Planetary Nebulae in the Solar Neighbourhood: Statistics, Distance Scale and Luminosity Function

David John Frew
B. App. Sc (Hons I), Dip. Ed.

A thesis submitted to Macquarie University in accordance with the requirements of the degree of Doctor of Philosophy

Department of Physics
Division of Information and Communication Sciences
Macquarie University
NSW 2109, Australia

July 2008

For Sofia and Darcy

Declaration of Originality

This thesis is submitted in fulfilment of the requirements of the degree of Doctor of Philosophy at Macquarie University, New South Wales. This thesis has not been submitted for a higher degree to any other university or institution, either in Australia or overseas. This research was carried out with formal advice from A/Prof Q.A. Parker and also Dr A.E. Vaughan.

I certify that to the best of my knowledge and belief, all sources used and assistance received in the preparation of this thesis have been duly acknowledged. Some of the text found within has previously been published in the list of refereed papers and conference proceedings found in the appendix, on which I have been the first author or a co-author.

Any views expressed in this dissertation are those of the author and do not represent those of Macquarie University.

David Frew
July 2008

Preamble

"One must say that the present knowledge of the masses and distances of planetary nebulae is, at best, uncertain. This is largely caused by the lack of reliable basic astrometric observations upon which to found a scale of masses and distances." (O'Dell 1962)

"At the Tatranská Lomnica meeting 10 years ago, there seemed little hope that one day soon planetary nebulae distances would become reliable. That day is near, if not here already." (Liller 1978)

"The distances to galactic planetary nebulae remain a serious, if not *the* most serious, problem in the field, in spite of literally decades of study, and of attempts to find a good solution." (Cahn, Kaler & Stanghellini 1992)

"It is unfortunately less obvious … how one could devise a new 'grand unification' calibration that simultaneously handles both the lower surface brightness objects that prevail among the nearby nebulae and the brighter PNe that dominate samples like those in the Galactic bulge and extragalactic systems. We leave this daunting task to future workers" (Ciardullo et al. 1999)

"A vacuum is a hell of a lot better than some of the stuff that nature replaces it with." Tennessee Williams, *Cat on a Hot Tin Roof* (1955)

Abstract

An accurate census of the nearest planetary nebulae (PNe) is needed for calculations of the total number, space density, scale height, and birth rate of PNe in the Galaxy, to understand the dynamics of an evolving nebula and its relationship to the cooling history of the central star, and also to provide an unbiased sample to investigate the frequency of binary central stars and their role in the formation and shaping of these objects. This study presents the most refined volume-limited survey of PNe known to date.

Integrated Hα fluxes for over 400 mostly evolved PNe are presented, based primarily on data from the Southern Hα Sky Survey Atlas (SHASSA) and the Virginia Tech Spectral-Line Survey (VTSS). Aperture photometry on the digital images was performed to extract Hα+[N II] fluxes. The [N II] contribution was then deconvolved using literature data, new data from slit spectra, or spectrophotometric data from the Wisconsin H-Alpha Mapper (WHAM) also obtained as part of this project. Comparison with previous work shows that the flux scale presented here has no significant zero-point error. The Hα fluxes are used to determine new Zanstra temperatures for those PNe with accurate central star photometry, calculating surface-brightness distances for each PN in the sample, and in conjunction with accurate [O III] fluxes, new absolute PN magnitudes for delineating the faint end of the PN luminosity function. A spectroscopic survey of a range of MASH PNe is also presented. New emission-line intensities for 60 PNe are given, including a preliminary discussion of the chemical abundances of this sample.

New distances have been determined for a large number of PNe, by either critically examining the literature, or by deriving new extinction and kinematic distances where suitable. For all PNe not amenable to these approaches, distances were estimated from a new Hα surface brightness – radius (SB–r) relation. The Hα SB–r relation covers >6 dex in SB, and while the spread in SB is ~1 dex at a given radius, optically thick (mainly bipolar and bipolar-core) PNe tend to populate the upper bound of the trend, while common-envelope PNe and high-excitation PNe fall along the lower boundary in SB-r space. Using sub-trends has allowed more precision in the determination of distances, as good as ±22% in the case of high-excitation PNe. The adopted SB-r zero point, set from 122 galactic calibrators, recovers the distances to the LMC, SMC and the Sagittarius dSph galaxy to within 5%.

With distances to all nearby PNe, I have generated the most *accurate* volume-limited sample of PNe ($D \leq 1.0$ kpc) yet considered, containing ~56 PNe. An extension sample to 2.0 kpc contains ~210 PNe. An accurate database of parameters for nearly all of these objects is presented, providing integrated fluxes, diameters, morphological classifications, distances, ionized masses,

expansion velocities, kinematic ages, chemical abundances, and central star properties for each PN in this volume-limited sample. Details are also given on a number of misclassified ‘PNe’ which contaminate the local volume, including, amongst others, Abell 35, DHW 5, Sh 2-68, Sh 2-174, Hewett 1, RE 1738+665, PG 0108+101, PG 0109+111, PHL 932 and EGB 5.

The observation that known close-binary PNe fall on a particular trend in SB-r space, is suggestive that these form a separate population to the majority of PNe. Recent conclusions that the great majority (or all) PNe go through a common-envelope phase are not supported at this point in time, though there is no doubt a modest frequency of common-envelope events has occurred in the solar neighbourhood. The exact number awaits a full multiplicity census of all objects within this volume. A preliminary estimate of the binary frequency of PN central stars in the solar neighbourhood is ∼52–58%, and hence I conclude that it is possible for single stars to produce PNe.

A deep local PN luminosity function is presented, extending to 10 magnitudes below the bright PN cutoff magnitude, M^*. The local [OIII] PNLF is seen to be much more bottom-heavy than previously recognised, with up to half of all PNe being fainter than 7 mag below M^*. An exponential increase in PN numbers occurs to ∼8.3 mag below M_*, where a marked turnover in the PNLF is seen. The very faintest PNe may represent a population of low-mass objects with low-luminosity central stars. New estimates for the number density, scale height, birth rate, and total number of Galactic PNe, as extrapolated from the solar neighbourhood sample, are also given. The total Galactic population is estimated to be 24,000 ± 4000 PNe with r <1.5 pc, and 13,000 ± 2000 PNe with r <0.9 pc. The MW/LMC luminosity ratio implies a total LMC PN population of ∼2400. Evidently many more PNe remain to be discovered in this system. The observed Galactic population leads to a PN birthrate of $0.8 \pm 0.3 \times 10^{-12}$ pc^{-3}yr^{-1}, fully consistent within the errors with the birthrate of white dwarfs.

A remarkable bow-shock nebula around a previously unnoticed, bright, nova-like cataclysmic variable, V341 Ara, has also been discovered as part of this study. The star has a high space motion, leading to the formation of the parabolic bow-shock at the interaction of the disk wind and the ISM. The proximity of this nebula to the Sun suggests the space density of such objects may quite high. Similar nebulae might be found through a narrowband search around other CVs with significant proper motion.

Contents

List of Figures

List of Tables

Acknowledgements

Firstly, I must gratefully thank my principal thesis supervisor A/Prof Quentin Parker of the Department of Physics, Macquarie University, for his continual encouragement, guidance, support and friendship over the time taken to complete this thesis. Thanks are also given to Dr Alan Vaughan, A/Prof Mark Wardle and A/Prof Judith Dawes of Macquarie University for their advice and guidance. I gratefully acknowledge Macquarie University for granting me a research scholarship, and for support throughout the tenure of my thesis, and also to the State Government of Western Australia, the Australian Nuclear Science and Technology Organisation and the International Astronomical Union for additional financial support.

This dissertation was completed while I was in full-time employment at Perth Observatory. I thank the directors of the Mount Stromlo and Siding Spring Observatories, the South African Astronomical Observatory, and the European Southern Observatory for the generous award of observing time. Thanks must go to the support staff at these various observatories for technical assistance. I also must thank the director and staff of the Anglo Australian Observatory, for providing me with an office and computing facilities at the AAO Epping headquarters, and for technical and logistical support while I was in Sydney. Thanks go to Brent Miszalski for his PNDR code which was of great assistance in the reduction of slit spectra of planetary nebulae, and whose wide-ranging computer expertise was always of great help. I also thank Greg Madsen with whom I collaborated on the WHAM Planetary Nebula project, for making this data available prior to publication. I also acknowledge the fruitful discussions I have had with various scientists at different times: Martin Cohen, Simon O'Toole, Delphine Russeil, Agnes Acker, Joachim Köppen, Hugh Harris and Brian Skiff, amongst others, and my fellow PhD students Mark Pierce, Alan Peyaud, Brent Miszalski, Milorad Stupar, Warren Reid, and Anna Kovacevic. Thanks are also due to Arsen Hajian (USNO) who kindly provided a list of expansion parallaxes prior to publication, and to Ralph Martin, Arie Verveer and Andrew Williams for technical support at Perth Observatory.

This research has made use of the SIMBAD database, operated at CDS, Strasbourg, France. This study used data from the AAO/UKST Hα Survey, produced with the support of the Anglo-Australian Telescope Board and the Particle Physics and Astronomy Research Council (UK). Additional data was used from the Southern Hα Sky Survey Atlas (SHASSA), the Virginia-Tech Spectral Line Survey (VTSS), and the Wisconsin H-Alpha Mapper (WHAM), which were all produced with support from the National Science Foundation. Data products from the Two Micron All Sky Survey (2MASS) were also utilised, which is a joint project of the University of Massachusetts and the Infrared Processing and Analysis Center/California Institute of Technology, funded by the National Aeronautics and Space Administration and the National Science Foundation. Data from the Sloan Digital Sky Survey (SDSS) has also been used in this work, supported by the Alfred P. Sloan Foundation, the Participating Institutions, the National Science Foundation, the U.S. Department of Energy, the National Aeronautics and Space Administration, the Japanese Monbukagakusho, the Max Planck Society, and the Higher Education Funding Council for England.

I leave my most special thanks to my wife Sofia, for her unwavering encouragement and support throughout the five years I spent completing this dissertation. I would like to dedicate this thesis to both her and our beautiful baby daughter Darcy, whose arrival during my tenure as a post-grad student, made life just that little bit more interesting.

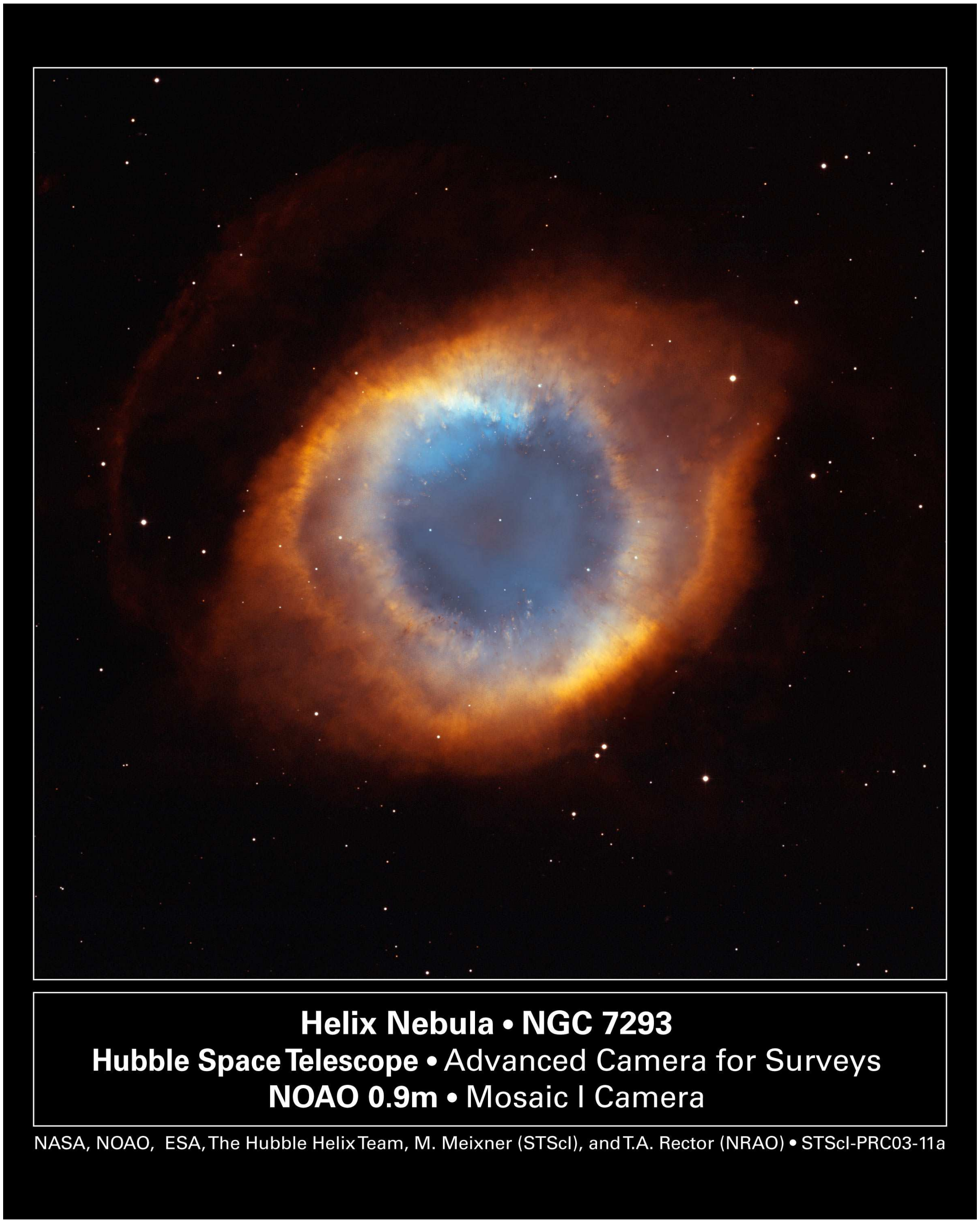

The Helix Nebula, NGC 7293

Chapter 1

Introduction

Planetary nebulae (PNe) are some of the most beautiful and fascinating objects in the heavens. In simple terms, a planetary nebula is a bubble or toroid of ionized gas, produced from a low- to intermediate-mass star ($\sim$1 to 8 $M_\odot$) towards the end of its evolution. Typically representing about a half solar mass of ionized gas, PNe are an important, albeit brief ($\sim$30,000 – 50,000 yr), evolutionary phase in the lifetimes of a significant fraction of Milky Way disk stars. They are an important tool in our understanding of the physics of mass loss for low- and intermediate-mass stars (Iben 1995), the chemical enrichment of our Galaxy, and in turn, its star formation history (e.g. Maciel & Costa 2003). Planetary nebulae also function as ideal test particles to probe the dynamics of the Galactic bulge, and by extension, the dynamics of external galaxies.

In order to refine our understanding of this brief evolutionary stage, a far more complete census of PNe in our Galaxy is needed, especially an accurate volume-limited survey centred on the Sun from which unbiased statistics can be determined. Such a census allows the total PN population in the Galaxy, the true proportion of different morphological and chemical classes, the range of central star properties, PN lifetimes, and the relative contribution of common-envelope systems to the PN population to be ascertained. These questions will be addressed in subsequent chapters in this work.

It is beyond the scope of this chapter to give an exhaustive summary of our current state of knowledge concerning planetary nebulae. For detailed reviews, the reader is referred to the works of Aller (1976), Terzian (1980), Kaler (1985), Khromov (1989), Peimbert (1992), Pottasch (1992), Iben (1993), Kwok (1994, 2005), Weinberger & Kerber (1997), Kerber (1998), and the monographs by Pottasch (1984), Gurzadyan (1997) and Kwok (2000). A good recent review of the processes that shape the morphology of PNe is presented by Balick & Frank (2002).

1.1 Historical Overview

Planetary nebulae were classed as a new type of celestial object on morphological grounds by William Herschel in the late eighteenth century. However, the first planetary nebula to be discovered, though not then classed as such, was M 27, found by Charles Messier in 1764. Fifteen years later, the Ring Nebula, M 57, was independently noted by Darquier and Messier in 1779. They were both observing the comet of that year (see Jones 1975). Messier, along with his compatriot Pierre Mechain, added two more PNe (M 76 and M 97) by 1782. Soon after, William Herschel began his extensive survey of the northern sky with reflecting telescopes of his own construction. His telescopes far exceeded the light grasp of the small instruments used previously, and consequently Herschel catalogued 2509 new non-stellar objects, dividing them into eight morphological classes. His class IV, which he termed planetary nebulae, were named in allusion to the circular disc-like appearance of some of the first known examples, which visually resembled the ghostly bluish-green disc of the newly-discovered planet Uranus.[1] Herschel included 79 objects in his new planetary nebula class, though most eventually turned out to be galaxies. Only twenty of them are now known to be true PNe.

Sir John Herschel continued his father's survey of the heavens with an 18-inch speculum[2] reflector, firstly from Slough, England (Herschel 1833) and later at the Cape of Good Hope to chart the southern sky from 1834 to 1838 (Herschel 1847). He found over 2000 nebulae and star clusters, including 20 new PNe, and eventually combined his and his father's work (including discoveries from other astronomers) into a *General Catalogue* (GC) of nebulae and clusters, totalling over 5000 objects. This was later revised by Dreyer (1888) as the venerable *New General Catalogue* (NGC).

Meanwhile, Huggins (1864) had noted that NGC 6543 (The Cat's Eye) had an emission-line spectrum, and was thus composed of a rarefied high-temperature gas.[3] Until then the nature of nebulae in general, and PNe in particular, was unknown, though the topic had been speculated on at length. Indeed, William Herschel, in a remarkably prescient statement, had postulated that the diffuse planetary NGC 1514 was not an unresolved mass of stars, but was indeed gaseous in nature. He wrote (Herschel 1790):

> A most singular phenomenon; a star of 8th magnitude with a faint luminous atmosphere of a circular form, about $3'$ in diameter. The star is perfectly in the centre, and the atmosphere is so diluted, faint and equal throughout that there can be no surmise of it consisting of stars, nor can there be a doubt of the evident connection between atmosphere and star.

Huggins and others (e.g. Secchi 1867, Herschel 1868) spectroscopically examined several of the brightest planetary nebulae, and it became apparent that three bright lines were almost ubiquitous in these objects — a line due to hydrogen (Hβ) and two bright "nebulium" lines of then unknown provenance. Even though the mystery of the nebulium lines was not solved until much later, being produced from metastable transitions of doubly-ionized oxygen (see Bowen 1927, 1928), the relative brightness of these lines in most PNe allowed the discovery of more

[1]It was Herschel himself who discovered Uranus on the night of March 13, 1781. He may have also been partly influenced by the statement of Darquier, who in 1779 described the Ring Nebula, M 57, as "very dim and perfectly outlined; it is as large as Jupiter and resembles a fading planet." Later, his son John Herschel (1847) discovered and described NGC 3918 as "...very like Uranus, only about half as large again and blue."

[2]Speculum metal is a reflective alloy of copper, tin and sometimes a trace of arsenic. It was commonly used to make the primary mirrors of reflecting telescopes in the early- to mid-nineteenth century.

[3]"On the evening of August 29, 1864, I directed the telescope for the first time to a planetary nebula in Draco. . . I looked into the spectroscope. No such spectrum as I expected! A single bright line only. . . A little closer looking showed two other bright lines on the side toward the blue, all the three lines being separated by intervals relatively dark. The riddle of the nebulae was solved. The answer, which had come to us in the light itself, read: Not an aggregation of stars, but a luminous gas." (Huggins 1897)

distant examples embedded in the star fields of the Milky Way (see section 1.5).[4] The first discoveries were found with the use of a visual spectroscope (e.g. Pickering 1880), but the great majority were discovered later by photographic techniques, pioneered at Harvard Observatory by Pickering and Fleming. Many of these new discoveries were included in the NGC, and the two supplemental Index Catalogues (Dreyer 1895, 1908). These catalogues listed in total >100 objects described as either 'planetary' or 'annular' nebulae; of these, 85 are true PNe.

Several other NGC/IC objects (e.g. NGC 246, NGC 1360, NGC 7293, and IC 4406, among others) were classified as true PNe only later, based on the spectroscopic work of other workers. Another example is the high-excitation object NGC 6026, which was shown to be a PN, and not a galaxy, by de Vaucouleurs (1955b) and independendently by the amateur astronomer E.J. Hartung in 1958 (Hartung 1968). The most recent NGC object 'discovered' to be a PN (Shaw & Bidelman 1987; Maehara et al. 1987) is another high-excitation object, NGC 2242 (see Swift 1887), long assumed to be a faint galaxy.

1.2 Planetary Nebulae: a working definition

There has been considerable controversy in the past over the working definition of a PN, based in part on differing morphological, spectroscopic, and physical or evolutionary criteria for classification, which have changed over the past two centuries. Indeed, as recently as 1967, at least one eminent commentator has described a PN as any object in a catalogue of PNe.[5]

A consensus taxonomic defintion remains elusive, even at present (e.g. Kohoutek 1983; Lutz 1993; Kohoutek 2001). Based on an overview of the literature, as well as an analysis of the properties of a volume-limited PN census derived in this work (see subsequent chapters), I consider a PN to be an ionized emission nebula with the following observational characteristics:

- A round or axisymmetric shape, sometimes with multiple shells or outer haloes. Note that many evolved PNe are perturbed through interaction with the interstellar medium (ISM);
- A photoionized emission-line spectrum characterised by recombination lines of hydrogen and helium as well as various collisionally-excited forbidden lines of heavier elements such as oxygen, nitrogen, sulfur and neon. The [O III] lines are usually, but not always, the strongest emission lines in the optical region (see §1.4);
- Thermal free-free emission in the radio spectrum;
- A nebular radius, $r \leq 2.5$ pc (the vast majority have $r < 1.5$ pc);
- An ionized mass roughly between the empirical limits of 0.01 and 3 $M_{\odot}$, to differentiate PNe from lower-mass nova shells and higher-mass ejecta shells from massive Population I stars;

[4] For a historical review of the key developments in PN spectroscopy, see Kaler (1973).

[5] During a session at IAU Symposium 34, R. Minkowski responded to a query from D.S. Evans, stating: "As to the question of how to define a planetary nebula, there is no better way than to accept any object in a catalogue of planetary nebulae if nobody has serious objections" (Osterbrock & O'Dell 1968, p. 290).

- A shell expansion velocity typically between 10–60 kms^{-1} though some strongly bipolar PNe can have higher expansion velocities along the major axis;

- A hot, low-mass central star with a temperature of at least 25,000 K (up to ∼250,000 K), and a mass between the empirical limits of ∼0.55 and 1 $M_{\odot}$. It is possible that lower mass stars might be formed via a common-envelope process. Corresponding surface gravities are generally in the range, $\log g \simeq 3.0$–7.5 cms^{-2}.

I argue that the term planetary nebula has a distinct physical or evolutionary meaning, and be restricted to the ionized shell ejected at the end of the asymptotic giant branch (AGB) evolutionary phase, either by a single star, or as part of a common-envelope ejection (e.g. Iben & Tutukov 1993). This basic definition was put in plain terms by Lutz (1993) who stated that "a PN is a star that ejects some material while evolving from the red giant to the white dwarf phase". In other words, the ionized gas was shed by the now hot central star, at the end of the previous AGB phase. This is a crucial point, as in many symbiotic systems, which are often confused with PNe, the gas has been donated by a *companion* red giant, and not the white dwarf, which is usually the source of the ionizing radiation field (e.g. Corradi et al. 2000; Corradi 2003). Further discussion of this point is given in §1.7, below.

I also argue that the term should not be applied to any hypothetical nebula around a post-EHB or AGB-manqué star (see §8.3 for a further discussion). Armed with a working evolutionary definition, the next section describes in detail the evolution of PNe between the AGB and white dwarf phases.

1.3 The Evolution of Planetary Nebulae

As a low- to intermediate-mass (0.8–8 $M_{\odot}$) star nears the end of its main-sequence (MS) lifetime (during which hydrogen is stably converted into ^{4}He), it begins to exhaust the supply of fuel in its core. Consequently, the core contracts under gravity and its temperature increases, which causes the outer layers of the star to expand. The star now moves away from the main sequence and climbs the giant branch in the Hertzsprung-Russell (HR) diagram. While the stellar luminosity increases by a considerable factor (∼10^{3} for a solar-mass MS star), the surface area of the star increases enormously, so the surface cools to an effective temperature of ∼3500 K (corresponding to an early M spectral type), a natural consequence of the Stefan-Boltzmann law. The star is now a first-ascent red-giant branch (RGB) star (see figure 1.1 for a schematic depiction of the full evolution of an intermediate-mass star in the HR diagram).

During this phase, the star's surface layers become less gravitationally bound, a consequence of the large increase in radius. Hence, the mass-loss rate increases markedly (Reimers 1975; Willson 2000). Convection becomes the dominant energy transport mechanism in the envelope due to increased hydrogen opacity at cooler temperatures. As a result the convective envelope can dip into the nuclear burning zone which causes an increase of ^{14}N and a simultaneous decrease in ^{12}C and ^{16}O in the envelope, a process termed the *first dredge-up*.

In stars less massive than $\sim 2M_\odot$, the He core is contracting as the star climbs the RGB, getting hotter, denser, and more electron-degenerate (Iben & Renzini 1983; Herwig 2005). When the temperature is high enough for He ignition in the degenerate core (via the triple-α process) the energy released simply increases the central temperature, as the core cannot expand due to its degenerate state. This causes the burning rate to further increase, ending up as a thermonuclear runaway. This is called the core helium flash (Iben & Renzini 1983).

Note that the luminosity flash is as high as 10^{10} $L_\odot$, yet the overall stellar luminosity is relatively unchanged. The energy released by the flash is used to change the equation of state of the core, 'lifting' the degeneracy and restoring an ideal-gas state. In general terms, it takes more than one of these flashes to remove the degeneracy in the core. Subsequent He flashes are much weaker and eventually the core reaches a state of steady He burning. As a result, the star rapidly cools and becomes less luminous, moving down and to the left in the HR diagram to become a zero-age horizontal branch (ZAHB) or red clump star, depending on the metallicity (see figure 1.1). For higher mass RGB stars ($>2\,M_\odot$), the core is hotter but less dense. Degeneracy is hence avoided, and the star ignites core helium gently. The star is now in an evolutionary phase with two energy sources: a He-burning core and a H-burning shell exterior to it.

As the core helium is exhausted, the star again increases in luminosity and cools, becoming a second-ascent red giant. Owing to the position of the evolutionary track in the HR diagram (closely parallel to the RGB track, but slightly blueward), these stars are called asymptotic giant branch (AGB) stars (figure 1.1). As the outer layers cool and become less dense, convection once again becomes the dominant heat-transfer mechanism. If the convective envelope penetrates the H-burning shell, it brings to the surface the products of H burning (He plus ^{14}N from the CNO cycle) during the so-called *second dredge-up*. However, this only occurs for stellar masses above $\sim 4M_\odot$ (Herwig 2005).

For detailed accounts of the varied facets of AGB evolution, see Becker & Iben (1979, 1980), Iben & Renzini (1983, 1984), Iben (1991), Groenewegen & de Jong (1993), Marigo, Bressan & Chiosi (1996), Busso, Gallino & Wasserburg (1999), Karakas, Lattanzio & Pols (2002), Habing & Olofsson (2003), Izzard et al. (2004), Herwig (2005) and Karakas & Lattanzio (2007).

AGB evolution is divided into two phases: the early-AGB (E-AGB) and the thermally pulsing AGB (TP-AGB). In the E-AGB phase, the star consists of a degenerate CO core surrounded by a He-burning shell, in turn surrounded by a convective hydrogen envelope (see figure 1.2). As the helium shell runs out of fuel, the thermally-pulsing AGB (TP-AGB) phase begins, characterised by separate (dual) shells of H and He which alternatively switch off and on to provide the energy source of the star. These shells are separated by an intershell region rich in ^{4}He and ^{12}C (see figure 1.2). As the shell helium is exhausted, the hydrogen shell compresses and fires up, exterior to the now dormant helium shell.

Approximately every 10^5 years, the helium shell beomes thick enough to reignite (the helium shell flash or thermal pulse), and as a result, expands the outer layers of the star; the H-burning shell is pushed outwards to a zone of lower temperature and density, so fusion there ceases. When He in the inner shell is exhausted, the hydrogen shell compresses and reignites again

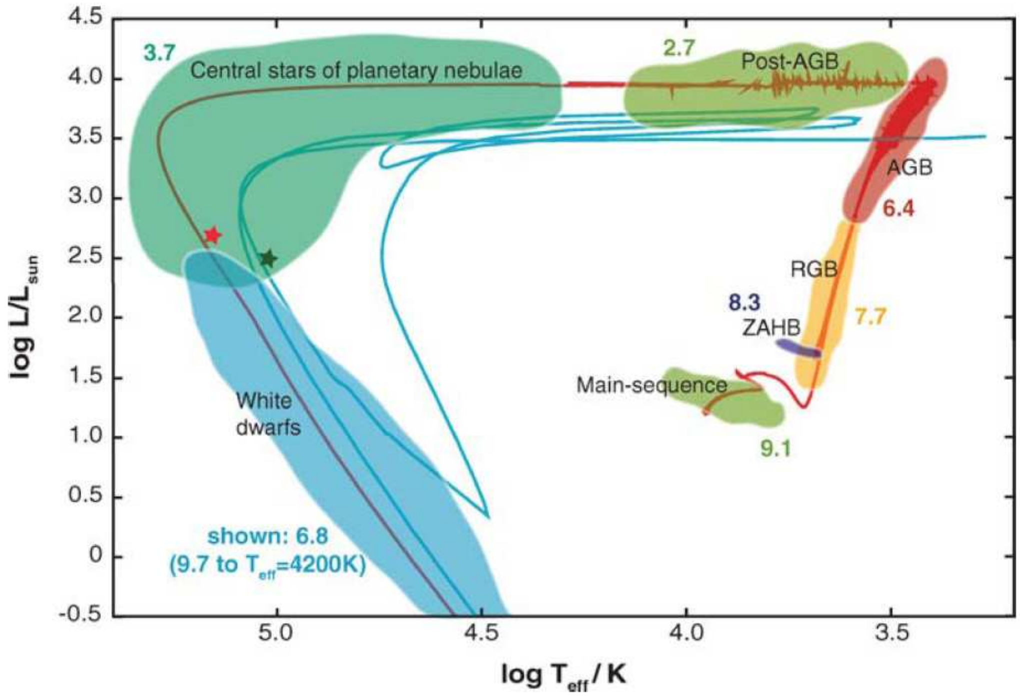

Figure 1.1: Hertzsprung-Russell diagram showing the evolution of a $2M_{\odot}$ solar-metallicity star from the main sequence to the white dwarf state (red track). The blue track shows a born-again scenario (triggered by a very late thermal pulse) for the same mass, but shifted slightly in $\log T$ and $\log L$ for clarity. The red and green stars represent the position of the central star of NGC 6853 (H-rich) and the naked PN nucleus PG 1159-035 (H-deficient). The numerical labels indicate the logarithm of the approximate time (in years) for each evolutionary phase. Figure adapted from Herwig (2005).

quiescently (the interpulse phase). Roughly a few dozen thermal pulses occur over the course of the TP-AGB phase. During each pulse, the ash of the innermost He-burning shell adds to the degenerate CO core, so it slowly gains in mass up to the end of the TP-AGB phase.

TP-AGB stars are generally larger and more luminous than RGB stars (L may exceed 10^4 solar luminosities, and diameters are of the order of $\sim$2 AU). Temperatures can be as cool as 2500 K (spectral type M8 or even later). As the star nears the tip of the TP-AGB, it typically shows Mira variability (with a periodicity of the order of $\sim$1 yr), a result of the internal instabilities in these objects. The mass loss rate increases with time, and after each thermal pulse, fusion products are brought up via convection to the surface (the *third dredge-up*). The surface becomes further enriched with helium, CNO, and slow neutron capture (s-process) elements (Iben & Renzini 1983, 1984; Herwig 2005; Sterling & Dinerstein 2008). In stars with main-sequence masses of $\sim$2 – 4 $M_{\odot}$, repeated dredge-up events completely alter the surface chemistry, giving rise to carbon stars (R Leporis and V Hydrae are well-known nearby examples).

In massive AGB stars ($\sim$4 to $\sim$8 $M_{\odot}$)[6], nuclear burning can occur in the deepest layers of the convective envelope. This process, known as hot-bottom burning (HBB) is the reason that

[6]Progenitor stars with masses of $\sim$8 to 10 $M_{\odot}$ are destined to form super-AGB stars, which end up producing ONeMg cores, or possibly neutron stars (Herwig 2005). Such stars are not likely to produce *observable* PNe and are not considered further here.

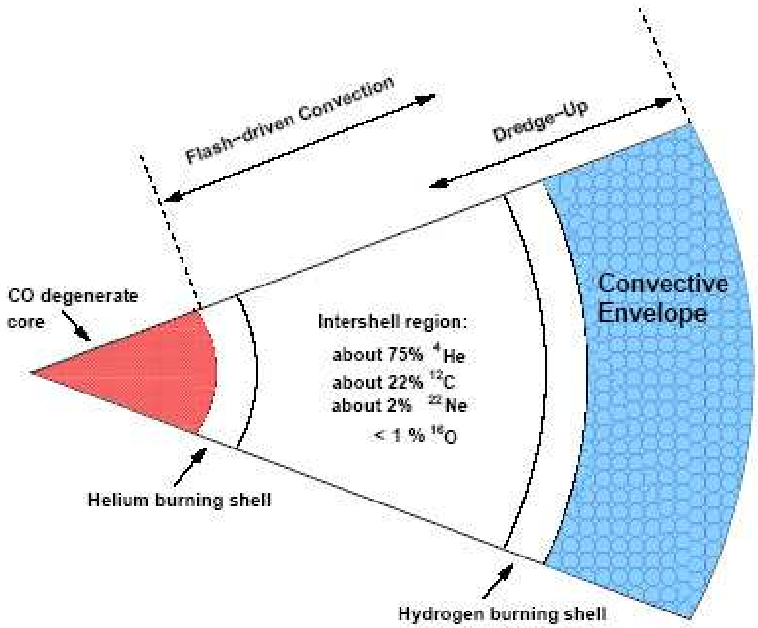

Figure 1.2: The schematic structure of a TP-AGB star, not to scale. Refer to the text for details. Figure adapted from Karakas (2007).

AGB stars in this mass range have O-rich surface chemistries, unlike the lower mass carbon stars (e.g. Izzard et al. 2004; Herwig 2005; Marigo 2007). In high-mass AGB stars, the envelope can be extremely enriched in nitrogen, as a result of dredged-up primary carbon being efficiently converted to nitrogen during envelope burning (Kingsburgh & Barlow 1994). The so-called Type I PNe (e.g. Peimbert 1978; Kingsburgh & Barlow 1994) are the offspring of these stars.

Eventually, as the star leaves the AGB, it ejects almost its entire outer envelope in a final extensive mass-loss phase via the so-called *superwind* (e.g. Renzini 1981; Wachter et al. 2002). This phase of enhanced mass-loss occurs at a rate of up to $\dot{M} = 10^{-4}$ $M_\odot\,yr^{-1}$ (Zijlstra 2006) at a relatively sedate velocity of ~10–20 $km\,s^{-1}$. Consequently, the outer layers of the star are eroded and shed into the surrounding ISM. The AGB star is surrounded by a large expanding, circumstellar envelope of dust and gas, which is often the site of maser emission. Masering molecules that have been detected in the winds of late TP-AGB stars are OH (hydroxyl), SiO, and H_2O (e.g. Zijlstra et al. 1989; Habing 2004). The more massive AGB stars have both strong OH masers and strong infrared emission from the ejected shell of dust and gas. Known as OH/IR stars (e.g. Cohen, Parker & Chapman 2005, and references therein), these are the immediate precursors of the pre-planetary nebulae (PPNe)[7].

When the star's outer envelope is reduced via mass loss to below ~10^{-2} $M_\odot$, the superwind

[7]The term pre-planetary nebula — formerly proto-planetary nebula (see Sahai, Sánchez Contreras & Morris 2005) — refers to the optical or near-IR (reflection) nebula visible prior to the onset of ionization by the CSPN. Supergiants of intermediate spectral type (B–K) without associated nebulae that are positioned in the HR diagram between the AGB and PN phases are usually referred to as post-AGB (PAGB) stars (see van Winckel 2003, for a review). PPNe and PAGB stars fall outside the scope of this dissertation, but a useful catalogue of PAGB objects is presented by Szczerba et al. (2007). Sahai et al. (2007) provide a very useful morphological catalogue of PPNe, including a library of HST images. Further images are given in Siódmiak et al. (2008).

effectively ceases and the star rapidly evolves to higher temperatures; the main mass-loss phase is assumed to be complete when the surface temperature of the core reaches $T_{\rm eff} = 5000\,{\rm K}$ (Schönberner 1983). The star moves to the left in the HR diagram (Figure 1.1) at approximately constant bolometric luminosity, which is primarily determined by the core mass of the star (Paczyński 1971; Kwok 1994) as given by the equation:

$$\frac{L}{L_\odot} \approx 59250\,(\frac{M_c}{M_\odot} - 0.52) \tag{1.1}$$

As the newly exposed core of the post-AGB star — hereafter the planetary nebula central star (CS) — reaches a surface temperature of ∼25,000 K, the ejected envelope begins to be ionized by the copious amount of hard ultraviolet radiation produced by the CS, and sculpted by the fast wind ($v \simeq 2000$ km s^{-1}; $\dot{M} = 10^{-7}$ M$_\odot$ yr^{-1}) from this hot star. The ejected envelope then becomes visible as a planetary nebula. The core mass also influences the maximum temperature, $T_{\rm max}$, the CS will eventually reach, which is typically 100,000 to 250,000 K. Tylenda (1989) gives an approximate formula as a function of the core mass:

$$\log T_{\rm max} \approx 5.72\, +\, 2.41 \log \frac{M_c}{M_\odot} \tag{1.2}$$

Eventually, hydrogen burning via CN-cycle reactions ends and the central star 'rounds the knee' in the HR diagram to descend along the white dwarf cooling track (see Figures 1.1 & 1.3). The time taken from the cessation of the superwind to the beginning of the WD cooling track is a steep function of the core mass, as empirically given by Tylenda (1989):

$$\log \Delta t \approx 4.96\,(\frac{M_c}{M_\odot} - 1.0) - \log\,(\frac{M_c}{M_\odot} - 0.52) \tag{1.3}$$

From this equation, the nuclear burning time is approximately 12,000 years for a $0.6\,M_\odot$ core, 1700 years for a $0.7\,M_\odot$ core and only 20 years for a $1.0\,M_\odot$ core! Such a brief lifetime for high mass cores effectively biases against the discovery of their PNe for two main reasons: (1) such stars come from high-mass B-type progenitors which are intrinsically rare compared to the F-type main-sequence stars which are considered to be the numerically dominant precursors of PNe, and (2) the rapidly-evolving core will already start to descend the WD cooling track well before the optically thick, high-density PN phase is over (Marigo et al. 2004). Furthermore, high-core mass PNe might preferentially have greater internal extinction, which makes them fainter at optical wavelengths (Ciardullo & Jacoby 1999), but see Shaw et al. (2001, 2006) for a contrary opinion. Hence it is not surprising that no CS has yet been definitively observed to have a mass $\geq 1\,M_\odot$, even though such WD masses are not uncommon (e.g. Sirius B, Holberg et al. 1998; Barstow et al. 2005).

As the star 'rounds the knee', the luminosity of the CS quickly drops by an order of magnitude (in less than 10^3 years for a $0.6\,M_\odot$ core; Schönberner 1983). After this epoch of rapid dimming, the star continues to slowly fade and cool at a decreasing rate. For detailed treatments of the evolutionary tracks of PN central stars in the theoretical HR diagram, refer to Schönberner (1983), Wood & Faulkner (1986), Blöcker & Schönberner (1990), Stanghellini &

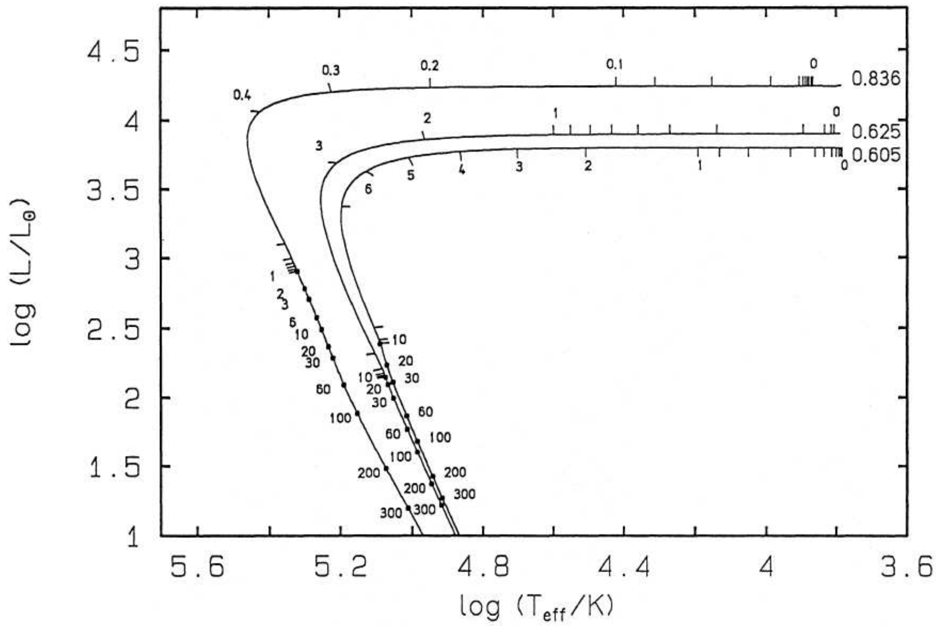

Figure 1.3: Evolution of post-AGB H-burning models for masses of 0.605 $M_\odot$, 0.625 $M_\odot$ and 0.836 $M_\odot$. Tick marks are in units of 10^3 years. Figure taken from Blöcker (1995).

Renzini (1993), Vassiliadis & Wood (1994), and Blöcker (1995; see figure 1.3). Detailed evolutionary cooling sequences for post-PN WDs are given by Bergeron, Wesemael & Beauchamp (1995).

Concurrent with the dramatic fading of the CS, the nebular gas has been expanding at a typical velocity of ~20 km s^{-1} (e.g. Weinberger 1989), and as a result, the PN eventually fades below the level of detectability as it disperses and dissolves into the ISM. The processes of AGB mass-loss and PN dispersal seed the ISM with CNO- and *s*-processed elements from which future generations of stars will be born. Consideration of the initial-final mass relation for WDs (e.g. Williams 2007; Kalirai et al. 2008, and references therein) leads to the conclusion that a PN progentor star may lose 50% to 80% of its mass during the RGB and AGB phases.

A minority of PN central stars are observed to have strongly hydrogen-deficient surface compositions (Iben et al. 1983; Iben 1984), and are now subdivided into two main types. The Wolf-Rayet central stars (e.g. Crowther, De Marco & Barlow 1998; Peña et al. 1998; Górny & Tylenda 2000; Górny 2001; Acker & Neiner 2003) are observed to be still on the horizontal track in the HR diagram, and show spectral features analogous to their massive Population I cousins of the carbon sequence (i.e., strong emission lines of ionized helium, carbon and sometimes oxygen). Others are typified by spectra showing absorption lines of highly ionized He, C, and O. These are the PG 1159 stars, named after the prototype of the group: PG 1159-035 (see Wesemael, Green & Liebert 1985; Quirion, Fontaine & Brassard 2007).

An evolutionary sequence from late-[WC] through early-[WC] (or [WO]) and PG 1159 stars to non-DA white dwarfs is now generally accepted (e.g. Werner & Herwig 2006, and references therein). The deficiency of surface hydrogen is likely caused by a (very) late thermal pulse (VLTP) or an AGB final thermal pulse (Iben et al. 1983). This causes complete envelope mixing with hydrogen being ingested and burned (Werner & Herwig 2006). Hence helium-shell burning recommences and the star is transformed back into an AGB star. This is the so-called "born-again" scenario (Herwig et al. 1999; De Marco 2002; Miller Bertolami et al. 2006; Werner & Herwig 2006). For a contrary opinion on the production mechanism for H-deficient stars, however, see De Marco (2008).

It turns out that about 20–25% of hot WD stars are H-deficient (e.g. Iben 1984; Althaus et al. 2008), though a higher fraction, 33%, is found in the local sample near the Sun (Holberg et al. 2008), which agrees with the fraction (26/88 or 30%) of PN central stars with known spectral types within 2.0 kpc (see §9.5). A recent catalogue of known hydrogen-deficient stars is given by Jeffery et al. (1996), and further reviews are provided by Althaus et al. (2005), Quirion, Fontaine & Brassard (2007) and Jeffery (2008). Evolutionary tracks of H-deficient central stars have been described by Werner & Herwig (2006) and Miller Bertolami & Althaus (2006, 2007).

Mention also needs to be made of the common-envelope (CE) ejection mechanism (e.g. Iben & Tutukov 1993; Iben 2000) in the formation of PNe. Such PNe have close-binary central stars, with periods typically of the order of days (e.g. Bond 2000; Bond & Livio 1990; De Marco 2006; De Marco, Hillwig & Smith 2008) and are the precursors of cataclysmic variables (e.g. Hillwig, Honeycutt & Robertson 2000), and potentially, Type Ia supernovae (e.g. Parthasarathy et al. 2007). Post-CE PNe are further discussed in §7.3.4.

1.3.1 The Interacting Stellar Winds (ISW) Model

As any cursory glance at the major PN imaging catalogues will reveal, PNe show a remarkably diverse range of morphologies (see Chapter 4). The interacting stellar winds (ISW) model, first proposed by Kwok, Purton & FitzGerald (1978; see also Kwok 1982; Balick 1987; Frank et al. 1993; Mellema & Frank 1997; Dwarkadas & Balick 1998) has now been refined into the general interacting stellar winds (GISW) model (e.g. Frank 1999; Kwok 2000). This GISW model explains PN structural features as the result of a spherical high-velocity post-AGB wind snow-plowing into the earlier, often-axisymmetric, AGB-superwind and shaping the nebular gas into a shell-like, elliptical or bipolar morphology. An example of a typical multiple-shell PN, NGC 2022, is illustrated in Figure 1.4.

The GISW model is now generally accepted in theory, but the range of observed PN morphologies requires that the original AGB wind was in the majority of cases obviously non-spherical. There is considerable debate at present regarding the mechanism needed to generate a strongly axisymmetric AGB wind. Proposed mechanisms include stellar rotation (e.g. Dwarkadas 2004), binary companions (e.g. Soker 1998, 2002a), circumstellar disks (Kastner & Weintraub 1995), magnetic fields (García-Segura, López & Franco 2005), or a combination of several processes (Balick & Frank 2002).

Soker (1997) argues that a planetary nebula will have a bipolar morphology if the CS has a close binary companion. However, PNe with bipolar morphologies are more concentrated to the Galactic plane (Corradi & Schwarz 1995), with a smaller scale height than elliptical and round PNe, suggesting that the mass of the progenitor star has a strong influence on the morphology

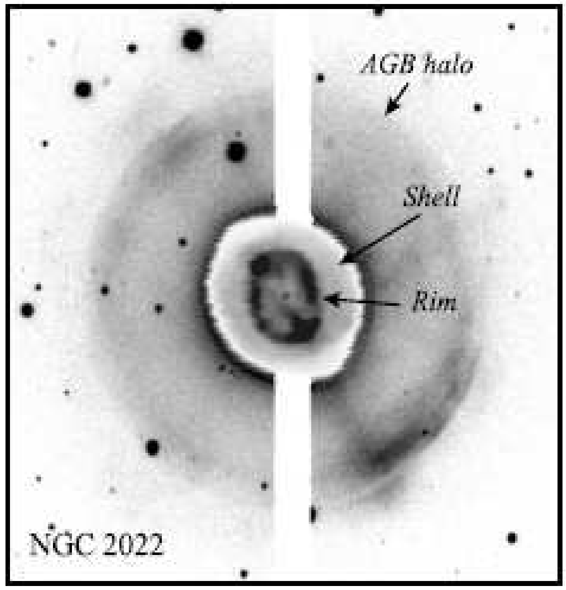

Figure 1.4: The basic morphological features of a typical multiple-shell PN. Figure taken from Corradi et al. (2003). The main structural features are labelled.

of the ejected PN (see §4.2). This would not be generally expected if binarity was the *sole* factor producing a bipolar morphology, though see the counter-arguments of Soker (1997). Furthermore, Soker & Subag (2005) have also argued that spherical PNe (akin to canonical Strömgren spheres) are less likely to be detected due to their intrinsic faintness. This point will be further discussed in Chapters 4 & 8.

1.4 The Spectra of PNe

The high temperature of most CS means the bulk of their photon flux is blueward of the Lyman limit. Hence, the gaseous shell ejected from the CS is photoionized and emits an emission-line spectrum. The main emission lines in the optical region are recombination lines of hydrogen and helium (plus a few of the strongest lines of oxygen, nitrogen and carbon in bright, compact PNe), with prominent optical emission from various collisionally-excited forbidden lines of heavier elements such as O, N, S, Ne, and Ar. There is also a nebular continuum present (usually only detected in PNe of higher surface-brightness) produced by recombination, two-photon emission, and free-free-emission. Planetary nebulae show a diverse variety of optical spectra and have spectral characteristics in common with symbiotic stars as well as with ordinary HII regions, Wolf-Rayet shells, and some supernova remnants (also see §1.7).

PNe range from very low excitation objects like BD +30°3639 and He 2-131 (with strong Balmer lines and [O II] emission) surrounding relatively cool cores ($T_{\rm eff} \simeq 30{,}000$ K) to higher excitation objects where the archetypal pair of [O III] lines at $\lambda\lambda$ 4959,5007Å are the dominant emission lines in the optical spectrum. There are also very high-excitation PNe such as NGC 246 and NGC 4361 (e.g. Kaler 1981), where HeII λ4686 emission is stronger than Hβ, and the relative strength of the [O III] λ4363 line indicates a high electron temperature. These PNe also show strong [Ne V] lines and generally have little or no trace of low-ionization species such as [O II], [N II], and [S II]. Fluorescent lines of OIII and NIII are sometimes seen in the highest-excitation PNe. Other PNe of high excitation belong to the bipolar class, but in these examples a wide range of excitation states are often seen, from [O I] to [Ne V]. Such PNe are often optically thick (Jacoby & Kaler 1989; Kaler & Jacoby 1989) and are often seen to have extensive molecular envelopes (e.g. Zuckerman & Gatley 1988; Kastner et al. 1996). Furthermore, these objects (e.g. NGC 2440 and NGC 6302) likely have very large density gradients between the central torus and the bipolar lobes, in order to explain the large range in ionization states.

Abundance variations can have a profound effect on the optical spectrum of a PN. Greig (1967, 1971) first drew attention to the correlation between certain PN morphologies, nebular excitation and chemistry, noting that some binuclear (now called bipolar) PNe usually had very strong [O II] and especially [N II] lines. In some cases, the [N II] lines for Type I PNe can be several times the strength of Hα (Corradi et al. 1997; Frew, Parker & Russeil 2006). Peimbert (1978) and Peimbert & Serrano (1980) defined 'Type I' PNe as those with N(He)/N(H) $\geq$ 0.14 *or* log(N/O) $\geq$ 0. Kingsburgh & Barlow (1994) have formalised the definition of a Type I PN (see §9.3.6), which for present purposes corresponds to log(N/O) ≥ -0.1. The spectrosocopic data, abundances and proportion of Type I PNe in the solar neighbourhood sample will be presented and discussed in more detail in Chapter 5.

In the great majority of PNe, the [O III] doublet lines are the strongest in the optical spectrum (after dereddening). The spectrum of M 1-57, a typical middle-aged PN, is shown in Figure 1.5, which can be compared with two more examples in Figure 1.13. To help elucidate the wide variety of spectral signatures seen in PNe, the concept of the Excitation Class (EC) has been introduced (e.g. Page 1942; Aller 1956; Feast 1968; Gurzadyan 1970, 1988; Webster 1975; Gurzadyan & Egikyan 1991). Primarily the EC is a direct proxy for the temperature of the CS, but the EC is also influenced by a number of second-order effects: the abundances of He, O and Ne (depending on the line species used in the definition), the stellar luminosity (manifested as the ionization parameter), and the optical depth of the PN (which reflects the size and density of the PN shell).

The most widely used of the earlier schemes was that of Aller (1956). His definition is a semi-quantitative measure of the excitation of the PN, on a scale of 1 to 10, and used the relative line strengths of [O II] λ3727 and [O III] λ4959, relative to Hβ, and for high-excitation nebulae, the strengths of HeII λ4686 and [Ne V] λ3426. Even though the 3426/Hβ ratio is a powerful diagnostic at highter temperatures, much of the spectrophotometric data in the literature does not extend far enough to the blue to record the [Ne V] line, especially for the fainter PNe, so this scheme is somewhat compromised for the current study.

More recently, Dopita & Meatheringham (1990) have introduced the decimal excitation class, and give two equations depending on whether He II emssion is detectable. They took this approach as the EC defined by the earlier workers was a discrete variable. Dopita & Meatheringham's approach considers EC as a continuous variable, which can be related to other PN parameters in a more formal way (see Chapter 9).

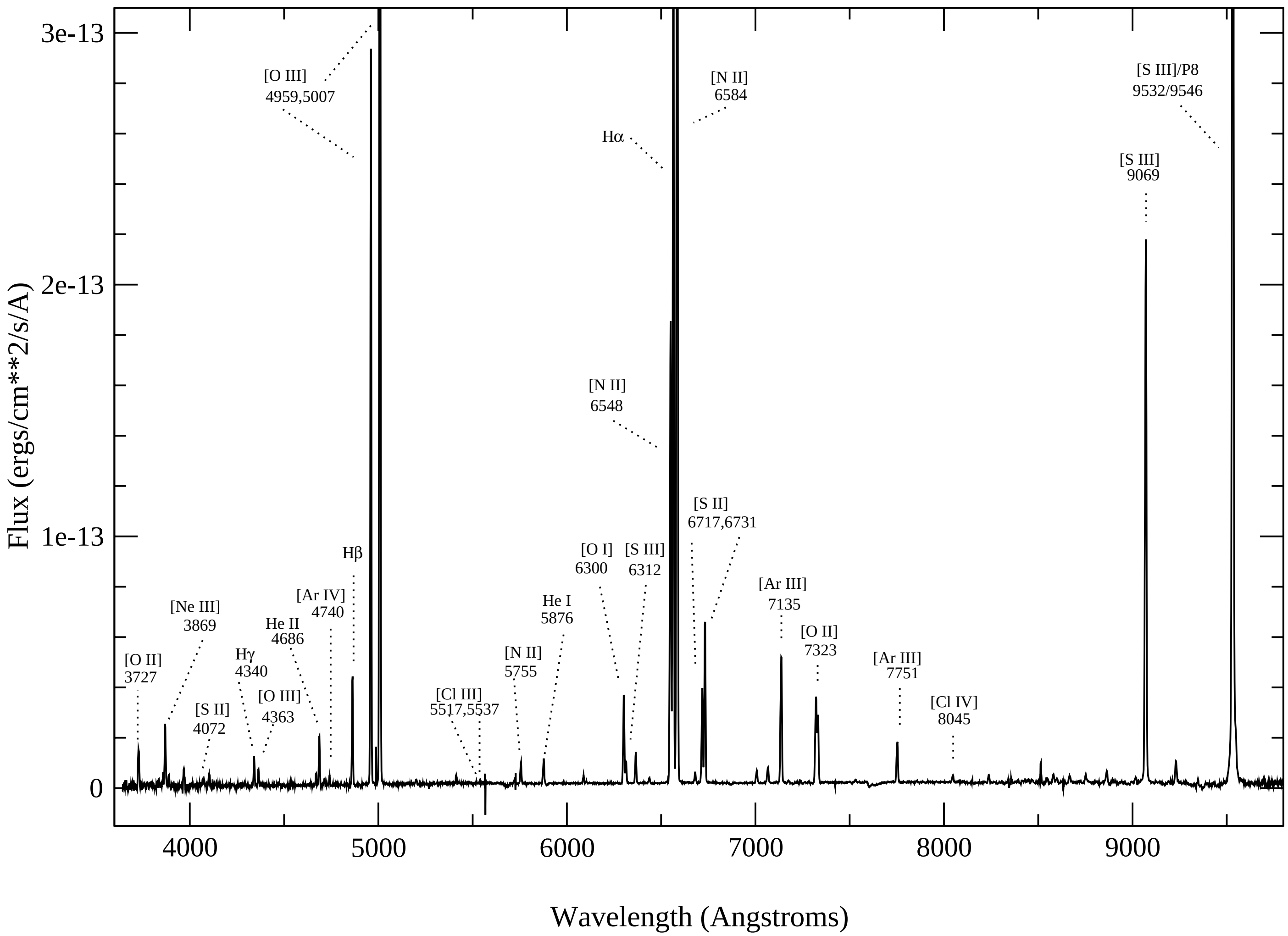

Figure 1.5: Flux-calibrated optical spectrum of the medium excitation PN Minkowski 1-57 taken from Kwitter & Henry (2001). The main diagnostic lines are labelled, and the brightest lines are cropped in order to show the relative intensities of the fainter lines.

1.5 Detection Techniques for PNe

As befits the large range in apparent size, integrated magnitude, surface brightness, coherence, and excitation class shown by individual PNe, a large and diverse range of detection methods has been used in their discovery. These various methods are summarised below, separated on the basis of the detector/technique used.

1. *Visual discoveries*:

   Some of the brightest and best-known PNe were found at the eyepiece by pioneering observers like Charles Messier, Pierre Mechain, and the Herschels, William and John (see section 1.1), and classified as PNe purely on morphological grounds. These were followed by later discoveries of more compact objects (e.g. Webb 1879; Barnard 1892; Espin 1907; Jonckheere 1913, 1916) and PNe of somewhat lower surface brightness (e.g. Gale 1896).

2. *Spectroscopic Techniques*:

   (a) Spectroscopic surveys conducted visually with a direct-vision prism in the optical train of the telescope (e.g. Pickering 1880, 1882; Copeland 1884a, b), leading to the discovery of several very compact (near stellar) PNe.

   (b) Spectroscopic discoveries made from objective-prism plates. The pioneering work by E.C. Pickering and Williamina Fleming was a by-product of the Henry Draper (HD) catalogue at Harvard Observatory from 1891 onwards, later continued by Annie Cannon and Margaret Mayall (see Hearnshaw 1986). The middle decades of the twentieth century provided a vast increase in the number of new PNe as photographic surveys reached greater depth, typified, for example, by the work of Hubble (1921), Humason (1921), Merrill (1942), Vyssotsky (1942), Minkowski (1946, 1947, 1948), Haro (1952), Perek (1960), Henize (1961, 1967), The (1964), Nassau, Stephenson & Caprioli (1964), Kohoutek (1965, 1969, 1972), Wray (1966), Stock & Wroblewski (1972), Sanduleak & Stephenson (1972), Stenholm (1975) and Sanduleak (1975, 1976).

   This technique has been particularly applicable to the Galactic Bulge, which contains large numbers of compact, relatively high-surface brightness PNe (see Kohoutek 1994, 2002). References to a number of additional papers that utilized this technique can be found in Acker et al. (1983, 1992, 1996).

   (c) Targeted long-slit spectroscopy around hot white dwarfs and subdwarfs (e.g. Méndez et al. 1988c). The serendipitous discovery of the putative PN Hewett 1 (Hewett et al. 2003) from Sloan Digital Sky Survey (SDSS) spectra is also noted, though its status as a PN is unlikely (see Chapter 8). Spectroscopy is, of course, the primary technique used to confirm the nature of PN candidates discovered from other methods.

3. *Photographic plates and films*:

   (a) Discoveries from visual inspection of *broadband* photographic plates. The earliest discoveries were mostly serendipitous (e.g. Curtis 1919; Menzel 1922; Baade 1935;

Shapley 1936; Jones & Emberson 1939; Miller & van Dien 1949a,b; see also Barbieri & Sulentic 1977). However, since the 1950s, there have been more systematic surveys utilizing large-format Schmidt telescope plates. Numerous discoveries (especially of old faint PNe) came from the Palomar Observatory Sky Survey (POSS) plates (e.g. Abell 1955, 1966; Vorontsov-Vel'yaminov 1961a; Kohoutek 1962, 1963, 1964, 1971; Ellis, Grayson & Bond 1984). Numerous discoveries in the southern hemisphere came from plates taken with the UK Schmidt and ESO Schmidt telescopes (e.g. Blaauw, Danziger & Schuster 1975; Schuster & West 1976; Longmore 1977; Kohoutek 1977; Longmore & Tritton 1980; Lauberts 1982; Hartl & Tritton 1983, 1985; see also Cappellaro et al. 2001).

By the close of the 20th century, the longest-running discovery program was that of the 'Innsbruck' group (e.g. Weinberger 1977; Purgathofer & Weinberger 1980; Dengel et al. 1980; Saurer & Weinberger 1987; Melmer & Weinberger 1990; Kerber et al. 1994; Kerber & Weinberger 1995; Kerber, Lercher & Weinberger 1996; Kerber et al. 1998, 2000a) who found ∼130 new (mostly evolved) PNe in both the northern and southern sky as a result of painstaking visual scrutiny of large numbers of POSS I and ESO/SERC UKST Schmidt plates and films. Additional faint PNe have been found from POSS II plates (e.g. Ali & Pfleiderer 1997), while Whiting, Hau & Irwin (2002) and Whiting et al. (2007) found several PNe in a search for dwarf galaxies from the POSS II and ESO/SERC surveys.

In addition, PNe have been discovered directly from Digitized Sky Survey (DSS) digital images (e.g. Bond et al. 2003), including nearly 70 candidates found from systematic visual scans conducted by several amateur astronomers (e.g. Kronberger et al. 2006; Teutsch, pers. comm., 2006, 2007; Kronberger pers. comm., 2007; Jacoby et al. 2008). These recent finds hint that there are still numerous faint PNe remaining to be discovered on broadband surveys outside the zones covered by the AAO/UKST Hα Survey and the Isaac Newton Telescope Photometric Hα Survey (IPHAS, see Chapter 2). It should be reiterated that spectroscopy or spectrophotometry has been generally used to confirm the PN candidates found on these surveys.

(b) Discoveries from direct inspection of *narrowband* (including interference-filter) photographic plates such as the six new evolved PNe announced by Weinberger & Sabbadin (1981). Heckathorn et al. (1982) and Fesen et al. (1983) added three more candidates from plates taken as part of the emission-line survey of Parker et al. (1979). In addition, a few true PNe were found on plates taken by Gum (1955), Hase & Shajn (1955), Johnson (1955), and Rodgers, Campbell & Whiteoak (1960) — these medium-band surveys were primarily for HII regions and diffuse Hα emission.

Recently there have been the numerous discoveries from narrowband AAO/ UKST Hα Survey films by Parker et al. (2001b, 2003, 2006a), on which much of this thesis is based (see Chapter 2). The recently published Macquarie/AAO/Strasbourg Hα (MASH) Catalogue of Galactic PNe (Parker et al. 2006a), contains 903 true, likely and possible PNe discovered *solely* from the Anglo-Australian Observatory UK

Schmidt Telescope (AAO/UKST) Hα survey of the Southern Galactic plane (Parker et al. 2005a). The MASH catalogue represents the largest ever incremental increase in Galactic PN numbers, and has increased the number of known Galactic PNe by $\sim$60%, revolutionising their statistics. This catalogue has recently been supplemented by the MASH-II catalogue, which contains 335 objects (Miszalski et al. 2008; see Chapter 2).

(c) Image comparison techniques (subtraction or quotient imaging) applied to *digitized* photographic survey plates and films. Sabbadin (1986), Cappellaro et al. (1990, 1994) and Turatto et al. (1990) have found new PNe by comparing digitized POSS red with infrared plates of the Palomar Near-Infrared Photographic Survey (PNIPS). Peyaud et al. (2003) have discovered numerous bulge PNe from difference imaging of digitized SHS data scanned from AAO/UKST Hα and short-red (SR) films as part of the MASH project (see also Peyaud et al. 2004; Peyaud 2005). Birkby et al. (2007) and Miszalski et al. (2008) searched the remainder of the SHS data in the same way. Pierce (2005) and Miszalski et al. (2008) have also mined the AAO/UKST digital data for PNe on a number of SHS fields by investigating colour-colour plots.

4. *Optical CCD Imagery*:

(a) Discoveries from direct inspection of narrow-band CCD survey imagery. For example, many large, highly evolved candidates (Corradi et al. 2005; Sabin 2007, pers. comm.) have so far been discovered on IPHAS Hα mosaics (see Drew et al. 2005). It should be noted that prior to IPHAS, only small areas of the sky have been surveyed in this way (see the next point). A catalogue of new PN candidates found from IPHAS is in preparation (see Corradi et al. 2005, and §2.6) while a couple of individual objects have already warranted separate publication (Mampaso et al. 2005, 2006).

(b) Comparison of deep on-band and off-band CCD imaging (Beaulieu, Dopita & Freeman 1999; Boumis et al. 2003, 2006) which has also been used successfully by Jacoby and co-workers for the discovery of numerous extragalactic PNe (e.g. Jacoby et al. 1990; Jacoby & de Marco 2002; Ciardullo et al. 2002, and references therein). The present author has found a number of emission nebulae, including some PN candidates (see Frew, Madsen & Parker 2006, and Chapter 2), on continuum-subtracted images from the Southern Hα Sky Survey Atlas (SHASSA; Gaustad et al. 2001) and the Virginia Tech Spectral line Survey (VTSS; Dennison, Simonetti & Topasna 1998). Additionally, the IPHAS consortium (see Chapter 2 and Drew et al. 2005) has discovered numerous compact PNe (Viironen et al. 2006; Viironen 2007; Corradi et al., in preparation) using colour-colour plots.

(c) Targeted CCD imaging around hot pre-white dwarfs and subdwarfs (Motch et al. 1993; Appleton et al. 1993; Tweedy & Kwitter 1994; Jacoby & Van de Steene 1995; Liebert et al. 1995). Details on a targeted search using SHASSA and VTSS images are given in Chapter 2.

5. *Discoveries at non-optical wavelengths*:

   Search techniques at infrared and longer wavelengths have the advantage of avoiding the worst effects of interstellar extinction, and are a very useful adjunct to the various optical methods, especially close to the Galactic plane.

   (a) New PNe selected from IRAS colours, followed by radio, IR or optical (imaging and/or spectroscopic) confirmation (Pottasch et al. 1988; Ratag et al. 1990; Ratag & Pottash 1991; Van de Steene & Pottasch 1993, 1995; Van de Steene, Jacoby & Pottasch 1996; Van de Steene, Sahu, & Pottasch 1996; García-Lario et al. 1997; Beer & Vaughan 1999; Suárez et al. 2006). However, there is always a question mark over these PN candidates until confirmatory spectra and high-resolution optical/NIR or radio images are obtained. Kistiakowsky and Helfand (1995) used [S III] λ9532 imagery to confirm candidate PNe selected from radio surveys using IRAS colour-colour plots.

   (b) Comparison of deep on-band and off-band CCD imaging in the near IR. Recently, Jacoby & Van de Steene (2004) have conducted an on-/off-band CCD survey of a 4×4 degree region of the Galactic bulge in the light of [S III] λ9532 which has the benefit of detecting extremely reddened PNe. They disovered 94 candidate PNe of which 63 were spectroscopically confirmed. Shiode et al. (2006) are currently using the 1.8-m Perkins Telescope to conduct a pilot [S III] imaging survey of the Galactic plane, searching for new PNe. Significant numbers of PNe are expected to be found.

   (c) Discoveries of very heavily reddened PNe at mid-infrared wavelengths with the Spitzer Space Telescope (SST) (e.g. Cohen et al. 2005; Kwok et al. 2006).

   (d) General surveys at radio wavelengths (e.g. Wouterloot & Dekker 1979)

Methods (2b) and (3) have led to the greatest number of PN discoveries, in the bulge and disk respectively, but in general, the majority to date of *highly-evolved* planetary nebulae have been found by methods (3a), (3b), (3c) and (4a) above. It should also be noted that a handful of recent PNe discoveries have resulted from the re-appraisal of objects previously catalogued as HII regions from earlier survey work (e.g. Arkhipova & Lozinskaya 1978; Fesen, Blair & Gull 1981; Fesen, Gull & Heckathorn 1983; Napiwotzki & Schonberner 1993; Frew 1997; Frew, Parker & Russeil 2006).

1.6 Catalogues of PNe

While the NGC and IC catalogues included most of the brightest members of the class, the first essentially accurate compilation of PNe was by Curtis (1918) who used both spectroscopic and morphological criteria. Illustrations (based on detailed photographs) of 78 individual PNe were also provided in the monograph. Only one object (the Crab Nebula, M 1, a well known SNR) was erroneously included and questionably so, by Curtis. He also undertook a spectroscopic survey of an additional sample of candidate nebulae from the NGC and IC in order to find new PNe, stating:

> The fact that but one object [NGC 7139] out of seventy-nine small nebulae has proved to be of the planetary type would further support the view that no very great increase in the proportion of planetary nebulae is to be expected from future surveys.

This vastly incorrect prediction should not prejudice the reader against the otherwise excellent standard of Curtis's pioneering paper.

The next working PN catalogue was that of Vorontsov-Velyaminov (1934). His *General Catalogue of Planetary Nebulae* included 131 PNe.[8] The next important compilation was the work of Minkowski (1950) who included a total of 371 PNe, with many of the new objects found by Minkowski himself. The considerable increase in numbers of PNe was a result of the objective-prism surveys which were then being undertaken.

A seminal catalogue of PNe was compiled by Perek & Kohoutek (1967). Their *Catalogue of Galactic Planetary Nebulae* (CGPN or the 'PK Catalogue') included 1036 PNe, discovered up to the beginning of 1965. Following its publication, six supplements outlining new discoveries and misclassified PNe (Kohoutek 1978, 1983, 1989, 1992, 1997b, 2000) were incorporated into the new *Version 2000 of the Catalogue of Galactic Planetary Nebulae* (Kohoutek 2001). As Kohoutek has emphasised, over 90% of known PNe have been discovered since 1945. This catalogue also includes a table of 334 pre-PNe and a list of 86 possible 'post-PNe'.

The *Catalogue of Central Stars of true and possible Planetary Nebulae* (Acker et al. 1982) included data on the 460 central stars known at that time, and this was followed by the *Index and Cross-identification of Planetary Nebulae* (Acker et al. 1983) which included information on 1518 PNe, including probable, possible and misclassified objects. This led eventually to the publication of the important *Strasbourg-ESO Catalogue of Galactic Planetary Nebulae* (SECGPN; Acker et al. 1992) and its *First Supplement* (Acker et al. 1996). A compilation of the most important catalogues of planetary nebulae in chronological order is given in Table 1.1.

Since these important compilations have been published, there have been significant new discoveries of PNe. The most important contribution is the MASH catalogue (Parker et al. 2006a) which represents the largest incremental increase in Galactic PN numbers to date. A key strength of the catalogue is that the new PNe have all been discovered from the same uniform, observational data, the AAO/UKST Hα Survey (Parker et al. 2005a). MASH PNe are typically more evolved, obscured, and of lower surface brightness than those found in most previous surveys (Parker et al. 2006a). MASH contains 578 true PNe (64% of the total), 186 likely PNe (21%) and 139 possible PNe (15%). The catalogue is described in more detail in Chapter 2, and the reader is also referred to the conference proceedings of Parker et al. (2003, 2005b, 2006b) and the preliminary CD-ROM (Parker et al. 2001b) for additional information.

The total number of true, likely and possible PNe known is currently around 3200, including the discoveries from the MASH Catalogue, new confirmed PNe found in the MASH-II supplement (Miszalski et al. 2008), the initial discoveries from the IPHAS survey (see Chapter 2), plus some new faint PNe found as part of the ongoing 'Deep Sky Hunters' project (Kronberger et al. 2006, Jacoby et al. 2008).

[8] Note that the SIMBAD database erroneously lists this first catalogue as having 288 objects. Later editions (Vorontsov-Velyaminov 1948, 1962) included 288 and 591 PNe respectively.

Table 1.1: Catalogues of planetary nebulae

Author	Year	No. of PNe
Pickering	1880	50*
Curtis	1918	78§
Vorontsov-Vel'yaminov	1934	131
Vorontsov-Vel'yaminov	1948	288
Minkowski	1950	371
Vorontsov-Vel'yaminov	1962	591
Perek & Kohoutek (CGPN)	1967	1036
Acker et al. (SECGPN)	1992	1143†
Acker et al. (SECGPN, 1st suppl.)	1996	1385‡
Kohoutek (CGPN 2000)	2001	1510
Parker et al. (MASH)	2006	903⋆
Miszalski et al. (MASH-II)	2008	335⋆
Viironen et al. (IPHAS)	2007	400⊕

* No details provided

§ Excludes southern PNe

† Another 347 objects were listed as possible PNe

‡ The total here refers to the 242 true PN in the first supplement added to the total in Acker et al. (1992). The supplement includes another 142 possible PNe. Note that the SECGPN and its supplement and the CGPN contain essentially the same objects.

⋆ The MASH and MASH-II catalogues contain newly discovered (true, likely or possible) and newly confirmed PNe only.

⊕ Unpublished list of candidate PNe. A program of spectroscopic confirmation is in progress.

1.7 PN Mimics

For one reason or another a huge range of different astrophysical objects have turned up in published catalogues of planetary nebulae. Similarly, PNe have been found lurking in lists of HII regions, reflection nebulae, and low-surface brightness galaxies, and even three candidate Galactic globular clusters have turned out to be PNe after spectroscopic analysis (Bica et al. 1995; Parker et al. 2006a).

Many PNe have been classified in the past using one criterion only. Either the emphasis was placed on morphology (for PNe discovered from photographic plates or CCD images) or on the object having a PN-like spectrum (for those found spectroscopically). As an example, figure 1.6 shows a bipolar PN and a symbiotic nebula with remarkably similar morphologies, so the potential for contaminants to appear in the various catalogues of PNe is high. Along with Q.A. Parker, the present writer has spent a good deal of time examining in detail most of the >1200 MASH PN *candidates* (and some of the MASH-II candidates) using a multiwavelength approach to reject non-PNe (see Parker et al. 2006a and Miszalski et al. 2008, for additional details). Furthermore, several known objects *currently accepted* as PNe in the literature have been shown herein to be ionized Strömgren zones in the ISM. Detailed multi-wavelength investigations of nearby examples of such nebulae (and their ionizing stars) will be found in Chapter 8.

Since a key science driver of this thesis is the definition of a cleaned, bias-free 'solar neighbourhood' PN sample for further detailed studies (see Chapter 9), it is germane to consider the nature of PN mimics (e.g. Kohoutek 1983; Acker et al. 1987) in some detail. Hence, for convenience, a review is given here, greatly extended from the work of Kohoutek (1983):

1. **Emission-line stars.** A wide range of stars with emission lines have been discovered over the years from objective-prism surveys. As a result, many of these objects (collectively regarded as point-source emitters, in the context of this thesis) have been misinterpreted as compact and 'stellar' PNe in previous catalogues. Lists of emission-line stars in PN catalogues have been given by Allen (1973) and Acker et al. (1987), and a more recent discussion is provided by Pierce (2005). Emission-line stars are generally not a PN contaminant in the solar neighbourhood, but are described here for completeness, subdivided into the main classes.

    (a) **Symbiotic stars.** The traditional definition encompasses those objects that show a composite spectrum with emission lines of H I and He I (and often [O III] and He II) present in conjunction with an absorption spectrum of a late-type (K, M, S, or carbon) giant star (e.g. Kenyon 1986). In reality, they show a wide variety of spectral characteristics (see Munari & Zwitter 2002, and figure 1.7). Symbiotic systems are usually subdivided into S-type systems which contain a normal (*stellar*) red giant which dominates the near-IR colours, and D-type systems where the central binary contains a Mira and the IR colours indicate the presence of *dust*. Symbiotic systems generally can be weeded out from PNe using near-IR photometric colours, and in optical spectra, the presence of a red continuum and/or strong [O III] λ4363 relative

Figure 1.6: Images showing the difficulty of PN classification. Here are two objects that are very similar morphologically. The top panel shows NGC 6537, a strongly bipolar Type I PN with a faint and very hot CS. The bottom panel shows the bipolar symbiotic outflow He 2-104, ejected from a binary system consisting of a WD and a cool Mira star. Strong bipolarity is also found in the nebulae around massive stars, such as the Homunculus around η Carinae and the hourglass nebula around Supernova 1987A. [Image credits: NGC 6537, G. Mellema et al., HST, ESA, NASA; He 2-104: R. Corradi et al., IAC, STScI, NASA].

to λ5007 in higher-excitation objects. Symbiotic stars are generally much denser than even the youngest PNe. Gutiérrrez-Moreno (1988) and Gutiérrrez-Moreno, Moreno & Cortés (1995) have used the [O III] $\lambda4363/\lambda5007$ ratio to separate PNe from symbiotics. This ratio is a good temperature indicator at densities typical of PNe, and a good density indicator at the densities characteristic of symbiotic stars. Therefore, diagnostic diagrams using emission-line intensities (Gutiérrrez-Moreno, Moreno & Cortés 1995, see Figure 1.8; Feibelman & Aller 1987) or optical and near-IR colours (e.g. Schmeja & Kimeswenger 2001; Ramos-Larios & Phillips 2005; Corradi et al. 2008; figures 1.9 and 1.10) are of great utility to help differentiate PNe from symbiotic stars. Raman-scattered OVI emission lines at $\lambda\lambda$6825, 7082Å are also a useful disgnostic for symbiotic stars when visible (Schmid 1989, 1992).

Catalogues of symbiotic stars have been presented by Allen (1984) and Belczyński et al. (2000), and they are the most common PN contaminant in the Galactic bulge (e.g. Acker et al. 1987). Corradi et al. (2008) have utilised a method of selecting candidate symbiotic stars by combining IPHAS and near-IR (2MASS) colours, which helps to differentiate symbiotic stars from both normal stars and other Hα point-source emitters, incuding compact PNe (see figure 1.10). An important new catalogue of 1183 candidates has been presented by them. A few yellow symbiotics with F- or G-type spectra are also known; M 1-2 (V471 Per; O'Dell 1966; Siviero et al. 2007), Cn 1-1 (HDE 330036; Lutz 1984; Munari & Zwitter 2002; Pereira, Smith & Cunha 2005, and figure 1.7) and PC 11 (HD 149427; Gutiérrez-Moreno & Moreno 1998; Munari & Zwitter 2002) have been catalogued as 'stellar' PNe in the past.

Note that *resolved symbiotic outflows* often show close morphological similarity to PNe, as illustrated in Figure 1.6, and are described in more detail below.

(b) **Be and B[e] stars.** Be stars are B-type main-sequence, subgiant or giant stars with prominent Balmer emission. The bright lines are generated in a circumstellar disk or envelope, due to rapid rotation or the influence of a magnetic field or a binary companion. B[e] stars are supergiants which have additional emission lines of species such as Fe II, [Fe II], [O II] and [S II], and occasionally P-Cygni absorption profiles. The B[e] stars are not a homogenous class of objects, and several appear to have large nebular shells associated (e.g. Marston & McCollum 2006). Curiously, the peculiar B[e] star He 2-90 has features in common with PNe, as it is surrounded by an extended bipolar nebula. Its evolutionary state is uncertain, but is a possibly a post-AGB object or PPN (see Sahai et al. 2002; Kraus et al. 2005).

(c) **Wolf-Rayet stars.** Wolf-Rayet (WR) stars are hot, evolved, massive stars with exceptionally strong stellar winds that have caused the loss of their hydrogen envelopes, leaving their helium cores exposed. The high mass-loss rates give rise to very broad emission lines of helium, carbon, nitrogen and oxygen. The ejecta nebulae and wind-blown bubbles surrounding Wolf-Rayets have occasionally been confused with PNe (see below). The stars themselves are also potential PN mimics, but the width of the lines is usually enough to differentiate them from PNe on spectra of adequate

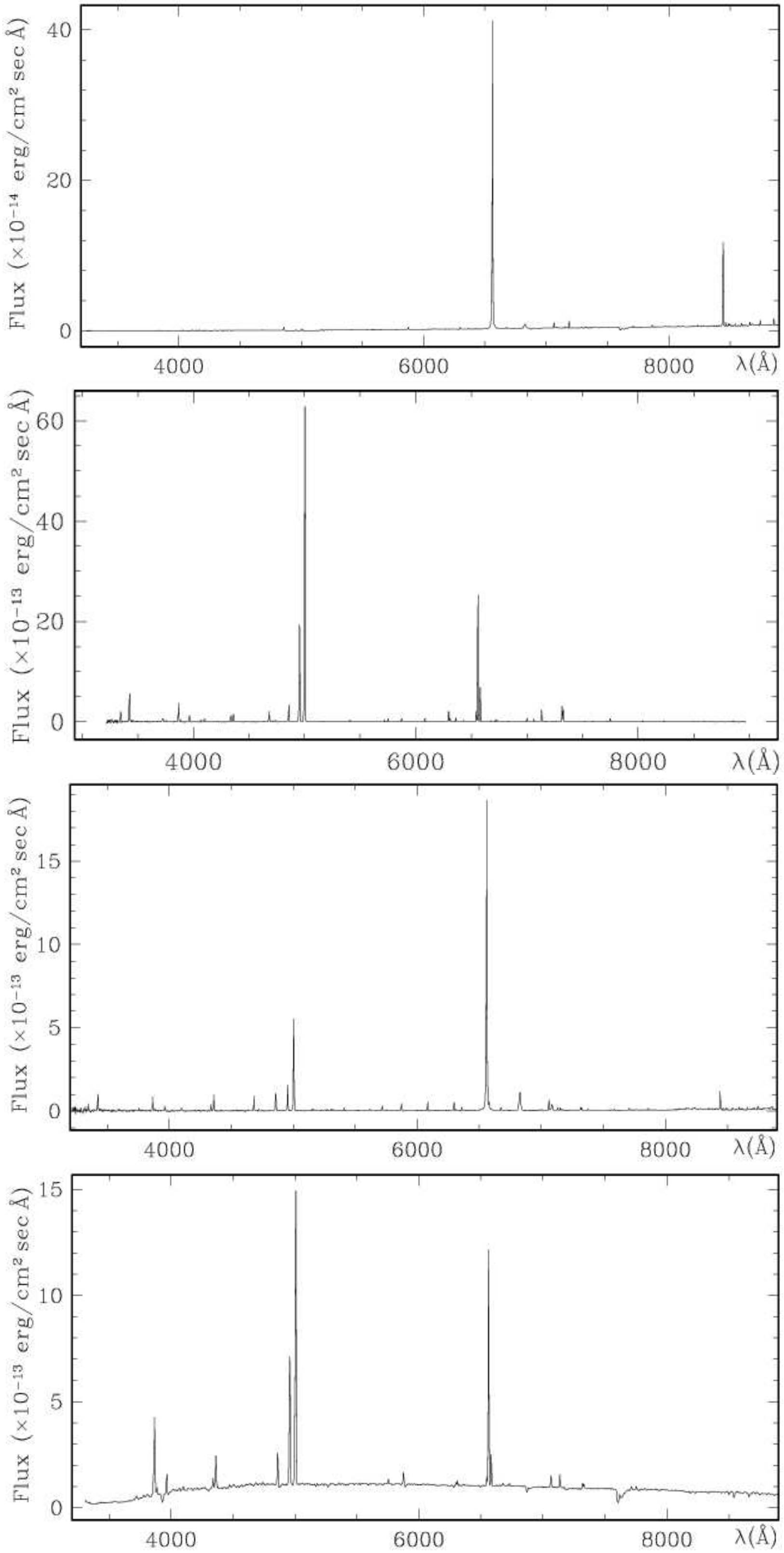

Figure 1.7: Spectra of the symbiotic stars H 1-25 (top), H 1-36, H 2-38, and the yellow symbiotic Cn 1-1 (HDE 330036) from Munari & Zwitter (2002) showing the variety present in the group.

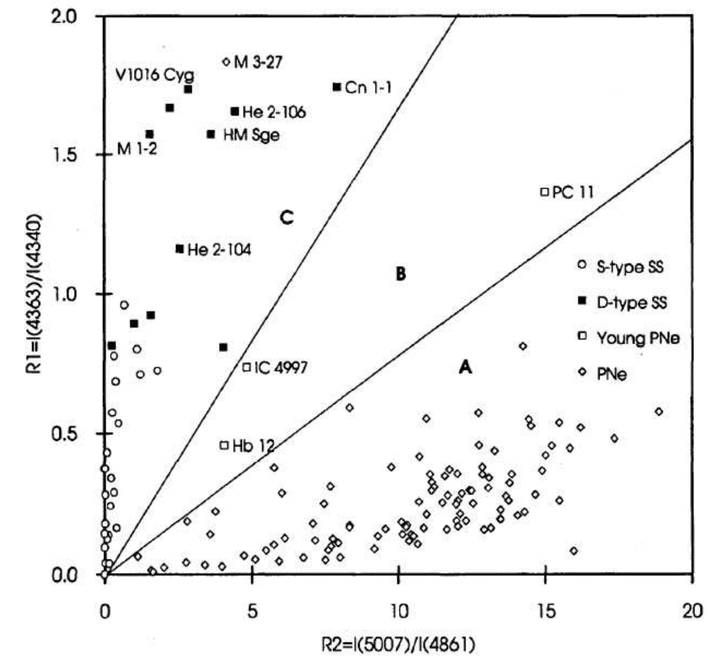

Figure 1.8: A diagnostic diagram for PNe and symbiotic stars from Gutiérrez-Moreno, Moreno & Cortés (1995). The diagram plots $R1 = [\mathrm{O\,III}]\ \lambda4363/\mathrm{H}\gamma$ versus $R2 = [\mathrm{O\,III}]\ \lambda5007/\mathrm{H}\beta$. Symbols show S-type symbiotics, D-type symbiotics, young PNe, and more evolved PNe. Three regions, A, B and C, have been defined, containing PNe, young dense PNe and symbiotic stars, respectively.

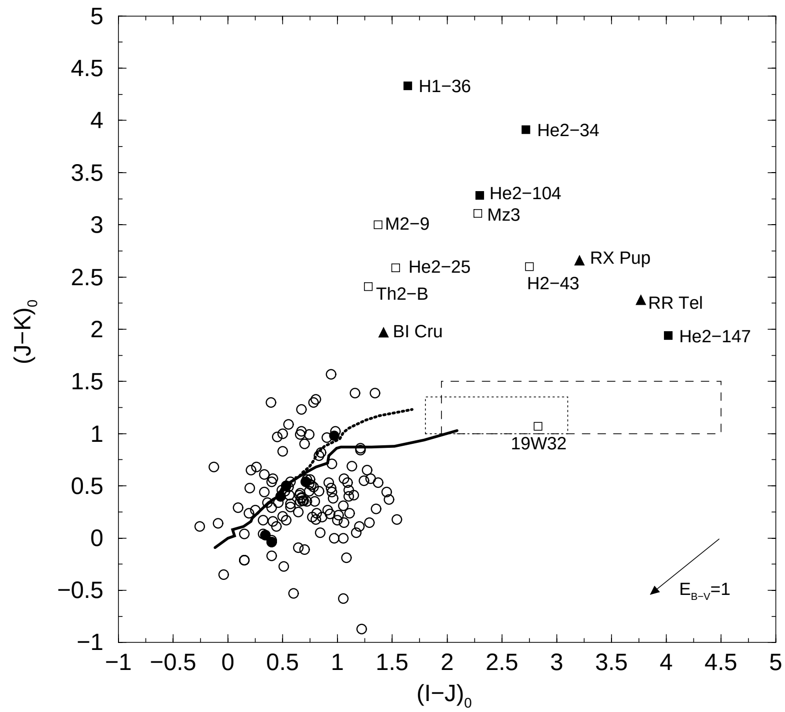

Figure 1.9: A diagnostic, reddening-corrected IJK two-colour diagram for PNe and symbiotic stars using DENIS data, taken from Schmeja & Kimeswenger (2001). The figure plots bona fide PNe (open circles), bipolar PNe without symbiotic features (filled circles), symbiotic Miras classed in the literature as PNe (filled squares), symbiotic Miras not classed as PNe (open triangles) and suspected symbiotic Miras (open squares). The stellar main sequence (solid line) and giant sequence (dotted line) are given as well as the regions of Miras and semi-regular variables (dashed and dotted boxes, respectively).

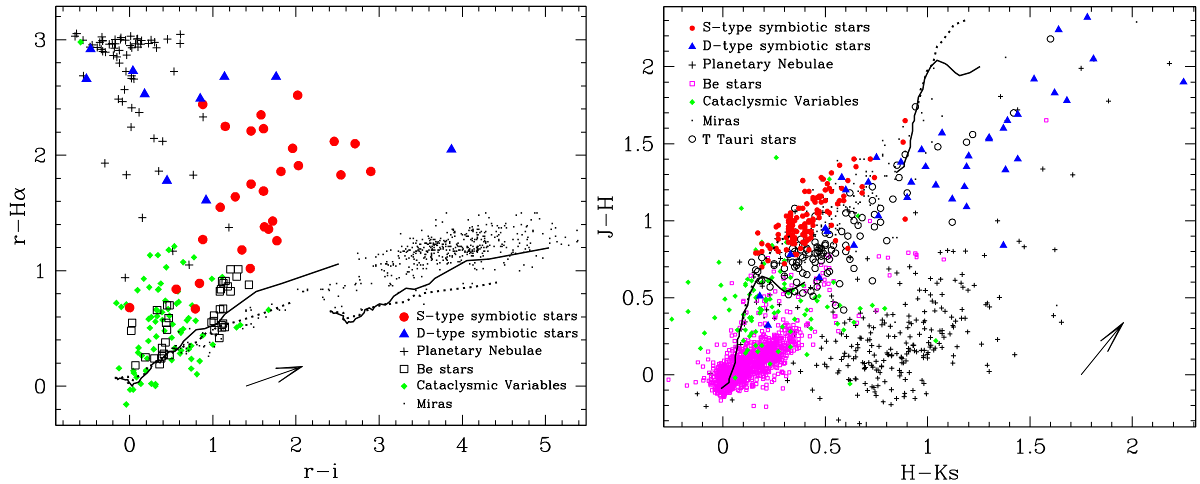

Figure 1.10: Diagnostic diagrams for symbiotic stars and other objects based on IPHAS and 2MASS data. Differing types of Hα emitter are given in the key, and plot in distinct regions in the $r'-\text{H}\alpha$, $r'-i'$ and $J-H$, $H-K_s$ colour-colour planes. The main loci show unreddened main sequence stars and giant stars as solid and dotted lines respectively. Separate loci, showing these sequences reddened by $E(B-V)$ = 4, are also plotted. They can be distinguished by referring to the reddening vectors, which represent $A_V = 3$. Figures taken from Corradi et al. (2008).

dispersion (e.g. Stenholm 1975). There are two spectral subclasses: WN stars, which have broad emission lines of helium and nitrogen, and WC stars, which show broad helium, carbon and oxygen lines. Wolf-Rayet features are present in the central stars of some PNe and are denoted [WR] to differentiate them from their Population I cousins. Almost all belong to the [WC]/[WO] sequence except for the rare [WN] objects N 66 in the LMC (Peña et al. 2004) and PM 5 (PHR 1619-4914) in the Galaxy (Morgan, Parker & Cohen 2003). However, further work is needed to completely rule out the possibility that this latter object is a Pop I WR ring nebula.

(d) **Luminous blue variables (LBVs).** These bright variable hypergiants display rich emission-line spectra from H, He and a number of permitted and forbidden metal species. These lines help to differentiate them from other emission-line stars and stellar-appearing PNe. For a review of LBVs, see Humphreys & Davidson (1994). Examples of LBV ejecta nebulae are discussed further below.

(e) **Pre-main sequence emission objects**, including T Tauri stars (Joy 1945), Herbig Ae/Be stars (Finkenzeller & Mundt 1984) and (compact) Herbig-Haro objects. Many HAeBe stars have rather similar spectra to the B[e] stars and are associated with regions of star formation, which can be used to ascertain their true nature.

(f) **Cataclysmic variable stars (CVs).** This large class of variable stars includes classical and recurrent novae, nova-like variables and dwarf novae. CVs are semi-detached binaries in which a white dwarf star is accreting material from a close, Roche lobe-filling companion, usually a main sequence G-, K- or M-type star.

Importantly, erupting novae in the 'nebular' phase show strong Balmer and [O III] emission and have been confused in the past with 'stellar' PNe on objective-prism plates. There are even three or four old novae in the NGC/IC catalogues (e.g. IC 4544 = IL Normae and IC 4816 = V1059 Sgr), erroneously classified as 'gaseous nebulae'. Curiously two objects discovered by Fleming (1895), IC 2189 and IC 2206 (see Dreyer 1908), have no known counterparts and it will be interesting to conduct a search for possible old nova candidates at the precessed IC positions. Contaminating novae have also been found in recent CCD surveys for PNe in the Magellanic Clouds (Jacoby 2006). *Resolved nova shells* and related objects are discussed in more detail below.

2. **Late-type stars.** On small-scale objective prism plates, the spectra of ordinary late-type (M-type) giant stars can present apparent 'emission' near Hα due to the relative brightness of the red continuum around 6600Å compared to the deep absorption dips from TiO band-heads at adjacent wavelengths. Several M-type stars were present in the CGPN (Perek & Kohoutek 1967). This property of M-stars has also led to contamination of candidate PN samples defined via H$\alpha - R$ versus R plots obtained from SuperCOSMOS IAM data (see Pierce 2005; Parker et al. 2005a) and in SHS quotient imaging and digital $B_J/SR/$Hα composite images (Miszalski et al. 2008; Parker et al., in preparation). Including IR photometry in the analysis is of great benefit in such cases. Many Mira-type variables can have intrinsic Balmer emission (classed as Me and Se stars), which may lead to misclassification as compact VLE PNe on poor-quality spectra, leading to further confusion (see Kohoutek 1983; Pierce 2005). In addition, variable stars can be confused as PN candidates in techniques which use on-band/off-band image subtraction or blinking. This can occur if the exposures are not contemporaneous and the star has changed brightness between exposures (e.g. Jacoby 2006, Reid 2007).

3. **HII regions.**

   (a) **Compact HII regions.** A number of compact HII regions have been picked up by the numerous objective-prism surveys over the years, with many of the higher excitation objects being misidentified as PNe (see figure 1.13). These compact HII regions form an important contaminant which have been removed from the MASH survey (see Parker et al. 2006a). Other examples of compact HII regions formerly classified as PNe include He 2-77 (Caswell & Haynes 1987), Abell 77 = Sh 2-128 (Mampaso et al. 1984; Bohigas 2003; and see figure 1.12), We 1-12 (Kimeswenger 1998) and Wray 16-185 (Acker et al. 1987; Ogura & Noumaru 1994; Gyulbadaghian et al. 2004; Roman-Lopes & Abraham 2006).

   Certain compact HII regions show a distinct cometary or bipolar form, e.g. Sh 2-106 and Sh 2-201 (Mampaso et al. 1987), and overlap with cometary reflection nebulae and bipolar PNe morphologically (see also Calvet & Cohen 1978, and Rodriguez 1992). NGC 2579 is an interesting case: this compact HII region has also been classified as a planetary nebula (=Ns 238; Nordström 1975; Schwarz, Corradi & Melnick 1992), a cometary nebula (Parsamyan & Petrosyan 1979) and an ordinary

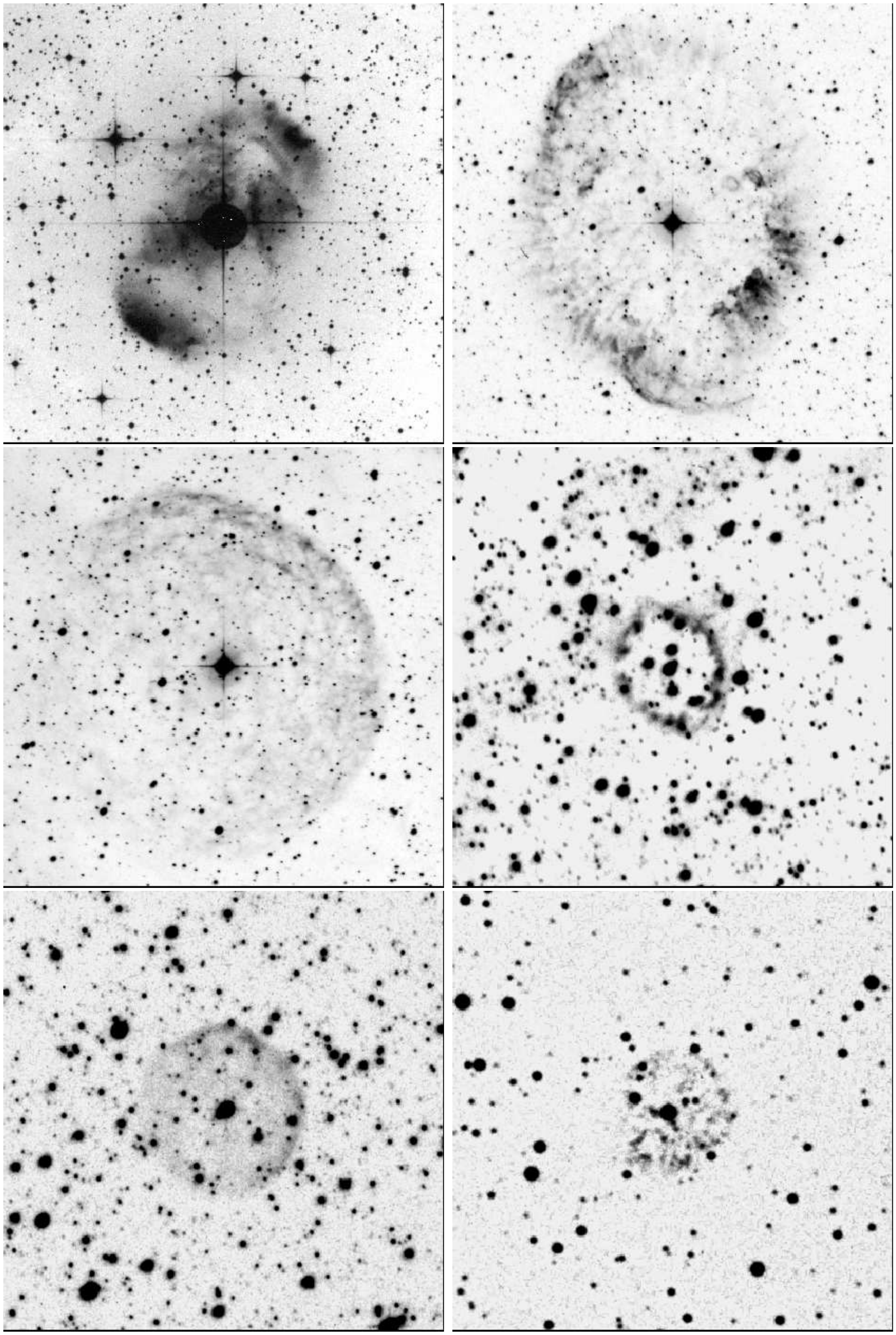

Figure 1.11: Images of various PN mimics, adapted from DSS and SHS images Top: (L): NGC 6164/65, a bipolar ejecta nebula around the Of star HD 148937 (B_J image, $10'$ wide). (R): Wolf-Rayet ejecta nebula RCW 58 (Hα image, $10'$). Middle: (L): A faint interacting shell around the Wolf-Rayet star WR 16 (Hα image, $10'$). (R) A newly discovered WR shell, PCG 11 (Hα image, $5'$). Bottom: (L): The true PN PHR 1424-5138 as a comparison object. Note the bright CS relative to the faint nebular surface brightness (Hα image, $5'$). (R): The old nova shell around GK Persei (R_F image, $5'$).

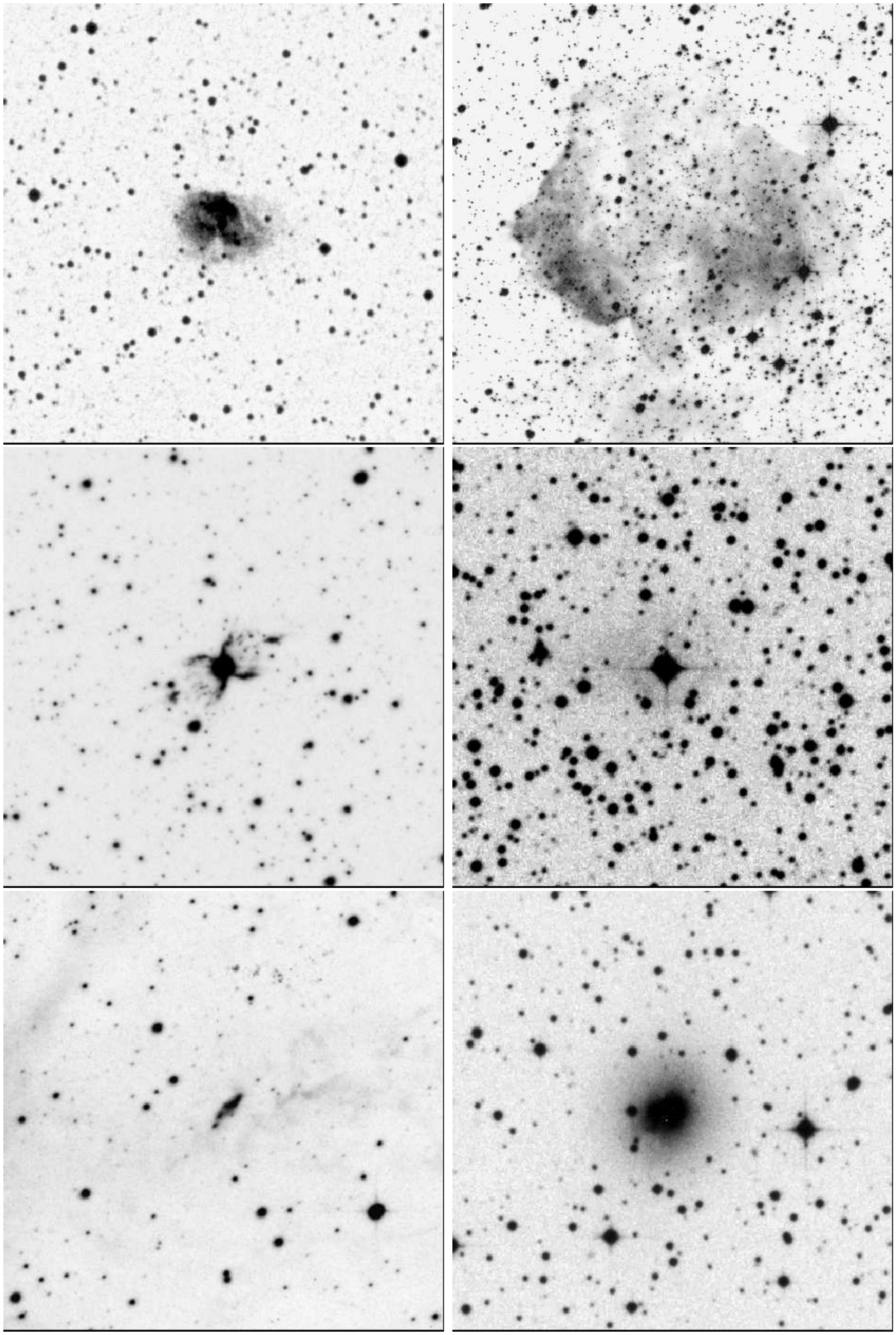

Figure 1.12: Top: (L): Abell 77 (Sh 2-128), a compact HII region (R_F image, $5'$ wide). (R): The low-surface brightness HII region, vBe 1 (Hα image, $10'$). Middle: (L): Bipolar symbiotic outflow, He 2-104 (Hα image, $5'$). (R) Longmore 14, a reflection nebula (B_J image, $5'$). Bottom: (L): PHR 0818-4728, a compact knot in the Vela SNR (Hα image, $5'$). (R): Blue compact galaxy He 2-10 (R_F image, $5'$).

reflection nebula in the past (see the discussion by Copetti et al. 2007). The peculiar nebula M 1-78 (Puche et al. 1988; Gussie 1995) is now interpreted as a compact HII region contaminated by N-rich ejecta from a Wolf-Rayet star (Martin-Hernández et al. 2008). Additional misclassified HII regions are discussed by Rubin (1970), Glushkov et al. (1974), Felli & Perinotto (1974) and Acker et al. (1987).

In general, consideration of the nebular spectral features, radio fluxes, environment, and near- and mid-IR characteristics (including any embedded sources) is usually enough to differentiate between PNe and compact HII regions. Compact HII regions in external galaxies can also be confused with PNe, but generally appear more extended (if not too distant), are of lower ionization, and usually show strong continua from embedded OB stars (Jacoby 2006).

(b) **Diffuse HII regions.** In the course of this work, a number of symmetrical, round, low-surface brightness nebulae were initially suspected to be PNe in the MASH working list. Spectra have shown most of them to be HII regions around OB stars, confirmed where possible by comparing optical images with Mid-course Space eXperiment (MSX) imagery/data (see Cohen & Parker 2003) and IRAS maps. HII regions (and young stellar objects) that have extensive amounts of warm dust show strong MIR emssion especially at 8.3μm and 21.3μm as seen in MSX data (Cohen & Parker 2003). Conversely, only 10–20% of bona fide PNe show detectable MIR emission, and most of these are fairly compact and of high surface brightness in Hα. Other nebulae in the MASH list are assumed to be HII regions due to their association with known star-forming complexes, molecular clouds, and neighbouring emission and reflection nebulosities. Several contaminants in MASH were removed based on *Spitzer* GLIMPSE Survey data in the zone $|b| < 1°$ (see Cohen et al. 2007).

One object from the literature that has had particular difficulty in classification is the faint HII region vBe1 = G339.2 − 0.4 (Murdin Clark & Haynes 1979; Shaver et al. 1980; Rosado 1986) due to its vaguely PN-like morphology. Further details on this object are provided in §8.17 and it is illustrated in figure 1.12. In general, diagnostic diagrams using a range of emission-line intensities are of great utility in differentiating HII regions from PNe (e.g. Sabbadin, Minello & Bianchini 1977; Canto 1981; Kennicutt et al. 2000; Riesgo-Tirado & López 2002; Riesgo & López 2006; Kniazev, Pustilnik & Zucker 2008).

As a caveat however, a slit spectrum of the peculiar high-latitude 'planetary nebula' around the sdOB star PHL 932 shows strong Balmer lines, only weak [N II] and almost undetectable [O III] emission, and is practically indistinguishable from spectra of these aforementioned H II regions. Some MASH objects may therefore turn out to be 'PHL 932-type' nebulae, which are very likely Strömgren zones in the ISM around hot subdwarfs and white dwarfs (see Chapter 8).

In fact, it is shown that several large, nearby nebulae currently accepted as PNe are also just Strömgren zones in the ISM, each one ionized by a hot pre-white dwarf or subdwarf. For example, the classification as PNe of Abell 35 (e.g. Jacoby 1981), Hewett 1 (Hewett et al. 2003), DeHt 5, Sh 2-68, Sh 2-174 (Tweedy & Napiwotzki 1994), RE J1738+665 (Tweedy & Kwitter 1994), and PG 0108+101 (Reynolds 1987), amongst others, is unlikely (see Frew & Parker 2006; Madsen et al. 2006). These nebulae, plus others, are discussed in Chapter 8. Demonstrated Strömgren spheres around hot 'naked' low-mass stars do exist, such as the large, extremely low surface brightness nebula around the subdwarf star PHL 6783 (Haffner 2001). Several optically-thin PNe also have faint surrounding haloes which are almost certainly ionized ISM; e.g. Abell 36 and Abell 15 (McCullough et al. 2001), NGC 246 (Haffner 2001) and Sh 2-200 (Madsen et al. 2006; Frew & Madsen 2008, in preparation, and §4.2.2). NGC 6751 (Chu et al. 1991) is a more distant example of a PN ionizing the surrounding ISM.

Mention should also be made of so-called 'lazy PNe', with low-mass, slowly-evolving central stars. Such nebulae may have expanded to large diameters (with consequent low surface brightness) before their CS have reached a sufficient temperature to ionize the AGB wind. Such nebulae would show up as faint diffuse objects primarily emitting in Hα and may not show an obviously PN-like morphology (i.e lack of a well defined rim), due to the late onset of the fast stellar wind. These nebulae would be very difficult to differentiate from diffuse HII regions. Isolated nebulae at high galactic latitudes with no obvious nearby dust clouds or star-forming regions may be candidates for such objects. FP 1054-7011 (discovered as part of this study) has a faint blue star within, and may be such an example.

4. **Population I Shell (and ejecta) nebulae.**

   (a) **Shell/ejecta nebulae around O- and B-type stars.** The 'Bubble nebula' NGC 7635, around the O6.5 III star BD+60°2522, was originally suspected to be a PN by Hubble (1922) and was considered to possibly be "a PN in an HII region" as late as 1973 (Johnson 1973, 1974). The peculiar nitrogen-rich bipolar ejecta nebula NGC 6164–65, catalogued as a PN by Henize (1967) surrounds the O(f) star HD 148937 (figure 1.11), which is closely related to the WR stars. Another example may be Sh 2-266, a ring nebula around MWC 137, a possible B[e] supergiant (Esteban & Fernández 1998).

   (b) **Wolf-Rayet (WR) nebulae.** These nebulae can be subdivided into ejecta nebulae and stellar wind-blown bubbles in the ISM. Again, morphological criteria alone has made differentiation between these objects and true PNe difficult in certain cases. Some ejecta nebulae have morphologies rather like PNe; e.g. M 1-67 (Merrill's star), which was suspected to be an unusual PN for many years (e.g. Perek & Kohoutek 1967), RCW 58 (Chu 1982; and see figure 1.12), and PCG 11 (Cohen, Green & Parker 2005; figure 1.11). Other nebulae are simple wind-blown shells in the ISM; examples are NGC 6888 (the Crescent Nebula), NGC 2359 (e.g. Johnson & Hogg 1965), NGC 3199, Sh 2-308, and the spherical limb-brightened shell around WR 16 (Marston et al. 1994; see figure 1.11). Another object that was formerly classified as a

PN is the compact nebula around the WN8 star, We 21 (Duerbeck & Reipurth 1990). A catalogue and atlas of nebulae associated with Wolf-Rayet stars was presented by Chu, Treffers & Kwitter (1983), with more recent discoveries summarised by Marston (1997, and references therein).

(c) **LBV ejecta nebulae.** One object which was classified as a PN for many years is the ring nebula He 2-58, associated with the luminous blue variable (LBV) star AG Carinae (Thackeray 1950; Henize 1967). It is an annular nebula made up of oxygen-poor ejecta (Johnson 1976, Thackeray 1977). The bipolar Homunculus nebula around the eruptive variable η Carinae is related. This remarkable object was ejected during the 'Great Eruption' of this star observed in the 1840s (Frew 2004). Another possible LBV, Wray 17-96, is also surrounded by a nebula (Egan et al. 2002).

5. **Reflection nebulae.** A few symmetrical reflection nebulae have been misclassified as PNe, such as NGC 1985 (Sabbadin & Hamzaoglu 1981; Lutz & Kaler 1983) and Lo 14 (Longmore 1977; and see figure 1.12); this latter object had been previously classified as a reflection nebula by van den Bergh & Herbst (1975). Furthermore, the occasional 'cometary' reflection nebula (e.g. Parsamyan & Petrosyan 1979; Neckel & Staude 1984) has been confused with a PN on morphological grounds. The continuous spectra of reflection nebulae allow them to be easily differentiated from PNe. Note that from the initial visual search of the AAO/UKST Hα Survey, reflection nebulae were weeded out by comparing short-red and I-band images with the Hα images. Conversely, a few objects classified as reflection nebulae are in fact PNe (e.g. DS 1 = GN 10.52.5.01; Neckel & Vehrenberg 1990). These authors likely classified this PN as a reflection nebula due to the presence of a bright central star, the nebula's irregular and amorphous morphology, and the fact that it is brighter on SERC J plates compared to red plates.

6. **Supernova remnants (SNRs).** At least one filamentary nebula initially classed as a PN has turned out to be a SNR, e.g. CTB 1 = Abell 85 (Abell 1966). Conversely, the one-sided filamentary PNe, Abell 21 (the Medusa nebula) and Sh 2-188, have been misclassified as a SNRs in the past. Indeed, Abell 21 was omitted from the CGPN (Perek & Kohoutek 1967) despite its earlier announcement as a PN by Abell (1966). Mention has already been made of the historical status of the Crab Nebula (M 1).

   A few individual compact knots of extended SNRs have also been misidentified as PN candidates, such as Haro 2-12 which is a bright knot in Kepler's SNR of 1604 (Acker et al. 1987; Riesgo & López 2005) and PHR 0818-4728 (Parker et al. 2001b), which turned out to be a compact knot in the Vela SNR (see figures 1.12 and 1.13). The unusual 'Paperclip' nebula, found as part of the MASH survey (see Parker, Frew & Stupar 2004) is the brightest part of a newly identified Galactic SNR (Reynoso & Green 2006; Stupar et al. 2007). Attention is also drawn to the unusual filamentary nebula FP 0821–2755 (see Appendix A and figure 2.10). It has been classified in the literature as a possible SNR by Weinberger (1995), Weinberger et al. (1998) and Zanin & Kerber (2000), though it might be a peculiar PN instead (Parker et al. 2006a). Diagnostic plots (see figures 1.14,

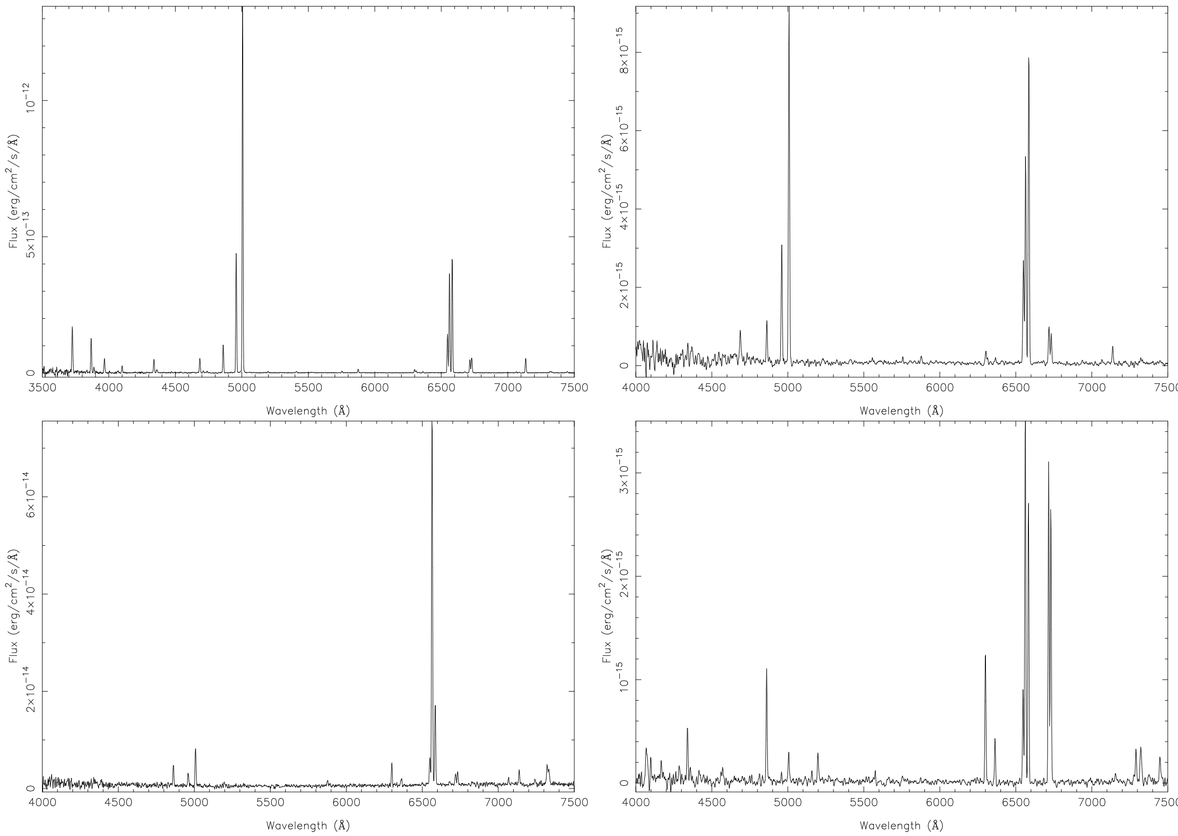

Figure 1.13: Representative spectra of two PNe, a reddened, compact HII region and a SNR. Top left: Spectrum of NGC 5189, a typical PN of medium/high excitation. Top right: Spectrum of PHR1315-6555, of special interest as it is very likely a bona fide member of the intermediate-age open cluster ESO 96-SC04 (Parker, Frew, Köppen & Dobbie 2008, in preparation, and §6.4.10). Bottom left: Spectrum of a highly-reddened, compact HII region, M 2-62 (Frew et al. 2008, in preparation). Bottom right: Spectrum of PHR 0818-4728, a small isolated knot from the Vela SNR, which was included in the preliminary MASH database (Parker et al. 2001b, 2003) as a PN candidate. Note the relative strength of the [SII], [OI], [NII] and [NI] lines in the knot.

5.2 and 5.3) are often very useful in differentiating SNRs from PNe and HII regions based on observed emission-line ratios (e.g. Sabbadin, Minello & Bianchini 1977; Canto 1981; Fesen, Blair & Kirshner 1985; Riesgo-Tirado & López 2002; Riesgo & López 2006).

SNRs in external galaxies may also be confused with PNe (Ciardullo, Jacoby & Harris 1991; Jacoby 2006), but are generally more extended (if not too distant to be resolved). Like their Galactic counterparts, they can be separated from PNe spectroscopically using diagnostic diagrams.

7. **Herbig-Haro (HH) objects and young-stellar objects (YSOs).** For a detailed review of Herbig-Haro objects, including a discussion of their spectra, see Schwartz (1983; see also Raga, Böhm & Cantó 1996). Proximity to star-forming regions, morphology, and spectral features such as the presence of strong [S II] and [OI] emission can usually be used to differentiate HH objects from PNe (e.g. Cantó 1981; Ogura & Noumaru 1994), A lack of non-thermal radio emission can be used to split HH obects from SNRs. Lists of YSOs and other compact nebulous objects in and around star forming regions are given by

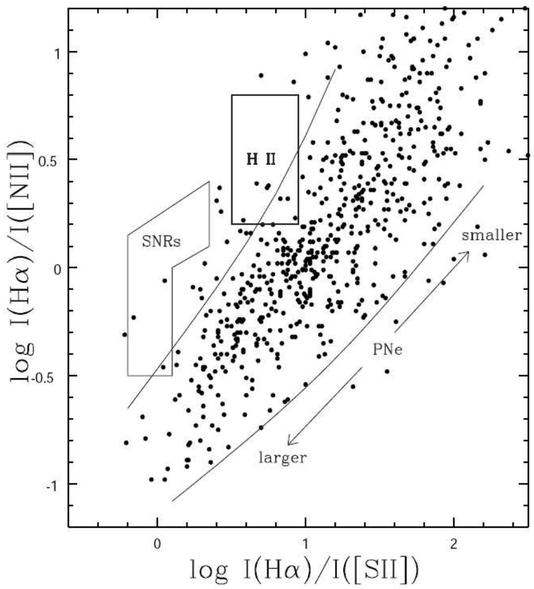

Figure 1.14: Log $I(\mathrm{H}\alpha)/I[\mathrm{N\ II}]$ versus log $I(\mathrm{H}\alpha)/I[\mathrm{S\ II}]$ diagnostic diagram from Riesgo-Tirado & López (2002), which can usefully separate HII regions, PNe, and shock-excited nebulae such as SNRs.

Parsamyan (1965), Gyulbadaghian & Magakyan (1977), Cohen (1980) and Gyulbadaghian et al. (2004). The reader is also referred to the recent survey of Urquhart et al. (2007).

8. **Bowshock nebulae.** These form a rather heterogeneous class of objects. Emission nebulae with PN-like morphologies and spectra are known around CVs, supersoft X-ray sources (e.g. Remillard, Rappaport & Macri 1995), and pulsars. There are currently only two bowshock nebulae known to be associated with nova-like CVs, but both have, at least initially, been offered as PN candidates. They are EGB 4 associated with BZ Cam (Ellis, Grayson & Bond 1984; Krautter, Klaas & Radons 1987; Hollis et al. 1992; Greiner et al. 2001) and a highly interesting nebula found by the author, Fr 2-11, associated with a previously unnoticed nova-like variable, V341 Ara (see Frew et al. 2008, in preparation, and Appendix B).

   Furthermore, the peculiar nebula Abell 35 may be a bowshock nebula inside a photoionized Strömgren sphere (see §8.2). Indeed the emission spectra of EGB 4, Fr 2-11, and Abell 35 are quite similar. Three *possible* PNe in the MASH catalogue (Parker et al. 2006a) may in fact be similar nebulae: PHR 1052-5042, PHR 1539-5325 and PHR 1654-4143. Further work is needed to elucidate their nature. Curiously, the compact core of the supernova remnant CTB 80 is morphologically like a PN in [O III] light (Blair et al. 1984; Fesen & Gull 1985), but has a strong non-thermal radio spectrum. It is probably a pulsar wind nebula seen relatively head on (Hester & Kulkarni 1988, 1989; Lozinskaya et al. 2005).

9. **Nova Shells.** These are shells of gaseous ejecta produced by classical and recurrent nova eruptions. Typically about $10^{-4}\,M_{\odot}$ of ejecta is produced in a nova eruption (e.g. Cohen & Rosenthal 1983), or 2 to 4 orders of magnitude less mass than is contained in a PN shell. However, nova shells show both spherical and axisymmetric structures and have

spectral signatures which can be reminiscent of PNe (e.g. Slavin, O'Brien & Dunlop 1995; Downes & Duerbeck 2000). A faint nebulosity around Q Cygni (Nova Cygni 1876) was designated as NGC 7114 and classed as a possible nebulous variable or planetary nebula by Dreyer (1888). This nebulosity seems to be no longer visible (Corwin 2006).[9] The shell around GK Persei (Nova Persei 1901) is one of the best-known examples of the class (figure 1.11). GK Persei is of further interest due to the claim by Bode et al. (1987) of a possible ancient PN surrounding it (see also Bond 1989, Tweedy 1995a, and Bode 2004). Recently, Shara et al. (2004, 2007) discovered a large extended fossil nova shell around the dwarf nova, Z Cam.

10. **Light echoes.** Light echoes have also been seen around erupting novae and nova-like transients, e.g. the recent eruption of V838 Mon (Bond et al. 2003, and references therein). While not *apparently* related to the CVs, the interesting case of V-V 1-7 (Vorontsov-Vel'yaminov 1961b; Perek & Kohoutek 1967) deserves mention. Méndez et al. (1980) have proposed it to be a transient reflection nebula or light echo in the interstellar medium (ISM). Alternatively it may be a peculiar plate defect[10] (see §2.3.4).

11. **Resolved Symbiotic Outflows**. While only about two dozen objects of this class were known prior to MASH/MASH-II, their strongly bipolar morphology has caused many of them to be classified as PNe (and pre-PNe), as illustrated in Figure 1.6, though there has been confusion in the literature (see Allen 1988; Schwarz, Aspin & Lutz 1989; Lutz et al. 1989; Corradi & Schwarz 1993a, 1993b, 1995; Corradi 1995, 2003; Corradi et al. 1999, 2000; Kwok 2003; López, Escalante & Riesgo-Tirado 2004; Schwarz & Monteiro 2004).

    Some authors use the term 'symbiotic PN' arguing that symbiotics and PNe (and pre-PNe) have physical, if not evolutionary links (e.g. Schwarz, Aspin & Lutz 1989; Smith & Gehrz 2005; Arrieta, Torres-Peimbert & Georgiev 2005). For an illustration of the confusion present in the literature, the bipolar outflow around BI Crucis has always been considered to be a symbiotic nebula since discovery (Schwarz & Corradi 1992), as has the bipolar nebula around the nearby Mira star R Aquarii (e.g. Merrill 1940; Kaler 1981a). However, He 2-104, the Southern Crab (Lutz et al. 1989; Schwarz, Aspin & Lutz 1989; Corradi et al. 2001; Corradi 2003; Santander-García et al. 2008, and figure 1.12) was initially classified as a PN (Henize 1967), but is ostensibly of the same class.

    Following on from §1.2, I use the definition given by Corradi (2003), that states that in resolved symbiotic nebulae, the ionized gas comes from a star in the red giant or AGB phase (i.e. it is a pre-PN). Corradi (2003) has also used a simple statistical argument to show it is highly improbable that a true PN central star would have a binary Mira companion. Nevertheless, evolutionary links between the symbiotic outflows and PNe are likely: many current symbiotic systems may have been PNe in the past when the white dwarf companion was at an earlier phase in its evolution. Similarly, many PNe with binary

[9] see http://www.ngcic.org

[10] A recent unattributed note in the SIMBAD database (dated July 2007) describes it as a "POSS-I artifact misidentified as a nebula."

central stars may go through a symbiotic phase in the future, when the companion star evolves to the AGB.

Hence, I separate true bipolar PNe (e.g. NGC 6537) from resolved symbiotic outflows like He 2-104 (see figure 1.6). As an aid to classification, Schmeja & Kimeswenger (2001) have used DENIS colour-colour plots (figure 1.9) to clearly differentiate symbiotic outflows (and unresolved symbiotic stars) from PNe. These authors have also suggested that the well-known bipolar nebulae M 2-9 (Schwarz et al. 1997; Livio & Soker 2001) and Mz 3 (Cohen et al. 1978) are probable symbiotic outflows. A search for new resolved symbiotic nebulae was undertaken by Kohoutek (1997a) and several new examples were discovered as part of the MASH survey (Parker et al. 2006a; Cohen et al. 2007); see the Miscellaneous Emission Nebula (MEN) Catalogue (Parker, Frew et al. 2008, in preparation) for further details.

The LMC object RP 916, one of the recently discovered RP planetaries in the LMC (Reid & Parker 2006b) is shown by Shaw et al. (2007) to be a very unusual object. However, the very red optical and IR colours of the central source, its intrinsic variability, along with the extreme bipolar morphology, may indicate that it is a symbiotic outflow analogous to its better studied Milky Way cousins. Its large size of 0.75 pc is notable, but not unprecedented amongst symbiotic nebulae (Corradi 2003; Santander-García et al. 2008). However, nebular and molecular emission and hot dust may have affected the observed central star colours. In the future, NIR spectroscopic observations should shed light on the true nature of this unusual object.

12. **Galaxies.**

    (a) **Low-surface brightness (LSB) galaxies.** Similarly to reflection nebulae, a few LSB dwarf galaxies were initially interpreted as evolved PNe on morphological criteria alone. Deep imaging (occasionally resolving the stellar population; e.g. Hoessel, Saha & Danielson 1988) or spectroscopy (detecting the redshift) has confirmed their identity as galaxies. Conversely, a number of candidate LSB galaxies have been shown to be bona fide PNe (e.g. Hodge, Zucker & Grebel 2000; Makarov, Karachentsev & Burenkov 2003).

    (b) **Emission-line galaxies.** A range of galaxy sub-types can have strong Balmer (and forbidden) emission lines, and are potentially confused with PNe on objective prism plates, where the lack of spectral resolution precludes an extragalactic identification without recourse to matching direct imaging, when of relatively low redshift. These range from nearby blue compact dwarf (BCD) galaxies (sometimes referred to as 'intergalactic giant HII regions'), HII region-rich late-type galaxies (e.g. Turatto et al. 1993), and Wolf-Rayet galaxies (Vacca & Conti 1992), to more distant LINER and Seyfert galaxies, and other active galactic nuclei. Two examples of nearby starburst dwarf galaxies are He 2-10 (figure 1.12) and IC 4662 (West & Kohoutek 1985), classed as possible PNe from objective prism plates by Henize (1967; see also Kondratieva

1972). A useful list of misclassified emission-line galaxies is given by Acker, Stenholm & Véron (1991). In addition, six initial PN candidates in the MASH survey have turned out to be low-redshift emission-line galaxies (Hα still falls within the filter bandpass out to $\sim$1100 kms^{-1}).

In addition, distant emission-line galaxies can contaminate on-band/off-band [O III] surveys for PNe in galaxies in and beyond the Local Group (e.g. Jacoby 2006; see §1.5). Ly-α emission from starburst galaxies at redshift, $z = 3.1$ falls in the bandpass of [O III] λ5007 interference filters, as do [O II] emitters at $z = 0.34$. Rarely, closer emission-line galaxies at $z = 0.03$ can have Hβ shifted into the filter bandpass (e.g. Jacoby 2006, figure 2), but these can generally be eliminated on other grounds.

(c) **Ring galaxies.** A few (non-emission-line) ring galaxies plus galaxies with compact nuclei found on small-scale photographic plates have also been confused with PNe morphologically. Shapley (1936) catalogued two round nucleated galaxies (NGC 6630 and IC 4723) as PNe, stating that "because of their appearance there is no doubt that [they] belong to the planetary class." Their identity was questioned by Evans & Thackeray (1950) before they were correctly omitted by Perek & Kohoutek (1967). The best known example of a ring galaxy masquerading as a PN is Abell 76 (Abell 1966) which was shown to be an extragalactic object by Chopinet (1971; see also Chopinet & Lortet-Zuckerman 1976). Another example is PHR 0950-5223, which is a curious emission-line ring galaxy at cz = 2300 kms^{-1}).

13. **Plate defects and flaws.** The photographic process is prone to a wide range of emulsion and processing defects (UKSTU Handbook 1983), and many defects are present on large-scale Schmidt plates such as the POSS. Comparison of first and second epoch plates can generally eliminate these flaws easily. However, when only a single epoch plate is available, the true identity of a PN candidate is less obvious. A number of entries in the Abell (1966) list of evolved PNe were only visible on the POSS E (red) plate, and some of these have turned out to be flaws (e.g. Abell 17 and Abell 32; K. Wallace, 2004, pers. comm.). Another example of a plate flaw on the POSS which had been identified as a possible PN is K 2-4 (Kohoutek 1963; see Lutz & Kaler 1983 for a discussion of this object).

    Note that the Kodak Technical-Pan film used for the AAO/UKST Hα Survey is especially sensitive to static charge build-up (Parker et al. 2005a) which attracts dust particles and other detritus. Furthermore, static discharges may generate faint diffuse spots on the emulsion (Reid 1991). Despite precautions, detritus can build up on the films and is hence present in the digital data, after scanning with the SuperCOSMOS measuring machine (these are further discussed in §2.3.4). Images of 'mandrel' marks on this survey can be remarkably like spherical PNe in appearance, but have been carefully eliminated from the MASH catalogue as they are always in the same relative position(s) on the field images (see §2.3.4 and figure 2.12).

1.8 Thesis Overview

The study of PNe opens a window to the critical phase of stellar evolution between the AGB and white dwarf phases. However, due to the relatively small numbers catalogued prior to MASH and MASH-II (i.e. ∼1,500), their potential to unlock the secrets of the late-stage evolution of low- to intermediate-mass stars has only been partially realised (Parker et al. 2006a). This is particularly true for the most highly evolved PNe where there was, until recently, a serious shortage of known examples.

Most prior statistical studies have used flux-limited samples of galactic PNe (e.g. Manchado et al. 1996). However, a volume-limited local sample of PNe has the potential to better answer some of the remaining unsolved questions of PN research, such as the intrinsic proportions of different morphological and compositional subtypes, to better pin down the scale height(s) and kinematics of different populations (which will help define the lower-mass bound for progenitors to produce visible PNe), and answer the very important question of whether binarity is an essential ingredient in the recipe of PN formation.

The science goals of this study are to provide the most accurate census of nearby PNe in the solar neighbourhood ($D < 1.0$ kpc) yet compiled (as well as an extension to 2.0 kpc), to refine the statistical distance scale(s) for PNe, to examine the faint end of the PN luminosity function (PNLF), to elucidate the binary frequency of PN central stars, and to give fresh estimates for the total Galactic PN population and birthrate.

In Chapter 2, I present the results of searches for new PN candidates based on the AAO/UKST Hα Survey, the Southern H-Alpha Sky Survey Atlas and the Virginia-Tech Spectral-line Survey, supplemented with new data from the INT Photometric Hα Survey and the Wisconsin H-Alpha Mapper.

Chapter 3 summarises new self-consistent estimates of global fluxes in the main emission-lines for a large number of PNe. Very few old PNe have accurate numbers for these quantities, and those that are published are heterogeneous and often very inconsistent (cf. Kaler 1983b; Hippelein & Weinberger 1990; Xilouris et al. 1996). I have generated the most accurate and complete database of fluxes for the nearest, most highly-evolved PNe yet compiled. This is important in the context of estimating reliable distances and ionized masses for these PNe.

In Chapter 4, I discuss the morphological charateristics of PNe, the adopted classification schema, and provide morphological classifications for all PNe in the local volume, with the goal of providing true proportions of the different morphological classes of PNe.

Chapter 5 presents the main results of our spectroscopic survey of nearby PNe, including a discussion of the preliminary chemical abundances of the solar neighbourhood sample.

Chapter 6 discusses the distance scale problem, and the definition of a reliable set of calibrating PNe for a new Hα surface brightness – radius (SB-r) relation, discussed in detail in Chapter 7. Distances are presented for all PNe studied herein, either obtained via the kinematic or extinction-distance methods, obtained with the new Hα SB-r relation developed here, or are revised distances critically evaluated from the literature. Chapter 8 details a number of misclassified PNe, especially those considered to be candidates for the local volume.

With new distances to all nearby PNe, I have generated the most *accurate* volume-limited sample of PNe yet considered, presented in Chapter 9, including an accurate database of parameters for nearly all of these objects and their central stars, as well as looking at the vexing question of single versus binary PN progenitors.

Chapter 10 presents the first volume-limited PN luminosity function (PNLF) centred on the Sun, emphasising the faint end, and Chapter 11 presents new estimates for the number density, scale height, birth rate and total number of Galactic PNe, as extrapolated from the solar neighbourhood sample. Chapter 12 summarises my main conclusions of the study.

Appendix A in the backmatter gives detailed notes on individual bona fide PNe in the solar neighbourhood. A summary of the nebulae found using SHASSA, VTSS and WHAM is presented as Appendix B, while a database of magnitudes and colour indices for a large set of PN central stars is given as Appendix C. Appendix D gives the abstracts of the relevant refereed papers and conference proceedings that have been authored or co-authored by me as a result of working on this project. Finally, the journal abbreviations used in the reference list are summarised in Appendix E.

Chapter 2

A Search for New Planetary Nebulae

2.1 Introduction

Any volume-limited sample of planetary nebulae will be dominated by large, evolved, hard-to-detect examples. A simple argument to elucidate this point follows: Kaler (1983b) defined a 'large' PN as having a radius, $r > 0.175$ pc, while Kaler, Shaw & Kwitter (1990) adopted a smaller limit of $r > 0.15$ pc. After considering the observable properties of a sample of well studied PNe with a range of surface brightness, an evolved PN is here defined as having $r >$ 0.20 pc (see later). Assuming a mean expansion velocity of 20 kms^{-1} (Weinberger 1989), this size corresponds to a nebular age of ∼10,000 years. The upper limit to the age of an observable PN is poorly known, but is of the order of $5{\times}10^4$ years or more (e.g. Zijlstra & Pottasch 1991; Pierce et al. 2004; Frew & Parker 2005, and Chapter 11). Thus, it is clear that at least ∼80% of all PNe are, by definition, evolved objects.

Since an accurate census of the nearest planetary nebulae is needed for reliable calculations of the total number, space density, scale height, and birth rate of planetary nebulae in the Galaxy, as well as relating the dynamics of an evolving nebula to the cooling history of the central star, it is important that a new search be undertaken for evolved PNe in the solar neighbourhood, defined here as the volume within 1.0 kpc of the Sun. Considerable additional effort has resulted in an 'extension sample' out to a radius of 2.0 kpc from the Sun, but as is shown later, this sample is much less complete at the faint end of the PN luminosity function (see Chapter 10).

Prior to the advent of the AAO/UKST and SHASSA surveys, a list of the largest PNe by angular size (38 examples), had only 10 situated south of the celestial equator — including two needing to be confirmed as true planetary nebulae (Frew 1997). In that article, the number of large PNe in the north polar cap above declination +50°, which included 10 PNe, was compared with the number of known PNe in the south (two PNe). As a result, it was suggested that a considerable number of low-surface-brightness objects remained undiscovered in the 'deep-south.' Other lists detailing the largest PNe in the sky were given by Borkowski, Sarazin & Soker (1990), Tweedy (1995b), and Tweedy & Kwitter (1996).[1] Cahn & Wyatt (1976), Jacoby

[1] Of further interest is the website by Jens Bohle (in German) summarising 'Die großen Planetarische Nebel',

(1980), Daub (1982), Weinberger (1986), Ishida & Weinberger (1987) and Terzian (1993) give lists of local PNe in the solar neighbourhood, dominated by large evolved objects.

As stated earlier, the first step to obtaining an accurate census of planetary nebulae in the solar neighbourhood is to conduct a search for new large PNe (see below). Fortunately, a number of recent deep surveys covering the Hα+[N II] lines have recently become available. The recently completed AAO/UKST Hα Survey (Parker et al. 2005a) was used to catalogue 903 new PNe candidates (the MASH catalogue), of which the majority of these new PNe are of low to very-low surface brightness (Parker et al. 2001b, 2003, 2006a). Some of the largest new MASH PNe were found by re-examining the blocked-down digitized SuperCOSMOS Hα Survey (SHS) data; these were missed by the original eyeball scans of the survey films. For the PNe of largest angular size, the overall MASH (+ MASH-II) sample has reversed the north-south bias, at least along the Galactic plane, with $\sim$15 new large PNe ($>5'$ across), and another 100 new examples $2'$–$5'$ across having been found so far in the southern sky.

For areas further from the Galactic plane that are not covered by the SHS, a visual inspection of all of the fields of the Southern H-Alpha Sky Survey (SHASSA), outside the zone of coverage of the SHS to look for additional diffuse nebulosities and PN candidates was undertaken. as well A supplemental search for similar nebulosities with the Virginia Tech Spectral-line Survey (VTSS) was also undertaken. Observations taken by the Wisconsin H-Alpha Mapper (WHAM; Haffner et al. 2003) will also be used as an adjunct to both search for new PNe, and to critically assess a number of poorly studied PN candidates (see Chapter 9 and Appendix 8).

The INT Photometric H-Alpha Survey (IPHAS; Drew et al. 2005) of the northern Galactic plane was directly motivated by the success of the SHS, and is also leading to the discovery of new evolved candidate PNe, though the numbers of likely solar neighbourhood PNe are predicted to be considerably less due to the smaller areal coverage of the survey and the fact that the northern hemisphere had previously been searched to greater depth.

In this chapter I will detail the results of these searches for new large PNe, using the AAO/UKST Hα survey and SHASSA, as well as a supplemental search of the northern sky with VTSS. I will examine each of these surveys in turn, detailing the discoveries that were made from each, and will examine the statistics of the new objects with regard to completeness. The new PNe will be combined with a critically-assessed 'refined sample' of previously known PNe to define a clean, relatively unbiased solar neighbourhood sample (plus the extension sample) which will be analysed in subsequent chapters.

2.2 The AAO/UKST Hα Survey

A key adjunct to this project is the Anglo-Australian Observatory/UK Schmidt Telescope (AAO/UKST) Hα Survey, now available online as the scanned SuperCosmos Hα Survey (SHS; Parker et al. 2005a). This is a high-resolution, narrow-band Hα+[N II] survey covering $\sim$4000 square degrees of the southern Galactic plane[2] extending to a galactic latitude of $|b| \sim 10 -$

located at: http://www.jens-bohle.de/projekt_grosse_pn.htm

[2]The survey also included a separate contiguous region of 700 square degrees covering the Magellanic Clouds.

Table 2.1: Summary details of various current Hα surveys

Survey	Coverage (sq. deg)	Depth (R)	Resolution (arcsec)	Field size (deg)	Filter FWHM	Coverage	Reference
SHS[1]	4000	2 – 5	1 – 2	5.5 × 5.5	70 Å	$\delta < +2^\circ$; $\lvert b\rvert \leq 12^\circ$	Parker et al. (2005a)
IPHAS[2]	1800	2 – 3	~ 1	0.3 × 0.3	95 Å	$\delta > -2^\circ$; $\lvert b\rvert \leq 5^\circ$	Drew et al. (2005)
SHASSA[3]	17000	0.5 – 2	48	13 × 13	32 Å	$\delta < +15^\circ$	Gaustad et al. (2001)
VTSS[4]	>1000	$\sim$1	96	10 × 10	17 Å	$\delta > -20^\circ$	Dennison et al. (1998)
WHAM[5]	17000	0.15	3600	1.0	0.25 Å	$\delta > -30^\circ$	Haffner et al. (2003)

[1] http://www-wfau.roe.ac.uk/ss/halpha/

[2] http://astro.ic.ac.uk/Research/Halpha/North/

[3] http://amundsen.swarthmore.edu/SHASSA

[4] http://www.phys.vt.edu/halpha

[5] http://www.astro.wisc.edu/wham

13°(see Figure 2.3).

2.2.1 Characteristics of the Survey

The survey, which commenced in early 1998 and was completed by 2003, used a large high-quality optical interference filter (see Parker & Bland-Hawthorn 1998) with a bandpass of 70 Å centred close to Hα. A graphical plot of the effective filter bandpass is shown in Figure 2.1, and the salient properties of the AAO/UKST survey, including a comparison with the other Hα surveys discussed in this chapter, are given in Table 2.1.

Matching 3-hour Hα and 15-min broadband (5900 – 6900Å) short red (SR)[3] exposures were taken over 233 overlapping fields of the Galactic plane. To allow full contiguous coverage in Hα, the fields were done on 4° centres because of the slightly smaller circular aperture ($\sim$305 mm diameter)[4] of the Hα interference filter (see Parker et al. 2005a for further details). Hence a new southern sky-grid[5] of over 1100 four-degree field centres was created (cf. the 893 standard 5° field centres of the UKST and ESO southern sky surveys).

The Hα survey was carried out using hypersensitised large-format Kodak Technical Panchromatic (Tech-Pan) film (Parker & Malin 1999). This emulsion has high quantum efficiency (with hypersensitised film having a DQE approaching 10%; Phillipps & Parker 1993), a very fine grain ($\sim 5\mu$m), and an extended red response to nearly 7000 Å with a useful sensitivity peak at Hα. Further details on the suitability of this emulsion for astronomical applications, as well as its adaptation for use at the UK Schmidt Telescope are found in Parker & Malin (1999) and Parker et al. (2005a).

Consequently the survey has arcsecond spatial resolution and very good sensitivity to faint diffuse Hα emission down to a surface brightness of $\sim$2 – 5 Rayleighs[6], corresponding to a

[3] Note that the short red moniker does not refer to exposure time, but instead refers to the use of a OG590 filter compared to the normally used RG630 red filter.

[4] This is probably the world's largest interference filter used for astronomical applications.

[5] An index map of the Hα survey region is available online at http://www-wfau.roe.ac.uk/sss/halpha/

[6] 1 Rayleigh = $10^6/4\pi$ photons cm^{-2} s^{-1} sr^{-1} = 2.41×10^{-7} erg cm^{-2} s^{-1} sr^{-1} = 5.66×10^{-18} erg cm^{-2} s^{-1} arcsec^{-2} at Hα

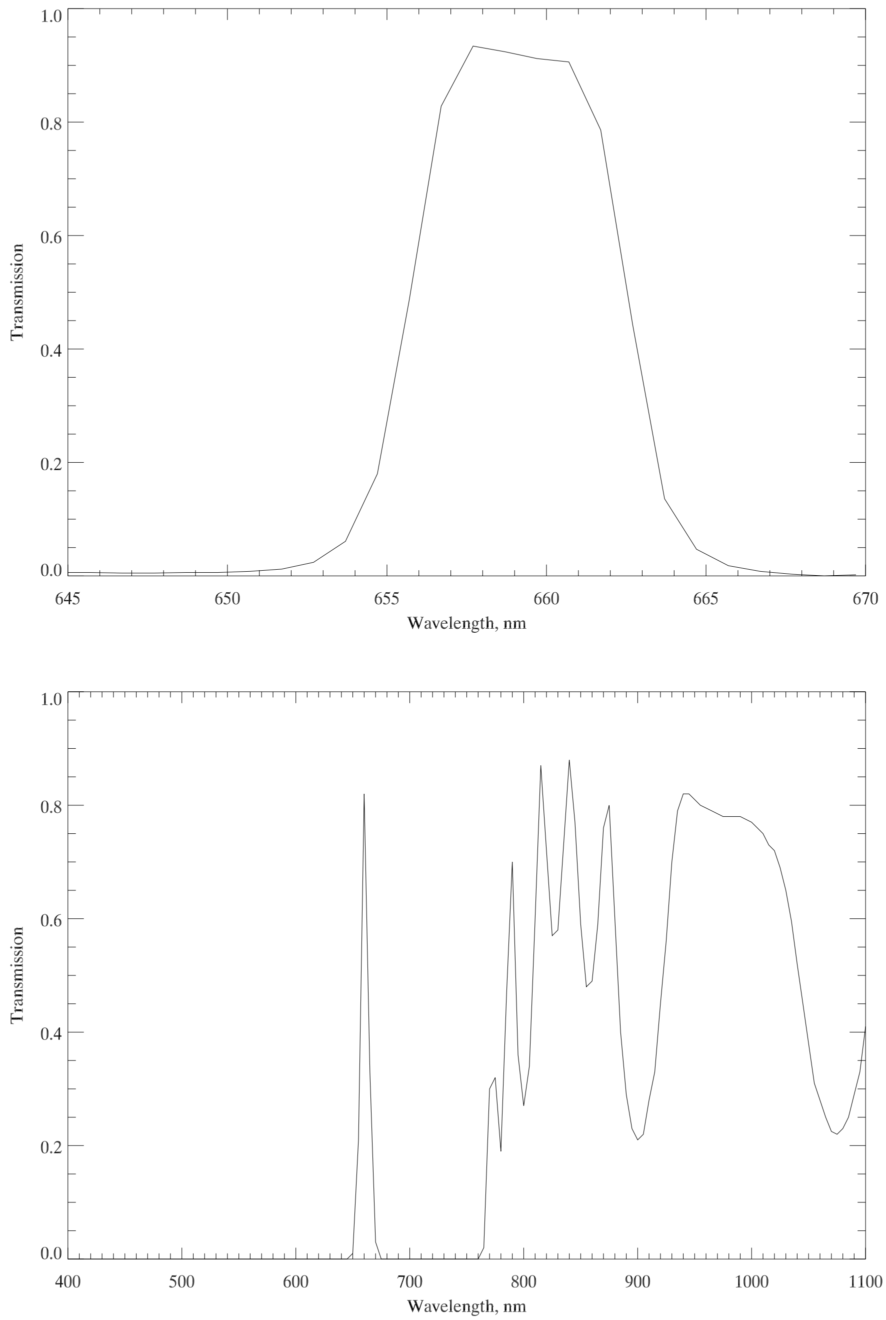

Figure 2.1: The top plot shows a high resolution transmission scan from the central area of the AAO/UKST Hα filter. The bottom plot shows a lower resolution scan showing the narrow peak around Hα and the extended response into the near-IR. The Tech-Pan emulsion long-wavelength cut-off is at 6990Å so longer wavelengths are not recorded. Figure reproduced from Parker et al. (2005a).

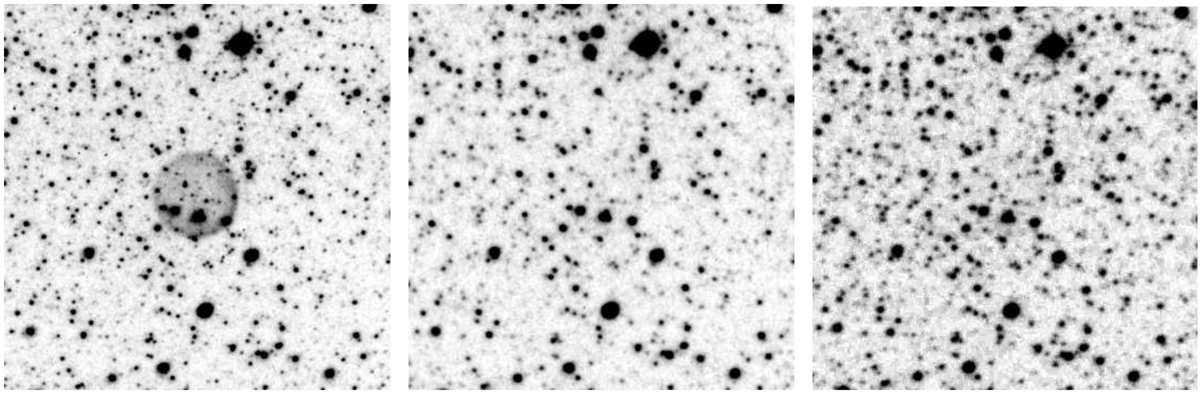

Figure 2.2: 3×3 arcminute extracts of SHS data around a newly discovered PN (PHR1706-3544) from the 3-hour Hα survey data (left), matching 15 minute Tech-Pan *SR* data (middle) and earlier epoch 60 minute IIIa-F *R*-band data (right). The new PN is only visible in the Hα image. Note the well matched depth for point sources between all three exposures and the better PSF of the Tech-Pan images compared with the IIIa-F exposure.

surface brightness of $\sim 1 - 3 \times 10^{-17}$ erg cm^{-2} s^{-1} arcsec^{-2}, or an emission measure of about 5 – 12 cm^{-6}pc. This can be compared to the approximate surface brightness limit of the Palomar Observatory Sky Survey (POSS) red plates, using the 103a-E emulsion, $\sim 10^{-16}$ erg cm^{-2} s^{-1} arcsec^{-2} or $\sim$20 R (Peimbert, Rayo & Torres-Peimbert 1975), a factor of 10 brighter than the SHS limit. Both the POSS-II (Reid 1991) and UKST Survey red plates used the IIIa-F emulsion; these plates have a sensitivity limit about twice as deep as the POSS, or $\sim 8 - 12$ R. In comparison, sky-limited narrowband CCD sensitivity limits are at the $\sim$1 R level (e.g. Xilouris et al. 1996), comparable to SHASSA and VTSS (see §2.4 and §2.5). Careful comparison shows that the CCD images of Tweedy & Kwitter (1996) reach the same sensitivity level.

Figure 2.2 illustrates the qualitative difference between the 3-hour Hα and contemporaneous 15-min *SR* Tech-Pan exposures, as well as a comparison with a standard first-epoch 60-min *R*-band IIIa-F UKST survey image. This region includes a newly discovered planetary nebula (PHR 1706-3544) found from the Hα survey data and included in the Macquarie/AAO/Strasbourg Hα planetary nebulae catalogue (Parker et al. 2003, 2006a, and see below). Note the improved resolution of the Tech-Pan image, the very similar depth of the Hα and SR exposures for point sources and the better point-spread function (PSF) for the Tech-Pan compared to the IIIa-F emulsion. The colour terms of the Tech-Pan emulsion have been derived by Morgan & Parker (2005), where these terms are shown to be stable and quite similar to those previously derived for the older IIIa-F emulsion.

To take advantage of the UKST's large, 6.5° field of view it was necessary to obtain a physically large narrow-band filter to be placed as close as possible to the telescope's focal plane (Parker et al. 2005a). An RG 610 glass substrate was cut to 356×356 mm, the standard size of UKST filters, and coated with a multilayer dielectric stack to give a clear aperture of ~ 305 mm diameter, making it probably the world's largest astronomical, narrow-band interference filter. At the UKST plate scale, the filter allows field coverage of approximately 5.7° in diameter on the sky (slightly less than the standard Schmidt field). Therefore, to ensure complete, overlapping survey coverage with the circular aperture interference filter it was necessary to use 4°-spaced field centres.

In addition, the central wavelength of the interference filter was set slightly longward of zero-velocity Hα for two reasons. Firstly, the UKST has a fast, f/2.48 converging beam. This leads to the interference filter 'scanning down' in wavelength for an off-axis beam compared to a beam normal to the filter. Secondly, the aims of the survey were to map diffuse Hα (+ [N II]) emission in the Milky Way (covering the full range of observed disk velocities as well as to map positive velocity gas in nearby galaxies out to the distance of the Virgo and Fornax clusters ($cz = \sim$1500 kms^{-1}). Given a bandpass (FWHM) of 70Å, the filter was hence centred at 6590Å where the peak filter transmission is around 90% (for further details see Parker & Bland-Hawthorn 1998 and Parker et al. 2005a).

2.2.2 The SuperCOSMOS Hα Survey (SHS)

Both the narrowband Hα and broadband short-red (SR) photographic images have been scanned and digitised by the high speed SuperCOSMOS plate scanning machine at the Royal Observatory, Edinburgh (Hambly et al. 1998). The resulting SuperCOSMOS Hα Survey (SHS; Parker et al. 2005a) is now available online,[7] both as as full 0.67″-resolution pixel data and also as 16× blocked-down (11″ resolution) images of each survey field[8]. A similar scanning and processing pipeline was employed to the analogous SuperCOSMOS broad-band sky surveys (SSS) outlined in detail by Hambly et al. (2001 a,b,c). Full details of the SHS are given in the definitive paper of Parker et al. (2005a), and are briefly described here.

Figure 2.3 shows all 233 survey fields in the southern Galactic plane (mosaiced together by M. Read) which together make up the entire Hα survey. The individual scanned images have been incorporated into an online mosaic within the freeware 'Zoomify' environment[9] which allows visualisation of the images. This interactive SHS map is available online[10], and can be zoomed-in to a level where each pixel represents about 12 arcseconds. Hence this map is a factor of 18× lower in resolution than the full 0.67 arcsecond data available online.

The full-resolution Hα and SR data for the 233 survey fields are also available online[11]. The data products are given as FITS files with the header information providing photographic, photometric, astrometric and scanning parameters in standard image-analysis mode (IAM) format (e.g. Hambly et al. 2001b). The FITS images also have an accurate built-in World Coordinate System (WCS). The scanned pixel data are processed through the standard SuperCOSMOS object detection and parameterisation software (Beard, MacGillivray & Thanisch 1990) to produce the associated Fits table extension data for each field. This process determines a set of 32 image-moment parameters which provide the astrometry, photometry and morphology of the detected objects in each SHS field (see Parker et al. 2005a).

[7] http://www-wfau.roe.ac.uk/sss/halpha/

[8] The blocked-down SR fields were not available at the commencement of this study. A new search for evolved PN candidates using difference imaging of the blocked-down data is described later in this chapter.

[9] see http://www.zoomify.com

[10] http://surveys.roe.ac.uk/ssa/hablock/hafull.html

[11] http://www-wfau.roe.ac.uk/sss/halpha

The calibration of the SHS was undertaken by Pierce (2005) and Parker et al. (2005a). It was shown that continuum emission can be successfully removed from the Hα images by subtracting a scaled SR image. Unlike CCD data, which enjoys a linear response frame to frame over a wide range of emission strength, photographic data is more difficult to calibrate because both the response of the Tech Pan emulsion and the SuperCOSMOS scanner behave non-linearly over wide dynamic ranges. Variations in sensitivity are also to be expected between exposures. Despite these caveats, Pierce (2005) showed the SHS can be calibrated with reasonable accuracy by means of a comparison with the SHASSA images (Gaustad et al. 2001).

The comparison showed that the SHS recorded diffuse Hα + [N II] emission over a wide range of intensties from ~ 5 R to more than 500 R, the approximate saturation limit of the SHS. Emission down to ~ 2 R has been measured on one field, HAL1109, comparable to the CCD-based IPHAS survey. A crude calibration scheme for all 233 SHS fields was based on comparison of a carefully selected binned $30'$ region from each SHS field with the equivalent area from the calibrated SHASSA Hα image. An important caveat is that the chosen SHS fields need to be carefully examined for flaws which can affect the SHS digital data (see §2.3.4).

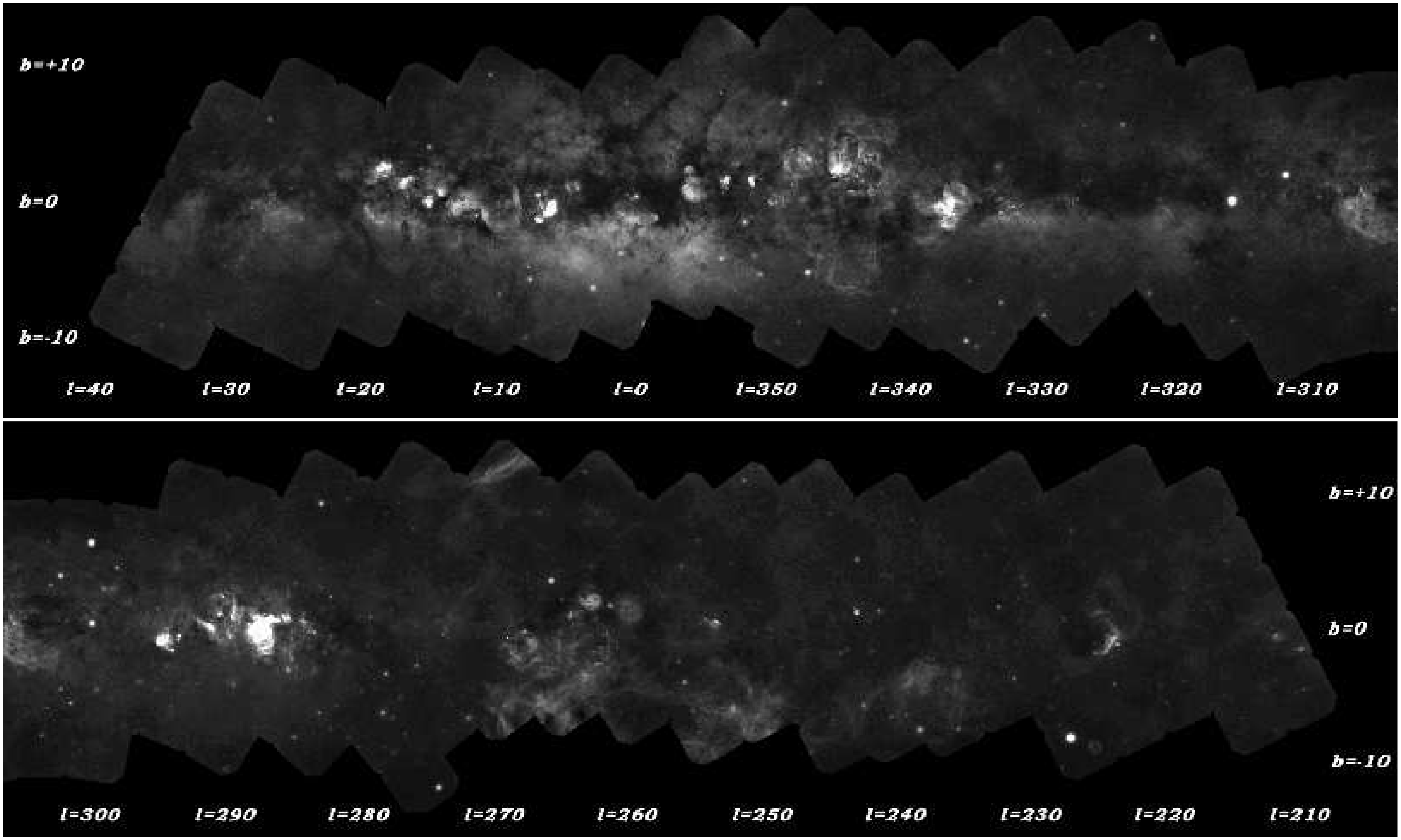

Figure 2.3: All 233 SHS fields mosaiced together by M. Read. The top panel covers galactic longitude $l = 40°$ to $310°$, and the bottom panel $l = 300°$ to $210°$.

2.3 The Macquarie/AAO/Strasbourg Hα (MASH) Catalogue

The Macquarie/AAO/Strasbourg Hα (MASH) Catalogue of PNe details the discoveries made from the AAO/UKST Hα Survey, and totals 905 new Galactic PNe (Parker et al. 2005b, 2006a). Excluding the bulge sample, most of these PNe are of very low surface brightness and are often heavily reddened. This catalogue supercedes the the preliminary version of the catalogue released on CD-ROM[12] in 2001 (Parker et al. 2001; see also Parker et al. 2003).

As the FWHM of the Hα filter bandpass is 70Å with a central wavelength of 6590Å, it is more accurately an Hα + [N II]$\lambda\lambda$6548, 6583 filter. This is an advantage for PN searches based around the Hα line as many Type I PNe can have [N II]$\gg$Hα by up to a factor of five or more (e.g. Guerrero, Manchado & Serra-Ricart 1996; Corradi et al. 1997; Kerber et al. 2000; Frew, Parker & Russeil 2006). As noted above, the central filter wavelength is redward of Hα to account for the scanning down of wavelength with off-axis flux as the filter encounters the f/2.48 converging beam of the UKST.

The MASH catalogue includes a good many PNe of very large angular diameter. The survey has increased by about 60% the number of Galactic PNe discovered from all sources over the last century. Furthermore, the new sample has the potential to better examine the poorly represented extremes of PNe evolution, and provide more statistically significant samples of both compact and old, highly-evolved PNe. The international MASH Consortium has been set-up to exploit this new sample of PNe.

Once the SHS Hα pixel data became fully available in 2003 it was possible to check all the previous visual identifications and in particular to obtain more accurate estimates of nebular size, position and morphology. All catalogue entries have been completely updated in this way and the current MASH release represents a more consistent description of the new PNe compared to what was available in the preliminary CD-ROM. This catalogue has been completely superceded with many contaminants such as HII regions removed and significant numbers of PNe added. The full catalogue is now accessible through the VizieR service[13] as Catalogue V/127. A few basic plots of the new MASH data are provided in Figure 2.4 (refer to the caption for details), where the MASH catalogue is compared with similar data from the Acker et al. (1992, 1996) catalogues. Greater numbers of PNe have been found at lower Galactic latitudes, which is due to the AAO/UKST survey's deep sensitivity in Hα which is less affected by dust than [O III] imagery.

To help the reader visualise the scope of the MASH project, a random example selection from the MASH online catalogue (Parker et al. 2006a) is presented as Figure 2.5. Figure 2.6 shows an example of an individual PN summary page from the MASH online catalogue. Figure 2.7 shows a mosaic (from a developmental database) of a set of PNe from the MASH catalogue. An updated version is available through VizieR.[14]

[12] formerly known as the Edinburgh/AAO/Strasbourg Catalogue
[13] http://vizier.u-strasbg.fr/vizier/MASH/
[14] http://vizier.u-strasbg.fr/vizier/MASH/gallery.htx

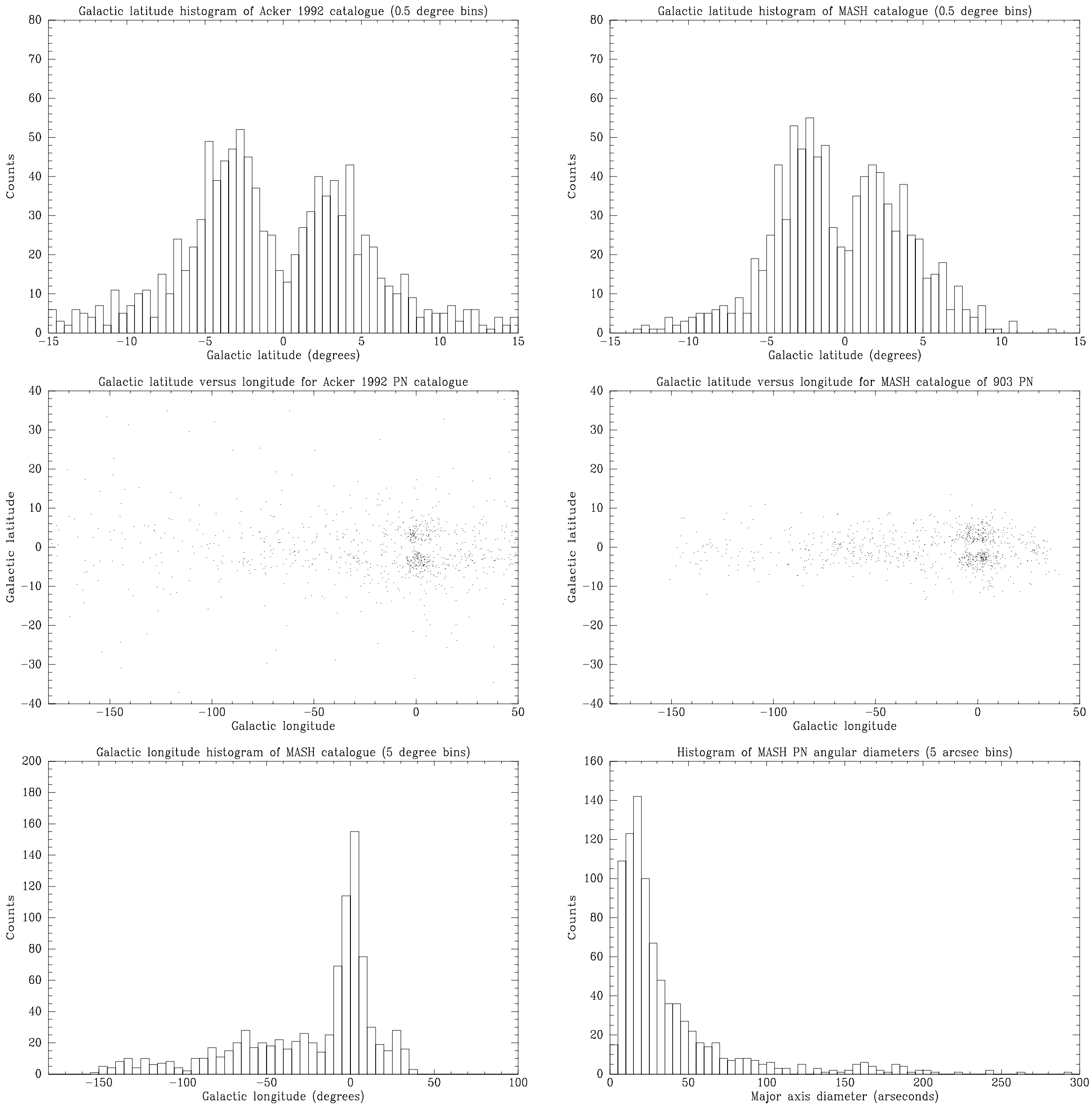

Figure 2.4: Basic comparison plots between the Acker et al. catalogues and the new MASH PN catalogue. The top two plots show the galactic latitude histograms of the Acker et al. and MASH catalogues respectively, but are restricted to a $|b|$ of 15 degrees (dictated by the SHS coverage). MASH PNe are found significantly closer to b=0° than previous samples, especially away from the heavily obscured bulge region. This improved low latitude coverage is a product of the survey's deep sensitivity in Hα which is less affected by dust than [O III] imagery. The middle two plots show the Galactic latitude versus longitude plots of Acker et al. (left) and MASH PNe (right) in the region of overlap in the southern Galactic plane. They show the increased PN number density of the MASH sample in the bulge region, and a more uniform disk distribution compared to the equivalent Acker sample. The final two plots give the MASH histograms of galactic longitude in degrees, and major axis in arcseconds. Figures taken from Parker et al. (2006a).

M	n	PNG	Name	RAJ2000 "h:m:s"	DEJ2000 "d:m:s"	GLon deg	GLat deg	MajDiam arcsec	MinDiam arcsec	Morph	Tel	Obs "Y:M:D"	HaExp	HaFld
	T	G209.1-08.2	PHR0615-0025	06 15 20.4	-00 25 49	209.1757	-8.2227	100.0	100.0	R	MS	2005-01-07	HA19062	HA1285
	P	G227.3-12.0	PHR0633-1808	06 33 24.9	-18 08 23	227.3207	-12.0289	17.0	15.0	Ea	SA	2003-02-02	HA18191	HA926
	T	G212.2-04.7	PHR0633-0135	06 33 09.3	-01 35 12	212.2603	-4.7910	56.0	50.0	Ea	SA	2004-02-16	HA19062	HA1285
	P	G214.2-02.4	PHR0645-0217	06 45 03.5	-02 17 52	214.2511	-2.4663	55.5	46.0	Es	SA	2003-01-29	HA18685	HA1196
	L	G223.6-06.8	PHR0646-1235	06 46 25.4	-12 35 56	223.6338	-6.8035	40.0	37.0	E	SA	2006-02-22	HA18194	HA1016
	L	G219.1-03.9	PHR0648-0719	06 48 43.8	-07 19 51	219.1592	-3.9343	35.0	33.0	Ea	SA	2000-02-08	HA18693	HA1107
	T	G212.6-00.0	PHR0650+0013	06 50 40.5	+00 13 40	212.6422	-0.0659	68.0	26.0	B	SA	2004-02-13	HA19075	HA1286
	T	G215.5-01.4	PHR0651-0257	06 51 07.2	-02 57 07	215.5234	-1.4162	8.5	8.5	R	SA	1999-01-13	HA17887	HA1197
	P	G221.8-04.2	PHR0652-0951	06 52 19.4	-09 51 36	221.8238	-4.2837	60.0	46.0	Ea	SA	2003-01-30	HA18693	HA1107
	P	G224.3-05.5	PHR0652-1240	06 52 20.3	-12 40 34	224.3504	-5.5463	187.0	180.0	I	SA	2003-01-31	HA18244	HA1017
	T	G222.8-04.2	PHR0654-1045	06 54 13.4	-10 45 38	222.8412	-4.2730	27.0	16.0	E	SA	2003-01-28	HA18244	HA1017
	T	G224.3-03.4	PHR0700-1144	07 00 05.8	-11 43 51	224.3616	-3.4280	49.0	47.0	Ea	SA	2003-01-29	HA18244	HA1017
	L	G221.0-01.4	PHR0701-0749	07 01 09.3	-07 49 21	220.9984	-1.4147	67.0	66.0	Ea	SA	2003-01-28	HA18693	HA1107
	T	G217.2+00.9	PHR0702-0324	07 02 34.2	-03 24 35	217.2356	0.9177	52.0	44.5	Ea	SA	1999-01-13	HA17887	HA1197
	T	G214.6+02.9	PHR0704-0011	07 04 56.6	-00 11 15	214.6399	2.9189	14.0	14.0	R	SA	2004-02-13	HA19046	HA1288
	T	G227.2-03.4	PHR0705-1419	07 05 38.5	-14 19 05	227.2852	-3.4029	15.0	15.0	E	SA	2003-01-29	HA18244	HA1017
	T	G222.9-01.1	PHR0705-0924	07 05 51.4	-09 24 11	222.9361	-1.1056	85.0	80.0	B	SA	2003-01-28	HA18693	HA1107
	P	G237.9-07.2	FP0711-2531	07 11 32.0	-25 31 24	237.9490	-7.2470	660.0	600.0	Ea	SA	2004-02-14	HA19099	HA756
	T	G226.4-01.3	PHR0711-1238	07 11 43.3	-12 38 03	226.4677	-1.3165	56.5	55.0	Ra	SA	2003-01-29	HA18263	HA1018
	L	G225.2+00.1	PHR0714-1051	07 14 28.8	-10 51 44	225.2104	0.1031	7.0	5.0	E	MS	2005-01-07	HA18263	HA1018
	T	G225.4+00.4	PHR0716-1053	07 16 08.0	-10 53 06	225.4195	0.4518	104.5	71.0	Em	SA	2000-02-08	HA18263	HA1018
	T	G227.1+00.5	PHR0719-1222	07 19 46.7	-12 22 47	227.1581	0.5422	193.0	188.0	Ea	SA	2000-02-08	HA18263	HA1018
	P	G215.0+07.4	FP0721+0133	07 21 41.0	+01 33 31	214.9990	7.4390	720.0	720.0	A	SA	2004-02-14	HA19046	HA1288
	T	G238.1-04.6	PHR0722-2431	07 22 14.3	-24 31 02	238.1645	-4.6301	21.0	20.0	R	SA	2003-01-28	HA19352	HA757
	T	G229.3+00.0	PHR0722-1434	07 22 14.9	-14 34 49	229.3826	0.0376	93.0	60.0	Es	MS	2005-01-08	HA18256	HA928
	T	G222.1+03.9	PFP1	07 22 17.7	-06 21 46	222.1292	3.9104	1150.0	1100.0	Ra	SA	2004-02-13	HA18771	HA1109
	P	G228.1+00.8	PHR0722-1305	07 22 30.6	-13 05 30	228.0997	0.7954	44.5	20.5	R?	MS	2005-01-08	HA18282	HA1019

Figure 2.5: Random example selection from the MASH online catalogue (list in RA order)

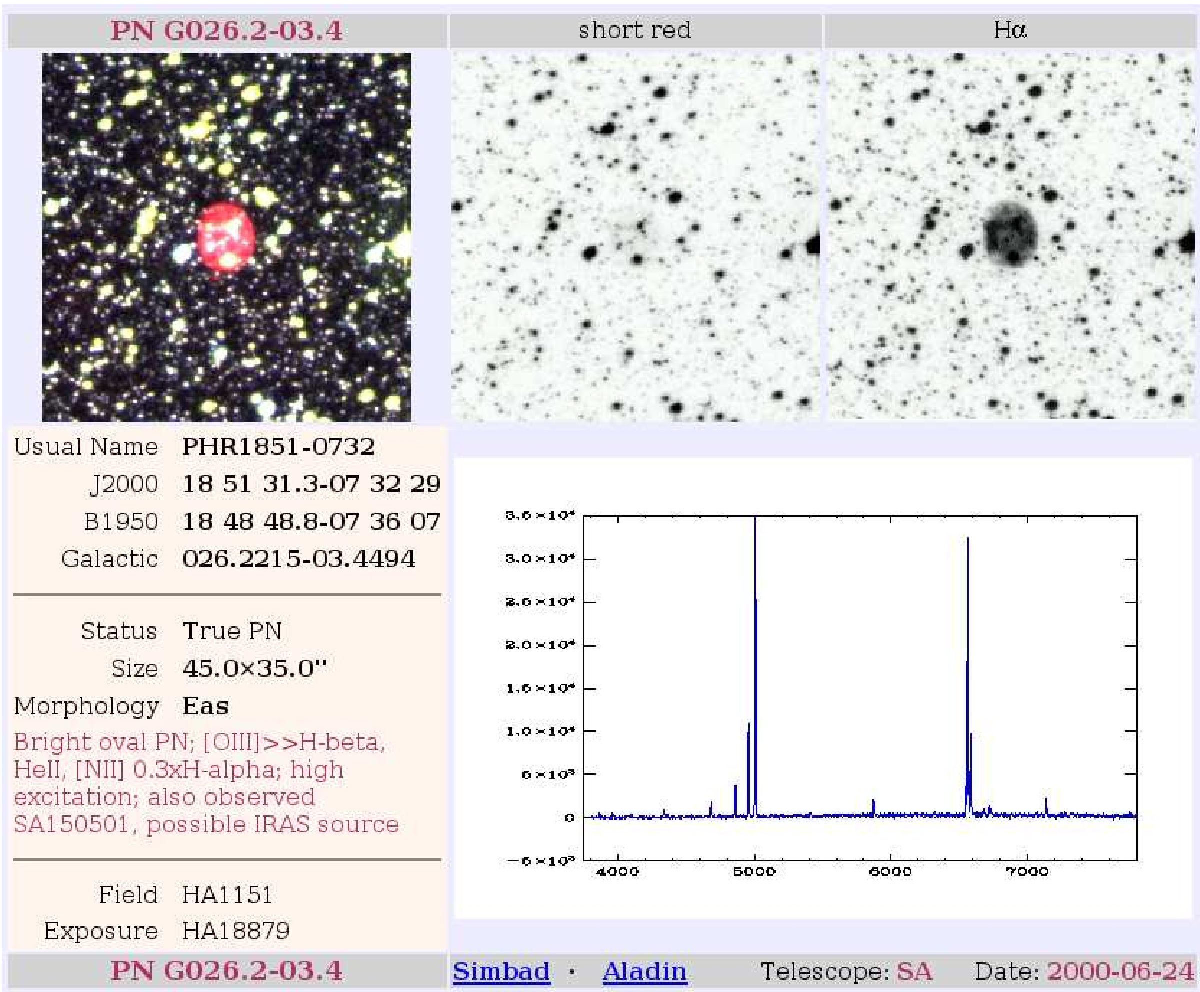

Figure 2.6: Example of an individual PN summary page from the MASH online catalogue: Top: Hα/SR/B combined colour image, SR and Hα images of size 4×4 arcmin; Bottom: summary information and 1-D spectrum

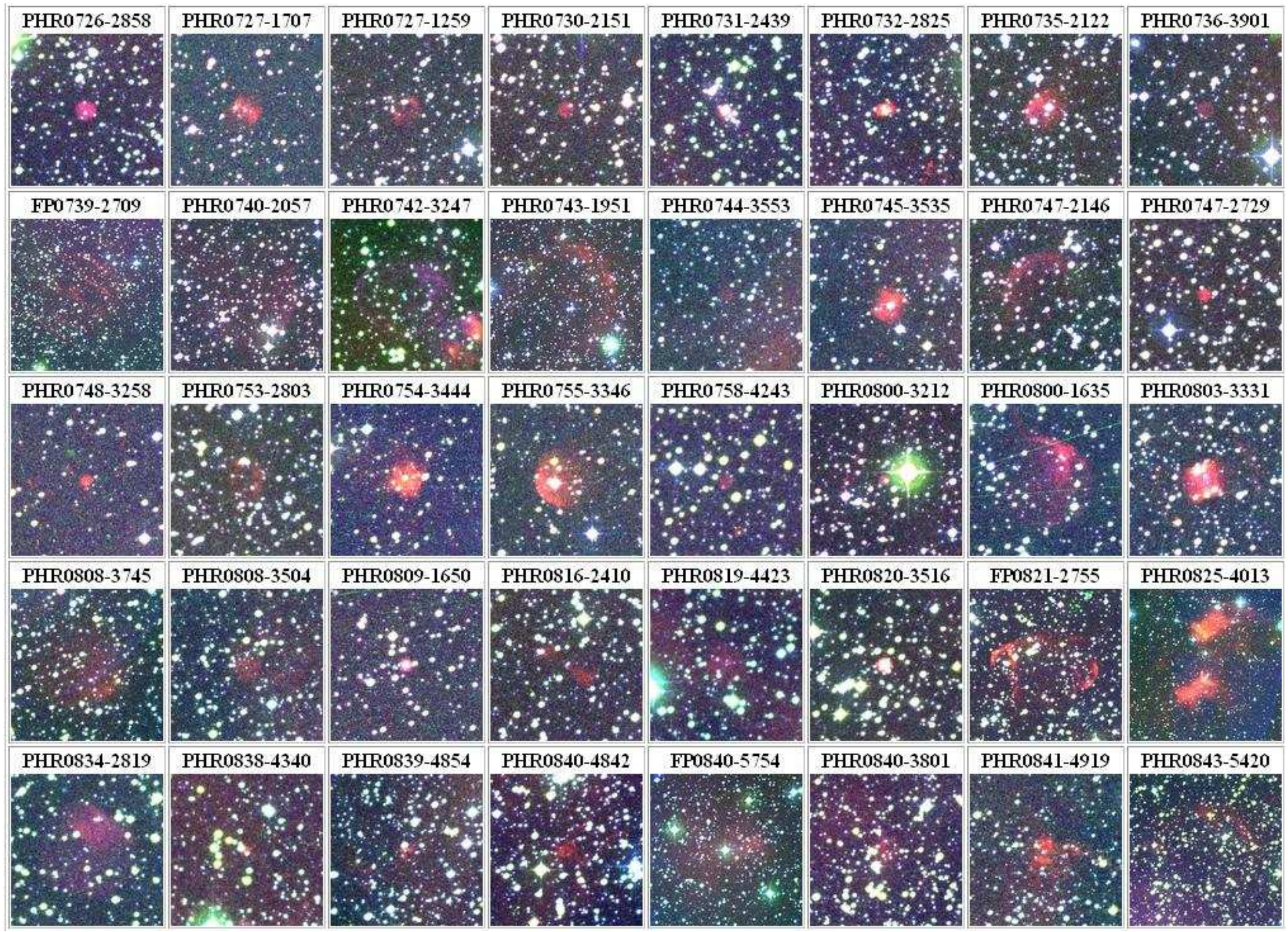

Figure 2.7: A mosaic showing a series of PNe from the MASH catalogue, in RA order. Figure courtesy of B. Miszalski.

2.3.1 MASH Discovery Techniques

Several different search techniques were necessary to fully utilise the SHS data, a consequence of the wide range in size and brightness of the PNe apparent on the survey. These are visual inspection of the original survey films, visual inspection of the blocked-down survey images, and inspection of the digital difference and/or quotient images.

Visual Inspection of Survey Films

The bulk of MASH PNe have been discovered from careful visual scrutiny of the original Hα *survey films* using a binocular microscope on a field-by-field basis, primarily by Q. Parker, M. Hartley, and D. Russeil (leading to the PHR prefix for the majority of MASH PNe). The process began in 1998 and all 233 survey fields, which each effectively cover ~ 25 square degrees, were examined by early 2003. Figure 2.8 shows 4×4 arcminute Hα, SR and quotient (i.e. Hα divided by SR) images of a typical example of a new PN discovered in this way.

Visual scanning was effective at finding resolved ($\geq 5''$) candidate PNe on the basis of morphology, and in general, isolation from extensive diffuse emission and dust clouds. However, because of the finite angular field of the microscope, very large PNe ($\geq 5'$) were sometimes missed. Some additional PNe of very large angular size were discovered by visually examining the blocked-down digital images (see the next point).

Blocked-down survey images

The Hα survey online digital data was useful for a complete re-appraisal of the entire survey, to hunt for extremely low surface brightness and large angular scale PNe, missed from inspection of the original films. Frew & Parker performed a careful systematic visual search of 16×16 (11 arcsecond resolution) blocked-down Hα FITS data of all 233 survey fields, downloaded from the SHS website in 2003. These blocked-down images effectively enhance large angular size, low-surface brightness features (e.g. Pierce et al. 2004), making them easier to detect. Since the fields have an accurate WCS coordinate system built into their FITS headers, reliable positions could be determined for each candidate; $10'$ fields were then downloaded at full resolution to discern the morphology of each candidate and to grade them for spectroscopic follow-up (several flaws were identified at this point).

This search revealed nearly 100 large-scale (>3 arcminute) faint candidate PNe and other nebulosities (including several SNR candidates and highly reddened HII regions), which have formed the basis for further follow-up. These additional confirmed and possible PNe are identified by the FP (Frew-Parker) prefix in the MASH catalogue. SHS Hα images of the 12 largest FP PNe are given in figures 2.10 and 2.11. Further details are given in the online MASH database and in Appendix A. Those objects currently not considered to be PNe are listed in table 2.2, which includes a brief description of their nature.

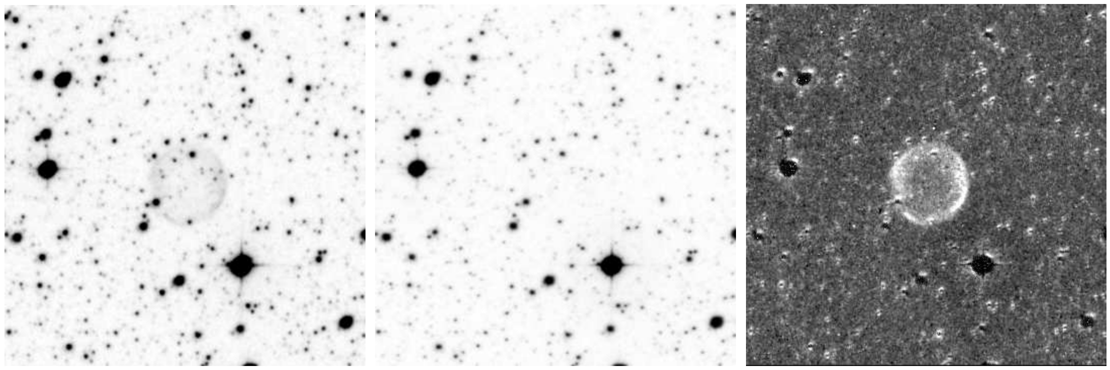

Figure 2.8: $4' \times 4'$ extracts of SHS data around a newly discovered PN, PHR1520-5243. Images show the 3-hr Hα survey data (left), matching 15 min SR data (middle) and a simple quotient image (right). The new PN is 53 arcseconds in diameter and is essentially visible only in the Hα image. Note the well matched depth for point sources between the two exposures.

Difference and/or quotient imaging

Another significant advantage of the SuperCOSMOS Hα and SR data was the ability to perform simple quotient (Hα and SR image division) or more sophisticated difference imaging. This is an effective way of revealing the underlying nebulosity (see fig 2.8), especially if the PN is extremely faint and diffuse, even more so than the nebulae found using the previous technique. The technique works extremely well for very small objects located in a crowded field (i.e. in the Galactic Bulge). This approach works well because the Hα and SR data point spread functions (PSFs) are very similar (e.g. same telescope, emulsion, and stellar limiting magnitude).

Many additional bulge PNe were discovered by the use of a sophisticated difference imaging technique developed by Bond et al. (2001). It is based on variable PSF matching between the Hα data and equivalent broad-band SR data, and gives better performance than simple quotient imaging. In Figure 2.9, three typical examples of new compact bulge PNe uncovered by this technique are presented. This technique has been used on 18 dense bulge fields to reveal 137 new PNe (to go with the 350 PHR PNe found visually in the bulge) which have been subsequently confirmed spectroscopically using the 6dF multi-fibre spectrograph on the UKST (Peyaud, Parker & Acker 2003, 2004, 2005; Peyaud 2005). This technique has also led to the discovery of several new symbiotic stars and other emission-line stars in the bulge.

Recently, the entire set of SR fields has also become available in blocked-down digital form. Hence, Birkby et al. (2007) and Miszalski et al. (2008) have performed quotient (Hα/SR) imaging of all the 16×16 (11 arcsecond resolution) blocked-down images to search for new nebulosities. Over 100 very faint PNe candidates (plus >100 more diffuse HII regions) have been found using this new technique, including two very large objects which are candidates for the solar neighbourhood sample, as well as more than 200 very compact, high surface brightness PNe along the Galactic plane outside of the bulge, missed from the inspection of the original films beacause of their small size. Those that were spectroscopically confirmed have been recently published in the MASH-II catalogue (Miszalski et al. 2008).

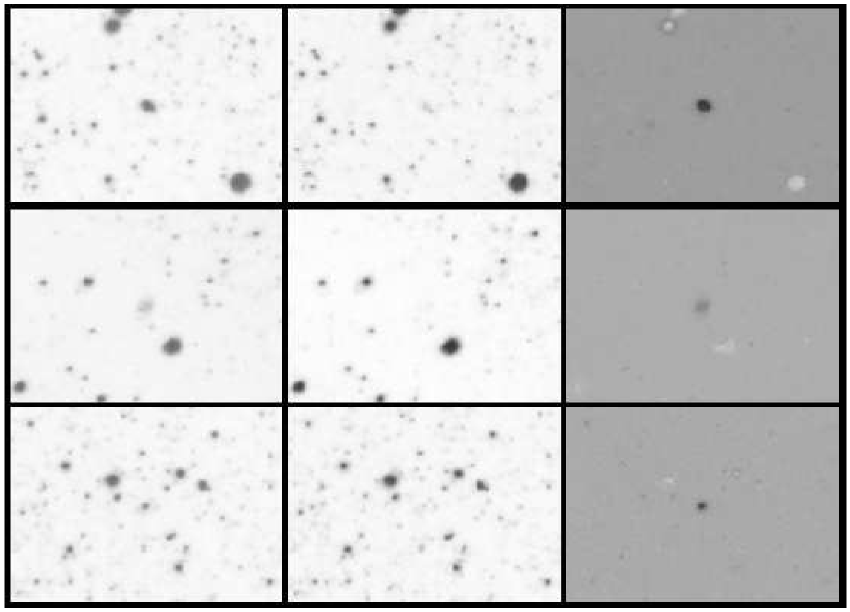

Figure 2.9: SHS extracts (dimensions $1.4' \times 1'$) three newly discovered PNe in the galactic bulge. The columns represent the 3-hr Hα survey data (left), matching 15 min SR data (middle) and difference images based on application of the point-spread function matching scheme of Bond et al. (2001) (right). This method has proven to be very effective in uncovering large numbers of compact emitters in the Galactic bulge (e.g. Peyaud 2005). Figure taken from Parker et al. (2005a).

IAM data

Point-source emitter candidates are also selected from the SuperCOSMOS IAM data (and not the pixel data), using a combination of H$\alpha - R$ versus $R - I$ colour-colour plots (see also Pierce 2005). In Parker et al. (2006a), only four PNe were discovered using this technique; a single PN found by E. Hopewell & Q. Parker during a 6dF spectroscopic follow-up run for emission-line star candidates, and two PNe confirmed at SAAO by R. Pretorius for a similar programme; these have PKP (Pretorius, Knigge, Parker) designations. Since then, Miszalski et al. (2008) used this approach to mine the entire SHS survey exterior to the Galactic Bulge, and have found more than 200 compact Hα emitters, most of which have already had spectroscopic confirmation.

New non-PN Hα point-source and compact emitters are a by-product of this technique. Drew et al. (2004) report the discovery of only the fourth known massive WO star in the Milky Way, while Hopewell et al. (2005) present five new WC9 stars discovered from the SHS data. Pierce (2005) demonstrated the utility of the SHS to reveal significant new populations of Hα emitters (e.g. T Tauri stars) in several star forming regions, in particular the Vela molecular ridge.

2.3.2 MASH projects

Several projects underway by the MASH team will result in major catalogue updates over the next two years. The current MASH catalogue largely contains well-resolved PNe because of the search techniques originally employed before the availability of the online digital SHS data in 2002. These visual scans were not particularly sensitive to compact/barely resolved sources. However, ∼30 per cent of PNe in previous catalogues have angular size $\leq 6''$, so large numbers of faint, barely resolved candidates were expected to be discovered from the survey. As outlined above, several hundred new emitting sources have been found as a result of recent large-scale difference imaging and colour-composite imaging of the survey outside of the bulge, and those objects spectroscopically confirmed as PNe are included in the MASH-II supplement (Miszalski et al. 2008).

A number of individual papers have already been published under the umbrella of the MASH project. The identification of a significant population of new PNe in the Galactic Bulge (e.g. Peyaud, Parker & Acker 2003, 2004, 2005; Peyaud 2005) has already been mentioned). Furthermore, a number of new Wolf-Rayet central stars have been found (Parker, Morgan & Russeil, 2000; Morgan, Parker & Russeil 2001; Parker & Morgan 2003) including the detection of the only [WN] PN central star in the Galaxy (Morgan, Parker & Cohen 2003).

An unusual PN also been reported around a strongly masing OH-IR star (Cohen, Parker & Chapman 2005; Cohen et al. 2006) which may represent a previously unobserved phase in PN evolution. *Spitzer* GLIMPSE observations of MASH PNe have been reported by Cohen et al. (2007). Other MASH papers have detailed the discovery of a very large PN in an early stage of interaction with the ISM, designated PFP 1 (Pierce et al. 2004), as well as two, very large bipolar Type I PNe previously misidentified as HII regions (Frew, Parker & Russeil 2006).

2.3.3 Other projects

New optical counterparts of supernova remnants (SNRs) in the SHS have already been noted by Walker, Zealey & Parker (2001) and in more detail in a parallel study to this one, by Stupar et. al. (2007) and Stupar (2007). One new Galactic SNR discovered serendipitously via the MASH programme has already been reported (Parker, Frew & Stupar 2004; Stupar et al. 2007), and several more have been found from a dedicated search of the SHS (e.g. Stupar, Parker & Filipović 2007, 2008, in preparation). A significant increase in the known population of optically detected Galactic SNRs is promised, comprised of both new discoveries and new optical detections of previously-known radio SNRs.

A new Population I Wolf-Rayet star and its ring nebula, PCG 11, was noted by Cohen, Parker & Green (2005), while many new optical HII regions have also been catalogued. Cohen & Parker (2003) refined the MASH PN database using Midcourse Space eXperiment (MSX) thermal-IR data (see also Cohen et al. 2002, 2007). In addition, a new sample of symbiotic stars and other emssion-line stars has been tabulated. These new discoveries will eventually be published as part of the Miscellaneous Emission Nebula (MEN) catalogue (Parker, Frew et al. 2008, in preparation).

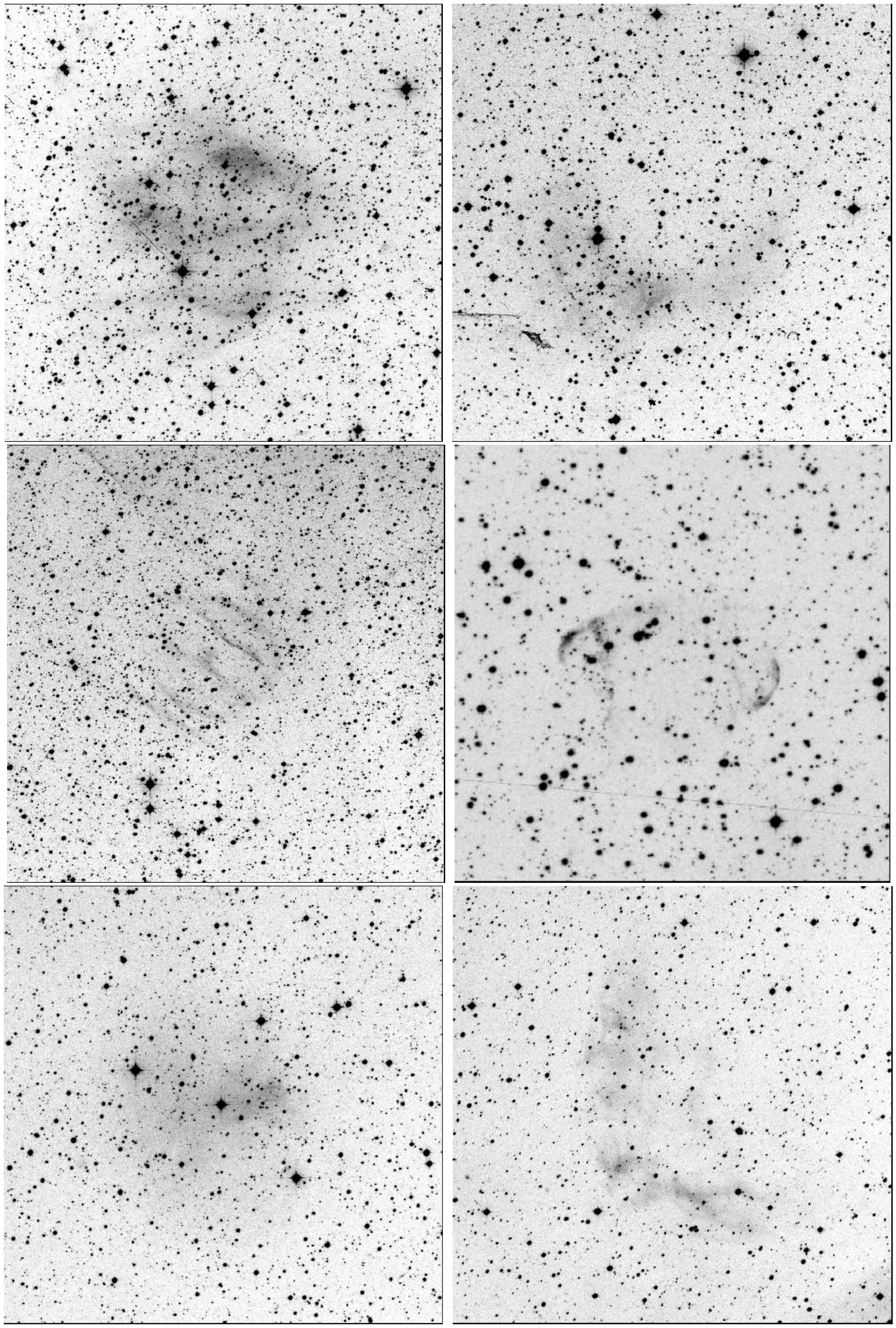

Figure 2.10: Hα images of six newly discovered candidate PNe from the SHS. Top panel: FP 0711-2531 (left, image 20′ wide), FP 0721+0133 (right, 20′); middle panel: FP 0739-2709 (left, 20′), FP 0821-2755 (right, 10′); lower panel: FP 0840-5754 = Fr 2-6 (left, 15′), FP 0905-3033 (right, 20′). North is up and east at left in all images.

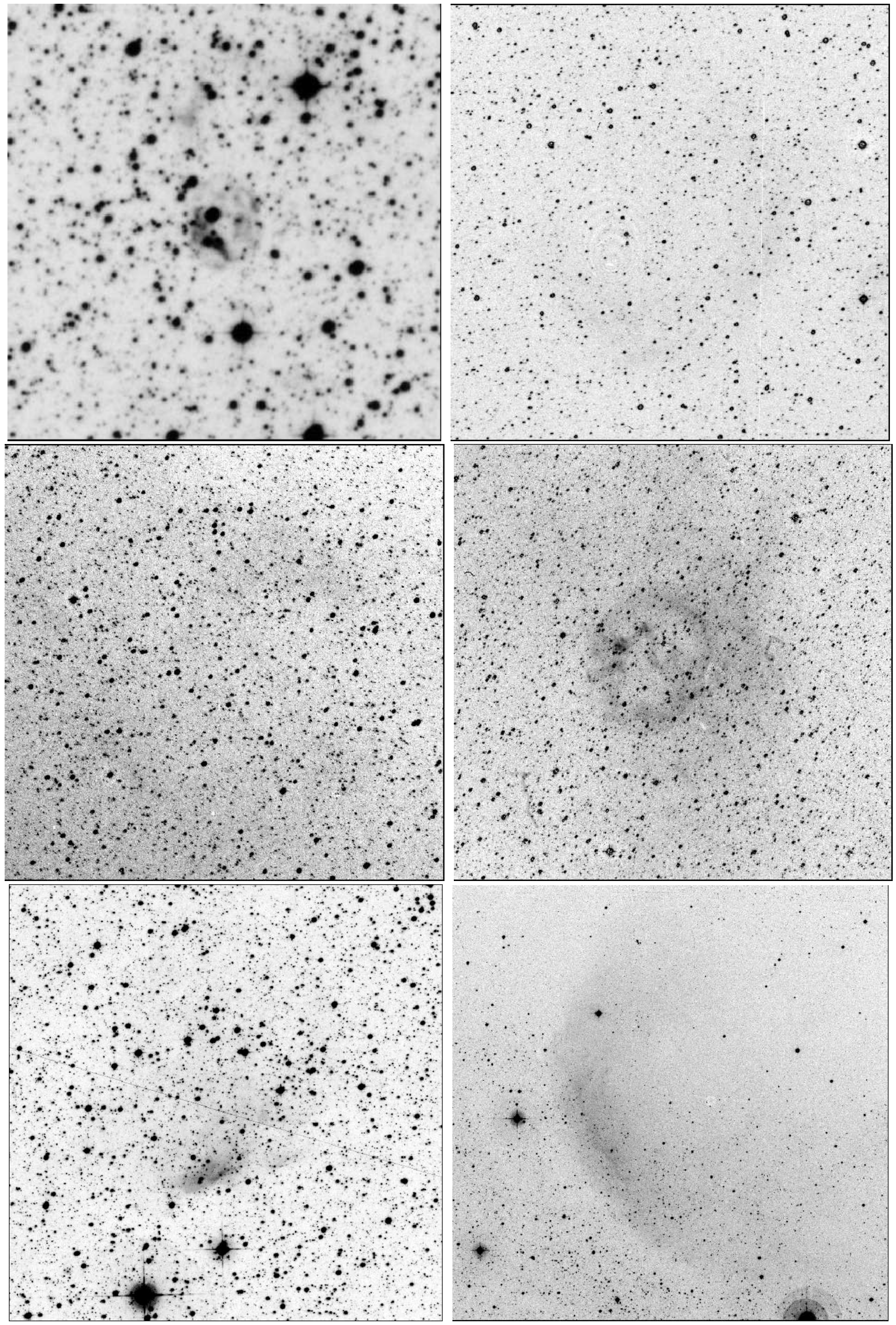

Figure 2.11: Hα images of six more newly discovered candidate PNe from the SHS. Top panel: FP 1554-5651 (left, image 5′ wide), FP 1556-4955 (right, 20′); middle panel: FP 1705-5415 (left, 20′), FP 1721-5654 = Fr 2-12 (right, 20′); lower panel: FP 1804-4528 (left, 15′), FP 1824-0319 (right, 30′). North is up and east at left in all images.

Table 2.2: Nebulae discovered from SHS blocked-down SHS images, rejected as PNe.

Name	Other	α	δ	l	b	a (′)	b (′)	Remarks
FP0646-0003	PMN J0646-0003	06 46 22	-00 03 16	212.40	-1.15	360	300	HII region
FP0648-0613	...	06 48 32	-06 13 44	218.15	-3.48	45	35	Flaw
FP0648-0611	...	06 48 55	-06 11 10	218.16	-3.38	400	340	probable HII region
FP0708-0831	...	07 08 42	-08 31 37	222.48	-0.08	...	...	HII region, ALS 192 involved
FP0709-2555	...	07 09 26	-25 55 57	238.11	-7.85	780	720	Diffuse nebulosity?
FP0723-1146	...	07 23 57	-11 46 50	227.11	1.72	1140	1140	Diffuse emission
FP0741-4107	...	07 41 11	-41 07 48	254.81	-8.95	...	...	elongated HII region
FP0742-1338	...	07 42 17	-13 38 24	230.90	4.75	840	840	Faint amorphous nebulosity
FP0745-2951	...	07 45 42	-29 51 55	245.38	-2.64	600	600	Aysmmetric PN candidate
FP0752-2616	...	07 52 46	-26 16 45	243.08	0.52	180	180	Round compact HII region
FP0800-2829	...	08 00 20	-28 29 40	245.84	0.81	3600	3800	Faint emission ring
FP0823-2722	...	08 23 30	-27 22 48	247.71	5.70	1200	1140	Possible one-sided PN
FP0828-2157	GN 08.26.9, Bran 152	08 28 31	-21 57 54	243.87	9.71	1200	900	Part of Gum nebula
FP0839-5217	...	08 39 05	-52 17 39	269.64	-6.57	450	420	ring or bubble in ISM
FP0850-2831	...	08 50 17	-28 31 50	252.19	9.77	900	720	Irregular HII region
FP0900-5150	...	09 00 15	-51 50 28	271.34	-3.76	1500	1420	large emission patch; real?
FP0904-4023	...	09 04 01	-40 23 40	263.18	4.31	540	540	Irregularly-round PN candidate
FP0911-4051	...	09 11 47	-40 51 32	264.52	5.08	240	170	Faint nebula with outer shell?
FP0917-5019	...	09 17 45	-50 19 10	272.08	-0.70	1200	900	probable HII bubble
FP0921-3828	...	09 21 22	-38 28 32	264.07	8.06	900	840	diffuse emission
FP0926-3737	...	09 26 12	-37 37 38	264.14	9.34	900	720	Probably just diffuse HII?
FP0930-5053	...	09 30 37	-50 53 44	273.94	0.31	15	13	Flaw
FP0931-5540	...	09 31 03	-55 40 40	277.26	-3.13	400	250	real object? flaw?
FP0939-5209	...	09 39 43	-52 09 16	275.84	0.33	360	360	probable HII region?
FP0941-5611	...	09 41 52	-56 11 46	278.74	-2.51	600	540	very faint, round nebula
FP0948-6417	...	09 48 44	-64 17 38	284.67	-8.11	...	...	Flaw
FP0953-6608	...	09 53 00	-66 08 00	286.20	-9.30	1200	1000	vague nebulous arc
FP1001-5458	Bran 279, Fest 2-74?	10 01 38	-54 58 07	280.14	0.21	1252	1082	Symmetric HII region
FP1004-5830	...	10 04 34	-58 30 27	282.57	-2.40	600	540	structured HII region
FP1018-6056	...	10 18 47	-60 56 45	285.44	-3.37	1260	1200	faint ring-shaped HII region
FP1022-5354	...	10 21 50	-53 44 56	281.86	2.89	1200	1140	HII region?
FP1022-5320	...	10 22 20	-53 19 50	281.70	3.27	300	300	Diffuse emission?

Continued on next page

Table 2.2 – continued from previous page

Name	Other	α	δ	l	l	a ($''$)	b ($''$)	Remarks
FP1029-4341	...	10 29 31	-43 41 27	277.52	12.07	720	660	large ring nebula?
FP1038-5802	RCW 51, vdBH 42a, Hf 30	10 38 34	-58 02 29	286.08	0.41	300	300	Round wispy HII region
FP1054-7011	Fr 2-7, MPA1054-7013	10 54 10	-70 11 45	293.25	-9.56	485	400	Isolated emission patch
FP1100-5816	...	11 00 22	-58 16 40	288.75	1.50	360	90	probable HII region
FP1116-5443	...	11 16 22	-54 43 50	289.41	5.63	...	...	possible filament of SNR?
FP1116-6129	Bran 351	11 16 34	-61 29 52	291.86	-0.86	120	100	Unusual HII region?
FP1200-5317	...	12 00 02	-53 17 36	295.20	8.81	480	240	probable flaw
FP1312-5819	...	13 12 32	-58 19 19	305.71	4.44	660	180	HII emission?
FP1333-5754	...	13 33 30	-57 54 00	308.51	4.52	1200	1200	large, faint emission patch
FP1337-6400	IRAS 13342-6345	13 37 41	-64 00 42	307.97	-1.59	35	20	peculiar HII region
FP1415-6714	...	14 15 45	-67 14 31	310.97	-5.70	2400	1500	large emission ring
FP1444-5950	...	14 44 48	-59 50 36	316.70	-0.05	600	300	peculiar knotty HII region
FP1448-5641	...	14 48 20	-56 41 24	318.50	2.61	540	540	diffuse emission ?
FP1514-5814	...	15 14 29	-58 14 26	320.85	-0.43	...	...	arcuate nebula
FP1538-4740	...	15 38 52	-47 40 26	329.80	6.27	...	...	filament or flaw?
FP1545-6801	...	15 45 55	-68 01 44	318.15	-10.48	...	...	no detection on spectrum; flaw
FP1549-5643	...	15 49 52	-56 43 54	325.60	-1.90	...	...	Flaw ?
FP1611-5202	...	16 11 13	-52 02 39	331.02	-0.42	...	...	probable diffuse emission region
FP1612-4952	LEDA 3077847	16 12 08	-49 52 18	332.61	1.07	14	12	small compact neby; YSO?
FP1612-5109	...	16 12 27	-51 09 08	331.77	0.10	...	...	probable HII region
FP1613-5405	...	16 13 03	-54 05 28	329.82	-2.10	330	160	faint nebula of uncertain nature
FP1615-4949	...	16 15 05	-49 49 09	332.99	0.78	200	180	probable HII region
FP1616-5117	G332.1-00.5	16 16 45	-51 17 54	332.20	-0.45	...	...	compact HII region
FP1634-3626	...	16 34 21	-36 26 09	345.06	7.61	480	480	irregularly round emission patch
FP1636-4032	...	16 36 41	-40 32 18	342.30	4.52	360	330	probable HII region
FP1639-5233	...	16 39 23	-52 33 00	333.67	-3.85	480	270	general emission
FP1644-5807	...	16 44 34	-58 07 35	329.91	-8.06	1800	900	SNR? HII region?
FP1648-5918	...	16 48 20	-59 18 30	329.31	-9.19	240	180	probable general emission
FP1648-6115	...	16 48 28	-61 15 30	327.78	-10.43	690	660	vaguely ringlike nebula
FP1659-5013	...	16 59 53	-50 13 30	337.51	-4.83	...	...	general emission?
FP1705-4609	...	17 05 15	-46 09 52	341.28	-3.06	300	300	HII region around B2II star
FP1706-4246	...	17 06 02	-42 46 01	344.13	-1.09	27	14	unusual flaw
FP1706-4242	...	17 06 05	-42 42 21	344.13	-1.09	540	540	diffuse emission / HII region
FP1710-3137	...	17 10 31	-31 37 21	353.56	4.82	...	...	diffuse emission?
FP1729-3637	...	17 29 28	-36 37 46	351.69	-1.26	...	...	known as SNR 351.7-01.2

Continued on next page

Table 2.2 – continued from previous page

Name	Other	α	δ	l	l	a ($''$)	b ($''$)	Remarks
FP1729-5423	...	17 29 58	-54 23 09	336.71	-10.97	...	...	faint diffuse HII region
FP1732-5100	...	17 32 30	-51 00 14	339.84	-9.51	...	...	faint irregular emission region
FP1739-4529	...	17 39 28	-45 29 15	345.20	-7.60	...	...	small emission patch
FP1755-1301	...	17 55 16	-13 01 44	14.86	6.18	420	390	probable HII region?
FP1756-4420	...	17 56 47	-44 20 32	347.76	-9.69	1500	1500	large, faint nebula around HR 6675?
FP1800-4416	...	18 00 25	-44 16 45	348.20	-10.20	1200	1000	general emission
FP1811-2206	...	18 11 05	-22 06 25	8.78	-1.56	780	600	WR bubble or SNR?
FP1819-0330	...	18 19 50	-03 30 57	26.17	5.41	270	100	v.v. faint arcuate object
FP1859-1049	...	18 59 46	-10 49 53	24.19	-6.75	720	720	probable diffuse emission
FP1900+0115	...	19 00 33	+01 15 40	35.09	-1.45	540	450	large dusty HII region

2.3.4 Spurious images in the SHS

It was noted in §1.7 that a number of catalogued PNe have turned out to be emulsion flaws. Since the source material for the MASH project is photographic film, it is germane to consider the nature of flaws and defects in some detail. Furthermore the production of the digital SHS from the survey films using SuperCOSMOS has introduced an additional population of spurious images that would not otherwise be present. In summary, flaws may be classed as spurious images in the emulsion itself due to processing defects or electrostatic marks, and those caused by contaminants on the surface of the emulsion or on the back of the film prior to scanning with SuperCOSMOS. Satellite trails and transient phenomena (asteroids, novae) produce real images which may have no counterpart in other survey bands of the same region, and are not considered here.

Flaws can sometimes be picked up by examination of the pixel images directly, though they are often missed, and can also appear as spurious detections in the IAM data. The spurious images have a variety of sizes and shapes and may be in or out of focus depending on whether the contaminating source is on the emulsion surface or on the platten used by SuperCOSMOS to sandwich the film flat for scanning.

The SuperCOSMOS machine is located in a class-100 clean room and each film is air-cleaned prior to scanning. However, contaminating dust particles (∼20–100 μm in size) are sometimes present on the emulsion before shipment to SuperCOSMOS. Unfortunately the *estar* base of the Tech-Pan film used for the exposures is prone to charge build-up. This occurs when the film is first inserted into its protective cellophane envelope after developing at the telescope. This is done in a non-clean room environment at the UKST and fine particles can be drawn onto the emulsion surface at this time (Parker 2003, pers. comm; Parker et al. 2005a). Hence Tech-Pan film exposures are particularly prone to spurious images from dust and crud which can lead to a higher level of artefacts in the SHS data compared to the other glass-plate based surveys of the SSS. A more detailed discussion of these spurios images is provided in Parker et al. 2005). In general flaws produced from particulate dust are not relevant to the present study through quasi-stellar spurious images may be mistaken for small PNe or PN central stars[15].

The SuperCOSMOS scanning system is highly specular so detritus present on the emulsion surface that is often invisible when viewed on a light table is revealed in bold relief in the scanned SuperCOSMOS data. Fortunately, having matched exposures in two bands (Hα & SR) makes identification of these artefacts more straightforward. For example, since the Hα and SR exposures are registered on the same pixel grid, quotient or difference imaging can reveal the locations of spurious images. We can also take advantage of the fact that the image properties of spurious images are usually quite distinct from real astronomical images, often being sharper than is possible from the combination of telescope optics and seeing disk, and therefore not consistent with any normal PSF. To illustrate some of the flaws visible on the Hα data, a 5×5 arcminute region extracted from HA273, a survey field with a particularly high level of spurious images, is shown in the two left panels of Figure 2.12. In general spurious images due to the

[15]Further details can be found at http://www-wfau.roe.ac.uk/sss/halpha/haspurious_images.html

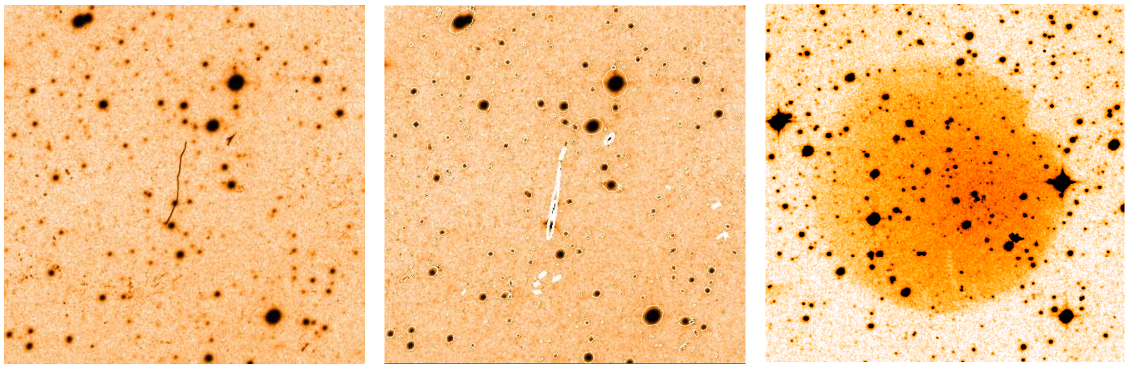

Figure 2.12: Left and Centre: 5 × 5 arcminute extracts of SuperCOSMOS Hα data highlighting a contaminating spurious image together with a matching image with the IAM data overlaid and with all the spurious images in the frame highlighted. Right: A 5 × 5 arcminute image showing a mandrel flaw. Note the typical spherical outline as well as a characteristic 'notch' at top right.

presence of crud only become evident on examining the full-resolution pixel data. That is, they may mimic a true astronomical object on the blocked-down images. A number of 'PN candidates' were noted during an examination of the blocked-down FITS whole-field images by Frew & Parker. These were only later noted as flaws or crud after examining the full-resolution data.

One unusual type of artefact is unique to the SHS, which derives from the use of a special vacuum-backed mandrel in the film/plate holder of the UKST. Small metal tubes attached to a vacuum pump are used in order to keep the flexible Tech-Pan film coincident with the curved focal surface (not necessary for glass plates). Unfortunately, in some cases as the film was being removed from the holder, stray light entered the metal tubes, forming circular artefacts on the film which look rather like faint spherical PNe. In general, the uniform surface brightness and very circular outline of these mandrel flaws belies their origin as does their consistent x, y coordinates from field to field (see the right panel of Figure 2.12).

2.4 SHASSA

Except for the Magellanic Cloud fields (see Reid & Parker 2006a,b), the AAO/UKST Hα survey is restricted to within about 10–12° of the Galactic Plane. To supplement the search for PNe from the AAO/UKST Survey, the writer visually searched the entire Southern Sky H-Alpha Survey Atlas (SHASSA; Gaustad et al. 2001)[16], outside a Galactic latitude of $|b| = 10°$, with the aim of discovering new evolved PNe in the Solar Neighbourhood.

2.4.1 Survey Characteristics

SHASSA is a robotic wide-angle digital imaging survey of the of the southern sky, with the aim of detecting Hα emission from the warm ionized interstellar medium. It is comprised of narrowband (Hα + [N II]) and continuum images of the entire southern sky ($\delta \leq +15°$). SHASSA

[16] http://amundsen.swarthmore.edu/SHASSA/

has coarse spatial resolution (48″ pixels) but is continuum-subtracted and flux calibrated.

SHASSA consists of 2168 images covering 542 fields south of +16° declination. There are four images available for each field: Hα, red continuum, continuum-corrected Hα (generated by subtracting each continuum image from the corresponding Hα image), and a smoothed Hα image. Each image subtends 1014 × 998 pixels (∼13° on a side). The Hα images have an effective resolution of 48″ and a limiting sensitivity of better than 2 R pixel^{-1}, corresponding to an emission measure of 4 cm^{-6} pc. The smoothed images are median-filtered to 5 pixels (4.0′) resolution and allow features as faint as 0.5 R to be detected. Additionally, the smoothed images generally remove star residuals better, though these images were not utilised in the search for new emission nebulosities, nor for determing flux measurements of new and known PNe (see the next chapter). Further details are given by Gaustad et al. (2001).

SHASSA is accurately flux-calibrated across the whole survey (see Chapter 3, and Finkbeiner 2003) and is of great utility for determining integrated fluxes for large and/or reasonably conspicuous PNe, as well as providing an accurate baseline calibration for the SHS data (see Pierce 2005; Parker et al. 2006a; Parker et al. 2008, in prep).

2.4.2 Search Technique and Results

The continuum-subtracted SHASSA Hα fields contain large numbers of filter artifacts (especially near bright stars), compact emitters and variable stars. This precludes the use of an automated search technique for new PN candidates. Hence a visual 'eyeball' search was conducted of all SHASSA fields, outside of a Galactic latitude of 10°. Candidates were selected as discrete, symmetric Hα enhancements, to differentiate them from the diffuse ISM background. As a result, seventeen nebulae were found from SHASSA images[17]. With one exception, Fr 2-8, all candidate nebulae are >5′ across (i.e. ∼7 SHASSA pixels)[18]. All previously known PNe larger than this size in the latitude zone examined were recovered in this blind search, as was the putative large PN Hewett 1 (Hewett et al. 2003), and the nebulae associated with the hot stars PHL 932, PG 0108+101 and PG 0109+111 (see Chapter 8). Figures 2.13 and 2.14 present image cutouts from SHASSA or VTSS for each of the discoveries.

Table 2.3 summarizes the main properties of the new nebulae, updated from the table published in Frew, Madsen & Parker (2006). Two additional objects (nos. 19 and 20) have been designated since the publication of that paper. The inividual nebulae are discussed in more detail in §B.3 in the backmatter. Most of the new discoveries are probable Stromgren zones in the ISM, and some were independently found as 'point-source' enhancements in the WHAM data, a product of the 1° beam size of the instrument (see Reynolds et al. 2005). Some nebulae show unusual line ratios for HII regions (e.g. strong [O III] or [N II] emission) based on slit spectroscopy and WHAM data (see Chapter 8, and Madsen et al. 2006 for further

[17]The 'Fr 2-' designation is applied to the 20 possible PNe and diffuse nebulae found from SHASSA and VTSS images, analogous to the true and possible nomenclature used by Kohoutek (1963b, and subsequent papers). The 'Fr 1-' designation refer to two *true* PNe found prior to the commencement of this thesis from broadband photographic plates (see Frew 1997 and Frew, Parker & Russeil 2006).

[18]The high-excitation PN Fr 2-8 was found serendipitously from SHASSA field 057. It had been independently noted as a PN by Côte et al. (1997), but no details were provided in their paper.

details), suggesting these are ionized by a hot subdwarf or white dwarf star, and may be possible PNe (see below). Arguably the most interesting discovery, though not a PN, is a remarkable bow-shock nebula, Fr 2-11, associated with the star V341 Ara, a previously unknown nova-like catalcysmic variable (Frew et al. 2008, in prep., and see §B.2).

In addition, a *targeted search* for emission nebulae was undertaken from the SHASSA survey, plus a few available VTSS fields (see below). To faciliate this, a working list of hot white dwarfs and subdwarfs culled from the literature was constructed. The stars were taken primarily from the updated list of McCook & Sion (1999)[19], sorted by spectral type (DO or DA) and/or by blue $U-B$ and $B-V$ colour indices. Additional stars were taken from the compilation of Napiwotzki (1999), while a set of sundry hot stars and subdwarfs were taken from Méndez et al. (1988c), Kwitter et al. (1989), Tweedy & Kwitter (1994), Werner et al. (1997) and Rauch (1999), to see if any nebulae had been missed by these authors. In addition, Reynolds (1987) conducted a high-sensitivity search for Hα emission enhancements around nine hot low-mass stars that have no associated emission nebulosity visible on the POSS (emission measures <60 cm^{-6}pc). These stars were also included in the working list.

The search technique was straightforward: for each hot star, the relevant SHASSA or VTSS fits image was examined in the GAIA image viewer, and the cursor was moved to the stellar position using the embedded WCS. Any discrete Hα enhancements, diffuse Hα emission, or other features were noted, though the vast majority of stars had no obvious detection. Table 2.4 lists the stars which were examined in this way. It should be noted that the number of catalogued hot white dwarfs in the northern hemisphere is greater than that in the south by roughly a factor of two, at the time this search was conducted (2004). This bias is being slowly remedied by new surveys in the south, e.g the Edinburgh-Cape Survey (Stobie, Kilkenny & O'Donoghue 2004), but the necessary observational follow-up to obtain accurate photometry and spectral typing for many stars remains to be done.

Disappointingly, only one possible PN candidate was noted as a result of this supplementary search, and a poor quality one at that, a faint diffuse nebula north following the DAO star, HS 2115+1148 (Dreizler et al. 1995; Rauch 1999). In addition, the previously known diffuse nebulae around PG 0108+101, PG 0109+111 and PG 1034+001 (see Chapter 8) were noted during this search, redundantly, as it turned out. Other nebular detections are noted in Table 2.4, but can be attributed to diffuse background emission, rather than being fossil PNe.

2.5 VTSS

A complementary survey to SHASSA, the Virginia Tech Spectral line Survey (VTSS; Dennison, Simonetti & Topasna 1998)[20] covers the northern hemisphere ($\delta > -15°$) along a wide strip around the Galactic plane ($|b| \leq 30°$). Like SHASSA, the combination of fast optics (f/1.2), narrowband interference filters, and a CCD gives this survey very deep sensitivity to diffuse Hα emission.

[19]see the Vizier online catalog III/235A at http://vizier.u-strasbg.fr/
[20]http://www.phys.vt.edu/halpha

The VTSS used the Spectral Line Imaging Camera (SLIC), which obtains 10° wide images in the light of Hα and [S II] λ6717,6731Å emission, using narrowband interference filters. The Hα filter has a narrower bandpass filters than SHASSA (17Å, with essentially no transmission of the flanking [NII] lines). The VTSS survey consists of a partial set of 10° diameter circular images with a sensitivity limit of ~1 Rayleigh, comparable to SHASSA. However, the resolution is approximately half that of SHASSA, with 96″ pixels. Each field name consists of the standard 3-letter IAU constellation abbreviation, plus a 2-digit running number (e.g. Cyg10).

Each field was planned to have four images available: Hα, [S II], continuum-corrected Hα, and continuum-corrected [S II]. The continuum-corrected Hα and [S II] images are produced by subtracting an aligned and scaled continuum image from the H-alpha or [S II] image. Continuum images are taken with a wide-bandpass filter, or a double-bandpass filter straddling the H-alpha line or [S II] doublet (Dennison, Simonetti & Topasna 1998).

2.5.1 Search Technique and Results

Available fields from the VTSS were also examined for nebulosities similar in character to those discovered on the SHASSA fields. Unfortunately less than half of the survey is complete at present (currently 107 fields), and no new data has been placed on the VTSS website since 2004. This has limited the utility of this survey to add to the discoveries made from the SHASSA survey.

The VTSS contains rather fewer numbers of artifacts, though the coarser resolution has made the identification of separate emission regions more difficult, especially in areas of widespread diffuse emission. As for SHASSA, these candidates were selected as discrete, morphologically symmetric Hα enhancements, though the symmetry criterion was relaxed somewhat for the VTSS survey due to its poorer inherent resolution. Only three new objects were found from the available fields of VTSS. All three nebulae are probable Strömgren spheres in the ISM, and their main properties are summarised in Table 2.3. The individual nebulae are discussed in more detail in §B.3.

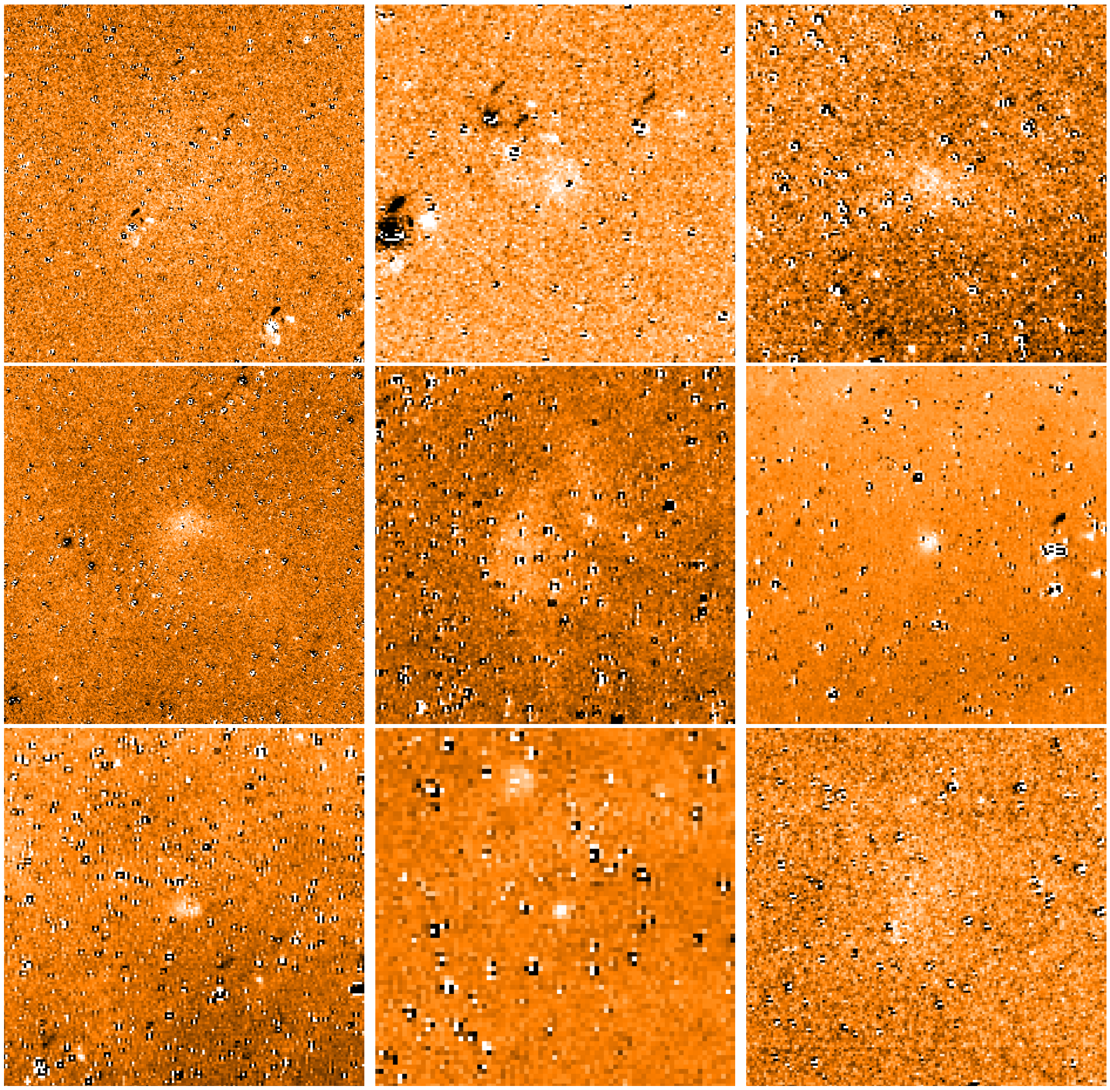

Figure 2.13: SHASSA discovery images of the emission nebulae Fr 2-1 to Fr 2-9. Top panel: (L): Fr 2-1 (image, 240′ wide). (C): Fr 2-2 (60′). (R): Fr 2-3 (240′). Middle panel: (L): Fr 2-4 (240′). (C): Fr 2-5 (60′). (R): Fr 2-6 (60′). Lower panel: (L): Fr 2-7 (60′). (C): Fr 2-8 (30′). (R): Fr 2-9 (60′). NE is at top left in all images.

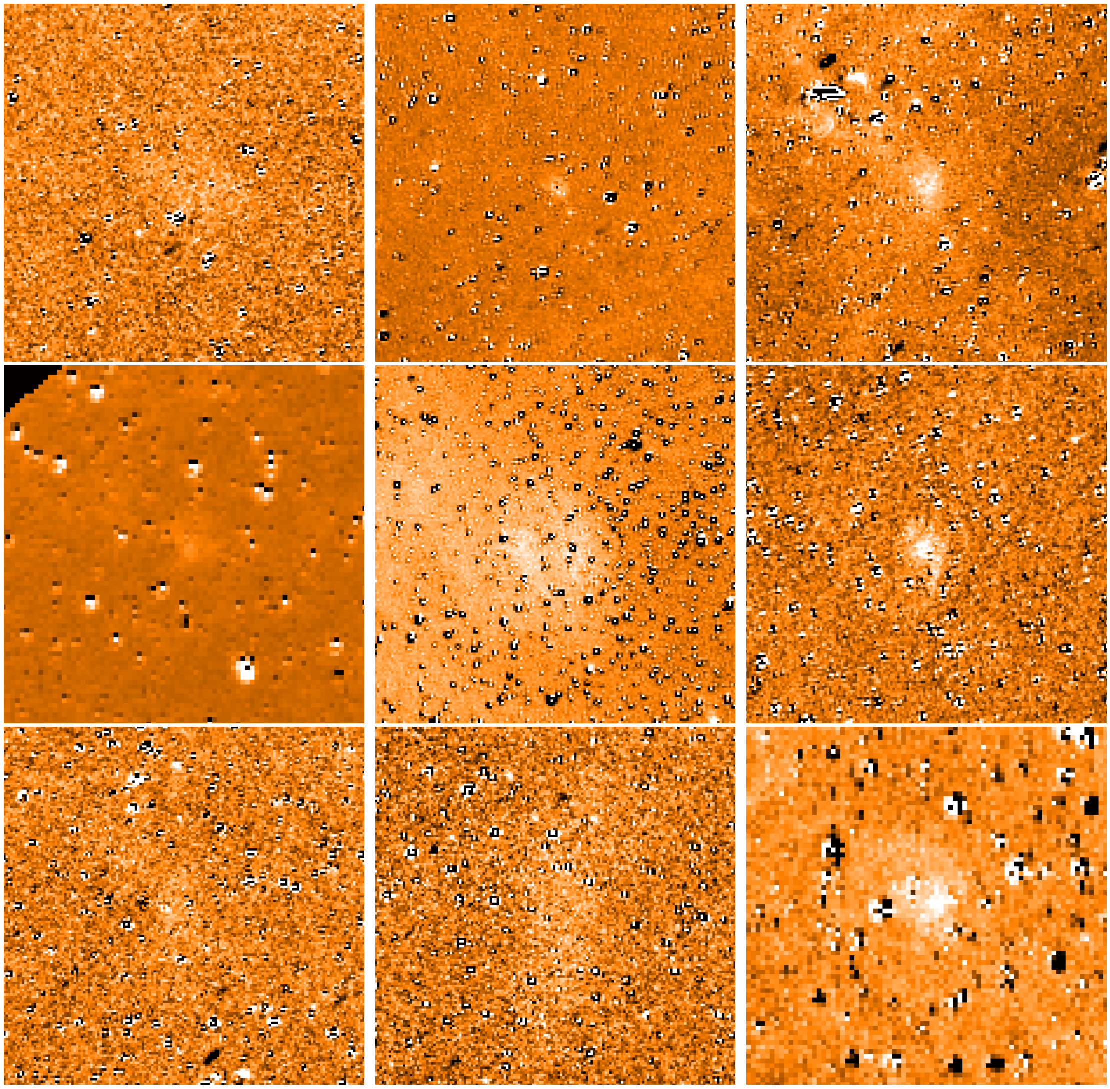

Figure 2.14: SHASSA and VTSS discovery images of the emission nebulae Fr 2-10 to Fr 2-18. Top panel: (L): Fr 2-10 (image, 240′ wide). (C): Fr 2-11 (60′). (R): Fr 2-12 (60′). Middle panel: (L): Fr 2-13 (60′). (C): Fr 2-14 (240′). (R): Fr 2-15 (60′). Lower panel: (L): Fr 2-16 (60′). (C): Fr 2-17 (60′). (R): Fr 2-18 (60′). NE is at top left in all images.

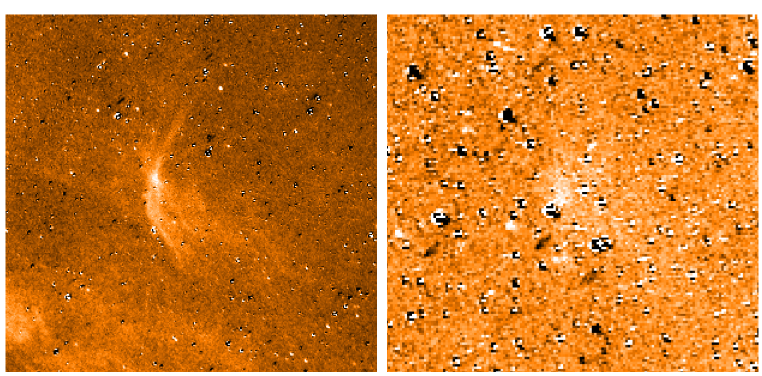

Figure 2.15: SHASSA discovery images of the emission nebulae Fr 2-19 (left) and Fr 2-20 (right). Images are 120′ and 240′ on a side respectively. NE is at top left in both images.

Table 2.3: Details for 20 Hα nebulae discovered from the SHASSA and VTSS surveys. The positions are for J2000. Column 7 gives the field number (SHASSA fields have the 3 digit code while VTSS fields include a constellation prefix), while columns 8 and 9 give the ID and V magnitude of the suggested ionizing star candidate. Columns 10 and 11 give the Hα flux (from SHASSA, VTSS and/or WHAM data) and the [O III]λ5007 flux from WHAM data (see Chapter 3). The last column gives alternative identifications for the nebulae, including objects from the WHAM Point Source Catalogue (WPS; Reynolds et al. 2005) and some nebulae which were independently picked up in the SHS data covering the overlap zone (FP objects).

Name	R.A.	Dec.	l	b	Size (arcmin)	Field	Star	V	F(Hα)	F(5007)	Type	Other ID
Fr 2-1	01 02 00	−61 18 00	300.9	−55.8	100 × 95	025	LB 3174	12.34	...	...	HII	...
Fr 2-2	02 40 46	+10 21 16	161.9	−44.1	20 × 15	238	...	...	−11.1	...	?	WPS 53
Fr 2-3	04 56 20	−28 07 48	229.3	−36.2	20 × 15	101	MCT 0455-2812	13.95	−10.8	−10.6	HII?	...
Fr 2-4	07 11 52	−82 03 03	294.1	−26.1	90 × 60	004	...	...	−10.35	...	HII?	...
Fr 2-5	08 10 14	−67 27 22	280.7	−17.8	80 × 45	015	...	...	...	...	HII?	...
Fr 2-6	08 40 23	−57 54 49	274.3	−9.8	8.2 × 6.3	031	...	...	...	...	PN?	FP 0840-5754
Fr 2-7	10 54 10	−70 11 45	293.2	−9.6	8.0 × 7.5	016	...	...	...	...	PN?	FP 1054-7011
Fr 2-8	14 00 43	−51 02 12	313.9	+10.4	2.0 × 1.9	057	...	...	−11.5	...	PN	AM 1357-504
Fr 2-9	14 23 31	−09 18 48	337.6	+47.3	80 × 60	184	G124-26	15.48	−10.3	−10.0	HII	WPS 82
Fr 2-10	15 09 19	−05 20 54	353.9	+43.5	30 × 30	720	PG 1506-052	14.0	−10.7	−11.2	HII?	...
Fr 2-11	16 57 48	−63 12 00	327.5	−12.5	8.0 × 6.0	037	V341 Ara	10.7$_v$	−10.9	...	CV	...
Fr 2-12	17 21 09	−56 54 25	333.9	−11.3	7.3 × 6.0	038	...	...	−11.0	...	PN?	FP 1721-5654
Fr 2-13	17 59 00	+34 29 36	60.5	+25.1	15 × 12	Her13	...	...	−11.1	...	HII	...
Fr 2-14	20 26 00	+76 37 00	109.8	+21.1	90 × 80	Cep08	...	...	...	...	HII	WPS 31
Fr 2-15	20 27 16	+11 49 20	55.1	−15.1	25 × 20	265	...	...	−10.4	−10.6	PN?	WPS 16
Fr 2-16	21 18 30	+12 01 36	62.9	−25.1	30 × 15	266	HS 2115+1148	16.7:	...	...	HII?	...
Fr 2-17	21 19 45	−56 23 45	339.7	−42.7	80 × 30	041	...	...	...	...	HII?	...
Fr 2-18	23 11 41	+29 27 54	98.2	−28.6	30 × 25	Peg13	...	...	−10.7	−11.0	HII?	...
Fr 2-19	16 10 30	−33 57 30	343.4	+12.8	120 × 70	116	...	...	...	...	?	...
Fr 2-20	20 20 08	+14 58 54	56.8	−11.9	25 × 15	265	...	...	...	...	HII?	...

Table 2.4: Targeted SHASSA and VTSS nebula search. The columns give the usual name of the white dwarf or subdwarf, J2000 position, spectral type of the star, V magnitude (blue magnitudes are denoted with the suffix B), SHASSA or VTSS field name, and a comment on the detection, if any. Some abbreviations used are: neb = nebulosity, f = fol = following, fil = filamentary, bg = background emission, p = preceding, poss = possible, nr = near.

Name	R.A.	Dec	Spectral type	V mag	Field	Detection
MCT 0130-1937	01 32 39	-19 21.6	DO.5	15.84	129	no
PHL 645	00 04 31	-24 26.3	sdO	13.90	627	no
KPD 0005+5106	00 08 17	+51 22.9	DOQZ.4	13.32	Cas01	bg
PHL 703	00 10 07	-26 12.9	sdO	12.88	627	no
MCT 0019-2441	00 21 59	-24 25.3	sdO4	14.49	127	no
RE 0029-632	00 29 56	-63 24.6	DA1	15.31	24	no
GD 619	00 33 54	-27 08.4	DA1	14.18	96	no
GD 8	00 39 56	+31 32.6	DA1	14.66	And12	no
LB 1566	00 40 13	-55 01.9	sdO	13.13	543	no
PG 0046+078	00 48 38	+08 02.7	DO.7	15.59	199	no
GD 659	00 53 17	-32 59.9	DA1.5	13.36	96	no
LB 3174	01 02 54	-60 33.4	sdB	12.34	25	poss
MCT 0101-1817	01 04 12	-18 03.0	DO	16.5	128	no
TON 191	01 06 46	-32 52.9	DA1	13.57	96	no
PG 0108+101	01 11 06	+10 21.5	DOZ.6	15.61	236	yes
PG 0109+111	01 12 23	+11 23.5	DOZ.7	15.40	236	yes
HS 0111+0012	01 13 46	+00 28.4	DOZ.8	14.5	200	no
WD 0123-842	01 21 56	-84 01.4	...	...	2	no
RX J0122.9-7521	01 22 55	-75 21.1	PG1159	15.45	11	no
PHL 1043	01 34 24	-16 07.1	DA1	13.98	664	no
SB 705	01 43 08	-38 33.3	sdO	13.03	69	no
MCT 0146-3426	01 48 37	-34 11.8	sdO6	15.45	69	no
KUV 01542-0710	01 56 42	-06 55.6	DA	16.30	700	no
PG 0205+13	02 08 03	+13 36.5	DA1	13.78B	237	no
LB 3241	02 13 12	-49 44.9	sdO	12.73	45	no
PG 0216+032	02 19 19	+03 26.9	sdOC	14.5	201	no
PG 0217+155	02 20 35	+15 44.1	sdO	15.0	238	no
PG 0226+151	02 28 50	+15 20.6	sdO	15.0	238	no
LB 1628	02 30 53	-47 55.4	DA	14.52	45	no
HS 0231+0505	02 33 42	+05 18.7	DAO	16.10	202	neb fol
Feige 24	02 35 08	+03 43.2	DAZQO1	12.25	202	no
HBQS 0253+0023	02 56 25	+00 36.0	DA	18.74	202	no
GR 270	03 04 37	+02 57.0	DA1.4	15.04	203	no
KUV 03301-0100	03 32 39	-00 49.9	DA	15.86	203	bg
KUV 03302-0143	03 32 43	-01 32.8	DA	17.30	203	bg
SDSS J034227.62-072213.2	03 42 27	-07 22.2	DO	17.88	168	bg
KUV 343-7	03 46 26	-00 38.5	DA1	14.91	204	no
QSF 2:01	03 46 47	-45 39.6	DAB?	18.09	47	no
GD 50	03 48 50	-00 58.4	DA1	13.99	204	fil nr
RBS529	04 15 39	-40 23.1	DA	16.44	72	no
RE 0443-034	04 43 07	-03 47.3	DA.70	16.7	205	bg
MCT 0455-2812	04 57 12	-28 07.8	DA	13.95	101	neb Sf
RE 0503-289	05 03 54	-28 55.1	DOZ1	13.91	102	no
FB 44	05 05 30	+52 48.8	DA.8	11.78	Cam01	ring Sp
050618-240415	05 06 19	-24 04.2	DO.7	15.2	134	bg?
HS 0505+0112	05 08 31	+01 16.6	DAOZ	14.9B	206	bg
RE J0521-102	05 21 19	-10 29.1	DA1.5	15.89	170	bg
GD 257	05 50 38	+00 06.0	DA	14.79	207	bg

Continued on next page

Table 2.4 – continued from previous page

Name	R.A.	Dec	Spectral type	V mag	Field	Detection
LTT 11733	05 52 27	+15 53.2	DA1.5	13.06	243	bg
RE J0558-373	05 58 10	-37 35.0	DA:	14.37	74	no
RE J0605-482	06 05 02	-48 20.4	DA1.4	15.82	49	bg
RE 0623-374	06 23 12	-37 41.4	DA	12.09	74	no
RE J0632-050	06 32 57	-05 05.7	DA	15.54	707	no
Lanning 14	06 43 14	+01 30.1	DO1	15.0B	208	bg
HD 49798	06 48 05	-44 19.0	sdO	8.27	75	bg
GD 080	06 54 13	-02 09.2	DA1.5	14.84	208	bg
RE 0720-314	07 20 48	-31 47.1	DAO1+dM5	14.82	105	bg
KPD 0720-0003	07 22 54	-00 09.1	sdO	15.78	209	no
LSS 630	07 39 42	-27 27.4	sdO	13.56	105	bg
RE J0841+032	08 41 03	+03 21.0	DA1.3	14.48	211	bg
PG 0916+064	09 18 42	+06 17.0	DA1	15.66	248	no
KS 292	09 20 10	-45 31.9	sdO	11.33	577	bg
PG 0928+085	09 31 09	+08 19.6	DA2	16.22B	248	no
EC 09423-1304	09 44 44	-13 18.4	sdO	16.48	176	no
GD 104	09 47 03	-09 19.8	DA1	15.95	177	no
PG 0950+023	09 52 45	+02 09.6	DA1	...	213	no
PG 0953+024	09 55 35	+02 12.6	sdO	15.0B	213	no
EC 09566-1144	09 59 07	-11 59.2	sdB	15.69	177	no
EC 09582-1151	10 00 43	-12 06.0	sdO	14.05	177	no
EC 10016-1923	10 04 01	-19 37.8	sdO	15.28	141	no
HE 1008-1757	10 10 33	-18 11.8	DA1	14.75	141	no
PG 1010+065	10 13 28	+06 12.1	DA1	16.58	249	no
EC 10112-1722	10 13 39	-17 37.3	sdO	16.47	142	no
RX J1016.4-0520	10 16 28	-05 20.5	DAO1+dM5	14.15	713	no
PG 1023+009	10 25 49	+00 39.0	DA2	16.3	213	no
EC 10300-1022	10 32 35	-10 38.5	sdO	16.96	178	no
PG 1034+001	10 37 04	-00 08.4	DOZ1	13.23	214	yes
EC 10346-1234	10 37 09	-12 49.8	DAs	16.14	178	no
EC 10475-2703	10 49 55	-27 19.2	sdO	13.49	109	no
EC 10479-2714	10 50 18	-27 30.7	sdO	13.90	109	no
EC 10481-1503	10 50 39	-15 18.9	DA1	16.86	178	no
PG 1057-059	11 00 09	-06 11.4	DO1	16.21B	178	no
110844-152408	11 08 45	-15 24.2	DA1	16.64	143	no
PG 1125-026	11 28 14	-02 50.4	DA1.5	15.32	715	no
PG 1125-055	11 28 16	-05 46.4	sdO	16.28	715	no
EC 11366-2504	11 39 10	-25 20.9	sdO	14.11	144	no
PG 1141+078	11 43 59	+07 29.0	DA1	14.11B	252	no
EC 11437-3124	11 46 18	-31 41.0	DA1	17.32	110	bg
PG 1144+005	11 46 35	+00 12.5	DO.34	15.10	216	no
EC 11481-2303	11 50 38	-23 20.5	DA0	11.76	144	bg
PG 1151-029	11 54 15	-03 12.1	DOZ1	16.04	715	no
EC 11575-1845	12 00 06	-19 02.1	sdO+dMe	12.89	144	no?
PG 1159-035	12 01 46	-03 45.6	DQZO.4	14.87	216	no
EC 12185-1950	12 21 07	-20 07.0	DA1	16.35	145	no
EC 12296-2113	12 32 19	-21 30.3	...	16.14	145	bg?
QNY 4:59	12 38 36	-00 40.7	DA	17.56	217	no
QNY 4:48	12 39 10	-01 00.1	DA	19.27	217	no
EC 12489-2750	12 51 40	-28 06.8	DA1	16.22	112	no
HE 1257-2021	13 00 27	-20 37.4	DO/PG1159	16.44	146	no
PG 1305+018	13 07 54	+01 32.1	DAO1	15.16	218	no
PG 1305-017	13 08 16	-01 59.1	DAO1	16.0	218	no
EC 13123-2523	13 15 04	-25 38.9	DA1	15.69	646	no
HE 1314+0018	13 17 25	+00 02.6	DO	15.6	218	no

Continued on next page

Table 2.4 – continued from previous page

Name	R.A.	Dec	Spectral type	V mag	Field	Detection
PG 1318+062	13 20 44	+05 59.0	sdOC	13.9	218	no
EC 13288-1515	13 31 34	-15 30.7	DA1	15.49	146	no
EC 13290-1933	13 31 46	-19 48.4	...	14.48	146	poss
LSE 44	13 52 41	-48 08.4	sdO	12.46	57	bg
LSE 153	13 53 08	-46 43.7	sdO	11.40	57	bg
PG 1403-077	14 06 06	-07 58.5	DA2	15.82	183	no
PG 1413+015	14 15 36	+01 17.3	DAO	17.01	219	no
141740+130211	14 17 40	+13 01.8	DA1	15.33	255	no
EC 14361-1832	14 38 58	-18 45.6	DA?	16.56	148	no
PG 1506-052	15 09 19	-05 20.9	...	14.56	221	yes
PG 1511-048	15 14 12	-04 59.5	DA	15.62	221	?
PG 1512-035	15 14 50	-03 42.8	sdO/DAO	16.32	221	no
QNZ 5:01	15 24 00	+02 18.6	DA	18.14	221	no
PG 1526+014	15 28 40	+01 13.0	DA2	16.69	221	poss
PG 1532+033	15 35 10	+03 11.2	DA.5	16.02	221	no
LB 898	15 46 45	+00 43.8	DA1	15.27	222	no
PG 1547+015	15 49 44	+01 25.9	DA2	...	222	no
PG 1609+044	16 11 48	+04 19.8	DA1.5	15.22	222	no
RE J161419-083257	16 14 19	-08 33.4	DA	14.01	186	bg
G 153-041	16 17 55	-15 35.8	DA1.5	13.45	686	bg
LS IV -12 1	16 23 44	-12 12.6	sdB	11.18	686	bg
SDSS J163200.34-001928.3	16 32 00	-00 19.4	DAO1	...	223	no
HD149499B	16 38 30	-57 28.2	DOZ1	11.7	37	neb nr
PG 1643+143	16 45 40	+14 17.7	DA1.5	15.38	259	no
PG 1646+062	16 49 07	+06 08.8	DAS	15.84	759	bg
LSE 259	16 53 55	-56 01.9	sdO	12.54	37	neb nr
Lanning 18	18 47 37	+01 57.5	DA	12.96	226	no
RE J1847-221	18 47 57	-22 19.6	DA2	13.72	154	no
LSE 263	19 02 12	-51 30.2	sdO	11.30	62	no
KPD 1903+2540	19 05 38	+25 45.5	sdOC	14.71	Lyr01	no
LS II +18 9	19 43 31	+18 24.6	sdO	12.13	Sge02	bg
WD 1948-389	19 52 19	-38 46.3	DA	14.63	90	no
RE J2013+400	20 13 09	+40 02.6	DAO	14.6	Cyg03	bg
KPD 2026+2205	20 28 20	+22 15.5	sdOC	...	Vul03	bg?
HS 2027+0651	20 29 32	+07 01.1	DOZ.7	16.9	265	fil nr
BPS CS 22940-0009	20 30 20	-59 50.8	sdB	14.07	40	bg
HS 2033+0507	20 35 45	+03 37.7	DAO	...	764	no
PG 2056+033	20 58 46	+03 31.8	DA1	16.26	765	no
HS 2115+1148	21 18 19	+12 01.6	DAOZ.7	16.5	266	neb Nf
PG 2120+054	21 22 35	+05 42.6	DA1.5	16.38	266	no
PG 2131+066	21 34 08	+06 50.9	DOZ.6	16.6	266	no
MCT 2146-4320	21 49 39	-43 06.2	DA	15.81	92	no
MCT 2148-294	21 51 18	-29 14.6	DO	16.2	123	no
PG 2150+021	21 53 22	+02 21.3	DA3	16.4	231	no
RE J2156-546	21 56 21	-54 38.4	DA	14.44	65	no
MCT 2153-4156	21 56 35	-41 42.3	DA	15.89	92	no
1RXS J215924-5946	21 59 24	-59 46.1	...	...	41	poss
MCT 2159-4129	22 02 28	-41 14.5	DA	15.54	92	?
RE 2214-491	22 14 11	-49 19.4	DA.76	11.77	65	no
PG 2215+151	22 17 49	+15 20.9	sdOC	13.88B	267	no
PG 2235+082	22 37 35	+08 28.8	DA1.5	15.23	268	bg?
EG 229	22 42 45	-04 14.2	DA	15.21	731	no
PG 2244+031	22 46 57	+03 24.6	DA1	16.02B	768	no
HS 2244+0305	22 47 22	+03 21.7	DA.70	16.02B	768	no
HS 2246+0640	22 49 25	+06 56.8	DA.51	...	768	no

Continued on next page

Table 2.4 – continued from previous page

Name	R.A.	Dec	Spectral type	V mag	Field	Detection
PHL 400	23 05 53	+02 00.0	DA2	15.76B	768	bg
PG 2308+050	23 11 17	+05 19.4	DA1.5	16.02	768	bg
GD 246	23 12 22	+10 47.0	DA.84	13.11	768	no
232030+125806	23 20 32	+12 58.2	DA	16.6	269	no
RBS 1999	23 24 31	-54 41.6	DA	15.2	66	no
PG 2231-4731	23 34 01	-47 14.4	DA.90	13.42	43	no
MCT 2341-3443	23 44 22	-34 27.0	sdB	10.98	625	no
MCT 2350-3026	23 52 36	-30 10.2	sdO6	12.14	126	no
PB 5617	23 56 28	+02 57.0	DA2	15.83	198	no
MCT 2356-4050	23 59 12	-40 32.0	sdO5	14.6	67	no

2.6 IPHAS

The new Isaac Newton Telescope (INT) Photometric Hα Survey of the Northern Galactic Plane (IPHAS; Drew et al. 2005)[21] was motivated by the success of the SHS. IPHAS is a survey of the Northern Galactic Plane being carried out with the 2.5-metre INT equipped with the Wide Field Camera (WFC), a mosaic of four CCDs. This survey, which is not quite complete at the time of writing, is an adjunct to the SHS, and a predecessor of new deep Hα surveys in the south, such as VPHAS+ (J. Drew, PI).

2.6.1 Survey characteristics

IPHAS covers 1800 deg^2 of the northern Milky Way along the Galactic plane between $-5° < |b| < +5°$, in narrow-band Hα, and the Sloan r' and i' broadband filters. The Hα filter has a FWHM of 95 Å, so like the SHS, the filter passes both [NII] lines. The survey reaches an equivalent red-continuum magnitude of $r' \simeq 20$ (10σ) at $1''$ resolution, and is sensitive to diffuse Hα emssion down to ~2 R.

The digital nature of the survey allows Hα emitters to be differentiated from the main stellar locus in the (r'−Hα, $r' - i'$) colour-colour plane. The utility of the survey to discover compact Hα emitters was illustrated after spectroscopic follow-up of a test field in Cepheus showed that the vast majority of sources selected using IPHAS colours were genuine compact Hα emitters. In this same field, examples of Hα deficit objects (e.g. a white dwarf and a carbon star) were readily distinguished by their IPHAS colours (Drew et al. 2005).

The SHS and IPHAS Hα surveys overlap at the celestial equator which allows a direct comparison to be made between them. Figure 2.16 shows a 3.3×2 arcminute region centred on $18^{\rm h}47^{\rm m}42.6^{\rm s}$, $+01°33'04''$ which includes the newly discovered planetary nebula PHR1847+0132, taken from a slightly shallow SHS survey field h1332 (exposure time cut short to 168 min, cf. 180 min normally). The data have been matched in coordinates but not otherwise processed. It is clear the two surveys achieve similar depth for diffuse emission but that the IPHAS survey generally goes deeper for point-sources due to its better resolution (cf. R. Morris 2006, pers. communication to Q. Parker). Further details are given by Drew et al. (2005).

2.6.2 Search Techniques and Results

Gonzalez-Solares et al. (2007) have presented the IPHAS Initial Data Release, which contains a photometric catalogue of about 200 million unique point-source objects, covering the northern hemisphere within the latitude range $-5°< b < 5°$, as well as associated image data covering about 1600 square degrees. Witham et al. (2008) have presented a catalogue of 4853 Hα point-source emitters, based on their IPHAS colours, covering the magnitude range $13.0 < r' < 19.5$. Spectral analysis for ~300 of these sources confirms more than 95% are genuine emission-line stars or compact nebulae. These authors find an increase of an order of magnitude in the number of faint ($r' > 13.0$) emission-line objects, compared to previous surveys. Of further

[21] http://www.iphas.org/

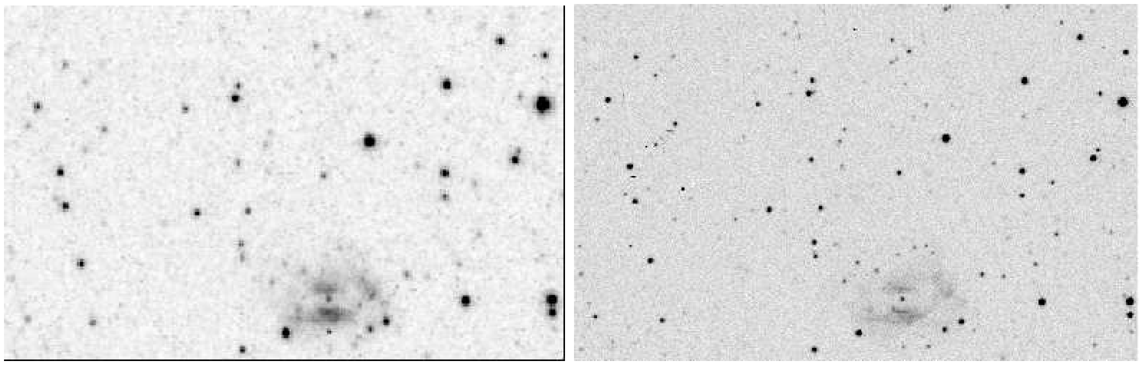

Figure 2.16: A $3.3' \times 2'$ comparison region between SHS (left) and IPHAS (right) data centred on $18^h47^m42.6^s, +01^o33'04''$ including the new planetary nebula PHR1847+0132.

interest is a new magnitude-limited catalogue of 1183 candidate symbiotic stars compiled from IPHAS data (Corradi et al. 2008), which is a subset of the catalogue of Witham et al. (2008). These discoveries will go some way towards reducing the disparity between the observed and predicted populations of symbiotics in the Galaxy, a situation analogous to PNe!

New compact PNe are confirmed from a dedicated programme of follow-up spectroscopy. Corradi et al. (2005) and Mampaso et al. (2006) have given a summary of the methods used to search for compact and extended ionized nebulae, and some preliminary results on ∼100 new candidate planetary nebulae identified so far. Viironen et al. (2006, 2007) reported on the first results of the specific search for compact PNe from IPHAS data (see also Witham et al. 2008).

Extended PNe (of greater importance to the present study) are also being found in considerable numbers. Preliminary visual scans of the of continuum-subtracted Hα image mosiacs, at a spatial sampling of 5×5 arcsec^2, have led to the discovery of numerous resolved PN candidates, including a number of obviously highly evolved nebulae (Corradi et al. 2005; Kovacevic 2005; Zijlstra 2005, pers. communication; Sabin 2007, pers. communication). However, the numbers of likely solar neighbourhood PNe predicted to be discovered are considerably less than in the south, due to the smaller areal coverage of the survey (i.e. $|b| \leq 5°$) and the fact that the northern hemisphere had previously been searched to greater depth (mainly on broad-band surveys). Nevertheless, several hundred PNe, both compact and resolved/extended, are expected to be discovered on completion of the project.

The IPHAS nebula database[22] was queried in December 2007, to obtain a list of PN candidates larger than 2′ across. A list of 37 objects was returned. Where available, SHASSA or VTSS images and/or blue and red DSS images were downloaded and examined, along with MSX cutouts, supplemented with a SIMBAD search around each object position. The majority of objects are considered to be likely HII regions, or areas of diffuse emission. Some very faint objects remain unclassified. Table 2.5 lists the four best candidates, along with data on two PN candidates supplied by A. Zijlstra and L. Sabin (pers. communication). The "Ear nebula" is a very good candidate for the solar neighbourhood volume (see the appendix).

In the literature to date, Mampaso et al. (2006) presented an in-depth study of the first

[22]http://catserver.ing.iac.es/IPHAS/Group_B/Search.php

Table 2.5: Likely large PNe (>2′ across) discovered from the IPHAS survey, listed at the end of 2007.

Name	Other	R.A.	Dec.	l	b	a (′)	b (′)	Morph	F(Hα)
IPHASX 0156	...	01 56 26.0	+65 28 30.0	129.61	+3.45	3.3	3.0	Ea	−11.5
IPHASX 0540	Teutsch 2	05 40 44.6	+31 44 32.0	177.06	+0.58	2.0	2.0	Raf	...
IPHASX 1906	PHR1906-0133	19 06 14.88	−01 33 18.6	033.25	−4.00	2.6	1.6	Ias	...
IPHASX 1925	...	19 25 10.80	+11 33 53.6	047.06	−2.09	2.3	2.3	B?	−12.0
IPHASX 1945	...	19 45 33.84	+21 07 50.9	057.80	−1.71	2.3	2.3	I	−11.9
IPHASX 2050	'Ear nebula'	20 50 13.74	+46 55 15.2	086.52	+1.83	5.9	5.2	Eas	−11.0

PN to be discovered from IPHAS. It is an unusual oxygen-poor Type I PN, located at a large galactocentric distance of 13 kpc. It shows an intricate morphology, with an inner ring surrounding the CS, bright inner lobes with an enhanced waist, and very faint extensions reaching up to more than 100″. The unusual quadrupolar morphology, the red CS colour, and possible evidence for a dense circumstellar disk, support the hypothesis that its morphology is related to a binary interaction. Another distant PN located near the Galactic anticentre direction has been reported by Mampaso et al. (2004). Its estimated galactocentric distance of 14 – 20 kpc makes it one of the farthest galactic PNe for which chemical abundances have been measured (see also the paper by Mampaso et al. 2007).

2.7 WHAM

The Wisconsin H-Alpha Mapper (WHAM; Haffner et al. 2003) is a Fabry-Perot spectrometer with high sensitivity and spectral resolution (R ≈ 25,000) and has been designed to produce a survey of Hα emission from the interstellar medium over the entire northern sky. The WHAM instrument consists of a 60 cm telescope combined with a 15 cm dual-etalon Fabry-Perot spectrometer, and can detect Galactic emission as faint as 0.05 Rayleighs in a 30 second exposure (Haffner et al. 2003). In primary mode, a single exposure covers a 200 kms^{-1}spectral region with a velocity resolution of 8–12 kms^{-1}, but with a low spatial resolution of 1° on the sky. For emitting gas at 10,000 K, this observed intensity corresponds to a Hα emission measure of about 0.1 cm^{-6} pc.

The first major product of the WHAM project is the Hα Northern Sky Survey (WHAM NSS; Haffner et al. 2003), which is a complete survey of the ionized gas in the Galaxy north of $\delta = -30°$. The survey totals 37,565 individual spectra, and provides the first absolutely calibrated, kinematically resolved map of the Hα emission in the Galaxy within $\pm\sim$100 kms^{-1} of the local standard of rest (Haffner et al. 2003).

Recently, a number of mainly high latitude Hα emission enhancements were found in the WHAM NSS and were catalogued as WHAM Point Source (WPS) objects (Reynolds et al. 2005). Greg Madsen and the present author have used WHAM to determine the status of a number of poorly studied PN candidates, including some of the WPS objects (see Chapter 8 and Appendix B), as well as obtaining integrated photometry in the main emission lines for most of the large PNe in the solar neighbourhood (see §3.3). The WHAM data will be published in detail in a separate paper (Madsen & Frew 2008, in preparation; see also Madsen et al. 2006; Frew, Madsen & Parker 2006, and Frew & Parker 2006).

2.8 Summary

This chapter presented the results of a search for new evolved PN candidates based primarily on the AAO/UKST Hα Survey. A complimentary search outside the area of the Galactic plane was undertaken using the complete Southern H-Alpha Sky Survey Atlas (SHASSA) and the available fields of the Virginia-Tech Spectral-line Survey (VTSS). Additional preliminary discoveries from the INT Photometric Hα Survey (IPHAS) and Wisconsin H-Alpha Mapper are also briefly discussed.

These new discoveries have helped generate a new accurate volume-limited local sample of PNe, discussed in more detail in later chapters. In the next chapter, I present new self-consistent estimates of global fluxes in the main emission-lines for a large number of PNe, including many of the new discoveries found as part of this work.

Chapter 3

Emission-line Photometry

3.1 Introduction

For a planetary nebula, the integrated flux in a Balmer line (e.g. Hα or Hβ) is one of the most fundamental parameters that needs to be determined, and is analogous to the apparent magnitude of a star. Calculations involving the surface brightness (i.e. in the $SB - r$ relation, defined below), the ionized nebular mass, the rms density, the Zanstra temperature of the CS (and hence its luminosity and mass), and the PN luminosity function are all dependent on accurate integrated line fluxes. However, most of the largest evolved PNe in the sky of low surface brightness (typified, for example, by the discoveries of Abell 1955, 1966) have poorly determined Hβ or Hα fluxes, if known at all. Those that are published are heterogeneous and often very inconsistent (cf. Kaler 1983b; Hippelein & Weinberger 1990; Xilouris et al. 1996).

The situation is obviously better for most of the brighter and/or more compact PNe in the Galaxy, with a large number of Hβ fluxes compiled by Acker et al. (1991, 1992), based on the efforts of a large number of workers over the last fifty years (see references therein). Global fluxes in the Hα line are less common, with most being contributed by Kaler (1983a, 1983b) and Shaw & Kaler (1989). A number of compact southern PNe have accurate Hα, Hβ, Hγ, [O III], [N II] and He II λ4686 fluxes determined by Kohoutek & Martin (1981), and several more were measured by Dopita & Hua (1997). Wright, Corradi & Perinotto (2005) presented accurate line fluxes for six compact northern PNe. Since the solar neighbourhood is dominated by low-surface brightness PNe with either poor-quality or no data, it was obvious that more work needed to be done.

In this section, I present new determinations of the Hα flux for a large number of PNe, including the most accurate and complete database of fluxes yet compiled for the nearest, most evolved PNe in the solar neighbourhood. This data is of great import for the calculation of Zanstra temperatures (and therefore stellar luminosities and masses; see §9.4.4) and underpins the new Hα SB-r relation derived later in this work (see Chapter 7).

3.2 Integrated Hα Fluxes

The Hα fluxes tabulated in this chapter are principally derived from the Southern Hα Sky Survey Atlas (SHASSA) of Gaustad et al. (2001). A smaller number of PNe were measured from the Virginia Tech Spectral line Survey (VTSS; Dennison, Simonetti & Topasna 1998) in the northern sky, outside the bounds of the SHASSA survey. Observations taken by the Wisconsin H-Alpha Mapper (WHAM; Haffner et al. 2003) are also given, as are a range of literature fluxes corrected to a common zero point. Details will be provided in the sections that follow.

3.2.1 Methodology

SHASSA

SHASSA provides narrowband (Hα + [N II]) and continuum images of the entire southern sky. The survey has a rather low spatial resolution (48$''$ pixels) but is continuum subtracted and accurately flux calibrated. Despite the relatively coarse resolution of the SHASSA data, a large number of PNe are either large enough or bright enough to be readily apparent on the survey, which allows for an accurate flux determination.

Gaustad et al. (2001) describe in detail how the SHASSA intensity calibration was derived using the planetary nebula spectrophotometric standards of Dopita & Hua (1997) after the continuum images had been scaled and subtracted from the Hα frames. However, a difficulty in applying PNe line fluxes to Hα narrow-band imaging is the proximity of the two [N II] $\lambda\lambda$6548, 6584 lines which are included in the flanks of the SHASSA Hα filter bandpass. These vary in strength relative to Hα between PNe and may significantly affect the flux determination if not taken into account, especially for Type I nebulae. Calculating the transmission properties of the interference filter to these lines is complicated by the blue-shifting of the bandpass with incident angle (e.g. Parker & Bland-Hawthorn 1998). These effects are considered in Section 4 of Gaustad et al. (2001) and are carefully accounted for in their calibration.

An additional uncertainty is introduced to the zero-point of the SHASSA intensity calibration from the contribution of geocoronal emission. Gaustad et al. (2001) estimate this by comparison with overlapping 1° field-of-view (FOV) WHAM data points and interpolating if there is no available WHAM data (Haffner et al. 2003). A by-product of the check of the intensity calibration against independent flux measures of bright PNe (see below) indicates that the geocoronal contribution to the SHASSA Hα images has been appropriately accounted for. Furthermore, Finkbeiner (2003) also showed there is no significant offset between WHAM and SHASSA data (cf. the VTSS data, see below).

The continuum-subtracted SHASSA data are available as either the original 48$''$ resolution data, or data smoothed to 4$'$. The full-resolution SHASSA data often shows unphysical, negative pixels which are residuals from poorly subtracted stellar images, largely removed in the smoothed images (see previous chapter). In order to ascertain the reliability of the SHASSA intensity calibration, a first-step analysis using 87 well-studied PNe with an independent measure of Hα flux given in the literature, showed that the aperture photometry from the full-resolution

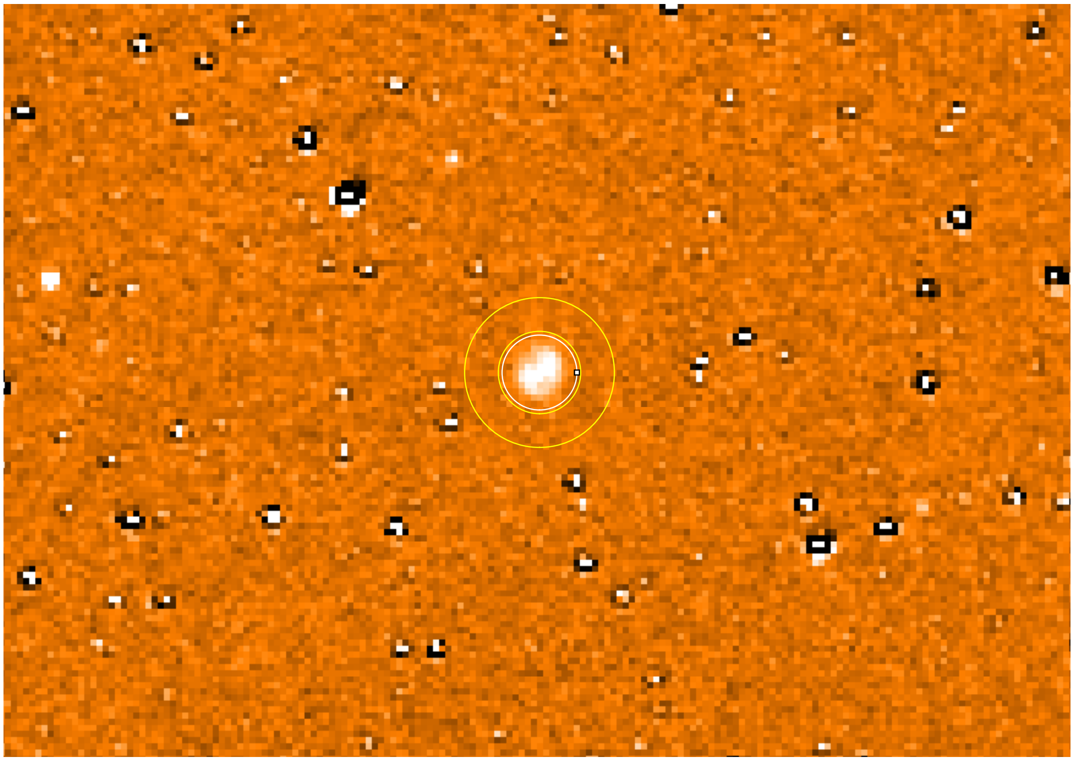

Figure 3.1: Obtaining PN photometry using SHASSA flux-calibrated unsmoothed images. Note the artifacts from the imperfect off-band continuum subtraction. This example, Longmore 1, is given to show how the aperture and background annulus are selected using the APERPHOTOM routine in GAIA. The resulting photometry counts are converted to a red flux using equation 3.1 (see text).

data returns the best measurement of the integrated Hα flux, despite the artefacts seen on these images (smoothing mingles the flux from the PN with the sky background). Available spectroscopic data were used to deconvolve the contribution from the [N II] lines passed by the SHASSA filter (see below) for these calibration PNe.

It was apparent that the deconvolved SHASSA Hα fluxes agree with published data to $\Delta\,\mathrm{F(H}\alpha) = -0.001$ dex, $\sigma = 0.07$ dex in the sense of SHASSA minus literature fluxes (see also my preliminary analyses in Pierce et al. 2004 and Parker et al. 2005a). There was also no correlation between $\Delta\mathrm{F(H}\alpha)$ and the [N II]/Hα ratio, showing that the adopted procedure is correct. Since the PNe literature fluxes themselves have associated errors, I find the SHASSA calibration to be calibrated to better than $\pm10\%$ across the whole survey, in agreement with the nominal error supplied by Gaustad et al. (2001).

To make the measurements of the Hα + [N II] integrated fluxes for the PNe reported here, the Starlink routine APERPHOTOM was used in the GAIA image analysis package. For each object, a circular aperture was carefully placed over the PN and an annulus for background subtraction defined; this is positioned to avoid residual stellar images and other image artifacts (see Figure 3.1). The routine automatically accounts for the differing relative areas of the aperture and annulus, and scales the sky subtraction accordingly. The total pixel counts and the error (due primarily to uncertainties in the background correction) were hence obtained from the routine.

For some PNe the presence of artifacts close to the PN preclude background estimation via the annulus method. Instead, measurements of the sky background were made through an aperture identical to the PN aperture at a number of representative regions immediately surrounding the nebula, in order to accurately account for the surrounding diffuse Hα emission. The standard deviation in these is the principal uncertainty in the flux measurement.

The SHASSA filter is centered at Hα and has a FWHM of 32Å. Hence the filter response passes Hα and both [N II] lines. The transmission factors for the λ6548, Hα and λ6584 lines are 39%, 78% and 26% respectively (Gaustad et al. 2001). Photometry using the SHASSA data is quite straightforward. A 'red' Hα+[N II] flux in cgs units is given by:

$$F_{\rm red} = 5.66 \times 10^{-18} \times 47.64^2 \times ({\rm COUNT}/10) \qquad {\rm erg\,cm^{-2}\,s^{-1}} \tag{3.1}$$

The constants in the expression are the conversion factor from Rayleighs to cgs units (at Hα and/or [N II]) and the pixel scale of the SHASSA survey (47.64 arcsec/pixel). Note that the native units of the SHASSA survey are deci-rayleighs, hence the photometry counts obtained from the APERPHOTOM routine need to be divided by 10.

As stated earlier, the SHASSA bandpass includes a contribution from the [N II] lines at $\lambda\lambda$6548, 6584 Å. In order to derive a pure Hα flux, the [N II]/Hα ratio is required to deconvolve the [N II] contribution to the SHASSA red flux. To do this the integrated [N II]/Hα ratios for each PN were taken from the literature (see table 3.1), spectroscopic data from table 5.3, other unpublished spectra taken as part of the Macquarie/AAO/Strasbourg/Hα (MASH) survey (Parker et al. 2006a, and see table 3.2), and from observations made with WHAM (see table 3.8). The WHAM data will be published in detail in a separate paper (see Madsen et al. 2006), and while *absolute* intensity calibration is difficult, the integrated [N II]/Hα ratios are reliable and are to be preferred as the WHAM field-of-view is larger than all of the PNe measured here.

Integrating the line strengths with the bandpass of the filter (see Gaustad et al. 2001) leads to the following expression (in log terms) for the correction due to the [N II] flux:

$$\log F(H\alpha) = \log F_{\rm red} + \log\left(\frac{1}{0.375\, R_{\rm [N\,II]} + 1}\right) \tag{3.2}$$

where $R_{\rm [N\,II]}$ is the [N II]/Ha ratio for the PN and the constant takes into account the throughput of the SHASSA filter for each [N II] line after integration. Note that the [N II] flux refers to the sum of the λ6548 and λ6584 lines. If only the brighter λ6584 line is measurable in a spectrum, F([N II]) is estimated as 1.333 x F(6584).

There is an important caveat to consider; as more often than not the adopted [N II]/Hα ratio for the PN is derived from long-slit spectroscopy (e.g. Acker et al. 1992), and may not be representative of the integrated ratio for the nebula. It is possible that the value of $R_{\rm [NII]}$ taken from long-slit spectra is systematically overestimated for some PNe, as spectrograph slits are often positioned (especially for evolved nebulae) on bright interacting rims which are expected to have enhanced [N II] emission. The derived Hα flux might therefore be slightly too faint in these cases (however the derived flux is only modestly sensitive to the exact value of $R_{\rm [NII]}$, for $R_{\rm [NII]} < 1$).

For all objects, the quoted zero-point calibration error of 9% from Gaustad et al. (2001) and our estimated error in the integrated [N II]/Hα ratio for the each PN have been added quadratically to get the overall uncertainty in the integrated Hα flux. Tables 3.1 and 3.2 contains all the Hα fluxes calculated from SHASSA images for 270 previously known objects and 95 new nebulae respectively. The adopted [N II]/Hα ratio is given in column 2, the 'red' flux count (including the contribution of the [N II] lines) as measured from the image is given in column 5, and the logarithms of the integrated red flux and the corrected Hα flux are given in columns 6 and 7 respectively. Column 8 lists the aperture diameter in arcmin.

Table 3.1: New Hα fluxes derived from SHASSA data for known PNe. Fluxes are given in log cgs units.

Name	NII/Hα	Ref	field	count	F$_{red}$	F(Hα)	aperture	Notes
NGC 246	0.01	5	163	6630 ± 100	−10.07 ± 0.01	−10.07 ± 0.04	9.0	
NGC 1360	0.01	5	100	13780 ± 150	−9.75 ± 0.01	−9.75 ± 0.04	15	1
NGC 1535	0.00	9	168	8680 ± 70	−9.95 ± 0.01	−9.95 ± 0.04	6.5	1
NGC 2022	0.01	10	242	2450 ± 50	−10.50 ± 0.01	−10.50 ± 0.04	4.1	
NGC 2346	2.5	4,11	209	3155 ± 40	−10.39 ± 0.01	−10.68 ± 0.05	5.1	
NGC 2438	1.5	4,9,10	138	3940 ± 100	−10.30 ± 0.01	−10.49 ± 0.04	6.0	1
NGC 2438	1.5	4,9,10	673	4000 ± 60	−10.29 ± 0.01	−10.48 ± 0.04	5.4	1
NGC 2440	3.2	4,7,9,10	138	23450 ± 670	−9.52 ± 0.01	−9.86 ± 0.06	12	
NGC 2452	0.62	7	105	1720 ± 60	−10.66 ± 0.01	−10.75 ± 0.04	4.9	
NGC 2610	0.15	7	139	1030 ± 40	−10.88 ± 0.02	−10.90 ± 0.04	3.8	
NGC 2792	0.02	4	78	1850 ± 80	−10.62 ± 0.01	−10.63 ± 0.04	4.3	
NGC 2818	2.2	7	78	2780 ± 100	−10.45 ± 0.02	−10.71 ± 0.05	5.6	
NGC 2867	0.29	7	31	11500 ± 400	−9.83 ± 0.01	−9.88 ± 0.04	6.5	
NGC 2899	3.72	7	31	6950 ± 130	−10.05 ± 0.01	−10.43 ± 0.06	5.7	
NGC 3132	2.06	4,9	79	20800 ± 100	−9.57 ± 0.01	−9.82 ± 0.05	6.0	
NGC 3195	1.50	7	5	4600 ± 60	−10.23 ± 0.01	−10.42 ± 0.04	4.8	
NGC 3211	0.06	7	32	2380 ± 40	−10.51 ± 0.01	−10.52 ± 0.04	4.0	
NGC 3242	0.01	9	142	38200 ± 90	−9.31 ± 0.01	−9.31 ± 0.04	6.5	2
NGC 3699	1.2	7	33	3490 ± 250	−10.35 ± 0.03	−10.51 ± 0.05	4.8	
NGC 3918	0.34	43	33	26900 ± 130	−9.46 ± 0.01	−9.51 ± 0.04	4.8	
NGC 4071	1.55	7	17	1420 ± 70	−10.74 ± 0.02	−10.94 ± 0.05	4.0	
NGC 4361	0.00	14	145	6020 ± 160	−10.11 ± 0.01	−10.11 ± 0.04	6.0	
NGC 5189	1.36	4,7,12	18	13780 ± 200	−9.75 ± 0.01	−9.93 ± 0.04	5.6	
NGC 5307	0.04	7	35	1880 ± 40	−10.62 ± 0.01	−10.62 ± 0.04	4.0	
NGC 5315	0.67	7	18	19660 ± 130	−9.60 ± 0.01	−9.70 ± 0.04	5.1	
NGC 5844	1.5	4	36	2880 ± 60	−10.43 ± 0.01	−10.62 ± 0.04	4.1	
NGC 5873	0.08	7	84	2150 ± 50	−10.56 ± 0.01	−10.57 ± 0.04	4.4	
NGC 5873	0.08	7	85	1980 ± 40	−10.59 ± 0.01	−10.61 ± 0.04	4.4	
NGC 5882	0.06	16	58	13400 ± 100	−9.76 ± 0.01	−9.77 ± 0.04	4.8	
NGC 5979	0.06	4	36	1740 ± 50	−10.65 ± 0.01	−10.66 ± 0.04	4.3	
NGC 6026	0.04	7	116	780 ± 20	−11.00 ± 0.01	−11.01 ± 0.04	3.8	
NGC 6072	1.67	7	86	4900 ± 70	−10.20 ± 0.01	−10.41 ± 0.04	9.5	
NGC 6153	0.22	17	86	9300 ± 150	−9.92 ± 0.01	−9.96 ± 0.04	7.9	
NGC 6302	2.80	4,16,19	142	41900 ± 500	−9.27 ± 0.01	−9.58 ± 0.05	5.6	
NGC 6302	2.80	4,16,19	87	41200 ± 500	−9.28 ± 0.01	−9.59 ± 0.05	5.6	

Name	NII/Hα	Ref	field	count	F_{red}	F(Hα)	aperture	Notes
NGC 6326	0.40	7	60	2250 ± 40	−10.54 ± 0.01	−10.60 ± 0.04	3.3	
NGC 6337	0.43	4	87	3230 ± 90	−10.38 ± 0.01	−10.45 ± 0.04	3.5	
NGC 6369	0.36	20	152	6050 ± 200	−10.11 ± 0.01	−10.16 ± 0.04	6.4	
NGC 6445	1.9	4,34	152	7600 ± 100	−10.01 ± 0.01	−10.24 ± 0.04	4.8	
NGC 6537	6.2	4,21	153	4550 ± 180	−10.23 ± 0.02	−10.76 ± 0.09	4.8	
NGC 6563	1.4	4,6	119	5470 ± 340	−10.15 ± 0.03	−10.34 ± 0.05	5.6	
NGC 6565	1.5	4	119	2900 ± 40	−10.43 ± 0.01	−10.62 ± 0.04	4.1	
NGC 6567	0.05	4	153	4300 ± 100	−10.26 ± 0.01	−10.27 ± 0.04	3.5	
NGC 6572	0.28	4	261	50500 ± 200	−9.19 ± 0.01	−9.23 ± 0.04	10	
NGC 6578	0.06	7	153	1400 ± 100	−10.75 ± 0.03	−10.76 ± 0.05	2.2	
NGC 6620	1.09	7	119	820 ± 40	−10.98 ± 0.02	−11.13 ± 0.04	3.5	
NGC 6620	1.09	7	653	740 ± 35	−11.02 ± 0.02	−11.17 ± 0.04	3.5	
NGC 6629	0.16	7	153	5400 ± 100	−10.16 ± 0.01	−10.18 ± 0.04	4.4	
NGC 6644	0.4	22	119	3000 ± 80	−10.41 ± 0.01	−10.47 ± 0.04	5.2	
NGC 6741	1.6		227	2850 ± 30	−10.44 ± 0.01	−10.64 ± 0.03	4.8	
NGC 6772	0.69	4	227	2310 ± 50	−10.53 ± 0.01	−10.63 ± 0.04	4.4	
NGC 6778	0.95	4	227	3340 ± 25	−10.37 ± 0.01	−10.50 ± 0.04	4.4	
NGC 6781	1.9	6,17,23	263	12280 ± 130	−9.80 ± 0.01	−10.04 ± 0.04	6.7	
NGC 6781	1.9	6,17,23	762	11500 ± 110	−9.83 ± 0.01	−10.06 ± 0.04	7.8	
NGC 6790	0.17	4	227	4500 ± 40	−10.24 ± 0.01	−10.26 ± 0.04	4.8	
NGC 6803	0.42	4	263	2780 ± 40	−10.45 ± 0.01	−10.51 ± 0.04	3.7	
NGC 6804	0.0	23	263	1920 ± 30	−10.61 ± 0.01	−10.61 ± 0.04	4.0	
NGC 6818	0.01	21	155	9680 ± 90	−9.91 ± 0.01	−9.91 ± 0.04	5.6	
NGC 6818	0.01	21	191	9400 ± 100	−9.92 ± 0.01	−9.92 ± 0.04	5.6	
NGC 6818	0.01	21	691	8950 ± 100	−9.94 ± 0.01	−9.94 ± 0.04	7.1	
NGC 6852	0.14	4	228	281 ± 14	−11.44 ± 0.02	−11.46 ± 0.04	3.2	
NGC 6891	0.05	4	264	5320 ± 100	−10.17 ± 0.01	−10.17 ± 0.04	4.4	
NGC 7009	0.08	1	194	41050 ± 150	−9.28 ± 0.00	−9.29 ± 0.04	8.4	1
NGC 7094	0.00	6	266	455 ± 14	−11.23 ± 0.01	−11.23 ± 0.04	4.8	
NGC 7293	1.8	2	159	187500 ± 5200	−8.62 ± 0.01	−8.84 ± 0.05	22	
NGC 7293	1.8	2	159	198200 ± 7500	−8.59 ± 0.02	−8.82 ± 0.05	37	3
IC 418	0.70	1	170	93000 ± 2500	−8.92 ± 0.01	−9.02 ± 0.04	6.4	
IC 972	0.72	4,5	147	320 ± 25	−11.39 ± 0.03	−11.49 ± 0.05	4.8	
IC 1266	0.55	7	61	7980 ± 120	−9.99 ± 0.01	−10.07 ± 0.04	4.8	
IC 1266	0.55	7	587	7200 ± 100	−10.03 ± 0.01	−10.12 ± 0.04	5.4	
IC 1295	0.15	3,4	190	1350 ± 80	−10.76 ± 0.03	−10.78 ± 0.05	4.8	
IC 1297	0.18	7	89	3120 ± 60	−10.40 ± 0.01	−10.43 ± 0.04	3.7	
IC 2165	0.15	4	171	4950 ± 70	−10.20 ± 0.01	−10.22 ± 0.04	5.4	
IC 2165	0.15	4	172	5150 ± 60	−10.18 ± 0.01	−10.20 ± 0.04	4.0	1
IC 2448	0.05	7	15	4130 ± 60	−10.28 ± 0.01	−10.28 ± 0.04	5.6	
IC 2501	0.33	8	32	8300 ± 90	−9.97 ± 0.01	−10.02 ± 0.04	4.8	
IC 2553	0.18	4,7	32	4800 ± 80	−10.21 ± 0.01	−10.24 ± 0.04	4.0	
IC 2621	0.72	8	16	2750 ± 80	−10.45 ± 0.01	−10.56 ± 0.04	4.1	
IC 4191	0.40	8	534	4650 ± 50	−10.22 ± 0.01	−10.28 ± 0.04	3.8	
IC 4191	0.40	8	18	4325 ± 62	−10.26 ± 0.01	−10.32 ± 0.04	3.8	1
IC 4406	2.0	4	84	8750 ± 80	−9.95 ± 0.01	−10.19 ± 0.05	4.8	
IC 4593	0.1	4	258	6710 ± 60	−10.06 ± 0.00	−10.08 ± 0.04	4.8	

Name	NII/Hα	Ref	field	count	F_{red}	F(Hα)	aperture	Notes
IC 4599	0.26	4,7	86	1150 ± 50	−10.83 ± 0.02	−10.87 ± 0.04	3.2	
IC 4634	0.04	4	151	4360 ± 50	−10.25 ± 0.01	−10.26 ± 0.04	4.3	
IC 4637	0.08	7	87	3240 ± 40	−10.38 ± 0.01	−10.39 ± 0.04	3.8	
IC 4642	0.00	4	560	1410 ± 40	−10.74 ± 0.01	−10.74 ± 0.04	3.8	
IC 4642	0.00	4	38	1210 ± 40	−10.81 ± 0.01	−10.81 ± 0.04	3.8	1
IC 4663	0.09	7	587	940 ± 40	−10.92 ± 0.02	−10.93 ± 0.04	4.0	
IC 4673	0.14	7	118	765 ± 40	−11.01 ± 0.02	−11.03 ± 0.04	3.3	
IC 4699	0.01	7	61	560 ± 50	−11.14 ± 0.04	−11.15 ± 0.05	3.5	
IC 4699	0.01	7	588	330 ± 40	−11.37 ± 0.05	−11.37 ± 0.06	3.5	
IC 4776	0.1	18	619	4500 ± 100	−10.24 ± 0.01	−10.25 ± 0.04	4.4	
IC 4846	0.09	7	191	1590 ± 80	−10.69 ± 0.02	−10.70 ± 0.04	3.7	
IC 5148	0.20	6	92	2950 ± 100	−10.42 ± 0.01	−10.45 ± 0.04	6.4	
Abell 7	0.8	3	134	3880 ± 485	−10.30 ± 0.05	−10.42 ± 0.06	22	
Abell 10	1.24	5	242	369 ± 30	−11.32 ± 0.03	−11.49 ± 0.05	3.5	
Abell 13	4.0	5,15,30	207	770 ± 60	−11.00 ± 0.03	−11.40 ± 0.07	6.4	
Abell 15	0.16	5	103	107 ± 20	−11.86 ± 0.07	−11.89 ± 0.08	2.7	
Abell 18	2.6	6	208	170 ± 28	−11.66 ± 0.07	−11.96 ± 0.08	2.9	
Abell 20	0.12	5	209	205 ± 15	−11.58 ± 0.03	−11.60 ± 0.05	3.5	
Abell 21	1.61	2	245	18150 ± 300	−9.63 ± 0.01	−9.84 ± 0.04	16	
Abell 21	1.61	2	245	21600 ± 300	−9.56 ± 0.01	−9.76 ± 0.04	40	3
Abell 22	1.8	4	209	400 ± 80	−11.29 ± 0.08	−11.51 ± 0.09	4.8	
Abell 23	1.0	4	105	140 ± 25	−11.75 ± 0.07	−11.88 ± 0.08	2.9	
Abell 24	5.2	5,30,32	210	6140 ± 120	−10.10 ± 0.01	−10.57 ± 0.08	8.7	
Abell 25	2.3	6	210	185 ± 30	−11.62 ± 0.07	−11.89 ± 0.08	6.4	4
Abell 27	3.6	4,6	106	205 ± 30	−11.58 ± 0.06	−11.95 ± 0.08	3.2	
Abell 29	4.5	3,4	139	2340 ± 140	−10.52 ± 0.03	−10.95 ± 0.07	8.4	
Abell 31	0.94	2	247	6700 ± 500	−10.07 ± 0.03	−10.20 ± 0.05	21	
Abell 33	0.17	5	212	> 500 ± 50	> −11.2	> −11.2	5.0	
Abell 34	0.64	5	177	510 ± 20	−11.18 ± 0.02	−11.28 ± 0.04	7.3	
Abell 35	0.86	2	145	10050 ± 250	−9.89 ± 0.01	−10.01 ± 0.04	18	7
Abell 36	0.00	5	146	2380 ± 100	−10.51 ± 0.02	−10.51 ± 0.04	10	
Abell 41	0.36	7	152	192 ± 15	−11.61 ± 0.03	−11.66 ± 0.05	2.7	
Abell 45	4.0	3	190	930 ± 100	−10.92 ± 0.04	−11.32 ± 0.08	4.8	
Abell 48	0.36	4	226	225 ± 25	−11.54 ± 0.04	−11.59 ± 0.05	3.7	
Abell 56	1.0	3	227	700 ± 70	−11.05 ± 0.04	−11.18 ± 0.06	4.8	
Abell 62	1.40	4,13,15	263	950 ± 50	−10.91 ± 0.02	−11.10 ± 0.05	3.5	
Abell 65	0.21	5,33,34	155	970 ± 30	−10.90 ± 0.01	−10.94 ± 0.04	4.8	
Abell 66	0.6	4,29	155	1197 ± 28	−10.81 ± 0.01	−10.90 ± 0.04	6.0	
BlDz 1	0.8	4	55	650 ± 100	−11.08 ± 0.06	−11.19 ± 0.07	4.4	5
BoBn 1	0.17	58	662	88 ± 8	−11.95 ± 0.04	−11.97 ± 0.05	4.5	
CTIO1230-275	0.0	4	111	18 ± 5	−12.64 ± 0.11	−12.64 ± 0.11	1.1	6?
CVMP 1	11.0	3,35	36	1030 ± 100	−10.88 ± 0.04	−11.59 ± 0.15	6.4	
DeHt 1	0.0	6	135	650 ± 200	−11.08 ± 0.12	−11.08 ± 0.12	4.8	4
DeHt 3	1.25	32	154	230 ± 50	−11.53 ± 0.09	−11.70 ± 0.09	4.8	
DS 1	0.0	3	54	1800 ± 90	−10.64 ± 0.02	−10.64 ± 0.04	5.2	
DS 2	0.0	3	85	210 ± 40	−11.57 ± 0.10	−11.57 ± 0.11	4.5	
EGB 5	0.3	3	246	100 ± 20	−11.89 ± 0.08	−11.94 ± 0.09	3.5	

Name	NII/Hα	Ref	field	count	F_{red}	F(Hα)	aperture	Notes
EGB 6	0.32	2	249	900 ± 50	−10.94 ± 0.02	−10.99 ± 0.04	15.9	
EGB 9	0.5	3	245	510 ± 60	−11.18 ± 0.05	−11.26 ± 0.06	6.8	
ESO 40-PN11	0.0	4	18	125 ± 30	−11.79 ± 0.09	−11.79 ± 0.10	4.8	
Fg 1	0.17	4	54	2670 ± 80	−10.46 ± 0.01	−10.49 ± 0.04	4.8	
Fg 2	0.37	4	87	610 ± 30	−11.11 ± 0.02	−11.16 ± 0.04	2.9	
G4.4+6.4	1.5	3	152	700 ± 100	−11.05 ± 0.06	−11.24 ± 0.07	4.8	
G247.8+4.9	10.0	3	106	420 ± 100	−11.27 ± 0.09	−11.94 ± 0.16	3.5	
H 1-3	1.43	7	86	175 ± 30	−11.65 ± 0.07	−11.83 ± 0.08	2.4	6
H 2-1	0.57	7	117	1750 ± 200	−10.65 ± 0.05	−10.73 ± 0.06	3.7	6
HaTr 1	0.6	4	533	220 ± 25	−11.55 ± 0.05	−11.63 ± 0.06	4.8	
HaTr 4	0.03	4	60	145 ± 20	−11.73 ± 0.06	−11.73 ± 0.06	0.0	
HaTr 7	0.3	3,4	38	380 ± 80	−11.31 ± 0.08	−11.36 ± 0.09	4.8	
HaTr 9	2.0	3	88	540 ± 50	−11.16 ± 0.04	−11.40 ± 0.10	4.8	
HaWe 7	0.78	4,31	172	695 ± 20	−11.05 ± 0.01	−11.16 ± 0.05	3.8	7?
HaWe 10	1.0	36	246	59 ± 10	−12.12 ± 0.07	−12.26 ± 0.08	3.0	
HaWe 13	0.0	4	227	75 ± 10	−12.02 ± 0.06	−12.02 ± 0.10	3.7	
Hb 4	0.40	7	152	1090 ± 25	−10.85 ± 0.01	−10.91 ± 0.04	4.3	
Hb 5	1.6	4	118	4940 ± 100	−10.20 ± 0.01	−10.41 ± 0.04	4.3	
Hb 6	0.63	7	153	1120 ± 40	−10.84 ± 0.02	−10.93 ± 0.04	4.0	
HbDs 1	0.0	3	53	220 ± 40	−11.55 ± 0.09	−11.55 ± 0.10	3.2	5
Hewett 1	0.61	2	214	7800 ± 1500	−10.00 ± 0.08	−10.09 ± 0.09	81.0	7
He 2-9	0.32	8	77	620 ± 25	−11.10 ± 0.02	−11.15 ± 0.04	3.5	
He 2-11	0.48	7	77	980 ± 50	−10.90 ± 0.02	−10.97 ± 0.04	3.7	
He 2-15	3.67	7	77	1500 ± 60	−10.72 ± 0.02	−11.09 ± 0.06	3.3	
He 2-25	0.05	7	52	410 ± 20	−11.28 ± 0.02	−11.29 ± 0.04	3.3	
He 2-34	0.02	8	53	65 ± 20	−12.08 ± 0.12	−12.08 ± 0.12	7.8	7
He 2-36	0.17	7	32	1110 ± 40	−10.85 ± 0.02	−10.87 ± 0.04	3.8	
He 2-41	0.20	8	32	480 ± 30	−11.21 ± 0.03	−11.24 ± 0.05	3.2	
He 2-47	1.12	8	32	4800 ± 80	−10.21 ± 0.01	−10.36 ± 0.04	2.5	6
He 2-62	0.23	8	17	295 ± 20	−11.42 ± 0.03	−11.46 ± 0.05	2.7	1
He 2-69	0.37	7	33	1325 ± 30	−10.77 ± 0.01	−10.83 ± 0.04	3.5	
He 2-70	7.6	4	33	600 ± 70	−11.11 ± 0.05	−11.70 ± 0.11	3.2	
He 2-71	0.44	8	17	740 ± 20	−11.02 ± 0.01	−11.09 ± 0.04	3.2	
He 2-73	0.57	8	17	665 ± 30	−11.07 ± 0.02	−11.15 ± 0.04	3.7	
He 2-73	0.57	8	533	630 ± 25	−11.09 ± 0.02	−11.18 ± 0.04	3.7	
He 2-77	0.12	7	33	360 ± 24	−11.33 ± 0.03	−11.35 ± 0.05	4.8	8
He 2-86	0.61	8	533	600 ± 40	−11.11 ± 0.03	−11.20 ± 0.05	3.2	
He 2-90	0.18	7	34	2530 ± 40	−10.49 ± 0.01	−10.52 ± 0.04	3.5	
He 2-96	0.31	8	35	470 ± 40	−11.22 ± 0.04	−11.27 ± 0.05	3.5	
He 2-97	1.33	8	18	1460 ± 40	−10.73 ± 0.01	−10.90 ± 0.04	3.5	
He 2-99	0.98	7	18	1040 ± 60	−10.87 ± 0.02	−11.01 ± 0.05	4.1	
He 2-104	0.15	8	57	1230 ± 30	−10.80 ± 0.01	−10.83 ± 0.04	3.2	7
He 2-108	0.46	7	57	1400 ± 20	−10.75 ± 0.01	−10.81 ± 0.04	3.5	
He 2-111	3.0	7,21	35	3210 ± 50	−10.38 ± 0.01	−10.71 ± 0.05	4.1	
He 2-113	0.71	8	58	1450 ± 20	−10.73 ± 0.01	−10.83 ± 0.04	3.5	
He 2-114	1.51	7	36	410 ± 80	−11.28 ± 0.08	−11.47 ± 0.09	2.7	6
He 2-117	0.75	8	36	640 ± 30	−11.09 ± 0.02	−11.19 ± 0.04	3.5	

Name	NII/Hα	Ref	field	count	F_{red}	F(Hα)	aperture	Notes
He 2-118	0.10	8	84	540 ± 30	−11.16 ± 0.02	−11.17 ± 0.04	3.2	
He 2-123	1.28	8	58	1050 ± 25	−10.87 ± 0.01	−11.04 ± 0.04	3.7	
He 2-125	1.09	8	58	240 ± 20	−11.51 ± 0.03	−11.66 ± 0.05	2.5	
He 2-131	1.2	43,61	19	28200 ± 2500	−9.44 ± 0.04	−9.60 ± 0.05	9.5	3
He 2-138	0.64	7	19	7040 ± 100	−10.04 ± 0.01	−10.14 ± 0.04	4.9	
He 2-140	1.44	8	37	640 ± 25	−11.09 ± 0.02	−11.27 ± 0.04	3.7	
He 2-142	1.31	8	37	1570 ± 30	−10.70 ± 0.01	−10.87 ± 0.04	3.2	
He 2-142	1.31	8	59	700 ± 70	−11.05 ± 0.04	−11.22 ± 0.06	3.2	1
He 2-180	0.4	4	151	640 ± 20	−11.09 ± 0.01	−11.15 ± 0.04	3.7	
He 2-182	0.24	8	37	3300 ± 100	−10.37 ± 0.01	−10.41 ± 0.04	3.2	
HFG 2	0.2	3	105	800 ± 600	−10.99 ± 0.24	−11.02 ± 0.25	4.8	
J 320	0.03	4	242	1040 ± 20	−10.87 ± 0.01	−10.88 ± 0.04	3.7	
K 1-2	0.51	4	107	95 ± 20	−11.91 ± 0.08	−11.99 ± 0.09	3.2	
K 1-9	9.0	37	173	130 ± 15	−11.78 ± 0.05	−12.42 ± 0.13	2.5	
K 1-10	3.0	3	137	130 ± 40	−11.78 ± 0.12	−12.10 ± 0.13	4.8	
K 1-22	0.21	5	110	1400 ± 40	−10.75 ± 0.01	−10.78 ± 0.04	5.7	1
K 1-23	0.61	4	81	540 ± 50	−11.16 ± 0.04	−11.25 ± 0.05	4.8	
K 1-27	0.00	4	4	65 ± 20	−12.08 ± 0.12	−12.08 ± 0.12	4.8	
K 2-2	0.33	5	244	3905 ± 650	−10.30 ± 0.07	−10.35 ± 0.08	12	6
KFR 1	4.0	3	33	305 ± 35	−11.41 ± 0.05	−11.80 ± 0.08	3.5	8
KLSS 1-8	10.0	3	637	150 ± 50	−11.72 ± 0.12	−12.39 ± 0.18	4.9	
Lo 1	0.1	3	70	906 ± 14	−10.93 ± 0.01	−10.95 ± 0.04	8.3	1
Lo 1	0.1	3	570	705 ± 20	−11.04 ± 0.01	−11.06 ± 0.04	8.7	
Lo 3	0.23	4	50	527 ± 112	−11.17 ± 0.08	−11.21 ± 0.09	3.3	
Lo 5	1.00	4	54	1005 ± 25	−10.89 ± 0.01	−11.03 ± 0.04	4.6	
Lo 6	1.54	4	55	230 ± 18	−11.53 ± 0.03	−11.73 ± 0.05	3.8	
Lo 8	0.0	4	82	120 ± 30	−11.81 ± 0.10	−11.81 ± 0.10	3.5	
Lo 9	2.56	4	59	120 ± 15	−11.81 ± 0.04	−12.10 ± 0.06	3.5	
Lo 11	0.80	4	86	95 ± 30	−11.91 ± 0.12	−12.03 ± 0.13	3.5	1
Lo 12	0.57	4	**	78 ± 11	−12.00 ± 0.06	−12.08 ± 0.07	2.9	
Lo 16	0.04	4	89	1410 ± 70	−10.74 ± 0.02	−10.75 ± 0.04	3.5	
Lo 17	0.42	29	88	240 ± 15	−11.51 ± 0.03	−11.57 ± 0.05	4.0	
M 1-6	0.64	8	208	520 ± 30	−11.18 ± 0.02	−11.27 ± 0.05	3.0	
M 1-11	0.95	8	137	1820 ± 35	−10.63 ± 0.01	−10.76 ± 0.04	4.3	
M 1-12	0.71	8	137	1250 ± 100	−10.79 ± 0.03	−10.90 ± 0.05	3.5	6
M 1-14	0.37	8	138	720 ± 30	−11.03 ± 0.02	−11.09 ± 0.04	2.7	4
M 1-16	3.51	8	173	1092 ± 20	−10.85 ± 0.01	−11.22 ± 0.06	3.5	
M 1-17	1.16	8	173	500 ± 25	−11.19 ± 0.02	−11.35 ± 0.05	3.7	
M 1-25	1.04	4	152	970 ± 20	−10.90 ± 0.01	−11.05 ± 0.04	3.8	
M 1-26	0.49	7	118	7120 ± 100	−10.04 ± 0.01	−10.11 ± 0.04	4.8	8?
M 1-28	6.2	32	152	690 ± 30	−11.05 ± 0.02	−11.57 ± 0.05	4.3	
M 1-40	1.34	7	153	700 ± 110	−11.05 ± 0.06	−11.22 ± 0.08	2.9	6
M 1-41	4.70	27,31	153	550 ± 100	−11.15 ± 0.10	−11.59 ± 0.15	2.9	
M 2-15	0.06	7	152	330 ± 20	−11.37 ± 0.03	−11.38 ± 0.05	3.3	
M 2-43	0.29	4	226	430 ± 20	−11.26 ± 0.02	−11.30 ± 0.04	4.6	
M 2-62	0.3	3	208	585 ± 20	−11.12 ± 0.01	−11.17 ± 0.04	4.1	8?
M 3-3	5.2	4,32	173	395 ± 10	−11.29 ± 0.01	−11.76 ± 0.04	3.7	

Name	NII/Hα	Ref	field	count	F_{red}	F(Hα)	aperture	Notes
M 3-3	5.2	4,32	708	330 ± 15	−11.37 ± 0.02	−11.84 ± 0.04	3.7	
M 3-5	1.8	32	638	450 ± 30	−11.24 ± 0.02	−11.36 ± 0.04	3.5	
Me 2-1	0.09	7	149	1120 ± 30	−10.84 ± 0.01	−10.86 ± 0.04	3.8	
MeWe 1-1	1.1	4	551	438 ± 25	−11.25 ± 0.02	−11.40 ± 0.05	4.0	
MeWe 1-2	1.8	3	32	500 ± 100	−11.19 ± 0.08	−11.42 ± 0.09	5.0	
MeWe 1-4	1.0	3	57	180 ± 30	−11.64 ± 0.07	−11.77 ± 0.08	4.0	
MeWe 1-10	0.25	39	560	95 ± 20	−11.91 ± 0.08	−11.95 ± 0.09	3.5	
MeWe 1-11	0.5	39	61	107 ± 30	−11.86 ± 0.11	−11.94 ± 0.11	3.2	
MeWe 2-4	1.0	3	57	630 ± 100	−11.09 ± 0.06	−11.23 ± 0.08	6.8	
Murrell 1	0.3	3	84	50 ± 15	−12.19 ± 0.11	−12.24 ± 0.12	3.3	
My 60	0.07	7	553	760 ± 40	−11.01 ± 0.02	−11.02 ± 0.04	3.5	
MyCn 18	1.30	8	534	4290 ± 80	−10.26 ± 0.01	−10.43 ± 0.04	3.8	
Mz 1	2.59	40	36	4320 ± 150	−10.26 ± 0.01	−10.55 ± 0.05	4.1	
Mz 2	0.8	4	59	750 ± 50	−11.02 ± 0.03	−11.13 ± 0.05	3.2	
Mz 3	1.0	41	59	5500 ± 80	−10.15 ± 0.01	−10.29 ± 0.04	4.0	
NeVe 3-3	3.2	38	105	100 ± 10	−11.89 ± 0.04	−12.23 ± 0.07	3.2	
Pe 1-1	0.55	8	553	510 ± 40	−11.18 ± 0.03	−11.26 ± 0.05	2.5	6
Pe 1-2	0.10	8	553	270 ± 100	−11.46 ± 0.14	−11.48 ± 0.14	2.4	6
PHL 932	0.4	2	235	1480 ± 80	−10.72 ± 0.02	−10.77 ± 0.04	11	7
PHL 932	0.3	2	236	1525 ± 75	−10.71 ± 0.02	−10.75 ± 0.04	11	7
SaWe 3	6.2	4,29	153	1200 ± 100	−10.81 ± 0.03	−11.33 ± 0.09	6.4	
SaWe 4	0.0	29	154	50 ± 10	−12.19 ± 0.08	−12.19 ± 0.09	4.8	
Sh 2-68	0.53	2	226	3080 ± 90	−10.40 ± 0.01	−10.48 ± 0.04	10	
Sh 2-68	0.53	2	226	5200 ± 150	−10.18 ± 0.01	−10.25 ± 0.04	17	3
Sh 2-71	6.0	4,31,44	226	3250 ± 150	−10.38 ± 0.02	−10.89 ± 0.09	6.4	
Sh 2-78	1.85	2	263	3300 ± 200	−10.37 ± 0.03	−10.60 ± 0.05	14	
Sn 1	0.01	7	223	503 ± 15	−11.19 ± 0.01	−11.19 ± 0.04	4.3	
Sp 1	0.12	7	59	770 ± 50	−11.00 ± 0.03	−11.02 ± 0.05	4.8	
Sp 3	0.32	4	61	3970 ± 150	−10.29 ± 0.02	−10.34 ± 0.04	4.8	
SuWt 2	7.0	3,4,63	35	580 ± 120	−11.13 ± 0.08	−11.69 ± 0.12	3.8	
SwSt 1	0.4	26	119	10200 ± 60	−9.88 ± 0.00	−9.95 ± 0.04	4.8	
vBe 1	0.4	3	60	7000 ± 1500	−10.05 ± 0.08	−10.11 ± 0.09	7.9	8?
vBe 2	5.0	25	36	100 ± 100	−11.89 ± 0.30	−12.35 ± 0.31	4.8	
VBRC 1	5.6	4	77	840 ± 80	−10.97 ± 0.04	−11.46 ± 0.09	4.8	
VBRC 2	1.7	45	31	1440 ± 60	−10.73 ± 0.02	−10.95 ± 0.05	4.4	
VBRC 4	5.3	4	533	720 ± 30	−11.03 ± 0.02	−11.51 ± 0.08	3.2	
VBRC 5	3.2	4	35	305 ± 30	−11.41 ± 0.04	−11.75 ± 0.07	2.9	
VBRC 7	1.55	4	59	170 ± 30	−11.66 ± 0.07	−11.86 ± 0.08	4.0	
Vy 2-2	0.07	7	263	1850 ± 40	−10.62 ± 0.01	−10.63 ± 0.04	4.0	
WDHS 1	4.0	3	243	6600 ± 1280	−10.07 ± 0.08	−10.47 ± 0.10	23	
We 2-34	2.5	3	208	142 ± 20	−11.74 ± 0.06	−12.03 ± 0.08	5.4	
We 3-1	0.33	13	262	320 ± 20	−11.39 ± 0.03	−11.44 ± 0.05	4.3	
WKG 3	4.3	28	35	110 ± 20	−11.85 ± 0.07	−12.26 ± 0.10	2.9	
Wr 16-122	0.8	4,32	34	140 ± 25	−11.75 ± 0.07	−11.86 ± 0.08	2.9	
YM 16	3.0	3	226	640 ± 50	−11.09 ± 0.03	−11.41 ± 0.06	5.6	

References for Table 3.1 and Table 3.2:

1. This work, table 3.7; 2. This work, table 3.8; 3. This work, table 5.3 and unpublished spectroscopy; 4. Acker et al. (1992); 5. Kaler (1980, 1981b, 1983a,b); 6. Kaler, Shaw & Kwitter (1990); 7. Shaw & Kaler (1989); 8. Dopita & Hua (1997); 9. Krabbe & Copetti (2006); 10. Kwitter, Henry & Milingo (2003); 11. Walsh (1983); 12. Kingsburgh & Barlow (1994); 13. Hippelein & Weinberger (1990); 14. Torres-Peimbert, Peimbert & Peña (1990); 15. Phillips, Cuesta & Kemp (2005); 16. Tsamis et al. (2003); 17. Lui et al. (2004); 18 Aller & Czyzak (1983); 19. Groves et al. (2002); 20. Monteiro et al. (2004); 21. Pottasch, Beintema & Feibelman (2000); 22. Aller, Keyes & Feibelman (1988); 23. Aller & Keyes (1987); Henry, Kwitter & Bates (2000); 25. Ruiz (1983, 1986); 26. De Marco et al. (2001); 27. Dopita (1977); 28. Weinberger, Kerber & Gröbner (1997); 29. Hua, Dopita & Martinis (1998); 30. Hua & Kwok (1999); 31. Bohigas (2001); 32. Bohigas (2003); 33. Pollacco & Bell (1997); 34. Perinotto et al. (1994); 35. Corradi et al. (1997); 36. Ali (1999); 37. Kondratyeva & Denissyuk (2003); 38. Kerber et al. (2000a); 39. Emprechtinger, Forveille & Kimeswenger (2004); 40. Monteiro et al. (2005); 41. Pottasch & Surendiranath (2005); 42. Boumis et al. (2006); 43. Kohoutek & Martin (1981); 44. Hua (1997); 45. Peña et al. (1997); 46. Boeshaar (1974); 47. Ercolano et al. (2003b); 48. Sabbadin, Falomo & Ortolani (1987); 49. Jacoby, Ferland & Korista (2001); 50. Bohigas & Tapia (2003); 51. Rodríguez, Corradi & Mampaso (1999); 52. Tajitsu et al. (1999); 53. Kimeswenger (1998); 54. Frew, Parker & Russeil (2006); 55. Costa, de Freitas Pacheco & De França (1996); 57. Barker (1978); 58. Wright, Corradi & Perinotto (2005); 59. Liu et al. (2006); 60. Liu et al. (2000); 61. Peimbert & Torres-Peimbert (1977); 62. Perinotto & Corradi (1998); 63. Smith, Bally & Walawender (2007). Notes for Table 3.1 and Table 3.2:

1. Nebula near edge of field;
2. sky taken outside halo;
3. flux includes halo;
4. uncertain count;
5. uncertain background correction;
6. symbiotic star;
7. not a PN;
8. PHR1200-5904;
9. Sh 2-42.

Table 3.2: SHASSA Hα fluxes for new MASH PNe (Parker et al. 2006a) and new objects found from SHASSA and VTSS (see Frew, Madsen & Parker 2006).

Name	NII/Hα	Ref	field	count	F_{red}	F(Hα)	aperture	Notes
Fr 2-2	1.4	2	238	950 ± 150	-10.94 ± 0.06	−11.01 ± 0.08	20	7?
Fr 2-3	1.6	2	101	1000 ± 300	−10.89 ± 0.11	−11.09 ± 0.12	19	7
Fr 2-4	0.5	3	4	4800 ± 900	−10.21 ± 0.07	−10.28 ± 0.10	38	7
Fr 2-8	0.1	3	57	307 ± 21	−11.40 ± 0.03	−11.42 ± 0.05	4.4	
Fr 2-9	0.87	2	184	4800 ± 3700	−10.21 ± 0.25	−10.33 ± 0.25	90	7?
Fr 2-10	1.4	2	720	1950 ± 250	−10.60 ± 0.05	−10.79 ± 0.07	40	7?
Fr 2-11	0.8	3	37	1120 ± 80	−10.84 ± 0.03	−10.96 ± 0.05	9.8	7
Fr 2-15	1.0	2	265	2900 ± 300	−10.43 ± 0.04	−10.57 ± 0.06	25	7?
Fr 2-16	...	...	266	700 ± 400	−11.05 ± 0.20	...	29	7
FP0709-2555	0.5	3	104	1570 ± 200	−10.70 ± 0.05	−10.77 ± 0.06	20	7
FP0711-2531	0.6	3	104	2550 ± 200	−10.48 ± 0.03	−10.57 ± 0.05	15	
FP0721+0133	0.5	3	209	600 ± 100	−11.11 ± 0.07	−11.19 ± 0.08	15	
FP0739-2709	2.0	3	105	700 ± 100	−11.05 ± 0.06	−11.29 ± 0.07	11	
FP0821-2755	10.0	3	106	350 ± 150	−11.35 ± 0.15	−12.02 ± 0.17	6.5	
FP0840-5754	0.4	3	31	2400 ± 400	-10.51 ± 0.07	-10.59 ± 0.08		
FP0904-4023	0.5	3	77	1170 ± 100	−10.82 ± 0.04	−10.90 ± 0.05	12	5,7?
FP0905-3033	1.0	3	107	3200 ± 800	−10.39 ± 0.10	−10.52 ± 0.10	16	
FP1001-5458	0.5	3	53	16600 ± 2000	−9.67 ± 0.05	−9.75 ± 0.06	20	7
FP1054-7011	0.4	3	16	1150 ± 200	−10.83 ± 0.07	−10.89 ± 0.08	10	7?
FP1721-5654	1.5	3	38	1120 ± 100	−10.84 ± 0.04	−11.04 ± 0.06	9.5	
FP1804-4528	1.0	3	61	500 ± 200	−11.19 ± 0.15	−11.33 ± 0.15	9.5	
FP1819-0330	1.0	3	225	450 ± 90	−11.24 ± 0.08	−11.38 ± 0.09	14	7?
FP1824-0319	1.1	2,3	226	4150 ± 250	−10.27 ± 0.03	−10.42 ± 0.05	29	
FP1859-1049	0.5	3	190	530 ± 100	−11.17 ± 0.08	−11.24 ± 0.08	9.5	7?
PFP 1	1.5	2,3	173	2430 ± 1020	−10.51 ± 0.15	−10.70 ± 0.16	21	
RCW 24	6.5	3	77	3000 ± 200	−10.41 ± 0.03	−10.95 ± 0.09	15	
RCW 69	6.5	3	34	3330 ± 180	−10.37 ± 0.02	−10.91 ± 0.09	13	
PHR0615-0025	0.0	3	207	95 ± 40	−11.91 ± 0.15	−11.91 ± 0.15	3.8	
PHR0633-0135	0.5	3	208	20 ± 8	−12.59 ± 0.15	−12.66 ± 0.15	3.0	
PHR0650+0013	2.7	3	208	210 ± 20	−11.57 ± 0.04	−11.87 ± 0.06	3.3	
PHR0652-1240	0.92	3	172	180 ± 20	−11.64 ± 0.05	−11.76 ± 0.06	4.0	
PHR0719-1222	2.7	3	173	160 ± 30	−11.69 ± 0.07	−11.99 ± 0.09	3.8	
PHR0724-1757	8.3	3	138	60 ± 20	−12.11 ± 0.12	−12.73 ± 0.16	3.5	
PHR0740-2057	1.0	3	138	50 ± 15	−12.19 ± 0.11	−12.33 ± 0.12	4.0	
PHR0743-1951	1.6	3	138	330 ± 35	−11.37 ± 0.04	−11.58 ± 0.06	7.1	
PHR0747-2146	0.55	3	138	170 ± 20	−11.66 ± 0.05	−11.74 ± 0.06	4.1	
PHR0755-3346	0.7	3	105	70 ± 20	−12.05 ± 0.11	−12.15 ± 0.12	3.2	
PHR0800-1635	1.7	3	138	60 ± 20	−12.11 ± 0.12	−12.33 ± 0.13	3.7	
PHR0808-3745	0.79	3	76	135 ± 40	−11.76 ± 0.11	−11.87 ± 0.12	4.1	
PHR0834-2819	1.0	3	106	110 ± 20	−11.85 ± 0.07	−11.99 ± 0.08	4.0	
PHR0905-4753	1.7	3	52	275 ± 40	−11.45 ± 0.06	−11.67 ± 0.07	3.3	
PHR0905-4753	1.7	3	275	218 ± 15	−11.55 ± 0.03	−11.77 ± 0.05	3.0	
PHR0941-5356	0.5	3	53	650 ± 200	−11.08 ± 0.12	−11.15 ± 0.12	10	7?
PHR0942-5220	0.55	3	53	250 ± 30	−11.49 ± 0.05	−11.57 ± 0.06	4.0	
PHR1032-6310	1.5	3	32	270 ± 30	−11.46 ± 0.05	−11.65 ± 0.06	3.8	

Name	NII/Hα	Ref	field	count	F_{red}	F(Hα)	aperture	Notes
PHR1040-5417	1.3	3	54	720 ± 100	−11.03 ± 0.06	−11.21 ± 0.07	7.9	1
PHR1052-5042	0.5	3	54	270 ± 30	−11.46 ± 0.05	−11.53 ± 0.06		
PHR1118-6150	1.5	3	33	400 ± 200	−11.29 ± 0.18	−11.48 ± 0.18	6.4	5
PHR1137-6548	0.5	3	55	190 ± 40	−11.61 ± 0.08	−11.69 ± 0.09	3.7	7?
PHR1200-5904	1.0	3	33	335 ± 20	−11.37 ± 0.03	−11.50 ± 0.05	4.1	
PHR1202-6307	0.3	3	33	180 ± 80	−11.64 ± 0.16	−11.68 ± 0.16	3.8	7?
PHR1202-7000	9.0	3	17	660 ± 60	−11.07 ± 0.04	−11.71 ± 0.12	5.1	
PHR1246-6324	0.8	3	34	53 ± 10	−12.17 ± 0.08	−12.28 ± 0.08	2.5	
PHR1250-6346	1.7	3	34	95 ± 10	−11.91 ± 0.04	−12.13 ± 0.06	3.2	
PHR1255-6251	10.0	3	34	40 ± 20	−12.3 ± 0.2	−13.0 ± 0.3	4.0	4
PHR1304-6024	1.5	3	34	26 ± 10	−12.48 ± 0.14	−12.70 ± 0.15	2.4	
PHR1318-5601	3.0	3	34	92 ± 15	−11.93 ± 0.07	−12.25 ± 0.08	3.5	
PHR1318-5601	3.0	3	35	53 ± 29	−12.17 ± 0.19	−12.49 ± 0.20	3.5	1
PHR1327-6032	3.3	3	35	345 ± 40	−11.35 ± 0.05	−11.70 ± 0.07	3.5	
PHR1337-6535	3.5	3	18	395 ± 30	−11.29 ± 0.03	−11.66 ± 0.07	4.1	
PHR1408-6106	1.9	3	35	360 ± 80	−11.33 ± 0.09	−11.57 ± 0.10	5.2	
PHR1408-6229	8.0	3	35	340 ± 100	−11.36 ± 0.11	−11.96 ± 0.15	2.5	
PHR1418-5144	1.4	3	57	490 ± 20	−11.20 ± 0.02	−11.39 ± 0.05	7.9	
PHR1424-5138	0.0	3	57	55 ± 10	−12.15 ± 0.07	−12.15 ± 0.07	4.0	
PHR1432-6138	2.6	3	35	1000 ± 90	−10.89 ± 0.04	−11.19 ± 0.06	4.8	
PHR1437-5949	8.0	3	35	30 ± 10	−12.41 ± 0.12	−13.0 ± 0.2	3.0	
PHR1501-4817	0.8	3	58	40 ± 15	−12.29 ± 0.14	−12.40 ± 0.14	3.0	7?
PHR1510-6754	4.8	3	19	540 ± 60	−11.16 ± 0.05	−11.60 ± 0.10	6.0	
PHR1517-5751	0.5	3	36	55 ± 15	−12.15 ± 0.10	−12.23 ± 0.11	3.2	
PHR1529-5458	1.5	3	36	60 ± 15	−12.11 ± 0.10	−12.44 ± 0.11	3.5	
PHR1533-4824	2.4	3	58	80 ± 20	−11.99 ± 0.10	−12.27 ± 0.11	3.2	
PHR1534-5829	1.5	3	36	120 ± 50	−11.81 ± 0.15	−12.01 ± 0.16	3.2	
PHR1537-6159	1.8	3	36	75 ± 30	−12.02 ± 0.15	−12.24 ± 0.15	2.7	
PHR1547-5929	0.8	3	36	500 ± 50	−11.19 ± 0.04	−11.31 ± 0.06	4.4	
PHR1553-5738	0.8	3	36	240 ± 20	−11.51 ± 0.03	−11.62 ± 0.05	4.1	
PHR1602-4127	1.2	3	86	430 ± 30	−11.26 ± 0.03	−11.42 ± 0.05		
PHR1619-4914	2.3	3	39	15 ± 3	−12.72 ± 0.08	−12.99 ± 0.10	2.7	
PHR1625-4523	0.98	3	59	590 ± 80	−11.12 ± 0.06	−11.26 ± 0.07	6.7	
PHR1651-3148	0.3	3	117	145 ± 30	−11.73 ± 0.08	−11.78 ± 0.09	3.3	
PHR1709-3629	2.5	3	87	16 ± 5	−12.69 ± 0.12	−12.97 ± 0.15	2.4	7?
PHR1757-1649	1.5	3	153	475 ± 30	−11.21 ± 0.03	−11.41 ± 0.05	4.0	
PHR1758-2139	1.5	3	153	110 ± 20	−11.85 ± 0.07	−12.04 ± 0.08	3.7	
PHR1806-1956	1.9	3	153	31 ± 5	−12.40 ± 0.06	−12.63 ± 0.08	1.9	
PHR1810-1647	1.0	3	153	970 ± 80	−10.90 ± 0.03	−11.04 ± 0.05	3.5	9
PHR1818-1526	5.0	3	153	35 ± 5	−12.35 ± 0.06	−12.8 ± 0.2	1.6	
PHR1831-1415	0.03	42	190	115 ± 20	−11.83 ± 0.07	−11.84 ± 0.08	2.2	
PHR1844-0452	7.0	3	190	40 ± 10	−12.29 ± 0.10	−12.9 ± 0.2	4.0	
PHR1911-1546	0.5	3	154	340 ± 20	−11.36 ± 0.02	−11.43 ± 0.05	4.0	

VTSS

A smaller number of PNe were measured from the VTSS survey (Dennison, Simonetti & Topasna 1998). The procedure is identical to that used for the SHASSA measurements with the important simplification that a correction for [NII] is not necessary as these lines are not passed by the narrowband VTSS Hα filter. The native units of VTSS are Rayleighs.

The resolution of VTSS is coarser than SHASSA and owing to the increased level of confusion at low intensities, the VTSS flux limit is brighter, $\log \mathrm{F(H\alpha)} \simeq -11.5$ compared to $\log \mathrm{F(H\alpha)} = -12.5$ for SHASSA. The raw VTSS Hα measurements are given in table 3.3, as well as the corrected VTSS fluxes based on the known zero-point offset between SHASSA and VTSS (see the next section). After scaling, the adopted VTSS zero-point error is assumed to be equivalent to SHASSA. This error has been added in quadrature to the measurement error determined from the APERPHOTOM routine to determine the final uncertainty on the Hα flux.

Table 3.3: VTSS Hα fluxes for PNe and other nebulae (see text).

Name	field	sum	F(Hα)	F(Hα)(corr)	aperture	Notes
NGC 650-1	Cas03	1150 ± 75	−10.22 ± 0.03	−10.12 ± 0.05	9.3	...
NGC 2022	Ori01	450 ± 45	−10.63 ± 0.04	−10.53 ± 0.06	6.4	...
NGC 2242	Aur11	43 ± 7	−11.65 ± 0.07	−11.55 ± 0.08	4.2	...
NGC 2346	Mon07	330 ± 16	−10.76 ± 0.02	−10.67 ± 0.04	8.3	...
NGC 2438	Mon05	760 ± 50	−10.40 ± 0.03	−10.30 ± 0.05	5.8	1
NGC 6720	Lyr01	4500 ± 50	−9.63 ± 0.01	−9.53 ± 0.04	10	...
NGC 6543	Dra14	12135 ± 100	−9.20 ± 0.01	−9.10 ± 0.04	13	...
NGC 6765	Lyr01	76 ± 10	−11.40 ± 0.05	−11.30 ± 0.07	5.1	...
NGC 6781	Aql04	1488 ± 50	−10.11 ± 0.01	−10.01 ± 0.04	11	...
NGC 6886	Sge01	320 ± 15	−10.78 ± 0.02	−10.68 ± 0.04	6.4	...
NGC 6905	Sge01	545 ± 15	−10.55 ± 0.01	−10.45 ± 0.04	8.5	...
NGC 7027	Cyg08	8150 ± 100	−9.37 ± 0.01	−9.27 ± 0.04	12	1
NGC 7048	Cyg08	215 ± 25	−10.95 ± 0.05	−10.85 ± 0.06	4.8	...
IC 289	Cas06	228 ± 20	−10.92 ± 0.04	−10.83 ± 0.05	5.8	...
IC 418	Ori11	14400 ± 140	−9.12 ± 0.00	−9.03 ± 0.04	14	...
IC 4997	Sge01	1920 ± 45	−10.00 ± 0.01	−9.90 ± 0.04	11	...
IC 5117	Cyg08	420 ± 25	−10.66 ± 0.03	−10.56 ± 0.05	6.7	...
IC 5217	Lac01	380 ± 15	−10.70 ± 0.02	−10.61 ± 0.04	7.0	...
Abell 2	Cas01	19 ± 7	−12.00 ± 0.14	−11.91 ± 0.14	3.8	...
Abell 13	Ori03	45 ± 8	−11.63 ± 0.07	−11.53 ± 0.08	6.1	...
Abell 20	Mon07	26 ± 7	−11.87 ± 0.10	−11.77 ± 0.11	3.8	...
Abell 31	Cnc02	1040 ± 150	−10.27 ± 0.06	−10.17 ± 0.07	22	...
Abell 53	Aql04	25 ± 5	−11.88 ± 0.08	−11.79 ± 0.09	5.8	...
Abell 56	Aql04	42 ± 15	−11.66 ± 0.13	−11.56 ± 0.14	6.4	...
Abell 61	Lyr03	64 ± 4	−11.48 ± 0.03	−11.38 ± 0.05	4.8	1
Abell 74	Vul04	355 ± 80	−10.73 ± 0.09	−10.64 ± 0.10	18	...
Abell 74	Peg05	310 ± 70	−10.79 ± 0.09	−10.69 ± 0.10	18	...
Abell 79	Cep00	59 ± 20	−11.58 ± 0.10	−11.49 ± 0.10	5.8	...
Abell 80	Lac01	54 ± 10	−11.55 ± 0.07	−11.45 ± 0.08	5.8	...
Abell 84	Cep01	105 ± 15	−11.26 ± 0.06	−11.16 ± 0.07	6.1	...

Name	field	sum	F(Hα)	F(Hα)(corr)	aperture	Notes
BD +30 3639	Vul01	6240 ± 20	−9.49 ± 0.00	−9.39 ± 0.04	9.6	...
DeHt 5	Cep06	500 ± 50	−10.58 ± 0.04	−10.49 ± 0.06	14	...
HaWe 4	Per05	240 ± 50	−10.90 ± 0.08	−10.81 ± 0.09	13	2
HaWe 15	Lac01	80 ± 13	−11.38 ± 0.07	−11.28 ± 0.08	11	...
Hu 1-1	Cas01	166 ± 12	−11.06 ± 0.03	−10.97 ± 0.05	6.4	...
IsWe 1	Cam00	200 ± 50	−10.98 ± 0.10	−10.88 ± 0.10	16	...
Jones 1	Peg16	261 ± 10	−10.87 ± 0.02	−10.77 ± 0.04	12	1
K 1-6	Cep08	74 ± 10	−11.41 ± 0.06	−11.32 ± 0.07	7.0	3
K 2-2	Mon11	900 ± 200	−10.33 ± 0.09	−10.23 ± 0.10	16	3,4
M 1-9	Mon09	120 ± 12	−11.20 ± 0.04	−11.11 ± 0.06	5.1	...
M 1-17	Mon05	70 ± 15	−11.44 ± 0.08	−11.34 ± 0.09	4.8	...
Me 2-2	Lac01	325 ± 60	−10.77 ± 0.07	−10.67 ± 0.08	6.4	...
PFP 1	Mon07	280 ± 100	−10.84 ± 0.13	−10.74 ± 0.14	22	...
Sh 1-89	Cyg08	70 ± 20	−11.44 ± 0.11	−11.34 ± 0.12	4.8	...
Sh 2-71	Aql04	230 ± 12	−10.92 ± 0.02	−10.82 ± 0.05	9.0	...
Sh 2-78	Aql15	380 ± 30	−10.70 ± 0.03	−10.61 ± 0.05	13	...
Sh 2-176	Cas01	...	...	...	...	5
Vy 1-1	Cas01	146 ± 16	−11.12 ± 0.05	−11.02 ± 0.06	6.1	...
Vy 1-2	Her13	135 ± 20	−11.15 ± 0.06	−11.06 ± 0.07	6.1	...
WDHS 1	Ori01	610 ± 220	−10.50 ± 0.13	−10.40 ± 0.14	24	...
We 1-6	Mon04	35 ± 15	−11.74 ± 0.15	−11.64 ± 0.16	5.1	...
We 2-34	Mon09	<18 ± 5		< −11.8 ± 0.11	7.0	...
WeSb 1	Cas03	11 ± 5	−12.24 ± 0.16	−12.14 ± 0.17	5.8	...
YM 16	Aql04	60 ± 12	−11.50 ± 0.08	−11.41 ± 0.09	8.3	...
Fr 2-13	Her13	135 ± 38	−11.15 ± 0.11	−11.06 ± 0.11	26	...
Fr 2-14	Cep08	2100 ± 300	−9.96 ± 0.06	−9.86 ± 0.07	60	...
Fr 2-18	Peg13	270 ± 40	−10.85 ± 0.06	−10.75 ± 0.07	25	...

Notes for Table 3.3:

1. Nebula near edge of field; 2. stars superposed; 3. nature uncertain; 4. uncertain background correction; 5. too diffuse for flux determination.

3.2.2 Comparison with other fluxes

Since Gaustad et al. (2001) used a number of well-studied PNe as calibrators for the SHASSA survey, it is to be expected that a comparison between PN literature fluxes and those derived here would have a small zero-point error. Not only does the expanded analysis here give a useful cross-check to the Gaustad et al. intensity calibration, but it also allows the veracity of the adopted aperture photometry technique used here to be ascertained, including the treatment of the deconvolution of the [N II] lines from the red flux for each PN.

To do this, published Hα fluxes for a large number ($\sim$100) of southern calibrating PNe were taken from Kohoutek & Martin (1981), Kaler (1983b), Shaw & Kaler (1989) and Dopita & Hua (1997) and compared with the values reported here. The comparisons are shown in Figure 3.2.

The fluxes from Kohoutek & Martin (1981) are in excellent agreement, while the Hα fluxes of Kaler (1983b) show the greatest scatter. This is attributed to the low surface brightness of the nebulae in Kaler (1983b), with consequent low photometer counts, and because the largest diaphragm is smaller than the diameter of some of the largest PNe he investigated. Hence, the total flux has been extrapolated upwards by a geometric factor (the ratio of the PN area to the aperture area). The SHASSA Hα fluxes measured here are integrated fluxes, measured through an aperture which was always larger than the nebula on the CCD image. They are to be preferred for these large evolved PNe.

The comparison was repeated for the VTSS fluxes derived here. The VTSS data has an arbitrary zero point (Dennison, Simonetti & Topasna 1998). Gaustad et al. (2001) found VTSS to be fainter than SHASSA by a factor of 1.25 in one overlap region near the equator (figure 3.3). Finkbeiner (2003) applied this same factor to all VTSS images in order compare it with SHASSA, using available WHAM data as a cross-check. The offset factor was assumed to be constant across the whole VTSS survey. Finkbeiner found the resulting agreement between VTSS and SHASSA to be good (see his figure 7), confirming this approach. After checking the VTSS fluxes for a selection of calibration PNe with known literature fluxes, the same factor was independently derived here (see figure 3.4). Table 3.3 gives both the raw VTSS Hα fluxes and the corrected Hα fluxes, after brightening by 25% (0.10 dex).

In addition, Xilouris et al. (1996) presented Hα+[N II] and [O III] fluxes for eight evolved PNe (see also Papamastorakis, Xilouris & Paleologou 1994). A comparison between their quoted surface brightness data and independent SHASSA measurements show the Xilouris et al. surface brightness data to be accurate, but the integrated fluxes were found to be too faint by a factor of $\sim$20 (see figure 3.4), presumably the result of a simple reduction error. In order to compare the Xilouris et al. (1996) data with those from other sources, firstly Hα fluxes were derived from their quoted 'red' fluxes by deconvolving the [N II] emission for each PN. Using the characteristics of the filter used by them (see Mavromatakis et al. 2000), the transmission for the [N II] doublet is identical to Hα making the calculation straightforward (i.e. the constant in equation 3.2 is unity). The adopted [N II]/Hα ratio was taken from either this work (table 3.1), or from Madsen et al. (2006), Hippelein & Weinberger (1990), Phillips, Cuesta & Kemp (2005), Gieseking, Hippelein & Weinberger (1986) and Ishida & Weinberger (1987).

Figure 3.4 shows the deconvolved Hα fluxes (points) from SHASSA against the Hα fluxes ([N II] deconvolved) from Xilouris et al. (1996; see Table 3.4) for each PN. Also plotted are the raw Xilouris et al. (1996) [O III] fluxes compared with the weighted mean [O III] fluxes from the literature and this work (crosses). The comparison data are taken from Kaler (1983b), the SHASSA fluxes from table 3.1 herein, plus the WHAM observations from Madsen et al. (2006). The Xilouris et al. (1996) fluxes are found to be offset in the mean by 1.31 ± 0.13 dex and this correction was hence applied to all their original fluxes. The *corrected* fluxes are presented in the last three columns of Table 3.4, and the flux errors are estimated to be $\pm\,0.15$ dex.

Another set of emission-line 'fluxes' in Hα, [N II] and [O III] is presented by Gieseking, Hippelein & Weinberger (1986) and Hippelein & Weinberger (1990). These authors used a Fabry-Perot spectrometer using $1'$ or $2'$ apertures (i.e. smaller than most of the PNe they

Table 3.4: Raw and corrected Hα, [O III] and [N II] fluxes from Xilouris et al. (1996)

Name	F(red) (raw)	[N II] /Hα	Ref	F(Hα) (raw)	F(6583) (raw)	F(5007) (raw)	F(Hα) (corr)	F(6583) (corr)	F(5007) (corr)
Abell 7	−11.59	0.8	1,2	−11.85	−12.07	−11.51	−10.53	−10.675	−10.20
Abell 62	−11.96	1.5	3,4	−12.29	−12.232	−12.30	−11.01	−11.00	−10.99
Abell 74	−11.51	1.3	2,5	−11.87	−12.03	−11.89	−10.56	−10.72	−10.58
HFG 1	−11.59	0.4	2,6	−11.77	−12.26	−11.54	−10.46	−10.94	−10.23
IsWe 1	−11.96	0.75	2,5,7	−12.07	−12.45	−12.40	−10.76	−11.14	−11.09
IsWe 2	−11.37	1.45	5,7	−11.76	−11.72	...	−10.45	−10.41	...
Sh 2-68	−11.66	0.53	2	−11.84	−12.26	−11.92	−10.53	−10.93	−10.61
Sh 2-176	−11.41	2.3	2	−11.93	−11.69	...	−10.62	−10.38	...
Sh 2-188	−10.87	1.9	2	−11.35	−11.18	−11.57	−10.04	−9.87	−10.26

Reference for [N II]/Hα ratio: (1) This work (MASH spectroscopic database); (2) This work, and Madsen et al. (2006), Madsen & Frew, in prep.; (3) Hippelein & Weinberger (1990); (4) Phillips, Cuesta & Kemp (2005); (5) Gieseking, Hippelein & Weinberger (1986); (6) Heckathorn, Fesen & Gull (1982); (7) Ishida & Weinberger (1987).

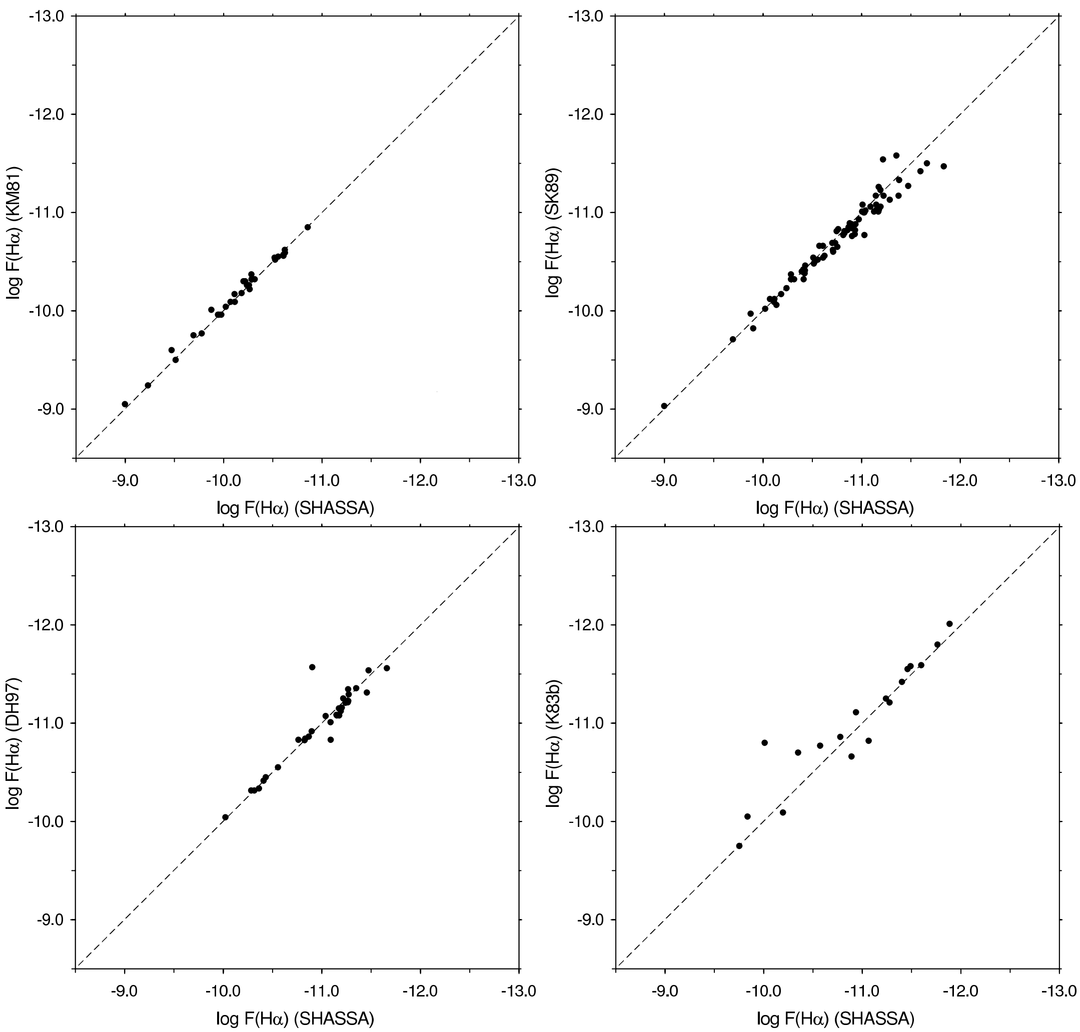

Figure 3.2: Comparison of new SHASSA Hα fluxes with fluxes from Kohoutek & Martin (1981) (top left), Shaw & Kaler (1989) (top right), Dopita & Hua (1997) (bottom left), and Kaler (1983b) (bottom right). The dashed lines represent a 1:1 correlation.

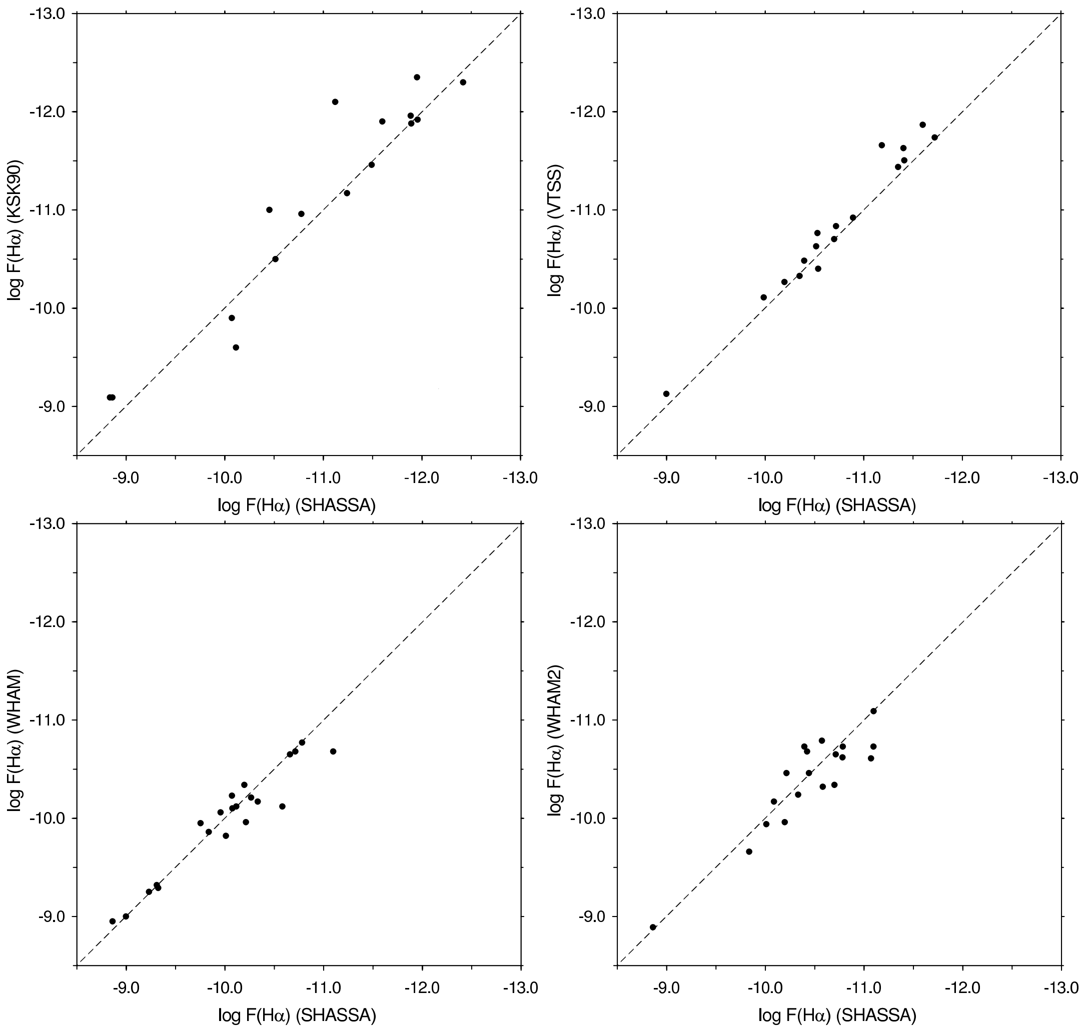

Figure 3.3: Comparison of new SHASSA Hα fluxes with fluxes from Kaler, Shaw & Kwitter (1989) (top left), new fluxes from VTSS (top right), fluxes from WHAM (Reynolds et al. 2005) (bottom left), and unpublished WHAM fluxes (Madsen & Frew 2008, in preparation) (bottom right). The dashed lines represent a 1:1 correlation.

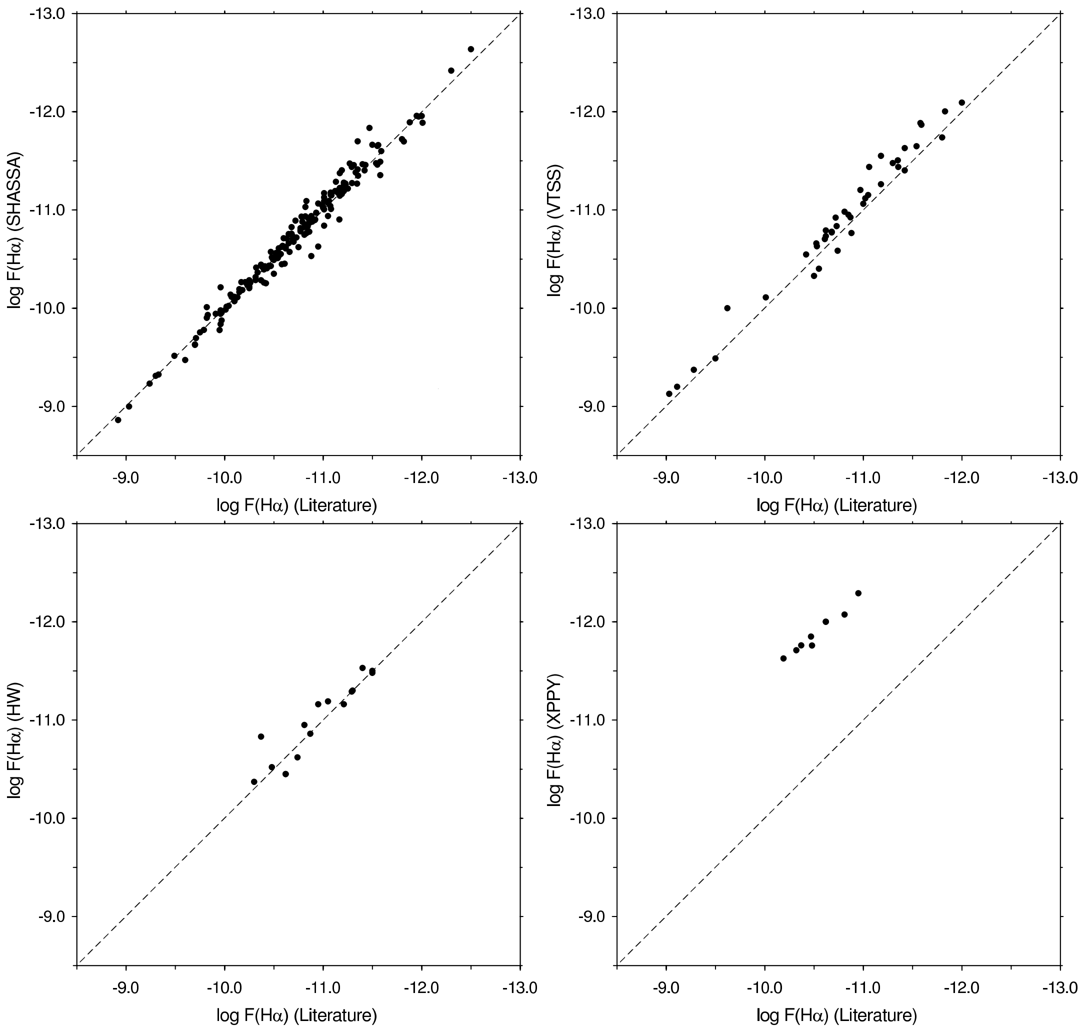

Figure 3.4: Comparison of Hα fluxes derived here with mean values from the literature. Comparison of new SHASSA Hα fluxes with literature fluxes (top left), uncorrected VTSS fluxes compared with literature fluxes (top right), fluxes from Gieseking, Hippelein & Weinberger (1986) and Hippelein & Weinberger (1990) compared with literature fluxes, as discussed in the text (bottom left), comparison of Hα fluxes (corrected for [N II] contribution) and [O III] fluxes from Xilouris et al. (1996), with other fluxes taken from the literature (bottom right).

studied), presenting surface brightness values (given in mag per arcsec^2) for each PN.

These surface brightness values were not immediately reconcilable with the fluxes of Xilouris et al. (1996) and Kaler (1983b), as the adopted formula to convert from magnitudes to cgs units is not given by either Gieseking, Hippelein & Weinberger (1986) nor Hippelein & Weinberger (1990). However, a comparison of the surface brightness measurements of Gieseking, Hippelein & Weinberger (1986) for IW 1 and IW 2 with the absolute surface fluxes for these same PNe presented by Ishida & Weinberger (1987), allowed the determination of the transformation equation used, which is that given by Pottasch (1984), viz:

$$m_\lambda = -2.5\log F(\lambda) - 15.77 \tag{3.3}$$

where λ is the emission line species of interest. Note that Gieseking, Hippelein & Weinberger (1986) and Hippelein & Weinberger (1990) use the same zero-point of 15.77 for [O III], [N II] and Hα, despite the range in wavelength of these emission lines (cf. Allen 1973, p. 197). Using equation 3.3, the surface brightness in $\mathrm{erg\,cm^{-2}\,s^{-1}arcsec^{-2}}$ in each emission line was determined for the other PNe in the lists of Gieseking, Hippelein & Weinberger (1986) and Hippelein & Weinberger (1990). However, to get the integrated flux in each line, one needs to know the dimensions of these PNe. The dimensions were taken from table 9.4 below, and the diameters in [N II] and Hα were assumed to be identical. However, for the higher-excitation [O III] line, the PN diameter is often smaller due to stratification effects, especially for highly evolved low-excitation PNe (the [O III] Strömgren zone is smaller than the Hα Strömgren zone). The diameters in [O III] were estimated from published images where available (e.g. Xilouris et al. 1996 and Tweedy & Kwitter 1996). Table 3.5 summarises the adopted dimensions in Hα, and derived emission-line fluxes for the PNe studied by Gieseking, Hippelein & Weinberger (1986) and Hippelein & Weinberger (1990).

There are a few other moderately-sized PNe which have no flux data at present, either because they are too faint for SHASSA, VTSS, and/or WHAM (see below), or because they are located outside the bounds of the available VTSS fields. Since any flux data on these poorly-studied objects are welcome, a re-investigation of the Abell (1966) photographic data is warranted.

The photored magnitudes of Abell (1966) were corrected for the contribution of the [NII] lines, assuming equal throughput for both Hα and the nitrogen lines through the broadband red Plexiglass filter used for the POSS I red plates. The conversion is given by:

$$m_{\,\mathrm{H}\alpha} = m_{\mathrm{pr}} - 2.5\log\left(\frac{1}{R_{[\mathrm{N\,II}]}+1}\right) \tag{3.4}$$

where $R_{[\mathrm{N\,II}]}$ is defined as before. The resulting 'Hα' magnitudes were compared with available Hα fluxes obtained from the references given in table 3.1, as well as additional fluxes from Kaler (1983a), Kwitter & Jacoby (1989), Kohoutek & Martin (1981), and Reynolds et al. (2005). A linear fit to the flux-magnitude relation gave:

$$\log F(\mathrm{H}\alpha) = -0.4\,(m_{\,\mathrm{H}\alpha} + 15.40) \tag{3.5}$$

Table 3.5: Corrected [O III], Hα, and [N II] fluxes from Gieseking, Hippelein & Weinberger (1986) and Hippelein & Weinberger (1990).

Name	diam ($''$)	S(5007) (mag/$\square''$)	S(5007)	F(5007)	S(Hα) (mag/$\square''$)	S(Hα)	F(Ha)	S(6584) (mag/$\square''$)	S(6584)	F(6584)	Δ(5007)	Δ(Ha)
Abell 25	166	23.9	-12.31	-11.53	...	...	...	...	...	...	...	...
Abell 28	320	25.0	-12.75	-11.40	25.1	-12.79	-11.44	26.7	-13.30	-11.95	...	0.00
Abell 29	438	24.7	-12.63	-11.01	...	...	...	...	...	...	...	...
Abell 31	1004	22.4	-11.71	-9.82	...	...	...	26.6	-13.26	-10.92	-0.08	...
Abell 34	292	23.8	-12.27	-11.00	24.1	-12.39	-11.12	24.9	-12.58	-11.31	-0.07	0.08
Abell 39	174	23.0	-11.95	-11.13	23.9	-12.31	-11.49	25.5	-12.82	-12.00	-0.37	-0.14
Abell 61	199	23.0	-11.95	-11.02	23.6	-12.19	-11.26	25.1	-12.66	-11.73	...	...
Abell 62	161	22.1	-11.59	-11.13	22.8	-11.87	-11.12	23.7	-12.10	-11.35	-0.31	-0.12
Abell 71	157	22.7	-11.83	-11.10	22.0	-11.55	-10.82	22.7	-11.70	-10.97	0.12	0.10
Abell 74	793	24.4	-12.51	-10.55	24.5	-12.55	-10.41	24.0	-12.22	-10.09	...	0.14
DHW 5	595	23.1	-11.99	-10.10	24.3	-12.47	-10.58	25.6	-12.86	-10.98	...	-0.58
EGB 6	780	25.4	-12.91	-10.79	26.3	-13.27	-11.15	25.5	-12.82	-10.70	...	-0.16
HFG 1	695	23.7	-12.23	-10.21	...	...	...	25.8	-12.94	-10.92	...	...
IsWe 1	744	25.2	-12.83	-11.00	25.6	-12.99	-10.91	...	...	...	...	-0.06
IsWe 2	969	26.6	-13.39	-11.08	25.1	-12.79	-10.48	25.0	-12.62	-10.31	...	0.02
Jones 1	336	23.3	-12.07	-10.68	...	...	...	...	...	...	-0.36	...
JnEr 1	380	23.0	-11.95	-10.45	23.5	-12.15	-10.65	24.2	-12.30	-10.81	-0.10	-0.05
K 2-2	709	24.4	-12.51	-10.47	...	...	...	...	...	...	-0.12	...
LoTr 5	509	23.2	-12.03	-10.28	...	...	...	...	...	...	0.13	...
PuWe 1	1211	24.2	-12.43	-10.18	25.2	-12.83	-10.33	25.0	-12.62	-10.12	0.02	-0.10
Sh 2-68	408	23.4	-12.11	-11.20	24.0	-12.35	-10.79	25.8	-12.94	-11.38	...	-0.33
Sh 2-176	775	26.1	-13.19	-11.07	...	...	...	...	...	...	-0.07	...
Sh 2-200	356	23.5	-12.15	-10.71	...	...	...	...	...	...	...	...
WDHS 1	1160	27.4	-13.71	-11.24	...	...	...	24.9	-12.58	-10.12	...	...
We 1-10	190	23.6	-12.19	-11.30	24.0	-12.35	-11.46	25.2	-12.70	-11.81	...	...
We 3-1	166	23.1	-11.99	-11.21	23.2	-12.03	-11.25	24.7	-12.50	...	...	...

This can be compared to the formula adopted by Cahn & Kaler (1971), relating the photored magnitude directly to a red flux, $F_{\rm red}$, which is a sum of the Hα and [NII] fluxes:

$$\log F(\text{red}) = -0.4\,(m_{\,\rm pr} + 14.97) \tag{3.6}$$

Equation 3.5 was used to determine approximate Hα fluxes for all the PNe with $m_{\rm pr}$ magnitudes listed in Abell (1966) that have [NII]/Hα ratios available. Similarly, approximate fluxes were also determined for PNe with photored magnitudes from Arp & Scargle (1967), Blaauw, Danziger & Schuster (1975), Weinberger (1977 a,b, 1978), Dengel, Hartl & Weinberger (1980), Weinberger & Sabbadin (1981), Weinberger et al. (1983), Fesen, Gull & Heckathorn (1983), Hartl & Tritton (1985), Hartl & Weinberger (1987), and Saurer & Weinberger (1987), which are all ostensibly on the same magnitude scale. Table 3.6 gives the derived fluxes, which are plotted against the average literature fluxes in figure 3.5. The 1σ error on each flux is $\sim \pm 0.30$ dex.

Table 3.6: Derived Hα fluxes from Abell (1966) and others. See the text for further details.

Name	Other	NII/Hα	Ref	m_{pr}	$m_{\rm H\alpha}$	F(Hα)	Notes
NGC 246	...	0.01	5	9.7	9.7	−10.04	...
NGC 650/1	M 76	2.00	10	9.1	10.3	−10.28	...
NGC 1501	...	0.04	47	10.7	10.7	−10.46	...
NGC 2610	...	0.15	7	11.9	12.1	−10.98	...
NGC 3587	M 97	0.36	46	8.6	8.9	−9.73	...
NGC 6742	Abell 50	0.31	4	13.1	13.4	−11.52	...
NGC 6772	...	0.69	4	10.7	11.3	−10.67	...
NGC 6781	...	1.9	6,17,23	9.0	10.2	−10.22	...
NGC 6804	...	0.0	23	11.2	11.2	−10.64	...
NGC 6842	...	0.07	6	12.5	12.6	−11.19	...
NGC 6894	...	1.04	5	11.2	12.0	−10.95	...
NGC 7008	...	0.06	5	10.0	10.1	−10.19	...
NGC 7076	Abell 75	0.04	5	14.2	14.2	−11.86	...
NGC 7293	...	1.8	2	6.3	7.4	−9.13	...
IC 289	Hb 1	0.01	4	11.9	11.9	−10.92	...
IC 972	Abell 37	0.72	4,5	12.7	13.3	−11.48	...
IC 1295	...	0.15	3,4	11.6	11.8	−10.86	...
IC 1454	Abell 81	0.33	48	12.6	12.9	−11.32	...
Abell 1	...	0.72	6,4	14.7	15.3	−12.28	...
Abell 2	...	0.36	5	14.1	14.4	−11.93	...
Abell 3	...	0.35	5	13.3	13.6	−11.61	...
Abell 4	...	0.61	5	14.3	14.8	−12.09	...
Abell 5	...	4.0	5	12.7	14.4	−11.94	...
Abell 6	...	0.17	5	12.6	12.8	−11.27	...
Abell 7	...	0.90	3	10.5	11.1	−10.62	...
Abell 8	...	1.5	5,15	14.0	15.0	−12.16	...
Abell 9	...	1.57	6	15.3	16.3	−12.69	...
Abell 10	K 1-7	1.24	5	12.7	13.6	−11.59	...
Abell 13	YM 28	4.0	5,15,30	11.5	13.2	−11.46	...
Abell 14	...	6.8	32	14.0	16.2	−12.65	...
Abell 15	...	0.16	5	14.1	14.3	−11.86	...
Abell 16	...	0.20	5	12.8	13.0	−11.36	...
Abell 18	...	2.6	6	12.8	14.2	−11.84	...
Abell 19	...	1.68	6	14.8	15.9	−12.51	...

Name	Other	NII/Hα	Ref	m_{pr}	$m_{\rm H\alpha}$	F(Hα)	Notes
Abell 20	...	0.12	5	13.6	13.7	−11.65	...
Abell 21	...	1.61	2	7.7	8.7	−9.66	...
Abell 22	...	1.8	4	12.2	13.3	−11.49	...
Abell 23	...	1.0	4	13.1	13.9	−11.70	...
Abell 24	...	5.2	5,30,32	9.3	11.3	−10.67	...
Abell 25	K 1-13	2.3	6	13.0	14.3	−11.88	...
Abell 26	...	1.38	4,31	14.3	15.2	−12.26	...
Abell 27	K 1-1	3.6	4,6	13.0	14.7	−12.02	...
Abell 28	...	1.0	5,13	13.4	14.1	−11.80	...
Abell 29	...	4.5	3,4	10.6	12.5	−11.14	...
Abell 30	...	0.05	30	13.5	13.6	−11.58	...
Abell 31	...	0.94	2	9.4	10.1	−10.21	...
Abell 33	...	0.17	5	11.1	11.3	−10.67	...
Abell 34	...	0.64	5	12.0	12.5	−11.17	...
Abell 35	...	0.86	2	9.7	10.4	−10.31	1
Abell 36	...	0.00	5	10.6	10.6	−10.40	...
Abell 38	K 1-3	10.6	29	11.7	14.4	−11.90	...
Abell 39	...	0.05	49	12.1	12.2	−11.02	...
Abell 40	...	0.0	4	13.4	13.4	−11.52	...
Abell 41	...	0.36	7	13.9	14.2	−11.85	...
Abell 42	...	0.0	4	14.6	14.6	−12.00	...
Abell 43	...	0.18	5	12.7	12.9	−11.31	...
Abell 44	...	1.9	4	12.6	13.8	−11.67	...
Abell 45	...	4.0	3	11.5	13.2	−11.46	...
Abell 46	...	0.01	33	13.2	13.2	−11.45	...
Abell 48	...	0.36	4	13.3	13.6	−11.62	...
Abell 49	...	1.3	4	13.2	14.1	−11.80	...
Abell 51	...	0.05	5b	13.0	13.1	−11.38	...
Abell 53	...	1.0	5	12.3	13.1	−11.38	...
Abell 54	...	1.16	6	14.5	15.3	−12.29	...
Abell 55	...	1.0	4	12.0	12.8	−11.26	...
Abell 57	...	0.0	4	14.9	14.9	−12.10	...
Abell 59	...	2.1	6	12.2	13.4	−11.52	...
Abell 60	...	0.0	4	13.7	13.7	−11.64	...
Abell 61	...	0.33	13	12.7	13.0	−11.36	...
Abell 62	...	1.40	4,13,15	10.3	11.3	−10.66	...
Abell 63	...	0.01	33	14.0	14.0	−11.77	...
Abell 65	...	0.21	5,33,34	12.7	12.9	−11.32	...
Abell 66	...	0.6	4,29	11.5	12.0	−10.96	...
Abell 67	...	0.6	4	14.2	14.7	−12.04	...
Abell 69	...	5.2	6	14.3	16.3	−12.67	...
Abell 70	...	1.07	5	12.7	13.5	−11.56	...
Abell 71	...	2.00	5	10.2	11.4	−10.72	...
Abell 72	...	0.06	5,15	12.8	12.9	−11.31	...
Abell 73	...	1.25	5	13.7	14.6	−11.99	...
Abell 74	...	0.67	2	10.0	10.6	−10.38	...
Abell 77	Sh 2-128	0.17	50	11.5	11.7	−10.83	1
Abell 78	...	0.08	5	14.3	14.4	−11.91	...
Abell 79	...	6.9	51	11.1	13.3	−11.50	...
Abell 80	...	1.9	5	11.3	12.5	−11.14	...
Abell 82	...	1.24	5	12.0	12.9	−11.31	...
Abell 83	...	0.83	15	14.9	15.6	−12.38	...
Abell 84	...	1.11	5	11.0	11.8	−10.88	...
BlDz 1	...	0.8	4	11.2	11.8	−10.90	...
DeHt 1	LoTr 1	0.0	6	14.2	14.2	−11.84	...

Name	Other	NII/Hα	Ref	m_{pr}	$m_{H\alpha}$	F(Hα)	Notes
DeHt 2	...	0.0	4	14.5	14.5	−11.96	...
DeHt 3	DHW 1-1	1.25	32	12.9	13.8	−11.67	...
DeHt 4	...	2.0	4	16.2	17.4	−13.12	...
DeHt 5	...	0.70	2	11.4	12.0	−10.95	1
EGB 1	HaWe 1	0.5	4	11.1	11.5	−10.77	2
HaTr 8	...	1.0	4	18.8	19.6	−13.98	...
HaTr 10	...	7.2	4,52	14.7	17.0	−12.95	...
HaTr 11	...	1.7	4	14.3	15.4	−12.31	...
HaTr 13	...	1.3	4	16.7	17.6	−13.19	...
HaTr 14	...	0.0	4	19.8	19.8	−14.08	...
HaWe 4	HDW 3	1.6	2	11.4	12.4	−11.13	...
HaWe 5	...	0.0	4	17.1	17.1	−13.00	...
HaWe 7	HDW 5	0.78	4,31	12.7	13.3	−11.49	2
HaWe 8	HDW 6	0.5	36	14.5	14.9	−12.14	...
HaWe 10	HDW 7	1.0	36	14.8	15.6	−12.38	...
HaWe 11	HDW 8	0.3	4	13.2	13.5	−11.54	...
HFG 2	Bran 63	0.1	3	13.6	13.7	−11.62	...
PHL 932	...	0.3	2	12.8	13.0	−11.38	1
PuWe 1	...	1.28	2	8.6	9.5	−9.96	...
SaWe 1	...	0.2	4	15.0	15.2	−12.24	...
SaWe 4	...	0.0	29	14.9	14.9	−12.12	...
Sh 2-68	...	0.53	2	8.8	9.3	−9.86	1
Sh 2-176	...	2.3	2	10.2	11.4	−10.74	...
Sh 2-200	HaWe 2	0.1	...	11.7	11.8	−10.88	3
Sh 2-216	...	1.31	2	5.2	6.1	−8.59	...
WDHS 1	...	3.0	3	10.5	12.0	−10.94	...
We 1-1	...	1.1	4	15.3	16.1	−12.60	...
We 1-2	...	1.75	4,6	13.3	14.4	−11.92	...
We 1-3	...	2.9	6	14.2	15.7	−12.44	...
We 1-4	...	5.3	31,4	14.0	16.0	−12.56	...
We 1-5	...	0.0	4,6	16.7	16.7	−12.84	...
We 1-9	...	0.90	4	13.6	14.3	−11.88	...
We 1-10	...	0.44	13	11.4	11.8	−10.88	...
We 1-11	...	2.0	4	14.9	16.1	−12.60	...
We 1-12	...	0.4	53	12.1	12.5	−11.15	1
We 2-34	...	2.5	3	11.7	13.1	−11.38	...
We 3-1	...	0.33	13	13.3	13.6	−11.60	...
WeSb 4	...	8.2	4	14.0	16.4	−12.72	...

Notes for Table 3.6: 1. Not a PN; 2. Status uncertain; 3. Flux excludes halo.

3.3 Integrated Hα, [O III], and [N II] Fluxes with WHAM

Additional integrated fluxes in Hα, [O III], and [N II] have been determined for a number of large northern and equatorial PNe by Madsen et al. (2006) and Madsen & Frew (2008, in preparation) using the WHAM Fabry-Perot spectrometer (Haffner et al. 2003). WHAM is a useful instrument for such a task, because of its large effective beam size, larger than all but one PN in the local sample.

The WHAM intensity calibration is not as easy to do as other instruments, because of the nature of the complex optical train. For Hα this is generally based on the absolute calibration

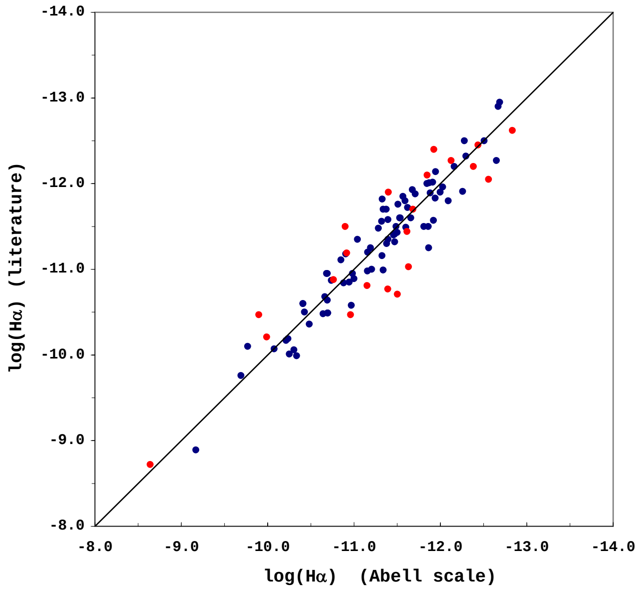

Figure 3.5: Comparison of derived Hα fluxes from Abell (1966) (blue dots) and others (red dots) with weighted-mean literature fluxes. Surprisingly good agreement is noted. The dispersion is $\pm$0.30 dex.

of the central 49′ region of the North American Nebula, NGC 7000 (Scherb 1981; Haffner et al. 2003). The [N II] intensity calibration follows, as the response of the etalons at [N II] is essentially identical to that at Hα. An additional calibrator for Hα and Hβ is the faint emission region around the nearby early B-type star Spica (Madsen, pers. comm. 2006). The Hα flux is bootstrapped to the NGC 7000 flux, and because of negligible reddening toward Spica, the measured Hβ flux is compared to the inferred Hβ flux assuming a normal Balmer decrement (e.g. Brocklehurst 1971; Osterbrock 1989).

However, the zero point of the WHAM [O III] intensity calibration was essentially unknown, and it was also deemed desirable to have as large a set of calibrating nebulae in the other emission lines as possible. Hence, it was necessary to glean a set of PNe from the literature with accurate integrated fluxes, covering a range of diameter and surface brightness, before the WHAM intensity zero point in each emission line could be accurately determined. A similar approach was taken by Reynolds et al. (2005) in the determination of Hα fluxes for objects from the WHAM Point Source Catalog (WPS).

Table 3.7 gives the fluxes in the main emssion lines for the calibration PNe. The adopted fluxes are derived from a carefully weighted mean of literature fluxes, taken from Liller & Aller (1954), Liller (1955), Capriotti & Daub (1960), Osterbrock & Stockhausen (1961), Collins, Daub & O'Dell (1961), O'Dell (1962, 1963, 1998), Gebel (1968), Peimbert & Torres-Peimbert (1971), Perek (1971), Kaler (1976, 1978b, 1981b, 1983a), Torres-Peimbert & Peimber (1977), Kohoutek & Martin (1981), Webster (1983), Carrasco, Serrano & Costero (1983, 1984), Shaw & Kaler (1989), Copetti (1990), Kaler, Shaw & Kwitter (1990) and Hua, Dopita & Martinis (1998), supplemented by additional line-ratio data from Acker et al. (1992). The Hα fluxes were further cross-checked against the fluxes of Reynolds et al. (2005) and the new SHASSA measurements determined herein. The older fluxes published before 1975 were decreased by

Table 3.7: Adopted logarithmic fluxes and radial velocities for WHAM primary calibrating nebulae.

Name	F(Hα)	F(6584)	F(5876)	F(5007)	F(Hβ)	Error	$v_{\rm LSR}$	Notes
NGC 246	−10.09	...	...	−9.65	−10.55	C	−50:	1
NGC 1360	−9.75	...	...	−9.34	−10.21	C	+31:	1
NGC 1535	−9.97	...	...	−9.35	−10.43	B	−20	...
NGC 2392	−9.90	...	...	−9.43	−10.39	C	+63	...
NGC 3242	−9.31	...	...	−8.66	−9.79	B	−3	2
NGC 3587	−9.99	...	...	−9.54	−10.42	C	+12	...
NGC 6543	−9.10	...	...	−8.78	−9.59	A	−51	2,3
NGC 6572	−9.24	−9.82	−10.53	−8.74	−9.81	A	+9	...
NGC 6720	−9.55	−9.57	...	−9.05	−10.08	C	+0	2
NGC 6853	−8.99	...	...	−8.45	−9.48	C	−24	...
NGC 7009	−9.29	−10.54	−10.56	−8.72	−9.79	A	−36	2
NGC 7293	−8.89	...	...	−8.59	−9.37	C	−26	2
NGC 7662	−9.51	−11.29	−11.08	−8.89	−9.99	B	−5	2
IC 418	−9.01	−9.29	−10.46	−9.38	−9.56	B	+43	3,4
NGC 281	−8.24	...	...	−8.84	−8.87	C	...	5
NGC 7000	−7.34	...	...	...	...	C	...	5,6

Notes:

1. Velocity is mean of disparate literature values;
2. Has outer halo;
3. Strong diffuse background emission;
4. [O III]/Hβ ratio may be variable over time (Frew et al., in prep.);
5. HII region;
6. Surface flux at centre.

Error on fluxes:
A $\leq$ 0.02 dex; B $\leq$ 0.04 dex; C $\leq$ 0.08 dex.

0.02 dex due to the recalibration of Vega (Cahn & Kaler 1988, quoted by Acker et al. 1991) before being averaged (see also Shaw & Kaler 1989). Similarly the fluxes of Kaler (1976) were made brighter by 0.07 dex (see the discussion by Kaler 1978b). The published Hα flux of Goldman et al. (2004) for NGC 1360 was found to be too bright by $\sim$0.24 dex, and was not used. The eighth column of table 3.7 also gives the systemic LSR velocities for each PN taken from Schneider et al. (1983) and Durand, Acker & Zijlstra (1998).

The raw WHAM data for the observed PNe were put through the WHAM calibration pipeline by G. Madsen; for each night, the zero point in each emission line was set using a weighted mean of fluxes for NGC 7000 and two or three the calibration PNe, as given in table 3.7. Standard mean extinction corrections were used each night. The results are given in Table 3.8 for bona fide PNe and Table 3.9 for doubtful PNe and HII regions (see Chapter 8 for details on some of these objects). Representative WHAM spectra are presented in figure 3.6. The left panel shows Hα, [NII] and [OIII] spectra for a bona fide PN, Abell 31. The right panel shows the spectra of a HII region, Sh 2-174 (Napiwotzki & Schonberner 1993; Tweedy & Napiwotzki 1994; §8.7). Note that some of the fainter nebulae will be reobserved again in the future. A fuller account of the calibration process, results, and detailed error analysis will be

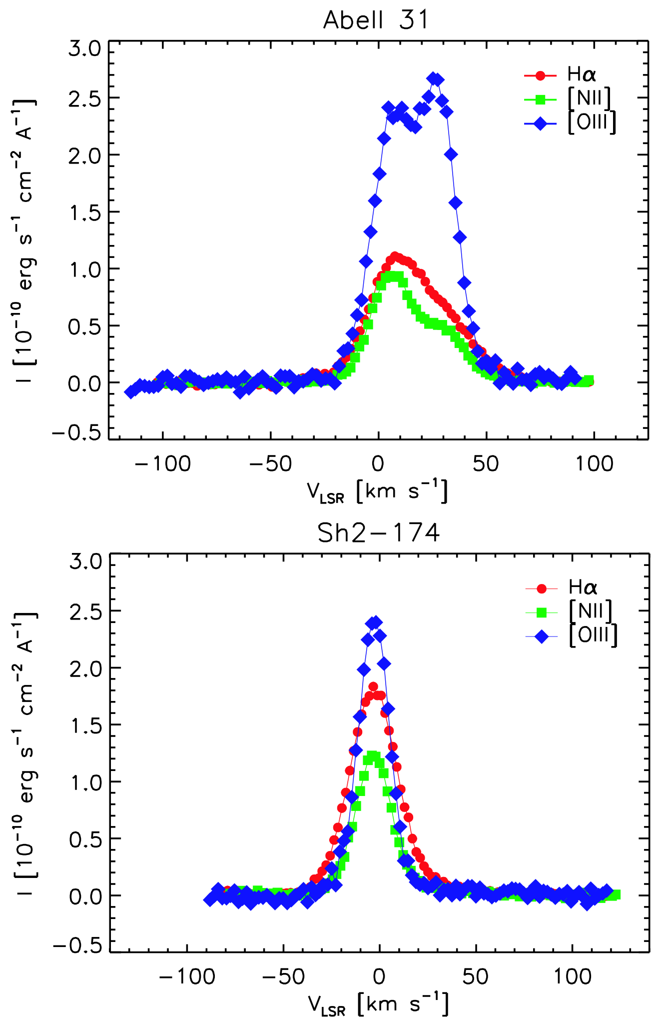

Figure 3.6: Representative WHAM spectra of a bona fide PN, Abell 31, and a HII region, Sh 2-174 (see §8.7).

published separately (Madsen & Frew 2008, in preparation.)

3.3.1 Systemic and Expansion Velocities from WHAM

Most of the WHAM line profiles can be approximated by least-squares Gaussian fits. Systemic radial velocities (in the LSR reference frame) were also measured from the centre of the Gaussian fit to the profile for each nebula. For double-peaked profiles (e.g. Abell 21), the radial velocity was taken as the mean velocity of the two components.

The radial velocities measured here are in excellent agreement with the literature values (quoted in table 3.7), with two exceptions, NGC 246 and NGC 1360. The literature velocities for these objects were uncertain, and were derived from slit spectra which may not represent the true systemic velocities of these large, high-expansion velocity PNe. The systemic values quoted in table 3.8 are to be preferred.

The expansion velocity was assumed to be half of the FWHM of the Gaussian fit to the observed velocity profile (i.e. the HWHM), after subtraction of the thermal and instrumental

Table 3.8: Integrated WHAM fluxes in Hα, [N II] and [O III] for true and likely PNe. Systemic LSR velocities and expansion velocities are also given.

Name	F(Hα)	F(6584)	F(5007)	$v_{\rm LSR}$	$v_{\rm exp}$	Notes
Abell 7	...	...	−10.26	+12	29:	1
Abell 21	−9.66	−9.58	−9.57	+18	32	...
Abell 24	−10.79	−10.02	−10.87	−7	20	...
Abell 28	...	...	...	...	...	1
Abell 29	...	...	−10.93	−27	20:	...
Abell 31	−9.96	−10.11	−9.77	+19	29	...
Abell 34	...	...	−10.87	+22	...	1
Abell 35	−9.94	−10.14	−10.05	−3	11	...
Abell 74	−10.12	−10.42	−10.78	...	...	1
EGB 1	...	...	−11.39:	0?	...	1
EGB 6	−10.61	−11.24	−10.78	−3	25:	...
FP 0905–3033	...	...	−10.45	+8	24:	1
FP 1824–0319	−10.67	−10.54	−10.78	...	12	...
HDW 3	−10.79:	−10.70	−10.64	...	11	1
HFG 1	...	−10.55	−10.05:	...	...	1
IC 418	...	...	...	+42	16	1,2
IsWe 1	−10.52	−10.77	−11.02	−17	12:	...
Jacoby 1	...	...	−10.96:	+30	...	...
Jones 1	−10.82	−11.26	−10.32	−1	36:	...
JnEr 1	−10.49	−10.36	−10.33	−61	24	...
LoTr 5	...	...	−10.44	−2	31	3
LTNF 1	...	...	−11.38	...	...	...
MWP 1	...	...	...	...	...	1,3
NGC 246	...	...	...	−33	35	2
NGC 1360	...	...	...	+45	34	2
NGC 1535	...	...	...	−20	21	2
NGC 2392	...	−10.47	...	+60	40:	2,4
NGC 3587	...	...	...	+8	34	2
NGC 6543	...	...	...	−53	19	2
NGC 6720	...	...	...	−4	22	1,2
NGC 6853	...	−8.96	...	−26	32	2,4
NGC 7009	...	...	...	−36	25	2
NGC 7293	...	−8.77	...	−24	21	2,4
NGC 7662	...	...	...	−4	27	2
PFP 1	...	−10.66	−10.42	+11	30:	1
PuWe 1	−10.21	−10.23	−10.20	+6	23	...
Sh 2-78	−10.34	−10.20	−10.40	+35	20:	1
Sh 2-176	...	−10.63	...	−24	22:	1
Sh 2-188	−10.09	−9.94	−10.56	−29	18	...
Sh 2-200	...	...	−10.49	−52:	...	5
Sh 2-216	−9.13	−9.13	−9.18	+8	12	6
Ton 320	−10.79	−10.89	−10.85	+14	15:	...
WDHS 1	−10.73	−10.32	>-11.0	−13	17	1

Notes:

1. diffuse emission in beam;
2. calibrating object;
3. [O III] emission in offset field;
4. new [N II] flux;
5. outer halo is ionized ISM;
6. surface flux; object larger than beam.

Table 3.9: Integrated WHAM fluxes in Hα, [N II] and [O III] for doubtful PNe and HII regions. Systemic LSR velocities and expansion velocities are also given.

Name	F(Hα)	F(6584)	F(5007)	$v_{\rm LSR}$	$v_{\rm exp}$	Notes
DHW 5	−10.00	−10.28	−10.49	−5	10	1
Fr 2-2	−11.09:	−11.08	...	+12	12:	...
Fr 2-3	−10.73	−10.66	−10.64	+11	9	...
Fr 2-9	−10.24	−10.43	−10.04	−17	11	2,3
Fr 2-10	−10.73	−10.70	−11.19	...	10	...
Fr 2-13	−11.14:	...	...	...	...	...
Fr 2-14	−10.06	−10.51	−11.28	−21	13	...
Fr 2-15	−10.32	−10.43	−10.58	+18	12	...
Fr 2-18	−10.66	−10.71	−11.02	−6	12	...
Hewett 1	−10.16	−10.50	−9.57	−5	13	2,3
KPD 0005+5106	−9.24	−9.60	−8.90	−5	13	2,3
PG 0108+101	−10.65	−10.82	−11.0	−9	10	3
PG 0109+111	−11.07	−11.01	−11.6	−10	10	...
PHL 932	−10.62	−11.34	...	−9	11:	...
RE 1738+665	...	...	−11.17:	...	...	4
Sh 2-68	−10.46	−10.86	−10.41	+5:	11	2,5
Sh 2-174	−9.87	−10.14	−10.09	−1	13	...
WPS 46	−10.61	−10.64	−10.61	−61	14	...
WPS 60	−10.23	−10.44	−10.94	−4	13	5,6
WPS 69	−10.13	−10.57	...	−4	10	...
WPS 75	−10.69	−11.13	...	−3	15	...

Notes:

1. diffuse emission in beam;
2. strong [O III] emission;
3. surface flux; object larger than beam;
4. off-beam Hα flux brighter than on-beam flux;
5. nature uncertain;
6. mean of 2 observations.

broadening components (following the approach of Gieseking, Hippelein & Weinberger 1986). Thermal broadening is only significant for the Balmer line profiles and is negligible for the [O III] and [N II] lines. The HWHM is, at least for statistical purposes, a valid approximation to the expansion velocity (see the discussion of Morisset & Stasińska 2008). However, two PNe had double-peaked profiles which could be fit with two Gaussian components. In these cases the expansion velocity was taken as half the velocity difference of the two peaks. Expansion velocities will be discussed in further detail later in this thesis.

3.4 Summary

This chapter presented a new set of Hα fluxes derived from SHASSA and the VTSS surveys for over 400 PNe, plus new Hα, [O III] and [N II] fluxes measured using WHAM for many of the largest PNe in the solar neighbourhood. Systemic and expansion velcities are also given from the WHAM line profile data. In addition, corrected fluxes from the works of Xilouris et al. (1996), Gieseking, Hippelein & Weinberger (1986), Hippelein & Weinberger (1990), Abell (1966) and others are presented, recalibrated here to a common zero-point. Weighted means of all available emission-line fluxes will be used in subsequent chapters of this work. In the future these new data will be of great utility, in calibrating the digitised SHS to derive fluxes for the numerous MASH PNe that are too faint for SHASSA and WHAM. This project is a work in progress (Miszalski, Frew & Parker 2008, in preparation) and details will be published elsewhere.

Chapter 4

PN Morphologies

4.1 Introduction

Planetary nebulae show a remarkably diverse range of morphologies, ranging from purely spherical shells to high axisymmetric bipolar forms (e.g. Kwok 2000; Balick & Frank 2002, and Chapter 1). In order to understand the relationships between PN morphology and the gamut of other properties such as binarity, ionized mass, CS mass, chemical composition, environment, and distance from the galactic plane, it is important firstly to devise a workable classification scheme, which can then be usefully applied to a statistical sample of PNe. Furthermore, any classification scheme needs to be internally consistent with the predictions of the GISW model for PN formation (Kwok, Purton & FitzGerald 1978; Kwok 1982; Balick 1987; Frank et al. 1993; Mellema & Frank 1997), as well as any additional factors that influence axisymmetry such as stellar rotation, magnetic fields, binarity, or a combination of several processes (Balick & Frank 2002). By utilising the volume-limited sample defined in this study (see Chapter 9), the true proportions of each morphological class can be determined with greater statistical certainty.

4.2 Morphological Classification of PNe

In this section, a summary of the various morphological classification schemes in current or former use is given. The diversity in PN forms has been suspected for a long time. Visual observations in the nineteenth century showed that there was wide variation in the sizes, ellipticities, and surface brightness of PNe, but there was little attempt to morphologically differentiate between them, or from other classes of object.[1] Early classification schemes were developed by Curtis (1918), based mostly on newly acquired, good-quality photographic images, and also by Vorontsov-Vel'yaminov (1934, 1948). The complex Vorontsov-Vel'yaminov (VV) system included a number of different classes and subclasses, though the scheme has now fallen into

[1]However, in the latter half of the nineteenth century, 'annular' nebulae were often considered to be a distinct class of object from the more disk-like 'planetary' nebulae. Annular nebulae were quite rare, with only half a dozen examples given by Clerke (1903). The two prototypes of the class were the Ring Nebula (M 57) and NGC 6894, both now considered to be pole-on bipolar PNe. Another annular nebula, NGC 6337, is now known to have a close-binary nucleus (see section 7.3.4, below). The reader is also referred to Secchi (1879; see Corradi 2004), Herschel (1887) and Clerke (1890) for other works on early morphological classification.

disuse.

Westerlund & Henize (1967) modified the VV system and used the following basic morphological categories: elliptical, bipolar, ring, peculiar, and doubtful. Other schemes were used by Evans & Thackeray (1950), Khromov & Kohoutek (1968) and Gurzadyan (1970). Greig (1967, 1971) classified PNe into two major groups, B and C (binebulous and centric respectively), plus two smaller groups, designated A and E. Greig (1967, 1971) noted that the binebulous (now called bipolar) objects had strong [N II] and [O II] emission relative to the Balmer lines, and used this fact to help classify PNe, even when the available plate material made the morphology indeterminate. This is a hybrid system, and explicitly assumes that morphology and spectrum are correlated, but a classification scheme based purely on a single criteriion is to be preferred.

Until the advent of modern CCD detectors, imaging catalogues of PNe were based on photographic plates, which were of varying depth, quality and resolution (e.g. the CGPN and the Acker et al. catalogues). The publication of large numbers of high-quality modern CCD images of PNe by Balick (1987), Schwarz, Corradi & Melnick (1992), Manchado et al. (1996) and Górny et al. (1999), amongst others, has allowed new, self-consistent PN classification schemes to be developed, further illuminated by the extraordinary range of high-resolution images prduced by the Hubble Space Telescope[2].

Balick (1987) divided planetary nebulae into three broad groups of round, elliptical, and butterfly. These classes were further differentiated with the 'types', early, middle, and late. A similar logical system of classification was developed by Schwarz, Corradi & Stanghellini (1993), further extended by Stanghellini, Corradi & Schwarz (1993) and Corradi & Schwarz (1995). Stanghellini et al. (2002) used a simplified scheme:

1. Round (R) PNe;
2. Elliptical (E) PNe, differentiated from round PNe if there is $> 5\%$ difference in the axial dimensions;
3. Bipolar (B) PNe, which have at least one pair of lobes and a pinched waist (this category includes quadrupolar PNe).

Determining the incidence of bipolarity amongst PNe has received considerable attention. Gurzadyan (1970) commented that "almost half of the planetary nebulae whose photographs permit the study of their structure are bipolar" while Zuckerman & Aller (1986) found that about half of 139 PNe displayed bipolar symmetry. However these conclusions are based on a looser definition of bipolarity (as many of these nebulae are ellipticals with varying degrees of point symmetry). A stricter definition of bipolarity (nebulae with a pinched waist) is adopted herein (following Corradi & Schwarz 1995 and Stanghellini et al. 2002). Additionally, Soker & Hadar (2002) have classified PNe on the basis of their departure from axisymmetry, while Soker (2002b) discussed the special case of the formation of spherical planetary nebulae.

The classification scheme adopted here is based (in general) on that of Schwarz et al. (1993), but with some modification, due to the fact we are exploring new parameter space with the

[2]see, for example, http://ad.usno.navy.mil/pne/gallery.html

MASH catalogue. It is noted here explicitly that spectral information was not used to classify any object morphologically (cf. Grieg 1971). However, many of the new evolved PNe from MASH are so highly asymmetric (due to an advanced ISM interaction, as seen in Sh 2-188), that the 'original' primary morphology is essentially unknown, though it is often ignored that bow-shock morphologies develop in the AGB stage (Villaver, García-Segura & Manchado 2003; Wareing, Zijlstra & O'Brien 2007a,b; Wareing et al. 2006b, 2007). Figure 4.1, taken from the main MASH paper (Parker et al. 2006a), illustrates SHS images of six newly discovered MASH PNe illustrating the basic morphological types of the scheme adopted here, and Figure 4.2 does the same for a number of bright PNe taken from the literature.

Throughout this work, the classification scheme tabulated in Table 4.1 is adopted. This scheme is identical to that used by Parker et al. (2006a) in the main MASH paper, but with three additional subclasses: 'b', used to describe elliptical PNe which have evidence for a bipolar core or inner structure (the Dumbbbell nebula, M27 is the prototype) and 'f', used to describe PNe with amorphous, *filled* centres; Abell 65 and NGC 1360 are typical examples[3] (both of these PNe may in fact be post-common-envelope systems). I have also subsumed the small group of quadrupolar and multipolar PNe into the broader bipolar class (cf. Mampaso et al. 2006). Finally the classifier '(h)' is added, used for PNe with evidence of a detached outer halo (AGB wind). A good in-depth review of the morphological diversity of PNe is by Balick & Frank (2002; see also Balick, Gonzalez & Frank 1992).[4]

For the PNe in the solar neighbourhood, a range of images from the literature, as well as digital images from the SSS and SHS were used to discern the morphology of each PN and give a classification under the scheme defined here (see table 9.4, below). It is hoped that systematic differences in classification can be avoided by having a single investigator classify all PNe in the local volume in an homogenous manner.

4.2.1 Proportion of Morphological Classes

About 12.5% of all PNe in the MASH catalogue show bipolar morphologies (Parker et al. 2006a, and table 4.2), though if the selection is restricted to PNe with diameters $>10''$ this fraction rises to 14.3%. This number is very similar to previous estimates of the incidence of bipolarity, despite the fact that there is no overlap between the MASH catalogue and previous compilations — Corradi & Schwarz (1995) found 14% of a sample of 359 PNe to be bipolar (those authors gave an additional sample of 37 probable/possible bipolar PNe). Manchado et al. (2000) found 13% from a sample of 255 PNe, revised to 17% by Manchado (2004). The percentage of round PNe in the MASH catalogue (including those $>10''$ in diameter) is 19%. The MASH-II catalogue estimates (Miszalski et al. 2007) for elliptical and bipolar PNe are similar but there are more round PNe in MASH-II (32%).

The small differences in the proportions of bipolar PNe between MASH and MASH-II and

[3]Note that the general appearance of some of these filled centre PNe is dependent on the emssion-line used; Abell 65 has two circular blobs present in [N II] but absent in Hα and [O III] (Hua, Dopita & Martinis 1998).

[4]A new comprehensive morphological catalogue of PN images is currently being compiled by Bruce Balick; see the Planetary Nebula Image Catalogue (PNIC) at http://www.astro.washington.edu/balick/PNIC/

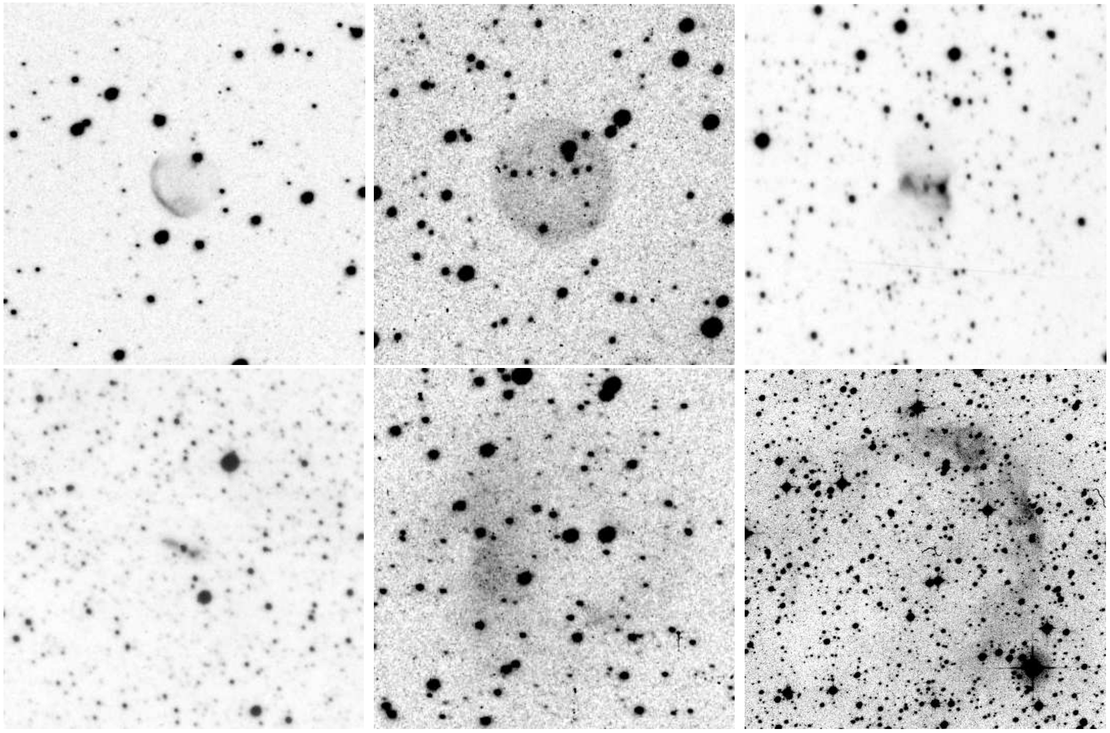

Figure 4.1: Extracts of SHS data around six newly discovered MASH PNe illustrating the basic morphological types. Top left: *Ea*, elliptical with asymmetric enhancement (PHR0700-1143), Top middle: *R*, round (PHR0843-2514) ; Top right: *Bs*, bipolar with resolved internal structure (PHR1408-6229), Bottom left: *Bp*, extreme bipolar / possible symbiotic outflow candidate (PHR1253-6350), Bottom middle: *Is*, irregularly shaped PN with some internal structure (PHR0652-1240), Bottom right: *As*, asymmetric PN, again with some structure (PHR0743-1951). The first five images have dimensions of $4' \times 4'$, while the bottom right image is $10' \times 10'$ in size. Figure adapted from Parker et al. 2006.

Table 4.1: Morphological codes adapted from Parker et al. (2006a)

Code	Meaning
B	Bipolar
E	Elliptical
R	Round
I	Irregular
A	Asymmetric (one-sided)
S	Stellar (unresolved)
a	asymmetry present
b†	bipolar core present
f†	filled (amorphous) centre
m	multiple shells present
p	point symmetry present
r	ring structure dominant
s	internal structure noted
(h)†	distinct outer halo

† subclass introduced in this work

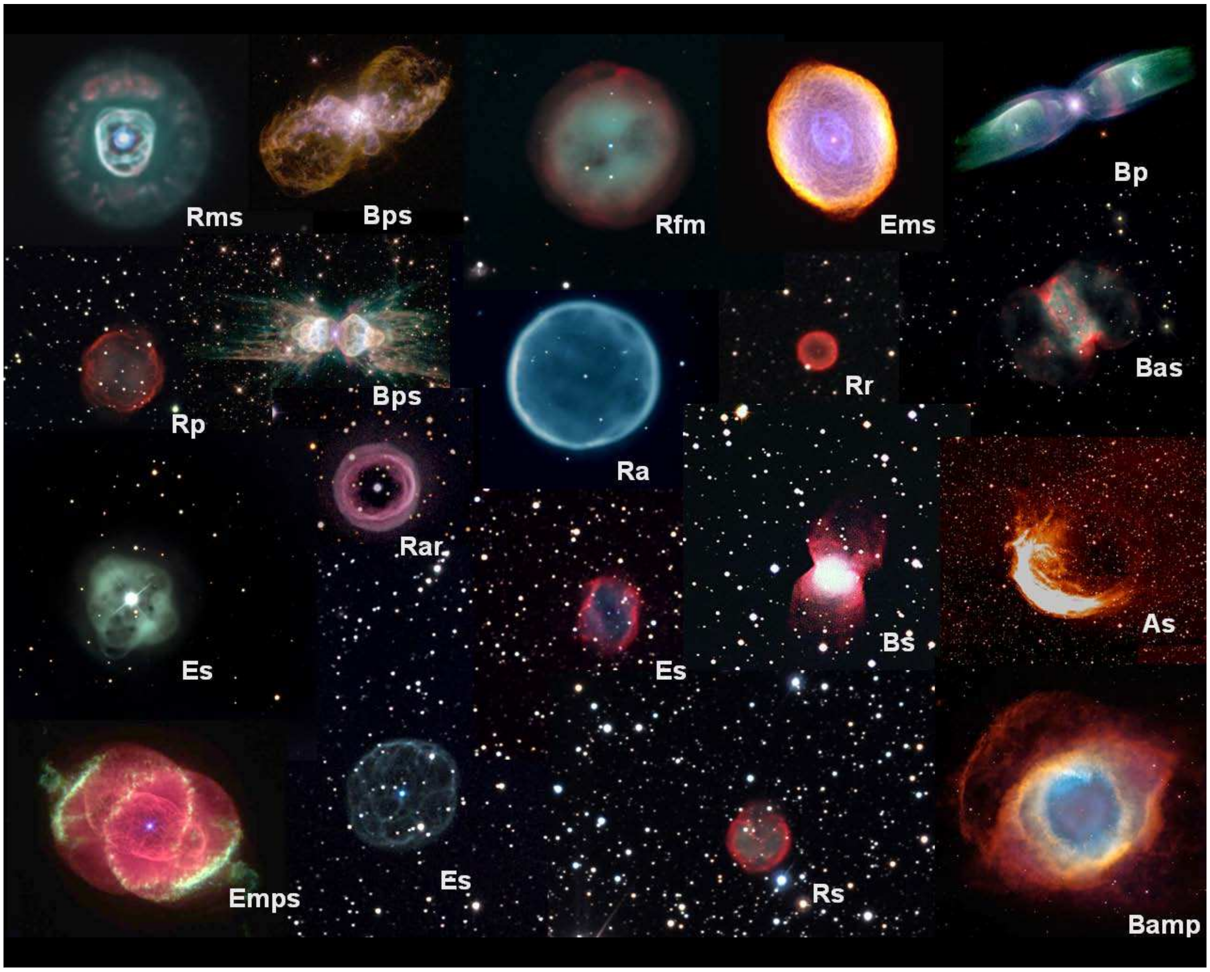

Figure 4.2: A mosaic showing a number of images of PNe taken from the literature, classified according to the scheme presented here. Note that M 2-9 (upper right) and Menzel 3 (second row, second from left) are likely symbiotic outflows rather than true PNe (see Chapter 8). Image credits: B. Balick, R. Sahai, A. Hajian, M. Meixner, P. Harrington, K. Borkowski et al. (STScI/AURA/NASA/ESA/NOAO), A. Block (NOAO/AURA/NSF), G. Jacoby (WIYN/NOAO/NSF), D. Malin (AAO) and A. Zijlstra (IPHAS).

Table 4.2: Summary details of morphological classifications for 903 new MASH PNe (Parker et al. 2006a).

Class	Number	% Fraction	$<\|b\|>$	σ	n> 10 arcsec
Bipolar	113	12.5	2.51	1.84	109
Elliptical	492	54.4	3.50	2.39	432
Round	175	19.3	4.05	2.51	146
Irregular	39	4.3	3.23	2.02	39
Asymmetric	36	4.0	3.44	2.80	36
Star-like	50	5.5	3.03	2.31	0

Note that at RAs greater than 17^h30^m the bulge increasingly dominates and a larger fraction are compact ($< 10''$ across) making morphological classification difficult. Note that there has been no pre-selection of this list into true, likely and possible PNe. The average $|b|$ values in degrees for each type are for PNe with major axes diameters $> 10''$ except for those of type S. The bipolar class contains 32 objects that are only possible bipolar PNe.

the older shallower surveys are not statistically significant. This was somewhat unexpected as it was thought initially that the better depth and red sensitivity of MASH (and especially MASH-II) would preferentially lead to the discovery of larger numbers of reddened bipolar Type I PNe, as most show strong [N II] emission lines relative to Hα (and extinction is less in the red compared to the blue). However, since the volume of the Galactic disk surveyed by MASH and MASH-II has increased, it may be that the more common elliptical and round PNe are being found to a greater completeness level (see Soker 2002b; Soker & Subag 2005). It is important to recall that most previous surveys are biased in principle, as they are magnitude-limited at relatively bright flux levels.

Furthermore, detailed kinematic studies (e.g. Graham et al. 2003; Mitchell 2006) are revealing that a number of elliptical PNe classified as such purely on morphological grounds, do in fact, possess bipolarity. Kwok (2000, 2005) has reiterated that apparent morphology alone is usually not sufficient to describe the intrinsic 3-D structure of a PN. The morphology of a PN is the result of a simple projection of an often complex 3-D structure on the sky, so orientation to the line of sight has a strong influence on the apparent morphology. However the acquisition of the necessary kinematic data will need a huge investment in appropriate telescope time, and it is also germane to note that over a quarter of the 3000+ currently known PNe do not even have accurate morphological classifications at present, mainly those of small angular size.

Nonetheless, in order to meaningfully compare the percentage of PN types in the solar neighbourhood with the flux-limited samples described above, it was deemed necessary here to only use the morphological criterion as a basis for classification (see table 4.1). The large angular size of most local PNe makes this task relatively straightforward. Note that Phillips (2001c) has analysed the observed disk aspect ratios in a sample of bright bipolar nebulae and has proposed that a number of pole-on bipolars have been misidentified as round or elliptical PNe, and that the true population of bipolars is $\sim 1.7\times$ greater than previously thought. Phillips estimates the overall fraction of bipolars to be $\sim$22%. Such bipolar PNe often have the appearance of a thick round annulus (e.g. Shapley 1, imaged by Bond & Livio 1990 and Mitchell et al. 2006) and can usually be differentiated from limb-brightened spherical shells like Abell 33 (Hua & Kwok 1999), Abell 34 (Tweedy & Kwitter 1994a), Abell 39 (Jacoby, Ferland & Korista 2001), PFP 1 (Pierce et al. 2004) and Patchick 9 (Jacoby et al. 2007). The morphological classification scheme used here (see Table 4.1) has been explicitly adopted to account for the presence of apparent ring structures in round PNe.

Phillips (2002b) has noted the presence of possible evolutionary effects in bipolar nebulae. He finds that the narrower-waisted, butterfly nebulae tend to have higher radio brightness temperatures than those nebulae which are more nearly cylindrical. There are probably several selection effects present here. Two recently discovered bipolar (butterfly) PNe have very low surface brightnesses (Frew, Parker & Russeil 2006), so more data are needed to see if the conclusions of Phillips (2002b) are justified. Furthermore, some of the extreme cylindrical nebulae may be the products of common envelope evolution (the other brighter examples are mostly Type I objects with massive progenitor stars). Most of the known close-binary PNe (e.g. Bond 2000, De Marco 2006) were found as a result of time-series photometry of their central stars. Central stars that are luminous mask the expected modulations from heating of the secondary component, while highly evolved nebulae have fainter central stars that have been observationally selected against. Consequently, the known common-envelope PNe have a somewhat restricted range in surface brightness. This problem will be re-examined later.

The increase in round PNe seen in MASH-II compared to MASH also needs a brief explanation. Numerous small and faint (hence distant) disk PNe at intermediate latitudes (4–10°) have been recorded in MASH-II. These PNe have large $|z|$ heights (>300 pc) and many of these have fairly round morphologies (if resolved). From flux-limited samples, round PNe are found to have a larger scale height than ellipticals and bipolars (Phillips 2001b; Manchado 2004), so the higher percentage of round PNe in MASH-II is a natural consequence of this survey probing the disk at greater $|z|$ distances. The local volume-limited sample (see Chapter 11) is less biased, but confirms unequivocally that round PNe have a larger scale height than the other types.

The true percentage of bipolar PNe in the solar neighbourhood, based on a volume-limited sample is 17 – 22%, depending on whether morphological or kinematic criteria are strictly used, in agreement with Phillips (2001c). This estimate is discussed further in Chapter 9. The proportion of Type I PNe is also estimated in Chapter 9 (see later).

4.2.2 Outer Haloes

Deep imaging of high surface brightness PNe facilitated the discovery of extended haloes around PNe[5]. One of the earliest systematic (albeit brief) studies was by Millikan (1974), who found haloes around several bright PNe. Another early-discovered example is the faint irregular halo around NGC 3242 (Minkowski 1965, quoted by Kaftan-Kassim 1966; Deeming 1966; Bond 1981). 'Giant halos' around four PNe were reported by Kaler (1974), who differentiated these structures from multiple shells. Somewhat later, Jewett, Danielson & Kupferman (1986), taking advantage of the better dynamic range of CCDs, presented the preliminary results of a Hα survey directly aimed at detecting faint haloes around PNe. They found that about two-thirds of the studied PNe had faint outer haloes[6].

One of the earliest investigations of the frequencey of multiple-shell structures in PNe was by Chu, Jacoby & Arendt (1987), who estimate that at least 50% of PNe show evidence for multiple shells, but note that their sample is a flux-limited one. Deep CCD imagery to identify faint outer haloes has also been conducted by Hua, Grundseth & Maucherat (1993), Papamastorakis, Xilouris & Paleologou (1993), Hua (1997), and Hua, Dopita & Martinis (1998).

Corradi et al. (2003) have provided the most comprehensive compilation of outer haloes around Galactic PNe (not including inner shells and rims). Observational data on the haloes of 50 PNe are presented in their paper and the associated website.[7] It is important to note that large features around PNe have been observed at other wavelengths (e.g. Hora et al. 2006). Weinberger (1999) and Weinberger & Aryal (2004) have noted cavities in the ISM around NGC

[5]Recall from Chapter 1, the morphology of a typical double-shell elliptical PN, NGC 2022 (see figure 1.4). The main body of the PN consists of a rim (the 'core' of Balick, Gonzalez & Frank 1992), surrounded by a shell of lower surface brightness. The faint haloes described in this section are exterior to these structures.

[6]Recently, Reid & Parker (2006 a,b) also found that 60% of LMC PNe have evidence for extended haloes.

[7]see http://www.ing.iac.es/∼rcorradi/HALOES/

4361, NGC 6826 and the Type I bipolar NGC 2899, amongst other objects. The feature around NGC 2899 is the more convincing, especially in the light of very faint point-symmetric, N-rich knots being noted by Parker (2000) on UKST Hα Survey images.

Corradi et al. (2003) have classified observed PN haloes into four groups: (i) circular or slightly elliptical AGB haloes; (ii) highly asymmetrical AGB haloes; (iii) candidate recombination haloes, i.e. limb-brightened extended shells that are expected to be produced by recombination as the CS descends the WD cooling track; and (iv) uncertain cases. Corradi et al. (2003) also appended group (v), non-detections, i.e. PNe in which no halo is found to a level of $< \sim 10^{-3}$ times the peak surface brightness of the inner shell.

To these I add another group, (vi) ISM haloes around optically thin PNe, of which the prototype is Sh 2-200 (figure 4.3). New WHAM data obtained here definitively show that the PN and halo are not physically associated (Madsen & Frew 2008, in preparation). In figure 4.4, two images centred at different velocities are presented. The left image is an [O III] image centred at $V_{\rm LSR} = -50\,{\rm kms}^{-1}$, the systemic velocity of the PN (Hippelein & Weinberger 1990). The right image is in [O III] centred at $V_{\rm LSR} = 0\ {\rm kms}^{-1}$, which shows the extended halo, at a velocity unrelated to the PN. Based on its velocity, this halo is assumed to be ambient ISM, ionized by radiation leaking out of this density bounded PN.

A preliminary list of PNe with possible ISM haloes is given in table 4.3. Local examples include Abell 36 (McCullough et al. 2001), probably NGC 3242 (figure 4.5) and NGC 1360 (found from SHASSA). In addition, ionizing radiation leaking from the optically-thin PN NGC 246 may contribute to the emission region associated with the sdO star PHL 6783 (Haffner 2001). These ionized ISM haloes have sizes of ∼2–40 pc, or typically an order of magnitude larger than the AGB haloes listed by Corradi et al. (2003) which mostly have diameters of 0.4–3 pc (comparable to the sizes of the very largest PNe).

It was also found during our program of integrated photometry with WHAM (see the preceding chapter, and table 3.8) that several local PNe were found to have low-velocity emission either contaminating the WHAM 60′ beam (e.g. Abell 7, Abell 28, Abell 34, Abell 74, HaWe 4, HFG 1 and EGB 1), or one of the offset fields (e.g. MWP 1, FP 0905-3033, LoTr 5, Sh 2-176 and WDHS 1). Whether this is unrelated emission on the same sight line or ambient gas ionized by these PNe is not completely clear at the present time; however the strong [O III] emission surrounding HaWe 4, LoTr 5 and MWP 1 suggests the latter (compare with the general low [O III]/Hβ ratio seen in the diffuse ISM: Madsen, Reynolds & Haffner 2006). NGC 6751 (Chu et al. 1991), HFG 2 (Fesen, Gull & Heckathorn 1983) and Abell 19 (Kaler, Shaw & Kwitter 1990; Hua & Martinis 2003) are other likely examples of leaky PNe ionizing the ISM.

Hence it is becoming apparent that optically-thin evolved PNe close to the Galactic plane may have ionised haloes in the ISM around them that are not physically associated with the central PNe. Since many LMC PN haloes have been found by Reid (2007) based on morphology alone, it may be that some of these are ionized ambient gas in the LMC ISM.

An interesting example is the bright object NGC 3242, which shows both an AGB halo (Monreal-Ibero et al. 2005) and the huge extended halo noted earlier (figure 4.5). This giant halo shows strong [O III] emission (Zanin & Weinberger 1997), and these authors suggest the very

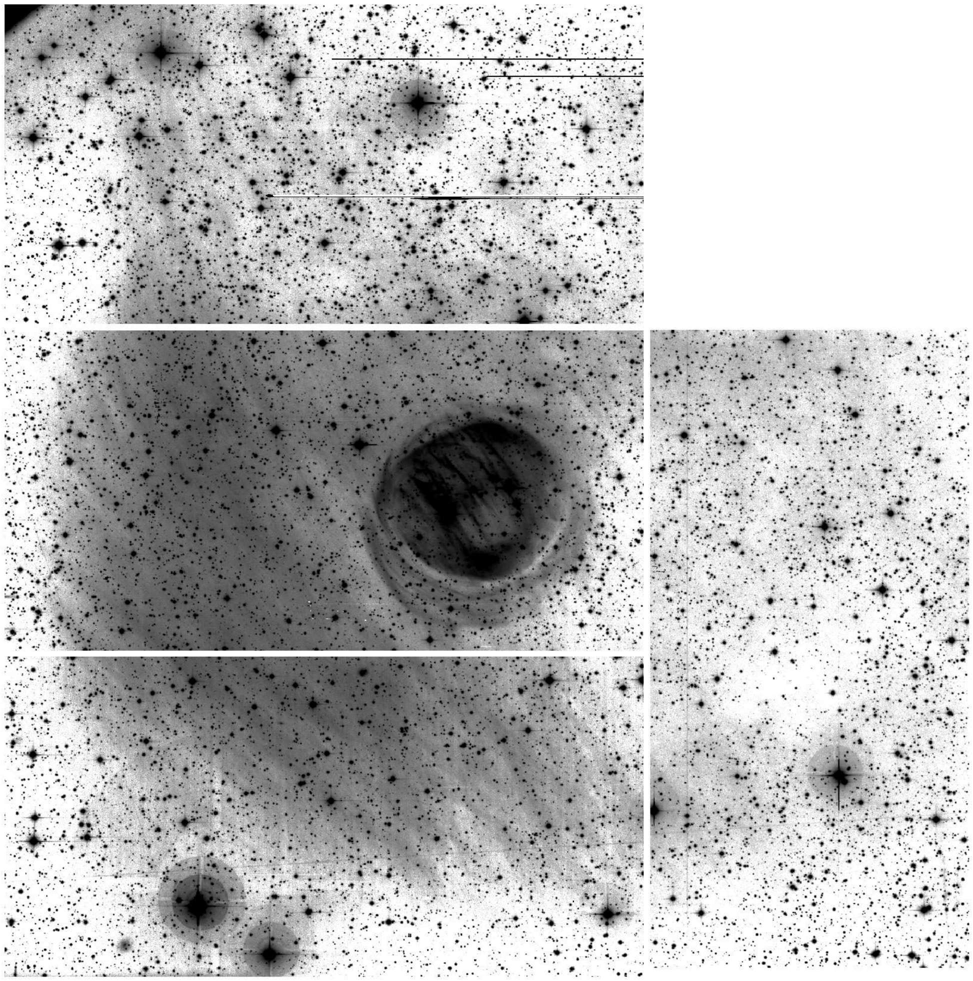

Figure 4.3: INT Hα image of the large halo around the evolved PN Sh 2-200. Image from Corradi et al. (2003).

high [O III]/Hα ratio is partly due to shocks, implying that the halo was physically produced from the CS. Available velocity data do not allow a conclusion to be drawn on its nature: unfortunately, both the systemic velocities of the PN and giant halo are coincidentally close to $V_{\rm LSR} = 0\,{\rm kms}^{-1}$(Durand, Acker & Zijlstra 1998; Rosado 1986), so there is no large velocity differential that proved useful in the case of Sh 2-200. The available kinematic data was used by Rosado (1986) to suggest PN and halo were associated, but it was noted that the expansion velocity of the filamentary halo was lower than that of the PN. Later, Meaburn, López & Noriega-Crespo (2000) obtained line profiles of the brightest western rim of the giant halo, and noted that the radial velocities are inconsistent with the model of a simple shell expanding radially from the PN. They suggested that it could be either an asymmetric lobe ejected from the PN or simply photoionized ambient ISM.

A Hα flux for the halo was estimated from SHASSA images by measuring the total flux of PN plus halo and subtracting the flux for the core only, to determine a halo flux, and then assuming a [NII]/Hα ratio of 0.5 for the halo (cf. Rosado 1986). The Hα halo flux was found to be $\sim$1.2 $\times$ 10^{-10} erg cm^{-2} s^{-1}. Following the procedure outlined in §7.7 below, an approximate

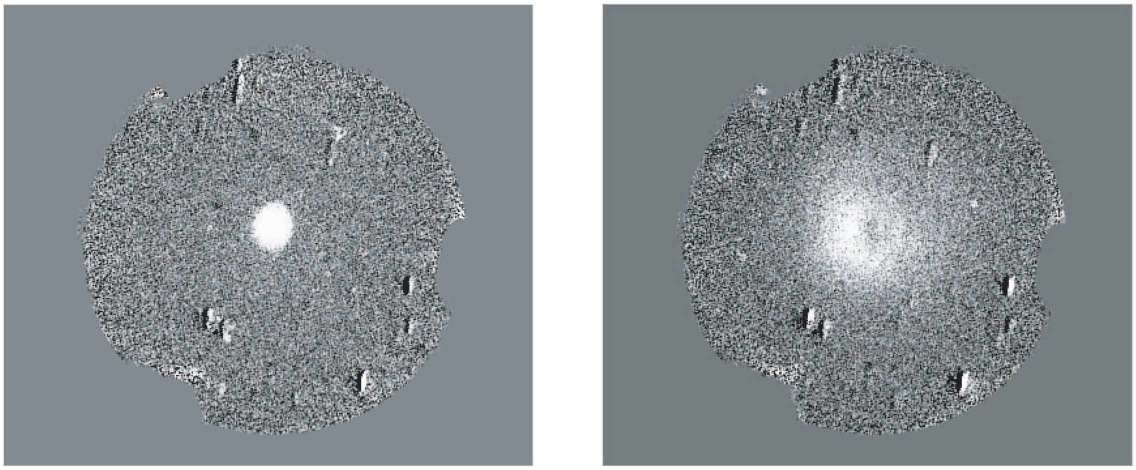

Figure 4.4: WHAM images for the high-excitation PN Sh 2-200. Each spectral window is 25 kms^{-1} wide. The left image is an [O III] image centred at $V_{\rm LSR} = -50\,{\rm kms}^{-1}$, the systemic velocity of the PN. The right image is in [O III] centred at $V_{\rm LSR} = 0$ kms^{-1}, which shows the extended halo. The halo is not physically associated with the PN, but is a Strömgren sphere in the local ISM, around this nearby optically-thin PN. Note the elongated PSFs of the PN and brighter stars in the field, a product of the imaging optics. Image from Madsen & Frew 2008, in preparation.

ionized mass of $\sim 34\sqrt{\epsilon}\, M_{\odot}$ was found, assuming a distance of 1.0 kpc. The low line-width of the halo and the small offset in systemic velocities is consistent with ambient ISM, unambiguously confirmed after taking into consideration the very high ionized mass of the halo at the adopted distance.

Note that the very high-excitation PN NGC 4361 has no detectable halo on SHASSA images (down to an emission measure of $\sim$2 cm^{-6}pc). Monreal-Ibero et al. (2005), using integral field spectroscopy, also found no evidence for a halo around this object. Therefore the nebulous filament 1.2° northwest of NGC 4361 seen on the POSS (Zanin & Weinberger 1997) is not an emission nebula. It may be faint interstellar cirrus.

Corradi et al. (2003) found that ionized AGB haloes are quite common around PNe, with 60% of elliptical PNe showing them where the necessary deep images are extant (many show sign of an ISM interaction, see below). Another 10% of PNe show possible recombination haloes. It is found here that up to 30% of *high-excitation, optically-thin PNe* show ISM haloes at low emission measures, despite the fact that many of these objects have large $|z|$ distances from the Galactic plane (see below).

Since the sizes and surface brightnesses of the visible shells of large evolved PNe and the AGB haloes seen around compact PNe are similar, to a first order the ionized masses are comparable. This is the best solution to the missing mass problem in PNe, where the mass budget of the PN plus central star is less than the inferred progenitor mass. However, the ionized masses of the optically-thin objects NGC 4361 and Abell 36 are $<$0.2 $M_{\odot}$, but neither has an observable AGB halo. In the latter case, there is a huge ionized ISM halo, but there is no evidence for additional PN mass. The CS has a mass of $\sim$0.56 $M_{\odot}$, so the observable mass total is well under a solar

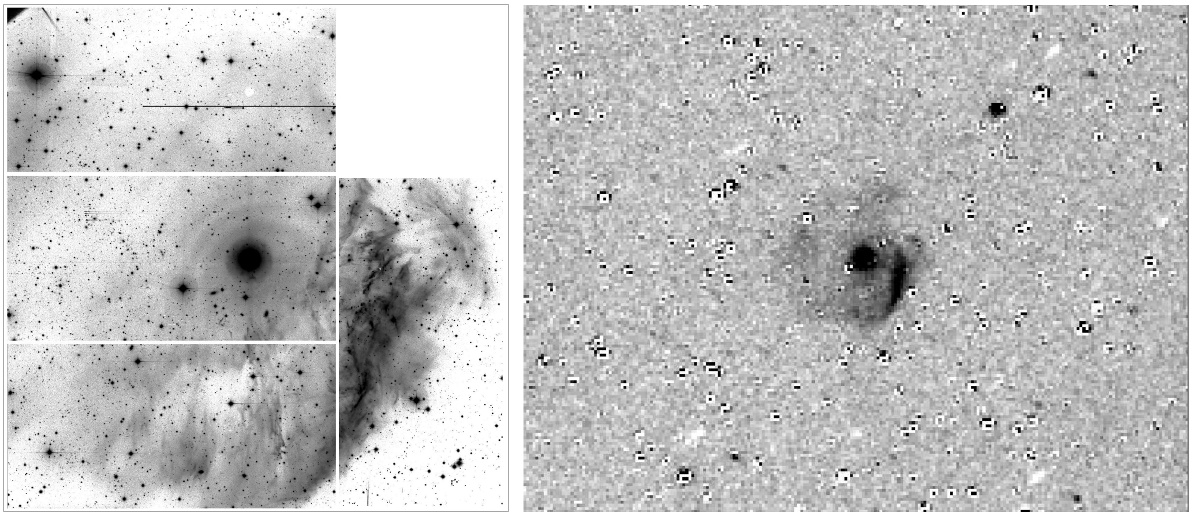

Figure 4.5: Left: INT Hα image of the very large halo around bright PN NGC 3242. Field is 30′ across. Image from Corradi et al. (2003). Right: [N II]+Hα image from SHASSA field #142, covering a wider angle, and showing the full extent of the halo. Image is 3° wide.

Table 4.3: Nearby PNe with definite or possible ionized ISM haloes. PNe are sorted in order of increasing distance, taken from table 9.5.

Name	Size (′)	Status	D (pc)	Size (pc)	Notes
NGC 1360	180 × 70	poss	375	20 × 8	1
Abell 36	300 × 240	yes	450	39 × 31	1, 2
NGC 246	>180:	poss?	495	>26	1, 3
MWP 1	>60	yes	497	>9	1
LoTr 5	>60	yes	500	>9	1
Abell 21†	23 × 18	poss?	540	4 × 3	1
Sh 2-200	30 × 30	yes	660	6 × 6	1, 4, 5
HaWe 4	20:	yes?	800	∼5	1, 6
NGC 3242	40 × 36	yes	1000	12 × 10	1, 4
HFG 2	7 × 5	yes	1900	4 × 3	1
NGC 2440	80 × 45	poss?	1900	44 × 25	1
NGC 6751	2.5 × 2.0	yes	2000	1.5 × 1.2	1, 7

Notes: † Possibly stripped PN material due to ISM interaction

1. This work; 2. McCullough et al. (2001); 3. Haffner (2001); 4. Corradi et al. (2003); 5. Hartl & Weinberger (1987); 6. Tweedy & Kwitter (1996); 7. Chu et al. (1991)

mass. A progenitor star with a mass of $\leq 1\,M_{\odot}$ should not have produced a visible PN (see Chapter 11). A possible solution to this problem is that RGB mass loss may be more efficient for low mass stars (e.g. Schröder & Smith 2008), hinting that any PN eventually produced may well be unobservable, i.e. a 'lazy' PN (see also the discussion in §9.5.1).

Balick, Wilson & Hajian (2001) have shown that the bright PN NGC 6543 has at least nine faint concentric ring-like shells in its halo, representing spherical bubbles of mass loss preceding the formation of the PN core. Using the dimensions and constraints on the ejection speeds, it seems the shells are formed during the AGB stage on time scales of $10^2 - 10^3$ yr. This is quite different to the time scales of thermal pulses ($\sim 10^5$ yr) and stellar surface pulsations ($\sim$1–3 yr).

Terzian & Hajian (2000) and Corradi et al. (2004) document the (mainly young) PNe containing rings or arcs in their haloes. Corradi et al. (2004) demonstrate that such rings, and hence the existence of mass loss fluctuations in the late AGB phase, is a common phenomenon; they estimate at least $\sim$35% of PNe show them. However, the formation mechanism is still uncertain: Meijerink, Mellema & Simis (2003) propose a dust-driven wind instability model as a production mechanism, but further work is needed.

Finally, it is important to note if any morphological classes have a greater incidence of haloes, based on the solar neighbourhood sample. The advantage is that the large angular size of PNe in the local sample makes it easier to describe the detailed morphogy of each PN. However, most highly-evolved PNe have no evidence for giant haloes; remembering that AGB haloes are typically a factor of 10^3 fainter than the main PN shell, then for the most evolved PNe the halo has expanded and faded well below detectability. In some cases it may have been swept up by the expanding PN shell. Some evolved bipolar PNe have detectable outer emission (e.g. RCW 24, see below), due to the greater ionized mass in their AGB haloes, which is attributed to the greater mass of the progenitor stars.

Recently, Hsia, Li & Ip (2007) have used SHASSA data to detect a number of haloes around a set of relatively nearby, mainly bipolar PNe. The haloes detected around NGC 2438, NGC 3242, NGC 7293, and He 2-111 were already known in the literature. Hsia, Li & Ip (2007) claimed to have detected new haloes around IC 4406, NGC 2818, NGC 2899, NGC 5189, NGC 6072, and NGC 6302. To test their claims, deep continuum-subtracted SHS images with a limiting surface brightness of $\sim$2 R at Hα (Parker et al. 2005a), were examined for each PN, except for IC 4406, which lies outside the coverage of the SHS. Since the diameters of all these PNe are larger than a SHASSA resolution element, it is inappropriate to use a PSF fitting function based on bright stars to infer the presence of a PN halo. Furthermore, the paper does not give details on the brightness of the stars used for the profile fitting or a detailed account of the procedure. Only for NGC 6302 is faint emission present exterior to the PN on SHS images, and this is considered to be unrelated diffuse emission. The SHS image of NGC 2899 shows two very faint emission knots in line with the polar axis (Parker 2000), but these are too faint and small to be recovered in the SHASSA data. No haloes were seen around the other objects, and I consider their detections to be artefacts of the reduction procedure of Hsia, Li & Ip (2007).

In summary, only 15–20% of solar neighbourhood ($D < 1.0$ kpc) PNe have detectable outer

(AGB) haloes, after referring to Table 9.4, later in this thesis. About the same fraction overall have surrounding haloes which are definitely, or very likely, ionized ISM. Comparing this frequency with the fraction of PNe in flux-limited samples (Corradi et al. 2003) is problematic, as such samples are dominated by bright PNe with proportionally brighter AGB haloes. The fraction determined here is significantly lower, due to the local volume being dominated by highly evolved PNe. The small numbers also preclude any conclusions being made on the frequency of haloes relative to morphological class.

4.3 Interaction of PNe with the Interstellar Medium

Since PNe have old-disk kinematics, the majority have non-zero space velocities relative to the interstellar medium (ISM). Morphological studies of evolved PNe show strong evidence of asymmetries which can attributed to an interaction with the ISM (Rauch et al. 2000). Observing interactions on a case-by-case basis allows the dynamics of the evolving nebula to be related to the cooling history of the central star (Tweedy & Kwitter 1994a, 1996; Tweedy 1995b; Jacoby & van de Steene 1995; Pottasch 1996; Wareing et al. 2006a). Borkowski, Sarazin & Soker (1990) and Borkowski (1993) consider the PN/ISM interaction process in detail. They find that the PN shell is compressed first in the *direction of the stellar motion*, which causes a dipole asymmetry in the surface brightness of the nebula. Eventually, an advanced interaction begins to strip the nebular gas away from the CS (Villaver, García-Segura & Manchado 2003; Wareing, Zijlstra & O'Brien 2007b, and references therein). Examples of such interacting nebulae are prevalent in the solar neighbourhood, and are in fact seen in the majority of local PNe (see below).

The population of interacting PNe in the solar neighbourhood can ultimately be used to verify current theories of PN/ISM interaction (e.g. Smith 1976; Borkowski, Sarazin & Soker 1990; Dgani 1995; Tweedy, Martos & Noriega-Crespo 1995; Rauch et al. 2000). Villaver et al. (2003) have shown that PNe with typical space velocities of $\sim$20 kms^{-1}, will interact with the ISM and have observable bow shock structures, confirmed by Wareing, Zijlstra & O'Brien (2007b). These authors find that the ongoing ISM interaction reduces the mass of the circumstellar envelope due to ram pressure stripping. This point will be further examined later.

4.3.1 A Case Study: PFP 1

This remarkable hollow-sphere PN was discovered serendipitously from AAO/UKST Hα Survey images by M. Pierce in 2003 (see Pierce et al. 2004 for a fuller account). At $\sim$19$'$ across, it is one of the largest examples of its type, with almost perfect circular symmetry, except for a brightened rim on the northwest edge. This beautiful object is a fine test case for current theories of ISM interaction (Borkowski, Sarazin & Soker 1990; Tweedy & Kwitter 1994a, 1996; Rauch et al. 2000).

Tweedy & Kwitter (1996) suggest three criteria to confirm that PN asymmetry is caused by a PN-ISM interaction. They propose that such interactions are characterised by three observable criteria:

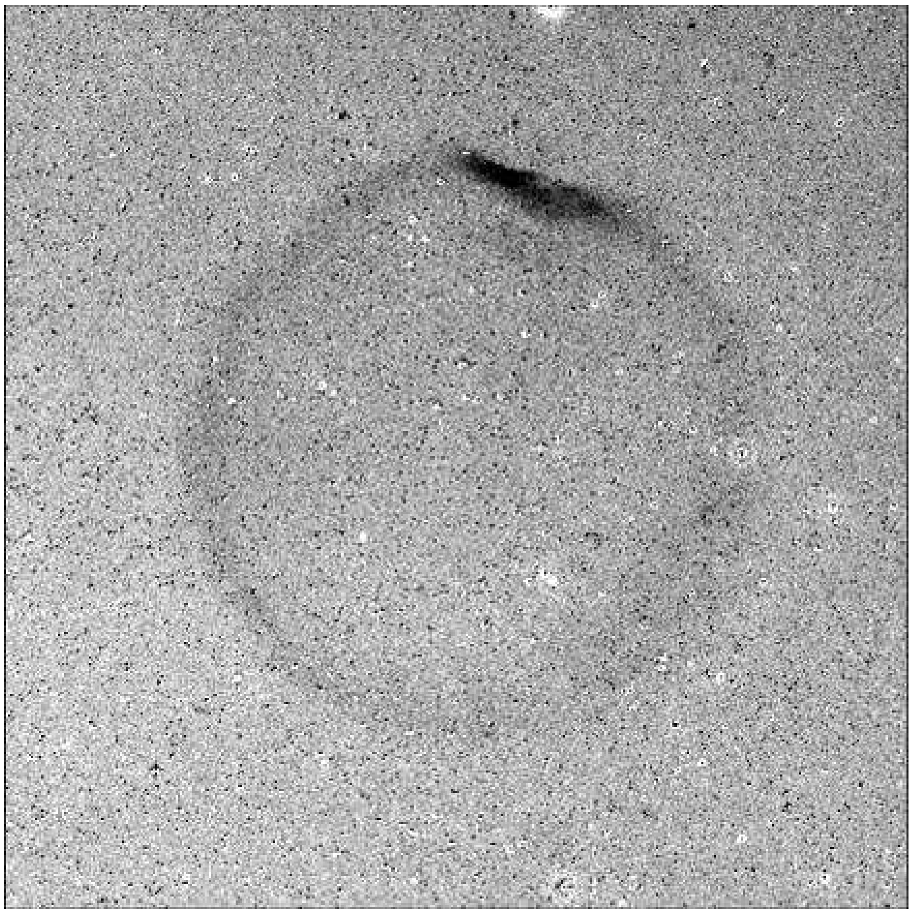

Figure 4.6: Continuum subtracted Hα + [NII] image of PFP 1. The field is $30'$ across, with north at top and east to the left.

1. an asymmetry in the periphery of the nebula;
2. an increase in surface brightness at the interacting edge;
3. that the rim exhibits a drop in the ionization level, i.e. an increased [N II]/Hα ratio with respect to the rest of the nebula. The higher [N II]/Hα ratio results from material being compressed at the PN-ISM boundary, increasing the density which, in turn, elevates the recombination rate and lowers the ionisation state of the gas (Tweedy & Kwitter 1994a, 1996; Kerber et al. 2000b). The giant nearby PN Sh 2-216 also shows these characteristics clearly (Fesen, Blair & Gull 1981; Tweedy, Martos & Noriega-Crespo 1995).

PFP 1 can be seen to satisfy the first two criteria of Tweedy & Kwitter (1996) purely from the SHS image (see Figure 4.6). The beginning of an asymmetry, coupled with an increase in brightness, can be clearly seen in the image. Emission-line spectroscopy shows the third criterion also is met, as the bright rim has an enhanced [N II]/Hα ratio of 3.2 compared with the east rim of the nebula where [N II]/Hα $\sim$ 1.5 (Pierce et al. 2004). The ratio for the whole nebula was estimated to be [N II]/Hα = 1.8 (based on weighted surface brightnesses of the different slit positions (Pierce et al. 2004) but recent WHAM data show that the *integrated* ratio is somewhat lower (see §3.3).

The ISM interaction in PFP 1 is at an early stage, since the CS is still close to the centre of the nebula, coupled with the fact that only the northwest rim is brightened, implying that the bulk of the nebula is still moving with the CS. Objects showing a more advanced interaction may have a substantially displaced CS from centre, such as the extreme cases of Sh 2-188 (Wareing et al. 2005, 2006a; Wareing, Zijlstra & O'Brien, 2007a) and Sh 2-216 (Cudworth & Reynolds 1985; Tweedy 1995b) where the CS is displaced by $24'$ from the geometric centre of this $1.6°$ diameter PN, due to the nebular material being slowed and re-absorbed into the ISM.

Borkowski, Sarazin & Soker (1990; see also Soker, Borkowski & Sarazin 1991) discuss PN-ISM interactions in terms of the expansion velocity of the PN and the velocity of the progenitor star with respect to its surroundings. In a homogeneous, isotropic ISM, the PN will start to interact on its leading edge. As the PN expansion causes the nebular density to fall below a critical value, the gas in the shell is compressed, resulting in a brightness enhancement in this direction and an increase in the recombination rate, manifested as an elevated [N II]/Hα ratio (Tweedy & Kwitter 1994, 1996; Kerber et al. 2000b). As the interaction develops the leading edge of the nebula is slowed by the ISM and the PN shell becomes distorted as is seen in the case of PFP 1 where an opposite concave curvature is present.

At first glance this appears to be a reasonable explanation for the morphology of PFP 1, especially as an examination of the local Galactic environment found that it sits in a low density region despite its small $|z|$ distance of 40 pc (Pierce et al. 2004). It is likely that the interaction is taking place because the PN is moving with respect to the local ISM, so it is predicted that the CS is moving north across the field. However, the central star of PFP 1 has no detectable proper motion from the available SSS and SHS images. A tentative upper limit for the proper motion of $\sim$8 mas.yr^{-1}, based on the SHS data for the field around the PN, corresponds to a upper limit for the transverse velocity of $\sim$20 km s^{-1} at the nominal distance of $\sim$ 550 pc (Pierce et al. 2004).

4.3.2 Discussion

About 65% of the PNe in the solar neighbourhood sample (defined below in Chapter 9) show evidence for an ISM interaction. This proportion rises to $\sim$90% amongst the evolved PNe (see §2.1) in the sample. Exceptions are RCW 24 (see Figure 4.7), Abell 7, Abell 24, and probably Abell 36. In the first three cases, the lack of ISM interaction is probably due to the CS having a small space motion component with respect to the ISM, at least in the direction transverse to the line of sight. Abell 36 has a moderately high $|z|$ distance and the root-mean-squared (RMS) electron density of the ISM is predicted to be low (though see McCullough et al. 2001). Other local evolved PNe only have a weak ISM interaction: examples are NGC 3587, Abell 74 and LoTr 5.

However, many of the nearest PNe show a pronounced bow shock structure as a signature of an ISM interaction. In broad terms, bow shocks are produced when wind-producing stars move supersonically through the ISM. Besides those seen around PNe (e.g. Tweedy & Kwitter 1994a; Zucker & Soker 1993; Wareing et al. 2006a), bow shocks are also noted around Herbig-Haro objects, Wolf-Rayet stars (e.g. Moffat et al. 1998), runaway OB stars (Gull & Sofia 1979; Van Buren & McCray 1988; Van Buren, Noriega-Crespo & Dgani 1995), high-mass X-ray binaries (Kaper et al. 1997), and pulsars (e.g. Kulkarni & Hester 1988).

Van Buren (1993) and Brown & Bomans (2005) discuss in detail the bow shock phenomenon. Villaver et al. (2003), Wareing et al. (2006b), Martin et al. (2007) and Wareing, Zijlstra & O'Brien (2007a,b) have shown that initial ISM interaction occurs between AGB wind and ISM, and well before the onset of the PN phase. Beautiful examples of one-sided evolved PNe are Sh 2-188 and Sh 2-176 which have morphologically-dominant bow shocks. Abell 35 is a particularly interesting case (Jacoby 1981; Hollis et al. 1996), as an inner bow shock morphology is visible in [O III] light, largely absent in Hα. However, the interpretation adopted here is that the emission nebula is not a PN at all, but a Strömgren zone in the ISM (see §8.2 for further details).

Other local PNe which have pronounced asymmetric shapes are Abell 21 (Kwitter, Jacoby & Lawrie 1983; Borkowski, Sarazin & Soker 1990; Hua & Kwok 1999), HaWe 4 (Tweedy & Kwitter 1996), HFG 1 (Heckathorn, Fesen & Gull 1982), IsWe 1 (Tweedy & Kwitter 1996; Xilouris et al. 1996), Abell 31 (Tweedy & Kwitter 1994a) and the newly discovered FP 0905-3033 (see figure 2.10). More distant examples include MeWe 1-4 (Kerber 1998), and KFR 1 and SuWt 1 (Rauch et al. 2000). New-epoch CCD images to determine accurate proper motions of their central stars will be of interest. An analysis of a sample of one-sided PNe has been given by Ali, El-Nawawy & Pfleiderer (2000); these authors found that 75% of their sample was found within 160 pc of the galactic plane (reflecting the scale height of the HI gas) and that about three times more PNe were found with features roughly parallel to the Galactic equator than PNe with features perpendicular to the equator.

It is should be re-emphasised that some morphologically unusual putative PNe have ionization structures and morphologies which are not consistent with an ISM interaction, assuming

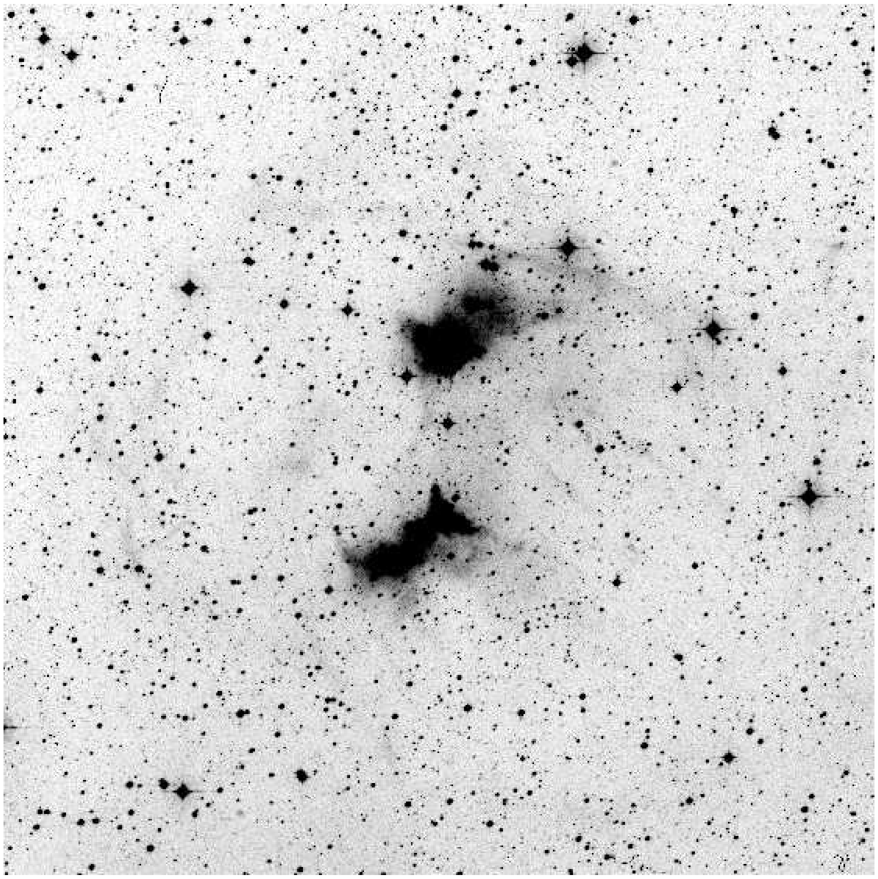

Figure 4.7: Hα + [NII] image of the faint bipolar PN RCW 24, showing little evidence for an ISM interaction. The field is 30$'$ across, with north at top and east to the left.

the CS is moving through the ISM, e.g. Sh 2-68, Sh 2-174 and PHL 932, amongst others. This fact has been used a discriminant for differentiating true PNe from H II regions. Some local nebulae are now thought to be HII regions ionised by hot stars rather then true PNe, and are discussed in more detail in Chapter 8.

It should also be noted that of the $\sim$20 PNe (e.g. De Marco 2006) which possess close binary central stars which have gone through a common-envelope stage, about $50 \pm 7\%$ show evidence of an ISM interaction (c.f. Bond & Livio 1990), which is slightly less (but not statistically different) to the overall proportion of interacting PNe in the volume-limited solar neighbourhood sample. The quoted uncertainty in this number is a 1σ Poissonian error.

Finally, the PN-ISM interaction may be influenced by the ISM magnetic field (e.g. Soker & Dgani 1997; Soker & Zucker 1997; Dgani & Soker 1998), as well as various hydrodynamic instabilities such as the Rayleigh-Taylor (RT) and possibly Kelvin-Helmholtz (KH) instabilities. The RT instability allows the ISM to stream into the interior of the PN (Dgani & Soker 1998), and is the most commonly seen in evolved PNe. RT instabilities are likely present in NGC 40 (Martin, Xilouris & Soker 2002), IC 4593 (Zucker & Soker (1993), DS 2 (Hua, Dopita & Martinis 1998), and Abell 43 and NGC 7094 (Rauch 1999).

In addition, a number of evolved PNe have almost perfectly linear 'stripes' manifested across the face of the PNe. Examples in the local volume include Sh 2-200 (Corradi et al. 2003), FP 0739-2709 (see figure 2.10), and probably Sh 2-216 and IsWe 2 (see Tweedy & Kwitter 1996). The stripes seen in the halo of NGC 6894 (Soker & Zucker 1997) are possibly examples of the same phenomenon. Dgani & Soker (1998) suggest that the ISM magnetic field makes the RT instability very efficient for PNe close to the Galactic plane, producing 'rolls' or stripes. The 'pipes' seen in Abell 35 (Jacoby 1981, Hollis et al. 1996) are superficially similar, but their formation mechanism remains uncertain (see §8.2).

Sophisticated computer modelling (e.g. Wareing et al. 2006a, 2006b, 2007; Wareing, Zijlstra & O'Brien 2007a, 2007b) has allowed the theory of PN/ISM interactions to be better compared observational data. Detailed modelling of the interacting PN Sh 2-188 succesfully predicted the shape of the downstream tail in this object (Wareing et al. 2006a). Furthermore turbulence is expected to produce vortices in the downstream wind. The vortices result from instabilities at the head of the bow shock upstream of the AGB star (or CSPN). These instabilities travel downstream and form vortices in the tail behind the bow shock. Such features appear to be visible in the planetary nebula Sh 2-188 (Wareing, Zijlstra & O'Brien 2007a) and the in the 'tail' of Mira (Martin et al. 2007; Wareing et al. 2007).

4.3.3 Summary

This chapter presented a discussion of the various PNe classification schemes used in the literature, including a detailed summary of the scheme adopted herein. Statistics are given on the relative proportions of the different morphological types in the solar neighbourhood sample.

AGB haloes have been observed around many compact PNe. Another type of halo, not often considered in the literature, is the ISM halo. It is found that ISM haloes are not rare around PNe, with up to 30% of local, optically-thin PNe showing evidence for them. Definite examples are the haloes around Sh 2-200 and NGC 3242.

About 65% of the PNe in the solar neighbourhood sample show evidence for an ISM interaction. This proportion rises to ∼90% amongst the evolved PNe in the sample. Some local evolved PNe only have a very weak or no ISM interaction, which is evidence of a low peculiar velocity relative to the ISM: examples are Abell 74, and RCW 24.

Chapter 5

Optical Spectroscopy of Evolved PNe

Data for this dissertation was taken from the unpublished MASH and MASH-II spectroscopic databases. Spectra of MASH PNe as well as a limited number of previously known evolved PNe were obtained on a number of telescope runs summarised in Table 5.1. The data was contibuted by several MASH team members (initials as noted in the last column of Table 5.1). The names of the observers can be found in the author list of Parker et al. (2006a). Additional runs for the MASH-II PN project are tabulated in the same format by Miszalski et al. (2008).

5.1 Observations

The spectroscopic runs observed by me concentrated on the most highly evolved PNe, starting in February 2004 with a run (with Q. Parker) using the SAAO 1.9m telescope at Sutherland, RSA. The standard 1.9-m grating spectrograph was used with a SITe 1798 x 266 pixel CCD, coupled to an f/2.2 camera with an 86 mm beam. Grating 7 was generally used (300 lines mm^{-1}) for the low dispersion observations, giving a spectral coverage of 3500–7400 Å, though Grating 4 (1200 lines mm^{-1}) was sometimes used to obtain higher dispersion; this grating is blazed for the red spectral range and has a spectral coverage of $\sim$6150–6900 Å.

On-chip binning ($2\times$) perpendicular to the dispersion direction was used to reduce readout noise. The slit width was set to 400μm ($\sim$2.4$''$ on the sky) to allow reasonable throughput for these faint PNe, and to allow for seeing effects when observing standard stars; the resulting spectral resolution is $\sim$7Å. The unvignetted slit length perpendicular to the dispersion was 1.6$'$ and was fixed east-west. Exposures were generally 600 to 1200 seconds, and repeat exposures were sometimes taken for especially faint objects, to improve the S/N ratio. Shorter exposures were used for flux and radial velocity standards. If the angular size of the nebula was larger than the slit length, separate offset sky frames were taken (e.g. for PFP 1; see Pierce et al. 2004).

Later spectroscopic runs used the double-beam spectrograph (DBS; Rodgers, Conroy & Bloxham 1988) at the Nasmyth focus of the MSSSO 2.3-metre reflector at Siding Spring Observatory, NSW. The 6.7′ slit was nominally oriented east-west, but was sometimes oriented at a different position angle in order to cover the brightest regions of the nebula, or to avoid bright field stars. The slit width was generally set to 2.5″, though sometimes wider in conditions of poor seeing (the median seeing at SSO is 1.5″). The separate blue and red spectra were recorded on identical-format Tek 1752×532 pixel CCDs, optimised for the blue and red. Since 2006, the detectors have been upgraded with Tek 2148×562 pixel chips.

For both the blue and red arms of the DBS, 600 and 1200 line/mm gratings were used, giving a spectral coverage of ∼3700–5600Å and ∼5700–7400Å respectively. On some later runs, a 300 line/mm grating was used which gave a coverage of 3600–7400Å. This reduced the number of frames to reduce, and had the benefit of giving a more robust estimate of the Hα/Hβ ratio in order to estimate the reddening; some resolution was sacrificed however. On-chip binning (2x), perpendicular to the dispersion direction, was typically used with the DBS. Exposures were generally 1200 seconds, though shorter exposures were used for brighter objects and flux and RV standards.

For all spectroscopic runs, dome flats and twilight sky flats were obtained, together with observations of spectrophotometric standard stars (Stone & Baldwin 1983) for flux calibration. Wavelength calibration was applied via suitable Fe-Ar, Cu-Ar or Ne-Ar arc exposures bracketing the observations. PN standards from Dopita & Hua (1997) were observed once a night as checks on the flux and wavelength calibrations, and to better quantify the errors on each. Observations of PNe were generally taken at low air-mass (<2) to minimize the effects of differential refraction, and standard stars were generally observed at air-mass <1.5. Differential refraction should not present a problem for these PNe as they are all are much larger than the chosen slit widths. However, this precludes obtaining line-flux ratios that are representative of the whole PN, as stratification effects are often present in these old, interacting PNe. For an excellent discussion of the sources of uncertainty in long-slit spectroscopy, see Jacoby & Kaler (1993).

Standard IRAF routines were used to reduce the long-slit spectra, supplemented with routines from the PNDR data reduction package written by fellow MASH team member Brent Miszalski.[1] All line fluxes were measured from the 1-D flux-calibrated spectra using the *splot* function in IRAF. Repeat observations from different spectra (where available) were taken and averaged, and the standard deviation is representative of the internal error in the absolute fluxes, which are accurate to ∼20% for the brightest lines in the more compact, high-surface brightness PNe, but to only ∼50% for lines in the very faintest nebulae. The relative flux ratios should be better; ∼10% for the [O III]/Hβ and [N II]/Hα ratios for the brighter PNe with better S/N.

Additional details on the earlier MASH spectroscopic runs, mainly taken with the FLAIR-II and 6dF fibre spectrographs on the 1.2m UKST have been given by Parker et al. (2006a) and Frew, Parker & Russeil (2006).

[1]See http://www.aao.gov.au/local/www/brent/pndr

5.2 Results

The nebulae selected for analysis from the MASH spectroscopic database were mostly candidates for the local volume, selected by their angular size and brightness. The observed flux values for 60 PNe are given in Table 5.2. All fluxes are normalized to Hβ = 100, and are uncorrected for reddening. For a few faint and highly reddened PNe, fluxes are given relative to Hα = 300. An upper case 'P' signifies that a line is present but too faint to measure, while an asterisk is used when the intensity of a faint doublet line has been estimated from the intensity of the brighter line such as [O III]λ5007. Roman letters immediately after the PN designation refer to different slit positions for those PNe with multiple observations.

The logarithmic extinction at Hβ, $c = \log F(H\beta) - \log I(H\beta$, is also derived for each PN based on the observed Balmer decrement. In this study, I have adopted the $R = 3.1$ Galactic reddening law of Howarth (1983), which is consistent with the Cardelli, Clayton & Mathis (1989) reddening law. From first principles,

$$\log\frac{F(H\alpha)}{F(H\beta)} = \log\frac{I(H\alpha)}{I(H\beta)} - 0.320\,c \tag{5.1}$$

Hence, the logarithmic extinction was determined from the following expression:

$$c = \frac{\left(0.456 - \log\frac{F(H\alpha)}{F(H\beta)}\right)}{0.320} \tag{5.2}$$

An intrinsic ratio of $I(\mathrm{H}\alpha/\mathrm{H}\beta) = 2.86$ was used ($\log I(\mathrm{H}\alpha/\mathrm{H}\beta) = 0.456$), appropriate for $\mathrm{T}_e = 10^4$K (Brocklehurst 1971) and low densities typical of the PNe studied in this work. The dereddened line fluxes, $I(\lambda)$, were determined from the observed fluxes, $F(\lambda)$, following:

$$I(\lambda) = F(\lambda)^{c(f(\lambda)-f(H\beta))} \tag{5.3}$$

where $f(\lambda)$ is the reddening function (normalized to Hβ) from the reddening law of Howarth (1983).

The derived extinctions are given in columns 2 and 3 of Table 5.3, which also includes a summary of the main de-reddened emission-line ratios. The last column gives an approximate N/O abundance ratio (see §5.4) for PN with available data. Figure 5.1 illustrates a set of representative 1-D flux-calibrated and wavelength-calibrated spectra of these mainly faint PNe. Further detailed results for MASH-II and other PNe will be presented in the future (Miszalski, Frew & Parker 2008, in preparation).

Table 5.1: Summary details of the MASH spectroscopic follow-up program, adapted from the equivalent table of Parker et al. (2006a). The telescope runs are listed in chronological order, with those observed by the writer in bold. Additional runs for the MASH-II catalogue are tabulated in Miszalski et al. (2008).

Telescope	Run dates (dd mm yy)	Instrument	Wavelength range (Å)	Resolution (Å) (FWHM)	Grating	Exposure (seconds)	Observer
MSSSO 2.3m	02 07 98	DBS B/R	3820–5680; 5290–6850	4.6/2.3	300B/600R	600-900	QAP/MH
UKST 1.2m	22 07 98	FLAIR B/R	4300–5800; 5900–7100	4.7/4.6	600V/600R	3 × 1800	QAP
UKST 1.2m	11 08 98	FLAIR B/R	4350–5780; 5810–7220	5.4/4.2	600V/600R	3 × 1800	QAP
SAAO 1.9m	12-18 01 99	CCD SPEC	3790–7700	5.9	300B	600–900	QAP/DR
UKST 1.2m	07-11 07 99	FLAIR B/R	3900–7200; 6310–7030	11/2.4	250B/1200R	3 × 1800	QAP
UKST 1.2m	12-13 08 99	FLAIR R	6310–7030	2.4	1200R	3 × 1800	QAP
MSSSO 1.9m	04-09 01 00	B&C CCD	5650–6785	2.0	600R	600-1200	QAP/MH
UKST 1.2m	04-09 01 00	FLAIR	3920–7350; 6270–7050	12/2.7	250B/1200R	3 × 1800	QAP
UKST 1.2m	04-05 07 00	FLAIR	6200–6940	2.8	1200R	3 × 1800	QAP
SAAO 1.9m	08-15 02 00	CCD SPEC	3790–7780	7.0	300B	600–900	QAP
SAAO 1.9m	20-27 06 00	CCD SPEC	3800–7800	7.2	300B	600–900	QAP/RAHM
MSSSO 2.3m	01-06 07 00	DBS B/R	4000–5940; 6060–7020	2.4/1.3	600B/1200R	600-1200	QAP/MH
ESO 1.5m	03 07 00	B&C CCD	2680–8050	5.6	300B	600-900	DR/SB
SAAO 1.9m	15-21 05 01	CCD SPEC	3810–7800	7.1	300B	600–900	QAP/SB
MSSSO 2.3m	22-27 06 01	DBS B/R	4320–6220; 5930–6870	2.5/1.3	600B/1200R	600-1200	RAHM/MH
MSSSO 2.3m	06-10 07 02	DBS B/R	4320–6240; 6180–7100	2.3/1.3	600B/1200R	600-1200	MH/AEV/SB
SAAO 1.9m	16-22 07 02	CCD SPEC	3240–7270	7.1	300B	600–900	QAP/RAHM
SAAO 1.9m	28-01 01-02 03	CCD SPEC	3230–7260	7.1	300B	600–900	QAP/RAHM
MSSSO 2.3m	04-07 07 03	DBS B/R	3870–5600; 6170–7110	2.5/1.2	600B/1200R	600-1200	RAHM/SB
SAAO 1.9m	24-30 06 03	CCD SPEC	3360–7520; 6150–6880	5.0/1.3	300B/1200R	600–900	QAP/AEJP
UKST 1.2m	16-21 08 03	6dF V/R	3920–5530; 5330–7590	4.9/5.8	580V/425R	3 × 1800	QAP/AEJP
SAAO 1.9m	10-16 02 04	CCD SPEC	3360–7520	7.1	300B	600–900	**DJF**/QAP
MSSSO 2.3m	24-27 02 04	DBS B/R	3870–5600; 6170–7110	2.5/1.2	600B/1200R	600-1200	**DJF**
MSSSO 2.3m	12-14 06 04	DBS R	3580–5520	2.8	600B	600-1200	QAP/MS
MSSSO 2.3m	15-19 07 04	DBS B/R	3870–5600; 6170–7110	2.5/1.2	600B/1200R	600-1200	**DJF**/AEV
SAAO 1.9m	22-26 07 04	CCD SPEC	3360–7520	7.1	300B	600–900	QAP/MS
UKST 1.2m	11-20 08 04	6dF V/R	3930–5600; 5310–7520	5.6/5.8	580V/425R	3 × 1800	QAP/AEJP
MSSSO 2.3m	06-11 01 05	DBS B	6040–6950	1.5	1200R	600-1200	**DJF**/QAP
MSSSO 2.3m	10-14 07 05	DBS B	3600–7400	5	300B	600-1200	**DJF**
MSSSO 2.3m	19-25 05 06	DBS B	3670–5650; 5480–7520	2.5/2.3	600B/600R	600-1200	QAP/BM
MSSSO 2.3m	18-23 02 07	DBS B	3600–7400	4.5	300B	300-1200	**DJF**/QAP/BM

Note: MSSSO 2.3m telescope spectrograph slit generally set to a width of 2.5″; SAAO 1.9m spectrograph slit set at 2.4″; ESO 1.5m was set to 2.0″; MSSSO 1.9m was set to 2.0″; FLAIR and 6dF fibres had an aperture of 6.7″.

Table 5.2: Observed line fluxes for 60 PNe, primarily from the MASH project, uncorrected for reddening. Nebulae were primarily selected as candidates for the local volume. Fluxes are normalised to Hβ = 100, or for a few very reddened objects, normalised to Hα = 300.

NAME	[OII] 3727	[NeIII] 3869	Hγ 4340	[OIII] 4363	HeII 4686	Hβ 4861	[OIII] 4959	[OIII] 5007	[NII] 5755	HeI 5876	[OI] 6300	[NII] 6548	Hα 6563	[NII] 6584	[SII] 6717	[SII] 6731	[ArIII] 7136	[OII] 7325
BMP0642-0422	522	...	...	...	...	100	50	146	...	...	...	280	385	846	...	...	...	...
BMP0733-3108	...	...	...	...	...	...	...	...	...	...	...	468	300	1318	100	45	...	...
BMP1808-1406	...	...	...	...	...	...	...	...	...	...	...	359	300	1076	141	98	...	...
FP0709-2555	197	...	...	...	...	100	...	...	...	...	...	...	297	113	...	...	...	...
FP0711-2531	665	...	...	...	...	100	102	289	...	...	...	72	295	195	82	68	...	...
FP0721+0133	848	...	...	...	...	100	39	91	...	...	...	135	463	341	70	81	...	...
FP0739-2709	373	...	...	...	...	100	15	50	...	...	...	274	338	794	93	75	...	...
FP0840-5754	527	...	...	...	...	100	32	79	...	...	...	72	335	224	97	79	...	...
FP0904-4023	605	...	...	...	...	100	30	93	...	...	...	78	302	235	163	92	...	...
FP1554-5651	...	77	37	...	79	100	565	1789	...	...	...	377	813	1185	180	146	131	...
PFP 1	585	77	45	...	...	100	50	141	...	18	108	228	301	727	133	85	...	...
PHR0652-1240	...	...	...	...	...	100	78	290	...	...	...	98	361	232	147	111	...	...
PHR0719-1222	...	...	...	...	...	100	153	397	...	...	37	368	536	1104	195	118	115	...
PHR0724-1757	...	...	...	...	...	...	...	...	...	...	...	697	300	1795	...	...	...	...
PHR0740-2057	...	...	...	...	...	100	578	1833	...	...	...	127	596	482	198	56	...	...
PHR0743-1951	...	...	...	...	...	100	30	104	...	...	...	195	524	640	385	356	...	...
PHR0747-2146	...	...	49	...	...	100	213	586	...	...	...	57	359	142	85	60	56	...
PHR0755-3346	...	...	...	...	...	100	57	168	...	...	...	76	377	224	125	114	...	...
PHR0800-1635	1045	...	59	...	...	100	175	516	...	...	...	141	339	434	61	72	47	...
PHR0808-3745	...	...	71	...	...	100	71	213	...	...	...	48	332	214	60	62	74	...
PHR0834-2819	560	71	52	...	...	100	344	986	...	...	...	110	438	322	43	21	...	...
PHR0905-4753A	199	86	44	...	55	100	328	1049	...	...	...	248	488	772	114	89	81	...
PHR0905-4753B	...	...	...	...	65	100	399	1276	...	...	...	179	589	561	65	60	84	...
PHR0907-4532	...	...	...	...	...	...	...	...	...	...	...	33	300	98	75	44	...	...
PHR0907-5722	...	...	...	...	...	100	96	235	...	...	...	209	306	607	186	149	...	...
PHR0942-5220	...	...	53	...	...	100	224	629	...	...	...	61	390	153	92	64	60	...
PHR1032-6310	...	...	63	...	...	100	142	422	...	...	...	148	357	402	178	125	44	...
PHR1040-5417	...	...	...	...	...	100	185	536	...	...	...	92	288	280	34	22	38	...
PHR1052-5042	...	...	...	...	...	100	27	77	...	...	...	59	445	172	83	75	...	...

Continued on next page

Table 5.2 – continued from previous page

NAME	[OII] 3727	[NeIII] 3869	Hγ 4340	[OIII] 4363	HeII 4686	Hβ 4861	[OIII] 4959	[OIII] 5007	[NII] 5755	HeI 5876	[OI] 6300	[NII] 6548	Hα 6563	[NII] 6584	[SII] 6717	[SII] 6731	[ArIII] 7136	[OII] 7325
PHR1115-6059	...	...	...	...	...	100	...	P	...	...	...	203	1686	523	193	165	...	...
PHR1255-6251	...	...	...	...	...	...	...	182	...	...	...	782	300	2243	178	113	...	...
PHR1315-6555A	...	...	...	...	67	100	244	729	...	...	...	...	...	...	...	...	...	...
PHR1315-6555B	...	85	29	...	79	100	276	841	...	16	33	252	500	726	94	69	41	19
PHR1315-6555C	...	120	23	...	77	100	303	959	...	19	41	294	628	939	116	84	56	...
PHR1318-5601	...	...	...	...	...	...	...	P	...	...	...	218	300	672	84	...	...	...
PHR1327-6032	...	...	...	...	62	100	119	230	...	13	...	389	440	1079	53	24	...	...
PHR1335-6349	...	...	...	...	...	100	51	205	...	...	...	358	416	1047	223	213	28	...
PHR1337-6535A	...	...	...	...	...	...	...	...	...	...	...	257	300	718	223	147	...	...
PHR1337-6535B	...	...	...	...	...	100	97	320	...	...	...	324	309	847	108	91	36	...
PHR1400-5536	...	...	...	...	...	100	...	...	...	...	...	22	287	52	23	...	...	...
PHR1408-6106	404	...	...	...	...	100	54	169	...	...	...	226	457	652	138	101	...	...
PHR1418-5144	...	...	...	...	...	100	204	724	...	...	...	90	398	455	...	...	...	...
PHR1424-5138	...	...	...	...	...	100	50*	159	...	...	...	...	496	...	...	...	...	...
PHR1429-6003	...	...	...	...	...	...	...	...	...	...	...	308	300	991	107	103	...	...
PHR1432-6138	...	...	...	...	...	100	134	360	...	...	...	241	378	756	120	120	25	...
PHR1510-6754A	...	...	...	...	...	100	105	311	...	...	...	285	268	1039	129	121	30	...
PHR1510-6754B	...	...	...	...	...	100	107	326	...	...	...	259	215	774	140	128	...	...
PHR1533-4824	...	...	...	...	...	100	84*	253	...	...	...	167	276	490	595	545	...	...
PHR1537-6159	...	...	...	...	...	100	417	1290	...	...	...	197	673	783	P	...	...	...
PHR1539-5325	...	...	...	...	...	...	...	...	...	...	...	85	300	205	132	102	...	...
PHR1551-5621	...	...	...	...	...	100	75	188	...	...	...	917	494	2609	110	59	...	...
PHR1602-4127	...	...	40	...	...	100	111	328	...	10	108	381	352	170	114	45	...	
PHR1625-4523A	...	...	28	...	...	100	98	268	...	8.1	...	93	462	360	140	97	45	...
PHR1625-4523B	...	...	...	...	...	100	80	218	...	...	...	113	400	274	176	136	...	...
PHR1720-3927	...	...	...	...	...	...	...	102	...	...	...	113	300	393	98	86	...	...
PHR1724-3859	...	...	...	...	...	100	109	269	...	...	...	1360	751	4107	209	147	...	...
PHR1808-3201	...	...	...	...	...	100	...	209	...	...	...	709	586	2100	255	244	...	...
PHR1906-0133	...	...	...	...	...	100	...	88	...	...	...	352	831	958	327	213	...	...
RCW 24A	...	...	47	...	...	100	150	352	...	...	...	681	331	1853	198	84	...	...
RCW 24B	255	...	40	...	16	100	78	186	30	25	57	466	315	1406	106	54	22	...
RCW 69A	...	...	...	...	28	100	169	485	...	...	...	859	499	2891	163	129	...	...
RCW 69B	...	...	...	...	...	...	...	...	...	...	...	418	300	1331	85	67	...	...
RCW 69C	264	...	28	...	...	100	175	409	...	...	...	924	458	2883	263	198	...	...
RCW 69D	219	...	40	...	...	100	131	377	30	40	...	944	543	2840	188	181	24	...

Continued on next page

Table 5.2 – continued from previous page

NAME	[OII] 3727	[NeIII] 3869	Hγ 4340	[OIII] 4363	HeII 4686	Hβ 4861	[OIII] 4959	[OIII] 5007	[NII] 5755	HeI 5876	[OI] 6300	[NII] 6548	Hα 6563	[NII] 6584	[SII] 6717	[SII] 6731	[ArIII] 7136	[OII] 7325
Abell 24	119	23	31	...	30	100	69	197	10	20	...	430	325	1214	40	31	...	...
Abell 31	...	...	...	...	45	100	280	833	...	...	...	...	301	...	...	...	...	...
DS 2	...	115	...	...	110	100	251	784	...	...	...	...	268	...	...	...	...	...
K 1-27	...	...	45	14	115	100	106	297	...	...	...	...	334	...	...	...	...	...
NGC 5189	168	119	52	15	55	100	370	1218	6	15	14	130	346	390	46	59	48	20
We 2-37	...	...	...	...	32	100	200	511	...	...	...	836	595	2476	40	37	32	...

Table 5.3: Extinctions and intrinsic line ratios for 60 PNe, primarily from the MASH project.

NAME	c	$E(B-V)$	A_v	[OIII]/Hβ	[NII]/Hα	[SII]/Hα	6717/6731	N/O
BMP0642-0422	0.40	0.28	0.86	1.96	2.92	0.00	...	0.49
BMP0733-3108	...	...	...	...	5.95	0.48	2.20	...
BMP1808-1406	...	...	...	...	4.78	0.80	1.43	...
FP0709-2555	0.05	0.04	0.11	0.00	0.51	0.00	...	0.28
FP0711-2531	0.04	0.03	0.09	3.91	0.90	0.51	1.21	0.14
FP0721+0133	0.65	0.45	1.39	1.30	1.03	0.33	0.86	0.09
FP0739-2709	0.22	0.15	0.48	0.65	3.16	0.50	1.23	0.82
FP0840-5754	0.21	0.15	0.46	1.11	0.89	0.53	1.23	0.17
FP0904-4023	0.08	0.05	0.16	1.23	1.04	0.84	1.76	0.18
FP1554-5651	1.42	0.98	3.03	21.13	1.91	0.37	1.24	...
PFP 1	0.07	0.05	0.15	1.90	3.17	0.72	1.57	0.59
PHR0652-1240	0.32	0.22	0.67	3.68	0.92	0.71	1.32	...
PHR0719-1222	0.85	0.59	1.82	5.16	2.74	0.56	1.66	...
PHR0724-1757	...	...	...	...	8.31	...	...	...
PHR0740-2057	0.94	0.65	2.01	21.54	1.02	0.41	...	...
PHR0743-1951	0.82	0.57	1.75	1.27	1.59	1.35	1.09	...
PHR0747-2146	0.31	0.21	0.66	7.80	0.55	0.40	1.42	...
PHR0755-3346	0.38	0.26	0.80	2.18	0.79	0.62	1.09	...
PHR0800-1635	0.23	0.16	0.49	6.79	1.70	0.39	0.85	0.16
PHR0808-3745	0.20	0.14	0.43	2.80	0.79	0.36	0.97	...
PHR0834-2819	0.58	0.40	1.24	12.73	0.98	0.14	2.01	0.14
PHR0905-4753A	0.64	0.44	1.37	12.82	2.09	0.40	1.28	0.77
PHR0905-4753B	0.83	0.57	1.77	15.54	1.26	0.20	1.09	...
PHR0907-4532	...	...	...	...	0.43	0.37	1.52	...
PHR0907-5722	0.09	0.06	0.20	3.28	2.66	1.09	1.25	...
PHR0942-5220	0.42	0.29	0.90	8.26	0.55	0.39	1.42	...
PHR1032-6310	0.30	0.21	0.64	5.51	1.54	0.83	1.43	...
PHR1040-5417	0.01	0.01	0.02	7.21	1.29	0.20	1.53	...
PHR1052-5042	0.60	0.41	1.28	0.99	0.52	0.34	1.12	...
PHR1115-6059	2.41	1.66	5.14	...	0.43	0.21	1.17	...
PHR1255-6251	>1.5	>1.0	>3.2	>6.5	10.04	0.89	1.57	...
PHR1315-6555A	...	...	...	...	...	...	...	...
PHR1315-6555B	0.76	0.52	1.62	10.54	1.95	0.31	1.36	...
PHR1315-6555C	0.95	0.64	1.97	11.63	1.96	0.30	1.38	...
PHR1318-5601	...	...	...	...	2.97	...	...	...
PHR1327-6032	0.58	0.40	1.25	3.35	3.33	0.17	2.20	...
PHR1335-6349	0.51	0.35	1.08	2.46	3.37	1.02	1.05	...
PHR1337-6535A	...	...	...	...	3.25	1.23	1.52	...
PHR1337-6535B	0.11	0.07	0.22	4.14	3.79	0.64	1.18	...
PHR1400-5536	0.00	0.00	0.01	...	0.26	...	...	...
PHR1408-6106	0.64	0.44	1.36	2.13	1.91	0.51	1.37	0.36
PHR1418-5144	0.45	0.31	0.95	8.96	1.37	...	...	...
PHR1424-5138	0.75	0.51	1.60	1.98	0.00	0.00	...	...
PHR1429-6003	...	...	...	...	4.33	0.70	1.04	...
PHR1432-6138	0.38	0.26	0.81	4.80	2.64	0.62	1.00	...

Continued on next page

Table 5.3 – continued from previous page

NAME	c	$E(B-V)$	A_v	[OIII]/Hβ	[NII]/Hα	[SII]/Hα	6717/6731	N/O
PHR1510-6754A	0.00	0.00	0.00	4.16	4.95	0.93	1.07	...
PHR1510-6754B	0.00	0.00	0.00	4.33	4.80	1.25	1.09	...
PHR1533-4824	0.00	0.00	0.00	3.37	2.38	...	...	...
PHR1537-6159	1.16	0.80	2.48	17.07	1.46	...	...	...
PHR1539-5325	...	...	...	...	0.85	0.60	0.96	...
PHR1551-5621	0.74	0.51	1.58	2.49	7.11	0.33	1.86	...
PHR1602-4127	0.39	0.27	0.83	4.26	1.20	0.73	1.50	...
PHR1625-4523A	0.65	0.45	1.39	3.49	0.98	0.50	1.45	...
PHR1625-4523B	0.46	0.31	0.97	2.87	0.97	0.76	1.30	...
PHR1720-3927	...	...	...	...	1.69	0.61	1.14	...
PHR1724-3859	1.31	0.90	2.80	3.43	7.24	0.44	1.44	...
PHR1808-3201	0.97	0.67	2.08	2.57	4.77	0.81	1.05	...
PHR1906-0133	1.45	1.00	3.09	1.17	1.58	0.65	1.54	...
RCW 24A	0.20	0.14	0.43	4.94	7.64	0.84	2.35	...
RCW 24B	0.13	0.09	0.28	2.61	5.94	0.51	1.96	2.41
RCW 69A	0.76	...	...	6.18	7.49	0.56	1.27	...
RCW 69B	0.76	...	...	...	5.81	0.49	1.28	...
RCW 69C	0.64	0.44	1.37	5.57	8.28	0.97	1.34	2.42
RCW 69D	0.87	0.60	1.86	4.76	6.94	0.65	1.04	2.11
Abell 24	0.18	0.12	0.37	2.62	5.05	0.22	1.28	4.2
Abell 31	0.07	0.05	0.15	8.28	11.07	...	...	...
DS 2	0.00	0.00	0.00	10.35	0.00	0.00	...	...
K 1-27	0.21	0.15	0.45	3.97	0.00	0.00	...	...
NGC 5189	0.26	0.18	0.56	15.57	1.50	0.30	0.78	0.85
We 2-37	0.99	0.69	2.12	7.11	5.56	0.13	1.08	...

5.3 Plasma Diagnostics

Once relative intensities of the observed emission lines in a PN are obtained, relative elemental abundances can be derived in a straightforward way. The simplest assumption is that the emission nebula is an isothermal and homogeneous volume of gas having the same degree of ionization throughout. However, the relative intensities of the collisionally excited forbidden lines depend on the electron temperature and density, so these diagnostics need to be determined prior to an abundance analysis. However owing to the very low surface brightness of most MASH PNe, only a very limited number of spectra were of sufficient depth to record the fainter diagnostic lines. Very deep integral field spectra will be needed to obtain the required data in the future. Such an observing program has just been commenced with the SPIRAL Integral Field Unit on the 3.9-m AAT (Parker, Frew et al., 2008, in preparation).

5.3.1 Electron temperature

The intensity ratios of certain collisionally excited lines, such as between [O III] λ5007Å and 4363Å, are very strongly dependent on the electron temperature of the gas. From first principles (e.g. Osterbrock & Ferland 2006), the electron temperature of a gas can be determined from the

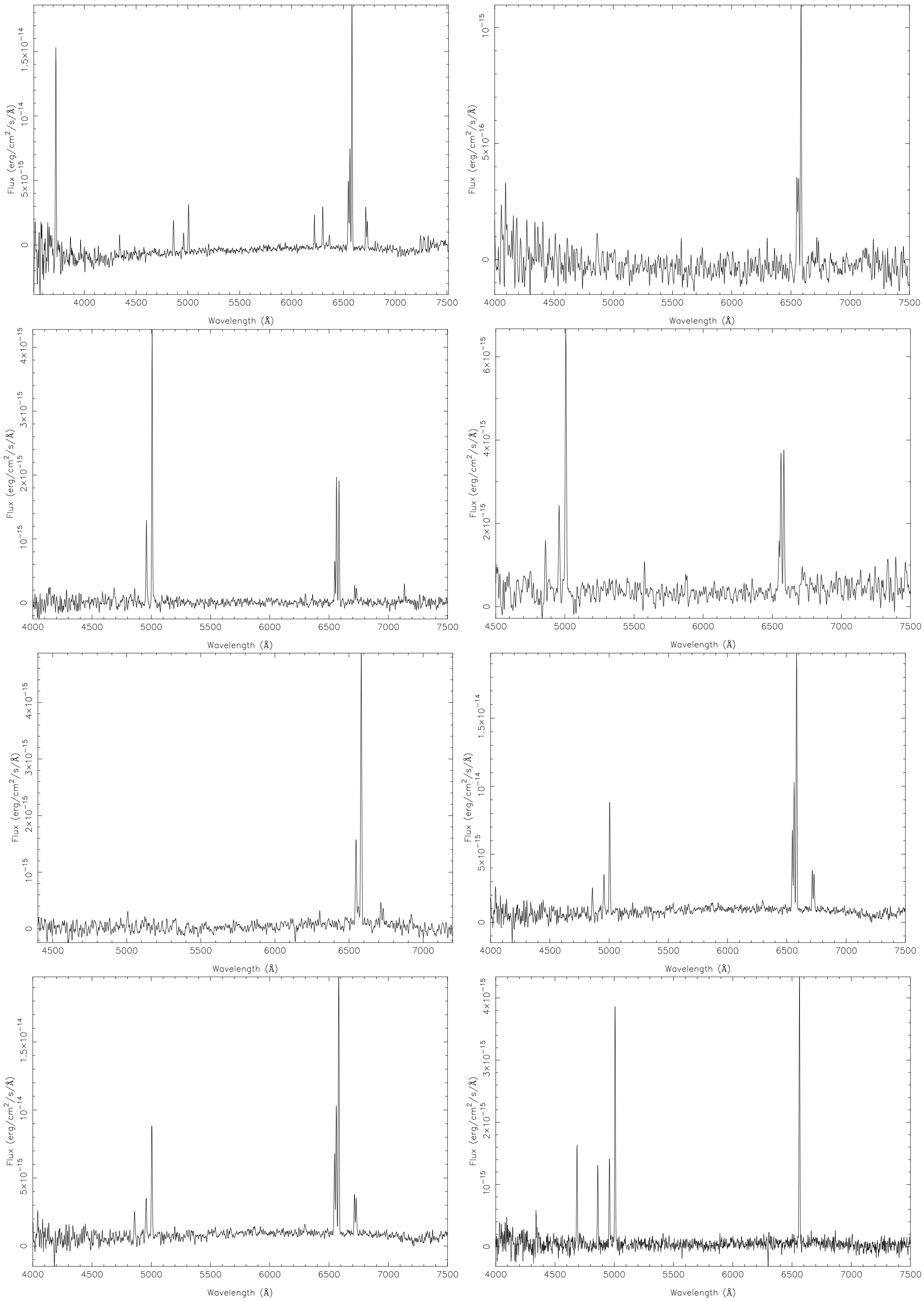

Figure 5.1: Representative flux-calibrated spectra for eight PNe, which were candidates for the local volume. Note the generally poor S/N ratios, which is a consequence of the very low surface brightness of these highly evolved PNe. Top row: PFP 1 (left), FP0739-2709 (right); second row: PHR0905-4753 (left), PHR1040-5417 (right); third row: PHR1255-6251 (left), PHR1432-6138(right); bottom row: PHR1602-4127 (left), K 1-27 (right). Wavelengths in Angströms (Å) are plotted on the x-axis and fluxes in erg $\mathrm{cm}^{-2}\,\mathrm{s}^{-1}\,\text{Å}^{-1}$ on the y-axis of each plot.

collision strengths and transition probabilities of the [O III] lines. Once the observed intensities of the [O III] lines are corrected for reddening, the following expression can be used to find the temperature:

$$\frac{I(\lambda 4959) + I(\lambda 5007)}{I(\lambda 4363)} = \frac{7.90\, e^{(32900/T)}}{1 + 4.5 \times 10^{-4}\, n_e/T^{0.5}} \tag{5.4}$$

From the coefficient in the denominator on the right-hand side of the equation, it is seen that there is only a very slight dependence on the electron density. An analogous expression can be derived for the [N II] lines:

$$\frac{I(\lambda 6548) + I(\lambda 6584)}{I(\lambda 5755)} = \frac{7.53\, e^{(25000/T)}}{1 + 2.7 \times 10^{-3}\, n_e/T^{0.5}} \tag{5.5}$$

5.3.2 Electron density

The line ratios of the [S II]$\lambda\lambda 6716, 6731$ and [O II]$\lambda\lambda 3726, 3729$ doublets are very sensitive to the electron density of the ionized gas, but only in the range ~100 to 10^5 cm^{-3} (see figure 5.8 from Osterbrock & Ferland 2006). The low- and medium-resolution blue spectra obtained for this study are not sufficient to resolve the [O II] doublet so the analysis is restricted to the red [S II] doublet. However, for most of the observed PNe, the [S II] doublet ratio is in the low density limit, so an alternative method is needed to calculate a density for the gas. If the distance to the PN is known, the ionized mass, M_i, can be determined (see §7.7). Once this is known, the root-mean-squared (RMS) electron density, n_e (in cm^{-3}) is simply derived using the following expression (McCullough et al. 2001):

$$n_e = \frac{1350\, M_i}{(4\pi/3)(\Theta D)^3\, \epsilon} \tag{5.6}$$

where Θ is in arcmin, D is in kpc, and ϵ is the volume filling factor. Further details are provided in Chapter 7. Alternatively, a RMS density can be determined from the Hα surface brightness at the respective slit position, either based on the flux from our own spectra, or measured directly from SHASSA images. The following expression has been derived (Pierce et al. 2004):

$$n_e^2 = 2.8 \times 10^{22} \frac{F(H\alpha)}{\epsilon \theta^3 D}, \tag{5.7}$$

Again the distance must be estimated for the PN in question (see Chapter 7).

5.4 Abundances

A detailed analysis of PN abundances was not attempted as part of this work, owing to the very faint surface brightness of most local PNe. Nonetheless, abundance data was derived for some of the brighter objects. For most of the known PNe in the local volume, available N/O ratios were also compiled from the literature, in order to derive a first estimate of the proportion of

Type I nebulae (Kingsburgh & Barlow 1994) in the local volume (see §9.3.6).

For six nebulae that had sufficient S/N to determine some fainter diagnostic lines, the line spectra were analysed using the plasma diagnostics program HOPPLA (Acker et al. 1989; Köppen, Acker & Stenholm 1991), and are presented in Table 5.4. The code computes temperature and density diagnostics by comparing the observed line ratios with those derived from accurate ionic models (see the previous section), and the code iteratively repeats until the results converge to better than 1 percent. In this code the [N II] temperature is used for the ions O^+, N^+, S^+, S^{2+} and the [O III] temperature is adopted for all other ions. If no accurate line ratio for the [O III] or [N II] electron temperature is available, a constant value of 10^4 K is assumed. Perinotto & Corradi (1998) found that T_e[N II] is usually higher than T_e[O III] for bipolar PNe, but see the contrasting discussion by McKenna et al. (1996). In the absence of temperature diagnostics, we formally set T_e[O III] = T_e[N II] and note that the derived abundances have a larger than average uncertainty.

Since for five of the six PNe, the [S II] doublet ratio is in the low density limit, a RMS density has been determined from the Hα surface brightness at the respective slit positions. However, it should be noted that at such low densities, none of the forbidden lines are sensitive to collisional de-excitation, so the derived elemental abundances are essentially independent of the assumed value of n_e.

Ultimately, the reddening corrected intensities of all observed emission lines, normalized to Hβ, are used to calculate the various ionic abundances of He, O, C, N, Ne and Ar relative to H. Since not all ions produce visible spectral lines, the analysis needs to take into account the unseen stages of ionization, using standard ionization correction factors (ICFs) taken from Köppen, Acker & Stenholm (1991). HOPPLA also assumes that the N^+ and O^+ ions share the same zone, and in PNe with He II lines, O^{3+} ions share the same zone as He^{2+} ions. It also assumes that Ne^{2+} and O^{2+} ions form in the same zone, and Ar^{2+} ions are present in the O^+ zone. For sulfur, a standard formula to a photoionization model is used, based on ionic abundances of oxygen (Acker et al. 1989; Köppen, Acker & Stenholm 1991).

Two newly discovered MASH objects have proven to be two of the largest and nearest Type I PNe known (Frew, Parker & Russeil 2006). The main results from that study are summarised here. For the available spectra of RCW 24, the [S II] doublet ratio is in the low density limit, so densities were estimated from the Hα surface brightness in each case. For RCW 24, the [OII] doublet intensity is only roughly determined, so the N/O value is only approximate. The data are insufficient to determine an accurate He/H ratio for RCW 24. The results are given in Table 5.4.

For RCW 69, the abundances generally have higher weight due to the better S/N of the available spectra. Helium appears to be enhanced above solar (He/H = 0.29) but the abundance has a significant error, since the HeI λ5876 flux is uncertain. The calculated log (N/O) ratio is +0.33 dex (N/O = 2.1), classifying it as a bona fide Type I PN according to Kingsburgh & Barlow (1994). The He abundance for RCW 69 is also enhanced above solar. Though the quality of the available spectra do not allow more than a first estimate of the elemental abundances, RCW 24 and RCW 69 are seen to be Type I PNe, with strongly enhanced nitrogen abundances.

Table 5.4: Elemental abundances by number for six PNe analysed using plasma diagnostics. The abundances are given in the usual notation of 12 + log(n(X)/n(H)). Abundances for Type I and non-Type I PNe are taken from Kingsburgh & Barlow (1994). Revised solar abundances are taken from Grevesse, Asplund & Sauval (2007).

PN / Element	He	N	O	Ne	S	Ar	log (N/O)
Abell 24	11.20	8.93	8.50	8.13	6.97	...	+0.43
NGC 5189	11.13	8.28	8.46	7.89	7.30	6.84	−0.18
PFP 1	11.11	8.44	8.67	8.86:	6.31	...	−0.23
PHR 1315-6555	11.15	8.32	8.67	8.31:	7.41	6.69	−0.35
RCW 24	>10.96	8.47	8.03:	8.31:	6.82:	...	+0.44:
RCW 69	11.46:	8.70	8.37	...	6.94	6.30:	+0.33
Type I	11.11	8.72	8.65	8.09	6.91	6.42	+0.07
non-Type I	11.05	8.14	8.69	8.10	6.91	6.38	−0.55
Solar	10.93	7.78	8.66	7.84	7.14	6.18	−0.88

Table 5.5: Abundances for NGC 5189 and Abell 24 taken from the literature, compared with the present work.

		He	N	O	Ne	S	Ar	log (N/O)
NGC 5189								
	This study	11.13	8.28	8.46	7.89	7.30	6.84	−0.18
	Girard, Köppen & Acker (2007)	10.72:	8.41	8.38	7.75	7.53	6.41	+0.03
	Stanghellini et al. (1995)	11.04	8.59	8.27	...	...	...	+0.31:
	Kingsburgh & Barlow (1994)	11.16	8.49	8.59	7.97	6.87	6.07	−0.10
	de Freitas Pacheco et al. (1991)	11.13	8.97	8.98	...	7.30	6.38	−0.01
Abell 24								
	This study	11.45	8.93	8.50	8.13	6.97	...	+0.43
	Bohigas (2003)	11.13	8.74	8.29	8.53	7.21	6.68	+0.46

Further details concerning these two interesting PNe are given in Frew, Parker & Russeil (2006).

The bright PN, NGC 5189 (see figure 1.13), was also observed to estimate the errors in the abundances derived here, as it has been studied by other investigators. The results derived here are in good agreement with the mean of the other studies (see Table 5.5), and an error of ±0.15 dex in the N/O abundance ratio is suggested. The other PN that has been independently studied is Abell 24 (Bohigas 2003). While the He abundance is somewhat discrepant, the N/O ratio derived here is in excellent agreement with the value from Bohigas (2003), showing this to be an extreme Type I PN. Abundances are also derived here for the distant PN, PHR 1315-6555, discussed in detail in §6.4.10 (also see figure 1.13). This object is classified as a Type I object according to the definition of Peimbert & Torres-Peimbert (1983; see below), but is slightly outside the cutoff of Kingsburgh & Barlow (1994). Finally, the abundances of PFP 1 have been discussed in detail in Pierce et al. (2004).

For the vast majority of the fainter PNe, an abundance analysis with HOPPLA is not possible. Since the N/O abundance ratio is an important diagnostic, approximate N/O ratios were determined using the precepts of Kaler (1983) for those PNe with [OII]λ3727 intensity data (see the ninth column of table 5.3). This approach is based on the well-known fact that the ionisation potentials for O^+ and N^+ are similar, so an estimate for the N/O ratio makes use of the relative strengths of the [OII] and [NII] lines in the optical part of the spectrum. At T_{eff}=10,000 K, equation (5) of Kaler (1983b) reduces to:

$$\frac{\mathrm{N}}{\mathrm{O}} = 0.52\,\frac{I(6584)}{I(3727)} \tag{5.8}$$

though it should be kept in mind that there may be a considerable range in electron temperatures in the most highly evolved PNe in the local volume. Approximate N/O ratios (uncertainty of ± 0.25 dex) calculated using equation 5.8 are given in the ninth column of table 5.3.

5.4.1 Type I PNe

The intrinsic proportion of Type I in a population can be related to evolutionary theory (Moe & De Marco 2006a). However, the working definition of a Type I PN has been rather fluid since the original investigations of Peimbert (1978) and Peimbert & Serrano (1980). Peimbert & Torres-Peimbert (1983) classified Type I PNe as having He/H ≥ 0.125 *and* log(N/O) ≥ -0.3 on the basis of improved data, while Kaler, Shaw & Kwitter (1990) adopted He/H > 0.15 *and* log(N/O) ≥ -0.1 for Type I PNe.

Kingsburgh & Barlow (1994) have formalised the definition, regarding a Type I PN as being produced by a progenitor star in which envelope-burning conversion of dredged-up primary carbon to nitrogen has occurred. The associated PN will therefore have a nitrogen abundance that exceeds the initial C+N abundance of the progenitor star. This abundance can be inferred from the average C+N abundance of an ensemble of local HII regions. For the nearby galactic neighbourhood, this corresponds to log(N/O) ≥ -0.1. Kingsburgh & Barlow (1994) find a large range in the He/H ratio for nitrogen-enhanced PNe and have consequently not used this criterion for differentiating Type I PNe. Their definition is used throughout this work.

In order to derive the intrinsic proportion of Type I PNe, a volume-limited sample of PNe is needed (see Chapter 9). Available N/O data were culled from the literature for all PNe with $D \leq 2.0$ kpc. For these, preference has been given to determinations based on multiwavelength (IR, UV and optical) data (e.g. Pottasch & Bernard-Salas 2006; Marigo et al. 2003) with other values taken, in approximate order of preference, from Perinotto, Morbidelli & Scatarzi (2004, and references therein), Liu et al. (2004), Henry, Kwitter & Balick (2004); Stanghellini et al. (2006), Krabbe & Copetti (2006), Pollacco & Bell (1997), Kingsburgh & Barlow (1994), Costa, Uchida & Maciel (2004), Howard, Henry & McCartney (1997) and Kaler (1983b).

The literature data has been supplemented with N/O values determined from this work, either taken from table 5.4 or determined approximately from reddening-corrected λ3727 and λ6584 fluxes using equation 5.8 (see table 5.3). Hence, each local PN with appropriate data could be classified as Type I or non-Type I. A fuller discussion on the statistics on the proportion of Type I PNe in the local volume are given in §9.3.6.

In addition, for all local PNe with spectroscopic data, observed line intensities for the [N II] and [S II] lines were tabulated (note the line fluxes are uncorrected for reddening, but these red lines are all close in wavelength so their ratios are not significantly affected). These data were then plotted on the $\log F(\mathrm{H}\alpha)/F[\mathrm{N\ II}]$ versus $\log F(\mathrm{H}\alpha)/F[\mathrm{S\ II}]$ empirical diagnostic diagram

(Sabbadin, Minello & Bianchini 1977; Riesgo-Tirado & López 2002; Riesgo & López 2006; Kniazev, Pustilnik & Zucker 2008), which is given here as figure 5.2. Red dots show Type I PNe following Kingsburgh & Barlow (1994), black dots show PNe of non Type I, while open circles plot PNe with unknown N/O ratios. The field boundaries are adapted from those plotted by Riesgo-Tirado & López (2002).

Figure 5.3 plots the same data, but with the boundaries separating PNe from SNRs and HII regions replotted, based on the best available data for the local sample. A new region of the empirical plot, the realm of Type I PNe, is suggested here, based on this data. This diagram suggests that PNe can be classified as Type I solely based on relative line intensities in the red. However, some of the abundances are only approximate and more data is needed before a definitive diagnostic diagram can be produced.

Note from this figure that some evolved non-Type I PNe can have surprisingly strong [N II] lines, at least over small regions sampled via long-slit methods, up to [N II]/H$\alpha \sim 5$ (e.g. Rosado & Kwitter 1982; Pierce et al. 2004). These high ratios are due primarily to a component of shock excitation in the interacting rims of these old objects. Interestingly, Jacoby & De Marco (2002) found that seven out of 25 newly discovered faint PNe in the SMC have[N II]/H$\alpha > 1$, and suggested they may have Type I chemistries. Remember that the lower mean metallicity of the SMC, [Fe/H]$\simeq -0.8$ (Jacoby & De Marco 2002) will influence the apparent [N II]/Hα ratio at the dividing line between Type I and non-Type I PNe (N/O$\geq$ 0.8; Kingsburgh & Barlow 1994), though this ratio is dependent on the mean excitation of the PN. Reid & Parker (2008, unpublished) also report that $\sim$1/3 of their newly discovered (mostly faint) LMC PNe have [N II]/H$\alpha > 1$.

However at the present time, with the available data, it is unclear if the enhanced [N II]/Hα ratios seen in *faint* Cloud PNe reflects a genuine abundance effect, or is instead a manifestation of a lower mean level of ionization typical of extended interacting PNe. Further work is needed. Similarly, more data are needed to better define the regions covered by HII regions and SNRs in figure 5.3. This is a work in progress (Frew et al. 2008, in preparation; Stupar & Parker 2008, in preparation).

5.5 Summary

This chapter described the ongoing program of spectroscopic follow-up for MASH, MASH-II and other evolved PNe. The observed fluxes for 60 mostly evolved PNe are presented, normalized to H$\beta = 100$. However, for a few faint and highly reddened PNe, observed fluxes are given relative to H$\alpha = 300$. Diagnostic line ratios and extinction coefficients are also determined for each PN.

Elemental abundances for six PNe were determined using plasma diagnostics, and approximate N/O ratios were determined for a number of other local PNe. In this work, discussion is largely restricted to relative N/O ratios, and the proportion of Type I nebulae in the local volume. Further details are given in §9.3.6. A new version of the $\log F(\mathrm{H}\alpha)/F[\mathrm{N\ II}]$ versus $\log F(\mathrm{H}\alpha)/F[\mathrm{S\ II}]$ diagnostic diagram is also given, based on new data for local PNe, especially for highly evolved objects. A new domain, the realm of Type I PNe, is suggested.

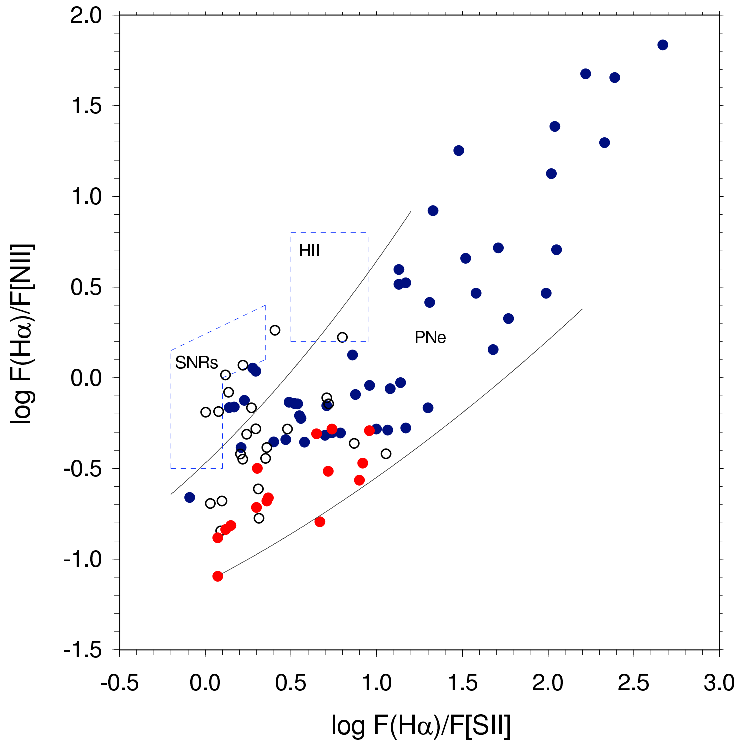

Figure 5.2: Log $F(\mathrm{H}\alpha)/F[\mathrm{N\ II}]$ versus log $F(\mathrm{H}\alpha)/F[\mathrm{S\ II}]$ diagnostic diagram adapted from Riesgo-Tirado & López (2002), for local PNe with [NII] and [SII] flux data. Red dots show Type I PNe following Kingsburgh & Barlow (1994), black dots plot PNe of non Type I, while open circles plot nebulae with unknown N/O ratios.

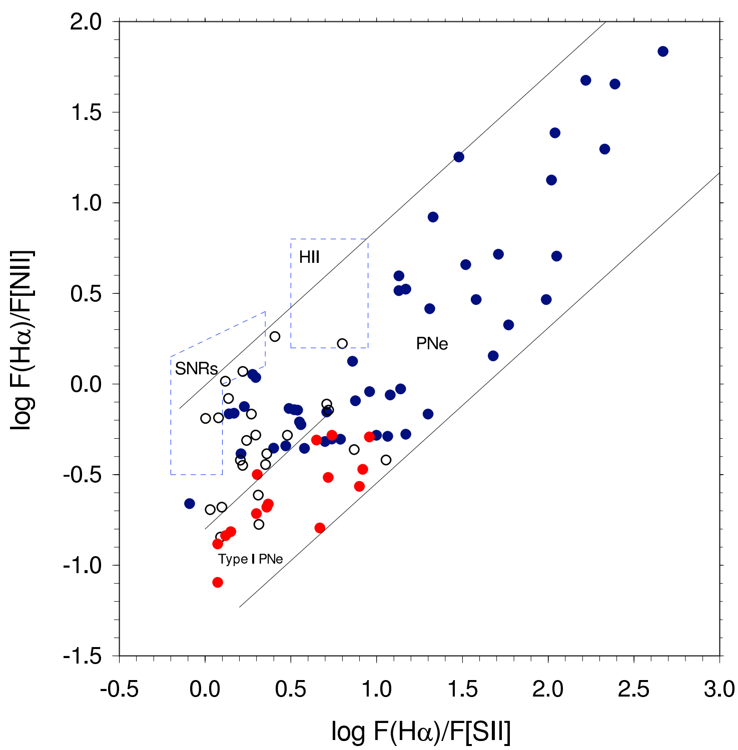

Figure 5.3: Log $F(\mathrm{H}\alpha)/F[\mathrm{N\ II}]$ versus log $F(\mathrm{H}\alpha)/F[\mathrm{S\ II}]$ diagnostic diagram with boundaries for the PN field modified here, based on new data for local PNe, especially for highly evolved objects. A new domain, the realm of Type I PNe, is suggested. Symbols are the same as figure 5.2.

Chapter 6

Towards a New Distance Scale for PNe

6.1 Introduction

One of the greatest difficulties facing the study of PNe in our own Galaxy has been the problem of determining accurate distances to them. This is due to the wide variation observed in both nebular and central star properties. Indeed, the most reliable distances are for those PNe belonging to external galaxies, such as the LMC and SMC, as well as those belonging to the central bulge population of our own Milky Way Galaxy. Cahn, Kaler & Stanghellini (1992) stated that the "...distances to galactic planetary nebulae remain a serious, if not *the* most serious, problem in the field, in spite of literally decades of study..."

So far accurate primary distances (with uncertainties <20%) are known only for a relatively small number of PNe, primarily from trigonometric parallaxes (e.g. Harris et al. 2007), though the situation is rapidly changing. Generally speaking, distance estimates are statistical in nature or rely on quantities whose measurements are uncertain and where there is a large observed dispersion (e.g. Daub 1982; Cahn, Kaler & Stanghellini 1992; Van de Steene & Zijlstra 1994, 1995; Buckley & Schneider 1995; Zhang 1995; Napiwotzki 2001; Bensby & Lundström 2001; Phillips 2004b). Uncertainties in the Galactic PN distance scale have been significant, up to factors of three or more (e.g. Zhang 1995; Terzian 1997; Ciardullo et al. 1999; Phillips 2002a, 2004c).

This uncertainty severely hampers attempts to derive meaningful physical quantities for PNe. Almost every quantity of interest, including radii, nebular luminosities, ionized masses, RMS densities, and the luminosities and masses of their central stars, depends on accurate knowledge of their distances (e.g. Ciardullo et al. 1999), as do all statistical determinations of the PN scale height, space density, and formation rate (see Chapter 11).

This chapter summarizes the various distance indicators currently in use in the literature, and gives a critique of each method and its caveats, limitations and errors. A set of high-quality distance estimates for more than 120 PNe is presented, based on an exhaustive and critical evaluation of the extant literature. New kinematic and extinction-distance determinations are also presented here, which are used as calibrating data for a new statistical distance indicator described in detail in the next chapter.

6.2 Distance Techniques

While techniques that are useful for estimating distances to PNe are many and varied, they are often problematic in their application, and usually have significant associated uncertainties, both internal and systematic. As a preamble to this chapter, the various distance techniques that have been used over the last few decades are described briefly below. They are divided into direct (primary) methods which generally have the highest accuracy, and statistical (secondary) methods, which in some cases, can have considerable uncertainties (factors of two or more).

6.2.1 Summary of Primary Distance Methods

A number of primary methods have been used with varying degrees of success (for earlier reviews, see for example, Acker 1978 and Sabbadin 1986), adopted for use here as detailed in § 6.4 onwards. These distance techniques include:

1. Direct trigonometric parallaxes of the CSPN, mainly from ground-based determinations (e.g. Harrington & Dahn 1980; Harris et al. 1997; Gutiérrez-Moreno et al. 1999; Harris et al. 2007), the Hipparcos satellite (Pottasch & Acker 1998; Acker et al. 1998), or from *HST* (e.g. Benedict et al. 2003; Benedict et al., in prep.) The recent ground-based CCD parallaxes of Harris et al. (2007) form a significant sample of accurate distances for several nearby evolved PNe. The method is susceptible to the so-called Lutz-Kelker bias (Lutz & Kelker 1973; Koen 1992; Smith 2003, 2006) which causes measured stellar parallaxes to be systematically greater than their actual values. This will be further discussed below.

2. Via a spectroscopic or photometric parallax of a companion star of 'normal' spectral type. The archetype is the well-studied high-excitation PN, NGC 246 (Minkowski 1965; Walsh, Walton & Pottasch 1993; Pottasch 1996; Bond & Ciardullo 1999) and the method has been applied to a number of more distant PNe with wide binary companions (e.g. Ciardullo et al. 1999).

3. Via the assumption of physical membership of a PN in a star cluster of known distance. This is essentially a subset of the previous method. Historically, the Type I nebula NGC 2818 has a distance determination based on the assumption of it being physically associated with the open cluster of the same name (Tifft, Connolly & Webb 1972; Dufour 1984; Pedreros 1989; Majaess, Turner & Lane 2007). However, recent radial velocity measurements (Mermilliod et al. 2001) have shown the objects are unrelated. Importantly, the Type I PN PHR 315-6555 is shown herein (§6.4.10) to be a physical member of the intermediate-age open cluster ESO 96-SC04 (Parker, Frew, Köppen & Dobbie 2008, in preparation). In addition, three or four globular clusters are currently thought to contain PNe (e.g. Jacoby et al. 1997). This method is critically discussed in more detail in §6.4.9,

below. Furthermore, an astrometric parallax has been applied to NGC 7293 by Eggen (1984), assuming Hyades moving group membership.

4. Spectroscopic 'gravity' distances for the CSPN (e.g. Méndez et al. 1988; Cazetta & Maciel 2000, 2001; Napiwotzki 2001), based on NLTE model atmospheres. This is, in principle, an elegant method, but is partly model dependent, and most distance scales have systematic errors, with the greatest uncertainty being the determination of $\log g$ (e.g. Pottasch 1996; Rauch et al. 2007). This method is discussed further in §6.4.6, below. Pauldrach, Hoffmann & Méndez (2004) have taken a somewhat different approach, also based on model atmospheres. The mass and radius of the CS are calculated from the mass loss rate, $\dot{M}$ and the terminal wind velocity v_∞, as estimated from a fit to the spectral lines. However, very high masses were determined for some CS, close to the Chandrasekhar limit, and the resulting very large distances have not been supported by other methods (see the discussion of Napiwotzki 2006).

5. Via an expansion parallax of the PN shell, in the optical (e.g. Liller, Welther & Liller 1966; Reed et al. 1999) or radio domains (Hajian, Terzian & Bignell 1995; Hajian & Terzian 1996; Terzian 1997). Initially thought to be an potentially accurate method (e.g. Liller, Welther & Liller 1966), it has been shown recently that there may be serious systematic errors in this technique. See the discussions by Mellema (2004) and Schönberner, Jacob & Steffen (2005), and in §6.4.5, below.

6. Extinction distances to either the PN shell (e.g. Lutz 1973; Acker 1978; Kaler & Lutz 1985; Gathier et al. 1986; Martin 1994; Saurer 1995), or the CSPN itself. An estimate of $E(B-V)$ is determined by observing the Balmer decrement, or another line pair of known intrinsic ratio, or by measuring the apparent $B-V$ colour of the CSPN, and assuming an intrinsic value for $B-V$. Extinction distances might be overestimated if dust internal to the PN is significant. However, this effect is only problematic for the youngest and most compact PNe, as the observed colours of the CS in most old PNe at high galactic latitude show no evidence for additional extinction from dust intrinsic to the PN (e.g. NGC 7293, Abell 7, Abell 31, etc.).

7. Kinematic distances (but only applicable to extreme Type I PNe in practice), assuming that the PN has little or no peculiar motion with respect to the local standard of rest, corrected for solar motion; i.e. the PN partakes of circular rotation around the Galaxy. However, some Type I (and Type I–II) nebulae have relatively high space motions (e.g. Sh 2-188, VV 47), so there are many caveats to this approach.

8. The 21cm hydrogen absorption method is essentially a hybrid kinematic/extinction method. Neutral hydrogen in the foreground of the PN causes an absorption line at 21 cm; if a distance for the absorbing cloud can be determined (usually via the kinematic method) this gives a lower limit to the distance of the PN (e.g. Gathier, Pottasch & Goss 1986; Maciel 1995, 1996), and in some cases constrains the distance quite well.

9. Na D absorption line distances. Similar in principle to point (8) above. See Napiwotzki (2001) for examples of its application.

10. Analysis of eclipsing binary CSPN (Bell, Pollacco & Hilditch 1994; Bell & Pollacco 1995) or CSPN showing a large reflection effect [e.g. Drilling (1985) for DS 1; Liebert et al. (1995) and Ferguson et al. (1999) for LTNF 1 around BE UMa]. These methods are partly model dependent however, but offer great promise if the systematics are well understood. Unfortunately, eclipsing binary central stars are very uncommon (see Chapter 9).

11. Modelling the PN/ISM interaction to determine the relative PN velocity in the plane of sky. This novel technique has been applied to the asymmetric PN Sh 2-188 by Wareing et al. (2005, 2006). Combining this data with a measured proper motion leads directly to a distance.

12. Photoionization modelling. This technique, as applied to individual PNe, holds promise (e.g. Monteiro et al. 2000, 2006; Monteiro et al. 2004; Schwarz & Monteiro 2006). Three dimensional photoionization codes used in conjunction with line mapping can self-consistently determine the nebular structure and ionization, central star characteristics, and the distance. The application of this technique to a number of PNe is given in §6.4.8, below.

13. Via the angular diameter of the HeII Strömgren zone at the centre of optically-thick PNe (Gurzadyan 1970). This is a crude proxy of the previous method, but saw little application owing to the wide variety of PN diameters, structural parameters, and excitation classes.

6.2.2 Summary of Statistical Distance Methods

A brief summary of the various statistical (secondary) distance methods follows:

1. The classical Shklovsky method was the first statistical method to be applied that had any claim to veracity. It assumes a constant ionized mass (typically 0.2 $M_\odot$) for the PN shell and was first applied by Minkowski & Aller (1954) and Shklovsky (1956a, b). Osterbrock (1960) applied this method to NGC 3587 and O'Dell (1962) used newly-determined Hβ fluxes to derive an early distance scale. In simple terms, and assuming a *constant ionized mass*, as the PN evolves, the radius increases, and the mean electron density falls. The quantities are related according to the equation:

$$\frac{4}{3}\pi r^3 n_e = \text{constant} \tag{6.1}$$

   If the mean electron density can be determined from measurements of [O II] or [S II] doublet intensities, or inferred from the mean Hα or Hβ surface brightness, the intrinsic radius can be calculated. Comparing this to the angular size of the PN leads directly to a distance. Variations on this technique, by assuming an ionized mass derived from a set of calibration objects at known distance (e.g. in the Magellanic Clouds), and using the observable electron density and Hβ flux to infer a distance, have been utilized by Kingsburgh & Barlow (1992) and Kingsburgh & English (1992).

It is now known that PNe have a considerable range of ionized masses, and the method can be inaccurate for the most evolved PNe (see Buckley, Schneider & van Blerkom 1993, for a brief critique). A derivation of the Shklovsky recipe uses an ionized mass that is a function of linear diameter, as estimated from the surface brightness (see Cahn & Kaler 1971; Daub 1982; Cahn, Kaler & Stanghellini 1992; and see Chapter 7). Milne (1982) assumed a constant Lyman continuum flux for all PNe on theoretical grounds to derive a mass-radius relationship of the form $M \propto R^{5/3}$ (see the discussion of Kwok 1985, and Chapter 7). Recently, the distance scale of Cahn, Kaler & Stanghellini (1992) has been recalibrated using Magellanic Cloud PNe by Stanghellini, Shaw & Villaver (2008).

2. A natural variant of the mass-radius relationship is the surface brightness-radius (SB-r) relationship. The primary observables are firstly the 5 GHz radio flux density (or an optical Hα or Hβ flux), and secondly the angular radius, from which a surface brightness can be calculated. The distance to each PN calibrator is estimated from a primary technique (or better still, a carefully weighted average from several such techniques). The data from an ensemble of PNe are used to define a SB-r and/or a mass-radius relationship (see Chapter 7). Various versions in the radio domain have been proposed by Amnuel et al. (1984), Van de Steene & Zijlstra (1994, 1995), Buckley & Schneider (1995), Zhang (1995), Bensby & Lundström (2001), and Phillips (2002a, 2005c), amongst others.

   Until the present study, optical relations have largely been neglected. The new Hα SB-r relation derived here is discussed in detail in the Chapter 7.

3. Statistical parallaxes based on observed proper motions and assumptions regarding the space motions of PN central stars (e.g. Berman 1937; Parenago 1946; O'Dell 1962; Cudworth 1974).

4. The timescale correlation method for PNe with haloes (Hajian et al. 1997). This method makes a comparison between multiple fine-scale shells and the thermal pulses of the PN nucleus. It is uncertain if this method has the potential to be an accurate distance estimator. By comparison with the PN distances presented herein, their scale seems too short.

5. Distance estimates based on IRAS fluxes (Tajitsu & Tamura 1998). The method assumes uniform dust mass and scales distances according to the observed IRAS four-band fluxes. A brief comparison shows that the accuracy may be less than the radio SB-r relations listed above.

6. The IRAS infrared excess (IRE) is the ratio of the observed total IR emission to the energy available in Lyman α photons (Pottasch et al. 1984), and hence is a distance independent quantity. In the bulge, Jacoby (1993) found that this parameter correlates with 6 cm radio flux, so this relationship can function as a distance indicator.

7. Distance extimates va the angular size of Type I bipolar PNe, assuming these have a similar intrinsic diameter (Phillips 2004b). This 'standard ruler' has been critiqued by Frew, Parker & Russeil (2006).

8. A quite novel method has been utilized by Meatheringham, Wood & Faulkner (1988) to determine distance to Galactic PNe. Dopita et al. (1988) found that Magellanic Cloud PNe fall on fairly tight plane in dynamical age/density/excitation class space. Meatheringham, Wood & Faulkner (1988) inferred a dynamical age from the observed electron density and exciation class. Since the dynamical age is assumed known, once the expansion velocity is measured, the intrinsic radius can be inferred. Comparing this number with the angular size leads directly to a distance.

9. 'Sosie' PNe. Following the sosie[1] concept as applied to galaxies by Paturel (1981) and de Vaucouleurs (1982), PNe with similar morphologies, surface brightnesses, relative central star (Δm) magnitudes (see Pierce et al. 2004), and/or abundances, can have distances estimated from either integrated fluxes, CS magnitudes, or diameters if one of the pair has a known distance. A related approach is to assume a constant absolute magnitude (i.e. a standard candle) for a homogenous sub-sample of PN central stars or nebulae themselves. Phillips (2005) took this approach for a set of evolved CSPN but there appears to be a significant spread in the absolute magnitudes of the central stars of old PNe (see also Harris et al. 2007, and Chapter 9).

10. Another distance technique which does not seem to have been applied is based on the subset of young PNe which have central stars still evolving left along the nuclear burning track in the theoretical HR diagram. If a canonical central star mass of $0.6\,M_\odot$ (or another value) is assumed (cf. Vennes et al. 1997; Madej, Należyty & Althaus 2004; Gesicki & Zijlstra 2007) and a temperature of the CS can be determined (from NLTE modelling or a Zanstra analysis), then an absolute visual magnitude can be predicted using an appropriate bolometric correction (e.g. Schönberner 1981; Vacca, Garmany & Shull 1996). If accurate reddening-corrected photometry for the CSPN is available (e.g. Ciardullo et al. 1999), a distance directly follows. The resultant distance scale depends on the adopted mean CS mass. Mal'kov (1997) seems to be the first to mention such a technique, but did not apply it in his paper.

6.3 Previous Distance Scales

Most published PN distance scales can be roughly divided into two camps, long and short, with ongoing debate between the two groups (e.g. Ciardullo et al. 1999; Phillips 2001a, 2002a, 2003e, 2004c), quite analogous to the well-known (former) controversy over the low and high values of the Hubble Constant (e.g. Rowan-Robinson 1985). Clearly, the recent literature provides no consensus on the distance scale for evolved PNe, with a factor of 2–3 discrepancy evident between the short and long scales (see §7.5).

[1] from the French, meaning look-alike.

One of the earliest attempts at a consistent distance scale was by O'Dell (1962), based on emission theory and the assumption of constant ionized mass, following Shklovsky (1956a; see also Shklovsky 1956b). It can readily be shown that the distance,

$$D \propto M^{2/5} F(H\beta)^{-1/5} \theta^{-3/5} \tag{6.2}$$

where M is the ionized mass, F(Hβ) is the reddening corrected Hβ flux and θ is the angular radius (O'Dell 1962; Milne & Aller 1975; Bensby & Lundström 2001). O'Dell (1962) gave an alternate expression, viz,

$$D = \frac{149}{K} \theta^{-3/5} F(H\beta)^{-1/5} \tag{6.3}$$

where K is a constant derived from the distances of calibrating PNe. O'Dell (1962) estimated K primarily from an expansion parallax for M 57, and spectroscopic distances for NGC 246 and NGC 1514. Like all constant-mass scales, distances to the youngest compact PNe and the largest evolved PNe were in general overestimated and underestimated respectively (see also Seaton 1968).

Various authors since then have used a sample of calibrating PNe (with distances determined using a primary technique) to derive a statistical distance scale (Van de Steene & Zijlstra 1994, 1995; Buckley & Schneider 1995; Zhang 1995; Bensby & Lundström 2001, and Phillips 2002a, 2004c, 2005c). Note however that Zhang (1995) used distances for 130 PNe as calibrators for his study, that were derived statistically from another method.

A common approach in the literature is a variable-mass derivation of the Shklovsky method or a version of the SB-r relationship. Pottasch (1980) was the first to find a correlation between ionized mass and radius for PNe, and around the same time, Maciel & Pottasch (1980) found empirically that $M_i = 1.225\,R - 0.0123$, where M_i is in solar masses and R in parsecs (i.e. a direct proportionality, or a power law with an index of 1).

In general terms the mass–radius relation can be expressed as $M_i \propto R^\beta$ where β is a power law index determined through observation. For more details the reader is referred to Kwok (1985, 1993) and Samland et al. (1993). While Maciel & Pottasch (1980) found $\beta = 1$, other authors have derived significantly different values for β: Milne (1982) and Pottasch (1984) found $\beta = 3/2$ from theoretical arguments, as did Kwok (1985) who suggested $\beta = 9/4$. Daub (1982) determined $\beta = 5/3$ and Zhang (1995) derived $\beta = 1.31$. Clearly, until now there has been no consensus on the correct value of β. These relations will be further discussed in §7.7.

Another approach was taken by Daub (1982), who related the ionized mass to a thickness parameter, based on the observed 5 GHz radio flux. The thickness parameter τ is defined as:

$$\tau = \log\left(\frac{\theta^2}{S_{5\mathrm{GHz}}}\right) \tag{6.4}$$

A value of $\tau = 3.65$ ($r = 0.12$ pc) was found to separate optically thick PNe from optically thin PNe which have a constant mass at larger radii. This approach was critiqued by Van de

Steene & Zijlstra (1995), who defined a brightness temperature, T_{b} as:

$$T_{\mathrm{b}} = 73200\frac{S_{5\mathrm{GHz}}}{\theta^2} \tag{6.5}$$

Van de Steene & Zijlstra (1995) derived a single expression for the distance, based on their new brightness temperature – radius relation, derived largely from a sample of Galactic bulge PNe.[2] Their relationship is:

$$\log D = 3.40 - 0.30\log\theta - 0.35\log S_{5\mathrm{GHz}} \tag{6.6}$$

which is nearly identical to the equivalent expression derived by Zhang (1995):

$$\log D = 3.39 - 0.27\log\theta - 0.36\log S_{5\mathrm{GHz}} \tag{6.7}$$

Bensby & Lundstrom (2001) have derived a relationship consistent with the distance scales of Van de Steene & Zijlstra (1995) and Zhang (1995), but slightly shorter:

$$\log D = 3.31 - 0.22\log\theta - 0.39\log S_{5\mathrm{GHz}} \tag{6.8}$$

Schneider & Buckley (1996) took a somewhat different approach, since they considered a single power-law inadequate to handle both young and old PNe. Their second-order fit can be described by the equation:

$$\log D = 3.37 - \log\theta - 0.026\,(\log I)^2 - 0.46\log I \tag{6.9}$$

However, in the next chapter, I show that a single power law does indeed fit the entire range of surface brightness seen in PNe, from young compact PNe down to the very faintest objects dissolving into the ISM. Some further general comments are worth emphasing here. When compiling a sample of PNe to calibrate the statistical scale, it is crucially important that the adopted distances are the best available, and that the sample be as free from systematic errors and bias as possible. Earlier authors have diluted the precision of their calibrating sample by including PNe with poorly known distances, or by not weighting the individual distance estimates to the PN calibrators with appropriate 1σ errors (cf. Bensby & Lundström 2001; Phillips 2002a, 2004c). Several of these works have also included HII regions, symbiotic outflows and other misclassified objects as 'PN calibrators', which adds significant noise (and probable biases) to the derived relationship (see Chapter 9). A comparison of these previous radio-based distance scales with the distance scale based on the new Hα SB-r relation is made in Chapter 7.

[2]This approach is open to bias if the bulge sample is not symmetrical around the Galactic centre.

6.4 Calibrating a new distance scale

6.4.1 Introduction

In Chapter 3, accurate fluxes in the main emission lines have been carefully determined for almost all local (and many more distant) PNe, a significant number for the first time. In this section, reliable distances have been estimated to over 120 PNe, including some very highly evolved objects, using a weighted mean technique *based on a variety of primary distance techniques.* This new data set has allowed a surface brightness – radius (SB-r) relationship in Hα to be defined over 6 dex in surface brightness. The Hα relation is analogous to the radio surface brightness – distance relationship that has been the basis of previous statistical distance scales (see Zhang 1995; Van de Steene & Zijlstra 1995; Phillips 2002a, 2004c), but with the added benefit of including the most extreme PNe at the very bottom of the PN luminosity function, which have been selected against in the radio regime (Zhang & Kwok 1993). The new Hα SB-r relation covers the full range of surface brightness parameter space.

Unfortunately, primary distances are of widely varying quality. The primary methods considered as potential sources of calibrating PNe for the Hα SB-r relation derived here (see Chapter 7) are trigonometric distances, extinction distances, expansion parallax distances, spectroscopic/photometric distances, gravity distances, kinematic distances, and cluster/association distance estimates. As a result, data on over 120 calibrating PNe have been carefully examined (in many cases revised with better systematics), including 10 new extinction distance determinations derived here (§6.4.4); 25 PNe have distances based on more than one primary method. For these PNe, a weighted average distance has been calculated based on the quoted errors of each individual distance determination. The following formula was used to determine the error on the weighted mean,

$$\sigma = \sqrt{\frac{\Sigma_{i=1}^{n} w_i (x_i - \bar{x}_w)^2}{\Sigma_{i=1}^{n} w_i}} \tag{6.10}$$

where $[x_1, x_2 \ldots x_n]$ are the distance estimates, with associated weights $[w_1, w_2 \ldots w_n]$ determined from the inverse variances, $w_i = 1/\sigma_i^2$, and $\bar{x}_w$ is the weighted mean distance. The final list of calibrating distances is given in §7.2. It should also be empasised that *no statistical distances* from other studies have been used as calibrators for the SB-r relation derived here (cf. Zhang 1995; Bensby & Lundström 2001).

A description of the primary distance methods used to define the calibrating sample are discussed in more detail in the following subsections. Individual PN distances are tabulated, and a critical assessment of their associated errors also follows.

6.4.2 Trigonometric distances

Accurate trigonometric distances have been presented by Harris (2006) and Harris et al. (2007) for 11 nearby PNe (expanding on the work of Harris et al. 1997) and these have been utilised in this work. Some debate is ongoing in the literature considering the application of the Lutz-

Table 6.1: Trigonometric distances for 16 bona fide planetary nebulae from the literature

Name	D (pc)	Reference
Abell 7	676^{+267}_{-150}	1
Abell 21	541^{+205}_{-117}	1
Abell 21	526^{+1141}_{-203}	5
Abell 24	521^{+112}_{-79}	1
Abell 29	459^{+677}_{-172}	2
Abell 29	303^{+173}_{-81}	5
Abell 31	568^{+131}_{-90}	1
Abell 36	234^{+407}_{-91}	4
Abell 74	752^{+676}_{-242}	1
NGC 1360	274^{+520}_{-108}	4
NGC 1514	265^{+196}_{-79}	4
NGC 6720	704^{+445}_{-196}	1
NGC 6853	379^{+54}_{-42}	1, 3
NGC 7293	219^{+27}_{-21}	1
PuWe 1	365^{+47}_{-37}	1
Sh 2-216	129^{+6}_{-5}	1
Ton 320	532^{+113}_{-80}	1

Reference: 1. Harris et al. (2007); 2. Harris et al. (1997); 3. Benedict et al. (2003); 4. van Leeuwen (2007); 5. Gutiérrez-Moreno et al. (1999).

Kelker (LK) bias to trigonometric parallax determinations. Owing to the uncertainty in the actual correction factor for PNe, the trigonometric distances used here (mainly the high-quality values from Harris et al. 2007) have not had a LK correction applied to them. As emphasised by van Leeuwen (2007), the LK bias is a statistical correction and has not been applied to individual PN distances.

Table 6.1 summarises the trigonometric determinations taken from the literature. The Hipparcos parallaxes (Acker et al. 1998; van Leeuwen 2007) are in the majority rejected, especially for the compact PNe where variations in the photocentre between epochs may have had an undue influence on the astrometric reductions. Additional lower limits on the distance can be determined from the data of Acker et al. (1998), van Leeuwen (2007) and Gutiérrez-Moreno et al. (1999); limits for NGC 246, LoTr 5 and He 2-11 are >195 pc, >431 pc and >335 pc respectively. For NGC 2392, no formal distance was determined by Acker et al. (1998). However a formal value of 178^{+359}_{-71} pc is given by van Leeuwen (2007), which is much too short. Similarly, formal parallaxes are given for the compact PNe SaSt 2-12, SwSt 1 and He 1-5 which place these objects at distances that are too close. These values has been disregarded.

6.4.3 Photometric distances

Distances for 16 PNe with results from this technique have been primarily adopted from Ciardullo et al. (1999). However, for two of these PNe, more accurate reddenings have been adopted for the companion stars (based in part on *HST* photometry of the primaries) and new revised distances have been calculated, as noted in Table 6.2, which summarises the determinations.

Of the probable associations listed in Ciardullo et al. (1999), the distance of K 1-27 has been rejected. The photometric distance for K 1-27 (based on the companion being a white dwarf

Table 6.2: Photometric (and spectroscopic) distances for 16 PNe from the literature.

Name	D (pc)	Reference
Abell 30	2020^{+390}_{-320}	1
Abell 31	<440	1
Abell 33	1160^{+180}_{-150}	1
He 2-36	780	3
K 1-14	3000^{+490}_{-420}	1
K 1-22	1330^{+220}_{-190}	1
K 1-27	470^{+130}_{-100}	1
LoTr 5	420 ± 200	3, 6, 7
LoTr 5	710^{+500}_{-360}	5
Mz 2	2160^{+530}_{-430}	1
NGC 246	495^{+145}_{-100}	2
NGC 1514	370 ± 100	3
NGC 1535	2310^{+430}_{-360}	1
NGC 2346	670 ± 210	3
NGC 3132	770^{+300}_{-210}	1
NGC 7008	690^{+180}_{-140}	1, 4
Sp 3	2380^{+660}_{-520}	1

Reference: 1. Ciardullo et al. (1999); 2. Bond & Ciardullo (1999); 3. Pottasch (1996); 4. this work (corrected value); 5. Wilson-Bappu relation (Strassmeier, Hubl & Rice 1997); 6. Longmore & Tritton (1980); 7. Feibelman & Kaler (1983)

which was fit to the cooling sequence) is less than a third of the gravity distance (see table 6.6) which in turn gives an ionized mass much smaller than the mean PN mass. Owing to the unusual nature of the central star, a member of the O(He) class, it may not be a conventional PN. The distance from Ciardullo et al. (1999) however, implies a space density that is at odds with the rarity of the O(He) class — only four examples are known (e.g. Rauch, Dreizler & Wolff 1998). If the companion to K 1-27 is in turn an unresolved red dwarf / WD pair, the true colour of the WD would be bluer and hence the luminosity larger. The greater distance might then be consistent with the gravity determination. Owing to these caveats, K 1-27 has not been used as a calibrator for the SB-r relation. The other companion-star associations have been re-evaluated using a better estimate for the reddening, derived from all available CS photometry (see §9.4.2).

Of the *possible* associations given by Ciardullo et al. (1999), only Abell 30 has been used. IC 4637 has been rejected after considering the separation of the putative companion as a function of the field star density, while the visual companion of the close-binary nucleus of Abell 63 gives a distance which seems too low (the third star might simply be an optical companion); the other possible associations are upper limits and are not considered further. It is important to note that none of the *doubtful* associations listed in Ciardullo et al. (1999) have been considered. Also, some distances from Pottasch (1996) have not been used: for He 2-36, the luminosity class of the A-type primary is uncertain, while WhMe 1 is a symbiotic star (see §8.17).

6.4.4 Extinction Distances

In general, extinction distances have been taken from the literature only if the PN is within 5° of the Galactic plane. At greater latitudes, the extinction distances can be greatly underestimated as the PN is effectively outside the main dust layer of the disk. This point has been recently emphasised by Phillips (2006). Furthermore, *only individual extinction distances have been considered*. In general, determinations based on *average* extinction-distance diagrams (e.g. Acker 1978; Pottasch 1984) have not been utilised. Similarly, the Na D absorption distances of Napiwotzki (2001) have been excluded as potential calibrating data.

The distance errors as given in the various literature individual determinations are rather inconsistent, with some being little more than rough estimates. If the error on an individual extinction distance is less than 25%, it has been reset to that value. While individual extinction distances have rather large errors, the method as a whole is not expected to be biased to a short or long distance scale, provided that a substantial number of nebulae are used as calibrators *and* that no high-latitude ($|b| > 5°$) PNe are included (see the discussion by Phillips 2006). Table 6.3 gives a summary of the adopted literature extinction distances, taken from the references listed following the table. These extinction distances might be overestimated if dust internal to the PN is significant (e.g. Ciardullo & Jacoby 1999). However most PNe to which this technique has been applied seem to show little or no extinction due to intrinsic dust. This is verified from the observed blue colours of the central stars in PNe at high galactic latitudes (e.g. NGC 246, NGC 1360 and NGC 7293).

New extinction distances

As an adjunct to the body of literature data, new extinction distances have been determined herein for a number of PNe in the Galactic plane, analogous to studies completed by, for example, Lutz (1973), Acker (1978), Kaler & Lutz (1985), Gathier, Pottasch & Pel (1986), and Saurer (1995). These PNe showed moderate, but well determined reddening, and were situated close to the Galactic plane well within the dust layer, and therefore showed promise as potential calibrating nebulae. A number of newly discovered MASH PNe also showed promise; reddenings for these objects were derived from slit spectra taken as part of this thesis (see Chapter 5 for more details).

Other PNe (e.g. NGC 2440) showed wildly disparate estimates for the published distance, and warranted reinvestigation. Hence, about 25 PNe were selected for detailed follow-up, and a search using the SIMBAD database was undertaken around each target PN, taking advantage of the recent increase in the availability of online photometric and spectroscopic data for stars in the Galactic plane.

In several cases (e.g. NGC 3699, Abell 79, YM 16, PHR 0652-1240, PHR 0808-3745, PHR 1032-6310), no suitable extinction-distance relation (EDR) could be generated for the PN field from the available data. For other cases (e.g. Abell 45, Abell 71, NGC 5315, RCW 24) only a lower limit could be determined for the PN distance. Despite this, new extinction distances are given in this section for 10 PNe, both previously known and from MASH. Detailed

Table 6.3: Published extinction distances for planetary nebulae. High-latitude PNe have been excluded from this table. Weighted averages are quoted for PNe with more than one independent distance determination.

Name	D (pc)	Reference
NGC 2346	980 ± 150	1, 2
NGC 2440	2200 ± 800	1, 3, 4, 5, 6
NGC 2452	3710 ± 360	1, 3, 4
NGC 2792	2020 ± 560	1, 4
NGC 2867	>2000	1
NGC 3211	1910 ± 500	1
NGC 3918	2240 ± 840	1
NGC 5189	1550 ± 160	1
NGC 5315	2620 ± 1030	1
NGC 6565	2000 ± 500	6
NGC 6567	1680 ± 170	1
NGC 6741	1860 ± 330	7, 8
NGC 6842	2300 ± 500	9
NGC 6853	310 ± 100	2
NGC 6881	>3200	3
NGC 6894	1310 ± 280	4, 7, 10
NGC 7026	2000 ± 280	4, 10, 11
NGC 7048	1970 ± 640	3, 9
NGC 7139	$2400\ ^{+600}_{-800}$	12
NGC 7354	2460 ± 1440	7
IC 289	2700 ± 1200	8, 10
IC 1747	2790 ± 270	3, 4, 7, 10
IC 2621	>5500	13
CVMP	2000 ± 500	14
HDW 3	800 ± 400	15
Hb 5	2000 ± 700	3
K 3-82	>2500	16
K 4-55	>1400	17, 19
M 1-26	1800 ± 500	3
M 1-77	2500 ± 1000	9
M 1-79	2700 ± 900	18
Sh 1-89	2000 ± 500	9
Sh 2-188	800 ± 300	15
We 1-6	1100 ± 300	15

Reference: 1. Gathier, Pottasch & Pel (1986); 2. Pottasch (1996); 3. Acker (1978); 4. Pottasch (1984); 5. Pollacco & Ramsay (1992); 6. Turatto et al. (2002); 7. Kaler & Lutz (1985); 8. Sabbadin et al. (2005); 9. Huemer & Weinberger (1988); 10. Lutz (1973); 11. Solf & Weinberger (1984); 12. Weinberger & Zeiner (1988); 13. Martin (1994); 14. Corradi et al. (1997); 15. Saurer (1995); 16. Saurer (1997); 17. Guerrero, Manchado & Serra-Ricart (1996); 18. Saurer (1998); 19. this work (see text).

Table 6.4: New extinction distances for planetary nebulae derived from this work.

Name	$E(B-V)$	D (pc)
NGC 2440	0.20	1770 ± 450
NGC 4071	0.37	>1000
NGC 5189	0.36	1500 ± 300
NGC 5315	0.41	>1900
Abell 45	0.78	>1000
Abell 71	0.72	>700
He 2-111	0.86	2200 ± 500
IPHAS-PN1	1.32	5900 ± 2200
Menzel 2	0.41	2000 ± 500
PHR0719-1222	0.59	2750 ± 700
PHR1255-6251	>1.0	>2000
PHR1327-6032	0.40	2150 ± 550
PHR1408-6106	0.46	1700 ± 300
RCW 24	0.30	>500
RCW 69	0.52	1200 ± 600
SaWe 3	0.75	2080 ± 250
Sh 1-89	0.72	2300 ± 300

accounts of three PNe are provided here to illustrate the methodology used to construct each EDR. A rather detailed method of Saurer (1995) was initially proposed for the error determination, but after consideration, the uncertainty derived from the best-fitting line was used instead. Table 6.4 summarises the results. Notes on individual PNe now follow.

RCW 24. This PN lies in a relatively transparent region of the Galactic plane (at least for the first 1–2 kpc), making the derivation of a useful extinction-distance relation somewhat problematic (see below). For RCW 24 we adopt $E(B-V) = 0.30 \pm 0.10$, derived from the average of the nebular values, combined with the reddening estimate from the CS photometry (Frew, Parker & Russeil 2006). This value can be compared to the approximate asymptotic extinction through the plane in this direction of $E(B-V) = 2.51$ ($A_v = 7.8$ mag) as determined from the extinction map of Schlegel et al. (1998). The most distant molecular cloud (G258.50 − 1.50) in this direction is at an inferred distance of 9.4 kpc (May, Alvarez & Bronfman 1997), showing the line of sight is extensive through the disk here. If we assume the edge of the disk is at D $\simeq$ 12 kpc, this gives an average absorption of 0.75 mag kpc^{-1}.

Fitzgerald's (1968) region at $l = 260.5°$ includes the position of the PN, and shows little reddening out to 800 pc where a sudden increase to $E(B-V) = 0.6$ is seen, confirmed by the equivalent data of Neckel & Klare (1980), which shows A_v = 1.8 mag at 1.0 kpc. Lucke (1978) found near l=260°, an increase in colour excess between 0.5 and 1.0 kpc. This increase in reddening at 1.0 kpc is probably due to dust associated with the Vela Molecular Ridge (Murphy & May 1991; see also Pettersson & Reipurth 1994).

In an attempt to refine the reddening distance for RCW 24, a literature search for all stars using the SIMBAD database was undertaken in a circular area of radius 45′ centred on the PN. Spectroscopic parallaxes were determined by adopting the intrinsic colours and absolute magnitudes for each spectral class from Schmidt-Kaler (1982). Figure 6.1 shows the extinction-distance diagram for the RCW 24 field, based on stars with the best quality photometry and spectroscopy. There is too much scatter in this direction to define an unambiguous trend, and hence an accurate distance to the PN. However, a possible lower limit to the distance of ∼500 pc is indicated, based on the available data.

RCW 69. For RCW 69 the observed reddening is $E(B-V)$ of 0.52 ± 0.08, due primarily to the foreground Coalsack nebula at a distance of 150 – 200 pc. Rodgers (1960) determined a distance to the Coalsack of ∼ 174 pc, and noted a relatively clear region immediately behind which extended to ∼1000 pc, beyond which an increase in absorption with distance was noted. Muzzio, Marraco & Feinstein (1974) analysed a region close to RCW 69, and found a general increase in visual absorption from $A_V = 1.0$ at 1300 pc to $A_V = 3.5$ at 2500 pc. This region has also been observed by Seidensticker (1989) and Seidensticker & Schmidt-Kaler (1989). They found that beyond 200 pc in this direction, A_V very slowly increases from 1.0 – 1.5 magnitudes, until $(m-M)_0 = 11.0$ ($D = 1600$ pc), where a steep increase in absorption sets in.

To refine the reddening distance for RCW 69, a search was similarly undertaken in a field of radius 45′ centred on the PN. Data were taken from Seidensticker (1989) where available, supplemented with additional spectroscopic distances as described above. An examination of UKST B and R plates shows this area to lack obvious clouds of heavy absorption, though there is modest differential extinction on small scales as indicated by dust lanes evident across the PN. The closest star to RCW 69 with accurate photometry and spectral typing is HD 110625, 2.5′ north-west of the nebula centre. This star was initially thought to be a possible ionizing source for RCW 69, but was shown by Vogt & Moffat (1975) to be unrelated. Seidensticker (1989) gives a distance of 1320 pc, and this distance is a first-guess estimate for RCW 69, based on the similar reddenings.

Figure 6.1 shows the extinction-distance relationship for the RCW 69 field. The increase in extinction at ∼180 pc corresponds to the near side of the Coalsack complex, and the trend between 180 pc and 3.1 kpc is based on a least-squares fit to the early-type (OBA) stars in the field with best-quality data. The diamond symbols are the open clusters NGC 4609 (Feinstein & Marraco 1971) and Hogg 15 (see the discussion by Piatti et al. 2002). Due to the presence of small scale absorption variations, the relationship has considerable scatter and a distance of 1200±600 pc for RCW 69 is adopted, based on its observed extinction.

IPHASX J012507.9+635652 (IPHAS PN-1). This nebula, hereafter designated IPHAS PN-1, is a small, strongly bipolar or quadrupolar PN (Mampaso et al. 2006) which was the first new object[3] discovered from the IPHAS Survey (Drew et al. 2005). As before the SIMBAD database was used to extract all available photometric and spectroscopic information for stars within 60′ of the PN. Spectroscopic parallaxes were determined after adopting the intrinsic colours and absolute magnitudes for each spectral class from Schmidt-Kaler (1982).

The EDR is shown in figure 6.3, based on a linear least-squares fit to the early-type (OBA) stars in the field with best-quality data. The upper dashed line shows the asymptotic reddening in this direction (Schlegel et al. 1998) and the lower line is the reddening determined from the

[3]Named the 'Príncipes de Asturias' nebula in dedication to the Spanish royal family.

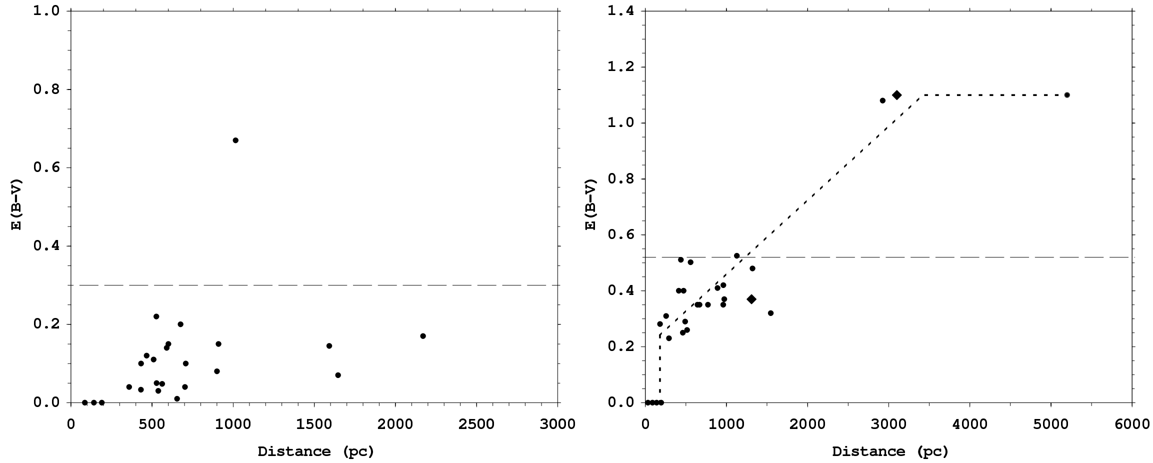

Figure 6.1: Extinction-distance relations (EDRs) for the fields containing RCW 24 (left) and RCW 69 (right), taken from Frew, Parker & Russeil (2006). Refer to the text for details.

Balmer decrement for the PN, taken from Mampaso et al. (2006). A monotonic relation of reddening versus distance is seen for this field, although with considerable scatter. Using the observed reddening to the PN ($A_V = 4.1 \pm 0.10$), a distance of $D = 5.9 \pm 2.2$ kpc is obtained. The error on the distance is probably optimistic as it does not account for any internal reddening in the nebula (if present, D is overestimated).

The diamond in the figure is the intermediate-age open cluster NGC 559 (Ann & Lee 2002), while the point at D=8 kpc is the high-mass X-ray binary, V635 Cas (Negueruela & Okazaki 2001). The point at lower right (open circle) is the B8 Ib star NGC 559#14 (Lindoff 1969), that is not actually a member star of NGC 559. The adopted spectral type is from Sowell (1987) which places it far off the observed trend, and so it is excluded from the fit. However if the star is a bright giant (luminosity class II) rather than a Ib supergiant, the star would essentially fall on the trend for the field.

6.4.5 Expansion parallaxes

Terzian (1997) and Hajian (2006) provide reviews of the technique. For this study, it was decided that expansion parallaxes based on ground-based optical photographs (Latypov 1957; Chudovicheva 1964; Liller 1965; Liller, Welther & Liller 1966) are not of sufficient quality to be useful as PN calibrators, despite the long time baselines. However, Meaburn (1997) and Meaburn et al. (2008) have used the proper motions of fast-moving outer optical knots (assuming ballistic motion) to derive distances for KjPn 8 of 1600 ± 230 pc, and NGC 6302, 1170 ± 140 pc, respectively. The latter value is consistent with the earlier radio-expansion estimate of $D = 1.6 \pm 0.6$ kpc (Gómez, Rodríguez & Moran 1993) and an earlier lower limit of 0.7 ± 0.3 kpc (Gómez et al. 1989).

A number of PNe have distance estimates based on multi-epoch *Very Large Array* (VLA) 6 cm radio observations (Masson 1986, 1989a,b; Hajian, Terzian & Bignell 1993; 1995; Hajian & Terzian 1996; Kawamura & Masson 1996), and are potentially far more accurate than the older optical determinations. Other distance determination are given by Christianto & Seaquist

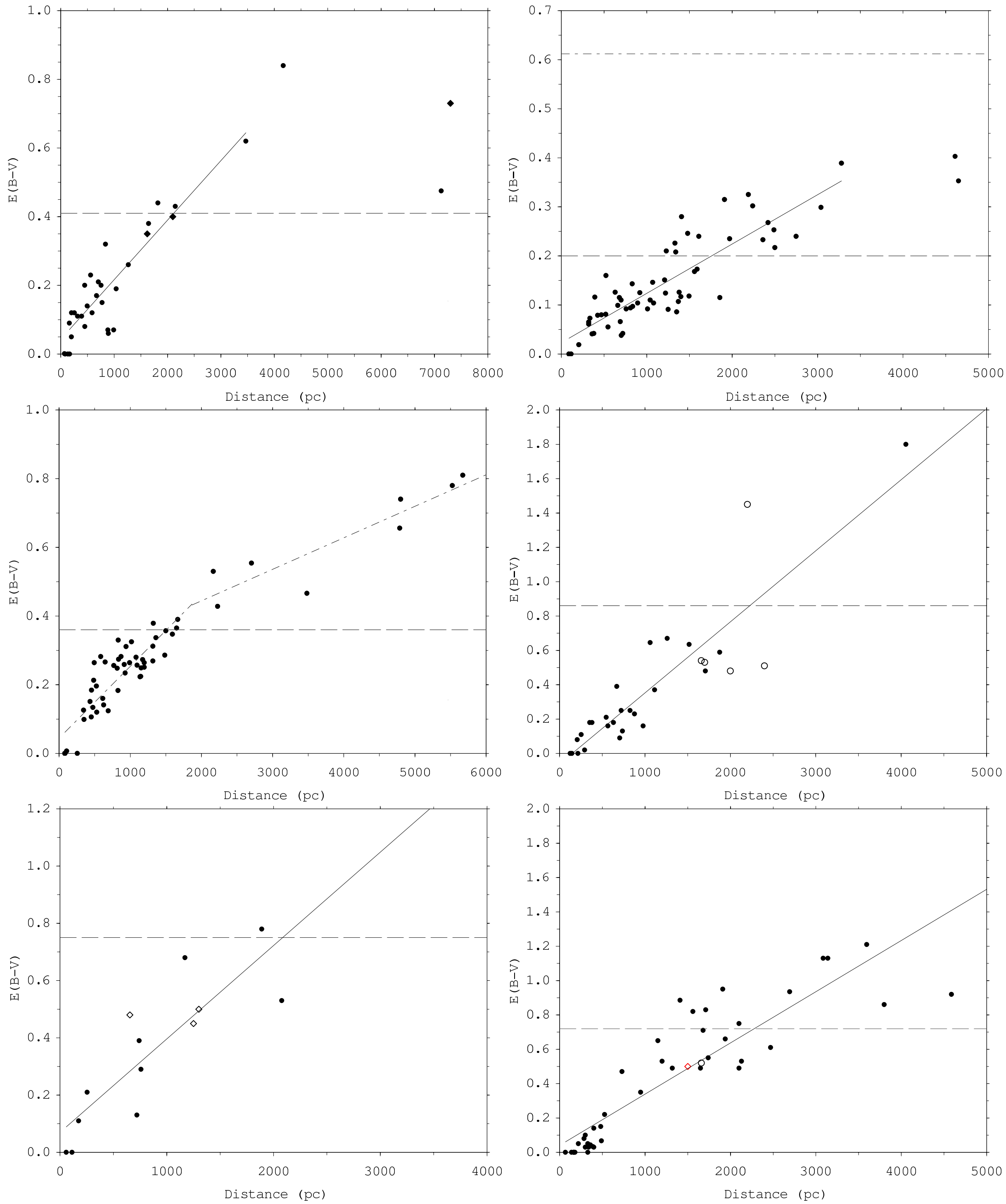

Figure 6.2: Extinction-distance relations for six previously known PNe in the galactic plane: Menzel 2 (top left), NGC 2440 (top right), NGC 5189 (middle left), He 2-111 (middle right), SaWe 3 (bottom left) and Sh 1-89 (bottom right). In each case the adopted EDR for the field is plotted, while the horizontal dashed line represents the extinction to the PN. Refer to the text for full details.

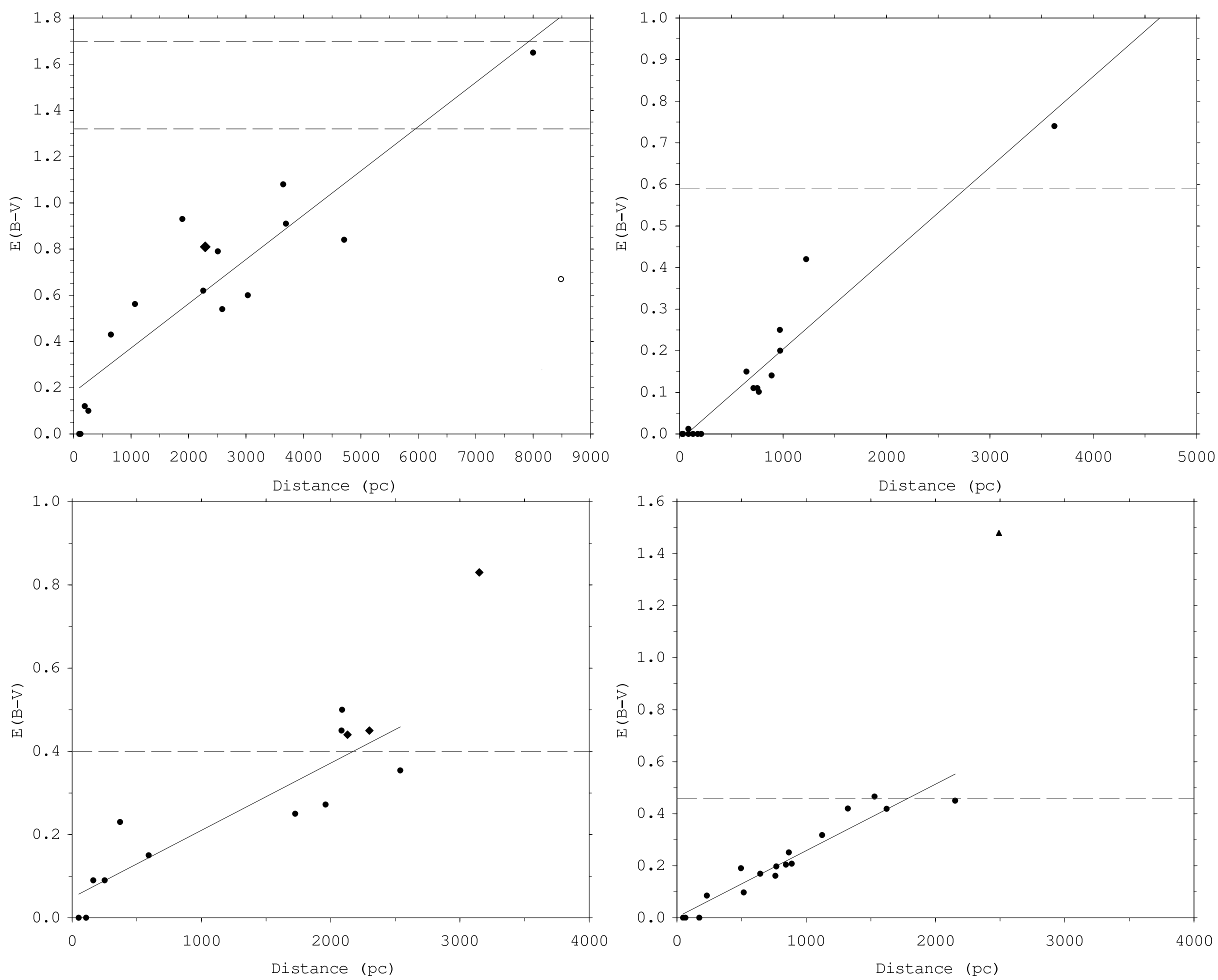

Figure 6.3: Extinction-distance relations for a newly discovered PN from the IPHAS survey, IPHAS-PN1 (top left), and three PNe from the AAO/UKST Survey, PHR0719-1222 (top right), PHR1327-6032 (bottom left) and PHR1408-6106 (bottom right). In each case the adopted EDR for the field is plotted, while the horizontal dashed line represents the extinction to the PN. Refer to the text for full details of individual diagrams.

(1998) for Vy 2-2, and Guzmán, Gómez & Rodríguez (2006) for M 2-43. More recently, precise optical parallaxes obtained with *HST* have become available (Reed et al. 1999; Li, Harrington & Borkowski 2002; Palen et al. 2002; Hajian 2006) which promise to have a significant impact on the local PN distance scale.

While expansion parallaxes were thought to be a relatively simple method, it has become apparent that there are serious sources of systematic error in the technique. Firstly the majority of PNe are not spherical, so various corrections for prolate ellipsoidal geometries have been applied (e.g. Li, Harrington & Borkowski 2002). Geometric corrections have been similarly applied by Wade, Harlow & Ciardullo (2000) for expanding nova shells.

Traditionally, in applying this technique, the angular expansion rate on the sky is compared to the spectroscopically measured gas velocity. However, this approach compares the former, a pattern velocity, with a matter velocity, and these are usually not identical (Mellema 2004; Schönberner, Jacob & Steffen 2005; Phillips 2005e). Mellema (2004) modelled the jump conditions for both shocks and ionization fronts, and found that the pattern velocity is typically ∼30% larger than the matter velocity, hence the calculated distances are too short by this amount. Schönberner, Jacob & Steffen (2005) took a different approach, based on 1-D hydrodynamical modelling, also finding that the pattern velocity is always larger than the material velocity. These authors found that the necessary correction factor ranged between 1.3 and 3, depending on the evolutionary state of the CS.

I have applied a numerical correction to all expansion distances taken from the literature to account for this effect, unless it had been specifically taken into account in the reduction, or the distance is based on the ballistic motion of high-proper motion features (e.g. Meaburn et al. 2005c, 2008). Following Mellema (2004), the exact value of the correction factor depends upon the Mach number[4] ($\mathcal{M}$) of the shock, given by:

$$\mathcal{M} = \frac{(\gamma+1)(u_1-u_0)+\sqrt{(\gamma+1)^2(u_0-u_1)^2+16a_0^2}}{4a_0} \tag{6.11}$$

where γ is the adiabatic index (for isothermal shocks[5], $\gamma = 1$), u_0 is the pre-shock velocity of the gas (taken to be ∼13 $\mathrm{kms^{-1}}$, noting that the correction factor is only weakly dependent on the exact value), u_1 is the spectroscopically derived expansion velocity, and a_0 is the pre-shock sound speed ($a_0 = 11.7$ $\mathrm{kms^{-1}}$ for nebular gas at 10^4 K, following Mellema 2004). The correction factor $\mathcal{R}$, is then found from equation (4) of Mellema (2004), viz:

$$\mathcal{R} = \frac{(\gamma+1)\mathcal{M}u_0+(\gamma+1)\mathcal{M}^2a_0}{(\gamma+1)\mathcal{M}u_0+2(\mathcal{M}^2-1)a_0} \tag{6.12}$$

The ratio tends to unity for high values of $\mathcal{M}$ (i.e. high spectroscopic expansion velocities).

Several PNe with optical expansion parallaxes have bright rims with attached shells, and so the rim can be considered to be shock bounded (Mellema 2004), and not indicative of an

[4]The Mach number is defined as $\mathcal{M} = v/v_s$, where v is the velocity of the object relative to the ambient gas and v_s is the sound velocity in the gas.

[5]Mellema (2004) shows that the isothermal case is justified as most PNe (at least the ones which have had expansion parallaxes determined), have relatively high densities and slow shocks.

ionization front. However, very young PNe (e.g. BD+30°3639 and Vy 2-2) need to be modelled as expanding (D-type) ionization fronts (see also Schönberner, Jacob & Steffen 2005) surrounded by neutral material. In this case the correction factor is more difficult to evaluate (Mellema 2004) but has been applied to BD+30°3639. He obtains $D = 1.3 \pm 0.2$ kpc, in agreement with Schönberner, Jacob & Steffen (2005). Kawamura & Masson (1996) estimate $D = 1.5 \pm 0.4$ kpc, while Li, Harrington & Borkowski (2002) estimate $D = 1.2 \pm 0.12$ kpc.

A. Hajian (2006, pers. comm.) has kindly provided preliminary *HST* expansion parallaxes for nearly 20 PNe, in advance of publication. An example is given here (the southern PN, NGC 5882) to show how the correction factor is calculated. For this object, the new expansion distance is $D = 1.32 \pm 0.2$ kpc, with the additional note that the [N II] and [O III] images give the same distance (see also Hajian 2006; Hajian et al. 2007). The [N II] and [O III] expansion velocities (Hajian et al. 2007) are also similar, with a mean of 25 kms^{-1}. Correcting for the jump condition, and assuming an isothermal shock ($\gamma = 1$) following Mellema (2004), equations 6.11 and 6.12 can be used to estimate $\mathcal{M} \simeq 1.64$ and a correction factor, $\mathcal{R} = 1.3 \pm 0.1$. The corrected distance is $D = 1.70$ kpc, and an error of 25% has been assumed. Table 6.5 includes the corrected expansion distances for the PNe observed by Hajian (2006, 2007), along with other distances (corrected as necessary) from the recent literature. These data will be used as calibrating PNe for the SB-r relation. For example, a recent *HST* expansion parallax for NGC 3242, which has taken shock jump conditions into account (Guerrero pers. comm., 2006) gives $D \simeq 1.0$ kpc (Ruiz et al. 2006).

Evidence to show that such biases do exist in expansion distances is provided by the study of the symbiotic nebula He 2-147 (Santander-García et al. 2007). They found that the expansion parallax method gave a distance of 1.5 ± 0.4 kpc, a factor of two lower than the distance of 3.0 ± 0.4 kpc obtained from the period-luminosity relationship for the central Mira variable. Corrected for the jump condition these authors find $D = 2.7 \pm 0.5$ kpc, in agreement with the period-luminosity distance. This example provides good independent evidence for the application of a correction factor, and that the measured expansion traces an expanding shock front rather than the bulk movement of matter.

However, Hajian (2006) states that for PNe with both [N II] and [O III] images, the [N II] distances are systematically higher. However, this hints that the jump condition needs to be applied. Indeed, Hajian (2007) notes that the [N II] velocities are higher than the [O III] velocities for all of the PN in the sample. Following Mellema (2004), the correction factor is less for higher spectroscopic velocities, tending to reduce the apparent distance discrepancy.

Of note is another ground-based expansion distance, applied to the unusual [WR] PN, PM 5 (Morgan, Parker & Cohen 2003). These authors gave a distance of 1.0 kpc, based on a scanned UK Schmidt plate in comparison with the SHS. Owing to the caveats described above, and the uncertain application of the shock front correction in this case, this object has also been omitted as a calibrating PN.

Table 6.5: Expansion distances for planetary nebulae. For PNe with more than one distance determination, the adopted values are weighted means.

Name	D (kpc)	Reference
NGC 2392	>1.5	1, 3
NGC 2440	>1.4	1, 3
NGC 3132	1.2 ± 0.4	2, 3
NGC 3242	1.0 ± 0.2	4
NGC 3918	1.4 ± 0.3	2, 3
NGC 5882	1.7 ± 0.4	2, 3
NGC 5979	2.0± 0.5	2, 3
NGC 6210	2.1 ± 0.5	1, 3, 5
NGC 6302	1.04 ± 0.16	6
NGC 6326	5.3 ± 1.3	2, 3
NGC 6543	1.5 ± 0.4	2, 3, 5, 8
NGC 6565	2.5 ± 0.5	2, 3
NGC 6572	2.0 ± 0.5	1, 3, 5, 9
NGC 6578	2.90 ± 0.78	5, 10
NGC 6720	0.56 ± 0.3	3, 7
NGC 6826	2.1 ± 0.5	2, 3, 15
NGC 6884	3.30 ± 1.24	3, 5, 10
NGC 6886	5.3 ± 1.0	2, 3
NGC 6891	2.9 ± 0.6	2, 3
NGC 7009	1.45 ± 0.5	11
NGC 7026	3.7 ± 0.8	2, 3
NGC 7027	0.82 ± 0.20	5, 12, 13, 14, 15, 21, 22, 23
NGC 7662	1.19 ± 1.15	5, 16
IC 418	1.1 ± 0.2	2, 3
IC 2448	2.2 ± 0.5	2, 3, 5, 10, 15
BD+30 3639	1.3 ± 0.2	2, 3, 5, 9, 15, 17
J 900	4.8 ± 1.0	2, 3
Hu 1-2	>1.5	1, 3
KjPn 8	1.6 ± 0.23	18
M 2-43	8.9 ± 1.8	3, 19
Vy 2-2	4.68 ± 1.20	5, 20

Reference: 1. Hajian, Terzian & Bignell (1995); 2. Hajian (2006, and pers. comm., 2006); 3. this work, correction applied (see text); 4. Ruiz et al. (2006); 5. Mellema (2004); 6. Meaburn et al. (2005); 7. O'Dell et al. (2002); 8. Reed et al. (1999); 9. Kawamura & Masson (1996); 10. Palen et al. (2002); 11. Sabbadin et al. (2004); 12. Masson (1986); 13. Masson (1989a); 14. Hajian, Terzian & Bignell (1993); 15. Schönberner, Jacob & Steffen (2005); 16. Hajian & Terzian (1996); 17. Li, Harrington & Borkowski (2002); 18. Meaburn (1997); 19. Guzmán, Gómez & Rodríguez (2006); 20. Christianto & Seaquist (1998); 21. Walsh et al. (1997); 22. Bains et al. (2003); 23. Zijlstra, van Hoof & Perley (2008).

6.4.6 Gravity Distances

This is potentially a very powerful method to determine distances directly for the central star, based on NLTE model atmosphere analysis. The observables are the central star visual magnitude and reddening, and from a detailed spectroscopic analysis, the temperature and surface gravity are determined. From this, the surface flux, mass and intrinsic radius of the star can be inferred, and using the reddening-corrected magnitude, a distance can be directly determined. The distance is derived using the following equation (cf. Méndez et al. 1988a):

$$D^2 = 3.82 \times 10^{-9} \ \frac{M_c F_*}{g} \ 10^{0.4 V_0} \tag{6.13}$$

where D is the distance in kpc, M_c is the stellar (core) mass in solar units, F_* is the monochromatic Eddington flux in units of $\mathrm{erg\,cm^{-2}\,s^{-1}\,\AA^{-1}}$ at $\lambda 5480$ Å, g is the surface gravity in $\mathrm{cm\,s^{-1}}$ and V_0 is the extinction-corrected visual magnitude, where $V_0 = V - 2.14c$, consistent with a Howarth (1983) reddening law.

In turn the Eddington flux can be approximated by the following linear equation if the effective stellar temperature, T_*, is known (Cazetta & Maciel 2000):

$$F_* = 1.85 \times 10^4 \ T_* \ - \ 9.97 \times 10^7 \tag{6.14}$$

where T_* is in K.

In order to compare the various determinations in a homogenous way, and to derive appropriately weighted mean gravity distances (in cases where more than one NLTE analysis exists in the literature), all suitable $T_{\rm eff}$ and log g determinations have been compiled from the literature to be used in conjunction with accurate reddenings and visual magnitudes (from the references detailed in §9.4.2) to calculate a new, internally consistent set of gravity distances.

Nonetheless there are caveats to this approach, and a number of criteria have been employed to minimize any bias in the adopted distance scale. In general, Lyman line $T_{\rm eff}$ determinations are preferred, as there is considerable error in the Balmer line determinations, compared with model fits utilising the Lyman lines (see the discussion by Good et al. 2004). This is because it is very difficult to simultaneously fit a model atmosphere to all the Balmer lines in the optical spectrum of a hot WD or subdwarf (the so-called Balmer line problem; e.g. Werner 1996), leading to significant errors in the effective temperature (and the gravity). The problem is thought to be due to the improper treatment of metal opacities in the models (Werner 1996).

To illustrate the Balmer line problem, it is seen that the Lyman temperatures of Good et al. (2004) are in much better agreement with the new Zanstra temperature determinations (see §9.4.4) for several nearby PNe with good quality data. These Zanstra determinations are considered to be much more reliable as a result of vastly improved Hα fluxes for many of these highly evolved PNe (see Chapter 3). However, since the spectroscopic estimations of the $\log g$ and $\log T_{\rm eff}$ values are not independent, it is prudent to question the reliability of the ground-based Balmer $\log g$ values as well.

Indeed, several lines of evidence point to problems with some of the gravity determinations,

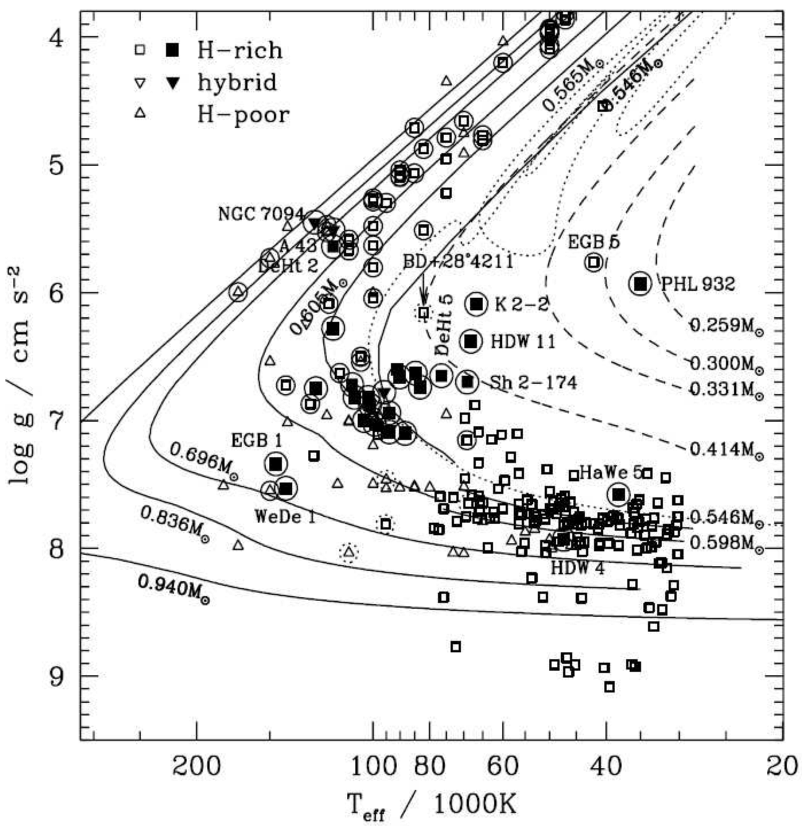

Figure 6.4: $T_{\text{eff}} - g$ diagram taken from Napiwotzki (1999). Hydrogen-rich CSPN are marked by squares and H-deficient objects by triangles. Stars with associated PNe are encircled. Post-AGB tracks are overlaid with solid lines, while post-RGB tracks are shown by dashed lines (see Napiwotzki 1999, for further details). A few nearby PNe and suspected local PNe are labelled. A few of these objects, such as Sh 2-174, HDW 11, PHL 932 and EGB 5 are shown here to be objects other than true PNe. Also worth noting is the mean mass of the ensemble of CSPN still undergoing nuclear burning, compared to the mean mass of CSPN on the cooling track. Approximate mean masses from the data presented in Napiwotzki (1999) are $0.65M_{\odot}$ and $0.56M_{\odot}$ respectively. They should be the same, and the discrepancy points to systematic errors in the $\log g$ values derived from NLTE modelling.

specifically that the $\log g$ value is underestimated, especially at low to moderate surface gravities (see figure 2 of Napiwotzki 1999, reproduced here as figure 6.4), where the mean mass of CSPN with $\log g < 6.0$ is considerably less than the mass of higher gravity objects. This problem has been noted previously by Pottasch (1996) and Pottasch & Acker (1998) who found that the $\log g$ values derived from the often-used Hγ line profile are often systematically too low.

However, despite recent advances in non-LTE modelling, systematic errors in the determination of the surface gravity persist. Traulsen et al. (2005) give a surface gravity for the CS of the Helix nebula, as $\log g = 6.3$ cgs units. The resulting distance of 780 pc is way outside the error bar of the recent trigonometric distance of 219^{+27}_{-21} pc (Harris et al. 2007). Even for the well-studied star LS V +4621, the CS of Sh 2-216, there remains an unexplained discrepancy between the spectroscopic distance based on UV lines (Rauch et al. 2007) and the well-determined parallax distance of Harris et al. (2007).

In this study, preference is given to values determined from the Lyman lines, or far-UV/X-ray spectroscopy. However, some published X-ray $\log g$ values for several PNe are treated with caution due to the coarse grid of model atmospheres applied and the subsequent resolution in $\log g$ being no better than $\pm$ 0.5 dex. (e.g. Hoare et al. 1995).

Compared with the high-quality trigonometric distances of Harris et al. (2007), the gravity distances derived here from the Lyman-line data of Good et al. (2004) are in somewhat better agreement than their Balmer determinations, and in turn, the Balmer determinations of Napiwotzki (1999, 2001). As another consistency check, the mean mass of an ensemble of DAO central stars (see table 5 of Good et al. 2005) using the Lyman method is in better agreement than the Balmer method, with the canonical WD mass of 0.6 $M_\odot$ (e.g. Vennes et al. 1997; Gesicki & Zijlstra 2007, and §9.4.6).

Table 6.6 gives the various PN central stars and the resulting gravity distances derived using equations 6.13 and 6.14 above. The stellar mass (needed for the equation 6.13) has been determined from the $\log g - T_{\rm eff}$ diagram from comparison with the evolutionary tracks of Blöcker (1995), interpolating linearly if necessary. Table 6.6 also gives data on the bolometric correction, stellar radius, and gravitational redshift for each central star. The bolometric correction ($BC = M_{\rm bol} - M_V$) is adopted from Vacca, Garmany & Shull (1996) and is given by:

$$\mathrm{BC} = 27.66 - 6.84 \log T_{\rm eff} \tag{6.15}$$

There is only a weak dependence of the bolometric correction on the surface gravity (Vacca, Garmany & Shull 1996) and the effect is ignored here. The stellar radius (in solar units) is calculated from the following standard expression, adopting the solar bolometric magnitude and effective temperature as $M_{\rm bol}^{\odot} = 4.74$ and $T_{\rm eff}^{\odot} = 5777\,\mathrm{K}$ respectively (Cox 2000):

$$R_* = 10^{0.2\,(4.74 - M_{\rm bol} - 10 \log (T_{\rm eff}/5777))} \tag{6.16}$$

The gravitational redshift (in $\mathrm{km\,s^{-1}}$) can be derived from the stellar mass and radius, expressed in solar units (e.g. Holberg et al. 1998; Barstow et al. 2005):

$$V_{\rm GR} = 0.636\, M_*/R_* \tag{6.17}$$

The gravitational redshifts are used in the next chapter to correct the observed CSPN radial velocities in order to compare with measured nebular velocities. This approach helps to eliminate HII regions and other nebulae currently masquerading as PNe, and hence better refine the solar neighbourhood sample.

Table 6.6: New PN gravity distances using updated data from the literature.

Name	V	$E(B-V)$	T_* (kK)	$\log g$ (cms^{-1})	M_* ($M_\odot$)	Ref	M_V	BC	$M_{\rm bol}$	R_* ($R_\odot$)	$V_{\rm GR}$ (kms^{-1})	D (pc)
A 7	15.48	0.00	99	7.68	0.67	1	7.58	-6.52	1.06	0.02	23.1	380
A 15	16.0	0.03	110	5.70	0.59	2	2.65	-6.82	-4.17	0.17	2.2	4480
A 20	16.56	0.05	119	6.13	0.57	3	3.67	-7.06	-3.38	0.10	3.6	3518
A 21	15.96	0.06	140	7.50	0.60	4	6.86	-7.54	-0.68	0.02	18.4	607
A 31	15.51	0.05	94	7.43	0.58	1	7.18	-6.35	0.83	0.02	15.9	435
A 33	15.50	0.31	100	6.20	0.60	6	3.99	-6.54	-2.55	0.10	4.0	1287
A 35	14.8	0.04	80	7.70	0.57	7	8.06	-5.88	2.18	0.02	21.2	213
A 36	11.53	0.03	113	5.60	0.60	8	2.35	-6.90	-4.55	0.19	2.0	656
A 39	15.60	0.03	117	6.58	0.58	1,2,5,9	4.80	-7.01	-2.21	0.06	6.1	1385
A 43	14.74	0.17	110	5.70	0.59	10	2.65	-6.82	-4.17	0.17	2.2	2053
A 52	17.6	0.1	110	6.00	0.58	4	3.42	-6.82	-3.40	0.12	3.1	5945
A 61	17.39	0.13	88	7.06	0.55	5	6.38	-6.17	0.21	0.03	10.1	1322
A 74	17.11	0.18	100	7.20	0.59	6	6.51	-6.54	-0.03	0.03	12.4	1020
A 75	17.2	0.80	80	6.00	0.60	4	3.75	-5.88	-2.13	0.12	3.1	1563
BlDz 1	18.4	0.15	128	6.85	0.57	3	5.39	-7.27	-1.88	0.04	8.4	3227
CRBB 1	10.72	0.04	27	3.10	0.55	11	-2.06	-2.65	-4.71	3.58	0.1	3399
DeHt 2	14.95	0.20	117	5.62	0.64	5	2.29	-7.01	-4.71	0.19	2.1	2556
DHW 5	15.47	0.16	60	6.75	0.41	1	6.37	-5.02	1.36	0.04	5.9	526
DS 1	12.26	0.21	90	5.25	0.60	6	1.74	-6.23	-4.49	0.29	1.3	942
DS 2	12.37	0.20	90	5.25	0.60	6, 12	1.74	-6.23	-4.49	0.29	1.3	1000
EGB 1	16.39	0.34	147	7.34	0.65	5	6.32	-7.68	-1.37	0.03	16.0	637
EGB 6	16.04	0.02	110	7.50	0.60	6	7.13	-6.82	0.31	0.02	17.9	588
HaWe 4	17.0	0.28	75	7.50	0.60	6	7.57	-5.69	1.89	0.02	17.2	515
HaWe 5	17.4	0.30	38	7.58	0.51	5	8.77	-3.67	5.10	0.02	16.5	347
HaWe 6	16.7	0.30	47	7.93	0.64	5	9.13	-4.32	4.81	0.01	28.1	213
HaWe 13	16.9	0.49	68	6.38	0.39	5	5.36	-5.40	-0.04	0.07	3.8	1012
HbDs 1	12.53	0.14	114	5.70	0.60	8	2.59	-6.93	-4.34	0.17	2.3	796
IC 1295	16.9	0.36	90	6.66	0.56	5	5.34	-6.23	-0.89	0.06	6.4	1229
IC 2149	11.34	0.25	42	3.60	0.60	13	-1.48	-3.96	-5.44	2.07	0.2	2562
IsWe 2	17.71	0.45	90	7.50	0.60	6	7.36	-6.23	1.14	0.02	17.5	617
Jacoby 1	15.52	0.00	150	7.50	0.68	10	6.65	-7.74	-1.10	0.02	19.7	596
Jacoby 1	15.52	0.00	150	7.50	0.56	14	6.86	-7.74	-0.89	0.02	17.9	541
Jn 1	16.3	0.00	120	7.00	0.60	6	5.78	-7.08	-1.30	0.04	10.2	1269
JnEr 1	17.14	0.02	120	7.40	0.60	6	6.78	-7.08	-0.30	0.02	16.1	1145
K 1-16	15.08	0.04	120	6.20	0.60	6	3.78	-7.08	-3.30	0.09	4.0	1716
K 1-16	15.08	0.04	139	6.00	0.60	15	3.12	-7.52	-4.40	0.12	3.3	2332
K 1-16	15.08	0.04	121	6.50	0.60	15	4.52	-7.11	-2.58	0.07	5.7	1220
K 1-16	15.08	0.04	140	6.40	0.58	10	4.15	-7.54	-3.39	0.07	5.1	1452
K 1-22	16.83	0.05	141	6.73	0.59	3	4.94	-7.56	-2.62	0.05	7.5	2219
K 1-27	16.13	0.05	105	6.50	0.52	16	4.84	-6.68	-1.84	0.06	5.2	1686
K 2-2	14.3	0.03	67	6.09	0.38	5	4.68	-5.35	-0.67	0.09	2.7	805
Lo 1	15.1	0.01	120	6.70	0.57	17	5.10	-7.08	-1.98	0.05	7.0	986
Lo 8	12.95	0.03	90	5.10	0.58	13	1.40	-6.23	-4.83	0.34	1.1	1956
LoTr 5	14.6	0.00	130	6.00	0.57	15	3.26	-7.32	-4.06	0.11	3.1	1855
NGC 246	11.84	0.02	150	5.70	0.72	10	2.08	-7.74	-5.66	0.18	2.6	869
NGC 246	11.96	0.02	120	6.50	0.57	15	4.59	-7.08	-2.49	0.07	5.6	290
NGC 650-1	17.48	0.10	140	7.40	0.60	6	6.61	-7.54	-0.93	0.02	16.4	1295
NGC 1360	11.34	0.01	140	6.00	0.57	15	3.17	-7.54	-4.37	0.11	3.2	424
NGC 1360	11.34	0.01	110	6.00	0.57	18	3.45	-6.82	-3.38	0.12	3.1	373
NGC 1360	11.34	0.01	97	5.30	0.65	8	1.69	-6.45	-4.76	0.28	1.5	839
NGC 1501	14.45	0.65	134	6.00	0.60	19	3.16	-6.80	-3.64	0.09	4.3	717
NGC 1535	12.11	0.05	70	4.60	0.65	20	0.32	-5.48	-5.16	0.65	0.6	2124

Continued on next page

Table 6.6 – continued from previous page

Name	V	$E(B-V)$	T_* (kK)	$\log g$ (cms^{-1})	M_* ($M_\odot$)	Ref	M_V	BC	$M_{\rm bol}$	R_* ($R_\odot$)	$V_{\rm GR}$ (kms^{-1})	D (pc)
NGC 2371	14.85	0.05	135	6.30	0.60	19	3.90	-7.43	-3.53	0.08	4.6	1442
NGC 2438	17.9	0.46	114	6.62	0.60	3	4.89	-6.93	-2.04	0.06	6.5	2072
NGC 2610	15.97	0.10	100	5.80	0.56		3.07	-6.54	-3.47	0.15	2.4	3301
NGC 2867	16.03	0.32	141	6.00	0.60	19	3.10	-7.56	-4.46	0.12	3.3	2440
NGC 3587	16.75	0.01	94	6.94	0.55	5	6.01	-6.35	-0.34	0.04	8.8	1387
NGC 4361	13.26	0.03	126	6.00	0.59	8	3.25	-7.23	-3.98	0.12	3.2	964
NGC 5189	14.53	0.36	135	6.00	0.60	19	3.15	-7.43	-4.28	0.12	3.3	1129
NGC 6720	15.78	0.05	80	7.00	0.56	2	6.32	-5.88	0.45	0.04	9.4	725
NGC 6720	15.78	0.05	101	6.88	0.56	5	5.75	-6.58	-0.82	0.04	8.4	943
NGC 6720	15.29	0.12	130	7.00	0.60	6	5.69	-7.32	-1.63	0.04	10.2	700
NGC 6842	16.7	0.70	80	5.00	0.60	4	1.25	-5.88	-4.63	0.39	1.0	4530
NGC 6853	13.94	0.10	120	6.90	0.60	6	5.53	-7.08	-1.55	0.04	9.0	416
NGC 6853	13.94	0.10	122	7.00	0.60	15	5.76	-7.13	-1.37	0.04	10.2	374
NGC 6853	13.94	0.10	126	6.50	0.58	8	4.51	-7.23	-2.71	0.07	5.6	665
NGC 6853	13.99	0.10	109	6.72	0.56	5	5.27	-6.79	-1.51	0.05	7.0	480
NGC 6905	14.6	0.15	141	6.00	0.60	19	3.10	-7.56	-4.46	0.12	3.3	1610
NGC 7094	13.61	0.10	126	5.45	0.87	5	1.45	-7.22	-5.77	0.27	2.1	2344
NGC 7094	13.61	0.03	110	5.70	0.59	10	2.65	-6.82	-4.17	0.17	2.2	1490
NGC 7293	13.48	0.00	90	7.00	0.56	2	6.19	-6.23	-0.04	0.04	9.5	287
NGC 7293	13.48	0.00	110	6.30	0.56	8	4.21	-6.82	-2.62	0.08	4.3	715
NGC 7293	13.48	0.00	104	7.00	0.57	5	6.01	-6.65	-0.64	0.04	9.7	312
PuWe 1	15.53	0.09	109	7.57	0.66	1	7.21	-6.80	0.41	0.02	20.4	407
RE 1738+665	14.60	0.01	71	7.53	0.54	21	7.82	-5.54	2.29	0.02	16.8	224
RE 1738+665	14.60	0.01	76	7.85	0.57	22	8.50	-5.72	2.79	0.01	25.0	162
RXJ 2117+34	13.10	0.03	163	6.61	0.57	23	4.53	-8.00	-3.47	0.06	6.5	497
Sanduleak 3	14.18	0.55	140	6.00	0.57	19	3.16	-7.54	-4.37	0.11	3.2	732
S 68	16.59	0.37	96	6.78	0.55	5	5.59	-6.41	-0.83	0.05	7.4	937
S 174	14.52	0.09	76	6.64	0.44	1	5.75	-5.71	0.04	0.05	5.5	501
S 176	17.70	0.30	65	7.50	0.60	6	7.74	-5.26	2.48	0.02	17.0	639
S 188	17.44	0.30	90	7.50	0.60	6	7.36	-6.23	1.14	0.02	17.5	675
S 188	17.44	0.30	102	6.82	0.56	5	5.59	-6.60	-1.00	0.05	7.8	1525
S 216	12.67	0.08	83	6.74	0.49	5	5.77	-5.99	-0.22	0.05	6.5	214
S 216	12.67	0.08	93	6.90	0.55	8	5.92	-6.32	-0.40	0.04	8.4	200
S 216	12.67	0.07	95	6.90	0.56	24	5.88	-6.39	-0.51	0.04	8.5	210
Ton 320	15.7	0.03	99	7.19	0.58	1	6.52	-6.51	0.01	0.03	12.1	658
WDHS 1	17.40	0.12	100	7.60	0.60	6	7.49	-6.54	0.95	0.02	19.9	808
WDHS 1	17.40	0.12	141	7.53	0.68	5	6.79	-7.56	-0.77	0.02	20.2	1116

References to table 6.6:

1. Good et al. (2004); 2. McCarthy, Méndez & Kudritzki (1997); 3. Rauch et al. (1999); 4. Rauch et al. (2004); 5. Napiwotzki (1999); 6. Pottasch (1996); 7. Herald & Bianchi (2002); 8. Traulsen et al. (2005); 9. Jacoby, Ferland & Korista (2001); 10. Werner & Herwig (2006); 11. McCarthy et al. (1991); 12. Méndez et al. (1988a); 13. Herrero, Manchado & Méndez (1990); 14. Werner et al. (2007); 15. Hoare et al. (1995); 16. Rauch, Köppen & Werner (1994); 17. Herald & Bianchi (2004); 18. Hoare et al. (1996); 19. Quirion, Fontaine & Brassard (2007); 20. Méndez, Kudritzki & Herrero (1992); 21. Bannister et al. (2003); 22. Barstow et al. (1994b); 23. Corsico et al. (2007); 24. Rauch et al. (2007).

6.4.7 Kinematic distances

This technique uses the position and measured radial velocity of the PN to infer a distance assuming a model for the rotation curve of the Galaxy. For examples of distances obtained via this method, see Aaquist (1993), Corradi & Schwarz (1993c) Maciel (1995, 1996), Costa, de Freitas Pacheco & De Franca (1996), Corradi et al. (1997), Phillips (2001a), Rodríguez, Corradi & Mampaso (2001) and Mampaso et al. (2006). Rosado & Kwitter (1982) applied this method to Sh 2-188, but this large asymmetric PN has been shown to have a very high space motion (Wareing et al. 2006), nullifying the utility of the method for this PN. In addition, kinematic distances (or limits) based on HI absorption measurements at 21 cm are available for 24 PNe, taken from the work of Gathier, Pottasch & Goss (1986).

In this work a galactic rotation curve slightly different to the IAU standard has been adopted: the adopted values are $v_{\odot} = 220\,\mathrm{kms}^{-1}$, and $R_{\odot} = 7.9\,\mathrm{kpc}$. A flat rotation curve in the range $4 \leq R \leq 14\,\mathrm{kpc}$ has been assumed (e.g. Gathier, Pottasch & Goss 1986). The galactocentric distance, R, to the PN is calculated from the observed LSR radial velocity, v_{LSR}, and the galactic coordinates l and b using the following expression:

$$R = \frac{k \sin l \cos b}{v_{LSR} + 220 \sin l \cos b} \tag{6.18}$$

where k depends on the adopted distance from the Sun to the galactic centre. The PN distance then follows from the geometric configuration formed by R, $R_{\odot}$, l, and b. The distance calculations have been made using a Perl script written by B. Miszalski.

Only a few kinematic determinations have been adopted as calibrating data. Extreme Type I PNe are in general the only objects for which this approach is valid, where a standard kinematic distance is derived based on the observed PN radial velocity, and assuming it has, like other extreme bipolar PNe, a low peculiar velocity relative to its local ISM. For PNe, which from other evidence, can be inferred to have a very low peculiar motion relative to the ISM (e.g. RCW 24; Frew, Parker & Russeil 2006), the peculiar velocity has been set equal to the zero-age velocity dispersion ($\sigma_u = 10$ kms^{-1}). For other bipolar PNe, the peculiar velocity is assumed to be equal to the velocity dispersion of main sequence stars of spectral type A0, $\sigma_u = 20$ kms^{-1} (Cox 2000; cf. Nordström et al. 2004), as such stars are plausible progenitors for Type I bipolar PNe. This uncertainty dominates the error budget for each PN distance determination, especially as most have accurate systemic velocities.

For the cases where there is a kinematic ambiguity, the overall interstellar extinction proved useful in determining that the near distance was the only solution in each case. Table 6.7 summarises the best distances (or limits) utilizing this technique. The radial velocities have been taken from Durand, Acker & Zijlstra (1998) unless otherwise noted, and have been converted to the LSR frame. For the more interesting cases, the new distance determinations are described in more detail below.

RCW 24. This is a highly evolved Type I bipolar PN (Frew, Parker & Russeil 2006). This PN is assumed to have a low peculiar velocity, for despite the large size and very low surface

Table 6.7: Kinematic distances for mostly Type I PNe.

PN	$v_{\rm LSR}$	D (kpc)	Reference
NGC 2899	$+2.8 \pm 1$	< 2.0	1, 7
NGC 3699	-25.4 ± 7.8	3 ± 1	1
NGC 5189	-15.7 ± 4	$1.3^{+1.6}_{-1.3}$	1
NGC 6537	$+8.6 \pm 2$	$1.6^{+1.1}_{-1.6}$	1
NGC 6741	$+57.5 \pm 1.4$	3.6 ± 0.6	1, 15
NGC 6751*	$+13 \pm 1$	2.0 ± 0.6	11
NGC 7026	-25.6 ± 0.6	4.2 ± 1.0	1
Abell 79	-44 ± 8	4.4 ± 0.8	1, 6
BV 5-1	-64 ± 4	5.5 ± 1.2	1, 13
CVMP 1	-28 ± 5	1.9 ± 0.5	3
IPHAS-PN1	-71.1 ± 1.5	$7.0^{+4.5}_{-3.0}$	4
He 2-84	-18 ± 10	1.8 ± 0.5	1, 8
He 2-111	-28 ± 5	2.1 ± 0.5	1, 5
HFG 2*	$+23.5 \pm 1$	1.9 ± 0.4	1, 9
K 3-72	$+29 \pm 10$	$3.8^{+2.0}_{-1.6}$	1, 8
M 3-3	$+55 \pm 2$	$5.5^{+1.8}_{-1.3}$	1, 7
M 3-28	$+32 \pm 3$	$2.5^{+1.1}_{-1.3}$	1, 14
Mz 1	-34 ± 3.2	2.3 ± 0.6	1
Mz 2	-28.3 ± 2.1	2.1 ± 0.6	1, 12
Na 2	$+97 \pm 3$	4.9 ± 1.0	1, 8, 14
RCW 24	-5 ± 5	0.8 ± 0.8	1, 2
RCW 69	-33 ± 3	$1.5^{+1.0}_{-0.5}$	1, 2
Sh 2-200*	-9.7 ± 1	0.66 ± 0.49	1, 10

References: 1. This work; 2. Frew, Parker & Russeil (2006); 3. Corradi et al. (1997); 4. Mampaso et al. (2006); 5. Meaburn & Walsh (1989); 6. Rodríguez, Corradi & Mampaso (2001); 7. Huggins et al. (1996); 8. Corradi & Schwarz (1993c); 9. Brand et al. (1987); 10. Fich & Blitz (1984); 11. Chu et al. (1991); 12. Costa, de Freitas Pacheco & de França (1996); 13. Josselin et al. (2000); 14. Huggins et al. (2005); 15. Phillips (2001a). PNe marked with an asterisk are non-Type I optically-thin objects that are ionizing ambient interstellar gas, for which a kinematic distance can be determined.

Table 6.8: Summary of optical radial velocity determinations for RCW 24 and RCW 69.

Object ID	Telescope	V_{hel} ($\mathrm{km\,s^{-1}}$)	V_{lsr} ($\mathrm{km\,s^{-1}}$)
RCW 24	SAAO	$+18 \pm 25$	$+1$
RCW 24	SAAO	$+26 \pm 28$	$+9$
RCW 69	UKST/FLAIR	-25.2 ± 8.6	-32.3
RCW 69	UKST/FLAIR	-29.9 ± 4.7	-37.0
RCW 69	SAAO	-20.4 ± 4.6	-27.5
RCW 69	SAAO	-23 ± 17	-30
RCW 69	Marseille F-P	...	-22
RCW 69	Marseille F-P	...	-48

brightness of this highly evolved object, there is very little sign of an ISM interaction such as a brighter asymmetric rim or an off-centred central star. Indeed, RCW 24 is one of the lowest surface brightness PNe without any strong evidence of an ISM interaction. Alternatively, the nebula is found in an extremely low-density environment where even a moderate velocity with respect to the ISM will have little effect on the morphology of the PN. However, this scenario is considered unlikely owing to the small z-distance of this PN, well within a disk scale height of the interstellar dust and molecular gas (Spitzer 1978).

The available low-dispersion SAAO spectra of RCW 24 are not ideal for radial velocity determination, and have significant associated uncertainties. The observed emission lines give a heliocentric radial velocity of $V_{\rm hel} = 22 \pm 5$ kms^{-1}, derived using the IRAF EMSAO package. The result is an average of the measurements from individual spectra taken over the two nights. The observations are summarised in Table 6.8. This translates to $V_{\rm lsr} = +5$ kms^{-1}, which is in reasonable agreement with the CO velocity measured by Brand et al. (1987), as part of their kinematic study of the outer Galactic disk. These authors observed each of the bipolar lobes separately in the CO(1–0) line, with concordant results. They observed a corrected antenna temperature $\mathrm{T}_A = 2.4\,\mathrm{K}$, $V_{\rm lsr} = +12.4\pm1.2$ kms^{-1}, and mean $\Delta \mathrm{V} = 2.3$ kms^{-1} for each lobe.

The narrow line widths of each lobe do not necessarily militate against a PN interpretation as Bachiller et al. (1993) observed low line widths in the lobes of the evolved PN JnEr 1 (= VV 47). However the measured CO velocities are very similar to those measured in the neighbouring Vela Molecular Ridge (Murphy & May 1991), so the association of the CO with the PN is ambiguous. As a precaution, only the optical RV measurements are used (see Table 6.8). Using $V_{\rm lsr} = +5$ kms^{-1} from the optical spectra, the derived kinematic distance is 0.8±0.8 kpc, the large uncertainty being due to the slow increase in velocity with distance in this direction.

RCW 69. This is another evolved bipolar Type I PN. Molecular emission is also probably present in this PN; a detailed discussion of the CO data is given in Frew, Parker & Russeil (2006). MIR emission has also been detected in *Spitzer* GLIMPSE data; see Cohen et al. (2007) for further details. The available FLAIR and SAAO data from Frew, Parker & Russeil (2006) are combined to obtain an average velocity of $V_{\rm hel} = -25.2 \pm 8.6\,\mathrm{kms^{-1}}$ based on the weighted fits to each set of emission lines as provided by the IRAF EMSAO package. A summary of the various velocity determinations is given in Table 6.8. Full details of the observing procedure are given in Frew, Parker & Russeil (2006).

This PN has also been observed in Hα with the Marseille Fabry-Perot (F-P) interferometer (see Frew, Parker & Russeil 2006) as part of a study of the spiral structure study of the Galaxy (e.g. Russeil et al. 1998; Russeil 2003). The quite poor spatial resolution (9″ pixel size) of the image is seen in Figure 6.5. Fortunately, the velocity resolution of the instrument allows determination of an accurate systemic velocity for the PN, as determined from a background corrected F-P Hα velocity plot (see fig 6.6, reproduced from Frew, Parker & Russeil 2006), which is a profile of the centre of the PN through a 45″ aperture. The Hα profile is approximately fit by two gaussians with mean LSR velocities of -22 and -48 kms^{-1}. These are interpreted as intrinsic to the PN as these components are absent in a nearby offset field. These velocity components are also seen in CO($1-0$) and CO($2-1$) profiles in this direction (for a full discussion of the CO data, see Frew, Parker & Russeil 2006). Further evidence of molecular material in this PN using *Spitzer* GLIMPSE data was presented by Cohen et al. (2007).

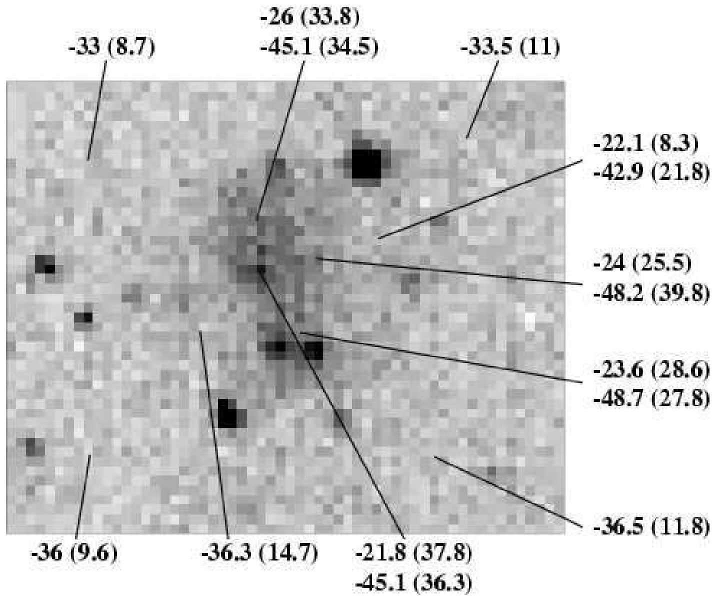

Figure 6.5: Hα image of RCW 69 with the Marseille Fabry-Perot interferometer. Radial velocities (LSR) are indicated with relative intensity values (in arbitrary units) in parentheses. The available data do not allow the internal kinematics to be modelled. The brightest star in the image is HD 110625, which is 2.5′ from the PN centre. Figure taken from Frew, Parker & Russeil (2006).

The offset field (not illustrated) has components centred at -1 kms^{-1} (Coalsack gas) and ~ -36 kms^{-1}, which traces the Carina arm, and which is seen to cover the field exterior to the body of the PN (see Figure 6.5). The Carina arm in this direction is generally considered to be at 2.5 kpc, but Franco (2000) has used the interstellar NaI D absorption-line profiles to a number of stars near to RCW 69 to suggest the near side of the Carina arm is as close as $D =$ 0.9–1.0 kpc in this direction.

A straight mean of the two intrinsic velocity components of the PN gives a systemic radial velocity of -35 kms^{-1} relative to the local standard of rest. Weighting with the velocities

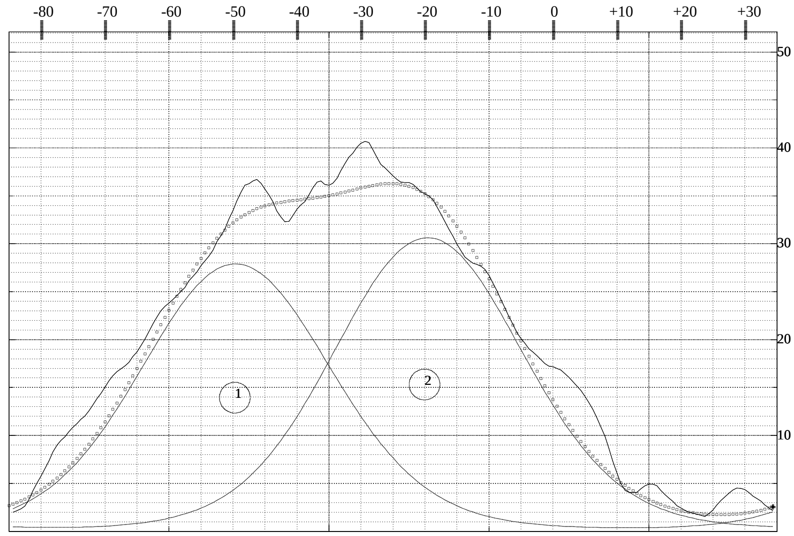

Figure 6.6: Background corrected Marseille F-P Hα spectrum at the centre of RCW 69 in an area of 45 arcsec diameter. Velocities in kms^{-1} are given with respect to the local standard of rest and the ordinate plots intensity (in arbitrary units). The overall profile can be modelled by two gaussian components (refer to text). Figure taken from Frew, Parker & Russeil (2006).

derived from our slit spectra leads to a final systemic velocity of -33 ± 3 kms^{-1}. This is, by coincidence, very similar to the diffuse emission tracing the near side of the Carina arm in this direction. Assuming the peculiar velocity of the PN is low (but possibly as high as ± 25 kms^{-1} following Nordström et al. 2004), the standard kinematic distance is ∼2–3 kpc; an earlier estimate by Russeil et al. (1998) placed RCW 69 at 2.1 kpc on the assumption that it was an HII region, following Brand (1986). However, if the near side of the arm is closer, then it may be as near as ∼ 1.0 kpc. Based on the available information, a kinematic distance of $1.5^{+1.0}_{-0.5}$ kpc is therefore adopted for RCW 69.

IPHAS PN-1. This PN is located at a favourable longitude ($l = 126\overset{\circ}{.}6$) for obtaining an estimate of a kinematic distance via its systemic radial velocity. The observed radial velocity as measured for the Hα and [N II] emission lines $V_{\rm hel} = -83.5 \pm 1.5$ kms^{-1} or $V_{\rm LSR} = -71.1 \pm 1.5$ corrected to the local standard of rest. The kinematic distance is calculated as $7.0^{+4.5}_{-3.0}$ kpc assuming a standard Galactic rotation curve (see Mampaso et al. 2006, for further details). The quoted error takes into account the observed velocity dispersion for young/intermediate-age stars (Nordström et al. 2004) along the line of sight.

HFG 2 (PHR 0742-3247). This high-excitation, optically-thin PN was discovered by Fesen, Gull & Heckathorn (1983) and confirmed as a true PN by Parker et al. (2006). The dimensions in this reference are given as $181'' \times 153''$. The 17th-mag central star is ionizing part of an extended HII region of dimensions $7' \times 5'$. That the source of ionization is the PN itself is shown by strong [O III] and weak HeII emission in the nebulosity immediately closest to the PN rim, on a SAAO spectrum taken in Feb 2004 (see Chapter 5). A CO detection to the surrounding HII region is reported by Brand et al. (1997). The measured LSR velocity, $+23.5$ kms^{-1}, leads to a kinematic distance for the PN of 1.9 ± 0.4 kpc.

Sh 2-200. A kinematic distance has been derived for the optically thin PN Sh 2-200 based on its 'physical' association with its ionized Strömgren sphere in the ambient ISM. The estimated distance is 660 ± 490 pc (Fich & Blitz 1984), based on a measured CO velocity from the surrounding ambient HII region (Blitz, Fich & Stark 1982). This object was discussed further in Chapter 4.

NGC 6751. Similarly for NGC 6751, a kinematic distance of 2.0 kpc has been adopted from Chu et al. (1991), using its association with a HII region ionized by the PN central star. See that reference for further details.

6.4.8 Model distances

Accurate distance determinations using photoionization modelling is a comparatively recent development. The development of powerful 2-D and 3-D photoionization codes (e.g. Ercolano et al. 2003a, b) allows the self-consistent determination of the PN structure, central star characteristics, and distance, once accurate spectrophotometric line mapping, narrowband imaging and/or kinematic data is available. A number of recent determinations using this techniques are given in table 6.9. However, the distance for Menzel 1 (Monteiro et al. 2005) has not been used, owing to no reliable CS magnitude (on which the photoionization modelling depends) existing.

Table 6.9: PN distances from photoionization modelling.

PN	D (pc)	Reference
NGC 3132	930	Monteiro et al. (2000, 2006)
NGC 6369	1550	Monteiro et al. (2004)
NGC 6781	950 ± 140	Schwarz & Monteiro (2006)
Abell 15	4010	Emprechtinger, Forveille & Kimeswenger (2004)
Abell 20	2350	Emprechtinger, Forveille & Kimeswenger (2004)
Hubble 5	1400 ± 300	Rice, Schwarz & Monteiro (2004)
Menzel 1	1050 ± 150	Monteiro et al. (2005)
Me 2-1	2300 ± 100	Surendiranath, Pottasch & García-Lario (2004)
MeWe 1-3	3950	Emprechtinger, Forveille & Kimeswenger (2004)

6.4.9 Cluster Distances

Physical membership of a PN in an open or globular star cluster is an important key that can help to unlock many of the problems facing PN research. Not only is a reliable distance obtained, for accurate estimation of the nebular properties, it also functions as a good calibrating object for a statistical distance indicator. Additionally, the age of the cluster indicates the mass of the progenitor star, which can be related to the chemistry of the resulting PN and also provides additional data for the WD initial-final mass relation (IFMR; Jeffries 1997; Weidemann 2000; Claver et al. 2001; Ferrario et al. 2005; Dobbie et al. 2006; Williams 2006; Kalirai et al. 2007).

The number of PNe thought to be genuine members of clusters is small (perhaps 1 or 2 at best within an open cluster, and 3 or 4 currently known in globular clusters). Köppen & Acker (2000) have discussed the occurrence of PNe in clusters, and derived a relationship between the age of a cluster and the expected number of PN candidates. Massive ($10^6\,M_\odot$) clusters should produce 1 PN per cluster of 2 Gyr age. The number is larger for younger clusters, but there are hardly any clusters of this age and mass in the Milky Way. The Magellanic Cloud 'blue globular' clusters may be excellent targets for a deep search for new PNe, but this topic goes beyond the scope of this work.

It should be noted that the recent increases in number of both Galactic PNe (see Chapter 2) and open clusters (e.g. Dias et al. 2002) have increased the probability of positional coincidences between these two classes of object. Table 6.10 includes the results of a critical literature search on the associations between PNe and star clusters in the Milky Way. Previous compilations of positional coincidences between PNe and clusters have been given by Žižňovský (1975) and Kohoutek (2001). Additional clusters have also been recently tabulated by Majaess, Turner & Lane (2007) which largely overlaps the list tabulated here. An additional association has been presented by Bonatto, Bica & Santos (2008).

However, some of the associations mentioned by these authors are omitted from Table 6.10. For example, the nearby open clusters NGC 6475 (M 7), Basel 5 and Trumpler 31 are projected on the Galactic bulge, so the distant, reddened, compact PNe in this direction, tabulated by Žižňovský (1975), Kohoutek (2001), and Majaess, Turner & Lane (2007), are obviously unrelated. The fourth column of the table gives a flag stating my opinion on the likelihood of a physical association, based on all available information, including new distance estimates and unpublished radial velocities. A discussion of the most interesting associations is given below.

Globular clusters: Pease 1 (K 648) (Buell et al. 1997; Alves, Bond & Livio 2000) and GJJC 1 (Cohen & Gillett 1989; Cudworth 1990; Borkowski & Harrington 1991) are bona fide members of their respective globular clusters M 15 and M 22. Pease 1 has been imaged with *HST* (Alves, Bond & Livio 2000) and has good estimates of its angular size and integrated flux which qualify it to be a primary SB-r calibrator (see below). However, an accurate flux for GJJC 1 is still wanting. Jacoby et al. (1997) conducted an extensive search for PN candidates in globular clusters,[6] finding two, JaFu 1 in Palomar 6 and JaFu 2 in NGC 6441. JaFu 2 is an almost certain member of NGC 6441. JaFu 1 was the less convincing candidate, owing to its large angular distance from the core of Palomar 6 (though still within the cluster tidal radius). Its radial velocity was marginally consistent with membership. However, a new velocity for Palomar 6, $V_{\rm hel} = +181 \pm 3\,{\rm kms}^{-1}$ (Lee, Carney & Balachandran 2004), greatly increases the probablity of membership. JaFu 2 is adopted as a primary SB-r calibrator but JaFu 1 has been excluded, pending a more accurate determination of an integrated Hα flux.

[6] Two possible PN candidates in metal-rich globular clusters were found as a by-product of the MASH-II catalogue (Miszalski et al. 2008), in Terzan 5 and NGC 6760. Both objects have been identified as late-type stars based on our unpublished spectroscopy and IR imagery (Parker et al., unpublished). Late-type stars can present apparent 'emission' near Hα due to the relative brightness of the red continuum around 6600Å compared to the deep absorption dips from TiO band-heads at adjacent wavelengths.

NGC 2818: Tifft, Connolly & Webb (1972) argued that NGC 2818 was a member of the open cluster of the same name, and this became entrenched in the literature as a valid association, still accepted today (e.g. Lee et al. 2007). Dufour (1984) and Pedreros (1989) assumed a physical association, but gave conflicting distances to the cluster. Other cluster studies have been those of Surendiranath et al. (1990), Geisler et al. (1992) and Stetson (2000). The PN radial velocity has been accurately measured by Meatheringham, Wood & Faulkner (1988) as $V_{\rm hel} = -1.0 \pm 3.0$ kms^{-1}, in agreement with the other values quoted by Durand et al. (1998). However Mermilliod (2001) obtained CORAVEL velocities for 12 red giant stars in the cluster to obtain a mean velocity of $<V_{\rm hel}> = +20.69 \pm 0.29$ kms^{-1}, showing unambiguously that the two objects are unrelated.

NGC 2438: This well-known annular PN is superposed on the bright open cluster NGC 2437 (Messier 46). Despite its brightness, this cluster was relatively unstudied until recently (e.g. Cuffey 1941; Stetson 1981). Sharma et al. (2006) derived $E(B-V) = 0.10$ mag, $D = 1.51$ kpc and an age of 250 Myr for the cluster. Based on 2MASS data, Majaess, Turner & Lane (2007) derive $E(B-V) = 0.13 \pm 0.05$, $D = 1.7$ kpc and an age of 220 Myr. Bonatto, Bica & Santos (2008), also using 2MASS data, give $E(B-V) = 0.10 \pm 0.02$, $D = 1.5 \pm 0.2$ kpc and an age of 250 Myr (corresponding to a turnoff mass of $\simeq 3.5\ M_{\odot}$).

Cuffey (1941) quoted a mean cluster velocity of +41.4 kms^{-1}, based on measurements of five stars by O. Struve (private communication to Cuffey). Cuffey noted that the velocity for the PN of +77 kms^{-1} (Campbell & Moore 1918) was different, making "its physical membership in the cluster very unlikely". O'Dell (1963) determined $V_{\rm hel} = 75 \pm 5$ kms^{-1} for the PN and $V_{\rm hel} = 48 \pm 3$ kms^{-1} based on one star in the cluster, confirming the earlier conclusion of Cuffey (1941) that the PN is unrelated. However, Pauls & Kohoutek (1996) measured $V_{\rm hel} = 60.3 \pm 3.6$ kms^{-1} and $V_{\rm hel} = 60.8 \pm 4.0$ kms^{-1} for PN and cluster respectively, concluding that they are indeed associated. The published reddening values are similar, and the Hα surface brightness distance for NGC 2438 of ∼1.4 kpc (see below), indirectly supports the association.

We measured a velocity for NGC 2438 with the same instrumentation on the same night as PHR 1315-6555 (see §6.4.10), and obtained $V_{\rm hel} = 73 \pm 6$ kms^{-1}, in excellent agreement with the estimates from Campbell & Moore (1918) and O'Dell (1963), and the values published by Meatheringham et al. (1988) and Corradi et al. (2000) of $V_{\rm hel} = 74 \pm 4$ kms^{-1} and $V_{\rm hel} = 74 \pm 5$ kms^{-1} respectively. Since Mermilliod et al. (1989, 2007) has determined an accurate cluster velocity of $V_{\rm hel} = 49.0 \pm 0.5$ kms^{-1} from two spectroscopic binaries in the cluster, there is little doubt that the PN is unrelated to the cluster, being just a chance superposition. This conclusion has been confirmed with new *AAOmega* radial velocity data (Kiss et al. 2008).

OH 231.8+4.2: Like NGC 2438, this object is also close to NGC 2437 (M 46). Commonly known as the Rotten Egg Nebula or Calabash Nebula, this strongly bipolar reflection/emission nebulosity is generally regarded as a preplanetary nebula (Kastner & Weintraub 1995; Sánchez Contreras et al. 2000; Meakin et al. 2003). There is an extensive literature on this object so only a brief sketch is provided here (see also Balick & Frank 2002). Unlike the case of NGC 2438, the systemic radial velocity is consistent with membership of M 46, and the phase-lag distance of $\sim$1.4 kpc (Bowers & Morris 1984; Reipurth 1987; Kastner et al. 1992; Shure et al. 1995) is also consistent with membership (Jura & Morris 1985). However, the fact that there is a Mira star (spectral type M9) at the centre, designated QX Pup (Cohen 1981; Kastner et al. 1998; Sánchez Contreras, Gil de Paz & Sahai 2004), combined with the strongly bipolar nature of the nebulosity, seems to indicate that the nebula has more in common with D-type symbiotic outflows (Corradi 1995; Corradi et al. 1999) rather than true pre-PNe. Either way, this object is not suitable as a calibrator for the SB-r relation.

Wray 17-31 (VBRC 2 = ESO 166-PN21): This evolved PN has been proposed to be a member of the open cluster IC 2488 (Pedreros 1987), despite the large angular separation of 53$'$ (19 pc at the nominal cluster distance). Pedreros gives a distance to IC 2488 of 1445 ±120 pc, while the more recent study of Clariá et al. has 1250 ±120 pc. The PN was studied by Peña et al. (1997) who estimated a distance of 1200 ±200 pc, though no systemic velocity was given. A new SB-r distance derived here is 1400 ±120 pc. A new velocity for the PN of $V_{\rm hel} = 61 \pm 8$ kms^{-1} is also determined here (observed on the same night as NGC 2438), which is very different to the cluster velocity of $< V_{\rm hel} > = -2.63 \pm 0.06$ kms^{-1} obtained by Clariá et al. (2003). The PN and cluster are not associated.

NGC 2899: This bipolar Type I PN (López et al. 1991) has about the same angular separation (54$'$) from IC 2488 as does Wray 17-31. The heliocentric radial velocity is $+3.4 \pm 2.8$ kms^{-1} (Bohuski & Smith 1974; Meatheringham, Wood & Faulkner 1988; Durand, Acker & Zijlstra 1998), which is marginally outside the error bar of the cluster velocity measurement (Clariá et al. 2003). Furthermore, the morphology and composition of this PN suggests a massive progenitor, so no large peculiar velocity with respect to the local standard of rest is expected. The distance to the PN from the high-trend SB-r relation is 1400 ±400 pc, which agrees with the cluster distance of 1450 pc (Pedreros 1987). However the different reddenings and velocities and importantly, the large angular separation between the two objects, suggests a physical association is possible but unlikely.

NGC 2452: An recent discussion of this interesting PN has been provided by Majaess, Turner & Lane (2007). The distance to the young open cluster NGC 2453 is 5900 pc (Mallik, Sagar & Pati 1995) or a somewhat closer distance of 5250 pc (Moitinho et al. 2006). A new SB-r distance for the PN is 3800 pc (using a high-trend SB-r relation, and 3100 kpc using a mean trend), suggesting the PN is in the foreground of the cluster. On the other hand, the heliocentric radial velocity for the PN is given as $+68 \pm 4$ kms^{-1} (Campbell & Moore 1918), $+65 \pm 3$ kms^{-1} (Meatheringham, Wood & Faulkner 1988), and $+62.0 \pm 2.8$ kms^{-1} (Durand, Acker & Zijlstra 1998), which agrees within the errors with the velocity of a single blue giant cluster member, $v = +67 \pm 14$ kms^{-1}, from one spectrogram (Moffatt & Fitzgerald 1974). These authors noted that the lines appeared to be double, so it is probably a spectroscopic binary. If that is the case, the systemic radial velocity remains unknown.

Table 6.10: A list of cluster / PN associations.

Cluster	Age (Myr)	PN	Name	Membership	References[⊕]
NGC 1912 (M 38)	250	G172.1 + 00.8	Abell 9	no	31, 39
NGC 2437 (M 46)	220	G231.8 + 04.1	NGC 2438	no	6, 7, 8, 31, 44, 57, 60
NGC 2437 (M 46)	220	...	OH 231.8+4.2	probable[†]	31, 44
NGC 2453	40	G243.3 − 01.0	NGC 2452	uncertain	15, 31, 48, 55, 56
NGC 2818	700	G261.9 + 08.5	NGC 2818	no	1, 2, 3, 4, 5, 31, 32, 57
NGC 2910	50	G275.5 − 01.3	Pe 2-4	no	31, 48, 54, 55
NGC 2925	110	G275.9 − 01.0	NeVe 3-1	no	31, 54, 55
NGC 3572	5	...	PhJa 1	not PN[§]	13, 14
NGC 4463	90	G300.7 − 02.0	He 2-86	no	31, 54
NGC 5617	80	G314.6 − 00.1	PHR 1429-6043[‡]	unknown	16, 17, 31
NGC 5999	400	G326.1 − 01.9	vBe 3	no	31, 51
NGC 6067	60	G329.5 − 02.2	HeFa 1	no	18, 19
NGC 6087	65	G327.7 − 05.4	KoRe 1	no	20, 21
NGC 6208	1000	G333.7 − 05.9	PHR 1650-5350	no	31, 50
NGC 6231	4	G343.5 + 01.2	PHR 1653-4143	no	31, 42, 43
NGC 6231	4	G343.6 + 01.1	PHR 1654-4143	no	31, 42, 43
NGC 6281	320	G347.7 + 02.0	Vd 1-8	no	31, 35, 36, 54
NGC 6469	250	G006.4 + 02.0	M 1-31	no	31, 57
NGC 6819	2500	...	PaTe 1	unknown	31, 38
NGC 6846	...	G068.7 + 01.9	K 4-41	unlikely	31, 55
NGC 7261	...	G104.1 + 01.0	Bl 2-1	no	31, 47
NGC 7423	1400	G107.7 − 02.2	M 1-80	no	31, 49, 55
IC 2488	180	G277.7 − 03.5	Wray 17-31	no	9, 10, 11, 31
IC 2488	180	G277.1 − 03.8	NGC 2899	unlikely	31
Anon	1000	G167.0 − 00.9	Abell 8	unlikely	31, 57
Anon	...	G076.3 + 01.1	Abell 69	unknown	31, 55
Berkeley 49	...	G070.9 + 02.4	KLW 6	unlikely	31, 55
Berkeley 51	...	G072.1 + 00.1	K 3-57	unknown	31, 55
Berkeley 81	1000	G033.8 − 02.6	NGC 6741	possible	31, 55
BH 91	160	G283.9 − 01.8	Hf 4	no	31, 54, 55
ESO 96-04	700	G305.4 − 03.2	PHR 1315-6555	probable	28, 29, 30, 31
ESO 165-09	900:	G274.8 − 05.7	PHR 0905-5548	no	31, 54
ESO 493-03	400	G242.3 − 02.4	FP 0739-2709	no	31, 54
Hyades moving group	600	G036.1 − 57.1	NGC 7293	possible	12
Lynga 5	50:	G324.8 − 01.1	He 2-133	no	41, 55
Melotte 111	500	G339.9 + 88.4	LoTr 5	no	40, 45, 46
Ruprecht 66	...	G258.4 + 02.3	PHR 0840-3801	unknown	31
Teutsch 110	...	G306.7 − 01.5	MPA 1326-6407	unknown	58, 59
NGC 6441	12000*	G353.5 − 05.0	JaFu 2	probable	27
NGC 6656 (M 22)	12500	G009.8 − 07.5	GJJC 1	certain	24, 25, 26, 34
NGC 7078 (M 15)	11800	G065.0 − 27.3	Pease 1 (K 648)	certain	22, 23, 33, 34
Palomar 6	12000*	G002.1 + 01.7	JaFu 1	probable	27, 53

Notes to Table 6.10:

⊕ The references refer to the listed open clusters, and if data is available, to the PN also.

† This object is a likely symbiotic outflow;

‡ Uncertain PN;

§ Probably a bright-rimmed globule;

* Age set to 12 Gyr.

References to Table 6.10:

1. Johnson (1960), 2. Tifft, Connolly & Webb (1972), 3. Dufour (1984), 4. Pedreros (1989), 5. Surendiranath et al. (1990), 6. O'Dell (1963), 7. Pauls & Kohoutek (1996), 8. Stetson (1981), 9. Peña et al. (1997), 10. Clariá et al. (2003), 11. Pedreros (1997), 12. Eggen (1984), 13. Phelps & Janes (1991), 14. Smith et al. (2003), 15. Mallik, Sagar & Pati (1995), 16. Clariá, Lapasset & Minniti (1989), 17. Haug (1978), 18. Henize & Fairall (1983), 19. Eggen (1983), 20. Koester & Reimers (1989), 21. Sagar & Cannon (1997), 22. Pease (1928), 23. Buell et al. (1997), 24. Cohen & Gillett (1989), 25. Cudworth (1990), 26. Borkowski & Harrington (1991), 27. Jacoby et al. (1997), 28. Andrews & Lindsay (1967), 29. Carraro et al. (1995), 30. Janes & Phelps (1994), 31. This work, see text, 32. Mermilliod et al. (2001), 33. Alves, Bond & Livio (2000), 34. Salaris & Weiss (2002), 35. Feinstein & Forte (1974), 36. Mermilliod (1981), 37. Kalirai et al. (2001), 38. M. Kronberger (2005, pers. comm.), 39. Subramaniam & Sagar (1999), 40. Odenkirchen et al. (1998), 41. Lynga (1964), 42. Sung et al. (1998), 43. Baume et al. (1999), 44. Sharma et al. (2006), 45. Graham et al. (2004), 46. Bounatiro (1993), 47. Janes & Adler (1982), 48. Moitinho et al. (2005), 49. Hasegawa et al. (2004), 50. Clariá et al. (2006), 51. Piatti, Claria & Bica (1999), 52. Sagar & Griffiths (1998), 53. Lee, Carney & Balachandran (2004), 54. Kharchenko et al. (2005), 55. Majaess, Turner & Lane (2007), 56. Moffatt & Fitzgerald (1974); 57. Bonatto, Bica & Santos (2008); 58. Kronberger et al. (2006); 59. Miszalski et al. (2008); 60. Kiss et al. (2008).

The accepted age of 25–40 million years for NGC 2452 (Moffatt & Fitzgerald 1974; Mallik, Sagar & Pati 1995; Moitinho et al. 2006) indicates a very high progenitor mass ($\sim 7\,M_{\odot}$ or greater) for the PN if it is a physical member. Using a standard IFMR, the CS mass must be at least $1.0\,M_{\odot}$, and very rapid evolution of the CS would be expected (refer to equation 1.3). This fact alone makes it unlikely that NGC 2452 is physically associated. However, Hasan, Kilambi & Hasan (2008) have estimated a closer distance of 3310 pc, $E(B-V) = 0.47$ and an age of $\sim$200 Myr for the cluster, in contradiction to the earlier studies. Futher work is needed to definitively state if the PN and cluster are related.

NGC 6741: This object is a SB-r calibrator: the adopted distance is 2.8 kpc from a combination of extinction-distance and kinematic measurements (see above). The adopted extinction value for the PN is $E(B-V) = 0.71$ ($c = 1.03$). The parameters of the old open cluster Berkeley 81 ($D = 3.0$ kpc and $E(B-V) = 1.0$) from Sagar & Griffiths (1998) are in reasonable agreement. A radial velocity for the cluster will allow a conclusion to be made on any association.

Abell 8: This faint round PN was discovered by Abell (1955, 1966). Bonatto, Bica & Santos (2008) have identified a new intermediate-age open cluster in the field of this PN, and give a reddening of $E(B-V) = 0.29 \pm 0.03$ and a distance, $D = 1.7 \pm 0.1$ kpc to it, based on 2MASS photometry. The reddening to the PN is determined from the spectroscopic data of Kaler (1983), Ali (1999) and Phillips, Cuesta & Kemp (2005), from which $c = 0.75 \pm 0.12$, or $E(B-V) = 0.51 \pm 0.09$ is adopted. The value of Kaler, Shaw & Kwitter (1989) has been rejected as being too high. A new flux derived here from VTSS is $F(\mathrm{H}\alpha) = -12.00 \pm 0.10$. A H$\alpha$+[NII] flux of $F(\mathrm{red}) = -11.60$ is also given by Ali, Pfleiderer & Saurer (1997). Correcting for the contribution of the [NII] lines, gives $F(\mathrm{H}\alpha) = -11.80 \pm 0.10$, where a mean [NII]/H$\alpha$ ratio of 0.6 has been adopted from Kondrateva (1971), Kaler (1983), Kaler, Shaw & Kwitter

(1989), Ali (1999) and Phillips, Cuesta & Kemp (2005). A final flux, $F(\mathrm{H}\alpha) = -11.90 \pm 0.10$, has been adopted.

Using the diameter of 60″ (Abell 1966) and the flux adopted here, a mean-trend SB-r distance is ∼3.2 kpc, which places the PN in the background of the cluster. This has been preferred to the low-trend distance, as despite its round morphology, the PN seems optically thick based on the available spectroscopic data. The reddenings of cluster and PN are in proportion with the distance ratios, providing additional evidence that the PN is very likely in the background of the cluster.

FP 0739-2709: This faint evolved PN was found by the writer and lies 8′ from the sparse open cluster ESO 493-SC03 (and also noted from the MASH catalogue by Majaess, Turner & Lane 2007). The SB-r distance for the PN is 2000 ± 600 pc, which is just consistent with the cluster distance of 1400 pc (Kharchenko et al. 2005). However, assuming that the brightened rim of the PN is a signature of an ISM interaction, the proper motion of the CS can be inferred to be a southwest direction. This is inconsistent with the proper motion components of μ_{α},μ_{δ} = +0.44, +2.31 mas yr^{-1} given by Kharchenko et al. (2005). The objects are not considered to be physically associated.

He 2-133 (ESO 177-10): This compact PN was noted by Majaess, Turner & Lane (2007) to be coincident in position with the poorly studied open cluster Lynga 5. Majaess et al. derived a CMD from 2MASS data to determine approximate values for the reddening and distance: $E(B-V) = 1.18 \pm 0.11$ and $D = 1.95 \pm 0.35$ kpc respectively for this young cluster (age of ∼ 50 million years). As noted by Majaess et al., the reddening of the PN (Tylenda et al. 1992) is much greater than the cluster. A new mean SB-r distance derived here, $D = 5.0 \pm 1.5$ kpc, confirms the PN is a background object.

HeFa 1 and KoRe 1: These two small and faint high-excitation PNe (Henize & Fairall 1983; Koester & Reimers 1989) have low-trend SB-r distances of ∼3.7 kpc and ∼4.8 kpc respectively, placing them in the far background of their putative open cluster hosts. Note that using a mean SB-r relation places them even further away. Neither PN is associated with an open cluster.

M 1-80: Following Majaess, Turner & Lane (2007), I adopt the parameters for the nearby open cluster NGC 7423 (=Berkeley 57) from Hasegawa et al. (2004): $D = 4.15$ kpc and $E(B-V)$ = 0.75. A new mean-trend SB-r distance for the PN is 6.1 ± 2.0 kpc, assuming a reddening of $E(B-V) = 0.4$. It is not clear at this point if the objects are physically associated. A radial velocity of the cluster is needed to confirm or reject any association.

NeVe 3-1: This faint PN was found by Kerber et al. (1998). A new SB-r distance is 3.5 kpc, which places it in the background of the cluster NGC 2925, which is at 770 pc (Kharchenko et al. 2005). The PN reddening is $E(B-V) = 0.75$ (Kerber et al. 1998), compared to $E(B-V)$ = 0.11 for NGC 2925 (Janes & Adler 1982), confirming that they are unrelated.

PHR 0905-5548: This MASH PN is located $\sim 9'$ from the open cluster ESO 165-SC09 (this coincidence also noted by Majaess, Turner & Lane 2007). The SB-r distance is 4.0 ± 1.0 kpc, which is an order of magnitude further than the cluster distance of just 450 pc (Kharchenko et al. 2005). The objects are not considered to be physically associated.

NGC 7293: In addition, Eggen (1984) proposed that the Helix Nebula is a member of the Hyades moving group, which includes the well-known Hyades and Praesepe open clusters, as well as numerous field stars in the solar neighbourhood. By forcing the space motion of the PN to agree with the moving group convergent point, he derived a distance of 180 pc, in reasonable agreement with the recent trigonometric distance of 219 pc (Harris et al. 2007). Hence the association is plausible on kinematic grounds. However recent work has indicated that the stars of the Hyades moving group are not coeval (Famaey et al. 2007, and reference therein), which favours a dynamical (resonant) origin for the stream. If that is the case, no age estimate for the Helix progenitor can be inferred.

Other candidates: The mean SB-r distances for the planetary nebulae Abell 9, Bl 2-1, He 2-86, Hf 4, M 1-31, Pe 2-4 (=He 2-31), PHR 1650-5350, Vd 1-8 (=Sa 2-167), and vBe 3 are all in the range 5–10 kpc, placing them far beyond the candidate open clusters listed in table 6.10, based on available data. A second candidate cluster (BH 72) has been proposed for Pe 2-4, but there is no astrophysical data available for it.

For the other associations listed here, no conclusions can be drawn at this stage. Lack of distance and/or reddening data for the clusters NGC 6846, Berkeley 49, Berkeley 51, Ruprecht 66 and Anon (Turner) listed in Majaess et al. (2007) precludes any inference being made on the validity of the proposed associations. However SB-r distances for K 4-41 and KLW 6 are $\sim$9.0 and $\sim$10 kpc respectively, suggesting they are in the background of the proposed clusters. No data are available on the possible association between the small cluster Teutsch 110 and the compact planetary MPA1326-6407 (Miszalski et al. 2008), nor for the new nebula Patchick-Teutsch 1 (P. Teutsch, pers. communication, 2006) located $27'$ northeast of the rich, intermediate-age cluster NGC 6819.

6.4.10 PHR 1315-6555

Of great interest is the discovery of a faint Type I bipolar planetary nebula (PHR 1315-6555) associated with the intermediate-age open cluster ESO 96-SC04, based on images from the AAO/UKST Hα Survey. This section will discuss the discovery, spectroscopic observations, and velocity determination of the PN, and the salient parameters of its host cluster, ESO 96-SC04. The importance of this PN/OC association to the WD initial-final mass relation is important, and will be the subject of a separate paper (Parker, Frew, Köppen & Dobbie 2008, in preparation).

The PN was discovered on Hα survey field h137 within $\sim 20''$ of the centre of the distant open cluster ESO 96-SC04. Despite the cluster being imaged with a CCD in B and V on the

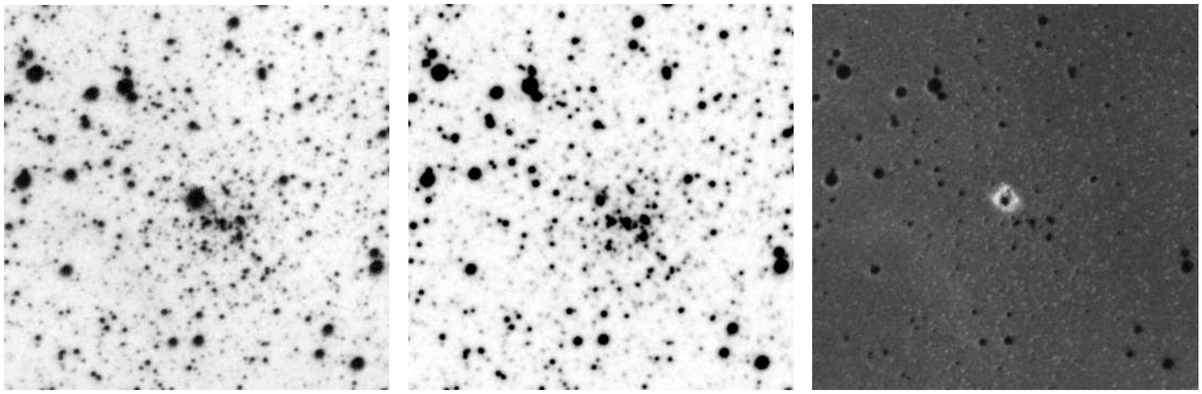

Figure 6.7: 4×4 arcminute extracts of SuperCOSMOS data around the newly discovered bipolar PN (PHR 1315-6555) from the 3-hour Hα survey data (left), matching 15 minute Tech-Pan SR data (middle) and a simple quotient image (right). The new PN is 15×12 arcseconds in size and is only *obvious* in the Hα image. Note the well matched depth for point sources between the two exposures and location of the PN well within the borders of the cluster.

ESO NTT 3.5-m telescope by Carraro et al. (1995) the PN was not seen due to its relatively low-surface brightness. Evidently the PN had been missed because no deep images were taken in the R-band (which passes Hα). It is the fine resolution and high sensitivity of the narrowband AAO/UKST Hα survey which allowed discovery of the the nebula. The morphology appears to be that of a compact bipolar PN approximately $19'' \times 18''$ in size, though its detailed morphology is uncertain (owing to its small angular size).

In Figure 6.7, $5' \times 5'$ images of the host cluster are presented, in Hα light (left), broadband SR (middle), and a quotient image (Hα/SR image) on the right. The quotient image is an effective means of revealing the nebula more clearly.

Nebular parameters

Both low and medium resolution spectra were obtained for PHR 1315 − 6555 at the 1.9-m SAAO telescope in June 2003 and February 2004. Spectra have also been taken with the 2.3-m MSSSO telescope at Siding Spring (Parker et al., in preparation). See Chapter 5 for a summary of the instrumentation and data reduction; figure 1.13 includes a low-resolution SAAO spectrum from June 2003. Two member stars from the cluster were also observed at higher resolution for radial velocity determination in Feb 2004 (see below). Additional spectra have been taken of these stars and the PN by Q. Parker, and will be the subject of a separate paper. The line ratios of the PN are summarised in Table 5.2 and Table 5.3.

Integrated Hα and Hβ fluxes were determined from the measured fluxes (knowing the dimensions of the slit) and scaling up by a geometric factor to the full dimensions of the PN. We estimate $\log \mathrm{F(H}\alpha) = -12.55 \pm 0.20$ and $\log \mathrm{F(H}\beta) = -13.35 \pm 0.20$. The adopted distance to the cluster (and hence to the PN) is 11.8 kpc (Carraro et al. 1995). The geometric mean angular radius of $9.3''$ leads to an intrinsic radius of 0.5 pc, typical of an evolved PN. We do not have detailed kinematic information, so assuming a mean expansion velocity of 24 kms^{-1}, typical of an old PN (see Chapter 9), this size corresponds to a nebular age of ∼21,000 years. As noted in

Chapter 5, this PN may be classified as a Type I object according to the definition of Peimbert & Torres-Peimbert (1983), but is slightly outside the cutoff of Kingsburgh & Barlow (1994).

The open cluster ESO 96-SC04: distance, reddening and age

ESO 96-SC04 (also previously identified as AL 1, BH 144 and AM 1311-653) is an interesting, compact open cluster first recorded by Andrews & Lindsay (1967) on ADH Schmidt plates. They described the cluster as being made up of "faint stars" and gave an angular diameter of 75″. It was independently discovered by van den Bergh & Hagen (1975) in their survey of southern clusters using the Curtis-Schmidt telescope at CTIO, before being noted on ESO Schmidt plates and designated ESO 96-SC04 (Lauberts 1982). Arp & Madore (1987) also included it in their Catalogue of Southern Peculiar Galaxies and Associations (under the category of miscellaneous objects) with the designation AM 1311-653. They described it as a "faint globular cluster".

The appearance of this remote open cluster is indeed rather globular-like on the ESO R plate as it is well defined and has a fairly stong central concentration. It is fainter on the SERC B plate due to the moderately high reddening in this direction (see below). There has been much confusion in the literature regarding the nomenclature of this cluster, a consequence of a number of published positions being in error (e.g. Tadross 2001, 2002).[7] Until recently the best position was that given by Carraro & Munari (2004), who quoted $13^{\mathrm{h}}15^{\mathrm{m}}09^{\mathrm{s}}$ $-65^{\circ}55'51''$. Other positions were given by Lauberts (1982) and by Carraro & Munari (2004); this position differs somewhat from Lauberts (1982) and is simply precessed from that quoted by Carraro et al. (1995), which is in turn taken directly from van den Bergh & Hagen (1975).

To help resolve the discrepancies in the literature, we measured the position from the online SHS short-red pixel data (Parker et al. 2005a) of the cluster region. Since the cluster appears compact, approximately circular and centrally concentrated, a 1′ diameter aperture was overlaid on the cluster SR-band pixel data in the GAIA image viewer, and appears a good match to the obvious cluster core in a high contrast image. The images have an accurate inbuilt WCS; the position of the centre of this aperture was measured and is taken as the cluster centre. The new determination is $13^{\mathrm{h}}15^{\mathrm{m}}16^{\mathrm{s}}$ $-65^{\circ}55'16''$ (J2000), which clearly differs from the position from Carraro & Munari (2004) by about 0.6′. In fact a new position determined by Carraro et al. (2005) is in excellent agreement with ours, and with the position published by Lauberts (1982).

A number of studies have been made of this cluster over the last decade. Janes & Phelps (1994) estimated a distance of 7.57 kpc (see also Phelps et al. 1994 and Friel 1995), though Carraro et al. (1995) determined a greater distance of 11.8 kpc, and dtermined a reddening of $E(B-V) = 0.75$. Carraro & Munari (2004) derived a distance of 12.0 kpc to the cluster, while Carraro, Janes & Eastman (2005) estimated a distance of 16.9 kpc, which is considerably higher than previous determinations, due to their low adopted value for the reddening of $E(B-V) = 0.35$. Instead, by using a value of $E(B-V) = 0.70$, the distance becomes 10.1 kpc, in good agreement with earlier determinations. The relevant data are summarised in Table 6.11. The reader is also referred to the summaries of Dias et al. (2002) and Tadross et al. (2002).

[7] At the time of writing, the Simbad database lists AM 1311-653 as a galaxy, despite the description in Arp and Madore (1987). However AL 1 and ESO 96-SC04 (BH 144) are listed separately in Simbad.

Table 6.11: Fundamental parameters from the literature for ESO 96-SC04

Reference	Telescope	D (kpc)	E(B-V)	Age (Myr)
PJM94, JP94	0.9m CTIO	7.57	0.72	...
CVO95	3.5m NTT	11.8	0.75	700
CM04	1.0m SAAO	12 ± 1	0.7 ± 0.2	800
CJE05	1.0m CTIO	19.9	0.35	800

References: CVO95, Carraro et al. (1995); PJM94, Phelps et al. (1994); JP94, Janes & Phelps (1994); CM04, Carraro & Munari (2004); CJE05, Carraro et al. (2005)

Dutra & Bica (2000) used DIRBE/IRAS 100μm dust emission to estimate a total line-of-sight reddening of $E(B-V) = 0.94$ in this direction. For the cluster, they assumed a reddening value of $E(B-V) = 0.72$ for a distance of 7.57 kpc, concluding that the difference of $E(B-V) = 0.22$ is due to obscuration behind the cluster. The cluster's distance from the Galactic plane is $|z| = 420$ pc if D = 7.6 kpc. and $|z| = 660$ pc if D = 12.0 kpc, so either the reddening determined from the CMD is underestimated, the total DIRBE reddening estimate is too high, or there is significant dust at large distances from the plane beyond the cluster. The last alternative is the least likely. Since the reddening of the PN estimated from our spectrophotometry is consistent with the various cluster determinations (Janes & Phelps 1994; Carraro et al. 1995; Carraro & Munari 2004), the total DIRBE reddening may be in error.

Carraro et al. (1995) give an age of 700 Myr for the cluster. Phelps et al. (1994; see also Janes & Phelps 1994) and Carraro et al (2005) give slightly greater ages of 800 Myr. Hence, the cluster is comparable to the Hyades in age or slightly older.

The Association of PHR 1355-6555 and ESO 96-SC04

We have used the SAAO medium-dispersion spectrum taken on 27/06/2003 with the 1200R grating to determine a radial velocity for the PN. The observed emission lines give a heliocentric radial velocity of $V_{\rm hel} = +51.6 \pm 15.0$ kms^{-1}, derived from the IRAF EMSAO package. For the cluster, Frinchaboy et al. (2006a) have measured a radial velocity of $V_{\rm hel} = +40 \pm 10$ kms^{-1} from spectra of three member stars obtained with the 4-m Blanco telescope. We have also determined a cluster velocity of $V_{\rm hel} = 50 \pm 10$ kms^{-1} based on observations of two cluster members, in agreement with the cluster velocity of Frinchaboy et al. (2006a), and with the PN radial velocity determined here. The equivalence of the radial velocities provides a very strong confirming argument for membership of the cluster, even though proper motion data are currently lacking. It seems quite certain that the PN is a bona fide member of ESO 96-SC04.

With a reliable Hα flux and distance, this PN is used as a calibrator in the Hα SB–r relation presented herein. As a confirmation, the bipolar trend equation (see Chapter 7) was recalculated without PHR 1355-6555 as a calibrator (to avoid a circular argument) and used to estimate a distance to the PN of 9.7 $\pm$ 3.1 kpc. This is consistent with the cluster distance and lends weight to the argument for membership, and its validity as a calibrating nebula.

Assuming an age for the cluster of 700–800 Myr, the progenitor mass was $\sim$2.5 M$_\odot$ (e.g. Girardi et al. 2000), the exact value of which depends on the metallicity. A preliminary estimate of the cluster metallicity is given by Frinchaboy et al. (2006a), [Fe/H] = -0.51, based on two stars. Accurate photometry of the central star is desirable (but will need a large telescope) in order to determine the CS luminosity and temperature via the Zanstra method. Fitting these parameters to the theoretical HR diagram will provide a CS mass which will be an important datum for the WD initial-final mass relation.

Did ESO 96-SC04 originate in the CMa Dwarf Galaxy?

The cluster ESO 96-SC04 has been proposed as a possible member of the Galactic Anticenter Stellar Structure (GASS), otherwise known as the Monoceros Stream. This stream was first identified by Newberg et al. (2002) from data obtained with the Sloan Digital Sky Survey, and confirmed by Yanny et al. (2003) and Ibata et al. (2003). The Monoceros stream has been proposed to be a tidal stream associated with a putative satellite galaxy, the Canis Major Dwarf galaxy (Martin et al. 2004). A comprehensive synthesis of the Monoceros Stream has been compiled by Peñarrubia et al. (2005). However, Rocha-Pinto et al. (2006) have suggested that the CMa dwarf is part of a larger Argo system. Bellazzini et al. (2005) showed that the original overdensity in Canis Major is real and that the 'Argo system' is probably the signature of a Galactic warp. The nature of the CMa overdensity as the core of a disrupted dwarf has been confirmed recently by Dinescu et al. (2005). However state that the CMa/Monoceros structure is not a disrupted satellite, but is instead the signature of the Galactic warp in this direction. At the time of writing, there is still no consensus on its origin.

A number of star clusters have been proposed to be asocciated with the CMa Dwarf/Monoceros Stream (Martin et al. 2004; Bellazzini et al. 2004; Forbes et al. 2004; Frinchaboy et al. 2004), including ESO 96-SC04. Frinchaboy et al. (2006a) measured a radial velocity for three stars in ESO 96-SC04 but were unable to conclude whether the cluster was physically associated with the GASS. Using our adopted heliocentric RV for the PN, we determined the galactocentic velocity using the equation provided by Frinchaboy et al. (2006b; see also Crane et al. 2003, and Frinchaboy et al. 2004):

$$V_{\rm gsr} = V_{\rm hel} + 9\cos b\cos l + 232\cos b\sin l + 7\sin b \tag{6.19}$$

For $V_{\rm hel} = 51.6 \pm 15.0$ kms^{-1}, this translates to $V_{\rm gsr} = -133 \pm 20$ kms^{-1}. The velocity is marginally consistent with GASS membership (see Frinchaboy et al. 2006b), but is also consistent with circular Galactic rotation at the adopted distance. Eventually a proper motion determination will confirm whether the cluster is a physical member of the putative GASS.

If ESO 96-SC04 and hence PHR 1315-6555 are shown to be part of the GASS, a possible tidal stream associated with the Canis Major Dwarf Galaxy, this should provide important new data on the initial-final mass relation and the relationship between bipolar morphology and Type I chemistry in a system of known metallicity.

6.5 Summary

This chapter presented a review of the various distance indicators currently in use in the literature. Each method was critically examined and a set of high-quality distance estimates for more than 120 PNe was compiled, using critically revised literature data and new kinematic and extinction-distance determinations. The newly discovered PN, PHR 1315-6555, is the best candidate at present for membership of an open cluster.

The set of critically evaluated distances for ∼120 PNe will be used as calibrating data for a new statistical distance indicator, the Hα surface brightness − radius relation, described in detail in Chapter 7.

Chapter 7

Hα surface brightness – radius relationship

7.1 Introduction

In this chapter, I present a newly established empirical Hα surface brightness – radius (SB-r) relation for Galactic PNe, which extends over 6 dex in surface brightness and a factor of $\sim$150 in physical diameter. This is analogous to the radio SB-r relationships that has been previously used as the basis of statistical distance scales (see Zhang 1995; Van de Steene & Zijlstra 1995; Phillips 2002a, 2004c, and references therein), but with the added benefit of including the most extreme PNe at the faint end of the PNLF, which have been selected against in the radio regime (Zhang & Kwok 1993; Ciardullo et al. 1999). Accurate fluxes in the main emission lines have been determined for almost all local PNe (see Chapter 3), and new and revised distances have been estimated using a variety of primary techniques (see the previous chapter), for each calibrating PN that defines the new relation.

The new SB-r relation is extremely simple in its application, requiring only an angular size, an integrated Hα flux, and the reddening to the PN. From these quantities, an intrinsic radius is calculated, which when combined with the angular size, yields the distance. The Hα SB-r relation has better utility than the equivalent [O III] and [N II] relations (e.g. Shaw 2006, and §7.2), as it includes both bright objects *and* the most senile PNe over a broad range of excitation, and best reflects the underlying ionized mass. The [N II] relation, especially, is strongly influenced by abundance variations between objects, and furthermore, there is negligible [N II] emission in the PNe of highest excitation. The Hα relation is also preferred to the equivalent Hβ relation, as at a minimum, Hα fluxes are a factor of approximately three brighter. Furthermore, a number of recent imaging surveys in Hα have become available, such as the SHS, IPHAS, SHASSA and VTSS surveys which have also allowed the determination of accurate integrated Hα fluxes (see Chapters 2 & 3).

Some previous authors (e.g. Schneider & Buckley 1996) have suggested that a single power-law approach is inadequate to handle both young and old PNe, while Ciardullo et al. (1999) stressed the importance of deriving a statistical calibration that simultaneously handles both the brighter PNe and the fainter objects that prevail among the nearby nebulae. The most evolved PNe represent a population that are usually avoided as calibrators of statistical distance scales, and this may be the reason for the systematic offsets that have plagued the various distance scales in the past (e.g. Pottasch 1996).

The Hα SB-r relation defined here is a first attempt at addressing the problem posed by Ciardullo et al. (1999), and the results show we are gradually moving towards a reconciliation of the long-running PN distance scale problem. As shown below, I find that a single power law does indeed fit the entire range of surface brightness seen in PNe.

7.2 Calibrating Sample

The reddening-corrected Hα SB-r relation (Figure 7.1) is wholly based on reliable data for over 120 calibrating nebulae with well-determined distances obtained from a primary technique ($0.13 \leq D \leq 18$ kpc) selected from the literature or determined anew (see the previous chapter); 25 PNe have distances based on more than one primary method. For these PNe, a weighted average distance has been calculated based on the quoted errors of each individual distance determination. For consistency, individual distances were combined within each method first, *before* being weighted with distances from other primary methods to determine the final weighted distance using equation 6.10.

We use data on the bipolar PN NGC 5189 to illustrate the procedure. Firstly the three available extinction determinations, from Pottasch (1984), Gathier, Pottasch & Pel (1986) and a new determination from Table 6.3 are combined to give a 'mean' extinction distance of 1550 $\pm$ 160 pc. The new determination is based on a revised reddening to the PN, of $E(B-V) = 0.36$, derived in part from a reappraisal of the integrated nebular Hα and Hβ fluxes (see Chapter 3).

The weighted extinction distance estimate was then combined with a gravity determination (using updated values for the extinction and visual magnitude of the CS) from table 6.6 of 1130 $\pm$ 280 pc, plus a kinematic determination (from table 6.7) of 1300 $\pm$ 500 pc. After weighting using inverse errors, a final distance was determined: $D = 1440 \pm 270$ pc which has been used along with a revised integrated Hα flux to provide a calibration point for the SB-r relation.

The Hα surface brightness for each PN is calculated from the integrated Hα flux and the angular geometric radius (in arcsecs), derived in turn from the observed major and minor dimensions. The linear radius in parsecs then follows from the angular radius and the adopted distance. The Hα fluxes are either taken from the literature or the new data presented in Chapter 3 (see this chapter for a detailed discussion of the observations).

Where possible, the angular dimensions of all calibrating PNe are measured at the 10%-of-peak surface brightness isophote (e.g. Tylenda et al. 2003, Ruffle et al. 2004). Some highly evolved PNe distorted by interaction by the ISM have been treated differently. In these cases a strict application of the 10% isophote rule may only give dimensions of the bright interacting rim, an example being Sh 2-188. In this case an isophote which includes the non-interacting part of the main shell is used to give the overall dimensions of the object. Similarly, the dimensions fro some evolved bipolar PNe are sometimes hard to define, and are dependent on the exact orientation of the 'waist'. In nearly all cases these are large or very large PNe, so the subjective effect of choosing an appropriate contour has only a relatively small percentage change on the overall dimensions of the nebula.

The SB-r relation is quite robust to any error in the angular dimensions. This is because any error in the dimensions flows through to *both* the surface brightness and the radius. For example, a 20% error in each angular dimension (40% error in the calculated surface brightness) leads to only a ~10% error in the distance.

Similarly, owing to the form of the SB-r relation, an uncertainty of 20% in the Hα flux leads to only a 5% error in the computed radius, i.e. the PN distance. Hence, errors introduced into the SB-r relation due to observational uncertainties in the angular dimensions or fluxes are generally minor compared to the uncertainties in the distances of the calibrating PNe, or the dispersion due to cosmic scatter.

Table 7.1 gives the relevant observational and derived data for the sample of all 122 calibrating PNe. The columns consecutively give the name, adopted distance in parsecs, the method of distance determination, a brief morphological code (E = elliptical, R = round, A = Asymmetric, B = bipolar), a comment on any other PN type classifier (I = Type I, C = close binary), the major and minor dimensions in arcsecs, the integrated fluxes in the Hα, [O III]λ5007 and [N II]λ6584 lines (in cgs units, taken from Chapter 3), the logarithm of the radius (in pc), the reddening-corrected Hα surface brightness (in cgs units per steradian), the ionized mass and logarithm of the electron density.

The codes for the distance method are as follows: 1. trigonometric parallax; 2. spectroscopic/photometric parallax; 3. extinction distance; 4. expansion parallax; 5. gravity method; 5a. asteroseismological (seismic) distance; 6. kinematic method; 7. cluster membership; 8. photoionization modelling; 9. eclipsing binary or reflection effect modelling; 10. HI absorption distance; 11. modelling the ISM interaction.

The individual distances and their associated errors are discussed in detail in the previous chapter. The calibrating PNe range in brightness from young, high-density, luminous objects like NGC 7027 through to some of the faintest known PNe (WDHS 1 and Ton 320). Such faint, evolved PNe have not been used before as calibrators.

The ordinary least-squares (OLS) bisector fit (Isobe et al. 1990) for the entire calibrating sample is represented by the equation:

$$\log S(\mathrm{H}\alpha) = -3.61(\pm0.11)\log R - 5.38(\pm0.09) \tag{7.1}$$

with a Pearson correlation coefficient, $r = -0.94$. An OLS bisector fit was used since observational errors are present in both fluxes and diameters (i.e. the surface brightness) and the distance (hence the radius). The justification for this approach was discussed by Isobe et al. (1990) and Feigelson & Babu (1992). The observed power-law slope of the Hα SB-r relation is between −3.0 and −3.7 (depending on the subset of PNe used; see table 7.6, below) which is broadly consistent with the R^{-3} law found for LMC and SMC PNe (e.g. Stanghellini et al. 2002; Shaw et al. 2001; Villaver, Stanghellini & Shaw 2003, and see §7.5).

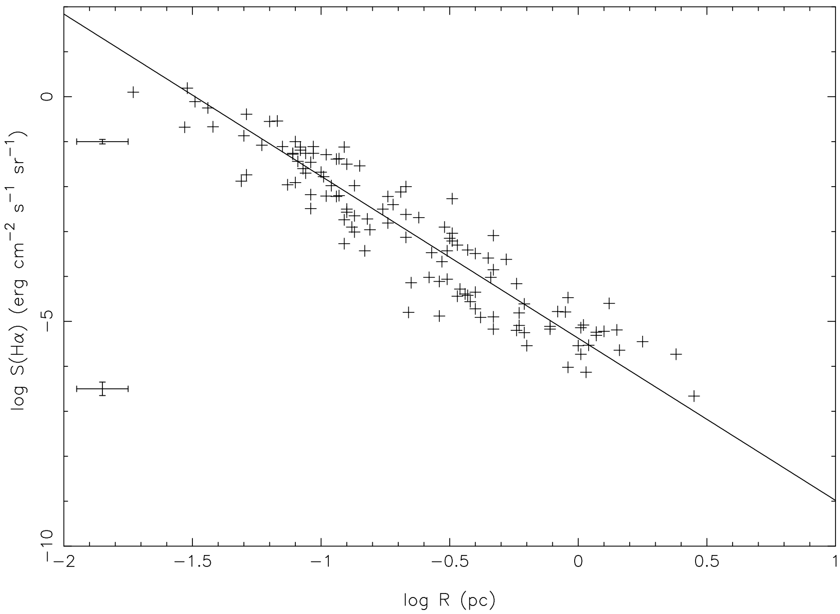

Figure 7.1: Newly derived Hα log surface brightness – log radius (SB-r) relation based on a sample of 122 calibrating PNe, spanning > 6.5 dex in SB. The line is a linear least-squares bisector fit (Isobe et al. 1990) to the entire sample. Representative error bars are shown.

Figures 7.2 and 7.3 show the equivalent reddening-corrected SB-r relations in the [O III] λ5007 and [N II] λ6584 lines respectively. Refer to table 7.1 for the flux and surface brightness data for the individual PNe. A similar distribution to the Hα relation is seen in [O III] SB-r space, but with a steeper slope and slightly more scatter. The least-squares bisector fit for the sample of 120 PNe that defines the [O III] relation yields:

$$\log S(5007) = -4.01(\pm 0.15) \log R - 5.35(\pm 0.12) \tag{7.2}$$

The correlation coefficient is $r = -0.91$. The steeper slope and greater scatter is due to the influence of excitation class on the [O III] surface brightness. The PN at $\log r = -1.73$, $\log S(5007) = -1.64$ is BD +30°3639, a young PN with a cool central star. Metallicity too, influences the position of a PN in [O III] SB-r space — the faint low-surface brightness object at $\log r = -0.40$, $\log S(5007) = -6.31$ is SBS1150+599A, a halo PN with a very low oxygen abundance. Also noteworthy is the tightening of the distribution at the largest radii. This effect is attributed to the most massive PNe having fast evolving, and therefore faint, central stars. In these nebulae, the shells are recombining, which manifests as weaker relative [O III] emission. Conversely, many of the largest round PNe have slowly evolving, optically-luminous central stars, so that the nebular excitation is still high (see figures 7.5 and 7.6).

The [O III] SB-r plot provides suggestive evidence for a change in slope. The PN sample was divided into two groups on the basis of size, young and compact versus large and evolved, separated at $\log r = -0.7$ ($r = 0.2$ pc) (see also Chapter 2). A bisector fit to the young PN sample ($n = 57$) is given by:

$$\log S(5007) = -3.67(\pm 0.38) \log R - 5.01(\pm 0.40) \tag{7.3}$$

with a correlation coefficient of -0.65, while the evolved sample ($n = 64$) is best fit by the equation:

$$\log S(5007) = -4.33(\pm 0.37) \log R - 5.43(\pm 0.14) \tag{7.4}$$

which has a correlation coefficient of -0.74. However, the two samples are not statistically different, with formally the same trend within the errors, though the overall impression is that of a steepening of the slope at larger radii. This may be due to an overall decrease in nebular excitation (with a commensurate reduction in [O III] surface brightness) seen in large nebulae, as the CS fades and cools.

Differences in excitation class and abundance are especially clear in [N II] SB-r space (figure 7.3), which increases the intrinsic scatter in the diagram. Of note is that many optically-thin high-excitation PNe (mostly round and elliptical objects) have very weak or no [N II] emission, so they fall off the bottom of the diagram. These PNe are not plotted, as the sensitivity limit is approximately at $\log S(6584) \simeq -7$ dex. The equation of the mean [N II] SB-r relation for 94 PNe with reliable data is:

$$\log S(6584) = -3.35(\pm 0.20) \log R - 5.48(\pm 0.17) \tag{7.5}$$

with a markedly lower correlation coefficient of $r = -0.81$, compared to the Hα trend.

Table 7.1: Calibrating nebulae for the SB-r relation.

Name	D (pc)	Meth	Mor	Type	a ($''$)	b ($''$)	c	$F(H\alpha)$ (cgs)	$F(5007)$ (cgs)	$F(6584)$ (cgs)	log r (pc)	$S(\mathrm{H}\alpha)$ (cgs)	M_i ($M_\odot$)	log N_e (cm^{-2})
Abell 7	510 ± 200	1,5	...	R	830	787	0.03	-10.48	-10.23	-10.75	0.00	-5.54	0.43	0.92
Abell 15	4010 ± 1000	8	...	R	37	35	0.06	-11.95	-11.89	-12.96	-0.46	-4.28	0.13	1.79
Abell 20	2350 ± 600	8	...	R	67	61	0.12	-11.60	-11.39	-12.05	-0.44	-4.39	0.13	1.72
Abell 21	575 ± 50	1,5	I	B	760	610	0.06	-9.84	-9.57	-9.58	-0.05	-4.73	0.81	1.36
Abell 30	$2020\,^{+390}_{-320}$	2	...	R	127	127	0.04	-11.81	-11.58	-13.23	-0.21	-5.25	0.18	1.17
Abell 31	481 ± 130	1,2,5	...	E	1145	890	0.06	-10.08	-9.77	-10.11	0.07	-5.31	0.83	1.00
Abell 33	$1160\,^{+180}_{-150}$	2	...	R	282	276	0.00	-10.95	-10.73	...	-0.11	-5.11	0.38	1.19
Abell 36	450 ± 200	1,5	...	E	468	315	0.04	-10.51	-10.38	...	-0.38	-4.91	0.10	1.43
Abell 39	1390 ± 400	5	...	R	174	174	0.03	-11.36	-10.76	-12.72	-0.23	-5.09	0.19	1.27
Abell 43	2050 ± 600	5	...	R	80	80	0.25	-11.82	-11.48	-12.69	-0.40	-4.72	0.11	1.54
Abell 46	1700 ± 600	9	...	E	97	84	0.23	-11.40	-11.40	-13.39	-0.43	-4.42	0.13	1.70
Abell 63	2400 ± 400	9	...	Eb	48	42	0.72	-11.95	-12.42	-13.92	-0.58	-4.02	0.09	1.98
Abell 74	$750\,^{+680}_{-240}$	1	...	Eb	810	776	0.11	-10.66	-10.68	-10.72	0.16	-5.64	0.94	0.79
Abell 79	4400 ± 600	6	I	B	59	49	0.45	-11.75	-11.67	-10.88	-0.24	-4.16	0.52	1.74
BD+30 3639	1300 ± 200	4	...	E	6.2	5.6	0.43	-9.39	-11.25	-9.35	-1.73	0.10	0.01	4.61
BV 5-1	5500 ± 1200	6	I	B	39	15	1.40	-11.22	-10.95	-10.64	-0.49	-2.27	1.08	2.80
CRBB 1	3400 ± 1000	5	...	E	17	13	0.06	-11.17	...	-11.62	-0.91	-2.74	0.056	2.78
CVMP 1	2000 ± 200	3,6	I	B	258	135	1.23	-11.52	-11.88	-10.43	-0.04	-4.47	1.14	1.48
DS 1	725 ± 75	9	...	E	354	315	0.22	-10.65	-10.35	...	-0.23	-4.81	0.26	1.41
DS 2	1000 ± 300	5	...	R	190	190	0.29	-11.55	-11.10	...	-0.33	-5.17	0.10	1.28
EGB 6	590 ± 150	5	...	E	780	660	0.07	-10.80	-10.78	-11.24	0.01	-5.73	0.36	0.83
Hb 5	1700 ± 300	3,8	I	B	52	18	1.66	-10.42	-10.37	-10.03	-0.90	-1.50	0.25	3.40
HbDs 1	795 ± 200	5	...	E	158	140	0.19	-11.40	-11.3	...	-0.54	-4.88	0.04	1.53
He 2-84	1800 ± 500	6	I	B	36	24	1.80	-11.64	-11.18	-11.10	-0.90	-2.57	0.07	2.86
He 2-111	2200 ± 500	3,6	I	B	29	15	1.18	-10.91	-10.72	-11.66	-0.96	-1.98	0.10	3.19
HFG 1	630 ± 320	2	...	E	540	540	0.67	-10.52	-10.23	-10.94	-0.08	-4.78	0.63	1.35
HFG 2	1900 ± 400	6	...	E	181	153	0.02	-11.53	-10.83	...	-0.12	-5.22	0.31	1.14
IC 289	2190 ± 1600	3	...	E	40	32	1.20	-10.87	-10.93	-12.99	-0.72	-2.40	0.25	2.85
IC 418	1200 ± 200	4	...	E	14	11	0.29	-9.01	-9.32	-9.29	-1.44	-0.26	0.05	4.29
IC 1295	1230 ± 300	5	...	E	110	89	0.52	-10.78	-10.13	...	-0.53	-3.67	0.17	2.12
IC 1747	2570 ± 200	3	...	E	13	13	0.81	-10.51	-10.41	...	-1.09	-1.44	0.09	3.52
IC 2448	2200 ± 600	4	...	R	22	22	0.12	-10.33	-9.77	-12.36	-0.93	-2.20	0.09	3.06
IPHAS PN-1	6300 ± 800	3,6	I	B	21	12	2.00	-12.43	-12.68	-12.03	-0.62	-2.69	0.33	2.66
IsWe 2	620 ± 150	5	...	E	1020	850	0.66	-10.45	-11.08	-10.41	0.15	-5.19	1.47	1.03

Continued on next page

Table 7.1 – continued from previous page

Name	D (pc)	Method	Morph	Type	a ($''$)	b ($''$)	c	$F(H\alpha)$ (cgs)	$F(5007)$ (cgs)	$F(6584)$ (cgs)	$\log r$ (pc)	$S(\mathrm{H}\alpha)$ (cgs)	M_i ($M_\odot$)	$\log N_e$ (cm^{-2})
J 900	4800 ± 1000	4	...	E	8.2	7.8	0.74	-10.71	-10.14	-11.42	-1.03	-1.26	0.15	3.58
Jacoby 1	570 ± 150	5	...	R	660	660	0.04	-11.14	-10.96	...	-0.04	-6.02	0.20	0.71
JaFu 2	12500 ± 1000	7	...	E	4.9	4.9	0.63	-13.22	-13.32	...	-0.83	-3.43	0.04	2.40
JnEr 1	1150 ± 300	5	...	Eb	398	362	0.03	-10.58	-10.33	-10.36	0.02	-4.98	0.93	1.19
K 1-14	3000^{+490}_{-420}	2	...	R	53	51	0.12	-11.95	-11.76	...	-0.42	-4.56	0.11	1.63
K 1-16	1670 ± 300	5	...	E	116	116	0.06	-11.55	-11.40	...	-0.33	-4.90	0.13	1.41
K 1-22	1330^{+220}_{-190}	2	...	E	200	186	0.07	-10.82	-10.42	-11.61	-0.21	-4.61	0.38	1.50
K 1-27	1700 ± 500	5	...	E	61	47	0.07	-12.13	-12.18	...	-0.66	-4.80	0.023	1.62
K 3-72	3800^{+2000}_{-1600}	6	I	B	54	25	1.16	-11.72	-11.93	-10.92	-0.47	-3.30	0.37	2.28
Lo 8	1990 ± 600	5	...	E	132	108	0.04	-11.81	-11.58	...	-0.24	-5.20	0.16	1.22
LoTr 5	450 ± 260	1,2	...	E	540	510	0.01	-10.84	-10.44	...	-0.20	-5.54	0.14	1.03
LTNF 1	2000 ± 300	9	...	E	230	215	0.05	-12.2	-11.38	...	0.03	-6.13	0.26	0.62
M 1-79	2700 ± 900	3	...	Eb	46	27	0.64	-11.00	-10.84	-10.97	-0.64	-2.91	0.22	2.56
M 3-3	5500^{+1800}_{-1300}	6	I	B	17	16	0.42	-11.74	-11.55	-11.05	-0.67	-3.13	0.15	2.46
M 3-28	2500 ± 600	6	I	B	24	12	2.60	-12.30	-12.31	-11.97	-0.99	-2.21	0.07	3.08
Me 2-1	2300 ± 100	8	...	E	8.9	8.6	0.15	-10.84	-10.17	...	-1.31	-1.88	0.01	3.41
Menzel 1	2300 ± 600	6	...	B	80	39	0.56	-10.56	-10.42	-10.25	-0.51	-2.93	0.46	2.49
Menzel 2	2100 ± 600	2,6	...	E	45	25	1.08	-10.94	-10.32	-11.13	-0.77	-2.50	0.17	2.83
MWP 1	497 ± 100	5a	...	E	840	505	0.03	-10.3	-10.80	...	-0.11	-5.17	0.35	1.16
NGC 246	495^{+145}_{-100}	2	...	E	260	227	0.03	-10.09	-9.65	...	-0.54	-4.11	0.10	1.91
NGC 650-1	1200 ± 300	5	I	B	168	111	0.15	-10.06	-9.55	-10.09	-0.40	-3.49	0.45	2.15
NGC 1360	380 ± 50	1,5	...	E	420	266	0.01	-9.75	-9.34	...	-0.51	-4.06	0.12	1.92
NGC 1501	720 ± 250	5	...	E	56	48	0.95	-10.46	-10.05	...	-1.04	-2.49	0.04	2.97
NGC 1514	400 ± 80	2	...	E	140	132	0.78	-10.28	-9.91	...	-0.91	-3.27	0.03	2.52
NGC 1535	2310^{+430}_{-360}	2	...	E	33	32	0.06	-9.97	-9.35	...	-0.74	-2.22	0.28	2.95
NGC 2346	900 ± 200	2,3	...	B	70	55	0.74	-10.65	-10.33	-10.26	-0.87	-2.98	0.05	2.64
NGC 2371/2	1410 ± 300	5	...	E	49	31	0.07	-10.51	-10.10	...	-0.88	-2.90	0.06	2.68
NGC 2440	1900 ± 400	3	I	B	59	25	0.45	-9.90	-9.32	-9.45	-0.75	-2.02	0.32	3.06
NGC 2452	3700 ± 400	3	...	Eb	18	12	0.62	-10.79	-10.29	-11.14	-0.87	-1.98	0.17	3.14
NGC 2792	2020 ± 560	3	...	E	18	16	0.58	-10.58	-10.31	-12.4	-1.08	-1.91	0.06	3.28
NGC 2867	2420 ± 600	5	...	E	14	14	0.46	-9.94	-9.45	-10.71	-1.08	-1.19	0.13	3.64
NGC 3132	810 ± 330	2,8	...	Eb	85	55	0.14	-9.82	-9.46	-9.59	-0.87	-2.65	0.08	2.80
NGC 3211	1910 ± 500	3	...	E	16	16	0.32	-10.51	-9.88	-12.13	-1.13	-1.96	0.04	3.28
NGC 3242	1000 ± 300	4	...	E	45	39	0.06	-9.31	-8.66	-11.27	-0.99	-1.78	0.11	3.30
NGC 3918	1840 ± 590	3,4	...	E	19	17	0.38	-9.50	-8.84	-10.09	-1.10	-1.00	0.14	3.74

Continued on next page

Table 7.1 – continued from previous page

Name	D (pc)	Method	Morph	Type	a ($''$)	b ($''$)	c	$F(H\alpha)$ (cgs)	$F(5007)$ (cgs)	$F(6584)$ (cgs)	$\log r$ (pc)	$S(\mathrm{H}\alpha)$ (cgs)	M_i ($M_\odot$)	$\log N_e$ (cm^{-2})
NGC 4361	950 ± 240	5	...	E	119	115	0.06	-10.11	-9.96	-12.62	-0.57	-3.47	0.17	2.25
NGC 5189	1440 ± 270	3,5,6	I	B	163	108	0.52	-9.94	-9.48	-9.93	-0.33	-3.09	1.05	2.32
NGC 5315	2620 ± 1030	3	I	B	10.7	9.2	0.60	-9.73	-9.54	-9.95	-1.20	-0.57	0.13	4.01
NGC 5882	1700 ± 400	4	...	E	16	13	0.39	-9.78	-9.38	-11.29	-1.23	-1.08	0.06	3.77
NGC 5979	1930 ± 100	3,4	...	E	20	19	0.48	-10.66	-10.18	-11.87	-1.04	-2.18	0.05	3.13
NGC 6210	2100 ± 500	4	...	E	14	14	0.08	-9.61	-9.07	-10.88	-1.15	-1.11	0.09	3.71
NGC 6302	1170 ± 140	4	I	B	89.9	34.8	1.28	-9.68	-9.40	-10.33	-0.80	-1.54	0.42	3.32
NGC 6326	5300 ± 1300	4	...	E	20.6	13.7	0.39	-10.56	-9.95	-11.17	-0.67	-2.00	0.54	3.03
NGC 6369	1550 ± 310	8	...	Eb	33	33	1.93	-10.17	-10.13	-10.74	-0.91	-1.12	0.37	3.59
NGC 6537	2000 ± 400	6,10	I	B	11	10	1.96	-10.49	-10.60	-10.31	-1.29	-0.43	0.09	4.13
NGC 6543	1500 ± 400	4	...	E	27	24	0.10	-9.10	-8.78	-10.07	-1.03	-1.11	0.18	3.66
NGC 6565	2250 ± 350	3,4	...	Eb	10.8	10.5	0.45	-10.62	-10.17	-10.42	-1.24	-1.63	0.03	3.50
NGC 6567	1640 ± 300	3,10	...	E	8.1	6.7	0.80	-10.24	-9.95	-11.60	-1.53	-0.68	0.02	4.12
NGC 6572	1860 ± 500	4	...	E	15	13	0.32	-9.24	-8.74	-9.82	-1.20	-0.58	0.13	4.01
NGC 6578	2900 ± 500	4	...	E	12.1	11.8	1.43	-10.70	-10.65	-11.98	-1.08	-1.12	0.14	3.67
NGC 6629	2000 ± 1000	10	...	E	17	16	0.83	-10.18	-10.09	-11.27	-1.11	-1.28	0.10	3.61
NGC 6720	704^{+445}_{-196}	1	...	Eb	86	63	0.07	-9.55	-9.05	-9.57	-0.90	-2.50	0.08	2.90
NGC 6741	2700 ± 500	3,6	...	Eb	9.1	6.5	1.01	-10.54	-10.12	-10.46	-1.30	-0.87	0.05	3.91
NGC 6751	2000 ± 600	6	...	E	24	23	0.56	-10.60	-10.37	-10.73	-0.94	-2.22	0.09	3.06
NGC 6781	950 ± 140	8	...	B	180	109	0.77	-10.02	-9.89	-9.87	-0.49	-3.04	0.45	2.42
NGC 6803	3000 ± 1000	3,10	...	E	5.4	5.1	0.80	-10.52	-10.14	-11.02	-1.42	-0.67	0.03	4.07
NGC 6842	2300 ± 500	3	...	E	55	53	1.04	-10.90	-10.81	-11.97	-0.52	-2.90	0.44	2.51
NGC 6853	379^{+54}_{-42}	1	...	Eb	470	342	0.07	-8.99	-8.45	-8.96	-0.43	-3.41	0.41	2.21
NGC 6884	2550 ± 750	3,4	...	E	17	15	0.74	-10.52	-9.93	-11.41	-1.01	-1.67	0.11	3.36
NGC 6886	5300 ± 1000	4	...	Eb	9.3	4.5	0.67	-10.68	-10.13	-10.77	-1.08	-1.10	0.14	3.69
NGC 6891	2900 ± 600	4	...	E	13.5	12.7	0.30	-10.17	-9.77	-12.04	-1.04	-1.46	0.12	3.48
NGC 6894	1310 ± 300	3	...	Eb	56	53	0.83	-10.65	-10.44	-10.75	-0.76	-2.81	0.12	2.67
NGC 6905	1580 ± 300	5	...	E	43	36	0.22	-10.42	-10.04	...	-0.82	-2.72	0.10	2.75
NGC 7009	1450^{+600}_{-400}	3	...	E	28	22	0.12	-9.29	-8.72	-10.54	-1.06	-1.26	0.13	3.59
NGC 7026	2500 ± 1000	3,6,10	...	Eb	27	11	0.95	-10.21	-9.92	-10.65	-0.98	-1.29	0.20	3.54
NGC 7027	890 ± 120	4	...	Eb	15.6	12.4	1.37	-9.25	-8.95	-9.70	-1.52	0.16	0.05	4.54
NGC 7048	1970 ± 640	3	...	Eb	63	60	0.38	-10.85	-10.43	-10.70	-0.53	-3.43	0.23	2.25
NGC 7094	1390 ± 350	4	...	R	103	99	0.12	-11.25	-11.06	...	-0.47	-4.44	0.10	1.71
NGC 7139	2400^{+600}_{-800}	3	...	E	86	67	0.76	-11.10	-10.96	-11.31	-0.35	-3.59	0.52	2.08
NGC 7293	219^{+27}_{-21}	1	...	B	1005	740	0.01	-8.89	-8.59	-8.77	-0.34	-4.02	0.35	1.86

Continued on next page

Table 7.1 – continued from previous page

Name	D (pc)	Method	Morph	Type	a ($''$)	b ($''$)	c	$F(H\alpha)$ (cgs)	$F(5007)$ (cgs)	$F(6584)$ (cgs)	log r (pc)	$S(\mathrm{H}\alpha)$ (cgs)	M_i ($M_\odot$)	log N_e (cm^{-2})
NGC 7354	1600 ± 600	3,10	...	E	22	18	1.77	-10.64	-10.42	-11.34	-1.11	-1.26	0.10	3.62
NGC 7662	1190 ± 1150	4	...	E	31	28	0.16	-9.51	-8.89	-11.29	-1.07	-1.60	0.08	3.43
Pease 1	12300 ± 1500	7	...	E	3.1	2.7	0.19	-11.64	-11.60	-13.50	-1.06	-1.70	0.08	3.38
PHR0719-1222	2750 ± 700	3	...	E	193	188	0.85	-11.99	-12.12	-11.68	0.10	-5.22	1.11	1.03
PHR1315-6555	11800 ± 1500	7	...	B	19	18	0.86	-12.42	-12.22	-12.26	-0.28	-3.62	0.79	2.03
PHR1327-6032	2150 ± 550	3	I	B	210	180	0.58	-11.70	-11.98	-11.31	0.02	-5.14	0.74	1.12
PHR1408-6106	1700 ± 300	3	...	E	307	264	0.67	-11.53	-11.98	-11.38	0.07	-5.24	0.90	1.04
PuWe 1	371 ± 30	1,5	...	R	1242	1180	0.16	-10.21	-10.20	-10.23	0.04	-5.53	0.53	0.91
SaWe 3	2080 ± 250	3	I	B	110	80	1.09	-11.40	-11.63	-10.92	-0.33	-3.85	0.46	1.93
SBS1150+599A	17800 ± 5000	5	...	E	9.2	9.2	0.06	-13.2	-15.17	...	-0.40	-4.35	0.17	1.72
Sh 1-89	2300 ± 300	3	I	B	68	48	0.98	-11.06	-11.56	-11.06	-0.50	-3.15	0.38	2.37
Sh 2-188	825 ± 160	3,11	...	A	702	610	0.52	-10.07	-10.41	-9.90	0.12	-4.60	2.44	1.34
Sh 2-216	129^{+6}_{-5}	1	...	R	6000	5400	0.07	-8.72	-9.18	-8.72	0.25	-5.45	2.00	0.85
Sp 3	2380^{+660}_{-520}	2	...	E	40	34	0.19	-10.35	-10.93	-10.97	-0.67	-2.62	0.26	2.72
SuWt 2	1500 ± 300	2	I	B	87	43	0.55	-11.69	-11.40	-10.97	-0.65	-4.14	0.05	1.95
Ton 320	570 ± 50	1,5	...	A	2300	1840	0.03	-10.79	-10.85	-10.89	0.45	-6.66	1.59	0.14
Vy 2-2	4680 ± 1200	4	...	E	3.1	2.6	0.98	-10.62	-10.65	-11.89	-1.49	-0.11	0.04	4.39
WDHS 1	850 ± 250	3,5	...	B	1320	1020	0.09	-10.40	...	-10.32	0.38	-5.73	3.00	0.64

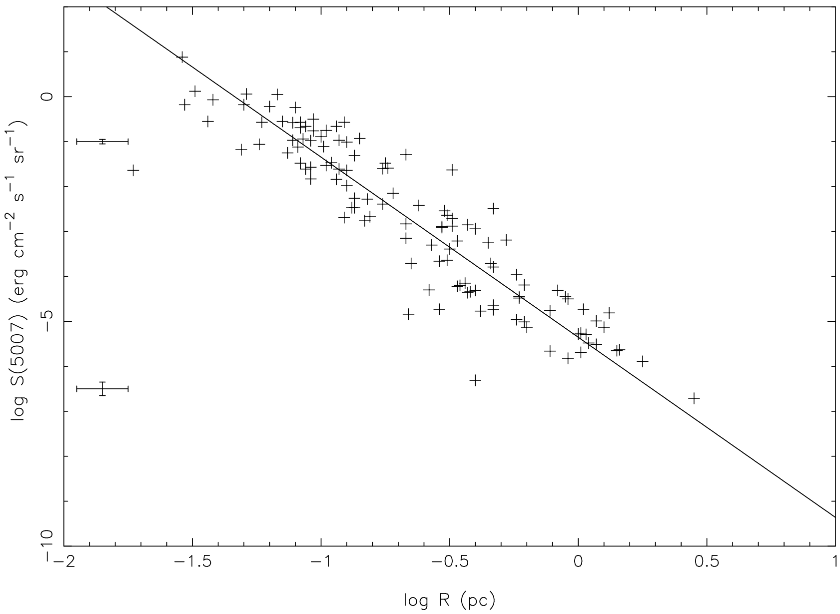

Figure 7.2: Newly derived [O III] SB-r relation based on a sample of 121 calibrating PNe. The line is a linear least-squares bisector fit and representative error bars are shown. The range in SB is somewhat more than in Hα, exceeding 7 dex.

7.3 Morphology, Chemistry and the SB-r relation

The 122 calibrating PNe in the Hα SB-r relation represent a broad range of PNe by morphological type, excitation class (CS temperature), evolutionary state and whether they are indentified as a post-common envelope object. Having new and revised data available for these calibrator PNe provides the opportunity to investigate the presence of any sub-trends within the relation. Figures 7.4, 7.5 and 7.6 show a breakdown of the calibrating PNe by morphological class (defined in Chapter 4). Some of the main conclusions are summarised here.

Bipolar PNe and elliptical PNe with bipolar-cores tend to populate the upper part of the broad trend in Hα SB-r space, with only one or two exceptions (i.e. bipolar PNe have higher ionized masses in the mean than other types; see below). Elliptical PNe without bipolar cores are more uniformly spread, while round PNe tend to fall along the bottom of the broad locus, beneath the mean trendline.

A similar distribution is seen in [O III] SB-r space, but the overall gradient is steeper. Again, bipolar PNe are seen to populate the upper part of the broad trend. Also noteworthy is the tightening of the distribution at the largest radii. This effect is attributed to bipolar PNe having faint central stars, so that the PN shells are recombining, with weaker [O III] emssion. Conversely, many of the largest round PNe have slowly evolving, optically-luminous CS, so that the nebular excitation is still high.

This difference between morphological types is especially clear in [N II] SB-r space, which responds to differences in excitation class and nitrogen abundance. In figure 7.6 it is especially clear that bipolar and bipolar-core PNe are largely separated from the other types of PNe. This diagram confirms what is already known: that bipolar and bipolar-core PNe are often enriched

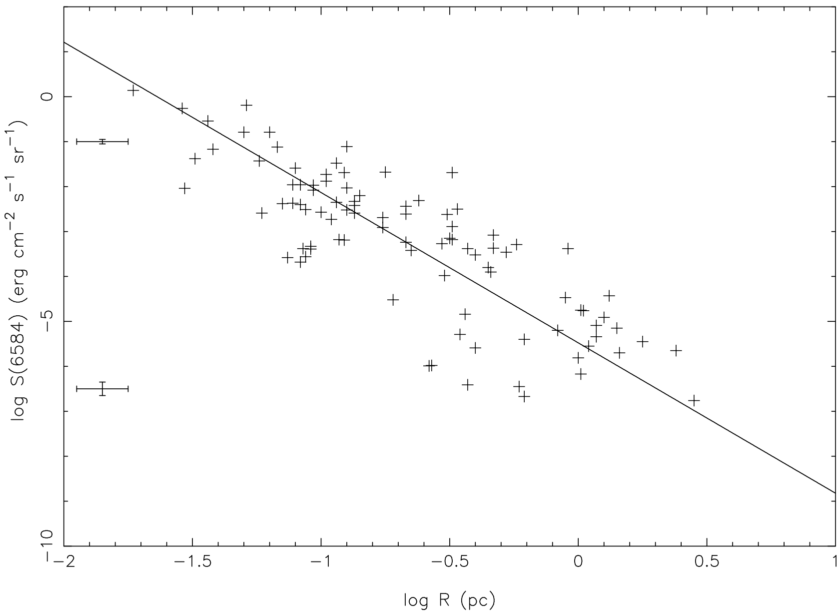

Figure 7.3: Newly derived [N II] SB-r relation based on a sample of 94 calibrating PNe with reliable data. The line is a linear least-squares bisector fit, and representative error bars are shown. Note the increased scatter compared to the Hα and [O III] relations.

in nitrogen (Peimbert's Type I). It should be reiterated that many optically-thin high-excitation PNe (mostly round and elliptical objects) have very weak or no [N II] emission, so they fall off the bottom of the SB-r diagram.

7.3.1 Bipolar PNe

Bipolar and bipolar-core (mainly optically thick) PNe (see Chapter 4) are systematically offset from the mean relation in Hα SB-r space (see Figure 7.7). Bipolars are seen to be larger, and hence more massive, at a given mean surface brightness.[1] A preliminary discussion of this point was given by Frew, Parker & Russeil (2006). A linear least-squares bisector fit to 39 bipolar and bipolar-core PNe is described by the equation:

$$\log S(\mathrm{H}\alpha) = -3.37(\pm 0.27) \log R - 4.87(\pm 0.19) \tag{7.6}$$

The apparent offset in SB-r space of bipolar PNe from the rest is important to note, and in principle allows this sub-trend to be used to derive more reliable distances for bipolar PNe. This approach has been taken herein, and 'high' trend distances have been determined for all bipolar and Type I PNe (see the next section) without primary distance estimates, to help define a more accurate solar neighbourhood sample (see Chapter 9).

[1] Or for a given radius, $M_{\mathrm{ion}} \propto S(\mathrm{H}\alpha)^{0.5}$

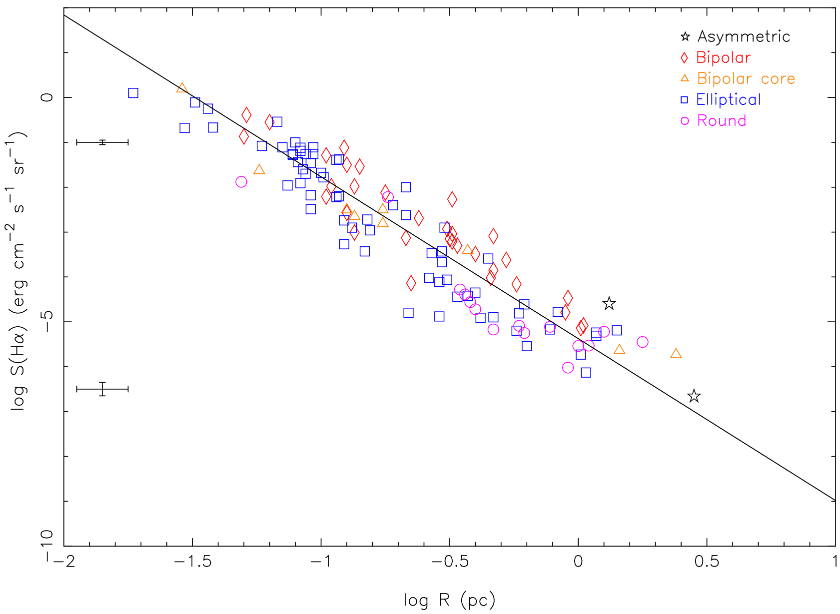

Figure 7.4: Hα SB-r relation for 122 calibrating PNe, with morphology indicated (refer to the text for more details). The line is a linear least-squares bisector fit.

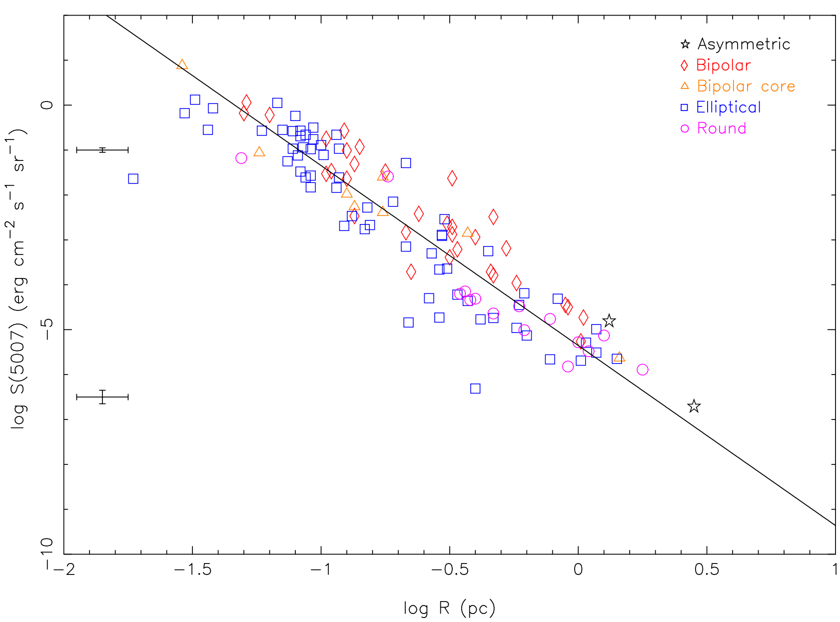

Figure 7.5: [O III] SB-r relation for 120 calibrating PNe, with morphology indicated. The line is a linear least-squares bisector fit.

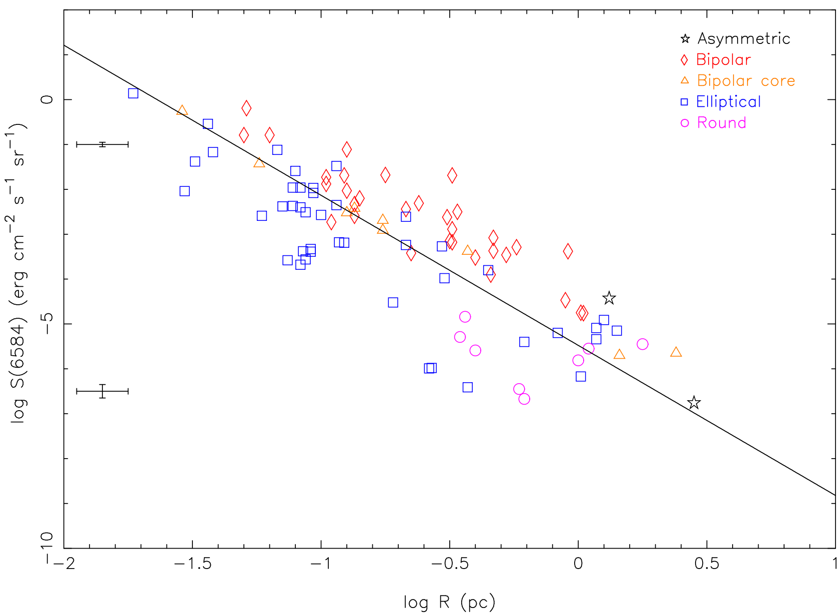

Figure 7.6: [N II] SB-r relation for 94 calibrating PNe, with morphology indicated. The line is a linear least-squares bisector fit.

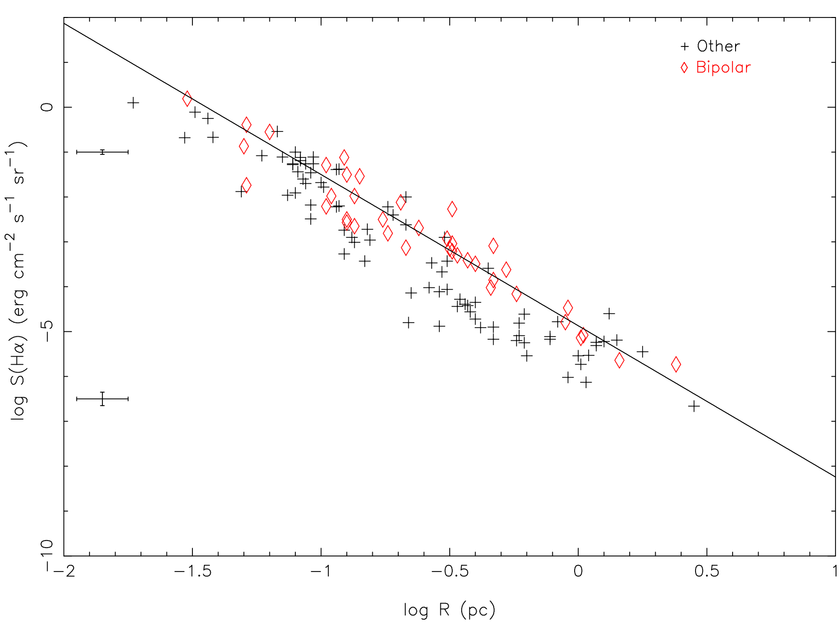

Figure 7.7: Hα SB-r relation plotting bipolar and bipolar-core PNe separately (red diamonds). Bipolar PNe are seen to be larger, and hence more massive, at a given mean surface brightness. Other calibrating PNe are marked with crosses. The line is a least-squares bisector fit to the bipolar PNe only.

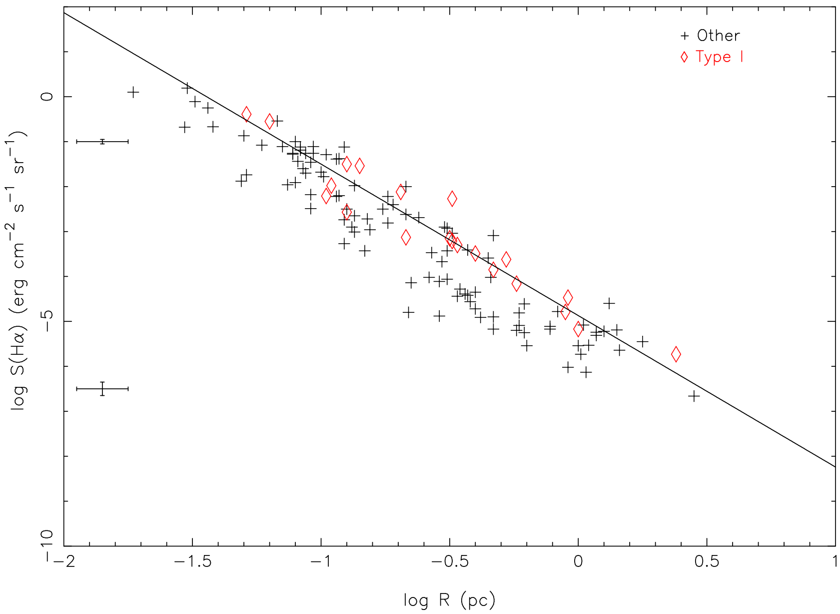

Figure 7.8: Hα SB-r relation plotting Type I PNe separately (red diamonds). Other calibrating PNe are marked with crosses. The line is a least-squares bisector fit to the Type I PNe only.

7.3.2 Type I PNe

Many of the bipolar PNe discussed in §7.3.1 also have Type I chemistries, using the Kingsburgh & Barlow (1994) definition, and there is high degree of overlap with the bipolar sample. A subset of known Type I PNe was extracted from the calibration sample, though the number of objects is only 19, all but one of which is bipolar. The trend is best described by the equation:

$$\log S(\mathrm{H}\alpha) = -3.35(\pm 0.25) \log R - 4.90(\pm 0.18) \tag{7.7}$$

which is statistically identical with the trend line defined by bipolar PNe. This is expected as the Type I sample is essentially a subset of the former.

7.3.3 High-excitation PNe

High-excitation (HE) PNe *sensu stricto* are defined here as a relatively homogenous subclass of PNe (at least spectroscopically), characterised by having $F(\mathrm{He\,II}) \geq 0.75\, F(\mathrm{H}\beta)$, and very weak or absent [N II], [S II] and [O II] emission (cf. Kaler 1981b). These PNe also appear to have simple round or elliptical morphologies (sometimes with amorphous filled centres), and relatively luminous central stars (Kaler 1981b). Based on published $\log g$ values (e.g. Napiwotzki 1999), the CS are still on the nuclear burning track in the HR diagram. These PNe are optically thin to the H I continuum and usually to the He II continuum as well, and consist essentially of a He^{2+} zone, i.e. $T_z(\mathrm{He\,II}) > T_z(\mathrm{H})$. Also typical are systematically lower ionized masses, and consequently, HE PNe plot near the lower bound of the SB-r relation (Figure 7.9), inhabiting a distinct locus in Hα SB-r space. A linear least-squares bisector fit to 19 calibrating HE PNe is described by the equation:

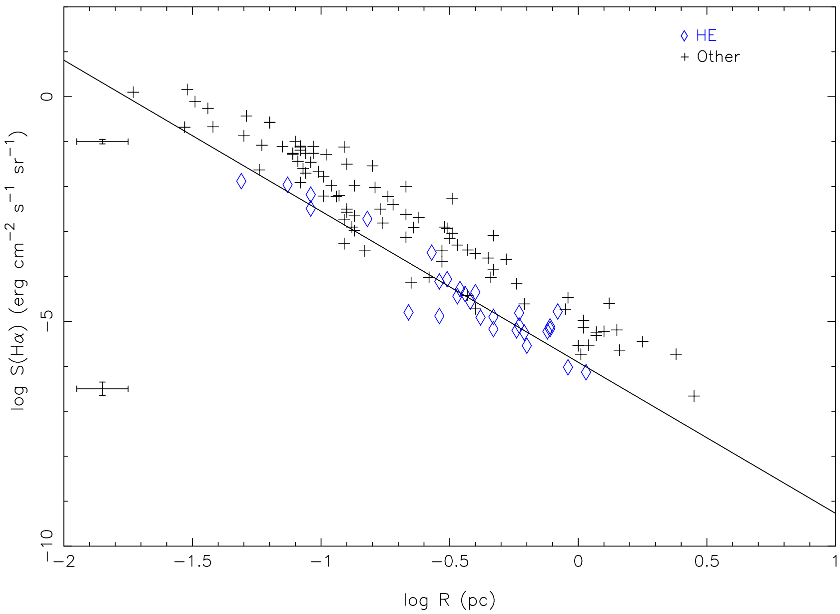

Figure 7.9: Hα surface brightness – radius relation plotting high-excitation (HE) PNe separately (red diamonds). These objects are characterised by having $F(\text{He}\,\textsc{ii}) \geq 0.75\,F(\text{H}\beta)$, weak or absent [N II], [S II] and [O II] emission, and low ionized masses. Consequently they plot close to the lower bound of the SB-r relation. Other calibrating PNe are marked with crosses. The line is a least-squares bisector fit to the HE PNe only.

$$\log S(\text{H}\alpha) = -3.16(\pm 0.45)\log R - 5.78(\pm 0.21) \tag{7.8}$$

The central stars of this group are rather heterogeneous, with both H-rich and H-deficient nuclei, and at least two belong to the born-again class (eg. Cohen et al. 1977). The spectroscopic uniformity of the nebulae as a whole is considered to be a product of the low shell mass of these PNe. Note that several post common-envelope PNe also have very high excitation, and are discussed further below.

7.3.4 Close-binary PNe

It is important to note that known post-CE PNe overlap in SB-r space with high-excitation PNe (Figures 7.10 and 7.11). These objects also plot close to the lower bound of the SB-r relation, showing that as a group, they too have systematically lower ionized masses. This was in fact first suggested by Bell, Pollaco & Hilditch (1994), based on data for Abell 63.

Summary lists of known post-common envelope PNe with close-binary central stars were given by Livio (1982), Bond (1989, 1994, 2000), Bond & Livio (1990), Livio (1993), De Marco (2006) and De Marco, Hillwig & Smith (2008). Table 7.2 lists the relevant data for all known close binary PNe. The list is adapted from De Marco (2006, and references therein), with three exceptions. Omitted are NGC 6302 for which the evidence of binarity is weak (see Zijlstra 2007), and Sh 2-71, for which the central star has until now been misidentified; the probable CS is a faint 19th magnitude star at the exact centre of the nebula (see Figure 7.13). Abell 35 is also excluded, not only because the companion is demonstrably too distant to be a close binary (Gatti et al. 1998), but is considered here not to be a PN at all (see §8.2). NGC 1514, LoTr 1 and LoTr 5 are included, following De Marco (2006), even though their orbital periods are currently unknown. WeBo 1 has also been added, as it shares morphological similarities with Sp 1 and SuWt 2.

The third column of Table 7.2 gives the orbital period in days. The distances in the last column are determined using the post-CE SB-r trend (equation 7.9), and may differ somewhat from the adopted distances for those PNe that are primary calibrators (see Table 7.3). However, the relative PN distances in table 7.2 should be fairly reliable, if the assumption that post-CE PNe have similar (and low) masses holds.

Bond (2005) and Moe & De Marco (2006 a,b) have suggested that close-binary PNe are very common, and may make up the majority of PNe. However, the known close binary PNe show a somewhat restricted range of Hα surface brightness ($S_{\mathrm{H}\alpha} = -2.5$ to -6.2 erg cm^{-2}s^{-1}sr^{-1}) compared to the full observed range for all PNe (+0.2 to −6.7). In other words, PNe of highest SB are not known to host close-binary nuclei. This has been traditionally interpreted as a selection effect (Bond & Livio 1990).

To help verify if close-binary PNe form a separate population to other objects, a subset of the latter CS that appear to be definitely single (e.g. NGC 7293 which has no NIR excess or any RV variability) or very likely single, based on data from Table 9.6, were plotted in Hα SB-r space (see figure 7.12). Again, a systematic offset between the post-CE PNe and non-close-binary PNe is observed. As a group, these post-CE nebulae seem to show quite distinctive filled-centre, bipolar, or toroidal morphologies, but not the more typical double-shelled forms (see Bond & Livio 1990). It is argued here that the known close binary PNe have a distinct spectrum of properties, which differentiate them from the more common 'typical' PNe.

It should be noted that 'merged binaries' may exist in the local volume, but probably not in large numbers. If mergers happen prior to the AGB, this might produce progenitor stars (and PN shells) of higher mass that will not be distinguishable in these plots. Indeed, Alves, Bond & Livio (2000) suggest that the PN Pease 1 (K 648) in the globular cluster M 15 probably evolved from a cluster blue-straggler, which was a product of a binary merger before the AGB phase. Blue stragglers are thought to be the possible progenitors of the [O III]-bright PNe which are seen to populate the top of the PNLF in elliptical galaxies (Ciardullo et al. 2005). These points are further discussed in §9.5.2 and §11.6.

It is found here that the average ionized mass of local, non-close-binary PNe (selected for SB within the same limits shown by close-binary PNe) is 0.64 ± 0.5 $M_{\odot}$. However, the average ionized mass for the objects from Table 7.3 is 0.17 ± 0.13 $M_{\odot}$, or 0.13 ± 0.08 $M_{\odot}$ if HFG 1 is excluded (due to a less reliable ionized mass). This result confirms what is apparent from the distinct locus of post-CE objects in SB–r space; that the known post-CE PNe have systematically lower ionized masses than other PNe of similar SB.

The linear least-squares fit to the eight post-CE PNe only is described by the equation:

$$\log S(\mathrm{H}\alpha) = -3.13(\pm 0.86)\log R - 5.86(\pm 0.49) \tag{7.9}$$

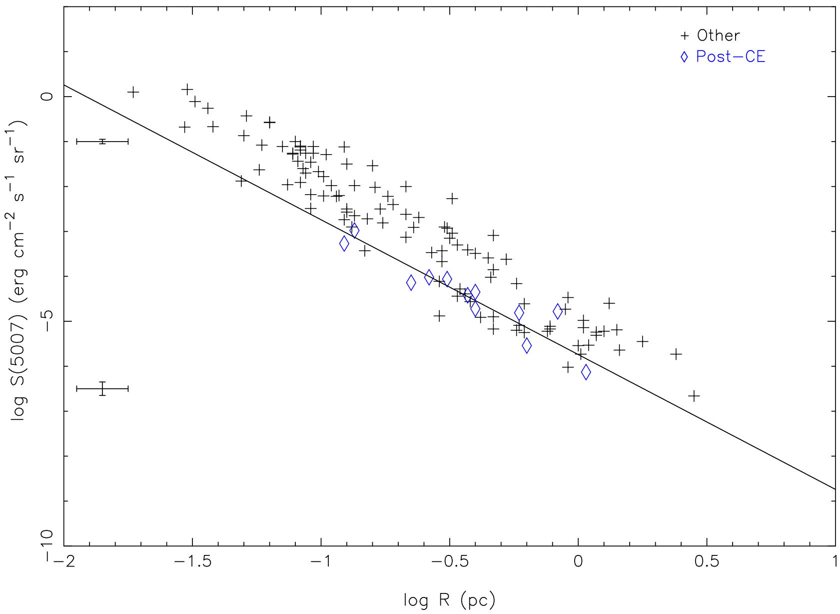

Figure 7.10: Hα surface brightness – radius relation plotting close-binary, common-envelope (post-CE) PNe separately (blue diamonds). These objects also plot close to the lower bound of the SB-r relation, showing that as a group, they have systematically lower ionized masses. Other calibrating PNe are marked with crosses. The line is a linear least-squares fit to the post-CE PNe only. If a common envelope phase is an universal prerequisite for PN formation, it is hard to reconcile this with the distinct trend occupied by known post-CE PNe in Hα SB-r space.

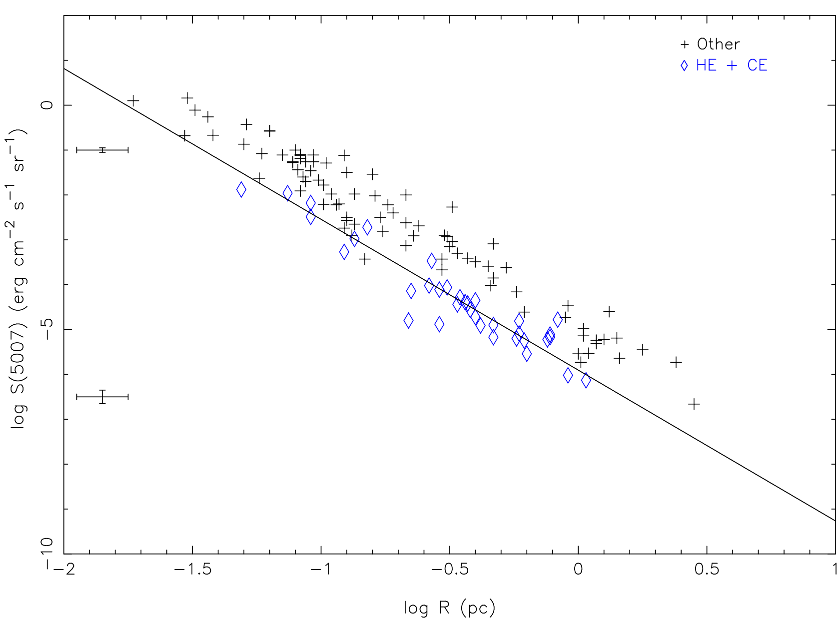

Figure 7.11: Hα surface brightness – radius relation grouping high-excitation and common-envelope PNe together (blue diamonds). Other calibrating PNe are marked with crosses. The line is a linear least-squares bisector fit to the HE and CE PNe only.

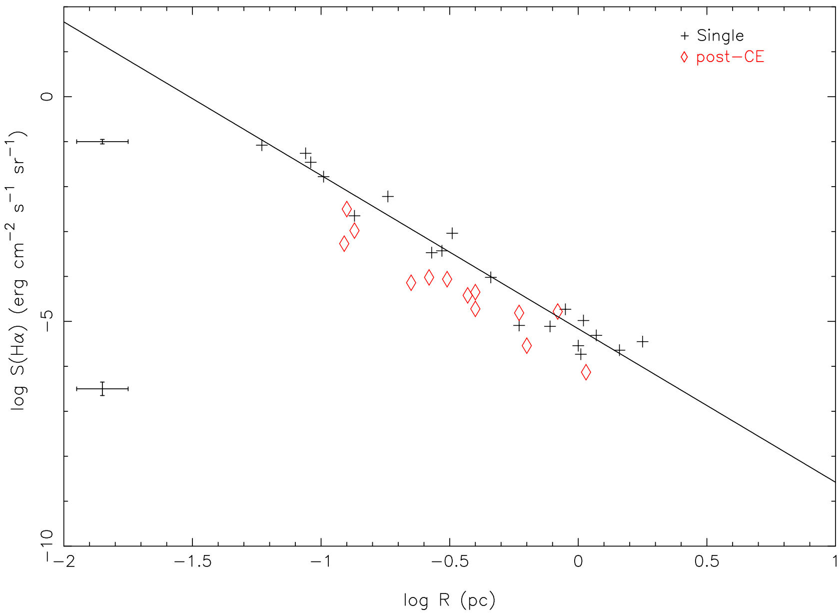

Figure 7.12: Hα SB-r relation comparing close-binary (post-CE) and definitely or very-likely non-close-binary PNe (refer to the text for more details). The line is a linear least-squares bisector fit to the non-close-binary PNe only.

It is of interest to determine what proportion of the HE PNe are in fact post-CE PNe. One object, NGC 1360 has morphological similarities with Abell 65, and its central star may be a close binary (Afşar & Bond 2005). However there is no photometric evidence for a companion from 2MASS data, though the limits are not overly stringent (the spectral type of any companion is later than M2V) because the central star is optically quite luminous.

The result that post-CE PNe are systematically lower in mass needs to be confirmed with more data from additional PNe, but is strongly suggestive of post-CE objects forming a distinct subset within the diverse family of PNe. This was first hinted at by Bell, Pollaco & Hilditch (1994) who noted a very low ionized mass for Abell 63. The low mean ionized mass of the post-CE sample also affects the shape of the PN luminosity function (PNLF), a point discussed further in Chapter 10.

This observation has significant implications for our understanding of the PN binarity issue. If *all* post-CE PNe are found to have lower masses, this conflicts with the hypothesis of Moe & De Marco (2006) which suggests that most, if not all, PNe are the result of close binary evolution. While recent radial velocity studies have lent support to this interpretation (e.g. Sorensen & Pollacco 2003; De Marco et al. 2004; Afşar & Bond 2005; cf. Méndez 1989 and Augensen 1985), there appears to be a range of selection biases in the samples studied to date. An often overlooked statistic is the percentage of radial velocity variables from the high-resolution spectroscopic study of Méndez (1989): only 5 out of 28 stars showed obvious radial velocity variations, and all of the others showed very small differences ($<$10 kms^{-1}) between the nebular and stellar velocities. If most CS are close binaries with periods of one to a few days, then a high fraction of CS should show velocities at random phase significantly different

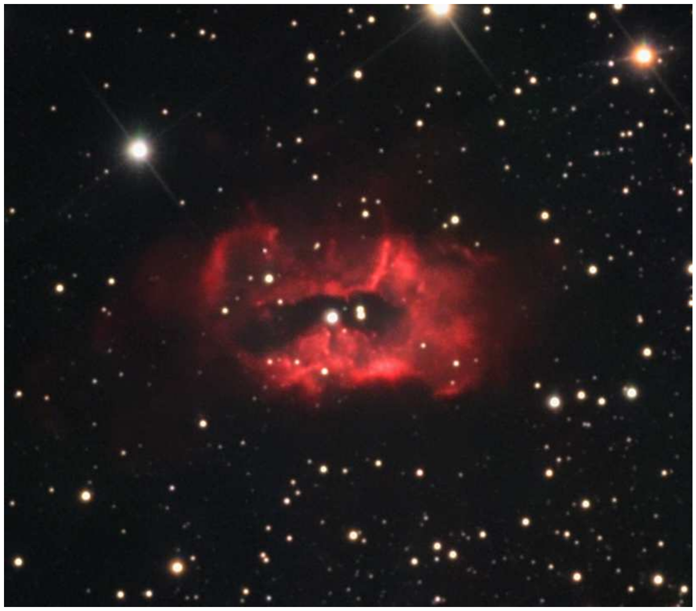

Figure 7.13: Tri-colour image of the bipolar Type I PN Sh 2-71. The true central star is the faint blue object at the *exact* centre of the nebula; the apparent V magnitude is $\sim$19. The star previously assumed to be the CS is the brightest star in the interior hole in the nebula (see the finder chart in Kohoutek 1979). This object should be removed from lists of close-binary PNe. Image credit: Adam Block/NOAO/AURA/NSF.

Table 7.2: Summary list of known and suspected close binary PNe (cf. De Marco 2006).

Name	Other	Period (days)	a ($''$)	b ($''$)	V^*	M_V^*	$D_{H\alpha}$ (pc)
Abell 41	...	0.11	26	22	16.45	2.33	2200
Abell 46	...	0.47	97	84	14.8	3.16	1760
Abell 63	...	0.46	48	42	15.14	1.69	2270
Abell 65	...	1.00	137	82	15.8	5.18	1170
DS 1	...	0.36	354	315	12.16	2.39	610
HaTr 4	...	1.74	30	18	17.06	2.32	3000
Hb 12	...	0.14	11	5	13.8	1.1:	2350
Hf 2-2	...	0.40	17	17	17.37	3.31	2900
HFG 1	...	0.58	540	540	13.38	3.33	380
K 1-2	...	0.68	110	53	16.83	3.96	2530
LoTr 1	DeHt 1	...	138	126	12.50	0.35	2440
LoTr 5	...	...	540	510	14.7[a]	5.9:	680
LTNF 1	BE UMa	2.29	230	215	16.15	4.54	2390
NGC 1514	...	...	140	132	9.512	−0.01	440
NGC 2346	...	15.99	70	55	11.27	−0.08	740
NGC 6026	...	0.53	53	46	13.33	1.13	1310
NGC 6337	...	0.17	48	47	15.3	2.65	800
SBSS 1150+599	PN G135.9+55.9	0.16	9	9	17.9	1.52	15800
Sp 1	...	2.91	72	72	13.69	1.82	1130
SuWt 2	...	2.45	90	45	11.95	−0.13	1760
WeBo 1	...	...	64	22	14.45	1.18	2700

[a] magnitude refers to hot component

Table 7.3: Known post-CE nebulae with primary calibrating distances. Ionized masses are calculated from the measured diameters and fluxes, and assuming a volume filling factor of 0.4 (see the text for further details).

PN	Distance (kpc)	Method	Ionized Mass ($M_\odot$)
Abell 46	1.7 ± 0.6	1	0.14
Abell 63	2.4 ± 0.4	1	0.08
BE UMa	2.0 ± 0.4	2	0.2:
DS 1	0.73 ± 0.07	2	0.26
HFG 1	0.6 ± 0.3	3	0.5:
LoTr 5	0.50 ± 0.20	3, 4, 5	0.13
NGC 1360	0.37 ± 0.10	5, 6	0.13
NGC 1514	0.37 ± 0.15	3	0.03
NGC 2346	0.90 ± 0.2	3, 7	0.06
SBS 1150+599A	18 ± 5	6	0.17
SuWt 2	1.5 ± 0.4	3	0.06

Distance method: 1. Eclipsing binary; 2. Reflection effect model; 3. Spectroscopic parallax; 4. Wilson-Bappu relation; 5. Trigonometric parallax; 6. Gravity method; 7. Extinction distance.

to the nebular (systemic) velocity; these differences should be at least ∼30–50 kms^{-1}. Instead, the data set of of Méndez (1989) suggests that close-binary CS are in the minority.

Since there is no consensus as yet on the frequency of close binaries, further efforts to discover more close-binary PNe, and determine accurate distances to them, are urged. To this aim, a new collaboration, the PLAN-B (PLAnetary Nebula Binaries)[2] group, has been set up in order to discover new PN binary central stars using a variety of observational techniques.

7.4 Precision and accuracy of the SB-r relation

The SB-r relation functions as a useful statistical distance indicator for *all* PNe, and especially for those for which no primary distance technique is available. A measure of the dispersion of the technique can be evaluated by comparing the primary distances of the PNe in the calibrating sample with the distances derived for these PNe from the SB-r relation. In figure 7.14, the primary calibrating distances (from table 7.1) and statistical distances from the *mean* SB-r relation for the full set of Galactic calibrating PNe are compared. The dispersion in the distance is ±40%, comparable to previous statistical distance scales. The right-hand panel of the figure plots uses high- and low-trend SB-r distances where appropriate, rather than one-size-fits-all mean distances. Using these sub-trends allows the overall dispersion to be reduced to ±28%.

Figure 7.15 plots individual PNe using the high- and low-trend statistical distances separately. Using the high-trend relation for bipolar and bipolar-core PNe only, a dispersion of ±32% is obtained. In addition, using the low-trend SB-r distance for just the subset of high-excitation and post-CE PNe gives a small resulting dispersion of only ±22%. This 1σ uncertainty is better than any previous statistical distance indicator, albeit for a rather restricted subset of PNe (see the discussion by Stanghellini, Shaw & Villaver 2008). The zero-point of the SB-r relation is

[2]see: http://www.wiyn.org/planb/

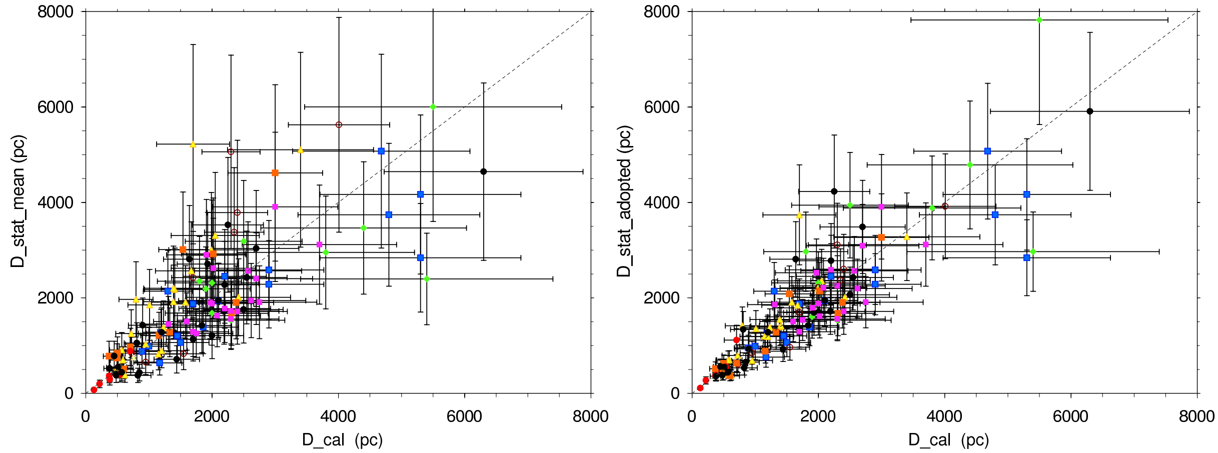

Figure 7.14: Comparison of primary distances and statistical distances from the Hα SB-r relation for the full set of 122 Galactic calibrating PNe. The left-hand panel plots the primary calibrating distance as the absicca and the mean SB-r distance as the ordinate. Individual distance techniques are colour-coded as follows: trigonometric distances (red dots), photometric/spectroscopic distances (orange squares), extinction distances (pink squares), gravity distances (yellow triangles), expansion distances (blue squares), kinematic distances (green dots), photoionization and other model distances (open circles) and distances based on two or more methods (black dots). The three cluster distances are off-scale. and are not plotted. The overall 1-sigma dispersion in the SB-r distance scale is $\pm 40\%$, represented by the y-axis error bars. Using sub-trends where appropriate (right panel), the dispersion can be reduced to $\pm 28\%$. The dashed lines in each panel have a slope of unity.

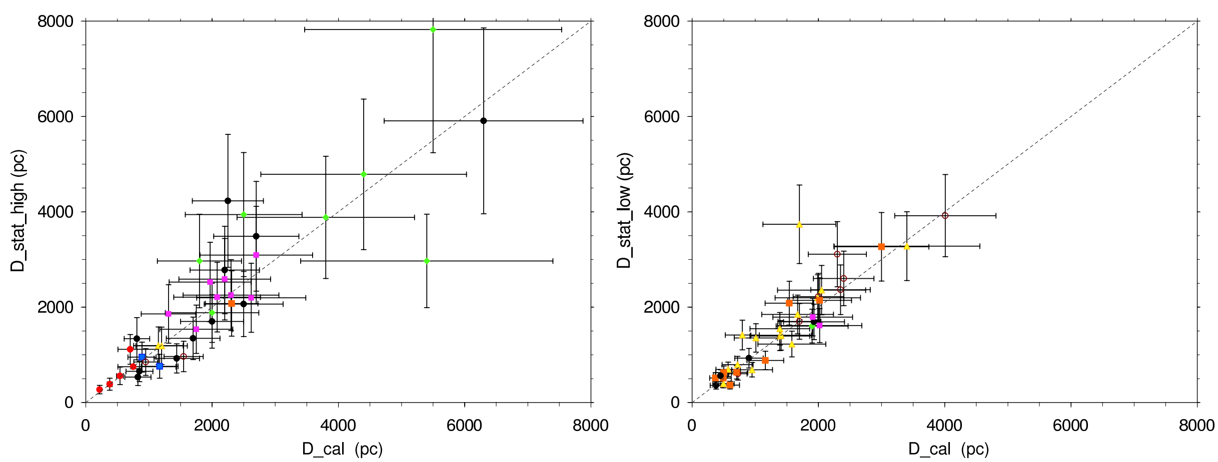

Figure 7.15: Comparison of primary distances and statistical distances from the Hα SB-r relation for two subsets of Galactic calibrating PNe. The left-hand panel plots the primary calibrating distance (abscissa) against the high-trend SB-r distance (ordinate) for bipolar and bipolar-core PNe only; the resulting dispersion is $\pm 32\%$. The right-hand panel plots the primary distance (abscissa) against the low-trend SB-r distance (ordinate) for high-excitation and post-CE PNe only; the resulting dispersion is only $\pm 22\%$, ignoring the 2.5σ outlier, the peculiar object K 1-27. The dashed lines in each panel have a slope of unity, and the symbols have the same meaning as figure 7.14. See the text for further details.

Table 7.4: Uncertainties of individual distance techniques. The quoted 1σ uncertainties are a convolution of the uncertainties in the individual distances and the uncertainties in the adopted SB-r distances (using subtrends).

Distance technique	Uncertainty
Trigonometric method	24%
Photometric/spectrsocopic parallax	25%
Extinction distance method	33%
Gravity method	34%
Expansion parallax method	30%
Kinematic method	37%
Model distances	20%
Cluster membership method	23%

estimated to be as good as ±5%, as shown by applying it to a set of Magellanic Cloud PNe at a known distance (see §7.5.2, below).

It is noted that the dispersion in the high-trend relation, applicable to bipolar PNe, is higher than the dispersion of the low-trend relation. Close inspection shows that for a few bipolar PNe, the high-trend relation is less accurate than the mean trend. This may be due in part to the difficulty of accurately measuring the angular dimensions of many bipolar PNe, but is more likely that the bipolar PNe are a relatively heterogeneous group: I speculate that bipolars may be produced by both high-mass single progenitors as well as lower-mass close-binary stars. Stanghellini, Shaw & Villaver (2008) also find that their distance scale does not work well for PNe with classic bipolar PNe.

The observed dispersion is actually a convolution of the uncertainties in both the calibrating distances and the statistical distances. In order to gauge the uncertainties of each primary distance technique, the distances for individual PNe were compared with the adopted SB-r distances. Table 7.4 shows the results. It is seen that the kinematic, gravity and extinction distance methods have the greatest uncertainties. The kinematic method was only applied to Type I PNe, but it seems even these can sometimes have significant peculiar velocities, meaning that the technique should be used with caution. The problems with the gravity method have already been discussed. The extinction method, while powerful in the sense that it can be applied to many PNe, should also be used with caution. Care should be taken to avoid using PNe that are found in fields with significant differential extinction.

7.5 Comparison with Previous Work

7.5.1 Previous Galactic Distance Scales

From a review of the literature, it is seen that most published PN distance scales can be roughly divided into two camps, long and short, with ongoing debate between the two groups (e.g. Ciardullo et al. 1999; Napiwotzki 2001; Phillips 2001a, 2002a, 2003e, 2004c), quite analogous to the well-known (former) controversy over the low and high values of the Hubble Constant (e.g. Rowan-Robinson 1985). Clearly, the recent literature provides no consensus on the distance scale for evolved PNe, with a factor of ~3 discrepancy evident between the short and long scales.

To compare the various published distance scales with one another, an index κ has been defined as $<D>_{\mathrm{reference}} \div <D>_{H\alpha}$, following Phillips (2002a), where the mean distances for an ensemble of PNe using one of the distance scales from the literature are compared with distances for the same PNe using the Hα SB-r relation. Table 7.5 shows a relative comparison of the most widely used distance scales discussed in the literature, expressed as approximate ratios relative to the present work (defined as κ = 1.00). This was done by normalising the older data taken from Peimbert (1990) onto the distance scale of Daub (1982) for all PNe in common between the two studies, before linking that with the more recent data presented in the various papers from Phillips (2001a, 2002a, 2004c, 2005c). The present distances derived here were directly related to the largest data sets of Cahn, Kaler & Stanghellini (1992), Zhang (1995), Phillips (2002a) and Phillips (2004c) (see Figures 7.16 and 7.17). Additional distances from Kingsburgh & English (1992), Mal'kov (1997) and Bensby & Lundstrom (2001) were then normalised to the same scale to get a fairly consistent set of ratios, relative to the present work.

Owing to the exact value of the κ-ratio being dependent on the subset of PNe used to make the comparison (i.e. whether the adopted distances of the calibrating PNe, or the statistical distances themselves were compared, or if subsets of compact or evolved PNe were used), statistical errors on the ratios are not formally given, but are estimated to be ± 20%. For example, for young, high-surface brightness PNe, the distance scale of Zhang (1995) agrees to within 10% with the present work, but for the most evolved PNe (which were not used as calibrators by Zhang), the Zhang scale predicts distances roughly a factor of two too large (see figure 7.16).

It can be seen from Table 7.5 that there is over a factor of three difference for the largest and smallest distance scales in the literature, that is Kingsburgh & English (1992; see also Kingsburgh & Barlow 1992) and Phillips (2002a) respectively. Another of Phillips's distance scales (Phillips 2005a) could not be consistently normalised with respect to the present scale, but appears to be a short one (note the high number of PNe within 500 pc in his sample).

7.5.2 Comparison with the Magellanic Clouds

It is readily apparent that the Hα SB-r relation for the Galactic sample is broadly consistent with that seen in Magellanic Cloud PNe. These PNe have the advantage of a known distance, and Stanghellini et al. (2002b, 2003) find a decline in surface brightness with nebular radius for both the LMC and SMC PNe that is well characterized by an R^{-3} law for all observed emission lines (see also Shaw et al. 2001, 2006). The relevant data (fluxes, reddenings, and major and minor axial dimensions) were taken from Shaw et al. (2001, 2006) and Stanghellini et al. (2002b, 2003). For consistency with the sample of Galactic calibrating objects, the angular dimensions at the 10% brightness contour have been used from these references, rather than the 'photometric' radii of the PNe (encompassing 85% of the total flux), as described by Stanghellini et al. (1999).

Intrinsic radii, assuming canonical distances of 50 kpc and 59 kpc to the LMC and SMC

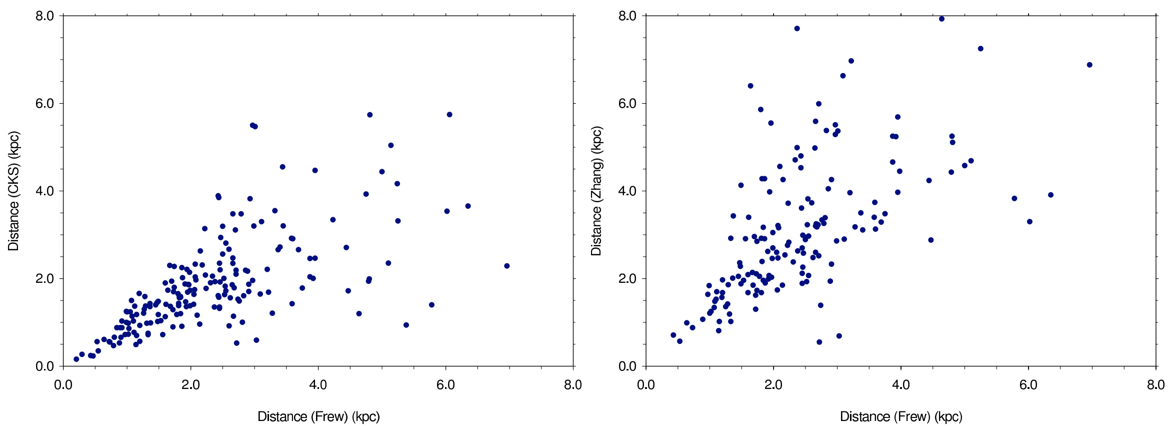

Figure 7.16: A comparison of the distance scales of Cahn, Kaler & Stanghellini (1992; CKS) and Zhang (1995) with the Hα SB-r distance scale from the present work. The data of Zhang (1995) show a relatively large scatter compared to the present distances. This is attributed to the Zhang scale breaking down for the largest, most evolved PNe, which have distances greatly overestimated by his relation. Distances for young compact PNe are in good agreement with those derived here.

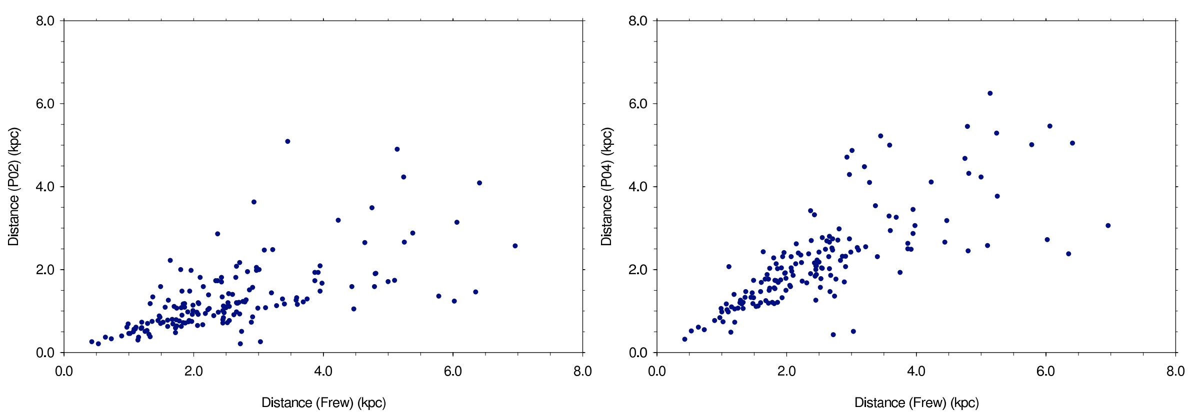

Figure 7.17: A comparison of two distance scales from Phillips (2002a, 2004c) with the present distance scale. The Phillips (2002a) scale is seen to be too short, based primarily on a range of incorrect distances to his calibrating nebulae. Non-PNe also contaminate his calibrating sample. The Phillips (2004c) scale is a better match to the present scale.

Table 7.5: Relative PN distance scales from the literature

Distance Scale	κ
O'Dell (1962)	0.87
Cahn & Kaler (1971)	0.74
Cudworth (1974)	0.91
Milne & Aller (1975)	0.74
Acker (1978)	0.69
Maciel & Pottasch (1980)	0.86
Daub (1982)	0.58
Mallik & Peimbert (1988)	0.95
Cahn et al. (1992)	0.83
Kingsburgh & English (1992)	1.29
Zhang (1995)	1.05
Van de Steene & Zijlstra (1995)	0.96
Schneider & Buckley (1996)	0.94
Mal'kov (1997)	1.08
Bensby & Lundström (2001)	1.00
Phillips (2001a)	0.99
Phillips (2002a)	0.38
Phillips (2004c)	0.98
Phillips (2005c)	0.80
Present work	1.00

Table 7.6: Summary of SB-r relation best-fit constants for different PN subsets.

Trend	a	b	n
Galactic (mean)	-3.61 ± 0.11	-5.38 ± 0.09	122
Bipolar (+ Bc)	-3.37 ± 0.27	-4.89 ± 0.19	39
High-excitation	-3.16 ± 0.45	-5.78 ± 0.21	19
Post-CE	-3.13 ± 0.86	-5.86 ± 0.49	8
non-close-binary	-3.41 ± 0.16	-5.16 ± 0.11	19
Type I	-3.35 ± 0.25	-4.90 ± 0.18	19
Solar Neighbourhood	-3.52 ± 0.44	-5.31 ± 0.53	32
Bulge	-3.35 ± 0.34	-4.83 ± 0.23	54
Magellanic Clouds	-3.49 ± 0.12	-5.14 ± 0.07	118
All	-3.66 ± 0.08	-5.34 ± 0.07	297

respectively (μ_0 = 18.50 and μ_0 = 18.85; van den Bergh 2000), and Hα surface brightnesses were calculated in the same way as for the Galactic sample. A linear least-squares bisector fit to 118 Cloud PNe is described by the equation:

$$\log S(\mathrm{H}\alpha) = -3.49(\pm 0.12)\log R - 5.14(\pm 0.07) \tag{7.10}$$

A systematic offset (and slightly different slope) is seen between the galactic sample (mean trend; figure 7.1) and the Magellanic Cloud sample (figure 7.18) when co-plotted in SB-r space.

Table 7.6 summarises the constants for the different SB-r fits for the various subsets described here. The small offset between the galactic and Magellanic Cloud samples is due to one or more of Malmquist bias (the MC sample is surface brightness limited), systematic errors in local distances, systematic errors in measuring PN diameters (much more difficult for extragalactic PNe, unless HST imaging is available), and age and/or metallicity differences between the samples from the different galaxies.

The relatively large observed uncertainties on these distances (∼20–40%) indicates that an application of the Galactic SB-r relation to external systems is likely to be affected by Malmquist bias[3] (Malmquist 1924) if the calibrating sample is different in make-up to the PN sample in the Magellanic Clouds. It is apparent from the data presented by Shaw et al. (2001, 2006) and Stanghellini et al. (2002b, 2003), that low mass, high excitation PNe *sensu stricto* (defined above) are essentially absent from their Cloud samples. Intuitively this is expected as they are intrinsically less luminous, with a fainter surface brightness at any given radius. However, one example has been noted by Shaw, Reid & Parker (2007), as a result of a deliberate search in archival *HST* images for PNe discovered by Reid & Parker (2006b; see also Reid 2008), based on deep Hα imaging.

A slight systematic offset in the LMC/SMC trendline is a natural consequence of slight biases in the flux-limited LMC sample compared to the local calibrating sample (figure 7.18). Cloud PNe have higher shell masses in the mean and will be displaced toward the upper envelope of the broad locus in SB-r space. I speculate this may be because the LMC (and SMC) disk field stars have a younger mean age than those of the galactic old thin disk. So a combination of Malmquist bias and population effects can explain the slight offset between the Cloud and local samples. It should be emphasised however, that no serious error in the zero point of the adopted (mean) distance scale is apparent.

Hence, the Hα SB-r relation can also be used as a crude extragalactic distance indicator (if an ensemble of extragalactic PNe is available across a range of SB). Distances to the Galactic Bulge, LMC, SMC and the Sagittarius dSph galaxy were determined using the mean galactic relation, a 'high' (optically-thick bipolar) trend and a 'low' HE/CE trend. The distances are tabulated in Table 7.7, based on Cloud PN data (maximum and minimum dimensions, Hα fluxes and reddenings) taken from Shaw et al. (2001), Stanghellini et al. (2003) and Shaw et al. (2006). Similarly, the Sgr dSph data is adopted from Zijlstra et al. (2006). Data for bulge PNe was taken from the sources discussed previously, with the comment that only objects with accurate angular dimensions, from Tylenda et al. (2003) or Ruffle et al. (2004), have been used. In summary, excellent agreement within the errors is achieved for all four systems compared to well determined literature values.

The average distances to the LMC and SMC PN samples derived using the mean SB-r relation can be used to estimate the zero-point error in the Galactic distance scale adopted here. Using the mean SB-r trend, the derived distances (Table 7.7) are 4.6% and 3.9% too short. I conclude that the SB-r zero-point is good to ±5%.

[3]Malmquist bias is present when the intrinsic (cosmic) dispersion of a sample of objects is significant. In other words, if a sample of objects (stars, PNe or galaxies, for example) is flux-limited, then only the most luminous objects are selected at large distances, so there is an observed increase in the average luminosity of a flux-limited sample as distance increases.

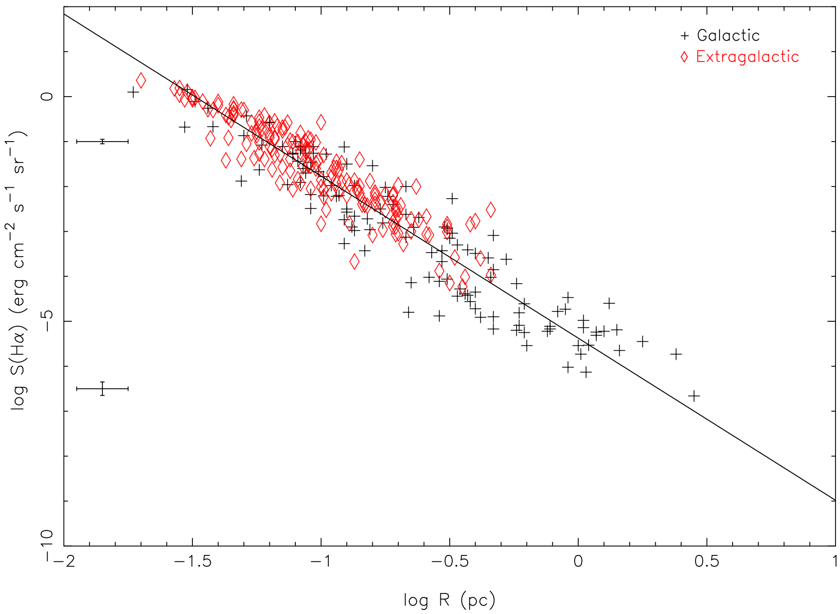

Figure 7.18: Hα SB-r relation plotting 121 extragalactic PNe from the LMC, SMC, and Sgr dwarf spheroidal galaxy (red diamonds), as well as the galactic calibrating sample of 122 PNe (crosses). The line is a least-squares bisector fit to the galactic sample. Note the absence of the largest PNe from the extragalactic sample, due to selection effects.

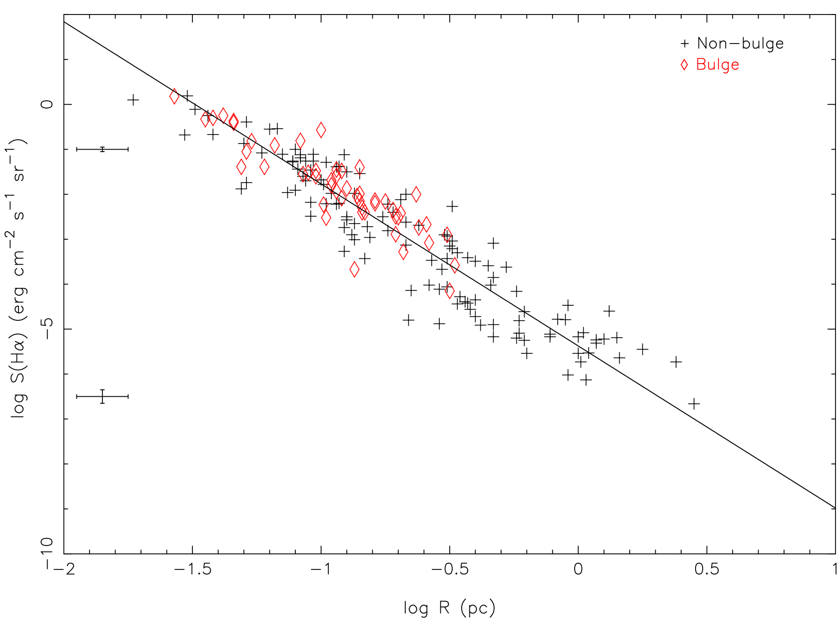

Figure 7.19: Hα SB-r relation plotting 54 PNe from the galactic bulge (red diamonds), as well as the galactic calibrating sample of 122 PNe (crosses). The line is a least-squares bisector fit to the galactic calibrating sample, excluding the bulge objects. The bulge PNe are seen to be mainly bright and compact, and show some additional scatter about the line of best-fit, due to observational uncertainties in their generally high extinctions, and the assumption of a common distance.

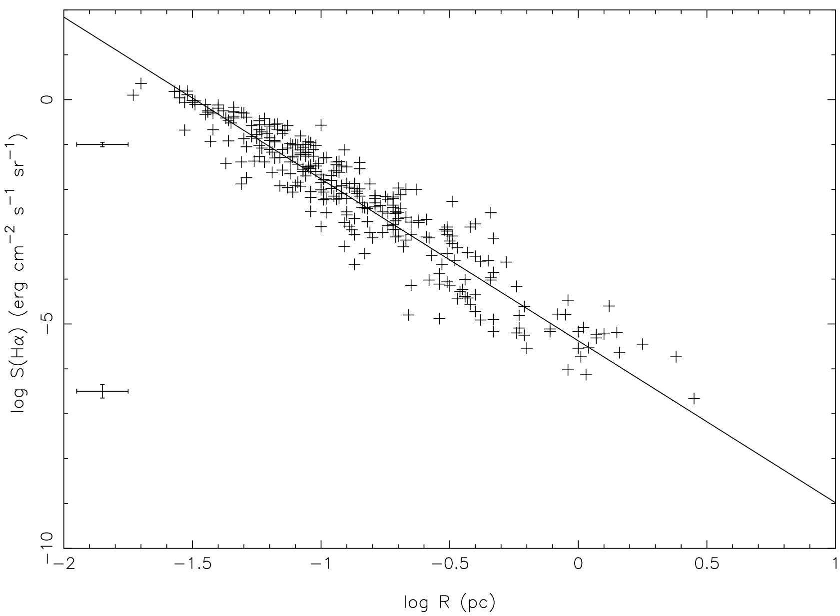

Figure 7.20: Hα SB-r relation for all 297 PNe from the previous samples. The line is a least-squares bisector fit to the Galactic calibrating sample. The shallower gradient of the relation at small radii can be compared with theoretical tracks (see figure 7.21).

Table 7.7: Distances to the Galactic bulge and three satellite galaxies

System	$n_{\rm PN}$	$D_{\rm lit}$ (kpc)	$D_{\rm mean}$ (kpc)	$D_{\rm low}$ (kpc)	$D_{\rm high}$ (kpc)	$D_{\rm local}$ (kpc)
Bulge	52	7.6 ± 0.3	7.5 ± 1.8	4.6 ± 1.2	9.2 ± 2.3	5.7 ± 1.5
LMC	91	50.0 ± 4.0	47.8 ± 17.8	29.0 ± 11.3	57.2 ± 22.4	35.1 ± 14.4
SMC	27	59.0 ± 5.0	56.6 ± 12.5	34.3 ± 8.9	67.7 ± 17.8	41.6 ± 12.7
Sgr dSph	3	25.0 ± 2.5	22.2 ± 2.9	13.2 ± 2.1	26.0 ± 4.2	15.7 ± 2.9

7.6 Malmquist Bias

The high trend overestimates the distances to the Clouds compared to the accepted literature values, showing that using a bipolar object as a proxy for an average PN is incorrect, as bipolar PNe have sytematically higher ionized masses than the mean. The difference in distance is least for the mean trend, which though slightly short, is consistent with truth. However, using the volume-limited SB-r trend (defined just using PNe in the solar neighbourhood), the derived distances are too short, due to the effect of Malmquist bias.

A quick-and-dirty correction for Malmquist bias can be determined as follows. In terms of magnitudes, the difference between the mean absolute magnitude ($\bar{M}$) of an observed flux-limited sample compared with the intrinsic mean magnitude ($\bar{M}_0$) of a population of PNe is:

$$\bar{M} = \bar{M}_0 - 1.38\,\sigma_0^2 \tag{7.11}$$

where σ_0 is the intrinsic dispersion of the population. For a derivation of this formula, see Rowan-Robinson (1985, p. 340).

For the 1.0 kpc *volume-limited calibrating sample* (32 calibrators, excluding K 1-27), an estimate of the intrinsic dispersion in the Hα surface brightness (at a given value of R) is taken as the residual standard deviation (standard error of the estimate) after regressing S against R. I find $\sigma_{\mathrm{S,R}} = 0.57$ (in log units of the Hα flux). After converting from flux units to magnitudes, a dispersion of $\sigma_0 = 1.43$ mag around the mean trend is derived.

From equation 7.11, the Malmquist bias in terms of modulus is 2.8 mag (or a factor of ∼3.6 in distance), larger than the factor of ∼1.4 difference in mean distance between the accepted distance to the LMC and the distance using the 'local' SB-r trend. The magnitude of the bias calculated this way is a firm upper limit, due to the assumption that all the dispersion is in the y-value (the surface brightness), but in fact the x-value (log R) has a significant intrinsic dispersion also. In reality, Malmquist bias is less of a problem as the *mean* SB-r trend is much more representative of the full admixture of PNe, and recovers the dstance to the Clouds to better than 5%.

The SB-r relation was never intended as a new extragalactic distance indicator, but applied to a representative sample of extragalactic PNe, can recover the mean distance to a nearby galaxy, though with a large associated error bar (typically $20 - 30\%$). Malmquist bias can be reduced by using the mean SB-r trend (rather than one based on a volume-limited sample), which is based on a wide sample of calibrating PNe that is fairly representative of the population in the Magellanic Clouds. However *HST* images are necessary to generate accurate angular dimensions for the application of the SB-r relation, so the technique is currently restricted to the very nearest galaxies of the Local Group, i.e. the companions of the Milky Way.

7.7 Mass, density and the SB-r relation

Detailed photoionization modelling of the SB-r relation (and its relationship to central star evolutionary tracks) is beyond the scope of this dissertation (see Kwok 1985; Van de Steene &

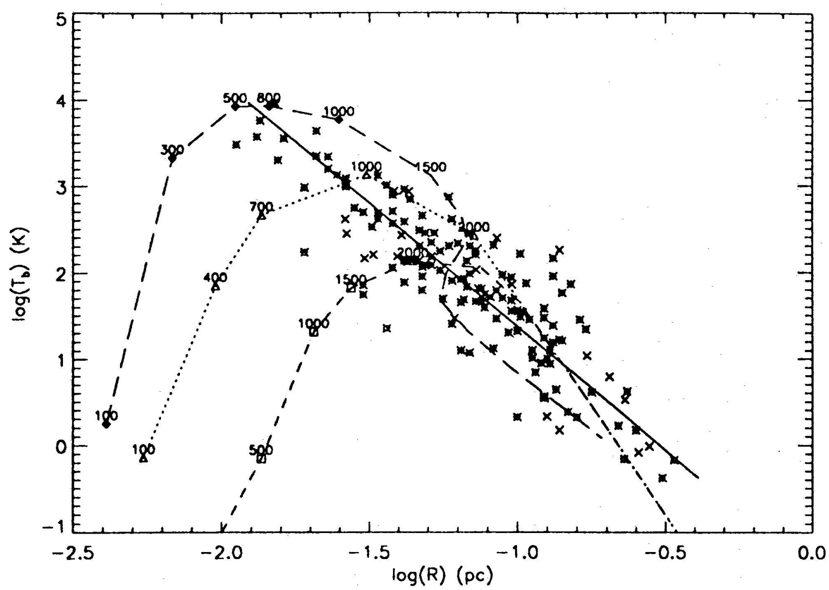

Figure 7.21: Radio (6 cm) brightness temperature versus radius diagram from Van de Steene & Zijlstra (1995). Model evolutionary tracks assuming a nebular mass of $0.2\,M_{\odot}$ and an expansion velocity of $20\,\mathrm{kms}^{-1}$ and various central star masses are overplotted (0.625, 0.605 and $0.565M_{\odot}$ models are plotted with long dashed, dotted and short dashed lines respectively). The numbers are post-AGB ages given by the models. The individual points are the calibrating PNe from Van de Steene & Zijlstra (1995) and the heavy solid line is the regression line of the sample.

Zijlstra 1995), but making some simple assumptions from emission theory, we can relate the observed power-law gradient of the SB-r relation to other PN parameters such as the ionized mass and mean electron density.

Following Hua & Kwok (1999), for an uniform spherical nebula of radius R, the integrated flux $F_0(\mathrm{H}\alpha)$ emitted by the Hα line is given by:

$$F_0(\mathrm{H}\alpha) = \frac{4\pi j_{\nu}}{4\pi D^2}\left(\frac{4\pi R^3}{3}\right) \tag{7.12}$$

where j_{ν} is the line emission coefficient, and D is the distance to the PN. The Hα flux is corrected for reddening using the Howarth (1983) reddening law, $F_0(\mathrm{H}\alpha) = F(\mathrm{H}\alpha) \times 10^{0.693 \times c_{\mathrm{H}\beta}}$.

For a recombination line, $j_{\mathrm{H}\alpha}$ is often expressed in terms of the effective recombination coefficient, as:

$$\alpha^{\mathrm{eff}} = \frac{4\pi j}{n_{\mathrm{e}} n_{\mathrm{p}} h\nu} \tag{7.13}$$

where n_{e} and n_{p} are the electron and proton densities respectively. The flux in the recombination line can then be written as:

$$F_0(\mathrm{H}\alpha) = \left(\frac{R^3}{3D^2}\right) h\nu_{\mathrm{H}\alpha} n_{\mathrm{e}} n_{\mathrm{p}} \alpha^{\mathrm{eff}}_{\mathrm{H}\alpha} \tag{7.14}$$

In practice, PNe are not spherically homogenous, and a volume filling factor ϵ is used to take this into account. Various values are presented in the literature, but a consensus value, $\epsilon = 0.4$, is adopted herein (Mallik & Peimbert 1988; Boffi & Stanghellini 1994; Pottasch 1996; Hua & Kwok 1999; Pierce et al. 2004). The ionized mass of the nebula is then given by:

$$M_i = \frac{4\pi}{3} n_{\rm p} \mu m_{\rm H} \epsilon R^3 \tag{7.15}$$

where μ is the mean atomic mass per H atom. Combining equations 7.14 and 7.15, the nebular ionized mass can be expressed in terms of the angular radius, Θ, and the Hα flux as

$$M_i = \frac{4\pi\mu \mathrm{m_H}}{\sqrt{3h\nu_{\mathrm{H}\alpha} x_e \alpha^{\rm eff}_{\mathrm{H}\alpha}}} \epsilon^{1/2} \Theta^{3/2} D^{5/2} F_0(\mathrm{H}\alpha)^{1/2} \tag{7.16}$$

where $x_{\rm e} = n_{\rm e}/n_{\rm p} \sim 1.16$ (Hua & Kwok 1999). The effective recombination coefficients for the Balmer recombination lines are taken frpm Osterbrock & Ferland (2006). The exact value of the recombination coefficient is a slowly varying function of $T_{\rm e}$, but in practice, a value of 10^4 K is used with little error.

Equation 7.16 can be finally expressed as a function of distance:

$$M_i = 0.035\, \epsilon^{1/2} \Theta^{3/2} D^{5/2} F_0(\mathrm{H}\alpha)^{1/2} \quad M_\odot \tag{7.17}$$

where $F_0(\mathrm{H}\alpha)$ is the reddening corrected total nebular Hα flux in units of 10^{-12} erg cm^{-2} s^{-1}, Θ is in arcmin and D in kpc. The rms electron density, n_e (in cm^{-3}) is simply derived from the ionized mass using the following expression (McCullough et al. 2001):

$$n_e = \frac{1350\, M_i}{(4\pi/3)(\Theta D)^3\, \epsilon} \tag{7.18}$$

where, as before, Θ is in arcmin and D is in kpc.

In terms of surface brightness at Hα, similar reasoning leads to the following expression:

$$S(\mathrm{H}\alpha) = \frac{\epsilon}{3} n_e^2\, R\, h\, \nu_{\mathrm{H}\alpha}\, \alpha^{\rm eff}_{\mathrm{H}\alpha} \tag{7.19}$$

where the various terms have the same explanation as before. Hence we can write:

$$S(\mathrm{H}\alpha) \propto n_e^2\, R \tag{7.20}$$

A natural consequence of the interacting stellar winds (ISW) model (Kwok, Purton & FitzGerald 1978; Kwok 1982) is that the mass of a PN shell increases with age (i.e. radius), due primarily to the expansion of the ionization front within the nebula, as well as the snowplow effect when the PN becomes evolved (see Villaver, Manchado & García-Segura 2002). Hence, unlike the Shklovsky method which assumes constant ionized mass, PNe manifest an observable mass-radius relation.

Uniform density has been assumed in order to determine the ionized mass (see the critique of Villaver et al. 2002). Note, however, that the volume emissivity of recombination lines is proportional to the square of the electron density. Therefore it is possible that a low-density but massive nebular halo around a PN contributes little to the integrated emission, and this may lead to an overall underestimate of the ionized mass for the PN. Nevertheless, the approach taken here is considered an acceptable assumption for a statistical study such as this.

Since, from equation 7.18, $n_{\rm e} \propto M\,(\Theta D)^{-3}$, or alternatively $n_{\rm e} \propto MR^{-3}$, it follows that $S(\mathrm{H}\alpha) \propto M^2\ R^{-5}$. Recalling that the mass-radius relation has the form:

$$M \propto R^{\beta} \tag{7.21}$$

where β is an observationally determined power law index, we can write:

$$S(\mathrm{H}\alpha) \propto R^{2\beta-5} \tag{7.22}$$

Note that the Shklovsky constant-mass assumption ($\beta = 0$) predicts a $S(\mathrm{H}\alpha) \propto R^{-5}$ power law (Seaton 1968), which is steeper than observed. Using the set of calibrating PNe defined here, the observed $R^{-3.5}$ relation predicts a value for $\beta = 0.75$, somewhat smaller than earlier determinations (e.g. Daub 1982; Milne 1982; Kwok 1985).

From the calibrating sample of ∼120 Galactic PNe, a mass-radius relation given by the following equation was derived:

$$\log M_i = 0.98(\pm 0.04)\log R - 0.04(\pm 0.04) \tag{7.23}$$

The correlation coefficient, $R^2 = 0.62$. The relation is plotted in figure 7.22, along with a fit to the PNe in the Magellanic Cloud sample. Data have been generated in the same way as for the Galactic sample, using fluxes, diameters and reddenings from Shaw et al. (2001), Stanghellini et al. (2003) and Shaw et al. (2006). The two lines are statistically identical, again showing there is no significant error in the adopted Galactic distance scale.

For $\beta = 0.98$, a SB-r relation with a power law index of -3 is then predicted. This is close to, but somewhat shallower than observed, but in agreement with the Cloud PN sample (Stanghellini et al. 2002b, 2003; Shaw et al. 2006). Since the temperature and luminosity of the ionizing star change markedly during the evolution of the PN, this has a direct influence on the index β. In fact it is quite remarkable that a set of simple relationships define the full population of PNe in simple parameter space, as illustrated in figures 7.22 and 7.23.

Furthermore, the relation between electron density and radius can be predicted, since from first principles, $n_e \propto R^{\beta-3}$. For $\beta = 0.98$, $n_e \propto R^{-2}$. From the derived data tabulated in table 7.1, supplemented with data from the Magellanic Cloud sample, I find:

$$\log n_e = -2.31(\pm 0.04)\log R + 1.02(\pm 0.04) \tag{7.24}$$

in reasonable agreement with the predicted relation (see figure 7.23). The correlation coefficient is high ($R = 0.96$), but the correlation is not independent, as errors in the distance (and hence radius) lead to correlated errors in the density. However, the figure illustrates that the intrinsic range in the adopted volume filling factor for the PN ensemble is relatively small, and

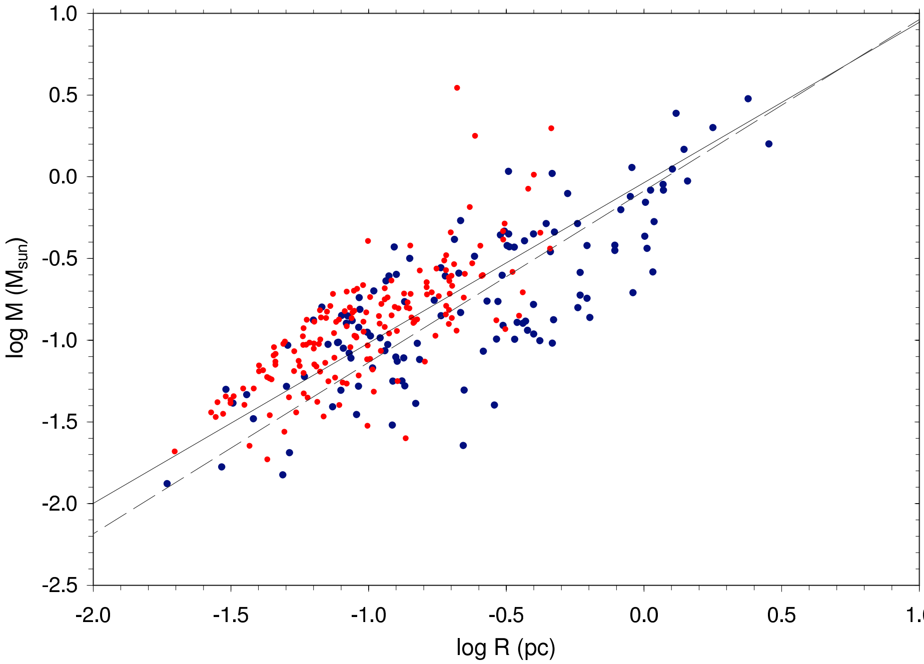

Figure 7.22: Plot of the logarithm of the ionized mass ($M_\odot$) versus log radius (pc), for Galactic PNe (large dots) and Magellanic Cloud PNe (small red dots). The dashed line plots the regression line for the Galactic sample of calibrating PNe. The solid line is the fit for the Magellanic Cloud PNe only. Data have been generated in the same way as for the Galactic sample, using fluxes, diameters and reddenings from Shaw et al. (2001), Stanghellini et al. (2003) and Shaw et al. (2006).

that using a constant value ($\epsilon = 0.4$) is justified.

It is important to emphasise that the electron densities plotted in figure 7.23 are RMS values derived from integrated fluxes and radii (which depend on the adopted distance scale used here). This approach was chosen since the solar neighbourhood sample is dominated by evolved PNe with mean densities less than the low-density limit of the [S II] line plasma diagnostic. The relation in figure 7.23 can potentially be used as a distance indicator, an approach taken by Zhang (1995). For the brighter nebulae it would be useful to get independent electron densities from the [S II] or [O II] doublet lines. Kingsburgh & Barlow (1992) and Kingsburgh & English (1992) have in fact adopted this approach, developing a distance scale for galactic PNe based on mean [O II] electron densities.

It also follows that $F(\mathrm{H}\alpha) \propto \Theta^{2\beta-3} D^{2\beta-5}$. If the Lyman continuum output is assumed constant (i.e. F is independent of Θ), then $\beta = 3/2$ and $F(\mathrm{H}\alpha) \propto D^{-2}$ (e.g. Milne 1982). Furthermore, Kwok (1985, 1993) and Samland et al. (1993) have shown that the errors in statistical distances increase rapidly as $\beta \longrightarrow 5/2$, at which point the method becomes degenerate (i.e. there is no dependence of surface brightness on radius). This is not the case in reality however, since a rather small value of β is determined herein.

The Hα SB-r relation as a new statistical distance indicator is hence reliable (cf. Kwok 1985; Marten & Schönberner 1991), with the only disadvantage being the quite large cosmic scatter. However, a first attempt undertaken herein to subdivide the ensemble of PNe into a number of subsets based on observable quantities, shows that with care, the statistical distances derived

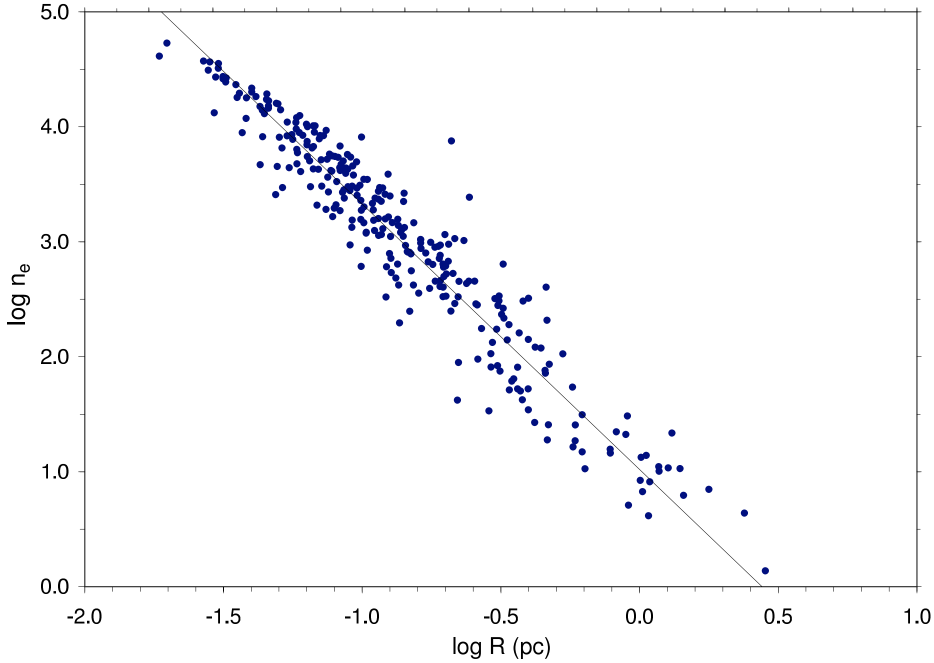

Figure 7.23: Plot of log electron density (cm^{-3}) versus log radius (pc) for a total sample of 240 Galactic calibrating and Magellanic Cloud PNe. The line is a least-squares fit to the whole sample.

here have comparable accuracy to most direct methods currently in use, and better than any other statistical distance indicator (cf. Stanghellini, Shaw & Villaver 2008). This justifies the use of the Hα SB-r relation(s) to provide distances for all local PNe without primary distance estimates, in order to build the most accurate volume-limited PN sample compiled to date (see Chapter 9).

Chapter 8

Identifying Impostors in the Solar Neighbourhood

8.1 Introduction

The integrity of any volume-limited sample of PNe, especially when the sample is relatively modest in number, is paramount when attempting to derive meaningful population parameters such as the accurate determination of the local PN column density, the PN scale height, the intrinsic distribution of morphological types, and the frequency of binarity. This is because small changes in the make-up of such populations have a significant impact on these derived properties.

Hence, while a search for previously overlooked PNe, especially evolved objects of extremely low surface brightness, is mandatory to improve the statistical completeness of the solar neighbourhood sample, it is equally important to ascertain the true nature of any suspect or doubtful nebula posing as a nearby PN in the current catalogues and remove them from consideration. For the definition of a PN adopted in this work, the reader is referred back to section 1.2.

Here we describe the range of tools now available to assist in this process of population refinement and show that several local 'PNe', still in the current catalogues are, in fact, impostors and need to be eliminated prior to any local volume study. As a starting point to achieve this goal, Table 8.1 lists all objects larger than $2'$ in size that have been previously identified in the literature as PNe, starting with the CGPN (Perek & Kohoutek 1967), or that have been newly identified as PN contaminants in this work (see also Frew & Parker 2006, and Madsen et al. 2006). The largest nebulae from Table 8.1 are potential contaminants in the immediate 'solar neighbourhood' sample, so it is very important to identify them, as the presence of such objects will seriously perturb the derivation of the local column density of PNe. This chapter describes the variety of techniques and observational evidence used to recognise non-PN contaminants, and details case studies of 15 objects which demonstrate the effectiveness of these tools in practice. These objects have been removed from the solar neighbourhood sample.

8.1.1 Identifying the Impostors

Post-PN hot white dwarfs are intrinsically far more common than actual PN central stars. The time for a post-PN nucleus to cool down to $T_{\rm eff}$ = 25,000 K (the minimum temperature needed for ionization of surrounding gas) is $\sim$3 $\times 10^7$ yr for a 0.6 $M_\odot$ H-burning core (Bergeron, Wesemael & Beauchamp 1995), compared to $\lesssim 10^5$ yr for the duration of the actual PN phase. Hence, the warm ISM is intuitively expected to contain numerous ionized Strömgren zones within it. These are found around hot stars including white dwarfs (e.g Tat & Terzian 1999) and hot subdwarfs, especially close to the Galactic midplane, where the H I density is highest (Spitzer 1978).

During my literature review, it also become apparent that a number of putative PNe currently in the literature such as Hewett 1 associated with the DO star PG 1034+001 (Hewett et al. 2003), Sh 2-174, DHW 5 and TK 2 (RE 1738+665) are actually Strömgren spheres in the ISM (Chu et al. 2004; Madsen et al. 2006; Frew & Parker 2006; Madsen & Frew 2008, in preparation). As other examples of such nebulae, Chu et al. (2004) have described the ionized nebula around the hot DO white dwarf KPD 0005+5106, suggested to be a possible PN by Otte, Dixon & Sankrit (2004), and Haffner (2001) has noted a large ionized nebula near the sdO star PHL 6783. Genuine evolved, optically thin PNe can also ionize the surrounding ISM, as seen in the case of the giant halo surrounding Abell 36 (McCullough et al. 2001). The large outer haloes around NGC 3242 and Sh 2-200 (Corradi et al. 2003) have also been shown to be ionized ISM (see Chapter 4 and Madsen & Frew 2008, in preparation). The well known runaway Population I star AE Aurigae (Herbig 1958) is also illuminating an extensive emission/reflection nebula, IC 405, far from its birthplace in the Orion nebula. So there is no *a priori* reason why we should not expect some of the more morphologically suspect PNe to be simply unrelated nebulae temporarily ionized by intruding hot stellar cores.

To ascertain the true status of each of the doubtful nebulae in the local volume, a number of different discriminatory criteria were used:

- The properties of the ionizing star, including its evolutionary age;
- Nebular morphology and ionization structure, including the consistency of any ISM interaction with the proper motion vector of the ionizing star;
- Nebular emission-line ratios;
- Nebular ionized mass;
- The line width of nebular gas, noting that some very evolved bona fide PNe (e.g. Sh 2-216) have narrow line widths;
- The systemic nebular velocity, and whether it differs from the radial velocity of the ionizing star.

The last dot point needs some elucidation here. The systemic velocity of the nebular shell is expected to be a good proxy for the radial velocity of the progenitor star (or the systemic velocity of a binary progenitor). However, the *measured* radial velocity of the ionizing star will generally not be the same. Evolved central stars are high gravity objects ($\log g > 6.5$ cm s^{-2}) and show a measurable gravitational redshift, though the effect is less severe for central stars still on the 'horizontal' nuclear-burning track in the HR diagram ($\log g = 3 - 6$). This correction has usually been ignored in the literature (cf. Méndez 1989). The expected gravitational redshift is $\sim$3 kms^{-1} at $\log g = 6$, comparable to the typical measurement uncertainties in both stellar and nebular radial velocities. However, the gravitational redshift is $\sim$10 kms^{-1} at $\log g = 7$ and $\sim$30 kms^{-1} at $\log g = 8$, so for a CSPN well down the white dwarf cooling track, ignoring the gravitational redshift can lead to serious systematic errors.

Furthermore, a single-epoch observation of the radial velocity of the CS may differ markedly from the nebular velocity if the CS belongs to a binary (though other evidence may indicate this fact). However, to allow comparison between stellar and nebular velocities in the cases discussed below, the stellar velocity has been corrected for gravitational redshift where appropriate. The values of the gravitational redshift for the nebulae discussed below are taken from the last column in Table 6.6.

Table 8.1: Misclassified PNe larger than 2′ in size. This list also includes a number of newly identified contaminants, uncovered as part of this work (indicated with an asterisk next to the name). The maximum and minimum dimensions (a and b) are given in arcminutes.

Name	Other	RA	Dec	l	b	a (')	b (')	Type
Sh 1-118	...	00 07 20	+64 57 20	118.28	+2.48	2.1	2.1	HII region
JoDi 1	Tycho's SNR	00 25 24	+64 09 00	120.07	+1.44	3.7	3.7	SNR
PHL 932*	...	00 59 57	+15 44 14	125.93	−47.08	5.0	4.1	HII region around sdOB⋆
PG 0108+101*	Re 1	01 11 06	+10 21 30	130.84	−52.21	60	60	HII region around sdO⋆
PG 0109+111*	...	01 12 23	+11 23 30	131.13	−51.15	10.0	5.0	HII region around sdO⋆
VV 1-1	...	01 50 05	+53 54 01	131.59	−7.98	2.5	2.1	reflection nebula
EGB 2*	...	01 57 59	+10 56 35	148.10	−48.62	8.3	8.3	reflection nebula
Sh 2-207	VV 1-2, LBN 708	04 19 51	+53 07 47	151.21	+2.11	3.6	3.0	HII region
EGB 3	Cam A, KK 41	04 25 16	+72 48 21	137.24	+16.20	2.6	2.0	dwarf 'Camel galaxy'
EGB 8	UGCA 92	04 32 05	+63 36 49	144.71	+10.51	2.0	1.5	dwarf galaxy
HDW 4	HaWe 6, We b	05 37 56	+55 32 16	156.31	+12.55	2.1	1.5	HII region?
Sh 2-269	VV 1-3, LBN 876	06 14 37	+13 49 41	196.45	−1.68	3.0	2.0	HII region
Sh 2-271	VV 1-4	06 14 53	+12 21 23	197.81	−2.31	2.0	1.9	HII region
Sh 2-267	VV 1-5, LBN 875	06 15 55	+14 17 57	196.19	−1.18	4.5	4.5	HII region
HaWe 7*	HDW 5	06 23 37	−10 13 24	218.99	−10.78	+3.7	3.0	HII region
KLSS 1-9*	KW 5	06 24 36	−33 04 48	240.86	−19.63	10.0	10.0	plate flaw or ref. nebula?
K 2-13	...	06 25 29	−39 51 48	247.77	−21.68	2.9	2.2	plate fault
EGB 4	...	06 29 34	+71 04 36	143.60	+23.82	4.3	2.5	nebula around CV
Sh 2-309	M 1-15, RCW 13	07 31 48	−19 26 05	234.74	−0.27	6.0	6.0	HII region
VV 1-7	...	07 41 14	−18 59 37	235.44	+1.89	3.0	3.0	transient ref nebula?
EGB 5*	...	08 11 13	+10 57 17	211.91	+22.62	4.0	2.0	HII region around sdOB⋆
NGC 2579	Ns 238	08 20 55	−36 13 23	254.68	+0.23	3.0	2.0	Compact HII region
K 2-15	...	08 48 48	−42 54 24	263.25	+0.51	3.0	2.6	HII region
Abell 32	...	09 16 25	+03 53 26	227.46	+33.77	2.2	2.2	plate fault
Hewett 1*	PG 1034+001	10 37 04	−00 08 20	247.55	+47.75	90.0	60.0	HII region?
Ced 109b	Wr 16-82/83	11 01 07	−60 47 38	289.87	−0.75	4.0	3.0	Bran 334; HII region
K 2-4	...	12 18 19	+11 03 08	275.49	+72.14	12.9	10.1	plate fault
NGC 5408	He 3-959	14 03 21	−41 22 44	317.15	+19.50	2.0	1.0	Emission-line dwf galaxy

Continued on next page

Table 8.1 – continued from previous page

Name	Other	RA	Dec	l	b	a (')	b (')	Type
RCW 87	Sa 2-110	15 05 18	−57 31 12	320.16	+0.80	2.0	2.0	HII region
RCW 88	Wr 16-166/7	15 07 08	−57 48 18	320.23	+0.44	3.0	2.0	HII region
RCW 99	Gum 50	15 59 38	−53 45 32	328.57	−0.53	4.0	2.0	HII region
Lo 14	vBH 69	16 11 45	−51 17 49	331.59	+0.07	2.1	2.0	HII region + ref nebula
RCW 107	NGC 6164/5	16 33 52	−48 06 40	336.37	−0.22	6.0	3.4	bipolar neb around Of ⋆
vBe 1*	G339.2-0.4	16 45 18	−46 09 12	339.12	−0.37	6.0	6.0	HII region
EGB 7*	...	16 47 36	+64 13	94.86	+37.57	20.0	11.0	reflection nebula
H 2-3	RCW 117	17 09 34	−41 36 12	345.40	−0.95	2.0	2.0	HII region
H 2-6	RCW 121, Sh 2-4	17 18 24	−39 19 06	348.24	−0.98	3.0	2.0	HII region
TK 2*	RE 1738+665	17 38 03	+66 53 48	96.89	+31.96	60.0	45.0	HII region
Sh 2-68*	LBN 96	18 24 58	+00 51 37	30.67	+6.28	8.0	5.5	HII region
Sh 2-61	VV 1-8, M 2-66	18 33 21	−04 58 02	26.45	+1.74	2.0	2.0	HII region
EGB 10	...	20 04 24	+71 48	104.50	+20.25	4.5	3.0	reflection nebula?
KLSS 1-3	KW 16	21 30 56	+66 48 52	104.99	+11.22	2.0	1.5	HII region
DeHt 5*	...	22 19 34	+70 56 03	111.09	+11.64	9.0	9.0	HII region
We 1-12	...	23 12 13	+59 35 59	110.67	−0.89	2.7	1.3	HII region
NGC 7635	...	23 20 48	+61 12 06	112.24	+0.23	3.4	3.0	HII region + wind-bubble
Sh 2-167	ARO 383	23 35 31	+64 52 28	114.98	+3.18	2.5	2.2	obscured HII region
Sh 2-174*	LBN 598	23 45 02	+80 57 00	120.22	+18.43	15.0	10.0	HII region
We 2-262	...	23 52 18	+62 32 11	116.17	+0.44	3.1	1.3	HII region
Abell 85	CTB 1	23 59 10	+62 26 30	116.93	+0.19	35.0	35.0	SNR
We 2-260	...	23 22 23	+57 46 24	111.26	−3.07	2.5	2.2	not PN in Simbad

In addition, it should be noted here that WHAM velocities (see Chapter 3) are referred to the local standard of rest (LSR). To convert stellar heliocentric velocities to LSR velocities, the following simplified expression is used:

$$v_{\rm LSR} = v_{\rm hel} + 19.5\,(0.5\sin\delta - 0.5\sin\alpha\sin\delta) \qquad (8.1)$$

which assumes a solar apex position of $\alpha, \delta = 18^{\rm hr}$, $+30°$. Comparison of the nebular and stellar LSR radial velocities can be used as evidence (or not) for a physical association.

In summary, no single discriminatory criterion is usually enough to define the status of a putative PN, so the *overall body of evidence* is used to classify each nebula. The following sections look in detail at a number of well-known nearby emission nebulae mostly classified as PNe, but shown here to be impostors. The majority are within ∼500 pc of the sun, so if included in the local sample, would heavily weight the determination of the local column density (discussed further in Chapter 11).

The following sections examine the nebulae around the sdOB stars PHL 932 and EGB 5 as well as the nebulae (associated with) Abell 35, DHW 5, Sh 2-68, Sh 2-174, TK 2 (RE 1738+665), Hewett 1, PG 0108+101, PG 0109+101, KPD 0005+5106, HDW 4, HDW 5, HaWe 5, and BD +28°4211. These nebulae are shown definitively in some, and highly likely in others, to be Strömgren zones (HII regions) in the ISM. EGB 2 and EGB 7 is shown to be reflection nebulae. These nearby nebulae should be struck out of any future compilation of PNe, and are not included in the refined solar neighbourhood PN sample, defined in the next chapter.

8.2 Abell 35

This peculiar nebula, discovered by Abell (1955, 1966) and independently by Sharpless (1959), is unusual in having a markedly different appearance in Hα compared to its appearance on [OIII] images (Jacoby 1981; Tweedy & Kwitter 1996; Hollis et al. 1996). In red light the nebula has as an amorphous morphology, about $17' \times 12'$ in size, with a pair of parallel filaments, or 'pipes' superposed south of the apparent central star BD$-22°$3467. Images in [O III] show smaller dimensions (about $10'$ across), including a curious parabolic bow shock centred on the star (Jacoby 1981; Hollis et al. 1996; Tweedy & Kwitter 1996). The proper motion vector of BD$-22°$3467 is parallel to the axis of this parabola, along with the orientation of the pipes, showing that this star is indeed associated with the bowshock. The calculated space motion of the star is fairly high, which has been traditionally used to explain the peculiar morphology of the nebula, as it interacts with the ISM (Borkowski, Sarazin & Soker 1990; Hollis et al. 1996; Tweedy & Kwitter 1996).

8.2.1 The Ionizing Star

BD $-22°$3467 is a yellow subgiant of spectral type G8 III-IV, or G8 IV (Jacoby 1981; Acker & Jasniewicz 1990; Thévenin & Jasniewicz 1997). The G-type star has an unresolved hot companion to provide the ionization for the nebula, first suspected by Jacoby (1981) as the colour indices of the G-type star are slightly too blue.

Acker & Jasniewicz (1990) suggested this object was a possible catalcysmic binary (the morphology is remarkably similar to the CV nebulae EGB 4 and Fr 2-11; see §B.2), but the very hot ionizing star had been confirmed with the IUE satellite (Grewing & Bianchi 1988; see also Hollis et al. 1996), and later imaged with *HST* (Gatti et al. 1998) at a separation of $\sim 0.1''$ from the primary. From the observed broadband colours of the G-star, Jacoby estimated the companion to have $V = 14.2$. An updated value can be determined from the spectrophotometric data given by Gatti et al. (1998). Based on IUE fluxes, the observed G-star to WD flux ratio for three HST filters was determined. Through the F547M filter (close to Johnson V) the primary/secondary flux ratio is predicted to be 115–122, or Δm = 5.15 – 5.22. Using the mean magnitude of the primary, $V = 9.64$ (Jacoby 1981; Jasniewicz, Lapierre & Monier 1994), the magnitude of the companion is $V = 14.8 \pm 0.1$.

BD $-22°$3467 is slightly variable (amplitude $\sim$0.05 mag) with a period of 0.766 days (Acker & Jasniewicz 1988, 1990; Jasniewicz et al. 1992; Jasniewicz, Lapierre & Monier 1994), and is now designated LW Hya. Originally thought to be a reflection effect variable (and hence a close binary), the variation is actually due to fast rotation of the spotted, chromospherically active subgiant. The observed MgII emission and Ca II H&K emission cores are signatures of strong chromospheric activity. The short period of variability had led Acker & Jasniewicz (1990) to consider a CV interpretation.

Vilhu, Gustafsson & Walter (1991) found no evidence for radial velocity variations in the star, but measured $V^{*}_{\rm hel} = -13$ kms^{-1}, which differed from the mean velocity from Jasniewicz & Acker (1988). The accurate RV measurements of Gatti et al. (1997) differ from these results, but are consistent with the velocity determined by Jacoby (1988, quoted by Acker & Jasniewicz 1990) of $V^*_{\rm hel} = -37$ kms^{-1}. Gatti et al. (1997) find *no evidence for variability* over 14 years (and hence no evidence for a close binary companion), and quote a mean velocity of $V^*_{\rm hel} = -40$ kms^{-1}, which is adopted hereafter.

Jacoby (1981) determined a spectroscopic distance for the G-star of 360 ± 80 pc. If the star is somewhat less bright (luminosity class IV), the absolute magnitude is ∼+3.1 (Schmidt-Kaler 1982), which leads to a distance of ∼190 pc, assuming $E(B-V) = 0.04$ (Herald & Bianchi 2002). Hollis et al. (1996), using the black-body characteristics of the ionizing star (a DAO white dwarf), infer a distance of ∼310 pc. However, the *Hipparcos* parallax suggests a considerably closer distance of 134^{+34}_{-23} pc (e.g. Acker et al. 1998), revised by van Leeuwen (2007) to 120^{+28}_{-19} pc. However the parallax may be subject to both a Lutz-Kelker bias (e.g. Koen 1992; Gatti et al. 1998) and photocentric errors due to the presence of the close companion.

Sandage, Lubin & VandenBerg (2003) show that the lower luminosity bound of the subgiant sequence in the solar neighbourhood ($0.85 \leq B-V \leq 1.05$) is at $M_V = 4.03 \pm 0.06$; these limits bracket the observed colour of the star (Jacoby 1981). Using the published magnitude of the G-star, a firm lower limit on the distance of $D \geq 125 \pm 5$ pc for BD$-22°3467$ is determined, which is actually consistent with the revised *Hipparcos* measurement.

Furthermore, an upper limit can be derived from the rotational period of the star. The rotation period is assumed to be identical to the photometric period, $T = 0.766$ d (Acker & Jasniewicz 1990). A mass of $1.1 M_\odot$ for the G-star is assumed (a suitable turnoff mass for the oldest disk stars), and the radius is kept as a free parameter. Following Jeffries & Stevens (1996), the critical rotation period for a star (at which the equatorial velocity equals the escape velocity) is given by:

$$P_c = 2\,\pi\sqrt{\frac{R^3}{2\,G\,M}} \tag{8.2}$$

The problem becomes one of finding the maximum radius consistent with the observed rotational period to prevent breakup. For a $1.1 M_\odot$ star, the critical radius is $\sim 4.6\,R_\odot$. For $T_{\rm eff}$ = 5000 K (Herald & Bianchi 2002), the predicted luminosity for a star of this radius is $11.7\,L_\odot$. After adopting an appropriate bolometric correction (Cox 2000), $M_V = +2.05$. The observed magnitude and reddening then leads to an upper limit on the distance of 310 pc. Adopting instead a slightly higher value for the temperature, $T_{\rm eff} = 5300$ K (Thévenin & Jasniewicz 1997), the maximum distance is 350 pc.

An arithmetic mean of the upper and lower limits points to a distance, $D = 220 \pm 100$ pc. Furthermore, a new gravity distance can be determined for the WD. Using the revised magnitude, $V = 14.8 \pm 0.1$, a reddening of $E(B-V) = 0.04$ and adopting $T_{\rm eff} = 80{,}000$ K and $\log g = 7.70$ cms^{-2} from Herald & Bianchi (2002), a distance of 215 ± 50 pc is determined, following the principles detailed in §6.4.6. The gravity distance is consistent within these limits, and is adopted in the discussion that follows.

8.2.2 The Emission Nebula

Spectroscopic and spectrophotometric data for the nebula is rather sparse in the literature. Jacoby (1981) gives [O III]/Hβ ratios at different points across the nebula. Integrated emission line fluxes were presented by Kaler (1978, 1980) and Kaler (1983b), superseded by the new data presented here in Chapter 3. The expansion velocity of this nebula is very low; Bohuski & Smith (1974) find $v_{\rm exp} = 4.2$ kms^{-1} (from the central regions of the nebula) while $v_{\rm exp} = 11$ kms^{-1} is determined here from new WHAM data for the whole nebula (see Chapter 3, and Reynolds et al. 2005). The line width either suggests the nebula is just ionized ambient interstellar material, or if a PN, that the shell has been significantly decelerated via interaction with the ISM. Indeed, Hollis et al. (1996) suggest the nebula is undergoing reverse expansion as a result of this interaction.

However, the adopted stellar radial velocity differs significantly from the systemic velocity of the nebula, which is $V_{\rm hel} = -5.8$ kms^{-1} (Bohuski & Smith 1974), $V_{\rm hel} = -16 \pm 14$ kms^{-1} (Jacoby 1981), $V_{\rm hel} = -12 \pm 1$ kms^{-1} (Reynolds et al. 2005) and $V_{\rm hel} = -3$ kms^{-1} from our new WHAM data through a $60'$ aperture (see Chapter 3). The large velocity difference suggests *the emitting gas does not originate from the star.*

8.2.3 Discussion

Tellingly, there is *no exterior bowshock on the leading side of the extended emission nebula.* Detailed modelling of PNe moving at significant velocities with respect to the ISM always show a strong bowshock in the direction of motion, a feature also seen in the winds of AGB stars (Villaver, García-Segura & Manchado 2003; Wareing et al. 2006b; Wareing, Zijlstra & O'Brien 2007b).

The sharp, inner bow shock morphology suggests a component of shock excitation as well as photoionization in this nebula, though Jacoby (1981) points out the lack of a density enhancement at the position of the bow wave (determined from the Hβ surface brightness, since $S \propto n_e^2$). In the case of Abell 35, the proximity of the bowshock to the ionizing star is due to the visible extended nebula being simply ionized ambient ISM, an interpretation which explains the very low line width of the emitting gas and its systemic velocity being very close to the local standard of rest (Bohuski & Smith 1974; Reynolds et al. 2005; Madsen et al. 2006, and Chapter 3). This object bears more than a passing resemblance to Fr 2-11 (see §B.2 for a fuller discussion), in that both nebular velocities consistent with the local standard of rest, both have coarse 'pipes' parallel to the proper motion vector, and both shocks are only seen in [OIII] light, and not in a Balmer line.

The emission line ratios of Abell 35 are also very similar to the nebulae EGB 4 and Fr 2-11, both nebulae located around two novalike CVs (see Greiner et al. 2001, and figure B.4, below). The strong [O III] emission seen in these bowshock nebulae is nicely explained by the high space motions of their respective stars, $\sim$125 kms^{-1} and $\gtrsim$80 kms^{-1} respectively (Greiner et al. 2001, and §B.2).

The observed bow shock is in dynamic equilibrium. This is achieved when the stellar wind pressure is equivalent to the ram pressure of the ISM (Weaver et al. 1977; Gull & Sofia 1979; Van Buren & McCray 1988; Hollis et al. 1992):

$$\frac{\dot{m}\, v_w}{4\,\pi\, l_1^2} = m_{\rm H}\, n_e\, v_{\rm rel}^2 \tag{8.3}$$

where $\dot{m}$ is the mass loss rate in cgs units, v_w is the terminal velocity of the stellar wind, l_1 is the distance from the star to the terminal wind shock front, $v_{\rm rel}$ is the velocity of the star relative to the surrounding ISM, $m_{\rm H}$ is the mass of the hydrogen atom, and n_e is the electron ($\approx$ proton) density in the surrounding medium. However, l_1 is not observable, as the high-temperature shocked wind does not produce any optical emission.

The shape of the bow wave is a paraboloid of revolution (Weaver et al. 1977), in which the distance along the z symmetry axis (as measured form the apex) is related to the perpendicular distance, y, from the axis to the paraboloid by the relation,

$$z = y^2/3\, l_2 \tag{8.4}$$

where l_2 is the "standoff" distance, defined as the distance from the stellar system to the stagnation point, or apex of the observable bow wave (see figure 8.1). The standoff distance is equivalent to:

$$l_2 = \frac{\sqrt{20 L_w}}{3\sqrt{33\,\pi\, m_{\rm H}\, n_e\, v_{\rm rel}^3}} \tag{8.5}$$

(Weaver et al. 1977; Van Buren et al. 1990; Hollis et al. 1996), where L_w is the mechanical luminosity of the wind, given by:

$$L_w = \frac{1}{2}\dot{m} v_w^2 \tag{8.6}$$

The model as applied to Abell 35 is illustrated in figure 8.1, taken from Hollis et al. (1996). The angular thickness of the [OIII] bow shock, Δr, was measured by Hollis et al. (1996) as $\sim$13.3$''$ from a [OIII] CCD image. The standoff distance, l_2 was measured to be 25.3$''$, hence the quantity $l_c = l_2 - r = 12''$, is the minimum distance from the star to the inner edge of the shocked wind, the contact discontinuity distance. Hence $l_2 > l_c > l_1$, and the relationships between the quantities are shown graphically in figure 8.1.

There is some foreshortening in this case, since the motion of the G-star is not in the plane of the sky. Using the Hipparcos proper motion, the tangential velocity of the G-star at the adopted distance is $\sim$64 kms^{-1}. Adopting the heliocentric radial velocity of -40 kms^{-1}, the star is moving at 75 kms^{-1} with respect to the Sun, at an angle, $\theta = 32°$ from the plane of the sky. The space velocity is 60 kms^{-1} with respect to the ISM.

From equation 8.5, we can simplify to:

$$L_w = 14.85\,\pi\,(l_2 \sec\theta)^2\, m_{\rm H}\, n_e\, v_{\rm rel}^3 \tag{8.7}$$

where the $\sec\theta$ term accounts for the fact that the symmetry axis of the parabola does not

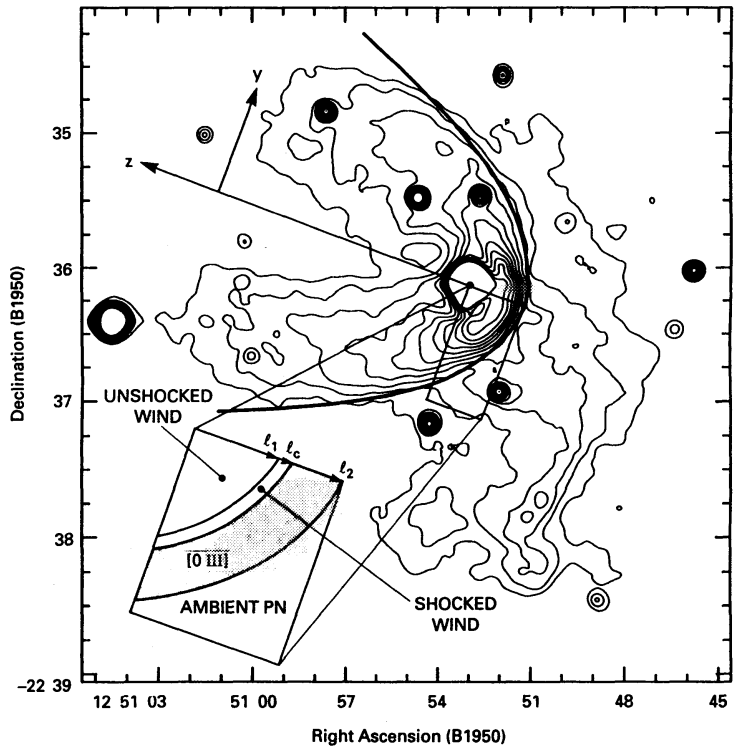

Figure 8.1: Schematic parabola for the Abell 35 bowshock, based on imaging data of Hollis et al. (1996). The shock speed at any point on the paraboloid of revolution is the orthogonal component to the surface. Figure taken from Hollis et al. (1996).

lie in the plane of the sky. The extimated wind power from the Abell 35 system is hence L_w $\sim$3 $\times$ 10^{33} erg s^{-1}, which is higher than estimated by Jacoby (1981) and Hollis et al (1996). Combining equations 8.3, 8.6 and 8.7, and solving for $\dot{m}$, we can also write:

$$\dot{m} = 0.54\,\pi\,\frac{l_1^4}{l_2^2}\,m_{\rm H}\,n_e\,v_{\rm rel} \tag{8.8}$$

The distance l_1 is unknown, but substituting l_c for l_1 in equation 8.8, an upper limit for the mass loss rate, $\dot{m} \lesssim 2.5 \times 10^{-9}\ M_\odot\,{\rm yr}^{-1}$ is found, a rate which is high, but not unprecedented for a G/K subgiant (e.g. Gull & Sofia 1979). Such a high mass loss rate is a product of the chromospheric activity and ultra-fast rotation of the G-star.

To explain fast rotation speeds in old, low-mass stars, Jeffries & Stevens (1996) have proposed that a detached secondary in a wide binary can accrete part of the slow massive wind from an AGB companion. The gain in mass and angular momentum can spin up the secondary to a state of very rapid rotation. As the AGB star evolves to a white dwarf, the companion now appears as a wind-accretion induced rapid rotator (or WIRRing star). In addition, the companion should show signs of enrichment in s-process elements, derived from the AGB wind. Indeed, Thévenin & Jasniewicz (1997) have observed barium enrichment in BD $-22°3467$.

To summarize, it is concluded that the emission nebula designated Abell 35 is a Strömgren zone in the ambient interstellar medium, ionized by a hot DAO white dwarf (the visual companion to the G8 subgiant), which has recently evolved from the PN phase. This system still produces a strong wind, probably from the active, fast-rotating subgiant, which interacts with the inner zone of the emission nebula (ambient ISM in this case) to produce the observed bowshock. This interpretation (cf. Frew & Parker 2007) best explains the available data.

8.3 PHL 932

Ever since a faint asymmetric emission nebula was discovered around the blue star PHL 932 (PG 0057+155) by Arp and Scargle (1967), this nebulosity has been assumed to be a planetary nebula (e.g. Acker et al. 1992). Along with EGB 5 (Ellis, Grayson & Bond 1984; see below), PHL 932 is an extraordinary object, as no other 'PNe' are associated with sdOB/sdB stars.

8.3.1 Ionizing Star

PHL 932 was first noted as a 12th-magnitude blue star by Haro & Luyten (1962), and was further studied by Arp & Scargle (1967) and Méndez et al. (1988b). PHL 932 was initially classified as a sdB star (Méndez et al. 1988b) but shows both broad Balmer emission lines and weak He I and He II absorption features, leading to a revised classification of sdOB (Edelmann 2003, Méndez 2006, pers. com.). Méndez et al. (1988b) determine $T_{\rm eff}$ = 37,000 ± 3000 K and log g = 5.5 ± 0.2, similar to the analogue EGB 5 (Méndez et al. 1988b). Edelmann (2003) estimated a lower temperature of $T_{\rm eff}$= 34,600 ± 1500 K and a higher gravity, log g = 5.8 ± 0.2. These values are in agreement with the values of Napiwotzki (1999), who determined $T_{\rm eff}$=35,000 ± 900 K and log g = 5.93 ± 0.12. Napiwotzki (1999) estimated a low mass of 0.28 $M_\odot$, but this assumed the star followed a post-AGB evolutionary track. Lisker et al. (2005) find $T_{\rm eff}$ = 33,600 K and log g = 5.74 ± 0.07, leading to an inferred $M_V = 4.25$ and a distance of 400 pc.

The star is relatively bright so the published photometry from the literature is quite accurate. A summary of the available optical photometry is presented in Table 8.2. Additional photometry has been taken from 2MASS (Cutri et al. 2003) and the SLOAN Digital Sky Survey (Adelman-McCarthy et al. 2008). The PSF magnitudes from the SDSS have been preferred to the model magnitudes returned through the VizieR service. These data have been converted from the AB system to Vega-based magnitudes following the prescription of Holberg & Bergeron (2006).

The available photometry (table 8.2) shows firstly that the star is not a large amplitude variable ($\Delta m \leq 0.10$ mag, and probably $\lesssim$0.05 mag). Furthermore, Bond & Grauer (1987) photometrically observed the central star for a total of 6.3 hours over 4 nights but found no evidence for any variation, making it unlikely to be a (very) close binary. In addition, the $V-K$ colour is consistent with no near-IR excess. On the other hand Saurer & Pfitscher (1989) state that it is a good candidate for a variable CS, but no data was published to back up their assertion. For now, the available data are consistent with the star being single.

Until recently the distance of the star was poorly known. Méndez et al. (1988b) derived a 'gravity' distance of ∼390 pc after assuming a stellar mass of ∼0.3 $M_\odot$, while Napiwotzki (1999) determined D = 235 pc using the gravity method. Both estimates disagreed with the Hipparcos trigonometric distance of 110^{+48}_{-26} pc (Pottasch & Acker 1998; Acker et al. 1998). On

Table 8.2: Literature multi-wavelength photometry of PHL 932

Band	Magnitude	Source
U	10.73	1
u'	10.602	2
B_T	11.917	3
B	11.83	1
B	11.803	4
B	11.853	5
b	11.967	6
g'	11.810	2
V_T	12.275	3
y	12.081	6
V	12.14	1
V	12.12	7
V	12.076	4
V	12.107	5
V	12.17	8
r'	12.132	2
R_C	12.211	4
I_C	12.43	7
I_C	12.378	5
I_C	12.387	4
i'	12.247	2
z'	12.429	2
J	12.696 ± 0.021	9
H	12.818 ± 0.030	9
K_s	12.865 ± 0.028	9
$B-V$	-0.29	adopted
$V-K$	-0.75	adopted
$J-K_s$	-0.17	9

1. Arp & Scargle (1967); 2. (Adelman-McCarthy et al. 2008; PSF magnitudes converted to Vega system); 3. Tycho-2 (Høg et al. 2000); 4. Allard et al. (1994); 5. Harris et al. (2007); 6. Wesemael et al. (1992); 7. Ciardullo et al. (1999); 8. ASAS3 (Pojmanski 2001); 9. 2MASS (Skrutskie et al. 2006).

Table 8.3: Proper motion of PHL 932

Survey	$\mu_\alpha cos\delta$ mas yr^{-1}	μ_δ mas yr^{-1}
Hipparcos	$+36.13 \pm 2.99$	$+7.09 \pm 2.00$
Tycho-2	$+36.2 \pm 1.9$	$+3.0 \pm 1.8$
UCAC2	$+36.3 \pm 1.4$	$+4.3 \pm 1.2$
USNO-B	$+36 \pm 4$	$+2 \pm 4$
NOMAD1	$+36.1 \pm 2.9$	$+7.0 \pm 2.0$
SSS	$+34.90 \pm 5.51$	$+3.28 \pm 4.09$
Harris et al. (2007)	$+36.4$	$+10.3$

the face of it, the Hipparcos parallax seems accurate, but the parallax error of $\pm$ 2.79 mas is large for a parallax of that magnitude, primarily due to the star being near the Hipparcos faint magnitude limit. However, a recent well-determined parallax of 3.36 $\pm$ 0.62 mas (Harris et al. 2007) has shown that the Hipparcos value is in error. The new parallax distance of 298^{+67}_{-47} pc removes the discrepancy with the gravity distance, and agrees far better with the expected properties of a hot EHB star (see below).

The total extinction along this sight line (Schlegel, Finkbeiner & Davis 1998) is $E(B-V)$ = 0.08, or A_V = 0.25, but this is probably an upper limit to the star itself. The Strömgren photometry of Wesemael et al. (1992) was compared with their grid of theoretical colours to estimate a reddening of $E(b-y) = 0.04$, or $E(B-V) = 0.05$. Using the theoretical colours of a 40kK WD (approximately applicable to a sdOB star) from Bergeron, Wesemael & Beauchamp (1995), I derive $E(B-V)$ = 0.02, 0.02 and 0.09 based on $B-V$, $V-I$ and $V-K$ colours respectively (see table 8.2). A final value of $E(B-V)$ = 0.05 $\pm$ 0.03 is adopted.

The mean visual magnitude is $V = 12.10 \pm 0.03$. The absolute magnitude, using the adopted extinction and the new distance from Harris et al. (2007), is $M_V = +4.6^{+0.4}_{-0.5}$, consistent with the observed absolute magnitudes of other EHB stars (e.g. Lisker et al. 2005) and field sdB stars (Thejll et al. 1997).

Arp & Scargle give $V_{\rm hel} = +15 \pm 20$ kms^{-1} based on a low-dispersion blue spectrum. Based on high-resolution echelle spectroscopy, Edelmann (2003) gives $V_{\rm hel} = +18 \pm 2$kms^{-1} with *no evidence* for radial velocity variability. Méndez (1989) also using echelle spectroscopy, found an identical value of $+18 \pm 2$ kms^{-1}, based on two spectra. More recently, Wade (2001) used spectra obtained with the Hobby-Eberly Telescope to show that no large radial velocity amplitude exists. In addition, Saffer, Green & Bowers (quoted by Wade 2001) also find no evidence for significant orbital motion. On the other hand, both De Marco et al. (2004) and Afşar & Bond (2005) claim the radial velocity is indeed variable, though no absolute velocity data has yet been published (the claim of De Marco et al. is based on one velocity outlier). Given the constancy of the high resolution data of Edelmann (2003), supported by Méndez (1989), Wade (2001) and Saffer, Green & Bowers, any claim for velocity variability is considered unproven.

The Hipparcos catalogue (Perryman et al. 2001) gives a significant proper motion for PHL 932, in accordance with the values in the Tycho-2 (Høg et al. 2000), UCAC2 (Zacharias et al. 2004), USNO-B1.0 (Monet et al. 2003) and SuperCOSMOS catalogues, and the new determi-

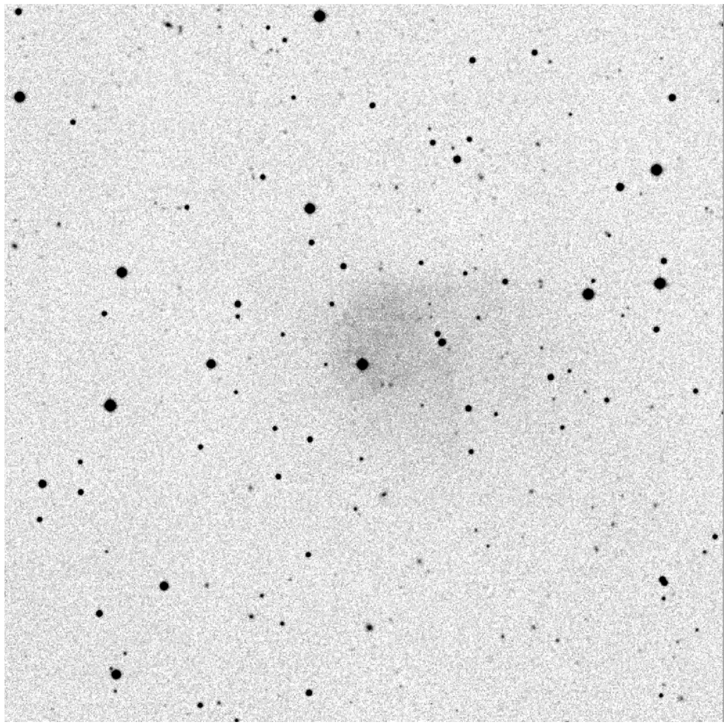

Figure 8.2: *R*-band SSS image of the nebulosity associated with PHL 932 (at centre). The field is 10′ on a side with NE at top left.

nation of Harris et al. (2007). The proper motion data are summarised in Table 8.3, where the errors on the USNO motions have been set to ±4 mas yr^{-1} following Gould (2003). The Hipparos value is adopted, i.e. 36.8 mas yr^{-1} in pa 79°. The tangential velocity at the adopted distance of 298 pc is then 52 ± 10 kms^{-1}.

Using the mean heliocentric radial velocity of +18 ± 2km^{-1} (Méndez 1989; Edelmann 2003) and following the precepts of Johnson & Soderblom (1987), the space motion vectors are determined to be $U = -54$kms^{-1}, $V = -12$kms^{-1}, $W = -5$kms^{-1}, so the star has rather typical old-disk kinematics. The total space motion is ∼55 kms^{-1} with respect to the Sun, or ∼43 kms^{-1} with respect to the local standard of rest. The space motion is consistent with the kinematics of sdB stars, most of which belong to the old disk (Thejll et al. 1997), though some halo objects are known.

8.3.2 The Emission Nebula

The emission nebula is elliptical and asymmetrically placed around the ionizing star PHL 932. The surface brightness is rather low, and it subtends about 300 × 245 arcsec on the POSS II red plate (see Figure 8.2). The nebula has been little studied since discovery. A spectrum was obtained by Arp & Scargle (1967) who noted strong [O II] λ3727 and weak Hα, confirmed by Méndez et al. (1988). The almost complete absence of [O III] emission suggests a rather cool ionizing field.

A highly evolved planetary nebula of low surface brightness travelling at moderate velocity through the ISM would normally show significant evidence of an ISM interaction. Arp &

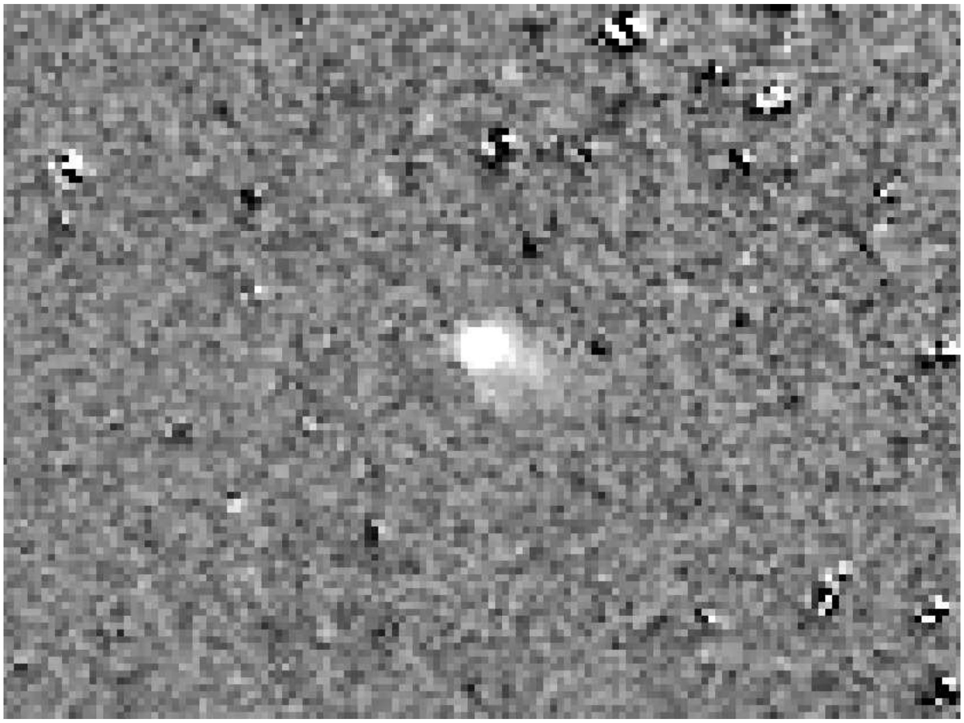

Figure 8.3: SHASSA Hα+ [N ii] image of the nebulosity associated with PHL 932. NE is at top left.

Scargle (1967) commented on the asymmetric cometary appearance of the nebula with an offset 'central' star. The SHASSA image from field #236, reproduced here as Figure 8.3, supports their interpretation. At first glance, the orientation of the nebula agrees with the proper motion vector of PHL 932 and there seems to be a stubby ionized tail or wake behind the ionizing star, à la Sh 2-68 (Kerber et al. 2002).

However, the detailed nebular morphology is not consistent with the nebula being ejected from PHL 932. From section 8.3.1, the total velocity with respect to the local standard of rest is $\sim$43 kms^{-1}. Despite the moderately fast space motion, there is no sign of an enhanced rim (bowshock) on the leading side of the nebula (figure 8.2; see also Manchado et al. 1996[1]), as expected from interaction theory (e.g. Wareing, Zijlstra & O'Brien 2007b), and there is no enhancement of the [N ii]/Hα ratio in our spectral data on an east-west cut through the nebula. Such an enhanced ratio is nearly ubiquitous in the interacting rims of old, highly evolved PNe (e.g. Kerber et al. 2000; Rauch et al. 2000; Pierce et al. 2004) where a higher recombination rate leads to a lower degree of ionization. In fact the morphology is rather amorphous and the surface brightness essentially drops of away from the ionizing star in all directions.

The WHAM Fabry-Perot interferometer (Haffner et al. 2003) was used to determine the integrated fluxes in the Hα and [N ii] lines (the nebula was too faint for WHAM in [O iii]). Preliminary values were published by Madsen et al. (2006) who gave $\log \mathrm{F(H\alpha)} = -10.67\pm0.05$ $\mathrm{erg\,cm^{-2}\,s^{-1}}$ and $\log \mathrm{F(6584)} = -11.32\pm0.05$ $\mathrm{erg\,cm^{-2}\,s^{-1}}$ through the 60$'$ WHAM beam. This aperture includes the ionized wake (see below). The nebula is also detected as WPS 37 by

[1]Image available at http://www.astro.washington.edu/balick/PNIC/

Reynolds et al. (2005). They quote an integrated Hα flux of $\log \mathrm{F(H\alpha)} = -10.75\pm0.10$ $\mathrm{erg\,cm^{-2}\,s^{-1}}$.

An integrated Hα flux was also determined from the Southern H-Alpha Sky Survey Atlas (SHASSA; Gaustad et al. 2001), following the precepts of Chapter 3. The estimated flux is $\log \mathrm{F(H\alpha)} = -10.73\pm$ 0.06 $\mathrm{erg\,cm^{-2}\,s^{-1}}$ through a 12′ aperture (mean of two SHASSA fields, #235 & 236), after adopting [N II]/H$\alpha = 0.3 \pm 0.1$ from our WHAM data. The Hα flux through a 60′ aperture is $\log \mathrm{F(H\alpha)} = -10.63\pm$ 0.06 $\mathrm{erg\,cm^{-2}\,s^{-1}}$ (mean of two fields). This value is in good agreement with the newly determined flux from WHAM (see above) and with the Hα flux reported by Reynolds et al. (2005).

Méndez et al. (1988b) argue from the emission measure of the nebula (~60 $\mathrm{cm^{-6}pc}$) that it is too dense to be ambient interstellar medium and must have been ejected from the star; i.e. it is a 'planetary nebula', albeit a peculiar one[2]. This argument is now considered in detail. The SHASSA survey was used to measure the peak surface brightness of the nebula. Both SHASSA fields give concordant results and give a Hα surface brightness (corrected for background and [N II] contribution) of 36 rayleighs, or 2.1×10^{-16} $\mathrm{erg\,cm^{-2}\,s^{-1}arcsec^{-1}}$. For ionized hydrogen, the surface brightness, $S_{\mathrm{H}\alpha}$ (in rayleighs) and the emission measure (EM, in units of $\mathrm{cm^{-6}pc}$) are related by the following expression (cf. Reynolds & Ogden 1982; Madsen, Reynolds & Haffner 2006):

$$\mathrm{EM} = 2.75\,T_4^{0.9}\,S_{\mathrm{H}\alpha}\,e^{2.2E(B-V)} \quad \mathrm{cm^{-6}pc} \tag{8.9}$$

where T_4 is the electron temperature in units of 10^4 K.

For the main body of PHL 932, the measured Hα intensity is roughly equivalent to an emission measure of ~80 – 100 $\mathrm{cm^{-6}pc}$, which considering the errors (in both the brightness and assumed electron temperature) is just consistent with the determination of Méndez et al. (1988b). Of further interest is that the nebula has a wake, trailing opposite to the direction of the proper motion vector. The wake, which extends ~18′ southwest from the ionizing star, has a mean corrected Hα surface brightness of ~5 R, or $S(\mathrm{H}\alpha) = 3 \times 10^{-17}$ $\mathrm{erg\,cm^{-2}\,s^{-1}arcsec^{-1}}$. This point will be revisited in §8.3.4, below.

The systemic radial velocity of the nebulosity as determined using WHAM data (Chapter 3) is $V_{\mathrm{LSR}} = -5\pm$ 3 $\mathrm{kms^{-1}}$ from Hα and $-13\pm$ 3 $\mathrm{kms^{-1}}$ from the [N II] λ6584 line. The mean is $V_{\mathrm{LSR}} = -9\pm$ 4 $\mathrm{kms^{-1}}$. The adopted radial velocity of PHL 932 (Méndez 1989; Edelmann 2003) is $V_{\mathrm{LSR}} = +16.4 \pm 2$ $\mathrm{kms^{-1}}$, which is a 6σ difference. Thus it can be categorically stated that the nebulosity and star are unrelated, especially since the star is *not* a radial velocity variable.

Reynolds et al. (2005) measure a FWHM ($\simeq 2v_{\mathrm{exp}}$) of 20 $\pm$ 2 $\mathrm{kms^{-1}}$ in Hα which is considerably less than the mean FWHM for *bona fide* PNe in their sample. The low line-width is confirmed with new WHAM data ($2v_{\mathrm{exp}}$) = 22 $\pm$ 4 $\mathrm{kms^{-1}}$, which is significantly less than the average width seen in evolved PNe.

The ionized mass of the nebula was calculated using equation 9.6. Using the dimensions

[2] I argue that the term 'planetary nebula' be restricted to the ionized shell ejected during the post-AGB evolutionary phase, and should not be applied to any hypothetical nebula around a post-EHB or AGB-manqué star.

and Hα flux quoted above, plus the adopted distance from Harris et al. (2007), we determine the ionized mass to be $0.041\sqrt{\epsilon}\ M_{\odot}$, where ϵ is the volume filling factor, much lower than the canonical PN mass of $0.2\,M_{\odot}$, which is in turn an underestimate for the most evolved PNe.

8.3.3 Environment

If the PHL 932 nebula is an HII region in the ISM, it is germane to look at the regional environment around the star. There are at least three high-latitude molecular clouds in the broad vicinity of PHL 932, part of a large arc of CO emission (Magnani et al. 2000) which may link a south-extending spur from the Taurus-Auriga dark cloud complex with the eastward extension of the Pegasus molecular cloud association. The molecular cloud MBM 3 (Magnani, Blitz & Mundy 1985) is found 4° northeast of PHL 932 and has a similar systemic radial velocity to the emission nebula around PHL 932. This cloud seems to be associated with the diffuse nebula LBN 131.35 − 45.88 (Lynds 1965), listed in SIMBAD as a HII region, but is more likely to be a reflection nebulosity, or galactic cirrus, as an enhancement is not present in the WHAM NSS data (Haffner et al. 2003). Other molecular clouds are nearby; MBM 4 (associated with LBN 133.57 − 44.96) is 2° east of MBM 3 and linked to it, while MBM 2 is 7.5° southwest of PHL 932.

Furthermore, the emission nebulae associated with the hot DO white dwarfs PG 0108+101 (Reynolds 1987; Frew, Parker & Madsen 2006; Madsen & Frew in prep.) and PG 0109+111 (Reynolds 1987; Werner et al. 1997) are only ∼6° southeast of PHL 932. The fairly similar apparent magnitudes, temperatures, and surface gravities of these two stars (e.g. Wesemael, Green & Liebert 1985) suggest they are at quite similar distances; gravity distances range between 200 and 400 pc (Pottasch 1996; Dreizler & Werner 1996). Considering the error bars on the published $\log g$ values, their distances are consistent both with each other, and with the distance to PHL 932.

It seems there is good evidence for widespread high-latitude gas and molecular material in this general direction. Table 8.4 summarises the radial velocities of the various emission nebulae and molecular clouds within a 10° radius of PHL 932. The velocities for the molecular clouds are taken from Magnani et al. (1985) and the velocities for the nebulae around PG 0108 and PG 0109 are unpublished data presented in table 8.4 (see also Madsen & Frew 2008, in prep.). In addition, Magnani et al. (2000) measured CO at $l, b = 127.4, -47.0$ on a sightline 1.5° from the position of PHL 932. They measured $V_{\rm LSR} = -10.5$ kms^{-1} and associated the emission with the MBM 3 cloud. The OH data for MBM 2 from Magnani & Siskind (1990) is also consistent in velocity, and a recent detailed study in CO of the extended Pegasus region has been undertaken by Chastain et al. (2006).

As seen in table 8.4, all features have a mean velocity near $V_{\rm LSR} = -8$ kms^{-1}, suggesting that the widespread molecular and ionized gas in this direction is at a common distance, ∼300 pc. However, Penprase (1992) has estimated a distance to the MBM 3/4 complex of 90 pc $\leq D \leq$ 190 pc, which is less than our preferred distance, so perhaps there is a considerable depth to the gas along this sightline.

Table 8.4: Summary of radial velocity determinations for emission nebulae (EN) and molecular clouds (MC) within 10° of PHL 932, ordered by Galactic longitude.

Object	Type	l	b	$V_{\rm LSR}$ (kms^{-1})	Line	Ref
MBM 2	MC	117.4	−52.3	−7.3	CO	1
				−7.4	OH	2
PHL 932	EN	125.9	−47.1	−9.0	Hα, [N II]	3
anon	(MC)	127.4	−47.0	−10.5	CO	5
PG 0108+101	EN	130.8	−52.2	−8.6	Hα, [N II], [O III]	3
				−11.0	Hα	4
PG 0109+111	EN	131.1	−51.2	−10.1	Hα	3
MBM 3	MC†	131.3	−45.7	−7.6	CO	1
MBM 4	MC†	133.5	−45.3	−8.7	CO	1

† associated with an LBN bright nebula; 1. Magnani et al. (1985); 2. Magnani & Siskind (1990); 3. This work; 4. Reynolds (1987); 5. Magnani et al. (2000)

8.3.4 Discussion

PHL 932 is on the extended horizontal branch (EHB) and is not the product of post-AGB evolution. Assuming a canonical EHB stellar mass of 0.50 M$_\odot$ (e.g. Theissen et al. 1993), we can use the adopted distance, magnitude and extinction to determine the surface gravity, following first principles (see equation 6.13). The derived gravity is $\log g = 5.8 \pm 0.2$, in excellent agreement with current measurements (Napiwotzki 1999; Edelmann 2003; Lisker et al. 2005). Therefore it can be concluded that the distance of Harris et al. (2007) gives parameters which make PHL 932 an ordinary sdOB star. The star plots squarely in the domain of EHB stars on the $T_{\rm eff} - \log g$ diagram (e.g. Figure 1 of O'Toole 2004).

However, is it reasonable to expect interstellar gas with the observed emission measure at this location, ∼220 pc from the Galactic midplane? There is considerable evidence that the multi-phase ISM is more clumpy than smooth (Redfield 2006). Furthermore, dense molecular gas can exist at remarkably large $|z|$ distances from the plane, as seen in the case of the Draco cloud which has $z \gtrsim 500$ pc (Mebold et al. 1985; Penprase, Rhodes & Harris 2000, and see §8.16). Hence it is concluded that molecular gas exists at moderate z distances in this direction.

Furthermore, is the surface brightness of the wake consistent with it being a fossil Strömgren tail (contrail)? By definition, the emission measure is proportional to the square of the electron density along the line of sight through the emitting region, formally written as:

$$\mathrm{EM} = \int_0^L n_{\rm e}^2 \,\mathrm{dl} = n_{\rm e}^2\, L \tag{8.10}$$

where the electron density, $n_{\rm e}$ is in cm^{-3}, and L is the path length (in pc) through the HII region. Measuring the Hα intensity in a HII region allows the determination of the emission measure and hence, the electron density if the line-of-sight path length can be determined (the distance to the HII region needs to be known). Combining equations 8.9 and 8.10, we get:

$$n_{\rm e} = \sqrt{\frac{2.75\, T_4^{0.9}\, S_{\rm H\alpha}\, e^{2.2E(B-V)}}{L}} \tag{8.11}$$

Now the recombination time, τ_r, for ionized hydrogen in a HII region is approximately given by:

$$\tau_r \approx \frac{1}{\alpha_H \, n_e} \tag{8.12}$$

where $\alpha_H = 2.59 \times 10^{-13}$ cm^{-3}s^{-1} is the ($n = 2$) hydrogen recombination coefficient taken from Osterbrock & Ferland (2006) at $T = 10^4 K$, and τ is in seconds.

For the downstream wake of PHL 932, the surface brightness is 5 R and the effective path length (assuming cylindrical geometry and a width of $8'$) is 0.70 pc (for D = 298 pc). The calculated mean electron density is 4.5 cm^{-3} and the recombination time is $\sim$2.3$\times$10^4 yr. Over this time interval, PHL 932 has travelled $\sim$20$'$ across the sky, in excellent agreement with the projected linear extent of the ionized tail. It is concluded that the wake is a slowly recombining ionized contrail in the ISM. Another example of this phenomenon is the interesting case of Sh 2-68, discussed in section 8.6 below. For another possible example, the reader is referred to McCullough & Benjamin (2001) and Benjamin, McCullough & Madsen (2001).

Taken together, the weight of available data make it extremely unlikely that the emission nebula around PHL 932 is a PN, and it is further concluded that the visible nebulosity does not represent a mass-loss event from this AGB-manqué star. It is instead argued that the nebula is a small, low-mass Strömgren sphere in the ISM, and that the wake is a fossil ionized contrail undergoing recombination, and not gas intrinsically associated with PHL 932.

8.4 EGB 5

EGB 5 is a small, faint, asymmetric nebula about $4' \times 2'$ in size, discovered by Ellis, Grayson & Bond (1984). The nebulosity is similar in several respects to the nebula around PHL 932. An unpublished spectrum of the nebula is similar to that of PHL 932, i.e. of low excitation with very weak [O III] emission and rather stronger [OII] and Balmer lines. The optical morphology of EGB 5 does not make it a convincing PN candidate either (with just a faint irregular patch of nebulosity visible, adjacent to the ionizing star on POSS II images. The much deeper SHASSA image (see figure 8.4) also faintly shows the nebulosity, without any faint extensions of low emission measure. The appearance is not typical of a PN, but a deep high-resolution image is needed to conclusively ditch this as a possible 'PN' on morphological grounds.

The ionizing star (Méndez et al. 1988a; Lisker et al. 2005) shows very strong similarities to PHL 932, and by inference, it is highly likely that the nebula EGB 5 is also a Strömgren sphere in the ISM. Méndez et al. (1988a) derived $T_{\rm eff}$ = 42,000 $\pm$ 5000 K and log g = 5.8 $\pm$ 0.2, and Méndez et al. (1988b) give a rough distance estimate of between 500 and 900 pc. Lisker et al. (2005) determined $T_{\rm eff}$ = 34060 K, log g = 5.85, D = 700 pc and M_V = +4.50. Extinction in this general direction is low, with $E(B-V)$ = 0.04 from Schlegel, Finkbeiner & Davis (1998). The UBV photometry of Ellis, Grayson & Bond (1984) implies $E(B-V)$ = 0.01 $\pm$ 0.01.

The UCAC2 proper motion is μ_α, μ_δ = -16.8, -3.2 mas yr^{-1} (17.1 mas yr^{-1} in pa 259°). Using the spectroscopically determined distance from Lisker et al. (2005), the transverse velocity

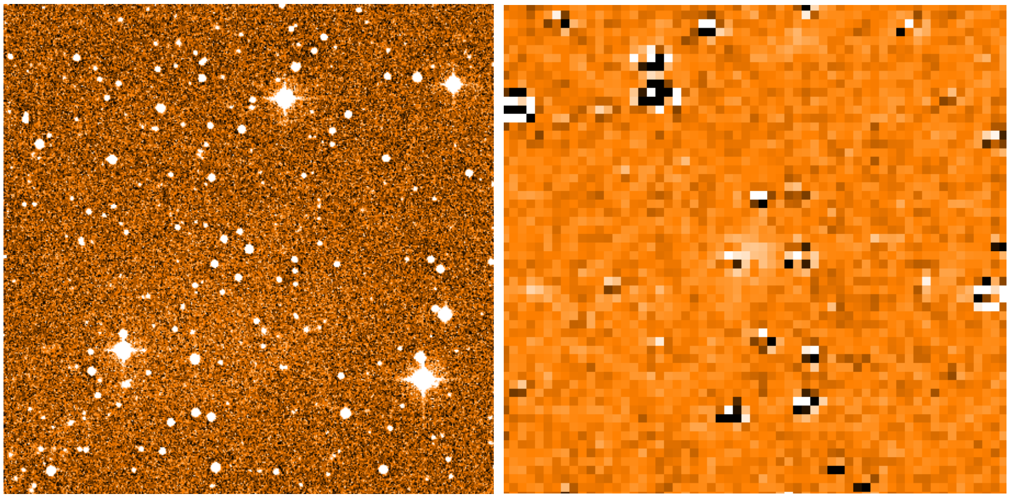

Figure 8.4: Left: SSS POSS II R-band image of EGB 5. A faint nebulous enhancement is visible, south-preceding the ionizing star ($V = 13.8$), which is at exact centre. Image is $10'$ across, with NE at top left. Right: SHASSA Hα+ [N II] image of the nebulosity EGB 5. Image is $45'$ across, with NE at top left. The small size and low surface brightness indicate a very low ionized mass at the accepted distance.

Table 8.5: Literature multiwavelength photometry for the ionizing star of EGB 5.

Band	Magnitude	Source
u'	12.30	1
U	12.37	2
B	13.51	2
g'	13.63	1
V	13.83	2
r'	13.90	1
i'	14.05	1
I	14.36	3
z'	14.22	1
J	14.482 $\pm$ 0.036	4
H	14.530 $\pm$ 0.055	4
K_s	14.692 $\pm$ 0.082	4

1. SDSS (Adelman-McCarthy et al. 2008; PSF magnitudes converted to Vega system); 2. Ellis, Grayson & Bond (1984); 3. Ciardullo et al. (1999); 4. 2MASS (Skrutskie et al. 2006).

is $\sim$57 kms^{-1} and total space velocity is $\sim$90 kms^{-1} with respect to the sun, using the radial velocity from Karl et al. (2003; see below). The magnitudes of the UVW vectors suggest the star has old disk kinematics.

The arguments of Méndez et al. (1988b) stating that the emission measure is too high for it to be ambient interstellar gas can be discounted in the light of our analysis of PHL 932, especially since the background-corrected Hα surface brightness is somewhat lower than PHL 932, about 16 R (as measured from SHASSA), corresponding to an emission measure of $\sim$45 cm^{-6}pc. Yet the faint enhancement on the southwest edge seen in figure 8.4, if interpreted as an ISM interaction, is in agreement with the orientation of the proper motion vector. The ionized mass of the nebula was determined the same way as for PHL 932, using an integrated flux for EGB 5 of $\log \mathrm{F(H}\alpha) = -11.9 \pm 0.2$ erg cm^{-2} s^{-1}. The result, $M_{\mathrm{ion}} = 0.03\sqrt{\epsilon}\ M_{\odot}$ is very low for a conventional PN, and supports an interpretation as either a small mass-loss event (perhaps through common-envelope ejection if the star is a close binary; see below) or alternatively, and favoured here, that the nebula is ionized ISM.

Confirmatory evidence on any association between star and nebula will come after determining the systemic velocity of the gas (the integrated flux is too faint for WHAM). Méndez (1989) determined the stellar velocity to be $V_{\mathrm{hel}} = +66.5 \pm 1.5$ kms^{-1}, from spectra taken on two consecutive nights; this implies it is not a short-period binary. On the other hand, Karl et al. (2003) find the star to be a single-lined spectroscopic binary with $\gamma_0 = 69.6$ kms^{-1} and $K = 16.1$ kms^{-1}. Their power spectrum has peaks at 1.1806 and 0.5505 days; they could not favour one period over the other. The systemic velocity is in good agreement with the observations of Méndez (1989). However, the velocity semi-amplitude is very small for such a short period system, but the orbit may be close to pole on. Alternatively, there could be stellar wind variability which mimics orbital variations in this star. Further work is needed.

There is some evidence from published photometry (Ellis, Grayson & Bond 1984; Tylenda et al. 1991) that the star may be variable, but the Ellis et al. V magnitude is consistent with the mean magnitude in the ASAS-3 database, $V = 13.80$. The dispersion in the ASAS photometry ($\sigma = 0.21$, from 94 measurements) is as expected for a star of that magnitude (i.e. close to the survey limit). Furthermore, Saurer & Pfitscher (1989) found no evidence for any photometric variability.

There is no signature of a near-IR excess using all available $UBVIJHK$ photometry and SDSS data from the literature. The dereddened optical and near-IR colours are practically identical to those of PHL 932 (see §8.3.1), so if a companion is present, it must be a faint WD or a very late M-dwarf (see also Karl et al. 2003, who class this object as a double degenerate). Hence there is conflicting evidence for binarity and the jury is still out on whether EGB 5 formed through a binary or single-star evolutionary channel. Of further note is that Jordan, Werner & O'Toole (2005) detected a probable magnetic field in this star (see this paper for a fuller discussion).

Along with PHL 932 and the central star of EGB 5, there seems to be only one other sdB star which may be ionizing a nebula, PG 1047+003 which has a large very faint, diffuse area of emission around it as seen in WHAM data (see Madsen, Reynolds & Haffner 2006), and which is also visible on SHASSA images. Line widths and systemic velocities imply this too is just ionized ISM. In summary, there is *currently no strong evidence* for any sdB or sdOB star to have an ejection nebula or putative 'PN' associated with it. Further work is needed to determine the origin of the nebulosity around EGB 5.

8.5 DHW 5

This large emission nebula (also designated DeHt 5) was first identified by Dengel, Hartl & Weinberger (1980) as a likely PN. It has an unusual irregular and stratified morphology, and shows a quite different appearance in [O III] light, compared to its morphology in [N II] and [SII] emission (see Dengel, Hartl & Weinberger 1980; Rosado & Moreno 1991; Tweedy & Kwitter 1996; and figure 8.5).

8.5.1 Ionizing star

The ionizing star of DHW 5 is WD 2218+706. The available photometry is summarised in table 8.6. There is some evidence from the reddening-corrected $V - K_s$ colour index of a slight near-IR excess, but the 2MASS K-band magnitude has a fairly large error bar.

Table 8.6: Literature photometry for WD 2218+706

Band	Magnitude	Source
B	15.253	1
V	15.474	1
I_C	15.640	1
J	15.566 ± 0.070	2
H	15.960 ± 0.196	2
K_s	15.576 ± 0.221	2
$B - V$	−0.22	

1. Harris et al. (2007)
2. 2MASS (Skrutskie et al. 2006)

A trigonometric distance has been recently determined by Harris et al. (2007), $D = 300^{+60}_{-44}$ pc, adopted here. Using the data given by Good et al. (2004), gravity distances were calculated from first principles, following the procedure outlined in §6.4.6). The resulting distances using the Balmer and Lyman lines respectively are $D = 390$ and 530 pc. This can be compared with the Balmer gravity distances of Pottasch (1996) of ∼460 pc and Napiwotzki (1999, 2001) of 510^{+170}_{-140} pc.

The available proper motion data presented in table 8.7 is inconsistent and no conclusion can be drawn on the consistency of the proper motion vector with the nebular morphology and ionization structure.

The best-fit heliocentric radial velocity of WD 2218+706 from Good et al. (2005) is −40.9 km s^{-1}, in good agreement with the velocity of Bannister et al. (2003) of −38.7 ± 0.2 km s^{-1}. The gravitational redshift from table 6.6 is $V_{\rm GR}$ = 5.9 km s^{-1}, which leads to a corrected

Table 8.7: Proper motion of WD 2218+706

Survey	$\mu_\alpha cos\delta$ mas yr^{-1}	μ_δ mas yr^{-1}
USNO-B	-12 ± 4	-18 ± 4
NOMAD1	-12 ± 4	-18 ± 2
Harris et al. (2007)	+36.4	+10.3

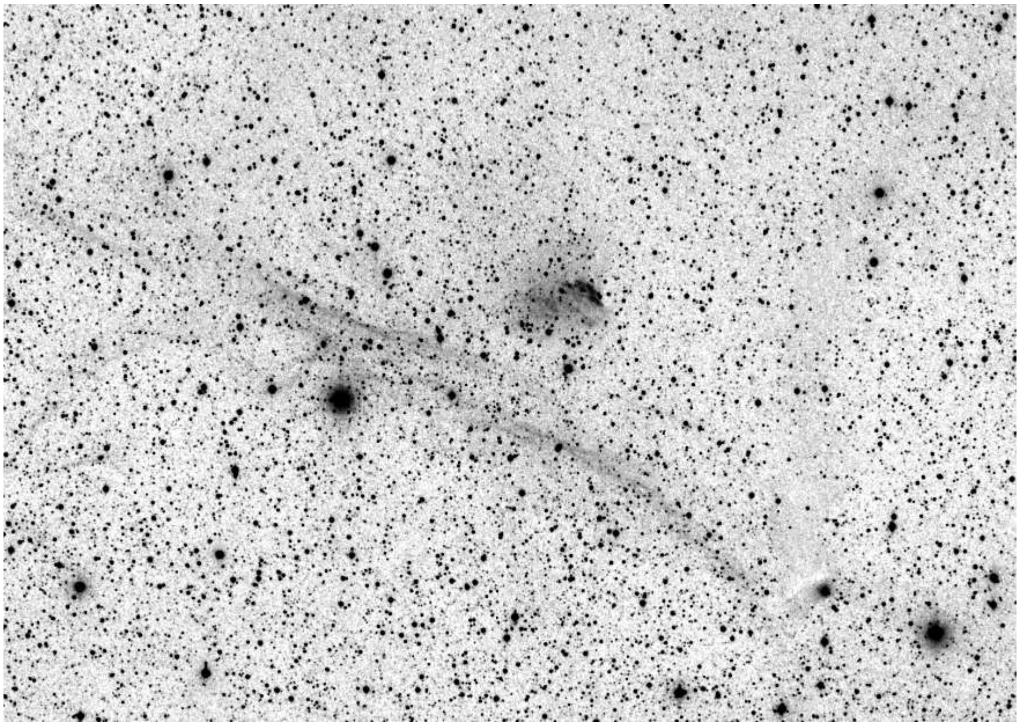

Figure 8.5: Narrow-band Hα+ [N II] image of the nebulosity DHW 5 (slightly above centre) and surrounding area. Image is 180′ wide. Note the extensive diffuse and striated emission across the field, evidence for irregular dust obscuration, and the cometary reflection nebula Ced 201 to the southwest (lower right). Image credit: Rick Schrantz, see http://www.grosse-pn.de.vu/

heliocentric velocity of -46.8 km s^{-1}, or -35.2 km s^{-1} referred to the LSR frame. Neither Bannister et al. (2003) or Good et al. (2005) found any evidence for radial velocity variations in the star.

8.5.2 Emission nebula

Detailed narrow-band images are presented by Rosado & Moreno (1991) and Tweedy & Kwitter (1996). The morphology and ionization stratification is atypical for a PN. The structure is somewhat filamentary and one-sided in the low-excitation [N II] and [SII] lines, but without an obvious bow shock structure, and there is a smaller Strömgren zone around the star in [O III]. A small dust patch abuts the nebula to the west (see Fig. 11 of Tweedy & Kwitter 1996, and figure 8.5).

The nebular gas surrounding WD 2218+706 has a very narrow line width determined from

Table 8.8: Summary of radial velocity determinations for emission nebulae (EN), reflection nebulae (RN), Bok globules (BG) and molecular clouds (MC) within 3° of DHW 5, ordered by Galactic longitude.

Object	Type	l	b	$V_{\rm LSR}$ (kms^{-1})	Line	Ref
[YDM97] 46	MC	109.20	+11.07	−20.6	CO	1
[YDM97] 52	MC	110.00	+13.33	−12.4	CO	1
[YDM97] 57	MC	110.40	+11.60	−4.6	CO	1
Ced 201/B175	RN/BG	110.60	+11.96	−5.3	CO	2
[YDM97] 61†	MC	110.67	+9.73	−4.9	CO	1
DeHt 5	EN	111.09	+11.64	−4.8	Hα, [N II], [O III]	3
DeHt 5	EN	111.09	+11.64	+1.6	Hα, [N II], [O III]	4

† associated with an LBN bright nebula; Yonekura et al. (1997); 2. Kutner et al. (1980); 3. This work ; 4. Gieseking et al. (1986), velocities converted to LSR frame.

our new WHAM data (HWHM = 10 ± 3 kms^{-1}, see table 3.9), confirming the earlier determination of Gieseking, Hippelein & Weinberger (1986). This is surprisingly small for an expanding PN, but consistent with the warm, diffuse ISM.

8.5.3 Environment

Extensive diffuse emission and reflection nebulosities surround DHW 5 (see figure 8.5). DHW 5 lies within the outer boundary of the Cepheus Flare, a nearby giant molecular cloud complex, ∼ 10 − 20° above the Galactic plane (e.g. Kun 1998). The literature on the Cepheus Flare is well summarised by Kun (1998) and by Bally & Reipurth (2001). Of historical note is the account by Hubble (1934) who noted a large area relatively free of galaxies above the Galactic plane in Cepheus. This void is due to the large area of obscuration associated with the Cepheus Flare.

One of the earliest detailed investigations of this region was undertaken by Grenier et al. (1989) who mapped the region in CO at 2.6 mm. They showed that CO emission was concentrated at a number of discrete distances, including a nearby molecular complex at ∼300 pc. Kun (1998) divided the Cepheus Flare region into subregions based on Galactic latitude and investigated the distribution of star counts with distance using Wolf diagrams. At the lowest latitudes (11° − 13°) she noted that the near side of the clouds were at $D \sim 300$ pc. This distance is in excellent agreement with the trigonometric distance of WD 2218+706 ($l = 111.1$, $b = +11.6$), $D = 300^{+60}_{-44}$ pc (Harris et al. 2007).

8.5.4 Discussion

Previous workers have assumed that DHW 5 is a bona fide PN. Bannister et al. (2003) had previously noted the proximity of WD 2218-706 to the giant molecular cloud complex described by Kun (1998), and stated that the star may lie in an area where the ISM is dense. However, these authors did not consider the possibility that the optical nebula might be in fact ionized ISM. Tweedy & Kwitter (1996) noted the extensive diffuse emission around the bright nebula, suggesting this might be ionized interstellar material, but assumed that the core was a true PN.

The velocity of the nebular gas is given in table 8.8, where the WHAM velocity is seen to be significantly different to the ionizing star, and identical to within the errors with the measured velocities of a neighbouring globule and two molecular clouds (see Table 8.8). Two other molecular clouds have greater negative velocities and are placed at a distance of ~1.0 kpc by Yonekura et al. (1997).

The overall body of evidence is again in favour of the ionized-ISM interpretation, rather than a PN. The morphology of the nebula is not typical of an evolved PN, and the gas is consistent with being ionized ambient material, as the systemic velocity agrees with the CO velocities of widespread neutral gas at ~300 pc, the distance of the star as determined by Harris et al. (2007). The narrow line width of the nebular gas is also consistent with the ionized ISM interpretation. Furthermore, the evolutionary position of the star in the HR diagram is *not* in agreement with a post-AGB track that is consistent with the timescale of PN evolution. All of the evidence is consistent with DHW 5 being a HII region ionized by WD 2218+706.

8.6 Sh 2-68 (HtDe 9)

This unusual nebula is also designated as Simeis 291, YM 15, LBN 93, and HtDe 9. It was first recorded by Gaze & Shajn (1954), and later by Johnson (1955), Sharpless (1959) and Lynds (1965) as a HII region. It was first classified as a PN by Fesen, Gull & Heckathorn (1983) based on its strong [O III] emission, and independently by Hartl & Weinberger (1987); both teams noted a faint blue 'central' star which gave support to a PN interpretation. It has generally been accepted as a PN ever since (Acker et al. 1992; Kohoutek 2001; Kerber et al. 2002).

8.6.1 Ionizing star

The ionizing star was photometrically measured by Forbes (1989), who quoted $V = 16.59$, $B - V = -0.01$. The star is moderately reddened: Adopting an intrinsic colour $(B - V)_0 = -0.35$, leads to a reddening of $E(B - V) = 0.34$. The star was spectroscopically investigated by Napiwotzki & Schönberner (1991), who showed it was one of a very rare class of hybrid PG 1159 stars, which show strong CIV and He II lines typical of PG1159 stars, as well as strong Balmer lines. Napiwotzki (2001) determines a gravity distance of 1100^{+500}_{-400} pc, but this will be shown below to be an overestimate.

Its large proper motion was determined by Kerber et al. (2002), who found a high value of 53.2 ± 5.5 mas yr^{-1}, from ground-based plates. This indicates that the distance is <500 pc for the star to belong to the old disk population, which seems certain based on its proper motion vector being aligned parallel to the Galactic equator.

8.6.2 Emission nebula

The morphology is highly unusual for a PN (Fesen, Gull & Heckathorn 1983; Xilouris et al. 1996), and it has an irregular comet-like tail of low emission measure extending for 45′ northeast (p.a. 212°) from the nebula (Kerber et al. 2003b; and figure 8.6). The most puzzling aspect is the complete lack of a well defined bowshock in the direction of the CSPN proper motion,

Table 8.9: Summary of radial velocity determinations for selected emission nebulae (EN), reflection nebulae (RN), young stellar objects (YSO) and molecular clouds (MC) within 2° of Sh 2-68, ordered by Galactic longitude.

Object	Type	l	b	$V_{\rm LSR}$ (kms^{-1})	Line	Ref
Sh 2-68	EN			+4.6	[O III]	1
Sh 2-68	EN			+1.6	Hα, [N II], [O III]	2
Sh 2-68	EN			+11.0	Hα	3
[YDM97] 61†	MC			−4.9	CO	4
'Serpens RN'	RN			+8.0	NH_3	5
SMM 1	YSO			+8.0	CO	6

†associated with an LBN bright nebula; 1. This work; 2. Gieseking et al. (1986), velocities converted to LSR frame; 3. Fich, Treffers & Dahl (1990); 4. Yonekura et al. (1997); 5. Ungerechts & Güston (1984); 6. White, Casali & Eiroa (1995).

expected from theoretical work and detailed modelling of PN/ISM interactions (see Chapter 4 and references therein). In fact the nebula has a pronounced density enhancement towards the east (see the next section). On the assumption that it is a PN, Kerber et al. (2003b) discuss the ionised tail downstream as a consequence of ram-pressure stripping of the nebula by the ISM as it moves through it. A similar phenomenon is seen in the gaseous tail of the well-known nearby AGB star, Mira (Martin et al. 2007; Wareing et al. 2007).

Integrated line fluxes were determined with the WHAM interferometer, in Hα, [N II] and [O III]. The systemic velocity of the nebular gas from the [O III] line is $V_{\rm LSR}$ = +4.6 kms^{-1} (the Hα and [N II] line profiles are affected by 'wings' of unrelated emission) and the expansion velocities in each line were found to be very low. The very largest, most highly evolved PNe do often have low expansion velocities (e.g. Ton 320, Sh 2-216), but at any reasonable distance (see below), the main body of Sh 2-68 (e.g. Fesen, Gull & Heckathorn 1983) is considerably smaller than these nebulae. The small line width, $2v_{\rm exp}$ = 10 kms^{-1} is difficult to explain if Sh 2-68 is a conventional PN, and the line width is more typical of diffuse ambient gas.

8.6.3 Environment

An alternative interpretation is that the hot star is ionizing a dense region of ambient interstellar material. Indeed the nebula is very close on the sky to the Serpens molecular cloud complex, which is ∼1° east of the nebula, in the direction of the bright rim on the edge. The moderate reddening seen towards the ionizing star is due to intervening dust associated with the complex.

Table 8.9 summarises a selection of radial velocity determinations taken from the literature for emission nebulae (EN), reflection nebulae (RN), and molecular clouds (MC) within 2° of Sh 2-68 (including the nebula itself), ordered by Galactic longitude. White, Casali & Eiroa (1995) show that widespread CO emission is present, at LSR velocities ranging from −10 to +25 kms^{-1}, but with a mean of +8 kms^{-1}, very close to the mean LSR velocity of the optical emission lines (Gieseking et al. 1986; Fich, Treffers & Dahl 1990; and this work).

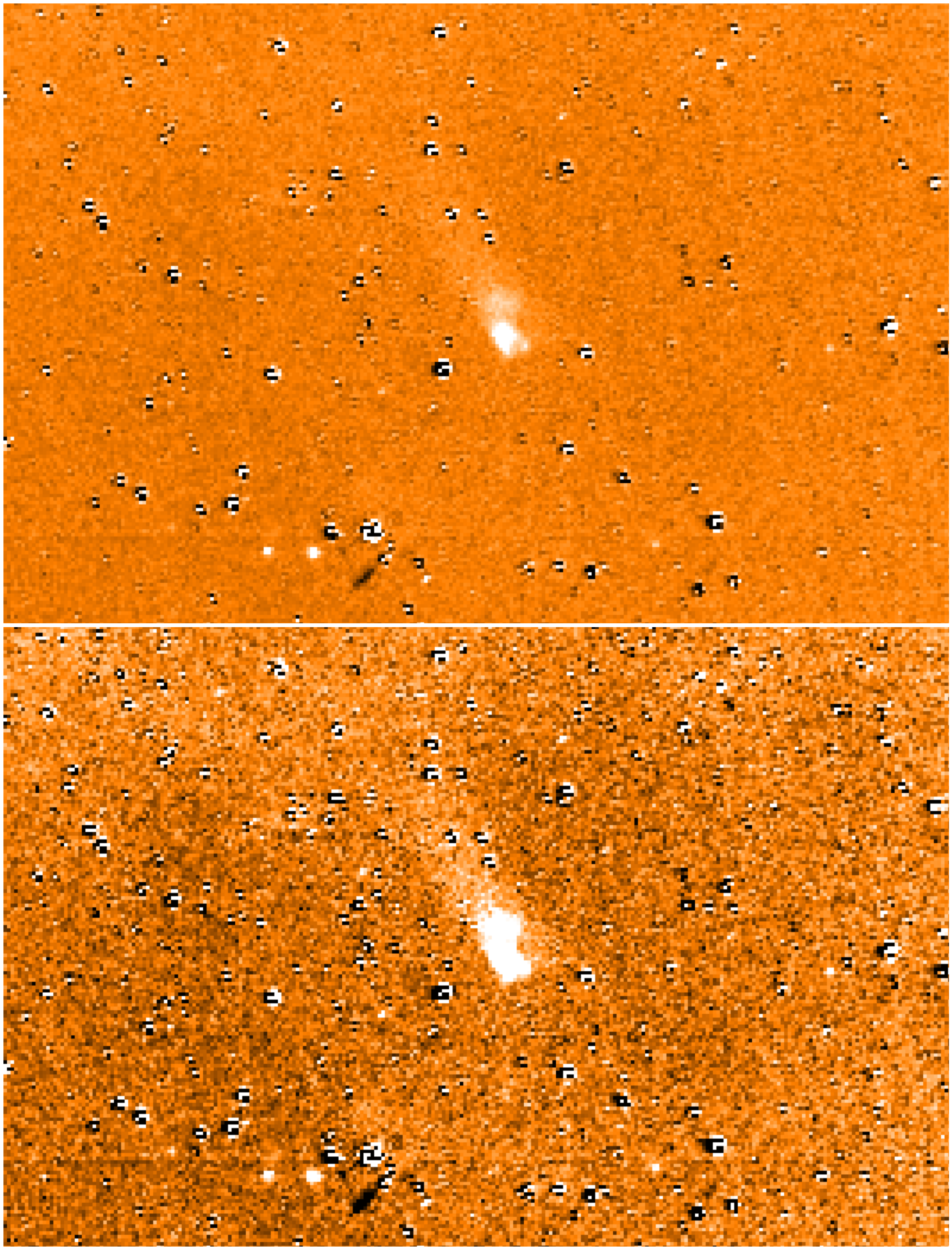

Figure 8.6: Low- and high-contrast SHASSA images of Sh 2-68. Each image is 3.5° wide, with NE at top left. See the text for further details.

8.6.4 Discussion

Traditionally, this nebula is interpreted to be a PN showing a strong interaction with the ISM (Tweedy & Kwitter 1996; Xilouris et al. 1996; Kerber et al. 2002), though the bright rim is on the *eastern* rim of the nebula which differs from that expected location on the southwest side, inferred from the p.a. of the proper motion vector. However, it is difficult to see how the observed nebular morphology could be produced if this was a genuine PN moving supersonically through the ISM. PNe moving through the ISM always have a bowshock oriented in the direction of motion (Borkowski, Sarazin & Soker 1990; Borkowski 1993; Villaver, García-Segura & Manchado 2003; Wareing et al. 2006a, 2007). The simplest solution is that this is a HII region in the ambient ISM around an unrelated hot PG1159 star.

If the star is ionizing part of the Serpens complex, which is 250–300 pc away (Chavarria et al. 1988; de Lara et al. 1991; Straizys, Cernis & Bartasiute 1996), then the determination of an accurate distance to the star naturally follows. The calculated transverse velocity is then $\sim$60 kms^{-1}, typical of disk white dwarfs (Sang-Gak 1984). Note that the NTLE gravity distance of 1100^{+500}_{-400} pc (Napiwotzki 2001) would lead to a transverse velocity of $\sim$280 kms^{-1} for this star, showing that there are often serious problems with the distance scale(s) based on NTLE model atmospheres, due primarily to the determination of the surface gravity (Pottasch 1996). Using a distance of 300 pc, and the adopted reddening, an absolute magnitude, $M_V = +8.15$ is determined. This is rather fainter than typical PN central stars.

Working with the hypothesis that this is a HII region in the ambient ISM, the tail noted by Kerber et al. (2003b) cannot be ram-pressure stripped gas from a putative PN. I propose here that the wake is an ionised contrail left behind as the unrelated hot star moves linearly through the ISM, analogous to that inferred for PHL 932. McCullough & Benjamin (2001) and Benjamin, McCullough & Madsen (2001) have argued that such contrails are feasible.

We proceed by using the same arguments as for PHL 932 (see §8.3.4). For the downstream wake of Sh 2-68, the corrected Hα surface brightness (midway down the tail) is $\sim$4 R. The effective path length (assuming cylindrical geometry and an average tail width of $15'$) is 1.3 pc (for $D = 300$ pc). The emission measure is calculated to be $\sim$16 cm^{-6}pc and the mean electron density is then $\sim$4 cm^{-3} (similar to the tail behind PHL 932). The hydrogen recombination time for ambient gas of this density is $\sim$30,000 yr. From the measured proper motion, the star was at the end of the tail about 45,000 years ago (Kerber et al. 2003b). Considering the coarse assumptions in this approach, the recombination time scale can explain the ionised tail behind the nebula, giving an answer correct to within a factor of two. For a recombination time of 45,000 years, the mean tail density should be about 2 cm^{-3}, somewhat lower than estimated. However, uniform density along the wake, or cylindrical geometry for the tail, may be incorrect assumptions.

To summarise, Sh 2-68 is considered to be a high-excitation HII region in a dense region of ISM associated with the Serpens molecular cloud complex. The hot star is moving quickly through the complex and has left an ionized contrail in its wake.

8.7 Sh 2-174 (LBN 598)

This large emission nebula is another 'putative PN' with a highly peculiar structure, rather like a 'cleft hoof'. The overall form lies outside the range of normal PN morphologies. The nebulosity was discovered by Sharpless (1959), and also noted by Lynds (1965), but it was first proposed to be a PN by Napiwotzki & Schonberner (1993) on the basis of its inferred association with the hot white dwarf GD 561. This star is actually located exterior to the main nebulosity as seen on red-light POSS images (figure 8.7), and Tweedy & Napiwotzki (1994) have termed it "the planetary nebula abandoned by its central star".

8.7.1 Ionizing Star

The ionizing star, designated GD 561, was discovered by Giclas et al. (1970), and it was later classified as a DAO white dwarf by Bergeron et al. (1992), confirmed by Tweedy & Napiwotzki (1994) and Napiwotzki & Schönberner (1995).

The available optical and NIR photometry for GD 561 is summarised in table 8.10. The dereddened $V - K_s$ colour is consistent with a DAO star of $T_{\rm eff} = 70000$ K, so there is no evidence for a companion star from the photometry (see also Farihi, Becklin & Zuckerman 2005). Since a companion is needed for the close-binary scenario, it seems that this star evolved from an alternative route, or that the putative companion is another, fainter degenerate.

While Tweedy & Napiwotzki (1994) accept it as a PN, the position of GD 561 in the HR diagram is highly unusual if this star is a product of post-AGB evolution; the star is considerably cooler than the other high-gravity stars of evolved PNe. Bergeron et al (1994) estimate $T_{\rm eff} =$ 65,300 K and $\log g = 6.71$, consistent with Napiwotzki (1994), who determined $T_{\rm eff} \simeq 65{,}000$ K and $\log g \simeq 6.8$ and from high S/N spectra, but these parameters are inconsistent with standard post-AGB evolutionary tracks. Napiwotzki (1999) found $T_{\rm eff} \simeq 69{,}100 \pm 3000$ K and $\log g =$ 6.70 ± 0.18, consistent with the earlier work. Good et al. (2004) determined $T_{\rm eff} = 64{,}400 \pm$ 2900 K and $\log g = 6.94 \pm 0.16$ from the Balmer lines, and $T_{\rm eff} = 75{,}600 \pm 4950$ K and $\log g =$ 6.64 ± 0.06 from the Lyman lines; the Lyman values are preferred. Using just the Hδ, Hϵ and the He II 4686 lines, these authors derive $T_{\rm eff} = 73{,}350 \pm 5400$ K and $\log g = 7.04 \pm 0.15$.

As an independent estimate for the stellar temperature, the new Hα flux from our WHAM data (see below) was used with the visual magnitude and reddening to determine a hydrogen Zanstra temperature (see §9.4.4). I derive $T_z(\mathrm{H}) = 71{,}000 \pm 8000$ K, in excellent agreement with the spectroscopic determinations.

The asymptotic reddening in this direction is $E(B-V) = 0.27$ mag ($A_V = 0.82$) from Schlegel, Finkbeiner & Davis (1998), higher than expected for a galactic latitude of $\sim$18°. This is evidence for dust and molecular material in this direction (see below). This is an upper limit to the star. The published $UBVrJHK$ photometry is best fit with a reddening of $E(B-V) =$ 0.06 which is consistent with the value adopted by Good et al. (2004) who determine $E(B-V)$ = 0.089 from a measurement of the hydrogen column density towards the star. The latter value is adopted in the discussion that follows.

Until recently the distance of the star was poorly known. Fich & Blitz (1984) estimate a

Table 8.10: Literature photometry of GD 561

Band	Magnitude	Source
U	13.07	1
B	14.28	1
B	14.19:	2
V	14.53	1
V	14.52	2
r	14.82	1
J	15.241 ± 0.052	3
H	15.539 ± 0.137	3
K_s	15.440 ± 0.221	3
$B - V$	-0.25	adopted
$V - K$	-0.91	adopted
$J - K$	-0.20	adopted

References: 1. Schwartz (1972); 2. Greenstein (1974); 3. 2MASS (Cutri et al. 2003).

distance of ~220 pc for Sh 2-174 from a Galactic rotation curve, but the error on the distance is expected to be substantial for such a low velocity relative to the ISM (see below). Tweedy & Napiwotzki (1994) derived a gravity distance of 420 ± 150 pc, and a new gravity distance using the data provided by Good et al. (2004) is 395 ± 120 pc, which will be adopted hereafter. The absolute magnitude of GD 561, using the adopted extinction and the distance is $M_V = +6.3 \pm 0.6$.

The heliocentric radial velocity of GD 561 from Good et al. (2004) is -12.5 ± 0.7 km s^{-1} from two spectra. The gravitational redshift from table 6.6 is $V_{\rm GR} = 6.9 \pm 1.2$ km s^{-1}, which leads to a corrected heliocentric velocity of -19.4 ± 1.4 km s^{-1}, or -9.6 ± 1.5 km s^{-1} referred to the LSR frame. The proper motion from USNO-B is μ_α, $\mu_\delta = -28 \pm 4$, $+4 \pm 6$ mas yr^{-1}. Note that Kerber et al. (2004) derived the space velocity and Galactic orbit using the nebular velocity combined with the stellar proper motion. Using the radial velocity from Good et al. (2004), the total space velocity is calculated to be 74 kms^{-1} with respect to the ISM.

8.7.2 Emission Nebula

Tweedy & Napiwotzki (1994) obtained narrowband images of Sh 2-174 with the Burrell Schmidt telescope. The cleft-hoof morphology apparent on the POSS is due to Hα + [N II] emission. However their [O III] images shows that the emission is centred on the white dwarf, which shows that GD 561 is the ionizing source, but does not necessarily confirm that the star and the nebula are physically related (cf. Tweedy & Napiwotzki 1994).

The ionization stratification of the nebulosity is not consistent with a star (and nebula) moving in a westerly direction. There is no enhanced rim to suggest a bowshock, and the region of highest ionization is at the preceding rim of the nebula. If the nebula had been moving in this direction, then a low-ionization front with relatively stronger [N II] emission would be expected on this side. The images presented by Tweedy & Napiwotzki (1994) and figure 8.7 are consistent with a star gradually moving through the *static ISM* and creating a (temporary) stratified HII region here.

Figure 8.7: Two-colour DSS $R + B_J$ image of Sh 2-174. Note the peculiar ionization stratification. The greenish-blue nebulosity to the right of the reddish 'cleft hoof' is the [O III] Strömgren zone around GD 561, which has a proper motion to the west (right). If the nebula was moving with the star, a low-excitation rim would be expected on the western edge of the nebula, opposite to what is seen. Note the extensive reflection nebulosity (also bluish) surrounding Sh 2-174. Image credit: Jens Bohle, see http://www.grosse-pn.de.vu/

Reynolds et al. (2005) found $\log F(H\alpha) = -10.15 \pm 0.06$ erg cm^{-2} s^{-1} through a 60′ beam (WHAM NSS data). Our new determinations (Madsen et al. 2006; Madsen & Frew 2008, in preparation) are $\log F(H\alpha) = -9.87 \pm 0.05$ erg cm^{-2} s^{-1}, $\log F(6584) = -10.14 \pm 0.05$ erg cm^{-2} s^{-1} and $\log F(5007) = -10.09 \pm 0.05$ erg cm^{-2} s^{-1} (see figure 3.6). The higher Hα flux is a consequence of the better centering of the nebula in the beam to recover all the flux; the nebula is smaller than the 60′ WHAM beam. From the new data, the integrated [N II]/Hα ratio is 0.72, higher than is typical for an ordinary HII region. This suggests that the electron temperature is elevated, owing to the high temperature of the ionizing star.

The systematic radial velocity of the nebulosity as determined by WHAM (see Chapter 3) is $V_{\mathrm{LSR}} = -1.4 \pm 2$ kms^{-1} from Hα, $V_{\mathrm{LSR}} = -5.2 \pm 2$ kms^{-1} from the [N II] 6584 line, and $V_{\mathrm{LSR}} = +2.5 \pm 2$ kms^{-1} from the [O III] 5007 line (see figure 3.6). This range in velocity between species is explained by the different spatial distribution of the stratified nebulosity (see Figure 1 of Tweedy & Napiwotzki 1994). The mean velocity, $V_{\mathrm{LSR}} = -1.4 \pm 3.9$ kms^{-1} is slightly different to the earlier determination from Hα of WHAM NSS survey data $V_{\mathrm{LSR}} = +4 \pm 1$kms^{-1}. The NSS beam was not in the same place as the pointed observation taken by G. Madsen, which probably explains the small velocity offset.

Reynolds et al. (2005) measure a FWHM of 20 ± 2 kms^{-1} in Hα which is considerably less than the mean FWHM for *bona fide* PNe in their sample. Our new WHAM data (see Chapter 3) confirms the narrow line-width of the emitting gas, which is significantly less than the average width seen in evolved PNe.

8.7.3 Discussion

The inferred stellar evolutionary age is 10^7 years, far longer than the typical PN lifetime of 10^4 to 10^5 years. To account for this anomaly, Tweedy & Napiwotzki (1994) suggested that GD 561 is part of a close binary, common-envelope system, that lost its outer envelope after the termination of core hydrogen burning. The small resultant mass of the WD of $\sim 0.4\ M_{\odot}$ is consistent with the range of masses expected for common-envelope scenarios (see Zijlstra 2007).

If Sh 2-174 is a HII region in the ISM, it is germane to look at the regional environment around the nebula. No molecular clouds, reflection nebulae or globules are catalogued within 10° of Sh 2-174. However, Blitz, Fich & Stark (1982) give CO velocity data for the nebula, the detection of which which would be unusual for a non-Type I PN of low surface brightness (see also Fich & Blitz 1984). Table 8.11 gives the available radial velocity data for Sh 2-174. The CO emission is consistent with the Hα velocity indicating they measure a common feature. From the data in table 8.11, the emitting gas is consistent with near to zero velocity with respect to the LSR, and therefore cannot be at too great a distance. This is also consistent with the high Galactic latitude of the nebulosity.

Note that the corrected stellar velocity (see above) of -9.6 ± 1.5 km s^{-1} is nearly 3σ less than the most negative nebular velocity: the WHAM [N II] velocity (Madsen & Frew, in prep.), so I consider the stellar velocity to be statistically different to the gas. Furthermore, a strong bowshock should be observed on the 'upstream' side of the nebula if it were co-moving with GD 561 (i.e. moving at 74 kms^{-1} with respect to the ISM). No such limb-brightening is observed.

Table 8.11: Summary of radial velocity determinations for Sh 2-174.

Object	Type	l	b	$V_{\rm LSR}$ (kms^{-1})	Line	Ref
Sh 2-174	EN/MC	120.17	18.40	-2.7	CO	1
Sh 2-174	EN	120.17	18.40	$+4.0$	Hα	2
Sh 2-174	EN	120.17	18.40	-1.4	Hα, [N II], [O III]	3
Sh 2-174	EN	120.17	18.40	$+5.9$	Hα	4

1. Blitz, Fich & Stark (1982); 2. Reynolds et al. (2005); 3. This work; 4. Fich, Treffers & Dahl (1990).

Taking these facts into account, and considering the great evolutionary age of the ionizing star, the overall impression is that Sh 2-174 is clearly a HII region in the ambient ISM and not a bona fide PN.

8.8 TK 2 (RE 1738+665)

The nebula around this hot DA white dwarf was discovered by Tweedy & Kwitter (1994) and was suggested to be a new remnant PN, but again the morphology is not convincing. The other faint nebula found by Tweedy & Kwitter (1994) is around the DAO star Ton 320, and is a very probable PN.

Preliminary values of $T_{\rm eff}$ and $\log g$ were determined by Barstow et al. (1994b). Bannister et al. (2003) determine $T_{\rm eff}$ = 71,300 K and $\log g$ = 7.53 cm s^{-2}, while Barstow et al. (2003a,b) using *FUSE*, determine $T_{\rm eff}$ = 66,800 ± 1200 K and $\log g$ = 7.77 ± 0.10 cm s^{-2} from the Balmer lines, and $T_{\rm eff}$ = 75,800 ± 700 K and $\log g$ = 7.85 ± 0.03 cm s^{-2} from the Lyman lines.

Harris et al. (2007) have measured a reliable trigonometric distance of only 169^{+13}_{-11} pc for RE 1738+665. The gravity distance from table 6.6 is 160–220 pc, consistent with the trigonometric distance. Using the Harris et al. distance, the derived absolute magnitude is $M_V = 8.29^{+0.14}_{-0.17}$ which would be very faint for a PN nucleus (cf. Phillips 2005a). The low luminosity and relatively cool temperature suggests the star is quite far down the WD cooling track, consistent with its DA spectral classification.

The heliocentric radial velocity for the star from Bannister et al. (2003) is +30.2 ± 0.3 km s^{-1}. The gravitational redshift from table 6.6 is $V_{\rm GR}$ = 16.8 km s^{-1} based on the parameters presented by Bannister et al. (2003), or $V_{\rm GR}$ = 25.0 km s^{-1} using the higher gravity Lyman determination of Barstow et al. (2003a,b). Using the latter result leads to a corrected heliocentric velocity of +5.2 km s^{-1}, or −20.8 km s^{-1} referred to the LSR frame. The circumstellar absorption features (Bannister et al. 2003) are assumed to be due to local gas in the vicinity of the star and have $V_{\rm hel}$ = −18.6 km s^{-1} or $V_{\rm LSR}$ = −3.0 km s^{-1}.

The systemic velocity of the emitting gas is difficult to determine. The WHAM Hα spectrum has a 'negative' flux, due to the offset fields having significant Hα emission. This can be interpreted as implying there is widespread faint diffuse gas in the area. Unfortunately the star is positioned just outside the coverage of VTSS, but diffuse Hα emission is visible on VTSS field *Dra14*, about 2° from RE 1738+665, and apparently surrounding the bright PN NGC 6543.

Furthermore, a number of WHAM offset fields for NGC 6543 have significant Hα emission (G. Madsen, pers. com. 2006).

The WHAM data shows the [N II] emission has a measured LSR velocity of close to zero, and is consistent with the velocity of the circumstellar features seen in RE 1738+665 (Bannister et al. 2003). Hence it is concluded that the nebular and stellar velocities are statistically different, and are not consistent with a PN interpretation. The distance from Harris et al. (2007) places the star within a Galactic scale height of the nebular gas, and coupled with the unconvincing nebular morphology and very low emission measure, this nebula is considered to be a faint, irregular HII region in the ISM.

8.9 Hewett 1

This nebula was first discovered serendipitously from Sloan Digital Sky Survey (SDSS) data (Hewett et al. 2003; Hewett & Irwin 2004) and was claimed to be "the largest known planetary nebula on the sky". The SDSS spectra revealed the presence of an extensive region of ionized gas roughly 2° across, centred at l, b = 248°, +48° (see figure 8.9). Hewett et al. (2003) noted strong [O III] emission, confirmed from our WHAM data and an unpublished MSSSO 2.3-m long-slit spectrum. Hewett et al. (2003) stated that the "combination of emission-line ratios, the close to zero heliocentric radial velocity, and the morphology of the structure is consistent with an identification as a very nearby planetary nebula".

The SHASSA image (figure 8.9) shows the main Hα region to subtend $100' \times 75'$. The integrated flux in Hα from SHASSA data (from field # 214), is $\log F(\mathrm{H}\alpha) = -10.13$ through a $60'$ aperture, consistent with the surface flux determined from WHAM (see Chapter 3), of $\log F(\mathrm{H}\alpha) = -10.16$. The total flux of the whole nebula from SHASSA is $\log F(\mathrm{H}\alpha) = -9.95 \pm 0.10$. The WHAM data also show the high excitation of the nebula, with $F(5007)/F(\mathrm{H}\alpha) = 3.9 \pm 0.5$, far higher than an ordinary HII region surrounding a Population I star, but expected for an emssion region around a hot DO white dwarf with T_{eff} = 100,000 K.

Using the new flux, the ionized mass is estimated to be $\sim 0.7 \sqrt{\epsilon} M_{\odot}$, which is typical for an evolved PN. However this parameter is not an overly useful discriminant, as the ionized masses of Strömgren spheres in the ISM excited by WD stars range from $\sim$0.02–50 $\sqrt{\epsilon} M_{\odot}$, including values typical of true PNe (see elsewhere in this chapter).

However, the systemic nebular velocity, $v_{\mathrm{LSR}} \sim 0\ \mathrm{km\,s^{-1}}$ (Hewett et al. 2003, and Chapter 3) is quite different from the photospheric velocity of the ionizing star, PG 1034+001, $v_{\mathrm{hel}} = +50.8\ \mathrm{km\,s^{-1}}$ (Holberg, Barstow & Sion 1998; c.f. Sorensen & Pollacco 2003). Corrected for gravitational redshift and converted to the local standard of rest, the stellar velocity is $v_{\mathrm{LSR}} \simeq 32\ \mathrm{km\,s^{-1}}$, not consistent with that of the nebular gas. Chu et al. (2004) suggested the nebula is simply ionized ISM, and this conclusion is substantiated here.

A spectroscopic distance to PG 1034+001 of 155 $\pm$ 50 pc was determined by Werner et al. (1995). Harris et al. (2007) give a new trigonometric distance of 211^{+26}_{-22}pc. which is consistent with the earlier determination. At this distance, the ionized nebula has an overall diameter of $\sim$7 pc. The measured proper motion of PG 1034+001 translates into a transverse velocity of 88

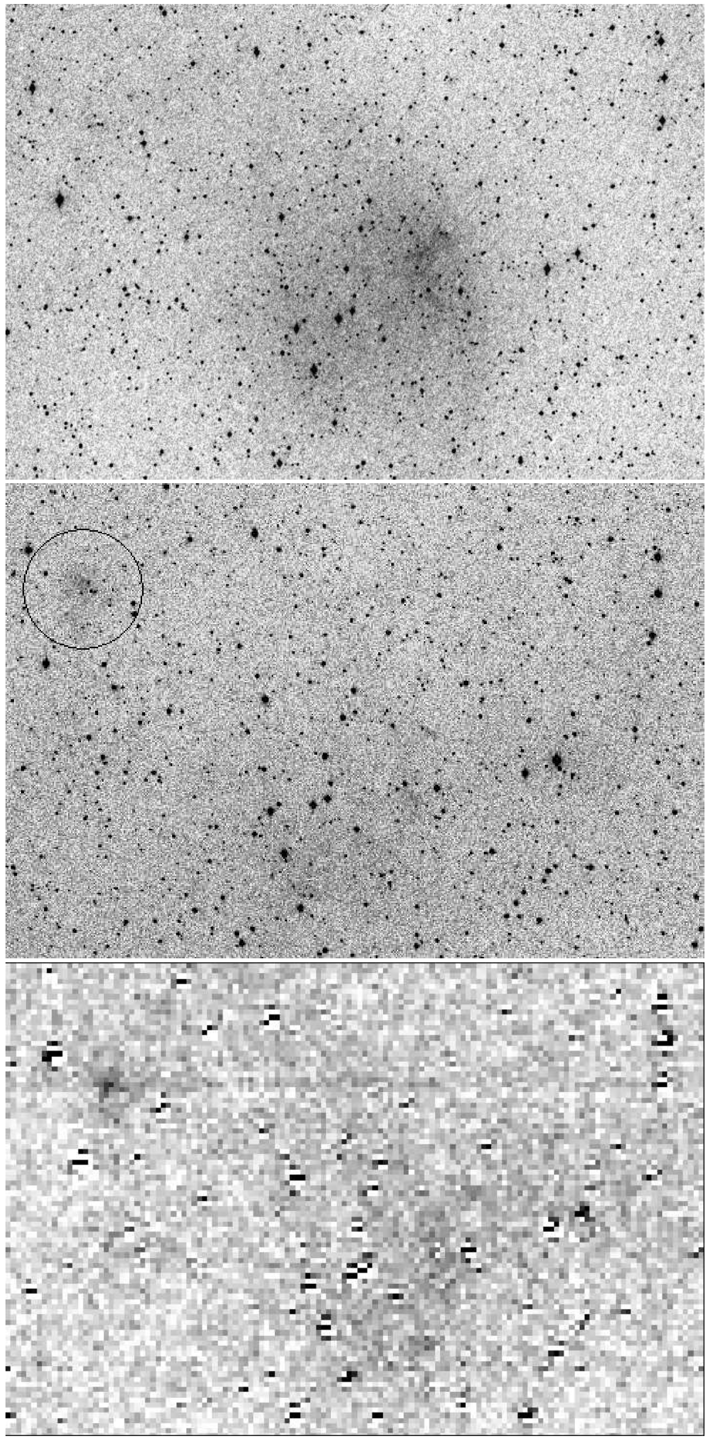

Figure 8.8: Narrowband images of the nebula Hewett 1. Top: Deep [O III] image obtained by Rick Schrantz, see http://www.grosse-pn.de.vu/. Middle: Hα + [N II] image; note the addtional HII region or emission patch to northeast, marked with a circle. Credit, Rick Schrantz. Bottom: Deep SHASSA continuum-subtracted Hα + [N II] image, at coarser resolution. NE is at top left in each panel and the field is 2° wide. See the text for further details.

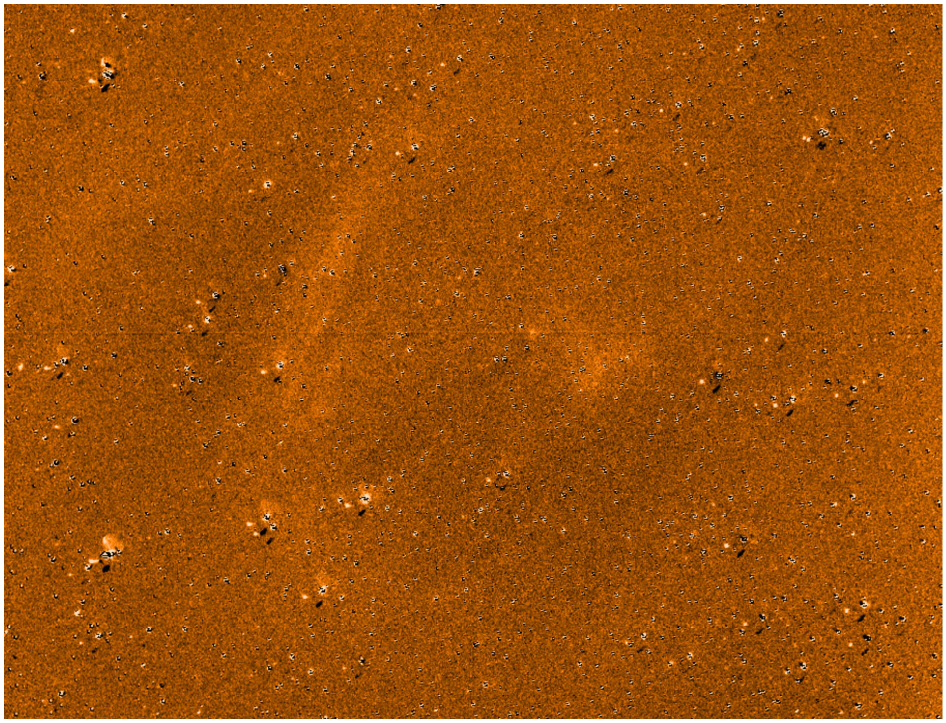

Figure 8.9: Wide SHASSA Hα + [N II] narrowband image around Hewett 1, which is the discrete nebulosity just right of centre. The large filamentary feature (centre left) was noted by Rauch, Kerber & Pauli (2004), but is part of a larger feature that extends over adjacent SHASSA fields. Image dimensions are $\sim$12° × 9°, and NE is at top left. See the text for further details.

± 10 kms^{-1} (Harris et al. 2007), and the total space motion is $\sim$94 kms^{-1} with respect to the local rest frame. Had the observed nebula been a bona fide PN travelling with PG 1034+001, a significant nebular bow shock would be expected in the direction of motion of the star. Deep CCD images presented by Hewett et al. (2003; see also Hewett & Irwin 2004), as well as the SHASSA image presented here (figure 8.9), show no obvious bow shock features.

Rauch, Kerber & Pauli (2004) discovered a giant 'halo' around PG 1034+001, with an apparent diameter of 6° × 9° on SHASSA images. Visual inspection shows the main part of the halo to be a curving arc of filamentary Hα emssion which extends for many degrees over adjacent SHASSA fields, and is probably not a halo feature associated with the HII region Hewett 1, but is just ionized ambient ISM, which can be remarkably filamentary on large angular scales (G. Madsen, pers. comm., 2006).

Hewett et al. (2003) also claimed that this nebula is the first PN to be unambiguously associated with a DO white dwarf. However, with the downgrading of the nebulae around PG 1034+001, PG 0108+101 and PG 0109+111 (§8.11) from PN status, as well as the interpretation of the nebula around KPD 0005+5106 as a Strömgren sphere (Chu et al. 2004; see also section 8.10 below), then there are currently *no DO white dwarfs known to be associated with a PN* (cf. Dreizler & Werner 1996; Kruk & Werner 1998; Napiwotzki 1999; Hewett et al. 2003; Otte, Dixon and Sankrit 2004; Chu et al. 2004).

8.10 KPD 0005+5106

KPD 0005+5106 is one of the very hottest DO (helium rich) white dwarfs with $T_{\rm eff}$ = 120,000 K and $\log g$ = 7.0 (Werner et al. 1994, 1996; Kruk & Werner 1998), though more recent work suggests it is even hotter, with $T_{\rm eff}$ = 200,000 K (Werner, Rauch & Kruk 2008). It was discovered by Downes, Liebert & Margon (1985) who measured it photoelectrically, determining $V = 13.32$, $B-V = -0.30$ and $U-B = -1.22$. The observed colours show that the star is lightly reddened, consistent with their determination of $E(B-V) = 0.07 \pm 0.04$ from the interstellar 2200 Å feature.

KPD 0005+5106 has a large [O III] emission region surrounding it, of diameter 3°, first found on interference-filter plates taken by T. Gull and Y.-H. Chu (unpublished). Kruk & Werner (1998) had detected, rather surprisingly, molecular H_2 absorption bands in the UV spectrum of KPD 0005+5106. They speculated that they might have been produced in a surrounding very old PN, but a deep search in Hα by Werner et al. (1997) failed to note any surrounding nebula, though the area covered was small. However Otte, Dixon and Sankrit (2004) found an O VI-emitting nebula around the star with the *Far Ultraviolet Spectroscopic Explorer* (FUSE), also postulating that the nebula is a high-excitation PN.

A detailed discussion of the ionized nebula around KPD 0005+5106 has been presented by Chu et al. (2004), so only the main points are repeated here. The velocities of the nebular gas in this direction enabled Chu et al. (2004) to separate the ionized nebula around KPD 0005+5106 from the background H II region, some 4° across, associated with the O9IIIn eclipsing binary star AO Cas. This HII region is primarily visible in Hα (see VTSS field *Cas01*, illustrated as figure 8.10), and has very little [O III] emission (see Chu et al. 2004, figures 2 & 3).

Chu et al. (2004) find that the velocity of the KPD 0005+5106 nebula is similar to that of the local ISM ($v_{\rm LSR} = -7$ from [O III]) and the interstellar/circumstellar absorption lines in the UV spectra of KPD 0005+5106, confirmed by our new WHAM data (see Chapter 3) where we find $v_{\rm LSR} = -5\pm$ 3 km s^{-1}. However, the photospheric velocity of the star is different, $v_{\rm hel}$ = +36.2 km s^{-1} (Holberg, Barstow & Sion 1998), transformed to $v_{\rm LSR}$ = +34 km s^{-1} (taking the gravitational redshift into account), showing that the star is not physically associated with the nebula. Werner et al. (1996) find the interstellar/circumstellar and photospheric lines to be different by ∼50 kms^{-1} and the velocity of the photospheric lines agrees with the velocity determined from Holberg, Barstow & Sion (1998).

The velocity-integrated Hα flux for the entire emssion region (i.e. AO Cas and KPD 0005) from VTSS is $\log$ F(Hα) = −8.2 ± 0.1, though this is a lower limit, as the nebula is truncated by the field edge. A separate Hα flux for the gas associated with KPD 0005+5106 is $\log$ F(Hα) = −8.62 (Y.-H. Chu, pers. comm. 2004), consistent with the VTSS aperture flux. Using this flux and the estimated distance of KPD 0005+5106 of 270 pc (Werner et al. 1994), the nebular ionized mass was estimated to be ∼70 $M_\odot$, far too high to be a PN, but consistent with it being a Strömgren zone in the ambient ISM (for further details, see Chu et al. 2004).

Such a large mass is consistent with the ionizing flux of the star, as demonstrated by Chu et al. (2004). Stasińska (1989) has shown that the maximum nebular mass that can be ionized

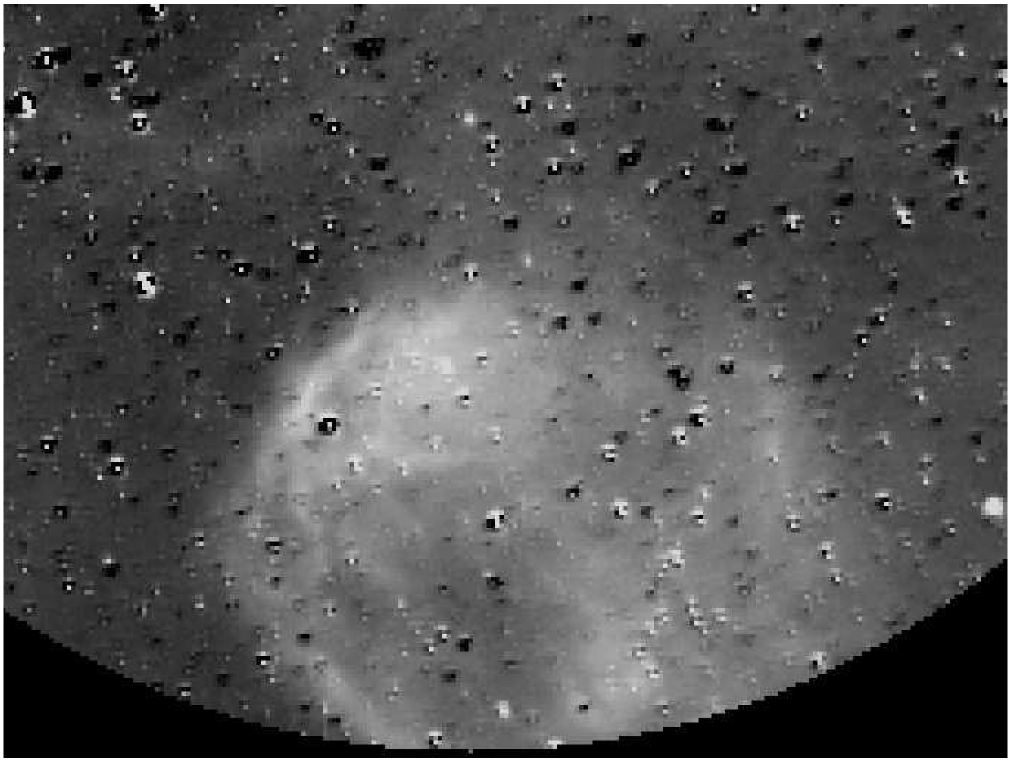

Figure 8.10: VTSS Hα narrowband image of the nebula associated with AO Cas. The edge of the curved VTSS field is visible at bottom. The image subtends $6^\circ \times 4.5^\circ$.

by a hot star is given by:

$$M_{\rm max} = 5 \times 10^{45}\, Q_{\rm H}\, n_e^{-1} \tag{8.13}$$

where $Q_{\rm H}$ is the Lyman continuum flux of the star in photons per second. From the data given by Stasińska (1989), a bare PN nucleus (age of 5 $\times 10^4$ yr) has $\log Q_{\rm H} \simeq 45.5$ photons s^{-1}. In an ambient medium with n_e = 0.5 cm^{-3}, approximately $30 M_\odot$ of material can be ionized, less in a denser medium. Hence, the existence of a faint HII region around KPD 0005, and the giant ISM haloes around Abell 36, NGC 3242, Sh 2-200 and others, are readily explained. In low density environments, hot WDs and central stars in density bounded PNe can ionize up to several tens of masses of surrounding interstellar material.

8.11 PG 0108+101 and PG 0109+111

Surrounding the hot DO white dwarf PG 0108+101 is a large ($\sim$60′) faint emission nebula first discovered by Reynolds (1987). Reynolds determined a nebular radius of 2.5 – 5 pc, and a root-mean-square electron density of just 0.3 –0.5 cm^{-3}, comparable to the mean ISM density in the galactic plane; Reynolds was unsure whether it was a faint evolved PN or an ionized HII region in the ISM. Another hot DO white dwarf, PG 0109+111 is just 1° north, and is also associated with some very faint emission (Reynolds 1987). This star is probably ionizing the small emission nebulosity (or knot) imaged by Werner et al. (1997). Again, the nature of this

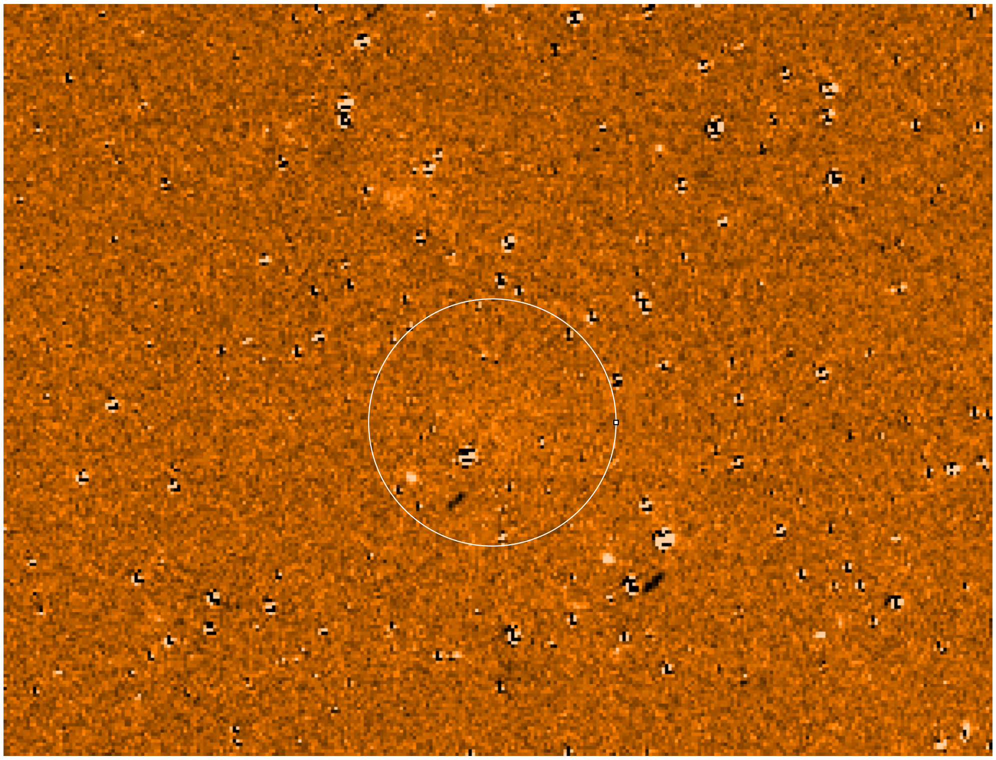

Figure 8.11: SHASSA Hα + [N II] narrowband image of the emission nebulae associated with PG 0108+101 and PG 0109+111. The circle has a diameter of 1° (the size of the WHAM beam) and is centred on PG 0108. The smaller, but higher surface brightness nebulosity northwest (noted by Werner et al. 1997) is probably associated with PG 0109. See the text for further details. North is up and east to the left.

object was unclear, but it is statistically very unlikely that two highly evolved PNe would occur in such close proximity, at this very high Galactic latitude ($b \simeq -52°$). Both nebulae are visible on SHASSA field 236, illustrated here as figure 8.11.

New WHAM data show that the systemic radial velocities of each nebula are identical within the errors and that there is probably one extended HII region here, ionized by one or both stars (see also Frew, Parker & Madsen 2006; Madsen & Frew 2008, in preparation). It should be reiterated that the nebula around PHL 932 is only a few degrees away, and is likely also associated with extensive high-latitude HI gas in the area, as the systemic velocity of this nebula is nearly identical (see §8.3).

The fairly similar apparent magnitudes, temperatures, and surface gravities of these two stars (e.g. Wesemael, Green & Liebert 1985) suggest they are at similar distances; gravity distances range between 200 and 400 pc (Pottasch 1996; Dreizler & Werner 1996) Considering the error bars on the published $\log g$ values, their distances are consistent with each other and with the distance to PHL 932. These nebulosities are also considered to be Strömgren spheres in the ISM.

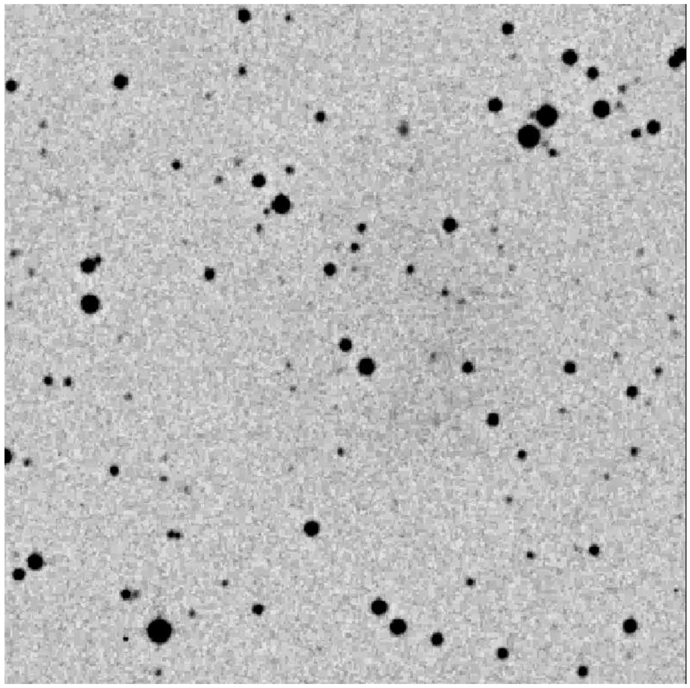

Figure 8.12: Red DSS image of HDW 4 (HaWe 6). Field is 5′ on a side with NE at top left. The ionizing star is the fainter of the two at centre.

8.12 HDW 4

Also designated HaWe 6, We b, and PN G156.3+12.5, this faint nebula (see figure 8.12) was noted by Hartl, Dengel & Weinberger (1983) and Hartl & Weinberger (1987). The dimensions quoted in the latter source are $128'' \times 87''$.

Harris et al. (2007) determine a trigonometric distance of to the ionizing star of only $D = 209^{+19}_{-16}$ pc. Napiwotzki (1999) performed a NLTE model atmosphere analysis, determining $T_{\rm eff}$ = 47,300 ± 1700 K and $\log g$ = 7.93 ± 0.16, and estimating a distance of 250 pc. The relatively low temperature and high gravity of the WD suggests a long cooling age, far greater than any feasible PN lifetime. Referring to Table 1 of Bergeron, Wesemael & Beauchamp, a cooling age of $3\text{–}4 \times 10^6$ years is suggested. The absolute magnitude is $M_V = 9.43^{+0.18}_{-0.19}$ which is considerably fainter than any PN nucleus. The very low ionized mass of the nebula ($5 \times 10^{-3}\ M_\odot$; Napiwotzki 1999) also rules out a PN interpretation. Napiwotzki speculates that the nebula might be a shell produced by an ancient nova outburst (the mass is about right) but the star shows no sign of any CV features in its spectrum (Napiwotzki & Schönberner 1995).

Napiwotzki (1999) obtained a spectrum of the HII region around this star and deduced an upper limit to the expansion of $2v_{\rm exp} < 47$ kms^{-1}. Hence an expanding nova shell hypothesis is ruled out. The expansion limit is consistent with ambient ISM, so the nebula may be another case of ISM ionization by an unrelated hot WD.

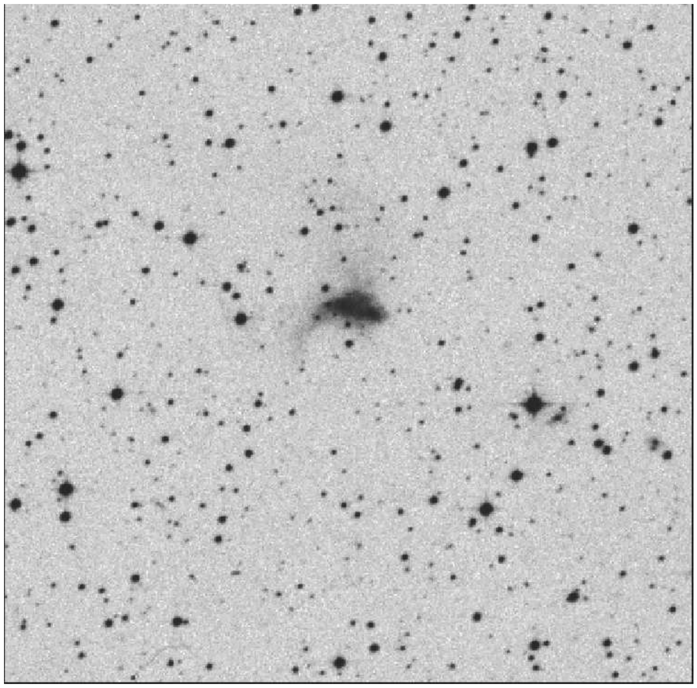

Figure 8.13: Red DSS image of HDW 5. Field is 10′ on a side with NE at top left. Note the faint extensions to the NE of the bright, sickle-shaped nebulosity. The morphology is unlike that of a PN.

8.13 HDW 5

This peculiar, sickle-shaped nebula (figure 8.13) is also listed as HaWe 7 and PN G218.9-10.7 in the literature. It is usually supposed to have been discovered by Hartl & Weinberger (1987), but had been noted several decades previously by Minkowski (1948), who designated it M 3-56. Cohen (1980) also noted it as a red nebulous object (= RNO 70) in his survey for nebulae in dark clouds. The morphology is peculiar (Manchado et al. 1996; Ali & Pfleiderer 1999) and somewhat similar to the HII region Sh 2-174 (see §8.7, above). The proposed ionizing star, which has $V = 16.29$ (Shaw & Kaler 1989), is also located outside of the visible nebulosity (Hartl & Weinberger 1987; Tylenda et al. 1991). By extension, it is argued that this is also an example of ionized ISM. The nebular spectrum is of low excitation with very weak [O III] emission (Acker et al. 1992; Ali & Pfleiderer 1999; Bohigas 2001). Bohigas (2001) could not determine whether it was an unusual bipolar PN or a HII region, and noted the possible presence of shocked H_2. Similarly, Ali & Pfleiderer (1999) also considered its nature, leaving open its status for future interpretation. More recently, Lee et al. (2007) investigated the ionizing star, but could not assign a spectral class for it. Earlier, Méndez (1991) has classified it as hgO(H).

HDW 5 is positioned close to an extensive area of reflection nebulae, dark nebulae and molecular clouds. Maddalena et al. (1986) mapped 850 deg^2 in the Orion/Monoceros region in the $J = 1 \rightarrow 0$ line of CO, finding evidence for widespread emission, including giant molecular cloud complexes associated with Orion A, Orion B and Mon R2. Another feature seen in CO emission, named the 'Southern Filament' by Maddalena et al. (1986), lies in very close proximity to HDW 5. One cloudlet associated with the nearby dark nebula LDN 1652, has $V_{\rm LSR} = +12.2$

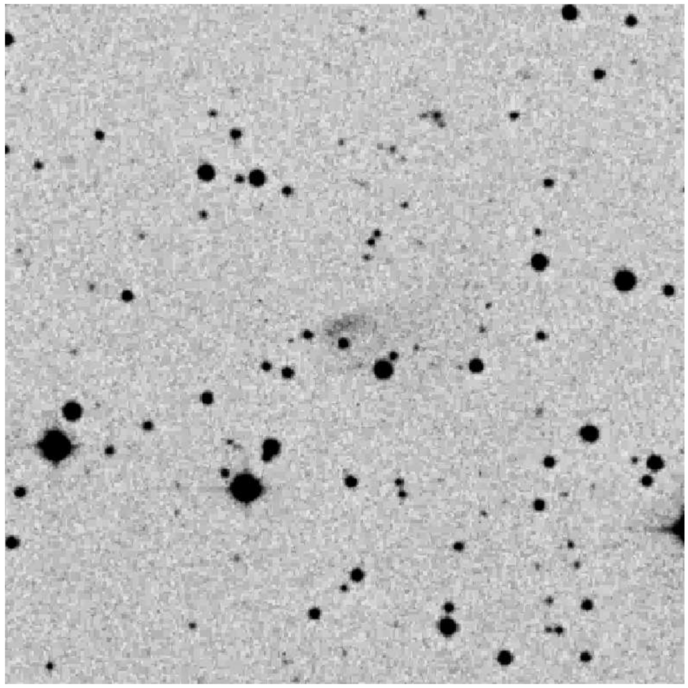

Figure 8.14: Red DSS image of HaWe 5. Field is 5′ on a side with NE at top left.

$\mathrm{km\,s^{-1}}$.

Even though there are no WHAM data to determine a systemic velocity of HDW 5, the most likely interpretation at this point is that HDW 5 is a HII region excited by the adjacent (pre)-white dwarf. The position of the star outside of the nebula, the aberrant morphology, the low nebular excitation, and its close proximity to extensive areas of molecular emission militate against a PN interpretation.

8.14 HaWe 5

This is PN G156.9-13.3, first reported as a new PN by Hartl & Weinberger (1987), who noted dimensions of $47'' \times 24''$. For the 'central' star, Napiwotzki (1999) determined $T_{\rm eff}$ = 38,100 $\pm$ 1500 K and $\log g = 7.58 \pm 0.20$ from an NLTE model atmosphere analysis. The estimated distance is $\sim$420 pc.

This small faint nebula shares characteristics in common with HDW 4, where the large evolutionary age of the star is at odds with the existence of a remnant PN. Napiwotzki (1999) also suggests that this may be an old nova shell (Napiwotzki estimated an ionized mass of only $2\times 10^{-4}\ M_{\odot}$). A red DSS image (figure 8.14) shows a vaguely PN-like elliptical nebula surrounding the ionizing star. The small size and faintness of the object would be remarkable if it was a real PN at the nominal distance. Instead, it could be a wisp of ionized ambient material.

8.15 BD +28°4211

The sdO star BD +28°4211 is a well-known spectrophotometric standard. Tweedy & Kwitter (1996) have investigated whether faint arcuate Hα filaments near this star provide evidence for a remnant PN; they present a deep Hα image of the filaments (see their figure 15). Zanin & Weinberger (1997) also found three very faint large filaments symmetrically centered on this star, over a diameter of ~5°. While no spectroscopic data referring to the individual filamentary nebulosities is available, WHAM NSS spectra show that widespread local gas of low emission measure is present in the vicinity of this star. Coupled with the fact that the proper motion of the star is taking it *towards* the innermost convex arcs (see the discussion by Tweedy & Kwitter 1994b, 1996), the nebulosity is considered to be ionized ISM.

8.16 EGB 7

This is a large, patchy elliptical nebula (dimensions $20' \times 11'$) discovered by Ellis, Grayson & Bond (1984) from the POSS. These authors noted there was no obvious central star and that its classification was uncertain. However, given its large size and possible proximity to the Sun, its status warranted evaluation. There is no published spectroscopic information on it, but its relative brightness on red and blue DSS images suggests it is almost certainly a large reflection nebula, coincident with a high-latitude molecular cloud (e.g. Herbstmeier, Heithausen & Mebold 1993).

Extensive faint reflection nebulosity is present over a wide area surrounding this object. A prominent reflection nebulosity is also associated with the HI cloud at l ~91°, b ~38° (Goerigk et al. 1983). Mebold et al. (1983) have called this the Draco nebula, with the brightest part nicknamed "Dracula". Mebold et al. (1985) studied this molecular cloud in detail, finding HI and CO emssion, associated with H_2CO absorption on this sightline; the mean CO velocity is $V_{\rm LSR} = -24\ {\rm km\,s^{-1}}$. Herbstmeier, Heithausen & Mebold (1993) looked at IRAS 100μm imagery along with CO and HI data to derive the extinction and total mass of the nebula. Their figures 1 and 3 respectively show the HI column density and 100μm flux of the entire cloud complex (see also Moritz et al. 1998). The Dracula condensation is seen to be linked to EGB 7, seen as the prominent condensation at l ~94.5°, b ~37.5°(their component 'H').

The Draco cloud is at a minimum distance of $D \gtrsim$800 pc (Mebold et al. 1985; Penprase, Rhodes & Harris 2000), with the height above the plane, $z \gtrsim$500 pc. This complex illustrates that that dense molecular gas can exist at remarkably large $|z|$ distances from the plane. The faint reflection nebulosity in the area is probably reflecting light from the Galactic disk, and is probably related to the high-latitude cirrus noted by Sandage (1976).

In summary, EGB 7 is a high latitude reflection nebula, probably shining by diffuse starlight, and is similar to another nebulosity catalogued by Ellis, Grayson & Bond (1984), EGB 2, located in Pisces at $l, b = 148.10°, -48.62°$. This is very similar in appearance to EGB 7 on the DSS red and blue images, and is also considered to be a reflection nebula. An unpublished MSSSO

2.3-m spectrum shows no emission lines present. A number of nearby molecular clouds extend in a zone west from the Aries molecular cloud complex (e.g. Straižys et al. 2002) at a distance of 325 pc. For example, MBM 5 (Magnani, Hartmann & Speck 1996) is only 88′ west.

8.17 Other rejected objects

Five more emission nebulae of different types are briefly described here, as they have been included in samples of local PNe in the past (e.g. Ishida & Weinberger 1987). For an additional brief list of PNe now shown to be at greater distances than first thought, and hence outside the 1.0 kpc volume, refer to §A.2 in the appendices.

Cn 1-1 (HD 330036). This stellar-appearing object has a distance of just 380 pc according to Ishida & Weinberger (1987), and was included in their sample of nearby PNe, and so it warrants briefly addressing here. The lack of any resolved nebulosity (despite its proximity to the Sun), the presence of a strong F-type continuum and the high density diagnostics in the spectrum point to it being a yellow symbiotic star (Lutz 1984; Munari & Zwitter 2002; Pereira, Smith & Cunha 2005). A spectrum from Munari & Zwitter (2002) is reproduced in figure 1.7.

EGB 4. This nebula is briefly mentioned here, as it is discussed elsewhere in this thesis (see §8.2 and §B.2). Discovered by Ellis, Grayson & Bond (1984) as a possible PN, EGB 4 has a remarkable bow-shock morphology (Krautter, Klaas & Radons 1987; Hollis et al. 1992; Greiner et al. 2001) and is associated with the cataclysmic variable BZ Cam. The visible nebula is considered to be HII region photoionized by the CV accretion disk with a strong component of shock excitation due to the star's significant space motion of $\sim$125 kms^{-1} with respect to the ISM (Greiner et al. 2001). The distance from this latter study is $\sim$830 pc, placing it in the solar neighbourhood volume, but it is not to be considered as a PN candidate.

He 2-77. This nebula was included by Ishida & Weinberger (1987) as a local PN candidate, with D = 330 pc! However, the unusual morphology, strong thermal IR emission (as seen in IRAS and MSX data), high radio flux density, and heavy extinction point to it being a distant compact HII region of quite high excitation (Cohen & Barlow 1980; Caswell & Haynes 1987).

M 2-9. An extensive literature (e.g. Schwarz et al. 1997; Doyle et al. 2000; Livio & Soker 2001; Smith & Gehrz 2005, and references therein) exists on this beautiful and remarkable bipolar nebula, discovered by Minkowski (1947) from objective-prism plates. It is considered here to be a resolved symbiotic outflow (included in figure 4.2 as a morphological comparison), based on its spectral characteristics and red near-IR colours (see Schmeja & Kimeswenger 2001, 2002 a,b), and as such, is not considered further here. The distance has been estimated as $\sim$650 pc, determined via an expansion parallax (Schwarz et al. 1997).

vBe 1 (G339.2 − 0.4). This object was first classified as a radio SNR (Clark, Caswell & Green 1975) though they noted its relatively flat radio spectrum ($\alpha = -0.2$, $S \propto \nu^{\alpha}$), suggested that it may not be a SNR after all. Van den Bergh (1978) classified it as a low-excitation PN, based on its appearance on red plates. It is essentially invisible on B and J plates (see figure 1.12). Murdin, Clark & Haynes (1979) re-examined its radio properties, confirming the relatively flat spectrum and low emission measure. It has very weak optical [O III] emission arguing against classifying it as a PN, but a SNR classification also seems ruled out as it has weak [SII] lines (Murdin, Clark & Haynes 1979).

Nevertheless they concluded it could be a probable PN based on its round, shell-like appearance on R plates, with a spectrum analogous to the low-excitation object NGC 40. Looking at their data more closely, the spectrum looks more like that of a HII region, but there does not seem to be any obvious population-I ionizing star(s) present. Deep red plates by Zealey, Elliott & Malin (1979) "show a complete shell 6 arcmin in diameter, with enhanced emission to the south." Shaver et al (1980) detected H109α and H137β radio recombination lines and concluded that it is an HII region, and certainly not a SNR. Rosado (1986) took interference images of this object as well as Fabry-Perot interferograms. Our spectrum confirms its nature as an HII region.

WhMe 1. This object was initially considered as a potential candidate PN for the 1 kpc sample. It was discovered by Whitelock & Menzies (1986), who argued that the central star is a binary comprising a B9 star and a hot subdwarf at a distance of 1.1 kpc. It was subsequently assumed to be a PN with a binary nucleus (e.g. De Marco et al. 2004). However, as discussed by Whitelock & Menzies (1986), this system may be another example of a yellow symbiotic. The [O III] λ4363 line is a factor of three brighter than Hγ, typical of symbiotic stars (e.g. Gutiérrez-Moreno, Moreno, & Cortés 1995), and the image is stellar (size $< 2''$). The near-IR magnitudes and colours are also more typical of dusty symbiotics. This object is not considered to be a candidate local PN.

8.18 Summary

In this chapter, a number of emission nebulae heretofore considered as PNe have been excluded from the solar neighbourhood sample on the basis of new and revised observational data. In summary, no single discriminatory criterion was usually enough to define the status of each putative PN, so the *overall body of evidence* was used to classify each nebula. Most objects have been shown to be Strömgren 'zones' (HII regions) in the ambient ISM, ionized by hot white dwarfs and subdwarfs. In the case of the former, they may have had PNe around them in the past, but these have long dispersed.

These nearby nebulae should be struck out of any future compilation of PNe, and are not included in the refined solar neighbourhood PN sample, defined in the next chapter.

Chapter 9

The Refined Solar Neighbourhood Sample

9.1 Introduction

As noted in Chapter 8, it is very important to eliminate nearby nebulae of doubtful provenence from any volume-limited sample. At least 15 nebulae in the solar neighbourhood, classified as PNe in the past, have been shown here to be non-PNe. Since an accurate determination of the local PN column density (see Chapter 11) is heavily dependent on the definition of a clean local sample, uncontaminated by PN impostors, it was important to classify each of these objects correctly, as the majority were within ∼500 pc of the sun.

As the next step towards defining the local census, all previously known 'large' PNe with mean diameters $>2'$ were tabulated in a working database, about 100 objects in total. All new discoveries larger than the same limiting size[1] from the MASH catalogue (Parker et al. 2006a) and its supplement, MASH-II (Miszalski et al. 2007) were also tabulated; a total of ∼80 objects.

To ensure that the local sample was as complete as possible, additional PNe and PN candidates of smaller diameter but with strong optical, radio, and/or infrared fluxes were tabulated separately. Such PNe could be local, especially if strongly reddened. For all objects, reddenings were taken from the literature, derived from nebular spectroscopy, or from $UBVRIJHK_s$ photometry of the CS (see below). Distances for these PNe were determined with the Hα SB-r relation developed in the previous chapter if a primary distance estimate was not available. As a result, data for over 450 PNe were tabulated and vetted, and sorted according to distance.

The tables at the end of this chapter (see §9.6) list the main observable and derived properties of all planetary nebulae now considered to be within 2.0 kpc of the Sun, a total of 210 PNe, including data on their central stars. More details on the various PN properties in the 2.0 kpc sample are provided in the following sections. Notes on individual PNe within a radius of 1.0 kpc (the '1 kpc' or solar neighbourhood sample) are given in Appendix A.

[1]Interestingly, Hubble (1922) used the term 'giant planetary' to describe those PNe with a diameter greater than $2'$. He noted just six such objects!

9.2 Completeness

The solar neighbourhood sample includes 56 PNe with $D \leq 1.0$ kpc, and there are 210 PNe with $D \leq 2.0$ kpc (and 220 with $D\sec(b) \leq 2.0$ kpc). Note that statistically obvious incompleteness begins by ~600 pc (see Chapter 11). For the 1.0 kpc sample as a whole, an incompleteness factor of 27% has been estimated (i.e. there should be ~73 PNe in this volume, down to current sensitivity limits). This was estimated from the run of column density with distance, as shown later (see figure 11.2).

Figure 9.1 plots distibution of local PNe on the sky, in both galactic and equatorial coordinates. Note the increased density of PNe along the galactic plane (l = 210°to 30° and $|b| \leq$ 10°), south of the celestial equator owing to the MASH and MASH-II surveys. The search for new PNe in the northern galactic plane, in the area covered by IPHAS, is not yet complete. Note also the distribution of high-latitude ($|b| \geq 15°$) PNe above and below the Galactic plane; there should be approximately the same number either side of the plane. However the observed distribution hints that this is not the case, though at low statistical confidence, with 11 PNe north and 7 PNe south of the plane in the solar neighbourhood sample ($D \leq 1.0$ kpc). Interestingly, this difference still holds at 2.0 kpc, with 31 PNe north and 20 PNe south of the plane. In such a volume, the sample size is consdierably more ($n = 210$) and the problem of small number statistics should be mitigated. In fact, at such an intermediate distance, there should be more PNe *south* of the plane than the north (which is a manifestation of the Sun's position slightly *north* of the Galactic midplane (e.g. Cohen 1995; Humphreys & Larsen 1995; Chen et al. 2001; Joshi 2007, and references therein). In fact, the mean $|z|$ distance for the 2.0 kpc sample is +30 pc (i.e. north). This observation suggests that there are a number of nearby PNe that remain to be discovered south of the plane (probably in the zone $-30 < b < -10$), which falls outside the zone covered by the SHS and IPHAS surveys.

An attempt to discover such high latitude PNe using SHASSA and VTSS was described in Chapter 2, but only a couple of convincing candidates were found, the majority being probable HII regions around hot white dwarfs or subdwarfs. A number of high latitude enhancements from the WHAM VTSS (Reynolds et al. 2005) remain to be properly investigated, as do some faint emssion regions found in SDSS data (A. West 2008, pers. communication). Perhaps some of these may turn out to be bona fide PNe in the future. Deep narrowband wide-field imaging will be needed in part to address this problem (see §B.4).

The reasons for the apparent deficit are not entirely clear at present. Widespread diffuse emission is present south of the plane in the zone covered by SHASSA, south of the galactic equator. This includes large areas associated with the Gum nebula, which extends over 40° × 30°, and the Orion-Eridanus complex. Faint extended PNe would be lost against the background emission and therefore missed in the visual search of SHASSA images (see Chapter 2). Curiously, the north polar cap has higher extinction than the region centred on the south galactic pole (Schlegel, Finkbeiner & Davis 1998), but reddening seems to be higher closer to the plane in the south (Joshi 2005). This extinction may help to mask very faint, evolved PNe that might otherwise have been found to date.

Soker & Subag (2005) argue that spherical PNe are much less likely to be detected at distances of several kiloparsecs. By analogy with the detection statistics of faint spherical AGB haloes around PNe (Corradi et al. 2003) which are similar in structure and surface brightness to round PNe, they claimed that there is a significant population of undiscovered spherical PNe. Perhaps a number are awaiting discovery in a wide zone south of the galactic plane. A few examples of higher-latitude PNe have been recently found by Kronberger et al. (2006; see also Jacoby et al. 2007). Interestingly, many of these have spherical morphologies.

A number of PN impostors in the local sample are detailed elsewhere in this work. It is possible that one or two of these objects may be returned to the PN fraternity based on new or better data in the future. In addition, the bipolar PN-like nebula (Bode et al. 1987; Tweedy 1995a) around the old nova GK Persei ($d = 450 \pm 30$ pc; Slavin, O'Brien & Dunlop 1995) is another object that might be added to the local sample in the future. Another putative old PN may exist around the (V)LTP star CK Vul (Evans et al. 2002; van Hoof et al. 2006) at a distance of $\sim$550 pc (Shara, Moffat & Webbink 1985).

9.3 PN Properties

The following sections summarise the main nebular observable properties (such as positions, angular radii, morphologies, fluxes and reddenings), derived nebular properties (distances, ionized masses, absolute magnitudes, abundances etc.), and parameters of the central stars of the PNe within 2.0 kpc of the Sun.

9.3.1 Fundamental observables

PN coordinates are taken from Parker et al. (2006a) and Miszalski et al. (2007) for MASH and MASH-II objects. For the 'FP' objects, preliminary coordinates were determined directly from the digital SHS images (see Chapter 2) using the embedded WCS, as part of this study. More accurate coordinates were then obtained for the central stars using the NOMAD astrometric database accessible via VizieR at the CDS, and checked for consistency against the positions from Acker et al. (1992), Kimeswenger (2001), Kerber et al. (2003a) and Kohoutek & Kühl (2002) for those previously known PNe.

For many bright, previously known PNe, angular dimensions have been taken from Tylenda et al. (2003) and Ruffle et al. (2004). These works quote diameters at the 10% level of the peak surface brightness isophote, which is adopted throughout this work. Major and minor dimensions for most of the largest PNe have been determined here anew (from available digital broadband red or Hα + [N II] images using the Starlink GAIA package), at the same isophote level.

For a few optically thin, very high excitation objects *sensu stricto* (e.g. Kaler 1981b), dimensions have been similarly determined from broadband B_J SSS images (a proxy for [O III]) using GAIA. Geometric mean diameters and radii have been calculated for all objects investigated here. Note that the adopted dimensions are of the main PN shell (see figure 1.4), which

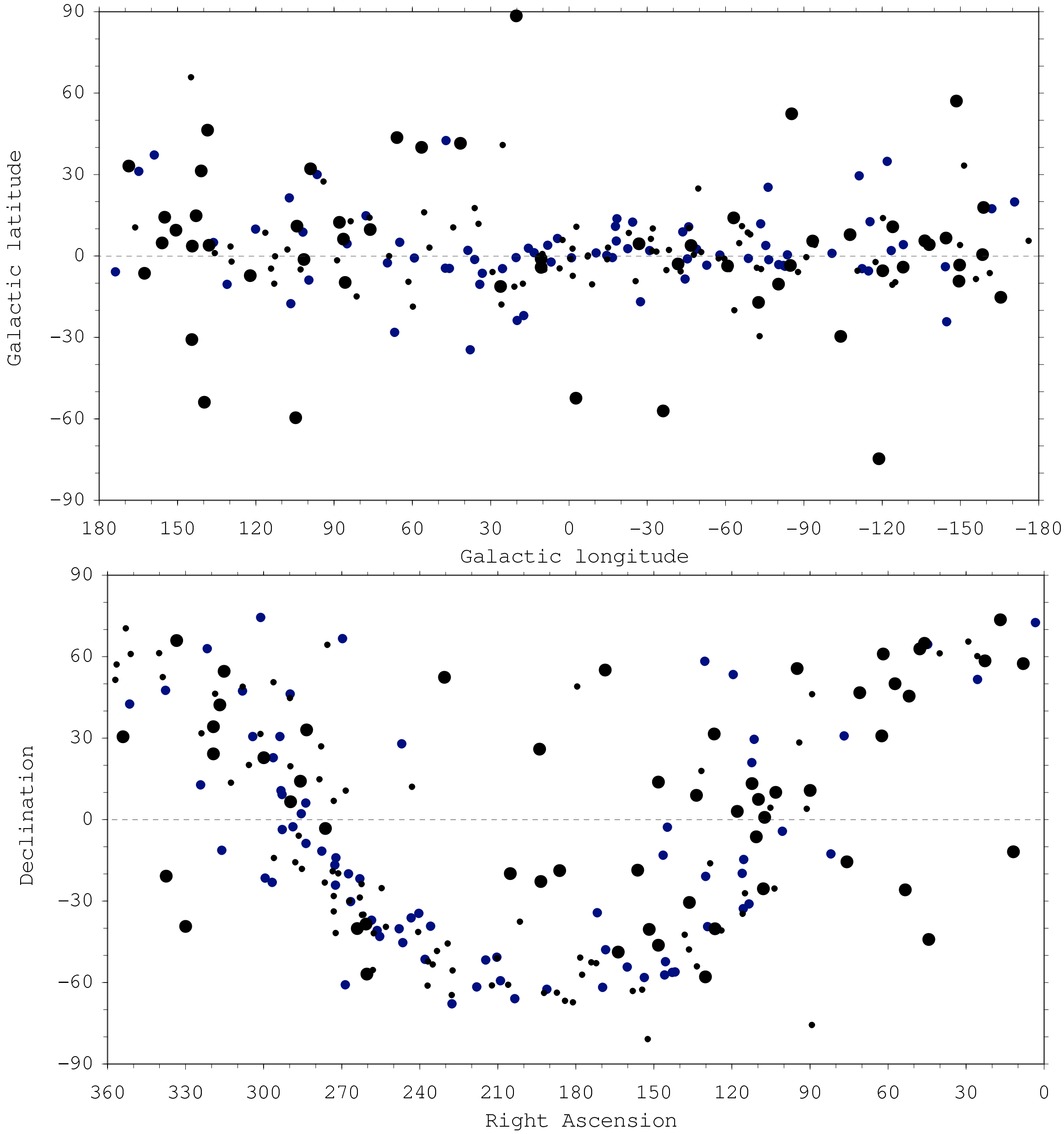

Figure 9.1: Plots showing the areal distribution of local PNe. Large dots represent PNe with D <1.0 kpc, medium dots represent PNe with D = 1.0—1.5 kpc, and small dots are PNe with D = 1.5—2.0 kpc. The top plot is in galactic coordinates and the bottom plot is in equatorial coordinates. Note that MASH and MASH-II have increased the number of PNe along the southern galactic plane within b = 10°, compared to the northern sky, but there is a deficit of nearby PNe south of the plane ($b < -20°$) in both hemispheres.

encloses the rim (or primary shock) if present, but *does not* include any faint outer halo(es) (e.g. Corradi et al. 2003).

The integrated Hα fluxes are mostly adopted from the tables in Chapter 3 (and references therein in a few cases). Integrated [O III] fluxes have been taken from Chapter 3 (and references therein), or, in those cases where no integrated fluxes are available, by bootstrapping to the integrated Hα fluxes using [O III]/Hα ratios obtained from other sources (e.g. Acker et al. 1992).

Hβ fluxes have been taken primarily from the compilation of Acker et al. (1991, and references therein) or determined from the Hα flux and an available Hα/Hβ ratio from the literature. In a few cases this is unknown, so a Hα/Hβ ratio is calculated from the reddening determined from the central star colours.

Apparent nebular magnitudes are also determined from the available flux data. The [O III] λ5007 nebular magnitude is derived following Jacoby (1989):

$$m_{5007} = -2.5 \log F(5007) - 13.74 \tag{9.1}$$

Following Méndez et al. (1993), the nebular Hβ magnitudes were similarly derived using:

$$m_{\beta} = -2.5 \log F(H\beta) - 13.74 \tag{9.2}$$

Finally nebular Hα magnitudes were calculated with the formula:

$$m_{\alpha} = -2.5 \log F(H\alpha) - 15.40 \tag{9.3}$$

equivalent to equation 3.6. This equation was confirmed using the data presented by Allen (1973).

Hα surface brightnesses have been calculated from the geometric radii and integrated Hα fluxes, expressed in units of $\mathrm{erg\,cm^{-2}\,s^{-1}\,sr^{-1}}$, using the formula:

$$S = \frac{F}{4\pi r^2} \tag{9.4}$$

To convert log values per steradian to log values per square arcsec, subtract the constant 10.629 dex. Quoted fluxes and surface brightnesses are reddening corrected.

New morphological classifications for every PN in the solar neighbourhood and extension samples follows the scheme adopted in Chapter 4 (see there for additional details). An estimate of the degree of any ISM interaction is also given, based on the recently published 'WZO' scheme of Wareing, Zijlstra & O'Brien (2007).

The logarithmic extinction constants, $c_{\mathrm{H}\beta}$, have been primarily taken from Cahn, Kaler & Stanghellini (1992), Tylenda et al. (1992) or individual papers from the literature where noted. The extinction constants are usually determined from the Balmer decrement, derived from optical spectroscopy, or by comparing the Hβ and radio fluxes. However, since these quantities were either unknown or unreliable for many of the faintest solar neighbourhood PNe, new extinction values are determined herein where applicable (see the appendix). New logarithmic extinctions for new MASH and MASH-II PNe have determined from the directly measured line fluxes, if available (see Chapter 5).

For PNe with adequate central star data, $E(B-V)$ values for the central stars have been calculated. Using published $UBVI$ photometry (see §9.4), the colour excess has been determined using the intrinsic values for an unreddened CSPN of $(B-V)_0 = -0.35$ and $(V-I)_0 = -0.40$ (Kaler 1983b; Bergeron, Wesemael & Beauchamp 1995; Ciardullo et al. 1999; cf. Harris et al. 2007). Note that the four bluest stars, including the Helix CS, in the list of photometric standards of Landolt & Uomoto (2007) have a mean $B-V = -0.348 \pm 0.012$, consistent with the adopted value.

The reddening $E(B-V)$ and the extinction constant, $c_{\mathrm{H}\beta}$ are related following the Howarth (1983) reddening law:

$$E(B-V) = 0.689\, c_{\mathrm{H}\beta} \tag{9.5}$$

9.3.2 Excitation Class

As discussed briefly in Chapter 1, the concept of the Excitation Class (EC) has been around for a long time. An early system was devised by Page (1942), which was modified by Aller (1956); this semi-quantitative system was in wide use for many years. Other schemes have been used by Feast (1968), Gurzadyan (1970, 1988), Webster (1975), Dopita & Meatheringham (1990), and Gurzadyan & Egikyan (1991).

The EC is often used as a direct proxy for the temperature of the CS (e.g. Gurzadyan & Egikyan 1991), but nebular excitation is also influenced nebular abundances, the stellar luminosity (manifested as the ionization parameter), and the optical depth of the PN. which is in turn influenced by the radius and density of the PN shell.

In this work, both the Dopita & Meatheringham (1990) and Gurzadyan & Egikyan (1991) schemes were considered. Both have weaknesses. The Dopita & Meatheringham approach uses a decimal excitation class, which has the benefit of treating the EC as a continuous variable.

The EC definition of Gurzadyan & Egikyan (1991) has two major problems. Firstly, the monotonic function relating EC to the stellar temperature is in serious error, as it ignores the effect of differing ionization parameters between nebulae. Secondly several workers have noted a lack of medium-excitation PNe using this definition (Gurzadyan & Egikyan 1991; Reid 2007; Kovacevic & Parker 2007). The distribution is a consequence of their definition of EC. Small changes in effective temperature lead to significant changes in the HeII λ4686 flux; in table 9.2, note the rapid increase (5 orders of magnitude) in the value of the integral G_4T as T_{eff} increases from 30,000 to 80,000 K. Hence the natural distribution is a large number of low- and high-excitation PNe with a dearth of medium excitation objects.

9.3.3 Distances

Distances have been taken from Chapter 7, if a calibrating PN, or derived here using the Hα SB-r relation for other objects. The mean relation is used, except for demonstrably high-

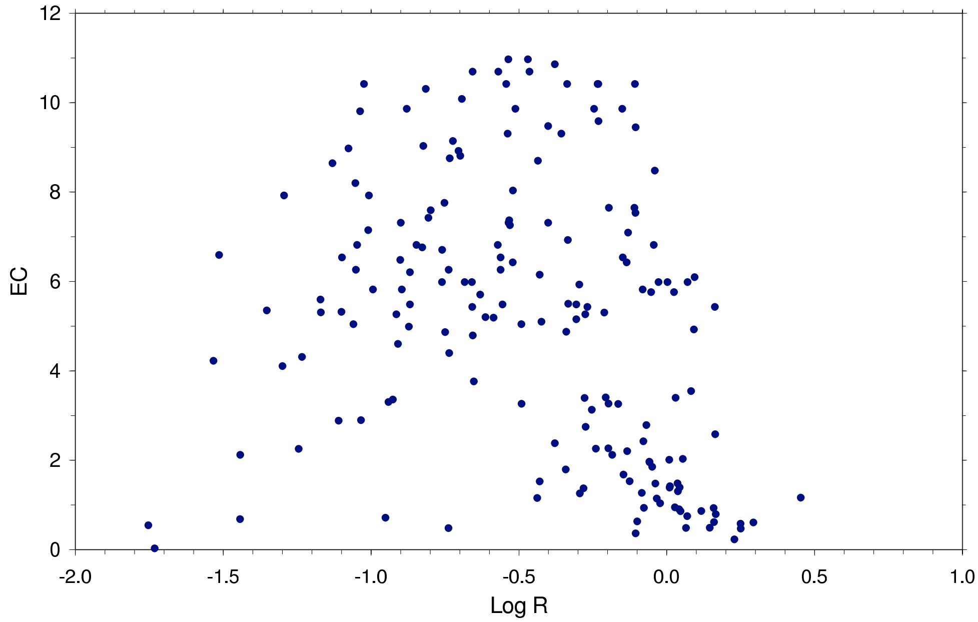

Figure 9.2: Excitation class of Dopita & Meatheringham (1990) plotted against log of the nebular radius.

excitation objects, following the criteria defined in Chapter 7, whereby a 'low' SB-r trend has been applied. This trend has also been used for the known close-binary PNe without primary distance determinations. Similarly, PNe of Type I, and/or with bipolar (or bipolar-core) morphologies have had distances determined using the 'high' SB-r trend (see Chapter 7 for further details).

For each PN in the local sample, the height from the plane z, and the projected distance q, were calculated from the respective formulae, $z = D \sin b$ and $q = D \cos b$, where D is the distance of the PN from the Sun and b is its Galactic latitude (all units in pc).

9.3.4 Ionized masses

Ionized masses are determined using the equation derived in §7.7 (see Hua & Kwok 1999), repeated here for convenience:

$$M_i = 0.035\, \epsilon^{1/2} \Theta^{3/2} D^{5/2} F_0(\mathrm{H}\alpha)^{1/2} \quad M_\odot \tag{9.6}$$

where $F_0(\mathrm{H}\alpha)$ is the reddening-corrected integrated nebular Hα flux in units of 10^{-12} erg cm^{-2} s^{-1}, Θ is in arcmin and D in kpc. The derived values of M_i (assuming a filling factor, $\epsilon = 0.4$) are given in Table 9.5. The geometric mean radius is always used. The greatest uncertainty is in the distance, but relative masses for a number of PNe with accurate distances should be reliable. Most ionized masses are less than 1 $M_\odot$, though there are some exceptions (e.g. Abell 74, Sh 2-216 and WDHS 1). However it is obvious that most large, highly-evolved, optically thick PNe have masses consistently higher than the canonical value of 0.2 $\mathrm{M}_\odot$, usually adopted in the literature (e.g. Ishida & Weinberger 1987). The subset of optically thin, high

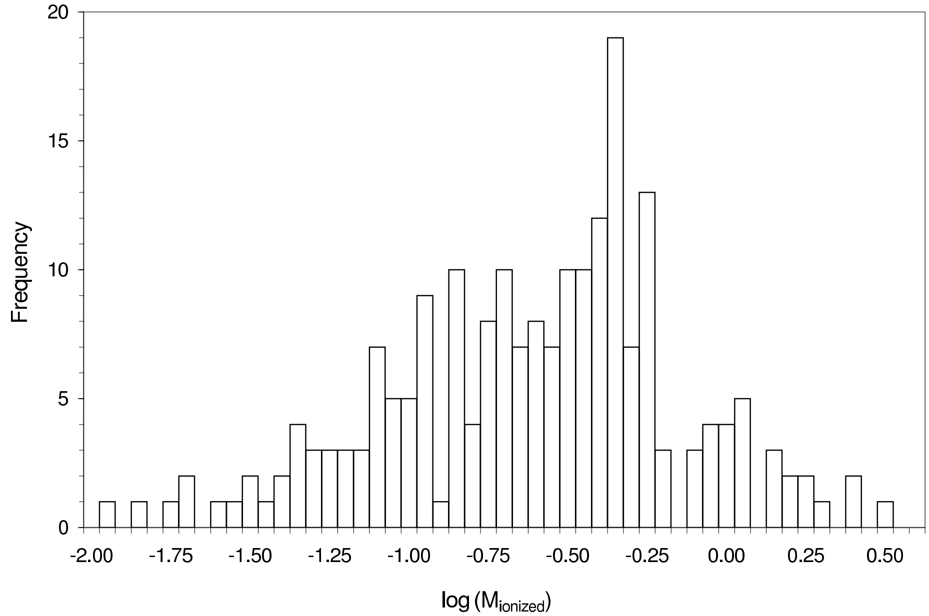

Figure 9.3: Frequency distribution of the ionized mass of PNe in the local volume. It is seen that the generally accepted average value of $\sim$0.2 M$_\odot$ is too low.

excitation PNe (e.g. Kaler 1981) have masses less than this value (see later). Figure 9.3 plots the distribution of ionized masses for all PNe within 2.0 kpc of the Sun. Ionized masses range from $\sim$0.01 – 3.0 M$_\odot$, and the modal value is $\sim$0.45 M$_\odot$.

As discussed in the preceding chapter, root-mean-squared electron densities for all PNe are derived from the ionized masses using equation 7.18. This approach has been taken, as most of the local PNe have densities too low to be determined from plasma diagnostics such as the [SII] λ6717/6731 ratio (this ratio is in the low density limit for these PNe).

9.3.5 Expansion Velocities

New data on a number of local PNe acquired with WHAM was discussed in Chapter 3. Most of the line profiles can be approximated by least-squares Gaussian fits. The expansion velocities were taken from table 3.8 for objects with WHAM data, or from the compilations of Weinberger (1989) and Acker et al. (1992), plus a few more recent papers in the literature (e.g. Goldman et al. 2004). If velocities were measured in more than one emission line, the adopted expansion velocities were taken as the mean of the Hα and [O III] λ5007 emission lines, as the majority of PNe have data in these lines. All the high excitation PNe *sensu stricto* have negligible or nil [N II] emission, so no expansion velocities in this line are available. Since expansion velocities are generally higher in the low-excitation lines (e.g. Hajian et al. 2007), to reduce possible systematic effects, [N II] expansion velocities were only utilised if no other data was available.

Hippelein & Weinberger (1990) found that the mean expansion velocity of the most hightly evolved nebulae was less than that of moderately evolved PNe. Furthermore they found that highly evolved PNe in the Galactic plane exhibit a smaller expansion velocity than those at large distances from the plane. This observation is confirmed here. Hippelein & Weinberger

(1990) suggested this might be caused by a reduction in the stellar wind from the CSPN, or by a population effect of the progenitors. They also considered a deceleration of the nebular gas by the ambient ISM, which seems to be the best mechanism to explain the low velocities seen in giant PNe like Sh 2-216. Furthermore, many PNe with higher than average expansion velocities are low-mass, optically thin, high excitation objects with relatively hot central stars still on the nuclear burning horizontal track in the HR diagram. The stellar winds of these stars are still significant and coupled with their slow evolution to high temperatures, enables efficient transfer of wind momentum to the PN shell, which may account for the high expansion velocities observed in this class of PNe (see also Gurzadyan & Egikyan 1991).

Phillips (2002c) also found evidence to indicate that there is a relationship between the mean expansion velocities of PNe and their morphological type. Phillips found that PNe with "bipolar rotating episodic jets" (BRETs) have the lowest velocities of expansion, with bipolar PNe, and elliptical and circular PNe having higher expansion velocities in the mean. In addition, he found that the distributions of circular, elliptical and bipolar sources were distinct, with bipolar PNe being biased towards lower expansion velocities, and circular PNe showing a greater range of velocities. It should be noted that bipolar PNe have very high expansion velocities in the polar direction (e.g. Dobrinčić et al. 2006), while the brighter sections of the nebulae (corresponding to equatorial toroids) have velocities of only $\sim$18 km s^{-1} on average (Phillips 2002c).

9.3.6 Nebular abundances

At the start of this dissertation it was hoped to gain accurate nebular abundances for the majority of PNe in the solar neighbourhood (within 1.0 kpc). However, the question of nebular abundances for the most evolved PNe in this volume is a problem for the future. The very low surface brightnesses ($\sim$10^6 times lower than for a young bright PN) requires deep integral field spectroscopy to obtain the essential plasma diagnostics. A few of the local nebulae have approximate abundances taken from Chapter 5, while available literature data is used to supplement the local sample. In this work, discussion is largely restricted to relative N/O ratios, and the proportion of Type I nebulae in the local volume.

In Frew, Parker & Russeil (2006), two nearby Type I bipolar PNe, RCW 24 and RCW 69 were investigated. These form an important addition to the small sample of evolved bipolar PNe within 1.5 kpc, showing that before the advent of MASH, the census of local Type I PNe was still incomplete. The new evolved Type I PNe identified from the MASH survey are especially important in the context that only one of Peimbert's (1978) original sample of relatively nearby PNe was a highly-evolved object (VV 47 = JnEr 1). Indeed, using the restricted definition of Kingsburgh & Barlow (1994), this is not a Type I object after all (see Bohigas 2001). It is important to note that morphology is not an exact proxy for chemistry (specifically the N/O ratio), and that not all bipolar PNe are classed as Type I (following Kingsburgh & Barlow 1994) and vice-versa, though overlap is strong.

Any attempt to estimate the true proportion of Type I PNe firstly needs a complete volume-limited sample, which will be dominated by evolved, hard-to-detect examples. A previous estimate for the fraction of Type I objects (using essentially a flux-limited sample) was given by Kingsburgh & Barlow (1994), who found a proportion of 21%. More recently, Perinotto, Morbidelli & Scatarzi (2004) compiled high-quality data for 131 PNe. Excluding the halo PN BoBn 1, some 16 PNe (12%) are Type I following the Kingsburgh & Barlow (1994) definition.

Within a volume of radius 1.0 kpc, there are ∼56 objects. However, only 3 or 4 objects are definite Type I PNe following Kingsburgh & Barlow (1994). These are Abell 21, Abell 24 and RCW 24. The extremely evolved object WDHS 1 is also a probable Type I PN, based on MSSSO spectra obtained by us, though poor flux calibration at the blue end means more data is required for a definitive answer. Revised distances to Abell 29, Abell 71, M 1-41, plus NGC 6302 (Meaburn et al. 2007) place these objects outside the solar neighbourhood volume, *sensu stricto* (cf. Frew, Parker & Russeil 2006). Seven more PNe: NGC 7293, M 27 (NGC 6853), M 57 (NGC 6720), NGC 2346, NGC 6781, Sh 2-188, and JnEr 1, have been classified as Type I nebulae by various workers in the past (e.g. Rosado & Kwitter 1982; Bohigas 2001, 2003; Perinotto, Morbidelli & Scatarzi 2004), but these all have N/O ratios below the cutoff of Kingsburgh & Barlow (1994).

Based on the number of number of nearby Type I PNe, it is concluded that only ∼6% of the local 1.0 kpc sample have Type I chemistries. Further work to refine this estimate is ongoing based on the larger though less complete '2 kpc' extension sample, which provides better numbers. A preliminary estimate is ∼11% (24/210), which is lower than the estimates derived from flux-limited samples. This estimate can be compared with the prediction of the population synthesis model of Moe & De Marco (2006a). These authors find that 6% ± 4% of PNe should be of Type I, following the Kingsburgh & Barlow (1994) definition. Allowing for the fact that most of the undiscovered PNe in the local volume are probably *not* Type I PNe, the Type I fraction found here is in agreement with the prediction from Moe & De Marco (2006a). Their model prediction assumed that a $4\,M_{\odot}$ progenitor star is needed to initiate hot bottom conversion of carbon to nitrogen (Becker & Iben 1980). Note that abundance data for other elements is too incomplete to warrant a similar discussion.

9.4 Central Stars

9.4.1 Identification

Of the 210 PNe within 2.0 kpc, 90% of PNe have identified central stars[2], but the fraction of these stars with spectral types is only 47% (see table 9.6). Central stars are known for all of the previously known solar neighbourhood PNe ($\leq$ 1.0 kpc) though Sh 2-200 has an uncertain identifcation; the most likely candidate is listed in table 9.6.

For all MASH PNe with a geometric mean diameter $>2'$, available digital Hα, SR, R_F, and B_J images were manually blinked in GAIA to try to identify any possible CSPN candidates within the photometric limits of each bandpass, for photometric follow-up. The coordinates are

[2]Most of the missing CS are in more distant, reddened PNe, though high internal extinction can also hide the CS (e.g. NGC 6302; Matsuura et al. 2005). This fraction can be compared with the fraction of CS detected with HST, 2/3, in a flux-limited sample of bright PNe in the Magellanic Clouds (Villaver, Stanghellini & Shaw 2003, 2004, 2007).

Table 9.1: $UBVRI_c$ photometry obtained at MSSSO for 11 central stars.

Name	Date	V	$U-B$	$B-V$	$V-R$	$R-I$	n
Abell 31	12/04/05	15.56	−1.20	−0.31	...	...	2
Abell 36	12/04/05	11.54	−1.22	−0.34	−0.14	−0.18	2
FP0905-3033	12/04/05	16.49	−1.25	−0.30	...	...	2
FP1824-0319	10/04/05	14.92	−1.18	−0.28	...	...	2
Fr 2-8	13/04/05	17.5:	...	...	...	...	1
PFP 1	12/04/05	15.78	−1.10	−0.35	...	...	2
PHR 0723+0036	13/04/05	13.88	−1.04	0.04	...	...	1
PHR 0905-4753	13/04/05	12.54	0.42	1.12	0.66	0.70	2
PHR 1424-5138	13/04/05	12.98	−1.02	0.06	0.11	0.14	4
PHR 1510-6754	09/04/05	15.2:	...	...	...	...	2
RCW 69	10/04/05	18.6:	−1.0:	0.2:	...	...	1

based on standard IAM data (Hambly et al. 2001) of the UKST broad-band B_J and R plates, and are tabulated in Table 9.6.

9.4.2 Central star photometry

For previously known PNe, there are numerous papers containing data on CSPN magnitudes in the literature. For the ∼210 PNe in the local volume, as well as other PNe at greater distances, magnitude data was compiled from the literature into a working database. Optical magnitudes were obtained from a large range of references described in Appendix C. In addition, relevant JHK_s data from the 2MASS Catalogue (Cutri et al. 2003) and IJK data from the DENIS Survey (DENIS Consortium, 2005) were compiled, if available. Care was taken to ensure the quoted near-IR magnitudes referred to the CSPN and not the integrated light from the nebula (e.g. Ramos-Larios & Phillips 2005).

In addition, $UBVRI$ photometry of several PN central star candidates (primarily aimed at MASH PNe) was obtained with the Direct Imager on the MSSSO 40-inch telescope on two runs in December 2004 and April 2005. Unfortunately, the Dec 2004 run was almost entirely clouded out, and several nights on the other run were non-photometric, so the total number of stars with new photometry is much less than first envisaged. For these runs, standard Bessell $UBVR_cI_c$ filters were used in conjunction with a thinned Tek 2048× 2048 CCD (24μm pixels) at the f/8 focus, giving an image scale of 0.5″/pixel. The field of view is approximately 21′ square. Seeing was generally poor throughout (>2″) so 2×2 binning was used, which also reduced readout time, and increased data throughput. Standard extinction coefficients were applied, and a range of standard stars from Landolt (1992) and Kilkenny et al. (1998) were measured to determine the colour equations used to convert from instrumental magnitudes. Table 9.1 gives the magnitudes and colours for 11 PN central stars. Owing to the generally poor observing conditions, the photometric errors are typically ±0.05 mag in each band (derived from repeat observations) and ±0.07 mag in the colour indices. Values marked with a colon have uncertainties of ±0.2 mag.

To supplement these measures, photometry based on standard image parameterisation (IAM) of SuperCOSMOS scanned data (Hambly et al. 2001) of the UKST broad-band B_J

and R plates was also included in the working database, as well as a search for complimentary data from the other scanned surveys available through VizieR on the worldwide web. Note that the photometric accuracy of the SuperCOSMOS data is limited to ± 0.15 mag (Hambly et al. 2001b), but this can be considerably larger close to the galactic plane due to image crowding and nebular contamination.

The various data were then combined to generate the best possible estimate of the CSPN magnitude in each waveband (see Appendix C). To do this, each individual magnitude estimate was vetted for quality (and sometimes omitted), before weighted mean $UBVRIJHK_s$ magnitudes were generated using only the most reliable estimates. The mean values are given in table C.1 in the appendix. The V magnitudes are also included in table 9.6. Using the adopted extinction of the PN shell (and/or the CSPN from $UBVI$ colours if available) from table 9.5, reddening-corrected optical and near-IR colour indices are also generated, summarised in table C.1. These data are then compared with the canonical colours of single hot stars (see Appendix C) to infer the presence of any unresolved late-type companions (see the discussion in §9.5.1)

In combination with the new integrated Hα fluxes taken from Chapter 3, the weighted V magnitudes from table 9.6 were utilised in the generation of Zanstra temperatures for all CSPN with adequate data in the solar neighbourhood. These are discussed further below.

9.4.3 Absolute magnitudes

For all PNe in the solar neighbourhood, CSPN absolute magnitudes were determined using the adopted distance, apparent V magnitude, and extinction from table 9.5. Absolute magnitudes are calculated via the standard distance modulus formula:

$$M_V = 5 \log D - 5 - V_0 \tag{9.7}$$

where V_0 is the reddening-corrected visual magnitude. The CSPN in the local volume span a wide range of absolute magnitudes. This effect is also seen in the calibrating sample for the SB-r relation (figures 9.4, 9.5 and 9.6). The observed scarcity of absolute magnitudes between $\mathrm{M}_V = +4.5$ and $+5.5$, is attributed to the rapid evolution of the stars as they begin their descent of the WD cooling track, an effect first seen clearly in figure 2 of Schönberner (1981). Note that the subset of bipolar PNe seem to have fainter stars in relatively compact PNe (figure 9.4), attributed to the faster stellar evolution of these higher-mass CS.[3] In figures 9.5 and 9.6, the domain of high-excitation and post-CE PNe is especially clear, where optically-luminous (slowly-evolving) CS are present inside evolved, faint, optically-thin PNe.

For the most evolved objects (with CS on the WD cooling track; $\mathrm{M}_V \geq 5.5$), the mean absolute magnitude is $\mathrm{M}_V = 7.0 \pm 0.3$, which is found to be consistent with Phillips (2005a) who found an average absolute magnitude of $\mathrm{M}_V = 7.05 \pm 0.26$ for a number of evolved CSPN of low radio surface brightness (log T_B between -0.5 and -4.0). Another set of independently

[3]This agrees with the finding that the fraction of detected CS in bipolar PNe in a flux-limited sample of LMC PNe was somewhat worse, compared to other morphological classes (Villaver, Stanghellini & Shaw 2003, 2004, 2007).

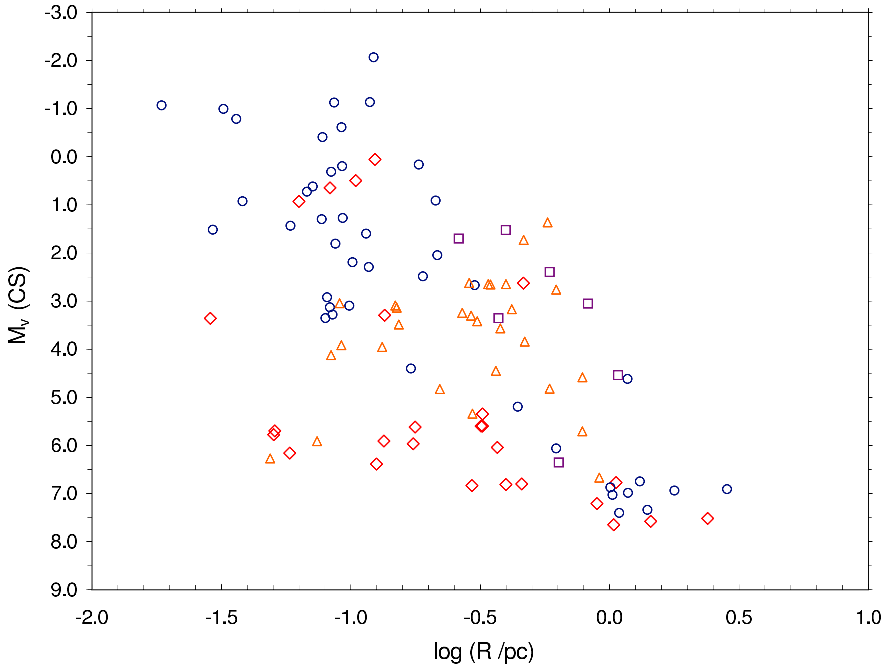

Figure 9.4: Plot of CS absolute magnitude against log radius of the PN for the sample of 122 calibrating PNe. Orange triangles plot high-excitation PNe *sensu stricto*, purple squres plot post-CE PNe, red diamonds plot bipolar PNe, and blue circles represent other objects. There is a large scatter present, but a broad trend showing the fading of the CS with PN expansion is seen. A subset of the bipolar PNe have faint stars in relatively compact PNe, attributed to the faster stellar evolution of these high-mass CS.

determined absolute magnitudes is given in Harris et al. (2007). These authors find a mean of M_V = 7.07 for eleven faint PN central stars in the same brightness temperature range as the Phillips sample. However, after omitting the ionizing stars of nebulae no longer considered to be PNe (see below), and using updated CS magnitudes as well as a slightly different prescription for reddening, I derive a mean magnitude of $M_V = 6.94 \pm 0.52$ for ten stars from the Harris sample, consistent with the value of Phillips (2005a) though with a higher dispersion.

9.4.4 Temperatures

Several methods are in use to determine the temperatures of the ionizing stars of PNe. The classical Zanstra method (Zanstra 1928, 1931) requires an integrated nebular flux in a Balmer Line (usually Hβ) and a B or V magnitude for the central star, assuming the nebula is optically thick in the Lyman continuum. A helium Zanstra temperature can also be calculated given the integrated flux in the HeII λ4686 line. Numerous determinations of Zanstra temperatures have been published in the literature (e.g. Harman & Seaton 1966; Pottasch 1981, 1984; Kaler 1983b; Gleizes, Acker & Stenholm 1989; Tylenda et al. 1994; Galli et al. 1997; Phillips 2004a.)

In addition, crossover (Ambartsumyan) temperatures (Kaler & Jacoby 1989) can be determined for optically thick PNe. This method calculates a temperature (and CSPN magnitude) by forcing agreement between the H and He Zanstra temperatures, and necessarily assumes that the nebula is optically thick. In addition, direct determinations of the CSPN tempera-

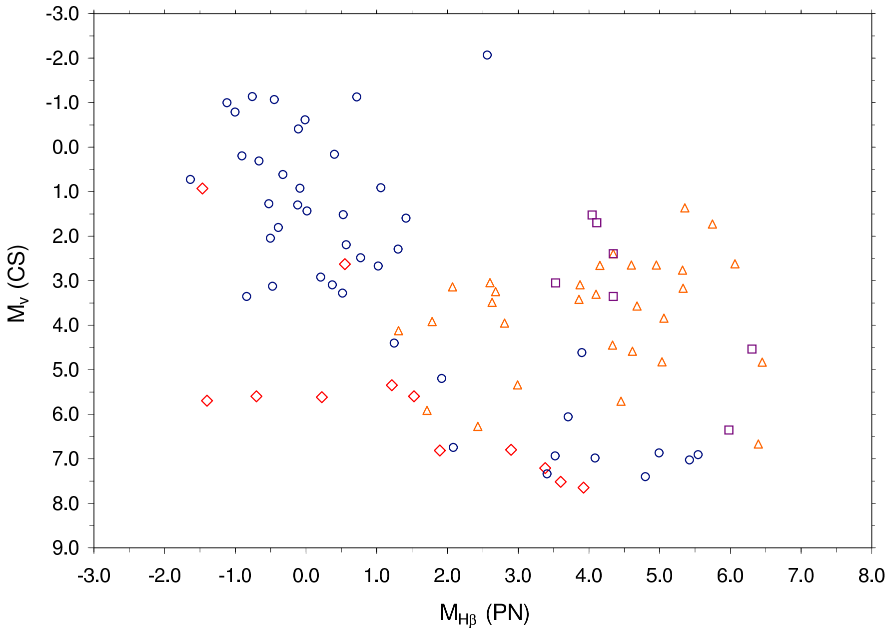

Figure 9.5: Plot of CS absolute magnitude against PN absolute Hβ magnitude for the sample of 122 calibrating PNe. Symbols are the same as for figure 9.4. The domain of high-excitation and post-CE PNe is especially clear in this plot, where optically-luminous (slowly-evolving) CS are present inside evolved, faint, optically-thin PNe.

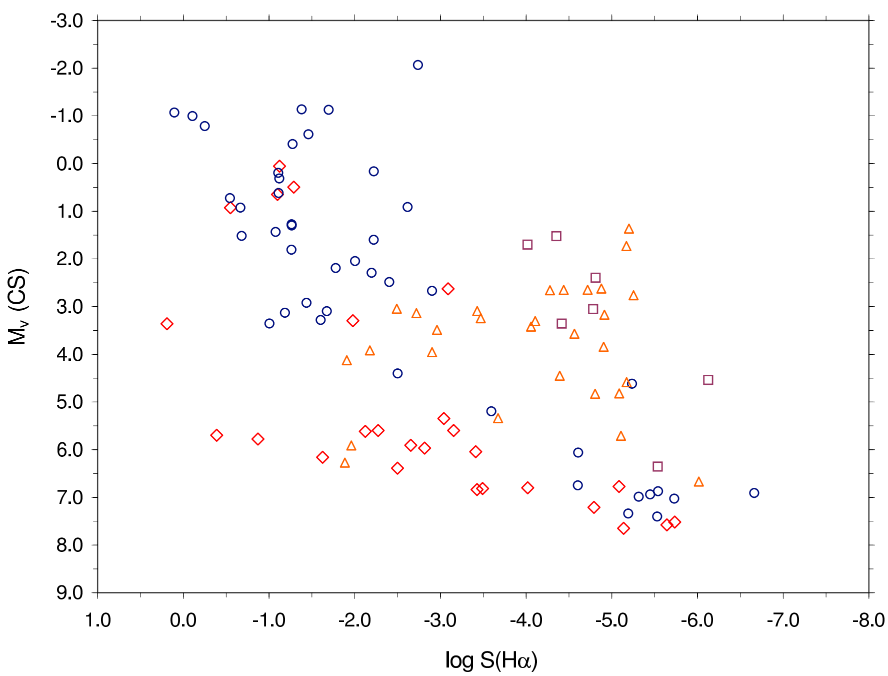

Figure 9.6: Plot of CS absolute magnitude against PN Hα surface brightness for the sample of 122 calibrating PNe. Symbols are the same as for figure 9.4. The split into the various subsets is quite similar to figure 9.5.

Table 9.2: Numerical value of the integral used for the calculation of Zanstra temperatures.

10^{-4} T	$G_1 T$	G_4T
2.0	2.987×10^{-2}	...
2.5	9.864×10^{-2}	...
3.0	2.088×10^{-1}	3.508×10^{-7}
4	4.956×10^{-1}	3.931×10^{-5}
5	7.902×10^{-1}	6.106×10^{-4}
6	1.048	3.591×10^{-3}
8	1.434	2.987×10^{-2}
10	1.688	9.864×10^{-2}
12	1.857	2.088×10^{-1}
15	2.019	4.202×10^{-1}
20	2.166	7.902×10^{-1}
25	2.243	1.106
30	2.288	1.353
40	2.336	1.688

tures are available from model atmosphere analyses, and are adopted from the literature (see section 6.4.6).

Zanstra Temperatures

The physics behind this approach is well understood. By using the nebular flux in a Balmer line or a Pickering-series line of ionized helium to count UV photons, and comparing this with the optical flux, a temperature for the ionizing star is determined. H and He Zanstra temperatures were determined following the recipe of Pottasch (1984), and are denoted T_z(H) and T_z(He). A black-body spectrum is also assumed for the CS, following Pottasch (1984), and which does not seem to introduce large errors to the method. See this reference for full details of the procedure.

The first step is to calculate an expression for the visual flux, F_λ(vis) which can be found from the visual magnitude (corrected for reddening), V_0, according to the following expression:

$$F_\lambda(\mathrm{vis}) = 3.68 \times 10^{-9} \times 10^{-0.4V_0} \tag{9.8}$$

The hydrogen Zanstra temperature, T_z(H), is given by the solution to the following equation:

$$\frac{F(\mathrm{H}\beta)}{F_\lambda(\mathrm{vis})} = 3.95 \times 10^{-11} T^3 G_1(T)(e^{26650/T} - 1) \tag{9.9}$$

where G_1(T) is an integral which can be used to count photons shortward of the hydrogen ionization limit, at 912Å. Similarly the helium Zanstra temperature, T_z(He), is given from the solution to the following equation:

$$\frac{F(\lambda4686)}{F_\lambda(\mathrm{vis})} = 8.49 \times 10^{-11} T^3 G_4(T)(e^{26650/T} - 1) \tag{9.10}$$

where G_4(T) is an integral which applies in this case to the He^+ ionization limit at 228Å. The numerical values of the integrals $G_1(T)$ and $G_4(T)$ are given by Harman & Seaton (1966) and Pottasch (1984), and are given here for convenience in table 9.2.

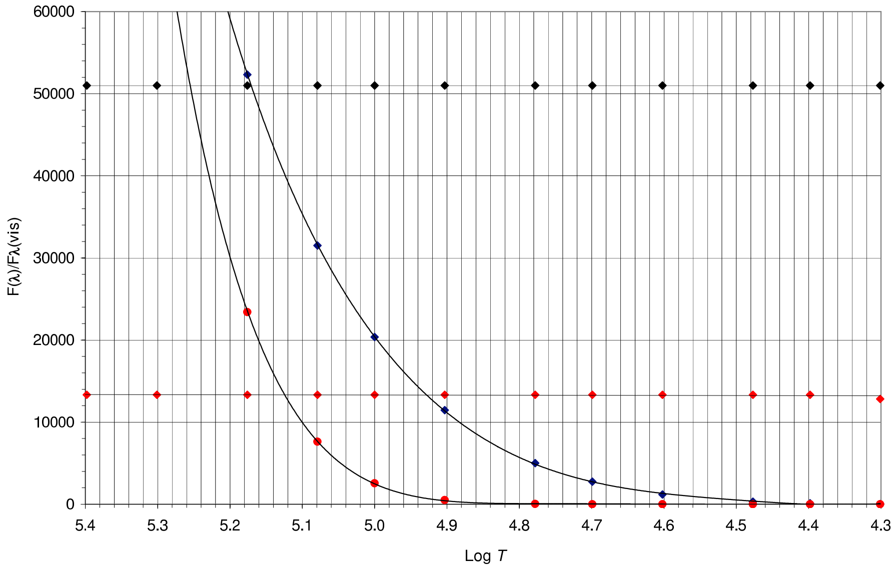

Figure 9.7: Determination of Zanstra temperatures for the large Type I PN, Abell 21. The blue dots fitted with a high-order polynomial represent the function F(Hβ)/F$_\lambda$(vis), while the red dots represent the function F(λ4686)/F$_\lambda$(vis). The temperatures are found from the intersection of these functions with the horizontal lines which represent the fluxes F(Hβ) and F(λ4686) respectively. Temperatures increase to the left, in the convention of the HR diagram.

As an example, the recipe is applied to the Type I PN, Abell 21, adopting the integrated Hα flux, reddening and CS magnitude from tables 9.4 and 9.6. The integrated HeII flux was determined from the data of Kaler (1983b). The resulting temperatures are $\log T_z(\mathrm{H}) = 5.170$ and $\log T_z(\mathrm{He}) = 5.125$, corresponding to temperatures of 148 ± 6 kK and 133 ± 6 kK respectively (see figure 9.7). Errors in the magnitudes and fluxes are propagated through the procedure to estimate errors in the derived Zanstra temperatures. For other nebulae, HeII fluxes are taken from the compilation of Tylenda et al. (1994).

Crossover Temperatures

For a few optically thick PNe without reliable *integrated* photometry or CS magnitudes, crossover (Ambartsumyan) temperatures (Kaler & Jacoby 1989) are determined using equation (1) of Kaler & Jacoby (1989):

$$\log T = 4.905 + 1.1116 \times 10^{-2} I(4686) - 1.1069 \times 10^{-4} I^2(4686) + 6.2057 \times 10^{-7} I^3(4686) \quad (9.11)$$

This method assumes optical thickness to both H and He$^+$ Lyman continua (and is generally applicable to massive bipolars with Type I chemistries). Criteria for optical thickness are discussed by Kaler (1983b) and Kaler & Jacoby (1989). Here I adopt optically thick PNe to have $F(\lambda 6584)/\mathrm{H}\alpha \geq 1.0$ and/or $F(\lambda 3727)/\mathrm{H}\beta \geq 1.0$.

A visual magnitude can also be predicted from the He II flux, again assuming optical thickness, and is given by the equation:

$$V_0 = -86.74 + 24.402\log T - 1.8242\log T^2 - 2.5\log I(\mathrm{H}\beta) \tag{9.12}$$

The predicted magnitude is good to about ±0.15 mag and can be used as a validation of the method for those PNe with independndent photometry of the CS (Kaler & Jacoby 1989; Jacoby & Kaler 1989). Alternatively, equation 9.12 can be used to estimate the luminosity of the central star, if a direct magnitude determination is unavailable (see §6.4.10).

9.4.5 Luminosities

By applying representative bolometric corrections, absolute bolometric magnitudes were estimated for each CSPN with reddening-corrected absolute magnitude and temperature data. The adopted bolometric correction was found from the following expression (Vacca, Garmany & Shull 1996) which is a consensus value for hot stars in the literature:

$$\mathrm{BC} = 27.66 - 6.84\log T_{\mathrm{eff}} \tag{9.13}$$

Absolute bolometric magnitudes were then converted to solar luminosities assuming $M_{\mathrm{Bol}} = +4.74$ for the Sun (Cox 2000; cf. Buzzoni 1989). The adopted luminosity values are tabulated in table 9.6.

The distribution of the central stars in $\log \mathrm{L} - \log \mathrm{T}$ space (figure 9.8) can be compared with predictions from stellar evolution theory (e.g. Shaw 1989; Méndez & Soffner 1997). There are some quantitative differences, such as the exact distribution on the nuclear-burning sections of the evolutionary tracks (specifically, there are fewer lower-luminosity CS than predicted), but this can be put down to relatively small numbers of bright PNe in the local volume, combined with uncertainties in the distances, and hence luminosities. Being based on a volume-limited sample, the plot is dominated by the intrinsically common, highly-evolved central stars, bunched at low luminosities. Figure 9.9 shows the frequency distribution of central star luminosities for PNe shown in Figure 9.8. The minimum in numbers at a luminosity near $10^3 L_\odot$ is due to rapid evolution as the stars first descend the WD cooling track (Schönberner 1981).

9.4.6 Masses

By interpolating between a set of standard post-AGB hydrogen burning evolutionary tracks on the theoretical HR diagram (Schönberner 1983, 1989; Blöcker 1995), the mass for each central star is estimated (see figure 9.8). This approach has been taken both in the Galaxy (e.g. Schönberner 1981, 1984; Kaler 1983b; Shaw & Kaler 1989; Kaler Shaw & Kwitter 1990; Cazetta & Maciel 1994) in the Magellanic Clouds (e.g. Villaver, Stanghellini & Shaw 2003, 2004, 2007), and in M 31 (Jacoby & Ciardullo 1999).

The derived values for the CS masses are tabulated in table 9.6. However, in many cases, the errors on both the temperatures and luminosities of these central stars are substantial, so the derived masses are uncertain. Furthermore, at low luminosites (evolved CSPN) the evolutionary tracks are fairly crowded. Nonetheless, useful statistical information can be recovered from the

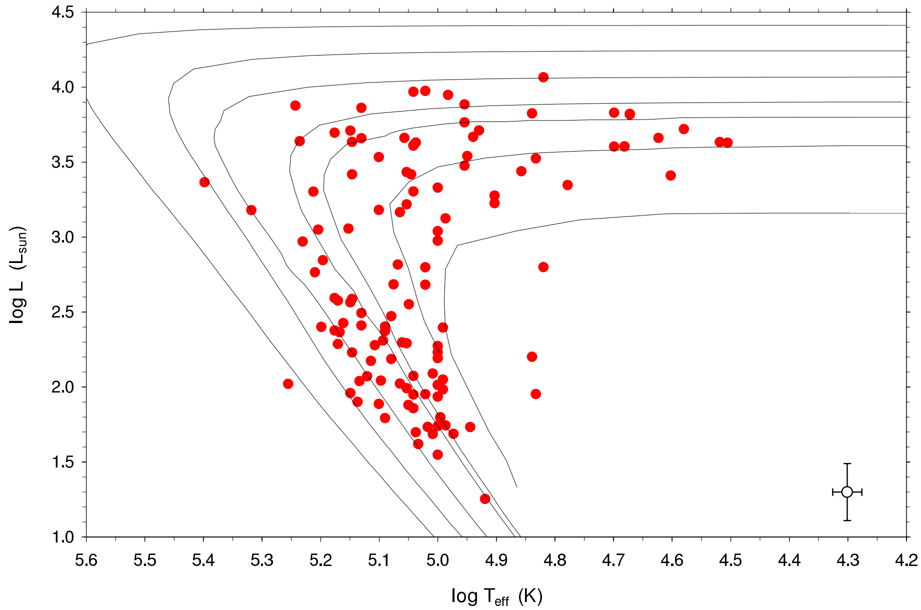

Figure 9.8: Luminosity versus $T_{\rm eff}$ diagram for the volume-limited ensemble of ∼125 PNe closer than 2.0 kpc with requisite data. Those PNe with only lower limits for the temperature (and luminosity) are omitted for clarity. A point showing representative error bars is plotted at lower right. Standard post-AGB evolutionary tracks are also plotted. With respect to the horizontal sections of the evolutionary tracks, from top to bottom, they are the 0.940, 0.836, 0.696, 0.625 and 0.605 $M_\odot$ tracks from Blöcker (1995), and the 0.565 and 0.546 $M_\odot$ tracks from Schönberner (1983). Note that the masses of He-burners are estimated using H-burning tracks, an approach deemed acceptable for a statistical study. The plot suggests that observable PN central stars are largely more massive than 0.55 $M_\odot$. The three stars less massive than this limit may either result from common-envelope evolution or are not true PNe.

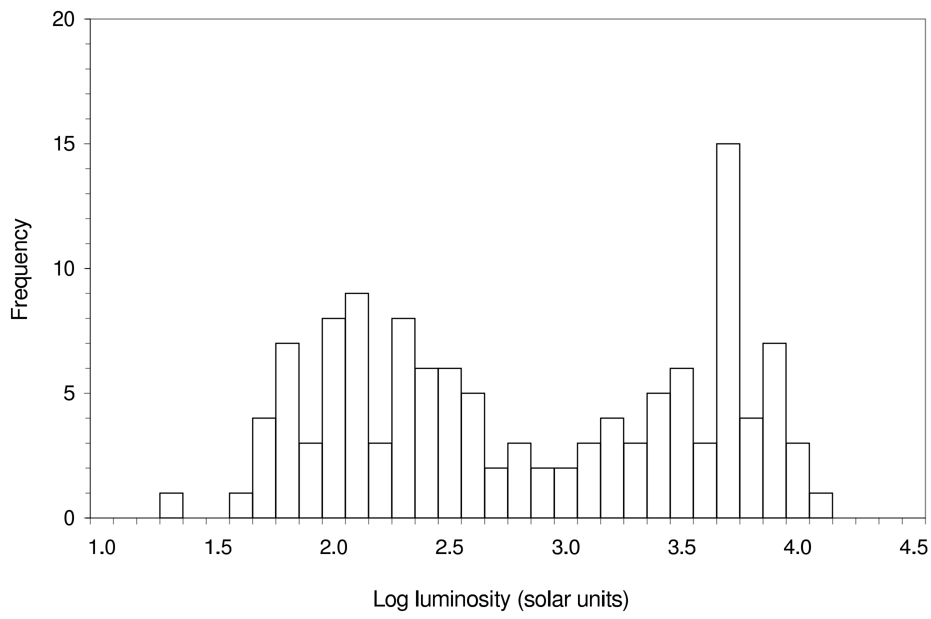

Figure 9.9: Frequency distribution of central star luminosities for PNe plotted in Figure 9.8. The minimum in numbers at a luminosity near $10^3 L_\odot$ is due to rapid evolution, as the stars first descend the WD cooling track.

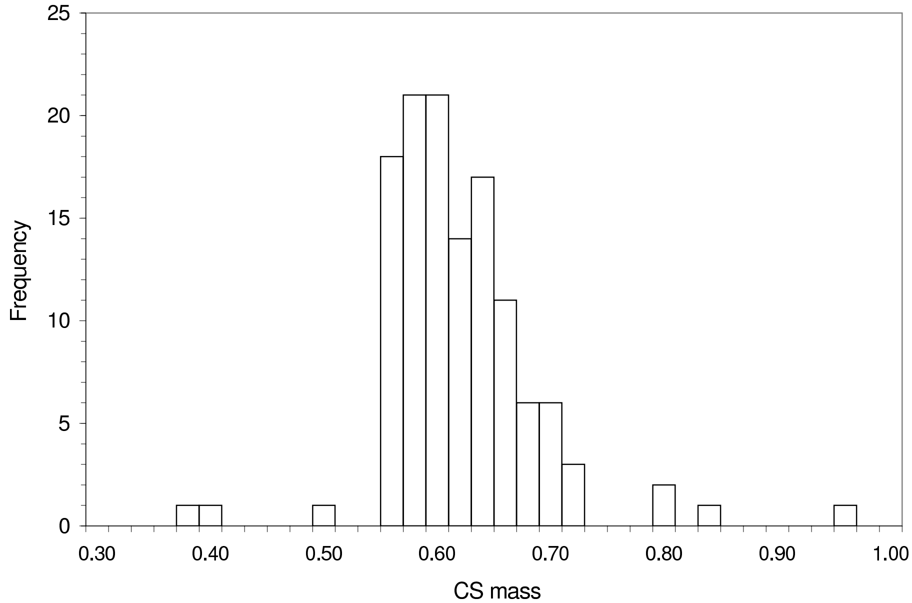

Figure 9.10: Frequency distribution of central star masses in the local volume, plotted in Figure 9.8. The mean mass (in solar masses) of the entire sample of CS is 0.61 ± 0.07 $M_\odot$. Almost all PN central stars are more massive than 0.55 $M_\odot$, which suggests this is the limit below which PNe become 'lazy'. The stars less massive than this limit may either result from common-envelope evolution or are not true PNe. Note the tail to higher masses. The CS at ∼0.95 $M_\odot$ is Abell 45, though this mass estimate is quite uncertain; this object deserves further study.

local sample using this approach, noting that more accurate values will follow from a better determination of the stellar temperatures and luminosities.

The mean mass of the entire sample of CS is 0.614 ± 0.066 $M_\odot$ in excellent agreement with the recent determination of by Gesicki & Zijlstra (2007), who find a mass distribution that is sharply peaked at 0.61 $M_\odot$ (see also Gesicki & Zijlstra 2000; Gesicki, Acker & Zijlstra 2003; Gesicki et al. 2006). The distribution of CS masses is shown in Figure 9.10, which is in good agreement with recent observational studies (e.g. Gesicki & Zijlstra 2007, and references therein) and theoretical work (e.g. Méndez et al. 2008).

Note that the canonical mean mass for hot white dwarfs of ∼0.56–0.60 $M_\odot$ (Finley, Koester & Basri 1997; Vennes et al. 1997; Madej, Należyty & Althaus 2004; Liebert, Bergeron & Holberg 2005; Kepler et al. 2007)[4], is somewhat lower, suggesting that CSPN with lower masses ($<\sim$0.55$M_\odot$) may not produce visible PNe; this fact is suggested by the distribution of points plotted in Figures 9.8, 9.10 and 9.11. This point will be further discussed in Chapter 11.

9.5 PN Statistics

Most prior statistical studies have used flux-limited samples of galactic PNe (e.g. Manchado et al. 1996). However, the volume-limited local sample of PNe defined here has much better potential to better answer some of the remaining unsolved questions of PN research. For

[4]The mean mass of the local sample within 20 pc of the Sun is higher, 0.665 $M_\odot$ (Holberg et al. 2008), dominated by older, cooler WDs.

Table 9.3: Statistical summary of PN properties in the solar neighbourhood and extension samples. All numbers are percentages, except for the numbers of close binary CS (marked with an asterisk).

Property	<1.0 kpc sample $n = 55$	$1.0 - 2.0$ kpc sample $n = 155$	<2.0 kpc sample $n = 210$
Morphology			
Bipolar	11	14	13
Elliptical	64	66	65
Round	13	17	16
Asymmetric	13	3	5
Irregular	0	1	1
ISM Interaction	69	50	55
Chemistry			
Type I	6	15	12
non-Type I	94	85	88
$< M_{\rm ion} >$	$0.53 \pm 0.61\ M_\odot$	$0.32 \pm 0.33\ M_\odot$	$0.37 \pm 0.43\ M_\odot$
Central stars			
$< M_* >$	$0.623 \pm 0.070\ M_\odot$	$0.610 \pm 0.063\ M_\odot$	$0.614 \pm 0.066\ M_\odot$
H-rich	20	37	30
H-deficient	80	63	70
Close binaries*	5	2	7
Inferred binarity fraction	52–58	...	...

example, what are the intrinsic proportions of the different morphological and compositional subtypes, and what is the exact lower-mass bound for *single* progenitors to produce visible PNe? Importantly, a volume-limited sample is a valuable tool to help answer the very important question of whether binarity is an essential ingredient in the recipe of PN formation and shaping.

Having defined a volume-limited sample of PNe in the previous sections, it can now be put to use to see the relationships between CS mass, scale height and shell mass. Similarly the sample can be used to investigate the true proportion of Type I PNe, the proportion of PNe with binary central stars, as well as investigate other characteristics such as the prevalance of ISM interactions, and the relations between these differing parameters. PN statistics in the volume-limited sample are summarised in table 9.3, divided between the 1.0 kpc (solar neighbourhood) and less complete 2.0 kpc (extension) samples. Further details on the scale heights of different populations of PNe are presented in §11.2.

There are some important differences between the solar neighbourhood and extension samples. As seen in table 9.3, the proportion of asymmetric PNe is substantially less in the 1.0–2.0 kpc sample, compared to the solar neighbourhood sample closer than 1.0 kpc. Asymmetric PNe are amongst the faintest and most evolved of all PNe, and completeness is expected to rapidly decrease with distance from the sun as the mean reddening increases, causing the apparent surface brightness to go below current detection limits. The general fraction of PNe showing an obvious ISM interaction similarly decreases with increasing distance, as many faint, senile PNe are preferentially lost from the sample due to increasing extinction.

The decreasing proportion of highly evolved PNe from the 2.0 kpc extension sample is also reflected in the lower mean ionized mass (a consequence of the observed mass-radius relation). Most interesting, however, is the significant change in the proportion of Type I PNe as a larger

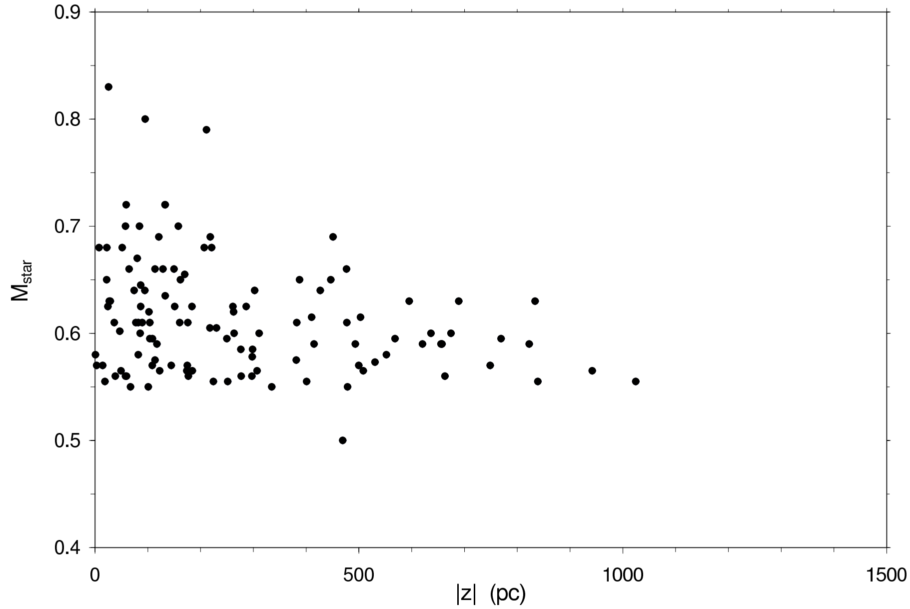

Figure 9.11: Plot of central star mass versus distance from galactic plane, $|z|$, for the 2.0 kpc sample. None of the high-mass central stars ($M \geq 0.7M_{\odot}$) are more than ∼220 pc from the plane. This is is agreement with standard IFMRs and the assumption that only low mass progenitors are found at large $|z|$ distances.

volume of space is surveyed. Type I PNe have very strong [N II] emission, making reddened examples much easier to find on deep red-sensitive surveys such as the SHS (or even the red DSS), compared to faint high-excitation objects with negligible [N II] emission. A corollary is that most of the Type I PNe within 2.0 kpc are currently known, or in other words, most of the missing PNe in this volume are non-Type I objects. Hence the 15% Type I PN fraction in the volume from $1.0 - 2.0$ kpc radius is a firm upper limit. Despite small number statistics, the 6% fraction is deemed more accurate, as the completeness of the extension sample is less (see Chapters 10 and 11).

Confirmation that high-mass progenitor stars produce higher-mass central stars comes from figure 9.11 which plots central star mass versus distance from galactic plane, $|z|$ for the 2.0 kpc sample. None of the high-mass central stars ($M \geq 0.7M_{\odot}$) are more than ∼220 pc from the plane. This is is agreement with standard WD initial-final mass relations (IFMRs) and the assumption that only low mass progenitors are found at large $|z|$ distances. Note that various versions of the IFMR exist in the literature. The reader is referred to the papers by Jeffries (1997), Weidemann (2000), Claver et al. (2001), Ferrario et al. (2005), Dobbie et al. (2006), Williams (2006) and Kalirai et al. (2008). This point will be discussed further in Chapter 11.

There seems a sharp lower mass cutoff at ∼0.55 $M_{\odot}$ in figure 9.11, which may indicate the limit below which PNe become 'lazy' (note, however, that this value is a product of the adopted evolutionary tracks). Furthermore, masses as high as ∼0.62 $M_{\odot}$ are seen to ∼800 pc above the plane. This may be due to errors in the mass determinations, or a hint that relatively high-mass progenitors or blue-stragglers are found in this population (see the discussion of Ciardullo et al. 2005, and also Chapter 11).

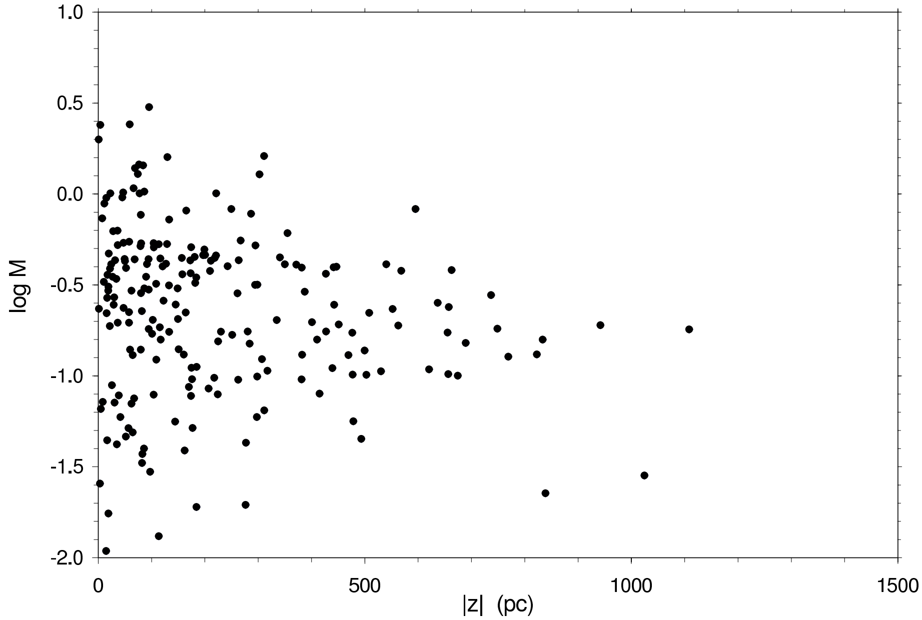

Figure 9.12: Plot of the logarithm of the nebular ionized mass versus distance from galactic plane, $|z|$ for PNe in the 2.0 kpc sample. At low $|z|$ distances, a large range of masses is observed (a reflection of the mass-radius relation with both young and old PNe being present). However, none of the high-mass PN shells ($M_{\rm ion} \geq 1.0 M_{\odot}$) are more than $\sim$300 pc from the plane. This strongly suggests that only low mass progenitors are found at large $|z|$ distances.

It is also germane to look at the distribution of nebular ionized masses with respect to the galactic plane. Figure 9.12 plots ionized mass versus distance from the plane, $|z|$ for all PNe in the 2.0 kpc sample. At low $|z|$ distances, a range of masses is observed (a reflection of the mass-radius relation, with both young and old PNe present). However, none of the high-mass PN shells ($M_{\rm ion} \geq 1.0 M_{\odot}$) are more than $\sim$300 pc from the plane. The upper envelope of the distribution is approximately fit by a straight line. Furthermore, Figure 9.13 plots the N/O abundance ratio relative to distance from the plane for 80 PNe with reliable data within 2 kpc. The enrichment of nitrogen in most PNe, compared to solar composition is noted, as is the fact that no Type I PN is more than 300 pc (3 scale heights) from the galactic plane.

The relationships shown in figures 9.11, 9.12 and 9.13 all strongly suggest that only low mass progenitors are found at large $|z|$ distances. Indeed, from the data of table 9.6, it is found that the mean $|z|$ distance from the Galactic plane is 360 $\pm$ 50 pc for low-mass central stars (mass $< 0.60\, M_{\odot}$) and 190 $\pm$ 27 pc for high-mass stars (mass $\geq 0.60\, M_{\odot}$). The difference between these populations is statistically significant.

The fraction of central stars in the local volume that are H-deficient is in broad agreement with previous work. However, only 88 of the 210 PNe within 2.0 kpc have CS with reliable spectral types. Of these, 59 are H-rich, 22 are classified as either [WR] or PG 1159 types, 6 are *wels* of which 3 are assumed to be H-deficient, and one is an O(He) star. Hence 30% $\pm$ 5% of local CS are considered to be H-deficient, though more data is needed to refine this estimate. Nevertheless, this estimate agrees with the proportion of nearby H-deficient white dwarfs, 33%, within 20 pc of the Sun (Holberg et al. 2008).

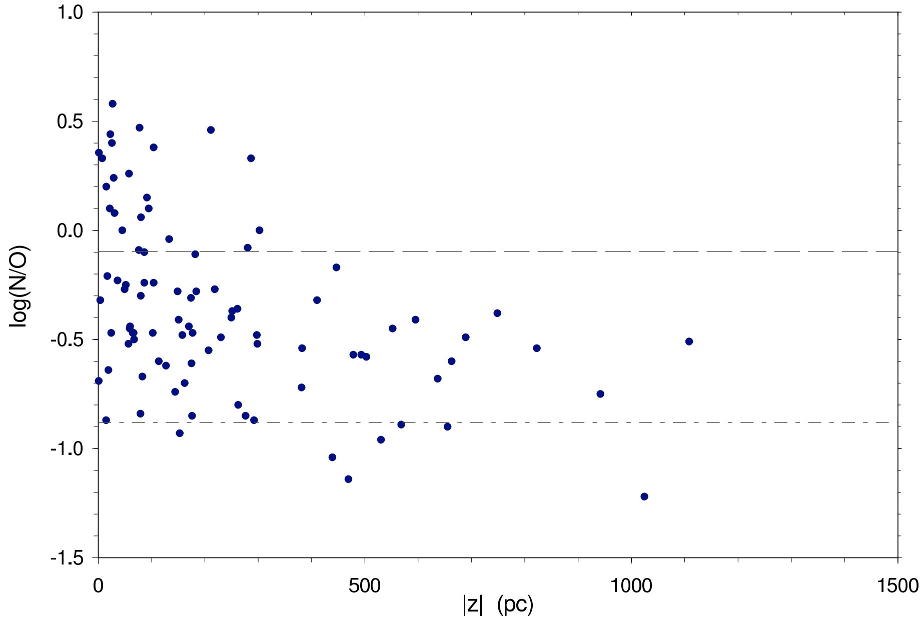

Figure 9.13: N/O abundance ratio relative to vertical height for 80 PNe with reliable data within 2 kpc. The horizontal dashed line is the cutoff for Type I PNe (N/O > 0.8) from Kingsburgh & Barlow (1994), while the dot-dash line plots the solar N/O ratio from Asplund, Grevesse & Sauval (2005). The enrichment of N in most PNe, compared to solar composition is noted, as is the fact that no Type I PN is more than 300 pc (3 scale heights) from the galactic plane.

9.5.1 Binarity

It is of great interest to determine the true proportion of binary (or multiple) central stars from an unbiased volume-limited sample. Furthermore, if all PNe are the product of CE evolution, for instance (Moe & De Marco 2006a, b), there should be direct observational evidence for the ubiquity of binary companions. Unfortunately, a systematic search for binary companions of the ∼55 closest central stars (within 1.0 kpc) has not been undertaken, though partial data exists, and will be summarised in this section.

There are several techniques used to discover or infer the presence of a binary companion to a PN central star. Briefly, they are:

- Direct imaging to detect resolved companions (e.g. Ciardullo et al. 1999);
- Detection of composite spectra in the optical regime, i.e. evidence for both cool and hot components (e.g. Rauch et al. 1999);
- Looking for cyclical photometric variations (e.g. Bond & Grauer 1987; Bond & Livio 1990; Hillwig 2004; Smith & De Marco 2007; Hajduk, Zijlstra & Gesicki 2008), which is sensitive to close binaries with orbital periods shorter than a few days, due to a reflection effect (or sometimes eclipses);
- Looking for radial velocity variability *with a definite periodicity* (e.g. Méndez 1989; Sorensen & Pollacco 2003; De Marco et al. 2004; Afşar & Bond 2005, and §7.3.4), as

distinct from wind-induced velocity variability (see Méndez 1989; Handler 2003, and references therein);

- Using optical and near-infrared (NIR) photometry to infer the presence of an unresolved cool companion (via a near-IR excess). Bentley (1989) and Zuckerman, Becklin & McLean (1991) applied this to a sample of ∼40 PNCS, inferring the presence of companions in several cases. This technique has also been widely applied to detecting cool companions of white dwarfs and subdwarfs (e.g. Wachter et al. 2003; Stark & Wade 2003; Holberg & Magargal 2005; Farihi, Becklin & Zuckerman 2005; Tremblay & Bergeron 2007; Hoard et al. 2007).

Zuckerman, Becklin & McLean (1991) found no excess at K in the CSPN of Sh 2-216, NGC 7293, NGC 3587 and NGC 2610. Only the last is not in the 1.0 kpc sample. These authors found the following nebulae to have a probable or possible excess at K: Abell 7 (confirmed here), Abell 78, Hu 1-2, IC 5217, J 900, NGC 2371, NGC 2452, NGC 3242, NGC 7009 and NGC 7662, but they also noted that the excess could be due to plasma emission from the PN, especially for the last three objects of high surface brightness, or alternatively from warm dust close to these luminous central stars.

Zuckerman et al. found a definite excess at K in NGC 2346, NGC 2392, NGC 7008, NGC 7026, EGB 6, and Abell 63. NGC 2346 is a known close binary with an IR excess due to warm dust (Schmeja & Kimeswenger 2001), while Abell 63 has an eclipsing close binary nucleus (Bond, Liller & Mannery 1978), also with a wider visual companion (Ciardullo et al. 1999). Resolved cool companions were also detected from *HST* images for NGC 2392 and NGC 7008 (Ciardullo et al. 1999), EGB 6 (Bond 1994), and curiously, for NGC 2610 (Ciardullo et al. 1999) as well.

Recently, Bilikova et al. (2008) found that four PNe out of a sample of 40 objects exhibit an IR excess using *Spitzer* archival data; these are NGC 2346, NGC 2438, NGC 6804 (independently found herein to have a near-IR excess from 2MASS data) and NGC 7139, though it is not yet clear if the excess is due to warm dust or a cooler, unresolved companion. All except NGC 7139 are within 2.0 kpc of the Sun.

9.5.2 A new search for binary companions

The known close binary PNe summarised by De Marco (2006) were primarily found via photometric monitoring. However, this technique has selected for bright CS in faint PNe, and seems to be biased *a priori* to finding binaries; note that the mean absolute magnitude of the known close binary sample (refer to table 7.2) is significantly brighter than the mean magnitude of all evolved PNe in the local volume (see §9.4.3). In the solar neighbourhood, definite post-CE PNe number only four. They are HFG 1, NGC 2346, DS 1, and NGC 6337. Based on morphological characteristics, NGC 1360 and LoTr 5 may also be possible examples, with NGC 1514 being a less likely candidate. The last two PNe have composite spectra, with G- and A-type primaries respectively.

Indeed, the local sample is ideal to gauge the true fraction of binary companions. We estimate there are 56 PNe with $D \leq 1.0$ kpc, including eight known *wide* binaries discovered from direct imaging, namely NGC 246, NGC 3132, NGC 6853, NGC 7008, Abell 7, Abell 31, Abell 35, and EGB 6 (Kohoutek & Laustsen 1977; Bond 1995; Gatti et al. 1998; Bond & Ciardullo 1999; Ciardullo et al. 1999). Zuckerman, Becklin & McLean (1990) also resolved two red companions to the CS of NGC 6853, but suggested from their available JHK photometry that both stars are optical companions in the foreground of the PN (cf. Ciardullo et al. 1999).[5]

From the discussion above, looking in the near-IR for signatures of cool companions is productive. By comparing reddening-corrected colours with the intrinsic colours of a 100kK DA white dwarf (e.g. Bergeron, Wesemael & Beauchamp 1995), the presence or absence of a cool companion can be inferred. Hence it is obvious that a search for undetected CS companions in the solar neighbourhood is very worthwhile. The 2MASS survey provides accurate photometry to $J \simeq 16$ and $K_s \simeq 14.7$. As long as the CS is brighter than these limits, the 2MASS data can be compared with optical magnitudes to infer the presence of an IR excess.

For local CSPN with 2MASS data, the detection threshold for a companion is a spectral type of ∼M0 V to M8 V, depending on the intrinsic luminosity of the true nucleus. Since most local PNe are highly evolved with the CS well down the WD cooling track, the practical limit is towards the *fainter* end of this range. For the local PNe with visual companions, only the K0 V secondary in NGC 246 is resolved in 2MASS data.[6] Of the rest, NGC 3132 and Abell 35 have 2MASS colours dominated by the brighter companion, but the remaining five CS *all* show a NIR excess compared to that expected from the optical magnitudes. If not already discovered as visual binaries by direct imaging, these stars would all be strongly suspected of binarity based on optical-NIR colours.

Of the seven possible close binary PNe within $D = 1.0$ kpc (of which four are bona fide, with known orbital periods), only the CS of NGC 6337 has inadequate data (poor optical magnitude). Of the remaining six, five are either dominated by the cooler companion or show an excess at J, H and/or K_s. The exception is NGC 1360, and it should be emphasised that binarity has *not* been proven for this object as yet (cf. Mendez & Niemela 1977; Wehmeyer & Kohoutek 1979; Afşar & Bond 2005). At any rate the limit is not particularly stringent; the companion, if present, has a spectral type later than M2 V. The return rate of using optical/NIR colours in finding known companions shows that this is a highly effective technique of inferring binarity at arbitrarily close separations.

Of the remaining PNe in the local volume, NIR data is wanting for 18 objects due to the faintness of the CS. Another three local PNe have a suspect CS identification, which might be taken as evidence of a likely companion, but are not considered further at this point, while three more have uncertain optical photometry. Of the 19 others which have adequate optical and NIR data, four show an excess at J, H and/or K_s. These are Ton 320, already shown to have an NIR excess by Holberg & Margargal (2005), plus Longmore 16, EGB 9 and HbDs 1.

[5] Of further interest is the recent announcement by Smith & De Marco (2007) of evidence for periodic variability in the CS of NGC 6853 (and NGC 6720), though this needs confirmation.

[6] Solheim, González Pérez & Vauclair (2008) suggest a possible companion to the PG1159 primary of NGC 246 with a period of just 72.5 min, based on a period analysis of time-series photometry.

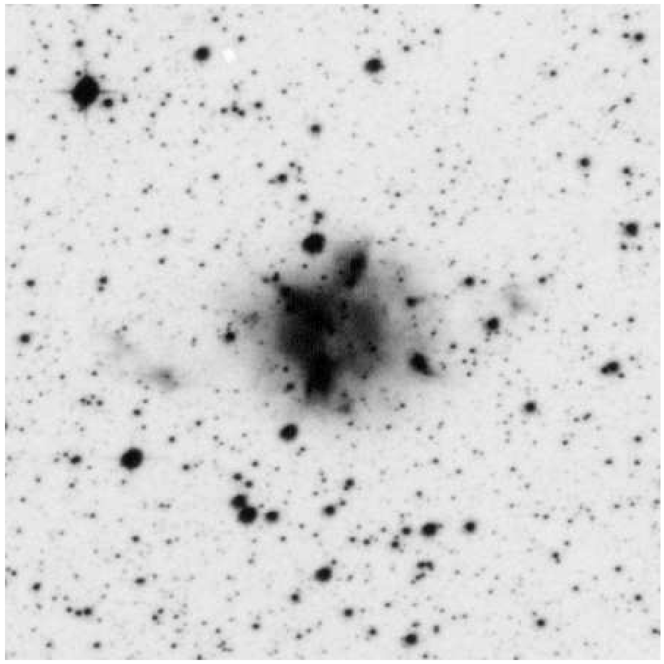

Figure 9.14: UKST SHS Hα+[N II] image of the remarkable point-symmetric PN Longmore 16. The assumed central star (at the centre of point symmetric features) has a clear NIR excess from 2MASS data. The image is 5′ wide, with NE at top left.

The last object has been monitored photometrically (Heber, Werner & Drilling 1988) but no variations were found. Lo 16 is an especially promising candidate for photometric follow-up, due to its unusual point-symmetric morphology (Figure 9.14).

In summary, considering the 33 local PNe with adequate data, the *total* binary fraction is 52% – 58%, and depending on the exact assumptions made (i.e. counting only confirmed close binaries, or including all unresolved stars with NIR excess), the total close-binary fraction is 12% to 33%, somewhat greater than, but in formal agreement with the estimate of 10% to 15% based on photometric variability (Bond 2000). This agreement may be due to previous samples concentrating on brighter (and often nearer) central stars. Hence, within wide limits, approximately 40% of all PN binaries are close ones. This fraction is consistent with the recent study of Schreiber et al. (2008), using SDSS data. These authors find that 35% ± 12% of WD/main-sequence binaries (the offspring of PN binaries) have gone through the common envelope phase.

My preliminary estimate for the CSPN binary fraction is comparable to that seen in Sun-like stars (Duquennoy & Mayor 1991; Lada 2006), and presumably F-type stars, which are the progenitors of at least the lower mass CS. This seems a valid assumption, as the multiplicity fraction of A-, F- and G-type stars is similar, based on a magnitude-limited sample of bright naked-eye stars (Eggleton & Tokovinin 2008).

There are also a number of CSPN in the extended sample (out to 2.0 kpc radius) with an NIR excess. Some are likely young PN with emission due to warm dust (e.g NGC 40, IC 2149, IC 4593 and M 1-26), including some with [WN] spectral types. Other more evolved PNe are better candidates for detailed follow up; these include NGC 2899, NGC 5189, NGC 6369, NGC 6751, NGC 6804, NGC 6905, NGC 7094, Abell 28, Patchick 5, PHR 1510-6754, PHR 1602-4127 and YM 16. Full details are given in table 9.6. No statistics are provided for the 2.0 kpc sample due to the majority of PNe in this volume having no IR photometry.

It should be re-emphasised that an enormous amount of work remains to be done in the search for binary companions in general. The ~21 post-CE PNe in table 7.2 (two without periods, excluding WeBo 1) represent just ~0.6% of the 3200 *confirmed* PNe and PN candidates currently known in the Galaxy (see Chapter 1).

Is there a population of undetected companions to PN central stars?

A comparison of optical and NIR photometry of central stars should be effective at detecting the majority of unresolved CS/red dwarf binaries. Since the observed binary fraction is slightly over half, and the close binary fraction lower still, there needs to be a large number of faint brown dwarf (BD) or cool WD companions present *if binaries are needed to generate PNe* (Moe & De Marco 2006a). However, this seems unlikely based on BD detection statistics. Recall the 'brown dwarf desert' (Marcy & Butler 2000; Grether & Lineweaver 2006, see figure 9.15); i.e. solar-type stars (i.e. PN progenitors) have an almost total absence of BD companions within 5 AU, the upper separation limit for a CE phase to occur during AGB evolution.

Confirmatory statistics are provided by WDs (Farihi, Becklin & Zuckerman 2005; Farihi, Hoard & Wachter 2006), the descendents of PN nuclei. The turnover in the companion star frequency distribution is approximately M3.5 V, the same as for field red dwarfs (Farihi, Becklin & Zuckerman 2005). These authors show that BDs are observed to be rare around WDs. The percentage of double-degenerate systems is also too low (Maxted & Marsh 1999) to readily account for the lack of observable companions around PN nuclei. Holberg et al. (2008) find only 6% of WDs in the solar neighbourhood are in double degenerate systems.

Alternatively, a single CS may be a merger product, but this is again considered unlikely. BDs are very rare at close separations around WDs, but the fraction is not nil. For example, one has recently been found to be in a short period orbit around a WD (Maxted et al. 2006); this system must be the result of CE evolution, therefore it is apparent that even *substellar* companions can survive a CE phase. So it seems unlikely that merger events are frequent enough to explain away the nearly 50% of nearby central stars which do not appear to have a detectable companion. Ockham's razor suggests that single stars can make PNe.

9.6 The PN sample: data tables

This chapter is rounded out with three extensive data tables which provide the main observable and derived properties of all planetary nebulae now considered to be within 2.0 kpc of the Sun, a total of 210 PNe, including data on their central stars. Note that individual PNe within a radius of 1.0 kpc (the '1 kpc' or solar neighbourhood sample) are described in more detail in Appendix A.

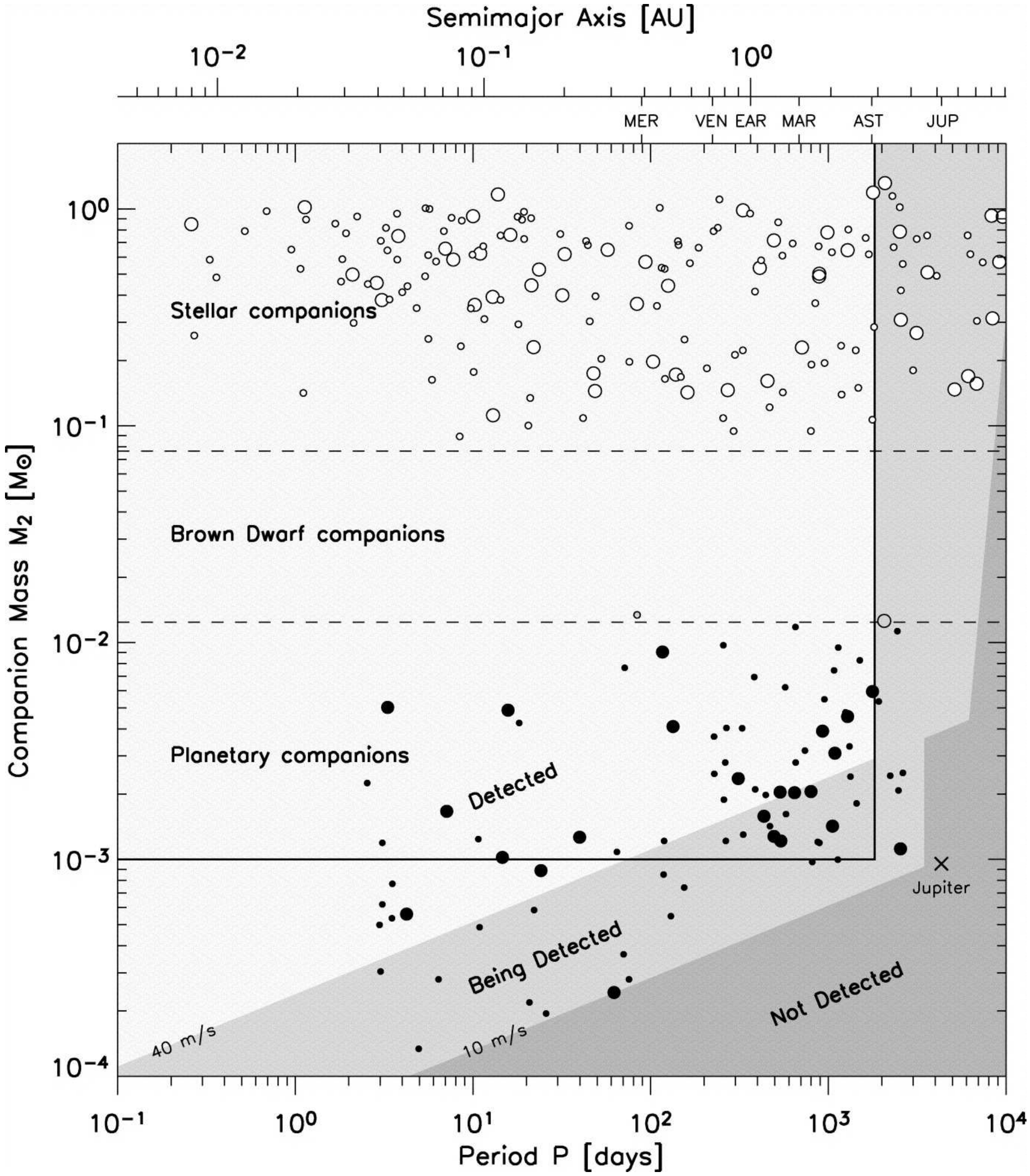

Figure 9.15: The brown dwarf desert in mass-period space, taken from Grether & Lineweaver (2006). The figure plots the estimated companion mass against orbital period for the companions to Sun-like stars closer than 25 pc (large symbols) and those between 25 and 50 pc away (small symbols). The stellar (open circles), brown dwarf (gray circles) and planetary (filled circles) companions are separated by dashed lines at the hydrogen and deuterium burning onset masses of $80M_J$ and $13M_J$, respectively. This plot clearly shows the brown dwarf desert for companions with orbital periods < 5 yr. See Grether & Lineweaver (2006) for further details.

Table 9.4 tabulates the main *observable properties* of these PNe. The column headings are generally self-explanatory. The running number (column 1) is provided to allow the reader to cross-reference between each of the three large tables in this section: it should not be interpreted as a strict ordering of PNe in distance. The next columns in order give the usual name, an alternative identifier, the PN G number, the position (epoch 2000.0) in equatorial and galactic cordinates, generally based on the CS, and the major and minor axial dimensions (in arcsec). The morphology is based on the scheme developed in Chapter 4, the column headed 'WZO' describes the degree of ISM interaction (Wareing, Zijlstra & O'Brien 2007; see §9.3.1), and the last four columns give the logarithmic extinction at Hβ, the logarithms of the integrated Hα and [O III] fluxes (cgs units), and lastly the expansion velocity in kms^{-1}.

Table 9.5 lists the *derived properties* for the PNe in the 2.0 kpc sample. The column headings sequentially give the running number (defined above), usual name, logarithm of the reddening-corrected Hα surface brightness (in cgs units), the distance in kpc and the method used to derive it (c = calibrating object; m = mean SB-r relation; h = high SB-r relation; l = low SB-r relation). The sixth and seventh columns give the projected distance from the Sun on the galactic plane, q, and the distance perpendicular to the plane, z, both in parsecs. The next eight columns give the excitation class, the Hα, Hβ, and [O III] λ5007 absolute magnitudes, the radius (in pc), the ionized mass (in solar masses), the log of the electron density, the dynamical age (derived from the radius and expansion velocity), and the log of the N/O abundance ratio, respectively. The last column notes if the nebula has a close-binary nucleus (C) or belongs to Peimbert's Type I (I).

Table 9.6 provides relevant parameters for the *central stars* of these 210 PNe, where unambiguously identified. The first nine columns sequentially give the running number, position, distance, apparent visual magnitude, absolute magnitude (corrected for reddening), stellar temperature, and the method used to derive the temperature (z = zanstra temperature; c = Ambartsumyan (crossover) temperature; m = model atmosphere method; or p = photoionization modelling). The next two columns give the stellar luminosity (in log solar units) and the stellar mass (in solar units). Columns 13 and 14 give an indication of any evidence for an infrared (IR) excess or radial velocity (RV) variability in the CS. Column 15 gives an overall indication if the CS is considered to be a binary (or multiple) star. Abreviations used in these columns are as follows: y = yes; n = no; nd = no data; c = close binary; w = wide binary; o = optical pair; s = secondary star spectrum dominates; u = uncertain; id = the CS identification is queried. The last two columns in the table give the spectral types of the central star and any companion star taken from the literature, or inferred here from a comparison of the optical and NIR colours; inferred spectral types are given in italics.

Table 9.4: Observed Quantities (2.0 kpc sample).

No.	Name	Other	PN G	α	δ	l	b	a (")	b (")	Mor.	WZO	c	F(Hα)	F(5007)	$V_{\rm exp}$ $\rm kms^{-1}$
1	Sh 2-216	LBN 744	G158.5+00.7	04 43 21.27	+46 42 05.8	158.49	0.48	6000	5400	Ra	2/3	0.07	-8.72	-9.18	5
2	NGC 7293	...	G036.1-57.1	22 29 38.51	-20 50 13.7	36.16	-57.12	1005	740	Bams(h)	1/2	0.01	-8.89	-8.59	21
3	FP1824-0319	...	G026.9+04.4	18 24 40.88	-03 19 59.6	26.89	4.44	1800	1500	Ea	2/3	0.15	-10.41	-10.78	12
4	NGC 1514	...	G165.5-15.2	04 09 16.99	+30 46 33.4	165.53	-15.29	140	132	Ems	1	0.78	-10.28	-9.89	25
5	PuWe 1	...	G158.9+17.8	06 19 33.96	+55 36 43.8	158.92	17.86	1242	1180	Ra	1/2	0.16	-10.21	-10.20	23
6	M 27	NGC 6853	G060.8-03.6	19 59 36.34	+22 43 16.1	60.84	-3.70	480	342	Ebm(h)	1	0.07	-8.99	-8.45	32
7	NGC 1360	...	G220.3-53.9	03 33 14.65	-25 52 17.9	220.36	-53.93	420	266	Efp	1	0.01	-9.75	-9.34	34
8	Abell 36	...	G318.4+41.4	13 40 41.34	-19 52 55.3	318.46	41.50	468	315	Ea	1	0.04	-10.51	-10.38	36
9	Abell 31	Sh 2-290	G219.1+31.2	08 54 13.16	+08 53 53.0	219.13	31.29	1145	890	Eas	2	0.06	-10.08	-9.77	29
10	NGC 246	...	G118.8-74.7	00 47 03.35	-11 52 19.0	118.86	-74.71	260	227	Ea	2	0.03	-10.09	-9.65	38
11	MWP 1	RX J2117.1+3412	G080.3-10.4	21 17 08.29	+34 12 27.2	80.35	-10.41	840	500	Eap	2	0.03	-10.3	-10.16	30
12	LoTr 5	...	G339.9+88.4	12 55 33.75	+25 53 30.6	339.90	88.46	540	510	Eabf	1/2	0.01	-10.84	-10.44	31
13	Abell 7	...	G215.5-30.8	05 03 07.52	-15 36 22.8	215.57	-30.85	830	787	Rs	1	0.03	-10.48	-10.23	29
14	IPHAS2050+4655	...	G086.5+01.8	20 50 13.74	+46 55 15.2	86.52	1.83	345	320	Es	2	2.2	-11.2	-11.48	...
15	PFP 1	...	G222.1+03.9	07 22 17.75	-06 21 46.4	222.13	3.91	1150	1100	Ra	2	0.07	-10.70	-10.42	30
16	Abell 21	YM 29	G205.1+14.2	07 29 02.71	+13 14 48.8	205.14	14.25	760	600	Bas(h?)	2	0.06	-9.84	-9.57	32
17	FP0905-3033	...	G255.8+10.9	09 05 05.34	-30 33 12.0	255.84	10.94	965	745	As	3	0.07	-10.60	-10.45	24
18	TK 1	Ton 320	G191.4+33.1	08 27 05.54	+31 30 08.8	191.40	33.08	2300	1840	As	3	0.05	-10.79	-10.85	15
19	Jacoby 1	PG 1520+525	G085.3+52.3	15 21 46.58	+52 22 04.1	85.37	52.35	660	660	Ra	2	0.05	-11.16	-10.96	30
20	EGB 6	...	G221.5+46.3	09 52 59.00	+13 44 34.5	221.59	46.36	780	660	Ea	2	0.07	-10.80	-10.78	25
21	HFG 1	...	G136.3+05.5	03 03 46.99	+64 54 35.4	136.38	5.55	540	540	Ea(h:)	2	0.67	-10.52	-10.23	15
22	IsWe 1	...	G149.7-03.3	03 49 05.89	+50 00 14.8	149.71	-3.40	780	710	Ea	3	0.26	-10.76	-11.02	12
23	IsWe 2	...	G107.7+07.8	22 13 22.53	+65 53 55.5	107.73	7.81	1020	850	Eas	2	0.65	-10.45	-11.08	12
24	FP0711-2531	...	G237.9-07.2	07 11 32.0	-25 31 24	237.95	-7.25	755	680	Eaf?	1/2	0.04	-10.61	-10.62	...
25	Sh 2-78	CTSS 3	G046.8+03.8	19 03 10.09	+14 06 58.9	46.83	3.85	680	620	Ebas	2	0.81	-10.52	-10.93	20
26	EGB 1	HaWe 1, LBN 624	G124.0+10.7	01 07 07.59	+73 33 23.1	124.07	10.73	570	540	As	3	0.33	-10.77	-10.69	...
27	Sh 2-200	LBN 674, HaWe 2	G138.1+04.1	03 10 58.87	+62 47 54.8	138.13	4.12	366	346	Eams(h:)	2	0.65	-10.90	-10.41	13
28	M 57	NGC 6720	G063.1+13.9	18 53 35.08	+33 01 45.0	63.17	13.98	86	63	Ebmr(h)	1	0.20	-9.55	-9.05	22
29	NGC 7008	...	G093.4+05.4	21 00 32.80	+54 32 35.3	93.41	5.49	98	82	Efp	1	0.54	-10.17	-10.02	37
30	NGC 1501	...	G144.5+06.5	04 06 59.19	+60 55 14.3	144.56	6.55	56	46	Es	1	0.95	-10.46	-10.05	40
31	DS 1	ESO 215-04	G283.9+09.7	10 54 40.57	-48 47 02.8	283.90	9.74	354	315	Efp	1	0.22	-10.65	-10.35	30
32	Abell 74	...	G072.7-17.1	21 16 52.27	+24 08 51.8	72.66	-17.15	810	776	Eab	1/2	0.12	-10.60	-10.78	26
33	M 97	NGC 3587	G148.4+57.0	11 14 47.73	+55 01 08.5	148.49	57.05	208	202	Rfm:	1	0.02	-10.00	-9.54	34

Continued on next page

Table 9.4 – continued from previous page

No.	Name	Other	PN G	α	δ	l	b	a (”)	b (”)	Mor.	WZO	c	$F(\mathrm{H}\alpha)$	$F(5007)$	V_{exp} kms^{-1}
34	Lo 1	K 1-26	G255.3-59.6	02 56 58.40	-44 10 17.9	255.32	-59.62	460	385	Eaf	2	0.00	-10.98	-10.66	30
35	Sh 2-176	...	G120.2-05.3	00 31 53.30	+57 22 49.0	120.26	-5.47	800	750	As	3	0.50	-10.7	-11.07	22
36	HbDs 1	DS 3, LSS 1362	G273.6+06.1	09 52 44.53	-46 16 47.4	273.67	6.19	158	140	Er?	1	0.19	-11.40	-11.43	...
37	K 2-2	...	G204.1+04.7	06 52 23.17	+09 57 55.8	204.17	4.76	720	540	As	3	0.00	-10.29	-9.85	10
38	HaWe 4	HDW 3	G149.4-09.2	03 27 15.44	+45 24 20.5	149.50	-9.28	725	560	A	3	0.29	-11.13	-10.64	11
39	NGC 3132	...	G272.1+12.3	10 07 01.76	-40 26 11.1	272.11	12.40	85	55	Er	1	0.15	-9.82	-9.46	21
40	Sh 2-188	Simeiz 22	G128.0-04.1	01 30 33.19	+58 24 50.2	128.07	-4.11	702	610	As	3	0.52	-10.07	-10.41	18
41	Abell 24	...	G217.1+14.7	07 51 37.55	+03 00 21.0	217.18	14.76	420	405	Ebp?	1	0.09	-10.69	-10.87	20
42	Lo 16	...	G349.3-04.2	17 35 41.80	-40 11 26.2	349.36	-4.23	90	80	Eps	1	0.84	-10.75	-10.46	...
43	WDHS 1	WeDe 1	G197.4-06.4	05 59 24.80	+10 41 40.2	197.40	-6.44	1320	1020	Eab	2	0.09	-10.40	<-11.2	17
44	IC 5148/50	...	G002.7-52.4	21 59 35.13	-39 23 08.1	2.71	-52.44	133	128	Rm	1	0.01	-10.45	-10.33	53
45	NGC 6337	...	G349.3-01.1	17 22 15.66	-38 29 03.5	349.35	-1.12	48	47	Epr	1	0.87	-10.45	-10.31	8
46	NGC 7027	...	G084.9-03.4	21 07 01.70	+42 14 09.5	84.93	-3.50	17	13	Bs/Ebs	1	1.37	-9.25	-8.94	22
47	NGC 2346	...	G215.6+03.6	07 09 22.55	-00 48 23.6	215.70	3.62	70	55	Bs	1	0.74	-10.65	-10.30	12
48	Jones 1	...	G104.2-29.6	23 35 53.32	+30 28 06.4	104.21	-29.64	363	315	Eap	2	0.13	-10.71	-10.32	36
49	FP1721-5654	Fr 2-12	G333.8-11.2	17 21 09.0	-56 54 25	333.87	-11.27	440	360	Eas?	2	0.30	-10.98	-10.92	...
50	NGC 6781	...	G041.8-02.9	19 18 28.09	+06 32 19.3	41.84	-2.99	180	109	Bam(h:)	1/2	0.77	-10.02	-9.89	12
51	NGC 4361	...	G294.1+43.6	12 24 30.75	-18 47 05.5	294.11	43.63	119	115	Es	1	0.06	-10.11	-9.96	32
52	EGB 9	...	G209.4+09.5	07 18 57.93	+07 22 23.2	209.43	9.50	377	234	Ea?	3?	0.10	-11.23	...	...
53	NGC 3242	...	G261.0+32.0	10 24 46.14	-18 38 32.3	261.05	32.05	45	39	Em(h)	1	0.06	-9.31	-8.66	28
54	RCW 24	Fr 1-1	G258.5-01.2	08 25 47.58	-40 13 10.0	258.52	-1.30	720	365	Bps	1	0.55	-10.95	-11.22	...
55	DS 2	LSE 125	G335.5+12.4	15 43 05.04	-39 18 14.6	335.58	12.45	190	190	Rs	1	0.32	-11.55	-11.10	...
56	HaWe 13	HDW 11, We e	G034.1-10.5	19 31 07.20	-03 42 31.5	34.15	-10.52	82	68	Efp?	1	0.71	-12.02	...	...
57	NGC 40	...	G120.0+09.8	00 13 01.02	+72 31 19.1	120.02	9.87	60	34	Eas(h)	1/2	0.61	-9.79	-10.24	25
58	Abell 34	...	G248.7+29.5	09 45 35.32	-13 10 15.6	248.71	29.54	291	278	Ra	2	0.06	-11.23	-10.82	35
59	MeWe 2-4	...	G314.0+10.6	14 01 15.42	-50 40 09.5	314.09	10.68	422	366	Ea	2	0.29	-11.20	-11.26	...
60	PHR1625-4523	...	G337.4+02.7	16 25 56.30	-45 23 14.4	337.40	2.66	330	300	Eas	2	0.56	-11.23	-11.41	...
61	Abell 66	...	G019.8-23.7	19 57 31.53	-21 36 44.7	19.85	-23.78	312	246	Eas	2	0.26	-10.96	-10.81	...
62	NGC 6153	...	G341.8+05.4	16 31 30.83	-40 15 14.2	341.84	5.44	28	23	Es	1	1.30	-9.96	-9.84	17
63	Abell 6	...	G136.1+04.9	02 58 41.87	+64 30 06.3	136.12	4.94	188	174	Ra	2	1.46	-11.48	-11.08	...
64	Sp 1	He 2-137	G329.0+01.9	15 51 40.93	-51 31 28.4	329.08	1.96	72	72	Rr	1	0.75	-11.02	-10.63	30
65	PHR1418-5144	...	G316.3+08.8	14 18 25.88	-51 44 37.4	316.35	8.83	404	375	Eas	2	0.45	-11.39	-11.11	...
66	He 2-11	Wr 16-23	G259.1+00.9	08 37 08.45	-39 25 08.1	259.15	0.94	122	64	Ebps	1	1.90	-10.93	-11.03	...
67	Sh 2-71	M 1-90, LBN 103	G035.9-01.1	19 01 59.95	+02 09 16.0	36.05	-1.36	157	76	Bs/Is	1	1.45	-10.75	-10.61	21
68	BMP0642-0417	...	G215.7-03.9	06 42 18.41	-04 17 48.9	215.72	-3.99	888	560	A	2/3	0.40	-11.8	-12.25	...

Continued on next page

Table 9.4 – continued from previous page

No.	Name	Other	PN G	α	δ	l	b	a (")	b (")	Mor.	WZO	c	$F(\mathrm{H}\alpha)$	$F(5007)$	V_{exp} kms^{-1}
69	JnEr 1	VV 47	G164.8+31.1	07 57 51.63	+53 25 17.0	164.81	31.18	398	362	Ebmp	1	0.03	-10.58	-10.33	24
70	Abell 33	...	G238.0+34.8	09 39 09.12	-02 48 31.5	238.02	34.86	282	276	Ra	2	0.00	-10.95	-10.73	32
71	Kronberger 9	Lanning 21	G059.1-00.7	19 44 59.13	+22 45 47.9	59.15	-0.78	260	240	Ea	2	0.3	-11.50	-11.34	...
72	NGC 6302	...	G349.5+01.0	17 13 44.21	-37 06 15.9	349.51	1.06	90	35	Bps	1	1.28	-9.68	-9.36	...
73	Abell 65	Sh 2-52	G017.3-21.9	19 46 34.20	-23 08 12.9	17.31	-21.96	137	82	Eafm:	1/2	0.29	-10.99	-10.55	11
74	PHR1432-6138	...	G314.5-01.0	14 32 09.73	-61 38 41.3	314.58	-1.07	269	230	Eas	2	0.38	-11.09	-11.10	...
75	NGC 6772	...	G033.1-06.3	19 14 36.37	-02 42 25.0	33.16	-6.39	81	71	Ep	1	0.92	-10.62	-10.25	11
76	IC 418	...	G215.2-24.2	05 27 28.20	-12 41 50.3	215.21	-24.28	14	11	Em(h:)	1	0.29	-9.01	-9.32	14
77	M 76	NGC 650/1	G130.9-10.5	01 42 19.95	+51 34 31.2	130.93	-10.50	168	111	Bas(h)	1	0.15	-10.06	-9.55	39
78	M 1-26	He 2-277	G358.9-00.7	17 45 57.65	-30 12 00.6	358.96	-0.72	6.4	6.0	R	1	1.52	-10.17	-11.55	12
79	Abell 28	...	G158.8+37.1	08 41 35.57	+58 13 48.4	158.82	37.18	320	315	Ra	2	0.00	-11.50	-11.78	8
80	IC 1295	...	G025.4-04.7	18 54 37.21	-08 49 39.1	25.41	-4.71	110	89	Efm:	1	0.52	-10.78	-10.13	27
81	NGC 7662	...	G106.5-17.6	23 25 53.97	+42 32 05.0	106.56	-17.60	31	28	Emp(h)	1	0.16	-9.51	-8.89	27
82	PHR1118-6150	...	G292.2-00.9	11 18 44.55	-61 50 19.4	291.22	-0.90	312	309	Ra	2	0.5	-11.43	-11.66	...
83	HaWe 15	HDW 13	G099.6-08.8	22 30 33.46	+47 31 23.6	99.65	-8.89	390	228	Eam?	2	0.30	-11.28	...	...
84	NGC 2392	...	G197.8+17.3	07 29 10.77	+20 54 42.4	197.88	17.40	48	44	Rm	1	0.23	-9.90	-9.43	53
85	YM 16	RCW 181	G038.7+01.9	18 54 57.72	+06 02 40.9	38.67	2.02	375	285	Eabs	2	1.2	-11.40	-11.59	...
86	NGC 6826	...	G083.5+12.7	19 44 48.16	+50 31 30.3	83.56	12.79	27	24	Emp(h)	1	0.15	-9.44	-9.07	16
87	IC 4637	...	G345.4+00.1	17 05 10.51	-40 53 08.4	345.48	0.14	19	14	Eam	2	0.85	-10.39	-10.27	21
88	BD+30 3639	He 2-438	G064.7+05.0	19 34 45.23	+30 30 58.9	64.79	5.02	6.2	5.6	Er	1	0.43	-9.39	-11.25	25
89	RCW 69	Fr 1-2, Gum 45	G302.1+00.3	12 44 27.3	-62 31 30.7	302.13	0.34	248	218	Bps	1	0.75	-10.90	-10.94	13
90	MeWe 1-2	PHR 1014-5811	G283.4-01.4	10 14 24.16	-58 11 52.3	283.44	-1.40	276	254	Ra	2	0.4	-11.30	-11.57	...
91	NGC 6894	...	G069.4-02.6	20 16 23.97	+30 33 53.2	69.48	-2.62	56	53	Emr	1	0.90	-10.58	-10.52	43
92	Abell 61	NSV 11917	G077.6+14.7	19 19 10.22	+46 14 52.0	77.70	14.77	203	196	Ra	2	0.07	-11.38	-11.16	30
93	NGC 6026	...	G341.6+13.7	16 01 21.07	-34 32 36.6	341.61	13.71	53	46	Ef	1	0.75	-11.01	-10.84	25
94	Abell 45	...	G020.2-00.6	18 30 15.42	-11 36 57.4	20.20	-0.66	302	281	Ers	1	1.13	-11.32	...	...
95	Abell 71	Sh 2-116	G084.9+04.4	20 32 23.22	+47 20 50.4	85.00	4.49	166	149	Ea	2	1.06	-10.92	-11.18	20
96	K 1-22	...	G283.6+25.3	11 26 43.79	-34 22 11.0	283.67	25.31	200	186	Ef	1	0.07	-10.82	-10.42	28
97	BMP0733-3108	...	G215.1-05.5	07 33 24.12	-31 08 05.1	245.19	-5.57	697	492	Bas	2	0.50	-11.32	...	...
98	NGC 2899	...	G277.1-03.8	09 27 03.12	-56 06 21.2	277.15	-3.83	152	80	Baps	1/2	0.62	-10.46	-10.23	25
99	PHR0743-1951	...	G236.4+01.9	07 43 51.13	-19 51 16.7	236.49	1.99	400	304	As	2/3	0.4	-11.58	-12.13	...
100	HaTr 7	...	G332.5-16.9	17 54 09.46	-60 49 57.6	332.51	-16.91	188	180	Ra?	2	0.08	-11.41	-10.82	...
101	Abell 62	...	G047.1-04.2	19 33 18.04	+10 37 00.7	47.30	-4.51	166	156	Ra	2	0.20	-10.90	-11.13	15
102	NGC 6445	...	G008.0+03.9	17 49 15.21	-20 00 34.5	8.07	3.91	45	36	Bs	1	1.23	-10.30	-10.02	38
103	NGC 6072	...	G342.1+10.8	16 12 58.08	-36 13 46.1	342.18	10.85	74	65	Ba	1/2	0.86	-10.37	-10.10	10

Continued on next page

Table 9.4 – continued from previous page

No.	Name	Other	PN G	α	δ	l	b	a (")	b (")	Mor.	WZO	c	$F(\mathrm{H}\alpha)$	$F(5007)$	V_{exp} kms^{-1}
104	Abell 29	...	G244.5+12.5	08 40 18.92	-20 54 36.3	244.59	12.58	485	385	Eb?	1	0.18	-10.98	-10.93	20
105	NGC 7094	K 1-19	G066.7-28.2	21 36 52.98	+12 47 19.3	66.78	-28.20	103	99	Ras	2	0.12	-11.24	-11.06	40
106	Abell 39	...	G047.0+42.4	16 27 33.74	+27 54 33.4	47.05	42.48	174	174	Ra	1	0.03	-11.36	-10.76	29
107	Wray 17-31	VBRC 2, RCW 44	G277.7-03.5	09 31 20.49	-56 17 39.4	277.73	-3.55	149	143	Es	1	0.35	-10.95	-10.68	28
108	BMP1808-1406	...	G015.5+02.8	18 08 35.08	-14 06 43.0	15.50	2.82	470	470	Rpr	1	1.0	-11.6	...	...
109	NGC 2371-72	...	G189.1+19.8	07 25 34.72	+29 29 25.6	189.16	19.84	49	31	Eps	1	0.07	-10.51	-10.10	43
110	PHR1040-5417	...	G284.5+03.8	10 40 48.21	-54 17 57.6	284.53	3.84	375	166	Ebps	1	0.13	-11.20	-10.91	...
111	NGC 2438	...	G231.8+04.1	07 41 51.43	-14 43 54.9	231.80	4.12	81	78	Emr(h)	1	0.27	-10.49	-10.14	23
112	NGC 5189	IC 4274	G307.2-03.4	13 33 32.97	-65 58 26.7	307.20	-3.45	163	108	Bps	1	0.52	-9.94	-9.48	25
113	Lo 5	...	G286.5+11.6	11 13 54.15	-47 57 00.6	286.52	11.79	152	150	Rar	1/2	0.20	-10.92	-10.56	...
114	NGC 7009	...	G037.7-34.5	21 04 10.88	-11 21 48.2	37.76	-34.57	28	22	Emps(h)	1	0.12	-9.29	-8.72	25
115	Sh 2-42	PHR 1810-1647	G013.3+01.1	18 10 13.6	-16 47 49	13.33	1.18	120	117	Eams	2	0.6	-11.04	...	...
116	PHR0942-5220	Bran 273	G276.2+00.4	09 41 59.42	-52 20 30.6	276.22	0.42	165	150	Ea	2	1.09	-11.58	-11.54	...
117	NGC 6804	...	G045.7-04.5	19 31 35.18	+09 13 31.9	45.75	-4.59	58	49	Eam	2	0.80	-10.61	-10.35	25
118	M 1-41	Ve 3-62	G006.7-02.2	18 09 29.90	-24 12 23.5	6.77	-2.25	50	35	Bs/Is	1	2.06	-10.97	-10.86	...
119	HaTr 5	...	G343.3-00.6	17 01 27.98	-43 05 55.1	343.30	-0.66	120	112	Rar	2	1.0	-11.31	...	...
120	NGC 7076	Abell 75	G101.8+08.7	21 26 23.60	+62 53 32.1	101.86	8.75	67	47	Ea	2	1.18	-11.55	-11.19	42
121	G4.4+6.4	PHR1731-2149	G004.3+06.4	17 31 51.71	-21 49 18.2	4.39	6.41	255	212	Ias	2?	0.8	-11.13	-11.11	...
122	K 1-6	...	G107.1+21.3	20 04 13.39	+74 26 28.3	107.10	21.38	240	195	Ea?	1/2	0.3	-11.29	...	...
123	He 2-36	...	G279.6-03.1	09 43 25.62	-57 16 55.6	279.61	-3.19	32	22	Bs	1	0.99	-10.88	-10.27	45
124	PHR1510-6754	...	G315.4-08.5	15 10 22.05	-67 54 24.0	315.44	-8.52	285	225	Eam?	2/3	0.28	-11.40	-11.43	...
125	K 2-1	UGCA 100	G173.7-05.8	05 07 08.33	+30 49 18.6	173.76	-5.87	145	122	Efp?	1	0.63	-11.18	-10.79	...
126	SuWt 2	...	G311.0+02.4	13 55 43.23	-59 22 40.0	311.05	2.47	87	43	Br	1	0.55	-11.69	-11.40	...
127	NGC 6543	...	G096.4+29.9	17 58 33.41	+66 37 58.8	96.47	29.95	27	24	Emps(h)	1	0.10	-9.10	-8.78	20
128	We 2-34	...	G210.0+03.9	07 00 28.40	+04 20 30.4	210.07	3.97	345	247	Eabr?	1/2	0.6	-11.70	-12.01	...
129	VBRC 5	SuWt 1	G309.2+01.3	13 44 00.03	-60 49 46.9	309.30	1.39	94	53	Ea?	2	2.10	-11.75	-11.82	...
130	IC 2149	...	G166.1+10.4	05 56 23.91	+46 06 17.3	166.16	10.48	12	8	E	1	0.36	-10.00	-9.90	20
131	Abell 80	...	G102.8-05.0	22 34 45.60	+52 26 06.2	102.83	-5.00	169	119	Ea	2	0.55	-11.20	-11.32	18
132	BMP1651-3930	...	G344.9+03.0	16 51 41.3	-39 30 27	344.96	3.01	315	305	Eas	2	0.3	-11.6	...	...
133	Abell 59	...	G053.3+03.0	19 18 40.00	+19 34 33.0	53.40	3.06	94	80	Ea	2	1.87	-11.76	-11.95	...
134	NGC 6369	...	G002.4+05.8	17 29 20.44	-23 45 34.2	2.43	5.85	33	33	Ebpr(h:)	1	1.96	-10.17	-10.00	42
135	IC 4593	...	G025.3+40.8	16 11 44.54	+12 04 17.1	25.33	40.84	15	15	Emp(h)	1	0.10	-10.12	-9.91	12
136	NGC 6905	...	G061.4-09.5	20 22 22.94	+20 06 16.8	61.49	-9.57	43	36	Eps	1	0.22	-10.42	-10.04	40
137	Fr 2-8	AM 1357-504	G313.9+10.3	14 00 41.75	-51 02 27.6	313.90	10.35	118	112	Ef	1	0.30	-11.48	-11.32	...
138	BMP0815-4053	...	G257.9-03.2	08 15 56.9	-40 53 08	234.95	-9.72	407	245	As	3	0.5	-11.8	...	...

Continued on next page

Table 9.4 – continued from previous page

No.	Name	Other	PN G	α	δ	l	b	a (")	b (")	Mor.	WZO	c	$F(\mathrm{H}\alpha)$	$F(5007)$	V_{exp} kms^{-1}
139	KjPn 8	K 3-89	G112.5-00.1	23 24 10.47	+60 57 30.8	112.54	-0.14	750	280	Bamps	2	0.74	-11.2	...	...
140	NGC 7354	...	G107.8+02.3	22 40 19.94	+61 17 08.1	107.84	2.32	25	21	Emp	1	1.77	-10.53	-10.42	25
141	We 3-1	...	G044.3+10.4	18 34 02.31	+14 49 10.2	44.32	10.48	180	154	Ea	2	0.50	-11.38	-11.32	...
142	NGC 6818	...	G025.8-17.9	19 43 57.84	-14 09 11.9	25.86	-17.91	25	25	Rmp	1	0.37	-9.94	-9.29	27
143	PHR1602-4127	...	G337.0+08.4	16 02 18.13	-41 26 49.5	337.03	8.45	200	175	Eaf	2	0.39	-11.42	-11.47	...
144	K 1-16	...	G094.0+27.4	18 21 52.21	+64 21 54.3	94.03	27.43	123	103	Ef	1	0.06	-11.55	-11.40	...
145	NGC 6563	...	G358.5-07.3	18 12 02.75	-33 52 07.1	358.50	-7.34	59	43	Ear	1/2	0.10	-10.30	-9.99	11
146	NGC 6567	...	G011.7-00.6	18 13 45.14	-19 04 33.7	11.74	-0.65	8.1	6.4	Em	1	0.80	-10.21	-9.95	18
147	Abell 84	...	G112.9-10.2	23 47 44.30	+51 23 56.3	112.91	-10.23	146	116	Eas	2	0.38	-11.18	-10.76	16
148	Hb 5	CD-29 13998	G359.3-00.9	17 47 56.19	-29 59 41.9	359.36	-0.98	52	18	Bps	1	1.66	-10.41	-10.37	...
149	Abell 46	...	G055.4+16.0	18 31 18.59	+26 56 12.1	55.41	16.03	97	84	Ebs	1	0.23	-11.40	-11.40	...
150	K 1-27	...	G286.8-29.5	05 57 02.14	-75 40 22.5	286.88	-29.58	61	47	Er	1	0.07	-12.13	-12.18	...
151	NGC 5882	...	G327.8+10.0	15 16 49.94	-45 38 58.4	327.82	10.08	16	13	Emp(h:)	1	0.39	-9.78	-9.38	...
152	PHR1408-6106	...	G312.1+00.3	14 08 48.07	-61 06 33.8	312.12	0.39	307	264	Eas	2	0.67	-11.53	-11.98	...
153	IC 4642	...	G334.3-09.3	17 11 45.02	-55 24 01.5	334.39	-9.35	24	22	Em	1	0.37	-10.68	-10.52	...
154	HaWe 11	HDW 8, M 3-57	G358.5+02.6	17 31 47.47	-28 42 03.4	358.61	2.68	40	36	Eps	1	1.7	-11.22	-11.07	...
155	NGC 2610	...	G239.6+13.9	08 33 23.32	-16 08 57.7	239.63	13.95	50	48	Em(h:)	1	0.00	-10.89	-10.70	24
156	Patchick 5	...	G076.3+14.1	19 19 30.53	+44 45 43.1	76.33	14.12	157	100	Ea	2	0.18	-11.6	-11.33	...
157	Abell 72	...	G059.7-18.7	20 50 02.06	+13 33 29.6	59.79	-18.73	160	118	Es	1	0.04	-11.56	-11.30	...
158	NGC 4071	...	G298.3-04.8	12 04 14.82	-67 18 35.6	298.39	-4.85	80	53	Eabp	2	0.55	-10.88	-10.52	17
159	Abell 51	...	G017.6-10.2	19 01 01.39	-18 12 15.3	17.62	-10.24	67	67	Ra	2	0.32	-11.35	-11.33	42
160	WeSb 2	...	G183.8+05.5	06 16 11.35	+28 22 11.0	183.81	5.55	154	148	Ea	2	1.5	-12.15	...	...
161	IPHAS 0156+65	...	G129.6+03.4	01 56 24.94	+65 28 30.5	129.61	3.45	198	180	Ea	2	0.3	-11.5	...	...
162	He 2-84	...	G300.4-00.9	12 28 46.82	-63 44 38.7	300.43	-0.98	35.8	23.7	Bp	1	1.8	-11.64	-11.18	...
163	We 1-10	...	G086.1+05.4	20 31 52.38	+48 52 49.9	86.19	5.46	195	185	Ea	2	0.20	-11.45	...	...
164	PHR1619-4914	PM 5	G333.9+00.6	16 19 40.18	-49 13 59.5	333.93	0.69	32	32	Rrs	1	4.8	-13.0	...	165
165	Fg 1	...	G290.5+07.9	11 28 36.21	-52 56 04.0	290.51	7.93	55	40	Emp	1	0.25	-10.49	-10.17	...
166	Abell 82	...	G114.0-04.6	23 45 47.81	+57 03 59.2	114.07	-4.68	133	94	Eab	2	0.32	-11.16	-10.74	...
167	NGC 5844	He 2-119	G317.1-05.7	15 10 40.75	-64 40 28.5	317.13	-5.71	63	60	Ebms(h)	1	0.93	-10.75	-10.18	...
168	Kronberger 24	...	G082.1-07.8	21 13 37.73	+37 15 37.6	82.12	-7.80	184	180	Ras	2	0.3	-11.5	...	...
169	NGC 3918	...	G294.6+04.7	11 50 17.73	-57 10 56.9	294.69	4.71	19	17	Ems(h)	1	0.38	-9.50	-8.84	25
170	PHR1533-4824	...	G328.6+06.2	15 33 06.87	-48 24 44.6	328.59	6.24	208	206	Ra	2	0.0	-11.40	-11.45	...
171	HaWe 9	...	G236.0-10.6	06 54 20.79	-25 24 33.5	236.09	-10.64	210	185	Ea	2/3	0.43	-11.66	...	...
172	Abell 78	...	G081.2-14.9	21 35 29.41	+31 41 45.4	81.30	-14.91	128	106	Eams	2	0.08	-11.57	-10.92	27
173	NGC 6572	...	G034.6+11.8	18 12 06.40	+06 51 12.2	34.62	11.85	15	13	Emp	1	0.32	-9.24	-8.76	18

Continued on next page

Table 9.4 – continued from previous page

No.	Name	Other	PN G	α	δ	l	b	a (")	b (")	Mor.	WZO	c	$F(\mathrm{H}\alpha)$	$F(5007)$	V_{exp} kms^{-1}
174	We 2-5	...	G129.2-02.0	01 42 38.00	+60 09 44.5	129.26	-2.08	210	165	E/Ba	2	0.50	-11.7	...	...
175	M 2-55	...	G116.2+08.5	23 31 52.71	+70 22 10.1	116.30	8.53	58	40	Ebp	1	1.24	-11.24	-11.07	...
176	PHR1539-5325	...	G326.4+01.5	15 39 46.82	-53 25 25.4	326.47	1.58	180	138	A	3	1.1	-12.0	...	...
177	HFG 2	PHR 0742-3247	G247.5-04.7	07 42 23.81	-32 47 50.4	247.58	-4.70	181	153	Eas	1/2	0.02	-11.53	-10.83	...
178	NGC 2440	...	G234.8+02.4	07 41 55.4	-18 12 33	234.84	2.42	59	25	Baps	2	0.45	-9.89	-9.32	25
179	H 1-7	...	G345.2-01.2	17 10 27.39	-41 52 49.4	345.28	-1.25	11	9	Ep	1	2.2	-10.8	-10.85	...
180	NGC 3211	...	G286.3-04.8	10 17 50.55	-62 40 14.6	286.30	-4.87	16	16	Em	1	0.32	-10.51	-9.88	27
181	H 1-13	...	G352.8-00.2	17 28 27.54	-35 07 31.6	352.83	-0.26	14	12	E	1	2.8	-11.4	-11.39	...
182	NGC 5979	...	G322.5-05.2	15 47 41.55	-61 13 06.3	322.58	-5.26	20	19	Em(h)	1	0.48	-10.66	-10.18	...
183	Abell 13	YM 28	G204.0-08.5	06 04 47.90	+03 56 35.8	204.02	-8.52	205	140	E/Bar(h:)	2	0.78	-11.32	-11.88	20
184	PHR1658-2515	...	G357.1+10.8	16 58 21.4	-25 15 44	357.10	10.76	302	302	Er	1	0.46	-12.1	...	...
185	PHR1911-1546	...	G020.9-11.3	19 11 04.46	-15 46 07.0	20.903	-11.373	157	154	R	1	0.23	-11.43	-10.77	...
186	FP0739-2709	...	G242.3-02.4	07 39 38.12	-27 09 30.3	242.49	-2.25	390	330	Eas	2	0.22	-11.39	-12.21	...
187	H 1-12	...	G352.6+00.1	17 26 24.24	-35 01 41.3	352.67	0.14	12	10	E	1	3.5	-11.76	-11.92	...
188	PHR1136-5235	...	G291.5+08.6	11 36 00.0	-52 35 33	291.47	8.64	268	201	Ea	2	0.3	-11.8	-11.87	...
189	NGC 7048	...	G088.7-01.6	21 14 15.22	+46 17 17.5	88.78	-1.68	63	60	Eab(h)	2	0.38	-10.85	-10.43	15
190	Lo 8	K 1-29	G310.3+24.7	13 25 37.51	-37 36 14.9	310.38	24.77	132	108	Ea	2	0.04	-11.81	-11.58	...
191	M 1-75	...	G068.8+00.0	20 04 44.09	+31 27 24.4	68.86	-0.04	63	23	Bp	1	2.49	-11.65	-11.50	...
192	K 2-7	...	G019.4-19.6	19 40 29.10	-20 27 05.9	19.41	-19.66	159	140	E/Ra	2	0.19	-11.90	...	...
193	CVMP 1	...	G321.6+02.2	15 09 25.17	-55 33 05.3	321.63	2.22	258	135	Baps(h:)	2	1.23	-11.60	-11.50	...
194	LTNF 1	BE UMa, Tw 1	G144.8+65.8	11 57 44.78	+48 56 18.7	144.81	65.85	230	215	Eab?	2	0.05	-12.2	-11.32	...
195	NGC 6537	...	G010.0+00.7	18 05 13.10	-19 50 34.9	10.10	0.74	11	10	Bmps	1	1.96	-10.49	-10.60	18
196	NGC 6629	...	G009.4-05.0	18 25 42.45	-23 12 10.6	9.41	-5.05	17	16	Em(h)	1/2	0.83	-10.18	-10.09	6
197	NGC 6751	...	G029.2-05.9	19 05 55.56	-05 59 32.9	29.23	-5.94	24	23	Emp(h:)	1	0.56	-10.60	-10.37	36
198	WeBo 1	...	G135.6+01.0	02 40 14.35	+61 09 17.0	135.67	1.00	64	22	Br?	1	0.86	-12.02	...	11
199	NGC 3195	...	G296.6-20.0	10 09 20.91	-80 51 30.7	296.62	-20.04	40	34	Ep	1	0.12	-10.38	-10.24	26
200	PHR0905-4753	Bran 229	G268.9-00.4	09 05 41.04	-47 54 05.2	268.97	-0.49	132	125	Eap	2	0.77	-11.72	-11.29	...
201	MeWe 1-1	ESO 165-6	G272.4-05.9	08 53 36.86	-54 05 09.8	272.14	-5.97	148	133	Ea	2	0.20	-11.40	-11.06	...
202	NGC 2792	...	G265.7+04.1	09 12 26.60	-42 25 39.9	265.75	4.10	18	16	Emp(h)	1	0.58	-10.58	-10.31	20
203	Abell 30	...	G208.5+33.2	08 46 53.51	+17 52 45.5	208.56	33.29	127	127	Rs	1	0.04	-11.81	-11.58	40
204	HaTr 1	...	G299.4-04.1	12 16 33.14	-66 45 45.1	299.49	-4.12	76	73	Ea	2	1.20	-11.63	-12.06	...
205	Wr 16-121	Lo 7, VBRC 4	G302.6-00.9	12 48 31.28	-63 49 57.9	302.61	-0.96	65	54	E/Baps	2	1.86	-11.51	-11.33	...
206	PHR1032-6310	WHI B1030-62	G287.9-04.4	10 32 14.4	-63 10 22	287.96	-4.42	180	175	Eas	2	0.30	-11.65	-11.57	...
207	IC 4406	...	G319.6+15.7	14 22 26.28	-44 09 04.4	319.69	15.74	46	30	Bps	1	0.30	-10.18	-9.72	7
208	BlDz 1	...	G293.6+10.9	11 53 06.60	-50 50 59.2	293.62	10.96	94	94	Ra	2	0.20	-11.13	-10.56	...

Continued on next page

Table 9.4 – continued from previous page

No.	Name	Other	PN G	α	δ	l	b	a (")	b (")	Mor.	WZO	c	F(Hα)	F(5007)	V_{exp} kms^{-1}
209	HaTr 9	...	G351.0-10.4	18 08 58.86	-41 48 37.6	351.09	-10.47	160	152	Ear	2	0.19	-11.49	...	...
210	Abell 43	...	G036.0+17.6	17 53 32.27	+10 37 23.7	36.06	17.62	80	80	E/Rs	1	0.25	-11.82	-11.48	...

Table 9.5: Derived Quantities (2.0 kpc sample)

No.	Name	$\log \mathrm{S}_0(\mathrm{H}\alpha)$	D (kpc)	meth	q (pc)	z (pc)	EC	M_α	M_β	M_{5007}	Radius (pc)	Mass ($M_\odot$)	$\log(n_e)$ cm^{-2}	Age (10^3yr)	log(N/O)	Type
1	Sh 2-216	-5.45	0.13	c	129	1	0.5	1.16	3.53	3.49	1.78	1.99	0.85	348	-0.69	...
2	NGC 7293	-4.02	0.22	c	119	-184	4.9	0.53	2.90	1.00	0.46	0.35	1.86	21	-0.28	...
3	FP1824-0319	-6.01	0.36	m	362	28	0.6	3.00	5.37	5.05	1.45	0.62	0.61	118	...	...
4	NGC 1514	-3.28	0.37	c	357	-98	5.3	1.56	3.92	1.25	0.12	0.03	2.51	5	...	C?
5	PuWe 1	-5.53	0.37	c	353	114	1.5	2.44	4.81	3.53	1.09	0.53	0.91	46	...	...
6	M 27	-3.42	0.38	c	378	-24	6.1	-0.51	1.84	-0.68	0.37	0.41	2.20	11	-0.47	...
7	NGC 1360	-4.06	0.38	c	224	-307	9.9	1.48	3.85	1.68	0.31	0.12	1.92	9	...	C?
8	Abell 36	-4.91	0.45	c	337	298	10.9	2.96	5.34	3.84	0.42	0.10	1.43	11	...	...
9	Abell 31	-5.31	0.48	c	411	250	6.0	1.72	4.09	2.13	1.18	0.83	1.00	40	-0.40	...
10	NGC 246	-4.11	0.50	c	131	-477	11.0	1.73	4.09	1.84	0.29	0.10	1.91	8	...	...
11	MWP 1	-5.17	0.50	c	489	-90	10.4	2.25	4.62	3.11	0.78	0.35	1.17	25	...	...
12	LoTr 5	-5.54	0.50	c	13	500	3.3	3.61	5.98	3.83	0.64	0.14	1.03	20	...	C?
13	Abell 7	-5.54	0.51	c	441	-264	6.0	2.62	5.00	3.21	1.01	0.43	0.92	34	...	...
14	IPHAS2050+4655	-4.04	0.52	m	519	17	7.1	0.78	3.15	1.18	0.42	0.27	1.86	...	...	...
15	PFP 1	-6.02	0.54	m	534	36	2.6	3.02	5.39	3.50	1.46	0.63	0.60	48	-0.23	...
16	Abell 21	-4.72	0.54	c	524	133	5.8	0.86	3.23	1.37	0.89	0.80	1.36	27	-0.12	...
17	FP0905-3033	-5.62	0.57	m	560	108	2.0	2.63	5.00	3.43	1.13	0.54	0.82	48	...	...
18	TK 1	-6.65	0.57	c	478	311	1.2	3.14	5.51	4.49	2.84	1.61	0.14	185	...	...
19	Jacoby 1	-6.03	0.57	c	348	451	8.5	4.07	6.44	4.76	0.91	0.19	0.70	30	...	...
20	EGB 6	-5.73	0.59	c	407	427	1.4	3.06	5.43	4.19	1.03	0.36	0.83	40	...	...
21	HFG 1	-4.80	0.60	c	597	58	9.4	1.31	3.68	1.34	0.79	0.55	1.35	51	...	C
22	IsWe 1	-5.59	0.62	m	616	-37	0.9	2.53	4.90	4.23	1.11	0.52	0.88	91	...	...
23	IsWe 2	-5.21	0.62	c	614	84	0.5	1.09	3.46	3.43	1.40	1.43	1.02	114	...	...
24	FP0711-2531	-5.56	0.63	m	623	-79	1.3	2.50	4.87	3.72	1.09	0.52	0.90	...	-0.84	...
25	Sh 2-78	-4.86	0.64	h	639	43	0.9	0.92	3.29	2.61	1.01	0.95	1.26	49	...	...
26	EGB 1	-5.30	0.65	c	639	121	2.0	2.33	4.70	3.13	0.87	0.40	1.08	...	...	...
27	Sh 2-200	-4.83	0.66	c	658	47	6.4	2.08	4.45	1.62	0.57	0.24	1.40	43	...	...
28	M 57	-2.41	0.70	c	683	170	6.5	-0.67	1.72	-0.83	0.13	0.09	2.94	6	-0.44	...
29	NGC 7008	-2.97	0.70	l	701	67	10.3	0.29	2.81	0.76	0.15	0.08	2.62	4	-0.50	...
30	NGC 1501	-2.49	0.72	c	715	82	8.2	0.28	2.80	-0.19	0.09	0.03	2.98	2	...	...
31	DS 1	-4.81	0.73	c	715	123	10.4	1.98	4.35	2.30	0.59	0.26	1.40	19	...	C
32	Abell 74	-5.58	0.75	c	717	-221	0.9	1.95	4.32	3.55	1.44	1.01	0.82	54	...	...
33	M 97	-3.88	0.76	m	413	637	5.1	0.60	2.86	0.66	0.38	0.25	1.97	11	-0.68	...

Continued on next page

Table 9.5 – continued from previous page

No.	Name	$\log S_0(H\alpha)$	D (kpc)	method	q (pc)	z (pc)	EC	M_α	M_β	M_{5007}	Radius (pc)	Mass ($M_\odot$)	$\log(n_e)$ cm^{-2}	Age (10^3yr)	log(N/O)	Type
34	Lo 1	-5.49	0.76	l	385	-658	7.6	3.07	5.44	3.50	0.78	0.24	1.00	25	...	...
35	Sh 2-176	-5.40	0.78	h	776	-74	0.8	1.47	3.84	3.27	1.46	1.29	0.91	65	...	...
36	HbDs 1	-4.88	0.80	c	790	86	10.4	3.71	6.08	4.88	0.29	0.04	1.53	...	...	...
37	K 2-2	-5.15	0.80	c	797	66	3.5	1.24	3.61	1.37	1.21	1.07	1.08	118	-0.47	...
38	HaWe 4	-5.81	0.80	c	790	-129	4.9	2.85	5.22	2.65	1.24	0.53	0.75	110	...	...
39	NGC 3132	-2.66	0.81	c	791	174	5.0	-0.21	2.16	0.02	0.13	0.08	2.80	6	-0.31	...
40	Sh 2-188	-4.61	0.83	c	823	-59	0.9	-0.26	2.11	1.45	1.31	2.42	1.33	71	-0.45	...
41	Abell 24	-5.13	0.83	m	803	211	5.8	2.01	4.38	3.62	0.83	0.43	1.17	41	0.46	I
42	Lo 16	-3.30	0.84	l	843	-62	6.0	0.84	3.21	0.75	0.17	0.07	2.42	...	...	...
43	WDHS 1	-5.73	0.85	c	845	-95	...	1.23	3.60	...	2.39	3.00	0.64	138	...	I?
44	IC 5148/50	-3.94	0.85	l	519	-674	6.8	1.49	3.86	2.41	0.27	0.10	2.01	5	...	...
45	NGC 6337	-2.47	0.86	l	862	-17	7.9	0.00	2.78	0.26	0.10	0.04	2.96	12	...	C
46	NGC 7027	0.07	0.89	c	888	-54	6.6	-3.92	-1.641	-4.44	0.03	0.05	4.48	1.4	-0.25	...
47	NGC 2346	-3.00	0.90	c	898	57	5.5	0.63	2.96	0.45	0.14	0.05	2.63	11	-0.52	C
48	Jones 1	-4.95	0.90	m	785	-447	7.1	1.80	4.17	1.97	0.74	0.40	1.29	20	-0.17	...
49	FP1721-5654	-5.24	0.93	m	908	-181	1.9	2.14	4.51	3.00	0.89	0.45	1.10	...	...	...
50	NGC 6781	-3.06	0.95	c	949	-50	5.0	-1.12	1.25	-0.76	0.32	0.44	2.41	26	-0.27	...
51	NGC 4361	-3.47	0.95	c	688	655	10.7	0.31	2.55	1.13	0.27	0.17	2.24	8	-0.90	...
52	EGB 9	-5.37	0.99	l	981	164	...	2.95	5.32	...	0.72	0.22	1.08	...	...	...
53	NGC 3242	-1.78	1.00	c	848	531	5.8	-1.80	0.58	-2.24	0.10	0.11	3.30	4	-0.96	...
54	RCW 24	-5.26	1.00	c	1000	-23	6.1	1.47	3.84	2.98	1.24	1.01	1.02	...	0.44	I
55	DS 2	-5.16	1.00	c	976	216	10.4	3.36	5.73	3.24	0.46	0.10	1.29	...	...	...
56	HaWe 13	-4.55	1.01	c	993	-184	...	3.85	6.22	...	0.18	0.02	1.79	...	...	...
57	NGC 40	-1.95	1.02	m	1007	175	0.7	-1.58	0.79	0.35	0.11	0.11	3.20	4	-0.61	...
58	Abell 34	-5.36	1.03	l	897	508	6.5	2.94	5.31	3.09	0.71	0.22	1.09	20	...	...
59	MeWe 2-4	-5.46	1.07	m	1055	199	1.4	2.38	4.75	3.56	1.02	0.49	0.96	...	...	...
60	PHR1625-4523	-5.11	1.08	m	1079	50	1.3	1.99	4.37	3.29	0.82	0.43	1.18	...	...	...
61	Abell 66	-4.93	1.10	m	1002	-442	2.2	1.79	4.16	2.46	0.74	0.40	1.30	...	...	...
62	NGC 6153	-1.15	1.10	m	1093	104	5.6	-2.48	-0.09	-2.48	0.07	0.08	3.71	4	-0.24	...
63	Abell 6	-4.27	1.10	m	1097	95	...	1.04	3.41	0.23	0.48	0.30	1.72	...	...	...
64	Sp 1	-3.49	1.13	l	1132	39	8.9	1.03	2.96	0.76	0.20	0.08	2.30	6	...	C
65	PHR1418-5144	-5.53	1.14	m	1122	174	3.4	2.46	4.84	2.68	1.07	0.51	0.92	...	...	...
66	He 2-11	-2.80	1.14	h	1140	19	5.2	-1.16	1.58	-1.02	0.24	0.29	2.60	...	...	...
67	Sh 2-71	-3.11	1.14	h	1140	-27	8.0	-0.85	1.52	-0.99	0.30	0.35	2.40	14	0.58	I
68	BMP0642-0417	-6.49	1.15	m	1146	-80	0.6	3.55	5.92	5.63	1.96	0.77	0.30	...	-0.30	...

Continued on next page

Table 9.5 – continued from previous page

No.	Name	$\log S_0(H\alpha)$	D (kpc)	method	q (pc)	z (pc)	EC	M_α	M_β	M_{5007}	Radius (pc)	Mass ($M_\odot$)	$\log(n_e)$ cm^{-2}	Age (10^3yr)	log(N/O)	Type
69	JnEr 1	-4.98	1.15	c	984	595	5.8	1.13	3.50	1.71	1.06	0.93	1.19	43	-0.41	...
70	Abell 33	-5.11	1.16	c	952	663	7.5	2.08	4.45	2.75	0.78	0.38	1.19	24	-0.60	...
71	Kronberger 9	-5.36	1.17	l	1169	-16	9.9	2.93	5.30	3.55	0.71	0.22	1.09	...	...	...
72	NGC 6302	-1.57	1.17	c	1170	22	7.6	-3.30	-0.93	-3.76	0.16	0.41	3.31	...	0.10	I
73	Abell 65	-4.11	1.17	l	1089	-439	6.4	1.66	4.03	1.59	0.30	0.11	1.90	27	-1.04	C
74	PHR1432-6138	-4.89	1.19	m	1185	-22	1.7	1.74	4.11	2.72	0.71	0.39	1.32	...	...	...
75	NGC 6772	-3.02	1.20	m	1189	-133	6.0	-0.37	2.00	-0.73	0.22	0.17	2.52	19	...	...
76	IC 418	-0.27	1.20	c	1094	-493	0.8	-3.33	-0.96	-1.53	0.04	0.05	4.28	3	-0.57	...
77	M 76	-3.49	1.20	c	1180	-219	7.3	-0.47	2.19	-0.62	0.40	0.44	2.15	10	-0.27	...
78	M 1-26	0.01	1.20	l	1200	-15	0.2	-2.53	-0.09	1.08	0.02	0.01	4.57	1	-0.87	...
79	Abell 28	-5.77	1.22	l	972	737	6.0	3.35	5.72	5.28	0.94	0.28	0.82	115	...	...
80	IC 1295	-3.68	1.23	c	1226	-101	7.3	0.65	3.02	-0.12	0.30	0.17	2.12	11	...	...
81	NGC 7662	-1.60	1.26	m	1203	-382	6.8	-1.97	0.33	-2.41	0.09	0.10	3.42	3	-0.72	...
82	PHR1118-6150	-5.34	1.26	m	1262	-20	1.1	2.25	4.62	3.71	0.95	0.47	1.04	...	...	...
83	HaWe 15	-5.29	1.27	m	1259	-197	...	2.19	4.56	...	0.92	0.46	1.07	...	...	...
84	NGC 2392	-2.33	1.28	m	1221	383	6.8	-1.15	1.13	-1.25	0.14	0.13	2.95	3	-0.54	...
85	YM 16	-4.88	1.29	h	1287	45	2.0	0.94	3.31	1.79	1.02	0.96	1.25	...	0.0	I?
86	NGC 6826	-1.42	1.30	m	1264	287	3.4	-2.18	0.19	-1.98	0.08	0.09	3.53	5	-0.87	...
87	IC 4637	-1.48	1.30	l	1296	3	4.1	-1.00	1.65	-0.68	0.05	0.03	3.60	2	...	...
88	BD+30 3639	0.10	1.30	c	1295	114	0.0	-2.80	-0.31	2.78	0.02	0.01	4.61	1	-0.60	...
89	RCW 69	-4.39	1.30	c	1300	8	6.4	0.44	2.81	1.24	0.73	0.73	1.57	55	0.33	I
90	MeWe 1-2	-5.14	1.30	m	1304	-32	0.9	2.02	4.39	3.64	0.84	0.43	1.16	...	...	...
91	NGC 6894	-2.71	1.31	c	1309	-60	6.7	-0.64	1.95	-0.19	0.17	0.14	2.72	4	-0.44	I?
92	Abell 61	-5.20	1.31	m	1270	335	2.3	2.77	5.14	3.39	0.64	0.20	1.20	21	...	...
93	NGC 6026	-3.15	1.31	l	1277	311	7.4	0.69	2.92	0.95	0.16	0.06	2.52	6	...	C
94	Abell 45	-4.75	1.32	h	1320	-15	...	0.81	3.18	...	0.93	0.95	1.37	...	...	I
95	Abell 71	-3.86	1.33	h	1324	104	5.9	-0.09	2.37	1.03	0.51	0.54	1.91	25	0.38	I
96	K 1-22	-4.61	1.33	c	1202	569	3.4	1.34	3.71	1.52	0.62	0.38	1.49	22	-0.89	...
97	BMP0733-3108	-5.78	1.34	h	1330	-130	...	1.85	4.22	...	1.90	1.60	0.67	...	...	I
98	NGC 2899	-3.39	1.37	h	1369	-92	8.7	-0.56	1.81	-0.35	0.37	0.41	2.22	14	0.15	I
99	PHR0743-1951	-5.66	1.37	m	1374	48	0.5	2.61	4.98	4.93	1.16	0.54	0.83	...	...	...
100	HaTr 7	-5.15	1.38	l	1319	-401	5.3	2.72	5.09	2.42	0.61	0.20	1.23	...	...	...
101	Abell 62	-4.44	1.38	m	1379	-109	5.4	1.24	3.61	2.90	0.54	0.32	1.61	35	...	...
102	NGC 6445	-1.94	1.39	h	1385	95	6.2	-2.02	0.35	-2.36	0.14	0.18	3.16	3	0.10	I
103	NGC 6072	-2.74	1.39	h	1364	261	5.7	-1.22	1.42	-1.28	0.23	0.28	2.64	23	-0.36	...

Continued on next page

Table 9.5 – continued from previous page

No.	Name	$\log \mathrm{S}_0(\mathrm{H}\alpha)$	D (kpc)	method	q (pc)	z (pc)	EC	M_α	M_β	M_{5007}	Radius (pc)	Mass ($M_\odot$)	$\log(n_e)$ cm^{-2}	Age (10^3yr)	log(N/O)	Type
104	Abell 29	-5.39	1.39	h	1356	303	5.4	1.46	3.83	2.44	1.46	1.28	0.92	71	>0.0	I
105	NGC 7094	-4.43	1.39	c	1225	-657	11.0	2.21	4.58	2.91	0.34	0.10	1.72	8		...
106	Abell 39	-5.09	1.40	c	1029	942	9.6	2.66	5.03	2.36	0.59	0.19	1.27	20	-0.75	...
107	Wray 17-31	-4.31	1.40	m	1396	-87	5.5	1.08	3.45	1.40	0.49	0.30	1.70	17	-0.24	...
108	BMP1808-1406	-5.53	1.40	h	1400	69	...	1.60	3.97	...	1.60	1.38	0.83	...	...	...
109	NGC 2371-72	-2.90	1.41	c	1326	479	9.9	0.44	2.81	0.59	0.13	0.06	2.68	3	-0.57	...
110	PHR1040-5417	-5.17	1.41	m	1409	95	2.8	2.06	4.43	2.46	0.85	0.44	1.14	...	...	...
111	NGC 2438	-3.37	1.42	m	1421	102	6.5	0.03	2.40	0.19	0.27	0.20	2.29	12	-0.47	...
112	NGC 5189	-3.10	1.44	c	1437	-87	6.9	-1.80	0.58	-2.09	0.46	1.03	2.31	18	-0.10	I
113	Lo 5	-4.41	1.44	m	1411	294	3.4	1.20	3.57	1.39	0.53	0.32	1.63	...	...	...
114	NGC 7009	-1.26	1.45	c	1194	-823	5.0	-2.76	-0.38	-3.04	0.09	0.13	3.59	3	-0.54	...
115	Sh 2-42	-4.04	1.46	m	1463	30	...	0.78	3.15	...	0.42	0.27	1.86	...	...	...
116	PHR0942-5220	-4.50	1.46	m	1464	11	3.1	1.30	3.67	1.66	0.56	0.33	1.57	...	...	...
117	NGC 6804	-2.78	1.47	m	1463	-117	9.1	-0.64	1.73	-0.63	0.19	0.16	2.67	7	...	...
118	M 1-41	-2.08	1.47	h	1468	-58	6.8	-1.88	0.49	-2.40	0.15	0.20	3.07	...	0.26	I
119	HaTr 5	-4.02	1.47	m	1473	-17	...	0.76	3.13	...	0.41	0.27	1.88	...	...	...
120	NGC 7076	-3.51	1.47	l	1457	224	8.8	1.06	3.43	0.55	0.20	0.08	2.29	5	...	...
121	G4.4+6.4	-4.58	1.48	h	1471	165	2.4	0.64	3.01	1.26	0.83	0.81	1.44	...	...	...
122	K 1-6	-5.02	1.48	m	1380	540	...	1.89	4.26	...	0.78	0.41	1.24	...	...	...
123	He 2-36	-2.16	1.49	l	1488	-83	5.3	-0.32	2.05	-1.31	0.08	0.04	3.17	2	-0.67	...
124	PHR1510-6754	-5.28	1.49	m	1476	-221	1.5	2.18	4.56	3.29	0.92	0.46	1.07	...	...	...
125	K 2-1	-4.27	1.50	m	1488	-153	8.5	1.04	3.41	0.86	0.48	0.30	1.72	...	-0.93	...
126	SuWt 2	-4.16	1.50	c	1499	65	3.8	2.44	4.81	2.55	0.22	0.05	1.94	...	...	I,C?
127	NGC 6543	-1.11	1.50	c	1300	749	2.9	-3.27	-0.90	-2.91	0.09	0.18	3.66	5	-0.38	...
128	We 2-34	-5.52	1.51	m	1503	104	0.9	2.46	4.83	4.07	1.07	0.51	0.92	...	...	...
129	VBRC 5	-3.29	1.52	m	1518	37	5.2	-0.07	2.30	-0.17	0.26	0.20	2.35	...	...	...
130	IC 2149	-1.00	1.52	l	1495	277	2.1	-1.49	0.88	-0.77	0.04	0.02	3.92	2	-0.85	...
131	Abell 80	-4.40	1.52	m	1517	-133	1.4	1.18	3.47	2.31	0.52	0.31	1.64	28	...	...
132	BMP1651-3930	-5.64	1.53	m	1530	81	...	2.59	4.96	...	1.15	0.54	0.84	...	...	...
133	Abell 59	-3.63	1.54	m	1534	82	3.3	0.32	2.69	0.71	0.32	0.23	2.13	...	...	...
134	NGC 6369	-1.14	1.55	c	1542	158	4.6	-3.83	-1.46	-4.40	0.12	0.36	3.58	3	-0.48	...
135	IC 4593	-1.67	1.57	l	1186	1025	2.3	-0.82	1.56	-0.18	0.06	0.03	3.48	5	-1.22	...
136	NGC 6905	-2.72	1.58	c	1558	-263	9.0	-0.29	2.08	-0.16	0.15	0.10	2.75	4	-0.80	...
137	Fr 2-8	-4.66	1.58	l	1555	284	9.3	2.23	4.60	2.85	0.44	0.15	1.54	...	...	...
138	BMP0815-4053	-5.72	1.58	m	1559	-267	...	2.68	5.05	...	1.21	0.55	0.79	...	...	...

Continued on next page

Table 9.5 – continued from previous page

No.	Name	$\log S_0(H\alpha)$	D (kpc)	method	q (pc)	z (pc)	EC	M_α	M_β	M_{5007}	Radius (pc)	Mass ($M_\odot$)	$\log(n_e)$ cm^{-2}	Age (10^3yr)	log(N/O)	Type
139	KjPn 8	-5.28	1.60	c	1600	-4	...	0.75	3.12	...	1.78	2.40	0.93	...	-0.32	...
140	NGC 7354	-1.31	1.60	c	1599	65	6.3	-2.67	-0.30	-2.98	0.09	0.13	3.57	3	-0.47	...
141	We 3-1	-4.75	1.62	m	1594	295	2.1	1.58	3.95	2.31	0.65	0.37	1.41	...	...	...
142	NGC 6818	-1.74	1.64	m	1556	-503	7.1	-1.82	0.55	-2.48	0.10	0.10	3.33	4	-0.58	...
143	PHR1602-4127	-4.96	1.65	m	1635	243	1.5	1.83	4.20	2.90	0.75	0.40	1.28	...	...	...
144	K 1-16	-4.88	1.67	c	1482	769	1.8	2.69	5.00	3.51	0.46	0.13	1.43	...	...	...
145	NGC 6563	-2.90	1.67	m	1657	-213	5.4	-0.50	2.26	-0.12	0.20	0.17	2.59	18	-0.49	...
146	NGC 6567	-0.65	1.68	c	1680	-19	4.2	-1.93	0.44	-1.92	0.03	0.02	4.14	2	-0.64	...
147	Abell 84	-4.42	1.68	m	1654	-299	5.3	1.21	3.53	1.12	0.53	0.32	1.63	32	-0.52	...
148	Hb 5	-1.52	1.70	c	1700	-29	7.3	-2.92	-0.24	-2.97	0.13	0.25	3.39	...	0.24	I
149	Abell 46	-4.42	1.70	c	1634	469	1.5	1.99	4.36	3.05	0.37	0.13	1.70	...	-1.14	C
150	K 1-27	-4.81	1.70	c	1478	-839	10.7	4.08	6.45	5.39	0.22	0.02	1.62	...	...	...
151	NGC 5882	-1.08	1.70	c	1674	298	4.3	-2.34	0.04	-2.38	0.06	0.06	3.77	...	-0.48	...
152	PHR1408-6106	-5.25	1.70	c	1700	12	0.7	1.56	3.93	3.44	1.17	0.88	1.04	...	...	...
153	IC 4642	-2.41	1.71	l	1685	-277	10.4	-0.06	2.40	0.51	0.09	0.04	3.00	...	...	...
154	HaWe 11	-2.49	1.71	m	1706	80	...	-0.97	1.40	-1.33	0.16	0.14	2.85	...	...	...
155	NGC 2610	-3.53	1.72	l	1672	415	10.1	1.07	3.53	1.83	0.20	0.08	2.28	8	...	...
156	Patchick 5	-4.94	1.75	l	1699	427	2.7	2.51	4.88	2.93	0.53	0.18	1.36	...	...	...
157	Abell 72	-5.07	1.75	l	1660	-563	10.4	2.64	5.01	3.18	0.58	0.19	1.28	...	...	...
158	NGC 4071	-3.40	1.77	m	1764	-150	5.5	0.05	2.43	0.00	0.28	0.21	2.27	17	...	...
159	Abell 51	-4.05	1.78	l	1756	-317	9.3	1.60	3.97	2.57	0.29	0.11	1.94	7	...	...
160	WeSb 2	-4.75	1.79	m	1785	173	...	1.59	3.96	...	0.66	0.37	1.41	...	...	...
161	IPHAS 0156+6528	-5.11	1.80	m	1797	108	...	1.99	4.36	...	0.82	0.43	1.18	...	...	...
162	He 2-84	-2.61	1.80	c	1800	-31	5.8	-0.21	2.16	-1.40	0.13	0.07	2.84	...	0.08	I
163	We 1-10	-5.14	1.82	m	1807	173	...	2.02	4.39	...	0.84	0.43	1.17	...	...	...
164	PHR1619-4914	-2.00	1.82	h	1823	22	...	-1.96	0.41	...	0.14	0.19	3.12	0.8	...	I?
165	Fg 1	-2.93	1.82	m	1806	252	6.0	-0.47	1.98	-0.22	0.21	0.17	2.57	...	-0.37	...
166	Abell 82	-4.31	1.82	m	1818	-149	5.2	1.08	3.45	1.03	0.49	0.30	1.70	...	-0.28	...
167	NGC 5844	-2.97	1.83	h	1821	-182	6.3	-0.99	1.38	-1.84	0.27	0.32	2.49	...	-0.11	...
168	Kronberger 24	-5.08	1.83	m	1813	-248	...	1.96	4.33	...	0.81	0.42	1.20	...	...	...
169	NGC 3918	-1.01	1.84	c	1834	151	6.5	-3.19	-0.82	-3.88	0.08	0.14	3.74	3	-0.41	...
170	PHR1533-4824	-5.30	1.84	m	1833	200	1.1	2.20	4.57	3.56	0.93	0.46	1.06	...	...	...
171	HaWe 9	-5.22	1.85	m	1815	-341	...	2.12	4.49	...	0.88	0.45	1.11	...	...	...
172	Abell 78	-4.91	1.85	l	1790	-477	14.7	2.48	4.82	2.02	0.52	0.17	1.38	19	...	...
173	NGC 6572	-0.58	1.86	c	1820	382	4.9	-3.75	-1.38	-3.95	0.06	0.13	4.01	4	-0.32	...

Continued on next page

Table 9.5 – continued from previous page

No.	Name	$\log S_0(H\alpha)$	D (kpc)	method	q (pc)	z (pc)	EC	M_α	M_β	M_{5007}	Radius (pc)	Mass ($M_\odot$)	$\log(n_e)$ cm^{-2}	Age (10^3yr)	log(N/O)	Type
174	We 2-5	-5.17	1.89	m	1885	-68	...	2.05	4.42	...	0.85	0.44	1.15	...	...	...
175	M 2-55	-3.03	1.89	m	1871	281	4.8	-0.36	2.01	-0.45	0.22	0.18	2.51	...	-0.08	I
176	PHR1539-5325	-4.91	1.90	m	1899	52	...	1.77	4.14	...	0.73	0.39	1.31	...	...	...
177	HFG 2	-5.22	1.90	c	1894	-156	9.9	2.43	4.80	1.89	0.77	0.31	1.14	...	...	...
178	NGC 2440	-2.02	1.90	c	1898	80	7.8	-2.40	-0.03	-2.92	0.18	0.32	3.06	7	0.06	I
179	H 1-7	-0.49	1.91	m	1909	-42	5.4	-3.23	-0.86	-3.35	0.04	0.06	4.13	...	...	...
180	NGC 3211	-1.97	1.91	c	1903	-162	8.6	-0.64	1.73	-1.22	0.07	0.04	3.28	3	-0.70	...
181	H 1-13	-0.94	1.91	m	1910	-9	...	-2.73	-0.36	-3.38	0.06	0.07	3.84	...	...	...
182	NGC 5979	-2.19	1.93	c	1922	-177	9.8	-0.56	1.81	-0.87	0.09	0.05	3.12	...	-0.47	...
183	Abell 13	-4.51	1.93	h	1913	-287	0.6	0.57	2.94	2.64	0.79	0.78	1.49	39	0.33	I
184	PHR1658-2515	-5.97	1.94	m	1901	361	...	2.96	5.34	...	1.42	0.62	0.63	...	...	...
185	PHR1911-1546	-4.92	1.94	m	1899	-382	...	1.78	4.15	1.21	0.73	0.39	1.30	...	...	...
186	FP0739-2709	-5.61	1.94	h	1942	-76	0.2	1.68	4.05	4.80	1.69	1.45	0.78	...	-0.09	I
187	H 1-12	-0.73	1.94	m	1944	5	...	-2.96	-0.59	-3.81	0.05	0.07	3.98	...	...	...
188	PHR1136-5235	-5.58	1.96	m	1941	295	1.4	2.52	4.89	3.70	1.11	0.52	0.88	...	...	...
189	NGC 7048	-3.44	1.97	c	1969	-58	7.4	0.04	2.41	-0.05	0.29	0.22	2.24	19	...	...
190	Lo 8	-5.20	1.99	c	1807	834	2.3	2.99	5.36	3.61	0.58	0.16	1.22	...	...	...
191	M 1-75	-2.38	1.99	h	1992	-1	8.8	-1.57	0.80	-2.50	0.18	0.23	2.87	...	0.36	I
192	K 2-7	-5.38	1.99	l	1878	-671	...	2.96	5.33	...	0.72	0.22	1.07	...	...	...
193	CVMP 1	-4.57	2.00	c	1998	78	6.8	0.43	2.80	0.55	0.90	1.01	1.43	...	0.47	I
194	LTNF 1	-6.13	2.00	c	818	1825	...	3.94	6.31	2.93	1.08	0.26	0.62	...	...	C
195	NGC 6537	-0.46	2.00	c	2000	26	7.9	-3.58	-1.21	-3.47	0.05	0.09	4.11	3	0.40	I
196	NGC 6629	-1.29	2.00	c	1992	-176	2.9	-2.45	-0.08	-2.02	0.08	0.10	3.61	14	-0.85	...
197	NGC 6751	-2.23	2.00	c	1989	-207	3.3	-0.93	1.44	-0.67	0.11	0.09	3.05	3	-0.55	...
198	WeBo 1	-3.85	2.00	c	2000	35	...	2.11	4.48	...	0.18	0.04	2.14	16	...	C?
199	NGC 3195	-2.69	2.01	m	1889	-689	4.9	-0.75	2.09	0.05	0.18	0.15	2.73	7	-0.49	...
200	PHR0905-4753	-4.68	2.01	m	2011	-17	7.6	1.50	3.87	1.10	0.63	0.35	1.46	...	-0.21	...
201	MeWe 1-1	-4.82	2.02	m	2006	-210	3.3	1.67	4.04	1.91	0.69	0.38	1.37	...	...	...
202	NGC 2792	-1.92	2.02	c	2015	144	9.0	-1.03	1.34	-0.89	0.08	0.06	3.27	4	-0.74	...
203	Abell 30	-5.25	2.02	c	1689	1109	11.6	2.96	5.33	3.58	0.62	0.18	1.17	15	-0.51	...
204	HaTr 1	-3.82	2.02	m	2016	-145	1.2	0.54	2.91	1.99	0.36	0.25	2.00	...	...	I?
205	Wr 16-121	-3.06	2.03	h	2032	-34	7.3	-0.90	1.47	-1.44	0.29	0.34	2.43	...	...	I?
206	PHR1032-6310	-5.21	2.03	m	2029	-157	2.0	2.10	4.47	2.91	0.88	0.44	1.12	...	...	...
207	IC 4406	-2.38	2.04	h	1960	552	4.4	-1.57	0.74	-1.71	0.18	0.23	2.87	26	-0.45	...
208	BlDz 1	-4.21	2.04	m	2001	388	5.5	0.97	3.34	0.64	0.46	0.29	1.76	...	...	...

Continued on next page

Table 9.5 – continued from previous page

No.	Name	$\log S_0(H\alpha)$	D (kpc)	method	q (pc)	z (pc)	EC	M_α	M_β	M_{5007}	Radius (pc)	Mass ($M_\odot$)	$\log(n_e)$ cm^{-2}	Age (10^3yr)	log(N/O)	Type
209	HaTr 9	-5.01	2.04	m	2010	-372	...	1.88	4.25	...	0.77	0.41	1.25	...	...	...
210	Abell 43	-4.72	2.05	c	1954	621	9.5	2.60	5.08	2.80	0.40	0.11	1.53	...	...	...

Table 9.6: Central star data (2.0 kpc sample)

No.	Name	α	δ	D (kpc)	V	M_V	T_* (kK)	meth	$\log T$ (K)	$\log L$ $L_\odot$	M_* $M_\odot$	IR	RV	Bin	ST_{CS}	ST_{sec}
1	Sh 2-216	04 43 21.27	+46 42 05.8	0.13	12.64	6.94	97	z,m	4.99	1.74	0.58	n	n	n	DAO	...
2	NGC 7293	22 29 38.51	-20 50 13.7	0.22	13.53	6.80	110	z,m	5.04	1.95	0.63	n	n?	n	DAO	...
3	FP1824-0319	18 24 40.88	-03 19 59.6	0.36	14.89	6.77	>52	z	>4.72	...	...	n	nd	n	...	...
4	NGC 1514	04 09 16.99	+30 46 33.4	0.37	9.52	0.01	60	m	4.78	...	...	s	u	c?	sdO:	A0III
5	PuWe 1	06 19 33.96	+55 36 43.8	0.37	15.59	7.40	109	m	5.04	1.70	0.66	u	n?	u	DAO	...
6	M 27	19 59 36.34	+22 43 16.1	0.38	14.09	6.05	135	z	5.13	2.49	0.63	y	u	o?	DAO	*dM*?
7	NGC 1360	03 33 14.65	-25 52 17.9	0.38	11.34	3.41	110	m	5.04	3.30	0.57	n	u	c?	O(H)	...
8	Abell 36	13 40 41.34	-19 52 55.3	0.45	11.53	3.17	113	m	5.05	3.43	0.58	n	nd	n?	O(H)	...
9	Abell 31	08 54 13.16	+08 53 53.0	0.48	15.52	6.99	94	m	4.97	1.69	0.60	y	n?	w	DAO	*dM6*
10	NGC 246	00 47 03.35	-11 52 19.0	0.50	11.84	3.30	140	m	5.15	3.63	0.61	n	n	w	PG1159	K0V
11	MWP 1	21 17 08.29	+34 12 27.2	0.50	13.13	4.58	163	m	5.21	3.30	0.61	n	n?	n	PG1159	...
12	LoTr 5	12 55 33.75	+25 53 30.6	0.50	14.88	6.35	100	m	5.00	2.01	0.57	s	n?	c?	sdO	G5III
13	Abell 7	05 03 07.52	-15 36 22.8	0.51	15.49	6.87	99	m	5.00	1.80	0.60	y	n?	w	DAO	*dM4*
14	IPHAS2050+4655	20 50 13.74	+46 55 15.2	0.52	16.7	3.51	...	...	...	...	...	id?	nd	u	...	...
15	PFP 1	07 22 17.75	-06 21 46.4	0.54	15.90	7.11	>56	z	>4.75	...	...	n	nd	n	...	...
16	Abell 21	07 29 02.71	+13 14 48.8	0.54	16.00	7.21	136	z,m	5.13	2.04	0.72	n	nd	n	PG1159	...
17	FP0905-3033	09 05 05.34	-30 33 12.0	0.57	16.49	7.55	>82	z	>4.91	...	...	nd	nd	nd	...	...
18	TK 1	08 27 05.54	+31 30 08.8	0.57	15.75	6.86	99	m	5.00	1.80	0.60	y	y?	y?	DAO	*dM*?
19	Jacoby 1	15 21 46.58	+52 22 04.1	0.57	15.54	6.65	150	m	5.18	2.38	0.69	n	nd	n	PG1159	...
20	EGB 6	09 52 59.00	+13 44 34.5	0.59	16.03	7.03	110	m	5.04	1.86	0.64	y	nd	w	DAO	*dM5*
21	HFG 1	03 03 46.99	+64 54 35.4	0.60	13.38	3.06	100	m	5.00	3.33	0.56	y	y	c	CB	*dG*
22	IsWe 1	03 49 05.89	+50 00 14.8	0.62	16.55	7.04	100	m	5.00	1.74	0.61	nd	nd	nd	PG1159	...
23	IsWe 2	22 13 22.53	+65 53 55.5	0.62	17.71	7.36	126	z	5.10	1.89	0.70	nd	nd	nd	DA	...
24	FP0711-2531	07 11 32.0	-25 31 24	0.63	...	...	...	...	...	...	...	id?	nd	u	...	...
25	Sh 2-78	19 03 10.09	+14 06 58.9	0.64	17.78	7.02	112	z	5.05	1.88	0.64	nd	nd	nd	PG1159	...
26	EGB 1	01 07 07.59	+73 33 23.1	0.65	16.39	6.62	147	m	5.17	2.37	0.69	n	nd	n	DA	...
27	Sh 2-200	03 10 58.87	+62 47 54.8	0.66	14.89	4.40	...	...	...	...	...	nd	nd	nd	...	...
28	M 57	18 53 35.08	+33 01 45.0	0.70	15.78	6.11	148	z	5.17	2.58	0.66	nd	nd	nd	hgO(H)	...
29	NGC 7008	21 00 32.80	+54 32 35.3	0.70	13.89	3.50	97	z	4.99	3.12	0.55	y	u	w	O(H)	*dG*:
30	NGC 1501	04 06 59.19	+60 55 14.3	0.72	14.45	3.13	135	m	5.13	3.66	0.61	y?	nd	y?	[WC4]	...
31	DS 1	10 54 40.57	-48 47 02.8	0.73	12.16	2.39	90	m	4.95	3.48	0.57	y?	y	c	O(H)	...
32	Abell 74	21 16 52.27	+24 08 51.8	0.75	17.20	7.57	108	m	5.03	1.62	0.68	nd	nd	nd	DAO	...
33	M 97	11 14 47.73	+55 01 08.5	0.76	16.10	6.66	105	z	5.02	1.95	0.60	u	nd	u	hgO(H)	...

Continued on next page

Table 9.6 – continued from previous page

No.	Name	α	δ	D (kpc)	V	M_V	T_* (kK)	meth	$\log T$ (K)	$\log L$ $L_\odot$	M_* $M_\odot$	IR	RV	Bin	$\mathrm{ST_{CS}}$	$\mathrm{ST_{sec}}$
34	Lo 1	02 56 58.40	-44 10 17.9	0.76	15.16	5.75	120	m	5.08	2.47	0.59	n	nd	n	hgO(H)	...
35	Sh 2-176	00 31 53.30	+57 22 49.0	0.78	17.70	7.17	104	z	5.02	1.73	0.64	nd	nd	nd	DA	...
36	HbDs 1	09 52 44.53	-46 16 47.4	0.80	12.53	2.62	114	m	5.06	3.66	0.60	y?	u	y?	O(H)	...
37	K 2-2	06 52 23.17	+09 57 55.8	0.80	14.30	4.78	69	z,m	4.84	2.20	0.38	u	u	u	hgO(H)	...
38	HaWe 4	03 27 15.44	+45 24 20.5	0.80	17.08	6.95	125	m	5.10	2.04	0.66	nd	nd	nd	DAO	...
39	NGC 3132	10 07 01.76	-40 26 11.1	0.81	15.76	5.91	100	z	5.00	2.19	0.57	s	n	w	...	A2IV-V
40	Sh 2-188	01 30 33.19	+58 24 50.2	0.83	17.44	6.75	158	z	5.20	2.40	0.72	nd	nd	nd	DAO	...
41	Abell 24	07 51 37.55	+03 00 21.0	0.83	17.36	7.57	137	z	5.14	1.90	0.79	nd	nd	o	...	...
42	Lo 16	17 35 41.80	-40 11 26.2	0.84	15.42	3.99	>82	z	>4.91	...	...	y	nd	c?	...	*dK*?
43	WDHS 1	05 59 24.80	+10 41 40.2	0.85	17.35	7.51	141	m	5.15	1.96	0.80	nd	nd	o?	DA	...
44	IC 5148/50	21 59 35.13	-39 23 08.1	0.85	16.16	6.49	110	z	5.04	2.07	0.60	nd	nd	nd	hgO(H)	...
45	NGC 6337	17 22 15.66	-38 29 03.5	0.86	15.67	4.13	105	m	5.02	...	...	u	y	c	...	*WD*?
46	NGC 7027	21 07 01.70	+42 14 09.5	0.85	16.04	3.37	175	z	5.24	3.87	0.67	nd	nd	nd	...	...
47	NGC 2346	07 09 22.55	-00 48 23.6	0.90	11.27	-0.08	>80	z	>4.90	...	...	s	y	c	sdO?	A5V
48	Jones 1	23 35 53.32	+30 28 06.4	0.90	16.17	6.11	150	m	5.18	2.59	0.65	n	nd	n	PG1159	...
49	FP1721-5654	17 21 09.0	-56 54 25	0.93	17.5	6.98	>69	z	>4.84	...	...	id?	nd	u	...	...
50	NGC 6781	19 18 28.09	+06 32 19.3	0.95	16.88	5.35	112	z	5.05	2.55	0.57	n	nd	n	DAO	...
51	NGC 4361	12 24 30.75	-18 47 05.5	0.95	13.26	3.24	126	m	5.10	3.53	0.59	n	n?	n	O(H)	...
52	EGB 9	07 18 57.93	+07 22 23.2	0.99	13.00	2.80	>25	z	>4.40	...	...	y	nd	y?	...	...
53	NGC 3242	10 24 46.14	-18 38 32.3	1.00	12.32	2.19	89	z	4.95	3.54	0.57	nd	n?	nd	O(H)	...
54	RCW 24	08 25 47.58	-40 13 10.0	1.00	18.21	7.04	132	z	5.12	2.07	0.68	nd	nd	nd	O(H)?	...
55	DS 2	15 43 05.04	-39 18 14.6	1.00	12.37	1.69	90	m	4.95	3.76	0.61	n	n?	n	O(H)	...
56	HaWe 13	19 31 07.20	-03 42 31.5	1.01	16.90	5.36	68	m	4.83	1.95	0.40:	y?	nd	y?	hgO(H)	...
57	NGC 40	00 13 01.02	+72 31 19.1	1.02	11.55	0.20	48	m	4.68	3.60	0.57	y?	nd	u	[WC8]	...
58	Abell 34	09 45 35.32	-13 10 15.6	1.03	16.40	6.21	98	z	4.99	2.05	0.57	nd	nd	o?	hgO(H)	...
59	MeWe 2-4	14 01 15.42	-50 40 09.5	1.07	17.0	6.23	>54	z	>4.73	...	...	nd	nd	nd	...	...
60	PHR1625-4523	16 25 56.30	-45 23 14.4	1.08	...	...	...	...	...	...	...	nd	nd	nd	...	...
61	Abell 66	19 57 31.53	-21 36 44.7	1.10	18.17	7.42	>93	z	>4.97	...	...	nd	nd	o?	...	...
62	NGC 6153	16 31 30.83	-40 15 14.2	1.10	15.55	2.57	109	z	5.04	3.63	0.60	nd	nd	nd	wels	...
63	Abell 6	02 58 41.87	+64 30 06.3	1.10	18.5	5.17	>57	z	>4.76	...	...	nd	nd	nd	...	...
64	Sp 1	15 51 40.93	-51 31 28.4	1.13	13.69	1.82	72	z	4.86	3.44	0.56	y	u	c	O(H)	...
65	PHR1418-5144	14 18 25.88	-51 44 37.4	1.14	17.4	6.16	>51	z	>4.71	...	...	nd	nd	nd	...	...
66	He 2-11	08 37 08.45	-39 25 08.1	1.14	18.3	3.99	>90	z	>4.95	...	...	n	nd	n	...	...
67	Sh 2-71	19 01 59.95	+02 09 16.0	1.14	19.0	5.62	157	z	5.20	2.85	0.63	nd	nd	nd	...	...
68	BMP0642-0417	06 42 18.41	-04 17 48.9	1.15	18.5	7.34	>60	z	>4.78	...	...	nd	nd	nd	...	...

Continued on next page

Table 9.6 – continued from previous page

No.	Name	α	δ	D (kpc)	V	M_V	T_* (kK)	meth	$\log T$ (K)	$\log L$ $L_\odot$	M_* $M_\odot$	IR	RV	Bin	$\mathrm{ST_{CS}}$	$\mathrm{ST_{sec}}$
69	JnEr 1	07 57 51.63	+53 25 17.0	1.15	17.14	6.77	116	z	5.06	2.02	0.63	n	nd	n	PG1159	...
70	Abell 33	09 39 09.12	-02 48 31.5	1.16	16.03	5.71	100	z	5.00	2.27	0.56	y	nd	w	O(H)	*dK3*
71	Kronberger 9	19 44 59.13	+22 45 47.9	1.17	16.17	5.19	>35	z	>4.54	...	...	nd	nd	nd	...	...
72	NGC 6302	17 13 44.21	-37 06 15.9	1.17	...	...	220	p	5.34	...	...	nd	nd	u	...	...
73	Abell 65	19 46 34.20	-23 08 12.9	1.17	15.60	4.63	>83	z	>4.92	...	...	y	nd	c	CB	...
74	PHR1432-6138	14 32 09.73	-61 38 41.3	1.19	18.7	7.52	100	z	5.00	1.55	0.65	nd	nd	nd	...	...
75	NGC 6772	19 14 36.37	-02 42 25.0	1.20	18.61	6.25	135	z	5.13	2.41	0.64	nd	nd	nd	...	...
76	IC 418	05 27 28.20	-12 41 50.3	1.20	10.23	-0.79	38	z	4.58	3.72	0.59	nd	y	u	Of(H)	...
77	M 76	01 42 19.95	+51 34 31.2	1.20	17.53	6.81	140	m	5.15	2.23	0.69	nd	nd	o	PG1159	...
78	M 1-26	17 45 57.65	-30 12 00.6	1.20	12.61	-1.03	33	m	4.52	3.65	0.57	y	nd	u	Of(H)	...
79	Abell 28	08 41 35.57	+58 13 48.4	1.22	16.57	6.14	>71	z	>4.85	...	...	y?	nd	y?	...	...
80	IC 1295	18 54 37.21	-08 49 39.1	1.23	16.9	5.34	98	z	4.99	2.40	0.55	nd	nd	nd	hgO(H)	...
81	NGC 7662	23 25 53.97	+42 32 05.0	1.26	14.00	3.15	111	z	5.05	3.42	0.58	nd	nd	nd	...	...
82	PHR1118-6150	11 18 44.55	-61 50 19.4	1.26	17.2	5.63	>47	z	>4.67	...	...	nd	nd	nd	...	...
83	HaWe 15	22 30 33.46	+47 31 23.6	1.27	17.9	6.73	>66	z	>4.82	...	...	nd	nd	nd	...	...
84	NGC 2392	07 29 10.77	+20 54 42.4	1.28	10.63	-0.40	47	m	4.67	3.82	0.61	y?	u	w	Of(H)	*dM?*
85	YM 16	18 54 57.72	+06 02 40.9	1.29	16.7	3.59	...	...	...	...	...	y	nd	y?	...	*dG?*
86	NGC 6826	19 44 48.16	+50 31 30.3	1.30	10.68	-0.19	50	m	4.70	3.81	0.61	y?	y?	u	O3f(H)	...
87	IC 4637	17 05 10.51	-40 53 08.4	1.30	12.70	0.32	50	z	4.70	3.60	0.57	y	n?	o?	O(H)	...
88	BD+30 3639	19 34 45.23	+30 30 58.9	1.30	10.42	-1.07	32	z	4.51	3.63	0.58	nd	nd	nd	[WC9]	...
89	RCW 69	12 44 27.3	-62 31 30.7	1.30	18.6	6.43	145	z	5.16	2.43	0.68	nd	nd	nd	...	...
90	MeWe 1-2	10 14 24.16	-58 11 52.3	1.30	18.8	7.4	>85	z	>4.93	...	...	nd	nd	nd	...	...
91	NGC 6894	20 16 23.97	+30 33 53.2	1.31	18.32	5.81	100	z	5.00	2.23	0.56	nd	nd	nd	...	...
92	Abell 61	19 19 10.22	+46 14 52.0	1.31	17.42	6.68	88	z	4.94	1.73	0.55	nd	nd	nd	hgO(H)	...
93	NGC 6026	16 01 21.07	-34 32 36.6	1.31	13.33	1.13	>35	m	>4.54	...	...	y?	y	c	...	...
94	Abell 45	18 30 15.42	-11 36 57.4	1.32	21.1	8.08	180	z	5.26	2.02	0.95	nd	nd	nd	...	...
95	Abell 71	20 32 23.22	+47 20 50.4	1.33	18.95	6.07	123	z	5.09	2.37	0.61	nd	nd	nd	...	...
96	K 1-22	11 26 43.79	-34 22 11.0	1.33	16.83	6.06	115	z	5.06	2.30	0.60	nd	nd	w	hgO(H)	*dK1*
97	BMP0733-3108	07 33 24.12	-31 08 05.1	1.34	18.5	6.80	>95	z	>4.98	...	...	nd	nd	nd	...	...
98	NGC 2899	09 27 03.12	-56 06 21.2	1.37	16.5	4.49	270	c	5.43	...	...	s	nd	y	...	*F5V:*
99	PHR0743-1951	07 43 51.13	-19 51 16.7	1.37	15.8	4.26	>32	z	>4.51	...	...	nd	nd	nd	...	...
100	HaTr 7	17 54 09.46	-60 49 57.6	1.38	14.66	3.79	100	m	5.00	3.04	0.56	n	nd	n	wels?	...
101	Abell 62	19 33 18.04	+10 37 00.7	1.38	17.5	6.37	98	z	4.99	1.98	0.57	nd	nd	nd	...	...
102	NGC 6445	17 49 15.21	-20 00 34.5	1.39	18.88	5.54	170	z	5.23	2.97	0.64	nd	nd	nd	...	...
103	NGC 6072	16 12 58.08	-36 13 46.1	1.39	18.47	5.92	140	z,c	5.15	2.59	0.63	nd	nd	nd	...	...

Continued on next page

Table 9.6 – continued from previous page

No.	Name	α	δ	D (kpc)	V	M_V	T_* (kK)	meth	$\log T$ (K)	$\log L$ $L_\odot$	M_* $M_\odot$	IR	RV	Bin	ST_{CS}	ST_{sec}
104	Abell 29	08 40 18.92	-20 54 36.3	1.39	18.33	7.23	102	z	5.01	1.69	0.64	nd	nd	nd	...	...
105	NGC 7094	21 36 52.98	+12 47 19.3	1.39	13.62	2.65	110	m	5.04	3.61	0.59	y	nd	y?	PG1159	...
106	Abell 39	16 27 33.74	+27 54 33.4	1.40	15.60	4.81	117	m	5.07	2.82	0.57	n?	n?	n?	hgO(H)	...
107	Wray 17-31	09 31 20.49	-56 17 39.4	1.40	17.94	6.46	120	z	5.08	2.19	0.63	nd	nd	nd	DAO	...
108	BMP1808-1406	18 08 35.08	-14 06 43.0	1.40	19.0	6.13	>65	z	>4.81	...	...	nd	nd	nd	...	...
109	NGC 2371-72	07 25 34.72	+29 29 25.6	1.41	14.85	3.95	100	z	5.00	2.98	0.55	nd	nd	nd	[WCE]	...
110	PHR1040-5417	10 40 48.21	-54 17 57.6	1.41	16.85	5.82	>40	z	>4.60	...	...	nd	nd	nd	...	...
111	NGC 2438	07 41 51.43	-14 43 54.9	1.42	17.6	6.25	124	z	5.09	2.31	0.62	y	nd	u	hgO(H)	...
112	NGC 5189	13 33 32.97	-65 58 26.7	1.44	14.53	2.63	135	m	5.13	3.86	0.65	y	nd	y?	[WO1]	...
113	Lo 5	11 13 54.15	-47 57 00.6	1.44	17.0	5.78	>66	z	>4.82	...	...	nd	nd	nd	...	...
114	NGC 7009	21 04 10.88	-11 21 48.2	1.45	12.87	1.81	87	z	4.94	3.67	0.59	y	n?	u	O(H)	...
115	Sh 2-42	18 10 13.6	-16 47 49	1.46	17.8	5.69	>70	z	>4.85	...	...	nd	nd	nd	...	...
116	PHR0942-5220	09 41 59.42	-52 20 30.6	1.46	18.8	5.64	>62	z	>4.79	...	...	nd	nd	nd	...	...
117	NGC 6804	19 31 35.18	+09 13 31.9	1.47	14.17	1.63	85	z	4.93	3.71	0.59	y	nd	y?	O(H)	...
118	M 1-41	18 09 29.90	-24 12 23.5	1.47	...	...	187	c	5.27	...	...	nd	nd	nd	...	...
119	HaTr 5	17 01 27.98	-43 05 55.1	1.47	16.4	3.42	>38	z	>4.58	...	...	nd	nd	nd	...	...
120	NGC 7076	21 26 23.60	+62 53 32.1	1.47	15.9	2.5	80	m	4.90	3.28	0.56	nd	nd	nd	...	...
121	G4.4+6.4	17 31 51.71	-21 49 18.2	1.48	...	...	...	...	...	...	...	nd	nd	nd	...	...
122	K 1-6	20 04 13.39	+74 26 28.3	1.48	...	...	...	...	...	...	...	nd	nd	nd	...	...
123	He 2-36	09 43 25.62	-57 16 55.6	1.49	11.48	-1.50	...	...	...	...	...	s	u	y	...	A2III
124	PHR1510-6754	15 10 22.05	-67 54 24.0	1.49	15.2	3.73	>35	z	>4.54	...	...	y	nd	y?	...	...
125	K 2-1	05 07 08.33	+30 49 18.6	1.50	17.4	5.18	113	z	5.05	2.63	0.60	nd	nd	nd	...	...
126	SuWt 2	13 55 43.23	-59 22 40.0	1.50	11.95	-0.11	...	...	...	...	...	s	nd	c	...	A0V+A0V
127	NGC 6543	17 58 33.41	+66 37 58.8	1.50	11.29	0.20	48	z	4.68	3.61	0.57	y?	y?	u	wels	...
128	We 2-34	07 00 28.40	+04 20 30.4	1.51	19.4	7.34	>72	z	>4.86	...	...	nd	nd	nd	...	...
129	VBRC 5	13 44 00.03	-60 49 46.9	1.52	...	...	...	...	...	...	...	nd	nd	nd	...	...
130	IC 2149	05 56 23.91	+46 06 17.3	1.52	11.34	-0.34	42	m	4.62	3.66	0.59	y	nd	u	Of(H)	...
131	Abell 80	22 34 45.60	+52 26 06.2	1.52	19.61	7.52	123	z	5.09	1.79	0.72	nd	nd	nd	...	...
132	BMP1651-3930	16 51 41.3	-39 30 27	1.53	19.0	7.43	>72	z	>4.86	...	...	nd	nd	nd	...	...
133	Abell 59	19 18 40.00	+19 34 33.0	1.54	21.15	6.22	102	z	5.01	2.09	0.58	nd	nd	nd	...	...
134	NGC 6369	17 29 20.44	-23 45 34.2	1.55	15.13	-0.01	66	z	4.82	4.07	0.70	y?	nd	y?	[WO3]	...
135	IC 4593	16 11 44.54	+12 04 17.1	1.57	11.33	0.14	40	m	4.60	3.41	0.56	y?	y	y?	O5f(H)	...
136	NGC 6905	20 22 22.94	+20 06 16.8	1.58	14.6	3.14	141	m	5.15	3.71	0.62	y?	nd	u	[WO2]	...
137	Fr 2-8	14 00 41.75	-51 02 27.6	1.58	15.83	4.19	>83	z	>4.92	...	...	n?	nd	u	...	...
138	BMP0815-4053	08 15 56.9	-40 53 08	1.58	20.0	7.94	...	...	...	...	...	nd	nd	nd	...	...

Continued on next page

Table 9.6 – continued from previous page

No.	Name	α	δ	D (kpc)	V	M_V	T_* (kK)	meth	$\log T$ (K)	$\log L$ $L_\odot$	M_* $M_\odot$	IR	RV	Bin	$\mathrm{ST_{CS}}$	$\mathrm{ST_{sec}}$
139	KjPn 8	23 24 10.47	+60 57 30.8	1.60	17.6	5.0	...	...	...	...	...	nd	nd	nd	...	...
140	NGC 7354	22 40 19.94	+61 17 08.1	1.60	16.2	1.40	96	z	4.98	3.95	0.66	nd	nd	nd	...	...
141	We 3-1	18 34 02.31	+14 49 10.2	1.62	...	...	...	...	...	...	...	nd	nd	nd	...	...
142	NGC 6818	19 43 57.84	-14 09 11.9	1.64	17.02	5.16	160	z	5.20	3.05	0.62	nd	nd	w	wels	*dK0?*
143	PHR1602-4127	16 02 18.13	-41 26 49.5	1.65	15.8	3.88	>35	z	>4.54	...	...	y	nd	y?	...	...
144	K 1-16	18 21 52.21	+64 21 54.3	1.67	15.08	3.84	140	m	5.15	3.42	0.60	n	nd	n	PG1159	...
145	NGC 6563	18 12 02.75	-33 52 07.1	1.67	17.49	6.16	123	z	5.09	2.34	0.61	nd	nd	nd	...	...
146	NGC 6567	18 13 45.14	-19 04 33.7	1.68	14.34	1.50	60	z	4.78	3.35	0.56	nd	nd	nd	wels	...
147	Abell 84	23 47 44.30	+51 23 56.3	1.68	18.49	6.55	100	z	5.00	1.94	0.59	nd	nd	nd	...	...
148	Hb 5	17 47 56.19	-29 59 41.9	1.70	18.6	3.90	172	z	5.24	3.64	0.63	nd	nd	nd	...	...
149	Abell 46	18 31 18.59	+26 56 12.1	1.70	14.8	3.16	66	z	4.82	2.80	0.5	u	y	c	O(H)	...
150	K 1-27	05 57 02.14	-75 40 22.5	1.70	16.13	4.83	105	m	5.02	2.68	0.56	nd	nd	w	O(He)	...
151	NGC 5882	15 16 49.94	-45 38 58.4	1.70	13.42	1.43	68	z	4.83	3.52	0.56	nd	n?	nd	Of(H)	...
152	PHR1408-6106	14 08 48.07	-61 06 33.8	1.70	17.2	4.62	>43	z	>4.63	...	...	nd	nd	nd	...	...
153	IC 4642	17 11 45.02	-55 24 01.5	1.71	15.66	3.71	113	m	5.05	3.22	0.56	nd	nd	nd	...	...
154	HaWe 11	17 31 47.47	-28 42 03.4	1.71	17.7	2.9	>54	z	>4.73	...	...	nd	nd	nd	...	...
155	NGC 2610	08 33 23.32	-16 08 57.7	1.72	15.97	4.79	142	m	5.15	3.06	0.59	y?	nd	w	...	...
156	Patchick 5	19 19 30.53	+44 45 43.1	1.75	15.3	3.70	>29	z	>4.46	...	...	y	nd	w?	...	...
157	Abell 72	20 50 02.06	+13 33 29.6	1.75	16.11	4.81	>86	z	>4.93	...	...	n?	nd	n?	...	...
158	NGC 4071	12 04 14.82	-67 18 35.6	1.77	19.15	6.73	130	z	5.11	2.17	0.66	nd	nd	nd	...	...
159	Abell 51	19 01 01.39	-18 12 15.3	1.78	15.47	3.53	>80	z	>4.90	...	...	n	nd	n	O(H)	...
160	WeSb 2	06 16 11.35	+28 22 11.0	1.79	...	...	...	...	...	...	...	nd	nd	nd	...	...
161	IPHAS 0156+6528	01 56 24.94	+65 28 30.5	1.80	18.6	6.68	>68	z	>4.84	...	...	nd	nd	nd	...	...
162	He 2-84	12 28 46.82	-63 44 38.7	1.80	17.1	2.0	>38	z	>4.58	...	...	nd	nd	nd	...	...
163	We 1-10	20 31 52.38	+48 52 49.9	1.82	17.85	6.13	>58	z	>4.76	...	...	nd	nd	nd	...	...
164	PHR1619-4914	16 19 40.18	-49 13 59.5	1.82	19.0	-2.56	...	...	...	...	...	y	nd	nd	[WN6]	...
165	Fg 1	11 28 36.21	-52 56 04.0	1.82	14.5	2.66	80	z	4.90	3.23	0.56	n?	nd	u	...	...
166	Abell 82	23 45 47.81	+57 03 59.2	1.82	14.90	2.91	...	...	...	...	...	s	nd	y?	...	*K0IV*
167	NGC 5844	15 10 40.75	-64 40 28.5	1.83	18::	...	...	...	...	...	...	nd	nd	nd	...	...
168	Kronberger 24	21 13 37.73	+37 15 37.6	1.83	18.56	6.61	...	...	...	...	...	nd	nd	nd	...	...
169	NGC 3918	11 50 17.73	-57 10 56.9	1.84	15.49	3.35	150	z,m	5.18	3.70	0.63	nd	nd	nd	O(H)?	...
170	PHR1533-4824	15 33 06.87	-48 24 44.6	1.84	...	...	...	...	...	...	...	nd	nd	nd	...	...
171	HaWe 9	06 54 20.79	-25 24 33.5	1.85	19.2	6.95	>72	z	>4.86	...	...	nd	nd	nd	...	...
172	Abell 78	21 35 29.41	+31 41 45.4	1.85	13.26	1.75	110	m	5.04	3.97	0.66	y	u	n?	[WC]-PG	...
173	NGC 6572	18 12 06.40	+06 51 12.2	1.86	13.0	0.98	69	z	4.84	3.72	0.60	y	nd	u	wels	...

Continued on next page

Table 9.6 – continued from previous page

No.	Name	α	δ	D (kpc)	V	M_V	T_* (kK)	meth	$\log T$ (K)	$\log L$ $L_\odot$	M_* $M_\odot$	IR	RV	Bin	$\mathrm{ST_{CS}}$	$\mathrm{ST_{sec}}$
174	We 2-5	01 42 38.00	+60 09 44.5	1.89	...	...	...	...	...	...	...	nd	nd	nd	...	...
175	M 2-55	23 31 52.71	+70 22 10.1	1.89	16.15	2.12	>55	z	>4.74	...	...	nd	nd	nd	...	...
176	PHR1539-5325	15 39 46.82	-53 25 25.4	1.90	18.6	4.86	>44	z	>4.64	...	...	nd	nd	nd	...	...
177	HFG 2	07 42 23.81	-32 47 50.4	1.90	16.7	5.26	>38	z	>4.58	...	...	nd	nd	nd	...	...
178	NGC 2440	07 41 55.4	-18 12 33	1.90	17.63	5.28	208	z,c	5.32	3.32	0.67	nd	nd	nd	...	...
179	H 1-7	17 10 27.39	-41 52 49.4	1.91	...	...	...	...	...	...	...	nd	nd	nd	...	...
180	NGC 3211	10 17 50.55	-62 40 14.6	1.91	18.0	5.91	162	z	5.21	2.76	0.65	nd	nd	nd	...	...
181	H 1-13	17 28 27.54	-35 07 31.6	1.91	...	...	...	...	...	...	...	nd	nd	nd	...	...
182	NGC 5979	15 47 41.55	-61 13 06.3	1.93	16.37	3.92	116	z	5.06	3.17	0.56	nd	nd	nd	...	...
183	Abell 13	06 04 47.90	+03 56 35.8	1.93	19.87	6.77	113	z	5.05	1.99	0.63	nd	nd	nd	...	...
184	PHR1658-2515	16 58 21.4	-25 15 44	1.94	...	...	...	...	...	...	...	nd	nd	nd	...	...
185	PHR1911-1546	19 11 04.46	-15 46 07.0	1.94	17.6	5.67	>90	z	>4.95	...	...	nd	nd	nd	...	...
186	FP0739-2709	07 39 38.12	-27 09 30.3	1.94	19.0	7.1	>95	z	>4.98	...	...	nd	nd	nd	...	...
187	H 1-12	17 26 24.24	-35 01 41.3	1.94	...	...	...	...	...	...	...	nd	nd	nd	...	...
188	PHR1136-5235	11 36 00.0	-52 35 33	1.96	17.2	5.05	>38	z	>4.58	...	...	nd	nd	nd	...	...
189	NGC 7048	21 14 15.22	+46 17 17.5	1.97	19.12	6.84	148	z	5.17	2.29	0.70	nd	nd	nd	...	...
190	Lo 8	13 25 37.51	-37 36 14.9	1.99	12.95	1.36	90	m	4.95	3.89	0.63	n	n	n	O(H)	...
191	M 1-75	20 04 44.09	+31 27 24.4	1.99	...	...	...	...	...	...	...	nd	nd	nd	...	...
192	K 2-7	19 40 29.10	-20 27 05.9	1.99	18.0	6.10	...	...	...	...	...	nd	nd	nd	...	...
193	CVMP 1	15 09 25.17	-55 33 05.3	2.00	20.2	6.07	123	z	5.09	2.37	0.61	nd	nd	nd	...	...
194	LTNF 1	11 57 44.78	+48 56 18.7	2.00	16.15	4.54	105	m	5.02	2.80	0.56	y	y	c	CB	dM0
195	NGC 6537	18 05 13.10	-19 50 34.9	2.00	21.56	5.87	250	c	5.40	3.30	0.83	nd	nd	nd	...	...
196	NGC 6629	18 25 42.45	-23 12 10.6	2.00	12.87	-0.41	47	z	4.67	3.82	0.61	nd	n?	nd	wels	...
197	NGC 6751	19 05 55.56	-05 59 32.9	2.00	14.30	1.60	105	m	5.02	3.97	0.68	y	nd	u	[WO4]	...
198	WeBo 1	02 40 14.35	+61 09 17.0	2.00	14.45	1.11	...	...	...	...	...	s	nd	y	...	K0IIIp
199	NGC 3195	10 09 20.91	-80 51 30.7	2.01	17.78	6.00	141	z	5.15	2.56	0.63	nd	nd	nd	...	...
200	PHR0905-4753	09 05 41.04	-47 54 05.2	2.01	12.67	-0.49	...	...	...	...	...	s	nd	u	pec	...
201	MeWe 1-1	08 53 36.86	-54 05 09.8	2.02	17.7	5.75	...	z	>4.61	...	...	nd	nd	o?	...	...
202	NGC 2792	09 12 26.60	-42 25 39.9	2.02	16.89	4.12	126	z	5.10	3.18	0.57	nd	nd	nd	...	...
203	Abell 30	08 46 53.51	+17 52 45.5	2.02	14.38	2.76	>66	z	>4.82	...	...	y	y?	w	[WC]-PG	...
204	HaTr 1	12 16 33.14	-66 45 45.1	2.02	...	...	...	...	...	...	...	nd	nd	nd	...	...
205	Wr 16-121	12 48 31.28	-63 49 57.9	2.03	...	...	...	...	...	...	...	id?	nd	nd	...	...
206	PHR1032-6310	10 32 14.4	-63 10 22	2.03	17.2	5.02	>42	z	>4.62	...	...	nd	nd	nd	...	...
207	IC 4406	14 22 26.28	-44 09 04.4	2.04	17.38	5.20	119	z	5.08	2.68	0.58	nd	nd	nd	...	...
208	BlDz 1	11 53 06.60	-50 50 59.2	2.04	18.40	6.43	128	m	5.11	2.28	0.65	nd	nd	nd	hgO(H)	...

Continued on next page

Table 9.6 – continued from previous page

No.	Name	α	δ	D	V	M_V	T_*	meth	$\log T$	$\log L$	M_*	IR	RV	Bin	ST_{CS}	ST_{sec}
				(kpc)			(kK)		(K)	$L_\odot$	$M_\odot$					
209	HaTr 9	18 08 58.86	-41 48 37.6	2.04	17.4	5.44	>72	z	>4.86	...	...	nd	nd	nd	...	...
210	Abell 43	17 53 32.27	+10 37 23.7	2.05	14.74	2.65	110	m	5.04	3.61	0.59	n	nd	nd	PG1159h	...

Chapter 10

The Local PN Luminosity Function

10.1 Definition

The planetary nebula luminosity function (PNLF; Jacoby 1980, 1989; Ciardullo et al. 1989) represents a snapshot of the collective luminosity evolution of an ensemble of PNe of different masses, powered by their evolving central stars. However, it is not well known that it was nearly forty years ago (Henize & Westerlund 1963; Hodge 1966) that the brightest PNe were first offered as a standard candle, even though the distances to individual galactic PNe were subject to large uncertainties. Henize & Westerlund (1963) proposed that PNe in the Milky Way and the SMC attain the same maximum brightness, leading the way to using bright PNe an extragalactic distance indicator. However, the first example of a PN-based distance was to a galaxy exterior to the Local Group, the large spiral M 81 (Ford & Jenner 1978).

Later work concentrated on the formal development of the PNLF and it has proven over the last two decades to be a powerful and widely used extragalactic distance indicator (e.g. Jacoby 1989; Ciardullo et al. 1989; Jacoby et al. 1992; Ferrarese et al. 2000; Ciardullo et al. 2002; for recent reviews, see Ciardullo 2003, 2005 & 2006a,b). Because the PNLF technique appears to be applicable to all kinds of galaxies, it provides an important link between the Population I and Population II distance scales (Jacoby et al. 1992; Ciardullo et al. 2002).

The PNLF plots the total number of PNe in each luminosity or absolute magnitude interval in a given volume. Because the [O III] λ5007 emission-line is the brightest in the optical part of the spectrum in the absence of extinction, the PNLF is traditionally expressed in [O III] magnitudes. An [O III] λ5007 apparent magnitude is derived from the measured monochromatic nebular flux using the formula of Jacoby (1989), given earlier as equation 9.1.

Jacoby (1980) first showed that the PNLF for the Magellanic Clouds agrees with the theoretical exponential function of Henize & Westerlund (1963), in which a PN is treated as a uniformly expanding homogeneous sphere ionized by a non-evolving central star. From first principles,

$$F(5007) \propto N_e \propto \frac{1}{R^3} \propto \frac{1}{t^3} \qquad (10.1)$$

It follows that the number of PNe in an ensemble of objects with λ5007 magnitudes between

M and $M + dM$ is given by:

$$N(M) \propto \frac{dt}{dm} \propto e^{0.307M} \tag{10.2}$$

In other words, the number of PNe in each luminosity interval is proportional to the PN lifetime spent within that luminosity bin (Jacoby 1980; Ciardullo et al. 1989; Ciardullo et al. 2004). This rising exponential represents the observed luminosity function in the LMC quite well (Jacoby 1980), except for the brightest part of the PNLF, where a sharp fall-off was observed. To allow for sharp turn-down observed at the bright end, Ciardullo et al. (1989) modified this model and introduced the widely-used truncated exponential function, which combines the slowly rising exponential of Henize & Westerlund (1963) with a sharp exponential cutoff at the bright end:

$$N(M) \propto e^{0.307M}[1 - e^{3(M^* - M)}] \tag{10.3}$$

where M^* is the absolute magnitude of the most luminous PNe (i.e. the bright cut-off magnitude), currently accepted to be $M^* = -4.47 \pm 0.05$ (Ciardullo et al. 1989, 2002; Jacoby et al. 1992). This universal PNLF is seen in all external galaxies which have statistically significant samples. The canonical truncated exponential is especially well shown in the new PNLF of M 31 (Merrett et al. 2006), plotted as figure 10.1.

However, there does appear to be a weak correction of M^* with galaxy metallicity (Dopita, Jacoby & Vassiliadis 1992; Ciardullo et al. 2002, 2005), given by the following relation:

$$\Delta M^* = 0.928[\mathrm{O/H}]^2 + 0.225[\mathrm{O/H}] + 0.014 \tag{10.4}$$

Following Méndez et al. (1993), a cumulative PNLF can be generated by integrating equation 10.3 which gives the following:

$$K(M) = \frac{k}{0.307}(e^{0.307M} - e^{0.307M^*}) - \frac{ke^{3M^*}}{-2.693}(e^{-2.693M} - e^{-2.693M^*}) \tag{10.5}$$

where K(M) is the cumulative number of PNe between M^* and M, and k is a suitable normalisation constant. Henize & Westerlund (1963) assumed that PNe become unrecognizable as they expand beyond a radius of ~0.7 pc (corresponding to a PN lifetime of ~30,000 years for a typical expansion rate), predicting that the faintest PNe should be about 7–8 mag below M_*. Hence, the 'standard' PNLF can be generated assuming that equation 10.3 applies and that there are no PNe fainter than 8 magnitudes below M^*, i.e. there is a faint-end cutoff. Based on this, the fraction of PNe in each magnitude interval of the standard PNLF has been summarised by Buzzoni, Arnaboldi & Corradi (2006), repeated here in column 2 of table 10.1 for convenience.

To fully understand the physical basis as to why the PNLF works so well requires complete, homogeneous PN samples in systems at a known distance, such as the Magellanic Clouds (Jacoby 2006; Reid 2008; Reid & Parker 2008, in preparation) which are sufficiently close that their PNe can be resolved and studied in detail with currently available technology.

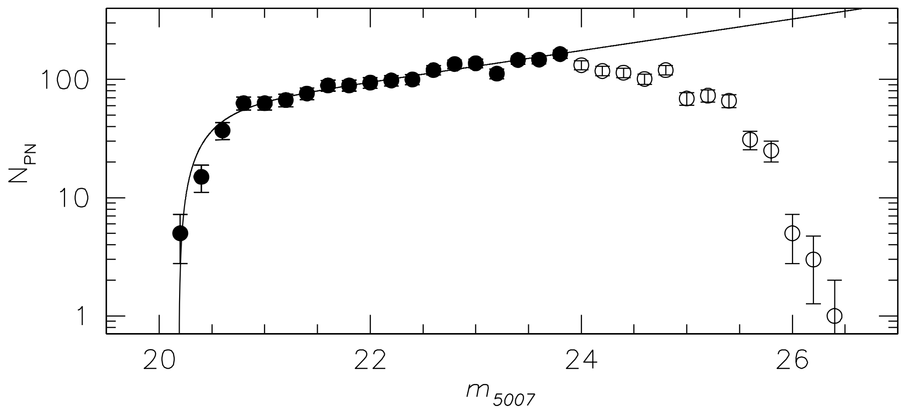

Figure 10.1: The [O III] PNLF for M 31 from Merrett et al. (2006). Note that the fit to the standard function is almost prefect at bright magnitudes. The sample is statistically complete (filled dots) down to 3.6 mag below M^*.

However even these samples remain incomplete at the faintest magnitudes (§10.3), hindering our undersatnding of the shape of the [O III] PNLF at the faint end, which has been essentially unknown till now (cf. Jacoby 1980; Jacoby & De Marco 2002). Thanks to the advent of new deep Hα surveys such as the SHS, which has facilitated the discovery of many highly evolved, senile PNe, combined with our ability to effectively eliminate non-PN contaminants (see Chapter 8), the most complete PNLF to date is found in the local volume where the SB-r relation can be used to generate an unprecedented sample of PNe out to 2 kpc.

The approach in this study is to concentrate on a critically-selected, volume-limited local sample of PNe. Though the number of PNe within 1.0 kpc of the Sun is relatively small (n = 56), one object, NGC 7027, is at the very top of the PNLF. However, within the small but statistically complete sample of 18 PNe out to 500 pc (see table 11.2), there are no 'bright' PNe at all, because this volume of space is not large enough to include these intrinsically less-common PNe. A rough estimate of the luminosity of the disk out to a radius of 500 pc is only $M_V \simeq -13$, comparable to a dwarf galaxy like the Fornax dwarf. Faint dwarf galaxies are not seen to have any PNe at the bright cutoff, partly due to metallicity effects (see above), but primarily because the overall PN population size is small (Méndez et al. 1993; Magrini et al. 2003).

Hence, bootstrapping the solar neighbourhood sample to the canonical bright end of the PNLF is actually a non-trivial problem. To alleviate this difficulty, a larger, but less complete 2.0 kpc sample is also analysed, as it contains a greater number of bright PNe (disk luminosity is $M_V \simeq -16.5$ out to 2.0 kpc). Based on this extensive new data set, a revision in the faint end of the PNLF is given in §10.3, below.

10.2 Invariance of the PNLF

One of the main unsolved questions concerning the [O III] PNLF technique is why there is such observational invariance (Ciardullo et al. 2002) in the bright cutoff magnitude, M_*, along the whole Hubble morphological sequence, i.e. between spirals undergoing active star formation on the one hand, and the old populations in elliptical and lenticular galaxies on the other (such old galaxies are not expected to contain a large population of massive stars). In fact, PNe are such robust standard candles that they are now used to calibrate Type Ia supernovae (e.g. Jacoby et al. 2006), but exactly how and why the PNLF works so well has not yet been firmly established.

Since the central star powers the line-emission of its surrounding PN, and the luminosity of the central star is a strong function of its mass (see §1.3), then relatively massive central stars are needed to produce PNe near the top of the PNLF. However, the low mass progenitors found in old populations produce residual central stars of lower mass, a consequence of the initial-final mass relation (IFMR), so these lower luminosity stars should power fainter PNe (see Chapter 1). Hence M^* should depend strongly on the age of the population, with fainter PNe being seen in ellipticals and spiral bulges (Jacoby 1997; Méndez & Soffner 1997; Marigo et al. 2004; Schönberner et al. 2007). However numerous studies have shown that [O III]-bright PNe are found in all population types, regardless of age (Jacoby et al. 1992; Ciardullo et al. 2002; Ciardullo 2003; Ciardullo et al. 2005).

The brightest PNe at the top of the PNLF have a luminosity of more than $600\,L_\odot$ in the λ5007Å emission line. Since observations and models indicate that only ∼10% of a central star's total luminosity is produced by this line (e.g. Jacoby 1989; Dopita, Jacoby & Vassiliadis 1992; Jacoby & Ciardullo 1999; Marigo et al. 2004; Ciardullo et al. 2005), it follows that the central stars of [O III]-bright PNe must have luminosities of at least $6000\,L_\odot$.

Referring to standard post-AGB evolutionary tracks (e.g. Blöcker 1995), this power is produced by central stars with $M_c \geq 0.62 M_\odot$ (Ciardullo et al. 2005; Schönberner et al. 2007; cf. Marigo et al. 2004), which is significantly larger than the mean of 0.56–0.60 $M_\odot$ found for nearby DA white dwarfs (Finley, Koester & Basri 1997; Vennes et al. 1997; Madej, Należyty & Althaus 2004; Liebert, Bergeron & Holberg 2005; Kepler et al. 2007). These higher-mass cores correspond to progenitor stars of >2.1 $M_\odot$ after referring to the most recent IFMRs of Williams (2007) and Kalirai et al. (2008). Similarly, Marigo et al. (2004) found that the brightest PNe are produced by progenitor stars of about 2 – 2.5 $M_\odot$. Such intermediate-mass stars *must be present in all population types*, to explain the universality of the bright-end of the PNLF. This point will be further discussed in the following sections.

10.3 The Local PNLF

Until this work, the faint end of the Galactic PNLF was essentially unknown (Jacoby 1980), and this lack of knowledge has led to a factor of 2–3 uncertainty in the estimated total number of PNe in the Galaxy. This uncertainty results from extrapolating from the observed number of PNe to the whole PN population size, usually through equation 10.5. This section seeks to address the long-standing problem of mapping the faint end of the PNLF.

Our new critically-appraised sample of local PNe (see Chapter 9) includes new discoveries from MASH and MASH-II (e.g. Pierce et al. 2004; Frew, Parker & Russeil 2006; Birkby et al. 2007) resulting from the greater depth and sensitivity of the SHS. The local sample has also been rigorously 'cleaned' of impostors (Chapter 8) which would otherwise bias and contaminate the

Table 10.1: Cumulative fractions of PNe by magnitude bin in five versions of the [O III] PNLF. The columns represent a standard (or universal) PNLF (generated using equation 10.5), the revised deep SMC PNLF of Jacoby (2006), the new deep LMC PNLF of Reid (2008), and two local PNLFs centred on the Sun, with volume radii of 1.0 kpc and 2.0 kpc respectively. Refer to the text for futher details.

$M - M^*$	f Standard	f SMC	f LMC	f 1.0 kpc	f 2.0 kpc
0.0	0	0	0	0	0
0.5	0.01	0.01	0.01	0.02	0.01
1.0	0.03	0.04	0.01	0.02	0.03
1.5	0.05	0.10	0.04	0.02	0.06
2.0	0.07	0.16	0.05	0.02	0.09
2.5	0.10	0.19	0.06	0.04	0.14
3.0	0.13	0.23	0.09	0.04	0.16
3.5	0.17	0.27	0.11	0.04	0.21
4.0	0.22	0.31	0.17	0.09	0.26
4.5	0.27	0.34	0.23	0.13	0.34
5.0	0.34	0.37	0.40	0.17	0.37
5.5	0.41	0.43	0.50	0.25	0.45
6.0	0.49	0.54	0.60	0.38	0.54
6.5	0.59	0.69	0.71	0.45	0.61
7.0	0.71	0.85	0.78	0.51	0.66
7.5	0.84	0.94	0.84	0.58	0.76
8.0	1.00	1.00	0.89	0.79	0.86
8.5	1.00	1.00	0.94	0.89	0.94
9.0	1.00	1.00	0.96	0.94	0.96
9.5	1.00	1.00	0.98	0.98	0.98
10.0	1.00	1.00	0.99	1.00	0.99
10.5	1.00	1.00	1.00	1.00	1.00

PNLF, especially at the faint end (see below). Both the new local PNLF and the complimentary deep LMC sample of Reid (2008) are probing down to 10 mags *below* M^*. These new samples are now addressing this issue for the first time.

To generate the local PNLF, the relevant data for the ensemble of PNe is taken from table 9.5. The [O III] apparent magnitudes were derived from the line fluxes, corrected for reddening, and absolute magnitudes calculated using the adopted distances. These distances are either calibrating distances, or are calculated from the SB-r relation (or one of its subtrends). The Hβ apparent magnitudes were similarly derived and absolute magnitudes calculated as before.

Table 10.1 provides the fraction of PNe by magnitude bin in the 'standard' PNLF, calculated from equation 10.5, the revised SMC PNLF of Jacoby (2006; see Buzzoni, Arnaboldi & Corradi 2006), the deep LMC PNLF of Reid (2008) and Reid & Parker (2008, in prep.), and two empirical PNLFs in the local volume, with volume radii of 1.0 kpc and 2.0 kpc respectively. Deep observations in the SMC (Jacoby & De Marco 2002; Jacoby 2006) show a decrease in the number of PNe ~6 mag fainter than M^*, compared to the predicted number from equation 10.3. Clearly, a volume limited sample is one way to improve the statistics at the faint end of the PNLF to see if this effect is also present in the solar neighbourhood.

Figure 10.2 plots the [O III] PNLFs for the 1.0 kpc solar neighbourhood sample and 2.0 kpc extension sample. PNe are binned in coarse 1-mag intervals to improve the statistics. The curves are derived from equation 10.3 and are normalized to the brightest (complete) magnitude bins. Despite poor statistics at the bright end, the 1.0 kpc sample is relatively complete to 8 mag down from M^*, and fully half of the PNe are fainter than 7 mag below M^*, compared with the standard and revised SMC PNLFs (see Jacoby 2006; Buzzoni, Arnaboldi & Corradi 2006) which have only 29% and 15% fainter than this limit respectively (see Table 10.1). Obvious incompleteness sets in at $M^* + 6$ mag, but it is unclear if the dip 5 magnitudes below M^* is real (see below).

The 2.0 kpc sample has much better statistics at the bright end, but is less populated at the faint end, with ∼34% of PNe more than 7 mag below M^*. The deep LMC sample of Reid (2008) goes practically as deep as the local samples, but nevertheless is quite incomplete at the faint end, with only ∼22% of PNe fainter than 7 mag below M^*.

The cumulative [O iii] and Hβ PNLFs, for PNe closer than 2.0 kpc, are shown in the top and bottom panels of figure 10.4. The faintest PNe in the local volume are ∼10 mag below M_*, which is in agreement with the faintest PNe seen in the LMC (Reid 2008; Reid & Parker 2008, in prep.). Considering the [O iii] PNLF, figure 10.4 shows that an exponential increase in PN numbers occurs to ∼8.3 mag below M_*, where a marked turnover in the PNLF is seen. The reason for the turnover at faint magnitudes is not entirely clear. The very faintest PNe may represent a population of low-mass objects with low-luminosity central stars (perhaps a consequence of long transition times from the AGB in the critical mass range; see Buzzoni, Arnaboldi & Corradi 2006), or the faint-end PNLF may be contaminated with other types of [O iii]-emitting objects.

Recall that PN contaminants in the local volume were carefully removed before the local PNLF was built. Table 10.2 lists the properties of some of the impostors that were removed in Chapter 8. These objects are mostly Strömgren spheres in the ISM, and span a large range of [O iii] magnitudes, though most are fainter than 8 mags below M^*. Note that the two bowshock nebulae around cataclysmic variables have very faint [O iii] magnitudes, suggesting that objects much fainter than $M^* + 10$ mag are not likely to be PNe. On the other hand, the HII region around KPD 0005+5106 is relatively bright but its large radius would have led to its classification as a non-PN at the distance of the Magellanic Clouds, but possibly not in the Andromeda spiral — recall that the ionizing source is very hot ($T \geq 120$ kK), and the observed emission-line ratios are typical of PNe (see the discussion in §8.10).

To investigate the PNLF faint-end cutoff further, Table 10.3 lists the properties of the 15 faintest PNe within 2.0 kpc of the Sun. Nine PNe are within 1.0 kpc, indicating that the census of these faint objects within 2.0 kpc is still incomplete and biased by extinction. Of this sample, four PNe are low excitation objects with large (∼2 pc) radii. Curiously, and somewhat disconcertingly, three objects have radii of less than 0.5 pc! Nominally, the PNLF faint-end cutoff of 8 mag below M^* corresponds to a radius of ∼0.9 pc, but this assumption appears to be incorrect. All three are high-excitation objects *sensu stricto*, with strong HeII λ4686 emission, and very low ionized masses. In fact K 1-27 may not be a conventional PN (Rauch, Köppen & Werner 1994) and Ciardullo et al. (1999) has already commented on its very faint [O iii] magnitude. HbDs 1 also has a peculiar morphology, and was intially thought to be a post-CE object, however the bright CS shows no evidence of short period light modulations (see §9.5.2).

I conclude that the majority of these [O iii]-faint nebulae are bona fide PNe, but they

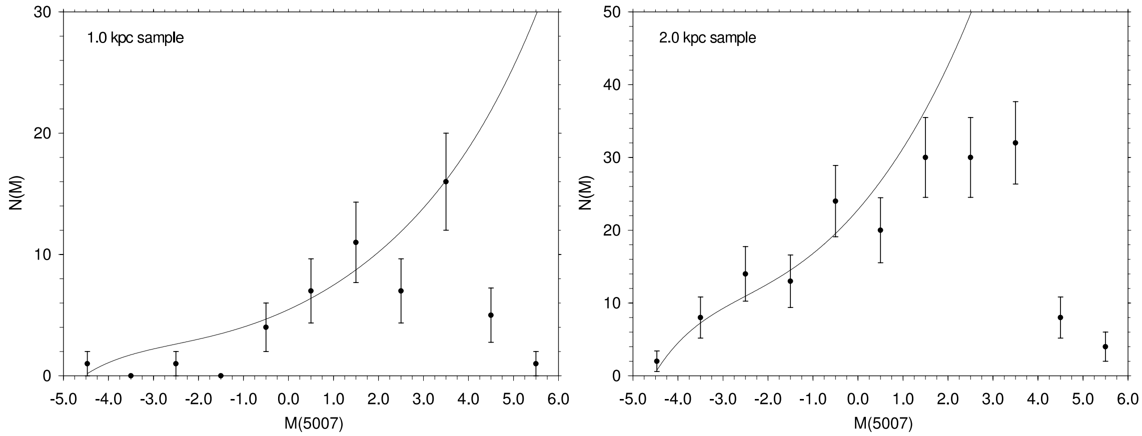

Figure 10.2: The [O III] PNLFs for the 1.0 kpc solar neighbourhood sample (left) and 2.0 kpc extension sample (right). PNe are binned in coarse 1-mag intervals to improve the statistics (note that the PNe in the samples are spread over 10 magnitudes). The curves are derived from equation 10.3 and are normalized to the brightest (complete) magnitude bins. Poisson error bars are shown. It can be seen that the 1.0 kpc sample is relatively complete to 8 mag down from M^*, while the 2.0 kpc sample is less populated at the faint end. Obvious incompleteness sets in at M^* + 6 mag, but it is unclear if the dip 5 magnitudes below M^* is real.

belong to two population types: (1) large low-excitation PNe of high ionized mass undergoing recombination, and (2) evolved optically-thin, (very) low-mass PNe. The relative proportions of the two types at the bottom of the PNLF are unknown at this point in time. Note that 24 faint, poorly-studied PNe in the local volume have no [O III] flux data at all (see table 9.4), while several others have only poor-quality fluxes. Spectrophotometric follow-up of these objects is urged.

10.3.1 Discussion

Henize & Westerlund (1963) assumed that PNe were uniformly expanding spheres around static central stars. However, central stars evolve concurrently over the dynamical timescale of a PN

Table 10.2: PN impostors and their relation to the [O III] PNLF. These objects are mostly Strömgren zones (HII regions) in the ISM. Two bowshock nebulae around catalcysmic variables are also listed.

Name	D (kpc)	$M - M^*$	S(Hα)	R (pc)	Type
KPD 0005+5106	0.27	3.9	-5.75	5.89	HII
Sh 2-174	0.42	7.1	-4.83	0.91	HII
Hewett 1	0.20	7.9	-6.33	1.45	HII
Sh 2-68	0.30	8.0	-4.51	0.30	HII
DHW 5	0.30	8.6	-5.03	0.43	HII
Abell 35	0.21	8.7	-5.09	0.43	HII?
HaWe 7	0.80	10.5	-4.62	0.39	HII?
PG 0108+101	0.30	10.8	-6.94	2.58	HII
EGB 4	0.83	11.9	-6.49	0.40	CV
PG 0109+111	0.30	12.2	-5.34	0.26	HII
Fr 2-11	0.20	13.6	-5.41	0.19	CV
HaWe 5	0.42	14.8	-5.18	0.04	HII?

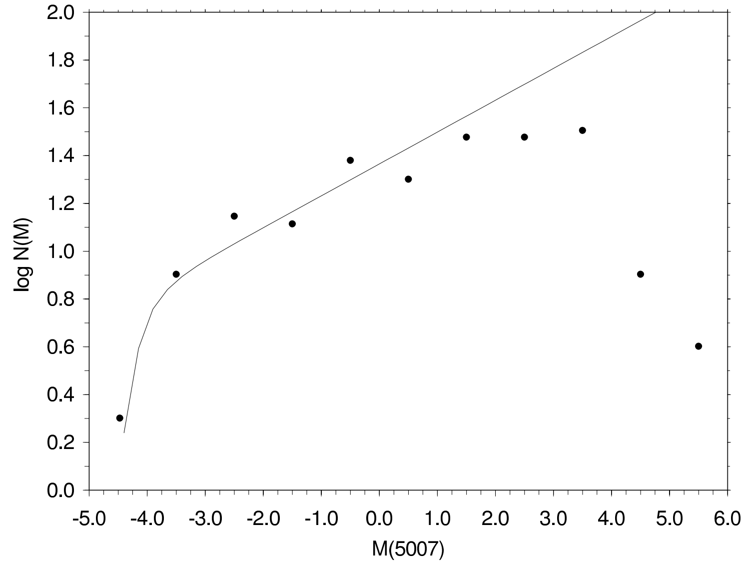

Figure 10.3: The observed [O III] PNLF for the 2.0 kpc extension sample, now plotting the logarithm of the PN number on the ordinate. The sharp drop in numbers at the bright cutoff is apparent, but the dip 5 magnitudes below M^* is of only marginal statistical significance (see figure 10.2). As shown in figure 10.2, incompleteness becomes obvious about 6 mag below M^*, but a more sudden turnover is apparent about 8.5 mag below M^*. The cause of this turnover is not yet clear.

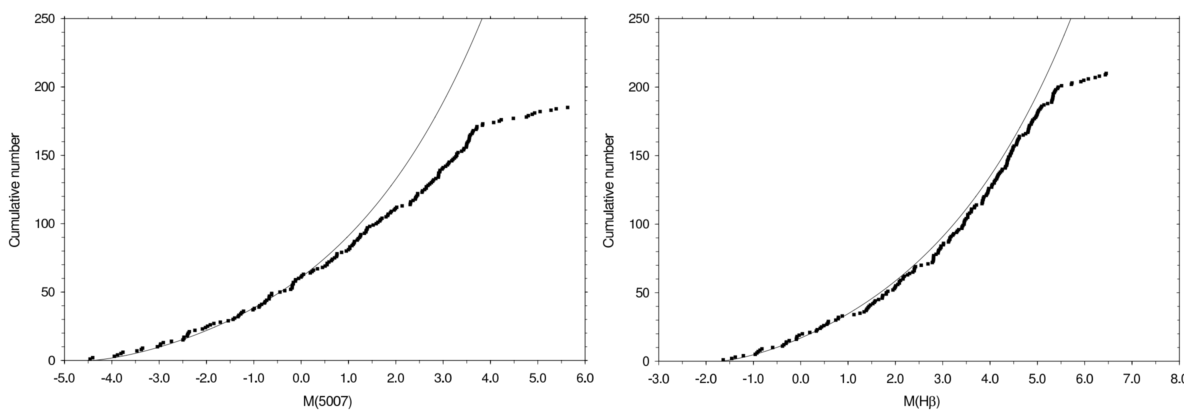

Figure 10.4: The cumulative PNLFs in [O III] and Hβ for the 2 kpc sample. The curves are derived from equation 10.5. The Hβ cutoff is set at $M^* = -1.75$. The Hβ data fits the predicted curve very well at the bright end down to 5 mags below M^*, but some incompleteness becomes apparent at the faintest magnitudes. Note the turnover 7 mags below M^*. The [O III] cumulative PNLF also fits the standard curve very well at bright magnitudes, but appears less complete than the Hβ curve at the faint end, primarily because over 20 PNe in this volume are excluded from the fit due to no available $\lambda 5007$ flux data.

Table 10.3: The 15 faintest PNe at the bottom of the [O III] PNLF. Optically-thin PNe of high excitation are denoted 'HE'.

Name	D (kpc)	$M - M^*$	S(Hα)	R (pc)	Type
LoTr 5	0.50	8.3	-5.54	0.64	HE
Abell 36	0.45	8.3	-4.91	0.42	HE
We 2-34	1.51	8.5	-5.52	1.07	...
EGB 6	0.59	8.7	-5.73	1.03	...
IsWe 1	0.62	8.7	-5.59	1.11	...
TK 1	0.57	9.0	-6.65	2.84	...
WDHS 1	0.85	>9.0	-5.73	2.39	...
Jacoby 1	0.57	9.2	-6.03	0.91	HE
FP0739-2709	1.94	9.3	-5.61	1.69	...
HbDs 1	0.80	9.4	-4.88	0.29	HE
PHR0743-1951	1.37	9.4	-5.66	1.16	...
FP1824-0319	0.36	9.5	-6.01	1.45	...
Abell 28	1.22	9.8	-5.77	0.94	...
K 1-27	1.70	9.9	-4.81	0.22	HE
BMP0642-0417	1.15	10.1	-6.49	1.96	...

(Kwok 1994; Marigo et al. 2001, 2004; Schönberner et al. 2007), and changes in stellar effective temperature, luminosity, and ionization parameter strongly influence the excitation of the PN. The overall result is that the faintest PNe in [O III] are considerably more than 8 magnitudes below M_* (cf. Henize & Westerlund 1963; Jacoby 1980; Buzzoni, Arnaboldi & Corradi 2006).

From the 2.0 kpc sample, there are 25 PNe within 2.5 mag of the bright cutoff. This suggests a total population of ~250 PNe in this volume, compared with 210 actually catalogued. However this number assumes a standard PNLF, and it is shown here that the local PNLF is more bottom-heavy than previously believed, i.e. the PNLF includes many PNe fainter than 8 mags below M_*. Using a mean surface density based on the PN complete population out to 500 pc (§11.3), there should be 300 PNe within a *projected* distance of 2.0 kpc from the Sun (198 actually known). A similar calculation shows there are about a dozen PNe remaining to be discovered within a projected distance of 1.0 kpc from the Sun. These are predicted to be have large diameters and very low surface brightnesses.

Recently, there is increasing observational evidence to show that the PNLF is not monotonic. Jacoby & De Marco (2002) found evidence of a dip in the PNLF of the SMC below the bright cut-off, and a similar effect has been noted in M 33 (Magrini et al. 2000; Ciardullo et al. 2004). However the MCELS survey of the SMC appears to be finding additional faint PNe in the SMC, so the reality of the dip remains unclear at this stage (R. Shaw, 2008, pers. comm.). Note that a similar dip has not been observed in the bulge of M 31 (Ciardullo et al. 2002), and the greatly enlarged sample of 2600 PNe in M 31 (Merrett et al. 2006) shows an almost canonical PNLF down to 3.6 mags below M_* (see figure 10.1).

Frew & Parker (2005) presented evidence for a dip in the PNLF at ~5 mag below M_* (based on preliminary data in the solar neighbourhood). However, this dip is only marginally identified in the much more extensive data set now obtained (see the bottom panel of figures 10.2 and figure 10.3). Roughly 50% of local PNe have a SB-r distance, rather than a distance derived from a primary technique. Considering the accuracy of the technique, and the often considerable errors in the distances of the calibrating PNe in this volume, any structure in the local PNLF would tend to be smeared out. In other words, the predicted 'Jacoby dips' are hidden by the errors on the distances for these local PNe. Furthermore, these dips are thought to be due to rapid evolution of central stars as they begin their descent of the WD cooling track (Schönberner 1983; Blöcker 1995), and this evolutionary effect is not accounted for when applying a linear SB-r relation.

Conventional wisdom holds that in very old populations, PN visibility is strongly reduced (Stanghellini & Renzini 2000; Buzzoni, Arnaboldi & Corradi 2006). For stars with $M_\mathrm{c} < 0.55\,M_\odot$, the transition time from the end of the AGB to the onset of ionization (see §1.3) increases markedly from 10^3 yr to more than 30,000 years (Schönberner 1983; Vassiliadis & Wood 1994; Blöcker 1995). This time interval may equal or exceed the dynamical time-scale for PN dissolution (Phillips 1989; Buzzoni, Arnaboldi & Corradi 2006). In other words, by the time the stellar core has reached a temperature sufficient for ionization, the nebula has already dispersed into the ISM. These are the so-called 'lazy' PNe.

Furthermore, cores of lower mass may not pass through the AGB and PN phases, partly as a result of higher metallicity-driven mass-loss on the RGB for these stars (e.g. Kalirai et al. 2007; Schröder & Smith 2008, and references therein). This so-called AGB-manqué pathway, is typified by stars that pass directly from the hot-HB directly to the WD cooling track (e.g. Dorman et al. 1993; Blöcker 1995; Castellani et al. 2006). The threshold mass is approximately $M_c < 0.50\,M_\odot$ (Buzzoni, Arnaboldi & Corradi 2006; Kalirai et al. 2007), but there is a dependence on metallicity (e.g. Kalirai et al. 2007).

The shape of the faint end of the PNLF is basically defined by the evolution of the central stars of lowest mass. Hence, the faintest PNe in the local volume are excellent objects to probe the phase change from the domain of observable PNe to the realm of white dwarfs without visible PNe. However, most of the objects in table 10.3 remain poorly studied due to their faintness; further work is needed on these PNe and their central stars. Recent work (e.g. Schröder & Smith 2008) suggest that the Sun may not be massive enough to produce a visible PN in the future, a point initially discussed by Jacoby et al. (1997; see the erratum in Jacoby et al. 1998). Results from this work (see the next chapter) also lead to the conclusion that progenitor stars less massive than ~1.4–1.5 $M_\odot$ may not produce visible PNe, otherwise the galactic PN population would be much larger than observed (cf. Moe & De Marco 2006a).

10.4 Bolometric luminosity-specific PN number

To better understand the relationships between a parent stellar population and its PN population, Jacoby (1980) and Peimbert (1990) have developed the concept of the luminosity-specific PN density. This ratio, usually referred to as the 'α ratio' (Buzzoni, Arnaboldi & Corradi 2006) is defined as the number of PNe seen in a galaxy, normalised to the bolometric luminosity of the galaxy, given by:

$$\alpha = \frac{N_\mathrm{PN}}{L_\mathrm{tot}} = \mathcal{B}.\tau_\mathrm{PN} \tag{10.6}$$

where $\mathcal{B}$ is the so-called 'specific evolutionary flux' (see Renzini & Buzzoni 1986; Buzzoni 1989), and τ_{PN} is the PN visibility lifetime, i.e. the time for the PN to be detectable in current [O III] and/or Hα surveys (Buzzoni, Arnaboldi & Corradi 2006). Hence just two parameters, $\mathcal{B}$ and τ_{PN} influence the value of α for a given stellar population. In fact the observed value of α is most dependent on the adopted PN visibility lifetime, since the specific evolutionary flux, $\mathcal{B}$, is nearly constant across most population types (Buzzoni 1989; Buzzoni, Arnaboldi & Corradi 2006). In general, $\tau_{\rm PN}$ sets an upper limit to the α value. For a Salpeter IMF, and using a representative value for $\mathcal{B}$ of $1.8 \times 10^{-11}\ L_\odot\,\mathrm{yr}^{-1}$, Buzzoni, Arnaboldi & Corradi (2006) derive:

$$\alpha_{\max} = 1.8\ \times\ 10^{-11}\,\tau_{PN} \quad = \quad 1\,\mathrm{PN}/1.85\ \times\ 10^{6}\,L_\odot \tag{10.7}$$

or $\log\alpha = -6.26$ (for $\tau_{PN} = 30{,}000$ yr). This value is fairly independent of metallicity. For $\tau_{PN} = 60{,}000$ yr (corresponding to a limiting radius of $\sim$1.5 pc; see §11.4.5), $\log\alpha = -6.0$.

The study of the α-ratio potentially sheds light on the characteristics of the PN population in different galaxy types, from pure ellipticals through to star-forming irregulars, and even to intracluster stars (e.g. Feldmeier et al. 2004; Arnaboldi et al. 2008). However, it is difficult to compare estimates of α between different galaxies, owing to large differences in the completeness limits for each galaxy's PNLF. Extrapolating to the total PN population from a sample of the brightest PNe is often plagued by small number statistics. Furthermore, star-forming galaxies like the SMC appear to have a non-monotonic PNLF that turns over two or three magnitudes below the cutoff (Jacoby & De Marco 2002; Ciardullo et al. 2004; Jacoby 2006) so any extrapolation based on equation 10.5 (or equivalently, the data in table 10.1) may not give accurate results. So to better compare data between galaxies, the parameter $\alpha_{2.5}$ has been introduced. This is the number of PNe within 2.5 mag of M^* normalised to the bolometric luminosity (Hui et al. 1993; Ciardullo et al. 2002; Buzzoni, Arnaboldi & Corradi 2006).

However, for the most distant galaxies studied to date (e.g. in the Virgo and Fornax clusters), even $\alpha_{2.5}$ is based on an extrapolation, since the observed sample often extends less than 1 mag down the PNLF. Hence another variant has been introduced, i.e., $\alpha_{0.5}$, which is the normalised number of PNe observed within 0.5 mag of M^*. Measurements of the α parameter in its various forms are now known for more than 30 galaxies in and beyond the Local Group (e.g. Hui et al. 1993; Ciardullo et al. 2002, 2005; Buzzoni, Arnaboldi & Corradi 2006), and the number is rising. Note that for a standard PNLF, $\alpha_{\rm tot} \simeq 10 \times \alpha_{2.5}$ which assumes that equation 10.5 applies, and that there are no PNe fainter than 8 magnitudes below M^*. Similarly, $\alpha_{0.5} \simeq \alpha/110$, where the necessary multiplicative 'completeness factor' is simply $1/f$, where f is given in column 2 of table 10.1 (see the discussion of Buzzoni, Arnaboldi & Corradi 2006).

Observationally, it has been found that the α-ratio appears to be correlated with galaxy colour, as the reddest ellipticals are a factor of $\sim$6 poorer in PNe per unit luminosity than spirals (Peimbert 1990; Hui et al. 1993; Buzzoni, Arnaboldi & Corradi 2006). This trend suggests the presence of a significant fraction of low-mass central stars in elliptical galaxies, with fewer PNe seen due to the low average luminosity of the CS in these populations. Another factor is the reduced visibility times for these objects, due to an increase in the AGB transition time (e.g. Buzzoni, Arnaboldi & Corradi 2006).

In high-metallicity populations, stars with $M_c < 0.50\,M_\odot$ bypass the PN phase, following an AGB-manqué path (Buzzoni, Arnaboldi & Corradi 2006; Kalirai et al. 2007). This contributes large numbers of hot post-HB stars (e.g. sdO stars), which will affect the integrated galaxy colours. Since this evolutionary pathway reduces the pool of potential PN progenitors, there should be a correlation between UV-upturn and the α-ratio in different galaxy populations. Indeed, the most UV-enhanced elliptical galaxies display the lowest values of α, as confirmed by members of the Virgo cluster (Ciardullo et al. 2005; Buzzoni, Arnaboldi & Corradi 2006).

It is now generally accepted that higher-mass CS must exist in early-type galaxies, such as the giant ellipticals of the Virgo cluster (Jacoby, Ciardullo & Ford 1990; Arnaboldi et al. 2008). However, Ciardullo et al. (2005) also find from the bolometric luminosity-specific PN number that in early-type galaxies, [O III]-bright PNe are relatively uncommon, with only ∼10% of central stars evolving to these bright magnitudes. They argue that the high mass cores seen in early-type galaxies derive from blue straggler stars, which result from mass transfer or mergers in a close binary, prior to the AGB phase. Such progenitor stars have masses up to twice the current turnoff mass, or $\sim 2\,M_\odot$, and are just massive enough to generate PNe in the top magnitude bin of the PNLF. The observed percentage of [O III]-bright PNe is in fair agreement with the observed proportion of blue stragglers seen in old populations (Ciardullo et al. 2005; Buzzoni, Arnaboldi & Corradi 2006, and references therein).

10.5 Summary

This chapter presented a deep, rigorously assembled PNLF in the local volume for the first time, which provides a platform on which to build our understanding of the physics of the PNLF. The solar neighhbourhood PNLF is seen to be much more bottom-heavy than previously recognised, with up to half of all PNe being fainter than 7 mag below M^*, and the faintest PNe being as faint as 10 mags below M^*. An extension sample out to 2.0 kpc confirms the faint limit of the PNLF, and provides much better statistical data at the bright end.

These new data have allowed a direct comparison with the revised SMC PNLF of Jacoby & De Marco (2002) and Jacoby (2006), and the deep LMC PNLF of Reid (2008) and Reid & Parker (2008, in preparation). However, the recent deep observations in the SMC (Jacoby & De Marco 2002; Jacoby 2006) appear to show a decrease in the number of PNe ∼6 mag fainter than M^*, compared to the predicted number from equation 10.3. These conflicting results may be due to differing sensitivity limits for the dimmest PNe. The very faintest PNe in the Clouds are seen against a bright background of widespread diffuse Hα emission and/or relatively high stellar densities, making them very difficult to detect. These problems might be alleviated in the peripheral regions of the Clouds, but the number density of observable PNe falls off there steeply as well.

Since the evolution of the CS slows markedly as it descends the WD cooling track (e.g. Schönberner 1983; Blöcker 1995), the integrated flux of an evolved PNe is not expected to vary much, even though the surface brightness continues to fade as the nebula undergoes dynamical expansion. Thus Magellanic Cloud PN samples are best thought of as surface-brightness limited, rather than magnitude limited. The Galactic PN with the lowest SB studied to date, Ton 320, has a latitude of 33°, which faciliitated its discovery in a targeted CCD image. It may not have been discovered had it been projected on a diffuse background of nebular emission, such as is seen close to the plane of the Galaxy, or against the LMC disk. However, at this stage a real deficit of faint PNe in the Clouds cannot be ruled out. Further work is obviously needed.

While the solar neighbourhood sample is of excellent statistical utility to derive better estimates for the scale height and surface density of local PNe (see Chapter 11), it does not quite deliver a 'perfect' PNLF to faint magnitudes. Despite the SB-r relation enabling significantly improved distance estimates for Galactic PNe in the absence of a distance from primary techniques, the dispersion of the relations is not insignificant, even allowing for the distinct subtrends. This would tend to smooth out structure in the local PNLF, and conversely introduce artificial structure to the exponential function as a result of these subtrends. In fact given the small number statistics, one might also expect structure to be seen in the PNLF due to Poisson errors (as seen at the bright end of the 1.0 kpc sample in figure 10.2). Since a linear relation is used for each trend, the 'Jacoby dips', if they indeed exist, are hidden by this statistical approach, as these dips are thought to be due to the fast evolution of CSs at the conclusion of nuclear burning, as they begin their descent of the WD cooling track (Schönberner 1983; Blöcker 1995). This evolutionary effect is not accounted for when using a linear SB-r relation(s).

A number of other key facts concerning the local PNLF that have come out of this work are summarised in the following bullet points:

• Based on observed PN surface densities in the solar neighbourhood, incompleteness sets in at around 500–600 pc from the Sun (see §11.3). There are no PNe within 2.5 mag of M^* inside this volume. The brightest PN, M 27, has $M_{5007} = -0.68$ (i.e. 3.8 mag fainter than M^*), while the next brightest (the Helix, NGC 7293) is 5.5 mag fainter than the bright cutoff.

• The nearest [O III]-bright PN is NGC 7027 at 850 pc, with $M_{5007} = -4.44$. This PN is either a bipolar object or a bipolar-core elliptical (e.g. Phiilips et al. 1991). There is one other PN closer than 2.0 kpc within 0.1 mag of M^*. This is NGC 6369 (D = 1550 pc, $M_{5007} = -4.40$), also classified as a bipolar-core object, seen relatively face-on (Monteiro et al. 2004). Hence, the bright end of the the Galactic PNLF is completely consistent with the extragalactic PNLF. There are no anomalously bright objects in the local volume.

• There are 25 PNe within 2.5 mag of M^* inside 2.0 kpc. Of these, 9 have bipolar morphologies, one is a bipolar-core object, and 14 are other elliptical PNe. Only one round PN is present, NGC 6818 with $M_{5007} = -2.48$. NGC 2392, with $M_{5007} = -1.25$ is the next brightest, though another bright, round PN, NGC 1535 ($M_{5007} = -2.33$) is just outside the volume, at D = 2.3 kpc. Hence we show conclusively that the brightest PNe in the local volume have bipolar or elliptical morphologies. *Round PNe are conspicuously absent from the top of the PNLF.* This result disagrees with the findings of Magrini et al. (2004), based however, on a flux-limited Galactic sample.

• Interestingly, two extreme butterfly nebulae, NGC 6537 and NGC 6302, are in the top 1 mag of the [O III] PNLF. Both are bona fide Type I PNe (following Kingsburgh & Barlow

1994). NGC 6537 is compact with a high surface brightness, but with a remarkably faint central star (Matsuura et al. 2005b); with $M_v = +5.9$, it is already descending the WD cooling track. Therefore NGC 6537 is a good test object to observe temporal changes in the ionization level of the nebula. With a massive, fast evolving central star, the nebula is probably out of photoionization equilibrium.

Chapter 11

The Galactic PN Population

11.1 Introduction

A secondary goal of this work was to improve the statistics of the total space density and birthrate of PNe, as these parameters are critically dependent on the adopted statistical distance scale for old PNe (Ishida & Weinberger 1987; Pottasch 1996). Ciardullo et al. (1999) have stressed the importance of deriving a statistical calibration that simultaneously handles both the brighter PNe and the lower surface brightness objects that prevail among the nearby nebulae. Napiwotzki (1999, 2001) has derived a 'long' statistical distance scale based on NLTE model atmospheres that gave considerably larger distances than trigonometric, spectroscopic, extinction, and Shklovsky distances for large old PNe. These evolved, optically-thin PNe represent a population that are usually avoided as calibrators of statistical distances (see Chapter 6), and this may be the reason for the systematic offsets that plague the various statistical distance scales (see Pottasch 1996; Ciardullo et al. 1999). The sample presented in this thesis has greatly increased the number of old objects, which has helped to reconcile the distance-scale problem.

In turn the total space density leads to an estimate for the total number of PNe in the Galaxy. However, the range of values seen in the literature over the last three decades is disconcertingly large, from 4,000 to 140,000 PNe (Alloin, Cruz-González & Peimbert 1976; Cahn & Wyatt 1976; Jacoby 1980; Daub 1982; Amnuel et al. 1984; Ishida & Weinberger 1987; Peimbert 1990, 1993; Zijlstra & Pottasch 1991; Pottasch 1996; Phillips 2002a; Peyaud 2005; Frew & Parker 2005, 2006).

Recent data on the current known population of Galactic PNe (e.g. Parker et al. 2006, and Chapter 1) range from 2500 to 3300 PNe and PN candidates. This number is uncomfortably close to the lower estimates in the literature for the Galactic population, especially considering that the most of the far side of the Galaxy beyond the bulge is entirely unsurveyed for PNe.

In this chapter, the determination of the scale height from both the 1.0 kpc and 2.0 kpc volume-limited samples is discussed. An estimate for the local space density of PNe is presented, and estimates for the total Galactic PN population based on this number and a variety of methods then follows. A discussion concludes the chapter, including visiting the vexing problem of whether close binaries are mandatory for PN production.

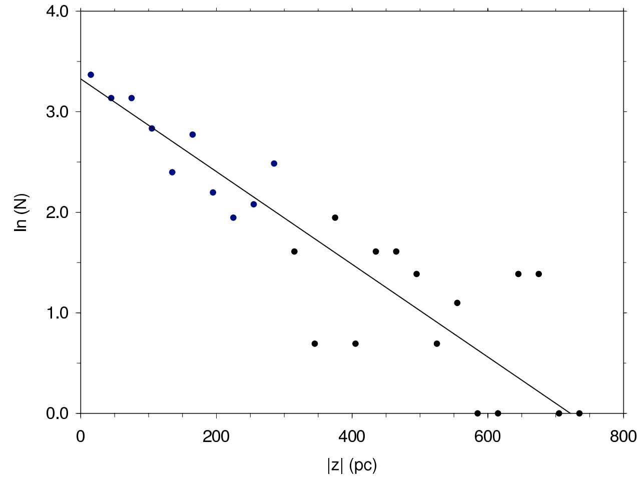

Figure 11.1: The distribution of local PNe as a function of z. The least squares fit gives a scale height of 217 ± 20 pc. Only PNe with $|z| \leq 300$ pc are used in the linear fit.

11.2 Scale height

From first principles, PNe are assumed to follow an exponential distribution with height in the Galactic disk. Therefore the number density of PNe, $\rho(z)$, at a distance $|z|$ from the midplane of the disk is equal to:

$$\rho(z) = \rho_0 e^{-z/h_z} \tag{11.1}$$

where ρ_0 is the planar number density in units of PN per kpc^{-3} and h_z is the scale height in kpc.

For each PN in the local sample, the height from the plane z, and the projected distance q were calculated[1] (see Chapter 8). Figure 11.1 shows the logarithmic distribution for all PNe within 2.0 kpc, as a function of $|z|$. After assigning the $|z|$ heights into 30 pc bins, the resulting distribution (see Figure 11.1) was fit with a least-squares line. A more robust fit was achieved using only PNe with $|z| \leq 300$ pc, since the bins at largest $|z|$ distance suffer from small number statistics; the resulting scale height is $h_z = 217 \pm 20$ pc.

This can be compared with the average $|z|$ distance of PNe in the 1.0 kpc and 2.0 kpc samples. For a uniform exponential distribution containing many points, the sample average is equivalent to the scale height. The mean $|z|$ distance for the 1.0 kpc sample is $|\bar{z}| = 195 \pm 21$ pc, while for the 2.0 kpc sample, $|\bar{z}| = 235 \pm 23$ pc. The total uncertainty includes an assumed zero-point error in the distance scale of 5% (see Chapter 7), with an additional 10% uncertainty added in quadrature to account for possible biases due to reddening in the Galactic plane and incompleteness at high latitudes (see below).

The estimate derived from the 2.0 kpc sample may be an overestimate as some PNe close to the plane are missing due to extinction (Phillips 2001b). Their absence would bias the number to a value somewhat higher than truth. Alternatively, some high-Galactic latitude PNe remain to be discovered, not unexpected since the MASH catalogue cuts out at $b \sim 11°$. Since, as

[1]This is the distance from the sun to the subnebular point, as measured in the Galactic plane

explained elsewhere, the search for new PNe in the local volume has been less complete at *high* latitudes, the PN scale height derived here might be slightly underestimated. However, a back-of-the-envelope calculation suggests that any correction is less than 10%. In the discussion that follows, I adopt a PN scale height for the local volume of $h_z = 216 \pm 24$ pc, where the error bar allows for the range of values determined from the three methods.

The value adopted here broadly agrees with other recent determinations in the literature. Zijlstra & Pottasch (1991) determined a value of 250 ± 50 pc, assuming an exponential disk, or 190 ± 40 pc for an isothermal disk. Corradi & Schwarz (1995) find $h = 259$ pc, but Phillips (2001b) found a somewhat lower value of 156 ± 37 pc. Older determinations have tended to be smaller, e.g. $h_z = 125$ pc (Daub 1982), $h_z = 130$ pc (Amnuel et al. 1984) and $h_z = 100$ pc (Ishida & Weinberger 1987), primarily due to the 'short' distance scales these authors used.

The WD scale height has been estimated as $h_z = 275 \pm 50$ pc (Boyle 1989), while Vennes et al. (2002) determined $h_z = 220 - 300$ pc from a large sample of DA white dwarfs discovered as part of the 2dF survey. These estimates broadly agree within the errors of the PN scale height derived here. Olivier, Whitelock & Marang (2001) have determined $h_z = 236 \pm 10$ pc for dust-enshrouded AGB stars, the immediate precursors of PNe. In fact, the PN scale height may be expected to be slightly smaller than the WD or AGB scale heights, as lower-mass progenitors will not evolve fast enough to ionize observable PNe (i.e. 'lazy' PNe). This point will be discussed further below, especially in the light of recent revisions to the initial-final mass relation (IFMR; e.g. Kalirai et al. 2007 a,b). Furthermore, since the mean PN scale height is dependent on the adopted distance scale, the fact that the PN scale height is in agreement with both AGB and WD scale heights provides independent evidence that the adopted PN distance scale zero point is accurate to ± ∼10–20%.

It is also worthwhile to compare the PN scale height with determinations based on star counts of low-mass, main-sequence stars which numerically dominate the thin disk. Phleps et al. (1999) derived a thin disk scale height of 213 ± 24 pc, but Chen et al. (2001) derive a scale height of 330 pc for late type dwarfs in the thin disk. These authors also determine a scale height of 580 – 750 pc for the thick disk, somewhat lower than the estimates of 860–1040 pc from Phleps et al. (1999) and Ojha (2001). Chen et al. (2001) also determine a local thick/thin disk normalisation ratio of 6.5% – 13%, but other determinations average about 5% (e.g. Ojha 2001; Wyse 2006). With ∼61 PNe with $q < 1000$ pc (table 11.2), ∼2 – 8 PNe are expected to be thick disk objects.

From the local sample data presented here, LTNF 1 (=BE UMa) is considered to be a probable thick-disk PN; note this is a post-CE object. The high-excitation PN NGC 4361 has been considered to be a halo object (e.g. Torres-Peimbert, Peimber & Peña 1990), but is here considered to also be a thick disk PN, on the basis of its kinematics and height from the galactic plane. The round PN IC 5148/50 might also be a thick disk member. Note that the scale heights derived here for high-excitation PNe and round PNe are similar (and significantly higher than the mean), and may imply a subset of these PNe may belong to the thick disk. One halo object near the North Galactic Pole (Haro 4-1) with a low q value, has been excluded from further discussion.

Table 11.1: Average $|z|$ distances for various subsets of PNe, based on volume-limited samples. The total uncertainty includes a 5% distance-scale zero-point error, with an additional 10% uncertainty added in quadrature to account for possible biases due to incompleteness at high latitudes and reddening in the Galactic plane.

Class	$\|z\|$ (pc) 1 kpc sample	$\|z\|$ (pc) 2 kpc sample
All	195 ± 21	235 ± 26
Asymmetric	...	119 ± 15
Round	310 ± 35	320 ± 35
Elliptical	200 ± 22	248 ± 27
Bipolar	...	95 ± 20:
Type I	...	85 ± 15
HE	260 ± 30	380 ± 40
WZO 1	212 ± 25	255 ± 30
WZO >1	180 ± 20	210 ± 25
low-mass CS	...	360 ± 40
high-mass CS	...	190 ± 20

Amnuel, Guseinov & Rustamov (1989) had previously found different scale heights for low- and high-mass PNe (see also Corradi & Schwarz 1995; Manchado et al. 2000; Phillips 2001b, 2001d). This work, utilising an accurate volume-limited sample of PNe allows a reinvestigation of this topic. A summary of the average $|z|$ distances for various subsets of PNe from this work is given in table 11.1.

In general, the numbers confirm previous work but are more robust, being based on a volume-limited sample. For example, the scale height for round PNe from Manchado et al. (2000) is considerably more than that determined here, but their estimate was not corrected for extinction (see the discussion by Phillips 2001b). Since the number of bipolar sources in the local volume is relatively small, only an approximate scale height of $|\bar{z}| \simeq 95$ pc is found, but this is statistically different to the average for all objects, confirming previous results which show they are more concentrated to the Galactic plane (e.g. Corradi & Schwarz 1995; Górny, Stasińska & Tylenda 1997; Phillips 2001b). This suggests that the mass of the progenitor star has a strong influence on the morphology of the ejected PN (see §4.2). Similarly, Type I PNe have a low mean $|z|$ distance of 85 ± 15 pc, implying that the progenitor stars of these PNe are main sequence stars of spectral type late-B to early-A (Miller & Scalo 1979; Phiilips 2001b), i.e., progenitor masses of >3–4 $M_{\odot}$.

A reliable scale height for common-envelope PNe could not be determined from the available data, due to small number statistics, but there is no compelling evidence for a different value to the estimate for all PNe. I have also divided the sample into two groups based on their degree of interaction with the ISM, based on the new scheme of Wareing, Zijlstra & O'Brien (2007b). Not unexpectedly, interacting PNe (WZO index > 1) are found closer to the plane than PNe showing no signature of an ISM interaction, but the difference is not statistically significant. However, the sample of aged, strongly distorted PNe termed 'Asymmetric' (see Chapter 4) have a mean $|z|$ distance of just 119 ± 15 pc, suggesting that only PNe close to the Galactic midplane, where the ambient ISM density is highest, can suffer such advanced deformation.

Table 11.2: Surface density of PNe in the solar neighbourhood

q (kpc)	0.3	0.4	0.5	0.6	0.7	0.8	0.9	1.0	1.5	2.0
n (all)	5	12	18	25	33	43	53	62	133	208
n (r <0.9 pc)	4	8	10	15	19	25	32	39	98	163
Area (kpc^2)	0.28	0.50	0.79	1.13	1.54	2.01	2.54	3.14	7.07	12.57
μ (PN kpc^{-2}) (all)	17.7	23.9	22.9	22.1	21.4	21.4	20.8	19.7	18.8	16.6
μ (PN kpc^{-2}) (r $<$ 0.9 pc)	14.1	15.9	12.7	13.3	12.3	12.4	12.6	12.4	13.9	13.0

11.3 Surface and Number Densities

The available data presented here allow a better quantification of the total space density of PNe. To determine the local surface (or column) density directly, PNe in the solar neighbourhood were binned into zones of radius q kpc projected onto the Galactic plane and centred on the Sun. From the data presented in Table 11.2 and Figure 11.2, the local PN column density was found to be $\mu = 23.4 \pm 2.3$ kpc^{-2}, with obvious incompleteness setting in at $q \simeq 600$ pc. The uncertainty of 10% is based on the adopted SB-r zero-point error of 5%, since the error in the surface density goes as D^2. This is a conservative approach as three quarters of the PNe within 600 pc have primary distance estimates, independent of any uncertainty in the SB-r relation and its subtrends.

A reciprocal scale height is defined as $k_z = 1/h_z$ kpc^{-1}, which for the local sample is $k_z = 4.63^{+0.58}_{-0.46}$ kpc^{-1}. It follows that the surface density, μ, and the planar number density, ρ_0, are related by the equation:

$$\mu = \int_{-\infty}^{\infty} \rho(z)dz = 2\rho_0 h_z \tag{11.2}$$

The local planar number density ρ_0 is then given by:

$$\rho_0 = \frac{\mu . k}{2} \tag{11.3}$$

Adopting for the surface density, $\mu = 23.4 \pm 2.3$ kpc^{-2}, ρ_0 is found to be 54.4 ± 10.1 kpc^{-3}, where the error takes into account the uncertainties in the SB-r zero-point and the scale height.

11.4 Number of Galactic PNe

Once the PN column density at the solar radius is known, there are three different approaches to determining the total Galactic disk PN population using the observed parameters of the Galactic disk as determined from other studies. A preliminary estimate of the *total* Galactic PN population, derived from three independent methods, was ~30,000 PNe (Frew & Parker 2005). Better data obtained since then has warranted a re-appraisal of the Galactic PN population.

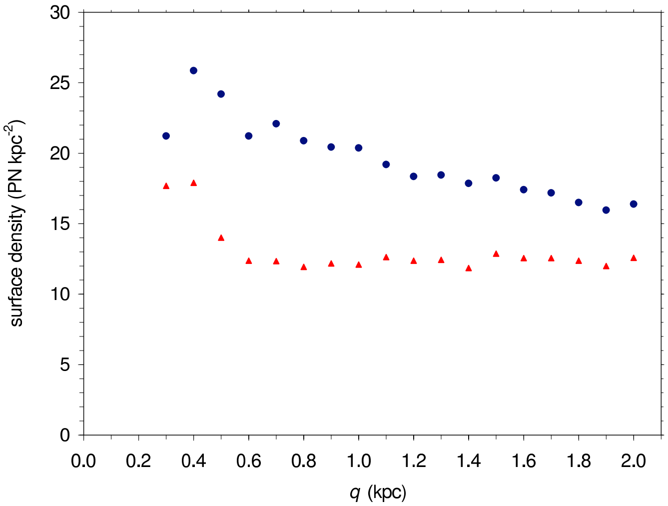

Figure 11.2: Plot of PN surface (column) density against distance from the Sun. Dark blue dots show all PNe, while red triangles plot PNe with radii ≤ 0.9 pc.

11.4.1 Number of Disk PNe from Galactic scale length

Via the exponential scale length of the disk, H, we calculate the number of PNe within any galactocentric distance R_G by:

$$n_{\mathrm{G}} = 2\pi\mu_0 \, e^{k_l R_\odot} \left[\frac{1 - (1 + k_l R_{\mathrm{G}})\, e^{-k_l R_{\mathrm{G}}}}{k_l^2} \right] \tag{11.4}$$

where $k_l = 1/H$ is the reciprocal disk scale length, $R_\odot$is the solar radius, taken to be 8 kpc (Reid 1993), and μ_0 is the surface density at the centre of the Galactic disk, given by:

$$\mu_0 = \frac{\mu}{e^{-k_L R_\odot}} \tag{11.5}$$

This approach assumes a constant scale length throughout the Galactic disk. However, some caveats are present: there is very likely a wavelength dependence on the radial scale length (e.g Naab & Ostriker 2006), which implies that the mass-to-light ratio is not constant across the disk. Furthermore, the disk scale height is also variable with radius (e.g. Kent, Dame & Fazio 1991), but modelling these second-order effects on the total PN population and birthrate is beyond the scope of this work.

Unfortunately, there is still considerable uncertainty in the exact value of the Galactic scale length. Brief reviews summarising earlier determinations have been presented by Bahcall & Soneira (1980), who adopt $H = 3.5$ kpc, Kent, Dame & Fazio (1991), Sackett (1997) and Ojha (2001). Gould, Bahcall & Flynn (1996) adopted $H = 3.0 \pm 0.4$ kpc based on the distribution of disk red dwarfs, and Zheng et al. (2001) similarly determine $H \simeq 2.75$ kpc from red dwarfs. López-Corredoira et al. (2002) determine an infrared radial scale length of $H \simeq 3.3$ kpc, based on 2MASS star counts, while Benjamin et al. (2005) measure $H = 3.9 \pm 0.6$ kpc from GLIMPSE mid-IR data. Hereafter, a value of $H = 3.3 \pm 0.6$ kpc is adopted, with the assumed error bar consistent with the range seen in recent literature determinations.

While there is modest sensitivity of the total PN number to the adopted radial scale length, the total number is fairly insensitive to the exact cutoff radius of the Galactic disk (for $R_{\rm co} \gg H$), assuming a truncated exponential for the disk. Robin et al. (1982) used optical star counts and a synthetic stellar population model to estimate $R_{\rm co} = 14 \pm 0.5$ kpc, while Ruphy et al. (1996) used near-IR star counts to find $R_{\rm co} = 15 \pm 2$ kpc. The most distant disk open clusters (e.g. MacMinn et al. 1994; Friel 1995) have galactocentric radii of ∼14 − 16 kpc, excluding objects like Be 29 (Tosi et al. 2004) which may have originated in an accreted dwarf galaxy. The most remote PNe (e.g. Mampaso et al. 2005, 2006) are at similarly large distances. However, Freudenreich (1998) finds a smaller value of $R_{\rm co} = 12.4 \pm 0.1$ kpc by fitting a model for the old disk to *COBE*-DIRBE NIR data. This cutoff radius may be underestimated, and the error seems optimistic. A weighted mean of $R_{\rm co} = 15.0 \pm 1.0$ kpc is adopted hereafter.

Of more import however, is that most reasonable estimates for the truncation radius of the Galactic disk place constraints on the Galactic scale length. Several studies (van der Kruit & Searle 1982, and references therein) have given a value of $R_{\rm co}/H = 4.2 \pm 0.5$, which would imply a scale length of ∼3.6 kpc for the Milky Way disk (consistent with the adopted value, above). However, Pohlen, Dettmar & Lütticke (2000) find from an ensemble of spiral disks that $R_{\rm co}/H = 2.9 \pm 0.7$. Using $R_{\rm co} = 15$ kpc, this suggests $h_l = 5.2^{+1.6}_{-1.0}$ kpc, which is higher than most recent determinations. More work is needed to explain this discrepancy.

Setting $H = 3.3 \pm 0.6$ kpc and $R_{\rm co} = 15.0 \pm 1.0$ kpc, and adopting a column density of $\mu = 23.4 \pm 2.3$ kpc^{-2}, leads to a total number of 19,800 ± 4000 PNe in the Galactic disk.

11.4.2 Number of disk PNe using mass-specific number

The *total* local column mass density determined in a column between 1.1 kpc above and below the plane (a distance which includes all but one PN in table 9.4) is $\Sigma_{1.1\rm kpc} = 71 \pm 6\ M_\odot$ pc^{-2}, which includes an undetected halo component (Kuijken & Gilmore 1989). The local *observed* column mass density, made up of stars, stellar remnants and gas is about $\Sigma_\odot = 45 \pm 5\ M_\odot$ pc^{-2} (e.g. Kuijken & Gilmore 1989, 1991; Gould, Bahcall & Flynn 1996; Naab & Ostriker 2006). Using the observed PN surface density derived in § 11.3, the local mass-specific PN number, is $5.3 \times 10^{-7} M^{-1}$.

The mass of the Milky Way is dominated by the dark halo, so multiplying the local mass specific number determined from the solar neighbourhood by the *total* Galactic mass will give a number for the total PN population that is overestimated (cf. Ishida & Weinberger 1987). Instead, adopting a galactic *disk* mass = (4.0 ± 0.7) $\times 10^{10}\ M_\odot$ (see Moe & De Marco 2006 for a review), leads to a total number of $N_{\rm disk}$ = 19,200 ± 4200 PNe.

11.4.3 Number of Galactic PNe using luminosity-specific number

An alternative approach is to directly find the local luminosity density, α, in the solar neighbourhood, and scale up to the total luminosity of the Galaxy. For a discussion of the α parameter, see §10.4. In this section the number of galactic PNe is averaged from four estimates of this parameter, $\alpha_{\rm bol}$, α_K, α_I and α_V.

The K-band absolute magnitude of the Milky Way is $M_K = -24.06$, set to $R_0 = 8.5 \pm 0.5$ kpc (Malhotra et al. 1996), as determined from *COBE*/DIRBE data, with an estimate for the disk alone of $M_K = -23.2$ (Naab & Ostriker 2006). The B-band absolute magnitude of the Milky Way has been determined by van der Kruit (1986) who gives $M_B = -20.3 \pm 0.2$. Additionally, using the integrated colour quoted by van der Kruit (1986), leads to $M_V = -21.1 \pm 0.25$.

A simple value for the V-band bolometric correction for the Milky Way disk is $BC_V = m_{bol} - V = -0.85$. This correction is accurate to within 10% (i.e. $\pm$ 0.1 mag) for almost all stellar population types and ages (Buzzoni 2005; Buzzoni, Arnaboldi & Corradi 2006). Hence, a bolometric absolute magnitude[2] of $M_{\rm bol} = -21.95 \pm 0.3$ is determined for the Milky Way.

The observed local luminosity densities are $k_l^K = 81\ L_\odot/{\rm pc}^2$, $k_l^I = 31\ L_\odot/{\rm pc}^2$ and $k_l^V = 26\ L_\odot/{\rm pc}^2$ at K, V and I respectively. After adopting the bolometric correction from Buzzoni, Arnaboldi & Corradi (2006), the local bolometric luminosity density is estimated as $k_l^{Bol} = 51\ L_\odot/{\rm pc}^2$.

Using the adopted PN surface density from §11.3, luminosity specific numbers in each band follow immediately. Adopting the respective Milky Way luminosities, $L_{\rm bol} = 4.7 \times 10^{10}\ L_\odot$, $L_K = 8.9 \times 10^{10}\ L_\odot$, $L_I = 4.0 \times 10^{10}\ L_\odot$, and $L_V = 2.3 \times 10^{10}\ L_\odot$, gives the total number in the Galaxy as respectively, 21,700 PNe (from the bolometric luminosity), 25,700 PNe (via K-band), 30,000 PNe (via I-band) and 21,100 PNe (via V-band). The weighted average from this technique is 24,600 $\pm$ 5100 PNe.

11.4.4 Total number of PNe in the Galaxy

Weighting the disk PN totals determined from the radial scale length (§11.4.1) and the local mass-specific number (§11.4.2) gives an average of $N_{\rm disk}$ = 19,500 $\pm$ 4000 PNe, which is in excellent agreement with Zijlstra & Pottasch (1991) who found the disk number to be 23,000 $\pm$ 6000.

The number of disk PNe can be added to the recent estimate of the number of PNe in the Galactic bulge by Peyaud (2005), based in part on recent MASH discoveries (see also Peyaud et al. 2006) to determine the number of PNe in the whole Galaxy. By utilising a new sample of $\sim$500 PNe in the bulge, Peyaud (2005) uses a 'de Vaucouleurs' density law to extrapolate the observed sample to the whole bulge, estimating $n_{\rm bulge}$ = 3500 $\pm$ 200, though the error seems underestimated; it has been reset to $\pm$700 PNe hereafter. Adding the bulge population to the disk population determined above, this leads to a total Galactic population of n = 23,000 $\pm$ 5000 PNe.

In the bulge, there is evidence for ongoing star formation, which has likely enhanced the PN production rate compared to pure Population II. For the purposes of this discussion, the same value of α is assumed for both disk and bulge. Hence, the estimate of Peyaud (2005) implies a bulge/disk mass ratio of $\sim$0.15, which is less than most estimates (see the discussion by Moe & De Marco 2006). This assumption probably does not apply, as the production rate in the bulge

[2]The following values for the solar bolometric magnitude and V-band bolometric correction are adopted throughout: $M_\odot^{\rm bol} = +4.74$ and $BC_\odot^V = -0.08$ (Cox 2000; cf. Buzzoni 1989).

is likely to be lower based on population synthesis models (e.g. Buzzoni, Arnaboldi & Corradi 2006), discussed further below. Using the data presented by Moe & De Marco (2006), it is seen that $\alpha_{\rm bulge} < \alpha_{\rm disk}$, which means the bulge is less efficient at producing PNe, due to its older mean age.

Combining the 'disk plus bulge' estimate from above with the weighted total Galactic number from §11.4.3, gives a final estimate for the total of $n_{\rm tot}$ = 24,000 ± 4000 Galactic PNe (with r < 1.5 pc).

11.4.5 Comparison with previous work

Jacoby (1980) estimated a total population of 10,000 ± 4000 PNe in the Galaxy, after considering the number of PNe known in external galaxies. He determined luminosity-specific and mass-specific numbers of PNe to be 6.1×10^{-7} PN $L_{\odot}^{-1}$ and 2.1×10^{-7} PN $M_{\odot}^{-1}$ respectively. Similarly, Peimbert (1990) estimated a Galactic population of n = 7,200 ± 1800 PNe with radius < 0.64 pc (cf. Peimbert 1993). Moe & De Marco (2006a) show that these estimates apply to PNe with radii <0.9 pc, corresponding to a brightness about 8 mag down the PNLF. Moe & De Marco (2006a) adopt a Galactic population of n = 8000 ± 2000 PNe with radii < 0.9 pc. However, the total population estimate derived here includes very large PNe (limiting radius of ∼ 1.5 pc) further down the PNLF (see §10.3). To better compare this total with these earlier estimates (see Moe & De Marco 2006a for a discussion), a simple scaling factor applied to their adopted radius limit (assuming uniform expansion velocity, which may not be strictly true) leads to a total number of 0.9/1.5 × 24,000 = 14,000 PNe with $r < 0.9$ pc

However, the completeness levels are different for the samples to each limiting radius. Hence, a better approach is to recalculate the local surface density in the solar neighbourhood from the observational data of Chapter 9, after excluding all PNe with r > 0.9 pc. The completeness of this sample is assumed to be 95% within q = 1.0 kpc (see §9.2). The resulting column density, $\mu_{0.9}$ = 12.7 PN kpc^{-2} (see Table 11.2), leads to a disk population (r < 0.9 pc) of 10,500 ± 2000 objects, or 13,000 ± 2000 PNe for the whole galaxy. This number is consistent with the estimate from Jacoby (1980), but slightly outside the error bar of Moe & De Marco (2006a).

The total number of Milky Way PNe found above is more than just of academic interest. It can be used to estimate the total number of PNe visible in an external galaxy, by scaling the relative luminosity of the galaxy to that of the Milky Way [the reverse of the procedure of Jacoby (1980) and Peimbert (1993)]. The ratio is best determined in a near-infrared photometric band, where the flux is dominated by the intermediate-age and older populations which include the precursors of PNe, or by comparing the bolometric luminosities of the systems.

The only two external galaxies with any claim for completeness in their PN populations at present are the LMC (Reid & Parker 2006a,b) and SMC (Jacoby & De Marco 2002; Jacoby 2006, and see the preceding chapter). The necessary integrated $IJHK$ photometry is non-existent for the Magellanic Clouds, so to estimate the luminosity ratios, the absolute magnitudes of the Clouds in the V-band are used instead. Table 11.3 summarises the available B and V integrated photometry for the Clouds.

The various SMC magnitudes are in good agreement, but there is much more scatter in the

Table 11.3: Integrated B and V magnitudes for the Magellanic Clouds

B_T SMC	V_T SMC	B_T LMC	V_T LMC	Reference
2.58 ± 0.05	1.97 ± 0.06	0.25 ± 0.05	....	1
2.79	2.29	0.63	0.08	2
2.70	2.25	0.91	0.40	3

1. Bothun & Thompson (1988)
2. De Vaucouleurs & Freeman (1972)
3. RC3 (de Vaucouleurs et al. 1991)

determinations of the integrated magnitude of the LMC, due undoubtedly to the huge angular size of this system. Hence, the adopted magnitudes are $B_T^{\mathrm{LMC}} = 0.7 \pm 0.2$, $V_T^{\mathrm{LMC}} = 0.2 \pm 0.2$, and $B_T^{\mathrm{SMC}} = 2.70 \pm 0.05$, $V_T^{\mathrm{SMC}} = 2.20 \pm 0.05$.

Using the consensus distances to the LMC and SMC of 50 kpc and 59 kpc respectively (μ_0 = 18.50 and 18.85), and the foreground reddenings from Schlegel et al. (1998), the absolute V-band magnitudes are determined to be $M_V^{LMC} = -18.6$ and $M_V^{SMC} = -16.8$. No correction for galaxy inclination has been adopted. Using $M_V^{MW} = -21.1$, the calculated V-band luminosity ratios are $\ell_{(MW/LMC)} = 10 \pm 2$ and $\ell_{(MW/SMC)} = 52 \pm 3$. Hence the total LMC population of PNe (limiting radius of $r < 1.5$ pc) is estimated as ∼2400 PNe, with a similar estimate of ∼460 PNe for the SMC. Just considering PNe with $r < 0.9$ pc, the Galactic number is ∼13,000, so there should be ∼1300 PNe in the LMC and ∼250 PNe in the SMC if the production rates are similar.

Reid & Parker (2006b) estimate a total LMC population of $n_{\mathrm{tot}} = 956 \pm 141$ PNe, while Jacoby & De Marco (2002) estimate $n_{\mathrm{tot}} \sim 216$ PNe in the SMC. These numbers are identical within the errors to the older estimates of Jacoby (1980) who derived $n_{\mathrm{tot}} = 996 \pm 253$ PNe for the LMC and $n_{\mathrm{tot}} = 285 \pm 78$ PNe for the SMC. Evidently, many more faint, *very large* PNe remain to be discovered in these systems, though the SMC population is now essentially complete to a radius limit of ∼0.9 pc (Jacoby & De Marco 2002; Jacoby 2006).

A hint that these previous magnitude-limited population estimates for the Clouds are too low is shown by the diameters of the faintest resolved PNe in the Clouds. In Jacoby (1980, table 3) the largest PN has a radius of ∼0.5 pc, a factor of three less than the adopted limiting radius for evolved PNe determined here[3]. Assuming constant expansion velocity over the course of PN evolution, one would expect the ratio of numbers of PNe in the bins $r < 0.5$ pc and $r <$ 1.5 pc to also be a factor of three, roughly what is found.

[3] Shortening the adopted distance scale decreases the limiting PN radius, but increases the local column density and therefore number estimates for the Milky Way and Magellanic Clouds.

11.5 PN birthrate

The kinematic age of a PN is equal to $r_{mean}/V_{\rm exp}$. Using convenient units, the kinematic age (in years) is calculated via:

$$t_{\rm kin} = \frac{9.78 \times 10^5\, r}{v_{\rm exp}} \tag{11.6}$$

where r is the PN radius (in pc) and $v_{\rm exp}$ is the expansion velocity in $\rm km\,s^{-1}$ for optically thin nebulae, and the velocity of the ionization front for optically thick nebulae. Since most PNe in the solar neighbourhood sample are very old and evolved (and at least partly optically thin), the first condition dominates.

Individual expansion velocities have been taken from Weinberger (1989) or are based on new WHAM data (see Chapter 3). If no such data is available, a constant expansion velocity of $20\,\rm km\,s^{-1}$ is generally assumed in the literature (e.g. Weinberger 1989; Ishida & Weinberger 1987, and other references). However, this may not hold for the most senile PNe as they interact with the ISM. A reasonable estimate of the average expansion velocity of a PN can be obtained by averaging the velocities of PNe in a volume-limited sample. Using the data for individual PNe given in table 9.5, the average expansion velocity of this ensemble is $24\,\rm km\,s^{-1}$.

If the limiting radius of this sample of optically visible PNe is known, equation 11.6 gives the mean PN lifetime, τ, in years. Adopting a mean PN limiting radius, $r = 1.5$ pc, the mean PN limiting age is $\tau = 6.1 \times 10^4$ yr. For a limiting radius of 0.9 pc, the age is $\tau = 3.7 \times 10^4$ yr.

The PN birthrate, $\chi_{(PN)}$, is then defined as

$$\chi_{(PN)} = \frac{\rho_0\, v_{\rm exp}}{\Delta\, r} \tag{11.7}$$

where, as before, ρ_0 is the local planar number density, $v_{\rm exp}$ is the adopted mean expansion velocity and $\Delta\, r$ is the change in radius over the mean observable lifetime of the PN. From this we get $\chi_{\rm (PN)} = 0.9 \pm 0.5 \times 10^{-12}\ \rm pc^{-3}yr^{-1}$. Using just the data for PNe with radii $<$ 0.9 pc (which are more complete), we get $\chi_{\rm (PN)} = 0.8 \pm 0.3 \times 10^{-12}\ \rm pc^{-3}yr^{-1}$. This value is in very good agreement with the white dwarf birthrate determined by Liebert, Bergeron & Holberg (2005) of $\chi_{\rm (WD)} = 1.0 \pm 0.25 \times 10^{-12}\,\rm pc^{-3}\,yr^{-1}$ and the value determined by Vennes et al. (2002) of $\chi_{\rm (WD)} = 0.75 \pm 0.25 \times 10^{-12}\,\rm pc^{-3}\,yr^{-1}$.

One of the earliest determinations of the PN birthrate was by Cahn (1968) who found $\chi_{\rm (PN)} = 0.5 \times 10^{-12}\,\rm pc^{-3}\,yr^{-1}$. He concluded that the "white-dwarf population must have received a major contribution from planetary nebulae." Phillips (1989) determined a higher rate of $2.4 \pm 0.3 \times 10^{-12}\,\rm pc^{-3}\,yr^{-1}$; he gives a useful discussion of the literature up to that date. Pottasch (1996) determined $\chi_{\rm (PN)} = 3 \times 10^{-12}\,\rm pc^{-3}\,yr^{-1}$, while Phillips (2002a) determined $\chi_{\rm (PN)} \simeq 1.6 \times 10^{-12}\,\rm pc^{-3}\,yr^{-1}$. Ishida & Weinberger (1987) found a much higher figure of $8.3 \times 10^{-12}\,\rm pc^{-3}\,yr^{-1}$, which strongly disagrees with the accepted WD birthrate. This can be attributed to the very high space density determined by these authors, based largely on a distance scale that was much too short. Ishida & Weinberger (1987) used the Shklovsky method but assumed a canonical mass of $0.2M_\odot$ for an evolved PN, a number which has been shown here (in Chapter 9) to be too low.

The predicted formation rate of Moe & De Marco (2006a) from single stars and binaries is $1.1 \pm 0.5 \times 10^{-12}\,\mathrm{pc}^{-3}\,\mathrm{yr}^{-1}$. Despite the different predictions on the total number of PNe in the Galaxy, their PN birthrate agrees with the value determined here. As Moe & De Marco (2006a) themselves state, this is due to the very different approach between the observationally-based estimates and the theoretical model derived by these authors.

Note that the production of WDs is also due to other post-RGB channels such as via AGB-manqué evolution (and possibly via the O(He) star route; Rauch et al. 2006), plus 'lazy PNe', which have central stars that evolve too slowly to ionize the ejected nebular shell. As a result, the observed WD birthrate should be somewhat greater than the observed PN birthrate. Considering the errors, the present estimate of the PN birthrate is in agreement with current estimates for the WD formation rate, after factoring in these alternative evolutionary scenarios (see also Chapter10).

Finally, using the preferred value of N_{G} = 24,000 PNe, the total Galactic production rate is given by:

$$\chi_{(G)} = \frac{\tau}{N_G} \sim 0.4\,\mathrm{year}^{-1} \qquad (11.8)$$

Using only PNe with $r < 0.9$ pc, the rate is ~0.35 year^{-1}, which is good agreement with Peimbert (1993)[4], but considerably less than estimated by Cahn & Wyatt (1976).

11.6 Discussion

It turns out that the total PN number in the Galaxy is of key interest to population synthesis calculations, in order to ascertain the mass range of PN progenitor stars. De Marco & Moe (2005) used a simple Drake equation-style approach to determine the number of PNe predicted to be in the Milky Way, ~114,000 PNe. Moe & De Marco (2006a) have used an elegant population synthesis model to estimate the number of PNe in the Galaxy if all stars in the mass range $1.05 < M < 10 M_\odot$ produced PNe, versus the numbers predicted if their hypothesis that PNe are the product of close binary (post-CE) evolution is true. Moe & De Marco (2006a) predict a Galactic population of PNe with radii < 0.9 pc to be 46,000 ± 13,000. From the observational work of Jacoby (1980) and Peimbert (1993), Moe & De Marco (2006a) adopt a Galactic population of n = 8000 ± 2000 PNe with radii < 0.9 pc, which can be directly compared with their theoretical prediction. Consequently, Moe & De Marco (2006a) claim that the difference between the observed and predicted PN populations is discrepant at the 2.9 σ level, and go on to conclude that only some of the stars thought to be able to make PNe, actually do so — namely close binaries. Similarly, Moe & De Marco (2006b) have predicted a total galactic population of 5000 ± 1600 PNe, if they directly result from CE evolution, which is in tolerable agreement with the estimated total number of PNe (Jacoby 1980; Peimbert 1993; Moe & De Marco 2006a).

A new observationally-based estimate for the total number of Milly Way PNe with r <0.9 pc

[4]Or put another way, roughly one new PN is born in the Milky Way in the time interval between IAU Symposia!

is 13,000 $\pm$ 2000 (§11.4.5), which is inconsistent with the theoretical prediction from Moe & De Marco (2006a). Furthermore, this is also inconsistent with the predicted number if *all PNe* are assumed to go through a common-envelope phase. The total number determined from this work is based on an accurate database of nearby PNe developed here and is considered to be robust. Recall that the observed space density derived here provides a PN birthrate of 0.8 $\pm$ 0.3 $\times$ 10^{-12} pc^{-3}yr^{-1}, fully consistent within the errors with the WD birthrate of 1.0 $\pm$ 0.25 $\times$ 10^{-12} pc^{-3}yr^{-1} (e.g. Liebert, Bergeron & Holberg 2005), and which allows for a population of low-mass stars that form WDs but not visible PNe ('lazy' PNe) and a modest frequency of common-envelope events.

Nevertheless, we need to explain why the theoretical prediction of Moe & De Marco (2006) disagrees with my determination of the total galactic population. There are a number of possible reasons to resolve this discrepancy. There may be many more PNe in the solar neighbourhood that remain to be discovered, especially at higher Galactic latitudes, which may be fainter on the average and harder to detect (see Soker & Subag 2005; and Chapter 9). Similarly, if the objects shown to be PN impostors in Chapter 8 are re-added to the local sample after further investigation, the local surface densities become $\mu_{1.5} \simeq 36$ PN kpc^{-2} and $\mu_{0.9} \simeq 20$ PN kpc^{-2} respectively, leading to a total Galactic PN population of 38,000 ($r \leq 1.5$ pc) or 23,000 PNe ($r \leq 0.9$ pc). If many or most of the doubtful SHASSA and WHAM nebulae (see Appendix B) are also considered to be PNe, these number estimates rise accordingly, and the discrepancy with the prediction of Moe & De Marco (2006) vanishes. However, hypothesising a large number of additional local PNe (with $r < 0.9$ pc) inflates the PN birthrate, forcing disgreement with the independently derived WD birthrate.

More feasably, there may be a number of incorrect inputs into population synthesis model that Moe & De Marco (2006a) have used. The upper mass limit for PN production is more generally accepted to be 8 $M_{\odot}$, and furthermore, these high-mass progenitors are expected to show extremely rapid evolution (see Equation 1.3) which effectively biases against the discovery of such objects. However, because of the relative rarity of B-type progenitors, a change in the upper mass limit will have only a very minor effect on the estimate of the total number of PN precursor stars.

Of more importance is the exact value of the lower progenitor mass limit for PN generation. This value is somewhat uncertain and depends on the adopted post-AGB evolutionary tracks, which differ somewhat amongst themselves (e.g. Schönberner 1983; Wood & Faulkner 1986; Blöcker & Schönberner 1991; Vassiliadis & Wood 1994; Blöcker 1995), as well as the metallicity (which determines the amount of mass loss in the AGB phase). We note that recent work on the low-mass end of the initial-final mass relation (Kalirai et al. 2008) hints at a revision of the lower mass bound for PN production. A central star below a minimum mass of $\sim$0.55 $M_{\odot}$ is considered to evolve too slowly to ionize a PN before it disperses into the interstellar medium [see the discussions in Buzzoni, Arnaboldi & Corradi (2006), and Moe & DeMarco (2006a)], a fact which is in agreement with the observed mass distribution of PN central stars (see §9.4.6).

Referring to the recent IFMR of Kalirai et al. (2008), the lower limit of a PN progenitor is now closer to 1.4–1.5 $M_{\odot}$, more than assumed by Moe & DeMarco (2006a). However, until more data points are added to the low-mass end of the IFMR, there remains a considerable uncertainty in this estimate. Nonetheless, if the lower mass limit is closer to $\sim$1.5 $M_{\odot}$, this will substantially decrease the number of PNe predicted by the population synthesis model (Moe & DeMarco 2006a), and bring it into closer agreement with the observations. Especially interesting is the data from the old metal-rich cluster NGC 6791; an average initial mass of 1.16 $M_{\odot}$ is found to produce an average WD mass of only 0.51 $M_{\odot}$ (Kalirai et al. 2008). Furthermore, it appears most of the lower mass WDs in NGC 6791 evolved directly from the extended horizontal branch (Kalirai et al. 2007a), a consequence of super-solar metallicity, further reducing the pool of potential PN progenitors. Further observational data to refine the low-mass end of the Population I IFMR, and the dependence on metallicity is urged.

In summary, a decrease in the upper limit from 10 to 5 $M_{\odot}$ (to produce *observationally detectable* PNe) combined with an increase in the lower limit from 1.05 to 1.5 $M_{\odot}$, effectively reduces the total number of precursor stars by $\sim$50%, after referring to a representative initial mass function (e.g. Kroupa 2001). Hence, the discrepancy between the predicted and observed PN populations is greatly reduced, to $\sim 1.5\sigma$. Empirically, precursor stars of lower mass had been thought capable of producing PNe, as they are found in globular clusters and the Galactic bulge. However, Alves, Bond & Livio (2000) postulate that the PN Pease 1 (K 648) in the globular cluster M 15 is likely the product of a star of greater mass than the current turn-off ($M = 0.8\,M_{\odot}$) as the measured CS mass of 0.60 $M_{\odot}$ is higher than the mean mass of globular cluster and halo WDs, 0.50 $M_{\odot}$. Hence, Pease 1 has possibly evolved from a cluster blue-straggler, which was the likely product of a binary merger before the AGB phase. Blue stragglers are thought to be the possible progenitors of [O III]-bright PNe which populate the top of the PNLF in elliptical galaxies (Ciardullo et al. 2005).

In addition, the observation that known close-binary PNe fall on a particular trend in SB–r space (see Chapter 7) is suggestive that *close-binary PNe form a separate population to the majority of PNe*. Zijlstra (2007) used another argument to show that the population synthesis model may be incorrect. That is, the observationally determined distribution of CS masses is different to that predicted by Moe & De Marco's population synthesis model.

To sum up, I consider the hypothesis that the great majority (or all) PNe go through a common-envelope phase is not supported at this point in time, though there is no doubt a modest frequency of common-envelope events has occurred in the solar neighbourhood. The exact number awaits a full multiplicity census of all objects within this volume. There is also strong evidence that binarity does affect the *shaping* of PNe, especially amongst the subset of demonstrably post-CE systems (e.g. Mitchell et al. 2007; Zijlstra 2007).

Chapter 12

Conclusions and Future Work

This dissertation has investigated in detail, for the first time, the properties of a critically-evaluated, volume-limited sample of Galactic PNe. Most prior statistical studies have used flux-limited samples of Galactic PNe, but a volume-limited local sample of PNe has much better potential to answer some of the remaining unsolved questions of PN research. The main conclusions of this work are summarised in the following bullet points. The reader is referred back to the relevant chapters for full details.

12.1 Summary

1. The results of a search for new evolved PN candidates based on the AAO/UKST Hα Survey, the Southern H-Alpha Sky Survey Atlas, and the Virginia-Tech Spectral-line Survey is presented. Preliminary data from the INT Photometric Hα Survey and the WHAM NSS are also discussed.

2. Integrated Hα fluxes for nearly all of the nearest evolved PNe (and many more distant examples) are presented. Aperture photometry on the SHASSA and VTSS digital images was performed to extract Hα+[N II] fluxes. For the SHASSA data, the [N II] contribution was then deconvolved using literature data, unpublished spectra, or data from the WHAM. Comparison with previous work shows that the flux scale presented here has no significant zero-point error. WHAM observations were also used to determine accurate integrated fluxes in Hα, [N II] and [O III] for many of the largest PNe.

3. The Hα fluxes are used to determine new Zanstra temperatures for those PNe with accurate central star photometry, and the calculation of surface-brightness distances for each PN. The [O III] fluxes are used to determine new absolute magnitudes for delineating the faint end of the PN luminosity function.

4. A spectroscopic survey of nearby PNe has been undertaken, including a brief discussion of the preliminary chemical abundances of this sample.

5. Distance estimates for a robust sample of calibrating PNe from the literature, plus new

distances for a number of highly evolved PNe, have allowed a new Hα surface brightness – radius relationship to be devised as a useful distance indicator. The SB–r relation covers >6 dex in SB, and while the spread in SB is ∼1 dex at a given radius, optically thick (mainly bipolar and bipolar-core) PNe tend to populate the upper bound of the trend, while common-envelope PNe and very high-excitation PNe form a sharp lower boundary. The SB-r zero point is consistent with new accurate trigonometric distances from Harris et al. (2007) and gravity distances derived from the high-quality data of Good et al. (2004). Distances to the LMC, SMC, Galactic Bulge, and Sagittarius dSph are recovered to within 5%.

6. Hence, new distances are presented for all nearby PNe, either obtained with the SB-r relation, the extinction-distance method, or revised distances critically evaluated from the literature. With distances to all nearby PNe, I have generated the most *accurate* volume-limited sample of PNe ($D \leq 1.0$ kpc) yet considered, containing ∼55 PNe. An extension sample to 2.0 kpc contains ∼210 PNe. An accurate database of parameters for nearly all of these objects is presented, providing integrated fluxes, diameters, morphological classifications, distances, ionized masses, expansion velocities, kinematic ages, chemical abundances, and central star properties for each PN in this volume-limited sample.

7. I also give details on a number of misclassified local 'PNe', showing that ∼10% of previously catalogued nearby PNe are in fact HII regions ionized by a hot evolved star. These include Abell 35, Sh 2-174, DHW 5, Hewett 1 (Chu et al. 2004), RE 1738+665, PG 0108+101, PG 0109+111, HDW 4, PHL 932, EGB 5, and Sh 2-68. Several other optically-thin evolved PNe have ionised haloes in the ISM around them, that are not physically associated with the central PNe. The LMC PN halo statistics of Reid & Parker may need to be reconsidered in light of this fact.

8. There are currently no DO white dwarfs known to be physically associated with a PN (cf. Werner et al. 1997). The nebulae around PG 0108+101, PG 0109+111, PG 1034+001 and KPD 0005+5106 are faint HII regions ionized by these hot stars.

9. Similarly no sdOB/sdB stars are physically associated with a PN (or other ejecta nebula). I also adopt the definitional statement that a PN must be the product of post-AGB evolution, and not be formed (hypothetically) from an alternative post-EHB or AGB-manqué path.

10. The observation that known close-binary PNe fall on a particular trend in SB–r space, shared by a subclass of high-excitation optically-thin PNe, strongly suggests that close-binary PNe form a *separate population* to the majority of PNe.

11. The present data suggest a CSPN binary fraction of 52% to 58%, comparable to that seen in sun-like stars (Duquennoy & Mayor 1991; Lada 2006), and presumably A-type and F-type stars (see Eggleton & Tokovinin 2008), which are the progenitors of most PNe. Post-CE nebulae are a fraction of these and are in the minority: the best estimate at

present is 12% to 33% of all PNe. Thus, the recent conclusion that the great majority (or all) PNe go through a common-envelope phase is not supported at this point in time, though there is no doubt a modest frequency of common-envelope events has occurred in the solar neighbourhood. The exact number awaits a full multiplicity census of all objects within this volume.

12. A first volume-limited PNLF centred on the Sun, emphasising the faint end, is presented here. The solar neighbourhood PNLF is more bottom-heavy than previously believed, with fully half of the PNe are fainter than 7 mag below M^*. The 2.0 kpc sample has better statistics at the bright end, but is less complete at the faint end, with ∼34% of PNe more than 7 mag below M^*. The faintest PNe in the local volume are ∼10 mag below M_*, which is in agreement with the faintest PNe seen in the LMC (Reid 2008; Reid & Parker 2008, in prep.). The new deep [O III] PNLF shows that an exponential increase in PN numbers occurs to ∼8.3 mag below M_*, where a marked turnover in the PNLF is seen. The very faintest PNe may represent a population of low-mass objects with low-luminosity central stars.

13. New estimates for the number density, scale height, birth rate, and total number of Galactic PNe, as extrapolated from the solar neighbourhood sample are also given. The total Galactic population is estimated to be 24,000 ± 4000 PNe with r <1.5 pc, and 13,000 ± 2000 PNe with r <0.9 pc, compared to the current total population of ∼3200 PNe and good PN candidates. The observed MW/LMC luminosity ratio implies a total LMC PN population of ∼2400. Evidently many more *evolved* PNe remain to be discovered in this system.

14. The observed Galactic population leads to a PN birthrate of $0.8 \pm 0.3 \times 10^{-12}$ pc^{-3}yr^{-1}, consistent with current estimates of the white dwarf birthrate.

15. In addition, a remarkable bow-shock nebula around a previously unnoticed, bright, nova-like cataclysmic variable, V341 Ara, has been discovered as part of this study. The star has a high space motion, leading to the formation of the parabolic bow-shock at the interaction of the accretion disk wind and the ISM. The proximity of this nebula to the Sun suggests the space density of such objects may be quite high. Similar nebulae might be found through a narrowband search around other CVs with significant proper motion.

12.2 Future Work

Refinement of the solar neighbourhood PN database will require a further improvement in the PN distance scale, which in turn will be dependent on all nearby PNe having distances known to better than ±10%, data which is currently lacking. This dearth of data may well be remedied by 2020, when the results from the GAIA astrometric satellite[1] are expected. This space mission, with its microarsecond positions, proper motions, and parallaxes, along with accurate

[1] http://www.rssd.esa.int/gaia/

radial velocities, promises to revolutionise our understanding of the Milky Way's stellar content, planetary nebulae included (see van Leeuwen 2007 for a fuller discussion).

For example, precise and accurate distances to hundreds of Galactic PNe will allow the PN luminosity function to be calibrated directly from the local volume. Hence the PNLF technique is destined to become a primary distance indicator in the near future.

The search for new PNe (especially for very evolved examples) will also continue. The completion of IPHAS will add to the total of known PNe in the northern sky, and new narrowband and wideband surveys such as VPHAS+[2] and SkyMapper[3] in the south have the potential to find even fainter PNe missed by MASH and MASH-II. Complimentary searches into longer-wavelength regimes will allow the discovery of highly reddened PNe in more obscured regions of the plane.

The question of progenitor star binarity as an essential ingredient in the PN formation recipe is still not properly resolved, though the evidence presented in this thesis is strongly supportive of the idea that single stars make PNe. Since the sample size of known post-CE PNe is still very small, there is urgent need to continue the search for close-binary nuclei. The ~21 post-CE PNe in table 7.2 (two without periods, excluding WeBo 1) represent just ~0.6% of the 3200 PNe currently known in the Galaxy (see Chapter 1), though several new close-binary PNe have been found from OGLE data (Miszalski et al. 2008, in preparation). A systematic program aimed at undertaking time-series photometry of local CSPN, as well as radial velocity monitoring (though these methods are difficult for faint CS) is needed.

Deep $(U)BVRIJHK(L)$ photometry of *all* CS in the solar neighbourhood sample is also required to ultimately get a better handle on the intrinsic binary fraction of PN nuclei. First steps towards these goals are underway as part of the PLAnetary Nebula Binaries (PLAN-B) project (De Marco, pers. comm., 2007). New deep imaging surveys becoming available now or in the near future should have an impact by producing extensive new optical and NIR datasets (e.g. UKIDSS, VHS, SkyMapper), while new radial velocity surveys aimed at fainter CS are planned.

The upcoming decade will be an exciting time in the history of PN research. Hopefully, by its end, the detailed mechanisms involved in the formation, shaping, and late-stage evolution of planetary nebulae and their ionizing stars will finally be understood.

[2] http://www.vphas.org/
[3] http://msowww.anu.edu.au/skymapper/

References

Aaquist O.B., 1993. Detailed radio morphology of the compact nebula K 3-35. A&A, 267, 260

Abell G.O., 1955. Globular clusters and planetary nebulae discovered on the National Geographic Society-Palomar Observatory Sky Survey. PASP, 67, 258

Abell G.O., 1966. Properties of some old planetary nebulae. ApJ, 144, 259

Acker A., 1976. Cinematique, age, et binarite des noyaux de nebuleuses planetaires. POStr, 4, 1

Acker A., 1978. A new synthetic distance scale for planetary nebulae. A&AS, 33, 367

Acker A. & Jasniewicz G., 1990. The nucleus of Abell 35: a cataclysmic binary? A&A, 238, 325

Acker A. & Neiner C., 2003. Quantitative classification of WR nuclei of planetary nebulae. A&A, 403, 659

Acker A. & Stenholm B., 1990a. A cataclysmic binary at the centre of the large planetary nebula HFG 1. A&A, 233, L21

Acker A. & Stenholm B., 1990b. Misclassified planetary nebulae. A&AS, 86, 219

Acker A., Jasniewicz G. & Gleizes F., 1985. Spectroscopic variations of the central star of LoTr5. A&A, 151, L13

Acker A., Marcout J. & Ochsenbein F., 1996. First Supplement to the SECPGN. Observatoire de Strasbourg

Acker A., Gliezes F., Chopinet M., Marcout J., Ochsenbein F. & Roques J.M., 1982. Catalogue of the central stars of true and possible planetary nebulae. PSCDS, No. 3. Observatoire de Strasbourg

Acker A., Marcout J., Ochsenbein F. & Lortet M.C., 1983. Index and cross-identification of planetary nebulae. A&AS, 54, 315

Acker A., Chopinet M., Pottasch S.R. & Stenholm B., 1987. Misclassified planetary nebulae. A&AS, 71, 163

Acker A., Stenholm B., Tylenda R. & Raytchev B., 1991. The absolute Hβ fluxes for galactic planetary nebulae. A&AS, 90, 89

Acker A., Ochsenbein F., Stenholm B., Tylenda R., Marcout J. & Schohn C., 1992. Strasbourg-ESO Catalogue of Galactic Planetary Nebulae. ESO, Garching

Acker A., Fresneau A., Pottasch S.R. & Jasniewicz G., 1998. A sample of planetary nebulae observed by HIPPARCOS. A&A, 337, 253

Adelman-McCarthy J.K., Agueros M.A., Allam S.S., et al., 2008. The sixth data release of the Sloan Digital Sky Survey. ApJS, 175, 297

Afşar M. & Bond H.E., 2005. Radial-velocity survey of central stars of southern planetary nebulae. MSAIt, 76, 608

Allard F., Wesemael F., Fontaine G., Bergeron P. & Lamontagne R., 1994. Studies of hot B subdwarfs. IX: Cousins *BVRI* photometry and the binary fraction of hot, hydrogen-rich subdwarfs in the Palomar–Green survey. AJ, 107, 1565

Allen C.W., 1973. *Astrophysical Quantities* (3rd edition). The Athlone Press.

Allen D.A., 1973. Near infrared magnitudes of 248 early-type emission-line stars and related objects. MNRAS, 161, 145

Allen D.A., 1984. A catalogue of symbiotic stars. PASA, 5, 369

Allen D.A., 1988. A Perspective on the symbiotic stars. In Mikolajewska J., et al. (ed), The Symbiotic Phenomenon, IAU Colloquium 103, 3. Dordrecht: Reidel

Aller L.H., 1956, Gaseous Nebulae. London: Chapman & Hall

Aller L.H., 1976. Planetary nebulae, survey and outlook. PASP, 88, 574

Aller L.H., 1987. Physics of Thermal Gaseous Nebulae: Physical Processes in Gaseous Nebulae. Springer (Astrophysics and Space Science Library)

Aller L.H. & Czyzak S.J., 1983. Chemical compositions of planetary nebulae. ApJS, 51, 211

Aller L.H. & Keyes C.D., 1987. A spectroscopic survey of 51 planetary nebulae. ApJS, 65, 405

Aller L.H., Keyes C.D. & Feibelman W.A., 1988. Two compact planetary nebulae of moderate excitation: NGC 6565 (3–4°.5) and NGC 6644 (8–7°.2). PASP, 100, 192

Ali A., 1999. Studies of four evolved planetary nebulae. NewA, 4, 95

Ali A. & Pfleiderer J., 1999. PN G218.9-10.7: a galactic emission nebula of unique morphology. A&A, 351, 1036

Ali A., El-Nawawy M.S. & Pfleiderer J., 2000. Statistical and physical study of one-sided planetary nebulae. Ap&SS, 271, 245

Ali A., Pfleiderer J. & Saurer W., 1997. Narrow band CCD imaging of four PNe. IAU Symp., 180, 204

Althaus L.G., Serenelli A.M., Panei J.A., Córsico A.H., Garca-Berro E. & Scóccola C.G., 2005. The formation and evolution of hydrogen-deficient post-AGB white dwarfs: The emerging chemical profile and the expectations for the PG 1159-DB-DQ evolutionary connection. A&A, 435, 631

Althaus L.G., Córsico A.H., Kepler S.O. & Miller Bertolami M.M., 2008. On the systematics of asteroseismological mass determinations of PG 1159 stars. A&A, 478, 175

Alves D.R., Bond H.E. & Livio M., 2000. Hubble Space Telescope observations of the planetary nebula K648 in the globular cluster M15. AJ, 120, 2044

Amnuel P.R., Guseinov O.H., Novruzova H.I. & Rustamov Y.S., 1984. Statistical survey of planetary nebulae: distances, masses, and distribution in the Galaxy. Ap&SS, 107, 19

Amnuel P.R., Guseinov O.H. & Rustamov Y.S., 1989. Planetary nebulae in the Galaxy. Ap&SS, 154, 21

Andrews A.D & Lindsay E.M., 1967. New southern clusters and nebulous ovals. IAJ, 8, 126

Appleton P.N., Kawaler S.D. & Eitter J.J., 1993. An enormous planetary nebula surrounding the X-ray source RXJ 2117+34. AJ, 106, 1973

Araya G., Blanco V.M., & Smith M.G., 1972. A new extension of the Helix Nebula. PASP, 84, 70

Arkhipova V.P., 1968. Photoelectric observations of the nuclei of planetary nebula He 1-5 and NGC 1514. AZh, 45, 6 [SvA, 12, 1036]

Arkhipova V.P. & Lozinskaya T.A., 1978. The nature of the nebulae A 21 (YM 29) and Simeiz 22. PAZh, 4, 16 [SvAL, 4, 7]

Arkhipova V.P., Lozinskaya T.A., Moskalenko E.I. and Sitnik T.G. 1989. New observations of planetary nebulae S 22 and YM 29. IAU Symp., 131, 50

Arnaboldi M., Doherty M., Gerhard, O., et al., 2008. Expansion velocities and core masses of bright planetary nebulae in the Virgo Cluster. ApJ, 674, L17

Arp H.C. & Madore B.F., 1987. A Catalogue of Southern Peculiar Galaxies and Associations. Cambridge University Press

Arp H & Scargle J.D., 1967. A high-latitude planetary nebula. ApJ, 150, 707

Arrieta A., Torres-Peimbert S. & Georgiev L., 2005. The proto-planetary nebula M 1-92 snd the symbiotic star MWC 560: two evolutionary phases of the same type of object? ApJ, 623, 252

Augensen H.J., 1985. A search for radial velocity variations in the central stars of southern planetary nebulae and planetary-like objects. MNRSA, 213, 399

Baade, W., 1935. A new planetary nebula. PASP, 47, 99

Bains I., Bryce M., Mellema G., Redman M.P. & Thomasson P., 2003. High-resolution radio structure and optical kinematics of NGC 7027. MNRAS, 340, 381

Balick, B.. 1987. The evolution of planetary nebulae. I. Structures, Ionizations, and morphological sequences. AJ, 94, 671

Balick, B. & Frank, A., 2002. Shapes and shaping of planetary nebulae. ARA&A, 40, 439

Balick, B., Gonzalez, G. & Frank, A. 1992. Stellar wind paleontology. II. Faint halos and historical mass ejection in planetary nebulae. ApJ, 392, 582

Balick, B., Wilson, J. & Hajian, A.R., 2001. NGC 6543: the Rings around the Cat's Eye. AJ, 121, 354

Bally J. & Reipurth B., 2001. When star birth meets star death: a shocking encounter. ApJ, 552, L159

Bannister N.P., Barstow M.A., Holberg J.B. & Bruhweiler F.C., 2003. Circumstellar features in hot DA white dwarfs. MNRAS, 341, 477

Barbieri, C. & Sulentic, J.W., 1977. The planetary nebula 164+31°.1. PASP, 89, 261

Barker T., 1978. Spectrophotometry of planetary nebulae. I. Physical conditions. ApJ, 219, 914

Barnard, E.E., 1884. New nebulae. AN, 108, 369

Barstow M.A., Wesemael F., Holberg J.B., et al., 1994a. A new hot DA white dwarf in a region of exceptionally low HI density. MNRAS, 267, 647

Barstow M.A., Holberg J.B., Marsh M.C., et al., 1994b. RE 1738+665: the hottest DA white dwarf detected by *ROSAT*. MNRAS, 271, 175

Barstow M.A., Bannister N.P., Holberg J.B., Hubeny I., Bruhweiler F.C. & Napiwotzki R., 2001. Far-ultraviolet spectroscopy of the hot DA white dwarf WD 2218+706 (DeHt 5) with STIS. MNRAS, 325, 1149

Barstow M.A., Good S.A., Holberg J.B., Hubeny I., Bannister N.P., Bruhweiler F.C., Burleigh M.R. & Napiwotzki R., 2003a. Heavy-element abundance patterns of hot DA white dwarfs. MNRAS, 341, 870

Barstow M.A., Good S.A., Burleigh M.R., Hubeny I., Holberg J.B. & Levan A.J., 2003b. A comparison of DA white dwarf temperatures and gravities from *FUSE* Lyman line and ground-based Balmer line observations. MNRAS, 344, 562

Barstow M.A., Bond H.E., Holberg J.B., Burleigh M.R., Hubeny I. & Koester D., 2005. *Hubble Space Telescope* spectroscopy of the Balmer lines in Sirius B. MNRAS, 362, 1134

Baume G., Vázquez R.A & Feinstein A., 1999. $UBVI$ imaging photometry of NGC 6231. A&AS, 137, 233

Beaulieu, S.F., Dopita, M.A. & Freeman, K.C., 1999. A survey of planetary nebulae in the southern Galactic bulge. ApJ, 515, 610

Becker S.A. & Iben I., Jr, 1979. The asymptotic giant branch evolution of intermediate-mass stars as a function of mass and composition. I. Through the second dredge-up phase. ApJ, 232, 831

Becker S.A. & Iben I., Jr, 1980. The asymptotic giant branch evolution of intermediate-mass stars as a function of mass and composition. II. Through the first major thermal pulse and the consequences of convective dredge-up. ApJ, 237, 111

Beer S.H. & Vaughan A.E., 1999. Two new planetary nebulae and an AGN in the Galactic plane. PASA, 16, 134

Belczyński K., Mikolajewska J., Munari U., Ivison R.J. & Friedjung M. 2000. A catalogue of symbiotic stars. A&AS, 146, 407

Bell S.A. & Pollacco D.L., 1995. Absolute dimensions and masses of the eclipsing planetary nebula central stars UU Sagittae and V477 Lyrae. In Harpaz, A. & Soker, N. (eds), Asymmetrical Planetary Nebulae. AnIPS, 11, 71

Bell S.A., Pollacco D.L. & Hilditch R.W., 1994. Direct optical observations of the secondary component of UU Sagittae. MNRAS, 270, 449

Bellazzini M., Ibata R.A., Monaco L., Martin N., Irwin M.J. & Lewis G.F., 2004. Detection of the Canis Major galaxy at $(l; b) = (244° \ -8°)$ and in the background of Galactic open clusters. MNRAS, 354, 1263

Bellazzini M., Ibata R., Martin N., Lewis G.F., Conn B. & Irwin M.J., 2006. The core of the Canis Major galaxy as traced by red clump stars. MNRAS, 366, 865

Benedict G.F., McArthur B.E., Fredrick L.W., et al., 2003. Astrometry with Hubble Space Telescope: a parallax of the central star of the planetary nebula NGC 6853. AJ, 126, 2549

Benjamin R.A., McCullough P.R. & Madsen G.J., 2001. A straight and narrow ionized filament: normal filamentation or stellar contrail? BAAS, 33, 1531

Bensby T. & Lundström I., 2001. The distance scale of planetary nebulae. A&A, 374, 599

Berdnikov L.N. & Szabados L., 1998. Study of neglected variable stars classified as Type II Cepheids. AcA, 48, 763

Bergeron P., Wesemael F. & Beauchamp A., 1995. Photometric calibration of hydrogen- and helium-rich white-dwarf models. PASP, 107, 1047

Bergeron P., Wesemael F., Beauchamp A., Wood M.A., Lamontagne R., Fontaine G. & Liebert J., 1994. A spectroscopic analysis of DAO and hot DA white dwarfs: the implications of the presence of helium and the nature of DAO stars. ApJ, 432, 305

Berman L., 1937. A study of the Galactic rotation from the data of the planetary nebulae. LicOB, 18, 57

Bhatt H.C. & Mallik D.C.V., 1986. Cn 1-1 – A peculiar compact planetary nebula. A&A, 168, 248

Bilikova J., Chu Y., Gruendl R.A. & Su K.Y.L., 2008. IR excesses of four central stars of planetary nebulae. AAS Meeting 211, poster 161.03

Birkby J., Parker Q., Miszalski B., Acker A. & Frew D., 2007. Examples of new evolved planetary nebulae from the SuperCOSMOS Hα Survey. AAONw, 111, 22

Blaauw, A., Danziger, I.J. & Schuster H.-E., 1975. A new southern planetary nebula. A&A, 44, 469

Blair W.P., Kirschner R.P., Fesen R.A. & Gull T.R., 1984. An optical investigation of the peculiar supernova remnant CTB 80. ApJ, 282, 161

Blitz L., Fich M. & Stark A.A., 1982. Catalog of CO radial velocities toward Galactic HII regions. ApJS, 49, 183

Blöcker T., 1995. Stellar evolution of low- and intermediate-mass stars. II. Post-AGB evolution. A&A, 299, 755

Blöcker T. & Schönberner D., 1990. On the fading of massive AGB remnants. A&A, 240, L11

Bode M.F., 2004. The evolution of nova ejecta. In Meixner M., Kastner J. & Soker N., eds., Asymmetric Planetary Nebulae III. ASP Conf. Series, 313, p. 504

Bode M.F., Roberts J.A., Whittet D.C.B., Seaquist E.R. & Frail D.A., 1987. An ancient planetary nebula surrounding the old nova GK Persei. Nature, 329, 519

Boeshaar G.O., 1974. Filamentary structure in planetary nebulae. ApJ, 187, 283

Boffi F.R. & Stanghellini L., 1994. Filling factors and ionized masses in planetary nebulae. A&A, 284, 248

Bohigas J., 2001. Infrared imaging and optical imaging and spectroscopy of (mostly) Type I planetary nebulae. I. RMxAA, 37, 237

Bohigas J., 2003. Infrared imaging and optical imaging and spectroscopy of (mostly) Type I planetary nebulae. II. RMxAA, 39, 149

Bohigas J. & Tapia M., 2003. Sh 2-128: an HII and star-forming region in the Galactic outback. AJ, 126, 1861

Bohuski T.J. & Smith M.G., 1974. Old planetary nebulae and the relation between size and expansion velocity. ApJ, 193, 197

Bonatto C., Bica E. & Santos J.F.C., 2008. Discovery of an open cluster with a possible physical association with a planetary nebula. MNRAS, 386, 324

Bond H.E., 1981. A giant halo around the planetary nebula NGC 3242. PASP, 93, 429

Bond H.E., 1989. Close-binary and pulsating central stars. In Torres-Peimbert S., (eds), Planetary nebulae. IAU Symp., 131, 251

Bond H.E., 1994. Binary nuclei of planetary nebulae. In *Interacting Binary Stars*, ASP Conference Series 56, ed. A.W. Shafter, pp. 179. San Francisco: Astronomical Society of the Pacific

Bond H.E., 2000. Binarity of central stars of planetary nebulae. In Kastner, J.H., Soker, N. & Rappaport, S. (eds), Asymmetrical Planetary Nebulae II: From Origins to Microstructures. ASP Conf. Series 199, 115

Bond H.E., 2005. Spectoscopic binaries in planetary nebulae. In Szczerba R., Stasińska G. & Górny S., eds., Planetary Nebulae as Astronomical Tools, AIP Conference Proceedings, 804, p. 165

Bond H.E. & Ciardullo R., 1999. Distance to the planetary nebula NGC 246 from the resolved companion of its central star. PASP, 111, 217

Bond H.E. & Grauer A.D., 1987. Close-binary central stars of planetary nebulae. IAU Colloquium 95, 221

Bond H.E. & Landolt A.U., 1971. The subluminous B-type star CD$-42°$14462. PASP, 83, 485

Bond H.E. & Livio M., 1990. Morphologies of planetary nebulae ejected by close-binary nuclei. ApJ, 355, 568

Bond H.E., Liller W. & Mannery E.J., 1978. UU Sagittae: eclipsing nucleus of the planetary nebula Abell 63. ApJ, 223, 252

Bond H.E., Pollacco D.L. & Webbink R.F., 2003. WeBo 1: A young barium star surrounded by a ringlike planetary nebula. AJ, 125, 260

Bond H.E., Ciardullo R., Fleming T.A. & Grauer A.D., 1989. HFG 1: a planetary nebula with a close binary nucleus. IAU Symp., 131, 310

Bond H.E., Meakes M.G., Liebert J.W. & Renzini A., 1993. HST observations of the nuclei of EGB 6 (0950+139) and Abell 58 (V605 Aql). In Weinberger R. & Acker A., (eds), Planetary nebulae. IAU Symp. 155, 499

Bond H.E., Henden A., Levay Z.G., et al., 2003. An energetic stellar outburst accompanied by circumstellar light echoes. Nature, 422, 405

Bond I.A., Abe F., Dodd R.J., et al.., 2001. Real-time difference imaging analysis of MOA Galactic bulge observations during 2000. MNRAS, 327, 868

Borkowski K.J., 1993. Interaction of planetary nebulae with the interstellar medium. In IAU Symp., 155, 307

Borkowski K.J. & Harrington J.P., 1991. A grain-heated, dusty planetary nebula in M22. ApJ, 379, 168

Borkowski K.J., Sarazin C.L. & Soker N., 1990. Interaction of planetary nebulae with the interstellar medium. ApJ, 360, 173

Bothun G.D. & Thompson I.B., 1988. Observations with the Parking Lot Camera. I. Surface photometry and color distribution of the Magellanic Clouds. AJ, 96, 877

Boumis P., Paleologou E.V., Mavromatakis F. & Papamastorakis J., 2003. New planetary nebulae in the Galactic bulge region with $l > 0° -$ I. Discovery method and first results. MNRAS, 339, 735

Boumis P., Akras S., Xilouris E.M., Mavromatakis F., Kapakos E., Papamastorakis J. & Goudis C.D., 2006. New planetary nebulae in the Galactic bulge region with $l > 0° -$ II. MNRAS, 367, 1551

Bounatiro L., 1993. Member stars of the open cluster Mel 111 in Coma Berenices. A&AS, 100, 531

Bowen I.S., 1927. The origin of the chief nebular lines. PASP, 39, 295

Bowen I.S., 1928. The origin of the nebular lines and the structure of the planetary nebulae. ApJ, 67, 1

Bowers P.F. & Morris M., 1984. The three-dimensional structure of a circumstellar maser. ApJ, 276, 646

Brand J., Blitz L. & Wouterloot J.G.A., 1986. The velocity field of the outer Galaxy in the Southern Hemisphere. I. Catalogue of nebulous objects. A&AS, 65, 537

Brand J., Blitz L., Wouterloot J.G.A. & Kerr F.J., 1987. The velocity field of the outer Galaxy in the Southern Hemisphere. II. CO observations of galactic nebulae. A&AS, 68, 1

Brocklehurst M., 1971. Calculation of level population for low levels of hydrogen ions in gaseous nebulae. MNRAS, 153, 471

Brosch N. & Hoffman Y., 1999. The shape of the LoTr 5 planetary nebula. MNRAS, 305, 241

Bruhweiler F.C. & Feibelman W.A., 1993. International Ultraviolet Explorer observations of the white dwarf nucleus of the very old, diffuse planetary nebula, IW-2. AJ, 105, 1477

Buckley D. & Schneider S.E., 1995. The ionized masses of planetary nebulae. ApJ, 446, 279

Buckley D., Schneider S.E. & van Blerkom D., 1993. The Shklovsky Paradox. In IAU Symp., 155, 179

Buell J.F., Henry R.B.C., Baron E. & Kwitter K.B, 1997. On the Origin of Planetary Nebula K648 in Globular Cluster M15. ApJ, 483, 837

Burkert A. & O'Dell C.R., 1998. The structure of cometary knots in the Helix Nebula. ApJ, 503, 792

Busso M., Gallino R. & Wasserburg G.J., 1999. Nucleosynthesis in asymptotic giant branch stars: relevance for Galactic enrichment and solar system formation. ARA&A, 37, 239

Buzzoni A., 1989. Evolutionary population synthesis in stellar systems. I – A global approach. ApJS, 71, 817

Buzzoni A., Arnaboldi M. & Corradi R.L.M., 2006. Planetary nebulae as tracers of galaxy stellar populations. MNRAS, 368, 877

Cahn J.H., 1968. The space distribution of planetary nebulae. In Planetary Nebulae, IAU Symp., 34, 44

Cahn J.H., 1984. Observational evolution of the central stars of planetary nebulae. ApJ, 279, 304

Cahn J.H. & Kaler J.B., 1971. The distances and distribution of planetary nebulae. ApJS, 22, 319

Cahn J.H., Kaler, J.B. & Stanghellini, L., 1992. A catalogue of absolute fluxes and distances of planetary nebulae. A&AS, 94, 399

Calvet N. & Cohen M., 1978. Studies of bipolar nebulae. V – The general phenomenon. MNRAS, 182, 687

Campbell, W.W. & Moore, J.H., 1918. The spectrographic velocities of the bright-line nebulae. PLicO, 13 (4), 75

Cannon, A.J., 1921. Stars having peculiar spectra. HarCi, 224, 1

Cantó J., 1981. Herbig-Haro objects: recent observational and theoretical developments. In Kahn F.D. (ed), Investigating the Universe. Astrophysics and Space Science Library, volume 91. Dordrecht: D. Reidel, p. 95

Cappellaro E., Turatto M., Salvadori, L. & Sabbadin F., 1990. Four newly identified planetary nebulae in the Palomar plate 18^h48^m+12°. A&AS, 86, 503

Cappellaro, E., Sabbadin, F., Salvadori, L., Turatto, M. & Zanin, C., 1994. New emission nebulae in the POSS field 18^h48^m+0°. MNRAS, 267, 871

Cappellaro E., Sabbadin F., Benetti. S. & Turatto M., 2001. New planetary nebulae towards the galactic center. A&A, 377, 1035

Capriotti, E.R. & Daub, C.T., 1960. Hβ and [O III] fluxes from planetary nebulae. ApJ, 132, 677

Cardelli J.A., Clayton G.C. & Mathis J.S., 1989. The relationship between infrared, optical, and ultraviolet extinction. ApJ, 345, 245

Carraro G. & Munari U., 2004. A multicolour CCD photometric study of the open clusters NGC 2866, Pismis 19, Westerlund 2, ESO96-SC04, NGC 5617 and NGC 6204. MNRAS, 347, 625

Carraro G., Janes K.A. & Eastman J.D., 2005. Photometry of neglected open clusters in the first and fourth Galactic quadrants. MNRAS, 364, 179

Carraro G., Vallenari A. & Ortolani S., 1995. CCD photometry of the faint old open clusters ESO 96-SC04 and ESO 92-SC18. A&A, 300, 128

Carrasco L., Serrano A., & Costero R., 1983. Photoelectric, absolute Hβ fluxes for 55 planetary nebulae. RMxAA, 8, 187

Carrasco L., Serrano A., & Costero R., 1984. Explanatory note to the paper: photoelectric, absolute Hβ fluxes for 55 planetary nebulae. RMxAA, 9, 111

Caswell J.L. & Haynes R.F., 1987. Southern H II regions: an extensive study of radio recombination line emission. A&A, 171, 261

Cazetta J.O. & Maciel, W.J., 1994. Location of PN central stars on the HR diagram. A&A, 290, 936

Cazetta J.O. & Maciel, W.J. 2000. Distances of Galactic planetary nebulae based on a relationship between the central star mass and the N/O abundance. RMxAA, 36, 3

Cazetta J.O. & Maciel, W.J., 2001. Gravity distances of planetary nebulae II. Application to a sample of galactic objects. Ap&SS, 277, 393

Cederblad S., 1946. Catalog of Bright Diffuse Galactic Nebulae. MeLuAO, Ser. 2, 12, No. 119.

Chastain R.J., Shelton R.L., Raley E.A. & Magnani L., 2006. A high-latitude molecular structure in Pegasus-Pisces. AJ, 132, 1964

Chavarria-K. C., de Lara E., Finkenzeller U., Mendoza E.E. & Ocegueda J., 1988. An observational study of the Herbig AE star VV Serpentis, and of stars with reflection nebula associated with its dark cloud. A&A, 197, 151

Chen B., Stoughton C., Smith J.A., et al., 2001. Stellar population studies with the SDSS. I. The vertical distaribution of stars in the Milky Way. ApJ, 553, 184

Chopinet M., 1963. Contribution a l'étude des nébuleuses planétaires grace a la caméra électronique. JObs, 46, 1

Chopinet M., 1971. Spectre nebuleuse planetaire A76. C.R. Acad. Sci. Paris B, 272, 290

Chopinet M. & Lortet-Zuckermann, M.C., 1971. Sur le spectre de la nebuleuse A 21. C.R. Acad. Sci. Paris, Sér. B, 273, 513

Chopinet M. & Lortet-Zuckermann, M.C., 1976. Interaction of hot stars and of the interstellar medium VIII. Low-dispersion spectra of galactic nebulae and planetary nebulae. A&AS 25, 179

Chromey, F.R., 1978. *UBV* photometry of faint blue stars near the Galactic anticenter. AJ, 83, 162

Chu Y.-H., Treffers, R.R. & Kwitter, K.B., 1983. Galactic ring nebulae associated with Wolf-Rayet stars. VIII. Summary and atlas. ApJS, 53, 937

Chu Y.-H., Manchado A., Jacoby G.H. & Kwitter K.B., 1991. The multiple-shell structure of the planetary nebula NGC 6751. ApJ, 376, 150

Chu Y.-H., Gruendl R.A., Williams R.M., Gull T.R. & Werner K., 2004. The nebular environment and enigmatic hard X-ray emission of the hot DO white dwarf KPD 0005+5106. AJ, 128, 2357

Chudovicheva O.N., 1964. O rasshirenii planetarnykh tumannostei NGC 6853 (Dumbbell Nebula) i NGC 7662. IzPul, 23, 154

Ciardullo R., 2003. Planetary nebulae as extragalactic distance indicators. In Dopita M., Kwok S., Sutherland R., eds, ASP Conf. Ser. vol. 209, Planetary nebulae and their role in the universe. Astron. Soc. Pacific, San Francisco, p. 617

Ciardullo R., 2005. Planetary nebulae and the extragalactic distance scale. In Szczerba R., Stasińska G. & Górny S., eds., Planetary Nebulae as Astronomical Tools, AIP Conference Proceedings, 804, p. 277

Ciardullo R., 2006a. The Planetary nebula luminosity function. In Stanghellini L., Walsh J.R., & Douglas N.G. (eds), Planetary nebulae beyond the Milky Way. ESO Astrophysics Symposium, p. 79

Ciardullo R., 2006b. Planetary Nebulae as Probes of Stellar Populations. In Barlow M.J. & Méndez R.H., eds, Planetary nebulae in our Galaxy and beyond, IAU Symp., 234, p. 325

Ciardullo R. & Jacoby G.H., 1999. The circumstellar extinction of planetary nebulae. ApJ, 515, 191

Ciardullo R., Jacoby G.H. & Harris W.E., 1991. Planetary nebulae as standard candles. VII. A test versus Hubble type in the NGC 1023 group. ApJ, 383, 487

Ciardullo R., Bond H.E., Sipior M.S., Fullton L.K., Zhang C.-Y. & Schaefer K.G., 1999. A Hubble Space Telescope survey for resolved companions of planetary nebula nuclei. AJ, 118, 488

Ciardullo R., Feldmeier J.J., Jacoby G.H., Kuzio de Naray R., Laychak M.B. & Durrell P.R., 2002. Planetary nebulae as standard candles. XII. Connecting the Population I and Population II distance scales. ApJ, 577, 31

Ciardullo R., Durrell P.R., Laychak M.B, Herrmann K.A., Moody K., Jacoby G.H. & Feldmeier J.J., 2004. The planetary nebula system of M 33. ApJ, 614, 167

Ciardullo R., Sigurdsson S., Feldmeier J.J. & Jacoby G.H. 2005. Close binaries as the progenitors of the brightet planetary nebulae. ApJ, 629, 499

Clariá J.J., Lapasset E. & Minniti D., 1989. Photometric metal abundances of high-luminosity red stars in young and intermediate-age open clusters. A&AS, 78, 363

Clariá J.J., Piatti A.E., Lapasset E. & Mermilliod J.-C., 2003. Multicolour photometry and Coravel observations of stars in the southern open cluster IC 2488. A&A, 399, 543

Claver C.F., Liebert J., Bergeron P. & Koester D., 2001. The masses of white dwarfs in the Praesepe open cluster. ApJ, 563, 987

Clerke, A.M., 1890. *The System of the Stars.* Longmans, Green & Co., London

Clerke, A.M., 1903. *Problems in Astrophysics.* Longmans, Green & Co., London

Cohen J.G. & Gillett F.C., 1989. The peculiar planetary nebula in M 22. ApJ, 346, 803

Cohen J.G. & Rosenthal A.J., 1983. Nova shells. ApJ, 268, 689

Cohen M., 1980. Red and nebulous objects in dark clouds: a survey. AJ, 85, 29

Cohen M., 1995. The displacement of the Sun from the Galactic plane using *IRAS* and FAUST source counts. ApJ, 444, 874

Cohen M. & Barlow M.J., 1980. Infrared photometry of southern planetary nebulae and emission-line objects. ApJ, 238, 585

Cohen M. & Parker Q.A., 2003. Refining the UKST Hα Survey's PN database using MSX. IAU Symp., 209, 33

Cohen M., Parker Q.A. & Chapman J., 2005. A circular planetary nebula around the OH/IR star OH 354.88–0.54 (V1018 Sco). MNRAS, 357, 1189

Cohen M., Hudson H.S., O'Dell S.L. & Stein W.A., 1977. A study of the planetary nebulae Abell 30 and Abell 78. MNRAS, 181, 233

Cohen M., FitzGerald M.P., Kunkel W., Lasker B.M. & Osmer P.S., 1978. Studies of bipolar nebulae IV. Mz 3 (= PK $331-1°1$). ApJ, 221, 151.

Cohen M., van Winckel H., Bond H.E. & Gull T.R., 2004. Hubble Space Telescope imaging of HD 44179, the red rectangle. AJ, 127, 2362

Cohen M.C., Green A.J., Roberts M.S.E., et al., 2005. G313.3+00.3: a new planetary nebula discovered by the Australia Telescope Compact Array and the Spitzer Space Telescope. ApJ, 627, 446

Cohen M.C., Parker Q.A., Green A.J., et al., 2007. *Spitzer* IRAC observations of newly-discovered planetary nebulae from the Macquarie-AAO-Strasbourg Hα Planetary Nebula Project. ApJ, 669, 343

Collins G.W., Daub C.T. & O'Dell C.R., 1961. Hβ and [O III] fluxes from planetary nebulae. II. ApJ, 133, 471

Combi J.A. & Romero G.E., 1995. On the origin of the γ-ray fields in the Ara region. A&A, 303, 872

Combi J.A., Romero G E. & Benaglia P., 1998. The gamma -ray source 2EGS J1703-6302: a new supernova remnant in interaction with an HI cloud? A&A, 333, L91

Conn B.C., Martin N.F., Lewis G.F., Ibata R.A., Bellazzini M. & Irwin M.J., 2005. A radial velocity survey of low Galactic latitude structures – II. The Monoceros Ring behind the Canis Major dwarf galaxy. MNRAS, 364, L13

Copeland R., 1884a. Spectroscopic observations made at the Earl of Crawford's Observatory, Dun Echt, Aberdeen. MNRAS, 45, 90

Copeland R., 1884b. Experiments in the Andes. Copernicus, 3, 193

Copetti M.V.F., 1990. Integrated photoelectric photometry of nine planetary nebulae. PASP, 102, 77

Copetti M.V.F., 2000. Integrated photometry of galactic HII regions. A&AS, 147, 93

Corradi R.L.M., 1995. He 2-25, Th 2-B, 19W32: further links between bipolar planetary nebulae and symbiotic stars? MNRAS, 276, 521

Corradi R.L.M., 2003. Large scale ionized outflows from symbiotic stars: a real link with planetary nebulae? In Corradi R.L.M., Mikolajewska J. & Mahoney T.J., (eds), Symbiotic Stars Probing Stellar Evolution. ASP Conference Proceedings, 303, 393. ASP, San Francisco

Corradi R.L.M., 2004. Planetary Nebulae Morphology According to Padre Angelo Secchi. In Meixner M., Kastner J.H., Balick B. & Soker N. (eds), Asymmetrical Planetary Nebulae III: Winds, Structure and the Thunderbird. ASP Conference Proceedings, 313, 25. ASP, San Francisco

Corradi R.L.M. & Schwarz H.E., 1993a. Bipolar nebulae and binary stars: the family of Crabs He 2-104, BI Crucis, and MyCn 18. A&A, 268, 714

Corradi R.L.M. & Schwarz H.E., 1993b. The bipolar outflow of He 2-36. A&A, 273, 247

Corradi R.L.M. & Schwarz H.E., 1993c. Kinematics of bipolar planetary nebulae. A&A, 278, 247

Corradi R.L.M. & Schwarz H.E., 1995. Morphological populations of planetary nebulae: which progenitors? I. Comparative properties of bipolar nebulae. A&A, 293, 871

Corradi R.L.M. & Schwarz H.E., 1997. Extended Optical Nebulae Around Symbiotic Stars. In Mikolajewska J. (ed.), Physical processes in symbiotic binaries and related systems. Copernicus Foundation for Polish Astronomy, Warsaw, p.147

Corradi R.L.M., Aznar R. & Mampaso A., 1998. Orientation of planetary nebulae within the Galaxy. MNRAS, 297, 617

Corradi R.L.M., Villaver E., Mampaso A. & Perinotto M., 1997. A new, evolved bipolar planetary nebula. A&A, 324, 276

Corradi R.L.M., Brandi E., Ferrer O.E. & Schwarz H.E., 1999. A narrowband imaging survey of symbiotic stars. A&A, 343, 841

Corradi R.L.M., Gonçalves D.R., Villaver E., Mampaso A., Perinotto M., Schwarz H.E. & Zanin C., 2000. High-velocity collimated outflows in planetary nebulae: NGC 6337, He 2-186, and K 4-47. ApJ, 535, 823

Corradi R.L.M., Livio M., Schwarz H.E & Munari U., 2000. Symbiotic Miras can do it. In Kastner, J.H., Soker, N. & Rappaport, S. (eds), Asymmetrical Planetary Nebulae II: From Origins to Microstructures. ASP Conf. Series 199, 175

Corradi R.L.M., Livio M., Balick B., Munari U. & Schwarz H.E., 2001. The Southern Crab from a new perspective. ApJ, 553, 211

Corradi R.L.M., Schönberner D., Steffen M. & Perinotto M., 2003. Ionized halos in planetary nebulae: new discoveries, literature compilation and basic statistical properties. MNRAS, 340, 417

Corradi R.L.M., Sánchez-Blázquez P., Mellema G., Giammanco C. & Schwarz H.E., 2004. Rings in the haloes of planetary nebulae. A&A, 417, 637

Corradi R.L.M., Mampaso A., Viironen K., et al., 2005. Detection of New Planetary Nebulae by IPHAS, the Hα Survey of the North Galactic Plane. In Szczerba R., Stasińska G. & Górny S., eds., Planetary Nebulae as Astronomical Tools, AIP Conference Proceedings, vol. 804, p. 7

Corradi R.L.M., Rodrguez-Flores E.R., Mampaso A., et al., 2008. IPHAS and the symbiotic stars. I. Selection method and first discoveries. A&A, 480, 409

Corsico A.H., Althaus L.G., Miller Bertolami M.M. & Werner K., 2007. Asteroseismological constraints on the pulsating planetary nebula nucleus (PG1159-type) RX J2117.1+3412. A&A, 461, 1095

Costa R.D.D., de Freitas Pacheco J.A. & De França J.A. Jr, 1996. Abundances in type I planetary nebulae: is the galactic disk presently oxygen deficient? A&A, 313, 924

Costa R.D.D., Uchida M.M.M. & Maciel W.J., 2004. Chemical abundances of planetary nebulae towards the Galactic anticenter. A&A, 423, 199

Côte S., Freeman K.C., Carignan C. & Quinn P.J., 1997. Discovery of numerous dwarf galaxies in the two nearest groups of galaxies. AJ, 114, 1313

Cox A.N. (ed), 2000. *Allen's Astrophysical Quantities* (4th edition). AIP Press, New York

Crane J.D., Majewski S.R., Rocha-Pinto H.J., Frinchaboy P.M., Skrutskie M.F. & Law D.R., 2003. Exploring halo substructure with giant stars: spectroscopy of stars in the Galactic Anticenter Stellar Structure. ApJ, 594, L119

Crowther P.A., De Marco O. & Barlow M.J., 1998. Quantitative classification of WC and WO stars. MNRAS, 296, 367

Cudworth, K.M., 1973. Visual binaries in planetary nebulae. PASP, 85, 401

Cudworth, K.M., 1974. New proper motions, statistical parallaxes, and kinematics of planetary nebulae. AJ, 79, 1384

Cudworth, K.M., 1977. A probable binary central star in the planetary nebula NGC 6853. PASP, 89, 139

Cudworth K.M., 1990. Further observations of the planetary nebula in the globular cluster M22. AJ, 99, 1863

Cudworth, K.M. & Reynolds, R.J., 1985. The proper motions of LS V+46°21 and AS 84, two "central" star candidates for S 216. PASP, 97, 175

Cuffey J., 1941. The Galactic clusters Messier 46, Messier 50, and NGC 2324. ApJ, 94, 55

Curtis, H.D., 1918. The planetary nebulae. PLicO, 13 (3), 57

Curtis, H.D., 1919. Three new planetary nebulae. PASP, 31, 285

Cutri R.M., Skrutskie M.F., van Dyk, S., et al., 2003. 2MASS All Sky Catalog of point sources. The IRSA 2MASS All-Sky Point Source Catalog, NASA/IPAC Infrared Science ArchiveVizieR On-line Data Catalog: II/246

Cuesta L. & Phillips J.P., 2000. Excitation and Density Mapping of NGC 3587. AJ, 120, 2661

Dachs J. & Isserstedt J., 1973. The dipole nebula IC 2220, a southern reflection nebula around the variable red giant HD 65750. A&A 23, 241

Dahn C.C., Behall A.L. & Christy J.W., 1973. Trigonometric parallax determination for the central star in the planetary nebula NGC 7293. PASP, 85, 224

Danziger I.J., Dennefeld M., Kunth D. & Schuster H.E., 1974. A large southern reflection nebula at high galactic latitude. A&A, 37, 419

Daub, C.T., 1982. A statistical survey of local planetary nebulae. ApJ, 260, 612

Deeming, T.J., 1966. A faint nebulosity near NGC 3242. ApJ,146, 287

de Freitas Pacheco J.A., Codina S.J. & Viadana L., 1986. New colour and Zanstra temperatures for 15 central stars of planetary nebulae. MNRAS, 220, 107

de Lara E., Chavarria-K., C. & Lopez-Molina G., 1991. Distance to the Serpens cloud. II. A&A, 243, 139

De Marco O., 2002. WC central stars of planetary nebulae and the born-again phenomenon. Ap&SS, 279, 157

De Marco O., 2006. Binary central stars. In Barlow M.J. & Méndez R.H., eds, Planetary nebulae in Our Galaxy and Beyond, IAU Symp., 234, p. 111

De Marco O., 2008. [WC] and PG 1159 central stars of planetary nebulae: The need for an alternative to the born-again scenario. In Werner K. & Rauch T. (eds), Hydrogen-Deficient Stars, ASP Conference Series, Vol. 391. San Francisco: Astronomical Society of the Pacific, p. 209

De Marco O., Hillwig T.C. & Smith A.J., 2008. Binary central stars of planetary nebulae discovered through photometric variability. I. what we know and what we would like to find out. AJ, 136, 323

De Marco O., Crowther P.A., Barlow M.J., Clayton G.C. & de Koter A., 2001. SwSt 1: an O-rich planetary nebula around a C-rich central star. MNRAS, 328, 527

De Marco O., Bond H.E., Harmer D. & Fleming A.J., 2004. Indications of a large fraction of spectroscopic binaries among nuclei of planetary nebulae. ApJ, 602, L93

Dengel J., Hartl H. & Weinberger R., 1979. Das Innsbrucker POSS-Durchmusterungsprogramm. MitAG, 45, 182

Dengel J., Hartl H. & Weinberger R., 1980. A search for planetary nebulae on the 'POSS'. A&A, 85, 356

DENIS Consortium, 2005. VizieR On-line Data Catalog: B/denis

Désert F.X., Bazell D. & Boulanger F., 1988. An all-sky search for molecular cirrus clouds. ApJ, 334, 815.

de Vaucouleurs G., 1955a. Emission nebulosities near the south pole. Obs, 75, 129

de Vaucouleurs G., 1955b. NGC 6026: a new planetary nebula. PASP, 67, 418

de Vaucouleurs G., 1960. Emission nebulosities near the south pole – II. Obs, 80 106

de Vaucouleurs G., 1982. Five crucial tests of the cosmic distance scale using the galaxy as a fundamental standard. PASA, 4, 320

de Vaucouleurs G. & Freeman K.C., 1972. Structure and dynamics of barred spiral galaxies, in particular of the Magellanic type. VA, 14, 163

de Vaucouleurs G., de Vaucouleurs A., Corwin H.G., Jr., Buta R.J., Paturel G. & Fouque P., 1991. Third Reference Catalogue of Bright Galaxies. Springer-Verlag, Berlin

Dgani, R., 1995. Planetary nebulae – Interstellar medium interaction: theory review. In Harpaz, A. & Soker, N. (eds), Asymmetrical Planetary Nebulae. AnIPS, 11, 219

Dgani, R. & Soker, N., 1998. Instabilities in moving planetary nebulae. ApJ, 495, 337

Dias W.S., Alessi B.S., Moitinho A., Lépine J.R.D., 2002. New catalogue of optically visible open clusters and candidates. A&A, 389, 871

Dinescu D.I., Martínez-Delgado D., Girard T.M., Peñarrubia J., Rix H.-W., Butler D., van Altena W.F., 2005. Absolute Proper Motion of the Canis Major Dwarf Galaxy Candidate. ApJ, 631, L49

Dobrinčić, M., Villaver, E., Guerrero, M.A. & Manchado, A. 2006. Kinematical analysis of bipolar planetary nebulae. In Barlow M.J. & Méndez R.H., eds, Planetary nebulae in our Galaxy and beyond, IAU Symp. 234, p. 38

Doi T., O'Dell C.R. & Hartigan P., 1997. Internal velocities in the Orion Nebula: large proper-motion features. AJ, 124, 445

Dopita M.A., 1977. PK 6-2°1, a remarkable nitrogen-rich southern planetary nebula. Ap&SS, 48, 437

Dopita M.A. & Meatheringham S.J., 1990. The evolutionary sequence of planetary nebulae. ApJ, 357, 140

Dopita M.A. & Meatheringham S.J., 1991. Photoionization modeling of Magellanic Cloud planetary nebulae. ApJ, 367, 115

Dopita M.A. & Hua C.T., 1997. Southern emission-line flux standards. ApJS, 108, 515

Dopita M.A., Jacoby G.H. & Vassiliadis E., 1992. A theoretical calibration of the planetary nebular cosmic distance scale. ApJ, 389, 27

Dopita M.A., Meatheringham S.J., Webster B.L. & Ford H. C., 1988. The internal dynamics of the planetary nebulae in the Large Magellanic Cloud. ApJ, 327, 639

Dopita M.A., Henry J.P., Tuohy I.R., Webster B.L., Roberts E.H., Byun Y.-I., Cowie L.L. & Songaila A., 1990. High-resolution imaging and the H-R diagram of galactic bulge planetary nebulae. ApJ, 365, 640

Doroshenko V.T., 1973. A study of the planetary nebula NGC 1360 and of its central star. Astron. Zh. 50, 501 [SvA, 17, 3]

Downes R.A. & Duerbeck H.W., 2000. Optical imaging of nova shells and the maximum magnitude–rate of decline relationship. AJ, 120, 2007

Downes R.A, 1984. Two bright peculiar galactic emission-line stars. PASP, 96, 807

Downes R.A, Liebert J. & Margon B., 1985. KPD 0005+5106: a post-PG 1159 type object? ApJ, 290, 321

Doyle S., Balick B., Corrradi R.L.M. & Schwarz H.E., 2000. The evolving morphology of the bipolar nebula M2-9. AJ, 119, 1339

Dreizler S. & Werner K., 1996. Spectral analysis of hot helium-rich white dwarfs. A&A, 314, 217

Drew J.E., Greimel R., Irwin M.J., et al., 2005. The INT Photometric Hα Survey of the northern Galactic plane. MNRAS, 362, 753

Dreyer J.L.E., 1888. A New General Catalogue of nebulae and clusters of stars, being the Catalogue of the late Sir John F.W. Herschel, Bart., revised, corrected, and enlarged. MmRAS, 49, 212

Dreyer J.L.E., 1895. Index Catalogue of nebulae found in the years 1888 to 1894, with notes and corrections to the New General Catalogue. MmRAS, 51, 185

Dreyer J.L.E., 1908. Second Index Catalogue of nebulae and clusters of stars, containing objects found in the years 1895 to 1907, with notes and corrections to the New General Catalogue and to the Index Catalogue for 1888–94. MmRAS, 59, 105

Drilling J.S., 1983. The spectra of 12 new subluminous O stars. ApJ, 270, L13

Drilling J.S., 1985. LSS 2018: A double-lined spectroscopic binary central star with an extremely large reflection effect. ApJ, 294, L107

Drilling J.S., 1991. UBV photometry of OB$^+$ stars in the Southern Milky Way. ApJS, 76, 1033

Drilling J.S., 1995. Individual UBV observations of LSS stars. VizieR On-line Data Catalog: II/154

Drilling J.S. & Bergeron L.E., 1995. An Extension of the Case-Hamburg OB Star Surveys. PASP, 107, 846

Drummond J.D., 1980. A photometric investigation of possible binary occurrence in the central stars of seventeen planetary nebulae. Unpublished PhD Thesis, New Mexico Univ., Albuquerque.

Duerbeck H.W. & Reipurth B., 1990. We 21: a WN8 star in a planetary nebula. A&A, 231, L11

Dufour R.J., 1984. The unique planetary nebula NGC 2818. ApJ, 287, 341

Duquennoy A. & Mayor M., 1991. Multiplicity among solar-type stars in the solar neighbourhood. II. Distribution of the orbital elements in an unbiased sample. A&A, 248, 485

Durand S., Acker A. & Zijlstra A., 1998. The kinematics of 867 galactic planetary nebulae. A&AS 132, 13

Dutra C.M. & Bica A.E., 2000. Foreground and background dust in star cluster directions. A&A, 359, 347

Dwarkadas V.V., 2004. Stellar rotation and the formation of asymmetric nebulae. In Meixner, M., Kastner, J., Balick, B. & Soker, N. (eds), Asymmetric Planetary Nebulae III. ASP Conf. Series, 313, 430

Dwarkadas V.V. & Balick B., 1998. The morphology of planetary nebulae: simulations with time-evolving winds. ApJ, 497, 267

Edelmann H., 2003. Unpublished PhD thesis, Friedrich-Alexander-Universität, Erlangen-Nürnberg

Egan M.P., Clark J.S., Mizuno D., Carey S., Steele I.A. & Price S.D., 2002. An infrared ring nebula around G358.5391+00.1305: the true nature of suspected planetary nebula Wray 17-96 determined via direct imaging and spectroscopy. ApJ, 572, 288

Eggen O.J., 1983. NGC 6067 and three cepheids. AJ, 88, 379

Eggen O.J., 1984. A systematic search for members of the Hyades Supercluster. I. The white dwarfs. AJ, 89, 830

Eggleton P.P. & Tokovinin A.A., 2008. A catalog of multiplicity among bright stellar systems. MNRAS, in press

Ellis G.L., Grayson E.T. & Bond H.E., 1984. A search for faint planetary nebulae on Palomar Sky Survey prints. PASP, 96, 283

Emprechtinger M., Forveille T. & Kimeswenger S., 2004. Spectroscopic investigation of unstudied southern PNe. A&A, 423, 1017

Ercolano B., Barlow M.J., Storey P.J. & Liu X.-W., 2003a. MOCASSIN: a fully three-dimensional Monte Carlo photoionization code. MNRAS, 340, 1136

Ercolano B., Morisset C., Barlow M.J., Storey P.J. & Liu X.-W., 2003b. Three-dimensional photoionization modelling of the planetary nebula NGC 3918. MNRAS, 340, 1153

Ercolano B., Wesson R., Zhang Y., Barlow M.J., De Marco O., Rauch T. & Liu X.-W., 2004. Observations and three-dimensional photoionization modelling of the Wolf-Rayet planetary nebula NGC 1501. MNRAS, 354, 558

ESA, 1997. The Hipparcos and Tycho Catalogues, ESA SP-1200. European Space Agency

Esipov V.F., Kaplan S.A., Lozinskaya T.A. & Podstrigach T.S., 1972. Spectrophotometric investigations of filamentary nebulae. AZh, 49, 105 [SvA, 16, 81]

Espin T.E., 1907. A new nebula. MNRAS, 67, 360

Esteban C. & Fernández M., 1998. S 266: a ring nebula around a Galactic B[e] supergiant? MNRAS, 298, 185

Evans A., van Loon J. Th., Zijlstra A.A., Pollaco D., Smalley B., Tyne V.H. & Eyres S.P.S., 2002. CK Vul: reborn perhaps, but not hibernating. MNRAS, 332, L35

Evans D.S., 1968. The central star of the planetary nebula NGC 3132. MNASSA, 27, 129

Evans D.S. & Thackeray A.D., 1950. A photographic survey of bright southern planetary nebulae. MNRAS, 110, 429

Exter K.M., Pollacco D.L., Maxted P.F.L., Napiwotzki R. & Bell S.A., 2005. A study of two post-common envelope binary systems. MNRAS, 359, 315

Farihi J., Becklin E.E & Zuckerman B., 2005. Low-luminosity companions to white dwarfs. ApJS, 161, 394

Farihi J., Hoard D.W. & Wachter S., 2006. White dwarf-red dwarf systems resolved with the Hubble Space Telescope. I. First results. ApJ, 646, 480

Feast M.W., 1968. The kinematics of planetary nebulae in the Magellanic Clouds. MNRAS, 140, 345

Feibelman W.A., 1997. The IUE spectrum of the binary nucleus of the planetary nebula NGC 1514. PASP, 109, 659

Feibelman W.A. & Aller L.H., 1987. The (C III λ1909/Si III λ1892) ratio as a diagnostic for planetary nebulae and symbiotic stars. ApJ, 319, 407

Feibelman W.A. & Kaler J.B., 1983. The binary central star of the planetary nebula LT-5. ApJ, 269, 592

Feibelman W.A. & Kondo Y., 2001. Planetary nebula He 2-36: still enigmatic, but getting less so. ApJS, 136, 735

Feigelson E.D. & Babu, G.J., 1992. Linear regression in astronomy II. ApJ. 397, 55

Feinstein A. & Forte J.C., 1974. The open cluster NGC 6281. PASP, 86, 284

Felli M. & Perinotto M., 1974. On the nature of some non radio emitting Sharpless HII regions. Ap&SS, 26, 115

Ferguson D.H., Liebert J., Haas S., Napiwotzki R. & James T.A., 1999. Masses and other parameters of the post-common envelope binary BE Ursae Majoris. ApJ, 518, 866

Fernández R., Monteiro H. & Schwarz H.E., 2004. Proper motion and kinematics of the ansae in NGC 7009. ApJ, 603, 595

Ferrarese L., Ford H.C., Huchra J., et al., 2000. A database of Cepheid distance moduli and tip of the red giant branch, globular cluster luminosity function, planetary nebula luminosity function, and surface brightness fluctuation data useful for distance determinations. ApJS, 128, 431

Ferrario L., Wickramasinghe D., Liebert J. & Williams K.A., 2005. The open-cluster initial–final mass relationship and the high-mass tail of the white dwarf distribution. MNRAS, 361, 1131

Fesen R.A. & Gull T.R., 1981. The optical structure of the central core in the peculiar supernova remnant CTB 80. ApL, 24, 197

Fesen R.A., Blair W.P. & Gull T.R., 1981. Sharpless 216: a curious emission-line nebula. ApJ, 245, 131

Fesen R.A., Blair W.P. & Kirshner R.P., 1985. Optical emission-line properties of evolved galactic supernova remnants. ApJ, 292, 29

Fesen R.A., Gull T.R. & Heckathorn J.N., 1983. Two new possible planetary nebulae. PASP, 95, 614

Fich M. & Blitz L., 1984. Optical HII regions in the outer Galaxy. ApJ, 279, 125

Fich M. & Terebey S., 1996. *IRAS* observations of the outer Galaxy. I. Discrete emission sources and large-scale (diffuse) emission. ApJ, 472, 624

Fich M., Treffers, R.R. & Dahl, G.P., 1990. Fabry-Perot Hα observations of Galactic HII regions. AJ, 99, 622

Finkbeiner D.P., 2003. A full-sky Hα template for microwave foreground prediction. ApJS, 146, 407

Finkenzeller U. & Mundt R., 1984. The Herbig Ae/Be stars associated with nebulosity. A&AS, 55, 109

Finley D.S., Koester D. & Basri G., 1997. The temperature scale and mass distribution of hot DA white dwarfs. ApJ, 488, 375

Fleming M., 1895. Stars having peculiar spectra. AN, 138, 175

Fluks M.A., Plez B., The P.S., de Winter D., Westerlund B.E. & Steenman H.C., 1994. On the spectra and photometry of M-giant stars. A&AS, 105, 311

Forbes D., 1989. Photometry and spectroscopy of stars in northern HII regions. A&AS, 77, 439

Forbes D.A., Strader J., Brodie J.P., 2004. The globular cluster system of the Canis Major Dwarf Galaxy. AJ, 127, 3394

Frank A., 1999. Bipolar outflows and the evolution of stars. NewAR, 43, 31

Frank A., Balick B., Icke V. & Mellema G., 1993. Astrophysical gasdynamics confronts reality: the shaping of planetary nebulae. ApJ, 404, L25

Fredrick L.W. & West R.M., 1984. A study of suspected planetary nebulae. A&AS, 56, 325

Freudenreich H.T., 1998. A COBE model of the Galactic bar and disk. ApJ, 492, 495

Frew D.J., 1997. The largest planetary nebulae. SthAs, 2, 6

Frew D.J., 2004. The historical record of η Carinae I. The visual light curve, 1595–2000. JAD, 10, 6

Frew D.J. & Parker Q.A., 2003. Two new large bipolar planetary nebulae. AAONw, 103, 6

Frew D.J. & Parker Q.A., 2005. Planetary nebulae in the solar neighborhood. In Szczerba R., Stasińska G. & Górny S., eds., Planetary Nebulae as Astronomical Tools, AIP Conference Proceedings, 804, p. 11

Frew D.J. & Parker Q.A., 2006. Towards a new distance scale and luminosity function for nearby planetary nebulae. In Barlow M.J. & Méndez R.H., eds, Planetary nebulae in our Galaxy and beyond, IAU Symp., 234, p. 49

Frew D.J. & Parker Q.A., 2008. Do post-common envelope objects form a distinct subset of planetary nebulae? In Corradi R.L.M., Manchado A. & Soker N. (eds), Proceedings of the APN-IV Conference (in press)

Frew DJ., Madsen G.J. & Parker Q.A., 2006. A search for new emission nebulae from the SHASSA and VTSS Surveys. In Barlow M.J. & Méndez R.H., eds, Planetary nebulae in our Galaxy and beyond, IAU Symp., 234, p. 395

Frew D.J., Parker Q.A. & Russeil D., 2006. Two new evolved bipolar planetary nebulae in the solar neighbourhood. MNRAS, 372, 1081

Friel E.D., 1995. The old open clusters of the Milky Way. ARA&A, 33, 381

Frinchaboy P.M., Majewski S.R., Crane J.D., Reid I.N., Rocha-Pinto H.J., Phelps, R.L., Patterson R.J. & Muñoz R.R., 2004. Star clusters in the Galactic Anticenter Stellar Structure and the origin of outer old open clusters. ApJ, 602, L21

Frinchaboy P.M., Muñoz R.R., Majewski S.R., Friel E.D., Phelps R.L. & Kunkel W.B., 2006a. Star Clusters in the Galactic Anticenter Stellar Structure: New Radial Velocities & Metallicities. In

Pasquini L., Randich S. (eds), Chemical Abundances and Mixing in Stars in the Milky Way Galaxy and its Satellites, ESO Astrophysics Symp., Springer-Verlag, p. 130

Frinchaboy P.M., Muñoz R.R., Phelps R.L., Majewski S.R. & Kunkel W.B., 2006b. Photometry and spectroscopy of old, outer disk star clusters: vdB-Hagen 176, Berkeley 29, and Saurer 1. AJ, 131, 922

Fulbright M.S. & Liebert J., 1993. JHK photometry of WD 0950+139. ApJ, 410, 275

Gale W.F., 1896. A new ring nebula. JBAA, 6, 218

Galli D., Stanghellini L., Tosi M. & Palla F., 1997. ^{3}He in planetary nebulae: a challenge to stellar evolution models. ApJ, 477, 218

Garcia-Diaz M.T., López J.A., Garcia-Segura G., Richer M.G. & Steffen W., 2008. The planetary nebula NGC 1360, a test case of magnetic collimation and evolution after the fast wind. ApJ, 676, 402

García-Lario P., Manchado A., Pych W. & Pottasch S.R., 1997. Near infrared photometry of IRAS sources with colours like planetary nebulae. III. A&AS, 126, 479

García-Segura G., López J.A., & Franco J., 2005. Magnetically driven winds from post-asymptotic giant branch stars: solutions for high-speed winds and extreme collimation. ApJ, 618, 919

Garrison R.F., Schild R.E., Hiltner W.A. & Krzeminski W., 1984. CPD $-48°1577$: the brightest known cataclysmic variable. ApJ, 276, L13

Gathier R., 1985. $VBLUW$-photometry of stars in small fields around planetary nebulae. A&AS, 60, 399

Gathier R., 1987. Properties of planetary nebulae. I. Nebular parameters and distance scales. A&AS, 71, 245

Gathier R. & Pottasch S.R., 1988. Magnitudes of central stars of planetary nebulae. A&A, 197, 266

Gathier R., Pottasch S.R. & Pel J.W., 1986. Distances to planetary nebulae I. The reddening distance method. A&A, 157, 171

Gathier R., Pottasch S.R. & Goss W.M., 1986. Distances to planetary nebulae. II. HI absorption observations. A&A, 157, 191

Gatti A.A., Drew J.E., Oudmaijer R.D., Marsh T.R. & Lynas-Gray A.E., 1998. The separation of the stars in the binary nucleus of the planetary nebula Abell 35. MNRAS, 301, L33

Gaustad J.E., McCullough P.R., Rosing W. & Van Buren D.J., 2001. A robotic wide-angle Hα survey of the southern sky. PASP, 113, 1326

Gaze V.F. & Shajn G.A., 1951. Second list of diffuse nebulae. IzKry, 7, 93

Gaze V.F. & Shajn G.A., 1954. Fourth list of diffuse nebulae. IzKry, 11, 39

Gaze V.F. & Shajn G.A., 1955. Catalogue of emission nebulae. IzKry, 15, 11

Gebel W.L., 1968. Interstellar reddening for HII regions and Lyman-visual colors of their exciting stars. ApJ, 153, 743

Georgelin Y.M., Georgelin Y.P. & Roux S., 1973. Observations de nouvelles regions HII galactiques et d'etoiles excitatrices. A&A, 25, 337

Gesicki K. & Zijlstra A.A. 2000. Expansion velocities and dynamical ages of planetary nebulae. A&A, 358, 1058

Gesicki K. & Zijlstra A.A. 2007. White dwarf masses derived from planetary nebulae modelling A&A, 467, L29

Gesicki K., Acker A. & Zijlstra A.A., 2003. Kinematics, turbulence and evolution of planetary nebulae. A&A, 400, 957

Gesicki K., Zijlstra A.A., Acker A., Górny S.K., Gozdziewski K. & Walsh J.R., 2006. Planetary nebulae with emission-line central stars. A&A, 451, 925

Gieseking F., Hippelein H. & Weinberger R., 1986. Late stages of the expansion of planetary nebulae. A&A, 156, 101

Gillett F.C., Jacoby G.H., Joyce R.R., Cohen J.G., Neugebauer G., Soifer B.T., Nakajima T. & Matthews K., 1988. The optical/infrared counterpart(s) of IRAS 18333-2357. ApJ, 338, 862

Gilmore G., Wyse R. & Kuijken K., 1989. Kinematics, chemistry and structure of the Galaxy. ARA&A, 27, 555

Girard P., Köppen J. & Acker A., 2007. Chemical compositions and plasma parameters of planetary nebulae with Wolf-Rayet and wels type central stars. A&A, 463, 265

Girardi L., Bressan A., Bertelli G., Chiosi, C., 2000. Evolutionary tracks and isochrones for low- and intermediate-mass stars: from 0.15 to $7M_\odot$, and from $Z = 0.0004$ to 0.03. A&AS, 141, 371

Gleizes F., Acker A. & Stenholm B., 1989. Zanstra temperatures of the central stars of southern planetary nebulae. A&A, 222, 237

Glushkov, Y.I., 1972. Spectrophotometric investigations of galactic nebulae. VI. NGC 2359, 1514. ATsir, 692, 2

Glushkov Y.I., Denisjuk E.K., Karyagina Z.V. & Kondratjeva L.N., 1974. Spectrophotometric studies of compact HII regions and objects with wide emission lines. MSAIt, 45, 361

Goerigk W., Mebold U., Reif K., Kalberla P.M.W. & Velden L., 1983. A high-latitude H I-cloud with optical emission. A&A, 120, 63

Goldman D.B., Guerrero M.A., Chu Y.-H. & Gruendl R.A., 2004. Physical structure of planetary nebulae. III. The large and evolved NGC 1360. AJ, 128, 1711

Gómez Y., Rodríguez L.F. & Moran J.M., 1993. Detection of the angular expansion rate and determination of the distance of the planetary nebula NGC 6302. ApJ, 416, 620

Gómez Y., Rodríguez L.F., Moran J.M. & Garay G., 1989. The distance to NGC 6302. ApJ, 345, 862

Gonzalez-Solares E.A., Walton N.A., Greimel R., et al. 2007. Initial data release from the INT Photometric H-alpha Survey of the Northern Galactic Plane (IPHAS). MNRAS, submitted

Good S.A., Barstow M.A., Holberg J.B., Sing D.K., Burleigh M.R. & Dobbie P.D., 2004. Comparison of the effective temperatures, gravities and helium abundances of DAO white dwarfs from Balmer and Lyman line studies. MNRAS, 355, 1031

Good S.A., Barstow M.A., Burleigh M.R., Dobbie P.D. & Holberg J.B., 2005. A search for binarity using *Far-Ultraviolet Spectroscopic Explorer* observations of DAO white dwarfs. MNRAS, 364, 1082

Górny S.K., 2001. Statistics of planetary nebulae with [WR] central stars. Ap&SS, 275, 67

Górny S.K. & Stasińska G., 1995. On the status of planetary nebulae with WR-type nuclei. A&A, 303, 893

Górny S.K. & Tylenda R., 2000. Evolutionary status of hydrogen-deficient central stars of planetary nebulae. A&A, 362, 1008

Górny S.K., Stasińska G. & Tylenda R., 1997. Planetary nebulae morphologies, central star masses and nebular properties. A&A, 318, 256

Górny S.K., Schwarz H.E., Corradi R.L.M. & Van Winckel H. 1999. An atlas of images of planetary nebulae. A&AS, 136, 145

Graham M.F., Meaburn, J. & López, J.A., 2003. Unveiling the morphology and kinematics of LoTr 5, the highest galactic latitude PN. RMxAA(SC), 15, 72

Graham M.F., Meaburn J.. López J.A., Harman D. J. & Holloway A.J., 2004. The bipolarity of the highest Galactic latitude planetary nebula, LoTr 5 (PN G339.9+88.4), around IN Com. MNRAS, 347, 1370

Grauer A.D., Bond H.E., Ciardullo R. & Fleming T.A., 1987a. The close-binary nucleus of the planetary nebula HFG1. BAAS, 19, 643

Grauer A.D., Bond H.E., Liebert J., Fleming T.A. & Green R.F., 1987b. A search for pulsating stars similar to PG 1159-035 and K1-16. ApJ, 323, 271

Greenstein J.L., 1972. The central star of NGC 1514. ApJ, 173, 367

Greenstein J.L. & Minkowski R., 1964. The central stars of planetary nebulae of low surface brightness. ApJ, 140, 1601

Greig W.E., 1967. Population discrimination among planetary nebulae. AJ, 72, 801

Greig W.E., 1971. The morphological classification of symmetrical nebulae. A&A, 10, 161

Greig W.E., 1972. Spatial and kinematic parameters of binebulous, centric and annular nebulae. A&A, 18, 70

Greiner J., 1998. Soft X-ray emission of VY Sculptoris stars during optical high state. A&A, 336, 626

Greiner J., Tovmassian G., Orio M., Lehmann H., Chavushyan V., Rau A., Schwarz R., Caselegno R. & Scholz R.-D., 2001. BZ Camelopardalis during its 1999/2000 optical low state. A&A, 376, 1031

Grenier I.A., Lebrun F., Arnaud M., Dame T.M. & Thaddeus P., 1989. CO observations of the Cepheus Flare. I. Molecular clouds associated with a nearby bubble. ApJ, 347, 231

Grether D. & Lineweaver C.H., 2006. How dry is the brown dwarf desert? Quantifying the relative number of planets, brown dwarfs, and stellar companions around nearby sun-like stars. ApJ, 640, 1051

Grewing M. & Bianchi L., 1988. The nucleus of Abell 35: A hot companion to SAO 181201. In A decade of UV Astronomy with the IUE Satellite, ESA SP-281, 2, 177

Groenewegen M.A.T. & de Jong T., 1993. Synthetic AGB evolution. I. A new model. A&A, 267, 410

Groves B., Dopita M.A., Williams R.E. & Hua, C.-T., 2002. The internal extinction curve of NGC 6302 and its extraordinary spectrum. PASA, 19, 425

Guerrero M.A., Manchado A. & Serra-Ricart M., 1996. K 4-55: a bipolar planetary nebula observed near pole-on. ApJ, 456, 651

Guerrero M.A., Chu Y.-H., Manchado A. & Kwitter K.B., 2003. Physical structure of planetary nebulae. I. The Owl Nebula. AJ, 125, 3213

Gull T.R. & Sofia S., 1979. Discovery of two distorted interstellar bubbles. ApJ, 230, 782

Gum C.S., 1955. A survey of southern HII regions. MmRAS, 67, 155

Gurzadyan G.A., 1970. Planetary Nebulae. Reidel, Dordrecht

Gurzadyan G.A., 1988. The temperatures of the nuclei of high-excitation planetary nebulae. Ap&SS, 149, 343

Gurzadyan G.A., 1997. The Physics and Dynamics of Planetary Nebulae. Springer-Verlag, Berlin

Gurzadyan G.A. & Egikyan A.G., 1991. Excitation class of nebulae – an evolution criterion? Ap&SS, 181, 73

Gussie G.T., 1995. The classification of M 1-78. PASA, 12, 31

Gutiérrez-Moreno A., 1988. Planetary nebulae and symbiotic stars. In Blanco, V.M. & Phillips, M.M. (eds), Progress and Opportunities in Southern Hemisphere Optical Astronomy, ASP Conf. Series, Vol. 1, p. 12. San Francisco: ASP

Gutiérrez-Moreno A. & Moreno H., 1998. New spectroscopic observations of the planetary nebula PC 11. PASP, 110, 458

Gutiérrez-Moreno A., Moreno H. & Cortés G., 1985. Studies of southern planetary nebulae. I. Fluxes from bright planetary nebulae. PASP, 97, 397

Gutiérrez-Moreno A., Moreno H. & Cortés G. 1995. A diagnostic diagram for planetary nebulae and symbiotic stars. PASP, 107, 462

Gutiérrez-Moreno A., Anguita C., Loyola P. & Moreno H., 1999. Trigonometric distances of planetary nebulae. PASP, 111, 1163

Guzmán L., Gómez Y. & Rodríguez L.F., 2006. Expansion parallax for the compact planetary nebula M2-43. RMxAA, 42, 127

Gyulbadaghian A.L. & Magakyan T.Y., 1977. New cometary nebulae. SvAL, 3, 58 [PAZh, 3, 113]

Gyulbudaghian A.L., Rodriguez L.F. & Villaneuva V.M, 1993. Nebulous objects on the ESO/SRC J plates. RMxAA, 25, 19

Gyulbudaghian A.L., May J., González L. & Méndez R.A., 2004. Nebulous objects in the Southern Hemisphere. RMxAA, 40, 137

Habing H.J., 2004. AGB Maser Stars as Tracers of Stellar Populations. In Kurtz D.W. & Pollard K.R. (eds), Variable Stars in the Local Group, IAU Colloquium 193, p. 138

Habing H.J. & Olofsson H., 2003. Asymptotic giant branch stars. Astronomy and astrophysics library. New York, Berlin: Springer

Haffner L.M., 2001. The Wisconsin H-Alpha Mapper Northern Sky Survey. In Tetons 4: Galactic Structure, Stars and the Interstellar Medium, ASP Conf. Ser., 231, ed., Woodward C.E., Bicay M.D., Shull J.M., San Francisco: ASP, p. 345

Haffner L.M., Reynolds R.J., Tufte S.L., Madsen G.J., Jaehnig K.P. & Percival J.W., 2003. The Wisconsin H-Alpha Mapper Northern Sky Survey. ApJS, 149, 405

Hajduk M., Zijlstra A.A. & Gesicki, K., 2008. An occultation event in a triple post-AGB star. A&A, submitted

Hajian A.R., 2006. Distances to planetary nebulae. In Barlow M.J. & Méndez R.H., eds, Planetary nebulae in our Galaxy and beyond, IAU Symp., 234, p. 41

Hajian A.R. & Terzian Y., 1996. Planetary nebulae expansion distances. III. PASP, 108, 258

Hajian A.R., Terzian Y. & Bignell C., 1993. Planetary nebulae expansion distances. AJ, 106, 1965

Hajian A.R., Terzian Y. & Bignell C., 1995. Planetary nebulae expansion distances. II. NGC 6572, NGC 6210, NGC 3242, and NGC 2392. AJ, 109, 2600

Hajian A.R., Frank A., Balick B. & Terzian Y., 1997. The timescale correlation method: distances to planetary nebulae with halos. ApJ, 477, 226

Hajian A.R., Movit S.M., Trofimov D., et al., 2007. An atlas of [N II] and [O III] images and spectra of planetary nebulae. ApJS, 169, 289

Hambly N., MacGillivray H.T., Read M.A., et al., 2001a. The SuperCOSMOS Sky Survey – I. Introduction and description. MNRAS, 326,1279

Hambly N.C., Irwin M.J. & MacGillivray H.T., 2001b. The SuperCOSMOS Sky Survey – II. Image detection, parametrization, classification and photometry. MNRAS, 326, 1295

Hambly N.C., Davenhall A.C., Irwin M.J. & MacGillivray H.T., 2001c. The SuperCOSMOS Sky Survey – III. Astrometry. MNRAS, 326, 1315

Han Z., Podsiadlowski P., Maxted P.F.L., Marsh T.R. & Ivanova N., 2002. The origin of subdwarf B stars – I. The formation channels. MNRAS, 336, 449

Han Z., Podsiadlowski P., Maxted P.F.L. & Marsh T.R., 2003. The origin of subdwarf B stars – II. MNRAS, 341, 669

Harman R.J. & Seaton M.J., 1966. The ionization structure of planetary nebulae IV. Optical thicknesses of the nebulae and temperatures of the central stars. MNRAS, 132, 15

Haro, G., 1952. Nuevas nebulosas planetarias y objetos con emision en la region del centro Galactico. BOTT, 1, 1

Haro G. & Luyten W.J., 1962. Faint blue stars in the region near the South Galactic Pole. BOTT, 3, 37

Harrington R.S. & Dahn C.C., 1980. Summary of U.S. Naval Observatory parallaxes. AJ, 85, 454

Harris H.C., 2007. Parallaxes of 16 planetary nebulae. In Barlow M.J. & Méndez R.H., eds, Planetary nebulae in our Galaxy and beyond, IAU Symp., 234, p. 415

Harris H.C., Dahn C.C., Monet D.G. & Pier J.R., 1997. Trigonometric parallaxes of planetary nebulae. In Habing H.J. & H. J. G. L. M. Lamers H.J.G.L.M. (eds), Planetary nebulae, IAU Symposium 180, 40. Dordrecht: Kluwer

Harris H.C., Dahn C.C., Canzian B., et al., 2007. Trigonometric parallaxes of central stars of planetary nebulae. AJ, 133, 631

Hartl H., Dengel J. & Weinberger R., 1983. Alte Planetarische Nebel: neue Kandidaten. MitAG, 60, 325

Hartl H. & Tritton S.B., 1983. Neuentdeckte südliche Planetarische Nebel. MitAG, 60, 328

Hartl H. & Tritton S.B., 1985. New planetary nebulae of low surface-brightness detected on UK-Schmidt plates. A&A, 145, 41

Hartl H. & Weinberger R., 1987. Planetary nebulae of low surface-brightness: gleanings from the "POSS". A&AS, 69, 519

Hartley L.E., Drew J.E., Long K.S., Knigge, C. & Proga D., 2002. Testing the line-driven disc wind model: time-resolved ultraviolet spectroscopy of IX Vel and V3885 Sgr. MNRAS, 332, 127

Hartung E.J., 1968. *Astronomical Objects for Southern Telescopes.* Melbourne University Press.

Hasan P., Kilambi G.C. & Hasan S.N., 2008. Ap&SS, 313, 363

Haug U., 1978. Photoelectric and photographic photometry in the open clusters NGC 5617, Tr 22 and NGC 5662. A&AS, 34, 417

Hawley S.A. & Miller J.S., 1978. Ionization and abundances in the Dumbbell nebula. PASP, 90, 39

Heap S.R., 1975. Spectroscopic studies of very old hot stars. I. NGC 246 and its exciting star. ApJ, 196, 195

Heap S.R. & Augensen H.J., 1987. Mass distribution and evolutionary schema for central stars of planetary nebulae. ApJ, 313, 268

Hearnshaw J.B., 1986. The analysis of starlight: One hundred and fifty years of astronomical spectroscopy. Cambridge University Press

Heber U. & Drilling J.S., 1984. High resolution spectroscopy of the CPN LSS 1362. MitAG, 62, 252

Heber U., Werner K. & Drilling J.S., 1988. High-resolution spectroscopy of central stars of planetary nebulae: LSS 1362. A&A, 194, 223

Heckathorn J.N. & Fesen R.A., 1985. Ultraviolet observations of the central star in the planetary nebula 136+5°1. A&A, 143, 475

Heckathorn, J.N., Fesen R.A. & Gull T.R., 1982. Discovery of a large, high-excitation planetary nebula at $l = 136°$, $b = +5°$. A&A, 114, 414

Henize K.G., 1961. Seven new planetary nebulae. PASP, 73, 159

Henize K.G., 1967. Observations of southern planetary nebulae. ApJS, 14, 125

Henize K.G. & Fairall A.P., 1981. The spectrum of planetary nebula K 1-27. PASP, 93, 435

Henize K.G. & Fairall A.P., 1983. A new planetary nebula with independently determined distance and mass. IAU Symp., 103, 544

Henry R.B.C., Kwitter K.B. & Bates J.A., 2000. A new look at carbon abundances in planetary nebulae. IV. Implications for stellar nucleosynthesis. ApJ, 531, 928

Henry R.B.C., Kwitter K.B. & Balick B., 2004. Sulfur, chlorine, and argon abundances in planetary nebulae. IV. synthesis and the sulfur anomaly. AJ, 127, 2284

Henry R.B.C., Kwitter K.B. & Dufour R.J., 1999. Morphology and composition of the Helix Nebula. ApJ, 517, 782

Herald J.E. & Bianchi L., 2002. The binary central star of the planetary nebula A35. ApJ, 580, 434

Herald J.E. & Bianchi L., 2004. A far-ultraviolet spectroscopic analysis of the central star of the planetary nebula Longmore 1. PASP, 116, 391

Herbig G.H., 1958. The spectrum of the nebulosity at AE Aurigae. PASP, 70, 468

Herbstmeier U., Heithausen A. & Mebold U., 1993. Tracing the molecular hydrogen content of the Draco nebula: very low $N\mathrm{H}_2/W(^{12}\mathrm{CO})$ ratios or varying FIR-emissivities? A&A, 272, 514

Herrero A., Manchado A. & Méndez R.H., 1990. NLTE analysis of high-resolution spectra of CSPN. Ap&SS, 169, 183

Herschel J.F.W., 1833. Observations of nebulae and clusters of stars, made at Slough, with a twenty-feet reflector, between the years 1825 and 1833. PhTrRS, 123, 359

Herschel J.F.W., 1847. *Results of Astronomical Observations Made ... at the Cape of Good Hope.* Smith, Elder & Co., London

Herschel J.F.W., 1864. Catalogue of nebulae and clusters of stars. PhTrRS, 154, 1

Herschel J.F.W., 1887. *Outlines of Astronomy.* Longmans, Green & Co., London

Herschel Lt. J., 1868. Observations of the spectra of some of the southern nebulae. ProcRS, 16, 417

Herschel W., 1785. On the construction of the heavens. PhTrRS, 75, 213

Herwig F., 2005. Evolution of asymptotic giant branch stars. ARA&A, 43, 435

Herwig F., Blöcker T., Langer N. & Driebe T., 1999. On the formation of hydrogen-deficient post-AGB stars. A&A, 349, L5

Hester J.J. & Kulkarni S.R., 1989. Optical imagery and spectrophotometry of CTB 80. ApJ, 340, 362

Hewett P.C., Irwin M.J., Skillman E.D., et al., 2003. Serendipity and the Sloan Digital Sky Survey: discovery of the largest known planetary nebula on the sky. ApJ, 599, L37

Hewett P.C. & Irwin M., 2004. The largest known planetary nebula on the sky. INGNw, 8, 6

Hillwig T.C., 2004. Two new close binary central stars of planetary nebulae from a critically selected southern hemisphere sample. In Meixner, M., Kastner, J., Balick, B. & Soker, N. (eds), Asymmetric Planetary Nebulae III. ASP Conf. Series, 313, 529

Hillwig T.C., Bond H.E. & Afşar M., 2006. Orbital parameters of the close binary central stars of NGC 6337 and NGC 6026. In Barlow M.J. & Méndez R.H., eds, Planetary nebulae in our Galaxy and beyond, IAU Symp., 234, 421

Hillwig T.C., Honeycutt, R.K. Robertson J.W., 2000. Post-common-envelope binary stars and the precataclysmic binary PG 1114+187. AJ, 120, 1113

Hippelein, H. & Weinberger, R., 1990. The expansion of highly evolved planetary nebulae. A&A, 232, 129

Hoard D.W., Wachter S., Clark L.L. & Bowers T.P., 2002. Infrared properties of cataclysmic variables in the 2 Micron All-Sky Survey Second Incremental Data Release. ApJ, 565, 511

Hoare M.G., Barstow M.A., Werner K. & Fleming T.A., 1995. ROSAT observations of EUV-bright planetary nebula central stars. MNRAS, 273, 812

Hoare M.G., Drake J.J., Werner K & Dreizler S., 1996. The extreme-ultraviolet spectrum of the central star of the planetary nebula NGC 1360. MNRAS, 283, 830

Hodge P.W., 1966. The physics and astronomy of galaxies and cosmology. McGraw-Hill Series in Undergraduate Astronomy, New York: McGraw-Hill

Hodge P.W., Zucker, D.B. & Grebel, E.K., 2000. An Emission Line Survey of Nearby Dwarf Galaxy Candidates. BAAS, 197, 3812

Hoessel, J.G., Saha, A. & Danielson, G.E., 1988. Deep CCD observations of nearby dwarf galaxy candidates. PASP, 100, 680

Hoffmeister C., 1956. Bearbeitung des Lichtwechsels von 75 kurzperiodischen veranderlichen Sternen zwischen 25 und 90 sudlicher Deklination. Veröff. Sonneberg, 3, 1

Høg E., Fabricius C., Makarov V.V., et al., 2000. The Tycho-2 catalogue of the 2.5 million brightest stars. A&A, 355, L27

Holberg J.B. & Bergeron P., 2006. Calibration of synthetic photometry using DA white dwarfs. AJ, 132, 1221

Holberg J.B. & Magargal K., 2005. Finding the cool companions of the PG DA white dwarfs. In Koester D. & Moehler S. (eds), *14^{th} European Workshop on White Dwarfs*, ASP Conference Series, 334, p. 419

Holberg J.B., Barstow M.A. & Burleigh M.R., 2003. An Archive of IUE Low-Dispersion Spectra of the White Dwarf Stars. ApJS, 147, 145

Holberg J.B., Barstow M.A. & Sion E.M., 1998. A high-dispersion spectrocopic survey of the hot white dwarfs: The *IUE* NEWSIPS SWP Echelle data set. ApJS, 119, 207

Holberg J.B., Barstow M.A., Bruhweiler F.C., Cruise A.M. & Penny A.J., 1998. Sirius B: a new, more accurate view. ApJ, 497, 935

Holberg J.B., Sion E.M., Oswalt T., McCook G.P., Foran S. & Subasavage J.P., 2008. A new look at the local white dwarf population. AJ, 135, 1225

Hollis J.M., Oliversen R.J., Wagner R.M. & Feibelman W.A., 1992. The 0623 + 71 bow shock nebula. ApJ, 393, 217

Hollis J.M., Van Buren D., Vogel S.N., Feibelman W.A., Jacoby G.H. & Pedelty J.A., 1996. The Abell 35 nebula inside out. ApJ, 456, 644

Honeycutt R.K., 2001. Similarities between stunted outbursts in nova-like cataclysmic variables and outbursts in ordinary dwarf novae. PASP, 113, 473

Honeycutt R.K., Robertson J.W. & Turner G.W., 1998. Unusual “stunted” outbursts in old novae and nova-like cataclysmic variables. AJ, 115, 2527

Hora J.L., Latter W.B., Marengo M., Fazio G., Allen L.E. & Pipher J. L., 2006. In Armus L. & W.T. Reach W.T., eds, The Spitzer Space Telescope: New Views of the Cosmos, ASP Conference Series, 357. San Francisco: Astronomical Society of the Pacific, p. 144

Howard J.W., Henry R.B.C. & McCartney S., 1997. A detailed abundance analysis of nine halo planetary nebulae. MNRAS, 284, 465

Howarth I.B., 1983. LMC and galactic extinction. MNRAS, 203, 301

Hua C.T., 1997. Deep morphologies of type I planetary nebulae. A&AS, 125, 355

Hua, C.T. & Kwok S., 1999. Monochromatic morphologies of Abell planetary nebulae. A&AS, 138, 275

Hua, C.T. & Martinis J., 2003. Discovery of a large-structure emission nebula near PN G200.7+08.4 (A 19). Ap&SS, 283, 263

Hua, C.T. & Nguyen-Trong T., 1983. Morphological study of three Abell planetary nebulae: A 33, A 36, and A 79. A&A, 117, 272

Hua C.T., Donas J. & Doan, N.H., 1980. Spectroscopic observations of galactic nebulae and galaxies with the imaging photon counting system (IPCS). A&A, 90, 8

Hua C.T., Dopita M.A. & Martinis J., 1998. Detection of new emission structures around planetary nebulae. A&AS, 133, 361

Hua C.T., Grundseth B. & Maucherat A.-J., 1993. Faint halos around compact planetary nebulae. A&AS, 101, 541

Hubble E., 1921. Twelve new planetary nebulae. PASP, 33, 174

Hubble E., 1922. A general study of diffuse galactic nebulae. ApJ, 56, 162

Hubble E., 1934. The distribution of extra-galactic nebulae. ApJ, 79, 8

Huemer G. & Weinberger R., 1988. Candidates for promising extinction distances: Sh 1-89, NGC 7048, and M 1-77. A&AS, 72, 383

Huggins P.J., Bachiller R., Cox P. & Forveille T., 1996. The molecular envelopes of planetary nebulae. A&A, 315, 284

Huggins P.J., Bachiller R., Planesas P., Forveille T. & Cox P., 2005. A CO survey of young planetary nebulae. ApJS, 160, 272

Huggins W., 1864. On the spectra of some of the nebulae. PhTrRS, 154, 437

Huggins W., 1897. The new astronomy: a personal retrospect. The Nineteenth Century Review, 41, 907

Humason M., 1921. Two new planetary nebulae. PASP, 33, 175

Humphreys R.M. & Larsen J.A., 1995. The Sun’s distance above the Galactic plane. AJ, 110, 2183

Ianna P.A. & McAlister H.A., 1974. Parallaxes of 20 stars determined from plates taken with the McCormick 26-in. refractor. AJ, 79, 1314

Ibata R.A., Irwin M.J., Lewis G.F., Ferguson A.M.N. & Tanvir, N., 2003. One ring to encompass them all: a giant stellar structure that surrounds the Galaxy. MNRAS, 340, L21

Iben I., Jr., 1984. On the frequency of planetary nebulae nuclei powered by helium burning and on the frequency of white dwarfs with hydrogen-deficient atmospheres. ApJ, 277, 333

Iben I., Jr., 1993. The evolution of planetary nebulae, their precursors and their progeny — a commentary. In Weinberger R. & Acker A., (eds), Planetary nebulae. IAU Symp. 155, p. 587

Iben I., Jr. & Renzini A., 1983. Asymptotic giant branch evolution and beyond. ARA&A, 21, 271

Iben I. & Renzini A., 1984. Single star evolution I. Massive stars and early evolution of low and intermediate mass stars. PhR, 105, 329

Iben I., Jr. & Tutukov A.V., 1993. Formation and evolution of binary planetary nebula nuclei and related objects. ApJ, 418, 343

Iben I., Jr., Kaler J.B., Truran J.W. & Renzini A., 1983. On the evolution of those nuclei of planetary nebulae that experience a final helium shell flash. ApJ, 264, 605

Iriarte B., 1959. Photoelectric photometry of faint blue stars. LowOB, 4, 130

Iriarte B. & Chavira E., 1957. Estrellas azules en el casquete galactico norte. BOTT, 2, 3

Ishida K. & Weinberger, R., 1987. Two senile planetary nebulae and the local PN population. A&A, 178, 227

Isobe T., Feigelson E.D., Akritas M.G. & Babu, G.J., 1990. Linear regression in astronomy. ApJ, 364, 104

Israel F.P. & Felli, M., 1976. Aperture-synthesis radio observations of three filamentary nebulae. A&A, 50, 47

Izzard R.G., Tout C.A., Karakas A.I. & Pols O.R., 2004. A new synthetic model for asymptotic giant branch stars. MNRAS, 350, 407

Jacoby G.H., 1979. Unusual structure in the planetary nebulae Abell 30 and Abell 78. PASP, 91, 754

Jacoby G.H., 1981. The peculiar planetary nebula Abell 35. ApJ, 244, 903

Jacoby G.H., 1988. Investigation of the central star of NGC 7027. ApJ, 333, 193

Jacoby G.H., 1989. Planetary nebulae as standard candles. I. Evolutionary models. ApJ, 339, 39

Jacoby G.H., 1993. Infrared excess (IRE) as an indicator of PN distance. In Weinberger R. & Acker A., (eds), Planetary nebulae. IAU Symp. 155, p. 176

Jacoby G.H., 2006. Surveys for planetary nebulae in the Magellanic Clouds. In Stanghellini L., Walsh J.R., & Douglas N.G. (eds), Planetary nebulae beyond the Milky Way. ESO Astrophysics Symposium, p.17

Jacoby G.H. & Ciardullo R., 1999. Chemical abundances of planetary nebulae in the bulge and disk of M31. ApJ, 515, 169

Jacoby G.H. & De Marco O. 2002. A survey for very faint planetary nebulae in the SMC. I. Identification, confirmation, and preliminary analysis. AJ, 123, 269

Jacoby G.H. & Kaler J.B. 1989. Magnitudes of central stars in optically thick planetary nebulae. AJ, 98, 1662

Jacoby G.H. & Kaler J.B. 1993. Improved observations of faint planetary nebulae in the Magellanic Clouds. ApJ, 417, 209

Jacoby G.H. & Van de Steene G. 1995. Identification of an old planetary nebula around the PG 1159 star: PG 1520+525. AJ, 110, 1285

Jacoby G.H. & Van de Steene, G. 2004. Planetary nebulae near the Galactic center: identifications. A&A, 419, 563

Jacoby G.H., Ciardullo R. & Ford H.C., 1990. Planetary nebulae as standard candles. V. – The distance to the Virgo Cluster. ApJ, 356, 332

Jacoby G.H., Ferland G.J. & Korista K.T. 2001. The planetary nebula A39: an observational benchmark for numerical modelling of photoionized plasmas. ApJ, 560, 272

Jacoby G.H., Branch D., Ciardullo R., et al., 1992. A critical review of selected techniques for measuring extragalactic distances. PASP, 104, 599

Jacoby G.H., Morse J.A., Fullton L.K., Kwitter K.B. & Henry R.B.C., 1997. Planetary nebulae in the globular clusters, Pal 6 and NGC 6441. AJ, 114, 2611

Jacoby G.H., Morse J.A., Fullton L.K., Kwitter K.B. & Henry R.B.C., 1998. Erratum: Planetary nebulae in the globular clusters, Pal 6 and NGC 6441. AJ, 115, 1688

Jacoby G., Kronberger M., Patchick D., Teutsch P., Saloranta J., Acker A. & Frew D., 2008. A search for faint planetary nebulae using the DSS. In Corradi R.L.M., Manchado A. & Soker N. (eds), Proceedings of the APN-IV Conference (in press)

Janes K.A. & Phelps R.L., 1994. The galactic system of old star clusters: The development of the galactic disk. AJ, 108, 1773

Jasniewicz G. & Acker A., 1988. Periodic light variations of the central star of Abell 35. A&A, 189, L7

Jasniewicz G., Duquennoy A. & Acker, A., 1987. The nucleus of LT-5: an unusual triple system? A&A, 180, 145

Jasniewicz G., Lapierre G. & Monier R., 1994. Ultraviolet variations in the spectrum of the visible central star of Abell 35. A&A, 287, 591

Jasniewicz G., Acker A., Freire-Ferrero R. & Burnet M., 1992. New photometric and spectroscopic observations of the central star of Abell 35. A&A, 261, 314

Jasniewicz G., Acker A., Mauron N., Duquennoy A. & Cuypers J., 1994. Further observations of the central star of LoTr5. A&A, 286, 211

Jasniewicz G., Thvenin F., Monier R. & Skiff B.A.,1996. The central star of LoTr 5 revisited. A&A, 307, 200

Jeffery C.S., 2008. Hydrogen-deficient stars: an introduction. In Werner K. & Rauch T. (eds), Hydrogen-Deficient Stars, ASP Conference Series, Vol. 391. San Francisco: Astronomical Society of the Pacific, p. 3

Jeffery C.S., Heber U., Hill P.W., Dreizler S., Drilling J.S., Lawson W.A., Leuenhagen U. & Werner K., 1996. A catalogue of hydrogen-deficient stars. In Jeffery C.S. & Heber U. (eds), Hydrogen deficient stars. ASP Conference Ser., 96, 471

Jeffries R.D., 1997. On the initial-final mass relation and the maximum mass of white dwarf progenitors. MNRAS, 288, 585

Jeffries R.D. & Stevens I.R., 1996. Wind-accretion induced rapid rotation and a new class of active star. MNRAS, 279, 180

Johnson D.R.H. & Soderblom D.R., 1987. Calculating galactic space velocities and their uncertainties, with an application to the Ursa Major group. AJ, 93, 864

Johnson H.M., 1955. Symmetric Galactic nebulae. ApJ, 121, 604

Johnson H.M., 1960. The planetary nebula NGC 2818. PASP, 72, 418

Johnson H.M., 1973. Spectra of NGC 7635, YM 29, and the central star of YM 29. MSRSL, 6^e Ser., 5, 367

Johnson H.M., 1974. On the comet like structure in NGC 7635. A&A, 32, 17

Johnson H.M., 1975. Luminous stars in Galactic supernova remnants. PASP, 87, 89

Johnson H.M., 1976. Spectra and Fabry-Perot interferometry of AG Carinae and the nebula. ApJ, 206, 469

Johnson H.M. & Rubin R.H., 1971. Observation and classification of the nebula YM 29. ApJ, 163, 151

Jonckheere R., 1913. Une étoile double nébuleuse. AN, 194, 47

Jonckheere R., 1916. A new stellar nebula. Observatory, 39, 134

Jones K.G., 1975. The Search for the Nebulae. Alpha Academic, Chalfont St. Giles, Bucks.

Jones R.B. & Emberson R., 1939. A large new planetary nebula. BHarO, 911, 11

Joshi Y.C., 2005. Interstellar extinction towards open clusters and Galactic structure. MNRAS, 362, 1259

Joshi Y.C., 2007. Displacement of the Sun from the Galactic plane. MNRAS, 378, 768

Josselin E., Bachiller R., Manchado A. & Guerrero, M.A., 2000. CO content of bipolar planetary nebulae. A&A, 353, 363

Joy A.H., 1945. T Tauri variable stars. ApJ, 102, 168

Jura M. & Morris M., 1985. Condensation onto grains in the outflows from mass-losing red giants. ApJ, 292, 487

Kafka S. & Honeycutt R.K., 2004. Detecting outflows from cataclysmic variables in the optical. AJ, 128, 2420

Kaftan-Kassim M.A., 1966. The planetary nebula NGC 3242. ApJ, 145, 658

Kaler J.B., 1973. The optical sectra of planetary nebulae. MSRSL , 6^e Ser., 5, 33

Kaler J.B., 1974. Planetary nebulae with multiple shells. AJ, 79, 594

Kaler J.B., 1976. Photoelectric filter photometry of planetary nebulae. ApJ, 210, 113

Kaler J.B., 1978a. The [O III] lines as a quantitative indicator of nebular central-star temperature. ApJ, 220, 887

Kaler J.B., 1978b. The enrichment of helium in planetary nebulae. ApJ, 226, 947

Kaler J.B., 1979. The enrichment of nitrogen and helium in planetary nebulae. ApJ, 228, 163

Kaler J.B., 1980. The oxygen enrichment of the Galaxy. ApJ, 239, 78

Kaler J.B., 1981a. The R Aquarii nebula. ApJ, 245, 568

Kaler J.B., 1981b. Large high-excitation planetary nebulae. ApJ, 250, L31

Kaler J.B., 1982. Bubbles from dying stars. S&T, 63, 129

Kaler J.B., 1983a. A photometric survey of compact and selected planetary nebulae. ApJ, 264, 594

Kaler J.B., 1983b. The evolution of large planetary nebulae and their central stars. ApJ, 271, 188

Kaler J.B., 1985. Planetary nebulae and their central stars. ARA&A, 23, 89

Kaler J.B. & Feibelman W.A., 1985. Ultraviolet spectra of the central stars of large planetary nebulae. ApJ, 297, 724

Kaler J.B. & Jacoby G.H., 1989. Central star temperatures of optically thick planetary nebulae and a distance-independent test of dredge-up theory. ApJ, 345, 871

Kaler J.B. & Jacoby G.H., 1990. The relation between chemical enrichment and core mass in planetary nebulae. ApJ, 362, 491

Kaler J.B. & Jacoby G.H., 1991. Central star temperatures of low-excitation planetary nebulae. ApJ, 372, 215

Kaler J.B. & Lutz J.H., 1985. Dust-distances to planetary nebulae. PASP, 97, 700

Kaler J.B., Aller, L.H. & Czyzak S.J., 1976. A spectroscopic survey of 21 planetary nebulae. ApJ, 203, 636

Kaler J.B., Shaw R.A. & Kwitter K.B., 1990. Large planetary nebulae and their significance to the late stages of stellar evolution. ApJ, 359, 392

Kalirai J.S., Bergeron P., Hansen B.M.S., Kelson D.D., Reitzel D.B., Rich R.M. & Richer H.B., 2007. Stellar evolution in NGC 6791: mass loss on the red giant branch and the formation of low-mass white dwarfs. ApJ, 671, 748

Kalirai J.S., Hansen B.M.S., Kelson D.D., Reitzel D.B., Rich R.M. & Richer H.B., 2008. The Initial-Final Mass Relation: direct constraints at the low mass end. ApJ, 676, 594

Kaper L., van Loon J.T., Augusteijn T., Goudfrooij P., Patat F., Waters L.B.F.M. & Zijlstra A.A., 1997. Discovery of a bow shock around Vela X-1. ApJ, 475, L37

Karakas A. & Lattanzio J.C., 2007. Stellar models and yields of asymptotic giant branch stars. PASA, 24, 103

Karakas A., Lattanzio J.C. & Pols O.R., 2002. Parameterising the third dredge-up in asymptotic giant branch stars. PASA, 19, 515

Karl C., Napiwotzki R., Heber U., Lisker T., Nelemans G., Christlieb N. & Reimers D., 2003. Double degenerates from the Supernova Ia Progenitor Survey (SPY). In D. de Martino, R. Silvotti, J.-E. Solheim & R. Kalytis (eds), White Dwarfs. NATO Science Series II, Vol. 105, p. 43. Kluwer Academic Publishers

Kastner J.H. & Weintraub D.A., 1995. Near-infrared polarimetric imaging of the bipolar nebula OH 231.8 +4.2: The death of a beta Pic-like system. AJ, 109, 1211

Kawamura J. & Masson C., 1996. Distances to planetary nebulae BD +30°3639 and NGC 6572. ApJ, 461, 282

Keeler J.E., 1899, The annular nebula $H IV.$13 in Cygnus. ApJ, 10, 266

Kent S.M., Dame T.M. & Fazio G., 1991. Galactic structure from the Spacelab infrared telescope. II - Luminosity models of the Milky Way. ApJ, 378, 131

Kennicutt R.C., Jr, Bresolin F., French H. & Martin P. 2000. An empirical test and calibration of HII region diagnostics. ApJ, 537, 589

Kenyon S.J., 1986. *The Symbiotic Stars*. Cambridge University Press, Cambridge

Kenyon S.J. & Truran J.W., 1983. The outbursts of symbiotic novae. ApJ, 273, 280

Kenyon S.J., Dobrzycka D. & Hartmann L., 1994. A new optical extinction law and distance estimate for the Taurus-Auriga molecular cloud. AJ, 108, 1872

Kenyon S.J., Mikolajewska J., Mikolajewski M., Polidan R.S. & Slovak M.H., 1993. Evolution of the symbiotic binary system AG Pegasi: the slowest classical nova eruption ever recorded. AJ, 106, 1573

Kepler S.O., Kleinman S.J., Nitta A., Koester D., Castanheira B.G., Giovannini O., Costa A.F.M. & Althaus L., 2007. White dwarf mass distribution in the SDSS. MNRAS, 375, 1315

Kerber F., 1998. Planetary nebulae: the normal, the strange, and Sakurai's Object. RvMA, 11, 161-76. (Schielicke, R.E., ed.) Astronomische Gesellschaft, Jena

Kerber F. & Weinberger R., 1995. A dozen new evolved planetary nebulae. In Harpaz, A. & Soker, N. (eds), Asymmetrical Planetary Nebulae. AnIPS, 11, 193

Kerber F., Lercher, G. & Weinberger R., 1996. Spectroscopy and imaging of newly discovered planetary nebulae. A&AS, 119, 423

Kerber F., Lercher G., Saurer W., et al., 1994. Newly detected galactic planetary nebulae (PNe). Astron. Ges. Abstr. Ser., 10, 172 (KLSS)

Kerber F., Kienel C., Weinberger R. & Danner R., 1997. Extinction distances: partly new access to an old problem. IAU Symp. 180, 48

Kerber F., Roth M., Manchado A. & Gröbner H. 1998. New evolved planetary nebulae in the Southern Hemisphere. A&AS, 130, 501

Kerber F., Furlan E., Galaz G., Chanamé J.C., 2000a. Investigating new planetary nebulae in the Southern Hemisphere. PASP, 112, 542

Kerber F., Furlan E., Rauch T. & Roth M., 2000b. PN-ISM interaction: the observational evidence. In Kastner, J.H., Soker, N. & Rappaport, S. (eds), Asymmetrical Planetary Nebulae II: From Origins to Microstructures. ASP Conf. Series 199, 313

Kerber F., Guglielmetti F., Mignani R. & Roth M., 2002. Proper motion of the central star of the planetary nebula Sh 2-68. A&A, 381, L9

Kerber F., Mignani R.P., Guglielmetti F. & Wicenec A., 2003a. Galactic Planetary Nebulae and their central stars. I. An accurate and homogeneous set of coordinates. A&A, 408, 1029

Kerber F., Guglielmetti F., Mignani R. & Roth M., 2003b. Sh 2-68 – A planetary nebula leaving it's [sic] mark on the interstellar medium. IAU Symp. 203, p. 525

Kerber F., Mignani R.P., Pauli E.-M., Wicenec A. & Guglielmetti F., 2004. Galactic orbits of planetary nebulae unveil thin and thick disk populations and cast light on interaction with the interstellar medium. A&A, 420, 207

Kharchenko N.V., Piskunov A.E., Röser S., Schilbach E. & Scholz R.-D., 2005. Astrophysical parameters of Galactic open clusters. A&A, 438, 1163

Khromov G.S., 1988. Planetary nebulae. SSRev, 51, 339

Khromov G.S. & Kohoutek L., 1968. Morphological study of planetary nebulae. In Osterbrock, D.E., & O'Dell, C.R. eds. Planetary Nebulae, IAU Symposium 34, Dordrecht, D. Reidel, p. 227

Kidder K.M., Holberg J.B. & Mason P.A., 1991. UBV photometry of hot DA white dwarfs. AJ, 101, 579

Kilkenny D., 1991. Photometry of faint blue stars – IX. MNRAS, 277, 920

Kilkenny D., Spencer Jones J.H. & Marang F., 1988. UBVI observations of LSS 2018, the binary central star of the planetary nebula DS-1. Obs, 108, 88

Kilkenny D., van Wyk F., Roberts G., Marang F. & Cooper D., 1998. Supplementary southern standards for UBV(RI)c photometry. MNRAS, 294, 93

Kim B.G., Kawamura A., Yonekura Y. & Fukui Y., 2004. ^{13}CO (J=1–0) survey of molecular clouds toward the Monoceros and Canis Major region. PASJ, 56, 313

Kimeswenger S., 1998. On the nature of the Galactic nebula We 1-12. MNRAS, 294, 312

Kimeswenger S., 2001. Optical coordinates of southern planetary nebulae. RMxAA, 37, 115

King D.J., Taylor K.N.R. & Tritton K.P., 1979. Nebulosity in the region of the South Celestial Pole. MNRAS, 188, 719

Kingsburgh R.L. & Barlow M.J., 1992. Distances for galactic planetary nebulae using mean [O II] doublet ratio electron densities. MNRAS, 257, 317

Kingsburgh R.L. & Barlow M.J., 1994. Elemental abundances for a sample of southern galactic planetary nebulae. MNRAS, 271, 257

Kingsburgh R.L. & English J., 1992. Distances for Galactic planetary nebulae – II. A southern hemisphere survey. MNRAS, 259, 635

Kiss L.L., Szabó G.M., Balog Z., Parker Q.A. & Frew D.J., 2008. AAOmega radial velocities out physical association between the open cluster M46 and the planetary nebula NGC 2438. MNRAS, submitted

Kiss Z.T., Tóth L.V., Krause O., Kun M. & Stickel M., 2006. Star formation in the Cepheus Flare region: implications from morphology and infrared properties of optically selected clouds. A&A, 453, 923

Klare G., Wolf B., Stahl O., Krautter J., Vogt N., Wargau W. & Rahe J., 1982. IUE observations of dwarf novae during active phases. A&A, 113, 76

Klemola A.R., 1962. Mean absolute magnitude of the blue stars at high galactic latitude. AJ, 67, 740

Kniazev A.Y., Pustilnik S.A. & Zucker D.B., 2008. Spectroscopy of two PN candidates in IC 10. MNRAS, 384, 1045

Koen C., 1992. Confidence intervals for the Lutz-Kelker correction. MNRAS, 256, 65

Koester D., Reimers D., 1989. Discovery of a planetary nebula in the field of the open cluster NGC 6087. A&A, 223, 326

Koester D., Napiwotzki R., Christlieb, N., et al., 2001. High-resolution UVES/VLT spectra of white dwarfs observed for the ESO SN Ia progenitor survey (SPY). I. A&A, 378, 556

Koesterke L. & Hamann W.-R.,1997. Spectral analyses of central stars of planetary nebulae of early WC-type: NGC 6751 and Sanduleak 3. A&A, 320, 91

Kohoutek L., 1960. On the determination of distances of planetary nebulae. BAC, 11, 64

Kohoutek L., 1962. New planetary nebulae. BAC, 13, 120

Kohoutek L., 1963a. A new distance scale and the optical thickness of planetary nebulae. BAC, 13, 71

Kohoutek L., 1963b. New planetary nebulae. BAC, 14, 70

Kohoutek L., 1964. New planetary nebulae. BAC, 15, 162

Kohoutek L., 1965. Hamburg Schmidt-camera survey of faint planetary nebulae. BAC 16, 221

Kohoutek L., 1967. A study of planetary nebula NGC 1514. I. The double-star hypothesis for the planetary nucleus based on photoelectric photometry. BAC, 18, 103

Kohoutek L., 1969. Hamburg Schmidt-camera survey of faint planetary nebulae: Galactic anticenter region. BAC, 20, 307

Kohoutek L., 1971. New planetary nebulae. A&A, 13, 493

Kohoutek L., 1972. Hamburg Schmidt-camera survey of faint planetary nebulae: Cygnus-Perseus region. A&A, 16, 291

Kohoutek L., 1977. New southern planetary nebulae. A&A, 59, 137

Kohoutek L., 1978. New and misclassified planetary nebulae. In Terzian Y. (ed), Planetary Nebulae. IAU Symposium, 76, 47

Kohoutek L., 1979. Sh 2-71 : new variable central star of a possible planetary nebula. IBVS, 1672, 1

Kohoutek L., 1983. New and misclassified planetary nebulae. In Flower, D.R. (ed), Planetary Nebulae. IAU Symp., 103, 17

Kohoutek L., 1989. New and misclassified planetary nebulae. In Torres-Peimbert S. (ed), Planetary Nebulae, IAU Symp. 131, 29

Kohoutek L., 1994. New planetary nebulae towards the galactic bulge. I. Objects in the central area. AN, 315, 235

Kohoutek L., 1997a. Search for envelopes of some steallr planetary nebula, symbiotic stars and further emission-line objects. A&AS, 125, 445

Kohoutek L., 1997b. New and misclassified planetary nebulae. AN, 318, 35

Kohoutek L., 2001. Catalogue of Galactic Planetary Nebulae (Updated Version 2000). Abhandlungen Hamburger Sternwarte, XII (2 volumes)

Kohoutek L., 2002. New Planetary Nebulae towards the galactic bulge. II. Objects surrounding the central area. AN, 323, 57

Kohoutek L. & Hekela, J. 1967. A study of planetary nebula NGC 1514. II. Spectroscopic investigation of the central star. BAC, 18, 203

Kohoutek L. & Kühl, D., 2002. Accurate coordinates of planetary nebulae. AN, 323, 484

Kohoutek L. & Laustsen, S., 1977. Central star of NGC 3132: a visual binary. A&A, 61, 761

Kohoutek L. & Martin, W., 1981. Study of compact planetary nebulae I. Absolute fluxes. A&AS, 44, 325

Kohoutek L. & Pauls, R., 1994. Spectroscopic verification of suspected planetary nebulae. III. AN, 315, 409

Kohoutek L. & Schnur, G.F.O., 1982. Study of planetary nebula K 1-2 and its variable nucleus. MNRAS, 201, 21

Kondratjeva L.N., 1971. Preliminary results on spectral investigation of some planetary nebulae. ATsirk, 629, 4

Kondratjeva L.N., 1972. He 2-10 extragalactic object. ATsirk, 683, 7

Kondratjeva L.N., 1979. Characteristics of planetary nebulae of low surface brightness. In Spectrophotometric studies of stars and nebulae, Trudy Ap. Inst. Kazakhstan, 34, 53

Kondratyeva L.N. & Denissyuk E.K., 2003. Planetary nebula K 1-9. A&A, 411, 477

Koornneef J. & Pottasch S.R., 1998. HST photometry of the stars near the center of PN NGC 650. A&A, 335, 277

Köppen J. & Acker A., 2000. Planetary Nebulae in Clusters. ASP Conf. Series, 211, 151

Köppen J., Acker A. & Stenholm B., 1991. Spectrophotometric survey of southern planetary nebulae. II – Chemical compositions. A&A, 248, 197

Kostjakova E.B., Savel'Eva M.V., Dokuchaeva O.D. & Noskova R.I., 1968. UBV photometry of the bright nuclei of the planetary nebulae. In Osterbrock D.E. & O'Dell C.R. (eds), Planetary Nebulae, IAU Symposium, 34, 317. Dordrecht, D. Reidel.

Kovacevic A.V., 2005. Using the IPAS Survey to find new extended objects in the plane of the Northern Milky Way. Unpublished report, Department of Physics, University of Bristol

Krautter J., Klaas U. & Radons G., 1987. On the nature of 623+71 – A cataclysmic binary surrounded by a bow-shock-like emission nebula. A&A, 181, 373

Krabbe A.C. & Copetti M.V.F., 2006. Chemical abundances in seven galactic planetary nebulae. A&A, 450, 159

Kronberger M., Teutsch P., Alessi B., et al., 2006. New galactic open cluster candidates from DSS and 2MASS imagery. A&A, 447, 921

Kroupa P., 2001. On the variation of the initial mass function. MNRAS, 322, 231

Kruk J.W. & Werner K., 1998. Far-Ultraviolet spectroscopy of PG 1159 stars with the Hopkins Ultraviolet Telescope. ApJ, 502, 858

Kuczawska E. & Mikolajewski M., 1993. Two different periods present in the binary nucleus of the planetary nebula LoTr5. AcA, 43, 445

Kulkarni S. & Hester J.J., 1988. Discovery of a nebula around PSR1957+20. Nature, 335, 801

Kuijken K. & Gilmore G., 1989. The mass distribution in the galactic disk – II. Determination of the surface mass density of the galactic disk near the Sun. MNRAS, 239, 605

Kuijken K. & Gilmore G., 1991. The Galactic disk surface mass density and the Galactic force K_z at z = 1.1 kiloparsecs. ApJ, 367, L9

Kun M., 1998. Star formation in the Cepheus Flare molecular clouds. I. Distance determination and the young stallar object candidates. ApJS, 115, 59

Kwitter K.B., Henry R.B.C. & Milingo, J., 2003. Sulfur, chlorine, and argon abundances in planetary nebulae. III. Observations and results for a final sample. PASP, 115, 80

Kwitter K.B. & Jacoby G.H., 1989. Properties of central stars in 13 faint, extended planetary nebulae. AJ, 98, 2159

Kwitter K.B., Henry R.B.C. & Milingo J.B., 2003. Sulfur, chlorine, and argon abundances in planetary nebulae. III. Observations and results for a final sample. PASP, 115, 80

Kwitter K.B., Jacoby G.H. & Lawrie D.G., 1983. Classification of the planetary nebula YM29 (= S274 = A21). PASP, 95, 732

Kwitter K.B., Jacoby G.H. & Lydon T.J., 1988. Identification of faint central stars in extended, low-surface-brightness planetary nebulae. AJ, 96, 997

Kwitter K.B., Massey P., Congdon C.W. & Pasachoff J.M., 1989. A search for remnant planetary nebulae around hot sdO stars. AJ, 97, 1423

Kwok S., 1982. From red giants to planetary nebulae. ApJ, 258, 280

Kwok S., 1985. On the distances of planetary nebulae. ApJ, 290, 568

Kwok S., 1993. Test of planetary nebula evolution models by distance-independent parameters. AcA, 43, 359

Kwok S., 1994. Planetary nebulae: a modern view. PASP, 106, 344

Kwok S., 2000. The origin and evolution of planetary nebulae. Cambridge University Press, Cambridge & New York

Kwok S., 2003. Symbiotic stars and planetary nebulae. In Corradi R.L.M., Mikolajewska J. & Mahoney T.J., (eds), Symbiotic Stars Probing Stellar Evolution. ASP Conference Proceedings, 303, 428. ASP, San Francisco

Kwok S., 2005. Planetary nebulae: new challenges in the 21st century. JKAS, 39, 271

Kwok S., Purton C.R. & FitzGerald P.M., 1978. On the origin of planetary nebulae. ApJ, 219, L125

Kwok S., Koning N., Huang H.H. & Churchwell E., 2006. Planetary nebulae detected in the Spitzer Space Telescope GLIMPSE Legacy Survey. AAS meeting 208, #45.02

Landolt A.U., 1992. *UBVRI* photometric standard stars in the magnitude range 11.5–16.0 around the celestial equator. AJ, 104, 340

Landolt A.U. & Uomoto A.K., 2007. Optical multicolor photometry of spectrophotometric standard stars. AJ, 133, 768

Latypov A.A., 1957. Trudy Tashkent Astron Obs., 2 (5), 31

Lauberts, A., 1982. The ESO/Uppsala Survey of the ESO (B) Atlas. European Southern Observatory, Garching

Lada C., 2006. Stellar multiplicity and the initial mass function: most stars are single. ApJ, 640, L63

Landoldt A.U., 1983. UBVRI photometric standard stars around the celestial equator. AJ, 88, 439

Landoldt A.U. & Uomoto A.K., 2007. Optical multicolor photometry of spectrophotometric standard stars. AJ, 133, 768

Lee J.-W., Carney B.W. & Balachandran S.C., 2004. Infrared echelle spectroscopy of Palomar 6 and M71. AJ, 128, 2388

Lee T.-H., Stanghellini L., Ferrario & Wickramasinghe D., 2007. High-resolution spectra of bright central stars of bipolar planetary nebulae and the question of magnetic shaping. AJ, 133, 987

Leibowitz, E.M., 1975. The optical spectrum of the nebula YM 29. ApJ, 196, 191

Lenz P. & Breger M., 2004. Period04: A software package to extract multiple frequencies from real data. In Zverko J., et al. (eds), The A-Star Puzzle, IAU Symposium, 224, 786. Cambridge: Cambridge University Press

Li J., Harrington J.P. & Borkowski K.J., 2002. The angular expansion and distance of the planetary nebula BD +30°3639. AJ, 123, 2676

Liebert J., Bergeron P. & Holberg J.B., 2005. The formation rate and mass and luminosity functions of DA white dwarfs from the Palomar Green Survey. ApJS, 156, 47

Liebert J., Bergeron P. & Tweedy R.W., 1994. A very hot, hydrogen-rich, white dwarf planetary nucleus. ApJ, 424, 817

Liebert J., Fleming T.A., Green R.F. & Grauer A.D., 1988. The nucleus of the planetary nebula VV 47: similarities with the pulsating PG1159-035/K1-16 variables. PASP, 100, 187

Liebert J., Green R., Bond H.E., et al., 1989. A compact planetary nebula around the hot white dwarf EGB 6/PG 0950+139. ApJ, 346, 251

Liebert J., Tweedy R.W., Napiwotzki R. & Fulbright M.S., 1995. BE Ursae Majoris: precataclysmic binary system and planetary nucleus. ApJ, 441, 424

Liller M.H., Welther B. & Liller W., 1966. Angular expansions of planetary nebulae. ApJ, 144, 280

Liller W., 1955. The photoelectric photometry of planetary nebulae. ApJ, 122, 240

Liller W., 1965. Expansions of planetary nebulae. PASP, 77, 25

Liller W., 1978. The distance scale of planetary nebulae. IAU Symp. 76, 35

Liller W. & Aller L.A. 1954. Photoelectric spectrophotometry of planetary nebulae. ApJ, 120, 48

Liller M.H. & Liller W. 1968. Observed Angular Motions in Planetary Nebulae. In Planetary Nebulae, Osterbrock, D.E., & O'Dell, C.R. (eds) IAU Symp. 34, Dordrecht: D. Reidel Pub. Co., p.38

Liller M.H., Welther B.L. & Liller W. 1966. Angular expansions of planetary nebulae. ApJ 144, 280

Lindoff U., 1969. The open cluster NGC 559. ArA, 5, 221

Lisker T., Heber U., Napiwotzki R., Christlieb N., Han Z., Homeier D. & Reimers D., 2005. Hot subdwarfs from the ESO Supernova Ia Progenitor Survey. I. Atmospheric parameters and cool companions of sdB stars. A&A, 430, 223

Liu X.-W., Storey P.J., Barlow M.J., Danziger I.J., Cohen M. & Bryce M., 2000. NGC 6153: a super-metal-rich planetary nebula? MNRAS, 312, 585

Liu X.-W., Barlow M.J., Zhang Y., Bastin R.J. & Storey P.J., 2006. Chemical abundances for Hf 2-2, a planetary nebula with the strongest-known heavy-element recombination lines. MNRAS, 368, 1959

Liu Y., Liu X.-W., Luo S.-G. & Barlow M.J., 2004. Chemical abundances of planetary nebulae from optical recombination lines – I. Observations and plasma diagnostics. MNRAS, 353, 1231

Livio M., 1982. Planetary nebulae with close binary central stars. A&A, 105, 37

Livio M. & Soker N., 2001. The "Twin Jet" Planetary Nebula M 2-9. ApJ, 552, 685

Longmore A.J., 1977. New and known planetary nebulae on plates taken with the UK 1.2-m Schmidt telescope. MNRAS, 178, 251

Longmore A.J. & Tritton S.B., 1980. A second list of new planetary nebulae found on United Kingdom 1.2-m Schmidt telescope plates. MNRAS, 193, 521

López J. A., Escalante K., Riesgo-Tirado, H., 2004. Links between symbiotic and planetary nebulae. RMxAA(SC), 20, 226

López J.A., Falcon, L.H., Ruiz, M.T. & Roth, M., 1991. The evolved bipolar planetary nebula NGC 2899. A&A, 241, 526

Louise R. & Hua C.T., 1984. Monochromatic observations of planetary nebulae. Ap&SS, 105, 139

Lozinskaya T.A., 1969. Interferometer observations of the filamentary nebula S 22. AZh, 46, 730 [SvA, 13, 573]

Lozinskaya T.A., 1972. Interferometry of the Medusa Nebula A21 (YM 29). AZh 49, 1158 [SvA, 16, 945]

Lozinskaya T.A., 1975. Supernova remnants as optical nebulae. AZh, 52, 39 [SvA, 19, 21]

Lozinskaya T.A. & Esipov, V.F., 1970. Spectrophotometry of three filamentary nebulae. AZh, 48, 449 [SvA, 15, 353]

Lozinskaya T.A., Sitnik T.G. & Toropova M.S., 1986. Monochromatic and spectral observations of the thin-filament nebula YM 29. AZh, 63, 255 [SvA, 30, 155]

Lozinskaya T.A., Sitnik T.G., Toropova M.S. & Klementeva A.Y., 1984. Observations of the filamentary nebula Simeiz 22. PAZh, 10, 122 [SvAL, 10, 48]

Lozinskaya T.A., Komarova V.N., Moiseev A.V. & Blinnikov S.I., 2005. New observations of the pulsar wind nebula in the supernova remnant CTB 80. AstL, 31, 245

Lucke P.B., 1978. The distribution of color excesses and interstellar reddening material in the Solar Neighborhood. A&A, 64, 367

Lutz J.H., 1973. Interstellar dust and distances to planetary nebulae. ApJ, 181, 135

Lutz J.H., 1977. Peculiar central stars of planetary nebulae. A&A, 60, 93

Lutz J.H., 1978. Observations of central stars. In Terzian Y. (ed), Planetary Nebulae. IAU Symposium, 76, 185

Lutz J.H., 1984. Ultraviolet and optical spectroscopy of CN 1-1 (=HDE 330036). ApJ, 279, 714

Lutz J.H., 1989. Distances to planetary nebulae. IAU Symp., 131, 65

Lutz J.H., 1993. Observational parameters: definitions and limits. In Weinberger R. & Acker A., (eds), Planetary nebulae. IAU Symp. 155, p. 19

Lutz J.H. & Kaler J.B., 1983. Misclassified and misidentified planetary nebulae and nuclei. PASP, 95, 739

Lutz J.H., Kaler J.B., Shaw R.A. Schwarz H.E. & Aspin C., 1989. He 2-104: a link between symbiotic stars and planetary nebulae. PASP, 101, 966

Lutz T.E. & Kelker D.H., 1973. On the use of trigonometric parallaxes for the calibration of luminosity systems: Theory. PASP, 85, 573

Lynds B.T., 1965. Catalogue of bright nebulae. ApJS, 12, 163

Lynga G., 1964. Studies of the Milky Way from Centaurus to Norma. II. Open clusters. MeLuAO, Ser. II, 140, 1

Lynga G., 1965. Studies of the Milky Way from Centaurus to Norma. IV. Galactic structure. MeLuAO, Ser. II, 142, 3

Maciel W.J., 1981. Distances of planetary nebulae II. A&AS, 44, 123

Maciel W.J., 1984. A catalogue of distances of planetary nebulae. A&AS, 55, 253

Maciel W.J., 1985. Extinction distance to the planetary nebula He 2-131. RMexAA, 10, 199

Maciel W.J., 1995. New kinematic distances of NGC 7009 and BD+30°3639 from UV and radio data. Ap&SS, 229, 203

Maciel W.J., 1996. New determinations of kinematic distances to Galactic planetary nebulae. RvMxAA(SC), 4, 126

Maciel W.J., & Cazetta J.O., 1997. Gravity distances of planetary nebulae. Ap&SS, 249, 341

Maciel W.J. & Costa R.D.D., 2003. PN and Galactic chemical evolution. In Dopita M., Kwok S., Sutherland R., eds, ASP Conf. Ser. vol. 209, Planetary nebulae and their role in the universe. Astron. Soc. Pacific, San Francisco, p. 551

Maciel W.J., & Pottasch S.R., 1980. Distances of planetary nebulae. A&A, 88, 1

MacMinn D., Phelphs R.L., Janes K.A. & Friel E.D., 1994. Berkeley 20: an unusual old open cluster. AJ, 107, 1806

Maddalena R.J., Morris M., Moscowitz J. & Thaddeus P., 1986. The large system of molecular clouds in Orion and Monoceros. ApJ, 303, 375

Madej J., Należyty M. & Althaus L.G., 2004. Mass distribution of DA white dwarfs in the First Data Release of the Sloan Digital Sky Survey. A&A, 419, L5

Madsen G.J., Reynolds R.J. & Haffner L.M., 2006. A multiwavelength optical emission line survey of warm ionized gas in the Galaxy. ApJ, 652, 401

Madsen G.J., Frew D.J., Parker Q.A., Reynolds R.J. & Haffner L.M., 2005. Emission line spectroscopy of large, diffuse planetary nebulae. *BAAS*, 37, 116

Madsen G.J., Frew D.J., Parker Q.A., Reynolds R.J. & Haffner L.M., 2006. An optical emission line survey of large planetary nebulae. In Barlow M.J. & Méndez R.H., eds, Planetary nebulae in our Galaxy and beyond, IAU Symposium, 234, 455

Maehara H., Okamura S., Noguchi T., He X.T., Liu J.Y., Huang Y.W. & Feng X.-C., 1987. NGC 2242 – A newly discovered planetary nebula. A&A, 178, 221

Magakian T.Y., 2003. Merged catalogue of reflection nebulae. A&A, 399, 141

Magnani L., Blitz L. & Mundy L., 1985. Molecular gas at high Galactic latitudes. ApJ, 295, 402

Magrini L., Corradi R.L.M., Greimel R., et al., 2003. The Local Group census: planetary nebulae in IC 10, Leo A and Sextans A. A&A, 407, 51

Magrini L., Corradi R.L.M., Leisy P., Scatarzi A., Morbidelli L & Perinotto M., 2004. The luminosity function of PNe with different morphology. In Meixner M., Kastner J.H., Balick B. & Soker N. (eds), Asymmetrical Planetary Nebulae III: Winds, Structure and the Thunderbird. ASP Conference Proceedings, 313, 42. ASP, San Francisco

Majaess D.J., Turner, D.G. & Lane, D.J, 2007. In search of possible associations between planetary nebulae and open clusters. PASP, 119, 1349

Malagnini, M.L., Morossi, C., Rossi, L. & Kurucz, R.L., 1986. The empirical BC versus T_{eff} scale for non-supergiant O9–G5 stars. A&A, 162, 140

Malin D.F., 1982. A look at some unstable stars. S&T, 63, 22

Malin D. & Murdin P., 1984. Colours of the Stars. Cambridge Univ. Press, pp. 97

Mal'kov Y.F., 1997. A self-consistent determination of the distances, physical parameters, and chemical composition for a large sample of Galactic planetary nebulae: the distances and parameters of central stars and the optical depths of envelopes. ARep, 41, 760

Mallik D.C.V., 1985. On the consequences of a new initial-final mass relation for low and intermediate mass stars and the birthrate of planetary nebulae. ApL, 24, 173

Mallik D.C.V., 1989. Initial masses. IAU Symp. 131, 493

Mallik D.C.V. & Peimbert, M., 1988. Filling factor determinations and their effects on planetary nebula studies. RMxAA, 16, 111

Mallik D.C.V., Sagar R., Pati A.K., 1995. A deep BVI photometric study of the open cluster NGC 2453. A&AS, 114, 537

Malmquist G., 1924. MeLuAO, 2, 64

Mampaso A., Gomez P., Sanchez-Magro C. & Selby M.J., 1984. Infrared observations of HII regions: S128 and G134.2+0.8 (GL 333). MNRAS, 207, 465

Mampaso A., Vilchez J.M., Pismis P., & Phillips J.P., 1987. The bipolar HII region S 201. RMxAA, 14, 474

Mampaso A., Viironen K., Corrradi R.L.M., Rodríguez M., Drew J.E., Greimel R. & Irwin J., 2005. IPHASX J052531.2+281946: a new planetary nebula towards the galactic anticentre. In Szczerba R., Stasińska G. & Górny S., eds., Planetary Nebulae as Astronomical Tools, AIP Conference Proceedings, 804, p. 14

Mampaso A., Corradi R.L.M., Viironen K., et al., 2006. The "Príncipes de Asturias" nebula: a new quadrupolar planetary nebula from the IPHAS survey. A&A, 458, 203

Mampaso A., Viironen K., Corradi R.L.M., Drew, J.E., Greimel R. & Sabin L., 2007. A search for new planetary nebulae located at large Galactocentric distances. In A. Vallenari, R. Tantalo, L. Portinari & A. Moretti (eds), *From Stars to Galaxies: Building the Pieces to Build Up the Universe*. ASP Conf. Series, 374, 199

Manchado, A., Guerrero, M.A., Stanghellini, L. & Serra-Ricart, M., 1996. The IAC Morphological Catalog of Northern Galactic Planetary Nebulae. Instituto de Astrofísica de Canarias

Manchado, A., Villaver, E., Stanghellini, L. & Guerrero, M.A., 2000. The morphological and structural classification of planetary nebulae. In Kastner, J.H., Soker, N. & Rappaport, S. (eds.), Asymmetrical Planetary Nebulae II: From Origins to Microstructures. ASP Conf. Series, 199, 17

Marcy G.W. & Butler R.P., 2000. Planets orbiting other suns. PASP, 112, 137

Marigo P., Bressan A. & Chiosi C., 1996. The TP-AGB phase: a new model. A&A, 313, 545

Marigo P., Girardi L., Groenewegen M.A.T. & Weiss A., 2001. Evolution of planetary nebulae I. An improved synthetic model. A&A, 378, 958

Marigo P., Bernard-Salas J., Pottasch S.R., Tielens A.G.G.M & Wesselius P.R., 2003. Probing AGB nucleosynthesis via accurate planetary nebulae abundances. A&A, 409, 619

Marigo, P., Girardi, L., Weiss, A., Groenewegen, M.A.T. & Chiosi, C., 2004. Evolution of planetary nebulae II. Population effects on the bright cut-off of the PNLF. A&A, 423, 995

Marsalkova P., 1974. A comparison catalogue of HII-regions. Ap&SS, 27, 3

Marsh M.C., Barstow M.A., Buckley D.A., Burleigh M.R., Holberg J.B., Koester D., O'Donoghue D., Penny A.J. & Sansom A.E., 1997. An EUV-selected sample of DA white dwarfs from the *ROSAT* All-Sky Survey – I. Optically derived stellar parameters. MNRAS, 286, 369

Marston A.P., 1997. A survey of nebulae around Galactic Wolf-Rayet Stars in the southern sky. III. Survey completion and conclusions. ApJ, 475, 188

Marston A.P. & McCollum B., 2006. Shells and bipolar structures around B[e] Stars. In Stars with the B[e] Phenomenon. ASP Conference Series, Vol. 355, p.189

Masson C.R., 1986. Angular expansion measurement with the VLA: the distance to NGC 7027. ApJ, 302, L27

Masson C.R., 1989a. The structure of NGC 7027 and a determination of its distance by measurement of proper motions. ApJ, 336, 294

Masson C.R., 1989b. The structures of and distances to BD $+30°3639$ and NGC 6572. ApJ, 346, 243

Masson C.R., 1990. On the structure of ionization-bounded planetary nebulae. ApJ, 348, 580

Marten, H. & Schönberner, D., 1991. On the dynamical evolution of planetary nebulae. A&A, 248, 590

Martin D.C, Seibert M., Neill J.D., et al., 2007. A turbulent wake as a tracer of 30,000 years of Mira's mass loss history. Nature, 448, 780

Martin N.F., Ibata R.A., Bellazzini M., Irwin M.J., Lewis G.F. & Dehnen W., 2004. A dwarf galaxy remnant in Canis Major: the fossil of an in-plane accretion on to the Milky Way. MNRAS, 348, 12

Martin W., 1981. Study of compact planetary nebulae. II. Temperatures, luminosities and problems of evolution of the central stars. A&A, 98, 328

Martin W., 1994. Extinction-distances to planetary nebulae. A&A, 281, 526

Martin-Hernández N.L., Esteban C., Mesa-Delgado A., Bik A. & Puga E., 2008. M1-78: a nitrogen-rich Galactic compact HII region beyond the Perseus arm. A&A, 482, 215

Matsuura M., Zijlstra A.A., Molster F.J., Waters L.B.F.M., Nomura H., Sahai R. & Hoare M.G., 2005a. The dark lane of the planetary nebula NGC 6302. MNRAS, 359, 383

Matsuura M., Zijlstra A.A., Gray M.D., Molster F.J. & Waters L.B.F.M., 2005b. The symmetric dust shell and the central star of the bipolar planetary nebula NGC 6537. MNRAS, 363, 628

Mavromatakis F., Papamastorakis J. & Paleologou E.V., 2001. The physical structure of the planetary nebula NGC 6781. A&A, 374, 280

Mavromatakis F., Papamastorakis J., Paleologou E.V. & Ventura J., 2000. Optical CCD imaging of the supernova remnant CTA 1. A&A, 353, 371

Maxted P.F.L. & Marsh T.R., 1999. The fraction of double degenerates among DA white dwarfs. MNRAS, 307, 122

Maxted P.F.L., Napiwotzki R., Dobbie P.D. & Burleigh M.R., 2006. Survival of a brown dwarf after engulfment by a red giant star. Nature, 442, 543

May J., Alvarez H. & Bronfman L., 1997. Physical properties of molecular clouds in the southern outer Galaxy. A&A, 327, 325

McCarthy J.K., Méndez R.H. & Kudritzki R.-P., 1997. Non-LTE model atmospheres analyses of faint PN central stars observed with Keck HIRES. In Habing H.J. & H. J. G. L. M. Lamers H.J.G.L.M. (eds), Planetary nebulae, IAU Symposium 180, 120. Dordrecht: Kluwer

McCarthy J.K., Mould J.R., et al. 1990. Evolutionary versus dynamical time scales for the evolution of the central stars of planetary nebulae. ApJ, 351, 230

McCarthy J.K., Rich R.M., Becker S R., Butler K., Husfeld D & Groth H.G., 1991. Echelle spectroscopy of CD $-41°13967$: the young central star of a new planetary nebula. ApJ, 371, 380

McCook G.P. & Sion E.M., 1999. A catalog of spectroscopically identified white dwarfs. ApJS, 121, 1

McCullough P.R. & Benjamin R.A., 2001. A straight and narrow ionized filament. AJ, 122, 1500

McCullough P.R., Bender, C., Gaustad, J.E., Rosing, W. & Van Buren, D., 2001. The 5°diameter ionized halo of the planetary nebula Abell 36. AJ, 121, 1578

McLaughlin D.B., 1942. The nucleus of the planetary nebula NGC 1514. PASP, 54, 31

Meaburn J., 1997. The proper motion distance to the remarkable bipolar planetary nebula KjPn 8. MNRAS, 292, L11

Meaburn J., & Walsh J.R., 1989. Echelle observations of the high speed motions in the extreme bi-polar nebula He 2-111 (PK 315–0°1). A&A, 223, 277

Meaburn, J., López, J.A. & Noriega-Crespo, A., 2000. The complex environment of the high-excitation planetary nebula NGC 3242. ApJS, 128, 321

Meaburn J., Clayton C.A., Bryce, M., Walsh J.R., Holloway A.J. & Steffen W., 1998. The nature of the cometary knots in the Helix planetary nebula (NGC 7293). MNRAS, 294, 201

Meaburn J., Boumis P., Christopoulou P.E., Goudis C.D., Bryce M. & López J.A., 2005a. The global kinematics of the Dumbbell planetary nebula (NGC 6853, M27, PN G060.8-03.6). RMxAA, 41, 109

Meaburn J., Boumis P., López J.A., Harman D.J., Bryce M., Redman M.P. & Mavromatakis F., 2005b. The creation of the Helix planetary nebula (NGC 7293) by multiple events. MNRAS, 360, 963

Meaburn J., López J.A., Steffen W., Graham M.F., & Holloway A.J., 2005c. The Hubble-type outflows from the high-excitation polypolar planetary nebula NGC 6302. AJ, 130, 2303

Meaburn J., Lloyd M., Vaytet N.M.H. & López J.A., 2008. Hubble-type outflows of the high-excitation, poly-polar planetary nebula NGC 6302 – from expansion proper motions. MNRAS, 385, 269

Meatheringham S.J., Dopita M.A. & Morgan D.H., 1988. Fluxes and ionised masses of Magellanic Cloud planetary nebulae. ApJ, 329, 166

Meatheringham S.J., Wood P.R. & Faulkner D.J.,1988. A study of some southern planetary nebulae. ApJ, 334, 862

Mebold U., Cernicharo J., Velden L., Crezelius C. & Reif K., 1983. Molekülwolken in hohnen Galaktischen breiten. MitAG, 60, 418

Mebold U., Cernicharo J., Velden L., Reif K., Crezelius C. & Goerigk W., 1985. The Draco nebula: a molecular cloud in the galactic halo? A&A, 151, 427

Meijerink R., Mellema G. & Simis Y., 2003. The post-AGB evolution of AGB mass loss variations. A&A, 405, 1075

Meixner M., McCullough P., Hartman J., Son M. & Speck A., 2005. The multitude of molecular hydrogen knots in the Helix nebula. AJ, 130, 1784

Melmer D. & Weinberger R., 1990. New old PN in the southern sky. MNRAS, 243, 236

Mellema G., 2004. On expansion parallax distances for planetary nebulae. A&A, 416, 623

Mellema, G. & Frank A., 1997. Outflow collimation in young stellar objects. MNRAS, 292, 795

Méndez R.H., 1975. The relationship between HD 87892 and NGC 3132. ApJ, 199, 411

Méndez R.H., 1978. A-type central stars of planetary nebulae – II. The central stars of NGC 2346, He 2-36 and NGC 3132. MNRAS, 185, 647

Méndez, R.H., 1989. Binarity and intrinsic variability in central stars of planetary nebulae. In Torres-Peimbert S. (ed), Planetary Nebulae, IAU Symp. 131, 261

Méndez R.H., 1991. Photospheric abundances in central stars of planetary nebulae, and evolutionary implications. In IAU Symp. 145 (ed. G. Michaud & A.V. Tutukov), p. 375

Méndez R.H. & Niemela V.S. 1977. The central star of NGC 1360: a spectroscopic binary within a planetary nebula. MNRAS, 178, 409

Méndez R.H. & Niemela V.S., 1978. Observations of three central stars of planetary nebulae. ApJ, 232, 496

Méndez R.H. & Niemela V.S., 1981. The binary central star of NGC 2346 and the extinction puzzle. ApJ, 250, 240

Méndez R.H. & Soffner T., 1997. Improved simulations of the planetary nebula luminosity function. A&A, 321, 898

Méndez R.H., Niemela V.S. & Lee P., 1978. A-type central stars of planetary nebulae – I. A radial-velocity study of the central stars of NGC 2346 and NGC 3132. MNRAS, 184, 351

Méndez R.H., Gathier R. & Niemela V.S., 1982. The unprecedented light variations of NGC 2346. A&A, 116, L5

Méndez R.H., Kudritzki R.P. & Herrero A., 1992. On central star luminosities and optical thicknesses in planetary nebulae. A&A, 260, 329

Méndez R.H., Lee P., O'Brien A. & Liller W., 1980. The disappearance of V-V 1-7 and the nature of its central star. A&A, 91, 331

Méndez R.H., Kudritzki R.P. & Simon K.P., 1985. SIT Vidicon and IDS spectra of central stars of planetary nebulae. A&A, 142, 289

Méndez R.H., Kudritzki R.P., Herrero A., Husfield D. & Groth H.G., 1988a. High resolution spectroscopy of central stars of planetary nebulae I. Basic atmospheric parameters and their interpretation. A&A, 190, 113

Méndez R.H., Groth H.G., Husfield D., Kudritzki R.P. & Herrero A. 1988b. PHL 932: another non-post-AGB central star of planetary nebula. A&A, 197, L25

Méndez R.H., Gathier R., Simon K.P. & Kwitter K.B. 1988c. Spectra of three planetary nebulae and a search for nebular emissions around 12 sdO stars. A&A, 198, 287

Méndez R.H., Kudritzki R.P., Ciardullo R. & Jacoby G.H., 1993. The bright end of the planetary nebula luminosity function. A&A, 275, 534

Méndez R.H., Teodorescu A.M., Schönberner D., Jacob R. & Steffen M., 2008. Toward better simulations of planetary nebulae luminosity functions. ApJ, 681, 325

Menzel D., 1922. Five new planetary nebulae. BHarO, 777, 3

Mermilliod J.-C., Mayor M., Andersen J., Nordström B., Lindgren H. & Duquennoy A., 1989. Red giants in open clusters. II – Orbits of ten spectroscopic binaries in NGC 2360, 2437, 2447, 5822, 5823, and 6475. A&AS, 79, 11

Mermilliod J.-C., Claria J.J., Andersen J., Piatti A.E. & Mayor M., 2001. Red giants in open clusters. IX. NGC 2324, 2818, 3960 and 6259. A&A, 375, 30

Mermilliod J.-C., Andersen J., Latham D.W. & Mayor M., 2007. Red giants in open clusters XIII. Orbital elements of 156 spectroscopic binaries. A&A, 473, 829

Merrett H.R., Merrifield M.R., Douglas N., et al., 2006. A deep kinematic survey of planetary nebulae in the Andromeda galaxy, using the Planetary Nebula Spectrograph. MNRAS, 369, 120

Merrill P.W. 1940. Spectra of the Long-Period Variable Stars. Chicago: University of Chicago Press

Merrill P.W., 1942. Two small planetary nebulae. PASP, 54, 107

Miller F.D. & van Dien E., 1949a. A large new planetary nebula. ApJ, 109, 537

Miller F.D. & van Dien E., 1949b. Erratum: a large new planetary nebula. ApJ, 110, 104

Miller G.E. & Scalo J.M., 1979. The initial mass function and stellar birthrate in the solar neighborhood. APJS, 41, 513

Miller J.S., 1974. Planetary nebulae and their central stars. ARA&A, 12, 331

Miller Bertolami M.M. & Althaus L.G., 2006. Full evolutionary models for PG 1159 stars. Implications for the helium-rich O(He) stars. A&A, 454, 845

Miller Bertolami M.M. & Althaus L.G., 2007. On the robustness of H-deficient post-AGB tracks. A&A, 470, 675

Miller Bertolami M.M., Althaus L.G., Serenelli A.M. & Panei J.A., 2006. New evolutionary calculations for the born again scenario. A&A, 449, 313

Milne D.K. & Aller L.H., 1975. Radio observations at 5 GHz of southern planetary nebulae. A&A, 38, 183

Minello S. & Sabbadin F., 1977a. The evolution of line intensity ratios in planetary nebulae. A&A, 58, L29

Minello S. & Sabbadin F., 1977b. Statistical properties of planetary nebulae: central stars. A&A, 60, L9

Minkowski R., 1942. Spectra of planetary nebulae of low surface brightness. ApJ, 95, 243

Minkowski R., 1946. New emission nebulae. PASP, 58, 305

Minkowski R., 1947. New emission nebulae (II). PASP, 59, 257

Minkowski R., 1948. New emission nebulae (III). PASP, 60, 386

Minkowski R., 1950. Galactic distribution of planetary nebulae and Be stars. PMicO, 10, 25

Minkowski R., 1958. Cygnus Loop and some related nebulosities. RvMPhys, 30, 1048

Minkowski R., 1965. Planetary Nebulae. In Galactic Structure, Blaauw, A. & Schmidt, M. (eds). Univ. of Chicago Press, p. 321

Minkowski R. & Aller L.H., 1954. The structure of the Owl Nebula. ApJ, 120, 261

Minkowski R. & Baum W.A., 1960. Ann. Rep. Mt. Wilson & Palomar Obs. pp. 18

Miszalski B., Parker Q.A., Acker A., Birkby J., Frew D.J. & Kovacevic A., 2008. MASH-II: More planetary nebulae from the AAO/UKST Hα Survey. MNRAS, 384, 525

Mitchell D.L., Pollacco D., O'Brien T.J., Bryce M., López J.A. & Meaburn J., 2006. The structures and kinematics of planetary nebulae with close-binary central stars. In Barlow M.J. & Méndez R.H., eds, Planetary nebulae in our Galaxy and beyond, IAU Symp., 234, 139

Mitchell D.L., Pollacco D., O'Brien T.J., Bryce M., López J.A., Meaburn J. & Vaytet N.M.H., 2007. Proof of polar ejection from the close-binary core of the planetary nebula Abell 63. MNRAS, 374, 1404

Moe M. & De Marco O., 2006a. Do most planetary nebulae derive from binaries? I. Population synthesis model of the Galactic planetary nebula population produced by single stars and binaries. ApJ, 650, 916

Moe M. & De Marco O., 2006b. Do all PNe come from binaries? In Barlow M.J. & Mendez R.H., eds, Planetary nebulae in our Galaxy and beyond, IAU Symp., 234, p. 463

Moehler S., Richtler T., de Boer K.S., Dettmar R.J. & Heber U., 1990. Hot subluminous stars at high galactic latitudes. I. Spectra and Strömgren photometry. A&AS, 86, 53

Moffatt A.F.J. & Fitzgerald M.P., 1974. NGC 2453, a moderately young open cluster in Puppis. A&AS, 18, 19

Moffat A.F.J., Marchenko S.V., Seggewiss W., et al., 1998. Wolf-Rayet stars and O-star runaways with HIPPARCOS. I. Kinematics. A&A, 331, 949

Monet D.G., Levine S.E., Canzian B., et al., 2003. The USNO-B Catalog. AJ, 125, 984

Monreal-Ibero A., Roth M.M., Schönberner D., Steffen M. & Böhm P., 2005. Integral field spectroscopy of faint halos of planetary nebulae. ApJ, 628, L139

Monteiro H., Morisset C., Gruenwald R. & Viegas S.M., 2000. Morphology and kinematics of planetary nebulae. II. A diabolo model for NGC 3132. ApJ, 537, 853

Monteiro H., Schwarz H.E., Gruenwald R. & Heathcote S., 2004. Three-dimensional photoionization structure and distances of planetary nebulae. I. NGC 6369. ApJ, 609, 194

Monteiro H., Schwarz H.E., Gruenwald R., Guenthner K. & Heathcote S.R., 2005. Three-dimensional photoionization structure and distances of planetary nebulae. II. Menzel 1. ApJ, 620, 321

Morgan, D.H., Parker, Q.A. & Russeil, D. 2001. New Wolf-Rayet central stars of planetary nebulae identified on the AAO/UKST Hα Survey. MNRAS, 322, 877

Morgan, D.H., Parker, Q.A. & Cohen, M., 2003. A unique Galactic planetary nebula with a [WN] central star. MNRAS, 346, 719

Morisset C. & Stasińska G., 2008. An atlas of synthetic line profiles of planetary nebulae. RMxAA, 44, 171

Moritz P., Wennmacher A., Herbstmeier U., Mebold U., Egger R. & Snowden S.L., 1998. A new method to determine total hydrogen column densities. A&A, 336, 682

Morrison N.D. & Liller W., 1968. Temperature, luminosity and distance of the exciting star of the planetary nebula NGC 1514. AJ, 73, S110

Motch, C., Werner, K. & Pakull, M.W., 1993. A new PG 1159 star discovered in the ROSAT XRT all sky survey: NLTE analysis of X-ray and optical spectra. A&A, 268, 561

Motch C., Haberl F., Guillout P., Pakull M., Reinsch K. & Krautter J., 1996. New cataclysmic variables from the ROSAT All-Sky Survey. A&A, 307, 459

Munari U., 1997. Outbursts of Symbiotic Stars. In Mikolajewska J. (ed.), Physical processes in symbiotic binaries and related systems. Copernicus Foundation for Polish Astronomy, Warsaw, p. 37

Munari U. & Zwitter T., 2002. A multi-epoch spectrophotometric atlas of symbiotic stars. A&A, 383, 188

Murdin P., Clark D.H. & Haynes R.F., 1979. G339.2 − 0.4: supernova remnant or planetary nebula? MNRAS ,189, 459

Murphy D.C. & May J., 1991. Molecular clouds in Vela. A&A, 247, 202

Mürset U. & Nussbaumer H., 1994. Temperatures and luminosities of symbiotic novae. A&A, 282, 586

Muthu C., 2001. Spectroscopic investigations of planetary nebulae. BASI, 29, 381

Muthu C., Anandarao B.G. & Pottasch S.R., 2000. A spatio-kinematic study of the interaction of the planetary nebula NGC 246 with the interstellar medium. A&A, 355, 1098

Napiwotzki R., 1993. White dwarfs in old planetary nebulae. AcA, 43, 343

Napiwotzki R., 1999. Spectroscopic investigation of old planetaries IV. Model atmosphere analysis. A&A, 350, 101

Napiwotzki R., 2001. Spectroscopic investigation of old planetaries V. Distance scales. A&A, 367, 973

Napiwotzki R., 2006. On near Chandrasekhar mass central stars of planetary nebulae. A&A, 451, L27

Napiwotzki R. & Schönberner, D., 1991. Spectroscopic investigation of old planetaries II. Detection of a "hybrid" central star. A&A, 249, L16

Napiwotzki R. & Schönberner, D., 1995. Spectroscopic investigation of old planetaries III. Spectral types, magnitudes, and distances. A&A 301, 545

Nassau J.J., Stephenson C.B., & Caprioli G., 1964. Spectral classification for new or unclassified late-type variables, emission-line stars, S stars, and planetary nebulae. ApJ, 139, 864

Neckel T. & Staude H.J., 1984. A survey of bipolar and cometary nebulae. Photographic and photometric observations. A&A, 131, 200

Neckel T. & Vehrenberg H., 1990. Atlas Galaktischer Nebel, Teil III. Treugesell, Verlag K.G.

Nordström B., 1975. A spectral survey of the Southern Milky Way. II. O–B5 stars, l=237° to 281°. A&AS, 21, 193

Norris J.E., Ryan S.G., Beers T.C., 1999. A search for stars of very low metal abundance. III. UBV photometry of metal-weak candidates. ApJS, 123, 639

Noskova R.I., 1989. The cyclic variability of IN Comae, the peculair central star of the planetary nebula LT 5. PAZh, 15, 346 [SvAL, 15, 149]

Noumaru J. & Ogura K., 1993. W 16-185: a heavily reddened, low-excitation planetary nebula. PASP, 105, 867

O'Dell C.R., 1962. A distance scale for planetary nebulae based on emission-line fluxes. ApJ, 135, 371

O'Dell C.R., 1963. Photoelectric photometry of the planetary nebulae. III. ApJ, 138, 293

O'Dell C.R., 1963. On the association of NGC 2437 and NGC 2438. PASP, 75, 370

O'Dell C.R., 1966. A new peculiar emission-line object. ApJ, 145, 487

O'Dell C.R., 1998. Imaging and spectroscopy of the Helix Nebula: the ring is actually a disk. AJ, 116, 1346

O'Dell C.R., 2000. The nature of the linear structures in the Helix and Orion nebulae. AJ, 119, 2311

O'Dell C.R., 2005. The 3-D structure of the Helix Nebula. RMxAA(SC), 23, 5

O'Dell C.R., McCullough P.R. & Meixner M., 2004. Unraveling the Helix Nebula: its structure and knots. AJ, 128, 2339

O'Dell C.R., Sabbadin F. & Henney W.J., 2007. The three-dimensional ionization structure and evolution of NGC 6720, the Ring Nebula. AJ, 134, 1679

O'Dell C.R., Balick B., Hajian A.R., Henney W.J. & Burkert A., 2002. Knots in nearby planetary nebulae. AJ, 123, 3329

Odenkirchen M., Soubiran C. & Colin J., 1998. The Coma Berenices star cluster and its moving group. NewA, 3, 583

Ogura K. & Noumaru J., 1994. Discovery of an extremely high excitation Herbig-Haro object in south-eastern Vela. AJ, 108, 1427

Ojha D.K., 2001. Radial scalelengths of the galactic thin and thick disc with 2MASS data. MNRAS, 322, 426

Oliveira C.M, Chayer P., Moos H.W., Kruk J.W. & Rauch T., 2007. Evidence for deuterium astration in the planetary nebula Sh2-216? ApJL, 661, L57

Olivier E.A, Whitelock P. & Marang F., 2001. Dust-enshrouded asymptotic giant branch stars in the solar neighbourhood. MNRAS, 326, 490

Osterbrock D.E & Ferland G.J., 2006. *Astrophysics of Gaseous Nebulae and Active Galactic Nuclei* (2nd ed). University Science Books, Sausalito, CA

Osterbrock, D.E., & O'Dell, C.R. (eds). *Planetary Nebulae.* IAU Symposium No. 34, D. Reidel Pub. Co., Dordrecht-Holland:

Osterbrock D.E. & Stockhausen R.E., 1961. Photometry and Radiometry of Gaseous Nebulae. ApJ, 133, 2

O'Toole S.J., 2004. Beyond the iron group: Heavy metals in hot subdwarfs. A&A, 423, L25

Otte B., Dixon W.V.D. & Sankrit R., 2004. Discovery of an O VI-emitting nebula around the hot white dwarf KPD 0005+5106. ApJ, 606, 143

Page T., 1942. Continuous emission in the spectra of planetary nebulae. ApJ, 96, 78

Palen S., Balick B., Hajian A.R., Terzian Y., Bond H.E. & Panagia N. 2002. Hubble Space Telescope expansion parallaxes of the planetary nebulae NGC 6578, NGC 6884, NGC 6891, and IC 2448. AJ 123, 2666

Papamastorakis J., Xilouris K.M. & Paleologou E.V., 1993. Morphological study of the extended halo around the Dumbbell Nebula (NGC 6853). A&A, 279, 536

Papamastorakis J., Xilouris K.M. & Paleologou E.V., 1994. CCD imaging of nearby aged planetary nebulae. In MacGillivray, H.T. et al. (eds.), Astronomy from Wide-Field Imaging. IAU Symp., 161, 484

Parenago, P.P. 1946. AZh., 23, 69

Parker Q.A., 2000. The largest PNe known? AAONw 94, 9

Parker Q.A. & Bland-Hawthorn J., 1998. Technical aspects of the new AAO/UKST H-alpha interference filter. PASA, 15, 33

Parker Q.A. & Phillipps S., 1998a. Background and first results from the new AAO/UKST Hα Survey. PASA, 15, 28

Parker Q. & Phillipps S., 1998b. Hidden secrets of the Milky Way. A&G, 39 (4), 10

Parker Q.A. & Malin D., 1999. The introduction of Tech Pan film at the UK Schmidt Telescope. PASA, 16, 288

Parker Q.A. & Morgan D.H., 2003. More Wolf-Rayet central stars of planetary nebulae identified on the AAO/UKST Hα Survey. MNRAS, 341, 961

Parker Q.A., Frew D.J. & Stupar M., 2004. G332.5-5.6: a new Galactic SNR identified from H-alpha imaging and optical spectroscopy. AAONw, 104, 9

Parker Q.A., Morgan D.H. & Russeil D., 2000. Discovery of two new Wolf-Rayet stars from the AAO/UKST H-alpha survey. AAONw, 93, 4

Parker Q.A., Malin D., Tritton S. & Hartley M., 2001a. The Helix nebula revisited – a planetary nebula the size of the Moon. AAONw, 96, 6

Parker Q.A., Hartley M., Russeil D., et al., 2001b. The Edinburgh/AAO/Strasbourg Catalogue of Galactic PN (Preliminary Version: 1.0 November 2001). On CD-ROM

Parker Q.A., Hartley M., Russeil D., et al., 2003. The Edinburgh/AAO/Strasbourg Catalogue of Galactic planetary nebulae. In Dopita M., Kwok S., Sutherland R., eds, ASP Conf. Ser. vol. 209, Planetary nebulae and their role in the universe. Astron. Soc. Pacific, San Francisco, p. 41

Parker Q.A., Phillipps S., Pierce M.J., et al., 2005a. The AAO/UKST SuperCOSMOS Hα Survey. MNRAS, 362, 689

Parker Q.A., Acker A., Peyaud A. & Frew D.J., 2005b. MASH: The Macquarie/AAO/Strasbourg Hα Planetary Nebula Catalogue. In Szczerba R., Stasińska G. & Górny S., eds., Planetary Nebulae as Astronomical Tools, AIP Conference Proceedings 804, p. 3

Parker Q.A., Acker A., Frew D.J., et al., 2006a. The Macquarie/AAO/Strasbourg Hα Planetary Nebula Catalogue: MASH. MNRAS, 373, 79

Parker Q.A., Acker A., Frew D.J., Reid W.A., 2006b. Milky Way and Magellanic Cloud Surveys for Planetary Nebulae. In Barlow M.J. & Méndez R.H., eds, Planetary nebulae in our Galaxy and beyond, IAU Symp. 234, p. 1

Parker R.A.R., 1964. Physical conditions in the Cygnus Loop and some other possible supernova remnants. ApJ, 139, 493

Parker R.A.R., Gull T.R. & Kirshner R.P., 1979. An Emission-Line Survey of the Milky Way. NASA SP-434

Parsamyan E.S., 1965. Index to cometary nebulae discovered on the Palomar charts. Isv. Akad. Nauk. Armyan. SSR. Ser 2, 18, 146

Parsamyan E.S. & Petrosyan V.M., 1979. Catalogue of cometary nebulae and related objects ($-42°$ $< \delta < +66°$). Soobsch. Byurakan Obs., 51, 1

Parthasarathy M., Branch D., Jeffery D.J. & Baron E., 2007. Progenitors of type Ia supernovae: binary stars with white dwarf companions. NewAR, 51, 524

Paturel G., 1981. Thèse de doctorat, Université de Lyon

Pauldrach, A.W.A., Hoffmann T.L. & Méndez R.H., 2004. Radiation-driven winds of hot luminous stars. XV. Constraints on the mass-luminosity relation of central stars of planetary nebulae. A&A, 419, 1111

Pauls R. & Kohoutek L., 1996. Study of the planetary nebula NGC 2438. I. Spectroscopy of the nebula and of some cluster stars. AN, 317, 413

Pease F.G., 1928. A planetary nebula in the globular cluster Messier 15. PASP, 40, 342

Pedreros M., 1987. Photometric study of the southern open cluster IC 2488. AJ, 94, 92

Pedreros M., 1989. The open cluster NGC 2818 and its associated planetary nebula. AJ, 98, 2146

Peimbert M., 1978. Chemical abundances in planetary nebulae. IAU Symp., 76, 215

Peimbert M., 1990. Total number of planetary nebulae in different galaxies and the PN distance scale. RMxAA, 20, 119

Peimbert M., 1993. Planetary nebula birth rates in the Galaxy and other galaxies. In Weinberger R. & Acker A., (eds), Planetary nebulae. IAU Symp. 155, p. 523

Peimbert M. & Torres-Peimbert S., 1971. Planetary nebulae. I. Photoelectric photometry. BOTT, 36 (6), 21

Peimbert M. & Torres-Peimbert S., 1977. Photoelectric photometry and physical conditions of planetary nebulae. RMxAA, 2, 181

Peimbert M., Rayo J.F. & Torres-Peimbert S., 1975. Observations of faint HII regions in our galaxy. RMxAA, 1, 289

Peña M. & Stasińska G., 2001. Planetary nebulae with [WR] nuclei. RMxAA(SC), 11, 61

Peña M., Stasińska G. & Medina S., 2001. Galactic planetary nebulae with Wolf-Rayet nuclei II. A consistent observational data set. A&A, 367, 983

Peña M., Ruiz M.T., Bergeron P., Torres-Peimbert S. & Heathcote S. 1997. The evolved central star of the planetary nebula ESO 166-PN21. A&A 317, 911

Peña M., Stasińska G., Esteban C., Koesterke L., Medina S. & Kingsburgh R., 1998. Galactic planetary nebulae with Wolf-Rayet nuclei I. Objects with [WC]-early type stars. A&A, 337, 866

Peñarrubia J., Martínez-Delgado D., Rix H.-W., et al., 2005. A Comprehensive Model for the Monoceros Tidal Stream. ApJ, 626, 128

Penprase B.E., Rhodes J.D. & Harris E.L., 2000. Optical observations of the Draco molecular cloud I. Catalog of B and V magnitudes for selected areas. A&A, 364, 712

Pereira C.B., Smith V.V. & Cunha K., 2005. High-resolution spectroscopic observations of the D'-type symbiotic stars HD 330036 and AS 201. A&A, 429, 993

Perek L., 1960. New planetary nebulae. BAC, 11, 256

Perek L., 1963a. Planetary nebulae in the central region of the Galaxy. BAC, 14, 201

Perek L., 1963b. Note on the distribution in space of planetary nebulae. BAC, 14, 218

Perek L., 1971. Photometry of southern planetary nebulae. BAC, 22, 103

Perek L. & Kohoutek L., 1967. Catalogue of Galactic Planetary Nebulae. Academia Publishing House, Prague

Perinotto M., 1991. Chemical abundances in planetary nebulae: basic data and correlations between elements. ApJS, 76, 687

Perinotto M. & Corradi R.L.M., 1998. The chemical structure of bipolar planetary nebulae II. 13 objects. A&A, 352, 721

Perinotto M., Purgathofer A., Pasquali A. & Patriarchi P., 1994. Spectrophotometry of southern planetary nebulae. A&AS, 107, 481

Perinotto M., Morbidelli L. & Scatarzi A., 2004. A reanalysis of chemical abundances in Galactic PNe and comparison with theoretical predictions. MNRAS, 349, 793

Perinotto M., Purgathofer A., Pasquali A. & Patriarchi P., 1994. Spectrophotometry of southern planetary nebulae. A&AS, 107, 481

Perinotto M., Schönberner D., Steffen M. & Calonaci C., 2004. The evolution of planetary nebulae I. A radiation-hydrodynamics parameter study. A&A, 414, 993

Peyaud A.E.J., 2005. Unpublished PhD thesis, Macquarie University

Peyaud A.E.J., Parker Q.A. & Acker A., 2003. Deep study of the Galactic bulge using new planetary nebulae discovered on the AAO/UKST Hαsurvey. In SF2A-2003: Semaine de l'Astrophysique Francaise, Conference Series, p. 311

Peyaud A.E.J., Parker Q.A. & Acker A., 2004. Dynamics of the Galactic bulge using a new planetary nebulae sample. In SF2A-2004: Semaine de l'Astrophysique Francaise, Conference Series, p. 625

Peyaud A.E.J., Parker Q.A. & Acker A., 2005. Deep AAO/UKST Hα images reveal large numbers of new Galactic bulge PNe. In Szczerba R., Stasińska G. & Górny S., eds., Planetary Nebulae as Astronomical Tools, AIP Conference Proceedings 804, p. 13

Peyaud A.E.J., Boily C., Acker A. & Parker Q.A., 2006. Kinematics and dynamics of the Galactic bulge through planetary nebulae. In Barlow M.J. & Méndez R.H., eds, Planetary nebulae in our Galaxy and beyond, IAU Symp. 234, p. 485

Phelps R.L. & Janes, K.A., 1991. A probable planetary nebula in the direction of the young open cluster NGC 3572. PASP, 103, 491

Phelps R.L., Janes K.A. & Montgomery K.A., 1994. Development of the Galactic disk: A search for the oldest open clusters. AJ, 107, 1079

Phillips J.P., 1989. Stellar evolution and the planetary nebulae formation rate. In IAU Symp. 131, ed. S. Torres-Peimbert, Dordrecht: Reidel, p. 425

Phillips J.P., 1998. Electron densities in planetary nebulae, and the unusual characteristics of the [S II] emission zone. A&A 340, 527

Phillips J.P., 2000a. The intrinsic structures of circular and elliptical planetary nebulae. A&A, 358, 1049

Phillips J.P., 2000b. Photometric constraints upon binaries in bipolar nebulae. AJ, 119, 342

Phillips J.P., 2000c. Recessional halos in planetary nebulae: an undervalues aspect of nebular morphology. AJ, 119, 2332

Phillips J.P., 2001a. The distances of planetary nebulae: a scaling factor based upon radial velocities. A&A, 367, 967

Phillips J.P., 2001b. The masses of the progenitors of planetary nebulae. PASP, 113, 839

Phillips J.P., 2001c. Bipolar nebulae: the missing population. PASP, 113, 846

Phillips J.P., 2001d. The determination of progenitor masses for planetary nebulae. MNRAS, 326, 1041

Phillips J.P., 2002a. The distances of planetary nebulae: a scale based upon nearby sources. ApJS, 139, 199

Phillips J.P., 2002b. A possible observational measure of evolution in bipolar nebulae. A&A, 385, 1008

Phillips J.P., 2002c. The correlation between expansion velocity and morphology in planetary nebulae. A&A, 393, 1027

Phillips J.P., 2003a. The use of high brightness temperature sources to constrain the scale heights and distances of planetary nebulae. NewA, 8, 29

Phillips J.P., 2003b. The radial distribution function in planetary nebulae. AN, 324, 191

Phillips J.P., 2003c. The relation between elemental abundances and morphology in planetary nebulae. MNRAS, 340, 883

Phillips J.P., 2003d. The relative sizes of planetary nebulae. Ap&SS, 288, 341

Phillips J.P., 2003e. The correlation between planetary nebula morphology and radio brightness temperature. A&A, 412, 791

Phillips J.P., 2004a. The statistical relation between Zanstra temperatures and emission-line ratios. MNRAS, 350, 196

Phillips J.P., 2004b. The distances of Type I planetary nebulae. NewA, 9, 391

Phillips J.P., 2004c. Planetary nebula distances re-examined: an improved statistical scale. MNRAS, 353, 589

Phillips J.P., 2005a. The distances of highly evolved planetary nebulae. MNRAS, 357, 619

Phillips J.P., 2005b. The mean properties of planetary nebulae as a function of Peimbert class. MNRAS, 361, 283

Phillips J.P., 2005c. The distances of less-evolved planetary nebulae: a further test of statistical distance scales. MNRAS, 362, 847

Phillips J.P., 2005d. Using planetary nebulae to probe the structure of the Galactic thin disk. RMxAA, 41, 407

Phillips J.P., 2005e. Biases in the kinematic parallaxes of Galactic planetary nebulae. RMxAA, 41, 471

Phillips J.P., 2006. The problem with reddening distances to planetary nebulae. RMxAA, 42, 229

Phillips J.P., Cuesta L. & Ortega V., 2001. The low-excitation structures of planetary nebulae. MNRAS,322, 866

Phillips J.P., Cuesta L. & Kemp S.N., 2005. Spectroscopy of six highly evolved Abell planetary nebulae. MNRAS, 357, 548

Phillips J.P., Mampaso A., Williams P.G. & Ukita N., 1991. The CO structure of NGC 7027: a bipolar nebula in the making. A&A, 247, 148

Phleps S., Meisenheimer K., Wolf C., Fuchs B. & Jahreiss, H., 1999. Faint stars and the structure of the Galaxy. Ap&SS, 265, 231

Pickering E.C., 1880. New planetary nebulae. AmJS, 20, 303

Pickering E.C., 1882. Small planetary nebulae discovered at the Harvard College Observatory. Obs, 5, 294

Pickering E.C., 1907. 71 new variable stars in Harvard Maps Nos. 9, 12, 21, 48 and 51. AN, 175, 333 (= Harvard Circ., No. 130)

Pier J.R., Harris, H.C., Dahn, C.C. & Monet, D.G., 1993. Trigonometric parallaxes of planetary nebulae. IAU Symp. 155, 175

Pierce M.J., 2005. Exploitation of the AAO/UKST SuperCOSMOS Hα Survey. Unpublished PhD thesis, University of Bristol

Pierce M.J., Frew D.J., Parker Q.A. & Köppen J., 2004. PFP 1: a large planetary nebula caught in the first stages of ISM interaction. PASA, 21, 334

Pigulski A. & Michalska G., 2002. NN Ser and V664 Cas: two pre-catalcysmic binaries with large reflection effect. IBVS, 5218, 1

Pirzkal N., Kerber F. & Roth M., 2000. Extinction distances of planetary nebulae interacting with the interstellar medium. Am. Astr. Soc. Meeting, 197, 610

Pohlen M., Dettmar R.-J. & Lütticke R., 2001. New constraints for the edge of the Galactic disk. ASP Conf. Series, 228, 547 [reformat reference]

Pojmanski G., 2001. The All Sky Automated Survey (ASAS-3) System – Its operation and preliminary data. In Small Telescope Astronomy on Global Scales, ASP Conf. Series, 246, p. 53

Pojmanski G., 2003. The All Sky Automated Survey. The Catalog of Variable Stars. II. 6^h–12^h quarter of the Southern Hemisphere. AcA, 53, 341

Pollacco D.L & Bell S.A., 1994. A preliminary analysis of the planetary nebula central star V477 Lyrae. MNRAS, 267, 452

Pollacco D.L & Bell S.A., 1997. Imaging and spectroscopy of ejected common envelopes. I. MNRAS, 284, 32

Pottasch S.R., 1980. Masses of planetary nebulae. A&A, 89, 336

Pottasch S.R., 1981. Hot central stars of planetary nebulae. A&A, 94, L13

Pottasch S.R., 1983. Distances of the central stars and their position in the HR diagram. IAU Symp., 103, 391

Pottasch S.R., 1984. *Planetary Nebulae: A Study of Late Stages of Stellar Evolution*. Reidel, Dordrecht

Pottasch S.R., 1992. Evolution of planetary nebulae. ARA&A, 4, 215

Pottasch S.R., 1995. Axial symmetry in planetary nebulae. In Harpaz, A. & Soker, N. (eds), Asymmetrical Planetary Nebulae. AnIPS, 11, 7

Pottasch S.R., 1996. Local space density and formation rate of planetary nebulae. A&A, 307, 561

Pottasch S.R. & Acker, A., 1989. Evolution of planetary nebulae in the Galactic bulge. A&A, 221, 123

Pottasch S.R. & Acker, A., 1998. A comparison of Hipparcos parallaxes with planetary nebulae spectroscopic distances. A&A, 329, L5

Pottasch S.R. & Surendiranath R., 2005. Abundances in planetary nebulae: Mz 3. A&A, 444, 861

Pottasch S.R., Beintema D.A. & Feibelman W.A., 2000. Abundance in the planetary nebulae NGC 6537 and He 2-111. A&A, 363, 767

Pottasch S.R., Goss, W.M., Arnal, E.M. & Gathier, R., 1982. The distance to the planetary nebula NGC 7027. A&A, 106, 229

Pottasch S.R., Baud B., Beintema D., et al., 1984. IRAS measurements of planetary nebulae. A&A, 138, 10

Pottasch S.R., Olling R., Bignell C. & Zijlstra A.A. 1988. Planetary nebulae near the Galactic center. I. Method of discovery and preliminary results. A&A, 205, 248

Preite-Martinez A. & Pottasch S.R., 1983. The temperature of central stars of planetary nebulae: the energy-balance method. A&A, 126, 31

Proga D., Mikolajewska J. & Kenyon S.J., 1994. He I emission lines in symbiotic stars. MNRAS, 268, 213

Puche D., Zijlstra A.A., Boettcher C., et al., 1988. The distance to the nebula M 1-78. A&A, 206, 89

Purgathofer A. 1978. A new planetary nebula of very low surface brightness near the galactic anticenter A&A 70, 589

Purgathofer A. 1980. A new faint planetary nebula behind the H II region S 232 and close to the galactic anticenter. A&A, 88, 275

Purgathofer A. & Weinberger R., 1980. A huge new nearby planetary nebula. A&A, 87, L5

Purgathofer A. & Schnell A., 1983. On the variability of the central star of the planetary nebula NGC 1514. IBVS, 2362, 1

Quirion P.-O., Fontaine G. & Brassard P., 2007. Mapping the instability domains of GW Vir stars in the effective temperature-surface gravity diagram. ApJS, 171, 219

Raga A.C., Böhm K.-H. & Cantó J., 1996. A compilation of optical spectrophotometry of HH objects and its tentative interpretation. RMxAA, 32, 161

Ragazzoni R., Cappellaro E., Benetti S., Turatto M. & Sabbadin F., 2001. 3-D ionization structure (in stereoscopic view) of planetary nebulae: the case of NGC 1501. A&A, 369, 1088

Ramos-Larios, G. & Phillips, J.P., 2005. An analysis of 2MASS near-infrared photometry for galactic planetary nebulae. MNRAS, 357, 732

Ramspeck M., Heber U. & Moehler S., 2001. Early type stars at high galactic latitudes. I. Ten young massive B-type stars. A&A 378, 907

Rappaport S., Chiang E., Kallman T. & Malina R., 1994. Ionization nebulae surrounding supersoft X-ray sources. ApJ, 431, 237

Ratag M.A. & Pottasch S.R., 1991. Planetary nebulae near the Galactic center. III. The WSRT measurements. A&AS, 91, 481

Ratag M.A., Pottasch S.R., Zijlstra A.A. & Menzies J., 1990. Planetary nebulae near the Galactic center. II. The second VLA measurements. A&A, 233, 181

Rauch T., 1999. Narrow-band imaging and a search for planetary nebulae. A&AS, 135, 487

Rauch T., Dreizler S. & Wolff B., 1998. Spectral analysis of O(He)-type post-AGB stars. A&A, 338, 651

Rauch T., Kerber F. & Pauli E.-M., 2004. On the discovery of an enormous ionized halo around the hot DO white dwarf PG 1034+001. A&A, 417, 647

Rauch T., Köppen J. & Werner K., 1994. Spectral analysis of the planetary nebula K 1-27 and its very hot hydrogen-deficient central star. A&A, 286, 543

Rauch T., Köppen J. & Werner K., 1996. Spectral analysis of the multiple-shell planetary nebula LoTr 4 and its very hot hydrogen-deficient central star. A&A, 310, 613

Rauch T., Köppen J., Napiwotzki R. & Werner K., 1999. Classification and spectral analysis of faint central stars of highly excited planetary nebulae. A&A, 347, 169

Rauch T., Furlan E., Kerber F. & Roth M., 2000. Survey of large planetary nebulae in decay. In Kastner, J.H., Soker, N. & Rappaport, S. (eds), Asymmetrical Planetary Nebulae II: From Origins to Microstructures. ASP Conf. Series, 199, 341

Rauch T., Kerber F., Furlan E. & Werner K., 2004. NLTE spectral analysis of central stars of PNe interacting with the ISM. In Meixner M., Kastner J. & Soker N., eds., Asymmetric Planetary Nebulae III. ASP Conf. Series, 313, 296

Rauch T., Ziegler M., Werner K., Kruk J.W., Oliveira C.M., Vande Putte D., Mignani R.P. & Kerber F., 2007. High-resolution FUSE and HST ultraviolet spectroscopy of the white dwarf central star of Sh 2-216. A&A, 470, 317

Reay N.K., Pottasch S.R., Atherton P.D. & Taylor K., 1984. The magnitudes and temperatures of central stars of planetary nebulae. A&A, 137, 113

Recillas-Cruz E. & Pismis P., 1981. Fabry-Perot radial velocities of S 274: a planetary nebula. A&A, 97, 398

Reed B.C., 1998. UBV beta database for Case-Hamburg northern and southern luminous stars. ApJS, 115, 271

Reed B.C., 2006. The Sun's displacement from the Galactic plane from spectroscopic parallaxes of 2500 OB Stars. JRASC, 100, 146

Reed D.S., Balick B., Hajian, A.R., Klayton T.L., Giovanardi S., Casertano S., Panagia N. & Terzian Y., 1999. Hubble Space Telescope measurements of the expansion of NGC 6543: parallax distance and nebular evolution. AJ, 118, 2430

Reed M. & Stiening R., 2004. A Search for Main-Sequence Companions to Subdwarf B Stars Using the Two Micron All Sky Survey. PASP, 116, 506

Reid I.N., Brewer C., Brucato R.J., et al., 1991. The second Palomar Sky Survey. PASP, 103, 661

Reid W.A., 2008. A new population of planetary nebulae discovered in the Large Magellanic Cloud. Unpublished PhD Thesis, Macquarie University, Sydney

Reid W.A. & Parker Q.A., 2006a. A new population of planetary nebulae discovered in the Large Magellanic Cloud – I. Preliminary sample. MNRAS, 365, 401

Reid W.A. & Parker Q.A., 2006b. A new population of planetary nebulae discovered in the Large Magellanic Cloud – II. Complete PN catalogue. MNRAS, 373, 521

Reimers D., 1975. Circumstellar envelopes and mass loss of red giant stars. In Problems in stellar atmospheres and envelopes. Springer-Verlag, New York, p. 229-256.

Remillard R.A., Rappaport S. & Macri L.M., 1995. Ionization nebulae surrounding CAL 83 and other supersoft X-ray sources. ApJ, 439, 646

Renzini A., 1981. Red giants as precursors of planetary nebulae. In Iben I., Jr & Renzini A. (eds), Physical Processes in Red Giants. Reidel, Dordrecht, p. 431

Renzini A. & Buzzoni A., 1986. Global properties of stellar populations and the spectral evolution of galaxies. In Spectral evolution of galaxies, Proceedings of the Fourth Workshop, Erice, Italy, March 12-22, 1985. Dordrecht: D. Reidel, p. 195

Reynolds R.J., 1985. Fabry-Perot observations of the unusual emission-line nebula S 216. ApJ, 288, 622

Reynolds R.J., 1987. Detection of an extremely faint emission nebula surrounding the hot white dwarf PG 0108+101. ApJ, 315, 234

Reynolds R.J. & Ogden P.M., 1982. HII regions surrounding high galactic latitude O stars. AJ, 87, 306

Reynolds R.J., Chaudhary V., Madsen G.J. & Haffner L.M., 2005. Unresolved Hα enhancements at high Galactic latitude in the WHAM Sky Survey maps. AJ, 129, 927

Rice M., Schwarz H. & Monteiro H., 2004. 3-D structure and distance of the planetary nebula Hb 5. BAAS, 36, 1572

Riesgo-Tirado H. & López J.A., 2002. Diagnostic diagrams of electron density versus excitation for planetary nebulae. RMxAA(SC), 12, 174

Riesgo H. & López J.A., 2006. Revised diagnostic diagrams for planetary nebulae. RMxAA, 42, 47

Ringwald F.A. & Naylor T., 1998. High-speed optical spectroscopy of a cataclysmic variable wind – BZ Camelopardalis. AJ, 115, 286

Robin A.C., Creze M. & Mohan V., 1992. The edge of the Galactic disk. ApJ, 400, L25

Rocha-Pinto H.J., Majewski S.R., Skrutskie M.F., Patterson R.J., Nakanishi H., Munoz R.R. & Sofue Y., 2006. The Dog on the Ship: the Canis Major Dwarf Galaxy as an outlying part of the Argo Star System. ApJ, 640, L147

Rodgers A.W., Campbell C.T. & Whiteoak J.B., 1960. A catalogue of Hα-emission regions in the southern Milky Way. MNRAS 121, 103

Rodgers A.W., Campbell C.T., Whiteoak J.B., Bailey H.H. & Hunt V.O., 1960. *An Atlas of H-Alpha Emission in the Southern Milky Way*, Australian National University

Rodgers A.W., Conroy P. & Bloxham G., 1988. A dual-beam Nasmyth spectrograph. PASP, 100, 628

Rodríguez L.F., 1992. Nebulae, cometary and bipolar. In S.P. Maran, ed., The Astronomy and Astrophysics Encyclopedia. New York: Van Nostrand Reinhold

Rodríguez L.F. & Gómez Y., 2007. Proper motions of the ansae in the planetary nebula NGC 7009. RMxAA, 43, 173

Rodríguez M., Corradi R.L.M. & Mampaso A., 2001. Evidence for binarity in the bipolar planetary nebulae A 79, He 2-428 and M 1-91. A&A, 377, 1042

Roman-Lopes A. & Abraham Z., 2006. The true nature of the alleged planetary nebula W16-185. AJ, 131, 2223

Rosado M., 1986. Kinematical Study of G 339.2-0.4, S 216, and the arc of the planetary nebula NGC 3242. RMxAA, 13, 49

Rosado M. & Kwitter K.B., 1982. The filamentary nebula S 188. RMxAA, 5, 217

Rosado M. & Moreno M.A., 1991. Deep narrow band interference filter photographs of selected extended planetary nebulae. A&AS, 88, 245

Rowan-Robinson M., 1985. *The Cosmological Distance Ladder.* W.H. Freeman, New York

Ruffle P.M.E., Zijlstra A.A., Walsh J.R., Gray M.D., Gesicki K., Minniti D. & Comeron F., 2004. Angular diameters, fluxes and extinction of compact planetary nebulae: further evidence for steeper extinction towards the bulge. MNRAS, 353, 796

Ruiz M.T., 1983. PL 1547.3-5612: a pure nitrogen ring nebula. ApJ, 268, L103

Ruiz M.T., 1986. On the nature of the unusual nebula PL 1547.3-5612. RMxAA, 12, 269

Ruiz N., Guerrero M.A., Chu Y.-H., Gruendl R.A., Kwitter K.B. & Meixner M., 2006. The physical structure of NGC 3242. In Barlow M.J. & Méndez R.H., eds, Planetary nebulae in our Galaxy and beyond, IAU Symp. 234, p. 497

Ruphy S., Robin A. C., Epchtein N., Copet E., Bertin E., Fouque P. & Guglielmo F.l., 1996. New determination of the disc scale length and the radial cutoff in the anticenter with DENIS data. A&A, 313, L21

Russeil D., 2003. Star-forming complexes and the spiral structure of our Galaxy. A&A, 397, 133

Russeil D. & Castets A., 2004. CO observations in the direction of southern HII regions. A&A, 417, 107

Russeil D., Georgelin Y.M., Amram P., Gach J.L., Georgelin Y.P. & Marcelin M., 1998. Deep Hα survey of the Milky Way IV. The $l = 301°$ to $l = 324°$ area. A&AS, 130, 119

Russeil D. & Parker Q.A., 2001. First results from the combination of the AAO/UKST and Marseille Hα Surveys. PASA, 18, 76

Sabbadin F., 1977. Spectroscopic observations of the planetary nebula NGC 6853. A&A, 57, 307

Sabbadin F., 1986. Planetary nebulae at known distance. A&AS, 64, 579

Sabbadin F. & Hamzaoglu E.,1981. Photographic and spectroscopic observations of planetary nebulae. A&A, 94, 25

Sabbadin F. & Minello S., 1978. Statistical properties of planetary nebulae: graphic presentation. A&AS, 33, 223

Sabbadin F., Falomo R. & Ortolani S., 1987. Spectroscopic observations of genuine and misclassified planetary nebulae. A&AS, 67, 541

Sabbadin F., Minello S. & Bianchini A., 1977. Sharpless 176: a large, nearby planetary nebula. A&A, 60, 147

Sabbadin F., Strafella F. & Bianchini A. 1986. Internal motions in thirty-two genuine planetary nebulae and in a misclassified object. A&AS, 65, 259

Sabbadin F., Ortolani S., Bianchini A. & Hamzaoglu E., 1983. The expansion velocity field within the planetary nebula NGC 7008. A&AS, 52, 399

Sabbadin F., Bianchini A., Ortolani S. & Strafella F., 1985. The structure of NGC 3587, the Owl nebula. MNRAS, 217, 539

Sabbadin F., Benetti S., Cappellaro E. & Turatto M., 2000. The tetra-lobed planetary nebula NGC 1501. A&A, 361, 1112

Sabbadin F., Turatto M., Cappellaro E., Benetti S. & Ragazzoni R., 2004. The 3-D ionization structure and evolution of NGC 7009 (Saturn Nebula). A&A, 416, 955

Sabbadin F., Benetti S., Cappellaro E., Ragazzoni R. & Turatto M., 2005. The 3-D shaping of NGC 6741: A massive, fast-evolving planetary nebula at the recombination-reionization edge. A&A, 436, 549

Saffer R.A., Green E.M. & Bowers T., 2001. The binary origins of hot subdwarfs: new radial velocities. ASP Conf. Series, 226, 408

Sagar R. & Cannon R.D., 1997. Multicolour deep CCD photometric study of the moderately young southern open star clusters NGC 3228, NGC 4103, NGC 5662 and NGC 6087. A&AS, 122, 9

Sagar R. & Griffiths W.K., 1998. *BVI* CCD photometry of the distant open star clusters Berkeley 81, Berkeley 99, NGC 6603 and NGC 7044. MNRAS, 299, 1

Sahai R., Bujarrabal V., Castro-Carrizo A. & Zijlstra A., 2000. The structure and momentum of multiple collimated outflows in the protoplanetary nebula Frosty Leo. A&A, 360, L9

Sahai R., Morris M., Sánchez Contreras C. & Claussen M., 2007. Preplanetary nebulae: A Hubble Space Telescope imaging survey and a new morphological classification system. AJ, 134, 2200

Salaris M. & Weiss A., 2002. Homogeneous age dating of 55 Galactic globular clusters. Clues to the Galaxy formation mechanisms. A&A, 388, 492

Salter C.J., Greve A., et al. 1984. Observations of the emission nebulae S 188 and S 274 at 2.7 and 5 GHz. A&A, 137, 291

Samland M., Köppen J., Acker A. & Stenholm B., 1993. A comparison of nebular distance scales. In Weinberger R. & Acker A., (eds), Planetary nebulae. IAU Symp. 155, p. 174

Samus N.N., Pastukhova E.N. & Durlevich O.V., 2007. New GCVS versions for three southern constellations. PZ, 27 (6), 1

Sandage A., 1976. High-latitude reflection nebulosities illuminated by the galactic plane. AJ, 81, 954

Sandage A., Lubin L.M. & VandenBerg D.A., 2003. The age of the oldest stars in the local Galactic disk from *Hipparcos* parallaxes of G and K subgiants. PASP, 115, 1187

Sanduleak N., 1971. On stars having strong OVI emission. ApJ, 164, L71

Sanduleak N., 1975. A catalog of confirmed planetary nebulae in the Southern Milky Way noted on low-dispersion objective-prism plates. Pub. Warner & Swasey Obs., 2, 1

Sanduleak N., 1976. Objective-prism spectroscopy of planetary nebulae in the Southern Milky Way. Pub. Warner & Swasey Obs., 2, 57

Sanduleak N. & Stephenson C.B., 1972. Very-low-excitation compact nebulae. ApJ, 178, 183

Santander-García M., Corradi R.L.M., Whitelock P.A., Munari U., Mampaso A., Marang F., Boffi F. & Livio M., 2007. HST and VLT observations of the symbiotic star Hen 2-147. Its nebular dynamics, its Mira variable and its distance. A&A, 465, 481

Santander-García M., Corradi R.L.M., Mampaso A., Morrisset C., Munari U., Schirmer M., Balick B., & Livio M., 2008. Hen 2-104: a close up look at the Southern Crab. A&A, 485, 117

Saurer W., 1995. Extinction distances for three planetary nebulae. A&A, 297, 261

Saurer W. & Weinberger R., 1987. The 33°–17°zone: probing SRC *J* film copies for planetary nebulae. A&AS, 69, 527

Saurer W., Werner K. & Weinberger R., 1997. Spectroscopy of the central stars of three evolved planetary nebulae. A&A, 328, 598

Saurer W., Pfitscher K., Weinberger R. & Hartl H., 1992. Photoelectric *UBV* photometry of stars in four fields near the galactic plane. A&AS, 93, 553

Savage B.D. & Mathis J.S., 1979. Observed properties of interstellar dust. ARA&A, 17, 73

Schechter P.L., Mateo M. & Saha A., 1993. DoPHOT, a CCD photometry program: description and tests. PASP, 105, 1342

Scherb F., 1981. Hydrogen production rates from ground-based Fabry-Perot observations of comet Kohoutek. ApJ, 243, 644

Schlegel D.J., Finkbeiner D.P. & Davis M., 1998. Maps of Dust Infrared Emission for Use in Estimation of Reddening and Cosmic Microwave Background Radiation Foregrounds. ApJ, 500, 525

Schmeja D., & Kimeswenger S., 2001. Planetary nebula or symbiotic Mira? Near infrared colours mark the difference. A&A, 377, L18

Schmeja D., & Kimeswenger S., 2002a. New IJK photometry of PNe with *DENIS*. HvaOB, 26, 45

Schmeja D., & Kimeswenger S., 2002b. A catalogue of IJK photometry of PNe with DENIS. RMxAA(SC), 12, 176

Schmid H.M., 1989. Identification of the emission bands at 6830, 7088Å. A&A 221, L31

Schmid H.M., 1992. Montecarlo simulations of Raman scattered OVI emission lines in symbiotic stars. A&A, 254, 224

Schmidt-Kaler T., 1982. In Landolt-Börnstein: Numerical Data and Functional Relationships in Science and Technology – New Series, Group 6, Astronomy and Astrophysics, volume 2, p. 1

Schneider S.E., Terzian Y., Purgathofer A. & Perinotto, M. 1983. Radial velocities of planetary nebulae. ApJS, 52, 399

Schnell, A. & Purgathofer, A., 1983. The binary nature of the central star of the planetary nebula LT-5. A&A, 127, L5

Schönberner D., 1981. Late stages of stellar evolution: central stars of planetary nebulae. A&A, 103, 119

Schönberner D., 1983. Late stages of stellar evolution. II. Mass loss and the transition of asymptotic giant branch stars into hot remnants. ApJ, 272, 708

Schönberner D., 1984. The HR diagram of central stars of planetary nebulae. In Maeder A. & Renzini A., (eds) Observational Tests of the Stellar Evolution Theory. IAU Symposium 105, 209. Dordrecht: D. Reidel

Schönberner D. & Drilling J.S., 1984. Effective temperatures and luminosities of very hot O type subdwarfs. ApJ, 278, 702

Schönberner D. & Napiwotzki R., 1990. Spectroscopic investigation of old planetaries I. Detection of two new 'PG 1159' central stars. A&A, 231, L33

Schönberner D. & Tylenda R., 1990. The observed Hertzsprung-Russell diagram for planetary nebula nuclei. A&A, 234, 439

Schönberner D., Jacob R. & Steffen M., 2005. The evolution of planetary nebulae. III. Internal kinematics and expansion parallaxes. A&A, 441, 573

Schönberner D., Jacob R., Steffen M., Perinotto M., Corradi R.L.M. & Acker A., 2005. The evolution of planetary nebulae. II. Circumstellar environment and expansion properties. A&A, 431, 963

Schreiber M.R., Gänsicke B.T., Southworth J., Schwope A.D. & Koester D., 2008. Post common envelope binaries from SDSS. II: Identification of 9 close binaries with VLT/FORS2. A&A, 484., 441

Schröder K.-P. & Smith R.C., 2008. Distant future of the Sun and Earth revisited. MNRAS, 386, 155

Schuster H.-E. & West R.M., 1976. Two new peculiar southern emission line objects. A&A, 46, 139

Schwartz R.D., 1972. $UBVr$ photometry of white dwarfs and white-dwarf suspects. PASP, 84, 28

Schwartz R.D., 1983. Herbig-Haro objects. ARA&A, 21, 209

Schwarz, H.E. & Corradi R.L.M., 1992. BI Crucis: a post PN nebula? A&A, 265, L37

Schwarz H.E. & Corradi R.L.M., 1995. Observational properties of bipolar planetary nebulae. In Harpaz A. & Soker N. (eds), Asymmetrical Planetary Nebulae. AnIPS, 11, 113

Schwarz H.E. & Monteiro H., 2003. Properties of bipolar planetary nebulae. RMxAA, 15, 23

Schwarz H.E. & Monteiro H., 2004. Binarity and symbiotics in asymmetrical planetary nebulae. In Meixner M., Kastner J. & Soker N., eds., Asymmetric Planetary Nebulae III. ASP Conf. Series, 313, p. 497

Schwarz H.E. & Monteiro H., 2006. Three-dimensional photoionization structure and distances of planetary nebulae. III. NGC 6781. ApJ, 648, 430

Schwarz, H.E., Aspin, C. & Lutz, J.H. 1989. He 2-104: a symbiotic protoplanetary nebula? ApJ, 344, L29

Schwarz H.E., Corradi R.L.M. & Melnick J., 1992. A catalogue of narrow band images of planetary nebulae. A&AS, 96, 23

Schwarz H.E., Corradi R.L.M. & Stanghellini L., 1993. Hα morphological classifications of planetary nebulae. IAU Symp., 155, 214

Schwarz H.E., Aspin C., Corradi R.L.M. & Reipurth B., 1997. M 2-9: moving dust in a fast bipolar outflow. A&A 319, 267

Seaton M., 1966. The ionization structure of planetary nebulae V. Radii, luminosities and problems of evolution. MNRAS, 132, 113

Seaton M., 1968. Distances of planetary nebulae. ApL, 2, 55

Seaton M., 1980. Spectra of gaseous nebulae. QJRAS, 21, 229

Secchi A., 1867. Spectral studies on some of the planetary nebul. AReg, 5, 40

Secchi A., 1879. Les Etoiles (2 vols). Germer, Baillière, et Cie, Paris

Shapley H., 1936, Five planetary nebulae and a globular cluster. BHarO, 902, 26

Shara M., Moffat A.F.J. & Webbink R.F., 1985. Unraveling the faintest and oldest recorded nova – CK Vulpeculae (1670). ApJ, 294, 271

Shara M.M., Martin C.D., Seibert M., et al., 2004. Direct imaging of a large dwarf nova shell. BAAS, 36, 1610

Shara M.M., Martin C.D., Seibert M., et al., 2007. An ancient nova shell around the dwarf nova Z Camelopardalis. Nature, 446, 159

Sharpless S., 1953. A catalogue of emission nebulae near the Galactic plane. ApJ, 118, 362

Sharpless S., 1959. A catalogue of HII regions. ApJS, 4, 257

Shaver P.A., McGee, R.X., Murdin, P.G. & Goss, W.M. 1980. Radio recombination lines in the supernova remnant candidate G339.2-0.4. MNRAS, 190, 527

Shaw R.A., 2006. The distribution of planetary nebula nuclei in the $\log \mathrm{L} - \mathrm{Log}\,\mathrm{T}$ plane: inferences from theory. In Torres-Peimbert S. (ed), Planetary Nebulae, IAU Symp. 131, 473

Shaw R.A., 2006. Magellanic Cloud planetary nebulae. In Barlow M.J. & Méndez R.H., eds, Planetary nebulae in our Galaxy and beyond, IAU Symp., 234, 305

Shaw R.A. & Bidelman W.P., 1987. NGC 2242: a newly-discovered planetary nebula. PASP, 99, 27

Shaw R.A. & Kaler J.B., 1982. The absolute Hβ flux from NGC 7027. ApJ, 261, 510

Shaw R.A. & Kaler J.B., 1985. Apparent magnitudes of luminous planetary nebula nuclei. I. Method and application. ApJ, 295, 537

Shaw R.A. & Kaler J.B., 1989. Apparent magnitudes of luminous planetary nebula nuclei. II. A survey of southern hemisphere planetary nebulae. ApJS, 69, 495

Shaw R.A., Reid W.A. & Parker Q.A., 2007. Confirmation of new planetary nebulae in the Large Magellanic Cloud. PASP, 119, 19

Shaw R.A., Stanghellini L., Mutchler M., Balick B. & Blades J.C., 2001. Morphology and evolution of the Large Magellanic Cloud planetary nebulae. ApJ, 548, 727

Shaw R.A., Stanghellini L., Villaver E. & Mutchler M., 2006. Hubble Space Telescope images of Magellanic Cloud planetary nebulae. ApJS, 167, 201.

Shaw R.A., Rest R., Damke G., Smith R.C., Reid W.A. & Parker Q.A., 2007. The unusual variability of the Large Magellanic Cloud planetary nebula RP J053059-683542. ApJ, 669, L25

Shimanskiĭ V.V., Borisov N.V., Sakhibullin N.A. & Surkov A.E., 2004. The nature of the unique precataclysmic variable V664 Cas with two-peaked Balmer lines in its spectrum. ARep, 48, 563

Shklovsky I.S., 1956a. A new scale of distances of planetary nebulae. AZh, 33, 222

Shklovsky I.S., 1956b. The nature of planetary nebulae and their nuclei. AZh, 33, 315

Shklovsky I.S., 1957. Once more on the distances to planetary nebulae and the evolution of their nuclei. Astron. Zh., 34, 403 [SvA 1, 397]

Shull C.F. & McKee J.M., 1979. Theoretical models of interstellar shocks. I. Radiative transfer and UV precursors. ApJ, 227, 131

Siódmiak N., Meixner M., Ueta T., Sugerman B.E.K., Van de Steene G.C. & Szczerba R., 2008. HST snapshot survey of post-AGB objects. ApJ, 677, 382

Simon V., 2003. Luminous binary supersoft X-ray sources: Optical colors and absolute magnitudes. A&A, 406, 613

Sion EM., Mikolajewska J., Bambeck D. & Dumm T., 2002. An IUE and HST archival study of the hot white dwarf in the symbiotic variable RW Hydrae. AJ, 123, 983

Siviero A., Munari U., Cherini G., et al., 2007. A fresh look to the yellow symbiotic star V471 Per. BaltA, 16, 52

Skrutskie M.F., Cutri R.M., Stiening R., et al., 2006. The Two Micron All Sky Survey (2MASS). AJ, 131, 1163

Skuljan J., Hearnshaw J.B. & Cottrell P.L., 1999. Velocity distribution of stars in the solar neighbourhood. MNRAS, 308, 731

Slavin A.J., O'Brien T.J. & Dunlop J.S.,1995. A deep optical imaging study of the nebular remnants of classical novae. MNRAS, 276, 353

Smith A. & De Marco O., 2007. Using photometric variability to detect binarity in the central stars of four planetary nebulae, A 43, A 74, NGC 6720, and NGC 6853. AAS Meeting 211, # 100.09

Smith H., 1976. Differential deceleration of nebular shells and the displacement of central stars. MNRAS, 175, 419

Smith H., Jr., 2003. Is there really a Lutz-Kelker bias? Reconsidering calibration using trigonometric parallaxes. MNRAS, 338, 891

Smith H., Jr., 2006. Beware λ-truncation! Sample truncation and bias in luminosity calibration using trigonometric parallaxes. MNRAS, 365, 469

Smith M.G. & Gull, T.L.,1975. Spectroscopic observations of the planetary nebula 283+25°1. A&A, 44, 223

Smith N. and Gehrz R.D., 2005. Bipolar symbiotic planetary nebulae in the thermal infrared: M 2-9, Mz 3, and He 2-104. AJ, 129, 969

Smith N., Bally J. & Walawender J., 2007. And in the darkness bind them: equatorial rings, B[e] supergiants, and the waists of bipolar nebulae. AJ, 134, 846

Smith N., Morse J.A., Bally J. & Phelps R.L., 2003. The mysterious ring in the open cluster NGC 3572: planetary nebula or photoevaporating globule? PASP, 115, 342

Soker N., 1997. Properties that cannot be explained by the progenitors of planetary nebulae. ApJS, 112, 487

Soker N., 1998. Binary Progenitor Models for Bipolar Planetary Nebulae. ApJ, 496, 833

Soker N., 2002a. Why every bipolar planetary nebula is 'unique'. MNRAS, 330, 481

Soker N., 2002b. Spherical planetary nebulae. A&A, 386, 885

Soker N. & Dgani R., 1997. Interaction of planetary nebulae with a magnetized ISM. ApJ, 484, 277

Soker N. & Hadar R., 2002. Classification of planetary nebulae by their departure from axisymmetry. MNRAS, 331, 731

Soker N. & Subag E., 2005. A possible hidden population of spherical planetary nebulae. AJ, 130, 2717

Soker N. & Zucker D.B., 1997. The interaction of the planetary nebula NGC 6894 with the ISM magnetic field. MNRAS, 289, 665

Soker N., Borkowski K.J. & Sarazin C.L. 1991. Interaction of planetary nebulae with the interstellar medium – Theory. AJ, 102, 1381

Solheim J.-E., González Pérez J.M. & Vauclair G., 2008. Search for pulsations in H-deficient planetary-nebula nuclei. In Werner K. & Rauch T. (eds), Hydrogen-Deficient Stars, ASP Conference Series, Vol. 391. San Francisco: Astronomical Society of the Pacific, p.195

Sorensen P.M., & Pollacco D.L., 2003. Binary central stars in planetary nebulae. ASP Conf. Series 303, p. 494

Spitzer L., 1978. Physical Processes in the Interstellar Medium. New York, Wiley-Interscience

Stanghellini L., 1995. Evolutionary tests of the planetary nebula luminosity function. ApJ, 452, 515

Stanghellini L. & Kaler J.B., 1989. Electron densities in planetary nebulae. ApJ, 343, 811

Stanghellini L. & Renzini A., 2000. Synthetic post-asymptotic giant branch evolution: basic models and applications to disk populations. ApJ, 542, 308

Stanghellini L., Corradi R.L.M. & Schwarz H.E., 1993. The correlations between planetary nebula morphology and central star evolution. A&A, 276, 463

Stanghellini L., Shaw R.A. & Villaver E., 2008. The Magellanic Cloud calibration of the Galactic planetary nebula distance scale. ApJ, in press

Stanghellini L., Kaler J.B., Shaw R.A. & di Serego Alighieri S., 1995. Broad emission line O VI planetary nuclei. A&A, 302, 211

Stanghellini L., Blades J.C., Osmer S.J., Barlow M.J. & Lu X.-W., 1999. Hubble Space Telescope images of Magellanic Cloud planetary nebulae: data and correlations across morphological classes. ApJ, 510, 687

Stanghellini L., Shaw R.A., Balick B. & Blades J.C., 2000. Large Magellanic Cloud planetary nebula morphology: probing stellar populations and evolution. ApJ, 534, L167

Stanghellini L., Villaver E., Manchado A & Guerrero M.A., 2002a. The correlations between planetary nebula morphology and central star evolution: analysis of the northern Galactic sample. ApJ, 576, 285

Stanghellini L., Shaw R.A., Mutchler M., Palen S., Balick B. & Blades J.C., 2002b. Optical slitless spectroscopy of Large Magellanic Cloud planetary nebulae: a study of the emission-lines and morphology. ApJ, 575, 178

Stanghellini L., Shaw R.A., Balick B., Mutchler M., Blades J.C. & Villaver E., 2003. Space Telescope Imaging Spectrograph slitless observations of Small Magellanic Cloud planetary nebulae: a study on morphology, emission-line intensity, and evolution. ApJ, 596, 997

Stanghellini L., Guerrero M.A, Cunha K., Manchado A. & Villaver E., 2006. Planetary nebula abundances and morphology: probing the chemical evolution of the Milky Way. ApJ, 651, 898

Stasińska G., 1989. Snapshots of evolving model planetary nebulae. A&A, 213, 274

Stasińska G. & Tylenda R., 1990. On the relation between the nitrogen enhancement in planetary nebulae and the mass of the central stars. A&A, 240, 467

Stasińska G., Tylenda R., Acker A. & Stenholm B., 1991. An extensive study of planetary nebulae in the Galactic bulge II. Statistical properties of the nebular envelopes. A&A, 247, 173

Stenholm B., 1975. Wolf-Rayet stars and Galactic structure. A&A, 39, 307

Stenholm B. & Acker A., 1987. Spectroscopic observations of faint and misclassified planetary nebulae. A&AS, 68, 51

Sterling N.C. & Dinerstein H.L., 2008. The abundances of light neutron-capture elements in planetary nebulae. II. s-process enrichments and interpretation. ApJS, 174, 158

Stetson P.B., 1981. Four-color and H-beta photometry for four southern open clusters. AJ, 86, 1500

Stobie R.S, Kilkenny D. & O'Donoghue D., 2004. The Edinburgh-Cape blue object survey. Ap&SS, 230, 101

Stock J. & Wroblewski H., 1972. A southern objective prism survey. Pub. Obs. Astron. Nac. Cerro Calan, 2, 59

Stone R.P.S. & Baldwin J.A., 1983. Southern spectrophotometric standards for large telescopes. MNRAS, 204, 347

Straižys V., Černis K.& Bartašiūtė S., 1996. Interstellar extinction in the area of the Serpens Cauda molecular cloud. BaltA, 5, 125

Straižys V., Černis K., Kazlauskas A. & Laugalys V., 2002. Photometric investigation of the MBM 12 molecular cloud area in Aries. II. Cloud distance. BaltA, 11, 231

Strassmeier K.G., Hubl B. & Rice J.B., 1997. Doppler imaging of stellar surface structure IV. The rapidly rotating G5III-IV star HD 112313 = IN Comae. A&A, 322, 511

Strassmeier K.G., Bartus J., Cutispoto G. & Rodonó M., 1997. Starspot activity with robotic telescopes. Continuous UBV and $V(RI)_C$ photometry of 23 stars in 1991–1996. A&AS, 125, 11

Stupar M., Parker Q.A., Filipović M.D., Frew D.J., Bojičić I. & Achsenbach, B. 2007. Multiwavelength study of a new Galactic SNR G332.5-5.6. MNRAS, 381, 377

Stupar M., Parker Q.A. & Filipović M.D. 2007. G315.1+2.7: a new Galactic supernova remnant from the AAO/UKST Hαsurvey. MNRAS, 381, 377

Suárez O., García-Lario P., Manchado A., Manteiga M., Ulla A. & Pottasch S.R., 2006. A spectroscopic atlas of post-AGB stars and planetary nebulae selected from the IRAS point source catalogue. A&A, 458, 173

Subramaniam A. & Sagar R., 1999. Multicolor CCD Photometry and Stellar Evolutionary Analysis of NGC 1907, NGC 1912, NGC 2383, NGC 2384, and NGC 6709 Using Synthetic Color-Magnitude Diagrams. AJ, 117, 937

Sung H., Bessell, M.S., Lee S.-W., 1998. UBVRI and H-alpha photometry of the young open cluster NGC 6231. AJ, 115, 734

Surendiranath R., Kameswara Rao N., et al., 1990. CCD photometry in VRI bands of the galactic cluster NGC 2818. JApA, 11, 151

Surendiranath R., Pottasch S.R., & García-Lario P., 2004. Abundances in planetary nebulae: Me 2-1. A&A, 421, 1051

Swift L., 1887. Catalogue No. 6 of Nebulae discovered at the Warner Observatory. AN, 117, 217

Swift L., 1899. List No. 12 of Nebulae discovered at Lowe Observatory, Echo Mountain, California, for 1900.0. MNRAS, 59, 568

Szczerba R., 1990. A distance-independent test of planetary nebulae nuclei evolution. A&A, 237, 495

Szczerba R., Siódmiak N., Stasińska G. & Borkowski J., 2007. An evolutionary catalogue of galactic post-AGB and related objects. A&A, 469, 799

Szentgyorgyi A., Raymond J., Franco J., Villaver E., López-Martín L., 2003. The high-excitation planetary nebula NGC 246: optical and near-ultraviolet observations and two-dimensional numerical models. ApJ, 594, 874

Tadross A.L., 2001. Morphological analysis of open clusters' propertiesI. Properties' estimations. NewA, 6, 293

Tadross A.L., Werner P., Osman A. & Marie M., 2002. Morphological analysis of open clusters' properties II. Relationships projected onto the galactic plane. NewA, 7, 553

Tajitsu A. & Tamura S., 1998. A new distance indicator to Galactic planetary nebulae based upon IRAS fluxes. AJ, 115, 1989

Tajitsu A., Tamura S., Yadoumaru Y., Weinberger R. & Köppen J., 1999. HaTr 10, a planetary nebula with extremely strong nitrogen lines. PASP, 111, 1157

Tamura S. & Weinberger R. 1995. An addition to the sample of evolved planetary nebulae. A&A, 298, 204

Taranova O.G. & Shenavrin V.I., 2007. Infrared photometry of eight planetary nebulae. AstL, 33, 584

Tat H.H. & Terzian Y., 1999. Ionization of the local interstellar medium. PASP, 111, 1258

Terzian Y., 1966. Radio emission from planetary nebulae. ApJ, 144, 657

Terzian Y., 1971. The Galactic nebula YM 29. ApJ, 166, 559

Terzian Y., 1977. Recent findings about planetary nebulae. S&T, 54, 459

Terzian Y., 1980. Planetary nebulae. QJRAS, 21, 82

Terzian Y., 1993. Distances of planetary nebulae. IAU Symp., 155, 109

Terzian Y., 1997. Expansion distances of planetary nebulae. IAU Symp., 180, 29

Terzian Y. & Hajian A.R., 2000. Planetary nebulae with the Hubble Space Telescope. In Asymmetrical Planetary Nebulae II: From Origins to Microstructures, ASP Conference Series, Vol. 199. Edited by J. H. Kastner, N. Soker, and S. Rappaport, p. 33

Thackeray A.D., 1950. Some southern stars involved in nebulosity. MNRAS, 110, 524

Thackeray A.D., 1977. Spectra of the low-excitation nebulosities around AG Carinae and HD 138403. MNRAS, 180, 95

The P.-S., 1964. Thirty six new planetary nebulae. Bosscha Contr., 26, 1

Theissen A., Moehler S., Heber U. & de Boer K.S., 1993. Hot subluminous stars at high galactic latitudes. IV. Physical parameters and distances of 18 hot subdwarf stars and their spatial distribution. A&A, 273, 524

Thejll P., Flynn C., Williamson R. & Saffer R., 1997. Proper motions of the hot subdwarfs. The kinematic population membership of the sdB. A&A, 317, 689

Thévenin, F. & Jasniewicz, G., 1997. Barium-rich G-stars in the nuclei of the planetary nebulae Abell 35 and LoTr5. A&A 320, 913

Thompson D.J., Bertsch D.L., Dingus B.L., et al., 1996. Supplement to the Second EGRET Catalog of high-energy gamma-tay sources. ApJS, 107, 227

Tifft W.G., Connolly L.P. & Webb D.F., 1972. NGC 2818, an open cluster containing a planetary nebula. MNRAS, 158, 47

Tinkler C.M. & Lamers H.J.G.L.M., 2002. Mass-loss rates of H-rich central stars of planetary nebulae as distance indicators? A&A, 384, 987

Torres-Peimbert S. & Peimbert M., 1977. Photoelectric photometry and physical conditions of planetary nebulae. RMxAA, 2, 181

Torres-Peimbert S., Peimbert M. & Peña M., 1990. Planetary nebulae with a high degree of ionization – NGC 2242 and NGC 4361. A&A, 233, 540

Tosi M., Di Fabrizio L., Bragaglia A., Carusillo P.A. & Marconi G., 2004. Berkeley 29, the most distant old open cluster. MNRAS. 354, 225

Tovmassian G.H., Napiwotzki R., Richer M.G., Stasińska G., Fullerton A.W. & Rauch T., 2004. A close binary nucleus in the most oxygen-poor planetary nebula PN G135.9+55.9. ApJ, 616, 485

Traulsen I., Hoffmann A.I.D., Rauch T., Werner K., Dreizler S. & Kruk J.W., 2005. HST and FUSE spectroscopy of hot hydrogen-rich central stars of planetary nebulae. In Koester D. & Moehler S (eds), 14th European Workshop on White Dwarfs. ASP Conference Series, 334, 325. San Francisco: Astronomical Society of the Pacific.

Tsamis Y.G., Barlow M.J., Liu X.-W., Danziger I.J. & Storey P.J., 2003. A deep survey of heavy element lines in planetary nebulae – I. Observations and forbidden-line densities, temperatures and abundances. MNRAS, 345, 186

Turatto M., Cappellaro E., Sabbadin F. & Salvadori L., 1990. The optical counterpart of the *IRAS* planetary nebula candidate 19170+1706. AJ, 99, 1170

Turatto M., Cappellaro E., Sabbadin F. & Salvadori L., 1993. Two emission line galaxies at low galactic latitude. AJ, 105, 142

Tweedy R.W., 1995a. Nova Persei 1901: Detection of the site of its brightest light echo. ApJ, 438, 917

Tweedy R.W., 1995b. Can ancient planetary nebulae be used to probe the non-local ISM? In Harpaz, A. & Soker, N. (eds), Asymmetrical Planetary Nebulae. AnIPS, 11, 209

Tweedy R.W. & Kwitter K.B., 1994a. The ionization structure of old planetary nebulae which interact with the interstellar medium. AJ, 108, 188

Tweedy R.W. & Kwitter K.B., 1994b. Two planetary nebula candidates around hot DA white dwarfs. ApJ, 433, L93

Tweedy R.W. & Kwitter K.B. 1996. An atlas of ancient planetary nebulae and their interaction with the interstellar medium. ApJS 107, 255

Tweedy R.W. & Napiwotzki R., 1992. The central star of S 216. MNRAS, 259, 315

Tweedy R.W. & Napiwotzki R., 1994. The planetary nebula abandoned by its central star. AJ, 108, 978

Tweedy R.W., Martos M.A. & Noriega-Crespo A., 1995. The closest planetary nebula, Sh 2-216, and its interaction with the interstellar medium. ApJ, 447, 257

Tylenda R., 1986. Outer haloes of planetary nebulae as probes of a fast luminosity decline in their nuclei. A&A, 156, 217

Tylenda R. & Stasińska G., 1994. Confrontation of theoretical tracks for post-AGB stars with observations of planetary nebulae. A&A, 288, 897

Tylenda R., Acker A. & Stenholm B., 1993. Wolf-Rayet nuclei of planetary nebulae. Observations and classification. A&AS, 102, 595

Tylenda R., Acker A., Stenholm B., Gleizes F. & Raytchev B., 1991. The B and V magnitudes of the central stars of planetary nebulae. A&AS, 89, 77

Tylenda R., Acker A., Stenholm B. & Köppen J., 1992. The extinction constants for galactic planetary nebulae. A&AS, 95, 337

Tylenda R., Stasińska G., Acker A. & Stenholm B., 1994. A catalogue of HeII line intensities in Galactic planetary nebulae. A&AS, 106, 559

Tylenda R., Siódmiak N., Górny S.K., Corradi R.L.M. & Schwarz H.E., 2003. Angular dimensions of planetary nebulae. A&A, 405, 627

UK Schmidt Telescope Unit, 1983. UKSTU Handbook, Royal Observatory, Edinburgh

Urquhart J.S., Busfield A.L., Hoare M.G., Lumsden S.L., Clarke A.J., Moore T.J.T., Mottram J.C. & Oudmaijer R.D., 2007. The RMS survey. Radio observations of candidate massive YSOs in the southern hemisphere. A&A, 461, 11

Urošević D., Vukotić B., Arbutina B. & Ilić D., 2007. The $\Sigma - D$ relation for planetary nebulae: an introductory analysis. SeAJ, 174, 1

Vacca W.D. & Conti P.S., 1992. Optical spectrophotometry of Wolf-Rayet galaxies. ApJ, 401, 543

Vacca W.D., Garmany, C.D. & Shull, J.M., 1996. The Lyman-continuum fluxes and stellar parameters of O and early B-type stars. ApJ, 460, 914

Van Buren D. & McCray R., 1988. Bow shocks and bubbles are seen around hot stars by IRAS. ApJ, 329, L93

Van Buren D., Mac Low M.-M., Wood D.O.S. & Churchwell E., 1990. Cometary compact H II regions are stellar-wind bow shocks. ApJ, 353, 570

Van Buren D., Noriega-Crespo, A. & Dgani, R., 1995. An IRAS/ISSA Survey of bow shocks around runaway stars. AJ, 110, 2914

van den Bergh S., 1978. A systematic search for Galactic supernova remnants. ApJS, 38, 119

van den Bergh S., 2000. The Galaxies of the Local Group. Cambridge University Press, Cambridge

van den Bergh S. & Hagen G.L., 1975. Uniform survey of clusters in the Southern Milky Way. AJ, 80, 11

van den Bergh S. & Herbst W. 1975. Catalogue of southern stars embedded in nebulosity. AJ, 80, 208

van den Bergh S., Racine R., van Agt S., Barnes T., Coutts C., Madore B.F. & Skill A., 1973. New southern planetary nebulae. ApJ, 179, 863

van der Hucht K.A., Jurriens T.A., Wesselius P.R., Olnon F.M., The P.S. & Williams P.M., 1985. IRAS observations of Sand. 3 and M 1-67: two new planetary nebulae with Wolf-Rayet nuclei. A&A, 145, L13

Van de Steene, G.C. & Pottasch, S.R. 1993. Radio continuum observations of southern planetary nebula candidates. A&A, 274, 895

Van de Steene, G.C. & Pottasch, S.R. 1995. Radio continuum observations of planetary nebula candidates from the northern hemisphere. A&A, 299, 238

Van de Steene, G.C. & Zijlstra, A.A., 1994. On an alternative statistical distance scale for planetary nebulae. Catalog with statistical distances to planetary nebulae. A&AS, 108, 485

Van de Steene, G.C. & Zijlstra, A.A., 1995. On an alternative statistical distance scale for planetary nebulae. A&A, 293, 541

Van de Steene, G.C., Jacoby, G.H. & Pottasch, S.R. 1996. Optical observations of planetary nebula candidates from the northern hemisphere. A&AS, 118, 243

Van de Steene G.C., Sahu K.C. & Pottasch S.R., 1996. Optical observations of southern planetary nebula candidates. A&AS, 120, 111

van Hoof P.A.M., Bryce M., Evans A., et al., 2006. The real-time evolution of Sakurai's Star (V4334 Sgr) and other (V)LTP objects. In Barlow M.J. & Méndez R.H., eds, Planetary nebulae in our Galaxy and beyond, IAU Symp., 234, p. 75

van Leeuwen F., 2007. Hipparcos, the new reduction of the raw data. Astrophysics and Space Science Library, vol. 350. Springer Dordrecht

van Maanen A. 1923. The photographic determination of stellar parallaxes with the 60- and 100-inch reflectors. Contrib. Mt. Wilson Obs., 12 (270), 229

van Winckel H., 2003. Post-AGB stars. ARA&A, 41, 391

Vasilevskis S., Harlan E., Klemola A. & Wirtanen C., 1975. Trigonometric parallaxes measured at Lick Observatory. I. PLicO, 22 (5), 1

Vassiliadis E. & Wood P.R., 1994. Post-Asymptotic giant branch evolution of low- to intermediate-mass stars. ApJS, 92, 125

Vauclair G., Solheim J.-E. & Østensen R.H., 2005. Abell 43, a second pulsating "hybrid-PG 1159" star. A&A, 433, 1097

Vauclair G., Moskalik P., Pfeiffer B., et al., 2002. Asteroseismology of RX J2117+3412, the hottest pulsating PG1159 star. A&A, 381, 122

Vázquez R., Kingsburgh R.L., López J.A., 1998. Spectrophotometry of the planetary nebula KjPn 8. MNRAS, 296, 564

Vega E.I., 1982. A search for H-alpha-emission objects in a region in Vela. AJ, 87, 794

Vennes S., Thejll P., Galvan R.G. & Dupuis J., 1997. Hot white dwarfs in the Extreme Ultraviolet Explorer Survey. II. Mass Distribution, Space Density, and Population Age. ApJ, 480, 714

Vennes S., Smith R., Boyle B.J., Croom S.M., Kawka A., Shanks T., Miller L. & Loaring N., 2002. White dwarfs in the 2dF QSO Redshift Survey – I. Hydrogen-rich (DA) stars. MNRAS, 335, 673

Verbunt F., Bunk W.H., Ritter H. & Pfeffermann E., 1997. Cataclysmic variables in the ROSAT PSPC All Sky Survey. A&A, 327, 602

Vilhu O., Gustafsson B. & Walter F.M., 1991. Spectroscopy of southern active stars II. HD 32918, HD 82558, BD$-22°$3467, AB Doradus (HD 36705) and RST 137B. A&A, 241, 167

Villaver E., García-Segura & Manchado A., 2003. Ram pressure stripping in planetary nebulae. ApJ, 585, L49

Villaver E., Manchado A. & García-Segura G., 2002. The dynamical evolution of the circumstellar gas around low- and intermediate-mass stars. II. The planetary nebula formation. ApJ, 581, 1204

Villaver E., Stanghellini L. & Shaw R.A., 2003. Post-asymptotic giant branch evolution in the Large Magellanic Cloud: the central stars of planetary nebulae. ApJ, 597, 298

Villaver E., Stanghellini L. & Shaw R.A., 2004. The low- and intermediate-mass stellar population in the Small Magellanic Cloud: the central stars of planetary nebulae. ApJ, 614 , 716

Villaver E., Stanghellini L. & Shaw R.A., 2007. The mass distribution of the central stars of planetary nebulae in the Large Magellanic Cloud. ApJ, 656, 831

Voges W., Aschenbach B., Boller T., et al., 1999. The ROSAT all-sky survey bright source catalogue. A&A, 349, 389

Volk K. & Kwok S., 1997. A self-consistent photoionization-dust continuum-molecular line transfer model of NGC 7027. ApJ, 477, 722

Vorontsov-Vel'yaminov B.A., 1934. General Catalogue of Planetary Nebulae with a statistical discussion of the subject. AZh, 11, 40

Vorontsov-Vel'yaminov B.A., 1948. Gaseous nebulae and Novae. Publishing House of the Academy of Sciences, USSR. Moscow

Vorontsov-Vel'yaminov B.A., 1956. On the distances of planetary nebulae and the evolution of their nuclei . AZh, 33, 809

Vorontsov-Vel'yaminov B.A., 1960. Visual remnants of three more supernovae. ATsir, 211, 25

Vorontsov-Vel'yaminov B.A., 1961a. A description of fifty planetary nebulae. AZh, 38, 75-82 [SvA, 5, 53]

Vorontsov-Vel'yaminov B.A., 1961b. New planetary and peculiar gaseous nebulae. Astron. Zh. 38, 375-6 [SvA, 5, 278]

Vorontsov-Vel'yaminov B.A., 1962. New catalogue of planetary nebulae. SoSht, 118, 3

Vorontsov-Vel'yaminov B.A., Kostyakova E.B., Dokuchaeva O.D. & Arkhipova V.P., 1965. ATsir, 348, 1

Vorontsov-Vel'yaminov B.A., Kostyakova E.B., Dokuchaeva O.D. & Arkhipova V.P., 1972. ATsir, 716, 7

Vyssotsky A.N., 1942. Four new planetary nebulae. PASP, 54, 152

Wachter A., Schröder K.-P., Winters J.M., Arndt T.U. & Sedlmayr E., 2002. An improved mass-loss description for dust-driven superwinds and tip-AGB evolution models. A&A, 384, 452

Wade R.A., 2001. Observations of the unusual PN central star PHL 932 with HET. ASP Conf. Series, 226, 199

Wade R.A. & Ward M.J., 1985. Cataclysmic variables: observational overview. In Pringle J.E. & Wade R.A. (eds), Interacting Binary Stars. Cambridge: Cambridge University Press, p.129

Wade R.A., Harlow J.J.B. & Ciardullo R., 2000. Biases in expansion distances of novae arising from prolate geometry of nova shells. PASP, 112, 614

Walsh J.R. 1983. NGC 2346: a bipolar nebula produced by mass-loss from a binary system. MNRAS 202, 303

Walsh J.R. & Walton N.A., 1996. Observations of the central star and nebula of Abell 65. A&A, 315, 253

Walsh J.R., Dudziak G. & Walton N.A., 1997. Modelling the expansion of NGC 7027. In Habing H.J. & H. J. G. L. M. Lamers H.J.G.L.M. (eds), Planetary nebulae, IAU Symposium 180, 286. Dordrecht: Kluwer

Walsh J.R., Walton N.A. & Pottasch S.R., 1993. A spectroscopic study of binary star planetary nebulae. IAU Symp. 155, 390

Walton N.A., Reay N.K., Pottasch S.R. & Atherton P.D., 1986. Magnitudes of selected central stars of planetary nebulae. In New Insights in Astrophysics, Proc. Joint NASA/ESA/SERC Conference. ESA SP-263

Wareing C.J., Zijlstra A.A. & O'Brien T.J., 2007a. Vortices in the wakes of asymptotic giant branch stars. ApJ, 660, 129

Wareing C.J., Zijlstra A.A. & O'Brien T.J., 2007b. The interaction of planetary nebulae and their AGB progenitors with the interstellar medium. MNRAS, 382, 1233

Wareing C.J., O'Brien T.J., Zijlstra A.A. & Drew J.E., 2005. Sh 2-188: a model for a speedy planetary nebula. MmSAI, 76, 477

Wareing C.J., O'Brien T.J., Zijlstra A.A., et al., 2006a. The shaping of planetary nebula Sh 2-188 through interaction with the interstellar medium. MNRAS, 366, 387

Wareing C.J., Zijlstra A.A., Speck A.K., et al., 2006b. Detached shells as tracers of asymptotic giant branch-interstellar medium bow shocks. MNRAS, 372, 63

Wareing C.J., Zijlstra A.A., O'Brien T.J. & Seibert M., 2007. It's a wonderful tail: the mass loss history of Mira ApJ, 670, 125

Warner B., 1987. Absolute magnitudes of cataclysmic variables. MNRAS, 227, 23

Warner B., 1995. *Cataclysmic Variable Stars.* Cambridge University Press, Cambridge

Webb T.W., 1879. Discovery of a gaseous nebula in Cygnus. AN, 96, 191

Weaver R., McCray R., Castor J., Shapiro P. & Moore R., 1977. Interstellar bubbles. II – Structure and evolution. ApJ, 218, 377

Webster B.L., 1969. The masses and galactic distribution of southern planetary nebulae. MNRAS, 143, 79

Webster B.L., 1975. A survey of planetary nebulae towards the galactic bulge. MNRAS, 173, 437

Webster B.L., 1978. Discovery of a giant halo with very high velocities around a planetary nebula. MNRAS, 185, 45P

Webster B.L., 1983. Emission-line fluxes of planetary nebulae and related objects. PASP, 95, 610

Wegner G., Africano J.L. & Goodrich B., 1990. Photoelectric photometry for 106 objects in the KISO survey. AJ, 99, 1907

Weidemann V., 1977. On the distance scale of planetary nebulae and white dwarf birth rates. A&A, 61, L27

Weidemann V., 2000. Revision of the initial-to-final mass relation. A&A, 363, 647

Weinberger R., 1977a. A list of possible, probable, and true planetary nebulae detected since 1966. A&AS 30, 335

Weinberger R., 1977b. New planetary nebulae of low surface-brightness. A&AS 30, 343

Weinberger R., 1978. A possible new planetary nebula in Hercules. Observatory 98, 137

Weinberger R., 1986. Lokale planetarische nebel – eine revision. MitAG, 67, 346

Weinberger R., 1989. A catalogue of expansion velocities of Galactic planetary nebulae. A&AS, 78, 301

Weinberger R., 1995. New interesting objects discovered in optical sky surveys. PASP, 107, 58

Weinberger R., 1999. Giant holes and emission structures around planetary nebulae on IRAS SkyView images. AGAb, 15, 119

Weinberger R. & Aryal B., Huge dust structures and cavities around PNe: NGC 6826 and NGC 2899. In Meixner M., Kastner J. & Soker N., eds., Asymmetric Planetary Nebulae III. ASP Conf. Series, 313, p. 112

Weinberger R. & Sabbadin F., 1981. Detection of six new planetary nebulae by means of interference filter photography. A&A, 100, 66

Weinberger R. & Kerber F., 1997. Planetary nebulae: understanding the physical and chemical evolution of dying stars. Science, 276, 1382

Weinberger R., Kerber F. & Gröbner H., 1997. New faint planetary nebulae in Centaurus/Musca. A&A, 323, 963

Weinberger R., Dengel J., Hartl H. & Sabbadin F., 1983. A newly discovered nearby planetary nebula of old age. ApJ, 265, 249

Weinberger R., Saurer W. Lercher G. & Seeberger R., 1994. PN G160.7 − 2.9: a new planetary nebula. A&A 282, 197

Weinberger R., Tajitsu A., Tamura S. & Yadoumaru Y., 1998. G247.8+4.9: A newly discovered optical supernova remnant in Puppis. PASP, 110, 722

Weinberger R., Hartl H., Temporin S., & Zanin C., 1999. A sample of new Galactic emission nebulae. ASP Conf. Series 168, 142

Wehmeyer R. & Kohoutek L., 1979. On the radial velocity of the central star of NGC 1360. A&A, 78, 39

Werner K., 1993. PG1159 stars and related objects. In M.A. Barstow ed., White dwarfs in Observation and Theory, Kluwer Academic, p. 67

Werner K., 1996. On the Balmer line problem. ApJ, 457, L39

Werner K. & Herwig F., 2006. The elemental abundances in bare planetary nebula central stars and the shell burning in AGB stars. PASP, 118, 183

Werner K., Dreizler S. & Wolff B., 1995. Spectral analysis of the hot DO white dwarf PG1034+001. A&A, 298, 567

Werner K., Heber U. & Fleming, T., 1994. Spectral analysis of the hottest known helium-rich white dwarf: KPD 0005+5106. A&A, 284, 907

Werner K., Rauch T. & Kruk J.W., 2008. KPD 0005+5106: Hottest DO white dwarf much hotter than assumed. In Werner K. & Rauch T. (eds), Hydrogen-Deficient Stars, ASP Conf. Series, 391. San Francisco: Astronomical Society of the Pacific, p.239

Werner K., Hamann W.-R., Heber U., Napiwotzki R., Rauch T. & Wessolowski, U., 1992. A spectacular mass-loss event of the central star of Longmore 4. A&A, 259, L69

Werner K., Dreizler S., Heber U., Rauch T., Fleming T.A., Sion E.M. & Vauclair G., 1996. High resolution UV spectroscopy of two hot (pre-) white dwarfs with the Hubble Space Telescope: KPD 0005+5106 and RX J2117+3412. A&A, 307, 860

Werner K., Bagschik, K., Rauch, T. & Napiwotzki, R., 1997. A search for planetary nebulae around hot white dwarfs. A&A 327, 721

Werner K., Drake J.J., Rauch T., Schuh S. & Gautschy A., 2007. Soft X-ray spectroscopy of the hot DA white dwarf LB 1919 and the PG 1159 star PG 1520+525. In Napiwotzki R. & Burleigh M.R. (eds), 15th European Workshop on White Dwarfs, ASP Conference Series, 372, 225. San Francisco: Astronomical Society of the Pacific

Wesemael F., Green R.F. & Liebert J., 1985. Spectrophotometric and model-atmosphere analyses of the hot DO and DAO white dwarfs from the Palomar-Green survey. ApJS, 58, 379

Wesemael F., Fontaine G., Bergeron P., Lamontagne R. & Green R.F., 1992. Studies of hot B subdwarfs. VIII - Stromgren photometry of hot, hydrogen-rich subdwarf candidates in the Palomar-Green and Kitt Peak-Downes surveys. AJ, 104, 203

West R.M. & Kohoutek L., 1985. Spectroscopic verification of suspected planetary nebulae. II. A&AS, 60, 91

Westerlund B.E. & Henize K.G., 1967. Dimensions of southern planetary nebulae. ApJS, 14, 154

Whitelock P.A. & Menzies J.W., 1986. A new binary planetary nebula. MNRAS, 223, 497

Whiting A.B., Hau G.K.T. & Irwin M., 2002. The southern dwarf hunt: Local Group candidates in the southern sky. ApJS 141, 123

Whiting A.B., Hau G.K.T., Irwin M. & Verdugo M., 2007. An observational limit on the dwarf galaxy population of the Local Group. AJ, 133, 713

Williams, J.P. & Maddalena R.J., 1996. A large photodissociation region around the cold, unusual cloud G 216-2.5. ApJ, 464, 247

Williams K.A., 2007. A new look at the empirical initial-final mass relation. In R. Napiwotzki & M. Burleigh (eds), Proceedings of the 15th European Workshop on White Dwarfs. ASP Conf. Series, Vol. 372. San Francisco: Astronomical Society of the Pacific, p.85

Witham A.R., Knigge C., Drew J.E., Greimel R., Steeghs D., Gaensicke B.T., Groot P.J. & Mampaso A., 2008. The IPHAS Catalogue of H-alpha emission line sources in the Northern Galactic Plane. MNRAS, 384, 1277

Wolff M.J., Code A.D. & Groth E.J., 2000. *Hubble Space Telescope* imaging of central stars of high-excitation planetary nebulae with WFC and WFPC2. AJ, 119, 302

Wood P.R. & Faulkner D.J., 1986. Hydrostatic evolutionary sequences for the nuclei of planetary nebulae. ApJ, 307, 659

Wouterloot J.G.A. & Dekker E., 1979. The detection of planetary nebulae near the galactic centre at radio wavelengths. I. A&AS, 36, 323

Wray J.D.,1966. A study of Hα objects in the southern Milky Way. Unpublished PhD thesis, Northwestern University

Wright S.A., Corradi R.L.M. & Perinotto M., 2005. Absolute spectrophotometry of northern compact planetary nebulae. A&A, 436, 967

Wyse R.F.G., 2006. Lessons from surveys of the Galaxy. MmSAI, 77, 1036

Xilouris K.M., Papamastorakis J., Sokolov N., Paleologou E. & Reich W., 1994. Discovery of the new emission nebula G 4.4+6.4. A&A, 290, 639

Xilouris K.M., Papamastorakis J., Paleologou E. & Terzian Y., 1996. The shaping of aging planetary nebulae. A&A, 310, 603

Yanny B., Newberg H.J., Grebel E.K., et al., 2003. A Low-Latitude Halo Stream around the Milky Way. ApJ, 588, 824

Yonekura Y., Dobashi K., Mizuno A., Ogawa H. & Fukui Y., 1997. Molecular clouds in Cepheus and Cassiopeia. ApJS, 110, 21

Zacharias N., Urban S.E., Zacharias M.I., Wycoff G.L., Hall D.M., Monet D.G. & Rafferty T.J., 2004. The Second US Naval Observatory CCD Astrograph Catalog (UCAC2). AJ, 127, 3043

Zacharias N., Monet D.G., Levine S.E., Urban S.E., Gaume R. & Wycoff G.L., 2005. NOMAD Catalog. VizieR On-line Data Catalog: I/297

Zanin C. & Weinberger R., 1997. Giant emission features at large distances from PNe: a preliminary investigation. IAU Symp. 180, 290

Zanin C. & Kerber F., 2000. G247.8+4.9, a nitrogen dominated nebula at the outskirts of Puppis. A&A, 356, 274

Zanstra H., 1928. Temperatures of stars in planetary nebulae. Nature, 121, 790

Zanstra H., 1931. Luminosity of planetary nebulae and stellar temperatures. Pub. Dominion Astr. Obs, Victoria, 4, 209

Zealey W.J., Elliott K.H. & Malin D.F., 1979. New optical observations of Galactic supernova remnants. A&AS, 38, 39

Zhang C.Y., 1993. On the distance to Galactic planetary nebulae. ApJ, 410, 239

Zhang C.Y., 1995. A statistical distance scale for Galactic planetary nebulae. ApJS, 98, 659

Zhang C.Y. & Kwok S., 1993. Trace of planetary nebula evolution by distance-independent parameters. ApJS, 88, 137

Zhang C.Y. & Kwok S. 1998. A morphological study of planetary nebulae. ApJS, 117, 341

Zijlstra A.A., 2007. Binary central stars of planetary nebulae. BaltA, 16, 79

Zijlstra A.A. & Pottasch S.R., 1991. On the scale height of planetary nebulae. A&A, 243, 478

Zijlstra A.A., Pottasch S.R. & Bignell C., 1989. A catalogue of VLA radio continuum observations of planetary nebulae with the Very Large Array. A&AS, 79, 329

Zijlstra A.A., Pottasch S.R. & Bignell C., 1990. Mis-classified planetary nebulae. A&AS, 82, 273

Zijlstra A.A., van Hoof P.A.M. & Perley R.A., 2008. The evolution of NGC 7027 at radio freqeuncies: a new determination of the distance and core mass. ApJ, 681, 1296

Zijlstra A.A., Te Lintel Hekkert P., Pottasch S.R., Caswell J.L., Ratag M. & Habing H.J., 1989. OH maser emission from young planetary nebulae. A&A, 217, 157

Žižňovský J., 1975. On the occurrence of planetary nebulae in open star clusters. BAC, 26, 248

Zucker D.B. & Soker N., 1993. The morphology and interaction with the interstellar medium of the planetary nebula IC 4593. ApJ, 408, 579

Zuckerman B. & Aller L.H., 1986. Origin of planetary nebulae: morphology, carbon-to-oxygen abundance ratios, and central star multiplicity. ApJ, 301, 772

Zuckerman B., Becklin E.E. & McLean I.S., 1991. Central stars of planetary nebulae in the infrared. In Astrophysics with Infrared Arrays, ed. R. Elston, ASP Conf. Ser., 14, 161

Appendix A

Individual PNe nearer than 1.0 kpc

Brief observational summaries and bibliographic notes are presented here for each of the 56 PNe currently considered to be within $D = 1.0$ kpc of the Sun, i.e. the solar neighbourhood sample. This list *excludes* a number of objects considered herein to be PN impostors (see Chapter 8) as well as post-AGB objects and pPNe such as the Red Rectangle (e.g. Cohen et al. 2004) and Frosty Leo (e.g. Sahai et al. 2000), the study of which lies outside the scope of this work.

For the most poorly-studied PNe in the local volume (mainly the fainter objects), an attempt has been made to include most of the primary references to the PN in the literature. For some well-known objects like NGC 7027, the reader is referred directly to the SIMBAD database, where this object has 1875 citations at the time of writing!

In addition, at the end of this chapter, a few objects are discussed that are considered unlikely to be local PNe. The reader is referred back to Chapter 8 for a more extensive discussion on this point. Objects are arranged alphabetically within each section.

A.1 Bona fide PNe

Abell 7. First reported by Abell (1955), this round, low-surface brightness PN (figure A.2) has a few brighter condensations superposed (Abell 1966; Tweedy & Kwitter 1996; Xilouris et al. 1996), and seemingly no evidence of an ISM interaction (Borkowski, Sarazin & Soker 1990). The central star has a possible red-dwarf companion (Ciardullo et al. 1999) which warrants further investigation in order to determine a photometric parallax; only an upper limit could be determined from the HST data of Ciardullo et al. (1999). Harris et al. (1997) measured a trigonometric parallax but gave only a lower limit for D of 700 pc, while Harris et al. (2007), on the basis of improved data, quote $D = 676^{+267}_{-150}$ pc. A gravity distance has been calculated herein, following first principles, using the Lyman-line $\log g$ and $\log T_{\rm eff}$ data of Good et al. (2004). The resulting distance is in agreement with the trigonometric determination (see §6.4.6). A weighted mean distance of 510 pc is used hereafter. As a result of a new integrated Hα flux, this PN is useful as a calibrator for the SB-r relation.

Abell 21 (YM 29 = Sh 2-274). This is the brightest of the photographically-discovered evolved PNe, reported by Johnson (1955), and independently noted by George Abell (Abell 1955, 1966) and Sharpless (1959) from the POSS plates (figure A.2). It has a peculiar shape, appearing as a one-sided arc of numerous overlapping filaments about $8' \times 6'$ in size (e.g. Abell 1966), causing it to be misclassified as a supernova remnant by Vorontsov-Vel'yaminov (1960, 1961), who termed it the 'Medusa Nebula' after its jellyfish-like shape. Consequently it was omitted from the *Catalogue of Galactic PNe* (Perek &

Kohoutek 1967). It was later identified as a peculiar PN (Johnson & Rubin 1971; Terzian 1971; Johnson 1973), confirmed by Leibowitz (1975) and Kwitter, Jacoby & Lawrie (1983). Additional multi-wavelength observations have been made by Chopinet & Lortet-Zuckerman (1971), Lozinskaya (1972), Arkhipova & Lozinskaya (1978), Recillas-Cruz & Pismis (1981), Salter et al. (1984), Lozinskaya, Sitnik & Toropova (1986) and Arkhipova et al. (1989).

The one-sided shape is due to a strong interaction with the ISM (Borkowski, Sarazin & Soker 1990); the western loop, while very faint, increases the total dimensions to more than $12' \times 8'$ (Kwitter, Jacoby & Lawrie 1983; Hua & Kwok 1999). The primary morphology appears to be bipolar, as there is evidence of a lightly pinched waist. There is additional emission apparent on SHASSA images and red DSS images northwest of the PN; it is uncertain whether this is material stripped off the PN as a result of its motion through the ISM (e.g. Wareing, Zijlstra & O'Brien 2007b), or unrelated ambient gas ionized by the CS. Harris et al. (1997, 2007) give a trigonometric distance of $D = 541^{+205}_{-117}$ pc. Accurate integrated fluxes are now known for this PN (see Chapter 3) and it is a primary calibrator for the SB-r relation.

Abell 24. Reported by Abell (1955, 1966), this planetary nebula shows a rather amorphous, bi-lobed structure figure A.2). The [N II] lines are very strong but [O III] emission is only moderate (Bohigas 2003, and Chapter 5); Kohoutek & Pauls (1985) give an excitation class of 4–6. An abundance analysis shows this is a bona fide Type I PN, confirmed by Bohigas (2003). Bohuski & Smith (1974) measured a heliocentric radial velocity, $V_{hel} = 12.7$ kms^{-1}, consistent with the observations of Kohoutek & Pauls (1985) and our WHAM data (see Chapter 3). Deep narrowband CCD images are presented by Tweedy & Kwitter (1996) and Hua & Kwok (1999).

Cudworth (1973) showed the CSPN was a close double, though Ciardullo et al. (1999) argue against this being a physical system. Harris et al. (1997) give a trigonometric distance of only ∼320 pc, which seems to be an underestimate, since then the CSPN is anomalously faint and the cooling time incompatible with the lifetime of the PN shell. The improved result of Harris et al. (2007) is $D = 521^{+112}_{-79}$ pc, which is still on the short side. Furthermore, at this distance, the PN lies well away from the SB-r relation (see Chapter 7) for other Type I PNe. Considering the morphology (the amorphous apparance is redolent of some post-CE objects), a mean SB-r trend was used to determine a distance of 830 ± 270 pc for this PN. Further work is needed to resolve these distance discrepancies.

Abell 31 (Sh 2-290). Discovered by Abell (1955, 1966) and Sharpless (1959), this object has a rather peculiar structure, with a rather sharply defined southern rim contrasting with the more diffuse northern edge (figure A.2). Like the other examples described here, this asymmetry is due to the nebula's interaction with the ISM as the central star moves through it. In addition, the nebula shows pronounced stratification with a brighter central zone of [O III] emission about $8'$ in diameter, compared to the [N II]+Hα apparent diameter of $17'$ across (Tweedy & Kwitter 1994). Ciardullo et al. (1999) give an upper limit to the distance of 440 pc (based on photometry of the resolved companion), marginally inconsistent with a direct trigonometric determination of $D = 568^{+131}_{-90}$ pc (Harris et al. 2007). This supersedes the result of Harris et al. (1997), who gave $D \simeq 211$ pc. With the new distance and an accurate Hα flux from Chapter 3, this PN is a primary calibrator for the SB-r relation.

Abell 36. Found by Abell (1955, 1966), this faint elliptical nebula is fairly symmetrical in appearance, with a bright central star of the 11th magnitude (figure A.2). Monochromatic images are presented by Hua & Nguyen-Trong (1983), Louise & Hua (1984) and Hua & Kwok (1999). Spectroscopic and spectrophotometric data is given by Kaler (1976; 1981b), Hua & Nguyen-Trong (1983) and Hua & Kwok (1999). This is a very high excitation nebula (Kaler 1976, 1981b) with strong HeII emission (>Hβ).

There is no real evidence for an ISM interaction (Borkowski, Sarazin & Soker (1990), even though there is a modest ISM density in the vicinity of the PN; a huge ionized halo was discovered from the SHASSA survey but this was conclusively shown to be ionized ISM rather than circumstellar matter by McCullough et al. (2001). Abell 36 is a primary calibrator for the SB-r relation.

Abell 74. This large, faint PN was discovered by Abell (1955, 1966). The morphology is roughly circular, with a bipolar core morphology, barely visible on the POSS blue plates, but brighter in the red (figure A.2). Monochromatic images are presented by Tweedy (1995b), Xilouris et al. (1996) and Tweedy & Kwitter (1996), showing it is stratified with [O III] emission concentrated at the centre. Harris et al. (2007) give a trigonometric distance of 752^{+676}_{-242} pc. A new, averaged Hα flux (from Chapter 3) allows this PN to be used as a faint-end calibrator for the SB-r relation.

DS 1 (ESO 215-PN4). This evolved nebula was found on ESO B plate (see Lauberts 1982) and independently detected around the 12th-magnitude sdO star LSS 2018 by Drilling (1983) (see figure A.3). A long-slit nebular spectrum published in Méndez et al. (1988c), shows strong HeII λ4686 emission; these authors quote a nebular excitation class of 9 (after Aller 1956). A deep [O III] image (Bond & Livio 1990; see also Zijlstra 2007) shows an unusual pseudo-bipolar structure, somewhat reminiscent of the bipolar reflection nebula, IC 2220, the 'Toby Jug' (e.g. Dachs & Isserstedt 1973.). The central star is a close binary, with a period of 0.357 days (Drilling 1985; Kilkenny, Spencer Jones & Marang 1988). The system was modelled by Drilling (1985), who determined a distance of ~725 pc. With a new accurate Hα flux from SHASSA (CHapter 3), it becomes a calibrator for the mean- and low-trend SB-r relations.

DS 2. This is a faint, spherical PN discovered by Drilling (1983) around the sdO star LSE 125 (figure A.3). An Hα image is shown in Hua, Dopita & Martinis (1998), where the inner network structure is similar to the 'Galactic Soccer Balls', Abell 43 and NGC 7094 (Rauch 1999). There is no [O III] emission according to Hua, Dopita & Martinis (1998), but it is brighter on blue-green IIIaJ plates than red plates, which suggested there was indeed strong [O III] emission. A spectrum obtained as part of this study confirms the strong [O III] emission (see Chapter 5) and shows strong HeII line emission, and it is in many respects spectroscopically similar to other high-excitation PNe like NGC 1360 and NGC 246. A new gravity distance derived herein is 1.0 kpc, so it is just at the cutoff for inclusion in the solar neighbourhood sample. It is a useful calibrator for the mean- and low-trend SB-r relations.

EGB 6. This large asymmetric PN was discovered from the POSS by H.E. Bond in 1978 (see Ellis, Grayson & Bond 1984) (see figure A.3). There is no published spectroscopic data, but deep narrowband CCD images have been presented by Jacoby & Van de Steene (1995) and Tweedy & Kwitter (1996). New WHAM and SHASSA data (see Chapter 3) has allowed integrated fluxes to be determined for the first time with reasonable accuracy. Liebert et al. (1989) studied the CS spectroscopically, deriving $T_{\rm eff}$ = 70 kK, log $g = 7.5 \pm 0.25$, and a distance of 460 pc for this DA white dwarf. Surprisingly, Liebert et al. (1989) found an unresolved, dense emission nebula surrounding the CS, with a tiny ionized mass of $\sim 10^{-9}$ $M_{\odot}$. Dopita & Liebert (1989) suggested that the compact nebulosity is evidence for photoionization-driven ablation of a gas-giant planet (or disk) in orbit around the WD. However, Zuckerman, Becklin & McLean (1990) found near-IR evidence for a probable red dwarf companion, confirmed by Fulbright & Liebert (1993) via JHK photometry of the CS. Note that Liebert et al. (1989) had previously put an upper limit on the luminosity (M3–M4 V) of any red dwarf companion based on the lack of a spectral signature in the optical. The companion has been imaged with *HST* (see Bond et al. 1993; Bond 1994) at a projected separation of 0.18″. Furthermore, the unresolved emission nebula corresponds in position to the red dwarf and not the CS (Bond 1994), suggesting there may be a small disk of material around the cool star (possibly accreted from the PN), and photoionized by the CS.

FP 0711-2531. This is a rather amorphous, wispy object, discovered by the writer from blocked-down SHS Hα images (see Parker et al. 2006a). However, no central ionizing star has yet been identified. The MASH spectrum shows moderately strong [O III] emssion, and this fact, coupled with its isolation from any star-forming regions, has led to its identification as a PN.

FP 0905-3033. A large one-sided PN discovered by the writer from blocked-down SHS images as part of the MASH survey (Parker et al. 2006a). A 16th-mag blue star has been identified at a position consistent with a PN interpretation. It is situated behind outlying nebulosities associated with the Gum nebula (Gum 1955), which complicates the interpretation of the WHAM spectra (Madsen & Frew 2008, in preparation). Only the WHAM [O III] flux seems reliable. The Hα flux is determined from SHASSA images (see Chapter 3). Deep CCD images will be needed to determine integrated fluxes in the other main emission lines.

FP 1721-5654 (Fr 2-12, Fr 1721-5654). This isolated PN candidate was also found on blocked-down SHS images in the overlap zone between the SHS and SHASSA surveys (see figures 2.11 and 2.14). It is one of the better FP candidates for a true PN (Parker et al. 2006a), as it has moderately strong [O III] emission as seen on a MSSSO spectrum, and a limb-brightened morphology, though there seems to be faint diffuse Hα emission to the west of the main body of the nebula. However, there is only one moderately blue star inside the nebula, nor is it at the centre. A spectrum is needed to see if this is the ionizing source.

FP 1824-0319. At nearly 30$'$ across, this is the largest PN discovered as part of the MASH survey (Parker et al. 2006a). The available SHS imagery suggests the nebula is partly veiled by dark clouds associated with the Serpens/Aquila dark rift, which sets a lower limit to the distance of $\sim$250–300pc (Chavarria et al. 1988; de Lara et al. 1991; Straizys, Cernis & Bartasiute 1996). Integrated fluxes and velocities for this very faint, stratified PN obtained with WHAM are given in Chapter 3. The morphology and ionization stratification of this PN is quite similar to the giant PN Sh 2-216 (e.g. Fesen, Blair & Gull 1981), and a blue ionizing star has been identified (see Chapter 9).

HaWe 4 (HDW 3, HtDe 3, We a, PN G149.4-09.2). A very faint one-sided nebula noted by Hartl, Dengel & Weinberger (1983) and Hartl & Weinberger (1987) (see figure A.3). Deep Hα and [O III] images are presented by Tweedy & Kwitter (1996), which show that it may be interacting with a strip of dense interstellar material ionized by the CSPN. Regardless if that is so, the integrated WHAM Hα flux through a 60$'$ beam is overestimated. The Hα flux from table 3.6 is adopted instead. Saurer (1995) gives an extinction distance of 800 $\pm$ 400 pc in reasonable agreement with the gravity distance from table 6.6 herein (see Napiwotzki 1999). Owing to the large error on the adopted flux, this nebula is not suitable as a calibrator for the SB - r relation.

HbDs 1 (LSS 1362). Heber & Drilling (1984) reported a faint irregular nebulosity (figure A.3) around the hot sdO star LSS 1362 (Drilling 1983), which was independently discovered by Brand, Blitz & Wouterloot (1986). A nebular spectrum is published by Mendez et al. (1988b), who note the extremely high excitation of the nebula; it shows He II λ4686 slightly stronger than [O III] 5007, confirmed by our spectra. Heber, Werner & Drilling (1988) analyse the central star and determine $T_{\rm eff}$ = 100 kK, log g =

5.3, and a distance of 1.1 kpc, revised herein to 0.8 kpc. They give an excitation class (after Aller 1956) of 10+. For any of the published literature distance estimates, the ionized mass of the PN is very low. Afşar & Bond (2005) have found good evidence for radial velocity variability, but further observations are needed to confirm this. However, Heber, Werner & Drilling (1988) found no optical variability in four hours of continuous monitoring (totalling 2000 frames).

HFG 1. An asymmetric PN, strong in [O III] emission, found by Heckathorn, Fesen & Gull (1982) from plates of the Emission-Line Survey of the Milky Way (Parker, Gull, & Kirshner 1979). Other images are presented by Heckathorn, Fesen & Gull (1982), Heckathorn & Fesen (1985) and Xilouris et al. (1996) (see also figure A.4) . The PN shows an outer halo with a diameter of 15′ with a strong ISM interaction on the southeast rim (Heckathorn, Fesen & Gull 1982; Xilouris et al. 1996; Tweedy & Kwitter 1996). Heckathorn, Fesen & Gull (1982) determine an approximate Hβ flux of 6×10^{-12} erg cm^{-2} s^{-1}, and use the Shklovsky method to estimate a distance of 350–400 pc.

A blue CS candidate was identified by Heckathorn, Fesen & Gull (1982), and confirmed using IUE ultraviolet spectroscopy (Heckathorn & Fesen 1985). Sinusoidal light variations with a period of 13.96 hr showed that the CS is a close pre-cataclysmic binary (Grauer et al 1987a; Bond et al. 1989; Acker & Stenholm 1990a) demonstrating a strong reflection effect. Hence, this PN is a product of common-envelope evolution. The CS (now designated V664 Cas) has an amplitude of ∼1.1 mag, fairly independent of wavelength (Grauer et al 1987a; Pigulski & Michalska 2002; Shimanskiĭ et al. 2004; Exter et al. 2005), and shows high excitation emission lines due to heating of the companion star by the hot primary (e.g. Grauer et al 1987a; Acker & Stenholm 1990a; Exter et al. 2005).

A detailed phase-resolved spectroscopic analysis of V664 Cas was undertaken by Exter et al. (2005), and they found that the spectral type of the companion was in the range F5–K0 V (on the assumption that the primary and secondary apparent magnitudes are comparable at R), and a distance estimated to be between 310 and 950 pc. We can use the spectroscopic information as well as the available 2MASS JHK photometry to put further constraints on the distance. Ciardullo et al. (1999) give HST single-epoch I-band photometry, I =13.00 consistent with V = 13.4 from Acker et al. (1992). The reddening is $E(B-V) = 0.43 \pm 0.07$ from nebular spectroscopy (Heckathorn, Fesen & Gull 1982) and $E(B-V) \simeq 0.5$ from the 2200Å interstellar absorption feature (Exter et al. 2005); a value of $E(B-V) = 0.46 \pm 0.04$ is adopted hereafter.

IC 5148/50. The beautiful round PN (figure A.4) was found visually by Gale (1896) and independently by Swift (1899)[1]. Spectroscopic observations have been made by Kaler, Shaw & Kwitter (1990), Acker et al. (1992) and Kingsburgh & Barlow (1994). Since this is a round PN at high galactic latitude, the low-trend SB-r relation has been used to determine a distance. The estimate is 850 pc, placing it 670 pc below the plane. This is consistent with an upper limit on the distance of 900 pc, determined by Kingsburgh & English (1992), derived from the Hβ flux, diameter and the density based on the [OII] doublet line-intensity ratio.

IPHASX J2050+4655. Nicknamed the Ear nebula, because of its unusual appearance[2], this is a highly-reddened, stratified PN (L. Sabin, 2008, pers. communication). The reddening is high, estimated as $c \simeq 2.2$ from the observed Balmer decrement (L. Sabin, pers. comm.) suggesting the nebula might be relatively nearby. Based on an approximate Hα flux derived from digital DSS images (using other

[1]Dreyer in his Second Index Catalogue (Dreyer 1908) catalogued the nebulae of Gale and Swift separately, not noting they were the same object. Hence the ‘double’ IC number for this canonical round PN.

[2]see http://zuserver2.star.ucl.ac.uk/ nwright/images/myastroimages/iphas1pn.jpg

northern PNe as calibrators), a SB-r distance of 520 pc has been estimated, placing it well within the solar neighbourhood volume. The relevant parameters are summarised in tables 9.4 and 9.5. No central star has yet been identified.

IsWe 1. This is a very large, diffuse, one-sided PN (figure A.4), and no accurate Hα flux was available until this study. Integrated [N II] and [O III] fluxes were also obtained with WHAM (see Chapter 3). The fluxes published by Xilouris et al. (1996) were erroneous, but once corrected (see §3.2.2, are broadly consistent with the WHAM data. Further details are provided by Ishida & Weinberger (1987), Schonberner & Napiwotzki (1990), Tweedy & Kwitter (1996) and Xilouris et al. (1996). The faint central star is a member of the hydrogen-deficient PG 1159 class (Schönberner & Napiwotzki 1990; Napiwotzki & Schönberner 1995). Photometry has been given by Chromey (1978) and Ishida & Weinberger (1987). The SB-r distance is 620 pc

IsWe 2. This faint elliptical PN was discovered by Ishida & Weinberger (1987), who summarise the basic details of the nebula (see figure A.4). They noted a faint CS with $V = 17.7$, and determined a reddening, $E(B-V) = 0.20$. Additional deep images have been published by Tweedy & Kwitter (1996) and Xilouris et al. (1996). Bruhweiler & Feibelman (1993) observed the CS with the IUE satellite, deriving a higher reddening of $E(B-V) = 0.45$, and via modelling the flux of the CS, estimated a distance of only 300 to 350 pc. Using the parameters of the CS adopted in table 6.6, a distance of 620 pc is estimated.

Jacoby 1. This very faint round PN was first reported by Jacoby & Van de Steene (1995), found after targeted narrowband imaging of the known PG 1159 star, PG 1520+525. The [O III] image in their paper shows an ISM interaction on the south side of the shell. It is barely visible on the blue POSS plates (figure A.4). Jacoby & Van de Steene critiqued the gravity distance of 1.1 kpc, preferring a closer distance of 600 pc. Additional images are presented by Tweedy & Kwitter (1996). Note that Kwitter et al. (1989) had recorded a deep long-slit spectrum of the central star for the purpose of detecting surrounding PNe, but did not note any emission lines. Jacoby & Van de Steene re-examined the Kwitter et al. photographic plates and noted [O III] and HeII emission around this star. The nebula was too faint in Hα for WHAM , but an [O III] flux of $\log F(5007) = -10.96$ erg cm^{-2} s^{-1} was determined, expected since the PN is brighter in [O III] based on imagery by Tweedy & Kwitter (1996) and the qualitative spectrum reproduced by Jacoby & van de Steene (1995). Their reproduction of the plate, shows the nebula belongs to the subset of evolved high-excitation objects, confirmed by the relative weakness of [N II] lines and strong HeII emission from this object (Tweedy & Kwitter 1996).

Jones 1. Rebecca Jones found this faint elliptical nebula in 1941 on a plate taken with Harvard Observatory's 40 cm wide-field Metcalf refractor (R. Minkowski, private communication to Miller & van Dien 1949b). It was independently discovered by Miller & van Dien (1949a). It is more than $5'$ in diameter and is roughly annular, with noticeably brighter arcs on the northern and southern sides (figure A.5). The CS is another example of the hydrogen-deficient PG 1159 class (Schönberner & Napiwotzki 1990; Napiwotzki & Schönberner 1995). A mean-trend SB-r distance estimate is 900 pc.

Longmore 1. This faint disc-shaped nebula was reported by Longmore (1977), following a search for faint planetary nebulae on the SERC J plates (figure A.5) , and independently by Lubos Kohoutek using the same plate material (Kohoutek 1977). It has reasonably strong [O III] and HeII emission (West & Kohoutek 1985), confirmed in an unpublished MSSSO 2.3-m spectrum. Herald and Bianchi (2004) use far-UV and UV data to determine the basic parameters of the central star, $T_{\rm eff}$ =120,000 ± 10,000 K and $\log g = 6.7\ ^{+0.3}_{-0.7}$ cms^{-2}. These authors adopt a distance of 800 pc, and derive an evolutionary age for the CS of $\tau_{\rm evol} \sim$ 65,000 years. A low-trend SB-r distance of 760 pc is estimated, adopted here, which is consistent with Herald and Bianchi (2004).

Longmore 16. This is a poorly studied, yet unusual point-symmetric PN (see figure 9.14). The assumed central star (at the centre of point symmetric features) has a clear NIR excess from 2MASS data. No other data is available for it other than spectroscopic data of the nebula from Acker et al. (1992). It may be a possible close-binary PN. To determine a distance, the low SB-r relation has been used, which gives $D = 840$ pc. This PN and its central star deserves detailed spectroscopic and photometric follow-up.

LoTr 5. This is a very faint elliptical PN, first reported by Longmore & Tritton (1980), following an examination of a non-survey UK Schmidt plate (figure A.5). It is situated in Coma Berenices, very close to the north Galactic pole. The apparent central star is quite bright at ninth magnitude, being a yellow giant of spectral type G5 III that has a hot blue companion. This, the true central star of the nebula, was detected spectroscopically with the IUE satellite (Feibelman & Kaler 1983), and forms a binary of unknown period with the G-type star. Feibelman & Kaler (1983), based on the UV flux, infer a visual magnitude for the hot star of $V = 14.7$, and a temperature, $T_{\rm eff} > 120{,}000$ K. Ciardullo et al. (1999) failed to detect a companion star with HST. The small-amplitude variable central star varies by $\sim$0.08 magnitude every 5.91 days (Schnell & Purgathofer 1983; Noskova 1989; Kuczawska & Mikolajewski 1993; cf. Jasniewicz et al. 1996; Strassmeier, Hubl & Rice 1997; Strassmeier et al. 1997) and was originally classified as a reflection effect variable, designated IN Comae (e.g. Schnell & Purgathofer 1983), but the variability is in fact due to rotation of the chromospherically active G-type component (Jasniewicz et al. 1994, 1996; Strassmeier, Hubl & Rice 1997).

Jasniewicz, Duquennoy & Acker (1987) proposed that the CS is a triple star; Malasan, Yamasaki & Kondo (1991) suggest a model with the hot subdwarf orbiting a binary comprising a G5 III-IV star and a faint companion. Radial velocity variations of the CS have been suspected by Acker, Jasniewicz & Gleizes (1985) and Malasan, Yamasaki & Kondo (1991). Jasniewicz et al. (1996) find no evidence for radial velocity variations, but suggest the fast rotation of the G-star is due to post-common envelope evolution. The distance to this object can be estimated from the apparent magnitude of the G-type star, and is given as 400 pc (Longmore & Tritton 1980). The *Hipparcos* parallax is indeterminate, but a probable lower limit of 430 pc is suggested (van Leeuwen 2007; cf. Acker et al. 1998). In contrast, Bounatiro (1993) proposed that the PN was a member of the nearby Coma star cluster (Melotte 111) at $D = 88$ pc (Odenkirchen, Soubiran & Colin 1998), based on similar proper motions of the nebula and cluster. However, the more accurate *Hipparcos* proper motion (Acker et al. 1998; van Leeuwen 2007) disagrees with that of the cluster. Strassmeier, Hubl & Rice (1997) derived a distance of 710^{+500}_{-360} pc, based on the Wilson-Bappu relation applied to the G5 star, consistent with the estimate of Longmore & Tritton (1980). A mean distance of 500 pc is adopted herein.

LoTr 5 was too faint for WHAM in Hα (see Chapter 3), but is much brighter in [O III], and a flux was determined herein. The Hα flux quoted in Table 9.4 was estimated by bootstrapping the observed [O III]/Hα ratio of 2.5 (Kaler, Shaw & Kwitter 1990) to the WHAM [O III] flux. With the new Hα flux, this PN becomes useful as a $SB - r$ calibrator. The morphology has been studied by Brosch & Hoffman (1999) and Graham et al. (2004; see also Graham, Meaburn, & López 2003). Brosch & Hoffman (1999) describe the lobed asymmetric appearance, while the latter authors determine the true morphology to be bipolar, as modelled from the nebular kinematics, which is unexpected given the spectroscopic characteristics and the large height above the Galactic plane. It may well be a close-binary (common-envelope) system, though no period is known (see De Marco 2006). The bipolar morphology in combination with the very small ionized mass is then typical of such PNe (see Chapter 7).

MWP 1. First discovered only in 1992 by Motch, Werner & Pakull (1993), and independently by Appleton, Kawalwer & Eitter (1993), this faint PN is only barely recognisable on the POSS blue plates (figure A.5). Deep images in the light of [O III] and Hα reveal a large bipolar planetary $13' \times 9'$ in size surrounding a recently identified 13.2-magnitude PG 1159 star, RX J2117.1+3412, detected as a strong X-ray source. An initial spectroscopic analysis of the central star by Motch et al. lead to a large distance of 1400 pc, giving a nebular diameter of $\sim$5 parsecs, the largest then known (Appleton, Kawaler & Eitter 1993). This seemed excessive, as the model atmosphere gravity method used by these authors has probably overestimated the central star distance. An asteroseismological distance of $\sim$452 pc has just been published (Córsico et al. 2007), which is significantly closer than previous work. This has been corrected here to $\sim$495 pc, based on a better estimate of the reddening, determined from the $V - I$ colour index of the CSPN from Ciardullo et al. (1999).

MWP 1 has no published flux or spectral data, but has extremely high excitation based on an unpublished long-slit spectrum taken with the MSSSO 2.3m telescope. This spectrum shows very strong HeII emission and no [N II] or [S II] emission (confirmed by narrowband images published by Tweedy & Kwitter (1996; see also Rauch 1999). An approximate Hα flux is determined from the surface brightness data of Appleton, Kawaler & Eitter (1993). Using the observed dimensions of the PN, I estimate $\log \mathrm{F(H\alpha)} = -10.9 \pm 0.3$.

NGC 246. This is a conspicuous nebula first found visually by William Herschel and later catalogued as a PN by Curtis (1918) (figure A.6). The spectrum is of very high excitation with $\mathrm{F(He\,II)} > \mathrm{F(H\beta)}$ (Minkowski 1942; Heap 1975; Kaler 1976, 1981b; Acker et al. 1992; Muthu, Anandarao & Pottasch 2000). The nebula is interacting with the ISM (Borkowski, Sarazin & Soker 1990; Muthu, Anandarao & Pottasch 2000; Szentgyorgyi et al. 2003). The CS is a visual binary (common-proper motion pair), with the companion being a cool main-sequence star of spectral type K0V (Minkowski 1965; Walsh, Walton & Pottasch 1993; Pottasch 1996; Bond & Ciardullo 1999). Hence, this PN was one of the very first to have an accurate distance determination via the spectroscopic parallax of the companion. A recent determination is 495^{+145}_{-100} pc (Bond & Ciardullo 1999; see also Pottasch 1996). Flux-calibrated imagery was published by Hua, Dopita & Martinis (1998), while Szentgyorgyi et al. (2003) present images in a variety of optical and UV emssion species. The space motion of this PN is $\sim$85 kms^{-1} with respect to the LSR and this accounts for the ISM interaction despite the large $|z|$ distance. Both Sorensen & Pollacco (2003) and Afşar & Bond (2005) found a low probablilty of radial velocity variability in the central star. Recently, Solheim, González Pérez & Vauclair (2008) suggested a possible companion to the PG1159 primary of NGC 246 with a period of just 72.5 min, based on a period analysis of time-series photometry. This is an unusually short period, and independent confirmation is neccesary before it is considered real.

NGC 1360. This evolved PN is also bright enough to have been discovered visually through the telescope (by Winnecke in 1868, see Dreyer 1888), though it was not classed as a PN until much later (Minkowski 1946). However, owing to its peculiar rather amorphous morphology, Khromov & Kohoutek (1968) thought it was not a true PN (figure A.6). Doroshenko (1973) classed it as a high-excitation object, and West & Kohoutek (1985) recorded a similar spectrum, observing HeII λ4686 comparable in intensity to Hβ, and giving an excitation class of 8–10 (see also Kaler 1978, 1981b). Deep CCD images show faint extensions to the north and south (Rauch 1999) of the main body of the PN. Mendez & Niemela (1977) proposed that the central star is a spectroscopic binary but Wehmeyer & Kohoutek

(1979) could not confirm this. However, Afşar & Bond (2005) have found evidence for radial velocity variability. Further monitoring will be worthwhile, as the amorphous, filled-centre morphology is redolent of Abell 65, a known close-binary PN (Pollacco & Bell 1997; De Marco 2006). Goldman et al. (2004) conducted a detailed spatio-kinematical study, modelling the PN as a prolate ellipsoidal shell with an age of 10,000 years. Note that the Hα flux determined by these authors is too bright by $\sim$0.24 dex. The adopted distance is 380 $\pm$ 50 pc, combined from a mean gravity determination (e.g. Hoare et al. 1996) and the Hipparcos distance from van Leeuwen (2007).

NGC 1501. This is a fairly bright, though strongly reddened, high-excitation, optically-thin PN (figure A.6). The central star is hydrogen deficient, classified as [WC4] or [WO4] (e.g. Tylenda, Acker & Stenholm 1993; Górny & Stasińska 1995; Crowther, De Marco & Barlow 1998; Acker & Neiner 2003). A detailed spectroscopic study of the PN shell (including a 3-D photoionization model) has been presented by Ercolano et al. (2004, and see references therein). Other detailed spatio-kinematic studies are those of Sabbadin et al. (2000) and Ragazzoni et al. (2001). A low-trend SB-r distance is 720 $\pm$ 150 pc, placing it well within the solar neighbourhood volume.

NGC 1514. This nearby elliptical PN was discovered by William Herschel in 1789, and it played a central role in the very early history of PN research (see Seaton 1980, and references therein, and §1.1). Despite its proximity and brightness, this PN is relatively unstudied spectroscopically (e.g. Chopinet 1963; Glushkov 1972; Kaler 1976), perhaps because the nebula is quite reddened, being located behind the nearby Taurus-Auriga dark cloud complex which is at 140 $\pm$ 10 pc from the Sun (Kenyon, Dobrzycka & Hartmann 1994). This is a lower limit for the PN distance. Narrow-band images have been presented by Balick (1987) and Hajian et al. (1997), and a spatiokinematic study was performed by Muthu & Anandarao (2003), who found no evidence for bipolarity (figure A.6).

The bright A-type star at the centre (Kohoutek 1967; Kohoutek & Hekela 1967; Morrison & Liller 1968; Greenstein 1972; Lutz 1977; Feibelman 1997; cf. McLaughlin 1942) shows an ultraviolet excess in its dereddened colours. The nebular and stellar velocities are in agreement so the A-star is a physical companion of the CS. The adopted distance, assuming a spectral type of A0 III for the companion, is D = 400 $\pm$ 80 pc (see Pottasch 1996; and this work). This distance is consistent with the revised Hipparcos trigonometric parallax from van Leeuwen (2007) is 3.78 $\pm$ 1.61 mas, corresponding to $D = 265^{+196}_{-79}$ pc. This PN is a calibrator for the SB-r relation.

The spectral class of the bright star suggests the progenitor star had a mass of $>2\,M_{\odot}$, but the low ionized nebular mass, relatively simple morphology, and the non-Type I chemistry suggest otherwise. These caveats might be accounted for if this is a post-common-envelope system, despite the present lack of evidence for short-period binarity. It has even been thought that the A-type star is a horizontal branch star (Greenstein 1972). Photometry of the CS has been obtained by Arkhipova (1968) and Purgathofer & Schnell (1983) but no obvious variability has been detected. Similarly, no RV variability was detected by Greenstein (1972) but Acker (1976) suggested a period of 0.41 day, but this has not been confirmed. Ciardullo et al (1999) failed to resolve the companion in HST data, which sets an upper limit of $\sim$40 AU for the projected separation.

NGC 2346. A peculiar bipolar PN with a unique eclipsing binary central star comprised of an A5V star and a hot companion (figure A.6). There is an extensive literature on the binarity of this object — see Kaler (1976), Lutz (1977), Méndez (1978), Méndez & Niemela (1981), Walsh (1983), Roth et al. (1984), Kohoutek & Celnik (1985), Acker & Jasniewicz (1985), Schaefer (1985), Jasniewicz & Acker (1986), Costero et al. (1986), Grothues & Kohoutek (1992), Costero et al. (1993), Kohoutek (1995), Smalley

(1997), Phillips & Cuesta (2000) and references within. The short period of the binary means this PN must be the product of a post-common envelope system. The ionized mass is rather low for a bipolar PN at the accepted distance; this provides additional evidence that post-CE PNe are undermassive and less luminous than the norm (see §7.3.4).

NGC 3132. This is a bright, well-known southern PN, nicknamed the "Eight-burst" nebula., as a result of its complex appearance (figure A.6 . A detailed summary will not be provided here, and the reader is referred to the SIMBAD database. Of note however is that the central star is a visual binary, with an A-type primary (Lutz 1977). The 16th mag ionizing star was first resolved from the ground by Kohoutek & Laustsen (1977). Ciardullo et al. (1999) give a spectroscopic distance determination of 770 pc, in agreement with the estimates of Méndez (1978) and Pottasch (1996). A detailed spatio-kinematic study of this bipolar object was presented by Monteiro et al. (2000), and a distance of 930 pc has been derived (see Schwarz & Monteiro 2006). An unpublished expansion parallax distance of 1200 ± 400 pc is larger (A. Hajian 2006, pers. comm.), but just consistent within the errors. The mean distance of 800 ± 300 pc is adopted here. This PN is a fundamental calibrator for the SB-r relation.

NGC 3242. This is a bright double-shell elliptical PN, well studied since discovery (figure A.7). Fundamental data has been given by Kaler (1974, 1976), Acker et al. (1992) and Perinotto et al. (1994), and the SIMBAD database can be used to retrieve more recent references. A recent expansion parallax distance places this PN at 1.0 kpc from the Sun (Ruiz et al. 2006). This PN shows both a AGB halo (e.g. Monreal-Ibero et al. 2005) as well as huge, tenous outer halo around it (Minkowski 1965, quoted by Kaftan-Kassim 1966; Deeming 1966; Bond 1981). A Hα flux for this halo was estimated from SHASSA images, and, with the adopted distance from Ruiz et al. (2006), an ionized mass of $\sim 34\sqrt{\epsilon}\ M_{\odot}$ was determined for the halo. This proves unequivocally that the outer halo cannot be produced by the PN central star, and is simply ionized ISM (see the discussion in §4.2.2).

NGC 3587 (M 97). This well-known PN (nicknamed the Owl Nebula) was first found by Pierre Méchain in 1781 (figure A.7). An early study of this object was by Minkowski & Aller (1954). The kinematics of the nebula were investigated by Sabbadin et al. (1985), while Guerrero et al. (2003) conducted a more detailed spatio-kinematical analysis, showing that the halo is undergoing an ISM interaction. Kaler (1976) give spectrophotometric data for this canonical middle-aged PN. Additional narrow-band images have been published by Cuesta & Phillips (2000). Distance estimates in the literature range from 500 to 1500 pc, but it is included here in the solar neighbourhood sample based on its SB-r distance of 760 pc.

NGC 4361. The high-excitation elliptical PN NGC 4361 is now considered to be a member of the solar neighbourhood sample (figure A.7). Adopting the parameters for the CS from Traulsen et al. (2005), a new gravity distance of 950 pc is estimated (see §6.4.6). It has been thought to be a halo object in the past (e.g. Torres-Peimbert, Peimber & Peña 1990), but is now considered to also be a thick disk PN, on the basis of its kinematics and height from the galactic plane.

Weinberger (1999) and Weinberger & Aryal (2004) have noted a large hole in the ISM around NGC 4361, and a nebulous filament 1.2° northwest of NGC 4361 seen on the POSS (Zanin & Weinberger 1997). However there is no detectable halo on SHASSA images (down to an emission measure of $\sim$2 cm^{-6}pc), and Monreal-Ibero et al. (2005), using integral field spectroscopy, also found no evidence for a surrounding halo. Therefore the nebulous filament found by Zanin & Weinberger (1997) is not an emission nebula, but may be faint interstellar cirrus.

NGC 6337. This is a beautiful, annular PN, with outer elliptical extensions of low emission measure, and is probably a bipolar PN seen nearly pole-on (Corradi et al. 2000) (figure A.7). The central star is a close binary; the variability was discovered by Hillwig (2004). The period is 0.173 days, confirmed by Hillwig, Bond & Afşar (2006). Spectra show this is a PN of medium-high excitation (e.g. Acker et al. 1992, Perinotto et al. 1994); the reddening is moderately high, at $c = 0.87$. A low-trend SB-r distance is 860 ± 200 pc, placing it in the solar neighbourhood volume.

NGC 6720 (M 57). The famous Ring Nebula (figure A.7) needs little introduction, and has been a favourite visual target for amateur astonomers since its discovery in the late eighteenth century (see Chapter 1). Harris et al. (1997, 2007) give a trigonometric distance of 704^{+445}_{-196} pc, adopted herein. The integrated fluxes are well determined (see Chapter 3) and it is a key calibrator for the SB-r relation. A detailed summary of this beautiful object will not be provided here; for a good recent spectroscopic and morphological study, the reader is referred to O'Dell, Sabbadin & Henney (2007, and references therein).

NGC 6781. This large bipolar-core PN (figure A.7) is a member of the solar neighbourhood sample at a distance of 950 ± 140 pc (Schwarz & Monteiro 2006), derived from a 3-dimensional photoionization modelling technique. It is quite heavily reddened, being projected behind the Aquila Rift, and would be a far better-known object if seen unobscured. A detailed imaging study in several emission lines was made by Mavromatakis, Papamastorakis & Paleologou (2001). Spectroscopic data has been given by Kaler, Aller & Czyzak (1976), Kaler, Shaw & Kwitter (1990) and Liu et al. (2004). A new, accurate integrated Hα flux has been determined from SHASSA and VTSS (see Chapter 3), and this PN is now an important calibrator for the SB-r relation.

NGC 6853 (M 27). This beautiful, bright planetary nebula needs little introduction. It was found by the French comet hunter Charles Messier in 1764 and was, in fact, the first of this class of object to be recorded. The morphology is best described as of two, broad wedge-shaped lobes forming the well-known 'Dumbbell' shape (figure A.8), while fainter nebulosity fills up the 'wings' of the nebula (morphological class Eb) (Hua & Louise 1981; Chu et al. 1987; Hua, Dopita & Martinis 1998). The wings are especially apparent in [O III] emission, and the overall dimensions are $\sim 8' \times 6'$. Spectroscopic data are given by Kaler, Aller & Czyzak (1976), Sabbadin (1977), Hawley & Miller (1978), Hua, Donas & Doan (1980), and Acker et al. (1992, and references therein).

Additionally, a very faint asymmetric halo with approximate dimensions $15' \times 12'$, and brightest in the north-west, is recorded on deep images (Papamastorakis, Xilouris & Paleologou 1993). The nebula shows a mild interaction with the ISM (Borkowski, Sarazin & Soker 1990; Papamastorakis, Xilouris & Paleologou 1993).

Harris et al. (1997) gave a trigonometric distance of 380 pc, updated to 420 pc by Benedict et al. (2003), and finally $379\,^{+54}_{-42}$ pc by Harris et al. (2007). Of note is the paper by Ciardullo et al. (1999), who discuss the companion to the CS discovered by Cudworth at Lick Observatory (Cudworth 1973, 1977). Assuming a physical association, a tentative spectroscopic parallax of 430 pc is derived, in agreement with the trigonometric distance, but a radial velocity measurement for the companion is needed.

NGC 7008. Although catalogued as a PN by Curtis (1918), it was suggested to be a diffuse nebula by Cederblad (1946). Recent work has shown this to be a high-excitation elliptical PN, with two low-excitation knots (FLIERS) positioned along the major axis either side of the nucleus (e.g. Sabbadin et al. 1983) (figure A.8). Additional monochromatic images have been published by Louise & Hua (1984). Ciardullo et al. (1999) showed the the CS is a close pair from HST imagery ($V = 13.89$ and 14.40, $0.42''$)

with the hot star being the brighter, and derived a spectroscopic distance determination of only 370 pc, which seems too low. A revised value of the reddening has been adopted, $E(B - V = 0.38$, based on the VI colours of the hot star from Ciardullo et al. (1999), rather than the poorly-determined nebular reddening. The de-reddened colours are then $(V - I)_0 = -0.41$ for the CS and $(V - I)_0 = 0.73$ for the companion. The companion has the colours of a G2–5 star (Ciardullo et al. 1999; Cox 2000) and a main sequence luminosity was assumed to fit a spectroscopic parallax. The resulting distance is 450 ± 100 pc which still seems low, even for a high-excitation PN.

However, the high radial velocity of the PN (Durand, Acker & 1998) suggests an old progenitor star, so the companion has probably evolved off the main-sequence. If so, the distance could be considerably greater, so until a spectrum of the companion star is obtained, it is prudent not to use the photometric method to determine the distance. The distance calculated from the HE SB$-r$ trend is 700 ± 150 pc. Adopting this, the absolute magnitude of the companion is then +4.0, typical of a IV-V luminosity class. This PN (and its CS) needs further study.

NGC 7027. Discovered by Webb (1879), this is a well-known, young luminous bipolar PN (e.g. Phiilips et al. 1991; Bains et al. 2003) at a distance of ∼850 pc, determined via the expansion parallax method (Masson 1986, 1989a; Hajian, Terzian & Bignell 1993; Bains et al. 2003; Mellema 2004; see also Zijlstra, van Hoof & Perley 2008). It is by far the most luminous PN in the solar neighbourhood sample (within 1.0 kpc), with ($M_{5007} = -4.5$; this luminosity places it at the very top of the PNLF (see Chapter 10). There is an extensive literature on this remarkable PN, with more papers having been published on this PN than any other. In the words of Volk & Kwok (1997), NGC 7027 “has been responsible for revolutionizing our understanding of the planetary nebula phenomenon.” A detailed bibliography is given in Acker et al. (1992), and the SIMBAD database can be used to retrieve more recent references (figure A.8).

NGC 7293. The famous Helix Nebula is an archetype of a moderately evolved planetary nebula (see figure A.8 and the illustration in the frontispiece). Missed by the Herschels, probably because of its large size, it was first discovered visually by Capocci and independently by Harding around 1827. One of the earliest photographs to show its form was taken by Wood in South Africa (Wood 1910). The main body subtends 15′× 12′, but a larger asymmetric halo surrounds this, a signature of ISM interaction, first detected by Araya, Blanco & Smith (1972). The brightest part forms a narrow curving arc of nebulosity north-east of the main body, about 10′from the central star. Photographically amplified plates (see Malin 1982; Malin & Murdin 1984; Parker et al. 2001a) reveal a complete asymmetric loop surrounding the Helix, and show a few, even fainter knots east of the loop, extending the total dimensions to about 35′× 18′. A red plate by Minkowski was the first to show the many small knots found in the disk (see Vorontsov-Velyaminov 1968). Spectral data are given by Warner & Rubin (1975), Hawley (1978), Acker et al. (1992), O’Dell (1998) and Henry, Kwitter & Dufour (1999).

Detailed morphological studies, especially concentrating on the radial network of small emission knots, are those by Meaburn et al. (1998), Burkert & O’Dell (1998), O’Dell (2000), O’Dell, McCullough & Meixner (2004), and Meixner et al. (2005). See also , and Corradi et al. (2003), Meaburn et al. (2005a), Meixner et al. (2005), and O’Dell (2001, 2005). The Helix is another moderately evolved PN showing evidence of an ISM interaction (e.g. Borkowski, Sarazin & Soker 1990).

The large apparent diameter made it an early target for parallax estimates but van Maanen’s (1923) determination was an order of magnitude in error. More recent trigonometric estimates of varying accuracy were those of Vasilevskis et al. (1975), Harrington & Dahn (1980) and Harris et al. (1997). The distance is now precisely known at 219^{+27}_{-21} pc (Harris et al. 2007), and is probably the second closest object of its kind to the Sun. Eggen (1984) has shown that the space motion of the central star makes it a likely member of the Hyades Supercluster. Forcing the space motion to be equal to the mean motion of the moving group leads to an astrometric distance of 180 pc, in reasonable agreement with the trigonometric estimate (see §6.4.9). If real, this association is an important one as it allows an approximate turnoff age and mass of the progenitor to be inferred.

PFP 1: This beautiful hollow-sphere PN, nearly 19′ across, is in the first stages of an interaction with the ISM (see figure 4.6). It was discovered serendipitously from digital AAO/UKST Hα Survey images by M. Pierce in 2003 (see Pierce et al. 2004). A detailed account of this beautiful but very faint PN is given in §4.3.1.

PuWe 1. This is a very faint round PN (figure A.8) discovered by Purgathofer & Weinberger (1980). It shows only a very modest ISM interaction despite its low surface brightness (see Tweedy & Kwitter 1996). Harris et al. (2007) give a trigonometric distance of 365^{+47}_{-37} pc (superseding the earlier estimate of Harris et al. 1997), while Ciardullo et al. (1999) discuss the nature of the CS companion(s). Now that the integrated Hα flux is known with accuracy, PuWe 1 is useful as a good primary calibrator for the faint end of the SB-r relation.

RCW 24 (Fr 1-1, Bran 147, PHR 0825-4013). This unusually large PN was noted serendipitously from first-epoch ESO-R Sky Survey films by the writer in 1995, and was later reported as a possible new PN (Frew 1997) based on its unusual morphology, despite the then accepted HII identification. It was independently found on the AAO/UKST Hα survey field h458 (exposure HA 18308) by Q. Parker in 1998 as part of the MASH identification program where it was more clearly identified as a probable evolved bipolar PN.

Earlier, Brand, Blitz & Wouterloot (1986) noted it in their list of HII regions, which also includes several reflection nebulae and a sprinkling of PNe. They gave no further comment on its nature and the two lobes of the PN were each given separate designations (Bran 147A/B). In addition, a red image is presented by Neckel & Vehrenberg (1990), where it was again assumed to be an HII region. At the time of discovery, the SIMBAD database placed the object RCW 24 a few arcminutes to the southwest of our position, based on the coordinates listed by Rodgers Campbell & Whiteoak (1960), but there is no obvious nebulous object at that position on Hα survey field h 458. Careful examination of the relevant plate from the RCW atlas (Rodgers et al. 1960) showed that the bipolar nebulosity is indeed present, and furthermore there is no visible object at their catalogued position. Acknowledging that positional errors of up to 5 arcmin are not unknown in the RCW catalogue (Rodgers, Campbell & Whiteoak 1960), RCW 24 is identified as an earlier observation of the two objects separately catalogued by Brand et al. (1986).

RCW 24 is readily visible on the standard UKST R-band survey image as two wedge-shaped lobes of emission, which extend about 8 arcmin. The extent is close to 11′ north–south in the new Hα image. It is likely that the object's large angular size, coupled with the faintness of the overall nebulosity on the previously available broad-band photographic images, mitigated against a previous PN identification. Deep AAO/UKST Hα images reveal the obvious bipolarity, and show very faint outer extensions (figure 4.7). These extensions are about 22′ × 18′ in size, with the major axis oriented east-west. In its surface brightness, spectrum and overall morphology, RCW 24 strongly resembles the bipolar Mask Nebula (PN G321.6+02.2 = CVMP 1; Corradi et al. 1997; see also Lynga 1965). A discussion of the chemical abundances of this interesting, evolved, Type I bipolar PN is given in §5.4.

A faint blue CSPN has been found symmetrically placed between the two bipolar lobes of RCW 24 (see Frew, Parker & Russeil 2006). UBV images were kindly obtained by Dr Patrick Woudt with the

SAAO 1.0-m reflector on the night of 2004 Feb 16, which gave $V = 18.21 \pm 0.03$, $B - V = 0.03 \pm 0.08$ and $U - B = -0.99 \pm 0.10$. The colours are consistent with a hot central star suffering some modest extinction. The distance to this PN is estimated as 1.0 kpc. A detailed summary of this PN is provided in Frew, Parker & Russeil (2006).

Sh 2-78 (CTSS 3, GS 162). A faint object discovered by Gaze & Shajn (1955) and independently by Sharpless (1959), but first shown to be an evolved PN by Cappellaro et al. (1990) (figure A.8). Deep images in Hα [O III] and [N II] are presented by Tweedy & Kwitter (1996), where a possible bipolar core morphology is apparent. The spectrum shows quite strong [N II] lines (Cappellaro et al. 1990) and it is possible that this is an evolved Type I PN, though there ar no published data on the UV [OII] lines. Against the interpretation is that the PN plots outside of the field of Type I PNe in the revised diagostic plot shown as figure 5.3. Capellaro et al. also give an approximate extinction distance of 700 pc. The radial velocity is $V_{\rm lsr} = +41.8$ kms^{-1} from Fich, Treffers & Dahl (1990), in broad agreement with our WHAM average systemic velocity of $V_{\rm lsr} = +34.4$ kms^{-1} from three emission species (see Chapter 3). The CS is another example of the hydrogen-deficient PG 1159 class (Napiwotzki & Schönberner 1995). CCD BV photometry of this star was given by Cappellaro et al. (1990).

Sh 2-176 (LBN 597). This one-sided filamentary nebula (figure A.9) was discovered by Sharpless (1959), and was also catalogued by Lynds (1965). In many respects, it resembles the brighter and better known, one-sided PN, Sh 2-188 (see below). Sabbadin, Minello & Bianchini (1977) identified it as an evolved PN, and obtained a slit spectrum of the brightest filaments, deriving a mean [N II]/Hα ratio of 2.9. Narrowband CCD images are presented by Tweedy & Kwitter (1996) and Xilouris et al. (1996). The [O III] emission is very weak (Gieseking, Hippelein & Weinberger 1986; Tweedy & Kwitter 1996; Xilouris et al. 1996), confirmed by our WHAM spectra, and by its absence on the [O III] plate in Parker, Gull & Kirshner (1979). It is unlikely that this object is a Type I PN; the strong apparent [N II] emission may be explained by shock excitation in the strongly interacting rim. Using the high-trend SB-r relation, applicable to old, optically thick nebulae, a distance of 780 pc is estimated.

Sh 2-188 (Simiez 22, Sh 1-134, LBN 633). This is a filamentary, one-sided, evolved PN (figure A.9), somewhat similar in appearance to Sh 2-176, but much brighter and better studied. It was first catalogued as an emission region by Gaze & Shajn (1951), and soon after by Sharpless (1953), before being classified as an HII region by Sharpless (1959) and Lynds (1965). It was also considered to be a possible SNR (Minkowski 1958; Parker 1964). Lozinskaya (1969) obtained Fabry-Perot observations of the nebula, estimating $V_{\rm hel} = -26 \pm 6$ kms^{-1} and an expansion velocity of 35 ± 2 kms^{-1}, preferring to classify it as a low-energy SNR (see also Lozinskaya 1975). Additional spectroscopic observations were conducted by Lozinskaya & Esipov (1970) and Esipov et al. (1972). It was not until Johnson (1975) re-examined it, that its true nature as an evolved, strongly asymmetric PN became clear, confirmed by Israel & Felli (1976) and Arkhipova & Lozinskaya (1978).

Detailed spectroscopic observations were made by Rosado & Kwitter (1982) who classified it as a PN of Peimbert's Type I, and Lozinskaya et al. (1984), who presented interference-filter photographs of the nebula. On the interference-filter plates of Parker, Gull & Kirshner (1979), it is obvious in Hα + [N II], [O III] and [S II], and faint in H$\beta\dot{\rm R}$adio observations have been made by Israel & Felli (1976), Salter et al. (1984) and Arkhipova et al. (1989). The central star was identified by Kwitter, Jacoby & Lydon (1988) who noted that the PN has the shape of an almost complete ellipse on the red POSS plates. The central star is off-centre confirming that a strong PN-ISM interaction exists (Borkowski, Sarazin & Soker 1990). An inferred Hβ flux was determined by Kwitter & Jacoby (1989). Tweedy & Kwitter

(1996) and Xilouris et al. (1996) present detailed images, which confirm the presence of a complete elliptical shell. The systemic velocity obtained with WHAM is $V_{\rm lsr} = -29\pm3$ kms^{-1} (Madsen & Frew 2008, in preparation, and table 3.8) in agreement with the earlier determinations of Lozinskaya (1969), and Rosado & Kwitter (1982), but in disagreement with the measurement of Georgelin, Georgelin & Roux (1973). An extinction distance of 800 ± 300 pc was derived by Saurer (1995). Wareing et al. (2005, 2006a) kinematically modelled the strongly one-sided shape of the nebula to infer a transverse velocity of ∼125 ± 25 kms^{-1}. Combined with a newly determined proper motion of 30 ±10 mas/yr, Wareing et al. (2006a) derived a distance of 850^{+500}_{-420} pc, which agrees within the errors with the extinction distance. With the new Hα flux from this work, this PN is a useful faint-end calibrator for the SB-r relation.

Sh 2-200 (HaWe 2). A large [O III]-bright PN that is very poorly studied, despite its far northern declination (see figure A.9). It was first noted by Sharpless (1959), but its probable PN classification came with Hartl & Weinberger (1987), who first recorded the large halo around this object. The central star identification is ambiguous; a possible candidate is given in table 9.6. The central nebula shows up as an obvious patch on the [O III] plate in Parker, Gull & Kirshner (1979); it is considerably fainter on their Hα + [N II] plate. A beautiful Hα + [N II] image is reproduced in Corradi et al. (2003), which reveals peculiar linear wisps which may be oriented in parallel with the proper motion vector, which is at present unknown. An accurate Hα flux is hard to determine with WHAM, owing to a large ionised halo around the PN (see Chapter 3). The large halo is in fact ionized ISM (see the discussion in §4.2.2) as the CO radial velocity (which is assumed to trace the diffuse HI) was measured by Blitz, Fich & Stark (1982) as $V_{\rm lsr} = -10$ kms^{-1}, a significantly different velocity to the PN itself ($V_{\rm lsr} = -50$ kms^{-1}). This interpretation was confirmed by new WHAM mapping data kindly obtained by Greg Madsen and presented herein (see figure 4.4). This demonstrates convincingly that the halo is unrelated to the PN, and is ionized by UV radiation escaping out of this porous, optically-thin PN. Curiously, stripes in the ISM halo are in the same orientation as the wisps seen in the PN. Their origin may be due to the interstellar magnetic field, or due to Kelvin-Helmholtz instabilities resulting from the motion of the PN through the ISM. Similar morphologies are present in Abell 35 and Fr 2-11, but the origin of these features is not yet known.

Sh 2-216 (Simiez 288). With an apparent diameter of ∼1.6°, this is the largest known planetary nebula (figure A.9), and with a accurately determined trigonometric distance of 129 pc (Harris et al. 1997, 2007), is currently the closest example known to our solar system. The brightest section (eastern rim) was discovered on red-filtered plates taken with an 8-inch f/1 Schmidt camera (Johnson 1954), and independently by Gaze & Shajn (1954) around the same time. Sharpless (1959) included it in his catalogue of HII regions. It is an interesting object, as the distribution of surface brightness across it is not uniform; it appears as a faint crescent on the POSS R print, which deep interference images show to be a bright rim on the eastern side of a roughly circular nebula (Parker, Gull & Kirshner 1979; Rosado 1986). Fesen, Blair & Gull (1981) showed the peculiar nature of this object, suggesting it may be a possible PN, though Weinberger et al. (1983) suggested it was a HII region, as it lacked the requisite faint blue star at its centre. Reynolds (1985) used spectra obtained with a Fabry-Perot interferometer through a 49′aperture, to infer it was probably an extremely old PN, despite the remarkably low expansion velocity of <4 kms^{-1} (Reynolds 1985), confirmed by our new WHAM data (Chapter 3). Cudworth & Reynolds (1985) identified the 'central' star as LS V +46°21, which lies about halfway between the bright rim and the apparent centre of the nebula.

The nebula shows a strong stratification effect, as [O III] images reveal a smaller, more circular region roughly centred LS V +46°21, confirming this to be the ionising source for the nebula (see the Hα+[N II] and [O III] images of Fesen, Blair & Gull 1981). Spectra of the ionizing star show that it is indeed a hot

DA white dwarf (Tweedy & Napiwotzki 1992). The peculiar appearance of this planetary is due entirely to its interaction with the ISM, as the nebulous gas is decelerated and left behind as the central star moves through it. Therefore the central star is predicted to be displaced from the geometric centre of the nebula in the direction of the central star's proper motion, just as observed for this object based on astrometric measurements (Cudworth & Reynolds 1985; Borkowski, Sarazin & Soker 1990; Tweedy, Martos & Noriega-Crespo 1995).

The large diameter of 3.6 pc leads to a dynamical age of nearly 350,000 yr, using the new WHAM expansion velocity of 5 kms^{-1} (cf. Reynolds 1985, who estimated an age of $\sim$ 300,000 yr). However, if considerable deceleration has occurred as a result of its interaction with surrounding ambient gas (the PN is very close to the Galactic midplane), then this age will be an upper limit. The position of this star in the HR diagram suggests a mass of $\sim$0.56 $M_{\odot}$ (a relatively low mass CS), however the ionized mass of the PN shell is quite large, 2.0 $M_{\odot}$. Sh 2-216 may well be an example of a grossly-decelerated shell which has swept up a significant portion of interstellar material (cf. Villaver, García-Segura & Manchado 2003). However, it seems from recent work that much of the nebular gas is not ionized ISM but processed material from the star. Based on *FUSE* data, Oliveira et al. (2007) observed a low D/H ratio, which is probably due to the nebular gas being processed through the star (astrated), and relatively unmixed with the ISM.

Ton 320 (TK 1). The DAO star Ton 320 was first noted by Iriarte & Chavira (1957) half a century ago, but the very faint one-sided PN was not found until much later (Tweedy & Kwitter 1994), as a product of a targeted search in Hα for faint nebulae around hot WD stars; it is invisible on the blue and red POSS plates (figure A.9). Until the present study, the morphology was the only characteristic suggesting this object may be a PN, as there were no spectral data, nebular velocities, or flux estimates in the literature.

For Ton 320, Good et al. (2004) determine $T_{\rm eff}$ = 99,000 $\pm$ 4000 K and $\log g$ = 7.26 $\pm$ 0.07 from the Lyman lines; the Balmer gravity is similar, but the derived $T_{\rm eff}$ is considerably lower. The Lyman values are preferred. The inferred gravity distance is $\sim$600 pc, consistent with the trigonometric distance of 532^{+113}_{-100} pc (Harris et al. 2007). The heliocentric radial velocity of Ton 320 from Good et al. (2005) is +33.8 $\pm$ 0.3 km s^{-1}. The gravitational redshift from table 6.6 is $V_{\rm GR}$ = 13.2 km s^{-1}, which leads to a corrected heliocentric velocity of +20.6 km s^{-1}, or +13.9 km s^{-1} referred to the LSR frame. The mean systemic nebular velocity (in Hα, [N II] and [O III]) from WHAM is $v_{\rm LSR}$ = +13.8 km s^{-1} identical to the stellar velocity, indicating they are physically associated. Despite the quite small line width of the emitting gas, this nebula is considered to be a bona fide PN; the low expansion velocity is explained by the deceleration of the nebular shell by the ISM. This is a truly ancient PN, with the lowest mean Hα surface brightness currently known. Adopting a distance of 570 pc, the observed angular size makes this the largest PN currently known, with a diameter of 5.7 pc. The derived age is 185,000 years, but the PN may have been decelerated by the ISM, so this age is an upper limit.

WDHS 1 (WeDe 1). This is an extremely faint PN with dimensions 17$'$ $\times$ 14$'$, was first reported by Weinberger et al. (1983) from a red POSS print (figure A.9). It is practically invisible on blue plates due primarily to the very weak [O III] emission in this object (see Chapter 3), and is invisible on the [O III] plate of Parker, Gull, & Kirshner (1979). Indeed, it is near the bottom of the [O III] luminosity function, despite evidence for it being a massive PN around a relatively hot and massive CS (see table 10.3). It emits more strongly in the red [N II] lines however, with Weinberger et al. (1983), showing that the ratio [N II]/Ha varies from 1.5 to 2.5 over the face of the nebula. The surface brightness is still rather low in red light, as it is fairly faint on the Hα + [N II] plate of the Parker, Gull, & Kirshner (1979) survey.

Tweedy & Kwitter (1996) present deep Hα and [N II] images; the nebula is considerably brighter in the latter line (see also Liebert, Bergeron & Tweedy 1994). An integrated [N II] flux has been obtained with WHAM (see Chapter 3).

The CS candidate has V ~17.40, and there is a possible faint companion to the CS (Weinberger et al. 1983), though it is more than likely to be an optical companion. These authors estimated a distance via the Shklovsky method of 320 pc. Liebert, Bergeron & Tweedy (1994) give detailed observations of the DA white dwarf nucleus. They determine a range of surface temperatures from 100 to 165 kK, and a high surface gravity, $g \simeq 7.6$. Based on these parameters, Liebert, Bergeron & Tweedy (1994) determine a much larger distance of 1.0 ± 0.25 kpc. They note this is one of the very largest PNe, with a diameter of ~6.4 pc. Napiwotzki & Schönberner (1995) and Napiwotzki (1999) also present analyses of the CS, giving a slightly larger distance of 1.1 kpc (see table 6.6), though Pottasch (1996) adopts a smaller gravity distance. Our new Hα integrated flux measurements from SHASSA and VTSS (see Chapter 3, and also Gieseking, Hippelein & Weinberger 1986) means this huge PN is now an important calibrator for the faint end of the SB-r relation.

A.2 Uncertain cases

EGB 1 (Simiez 280, LBN 624, HtDe 1, HaWe 1). A relatively bright, somewhat irregular, one-sided nebulosity found independently by Gaze & Shajn (1954), Lynds (1965), Hartl et al. (1983), Ellis, Grayson & Bond (1984) and Hartl & Weinberger (1987). Traditionally classed as a PN. it is poorly studied, but spectra shows relatively bright [O III] emission relative to Hα (Acker et al. 1992), but less so according to our WHAM data. The WHAM fluxes are uncertain due to poor background subtraction. The lack of a limb-brightened bow shock (expected for such a one-sided nebula with an off-centre CS), the small line-width, the systemic nebular velocity close to zero LSR, and the moderate excitation lead to questions regarding its status. It may be another case of ionized ISM, but more observations need to obtained before a definitive answer can be given.

EGB 9. Discovered by Ellis, Grayson & Bond (1984) from the POSS. Hoessel, Saha & Danielson (1988) obtained images of it, and suggested it was either a faint emission or reflection nebula. It shows up on SHASSA images as a irregular elongated patch (see figure A.1). CCD images (though not reproduced in their paper) have been obtained by Kerber et al. (2000). The emission spectrum is also confirmed here, on a MSSSO 2.3m spectrum. The CS is quite bright (V = 13.0) relative to the Hα flux, so the nebula must be of relatively low mass. If the nebula is near (<0.7 kpc), the small size and low flux indicates it may be another case of ionized ISM. Using a low-trend SBr relation, a distance of ~1.0 kpc is suggested. For now it is considered as a PN candidate, but further work is needed to clarify its nature.

FP 0721+0133. This large, one-sided PN candidate has rather weak [O III] emission. No CS has been identified, leading to question marks over its true status. Further work is needed, including obtaining deep narrowband images in various wavelengths.

FP 0821–2755. This interesting object has an elliptical, somewhat filamentary appearance (see figure 2.10) and has been classified as a possible SNR by Weinberger (1995), Weinberger et al. (1998) and Zanin & Kerber (2000); it has the designation SNR G247.8+04.9 in the SIMBAD database. There is a weak radio detection in the PMN survey, though it is not coincident with the optical nebulosity. Our new unpublished optical spectra confirm the extremely strong [N II] emission ($\gg$Hα), but only weak [S II] is

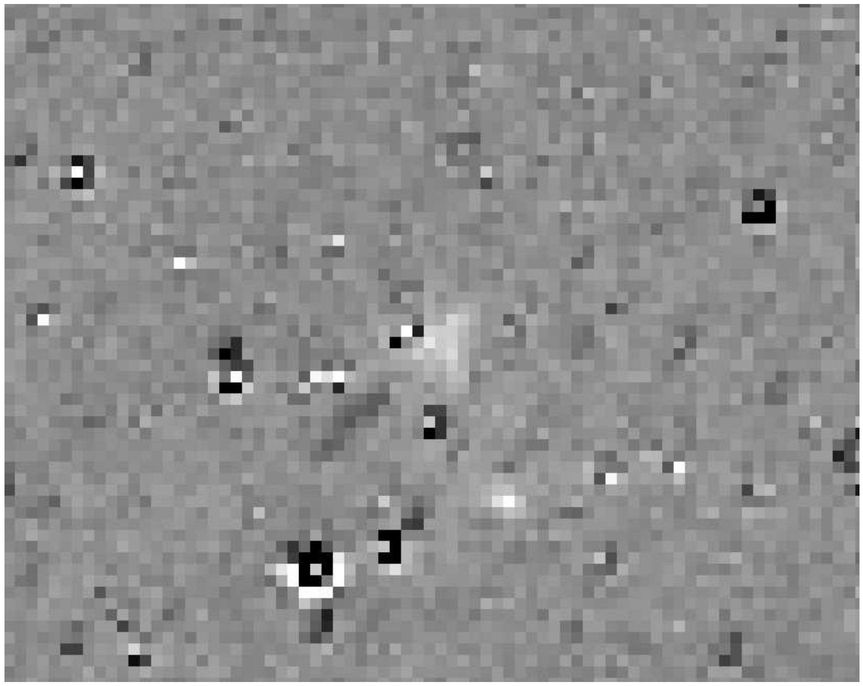

Figure A.1: Image of EGB 9 from SHASSA field 245. The image is 60′ wide.

seen, and [O III] is also clearly detected in the blue, stronger than Hβ. On this basis, an interpretation as a peculiar PN is more likely (Parker et al. 2006a), but more work is needed to definitively classify this object. If a PN, the Hα flux measured from SHASSA (corrected for the dominant [N II] line-emission) places it at an approximate distance of $\sim$ 2–3 kpc using the SB-r relation, so it is likely to be beyond the local volume.

FP 1556–4955. A HαSR difference image (shown in figure 2.11) illustrates the morphology of this large, very faint and asymmetric nebula, of dimensions 805″ by 680″. The elliptical one-sided shape is consistent with a PN interpretation, but no CS candidate has been identified. However, no evidence of star formation is present near the PN, which has a galactic latitude of +2.7°. There is evidence for stratification in the 2D-slit spectrum obtained by us. However, deeper observations are needed to unambiguously determine its nature.

FP 1705–5415. A HαSR difference image (shown in figure 2.11) reveals a very faint, round nebula, with an asymmetric brightness distribution. The overall dimensions are 860″ by 850″. SHASSA image 060 shows diffuse emission surrounding this object, which may be simply a brighter section of the diffuse nebulosity. Again, no CS has been identified, so its status as a PN is uncertain.

FP 1804-4528. This isolated, asymmetric nebula is considered to be a possible PN by Parker et al. (2006a), despite its low excitation (very weak [O III] emission). It shows a bright rim on the southern side, and faint extensions are seen to the north of the main body (figure 2.11); the overall diameter is nearly 10′. No ionizing star has been identified as yet, leaving open its true status. It may be another example of a Strömgren zone in the ISM; its morphology is somewhat like DeHt 5 (see §8.5).

Fr 2-6 (Fr 0840-5754, FP 0840-5754). This isolated nebula was also found on blocked-down SHS images in the overlap zone between the SHS and SHASSA surveys; both designations are included for completeness. It has a moderate surface brightness, and is located in a region with little diffuse emission or evidence of star formation, at a galactic latitude of $-9.8°$. The morphology is rather amorphous, as seen on the SHS Hα image (figure 2.10). A newly identified CS candidate is located at $08^{\rm h}40^{\rm m}16.47^{\rm s}$, $-57°54'45.3''$, in the brightest section of Hα emission. This star has $V \simeq 14.37$ (NOMAD catalogue; Zacharias et al. 2005) and has bluish colours; it is $56''$ west of CD$-57°2232$ (the bright star near the apparent centre of the nebula). The reddening in this direction is $E(B-V) = 0.18$ (Schlegel, Finkbeiner & Davis 1998). It is too far south for WHAM, and further work is needed to elucidate its true nature.

K 2-2 (LBN 926). Like Abell 21, Sh 2-176 and Sh 2-188, this is a one-sided arc-shaped nebula, first discovered from the POSS (Kohoutek 1963b; Lynds 1965). Until recently, it was relatively unstudied: Kaler (1983b), Kaler, Shaw & Kwitter (1990) and Gieseking, Hipplelein & Weinberger (1990) presented emission-line fluxes, and photometry of the proposed CS was given by Kwitter, Jacoby & Lydon (1988). Ali, El-Nawawy & Pfleiderer (2000) included it it their census of one-sided PNe. The ionizing star has a low mass (Napiwotzki & Schönberner 1995; Napiwotzki 1999) and the inferred post-AGB lifetime is not consistent with the kinematic age of the nebula. This object may turn out to be another case of ionised ISM à la Sh 2-174. Alternatively, this PN may be a senile example of a common-envelope ejection event. Afşar & Bond (2005) have suggested that the CS is a likely close binary, based on radial velocity variability. Photometric monitoring will be of interest.

A.3 Other PNe rejected from the 1.0 kpc sample

This section is a brief, partial list of other PNe which have recently been offered as candidate nebulae for the solar neighbourhood sample. All are shown here to be at distances beyond the 1.0 kpc cutoff.

Abell 29. This is a bona fide PN discovered by Abell (1955; see also Abell 1966), though now considered to be beyond the cutoff for inclusion in the solar neighbourhood sample, *sensu stricto*. Deep red-light images show an incomplete annulus with enhancements on the north-east and south-west edges (Tweedy & Kwitter 1996). Like Abell 24, the [N II] emission is remarkably strong. The distance is uncertain. Gutiérrez-Moreno et al. (1999) measure a ground-based trigonometric parallax of $\pi = 3.3 \pm 1.2$ mas. Harris et al. (1997) give a trigonometric parallax of 2.18 ± 1.30 mas ($D = 460$ pc), which has been superseded by the result of Harris et al (2007). This distance seems too close, for the reasons outlined for Abell 24 (see Appendix A. However, Harris et al. (2007) note that the preliminary parallax was not reliable and the star has been dropped from the USNO program. A high-trend SB-r distance is 1390 pc, placing it outside the formal solar neighbourhood volume. Using the apparent CS magnitude from Abell (1966) and Harris et al. (1997), and a reddening derived from the available $UBVI$ photometry, this distance leads to an absolute magnitude for the CS of $M_V = +7.22$, consistent with the mean magnitude for evolved CS (Phillips 2005a, and see §9.4.3).

FP 0739–2709. This curious PN has, like Sh 2-200 (Corradi et al. 2003), a set of linear stripes across the face of the PN (see figure 2.10), of uncertain origin. Dgani & Soker (1998) suggest that the ISM magnetic field makes the RT instability very efficient for PNe close to the Galactic plane, like this one, producing 'rolls' or stripes in the PN. However, without further evidence, their formation mechanism remains uncertain (see §4.3.2). The PN lies just $8'$ from the sparse open cluster ESO 493-SC03 (see also Majaess, Turner & Lane 2007), but it is not considered to be physically associated with the cluster (see

§6.4.9). A faint blue CS has been identified at the centre of the PN. FP 0739–2709 was originally thought to be a candidate for the solar neighbourhood, but the SB-r distance for the PN is 2000 ± 600 pc. It is hence included in the extension sample.

IC 4637. Ciardullo et al (1999) give a possible spectroscopic distance of just 500 pc for this compact elliptical PN, which seems much too low for a PN of its size and and realtively bright flux. However, as discussed by those authors the physical association of the companion star with the CS is very doubtful. The field star density is sufficiently high, and the separation of the stars sufficiently large, that the putative companion is certainly optical. It is no longer considered to located in the solar neighbourhood.

K 1-27. A peculiar, high-excitation PN independently discovered by Kohoutek (1977), Holmberg et al. in 1978 (see Lauberts 1982) and Fairall (1980). The spectral characteristics have been confirmed by West & Kohoutek (1985), Henize & Fairall (1981) and Rauch, Köppen & Werner (1994). Ciardullo et al. (1999) resolved the CS into a close pair on *HST* images, and proposed that the companion star is a white dwarf. Fitting the companion to the WD cooling sequence led to a spectroscopic distance of only 470 pc, though the considerably greater gravity distance of 1.3 kpc (Rauch, Köppen & Werner 1994), revised here with an updated reddening to 1.7 kpc (see table 6.6). This distance still places this object way off even the high-excitation $SB - r$ relation, with a very low ionized mass of 0.018 $M_{\odot}$. The central star is hydrogen deficient and helium rich, and is similar in many respects to the CS of another faint PN, LoTr 4 (Rauch, Köppen & Werner 1996). This peculiar PN warrants further investigation, and may originate in a non-standard formation process, such as the PN ejection taking place at the final He flash.

YM 16 (RCW 181). This faint, poorly studied PN was independently found by Johnson (1955) and Rodgers, Campbell & Whiteoak 1960). A new Hα flux has been determined from VTSS and SHASSA data (see Chapter 3). The observed $IJHK$ colours of the apparent central star can be fit by a mid-G-type dwarf with a reddening of $E(B - V) = 0.80$ (see tables 9.5 and 9.6). Using this reddening, a high-trend SB-r distance estimate of 1.3 kpc follows. Further work on the putative binary CS is needed however.

A.4 An Image Gallery of Solar Neighbourhood PNe

A gallery of images of PNe in the solar neighbourhood volume is presented here. Images of PNe discovered as part of the MASH project have been given earlier: the FP objects in Chapter 2, and images of PFP 1 and RCW 24 in Chapter 4. Images of nebulae discovered from SHASSA and VTSS are similarly presented in Chapter 2.

The approach taken here was not to provide a set of the most detailed narrowband images of each object (copyright restrictions prevented that), but instead to provide a set of *broadband* DSS images of these objects (R_F or B_J emulsions), to provide an easy visual comparison of the huge range in surface brightness presented by these nearby PNe. For some objects, e.g. Jacoby 1 and Ton 320, this meant that the nebulae were invisible on this material. This is itself instructive, since the Helix nebula (NGC 7293) or Medusa nebula (Abell 21) are often considered to be the archetypes of low-surface brightness nebulae. To see deep CCD images of the very faintest PNe, the reader is referred to the detailed references for each object provided in the previous section.

The PNe are arranged in in alphabetical order, with six objects in each figure. The emulsion and image scale are given for each PN. All images have NE at top left.

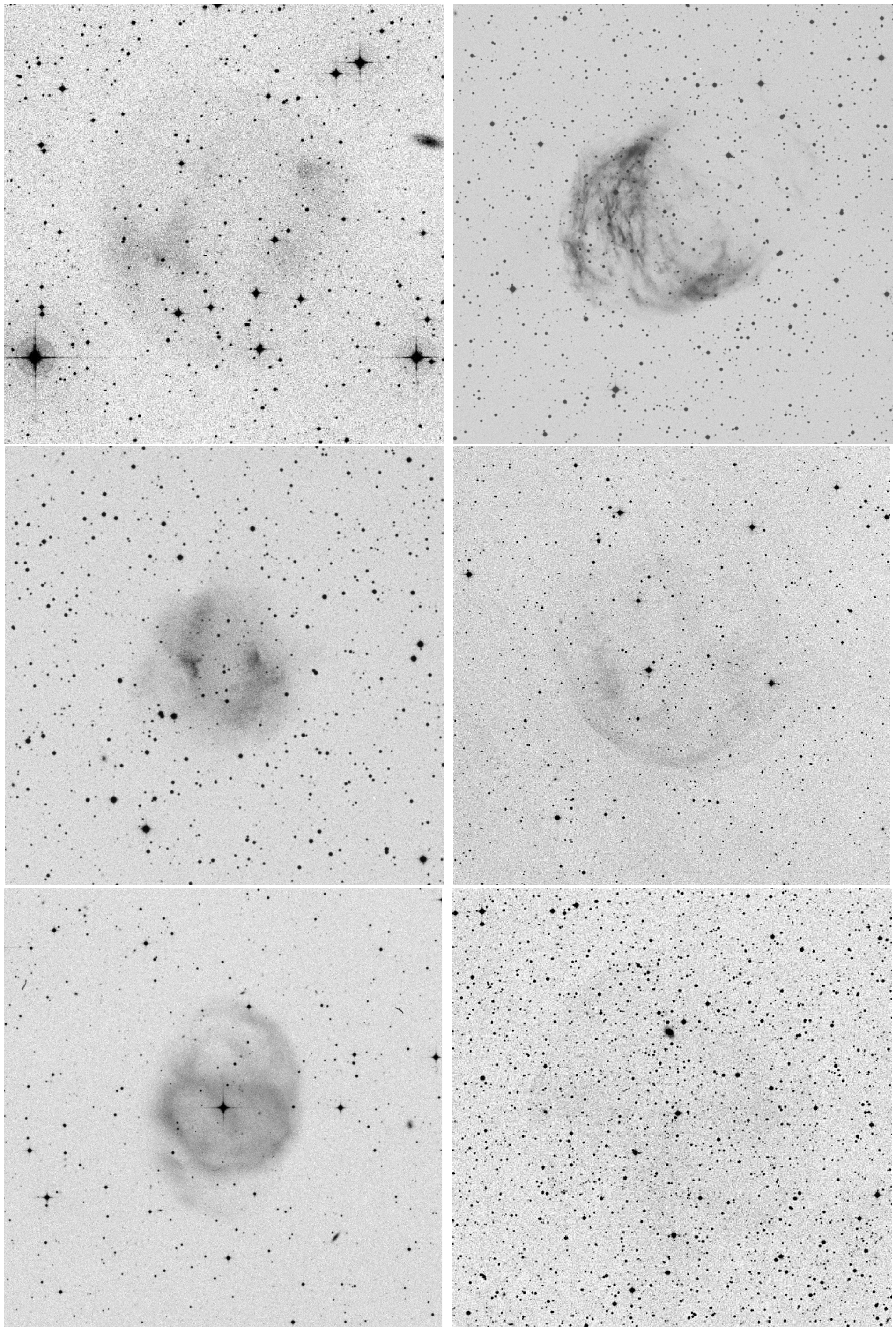

Figure A.2: Six PNe in the solar neighbourhood. Top panel: (L): Abell 7 (R_F image, $20'$ wide). (R): Abell 21 (R_F image, $20'$). Middle panel: (L): Abell 24 (R_F image, $15'$). (R): Abell 31 (R_F image, $30'$). Lower panel: (L): Abell 36 (B_J image, $15'$). (R): Abell 74 (R_F image, $20'$). North is up and east at left in all images.

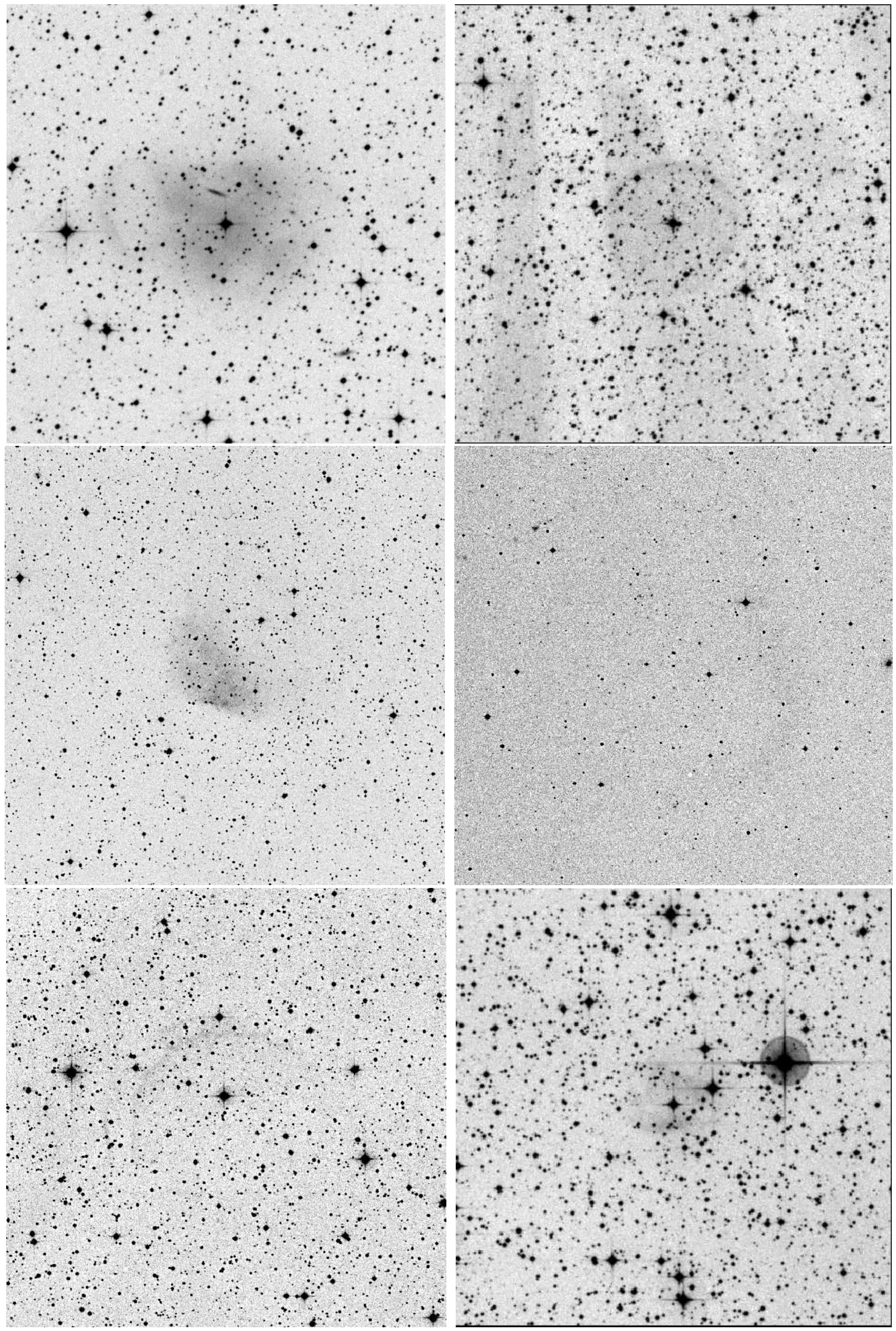

Figure A.3: Six more PNe in the solar neighbourhood. Top panel: (L): DS 1 (B_J image, 10′). (R): DS 2 (B_J image, 10′). Middle panel: (L): EGB 1 (R_F image, 20′). (R): EGB 6 (R_F image, 20′). Lower panel: (L): HaWe 4 (R_F image, 20′). (R): HbDs 1 (B_J image, 10′). North is up and east at left in all images.

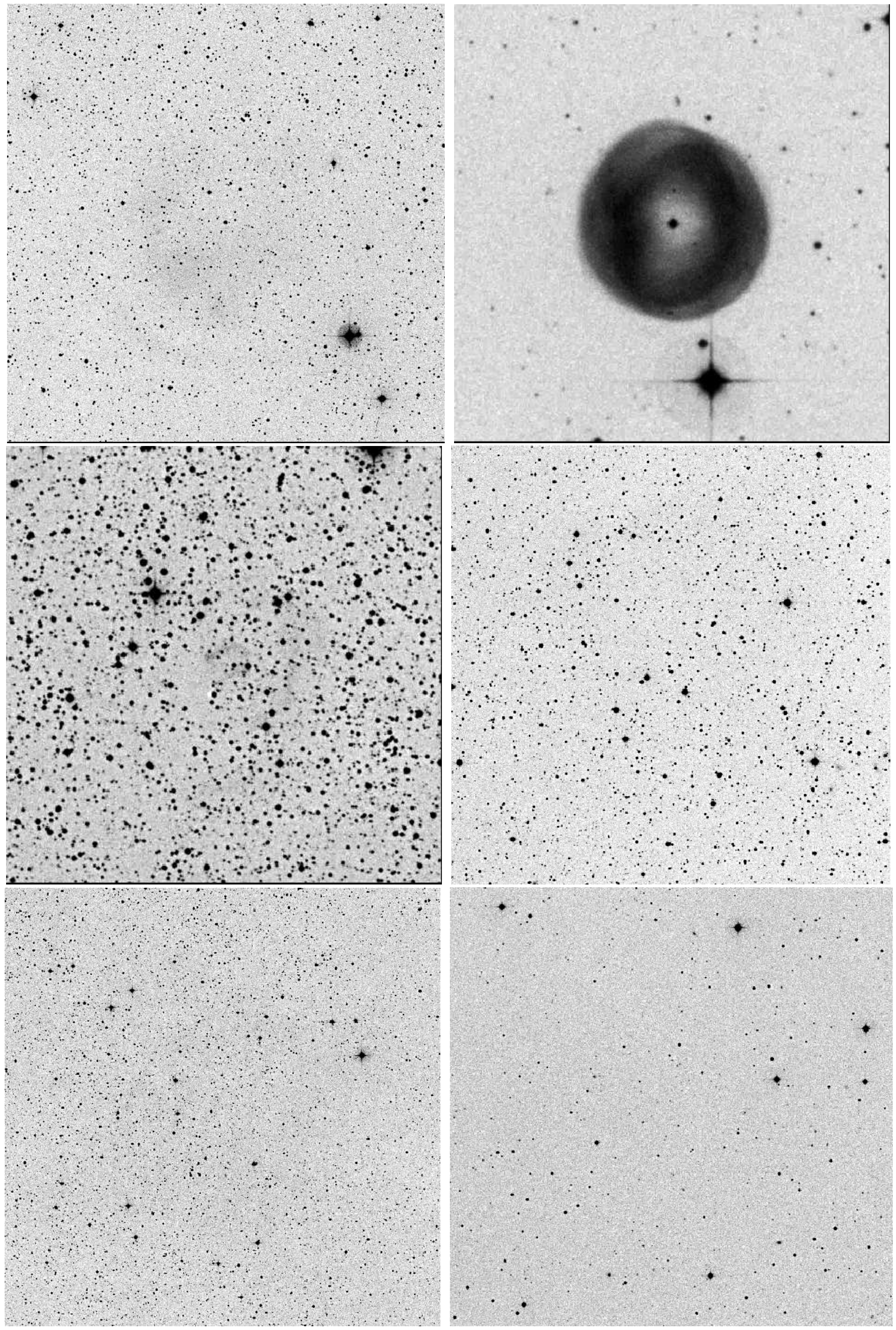

Figure A.4: Six more PNe in the solar neighbourhood. Top panel: (L): HFG 1 (B_J image, $20'$). (R): IC 5148/50 (B_J image, $5'$). Middle panel: (L): IPHAS2050+4655 (R_F image, $10'$). (R): IsWe 1 (R_F image, $20'$). Lower panel: (L): IsWe 2 (R_F image, $30'$). (R): Jacoby 1 (B_J image, $20'$). North is up and east at left in all images.

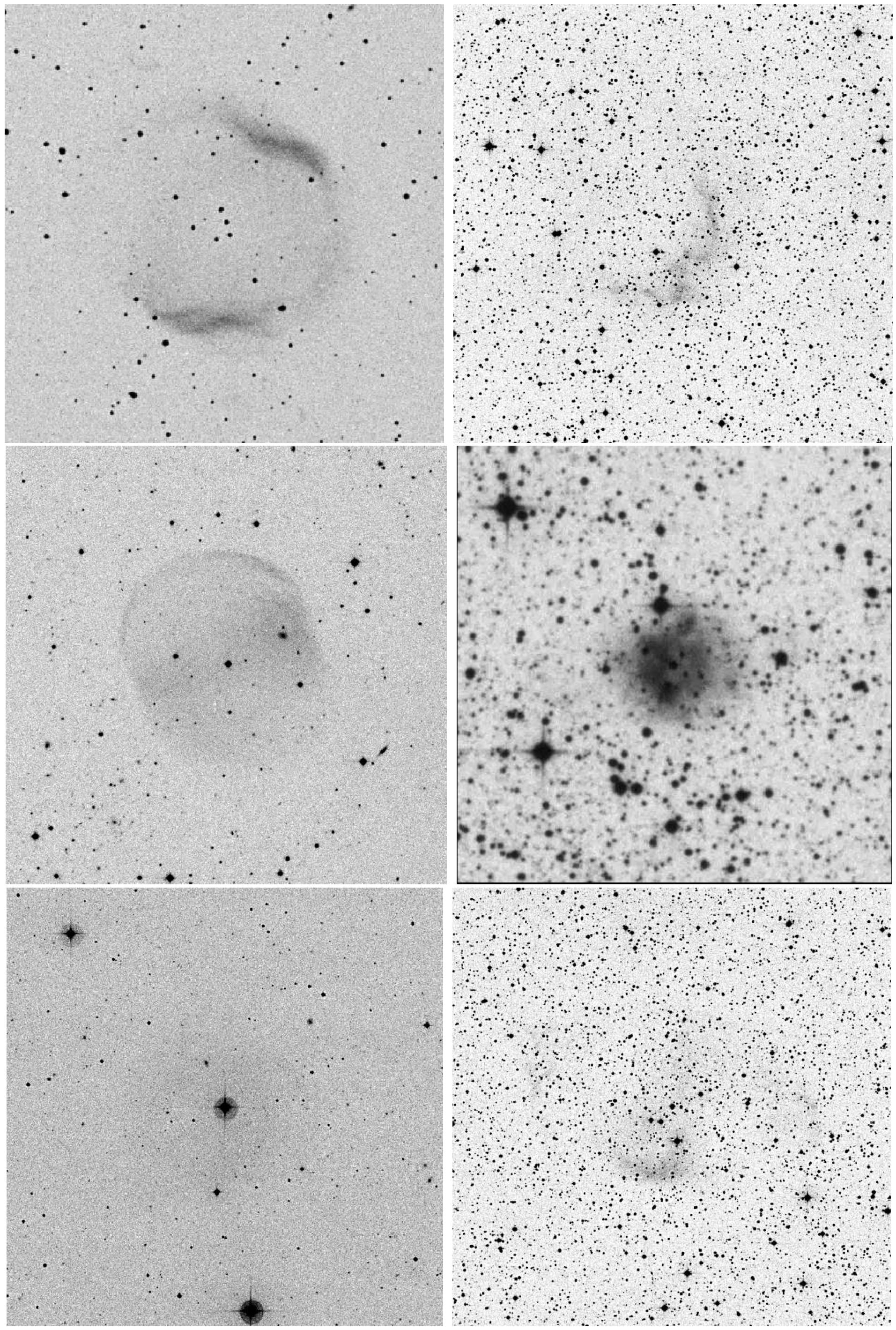

Figure A.5: Six more PNe in the solar neighbourhood. Top panel: (L): Jones 1 (B_J image, 10′). (R): K 2-2 (R_F image, 20′). Middle panel: (L): Lo 1 (B_J image, 15′). (R): Lo 16 (B_J image, 5′). Lower panel: (L): LoTr 5 (B_J image, 20′). (R): MWP 1 (B_J image, 20′). North is up and east at left in all images.

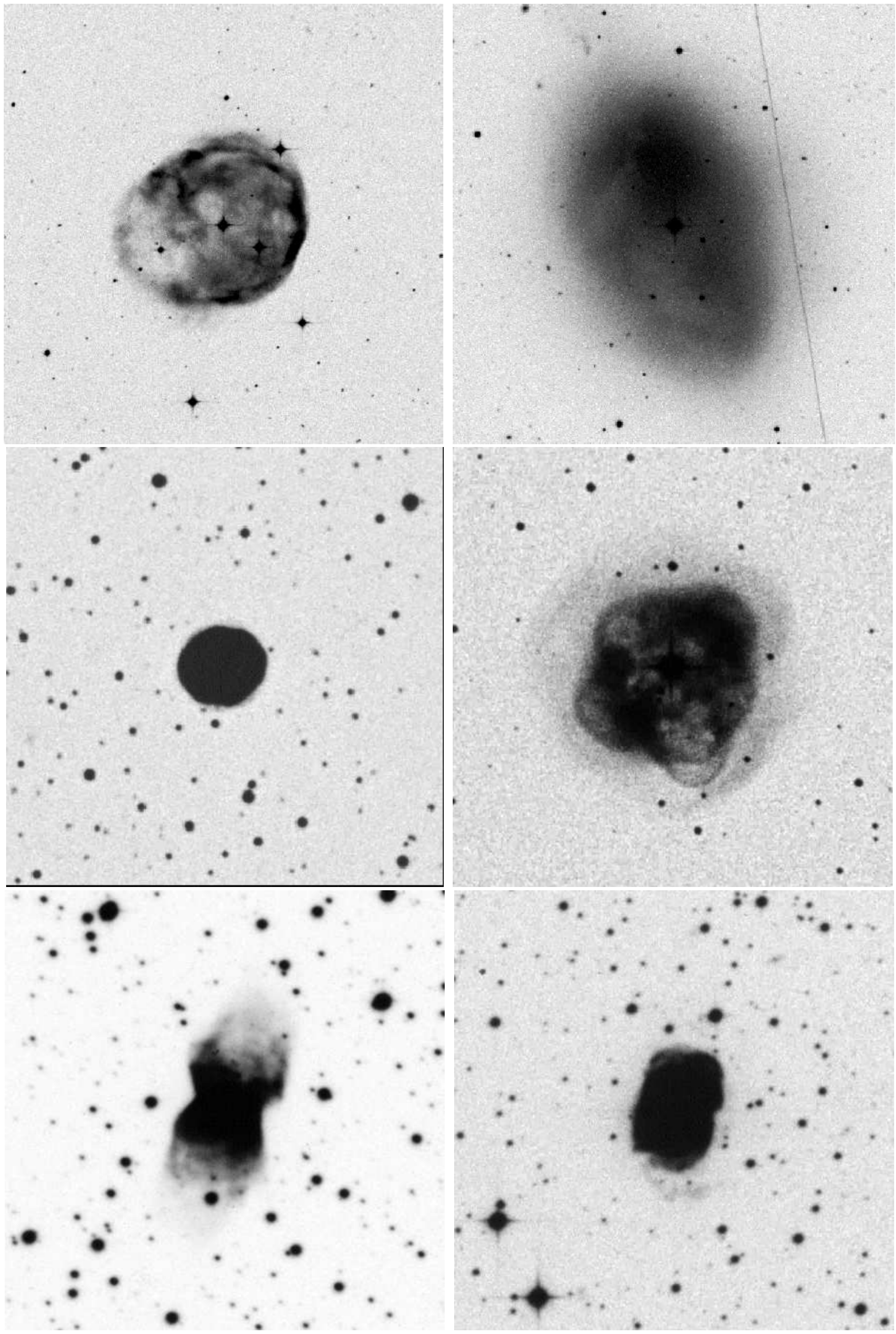

Figure A.6: Six more PNe in the solar neighbourhood. Top panel: (L): NGC 246 (B_J image, $10'$). (R): NGC 1360 (B_J image, $10'$); Middle panel: (L): NGC 1501 (B_J image, $5'$). (R): NGC 1514 (B_J image, $5'$). Lower panel: (L): NGC 2346 (R_F image, $5'$). (R): NGC 3132 (R_F image, $5'$). North is up and east at left in all images.

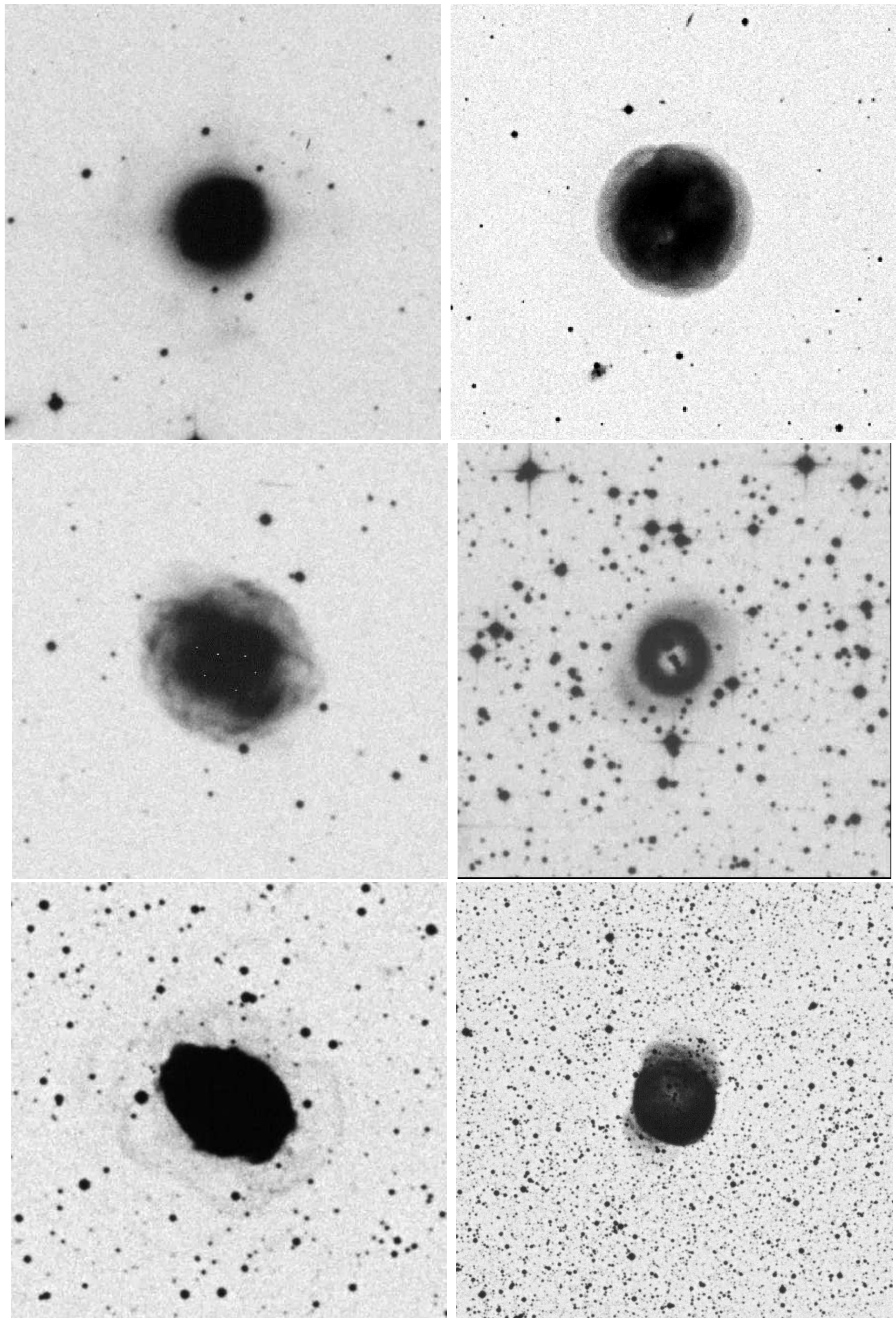

Figure A.7: Six more PNe in the solar neighbourhood. Top panel: (L): NGC 3242 (B_J image, $5'$). (R): NGC 3587 (M 97) (B_J image, $10'$). Middle panel: (L): NGC 4361 (B_J image, $5'$). (R): NGC 6337 (B_J image, $5'$). Lower panel: (L): NGC 6720 (M 57) (R_F image, $5'$). (R): NGC 6781 (R_F image, $10'$). North is up and east at left in all images.

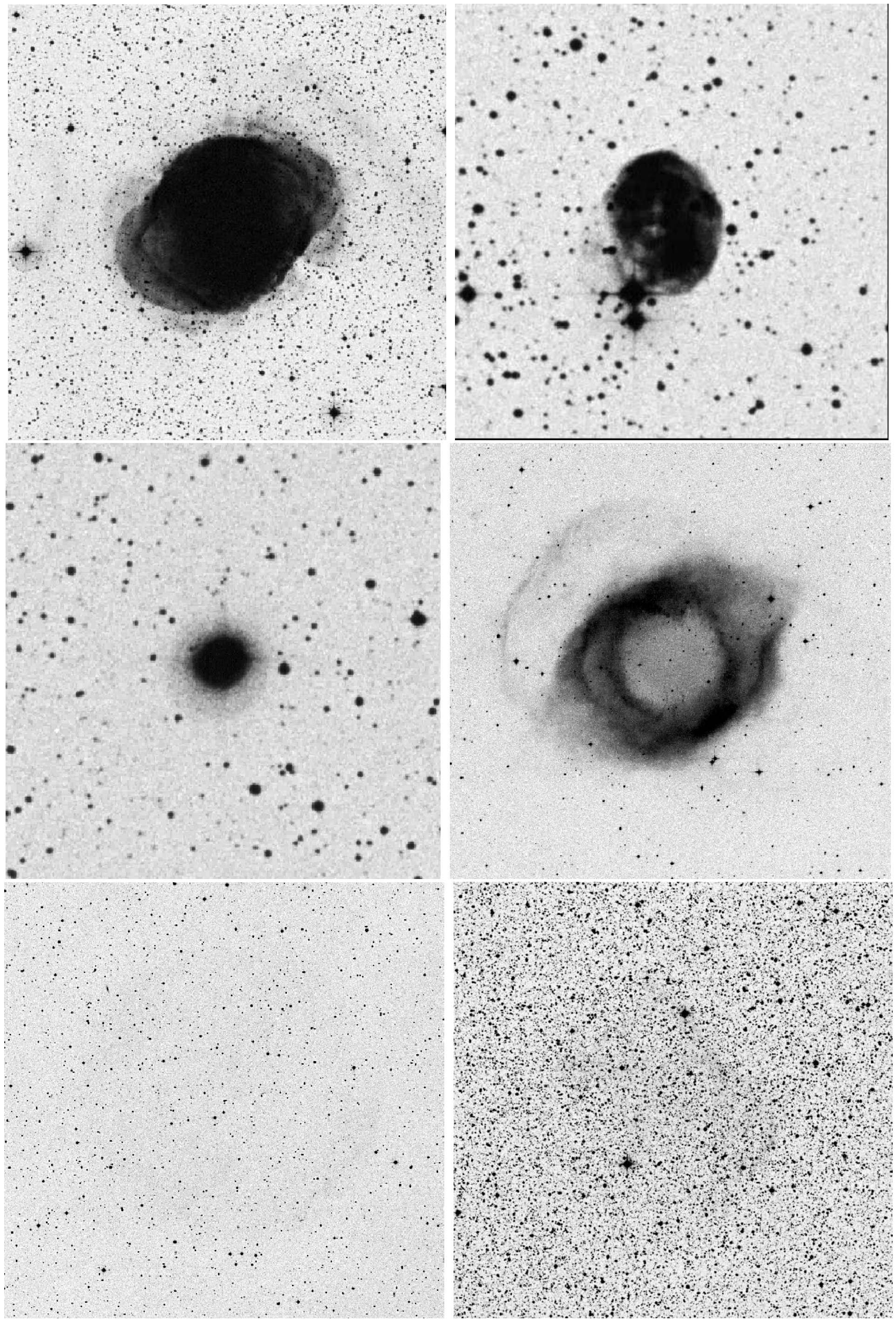

Figure A.8: Six more PNe in the solar neighbourhood. Top panel: (L): NGC 6853 (M 27) (R_F image, 15′). (R): NGC 7008 (B_J image, 5′). Middle panel: (L): NGC 7027 (B_J image, 5′). (R): NGC 7293 (R_F image, 30′). Lower panel: (L): PuWe 1 (R_F image, 30′). (R): Sh 2-78 (R_F image, 20′). North is up and east at left in all images.

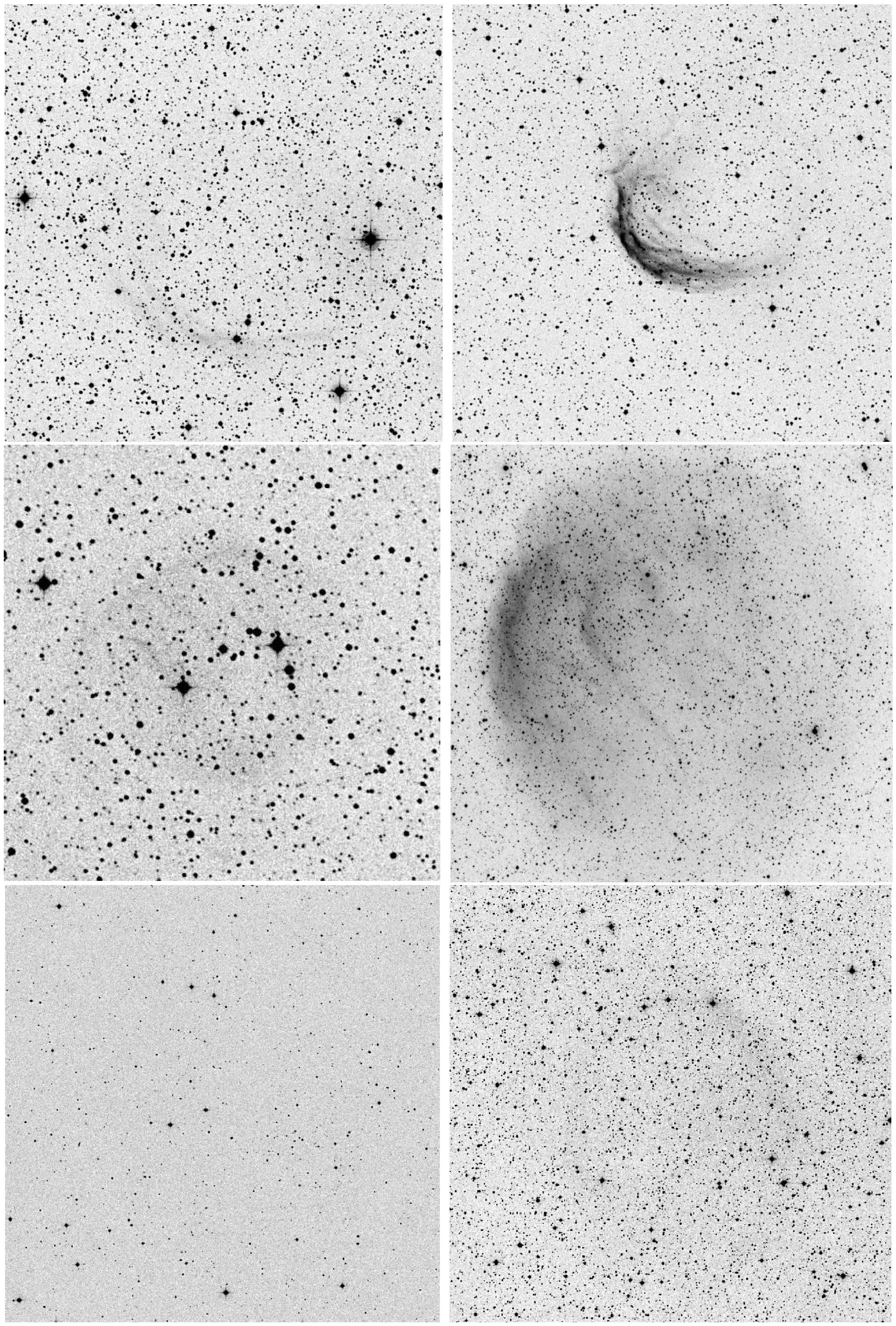

Figure A.9: Six more PNe in the solar neighbourhood. Top panel: (L): Sh 2-176 (R_F image, 20′). (R): Sh 2-188 (R_F image, 20′). Middle panel: (L): Sh 2-200 (B_J image, 10′). (R): Sh 2-216 (Hα image, 100′). Lower panel: (L): Ton 320 (R_F image, 30′). (R): WDHS 1 (R_F image, 30′). North is up and east at left in all images [Image credit for Sh 2-216: Steve Mandel].

Appendix B

New Nebulae from SHASSA, VTSS and WHAM

B.1 Introduction

This appendix includes brief notes on each of the new nebulae found from SHASSA and VTSS data (see Chapter 2), as well as a brief appraisal of some of the higher quality 'WHAM point source' nebulae noted by Reynolds et al. (2005). However, it seems that most are unlikely to be bona fide PNe based on currently available data. Because of the highly interesting nature of the nebula Fr 2-11, a detailed account is presented first.

B.2 Fr 2-11

While not a PN, one object (Frew 2-11) discovered during this study from SHASSA images (see Frew, Madsen & Parker 2006, is of particular interest (see Figure 2.13), and warrants an extended discussion. The size of this new nebula is nearly 10×8 arcmin, but the coarse resolution of the SHASSA data (48 arcsec pixels) precluded any further analysis of its morphology, and it was placed on a list of targets to be imaged in Hα and [O III] with the 2.2-metre ESO/MPEG telescope in May 2004. It is only barely visible on the broadband UKST B_J and R survey plates (Figure B.1).

B.2.1 The Nebula

Images were taken with the wide-field imager (WFI) of the 2.2-metre ESO/MPEG telescope on 27 May 2004, in the Hα and [O III] λ5007 lines (figures B.2 and B.3). The [O III] image in particular shows an extraordinary parabolic bow-shock structure, $\sim$1 arcmin across, with an 11^{th} mag star, V341 Ara, near the apex of the parabola, along the symmetry axis of the nebula. This object is very similar in morphology to Abell 35 (Abell 1966, Jacoby 1981; Hollis et al. 1996) and the 'bow-shock' nebula EGB 4 discovered by Ellis, Grayson & Bond (1984), and which was intially though to be a planetary nebula.

EGB 4 has a remarkable bow-shock morphology (Krautter, Klaas & Radons 1987; Hollis et al. 1992) and is associated with the cataclysmic variable BZ Cam. Abell 35 is traditionally thought to be a PN, albeit a peculiar one (Jacoby 1981; Hollis et al. 1996), but is considered here to be a Strömgren zone in the ISM (see §8.2). As considered below, the nebula around V341 Ara is closely related to EGB 4, and not to be a true PN.

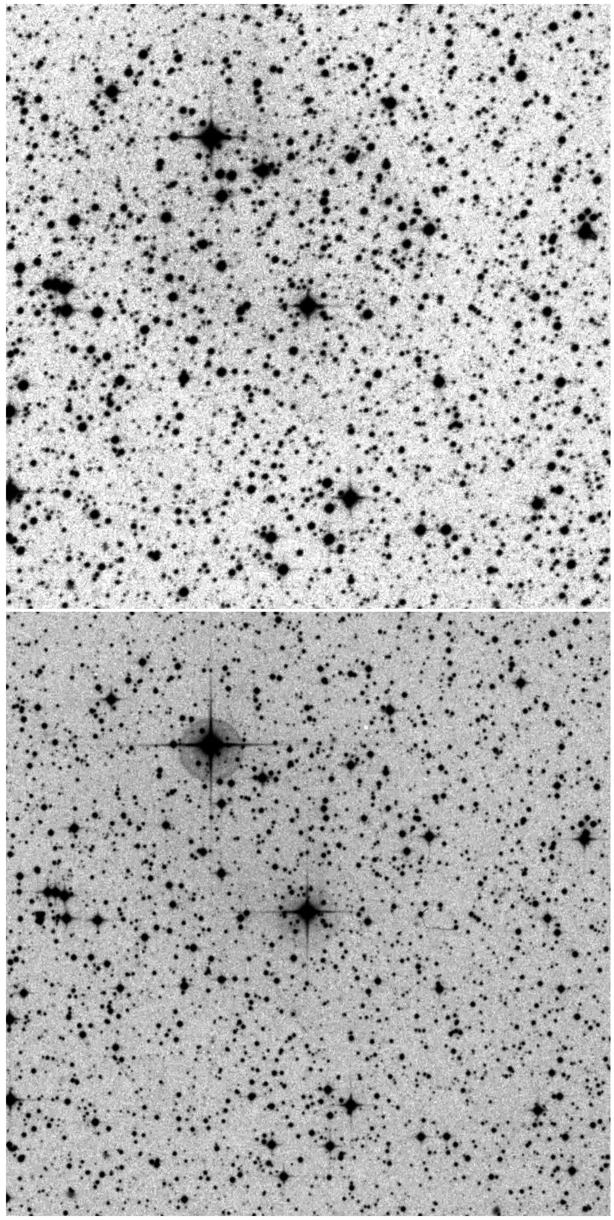

Figure B.1: R-band DSS image (above) and B_J image (below) of the faint nebula around V341 Ara. The star is at centre in these images which are 10 arcmin on a side, with NE at top left. The main body of the nebula extends NE from the star. The bow shock morphology is not apparent on these images.

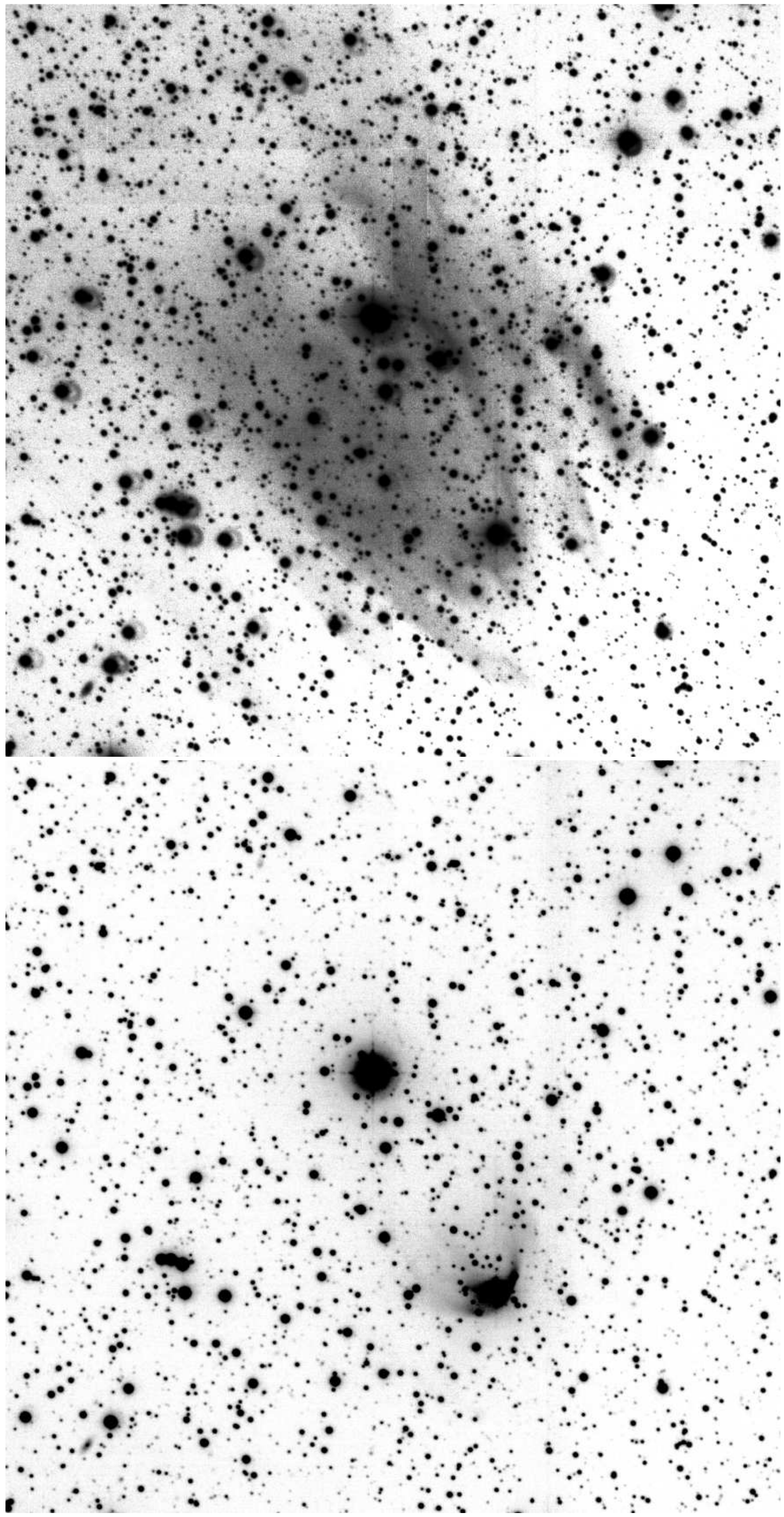

Figure B.2: ESO-MPEG Hα (left) and [O III] (right) images of the nebulosity around V341 Ara, designated Fr 2-11. The [O III] bow shock is restricted close to the star. The brightest star in the field, $3.2'$ northeast of V341 Ara, is HD 152512, which is unrelated. North is at top and east is at left.

Figure B.3: Composite Hα+[O III] two-colour ESO/MPEG image of the new nebula around V341 Ara. The [O III] bow shock is restricted close to the star. The brightest star in the field, 3.2′ northeast of V341 Ara, is HD 152512, which is an unrelated B9 III background star. North is at top and east is at left. Vertical and horizontal linear features in the image are residual structure left over from the mosaicing process. Image reduction by B. Miszalski.

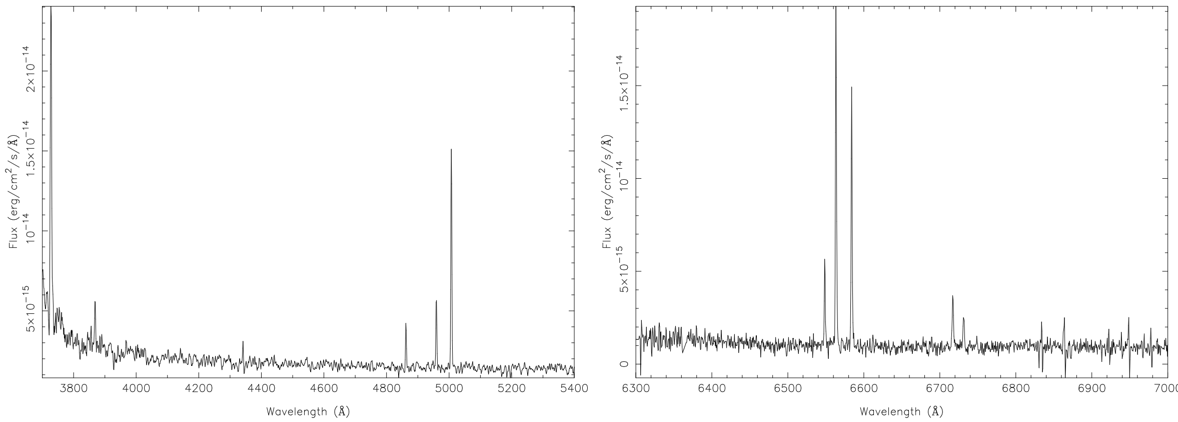

Figure B.4: Flux-calibrated blue and red MSSSO spectra of the bow shock nebula, Fr 2-11.

Spectroscopy

The nebula was observed on the night of July 16, 2004 with the Double-Beam Spetrograph (DBS) on the MSSSO 2.3m telescope. The unvignetted slit length perpendicular to the dispersion was 6.7′ and was oriented north-south, centered 7″ east of V341 Ara; the slit width was set to ∼2.5″. Dome screen and twilight flats were also obtained together with an observation of the spectrophotometric standard star EG 274. Wavelength calibration was applied via Fe-Ar (blue) and Ne-Ar (red) arc exposures bracketing the observation. The spectra were reduced and examined using standard IRAF routines, in conjunction with the add-on utility suite, PNDR (B. Miszalski 2005, pers. comm.). The blue and red MSSSO spectra are illustrated in Figure B.4.

The observed and reddening-corrected line intensities are summarised in Table B.1. The fluxes are normalized to Hβ = 100 and are corrected for reddening using the R = 3.1 galactic reddening law of Howarth (1983). An intrinsic ratio of I(Hα/Hβ) = 2.86 was adopted, after Brocklehurst (1971). The observed logarithmic extinction at Hβ, $c = \log F(H\beta) - \log I(H\beta)$, was found to be 0.06, which leads to $E(B-V) = 0.04 \pm 0.04$ and a total visual absorption, $A_V = 0.13$.

The line ratios in Fr 2-11 are quite similar to those seen in EGB 4 (Krautter, Klaas & Radons 1987; Greiner et al. 2001), Abell 35 (Jacoby 1981, and §8.2) and the central core of CTB 80 (e.g. Blair et al. 1984), suggesting all are dominantly produced by shock-excitation (see below). The strong [O III] emission seen in these bowshock nebulae is nicely explained by the high space motions of their respective stars.

Integrated flux

The SHASSA survey (Gaustad et al. 2001) was used to provide an estimate of the Hα flux from the nebula, following the procedure detailed in Chapter 3. Our long-slit spectra were used to deconvolve the [N II] contribution from the SHASSA 'red' flux determined via aperture photometry with the STARLINK GAIA package. The Hα flux is $\log F$(Hα) = −10.95 through an aperture of 10′, averaged from two SHASSA fields. Using the Hα/Hβ ratio from our spectra, we also quote $\log F$(Hβ) = −11.4.

B.2.2 Ionizing star

The 11th magnitude star behind the apex of the bow-shock nebula is V341 Arae (= CPD −63°4037 = LSE 246 = HIP 83003), currently classified in the SIMBAD database as a Cepheid variable star. Its variability was first discovered a century ago by Henrietta Leavitt from Harvard patrol plates (Pickering

Table B.1: Line fluxes and ratios for the bow shock nebula around V341 Ara.

Line	Wavelength (Å)	F(λ)	I(λ)
[O II]	3727	952::	987::
[Ne II]	3869	114:	118:
Hγ	4340	48	48
[O III]	4363	17:	17:
Hβ	4861	100	100
[O III]	4959	169	168
[O III]	5007	528	525
[N II]	6548	65	62
Hα	6563	299	286
[N II]	6584	214	205
[S II]	6717	57	54
[S II]	6731	36	35
[Ar III]	7136	26	24
[O III]/Hβ	...	...	6.93 ± 0.20
[N II]/Hα	...	...	0.93 ± 0.05
[S II]/Hα	...	...	0.31 ± 0.05
[S II] 6717/6731	...	...	1.56 ± 0.08

F(Hβ) = 1.05 $\times 10^{-14}$ erg cm^{-2} s^{-1}, c(Hβ) = 0.06

: Denotes higher uncertainty.

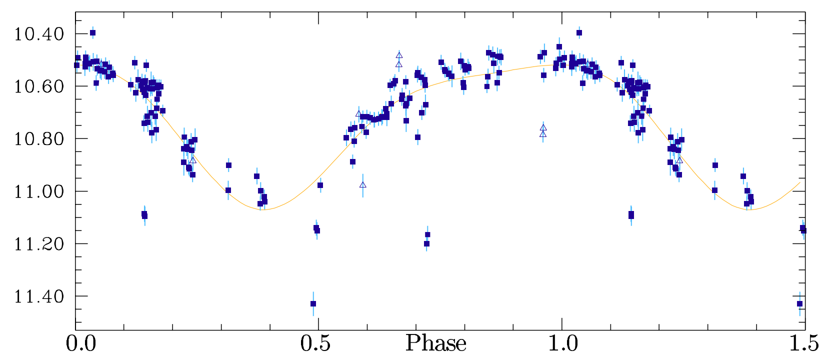

Figure B.5: The light curve for V341 Ara based on Hipparcos data. The phase is keyed to the nominal period of 10.919 d.

1907) though the star was basically ignored for half a century thereafter. Hoffmeister (1956) used new photographic and visual observations to classify the star as a Cepheid, determining a period of 11.95 days. These parameters were adopted by the General Catalogue of Variable Stars (GCVS) and hence by Simbad.[1]

The star was extensively observed by the Hipparcos satellite, and a period of 10.919 days is given in the variability annex (ESA 1997), where a CWA (W Virginis) classification is assumed. The magnitude range given is $m_{\mathrm{HIP}} = 10.52 - 11.07$. However, the Hipparcos data indicate a quasi-periodic light curve that is atypical for a Cepheid, illustrated here as Figure B.5. Note the significant number of points that do not phase up with the remainder.

Berdnikov & Szabados (1998) obtained photoelectric VI observations and derived a revised period of 14.11 days. These authors folded the Hipparcos data with the 14.11 day period but the scatter in their magnitude versus phase diagram is considerably worse. They suggested the light curve was consistent with its status as a Type II Cepheid, even though their $\langle V - I \rangle$ colour index is not consistent with this classification.

[1] Samus, Pastukhova & Durlevich (2007) have recently noted that this star is a possible CV.

Table B.2: Summary of literature photometry for V341 Ara

Waveband	Magnitude	Source
B_T	10.631	Tycho
V_T	10.675	Tycho
V	10.747	Berdnikov & Szabados (1998)
V	10.739	ASAS
m_H	10.609	Hipparcos
I_C	10.610	Berdnikov & Szabados (1998)
J	10.448	2MASS
H	10.379	2MASS
K	10.290	2MASS

Table B.3: Quasi-periodicities for V341 Ara.

Mean Date JD − 2400000	Frequency (c/d)	Period (d)	Source
48404.2	...	10.919	Hipparcos
50908.8	...	14.110	BS98
52067.0	0.105311	9.496	ASAS
52485.0	0.087351	11.448	ASAS
52813.1	0.079366	12.600	ASAS
53139.4	0.068650	14.567	ASAS
53425.8	0.061193	16.342	ASAS

The star is also included in the ASAS-3 Catalogue (All Sky Automated Survey; Pojmanski 2001). The derived mean magnitude from ASAS-3 is $V = 10.743 \pm 0.188$ (1σ) from 325 measurements (data retrieved December 2005). However, it is not listed in the ASAS variable star catalogue of Pojmanski (2003). A summary of the available literature photometry is presented in Table B.2.

Additional photoelectric observations were made with the ANU 1.0-m reflector at Siding Spring Observatory on the nights of Apr 12–13, 2005. A preliminary reduction (mags in the instrumental system) gave V =10.62, $B - V = 0.00$, $U - B = -0.78$. The colours are typical of other nova-like CVs (e.g. Bond & Landolt 1971; Garrison et al. 1984). Note also that the photometry of Berdnikov & Szabados (1998) shows a small but definite colour change with phase, with $V - I$ increasing at minimum.

A period analysis was attempted for each of the various data sets using the software Period04 (Lenz & Breger 2004). Owing to sampling problems and seasonal gaps, separate Fourier analyses were performed for each season of data. Since the light variations are not sinusoidal, the power spectra are noisy. Table B.3 shows the derived quasi-periods for each yearly ASAS data set. The FT frequencies are weak and the phase diagrams are ambiguous, showing that the lightcurve is only quasi-periodic, and not indicative of binary motion. However, there is also evidence of a long period evident in the data subtending over the last decade.

To determine the orbital period of V341 Ara, time-series photometry by D.J. Frew in the Cousins I-band was undertaken with the 61 cm Perth-Lowell Automated Telescope, at Perth Observatory, on three nights in August 2006. The data were reduced by A. Williams using the DoPHOT PSF-fitting routine (Schechter, Mateo & Saha 1993), running under the PLANET pipeline. Figure B.6 shows 5.3 hours of data from the night of 2006 Aug 29/30. Characteristic flickering with a period of $\sim$ 30 min was observed on all three nights, but unfortunately, we cannot extract the expected orbital period of a few hours from the present data, so more time-series photometry is needed. Time-resolved spectroscopic observations have also been commenced with the SMARTS 1.5m telescope in Chile. This should allow a definitive determination of the orbital period (Bond & Miszalski 2008, in preparation).

The light-curve, along with other evidence presented here, clearly classes the star as a nova-like CV.

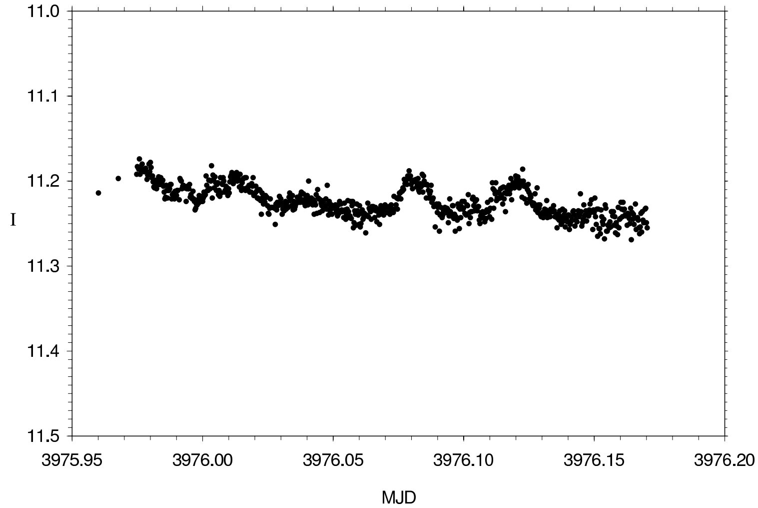

Figure B.6: *I*-band time-series photometry of V341 Ara taken with the 61 cm Perth-Lowell Automated Telescope, at Perth Observatory, on 2006 Aug 29/30. Magnitudes are in the instrumental system.

The quasi-periodic modulations are probably an example of the 'stunted' outbursts seen in other novalike CVs (Honeycutt, Robertson & Turner 1998; Honeycutt 2001). The mechanism for these modulations is still uncertain, but may be due to episodes of enhanced mass transfer, a variable hot spot, or a precessing accretion disk.

Spectroscopy

Drilling & Bergeron (1995) classified the star as 'OB' based on plates taken with the Curtis Schmidt telescope and a 4° objective prism. The observation was made as part of an extension of the Case-Hamburg OB-star surveys. The nominal $B - V$ colour index of the star is in agreement with the OB classification.

MSSSO DBS spectra were obtained on the night of July 12, 2004 (see Chapter 5 for more details of the reductions). The star shows broad Balmer absorption lines to H10 with emission cores observed to H8, and double emission cores seen in the H9 and H10 absorption lines. At Hα the emission core has almost filled in the absorption line. Absorption lines due to Ca II and He I are also present and weak emission cores are visible in the λ 4471, 4388 and 4026 He I lines. On the basis of these spectra, we consider the star to be a previously unnoticed novalike variable of the UX UMa subclass. The spectrum is very similar to other high-state nova-like variables such as RW Sex and V3885 Sgr. The blue spectrum is shown as Figure B.7.

Distance and Luminosity

The distance is rather uncertain. The revised Hipparcos parallax (van Leeuwen 2007) is 6.14±1.81 mas, leading to a distance of 163^{+231}_{-37} pc. At the upper limit of ∼394 pc, the derived space motion (§3.3) is unlikely for a disk star, Furthermore, as the star has old-disk kinematics (its proper motion vector is fairly parallel to the galactic plane), the space motion is probably less than ∼130 kms^{-1} (e.g. Skuljan, Hearnshaw & Cottrell 1999), which puts a useful upper bound on the distance estimate.

The asymptotic line-of-sight reddening is $E(B - V) = 0.144$ ($A_V = 0.48$ mag) from the extinction maps of Schlegel, Finkbeiner & Davis (1998). The reddening of HD 152512, 3.2′ NE, is only $E(B - V) = 0.10$ at D ∼ 0.9 kpc. For V341 Ara, we adopt $E(B - V) = 0.04 \pm 0.04$, from the nebular Balmer decrement. Unfortunately, the very low extinction along the line of sight precludes the calculation of

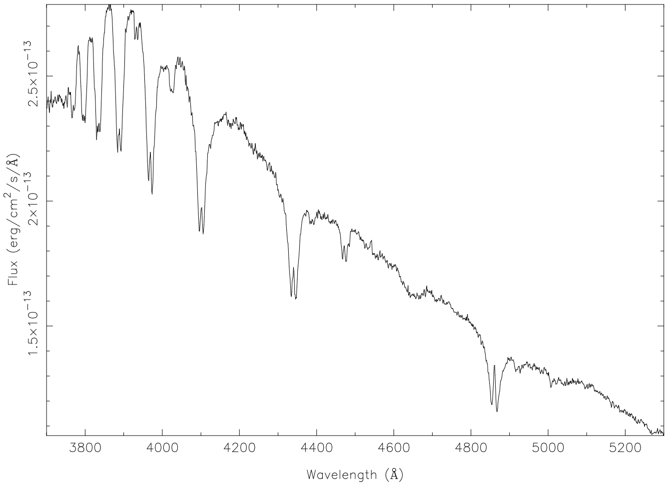

Figure B.7: MSSSO blue spectrum of the nova-like variable, V341 Ara. Note the broad Balmer absorption lines with emission cores observed to H10.

Table B.4: Proper motion of V341 Ara

Survey	μ_α mas yr^{-1}	μ_δ mas yr^{-1}
Hipparcos	-49.19 ± 2.49	-85.79 ± 2.32
Tycho-2	-46.6 ± 3.0	-82.5 ± 2.9
UCAC2	-48.4 ± 1.7	-83.7 ± 1.9
USNO-B	-48 ± 4	-84 ± 4
SSS	-54.86 ± 11.22	-100.4 ± 11.06

a meaningful extinction distance. For the discussion that follows, we adopt a distance of 200 $\pm$ 50 pc, which gives V341 Ara an absolute magnitude of $M_V = +4.0$, a representative value for novalike variables, nova remnants, and dwarf novae at maximum (e.g. Wade & Ward 1985; Warner 1987, 1995).

Space motion

The revised Hipparcos catalogue (van Leeuwen 2007; cf. ESA 1997) gives a significant proper motion for V341 Ara, in accordance with the values in the Tycho-2 (Høg et al. 2000), UCAC2 (Zacharias et al. 2004), and USNO-B1.0 (Monet et al. 2003) catalogues. The proper motion data are summarised in Table B.4, where the errors on the USNO motions have been set to ± 4 mas yr^{-1} following Gould (2003). The δ component of the proper motion as measured by the SuperCOSMOS Sky Survey (Hambly et al. 2001), is in mild disagreement. Owing to the concordance of the other values, we have confidence in their accuracy, and we adopt the Hipparcos proper motion hereafter, viz. 98.9 mas/yr in p.a. 215°.

At a distance of 200 pc, then the transverse velocity component (relative to the Sun) is $\sim$90 kms^{-1}. Assuming a radial velocity of zero (the morphology of the bowshock is suggestive that most of the motion is in the plane of the sky), the space motion with respect to the local standard of rest is $\sim$75 kms^{-1}.

Discussion

V341 Ara is considered to be a previously unknown, bright nova-like cataclysmic variable, and is one of the very brightest of its class. Only IX Vel, V3885 Sgr and possibly RW Sex have mean V magnitudes that are brighter (e.g. Hartley et al. 2002). Table B.5 compares the properties of the brightest nova-like

Table B.5: Summary of properties of the brightest nova-like variables. For comparative purposes, the *mean* V magnitudes have been retrieved from the ASAS-3 database. Distances are taken from the available literature.

Name	$<V>$	Period (hr)	Distance (pc)
IX Vel	9.6	4.654	96
V3885 Sgr	10.2	5.191	110
RW Sex	10.6	5.882	(180)
V341 Ara	10.7	?	165
TT Ari	11.0	3.301	(300)
QU Car	11.4	10.90	$\geq$500

variables.

V341 Ara shows marked quasi-periodic variations. However, it is unclear what the 9–16 day quasi-period is representing. The best guess is that these variations represent the 'stunted' eruptions seen in a few other CVs by Honeycutt et al. (1998) and Honeycutt (2001). The 2MASS data only provides marginal evidence for a late-type component in the system. The dereddened $J - H$ and $H - K_s$ colour indices are quite similar to other NL variables (see Figure 5 of Hoard et al. 2002) in which the integrated light is dominated by the accretion disk. There is also an associated ROSAT X-ray source, designated 1RXS J165743.7-631237 (Voges et al. 1999). The hardness indices are HR1 = 0.48±0.28 and HR2 = 0.11±0.36, consistent with other CVs in the ROSAT PSPC All Sky Survey (Motch et al. 1996; Verbunt et al. 1997). The association of the X-ray source with V341 Ara has been independently noted by Samus, Pastukhova & Durlevich (2007); these authors tentatively classified this star as a CV.

Following the procedure outlined in §9.3.4, the ionized mass of the main body of the nebula is found to be $\sim$0.005 $M_\odot$, much less than the canonical PN mass of $\sim$0.2 $M_\odot$. There may be objections to this approach, but as a point of comparison, note that the Helix nebula (NGC 7293) is at a similar distance as this object but has a Hα flux $\sim 100\times$ higher, so the mass estimate is probably reasonable. In fact the mass is more in line with the mass of an old nova shell (e.g. Cohen & Rosenthal 1983), though our slit spectra of the nebula show no evidence for a large line-width. In summary, Fr 2-11 is not considered to be a PN for the following reasons:

1. the nebular ionized mass is nearly two orders of magnitude less than is typical for an evolved PN;
2. the dereddened $U - B$ and $B - V$ colours of the star are not blue enough for a PN nucleus (unless it is a unresolved binary), but are instead consistent with other nova-like variables. Importantly, it shows characteristic flickering on short time-scales;
3. V341 Ara has a typical nova-like CV spectrum, and there is an associated ROSAT X-ray point source with hardness indices consistent with other nova-like CVs.

The overall body of evidence suggests this is a rare bow shock nebula probably analogous to EGB 4. As is seen in Abell 35, there is no forward bowshock in Fr 2-11 at the SE edge of the Hα emission region. Also, the velocity of the nebular gas is close to zero with respect to the LSR, so it is assumed to be ambient gas. The interpretation adopted here is that Fr 2-11 is a small low-excitation HII region photoionized by the system's accretion disk and/or the hot WD. The accretion-disk wind forms a bow shock with the ISM as a result of the star's significant space motion. So far only one bona fide CV, BZ Cam (Krautter, Klaas & Radons 1987; Hollis et al. 1992), had been known to be associated with a prominent bow shock nebula.

Like the nebula around BZ Cam, the nebular morphology of the bow wave associated with V341 Ara can be considered as a paraboloid of revolution. The orientation of the parabolic axis, as measured from the [O III] image, is p.a. 213°± 4°, and this agrees perfectly with the orientation of the proper motion vector of the star. Furthermore the strong [O III] emission is nicely explained by the high space motion of ∼80 $\mathrm{kms^{-1}}$. BZ Cam was the first CV to have a wind signature evident in its *optical* spectrum (Ringwald & Naylor 1998), so high resolution time-resolved spectroscopy may reveal the same features in V341 Ara (see the discussion by Kafka & Honeycutt 2004).

Some physical parameters for V341 Ara can be estimated from our 2.2-m MPEG [O III] image (figure B.2), following the procedure outlined in §8.2, regarding Abell 35. Considering figure 8.1 we define a standoff distance, l_2, which is the distance from the stellar system to the stagnation point, or apex of the observable bow wave (see figure 8.1). The quantity l_1, which is the distance from the star to the terminal wind shock front, is not observable as the shocked wind does not produce any optical emission. The angular thickness of the [O III] bow shock, Δr, was measured $\sim 6''$ from the [O III] CCD image. The standoff distance, l_2 is $11'' \pm 1''$, hence the the contact discontinuity distance is $l_c = l_2 - r = 5'' \pm 1''$ (see figure 8.1). At the adopted distance of V341 Ara, $l_2 = 3.3{\times}10^{16}$ cm, and $l_c = 1.5{\times}10^{16}$ cm.

For V341 Ara, $v_{\rm rel} = 75$ $\mathrm{kms^{-1}}$ which is sufficient to produce observable [O III] emission. For a normal oxygen abundance, shock speeds of >60 $\mathrm{kms^{-1}}$ are needed to produce significant [O III] emission (Shull & McKee 1979). We estimate an ISM electron density of 10 $\mathrm{cm^{-3}}$ using the observed Hα surface brightness of the surrounding emisson nebula. Using equation 8.7, we calculate a wind power, $L_w \sim 4 \times 10^{32}$ $\mathrm{erg\,s^{-1}}$ for the V341 Ara system. Similarly, using equation 8.8, and substituting l_c for l_1 as before (see §8.2), an upper limit for the mass loss rate, $\dot{m} \lesssim 1.6 \times 10^{-10}$ $M_\odot\,\mathrm{yr^{-1}}$ is found, a rate which is typical for similar CVs (Klare et al. 1982). A lower limit for the terminal wind velocity can also be estimated. The value derived here, 2700 $\mathrm{kms^{-1}}$, is again typical of CVs (Hollis et al. 1996; Ringwald & Naylor 1998; Kafka & Honeycutt 2004).

Summary

V341 Ara is a previously unnoticed CV at a distance of about 200 pc. It was shown to be a novalike (UX UMa) variable on the basis of its dereddened $U - B$ and $B - V$ colours, characteristic flickering on short time-scales, typical nova-like CV spectrum, and an associated ROSAT X-ray point source with hardness indices consistent with other nova-like CVs.

The nebula Fr 2-11 is a bowshock nebula analogous to EGB 4, only the second member of its class. The surrounding HII region is considered to be ambient ISM since the velocity of the nebular gas is close to zero with respect to the LSR, and there there is no forward bowshock at the SE edge of the emission region. The interpretation adopted here is that Fr 2-11 is a small low-excitation HII region photoionized by the system's accretion disk and/or the WD. In the case of V341 Ara, the accretion-disk wind forms a bow shock with the ISM which is moderately dense here; the strong [O III] emission is a result of the star's significant space motion of 75 $\mathrm{kms^{-1}}$.

There is other evidence for moderately dense ISM in this region. The area has been mapped at radio wavelengths by Combi, Romero & Benaglia (1998). The V341 Ara nebula seems coincident with a brighter section of a large, ring-shaped radio nebula (see also Combi & Romero 1995). This may be associated with the γ-ray source 2EGS J1703-6302 (Thompson et al. 1996), and is postulated to be an old supernova remnant in interaction with an H I cloud. Note that V341 falls within the 95% confidence error ellipse contour for the γ-ray source, but this is very likely a line-of-sight coincidence. Further studies of V341 Ara and its nebula are urged.

B.3 Other SHASSA/VTSS objects

A data summary for these nebulae was presented as table 2.3. The bow shock nebula Fr 2-11 has been discussed in detail above. The discovery images are presented in figures 2.13, 2.14 and 2.15.

Fr 2-1 (Fr 0102 − 6118). This an extremely faint and diffuse emission nebulosity of very low emission measure, though quite isolated. A slit spectrum obtained with the 2.3m ANU telescope on 2004 July 16, shows very faint Balmer emission lines, but no [O III]. A search for a blue star within the nebula using blue, red and infrared DSS images was not successful, so little more can be said about this object at this stage.

Fr 2-2 (Fr 0240+1021, WPS 53). This is a potential new large PN discovered from SHASSA survey and was independently noted in the WHAM point source catalogue (Reynolds et al. 2005). There is a fairly bright star, HD 16686, located near the centre of the apparent nebulosity, but it is uncertain if this star is related to the nebula. Published photometry of HD 16686 from SIMBAD is $V = 9.09$, $B - V = 0.10$. The spectral type, A0, is from the HD catalogue and cannot be used to derive an accurate reddening. However, the asymptotic reddening (Schlegel, Finkbeiner & Davis 1998), $E(B-V) = 0.16$, is quite high for a Galactic latitude of $-43.5°$. An ionizing source is yet to be identified, though the absence of [O III] emission suggests a relatively cool ionizing field ($T_{\rm eff} \leq 30{,}000\,$K). The radial velocity from new WHAM data is $V_{\rm LSR} = +12.3$ kms^{-1} from the [N II]λ6584 line, and the line full-width at half maximum ($2v_{\rm exp}$ $\simeq 23 \pm 4$ kms^{-1}), is significantly less than the average width seen in evolved PNe, suggesting the nebula is ionized ISM.

Fr 2-3 (Fr 0456-2755). This is a rather isolated emission nebula of low emission measure. The radial velocity from new WHAM data is $V_{\rm LSR} = +11 \pm 3$ kms^{-1}, averaged from the Hα, [O III] and [N II] lines. The line width at half maximum ($v_{\rm exp} \simeq 9 \pm 3$ kms^{-1}), in conjunction with the systemic velocity, again suggests the nebula is ionized ISM. A likely ionizing source is RE J0457-281 = MCT 0455-2812, a DA white dwarf with $V = 13.95$ (Barstow et al. 1994a, 2003b). These authors determine $T_{\rm eff} = 67{,}000\,$K and $\log g = 8.00$ cms^{-2} from Lyman line profile fitting. With this temperature, the star has a cooling age of 10^6 yr (Bergeron, Wesemael & Beauchamp 1995), which means it is far too old to retain a remnant PN. A gravity distance of $\sim$100 pc was determined following the principles outlined in §6.4.6, consistent with the estimate of Holberg, Barstow & Sion (1998).

Bannister et al. (2003) measure a velocity (converted from heliocentric to the LSR frame) of $V_{\rm LSR}$ $= -4.4 \pm 2.1$ kms^{-1} for the interstellar absorption features in the IUE spectrum of the star, identical within the errors with the measurement of Holberg, Barstow & Sion (1998). Both papers note the large velocity difference of $\sim$50 kms^{-1} between the interstellar and photospheric absorption features. The relatively strong [O III] emission measured with WHAM ([O III]5007/Hα= 1.23, see table 3.9) is consistent with an ionizing source of the effective temperature estimated by Barstow et al. (2003b). Dixon, Sankrit & Otte report a 3σ detection of O II λ1032 towards this star. The emitting gas has $V_{\rm LSR} = -12 \pm$ 9 kms^{-1}, broadly consistent with the IUE and WHAM data. This nebula is considered to be ionized ISM.

Fr 2-4 (Fr 0711-8203). This far southern emission region is also very diffuse, with a brighter region about 25′ across centred at $\alpha, \delta = 07^{\rm h}11.5^{\rm m}$, $-82°03'$, with a faint loop like extension to the SW; the overall dimensions are about $90' \times 60'$. A search using the USNO-B catalogue failed to find a convincing ionzing source for the emission nebula. A spectrum (20 minute exposure) on 2004 July 16, with the DBS on the 2.3m ANU reflector, showed possible Hα and Hβ line emission, but no [O III]. The ionizing source is probably fairly cool, making this a very poor candidate for a fossil PN.

This emission nebula was first thought to be coincident with a faint, bifurcated nebulosity reported over 50 years ago by de Vaucouleurs (1955a). It was found using an Aero-Ektar f/2.5 camera of 7-inch focus, with Kodak 103a-E plates as the detector, behind a Parra-Mantois VR2 glass filter to pass red light including Hα. From long-exposure plates two nebulosities were detected; one, an elongated nebula measuring 3° by 1°, and centred at $8^{\rm h}00^{\rm h}$ $-80°$ [1950], is broadly consistent in position with a filamentary emission feature seen on SHASSA image 004. The other, centred at $7^{\rm h}40^{\rm h}$ $-78°$ and apparently surrounding θ Mensae, is not seen on SHASSA images; this feature may be primarily due to reddened galactic cirrus. Indeed, extensive reflection nebulosity is found over the south polar cap, as noted by de Vaucouleurs (1960), Danziger et al. (1974) and King, Taylor & Tritton (1979).

Fr 2-5 (Fr 0810-6727). This is a large, diffuse, rather one-sided nebula with a fairly sharp eastern edge. No ionizing source is known, and it is tentatively classified as a HII region, pending a detailed spectroscopic and imaging investigation.

Fr 2-6 (Fr 0840-5754, FP 0840-5754). A discussion of this isolated PN candidate (Parker et al. 2006a) was presented in §A.2.

Fr 2-7 (Fr 1054-7011, FPM 1054-7011). Like the preceding object, this was also found on blocked-down SHS images in the overlap zone between the SHS and SHASSA surveys. It is also located in a region with little obvious obscuration or evidence of star formation (see figure 2.13). It may be a small HII region in the ambient ISM ionized by a hot WD, or an example of a so-called 'lazy PN', with a low-mass, slowly-evolving central star (see §1.7). Such an object may not show an obviously PN-like morphology (i.e. lack of a well defined rim), due to the late onset of the fast stellar wind. This nebula has a faint blue star within (see Miszalski et al. 2008), however, further work is needed to elucidate its true nature.

Fr 2-8 (Fr 1400-5102, AM 1357-504, LEDA 49877). This small nebula, about 2′ across, was found serendipitously from SHASSA field 057, while measuring a Hα flux from the nearby PN MeWe 2-4, and has been confirmed spectroscopically as a high-excitation PN, with the 2.3m MSSSO telescope. The position is coincident with the SIMBAD 'galaxy' AM1357-504 (Arp & Madore 1987). It had been independently noted as a PN by Côte et al. (1997), but no details were provided in their paper.

Fr 2-9 (Fr 1423-0918, WPS 82). Potential new giant PN discovered from SHASSA survey and independently in the WHAM point source catalogue (Reynolds et al. 2005). The SHASSA image shows the emission nebula to be centred at $14^{\rm h}22.6^{\rm m}$, $-09°14'$. It has strong [O III] emission from both WHAM data (see figure B.8) and an unpublished MSSSO spectrum. The DA white dwarf G 124-26, lies within the nebula (Reynolds et al. 2005), though the UBV colours indicate the star is too cool to be an ionization source ($V = 15.48$, $B - V = +0.31$, $U - B = -0.59$; Mermilliod 1991), confirmed by the detailed spectroscopic study of Koester et al. (2001) who derive $T_{\rm eff} = 8240\,{\rm K}$ and $\log g = 8.23$ cms^{-2} (mean of 2 spectra).

The mean systemic velocity from WHAM is $V_{\rm LSR} = -17 \pm 2$ kms^{-1}. The line width is fairly low, so the interpretation as a PN is equivocal. Deep, narrowband imaging with good resolution will be of use in determining its nature.

Fr 2-10 (Fr 1509-0520). A candidate ionizing star is PG 1506-052, spectral type sdOB (Moehler et al. 1990). Strömgren photometry by Wesemael et al. (1992) yields $y = 13.974$, $b - y = -0.087$ and $u - b = -0.327$, showing it is little reddened. WHAM spectrophotometry of the nebula yields [N II]λ6584/Hα =

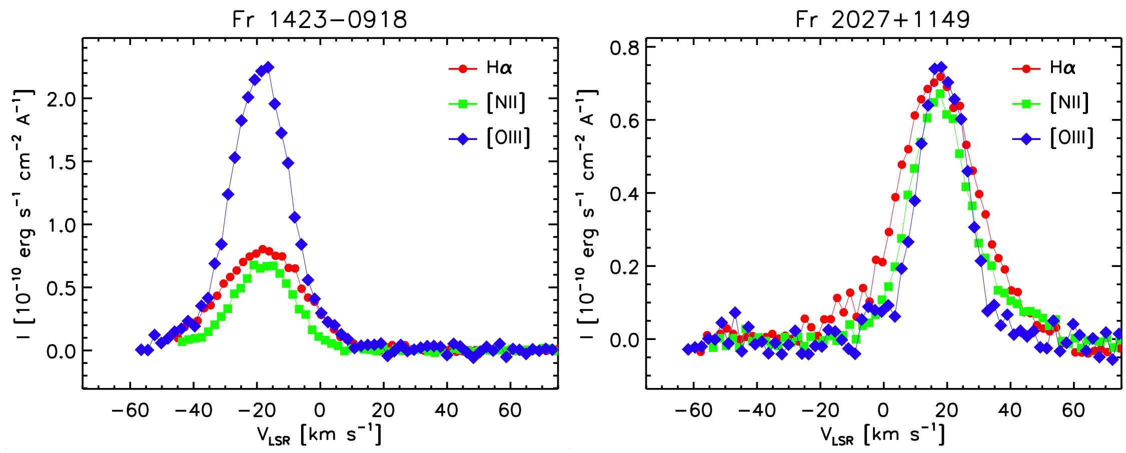

Figure B.8: WHAM spectra for two new nebulae, Fr 2-9 (left) and Fr 2-15 (right).

1.1, but rather weak [O III] emission. The line widths and systemic velocity from WHAM (see chapter 3) are consistent with ionized ISM.

Fr 2-12 (Fr 1721-5654, FP 1721-5654). A discussion of this isolated PN candidate was presented in §A.2.

Fr 2-13 (Fr 1759+3429). Large diffuse emission nebula discovered from the VTSS survey (field Her13). The object is very faint and WHAM data show weak Hα at close to zero velocity, and no [O III] emission. It is most likely ionized ambient ISM.

Fr 2-14 (Fr 2026+7637, WPS 31). Large diffuse emission nebula noted on VTSS field Cep08, and independently catalogued as a WHAM 'point source' emitter (Reynolds et al. 2005). WHAM data show [N II]6584/Hα = 0.35, and [O III] emission is very weak, showing the ionizing source is fairly cool. The mean velocity from the [N II] and Hα lines is $V_{\rm LSR} = -22 \pm 1$ kms^{-1}. A possible ionizing source, the sdO star KUV 20417+7604, was idenitified by Reynolds et al. (2005). Photometry by Wegner, Africano & Goodrich (1990) gives $V = 12.74$, $B - V = -0.11$ and $U - B = -0.88$. Reddening is non-negligible in this direction; the asymptotic reddening from Schlegel, Finkbeiner & Davis (1998) is $E(B - V) = 0.28$. The stellar photometry suggests somewhat less reddening if it has typical sdO colours, viz. $E(B-V) \simeq 0.18$. The most likely interpretation is that this is a HII region in the ambient ISM, probably associated with the Cepheus Flare (see §8.5).

Fr 2-15 (Fr 2027+1149, WPS 16). Potential new large PN discovered from the SHASSA survey and independently in the WHAM point source catalogue (Reynolds et al. 2005). The morphology is arcuate and somewhat filamentary, with a well defined western edge, as seen on the POSS-II R-band image (figure B.9). It presents a resemblance to the one-sided PN around Ton 320. Fr 2-15 has [O III] > Hβ from an unpublished, low S/N, MSSSO spectrum, confirmed with new WHAM data (see figure B.8, and §3.3). The systemic velocity is +18kms^{-1}, though the HWHM line-width is only 12 kms^{-1}, so an interpretation based on WHAM data is equivocal. No ionizing star has been found, so the possibility remains that this is something other than an evolved PN.

This new nebula is located near the nebula LBN 132 ($\alpha, \delta = 20^{\rm h}25.0^{\rm m}\ +14°12'$). LBN 132 is classified as a HII region in SIMBAD, but this nebula is not apparent on SHASSA images, and may be a reflection nebula. There is another emission patch west of this position at $20^{\rm h}20.1^{\rm m}$, $+14°50'$, as seen on SHASSA images, designated Fr 2-20.

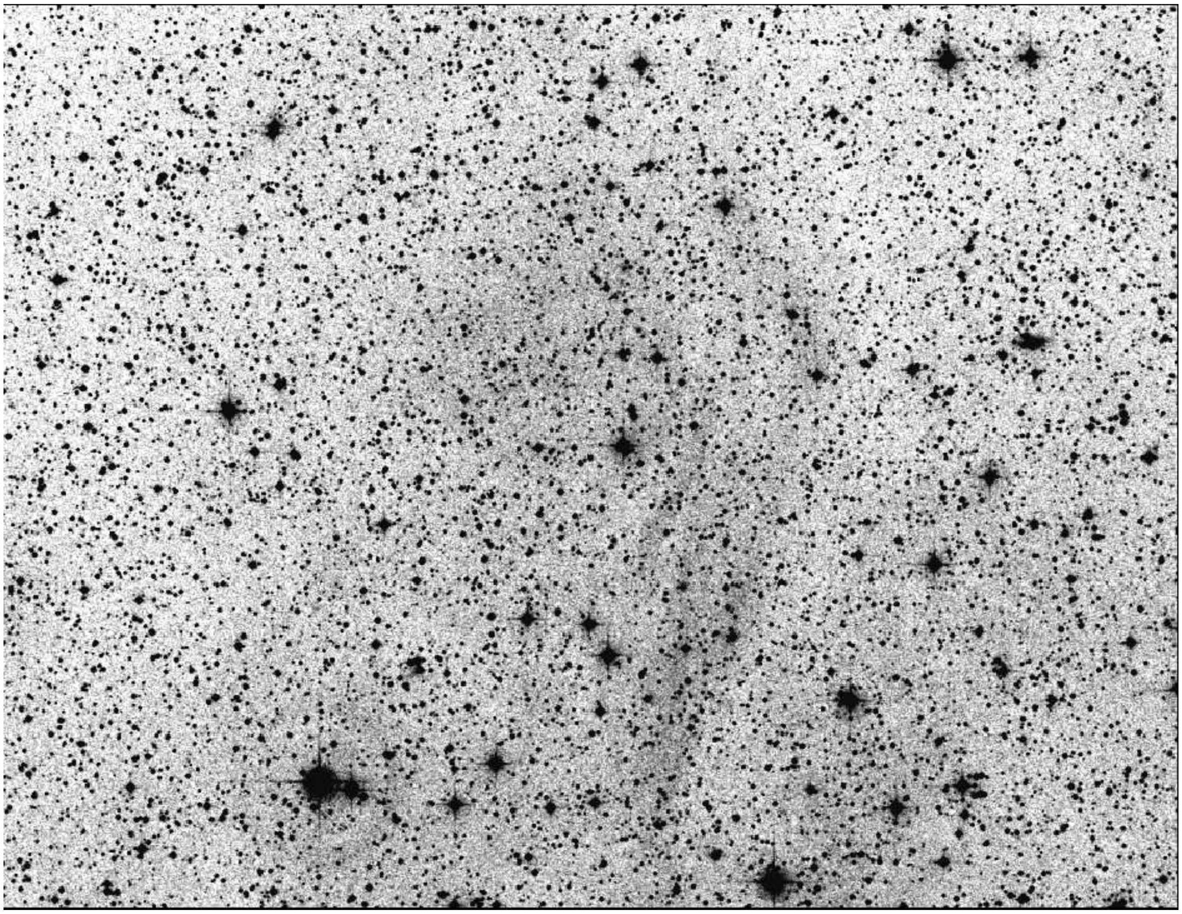

Figure B.9: Red DSS image of the PN candidate Fr 2-15. The image is 30′ wide, with NE is at top left. An ionizing star has yet to be identified.

Fr 2-16 (Fr 2118+1201). This is a very faint, diffuse emission region, and is possibly contiguous with widespread filamentary emission noted on SHASSA field 266. The most probable ionizing source is the DAO white dwarf HS 2115+1148. The fundamental parameters of this star are $B = 16.5$, $T_{\rm eff} = 67{,}000\,{\rm K}$ and $\log g = 6.9$ cms^{-2} (Dreizler et al. 1995). Rauch (1999) searched for Hα emission around HS 2115+1148 but did not note any. The centre of the apparent nebula is $\sim$15′ from this star, and therefore would have been outside the CCD field of the instrument used by Rauch (1999).

Fr 2-17 (Fr 2119-5623). A very faint emission patch which is probably ionized ambient ISM, despite the fact that no ionizing star has been found.

Fr 2-18 (Fr 2311+2927). Discovered from VTSS field Peg13. WHAM data show that F[N II] $\sim F$(Hα), with moderately weak [O III] emission. No ionizing star is known, but the observed line widths and systemic velocities from WHAM (chapter 3) are consistent with ionized ISM.

Fr 2-19 (Fr 1610-3357). A huge filamentary, arcuate nebula with dimensions of 120′ × 70′. No ionizing star is located near the centre of curvature of this object, which is unlikely to be a SNR owing to the high galactic latitude. However, the pulsating [WC] star Sanduleak 3 (Sanduleak 1971) is located at $16^{\rm h}06^{\rm m}28.4^{\rm s}$, $-35°45'13''$. This star is often considered as a 'naked' PN nucleus (e.g. van der Hucht et al. 1985; Koesterke & Hamann 1997), and the putative PN is designated PN G341.5+12.1 in SIMBAD, even though no visible nebula has been detected around this star. However, Sanduleak 3 is nearly 2° SW of the centre of curvature of the arcuate nebula discovered here, so a physical association seems unlikely. The proper motion of the star also seems inconsistent with an origin at the centre of the nebula. However, detailed spectroscopy of the emssion nebula is needed to shed light on its origin.

Fr 2-20 (Fr 2020+1450). This small faint emission nebula was noticed on SHASSA image 265, while determining a Hα flux for Fr 2-15 (see above). No other data is available for it, so its status is currently unknown.

B.4 WHAM point source nebulae

Several nebulae from the WPS catalogue (Reynolds et al. 2005) have either large half line-widths or systemic velocities considerably different to the local standard of rest, and are potential large remnant PNe. A systematic survey of these objects in Hα, [N II] and [O III] is being undertaken using WHAM by Madsen & Frew (2008, in prep.). Some of the more interesting candidates are as follows:

WPS 1. This nebulosity has a bright Hα flux, fairly high half line-width and a systemic velocity of $V_{\rm LSR} = +38 \pm 3$ kms^{-1} (Reynolds et al. 2005), suggesting it is not an ordinary HII region. However SHASSA images (figure B.10) show a large filamentary emission region brighter than the background, and not indicative of an evolved PN morphology. Reynolds et al. (2005) give a possible ionizing star, LSE 22, a probable O-type subdwarf.

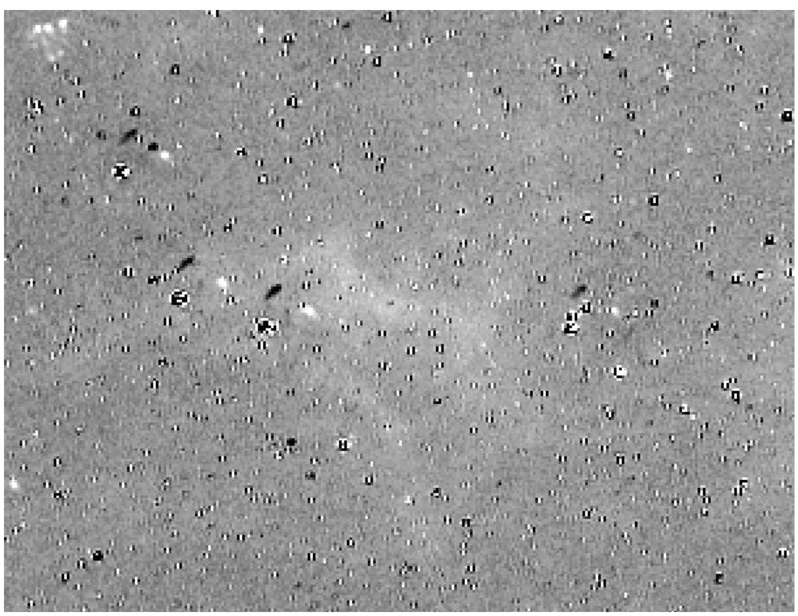

Figure B.10: SHASSA image of the diffuse emission nebulosity (WPS 1) near LSE 22. The image is 4° wide, with NE is at top left.

WPS 4. Reynolds et al (2005) give a broad FWHM ($\simeq 2v_{\rm exp}$) of 56 ± 15 kms^{-1} from WHAM NSS data, noting a possible ionizing star in the vicinity, PG 1548+149. However, there is no diffuse emission visible on SHASSA at the WHAM coordinates, but the beam includes R Ser, a bright Mira variable with emission lines, classified M7 IIIe (e.g. Fluks et al. 1994). This star is visible on SHASSA as a compact emitter. However, neither the radial velocities of R Ser or PG 1548+149 (taken from Simbad) agree with the systemic nebular velocity. In summary, there is no evidence that there is a PN here.

WPS 17. While the line width of this enhancement is typical of the diffuse ISM, the systemic velocity, $V_{\rm LSR} = -69 \pm 4$ kms^{-1}, is not. No nebulosity is visible on the DSS at this position (it is outside the VTSS), nor are there any good candidates for the ionizing source, so no conclusions can be drawn at this stage. Deep, wide-angle, narrowband imaging of this object is needed.

WPS 19. This object is also located outside the coverage of VTSS, and there is nothing obvious on the DSS R-band field. The HWHM from Reynolds et al. (2005) is only 14 kms^{-1}, and the systemic velocity is $V_{\rm LSR} = -37 \pm 3$ kms^{-1}. Needs follow-up.

WPS 20. Similar in characteristics to WPS 17, with $V_{\rm LSR} = +64 \pm 1$ kms^{-1}. There is diffuse emission and what looks like a cometary globule(s) visible on the R-band DSS. Unlikely to be a PN candidate.

WPS 21. Another WHAM point source with a non-zero systemic velocity, $V_{\rm LSR} = +52 \pm 2$ kms^{-1}, but a relatively narrow HWHM = 14 ± 5 kms^{-1}. No candidate ionizing star is known, but there may be some very faint nebulosity present on the red DSS image. Deep, wide-angle, narrowband imaging is needed to help determine the nature of this object.

WPS 22. With a HWHM of 18 kms^{-1} and $V_{\rm LSR} = +30 \pm 4$ kms^{-1}, this is potentially a PN. This may be the same object catalogued by Lynds (1965) as LBN 157. However, the Simbad database indicates the peculiar symbiotic nova AG Peg (Kenyon et al. 1993) is located just within the WHAM beam, and this may contribute to the Hα excess.

WPS 26. This Hα enhancement has $V_{\rm LSR} = -24 \pm 5$ kms^{-1}, and a quite broad HWHM = 19 $\pm$7 kms^{-1}. Deep, wide-angle, narrowband imaging is needed to help determine the nature of this object.

WPS 40. Reynolds et al. (2005) give $V_{\rm LSR} = -36 \pm 4$ kms^{-1} for this object, and suggested PG 0122+214 was a possible ionizing star. However, this is apparently a B-type main sequence runaway at a distance of 9.6 kpc from the Sun, and 6.2 kpc from the galactic plane (Ramspeck, Heber & Moehler 2001). Futhermore, with a spectroscopically determined temperature of 18,300 K, it is also too cool to be an ionizing source for a HII region. The field is not covered by SHASSA, but some possible faint diffuse emission is visible on the relevant R-band POSS-II plate. Needs follow-up.

WPS 41. A considerable negative systemic velocity, $V_{\rm LSR} = -63 \pm 2$ kms^{-1}, suggests it may be diffuse gas associated with the Perseus arm, though it is considerably off the galactic plane. At present, no conclusions can be drawn on its nature.

WPS 42. With $V_{\rm LSR} = -57 \pm 7$ kms^{-1}and a HWHM of 24 ± 7 kms^{-1} (Reynolds et al. 2005), this does not seem like a regular HII region, but no ionizing source is known. However, our new WHAM data fails to confirm any emission enhancement here, with null detections in Hα, [N II] and [O III]. Further observations are planned to resolve this discrepancy.

WPS 44. This enhancement has $V_{\rm LSR} = -26 \pm 2$ kms^{-1} and a very broad line width, with HWHM = 29 ± 4 kms^{-1}. No ionizing source is known in the vicinity, and there is nothing obvious on POSS II red images. Further observations are planned.

WPS 46. This object has $V_{\rm LSR} = -52 \pm 2$ kms^{-1} in Hα (Reynolds et al. 2005), confirmed here. The Hα, [N II] and [O III] fluxes are similar, showing that there is a fairly hot ionizing source present. Reynolds et al. (2005) suggest PG 0931+691 might be the ionizing star. However the nebula is in the direction of the Perseus spiral arm, and the negative systemic velocity might refer to background gas at a distance of $\sim$2 kpc in this direction. The line width is equivocal. Deep imaging data is necessary before its true nature can be ascertained.

WPS 47. Reynolds et al. (2005) give $V_{\rm LSR} = +30 \pm 4$ kms^{-1} and a HWHM of 20 ± 4 kms^{-1} kms^{-1}; a potential ionizing source is located in the vicinity, the sdB star KUV 02335+3343. There is possible faint emission seen on the DSS *R* image. Needs follow-up.

WPS 64. Widespread diffuse emission covers the SHASSA image in this direction. Despite the high negative velocity, $V_{\rm LSR} = -63 \pm 2$ kms^{-1}, this object is considered to be nebulosity associated with the Orion arm (see figure B.11), though there is no obvious enhancement at the WPS position.

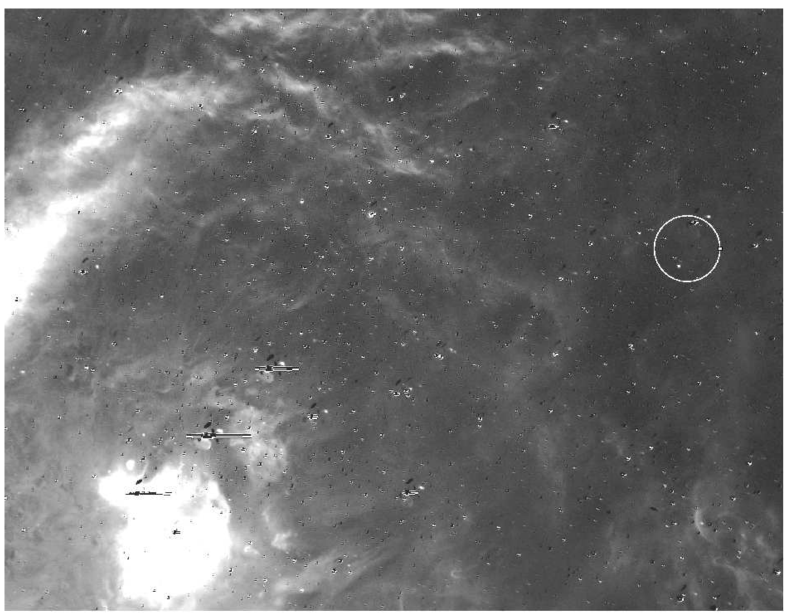

Figure B.11: SHASSA field 206, including WPS 64. The WHAM 1° diameter beam is represented by the circle at the position given by Reynolds et al. (2005). The very bright Orion nebula is at lower left. The field is $\sim$12° wide.

WPS 81. This is an enhancement with both a broad HWHM of 20 ± 7 kms^{-1} kms^{-1}, and a systemic velocity, $V_{\rm LSR} = +39 \pm 5$ kms^{-1}, significantly different from rest. Reynolds et al. (2005) note a hot blue star in the vicinity, EC 13331-2540, but the WHAM beam probably includes Hα emission from RW Hya, a bright symbiotic star (Sion et al. 2002, and references therein), which shows up as a compact Hα emitter on SHASSA image 113.

Appendix C

Database of $UBVIJHK_s$ Central Star Photometry

There are numerous papers containing magnitude data on PN central stars in the literature. This appendix provides a summary of the available $UBVI_cJHK_s$ photometry for all PNe which have photometry in at least two different bands, i.e. those PNe for which at least one colour index can be determined.

To generate table C.1 below, magnitude data was compiled from the literature into a working database. Optical magnitudes were obtained from Iriarte (1959), Klemola (1962), Abell (1966), Kohoutek (1967), Kostjakova et al. (1968), Evans (1968), Shao & Liller (1972, quoted by Acker et al. 1982), Dahn, Behall & Christy (1973), Kaler (1976, 1978), Chromey (1978), Drummond (1980, quoted by Acker et al. 1982), Martin (1981), Jacoby (1981), Landolt (1983), Downes (1984), Ellis, Grayson & Bond (1984), Reay et al. (1984), Shaw & Kaler (1985), Kaler & Feibelman (1985), de Freitas Pacheco, Codina & Viadana (1986), Walton et al. (1986), Hartl & Weinberger (1987), Grauer et al. (1987b), Jacoby (1988), Gathier & Pottasch (1988), Kwitter, Jacoby & Lydon (1988), Jacoby & Kaler (1989), Shaw & Kaler (1989), Liebert et al. (1989), Drilling (1991, 1995), Kidder, Holberg & Mason (1991), Tylenda et al. (1991), Saurer et al. (1992), Napiwotzki & Schönberner (1995), Kilkenny (1995), Walsh & Walton (1996), Acker et al. (1998), Reed (1998), Norris, Ryan & Beers (1999), Bond & Ciardullo (1999), Ciardullo et al. (1999), Wolff, Code & Groth (2000), Matsuura et al. (2005b), Frew, Parker & Russeil (2006), Harris et al. (2007) and Landolt & Uomoto (2007). Observations acquired with the MSSSO 1-m reflector at Siding Spring were also included (see Table 9.1) in the database.

In addition, relevant V data from the ASAS database (Pojmanski 2001), JHK_s data from the 2MASS Catalogue (Cutri et al. 2003), iJK data from the DENIS Survey (DENIS Consortium, 2005) and other sources were compiled, if available. Care was taken to ensure the quoted near-IR magnitudes referred to the just the CSPN and not the integrated light from the nebula (e.g. Ramos-Larios & Phillips 2005; Taranova & Shenavrin 2007). In some cases, such as IC 418, the near-IR stellar magnitudes are suspected to be contaminated by the bright background nebula.

The various data sets were then combined to generate the best estimate of the CSPN magnitude in each waveband. To do this, each individual magnitude estimate was vetted for quality (and sometimes omitted), before weighted mean $UBVIJHK_s$ magnitudes were generated using only the most reliable estimates. To illustrate the variable quality of the data-sets, figure C.2 shows a comparison between six large sets of V-band photometry. The *HST V* magnitudes from Ciardullo et al. (1999) are shown as the abscissae in each plot, as these magnitudes are considered to be free of nebular contamination. Comparison is made between these V magnitudes and those from Abell (1966), Harrris et al. (2007), Shao & Liller (1972), Shaw & Kaler (1985), Shaw & Kaler (1985), Tylenda et al. (1991), Napiwotzki &

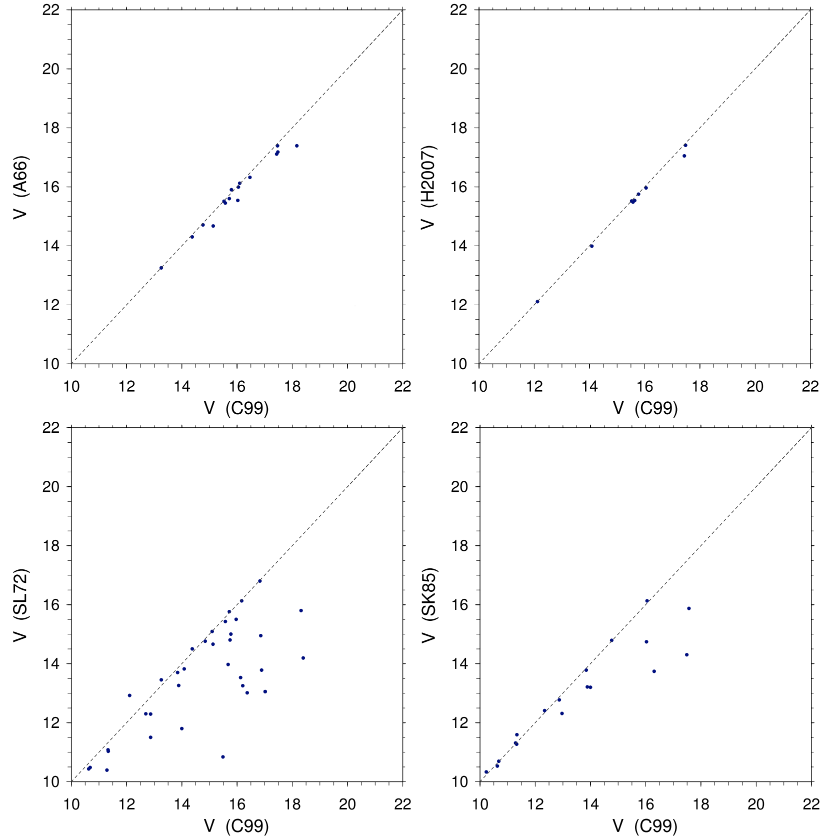

Figure C.1: Comparison of central star photometry between different studies. The HST V magnitudes from Ciardullo et al. (1999, hereafter C99) are plotted on the abscissae in each plot, as these magnitudes are considered to be free of nebular contamination. In the top-left plot, these V magnitudes are plotted against those from Abell (1966; A66). The other codes are: H2007, Harrris et al. (2007); SL72, Shao & Liller (1972); SK85, Shaw & Kaler (1985). In all cases, the dashed lines represent a 1:1 correlation.

Schönberner (1995) and Gathier & Pottasch (1988).

The magnitudes from Abell (1966), Napiwotzki & Schönberner (1995) and Harrris et al. (2007) are in excellent agreement, expected as these studies concentrated on hightly evolved PNe. The magnitudes from Shao & Liller (1972) are often heavily contaminated by nebular emission in the photometer diaphragms used, and can be considered upper limits. Only for a few low-surface brightness nebulae are the magnitudes reliable (see the discussion of Shaw & Kaler 1985). Magnitudes from Shaw & Kaler (1985, 1989) are in good agreement with the HST data at brighter magnitudes but are systematically overestimated at faint magnitudes, again due to nebular contamination. The data from Tylenda et al. (1991) show considerable scatter, but no obvious trend with CS magnitude, while the magnitudes from Gathgier & Pottasch (1988) are too faint at the fainest magnitudes.

The final weighted averaged values for the central star magnitudes are given in the table below. Using the adopted extinction of the PN shell (and/or the CS), reddening-corrected optical and near-IR colour indices are also generated. The best quality data for 17 PN central stars and 'naked' hot white dwarfs with low reddening were averaged to generate empirical, dereddened colour indices appropriate for very hot central stars with $T_{\rm eff} \simeq 100{,}000$ K. The averaged colours are: $(U-B)_0 = -1.27$, $(B-V)_0 = -0.35$, $(V-I)_0 = -0.41$, $(V-J)_0 = -0.78$, $(V-K)_0 = -1.07$, $(J-H)_0 = -0.14$, and $(H-K)_0 = -0.11$. These data are then used to infer the presence of any unresolved late-type companions (see the discussion in §9.5.1), after comparing the CS dereddened colours with these canonical values.

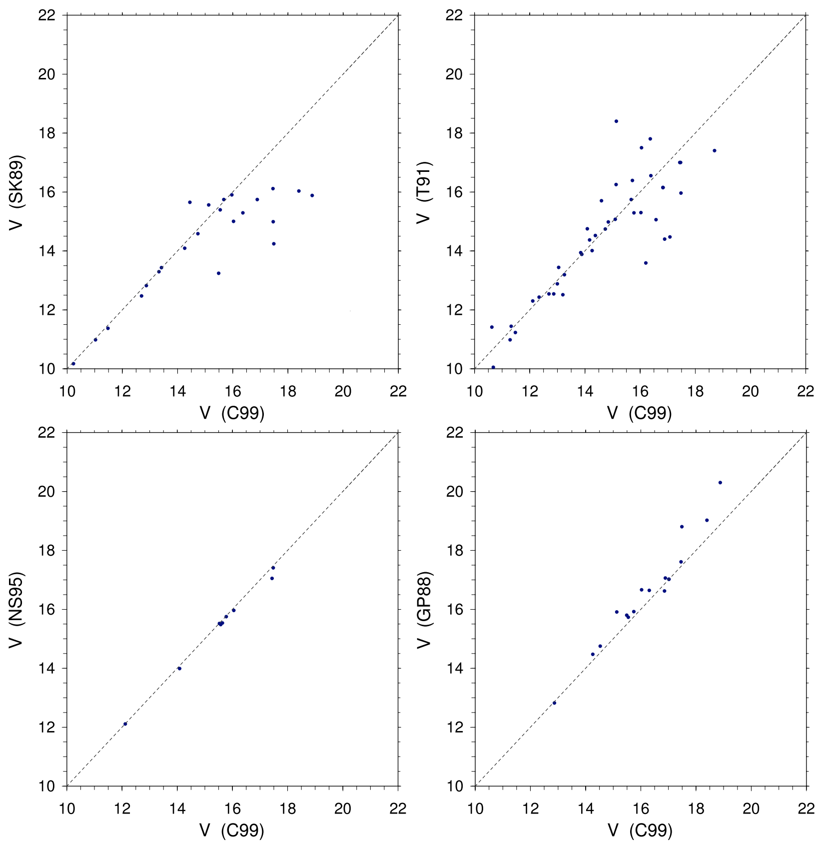

Figure C.2: Comparison of central star photometry between different studies. The HST V magnitudes from C99 are plotted on the abscissae in each plot. The codes are as follows: SK89, Shaw & Kaler (1989); T91, Tylenda et al. (1991); NS95, Napiwotzki & Schönberner (1995); GP88, Gathier & Pottasch (1988). In all cases, the dashed lines represent a 1:1 correlation.

Table C.1: Database of $UBVI_cJHK_s$ central star photometry, including dereddened optical and near-IR colours.

Name	E_{B-V}	V	$U-B$	$B-V$	I_c	J	H	K_s	V_0	$(U-B)_0$	$(B-V)_0$	$(V-I)_0$	$(V-J)_0$	$(V-K)_0$	$(J-H)_0$	$(H-K)_0$
Abell 7	0.02	15.49	-1.35	-0.33	15.92	16.10	16.16	...	15.42	-1.36	-0.35	-0.47	-0.66	...	-0.07	...
Abell 13	0.54	19.87	-1.00	0.19	...	...	...	...	18.20	-1.39	-0.35	...	...	...	...	...
Abell 14	0.68	15.24	-0.01	0.51	...	14.04	13.90	13.75	13.15	-0.50	-0.17	...	-0.31	-0.37	-0.05	-0.01
Abell 15	0.04	15.80	...	-0.31	...	...	...	...	15.68	...	-0.35	...	...	...	...	...
Abell 16	0.15	18.70	...	...	18.84	...	...	...	18.23	...	...	-0.39	...	...	...	...
Abell 20	0.08	16.56	-1.12	-0.27	...	...	...	...	16.31	-1.18	-0.35	...	...	...	...	...
Abell 21	0.04	16.00	-1.26	-0.31	16.35	16.58	...	...	15.88	-1.29	-0.35	-0.41	-0.67	...	...	...
Abell 23	0.65	18.50	...	...	...	...	...	...	16.49	...	...	...	...	...	...	...
Abell 24	0.06	17.36	-1.15	-0.29	17.82	...	...	...	17.17	-1.19	-0.35	-0.56	...	...	...	...
Abell 28	0.00	16.57	...	...	16.87	...	...	...	16.57	...	...	-0.30	...	...	...	...
Abell 29	0.10	18.33	-1.08	-0.23	...	...	...	...	18.02	-1.15	-0.33	...	...	...	...	...
Abell 30	0.03	14.38	-1.03	-0.07	14.53	14.56	14.57	14.04	14.29	-1.05	-0.10	...	-0.25	0.26	-0.02	0.53
Abell 31	0.04	15.51	-1.28	-0.30	15.95	15.87	15.57	15.67	15.38	-1.31	-0.34	-0.51	-0.46	-0.27	0.29	-0.11
Abell 33	0.00	16.03	-1.15	-0.16	16.47	14.92	14.35	14.15	16.03	...	...	-0.44	1.11	1.88	0.57	0.19
Abell 34	0.04	16.40	...	...	16.81	16.81	>17.2	...	16.27	...	...	-0.48	-0.51	...	...	...
Abell 36	0.02	11.53	-1.23	-0.33	11.83	12.23	12.36	12.48	11.47	-1.24	-0.35	-0.34	-0.75	-1.01	-0.13	-0.13
Abell 39	0.02	15.60	-1.23	-0.33	15.96	16.13	...	...	15.54	-1.24	-0.35	-0.39	-0.58	...	...	...
Abell 41	0.45	16.05	-0.87	0.11	15.73	15.69	15.81	15.16	14.66	-1.19	-0.34	-0.41	-0.64	-0.35	-0.24	0.54
Abell 43	0.17	14.74	-1.12	-0.18	14.86	14.98	15.05	15.33	14.21	-1.24	-0.35	-0.40	-0.62	-1.06	-0.12	-0.33
Abell 45	0.78	21.1	-1.00	0.40	...	...	...	...	18.68	-1.56	-0.38	...	...	...	...	...
Abell 46	0.16	14.83	-1.11	-0.19	15.48	15.63	15.67	...	14.33	-1.23	-0.35	-0.91	-1.16	...	-0.09	...
Abell 51	0.23	15.47	-1.04	-0.12	15.38	15.60	16.12	...	14.76	-1.21	-0.35	-0.28	-0.64	...	-0.59	...
Abell 61	0.05	17.42	-1.23	-0.34	17.69	...	...	...	17.27	-1.27	-0.39	-0.35	...	...	...	...
Abell 63	0.50	15.35	-0.70	0.38	14.78	14.95	13.79	13.66	13.80	-1.06	-0.12	-0.24	-0.71	0.32	1.02	0.01
Abell 65	0.20	15.60	-0.98	0.06	15.52	15.11	14.99	14.85	14.98	-1.12	-0.14	-0.24	0.04	0.20	0.07	0.09
Abell 66	0.18	18.17	-0.87	0.32	18.29	...	...	...	17.61	...	0.14	-0.41	...	...	...	...
Abell 71	0.73	18.95	-0.66	0.37	...	...	...	...	16.69	-1.19	-0.36	...	...	...	...	...
Abell 72	0.03	16.11	-1.24	-0.33	16.43	16.67	...	...	16.02	-1.26	-0.36	-0.37	-0.62	...	...	...
Abell 74	0.08	17.20	-1.19	-0.33	17.47	...	...	...	16.95	-1.25	-0.41	-0.40	...	...	...	...
Abell 78	0.05	13.26	-1.14	-0.22	13.45	13.51	13.42	13.28	13.11	...	-0.27	-0.27	-0.36	-0.16	0.08	0.12
Abell 79	0.60	16.7	...	...	...	15.05	14.64	14.44	14.84	...	...	...	0.32	0.61	0.24	0.06
Abell 82	0.22	14.90	...	1.28	13.54	12.44	11.82	11.69	14.22	...	1.06	1.00	1.97	2.60	0.56	0.07
Abell 84	0.26	18.49	-1.00	0.18	...	...	...	...	17.68	-1.19	-0.08	...	...	...	...	...

Continued on next page

Table C.1 – continued from previous page

Name	E_{B-V}	V	$U-B$	$B-V$	I_c	J	H	K_s	V_0	$(U-B)_0$	$(B-V)_0$	$(V-I)_0$	$(V-J)_0$	$(V-K)_0$	$(J-H)_0$	$(H-K)_0$
BD +30 3639	0.30	10.42	...	...	...	9.31	9.23	8.11	9.49	...	...	...	0.45	1.49	-0.01	1.05
BD +33 2642	0.06	10.82	-0.86	-0.17	10.96	11.09	11.14	11.20	10.65	-0.90	-0.22	-0.23	-0.39	-0.53	-0.06	-0.08
BMP0739-1418	0.43	16.00	...	...	15.71	15.80	15.80	...	14.67	...	...	-0.40	-0.76	...	-0.12	...
BMP1455-4727	0.26	13.64	...	...	12.83	12.34	12.12	12.09	12.85	...	...	0.39	0.73	0.84	0.15	-0.04
BMP1858-1430	0.10	15.83	...	...	16.22	16.13	...	...	15.52	...	...	-0.55	-0.53	...	...	...
Cn 1-1	0.41	10.90	...	...	10.05	9.12	8.08	7.57	9.63	...	...	0.19	0.87	2.20	0.92	0.41
CRBB 1	0.05	10.72	-0.96	-0.16	10.83	11.02	11.14	11.09	10.57	-1.00	-0.21	-0.19	-0.41	-0.51	-0.14	0.04
DeHt 2	0.25	15.00	...	0.01	...	15.32	15.49	15.50	14.23	...	-0.24	...	-0.88	-1.18	-0.23	-0.07
DS 1	0.15	12.06	-1.09	-0.19	...	12.61	12.63	12.65	11.60	-1.20	-0.34	...	-0.89	-1.00	-0.06	-0.05
DS 2	0.20	12.37	-1.12	-0.15	12.45	12.68	12.80	12.93	11.75	-1.26	-0.35	-0.40	-0.76	-1.11	-0.17	-0.18
EGB 1	0.23	16.39	-1.05	...	16.52	16.64	...	...	15.68	-1.22	-0.23	-0.50	-0.76	...	...	...
EGB 6	0.05	16.03	-1.22	-0.30	...	16.52	15.95	16.10	15.87	-1.26	-0.35	...	-0.60	-0.21	0.56	-0.17
EGB 9	0.07	13.00	...	...	13.04	12.96	12.98	13.00	12.79	...	...	-0.15	-0.11	-0.19	-0.04	-0.04
ESO 40-11	0.03	15.23	...	...	15.91	16.33	>17.32	...	15.14	...	...	-0.72	-1.17	...	...	...
Fg 1	0.17	14.5	...	...	14.61	14.88	15.08	14.73	13.97	...	...	-0.39	-0.76	-0.70	...	...
FP0840-5754	0.00	14.44	...	...	14.92	15.36	15.44	...	14.44	...	...	-0.48	-0.92	...	-0.08	...
FP0905-3033	0.05	16.49	-1.25	-0.30	16.77	...	...	...	16.34	-1.29	-0.35	-0.36	...	...	...	...
FP1721-5654	0.18	17.56	...	...	17.67	...	...	...	17.00	...	...	-0.40	...	...	...	...
FP1824-0319	0.08	14.92	-1.18	-0.28	15.14	15.51	15.62	...	14.67	-1.24	-0.36	-0.34	-0.76	...	-0.14	...
Fr 2-8	0.20	...	...	...	16.08	16.17	>16.66	...	...	...	...	...	...	...		...
Fr 2-10	0.05	13.97	...	...	...	14.42	14.54	14.66	13.94	...	...	...	-0.56	-0.83	-0.13	-0.13
H 2-1	0.52	13.25	...	...	...	11.40	11.18	10.30	11.65	...	...	...	0.69	1.52	0.08	0.75
H 3-75	0.25	14.24	...	...	13.08	12.00	11.46	11.33	13.47	...	...	0.75	1.68	2.22	...	...
HaTr 7	0.10	14.66	...	...	14.80	15.37	15.48	15.75	14.36	...	...	-0.29	-0.92	-1.35	-0.14	-0.29
HaWe 4	0.21	17.08	-0.83	-0.14	...	...	...	...	16.42	-0.98	-0.35	...	...	...	...	...
HaWe 6	0.08	16.53	...	-0.22	16.76	...	...	...	16.28	...	-0.30	-0.36	...	...	...	...
HaWe 7	0.41	15.8	...	...	15.85	15.80	15.83	...	14.51	...	...	-0.73	-0.93	...	-0.14	...
HaWe 13	0.49	16.9	...	...	16.48	16.29	15.97	...	15.38	...	...	-0.37	-0.48	...	0.18	...
HbDs 1	0.13	12.53	-1.19	-0.22	12.67	12.81	12.74	12.81	12.13	-1.28	-0.35	-0.35	-0.57	-0.64	0.04	-0.10
He 2-11	1.31	18.33	...	...	16.32	15.55	15.03	14.89	14.27	...	...	-0.11	-0.14	-0.17	0.15	-0.18
He 2-36	0.68	11.48	...	...	10.63	9.87	9.62	9.46	9.37	...	...	-0.26	0.10	0.15	0.05	0.00
He 2-86	1.51	15.91	...	...	13.91	12.16	11.85	10.79	11.23	...	...	-0.45	0.39	0.97	-0.12	0.70
He 2-111	0.81	16.1	...	...	15.38	14.25	13.73	13.45	13.59	...	...	-0.59	0.04	0.42	0.30	0.08
He 2-131	0.20	10.97	-1.05	-0.23	10.91	10.18	10.20	9.36	10.35	-1.20	-0.43	-0.26	0.34	1.06	-0.08	0.79
He 2-138	0.28	11.03	...	...	10.97	10.55	10.53	10.07	10.16	...	...	-0.39	-0.15	0.19	-0.05	0.38

Continued on next page

Table C.1 – continued from previous page

Name	E_{B-V}	V	$U-B$	$B-V$	I_c	J	H	K_s	V_0	$(U-B)_0$	$(B-V)_0$	$(V-I)_0$	$(V-J)_0$	$(V-K)_0$	$(J-H)_0$	$(H-K)_0$
He 2-151	0.25	13.08	...	0.22	12.50	12.12	12.08	11.76	12.31	...	-0.03	0.18	0.41	0.64	-0.03	0.26
HFG 1	0.46	13.38	...	...	13.00	12.93	12.68	12.58	11.95	...	...	-0.37	-0.57	-0.46	0.12	-0.01
HFG 2	0.01	16.8	...	...	17.20	...	...	...	16.76	...	...	-0.42	...	...	...	...
IC 289	0.82	16.8	...	...	15.92	15.59	15.62	15.14	14.21	...	...	-0.50	-0.67	-0.65	-0.26	0.28
IC 418	0.20	10.23	-0.91	0.16	10.22	9.79	9.75	9.06	9.61	-1.05	-0.04	-0.31	0.00	0.62	-0.02	0.64
IC 1266	0.12	11.38	...	...	...	11.18	11.18	10.64	11.00	...	...	...	-0.08	0.40	-0.04	0.51
IC 2149	0.25	11.34	...	...	11.32	...	...	10.61	10.57	...	...	-0.39	...	0.04	...	...
IC 2165	0.38	17.47	...	0.03	...	...	...	...	16.29	...	-0.35	...	...	...	...	...
IC 2448	0.08	14.26	...	...	14.54	...	...	...	14.01	...	...	-0.41	...	...	...	...
IC 3568	0.18	12.97	...	...	13.07	12.43	12.48	11.90	12.41	...	...	-0.39	0.14	0.58	-0.10	0.53
IC 4406	0.21	17.38	...	...	17.52	...	...	...	16.73	...	...	-0.48	...	...	...	...
IC 4593	0.10	11.33	...	...	11.52	11.28	11.32	11.01	11.02	...	...	-0.35	-0.18	0.05	-0.07	0.29
IC 4637	0.59	12.70	...	...	12.15	11.36	11.34	10.96	10.89	...	...	-0.40	0.03	0.13	-0.14	0.24
IC 4637 B	0.59	14.60	...	...	13.19	...	...	...	12.79	...	...	0.46	...	...	...	...
IC 5148-50	0.01	16.16	...	...	16.59	...	...	...	16.13	...	...	-0.45	...	...	...	...
IsWe 1	0.18	16.55	-1.04	-0.18	16.66	...	...	...	15.99	-1.17	-0.36	-0.40	...	...	...	...
IsWe 2	0.45	17.71	-1.04	0.35	...	...	...	...	16.32	-1.36	-0.10	...	...	...	...	...
Jacoby 1	0.03	15.54	...	...	...	16.38	...	...	15.45	...	...	...	-0.91	...	...	...
Jn 1	0.05	16.17	...	...	16.46	16.70	...	¿17.16	16.02	...	...	-0.37	-0.64	...	...	...
JnEr 1	0.02	17.14	...	...	17.56	...	...	...	17.08	...	...	-0.45	...	...	...	...
K 1-2	0.17	16.83	...	...	16.63	16.44	16.33	...	16.30	...	...	-0.08	0.01	...	...	...
K 1-14	0.08	16.21	...	...	16.48	...	...	...	15.96	...	...	-0.40	...	...	...	...
K 1-16	0.04	15.08	...	...	15.48	15.78	16.00	...	14.96	...	...	-0.46	-0.79	...	-0.22	...
K 1-22	0.05	16.83	...	...	17.14	...	...	...	16.68	...	...	-0.39	...	...	...	...
K 1-22 B	0.05	17.13	...	...	16.01	15.03	14.46	14.27	16.98	...	...	1.04	1.99	2.73	0.56	0.19
K 1-27	0.05	16.13	...	...	16.46	16.40	>16.49	>15.82	15.98	...	...	-0.41	-0.38	...	...	...
K 2-2	0.03	14.30	...	-0.70	...	14.94	14.99	15.09	14.21	...	...	...	-0.71	-0.87	-0.06	-0.10
K 648	0.13	14.73	-1.05	-0.13	14.93	...	...	...	14.33	-1.14	-0.26	-0.41	...	...	...	...
Lo 1	0.00	15.16	...	...	15.59	15.90	16.16	...	15.16	...	...	-0.44	-0.74	...	-0.26	...
Lo 3	0.17	16.6	...	...	16.68	16.84	15.97	15.49	16.07	...	...	-0.36	-0.61	0.64	0.82	0.44
Lo 8	0.03	12.95	...	-0.22	13.33	13.67	13.83	14.00	12.86	...	-0.25	-0.43	-0.79	-1.13	-0.16	-0.18
Lo 13	0.20	17.9	...	...	18.20	...	...	...	17.28	...	...	-0.63	...	...	...	...
Lo 16	0.58	15.42	...	...	14.88	13.98	13.74	13.55	13.62	...	...	-0.40	0.15	0.28	0.07	0.06
LoTr 1	0.01	12.6	...	...	11.79	10.87	10.21	10.03	12.57	...	...	0.79	1.70	2.54	0.66	0.18
LoTr 5	0.01	8.92	...	...	7.95	7.37	6.95	6.86	8.89	...	...	0.95	1.53	2.04	0.42	0.09

Continued on next page

Table C.1 – continued from previous page

Name	E_{B-V}	V	$U-B$	$B-V$	I_c	J	H	K_s	V_0	$(U-B)_0$	$(B-V)_0$	$(V-I)_0$	$(V-J)_0$	$(V-K)_0$	$(J-H)_0$	$(H-K)_0$
LS IV-12 111	0.20	11.33	-0.81	...	...	10.99	10.94	10.79	10.72	-0.95	-0.20	...	-0.10	0.00	-0.01	0.10
LTNF 1	0.01	16.15	...	...	...	13.96	13.71	13.63	16.12	...	...	...	2.17	2.49	0.25	0.08
M 1-2	0.13	13.07	...	0.98	11.95	11.02	10.40	9.93	12.67	...	0.85	0.91	1.76	2.78	0.59	0.43
M 1-26	1.05	12.61	...	...	11.32	9.92	9.65	8.93	9.36	...	...	-0.41	0.35	0.79	-0.02	0.47
M 1-77	0.8	12.10	...	...	11.24	10.48	9.93	9.20	9.62	...	...	-0.44	-0.17	0.70	0.33	0.54
M 1-77	0.83	12.13	-0.35	0.60	11.24	10.48	9.93	9.20	9.55	-0.95	-0.23	-0.46	-0.21	0.64	0.32	0.53
M 1-80	0.39	14.8	...	...	...	14.81	14.65	...	13.59	...	...	...	-0.87	...	0.05	...
M 2-54	0.35	12.22	...	0.00	12.09	11.82	11.74	11.57	11.14	...	-0.35	-0.43	-0.38	-0.30	-0.02	0.10
M 2-55	0.85	16.15	...	...	...	14.57	13.76	13.56	13.52	...	...	...	-0.32	0.25	...	...
M 3-20	0.99	15.95	...	...	...	13.67	13.51	12.76	12.88	...	...	...	0.07	0.47	-0.12	0.52
Me 1-1	0.46	13.86	...	1.51	...	9.94	9.23	8.94	12.43	...	1.05	...	2.90	3.65	0.57	0.18
Me 2-1	0.10	18.40	...	-0.25	...	...	...	...	18.09	...	-0.35	...	...	...	...	...
MPA1508-6455	0.60	13.58	...	...	12.92	12.09	11.47	11.28	11.72	...	...	-0.32	0.15	0.65	0.45	0.05
MWP 1	0.02	13.13	...	...	13.50	13.82	13.92	14.18	13.07	...	...	-0.40	-0.73	-1.11	-0.11	-0.26
Mz 2	0.55	18.32	...	...	17.82	...	...	...	16.62	...	...	-0.39	...	...	...	...
NGC 40	0.42	11.55	...	...	...	10.89	10.80	10.38	10.25	...	...	-0.41	-0.28	0.01	-0.02	0.31
NGC 246	0.02	11.84	-1.33	-0.33	12.21	12.61	12.80	12.87	11.78	-1.34	-0.35	-0.40	-0.81	-1.08	-0.19	-0.08
NGC 246 B	0.02	14.39	...	0.74	13.53	12.92	12.53	12.45	14.32	...	0.72	0.82	1.43	1.88	0.38	0.07
NGC 650-1	0.14	17.53	...	...	17.73	...	...	...	17.09	...	...	-0.43	...	...	...	...
NGC 1360	0.01	11.34	...	...	11.75	12.08	12.29	12.37	11.31	...	...	-0.43	-0.77	-1.06	-0.21	-0.08
NGC 1501	0.65	14.45	-0.86	0.33	13.80	13.20	12.92	12.79	12.43	-1.33	-0.32	-0.41	-0.20	-0.13	0.10	-0.03
NGC 1514	0.54	9.52	-0.01	0.55	8.71	8.19	8.10	8.00	7.85	-0.40	0.01	-0.06	0.13	0.03	-0.06	-0.03
NGC 1535	0.04	12.11	...	...	12.46	12.54	12.65	12.58	11.99	...	...	-0.41	-0.52	-0.58	-0.12	0.06
NGC 1535 B	0.04	17.65	...	...	16.71	...	...	...	17.53	...	...	0.88	...	...	...	...
NGC 2022	0.05	15.75	...	...	16.14	15.42	...	...	15.60	...	...	-0.47	0.22	...	...	...
NGC 2346	0.51	11.27	...	...	11.01	10.26	9.44	8.41	9.69	...	...	-0.57	-0.12	1.46	0.67	0.91
NGC 2371-2	0.05	14.85	...	...	15.16	...	...	...	14.70	...	...	-0.39	...	...	...	...
NGC 2392	0.16	10.63	...	...	10.77	10.87	10.92	10.94	10.13	...	...	-0.40	-0.60	-0.75	-0.09	-0.06
NGC 2440	0.20	17.63	...	-0.15	17.56	...	...	...	17.01	...	-0.35	-0.25	...	...	...	...
NGC 2452	0.43	17.46	...	0.24	16.95	15.34	15.00	14.29	16.13	...	-0.19	-0.19	1.16	1.99	0.22	0.61
NGC 2610	0.05	15.97	...	...	16.32	16.71	16.29	...	15.82	...	...	-0.43	-0.85	...	...	...
NGC 2792	0.40	16.89	...	...	16.67	...	...	...	15.65	...	...	-0.43	...	...	...	...
NGC 2867	0.32	16.03	...	...	15.83	...	...	...	15.04	...	...	-0.32	...	...	...	...
NGC 2899	0.43	16.5	...	...	14.58	13.94	13.59	13.60	15.17	...	...	1.22	1.60	1.72	0.23	-0.12
NGC 3132	0.10	10.09	...	...	9.90	9.75	9.73	9.72	9.78	...	...	0.02	0.11	0.09	-0.01	-0.02

Continued on next page

Table C.1 – continued from previous page

Name	E_{B-V}	V	$U-B$	$B-V$	I_c	J	H	K_s	V_0	$(U-B)_0$	$(B-V)_0$	$(V-I)_0$	$(V-J)_0$	$(V-K)_0$	$(J-H)_0$	$(H-K)_0$
NGC 3132	0.10	15.76	...	...	16.00	...	...	...	15.45	...	...	-0.40	...	...	...	...
NGC 3195	0.09	17.78	...	...	18.04	...	...	...	17.52	...	...	-0.40	...	...	...	...
NGC 3242	0.04	12.32	...	...	12.66	12.10	12.46	12.26	12.20	...	...	-0.40	0.13	-0.05	-0.37	0.19
NGC 3587	0.01	16.1	...	...	17.15	16.71	...	...	16.10	...	...	-1.04	-0.61	...	...	...
NGC 3918	0.26	15.49	...	...	15.48	...	...	...	14.68	...	...	-0.41	...	...	...	...
NGC 4361	0.04	13.26	...	...	13.59	13.94	14.00	14.02	13.14	...	...	-0.39	-0.77	-0.87	-0.07	-0.03
NGC 5189	0.36	14.53	...	...	14.35	14.02	13.84	13.53	13.41	...	...	-0.40	-0.29	0.01	0.08	0.23
NGC 5307	0.30	14.74	...	...	14.71	...	...	...	13.81	...	...	-0.46	...	...	...	...
NGC 5844	0.64	...	...	...	17.60	...	...	...	...	...	...	...	...	...	...	...
NGC 5882	0.27	13.42	...	...	13.35	...	...	...	12.49	...	...	-0.42	...	...	...	...
NGC 5979	0.27	16.37	...	...	16.33	...	...	...	15.53	...	...	-0.40	...	...	...	...
NGC 6026	0.35	13.33	...	...	13.20	13.05	13.04	13.04	12.25	...	...	-0.44	-0.50	-0.68	-0.09	-0.09
NGC 6058	0.03	13.85	...	...	14.21	14.46	14.62	14.58	13.76	...	...	-0.41	-0.67	-0.81	-0.17	0.04
NGC 6153	0.89	15.55	...	...	15.13	13.12	13.33	12.15	12.79	...	...	-1.02	0.45	0.95	-0.46	0.96
NGC 6210	0.06	12.43	...	0.05	...	11.05	...	...	12.26	...	-0.01	...	1.25	...	...	...
NGC 6337	0.59	15.67	...	...	...	15.21	...	...	13.84	...	...	...	-0.86	...	...	...
NGC 6369	1.33	15.13	...	...	14.20	12.45	11.87	11.48	11.01	...	...	-1.22	-0.29	0.00	0.21	0.08
NGC 6537	1.45	21.56	...	...	...	...	...	18.63	17.07	...	...	...	...	-1.06	...	...
NGC 6543	0.07	11.29	...	...	11.47	...	...	...	11.07	...	...	-0.29	...	...	...	...
NGC 6567	0.47	14.34	...	...	12.67	11.76	11.56	10.30	12.88	...	...	0.91	1.53	2.75	...	...
NGC 6578	0.75	15.68	...	...	14.90	...	...	...	13.36	...	...	-0.44	...	...	...	...
NGC 6629	0.57	12.87	...	...	12.36	...	...	...	11.10	...	...	-0.41	...	...	...	...
NGC 6720	0.01	15.78	...	-0.38	16.16	14.98	14.42	14.69	15.75	...	-0.39	-0.40	0.78	1.07	0.55	-0.26
NGC 6751	0.39	14.30	-0.45	0.21	13.65	13.37	13.23	12.63	13.09	-0.73	-0.18	0.01	0.05	0.59	0.04	0.50
NGC 6781	0.53	16.88	...	...	16.45	16.24	...	...	15.24	...	...	-0.43	-0.54	...	...	...
NGC 6790	0.58	16.13	...	...	15.60	10.61	10.45	9.47	14.33	...	...	-0.41	4.23	5.07	0.00	0.84
NGC 6804	0.55	14.17	...	0.08	13.64	13.23	12.45	11.28	12.47	-1.10	-0.47	-0.36	-0.28	1.38	0.62	1.04
NGC 6826	0.10	10.69	...	...	10.92	...	10.88	...	10.38	...	...	-0.40	...	...	...	...
NGC 6853	0.05	14.09	...	-0.30	14.47	14.75	14.70	14.61	13.94	...	-0.35	-0.46	-0.77	-0.65	0.04	0.08
NGC 6884	0.55	16.71	...	...	16.22	...	...	...	15.01	...	...	-0.40	...	...	...	...
NGC 6891	0.15	12.34	...	...	12.50	11.86	11.96	11.73	11.88	...	...	-0.40	0.15	0.20	-0.14	0.19
NGC 6894	0.45	18.32	...	...	17.99	...	...	...	16.93	...	...	-0.40	...	...	...	...
NGC 6905	0.15	14.6	...	...	14.74	14.54	14.44	14.35	14.14	...	...	-0.38	-0.28	-0.16	0.06	0.06
NGC 7008	0.38	13.89	...	...	13.68	...	...	...	12.72	...	...	-0.40	...	...	...	...
NGC 7008 B	0.38	14.40	...	...	13.06	11.87	11.52	11.41	13.24	...	...	0.73	1.70	1.96	0.24	0.02

Continued on next page

Table C.1 – continued from previous page

Name	E_{B-V}	V	$U-B$	$B-V$	I_c	J	H	K_s	V_0	$(U-B)_0$	$(B-V)_0$	$(V-I)_0$	$(V-J)_0$	$(V-K)_0$	$(J-H)_0$	$(H-K)_0$
NGC 7009	0.08	12.87	...	...	13.10	...	...	...	12.62	...	...	-0.36	...	...	...	...
NGC 7026	0.6	14.20	...	...	13.62	12.67	...	...	12.34	...	...	-0.39	0.20	...	...	...
NGC 7027	0.98	16.04	...	0.66	16.06	...	...	...	13.00	...	-0.32	-1.61	...	...	...	...
NGC 7076	0.81	15.9	...	...	15.30	...	...	...	13.39	...	...	-0.71	...	...	...	...
NGC 7094	0.08	13.62	-1.19	-0.25	13.92	14.14	14.13	14.19	13.37	-1.25	-0.33	-0.43	-0.70	-0.79	-0.01	-0.08
NGC 7293	0.01	13.53	-1.26	-0.36	13.93	14.33	14.49	14.55	13.50	-1.27	-0.37	-0.41	-0.82	-1.05	-0.16	-0.06
NGC 7354	1.17	16.2	...	...	...	14.26	14.13	...	12.57	...	...	...	-0.67	...	-0.20	...
NGC 7662	0.11	14.00	...	...	14.23	12.20	...	...	13.66	...	...	-0.41	1.55	...	...	...
Patchick 5	0.12	15.3	...	...	...	15.83	15.39	15.48	14.93	-0.09	-0.12	...	-0.79	-0.51	0.40	-0.11
PFP 1	0.05	15.9	...	...	16.31	16.64	...	...	15.75	...	...	-0.49	-0.85	...	...	...
PHR0719-1222	0.59	15.4	...	...	14.78	14.18	13.93	13.82	13.57	...	...	-0.33	-0.09	-0.04	...	...
PHR0723+0036	0.38	13.88	-1.00	0.05	13.97	13.90	13.91	13.83	12.70	-1.27	-0.33	-0.70	-0.87	-0.99	-0.11	-0.01
PHR0743-1951	0.8	15.8	...	...	14.96	14.33	14.02	13.93	13.43	...	...	-0.42	-0.25	-0.24	0.10	-0.08
PHR0905-4753	0.57	12.67	0.41	1.13	11.19	9.97	9.10	8.22	10.89	0.00	0.55	0.55	1.42	2.88	0.71	0.74
PHR1424-5138	0.43	12.93	-0.96	0.08	12.70	12.67	12.50	12.57	11.56	-1.27	-0.35	-0.50	-0.74	-0.86	0.05	-0.17
PHR1510-6754	0.19	15.2	...	...	14.75	14.41	14.26	14.04	14.61	...	...	0.14	0.37	0.64	0.10	0.17
PHR1539-5325	0.7	18.6	...	...	17.76	...	...	...	16.43	...	...	-0.30	...	...	...	...
PHR1602-4127	0.30	15.8	...	...	16.04	15.36	14.54	14.38	14.87	...	...	-0.72	-0.23	0.59	0.74	0.08
PHR1625-4522	0.38	17.5	...	...	16.01	14.30	13.61	13.46	16.30	...	...	0.86	2.34	2.98	0.58	0.06
PHR1654-4143	0.9	14.88	0.40	0.80	13.87	13.14	12.84	12.72	12.09	-0.25	-0.11	-0.45	-0.27	-0.32	0.06	-0.10
PHR1757-1649	0.9	15.38	...	...	14.68	13.84	13.49	13.26	12.59	...	...	-0.76	-0.47	-0.35	0.10	0.01
PHR1911-1546	0.16	17.6	...	...	17.75	...	...	...	17.09	...	...	-0.43	...	...	...	...
PuWe 1	0.11	15.59	...	-0.24	15.86	15.90	...	...	15.25	...	-0.35	-0.45	-0.56	...	...	...
RCW 24	0.30	18.21	-0.99	0.03	...	...	...	...	17.28	-1.21	-0.27	...	...	...	...	...
RCW 69	0.52	18.60	-1.00	0.20	...	...	...	...	16.99	-1.37	-0.32	...	...	...	...	...
Sa 3-151	0.7	12.99	...	...	12.06	11.40	11.18	11.04	10.82	...	...	-0.21	0.03	0.03	0.02	-0.03
Sa 4-1	0.03	13.85	...	...	14.02	14.40	14.52	14.58	13.77	...	...	-0.21	-0.60	-0.80	-0.13	-0.07
Sanduleak 3	0.55	14.18	...	...	13.53	13.28	12.97	12.87	12.49	...	...	-0.23	-0.32	-0.20	0.16	-0.04
Sh 2-68	0.4	16.59	-0.89	-0.01	16.09	16.04	16.01	...	15.35	-1.18	-0.41	-0.14	-0.35	...	-0.08	...
Sh 2-78	0.56	17.78	...	0.20	...	...	...	...	16.04	...	-0.36	...	...	...	...	...
Sh 2-188	0.36	17.44	-1.00	0.01	...	...	...	...	16.32	-1.26	-0.35	...	...	...	...	...
Sh 2-216	0.05	12.64	...	-0.30	12.99	13.41	13.52	13.66	12.48	...	-0.35	-0.44	-0.89	-1.16	-0.12	-0.15
Sn 1	0.10	15.0	...	...	14.48	14.06	14.35	13.79	14.69	...	...	0.36	0.72	0.94	-0.32	0.54
Sp 1	0.52	13.69	...	...	13.25	12.70	12.49	12.37	12.08	...	...	-0.40	-0.17	-0.11	0.06	0.00
Sp 3	0.13	13.20	...	...	13.39	13.42	13.37	13.44	12.80	...	...	-0.40	-0.50	-0.60	0.00	-0.10

Continued on next page

Table C.1 – continued from previous page

Name	E_{B-V}	V	$U-B$	$B-V$	I_c	J	H	K_s	V_0	$(U-B)_0$	$(B-V)_0$	$(V-I)_0$	$(V-J)_0$	$(V-K)_0$	$(J-H)_0$	$(H-K)_0$
Sp 3 B	0.13	16.86	...	...	16.03	...	...	...	16.46	...	...	0.62	...	...	...	...
SuWt 2	0.38	11.95	...	...	11.41	11.09	...	10.90	10.77	...	...	-0.07	0.01	0.00	...	...
Th 2-A	0.74	17.08	...	...	16.37	...	...	...	14.79	...	...	-0.49	...	...	...	...
Ton 320	0.02	15.75	-1.22	-0.34	16.11	16.59	...	15.73	15.69	...	-0.36	-0.39	-0.88	-0.03	...	...
VBRC 6	0.89	17.1	...	...	17.30	14.93	13.84	12.83	14.34	...	...	-1.64	0.19	1.82	0.84	0.79
VBRC 7	0.7	19.5	...	0.71	17.83	15.88	14.86	14.31	17.33	...	0.01	0.54	2.06	3.26	0.83	0.38
VV 3-5	0.86	13.27	0.39	0.39	12.60	11.99	11.84	11.72	10.60	-0.23	-0.47	-0.72	-0.63	-0.82	-0.10	-0.09
WDHS 1	0.06	17.35	-1.31	-0.26	...	...	...	...	17.16	-1.35	-0.32	...	...	...	...	...
We 1-6	0.30	15.76	-0.97	-0.08	...	...	...	...	14.83	-1.19	-0.38	...	...	...	...	...
WeBo 1	0.57	14.45	...	1.72	12.68	11.35	10.67	10.45	12.68	...	1.15	0.85	1.83	2.43	0.53	0.08
WeSb 5	0.49	17.12	...	...	...	16.59	...	...	15.60	...	...	...	-0.56	...	...	...
Wr 17-31	0.24	17.94	...	-0.18	17.89	...	...	...	17.20	...	-0.42	-0.34	...	...	...	...
YM 16	0.8	16.7	...	...	14.50	13.67	13.14	12.91	14.22	...	...	0.90	1.25	1.59	0.31	0.04

Appendix D

Published Papers

This section summarises the main details of the various refereed and non-refereed papers that have been produced as part of (or linked to) my PhD dissertation (papers listed in reverse chronological order).

D.1 Refereed Papers

1. ***Title:*** MASH-II: More planetary nebulae from the AAO/UKST Hα Survey.

   Authors: Miszalski, B., Parker, Q.A., Acker, A., Birkby, J.L., **Frew, D.J.** & Kovacevic, A.

   Reference: *MNRAS*, 384, 525 (2008)

   Abstract: We present a supplement to the Macquarie/AAO/Strasbourg Hα planetary nebulae (PNe) catalogue (MASH), which we denote MASH-II. The supplement consists of over 300 true, likely and possible new Galactic PNe found after re-examination of the entire AAO/UKST Hα Survey of the southern Galactic Plane in digital form. We have spectroscopically confirmed over 240 of these new candidates as bona-fide PNe and we include other high quality candidates awaiting spectroscopic confirmation as possible PNe. These latest discoveries largely comprise two distinct groups: small, star-like or moderately resolved PNe at one end and mostly large, extremely low surface brightness PNe at the other. Neither group were easy to discover from simple visual scrutiny of the original survey exposures as for MASH but were relatively straightforward to uncover from the digital images via application of semi-automated discovery techniques. We suspect the few PNe still hidden in the Hα survey will lie outside our search criteria or be difficult to find.

2. ***Title:*** *Spitzer* IRAC observations of newly-discovered planetary nebulae from the Macquarie-AAO-Strasbourg Hα Planetary Nebula Project.

   Authors: Cohen, Martin, Parker, Quentin A., Green, Anne J., Murphy, Tara, Miszalski, Brent, **Frew, David J.**, Meade, Marilyn R., Babler, Brian, Indebetouw, Rémy, Whitney, Barbara A., Watson, Christer, Wolfire, Mark, Wolff, Mike J., Mathis, John S. & Churchwell, Edward B.

   Reference: *ApJ*, 669, 343 (2007)

   Abstract: We compare Hα, radio continuum, and *Spitzer* Space Telescope (SST) images of 58 planetary nebula (PNe) recently discovered by the Macquarie-AAO-Strasbourg Hα PN Project (MASH) of the SuperCOSMOS Hα Survey. Using InfraRed Array Camera (IRAC) data we examine the relationships between optical and MIR morphologies from 3.6 to 8.0μm, and explore the ratio of mid-infrared (MIR) to radio nebular fluxes, which is a valuable discriminant between thermal and nonthermal emission. MASH empasizes late evolutionary stages of PNe compared with previous caalogs, enabling study of the changes in MIR and radio flux that attend the aging process.

Spatially integrated MIR energy distributions were constructed for all MASH PNe observed by the GLIMPSE Legacy Project, using the Hα images to establish the dimensions for the calculations of the Midcourse Space Experiment (MSX), IRAC, and radio continuum (from the Molonglo Observatory Synthesis Telescope and the Very large array) flux densities. The ratio of IRAC 8.0-μm and MSX 8.3-μm flux densities provides a measure of the absolute diffuse calibration of IRAC at 8.0μm. We independently confirm the aperture correction factor to be applies to IRAC at 8.0μm to align it with the diffuse calibration of MSX. The result is in accord with the recommendations of the *Spitzer* Science Center, and with our own results from a parallel study of HII regions in the MIR and radio. However, these PNe probe the diffuse calibration of IRAC on a spatial scale of 9–77$''$, as opposed to the many arcmin scale from the HII regions' study.

3. ***Title:*** Multi-wavelength study of a new Galactic SNR, G332.5–5.6.

   Authors: Stupar, M., Parker, Q.A., Filipović, M.D., **Frew, D.J.**, Bojičić, I. & Aschenbach, B.

   Reference: *MNRAS*, 381, 377 (2007)

   Abstract: We present compelling evidence for the confirmation of a new Galactic supernova remnant (SNR), G332.5–5.6, based initially on identification of a new, filamentary, optical emission-line nebulosity in the arcsecond resolution images from the AAO/UKST Hα survey. The extant radio observations and X-ray data which we have independently re-reduced, together with new optical spectroscopy of the large-scale fragmented nebulosity, confirms the identification. Optical spectra, taken across five different, widely separated nebula regions of the remnant as seen on the Hα images, show average ratios of [N II]/Hα = 2.42, [S II]/Hα = 2.10, and [S II] 6717/6731 =1.23, as well as strong [O I] 6300, 6364Å and [O II] 3727Å emission. These ratios are typical of SNRs. Here, we also present the radio-continuum detection of the SNR at 20/13cm with the Australia Telescope Compact Array (ATCA). Radio emission is also seen at 4850 MHz, in the PMN survey (Griffith & Wright 1993), and at 843MHz from the Sydney University Molonglo Sky Survey (SUMSS) survey. We estimate an angular diameter of $\sim$30$'$ and an average radio spectral index of $\alpha = -0.6 \pm 0.1$, indicating the non-thermal nature of G332-5.6. Fresh analysis of existing *ROSAT* X-ray data also confirms the existence of the SNR. The distance to G332.5-5.6 has been independently estimated by Reynoso and Green as 3.4 kpc based on measurements of the H I λ21 cm line seen in absorption against the continuum emission. Our cruder estimates via assumptions on the height of the dust layer (3.1 kpc) and using the $\Sigma - D$ relation (4 kpc) are in good agreement.

4. ***Title:*** Macquarie/AAO/Strasbourg Hα planetary nebula catalogue: MASH.

   Authors: Parker, Quentin A., Acker, A., **Frew, D.J.**, Hartley, M., Peyaud, A.E.J., Ochsenbein, F., Phillipps, S., Russeil, D., Beaulieu, S.F., Cohen, M., Köppen, J., Miszalski, B., Morgan, D.H., Morris, R.A.H., Pierce, M.J. & Vaughan, A.E.

   Reference: *MNRAS*, 373, 79 (2006)

   Abstract: We present the Macquarie/AAO/Strasbourg Hα Planetary Nebula Catalogue (MASH) of over 900 true, likely and possible new Galactic planetary nebulae (PNe) discovered from the AAO/UKST Hα survey of the southern Galactic plane. The combination of depth, resolution, uniformity and areal coverage of the Hα survey has opened up a hitherto unexplored region of parameter space permitting the detection of this significant new PN sample. Away from the Galactic bulge the new PNe are typically more evolved, of larger angular extent, of lower surface brightness and more obscured (i.e. extinguished) than those in most previous surveys. We have also doubled the number of PNe in the Galactic bulge itself and although most are compact, we have also found more evolved examples. The MASH catalogue represents the culmination of a seven-year programme of identification and confirmatory spectroscopy. A key strength is that the entire sample has been derived from the same, uniform observational data. The 60 per cent increase in known Galactic PNe represents the largest ever incremental sample of such discoveries and will have a significant impact on many aspects of PN research. This is especially important for studies at the faint end of the PN luminosity function which was previously poorly represented.

5. ***Title:*** Two new evolved bipolar planetary nebulae in the solar neighbourhood.

   Authors: **Frew, David J.**, Parker, Q.A. & Russeil, D.

   Reference: *MNRAS*, 372, 1081 (2006)

   Abstract: We present AAO/UKST Hα+[N II] narrow-band imagery and low- and medium-resolution optical spectroscopy of RCW 24 and RCW 69. These nebulae were previously classified as HII regions, but we now show them to be two of the largest and nearest bipolar Type I PNe yet discovered. Distances were estimated using extinction-distance and kinematic methods, and via a new Hα surface brightness–radius relation. The adopted distances are 1.0 ± 0.3 kpc for RCW 24 and 1.2 ± 0.2 kpc for RCW 69. Both objects have enhanced nitrogen abundances, with $\log \mathrm{N/O} \simeq +0.44$ for RCW 24, and $\log \mathrm{N/O} = +0.33$ for RCW 69. Systemic velocities and $|z|$ distances are $\mathrm{V_{LSR}} = +5$ kms^{-1} and $|z| \sim 23$ pc for RCW 24, and $\mathrm{V_{LSR}} = -33$ kms^{-1} and only $|z| \sim 7$ pc for RCW 69. Both PNe originated from massive progenitors (>2.0–$2.5\,\mathrm{M_\odot}$), as deduced from their chemical abundances, large ionised masses, small $|z|$ distances, low peculiar velocities, and relatively hot central stars. These two objects form an important addition to the small sample of evolved bipolar PNe in the solar neighbourhood.

6. ***Title:*** The "Príncipes de Asturias" nebula: a new quadrupolar planetary nebula from the IPHAS survey.

   Authors: Mampaso, A., Corradi, R.L.M., Viironen, K., Leisy, P., Greimel, R., Drew, J.E., Barlow, M.J., **Frew, D.J.**, Irwin, J., Morris, R.A.H., Parker, Q.A., Phillipps, S., Rodrguez-Flores, E.R., Zijlstra, A.A.

   Reference: *A&A*, 458, 203 (2006)

   Abstract: Context: The Isaac Newton Telescope Photometric Hα Survey (IPHAS) is currently mapping the Northern Galactic plane reaching to $r' = 20$ mag with typically $1''$ resolution. Hundreds of Planetary Nebulae (PNe), both point-like and resolved, are expected to be discovered. We report on the discovery of the first new PN from this survey: it is an unusual object located at a large galactocentric distance and has a very low oxygen abundance.

   Aims: Detecting and studying new PNe will lead to improved estimates of the population size, binary fraction and lifetimes, and yield new insights into the chemistry of the interstellar medium at large galactocentric distances.

   Methods: Compact nebulae are searched for in the IPHAS photometric catalogue, selecting those candidates with a strong Hα excess in the $r' - \mathrm{H}\alpha$ vs. $r' - i'$ colour-colour diagram. Searches for extended nebulae are by visual inspection of the mosaics of continuum-subtracted Hα images at a spatial sampling of 5×5 arcsec^2. Follow-up spectroscopy enables confirmation of the PNe, and their physico-chemical study.

Results: The first planetary nebula discovered via IPHAS imagery shows an intricate morphology: there is an inner ring surrounding the central star, bright inner lobes with an enhanced waist, and very faint lobular extensions reaching up to more than 100″. We classify it as a quadrupolar PN, a rather unusual class of planetary showing two pairs of misaligned lobes. From long-slit spectroscopy we derive T_e[N II] =12 800±1000 K, N_e = 390±40 cm^{-3}, and chemical abundances typical of Peimbert's type I nebulae (He/H =0.13, N/O =1.8) with an oxygen abundance of 12+log(O/H)=8.17±0.15. A kinematic distance of $7.0^{+4.5}_{-3.0}$ kpc is derived, implying an unusually large size of >4 pc for the nebula. The photometry of the central star indicates the presence of a relatively cool companion. This, and the evidence for a dense circumstellar disk and quadrupolar morphology, all of which are rare among PNe, support the hypothesis that this morphology is related to binary interaction.

7. ***Title:*** The AAO/UKST SuperCOSMOS Hα Survey.

   Authors: Parker, Quentin A., Phillipps, S., Pierce, M.J., Hartley, M., Hambly, N.C., Read, M.A., MacGillivray, H.T., Tritton, S.B., Cass, C.P., Cannon, R.D., Cohen, M., Drew, J.E., **Frew, D.J.**, Hopewell, E., Mader, S., Malin, D.F., Masheder, M.R.W., Morgan, D.H., Morris, R.A.H., Russeil, D., Russell, K.S., Walker, R.N.F.

   Reference: *MNRAS*, 362, 689 (2005)

   Abstract: The UK Schmidt Telescope (UKST) of the Anglo-Australian Observatory completed a narrow-band Hα plus [N II] 6548, 6584Å survey of the Southern Galactic Plane and Magellanic Clouds in late 2003. The survey, which was the last UKST wide-field photographic survey and the only one undertaken in a narrow-band, is now an online digital data product of the Wide-Field Astronomy Unit of the Royal Observatory Edinburgh (ROE). The survey utilized a high specification, monolithic Hα interference bandpass filter of exceptional quality. In conjunction with the fine-grained Tech-Pan film as a detector it has produced a survey with a powerful combination of area coverage (4000 square degrees), resolution (∼1 arcsec) and sensitivity (≤5 Rayleighs), reaching a depth for continuum point sources of $R \simeq 20.5$. The main survey consists of 233 individual fields on a grid of centres separated by 4° at declinations below +2° and covers a swathe approximately 20° wide about the Southern Galactic Plane. The original survey films were scanned by the SuperCOSMOS measuring machine at the Royal Observatory, Edinburgh, to provide the online digital atlas called the SuperCOSMOS Hα Survey (SHS). We present the background of the survey, the key survey characteristics, details and examples of the data product, calibration process, comparison with other surveys and a brief description of its potential for scientific exploitation.

8. ***Title:*** PFP 1: A Large Planetary Nebula Caught in the First Stages of ISM Interaction.

   Authors: Pierce, Mark J., **Frew, David J.**, Parker, Quentin A. & Köppen, Joachim

   Reference: *PASA*, 21, 334 (2004)

   Abstract: This paper presents (Hα+[N II]) imaging and spectroscopy of a previously unknown, highly evolved planetary nebula of low excitation which is in the first stages of an interaction with the interstellar medium (ISM). It was discovered serendipitously from AAO/UKST Hα Survey images as part of a project to exploit the survey data and has evaded detection by previous surveys due to its very low surface brightness. It is a remarkable hollow-sphere planetary nebula, some 19′ across, making it one of the largest examples of its type. We estimate a radius of 1.5 pc and a distance of 550 pc as derived from a new Hα surface brightness-radius relation. PFP 1 has near-perfect circular symmetry, broken only at the north-western edge which is coupled with significantly increased (Hα+[N II]) intensity, both of which provide evidence for an interaction with the ISM. We find a near solar composition for this object with possibly enhanced He and N abundances. A blue central star candidate has been identified from the SuperCosmos Sky Survey data.

D.2 Conference Proceedings and Abstracts

1. ***Title:*** Do post-common envelope objects form a distinct subset of planetary nebulae?

   Authors: **Frew, D.J.** & Parker, Q.A.

   Reference: In Proceedings of the APN-IV Conference, ed. Corradi, R.L.M., Manchado, A. & Soker, N. (2008, in press)

   Abstract: A new Hα surface brightness – radius (SB–r) relation has proved to be a useful statistical distance indicator for planetary nebulae. Known close binary PNe with reliable primary distances are shown to inhabit a distinct locus in SB–r space. Comparing the ionized masses of this sample with a volume-limited ensemble of PNe with the same range of surface brightness leads to the conclusion that post common-envelope (CE) PNe have systematically lower ionized masses than 'normal' PNe. Post-CE PNe are also morphologically distinct from the majority of elliptical PNe. A comparison of optical and near-infrared colours of the central stars of PNe in a volume limited sample leads to an estimated binary fraction of 52 – 58 per cent, similar to the known binary fraction of G-type main-sequence stars. Close binaries form a subset of these so we conclude that only a minority (12 – 33 per cent) of PNe have passed through a CE phase.

2. ***Title:*** A search for faint planetary nebulae using the DSS.

   Authors: Jacoby, G., Kronberger, M., Patchick, D., Teutsch, P., Saloranta, J., Acker, A. & **Frew, D.**

   Reference: In Proceedings of the APN-IV Conference, ed. Corradi, R.L.M., Manchado, A. & Soker, N. (2008, in press)

   Abstract: A group of amateur astronomers (Deep Sky Hunters) has identified ~50 candidate PNe by visually searching the 1st and 2nd generation red Digital Sky Survey images. Candidate PNe are then observed in Hα with larger telescopes, primarily the WIYN 3.5-m on Kitt Peak, and the 1.2-m and 1.5-m at Haute Provence Observatory (OHP). Thus far, ~20 new PNe have been found. These objects have a strong tendency to have low surface brightness and to be relatively round.

3. ***Title:*** Milky Way and Magellanic Cloud Surveys for Planetary Nebulae.

   Authors: Parker, Q.A., Acker, A., **Frew, D.J.** & Reid, W.A.

   Reference: In Barlow M.J. & Mendez R.H., eds, Planetary nebulae in our Galaxy and beyond, *IAU Symposium*, vol. 234, p. 1 (2006)

Abstract: The recent on-line availability of large-scale, wide-field surveys of the Galaxy and Magellanic Clouds in several optical and near/mid-infrared passbands has provided unprecedented opportunities to refine selection techniques and eliminate contaminants in PN surveys. This has been coupled with new surveys offering improved detection rates via higher sensitivity and resolution. This will permit more extreme ends of the PN luminosity function to be explored and enable studies of under represented PN evolutionary states. Known PNe in our Galaxy and LMC have thus been significantly increased over the last few years due primarily to the advent of narrow-band imaging in important nebula lines such as Hα, [O III] and [S III]. These PNe are generally of lower surface brightness, larger angular extent, in more obscured regions and in later stages of evolution than those in most previous surveys. A more representative PN population for in-depth study is now available, particularly in the LMC where the known distance adds considerable utility for derived PN parameters. Future prospects for Galactic and LMC PNe research are briefly highlighted.

4. ***Title:*** Towards a New Distance Scale and Luminosity Function for Nearby Planetary Nebulae.

   Authors: **Frew, David J.** & Parker, Q.A.

   Reference: In Barlow M.J. & Mendez R.H., eds, Planetary nebulae in our Galaxy and beyond, *IAU Symposium*, vol. 234, p. 49 (2006)

   Abstract: The local planetary nebula (PN) census is dominated by extremely evolved examples, and until recently, was incomplete. New discoveries from the AAO/UKST Hα Survey and SHASSA, have partially remedied this problem. In addition, we find that some currently accepted nearby PNe are in fact Strömgren spheres in the ISM ionised by a hot white dwarf. Distance estimates for a robust sample of calibrating PNe from the literature, plus new distances for a number of highly evolved PNe, have allowed a new Hα surface brightness – radius relationship to be devised as a useful distance indicator. It covers >6 dex in SB, and while the spread in SB is $\sim$1 dex at a given radius, optically thick (mainly bipolar and bipolar-core) PNe tend to populate the upper bound of the trend, while common-envelope PNe and very high-excitation PNe form a sharp lower boundary. Hence, distances can be estimated for all remaining local PNe, allowing the definition of a relatively complete census of PNe in the solar neighbourhood within 1.0 kpc. This provides a first look at the faint end of the PN luminosity function, and new estimates of the space density, scale height, total number, and birth rate of Galactic PNe.

5. ***Title:*** A Search for New Emission Nebulae from the SHASSA and VTSS Surveys.

   Authors: **Frew, David J.**, Madsen, G.J. & Parker, Q.A.

   Reference: In Barlow M.J. & Mendez R.H., eds, Planetary nebulae in our Galaxy and beyond, *IAU Symposium* vol. 234, p. 395 (2006)

   Abstract: As an adjunct to the planetary nebula (PN) search from the AAO/UKST Hα survey, a visual search was conducted for new emission nebulae from the SHASSA and VTSS surveys, outside a Galactic latitude of mid bmid = 10°. Fifteen new objects were found from SHASSA and three from the available fields of VTSS. With one exception, all objects are $>5'$ across, as smaller nebulae are confused with large numbers of artifacts and compact emitters on these surveys. All previously known PNe larger than this size in the search area, as well as Hewett 1, PG 0108, and PG 0109 were recovered in this blind search. Candidates were selected as discrete, morphologically symmetric Hα enhancements, to differentiate them from the ubiquitous diffuse emission structure of the ISM. These criteria were relaxed for the VTSS survey due to its poorer inherent resolution. Most of the new discoveries are probable Stromgren spheres in the ISM. Some show unusual line

ratios (e.g. strong [O III] or [N II] emission) based on slit spectroscopy and WHAM data (see Madsen et al. 2006, this volume), suggesting these are ionised by a hot subdwarf or white dwarf star, and may be possible PNe. Our most interesting discovery is a rare bowshock nebula around a bright, previously unnoticed, nova-like cataclysmic variable.

6. ***Title:*** An Optical Emission Line Survey of Large Planetary Nebulae.

   Authors: Madsen, G.J., **Frew, D.J.**, Parker, Q.A., Reynolds, R.J. & Haffner, L.M.

   Reference: In Barlow M.J. & Mendez R.H., eds, Planetary nebulae in our Galaxy and beyond, *IAU Symposium* vol. 234, p. 455 (2006)

   Abstract: Accurate emission line fluxes from planetary nebulae (PNe) provide important constraints on the nature of the final phases of stellar evolution. Large, evolved PNe may trace the latest stages of PN evolution, where material from the AGB wind is returned to the interstellar medium. However, the low surface brightness and spatially extended emission of large PNe have made accurate measurements of line fluxes difficult with traditional long-slit spectroscopic techniques. Furthermore, distinguishing these nebulae from H II regions, supernova remnants, or interstellar gas ionized by a hot, evolved stellar core can be challenging. Here, we report on an ongoing survey of large Galactic PNe ($r > 5'$) with the Wisconsin H-Alpha Mapper (WHAM), a Fabry-Perot spectrograph designed to detect faint diffuse optical emission lines with high sensitivity and spectral resolution. Our sample includes newly revealed Hα enhancements from the AAO/UKST and WHAM H? surveys of Parker et al. and Haffner et al. We present accurate emission line fluxes of Hα, [N II]λ6583, and [O III]λ5007, and compare our data to other measurements. We use the emission line ratios and kinematics of the ionized gas to assess, or in some cases reassess, the identification of some nebulae.

7. ***Title:*** Emission Line Spectroscopy of Large, Diffuse Planetary Nebulae.

   Authors: Madsen, G.J., **Frew, D.J.**, Parker, Q.A., Reynolds, R.J. & Haffner, L.M.

   Reference: *Bulletin of the American Astronomical Society*, 37, 116 (2005)

   Abstract: Accurate emission line fluxes of planetary nebulae (PN) provide important constraints on the nature of the late stages of stellar evolution. Large (r >10$'$), diffuse PN may trace the latest stages of PN evolution, where material from the AGB wind is returned to the interstellar medium. However, the low surface brightness and spatially extended emission of large PN have made accurate measurements of line fluxes difficult with traditional long-slit spectroscopic techniques. Furthermore, the distinction of these nebulae from HII regions, supernova remnants, or interstellar gas ionized by a hot, evolved stellar core can be challenging. Here, we report on observations of >20 large PN with the Wisconsin H-Alpha Mapper (WHAM), a Fabry-Perot spectrograph designed to detect faint, diffuse optical emission with high sensitivity and spectral resolution (R ~25,000). Our sample includes newly revealed Hα enhancements from the MASH and WHAM surveys. We present emission line fluxes of Hα, Hβ, [N II]λ 6583, and [O III]λ 5007, and compare our data to previous measurements. We use the emission line ratios and kinematics of the ionized gas to characterize and identify the nature of the nebulae.

8. ***Title:*** MASH: The Macquarie/AAO/Strasbourg Hα Planetary Nebula Catalogue.

   Authors: Parker, Quentin A., Acker, Agnes, Peyaud, Alan, **Frew, David J.** & the MASH Consortium

Reference: In Szczerba R., Stasińska G. & Górny S., eds., Planetary Nebulae as Astronomical Tools, *AIP Conference Proceedings*, vol. 804, p. 3 (2005)

Abstract: The Macquarie/AAO/Strasbourg Hα Planetary Nebula Catalogue (MASH) of nearly 1000 new Galactic Planetary Nebulae (PNe) discovered from the AAO/UKST Hα survey of the southern Galactic plane is now essentially complete. The survey's excellent combination of resolution, uniformity, areal coverage and depth has enabled detection of this unprecedented new PN sample. MASH PNe are typically more evolved, obscured, of larger angular extent, and of lower surface brightness than those in most previous surveys. The number of PNe in the Galactic bulge has also been doubled. Though most of these are quite compact, more evolved examples have been found. The MASH catalogue represents a seven year programme of discovery and spectroscopic confirmation and will form the basis for significant studies. A key strength is that the whole sample has been obtained from the same, uniform survey data. The 75% increase in known Galactic PNe represents the largest single increase in such discoveries. MASH PNe will have a significant impact on many aspects of PNe research, especially for studies at the extremes of the luminosity function which were previously poorly represented.

9. ***Title:*** Detection of New Planetary Nebulae by IPHAS, the Hα Survey of the North Galactic Plane.

   Authors: Corradi, R.L.M., Mampaso, A., Viironen, K., Kovacevic, A., Zijlstra, A., Greimel, R., Irwin, J., Drew, J.E., Wright, N., Morris, R., Phillipps, S., Irwin, M., Barlow, M., **Frew, D.J.**, Groot, P., Hopewell, E.C., Leisy, P., Parker, Q.A., Sokoloski, J.L., Walton, N. & Zurita, A.

   Reference: In Szczerba R., Stasińska G. & Górny S., eds., Planetary Nebulae as Astronomical Tools, *AIP Conference Proceedings*, vol. 804, p. 7 (2005)

   Abstract: IPHAS is an ongoing Hα imaging survey of the North Galactic plane. When completed, it is expected to discover several hundred new Galactic planetary nebulae, in addition to a huge number of Hα emitters.

   We present here the project, the methods used to search for compact and extended ionized nebulae, and some preliminary results about the ~100 new candidate planetary nebulae identified so far.

10. ***Title:*** Planetary Nebulae in the Solar Neighborhood.

    Authors: **Frew, David J.** & Parker, Quentin A.

    Reference: In Szczerba R., Stasińska G. & Górny S., eds., Planetary Nebulae as Astronomical Tools, *AIP Conference Proceedings*, vol. 804, p. 11 (2005)

    Abstract: The AAO/UKST Hα Survey has been used to discover a number of new, large, nearby planetary nebulae (PNe) These discoveries, combined with a critical re-analysis of all previously known large PNe, have allowed the compilation of a relatively complete census of PNe in the solar neighbourhood within 1.0 kpc. Distances are based in part on a new Hα surface brightness – radius relation. The census is relatively bias-free, and will provide more accurate estimates of the PN formation rate, average PN lifetime, and the total number of PNe in the Galaxy, as well as a first look at the faint end of the PN luminosity function (PNLF).

D.3 Other Non-Refereed Articles

1. ***Title:*** Examples of new evolved planetary nebulae from the SuperCOSMOS Hα Survey.
   Authors: Birkby, Jayne, Parker, Quentin, Miszalski, Brent, Acker, Agnes & **Frew, David**
   Reference: *AAO Newsletter*, 111, 22 (2007)

2. ***Title:*** G332.5–5.6: a new Galactic SNR identified from H-alpha imaging and optical spectroscopy.
   Authors: Parker, Q.A., **Frew, D.J.** & Stupar, M.
   Reference: *AAO Newsletter*, 104, 9 (2004)

3. ***Title:*** Two new large bipolar planetary nebulae.
   Authors: **Frew, David J.** & Parker, Quentin A.
   Reference: *AAO Newsletter*, 103, 6 (2003)

Appendix E

Journal Abbreviations

Table E.1: Journal abbreviations used in this work.

Abbreviation	Journal Title
AAHam	Astronomische Abhandlungen der Hamburger Sternwarte
AAONw	Anglo-Australian Observatory Newsletter
A&A	Astronomy and Astrophysics
A&AS	Astronomy and Astrophysics Supplement Series
AcA	Acta Astronomica
AJ	Astronomical Journal
AmJS	American Journal of Science
AN	Astronomische Nachrichten
AnHar	Annals of Harvard College Observatory
AnIPS	Annals of the Israel Physical Society
Ap&SS	Astrophysics and Space Science
ApJ	Astrophysical Journal
ApJS	Astrophysical Journal Supplement Series
ApL	Astrophysical Letters
AReg	Astronomical Register
ArA	Arkiv för Astronomii
ARA&A	Annual Reviews of Astronomy and Astrophysics
ARep	Astronomy Reports
AstL	Astronomy Letters
ATsir	Astronomicheskij Tsirkulyar
AZh	Astronomicheskii Zhurnal
BaltA	Baltic Astonomy
BAAS	Bulletin of the American Astronomical Society
BAC	Bulletin of the Astronomical Institutes of Czechoslovakia
BASI	Bulletin of the Astronomical Society of India
BHarO	Harvard College Observatory Bulletin
BOTT	Boletin de los Observatorios de Tonantzintla y Tacubaya
ChJA&A	Chinese Journal of Astronomy and Astrophysics
CoBos	Contributions from the Bosscha Observatory
CoLic	Contributions of Lick Observatory
HarCi	Harvard College Observatory Circular
HvaOB	Hvar Observatory Bulletin

Continued on next page

Table E.1 – continued from previous page

Abbreviation	Journal Title
IBVS	Information Bulletin on Variable Stars
INGNw	ING Newsletter
IzKry	Izvestiya Krymskoj Astrofizicheskoj Observatorii
IzPul	Izvestiia Glavnoi Astronomicheskoi Observatorii v Pulkove
JAD	Journal of Astronomical Data
JApA	Journal of Astrophysics and Astronomy
JObs	Journal des Observateurs
JKAS	Journal of the Korean Astronomical Society
JRASC	Journal of the Royal Astronomical Society of Canada
LicOB	Lick Observatory Bulletin
LowOB	Lowell Observatory Bulletin
MeLuAO	Meddelanden fran Lunds Astronomiska Observatorium
MitAG	Mitteilungen Astronomische Gesellschaft
MmRAS	Memoirs of the Royal Astronomical Society
MmSAI	Memorie della Societa Astronomica Italiana
MNASSA	Monthly Notes of the Astronomical Society of South Africa
MNRAS	Monthly Notices of the Royal Astronomical Society
MSRSL	Mémoires de la Societe Royale de Sciences de Liege
NewA	New Astronomy
NewAR	New Astronomy Reviews
Obs	The Observatory
PASA	Publications of the Astronomical Society of Australia
PASJ	Publications of the Astronomical Society of Japan
PASP	Publications of the Astronomical Society of the Pacific
PAZh	Pis'ma v Astronomicheskii Zhurnal
PhR	Physics Reports
PLicO	Publications of the Lick Observatory
PMicO	Publications of the Michigan Observatory
POStr	Publications de l'Observatoire de Strasbourg
PSCDS	Publication Speciale du Centre Donnees Stellaires
PW&SO	Publications of the Warner and Swasey Observatory
PZ	Peremennye Zvezdy
QJRAS	Quarterly Journal of the Royal Astronomical Society
RMxAA	Revista Mexicana de Astronomia y Astrofisica
RMxAA(SC)	Revista Mexicana de Astronomia y Astrofisica (Serie de Conf.)
PhTrRS	Philosophical Transactions of the Royal Society of London
ProcRS	Proceedings of the Royal Society of London
RvMA	Reviews of Modern Astronomy
RvMPhys	Reviews of Modern Physics
S&T	Sky and Telescope
SeAJ	Serbian Astronomical Journal
SoSht	Soobshcheniia Gosudarstvennogo Astronomicheskogo Instituta Shternberga
SvA	Soviet Astronomy
SvAL	Soviet Astronomy Letters
SSRev	Space Science Reviews
SthAs	Southern Astronomy
VA	Vistas in Astronomy